

AD-A090 850

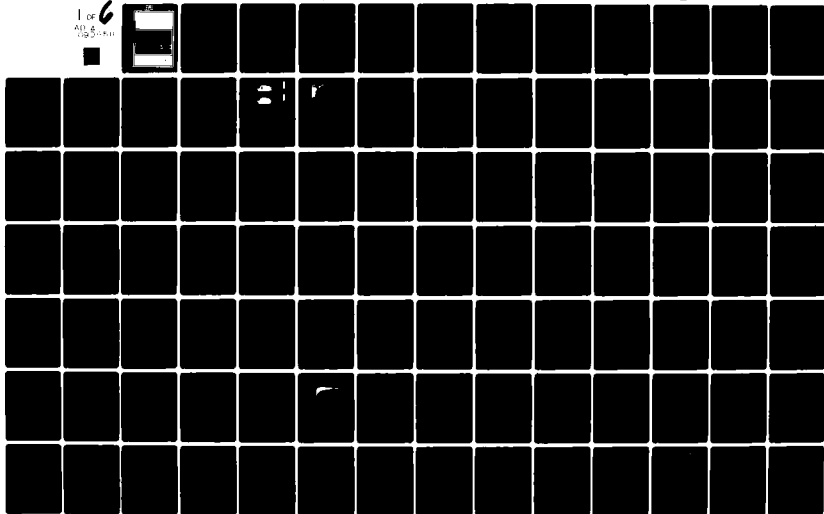
ADVISORY GROUP FOR AEROSPACE RESEARCH AND DEVELOPMENT--ETC F/6 20/14  
PROPAGATION EFFECTS IN SPACE/EARTH PATHS. (U)  
AUG 80 H J ALBRECHT

UNCLASSIFIED

AGARD-CP-284

NL

1 of 6  
AD 6  
1990-11



**LEVEL II**

①

AGARD-CP-284

AGARD-CP-284

**AGARD**

ADVISORY GROUP FOR AEROSPACE RESEARCH & DEVELOPMENT

7 RUE ANCELLE 92200 NEUILLY SUR SEINE FRANCE

AD A090850

AGARD CONFERENCE PROCEEDINGS No. 284

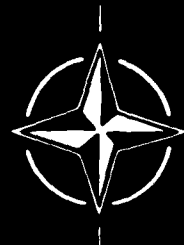
**Propagation Effects in  
Space/Earth Paths**

**S DTIC ELECTE D**  
OCT 28 1980  
**E**

**DISTRIBUTION STATEMENT A**

Approved for public release;  
Distribution Unlimited

**NORTH ATLANTIC TREATY ORGANIZATION**



DDC FILE COPY

**DISTRIBUTION AND AVAILABILITY  
ON BACK COVER**

80 10 10 10 10

14

AGARD-CP-284

NORTH ATLANTIC TREATY ORGANIZATION  
ADVISORY GROUP FOR AEROSPACE RESEARCH AND DEVELOPMENT  
(ORGANISATION DU TRAITE DE L'ATLANTIQUE NORD)

11) Aug 87

12) 403 C

9

AGARD Conference Proceedings No. 284

6

PROPAGATION EFFECTS IN SPACE/EARTH PATHS

Edited by

10

Dr H.J./Albrecht  
FGAN

Königstrasse 2  
D-5307 Wachtberg-Werthhoven  
Germany

**DISTRIBUTION STATEMENT A**

Approved for public release;  
Distribution Unlimited

Copies of papers and discussions presented at the Electromagnetic Wave Propagation Panel  
Symposium held in London, UK on 12-16 May 1980.

400043 all

## THE MISSION OF AGARD

The mission of AGARD is to bring together the leading personalities of the NATO nations in the fields of science and technology relating to aerospace for the following purposes:

- Exchanging of scientific and technical information;
- Continuously stimulating advances in the aerospace sciences relevant to strengthening the common defence posture;
- Improving the co-operation among member nations in aerospace research and development;
- Providing scientific and technical advice and assistance to the North Atlantic Military Committee in the field of aerospace research and development;
- Rendering scientific and technical assistance, as requested, to other NATO bodies and to member nations in connection with research and development problems in the aerospace field;
- Providing assistance to member nations for the purpose of increasing their scientific and technical potential;
- Recommending effective ways for the member nations to use their research and development capabilities for the common benefit of the NATO community.

The highest authority within AGARD is the National Delegates Board consisting of officially appointed senior representatives from each member nation. The mission of AGARD is carried out through the Panels which are composed of experts appointed by the National Delegates, the Consultant and Exchange Programme and the Aerospace Applications Studies Programme. The results of AGARD work are reported to the member nations and the NATO Authorities through the AGARD series of publications of which this is one.

Participation in AGARD activities is by invitation only and is normally limited to citizens of the NATO nations.

The content of this publication has been reproduced directly from material supplied by AGARD or the authors.

Published August 1980

Copyright © AGARD 1980

All Rights Reserved

ISBN 92-835-0269-8



*Printed by Technical Editing and Reproduction Ltd  
Harford House, 7-9 Charlotte St, London, W1P 1HD*

## PREFACE

With its symposium "Propagation Effects in Space/Earth Paths", the Electromagnetic Wave Propagation Panel adhered to its practice of permitting, in intervals of several years, a complete coverage of interim results and advancement of knowledge in a field of continuous interest. The meeting took place in London, United Kingdom, from 12th to 16th May 1980. These Conference Proceedings contain papers and contributions to discussions, as well as summaries on the sessions of the meeting.

For more than two decades, satellites have been used as relay stations in space for communication purposes, as references for navigation and positioning systems, for remote sensing, as well as for other tasks. The effects of electromagnetic wave propagation on paths between locations on or near the earth surface and a position in space is usually addressed in connection with or as part of meetings dealing with other main topics. The more concentrated effort undertaken in this meeting has enabled the Panel to account for the increasing importance of appropriate parameters in modern research projects and engineering applications concerning influence of propagation media on space/earth paths.

The entire subject of the meeting was dealt with in six sessions, concerning General Tropospheric Effects, Experimental Data on SHF/EHF Paths, Remote Sensing, General Ionospheric Dispersion Effects, New Data on Ionospheric Irregularities, and Propagation Limitations in Systems. In addition to a review and a general evaluation of recent data, papers and discussions at the meeting covered the variability of parameters, their geographical distributions, limitations to their validity, and system aspects.

In summary, this Symposium provided the intended review on the state of the art in this field of research, discussed theoretical and practical aspects, also concerning system planning, and indicated promising areas for further research. These Conference Proceedings give a full account of papers and discussions.

Gratefully acknowledged herewith are the excellent cooperation and assistance rendered by Dr E. Altshuler as co-chairman of the programme committee, and by its members: Prof. P.F. Checcacci, Prof. R. Viddeleer, and Dr P.A. Watson. It is with deep regret that we have to record the untimely death of Prof. P.F. Checcacci, on 21st June 1980; his assistance with the preparations of this AGARD meeting was his last activity of this kind. He will be remembered as a friend and as a scientist of high reputation.

Appreciation is furthermore expressed to all who assisted in the organization of the Symposium as well as in the compilation of these Proceedings, to authors and contributors to discussions, to session chairmen, to the host coordinator, to AGARD-staff and other collaborators.

H.J. ALBRECHT  
Editor

Accession For	
NTIS GRA&I	<input checked="" type="checkbox"/>
DDC TAB	<input type="checkbox"/>
Unannounced	<input type="checkbox"/>
Justification	
By _____	
Distribution/ _____	
Availability Codes	
Dist	Avail and/or special
A	

## PROGRAM AND MEETING OFFICIALS

### CHAIRMEN

Dr H.J.Albrecht  
FGAN  
Königstrasse 2  
D-5307 Wachtberg-Werthhoven  
Germany

Dr E.Altshuler  
Electromagnetic Sciences Division  
EPP/Rome Air Development Center  
(AFSC) Hanscom Air Force Base  
Massachusetts 01731, USA

### MEMBERS

Prof. P.F.Ceccacci  
IROE  
Via Panciatichi 64  
50127 Firenze  
Italy

Prof. ir. R.Viddeleer  
Akkerhoornbloem 41  
2317 KS Leiden  
Netherlands

Dr P.A.Watson  
University of Bradford  
Bradford BD7/CP  
UK

### ELECTROMAGNETIC WAVE PROPAGATION PANEL

CHAIRMAN: Dr J.Aarons  
AF Geophysics Lab.  
Hanscom Field  
Bedford, Mass. 01731  
USA

DEPUTY CHAIRMAN: Dr J.Belrose  
Communications Research Center  
Department of Communications  
P. Box 11490, Station H  
Ottawa K2H8S2  
Canada

PANEL EXECUTIVE: Lt Col. J.B.Catiller  
USAF

### SESSION CHAIRMEN

Dr E.Altshuler (I)  
Electromagnetic Sciences Division  
EPP/Rome Air Development Center  
(AFSC) Hanscom Air Force Base  
Massachusetts 01731, USA

Prof. ir. R.Viddeleer (II)  
Akkerhoornbloem 41  
2317 KS Leiden  
Netherlands

Prof. D.T.Gjessing (III)  
NTNF/PFM  
P.O. Box 25  
N-2007 Kjeller  
Norway

Dr H.Soicher (IV)  
US Army Communications  
Research and Development Command  
DRDCO-COM-RF5  
Fort Monmouth, N.J. 07703  
USA

Dr C.L.Rino (V)  
SRI International  
333 Ravenswood Ave  
Menlo Park  
CA 94025, USA

Dr H.J.Albrecht (VI)  
FGAN  
Königstrasse 2  
D-5307 Wachtberg-Werthhoven  
Germany

CONTENTS

	Page
<b>PREFACE</b> by H.J.Albrecht	iii
<b>PROGRAM AND MEETING OFFICIALS</b>	iv
	Reference
<b><u>SESSION I – GENERAL TROPOSPHERIC EFFECTS</u></b>	
<b>SESSION SUMMARY</b>	SS1
<b>CHARACTERISATION OF THE EFFECTS OF THE LOWER ATMOSPHERE</b> by P.A.Watson	1
<b>TROPOSPHERIC PROPAGATION EFFECTS ON EARTH-SPACE LOW ELEVATION ANGLE PATHS</b> by R.K.Moore	2
<b>A REVIEW OF THEORETICAL PREDICTION TECHNIQUES OF TRANSMISSION PARAMETERS FOR SLANT-PATH, EARTH-SPACE COMMUNICATIONS</b> by B.G.Evans and A.R.Holt	3
<b>PLANE WAVE SPECTRUM TREATMENT OF MICROWAVE SCATTERING BY HYDROMETEORS ON AN EARTH-SATELLITE LINK</b> by D.P.Haworth	4
<b>THE FREQUENCY DEPENDENCE OF MICROWAVE PROPAGATION THROUGH RAINFALL</b> by P.T.Thompson, A.W.Dissanayake and P.A.Watson	5
<b>SIMULATION OF EHF PROPAGATION THROUGH THE ATMOSPHERE</b> by J.D.Hopponen	6
<b>RADAR ESTIMATION OF SLANT PATH RAIN ATTENUATION AT FREQUENCIES ABOVE 10 GHz AND COMPARISONS WITH MEASURED MULTI-SEASON RESULTS</b> by J.Goldhirsh	7
<b>DUAL-POLARISATION RADAR DATA FOR EVALUATION OF EARTH-SPACE RADIO LINK ATTENUATION</b> by M.P.M.Hall, S.M.Cherry and J.W.F.Goddard	8
<b><u>SESSION II – EXPERIMENTAL DATA OF SHF/EHF PATHS</u></b>	
<b>SESSION SUMMARY</b>	SS2
<b>REVIEW OF SLANT PATH PROPAGATION MEASUREMENTS MADE AT THE APPLETON LABORATORY, SLOUGH, UK</b> by P.G.Davies and E.C.Mackenzie	9
<b>20 AND 30 GHz SLANT-PATH PROPAGATION MEASUREMENTS AT MARTLESHAM HEATH, U.K.</b> by J.Thirlwell and R.G.Howell	10
<b>A REVIEW OF SOME CROSS-POLARIZATION EFFECTS ON SLANT PATHS IN THE 11–30 GHz FREQUENCY RANGE</b> by T.Pratt	11
<b>ATTENUATION, DEPOLARIZATION AND DISPERSION BY ATMOSPHERIC HYDROMETEORS ALONG A 19 AND 28 GHz EARTH-SPACE RADIO PATH</b> by D.C.Cox, H.W.Arnold, H.H.Hoffman and R.P.Leck	12

	Reference
<b>RESULTS OF PROPAGATION EXPERIMENTS AT ITALIAN TERMINALS USING THE SIRIO SATELLITE</b> by F.Carassa, M.Mauri and A.Paraboni	13
<b>UTILISATION D'UN RADAR POUR ETUDIER L'ATTENUATION ET LA DEPOLARISATION DES HYPERFREQUENCES OBSERVEES SUR UN TRAJET OBLIQUE</b> par P.Golé, J.P.Mon et P.Ramat	14
<b>JOINT STATISTICS OF ATTENUATION AND CROSS-POLARIZATION MEASURED WITH THE OTS SATELLITE</b> by J.van Cappellen, A.Mawira, J.Neessen and F.Zelders	15
<b>RAIN ATTENUATION PREDICTION AT THE NETHERLANDS OTS/SIRIO RECEIVING SITE USING INEXPENSIVE X-BAND RADAR</b> by E.P.W.Attema and H.J.M.Heemskerck	16
<b>OTS PROPAGATION MEASUREMENTS AT EINDHOVEN UNIVERSITY, NETHERLANDS</b> by J.Dijk, C.N.F.Hansen and E.J.Maanders	17
<b>11-GHz PROPAGATION MEASUREMENTS ON SATELLITE LINKS IN THE FEDERAL REPUBLIC OF GERMANY</b> by F.Dintelmann and F.W.Rücker	18
<b><u>SESSION III – REMOTE SENSING</u></b>	
<b>SESSION SUMMARY</b>	SS3
<b>TARGET ADAPTIVE RADAR, PROPAGATION MEDIUM ADAPTIVE COMMUNICATION SYSTEMS, PRESENT DAY METHODOLOGY AND FUTURE PERSPECTIVES – A REVIEW</b> by D.G.Gjessing	19
<b>USE OF A SATELLITE MULTI-FREQUENCY RADIOMETER TO DETERMINE ATTENUATION SUFFERED BY A SATELLITE RADAR</b> by G.J.Dome, R.K.Moore, I.J.Birrer and K.van Sickle	20
<b>THE EFFECT OF TURBIDITY ON REMOTE SENSING OF OCEAN COLOR</b> by G.Metzig and E.Raschke	21
<b><u>SESSION IV – GENERAL IONOSPHERIC DISPERSION EFFECTS</u></b>	
<b>SESSION SUMMARY</b>	SS4
<b>RADIO BEACON STUDIES OF IONOSPHERIC IRREGULARITIES</b> by K.Davies	22
<b>AN EMPIRICAL MODEL OF IONOSPHERIC SLAB THICKNESS</b> by L.Kersley	23
<b>ANISOTROPIC MEDIUM EFFECTS ON THE PROPAGATION OF 1.5 GHz SIGNALS CODED BY PHASE REVERSALS: FULL-WAVE SOLUTIONS</b> by E.Bahar and B.S.Agrawal	24
<b>1979–1980 DATA PROCESSING AND RESULTS FROM THE OTS BEACONS B0/B1 AND TM, AND RADIOMETRY AT 11.4 AND 35 GHz</b> by A.Vander Vorst and P.Sobieski	25
<b>IONOSPHERIC DISPERSION EFFECTS ON WIDEBAND TRANSMISSIONS</b> by G.H.Millman and K.A.Olsen	26
<b>ELECTRON CONTENT MEASUREMENTS AT LANCASTER: HARMONIC ANALYSIS OF ATS-6 MEASUREMENTS</b> by E.M.Poulter and J.K.Hargreaves	27



SESSION V - NEW DATA ON IONOSPHERIC IRREGULARITIES

SESSION SUMMARY	SS5
TRANSIONOSPHERIC RADIOWAVE PROPAGATION AND SIGNAL STATISTICS by C.L.Rino	28
RECENT ASPECTS OF IONOSPHERIC SCINTILLATION OBSERVATIONS by G.K.Hartmann	29
STATISTICAL PROPERTIES OF TRANSIONOSPHERICALLY PROPAGATED RADIO SIGNALS UNDER THE INTENSE SCINTILLATION CONDITIONS by K.C.Yeh and C.J.Liu	30
RECENT OBSERVATIONS OF EQUATORIAL AND HIGH LATITUDE SCINTILLATIONS by J.Aarons and H.E.Whitney	31
Paper 32 cancelled	
4/6-GHz IONOSPHERIC SCINTILLATION MEASUREMENTS by D.J.Fang	33
PROPAGATION ANOMALIES AFFECTING AIRBORNE SATELLITE COMMUNICATIONS by A.L.Johnson	34

SESSION VI - PROPAGATION LIMITATIONS IN SYSTEMS

SESSION SUMMARY	SS6
ENVIRONMENTAL CONSTRAINTS IN EARTH-SPACE PROPAGATION - A REVIEW PAPER by J.M.Goodman	35
A PRELIMINARY EVALUATION OF THE TWO-FREQUENCY IONOSPHERIC CORRECTION FOR THE NAVSTAR-GLOBAL POSITIONING SYSTEM by J.A.Klobuchar, H.Soicher and J.A.Pearson	36
Paper 37 cancelled	
THE INTERACTIONS OF A SOLAR POWER SATELLITE TRANSMISSION WITH THE IONOSPHERE AND TROPOSPHERE by K.A.Hughes	38
Paper 39 cancelled	
ON MICROWAVE POWER TRANSMISSION AND THE FEASIBILITY OF POWER SATELLITES FOR EUROPE by D.Koehn	40
POTENTIAL IMPACT OF THE SATELLITE POWER SYSTEM ON COMMUNICATION AND ELECTRONIC SYSTEMS AND THE IONOSPHERE by W.B.Grant, C.M.Rush and E.L.Morrison	41
DISCUSSION ON PAPERS	D
APPENDIX - LIST OF ATTENDEES	A

### EDITOR'S BRIEF SUMMARY OF SESSION I – GENERAL TROPOSPHERIC EFFECTS

In this session, review and contributed papers dealt with the present state of the art and, in particular, with the evaluation of data collected during the last few years on general tropospheric characteristics effective upon propagation paths.

With regard to space/earth paths, reflections, refraction, scattering, and absorption in the troposphere are of varying importance, depending upon the frequency of operation. As a consequence of the extension of their range towards higher frequencies, the effects of precipitation have gained in importance, even if dealing with tropospheric effects generally and mainly for the purpose of modelling and forecasting. Specific features of the medium may require some consideration of polarization influence.

With its papers and discussions, the session provided a full coverage of all relevant problem areas. Especially the results in operational models and prediction methods are directly applicable to engineering development and system planning.

## CHARACTERISATION OF THE EFFECTS OF THE LOWER ATMOSPHERE

P.A. Watson, University of Bradford, U.K.

### Introduction

Characterisation of the effects of the lower atmosphere on the radio transmission path between earth and space, lies in the interests of the satellite radio system designer, the radio scientist and the radio meteorologist. A system designer wishes to be able to describe the performance of earth-space radio links for any location of earth station or satellite. To the radio scientist the earth-space propagation medium offers the challenge of studying a complex time varying medium using only remote sensing instrumentation such as radars, radiometers or radio links. For the meteorologist radio methods offer the possibility of wide scale quantitative measurement completely beyond the scope of other techniques.

This review will be concerned in the main with the interests of the radio system designer which one may attempt to summarize as follows:

- (i) The ability to predict the attenuation experienced on earth-space radio links for any satellite-earth station configuration in terms of the percentage time given attenuation thresholds are exceeded on average, and in terms of statistics of fade durations.
- (ii) Prediction of the on-average occurrence of cross-polarisation and, if possible, the relationship of this to the occurrence of attenuation.
- (iii) Prediction of the magnitude of incoherent emissions (thermal and forward scatter) causing an enhanced noise background on coherent radio systems.
- (iv) Characterisation of off-axis scattering from atmospheric structures, causing interference between systems.
- (v) Characterisation of any other channel impairments, for example dispersion, which may place limits on broadband systems operation.

In characterising the effects of the lower atmosphere from the viewpoint of the system designer, it is not at all obvious how much scientific understanding is necessary. An extreme, entirely empirical approach, might be to gather as much statistical radio data from radiometers and beacon receivers as practically possible, and to base predictions of link budgets entirely on that data. This approach requires little or no understanding of the propagation mechanisms at play. However, despite the recent proliferation of satellite beacons in the 10-30 GHz bands with ATS-5, ATS-6, Comstar, CTS, SIRIO and OTS as the prime examples, at the conclusion of these programmes we will still possess only a very limited data base from the point of view of sample length and geographical coverage. Furthermore, the next two decades are likely to see extensive exploitation of the 10-30 GHz bands for in-service systems. The system designer thus requires global predictions now, not after 20 years of gathering radio data. For that reason, it is important that propagation mechanisms are fully investigated in current experimental programmes, so that with this knowledge, predictions for arbitrary locations may be attempted from long-term meteorological data.

### Attenuation

Except for elevations less than  $5^{\circ}$ , the most important attenuation mechanism in the 2-50 GHz range is, of course, due to the occurrence of intense rainfall in the radio path. At higher frequencies, particularly above 30 GHz we also must consider the effects of clouds, fogs and gaseous absorption. The background loss in the various atmospheric windows occurring above 70 GHz appears to be higher than expected and is currently attributed to anomalous water vapour absorption.<sup>1</sup> In this paper my main concern will be in the frequency range 2 - 50 GHz.

#### (a) Characterisation of world climatic zones of rainfall intensity

This is a most important intermediate step. We look towards the synthesis of rainfall intensity maps for short duration rainfalls (1-5 mins) from which the system designer should be able to make viable predictions. Until now the classification of rainfall climates used by system designers has been on the basis of total annual rainfall,<sup>2</sup> a figure which barely relates to the occurrence of extreme intensities. Recently, Dutton and Dougherty<sup>2</sup> have used the maximum monthly fall and the number of thunderstorm days as indicators of intense rainfall climates. However, their classification of climatic zones and also those of Crane<sup>3</sup> are still based on broad climatological criteria and do not represent climatic zones of rainfall intensity.

An important consideration in the collation of data<sup>4</sup> for the characterisation of climatic zones of rainfall intensity, is the role of orographic features. Evidently such features should appear on the fine scale of any rain intensity maps used by the system designer, but should be removed by suitable scaling when making an initial assessment of intensity climates.

In some countries with long traditions of meteorological research, adequate data for the preparation of short duration rainfall maps are probably already available. In the U.K. for example, the Meteorological Office has published<sup>5</sup> contour maps for short duration rainfalls covering any part of the country. It is possible to use these maps with suitable rainstorm models to produce satisfactory rainfall-attenuation

predictions for terrestrial radio systems <sup>6</sup>. Fig. 1 shows an illustrative example of this procedure. Attenuation-rainfall rate relationships can be derived from single drop extinction coefficients, an assumed drop size distribution and a spatial rain intensity model. By following this procedure it should be possible to avoid difficulties with empirical, directly measured, A-R, relationships obtained with imperfect instrumentation.

(b) Development of models for the spatial structure of rainfall for use with point rainfall data

To move from contours of short duration point rainfall intensity to that occurring along a line (i.e. a radio path) we require a knowledge of the spatial structure of rainfall in each climatic zone. Here radars are perhaps the most powerful instrumentation, particularly the two polarisation type developed by Hall and Cherry <sup>7</sup>, though useful data has been obtained with single polarisation radars <sup>8,9</sup>. Alternatively a network or line of raingauges may be deployed, as in the UK by Harden et al. <sup>10</sup>. The climatic and orographic variations in rainfall intensity spatial distribution would appear at present to be a major uncertainty in modelling. Much more data are required.

(c) Characterisation of drop-size distributions in rainfall on slant paths

A knowledge of drop-size distribution is particularly useful when relating data collected at one frequency to that collected at another, since the contribution to extinction from a given population of drops varies considerably with size in the frequency range 2 - 50 GHz. Here the dual polarisation radar technique shows considerable promise (see later).

(d) Representation of the melting-zone in terms of radio path attenuation

In climates with frequent light and widespread rain, the region below the base of rainclouds in which ice structures melt to produce rain will assume a greater importance with increasing frequency in the range 20 - 50 GHz. Such considerations have particular relevance to systems operating with low fade margins (<10dB) in this frequency range, perhaps though not necessarily in a diversity mode. Fig. 2 shows what is believed to be the first direct characterisation of this region in terms of attenuation <sup>11</sup>, made by comparison of radar measurements with 20 GHz beacon attenuation on ATS-6.

(e) Collection of radio attenuation data for comparison with models

The value of radiometric and radar data is emphasized, as well as directly collected beacon data. Both radiometers and radars may be arbitrarily pointed. Hence if calibrated against a satellite beacon or beacons on one or more fixed paths, these instruments may be used to produce predictions of the dependence of attenuation upon satellite elevation for a given site <sup>12</sup>. Furthermore, the data collected by such instruments of any elevation can add substantially to the total data base. However, the question of the calibration of these instruments is an important one.

Radiometers

The basic expression relating sky noise temperature to the attenuation along a radio path for a thick slab of scatterers, neglecting high order scattering <sup>14</sup> may be written:  $\alpha(\text{dB}) = [1/(1-\omega)] 10 \log [T_m/(T_m - T_A)]$  where  $\omega$  is the scattering albedo and  $T_m$  the effective medium temperature. For a pure absorber, the effects of inhomogeneities may be evaluated using:

$$T_A = \int_0^L \int_{\Omega} \frac{4\pi}{4\pi} G(\underline{u}) T(z) B(z) e^{-\int_0^z B(z') dz} dz d\Omega$$

where  $G(\underline{u})$  is the antenna gain function in direction  $\underline{u}$ ,  $T(z)$  is the medium temperature profile along  $z$  and  $B(z)$  is the extinction cross section of the medium at position  $z$  along the path.

The major uncertainty in radiometer calibration lies in the determination of  $T_m$ , in particular in the mean value to be used. During the ATS-6 series of measurements over Europe <sup>15,16</sup>, radiometers calibrated against the satellite at beacons at 20 and 30 GHz gave effective medium temperatures of the same order as the expected medium physical temperature, i.e.  $\sim 270^\circ\text{K}$ . However, more recent measurements in association with OTS at 11 GHz have indicated that a temperature near  $260^\circ\text{K}$  should be used to obtain agreement with beacon data <sup>17</sup>. The reason for this is not understood, though may be related to the spatial structure of rain, bearing in mind that the rain observed at 20/30 GHz for fades <10dB must be of a considerably more widespread nature than that observed at 11 GHz for the same range of attenuation. However, using a gaussian correlation function to represent the large scale spatial structure in rain and evaluating the error expected from the integral given above, does not predict significant deviation from the attenuation as measured on a coherent beacon. Small scale structure within rain should, however, also be considered.

Radars

Radars can collect data on rainstorms at a much greater rate than either beacon receivers or fixed pointing radiometers. Instead of waiting for storms to intercept a fixed radio path, storms in the vicinity of a radar in any direction can be viewed. However, the question of calibration has been a major difficulty with this technique when quantitative predictions are required.

For accurate results a non-attenuating or lightly attenuating wavelength is chosen for the radar (usually 3 or 5 GHz) at which wavelength the radar reflectivity, represented by Rayleigh scattering shows a sixth power dependence on drop-size. Attenuation-reflectivity relationships of the form  $A = \alpha(f)z^{\beta(f)}$  may then be used for attenuation predictions <sup>11</sup>, with  $\alpha$  in the range  $2 \times 10^{-4}$  to  $4 \times 10^{-3}$  and  $\beta$ , 0.73 to 0.58 for predictions between 11 and 30 GHz for a 2.86 GHz radar.

When all equipment uncertainties are calibrated out of a single polarisation radar <sup>18</sup>, there remains an irreducible uncertainty associated with the sixth power dependence of  $z$  on drop-size. Recently a method has

been proposed for overcoming this problem<sup>19</sup> and is showing considerable promise<sup>7</sup>. The method uses two linear (near H-V) polarisations and takes advantage of the observed relationship between drop eccentricity and drop size, assuming that on elevated paths small mean drop canting angles are prevalent. The latter assumption appears to be born out by radio link and radar measurements<sup>7, 20</sup>. The two polarisation radar technique also appears to have potential for identifying and perhaps quantifying structure within and above the melting zone in rainstorms<sup>21</sup>. Fig. 3 shows some early results.

Given a characterisation of drop size as an integral part of a two-polarisation radar measurement, it should then be possible to produce attenuation predictions for any frequency band in the range 2 - 50 GHz from a single series of measurements. This is a most attractive prospect.

(f) Frequency scaling of attenuation

Here an empirical approach involving measurement with multi-frequency beacons and for radars is essential. Statistics of attenuation gathered at one frequency, cannot be scaled by simple deterministic transformations to other frequency bands, in view of the varying contributions made by the various particle populations over the frequency range<sup>22</sup>. Further multi-frequency beacon measurements, such as the limited scale measurements carried out during the ATS-6 programme<sup>23</sup> are required, backed up where possible with radar measurements.

Cross-polarisation

Two distinct particle populations are known to contribute to cross-polarisation on earth-space paths, namely raindrops and ice particles. The melting zone, a third region, appears from existing rather limited evidence to be fairly isotropic<sup>24, 25</sup>, though the two polarisation radar results from Hall and Cherry show an interesting region of high differential reflectivity immediately below the bright band<sup>21</sup>. The two heavily cross-polarising regions will now be discussed briefly:

(a) Rain

The model for cross-polarisation in rainfall is now well established<sup>26-28</sup>, involving raindrops approximated by oblate spheroids each with a preferred alignment of their axis of rotational symmetry to the local vertical. The cross-polarisation produced for a given attenuation on earth-space or terrestrial paths can be described accurately by a model with a distribution of raindrop tilt (or canting) angles around the local vertical. A gaussian distribution with near zero mean ( $<4^\circ$ ) and 20 to 25° standard deviation can be used<sup>27, 29</sup>. The theory can be represented in terms of small attenuation and phase approximations<sup>30</sup> giving a cross-polarisation law as follows:-

$$XPD = -20 \log A - 40 \log(\cos \alpha) - 20 \log(\sin 2\theta) + B + 17.37 \sigma^2$$

where A is the copolar attenuation,  $\alpha$  is the elevation angle of the satellite,  $\theta$  is the mean polarisation angle relative to the mean-drop tilt or canting angle and  $\sigma$  is the deviation of the canting angle distribution in radians. B is a frequency dependent term given by

$$B = 84.18 - 90.95 x f^y + (52.56 x f^y - 21.48) \log f$$

where  $x = 0.625$  and  $y = 0.145$

This expression is valid between 9 and 30 GHz and for local polarisation angles  $>5^\circ$ . The performance of circular polarisation can be approximated by making  $\theta = 45^\circ$ .

Figs. 4 and 5 show two sets of measurements of cross-polarisation, one a cumulative scattergram of 18 events at 36.5 GHz with  $45^\circ$  polarisation on a terrestrial path and the other a single storm measured at 11.8 GHz using OTS. In both cases the cross-polarisation-attenuation law is seen to be well described by the theory.

(b) Ice Particles

It is now well established that on earth-space paths an additional source of cross-polarisation is evident to that from distorted raindrops, namely cross-polarisation from ice-particles<sup>31-33</sup>. This form of cross-polarisation occurs with little or no attenuation, as would be expected in a medium exhibiting pure differential phase. Radar evidence<sup>31, 32, 34</sup> suggests that the major contribution to this form of attenuation comes from populations of large numbers of small particles, and this observation is consistent with the low attenuations observed, at 20 and 30 GHz. In modelling the medium it is useful to distinguish two particle types which will exhibit different properties, namely needle-like and plate-like particles<sup>35, 36</sup>. The greatest uncertainty in modelling arises at present from an incomplete knowledge of the role played by orientation effects, in particular with needle-like particles. The most simplistic model involves a population of ice plates showing a preferred orientation in the horizontal plane. In that case the received complex cross-polarisation field for linear and circular polarisations may be written<sup>35, 36</sup>

$$x_L = \frac{i \tan(\frac{1}{2} \beta \cos^2 \alpha) \sin 2\theta}{1 - i \tan(\frac{1}{2} \beta \cos^2 \alpha) \cos 2\theta} \quad \text{for linear polarisation.}$$

$$\text{and } x_C = -i \tan(\frac{1}{2} \beta \cos^2 \alpha) \exp(i2\theta) \quad \text{for circular polarisation}$$

where  $\beta$  is the intrinsic differential phase shift in the medium,  $\alpha$  is the satellite elevation and  $\theta$  the polarisation angle to the local vertical.

For small differential phase (as frequently observed in practise below 30 GHz) the following ratio may be extracted:

$$\left| \frac{x_L}{x_C} \right| = \sin 2\theta$$

Hence, during ice-particle cross-polarisation the ratio of linear to circular cross-polarisation will always be  $\sin^2\theta$  unless significant orientation effects are present, represented by alignment of needle-like particles in the horizontal plane or by alignment of either type of particle out of the horizontal plane. Recent evidence<sup>34</sup> has shown that whilst on most occasions horizontal alignment is adequate to explain measured values of cross-polarisation, there are occasions when the linear/circular cross-polarisation can only be explained in terms of alignment out of the horizontal.

Simultaneous co-sited comparison of linear and circular cross-polarisation from satellite beacons is particularly useful for the development of a model for the medium<sup>34</sup> and can give almost as much information as a full polarisation matrix characterisation involving both bands of either linear or circular polarisation. The latter technique is possible with the Comstar beacons<sup>33,37</sup> in the U.S.A. and the former with the ESA OTS satellite over Europe. Fig. 6 shows an example of an OTS simultaneous linear-circular cross-polarisation measurement, showing also the predicted linear cross-polarisation from the circular measurement. Such prediction is possible through the use of the circular cross-polarisation phase information to infer particle orientation.<sup>34</sup>

An alternative and more powerful technique of investigating orientation effects in ice particle populations is to use dual circularly polarised radar as developed by Hendry and McCormick<sup>38</sup>. Both the radar and the radio beacon measurements show that rapid jumps in mean particle orientation can take place<sup>39,40</sup>, though to date only the beacon measurements<sup>40,34</sup> have been able to give sufficient time resolution to quantify these as occurring in typically 0.1 to 0.25 s. There is strong evidence that such rapid jumps are due to re-orientation effects at the incidence of lightning strokes<sup>34,40</sup>.

#### Incoherent emissions

Received incoherent energy will raise the noise background for coherent radio systems. Below approximately 30 GHz the thermal emissions from rain appear to be adequately described by the radiometer equation given earlier, within the uncertainty connected with the choice of medium temperature. Above 30 GHz multiple scattering should be included<sup>14</sup>.

With highly directive antennas incoherent forward scattered radiation from rainfall should not be significant until at least 100 GHz<sup>41,42</sup>. However, with broad-beam antennas it may be necessary to consider this effect at lower frequencies and also to consider the correlation properties of incoherent signals associated with far from axis returns<sup>41</sup>. Experimental data is in short supply here.

#### Off-axis scattering

Off-axis or bistatic scattering from rainfall might be evident in circumstances where a common scattering volume is viewed by satellite and terrestrial radio relay links. Although the total scattering cross-section for a rain volume will increase with increasing frequency in the range 2 - 50 GHz, whenever significant common volume scattering occurs, there is invariably rain also present on the rest of the radio path, giving rise to attenuation of the scattered signal. Making the simplifying assumption that rain is uniform along the path, it can be shown<sup>42</sup> that the interference-to-signal ratio is given by  $\frac{\beta A}{4.34G}$  where A is the rain fade margin,  $\beta$  is the ratio of the scattering to extinction coefficients for the rain volume and G is the receive antenna gain.

However, from a practical point of view, other trans-horizon propagation mechanisms are likely to be much more significant than rain scatter in causing interference between systems. In a recent series of measurements<sup>43,44</sup> at 11 GHz on a number of over-land and over-sea trans-horizon radio paths, no evidence of rain scatter above a measurement threshold of -53dB on the free space value was detected, whereas super-refractive and ducting effects were observed for significant percentages of time (~0.01%) giving interference -10dB to -20 dB relative to the free space value.

#### Dispersion

For elevations  $>5^\circ$  there should be little or no mean phase-frequency distortion on earth-space radio links using 2-50 GHz, as confirmed by a recent measurements<sup>45</sup> at 20 and 30 GHz. Amplitude-frequency distortion from coherent returns should only be detectable on extremely broadband systems (GHz bandwidth) and can be predicted from published rain attenuation data<sup>30</sup>. Amplitude and phase scintillations due to incoherent returns<sup>41</sup> should also be negligible up to at least 50 GHz for most practical systems, however measurements using broadband data streams ( $G_b$ ) have not yet been reported.

A more serious dispersion mechanisms may come into play at low elevations ( $<5^\circ$ ) where deep fading is observed from stable anomalous refractive index gradients. Recently Strickland<sup>4</sup> has reported that such fading is not frequency selective over bandwidths of several MHz.

#### References

1. Liebe, H.J. "Millimeter wave attenuation in moist air - a review". Workshop on millimeter and submillimeter atmospheric propagation, Alabama, USA, March 1979.
2. Dutton, E.J. "Estimating year-to-year variability of rainfall for microwave propagation".  
and  
IEEE Trans. COMM-26, 8, Aug. 1978, p. 1321 - 1324.  
Dougherty, H.T.
3. Crane, R.K. "Prediction of attenuation by rain". Environmental Res. and Tech. Inc. Report 1979, Concord, MA. USA.
4. Rucker, F. "Simultaneous propagation measurements in the 12 GHz band on the SIRIO and OTS satellite links". URSI Commission F Symposium, Canada, 1980, preprints, p 4.1.1 to 4.1.5.
5. U.K. Meteorological Office. "Flood Studies Report". Vols. 1 - 5.  
National Environmental Research Council, 1975.

6. Watson, P.A., Ahmed, H.J. and Papaioannou, C. "Long term prediction of attenuation on terrestrial radio links from rainfall data". IEE Conf. on Antennas and Propagation, London 1978, p 92-96.
7. Bringi, V.N. et al. "A new accuracy in determining rainfall rates and attenuation due to rain by means of dual polarization radar measurements". *ibid* p. 120-124.
8. Strickland, J. "Radar measurements of site-diversity improvement during precipitation". *Jour. de Recherches Atmosphériques*, 8, Jan. 1974, p. 451 - 464.
9. Goldhirsh, J. and Robison, F.L. "Attenuation and space diversity statistics calculated from radar reflectivity data of rain". *IEEE Trans. AP-23* (2), March 1975, p. 221 - 227.
10. Harden, B.N., Norbury, J.R. and White, W.J.K. "Model of intense convective rain cells for estimating attenuation on terrestrial millimetric radio links". *El. Letts.* Nov. 1974, p. 483-484.
11. Dissanayake, A.W. and McEwan, N.J. "Radar and attenuation properties of the bright band". IEE Conf. on Antennas and Propagation, London 1978, p.125 - 129.
12. Jarvis, E.G. and Turner, D. "Aerial noise temperature variations at 3.95, 11.75 and 17 GHz due to atmospheric changes". *British Post Office Res. Dept.* Report 399, August 1973.
13. Crane, R.K. "Propagation phenomena affecting satelliting communications systems operating in the centimeter and millimeter wavelength bands. *Proc. IEEE* 59, No. 2, Feb.1971 p. 173-188.
14. Zavody, A.M. "Effect of scattering by rain on radiometer measurements at millimetre wavelengths" *Proc. IEE*, 121, 1974, p. 257 - 263.
15. Allnutt, J.E. and Shutie P.F. "Slant path attenuation and space diversity results at 30 GHz using radiometer and satellite beacon receivers". *ESA Report on ATS-6 propagation experiments in Europe* ESA SP-131, 1977, p. 69 - 78.
16. Bell, R.R. et al. "Calibration of 20 and 30 GHz radiometers by using the ATS-6 satellite beacons", *ibid* p. 135 - 148.
17. Davidson, C. and Hansander, L. "Comparison between attenuations measured by means of a radiometer and satellite signal receivers". Report RLO7/79 of the Radio Lab. of the Swedish Telecomms. Administration. Feb. 1979.
18. McEwan, N.J. et al. "A self-calibrating 9.4 GHz meteorological radar". *Proc. of Radar Workshop Graz. Austria*, Nov. 1978, p. 97 - 118.
19. Seliga, T.A. and Bringi, V.N. "Potential use of radar differential reflectivity measurements at orthogonal polarisations for measuring precipitation". *J. Appl. Meteor.* 15 (1), 1976, p. 69 - 76.
20. Neves, J. and Watson, P.A. "Propagation coefficients for vertically and horizontally polarised waves at 36.5 GHz". *El. Letts.* 13 (21), Oct. 1977, p. 649 - 650.
21. Cherry, S.M., Goddard, J.W.F., Hall, M.P.M. and Kennedy, G.R. "Measurement of raindrop-size distributions using dual polarisation radar". *Proc. 5th Int. Conf. on Erosion by Solid and Liquid Impact*, Cambridge, U.K., 1979.
22. Watson, P.A. "Propagation factors in the design of 20 and 30 GHz telecommunications satellite systems". *IEE Conference on Antennas and Propagation, London 1978, Proceedings* p. 130 - 134.
23. Howell, R.G. et al. "20 and 30 GHz attenuation measurements using the ATS-6 satellite". *ESA Report on ATS-6 propagation experiments in Europe* ESA SP-131, 1977, p. 55 - 68.
24. McEwan, N.J. et al. "Satellite path attenuation at 20 GHz compared with 9.4 GHz radar measurements". *ibid.* p 21 - 30.
25. Hendry, A., McCormick, G.C. and Antar Y.M.N. "Differential propagation constants on slant paths through snow, as measured by 16.5 GHz radar". *URSI-F Symposium, Canada, 1980. Preprints* p. 6.7.1 to 6.7.7.
26. Watson, P.A. and Arbabi, M. "Rainfall cross-polarisation at microwave frequencies". *Proc. IEE* 120, April 1973, p. 413 - 418.
27. Chu, T.S. "Rain induced cross-polarisation at centimeter and millimeter wavelengths". *BSIJ*, 53, Oct. 1974, p. 1557 - 1578.
28. Brussaard, G. "A meteorological model for rain induced cross-polarisation". *IEEE Trans. AP-24* Jan. 1976, p. 5 - 11.
29. Neves, J. and Watson, P.A. "Cross-polarisation, differential attenuation and differential phase shift measured on a 36.5 GHz terrestrial link". *URSI Commission F Symposium, Canada, 1980, Preprints* p. 5.1.1. to 5.1.6.
30. Dissanayake, A.W., Haworth, D.P. and Watson, P.A. "Analytical models for cross-polarisation in rainstorms on Earth-space radio links". *ibid.* p. 1.7.1 to 1.7.6.
31. McEwan, N.J. et al. "Cross-polarisation from high altitude hydrometeors on a 20 GHz satellite radio path". *El. Letts.* 13, No. 1, Jan. 1977, p. 13 - 14.
32. Shutie, P.F., Allnutt, J.E. and MacKenzie, E.G. "Satellite-earth signal depolarisation at 30 GHz in the absence of significant fading". *El. Letts.* 13, No. 1 Jan.1977, p. 1 - 2.

33. Cox, D.C., Arnold, H.W. and Rustako, A.J. "Some observations of anomalous depolarisation on 19 and 12 GHz earth-space propagation paths". Radio Sci. 12, May/June 1977, p. 435-440.
34. McEwan, N.J. et al. "OTS propagation measurements with auxiliary instrumentation". URSI Commission F Symp., Canada. 1980, Preprints p. 6.2.1 to 6.2.8.
35. Haworth, D.P., McEwan, N.J. and Watson, P.A. "Model for the effects of electric fields on satellite-earth microwave radio propagation". El. Letts. 13 (19) Sept. 1977, p. 562-564.
36. Haworth D.P., McEwan, N.J. and Watson, P.A. "Cross-polarisation for linearly and circularly polarised waves propagating through a population of ice-particles on satellite-earth paths". El. Letts. 13 (23) Nov. 1977, p. 703 - 704.
37. Cox, D.C. "An overview of the Bell Laboratories 19 and 28 GHz Comstar beacon propagation experiments". BSTJ May/June 1978, 57 (5) p. 1231-1256.
38. McCormick, G.C. and Hendry A. "Techniques for the determination of the polarisation properties of precipitation". Proc. of Radar Workshop, Graz, Austria. Nov. 1978, p. 133-172.
39. McCormick, G.C. "Dual polarisation radars, depolarisation measurements". *ibid* p. 173 - 190.
40. Haworth, D.P., McEwan, N.J. and Watson, P.A. "Relationship between atmospheric electricity and microwave radio propagation". Nature 266, April 1977, p. 703 - 704.
41. Capsoni, C., Mauri, M. and Paraboni A. "Incoherent effects in electromagnetic propagation through rain". Ann. Telecomm. 32, Nos. 11-12, 1977, p. 407 - 414.
42. Chu, T.S. "Rain-scatter interference on an earth-space path". IEEE Trans. AP March 1977, p.287-8.
43. Hewitt, M.T. and Adams, A.R. "Trans-horizon interference propagation measurements at 11 and 17 GHz in the UK North Sea region". URSI - Commission F Symposium, Canada 1980. Preprints, p. 7.1.1. - 7.1.7.
44. Hewitt, M.T. and Adams, A.R. "The identification of trans-horizon interference propagation conditions from meteorological data". *ibid*. p. 7.2.1. - 7.2.6.
45. Cox, D.C., Arnold, H.W. and Leck, R.P. "Phase and amplitude dispersion for earth-satellite propagation in the 20 to 30 GHz frequency range". To be published.
46. Strickland, J. "Site diversity measurements of low angle fading and comparison with a theoretical model". URSI Commission F Symposium, Canada 1980, Preprints p. 3.2.1 - 3.8.6.
47. G. Brussaard "Report on OTS in-orbit measurements", Vol. 2, ESA JCB(80)1. Dec. 1979.

#### Acknowledgements

Acknowledgement is made to the Rutherford-Appleton Laboratory of the U.K. Science Research Council for making available Fig. 3.



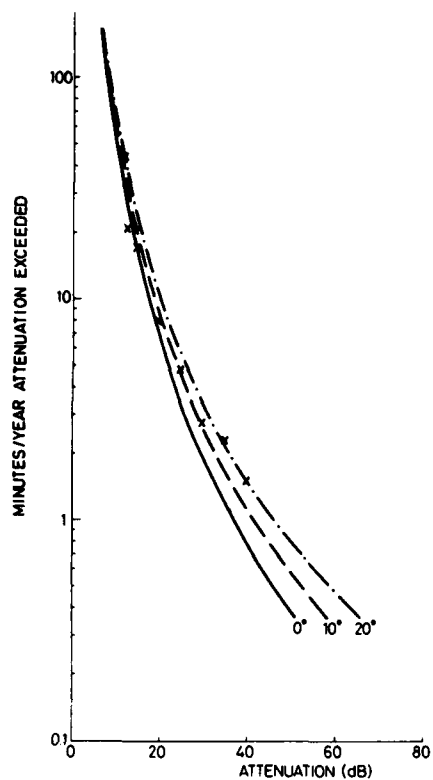


Fig. 1. Example of terrestrial radio link attenuation at 11 GHz predicted from long-term rainfall data. Crosses are data points from 3 years radio measurements on a 26 km link. Curves are predictions from 44 years rain gauge data using an exponential raincell model, Laws-Parsons drop sizes and drop temperatures as indicated (ref. 6).

Fraction of time  
attenuation is greater  
than given value

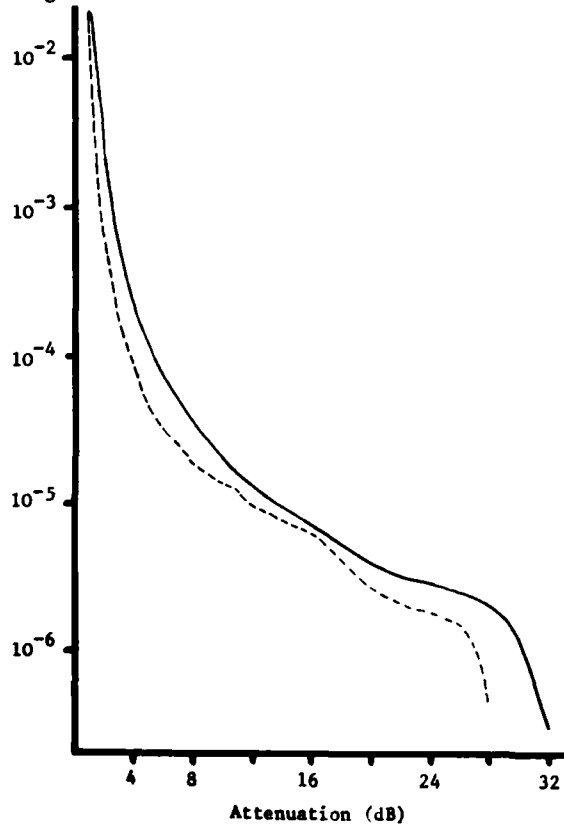


Fig. 2. Comparison of total attenuation measured on the ATS-6 20 GHz beacon with attenuation predicted from a co-sited radar for rainfall only. The difference is attributed to the effects of the melting layer and ice particles (ref. 11, Dissanayake and McEwan).

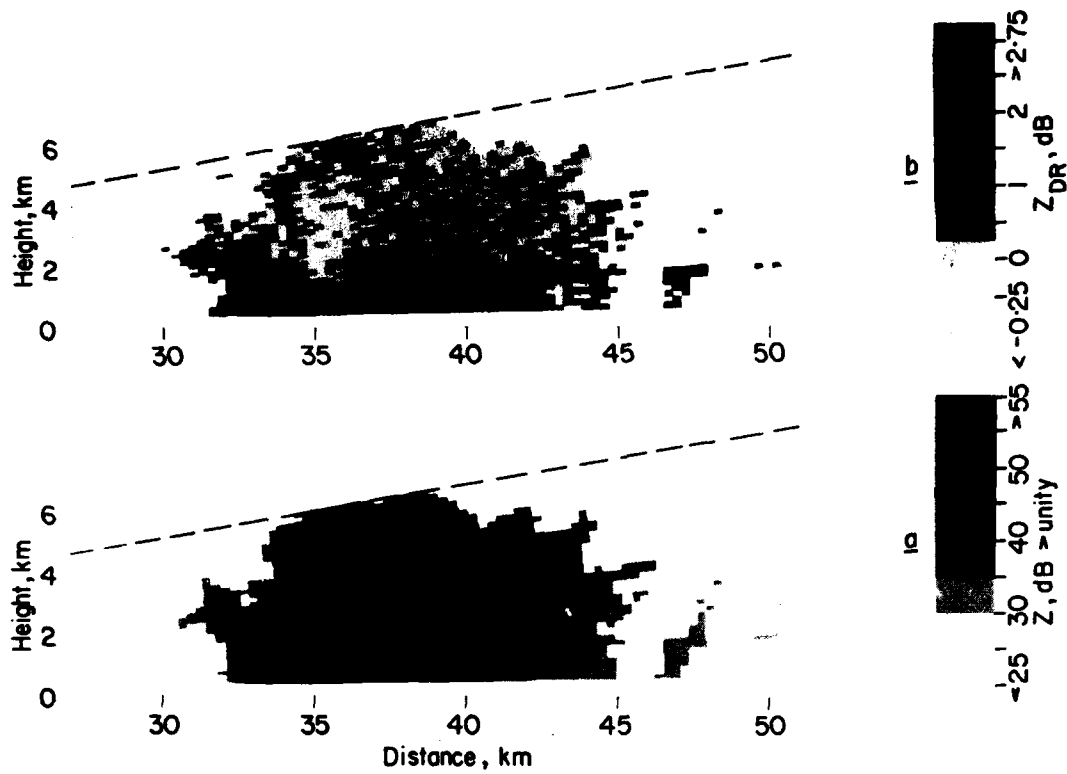


Fig. 3. Example of differential reflectivity through a thunderstorm, seen on a dual linearly polarised radar compared with the total reflectivity, (ref. 21 Cherry et al.). Note region of high total reflectivity near centre of convective cell corresponding with a region of low differential reflectivity.

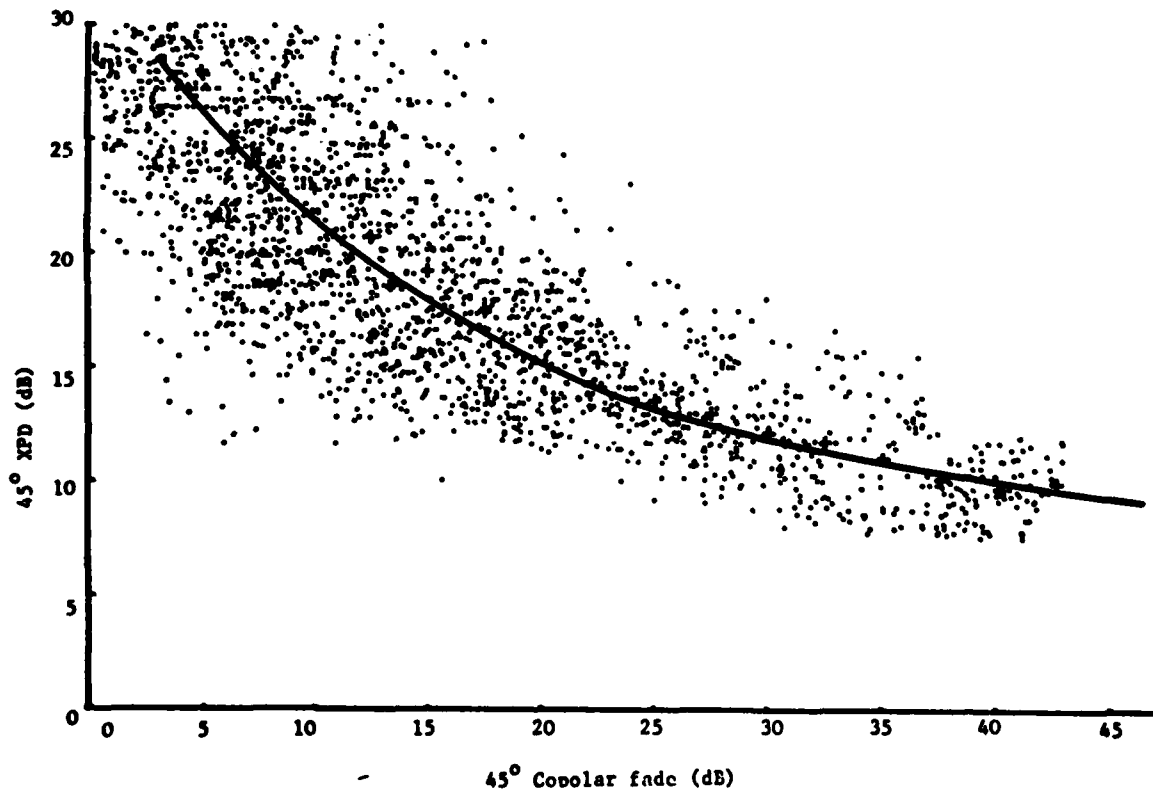


Fig. 4. Cross-polarisation discrimination for 45° pol. versus attenuation measured on a 36.5 GHz, 13 km terrestrial radio link. Theoretical curve is for zero mean canting angle with standard deviation 20° (ref. 29 Neves and Watson).

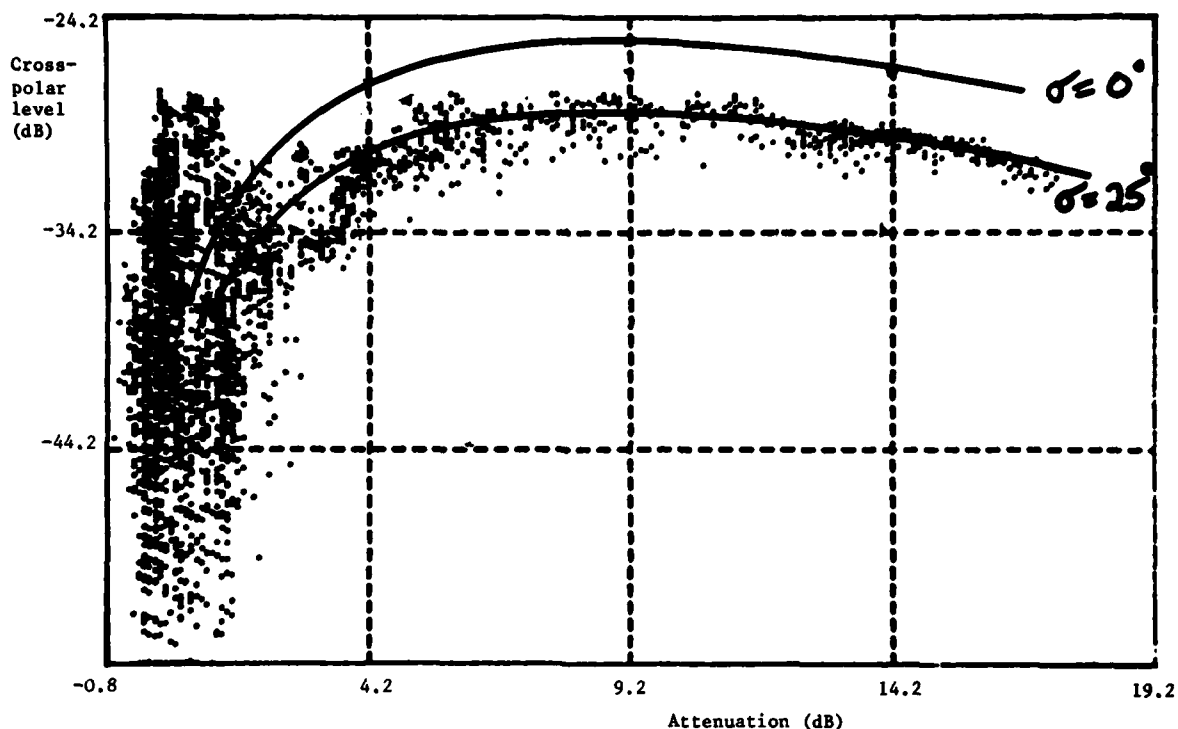


Fig. 5. Cross-polarised signal level versus attenuation measured at Funcino, Italy, using the BI circularly polarised beacon of OTS at 11.8 GHz. The theoretical curves use the relationship given in the text with zero mean canting angle and standard deviation,  $\sigma$ , as shown. Data supplied by Mr. G. Brussard of ESA-ESTEC (ref. 47).

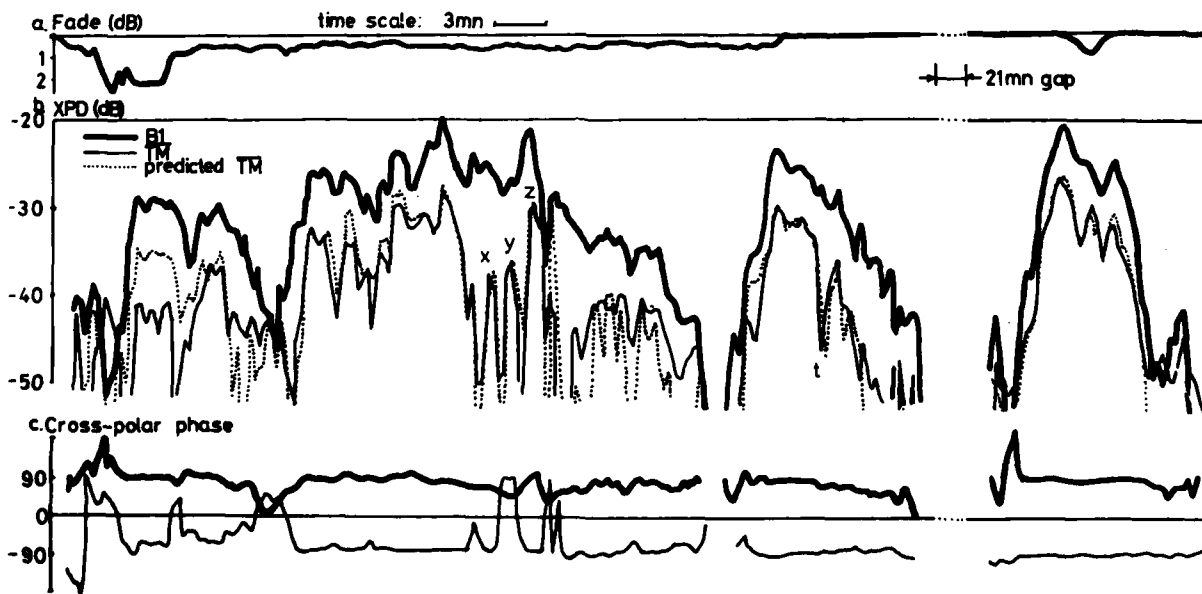


Fig. 6. Cross-polarisation measured using the OTS linearly and circularly polarised beacons (TM and BI respectively). Note the predicted XPD for linear polarisation, using the circular polarisation amplitude-phase data and assuming a lossless medium. The predictions are excellent in conditions of low loss. The observed cross-polarisation correlates well with high altitude radar returns (5-10 km, ref. 34 McEwan et al.)

## TROPOSPHERIC PROPAGATION EFFECTS ON EARTH-SPACE LOW ELEVATION ANGLE PATHS

Richard K. Moore  
Remote Sensing Laboratory  
The University of Kansas Center for Research, Inc.  
Lawrence, Kansas 66045

## SUMMARY

Extensions and reductions of horizon distance have been determined for a satellite transmitter under climatologically realistic conditions for refraction in the troposphere. The increase in elevation (grazing) angle has been determined under the same conditions. The computations have been made, where possible, using parameters available climatologically on a global basis in the World Atlas of Atmospheric Radio Refractivity. The effects of normal variations in refractivity, of ducting, and of subrefraction have all been considered. Likely limits have been placed on the basis of climatology.

Examples considered show possible variations in horizon distance from 22 km closer than for a vacuum under extreme conditions of subrefraction to 340 km beyond the free space horizon for an extreme duct condition. Horizon variations due to variations in surface refractivity with normal refraction amount to 109 km. Grazing angle variations between minimum and maximum surface refractivity amount to only about 5 mr, but in a duct they may become as great as 32 mr.

## 1. INTRODUCTION

The communication or radar range possible from a satellite is set by the horizon distance, and to some extent by atmospheric attenuation. Straightforward calculations of horizon distance, assuming the rays travel from satellite to ground through a vacuum, can be significantly in error because of bending in both ionosphere and troposphere. This problem has been treated in connection with other kinds of studies by Millman (1965, 1966), and Weisbrod and Anderson (1959). However, climatological variations in the troposphere have been largely ignored in these earlier studies. Hence, the purpose of this study is to show the effects of the very considerable variations in tropospheric properties on the distances seen from a satellite at microwave frequencies. The effects of the ionosphere have been ignored here, although they are important at frequencies up to 1 GHz or so.

Computations made here are largely independent of satellite height above the earth. Except for total horizon range, the 900 km computations presented are essentially the same as they would be for higher satellites, such as those in synchronous orbit. To illustrate how strongly the tropospheric effects depend upon the ray being nearly tangent to the earth, some computations have also been made for 4° elevation angle.

Although the troposphere only occupies the lowest 8 to 16 km of the atmosphere, it has a disproportionate effect on satellite-to-ground signals that reach the ground near grazing incidence. This happens because ray paths nearly tangent to the earth extend so far through the troposphere; for example, the tangent ray through only the first kilometer of height is 113 km long in the absence of refraction, and with refraction it often exceeds 150 km. Thus, the lowest 0.11% of the height for a 900 km satellite occupies about 3.2% of the total distance between satellite and ground. Furthermore, the most important ray bending effects take place in the lower few kilometers and in the ionosphere. This point is illustrated in Table 1.

TABLE 1: Unrefracted-Path Distances

Path or Range	Distances in Kilometers	
	Grazing	4° Elevation
Satellite-ground path-900 km	3500	3085
Ionosphere path-900 km	2370	2315
Below-ionosphere (h<100 km) path	1130	770
Troposphere (h<20 km) path	505	228
Troposphere path below h - 1 km	113	14
Ground range-900 km	3200	2780
Local ray elevation angle (900 km)	28.8°	29.0°
Local ray elevation angle (100 km)	10.0°	10.51°
Local ray elevation angle (20 km)	4.50°	6.05°
Local ray elevation angle (1 km)	1.02°	4.13°

Although most of the refraction and attenuation below the ionosphere occur in the troposphere, some refraction takes place in the stratosphere, above the boundary between the two regions called the tropopause. In the discussion that follows, the term "troposphere" will be used without qualification, even though some parts of the discussion apply to the combined troposphere-stratosphere region, since the same kind of considerations are applicable throughout the region.

Bending (refraction) takes place in the troposphere because of variations in the refractive index  $n$  of air. The refractive index is the square root of the relative permittivity (dielectric constant):

$$n = \sqrt{\epsilon_r} \quad (1)$$

The refractive index of air is a function of temperature, pressure and water vapor density (Bean and Dutton, 1966, p. 7):

$$N = (n - 1) \times 10^6 = \frac{77.6}{T} (p + \frac{4810e}{T}) \quad (2)$$

where  $N$  is the refractivity, a standard measure of refractive index, in  $N$ -units,

$T$  is the temperature in  $^{\circ}K$ ,

$P$  is the pressure in millibars,

and  $e$  is the partial pressure of water vapor in millibars. At sea level, the value of  $N$  ranges from about 270 to 430  $N$ -units; i.e., the refractive index differs from unity by between 0.27 and 0.43 parts per thousand. For this small difference to be significant, the ray must travel nearly horizontally. Although Bean and Dutton discuss alternate forms of (2), for practical purposes the values used in (2) are sufficiently accurate for this analysis.

The refractivity tends to decrease with altitude, since its value is zero (refractive index one) outside the atmosphere. In some cases, however, the refractivity actually increases over a small range of increasing altitude. The amount of bending of a radio wave is proportional to the gradient of refractive index or refractivity, since a ray in a homogeneous medium travels in a straight line.

A decrease in refractivity with altitude causes a ray from a satellite to be bent toward the earth, whereas an increase causes bending away from the earth. Figure 1 shows a ray AD from a satellite to the earth labelled "normal refraction" and bent toward the earth. Subrefraction can occur near the surface, as shown by ray AEB, with a resulting decrease in range. In this ray, the region of positive gradient is from B to E.

Superrefraction occurs when the refractivity decreases more rapidly than normal; it results in increases in the horizon distance, because a ray can be bent farther around the spherical earth. AF in Figure 1 shows this. The extreme case of superrefraction is formation of a "duct", which occurs when the bending of the ray equals or exceeds the curvature of the earth. For rays entering the atmosphere from above, the effect of the duct is to extend the possible range although any particular ray is bent downward more sharply so its range is decreased.

Refraction also changes the incident angle at which a ray from a spacecraft strikes the earth at any particular point, or the elevation angle that an earth station must use to reach a particular point in space. This effect is relatively small except in a duct, and the effect is negligible for all atmospheric conditions at angles more than 4 or 5 degrees from grazing (unless the angle is used in a position measurement).

The study of refractive effects is greatly simplified by the availability of Bean, et al., A World Atlas of Atmospheric Radio Refractivity (1966). Although the Atlas is necessarily unreliable in some parts of the world because of lack of data, it was specifically designed for the radio engineer and the results are therefore presented in appropriate form for use in a study such as this one. Accordingly, the analysis of refraction presented here has been designed to fit the data presented in the Atlas.

## 2. NORMAL REFRACTION

### 2.1 Choice of Model

Calculation of refractive effects requires use of a model for the variation of refractivity with altitude. If refractivity always varied the same way, the problem would only be a computational one, but in fact refractive index profiles are quite complicated and variable. The normal procedure for determining the refractive index variation with height is to use equation (2) and values of the pressure, temperature, and moisture content obtained from meteorological radiosondes. This method gives an incomplete picture for two reasons: the radiosonde sensors are sluggish and values are only read out at rather wide intervals, and radiosonde measurements are not made frequently enough or in enough places to give a complete picture even of the information the instruments could provide.

Measurement of detailed variations is possible with a microwave refractometer, but these are too expensive to be sent aloft in balloons like radiosondes. Hence, only occasional samplings are made by refractometers carried in aircraft.

Any climatological study like this one must use grossly simplified profiles or become so large that it is unusable. Bean and Dutton (1966) have studied the various approaches to evaluation of the tropospheric bending, both in terms of models of the atmosphere and methods of calculation. Fortunately, they conclude that relatively simple computations are adequate for climatological and system prediction purposes when the wave passes through nearly the entire atmosphere, although more complex techniques are necessary if both terminals are near the ground.

In view of the nature of the climatological information available in the Atlas (Bean et al., 1966) we shall use the "statistical regression" method, as Bean and Dutton suggest. This is described in Bean and Dutton on p. 54, and much of the book is devoted to verification of its applicability.

The statistical regression method is based on an extensive study of refraction through numerous atmospheres measured by radiosonde techniques at many places in the world. Regression equations are given for both the total refraction angle  $\tau$  and the "elevation error"  $\epsilon$ . Thus:

$$\tau = bN_s + a \pm SE \text{ } m r \quad (3)$$

$$\epsilon = mN_s + n \pm SE \text{ } m r \quad (4)$$

where  $a$ ,  $b$ ,  $m$ , and  $n$  are regression coefficients that are functions of the altitude difference between ground and aircraft or satellite and of the angle of incidence (or elevation) at the ground. The values of these coefficients are given by Bean and Dutton in a set of tables on pp. 382-384 and 420-422. For the spacecraft problem only the tables for 70 km height need be used, since these are considered to be appropriate for waves that pass completely through the troposphere. The terms SE in (3) and (4) refer to the standard error of the regression, which is also listed in the tables.

2.2 Climatology of Surface Refractivity  $N_s$ 

The World Atlas of Atmospheric Radio Refractivity contains world maps of surface refractivity for February, May, August, and November. Rather than giving the total refractivity on a single map, the "dry" and "wet" terms in equation (2) are separated out, and a map is given of each for each month. With this technique it is possible to model the atmosphere with a double exponential decay of refractivity, and the Atlas gives maps of the "scale height" for each term separately. In use of the regression method at sea level, the scale height maps are not necessary. Figure 2 shows the dry and wet term maps for February. Clearly, the dry term is most important in the polar regions and the wet term is usually important in the tropics; this occurs because the absolute humidity cannot be large in the polar regions because of the low temperatures. Note also that the dry term is given with contour intervals of four N-units, whereas the wet term has contour intervals of 20 N-units. This is indicative of the relative variability of the two; the wet term is much more variable.

In addition to the maps, the Atlas contains in Table A-1 cumulative distributions of the refractivity for 110 stations around the world. Examination of data from some sample stations, and computation of the resulting total bending gives an indication of the variability to be expected in different parts of the ocean. Consider three cases: Anchorage, a near-polar station; Singapore, a tropical station; and Nicosia, Cyprus. Tables 2 - 7 show the surface refractivity exceed 5%, 50%, 95% and 99% of the time for these stations, and the corresponding total bending. Anchorage shows little variation either within or between seasons. Singapore is much more variable between seasons, and even within the months of May and August. The total bending at Anchorage is seldom as great as the 99% value for Singapore.

The Eastern Mediterranean is a region of extremes. Tables 6 and 7 show the situation at Nicosia, Cyprus. The minimum bending is lower there in May and August than in Anchorage during the tabulated months, but the maximum during August is almost as much as for Singapore. During August the range of surface refractivity at Nicosia is almost a full 100 N-units, far more than the range at any of the other example stations in any month.

TABLE 2  
Refractivity at Anchorage, Alaska

Month	Percent Time Refractivity Exceeded			
	5	50	95	99
February	317.5	307.2	299.8	294
May	318.9	308.9	296.2	293
August	336.3	324.3	308.5	297
November	314.2	306.6	298.7	296

TABLE 4  
Refractivity at Singapore

Month	Percent Time Refractivity Exceeded			
	5	50	95	99
February	385	379	369	367
May	396	388	377	338
August	393	386	376	331
November	389	382	374	365

TABLE 6  
Refractivity at Nicosia, Cyprus

Month	Percent Time Refractivity Exceeded			
	5	50	95	99
February	326	312	294	288
May	342	314	280	270
August	366	327	281	267
November	338	315	274	288

TABLE 3  
Total Bending in Troposphere (milliradians)  
Anchorage, Alaska

Month	Percent Time Bending Exceeded			
	5	50	95	99
February	11.0	10.5	10.1	9.8
May	11.1	10.6	10.0	9.7
August	11.5	11.4	10.6	9.9
November	10.9	10.4	10.1	9.9

TABLE 5  
Total Bending in Troposphere (milliradians)  
Singapore

Month	Percent Time Bending Exceeded			
	5	50	95	99
February	14.5	14.2	13.7	13.6
May	15.1	14.7	14.1	12.1
August	14.9	14.6	14.0	11.7
November	14.7	14.4	13.9	13.5

TABLE 7  
Total Bending in Troposphere (milliradians)  
Nicosia, Cyprus

Month	Percent Time Bending Exceeded			
	5	50	95	99
February	11.0	10.8	9.8	10.1
May	12.3	10.9	9.1	8.6
August	13.6	11.6	9.2	8.4
November	12.1	11.0	10.8	10.1

To give an idea of worldwide extremes of refractivity, the level of refractivity exceeded only 1% of the time for stations having the highest values has been compiled in Table 8. Also in the table are the values of refractivity exceeded 99% of the time for the stations having the lowest values. The extremely high values of refractivity occur only in warm climates. The extremely low values, however, are found in both warm and cold climates.

## 2.3 Refractive Extension of Ground Range

The effect of normal refraction is to extend the ground range, as shown in Figure 1. This extension may be computed in terms of the total refraction given in (3). Figure 3 shows the geometry associated with this computation.  $R_0$  is the earth's radius and  $(R_0 + h)$  is the radius to the top of the troposphere-stratosphere, assumed to be 70 km above the earth's surface. AD is the ray at angle  $\alpha_0$  from a point on the ground to the top of the troposphere in the absence of atmosphere, and AE is the bent ray actually present.  $\phi_0$  is the central angle for the free-space ray and  $\Delta\phi$  is the extension due to bending. AD has an elevation angle at D of  $\alpha_h^0$  and AE an elevation angle at E of  $\alpha_h$ .

The sizes of these angles may be determined from Snell's Law for a spherical geometry. Thus

$$(R_0 + h) \cos \alpha_h^0 = R_0 \cos \alpha_0 \quad (\text{Vacuum})$$

$$(R_0 + h) \cos \alpha_h = n_s R_0 \cos \alpha_0 \quad (\text{Atmosphere})$$

where  $n_s$  is the refractive index at the surface. The maximum difference between these angles occurs for grazing incidence ( $\alpha_o = 0$ ).

TABLE 8: Extreme Values of Refractivity

Value exceeded 1% of time		Value exceeded 99% of time	
FEBRUARY		FEBRUARY	
Darwin, Australia	411	Perth, Australia	281
Lae, New Guinea	490	Tripoli, Libya	285
Abidjan, Ivory Coast	405	Adelaide, Australia	282
Nandi, Fiji Islands	403		
MAY		MAY	
Calcutta, India	421	Nicosia, Cyprus	270
Aden	411	Tripoli, Libya	284
Bahrain Island	409	Ezeiza, Argentina	284
Saigon, Viet Nam	404	Perth, Australia	290
Hongkong	401	Anchorage, Alaska	293
Singapore	401		
AUGUST		AUGUST	
Bahrain Island	429	Nicosia, Cyprus	267
Calcutta, India	412	Ship A(62° N, 33° W)	277
Mazatlan, Mexico	406	Coppermine, NWT, Canada	280
Key West, Florida	405	Lourenco Marques, Angola	280
Cocoa Beach, Florida	403		
Aden	401		
NOVEMBER		NOVEMBER	
Lae, New Guinea	417	Adelaide, Australia	282
Majuro Island	401	Townsville, Australia	282
		Perth, Australia	283
		San Diego, California	283
		Nicosia, Cyprus	288

For a height of 70 km,

$$\alpha_h^o = 0.15 \text{ radians}$$

Weisbrod and Anderson (1959) show that

$$\alpha_h^o - \alpha_h \sim N_s \times 10^{-6} \cot \alpha_h$$

If we assume  $N_s = 400$  N-units, this means that

$$\alpha_h^o - \alpha_h = 2.60 \times 10^{-3}$$

which means that the error in assuming the two angles are equal is only 1.8% so we shall assume that they are equal in the development that follows.

Bean and Dutton show in their equation (3.61) that the total refraction  $\tau$  is

$$\tau = \phi + (\alpha_o - \alpha_h) \quad (5)$$

By examining triangle OAD, we can show

$$\tau = \phi + (-\phi_o) = \Delta\phi \quad (6)$$

The range extension due to refraction is given by

$$\Delta G = R_o \Delta\phi = R_o \tau \quad (7)$$

This may be expressed in terms of the statistical model by substituting the value of  $\tau$  from (3) into (5):

$$\Delta G = R_o (bN_s + a) \pm R_o (SE) \quad (8a)$$

Using the polar value for the radius of the earth,  $6.36 \times 10^3$  km, and noting that (3) gives  $\tau$  in milliradians, the range extension in kilometers is

$$\Delta G_{km} = 6.36(bN_s + a) + 6.36(SE) \quad (8b)$$

From this a modified set of regression coefficients for  $\Delta G$  can be written, so we can express

$$\Delta G_{km} = BN_s + A + SE_{km} \quad (8c)$$

Using Bean and Dutton's Table 9.9 and converting it from  $b$ ,  $a$ , and  $SE$  to  $B$ ,  $A$ , and  $SE_{km}$ , the values to use for different grazing angles are given in Table 9.

Although the standard errors are quite large at grazing incidence, they are of negligible importance even at 5 mr. Table 9 can be used with the tables and maps in the Atlas to produce maps with contours of constant range extension for a given grazing angle. Such a map could be made from Fig. 2, using the values shown in Figure 4, where  $\Delta G$  is plotted vs.  $\alpha_o$  for various values of  $N_s$ .

TABLE 9: Coefficients to Use in Regression Method for Computing Range Extension

$\alpha_o$ (mr)	B	A	SE <sub>km</sub>
0	0.731	-112	47
1	0.585	-82.0	27.3
2	0.512	-68.1	18.1
5	0.410	-48.6	8.4
10(0.57°)	0.325	-34.0	6.0
20(1.15°)	0.224	-18.6	1.8
52.4(3.0°)	0.108	- 3.9	0.25
100(5.7°)	0.060	- 0.9	0.06

TABLE 10: Ground Ranges for Different Values of Surface Refractivity for Satellite Altitude of 900 km

(mr)	G <sub>900</sub> Vacuum	G <sub>900</sub> N <sub>s</sub> =270	G <sub>900</sub> N <sub>s</sub> =430
0	3200	3286	3403
1	3194	3270	3364
2	3187	3257	3339
5	3168	3230	3295
10	3136	3190	3242
20	3075	3116	3152
52.4	2882	2906	2925

To show how these range extensions relate to the total ground range, Table 10 has been prepared. While these give the extreme values to be expected for the stations in Table 8 with 98% certainty, the values found for the remaining 2% of the cases at these stations may be considerably outside the extremes of Table 10.

Summary of Effects of Ground-Range Extension. Except in the special case of subrefraction treated later, the ground range is always extended significantly over the value it would have in a vacuum. This range extension means that a radar or communication system will "see" some points beyond the horizon. The "slant range" for these points is actually the length of the curved path shown as AD in Figure 1. Because the horizon range is extended, the elevation angle for rays to points within the new horizon is greater than it would be in a vacuum.

2.4 Elevation-Angle Changes Due to Normal Tropospheric Refraction

Radars usually determine the position of airborne objects by measuring a range and an elevation angle. The range measurement is not seriously modified by the difference in velocity of propagation in the troposphere, but the elevation angle measurement is strongly affected by refraction. Here, however, the problem is to establish the elevation angle error when both ground and airborne locations are known, as shown in Figure 5. Here one has a satellite at point B and wishes to know the increase in angle of incidence on the ground at point A. Path 1 is the direct path in a vacuum; path 2 is the path with a selected standard refraction; and path 3 is the path for a different refractive index profile.

It can be shown that the refraction in the ionosphere and troposphere may be treated separately, and here only the troposphere is considered.

Since Path 1 in Figure 5 is never possible, the change in angle of incidence should be computed between, say, the minimum readily possible angle (Path 2) and that for the particular refractivity under consideration (Path 3). Thus, the increase in  $\alpha_o$  is referenced to a feasible value rather than a fictional one.

The constraint on the various paths in Figure 5 is that they all must correspond to the same ground range, so

$$\phi = \phi_s \tag{9a}$$

where  $\phi_s$  is the central angle for the standard refractivity. Thus, in terms of Figure 4,

$$\phi_o(\alpha_o) + \Delta\phi(\alpha_o) = \phi_s(\alpha_{s0}) \tag{9b}$$

where  $\alpha_{s0}$  is for the standard refractivity of Path 2. This equation must be solved for  $\alpha_o(N_s, \alpha_{s0})$ .

The value of  $\phi_s(\alpha_{s0})$  may be readily calculated by the methods indicated above.  $\phi_o(\alpha_o)$  is obtained from triangle AOD of Figure 3 by applying the law of sines.  $\Delta\phi_s$  may be obtained from (4) and (2a). The approximate equation that must be solved is

$$\sqrt{\frac{2h+R_o \alpha_o^2}{R_o+h}} - \alpha_o + N_s b(\alpha_o) + a(\alpha_o) = \phi_s(\alpha_{s0}) \tag{10}$$

Not only is the equation non-linear, but the functions  $b(\alpha_o)$  and  $a(\alpha_o)$  must be established numerically from Bean and Dutton's tabulated values.

Figure 6 illustrates the same points differently by plotting the increase in  $\alpha$  due to different values of  $N_s$ . Also shown, to indicate the value of choosing a more realistic reference than the vacuum ray, is the additional grazing angle compared with that for the grazing vacuum ray. The total difference for  $N_s = 430$  is almost a degree, so one might think the increased angle more important if he chose the vacuum ray as a reference.

The additional elevation angle has been plotted in Figure 7 for two values of  $N_s$ , assuming a standard minimum of 280 N-units. The upper curve, for  $N_s = 430$  is an extreme case for ordinary refraction, and the maximum increase in grazing angle is only 6 mr. For the more typical situation of  $N_s = 360$  the maximum is only 4 mr. Thus, this is not a highly important factor except in a system depending on this angle for location.

3 DUCTING

3.1 Basic Conditions for Ducting



A surface duct exists when radio waves starting from near the surface at a small enough elevation angle do not leave the atmosphere, but rather are bent around the earth. For waves entering the lower atmosphere from above, the duct results in an extension in range, and possible reductions in signal strength at some ranges, as discussed in this section.

A duct is present at the surface when the gradient of refractivity there is sufficiently negative. Figure 8 shows a normal profile of refractivity compared with the profile that produces "superrefraction" or a duct (extreme case of superrefraction).

Figure 9 shows the lapse rate required to trap waves in ducts of different thicknesses as a function of the elevation angle. The duct must be quite thick for any reasonable lapse rate to result in trapping of waves if the elevation angle exceeds about half a degree. Since the Atlas gives the percentage of ducts greater than 100 meters, the curve for that thickness is particularly useful in estimating the situation in any specified part of the world.

### 3.2 Duct Climatology

Since the ducting is so dependent on climatology, Bean and Cahoon in their Atlas give considerable climatological information for duct and superrefraction conditions. Maps for the months of February, May, August, and September are given with contours of the following types:

% of time -  $\Delta N/\Delta R \geq 100$  N-units/km (superrefractive conditions)  
 % time superrefractive layers are thicker than 100 meters  
 % time -  $\Delta N/\Delta R \geq 157$  N-units/km (ducting conditions)  
 % of ducting layers thicker than 100 meters  
 % time trapping frequency  $\geq 300, 1000, 3000$  MHz  
 Lapse rate exceeded 25, 10, 5, 2% of the time for 100 meter layer.

Superrefraction is quite common in some parts of the world. For example, it exists 90% of the time in August in the Persian Gulf and 75% of the time off the "bulge" of Africa in February. Actual ducting is present 75% of the time in May and August in the Persian Gulf region, where the identification of the phenomenon was made during World War II because radars on the coast of India persistently received echoes from the coast of Arabia. Furthermore, about half of these ducts are more than 100 meters thick.

To give an indication of the situation at specific stations, Bean et al., give cumulative distributions of refractivity gradient for a 100 meter layer for 18 coastal and ocean stations. An example is presented here for Aden, an extreme case, in Figure 10. The range of refractivity gradient at Aden is tremendous, with both subrefractive and ducting conditions occurring for significant parts of the time.

Elevated ducts are exceedingly common. Such ducts exist when there is a sudden drop in refractivity over a range of elevations. The elevated duct can cause dropouts of radio signals between aircraft flying within "line of sight" of each other. However, the angle of incidence on these ducts for a ray that also contacts the ground is usually large enough so that the ducts cannot trap or otherwise significantly affect these rays, so they are ignored here.

### 3.3 Effects of Ducts on Range

For propagation from a satellite the effect of a duct is to reduce the range for any particular ray, but to increase the total range. Figure 11 shows how this can happen. Ray B would go to the horizon in the absence of a duct. It is shown straight from the satellite to the top of the troposphere (the ionosphere may be treated separately); from there it follows a curved path to point 2 on the earth, at which it is tangent to the surface. If a duct is present, the additional refractivity lapse rate in the duct causes additional curvature from the top of the duct to the ground, and the ray strikes the ground at point 1. Not only is this closer to the sub-satellite point, but the angle of incidence is steeper as shown. If this horizon ray for the normal atmosphere were the shallowest ray leaving the satellite that could reach the ground in the presence of a duct, the net ground area within "sight" would be reduced. Ray A, however, reaches the ground in the duct, even though it would normally be tangent to the sphere whose surface is the top of the duct, and would then pass on out of the atmosphere as shown. With the duct, the ray that is tangent at its top is bent on into the duct and strikes the earth at point 3. Since this is beyond point 2, the actual coverage is extended by the presence of the duct. This ray strikes the ground at an incidence angle greater than zero; no tangent ray exists for the duct situation. A ground station at point 2 would see the satellite on the horizon (zero elevation angle) in the absence of the duct, but in the presence of the duct the satellite will appear at a significant elevation angle.

This picture cannot properly describe Ray A because a ray tangent to the top of the duct does not satisfy the conditions for use of geometric optics (Kerr, 1951, p. 53). Wave theory (physical optics) should be used to determine the amplitude of waves arriving at the top of the duct at this angle and detected at point 3, but this is beyond the scope of the treatment here. As the wave strikes the duct at steeper angles, the use of rays (geometric optics) becomes increasingly valid.

The procedure used here to determine the extension in range due to the presence of the duct is based on the assumption that refraction above the duct is identical to what it would be in the absence of the duct. A standard model (the CRPL exponential standard used before) is assumed, and the refractive index at duct height is assumed to be that which would be present if the standard model were extended to the surface. The steps in the procedure are as follows:

The net effect on the range may be expressed as

$$\text{Net increase in range} = -(\text{Reduction in } R_{\phi_0}) - (\text{Reduction in } \Delta G) + (\text{Distance in duct}) \quad (11)$$

For 900 km altitude this can be shown to be (Moore, 1970, pp. 55-59)

$$\text{net increase} = -1.82h_d - 0.731\Delta N_s + \sqrt{2h_d/(\kappa)} \quad (12)$$

where

$$\kappa = \frac{\Delta n}{\Delta R} + \frac{1}{R_0} < 0 \quad (13)$$

Here  $h_d$  is the height of the duct in km and  $\Delta N_s$  is the total change of  $N$  in the duct. This increase in range has been plotted in Figure 12 for the 900 km satellite altitude and the  $N_s = 350$  N-units CRPL standard exponential reference atmosphere. The difference with typical variation in  $N_s$  for the standard atmosphere is small, so additional plots for this variation have been omitted.

The range extension shown in Figure 12 is greatest when the lapse rate is close to the minimum value for trapping. In the limiting case, the range extension appears to be infinite, but this is of course impossible. Two factors limit the range increase at this value of lapse rate: the horizontal extent of the duct is finite, and the situation at this point is one in which ray theory (geometric optics) must be replaced by wave theory (physical optics).

A further consequence of the limiting case is possibly significant; a large reduction in field strength very probably accompanies this large range extension. Although rays have not been traced for the near-limiting angles for this kind of lapse rate, intuition indicates that the rays will spread a long distance on the ground for small variations in angle. Such a spreading of rays is accompanied in geometric optics by a reduction in signal intensity, since the bundle of rays containing a given flux of power spreads this power over a greater range of distances. Hence, because of decreased signal intensity, the apparently large increase in range for near-critical lapse rates may in fact be fictitious because the signals are so reduced in power that they are unusable at the larger ranges.

In spite of these possible limitations, range extensions of 50 to 150 km may occur because of ducts.

### 3.4 Increased Angle of Elevation Due to Ducts

Figure 11 shows that the angle of incidence with which any ray from above the duct strikes the earth is greater than it would be in the absence of the duct.

Since the largest increase in angle of incidence occurs for the ray that would have been tangent to the earth in the absence of the duct, we evaluate here the increase for this ray only. A similar development could be performed for steeper rays.

It can be shown (Moore, 1970, pp. 61-62) that

$$\alpha \approx \sqrt{2h\kappa + \alpha_0^2} \quad \text{radians} \quad (14a)$$

Expressing  $\kappa$  in N-units/km as  $\kappa_N$ , this is

$$\alpha \approx \sqrt{2h\kappa_N + \alpha_0^2} \quad \text{mr} \quad (14b)$$

If  $\alpha_0$  is also expressed in milliradians.

This expression applies either to the ray in the normal atmosphere or to a ray in a duct. At the top of the duct,  $\alpha$  for the ray in the duct is the same as  $\alpha$  for the ray in the normal atmosphere, so we may equate the two, obtaining

$$2h_d\kappa_{Nd} + \alpha_0^2 = 2(-N_s c_e + \frac{1}{R_0} \times 10^6)h_d \quad (15)$$

where  $\kappa_{Nd}$  is the modified refractivity gradient (N units/km) in the duct, and  $c_e(N_s)$  is the constant in

$$N = N_{se} \exp[-c_e(N_s)h] \quad (16)$$

$c_e(N_s)$  is 0.159 for  $N_s = 350$  and 0.187 for  $N_s = 400$  (Bean and Dutton, pp. 65-66).

This may be solved for the value of  $\alpha_0$  in the duct at point 1 on Figure 11:

$$\alpha_0 = \sqrt{2h_d(-N_s c_e - \kappa_{Nd})} \quad \text{mr} \quad (17)$$

Examples of this effect have been plotted in Figure 13. The curves have been continued from the critical lapse rate back to the lapse rate for the model atmosphere, since these rays are not trapped by the duct, but rather are merely refracted more in the duct. Clearly, for thick ducts, the angle of incidence for this ray is quite large, even though the ray would have been tangent ( $\alpha_0 = 0$ ) in the absence of the duct. For a 1 km thick duct  $\alpha_0$  approaches  $2^\circ$ .

The problem of increased angle of incidence for a given location on the earth is not as severe as it is for a given ray, because the ray strikes the earth at shorter range from the satellite, and the ray that would normally strike the earth at that point may also have a significant angle of incidence. This ray may be tracked to the earth from the top of the duct using the methods applied above.

The decrease in range for the ray that would be tangent in the standard atmosphere is plotted in Figure 15. For thick ducts, the reduction in distance may be as great as 100 km, but it is relatively independent of lapse rate in the duct. Figure 13 shows the elevation angle for this ray, and Figure 14 shows the range decrease. Thus, we may use Figure 4 to find the value of  $\alpha_0$  for a ray having the  $\Delta G$  given by reducing that for grazing by the amount shown in Figure 14. The result is plotted in Figure 15. The difference between the results shown in Figure 15 and those shown in Figure 13 is striking--the effect of

duct height is reversed. Physically this can be explained because the ray entering the thicker duct enters at a steeper angle, so the difference in effect due to the different refractivity lapse rates in duct and standard atmosphere is less. The ray for the thinner duct enters the top of the duct more nearly horizontally, so the difference in refractivity makes a bigger difference in distance.

#### 4. SUBREFRACTION

Subrefraction occurs when the refractivity gradient is less negative than normal or is actually positive. This was indicated in Figure 1 where the reduction in range associated with subrefraction was diagrammed. Subrefraction, like ducting and superrefraction, commonly occurs for short distances above the earth or in elevated subrefractive layers. If the refractivity gradient is negative, but with smaller magnitude than normal (lapse rate smaller), the curvature of the rays is less than with normal refractivity gradients. If the refractivity gradient is positive, the rays actually curve upwards, whereas normal and superrefraction cause downward curvatures.

Calculated values for this reduction in range are shown in Figure 16. For slight subrefractivity (refractivity gradient = 0), the range reduction is really significant only for a thick subrefractive layer with a fairly large  $N_s$ . On the other hand, when the refractivity gradient is strongly positive, all the cases plotted give loss in horizon exceeding 50 km except for the thinnest region (0.1 km) and the smaller  $N_s$  (270).

#### 5. SUMMARY OF TROPOSPHERIC REFRACTION EFFECTS

The troposphere affects radio waves traveling through it because its refractive index differs from that of a vacuum, and this refractive index varies with position in the troposphere. The deviation of the refractive index from unity is only a few parts in ten thousand, so its effect is most significant for waves traveling nearly horizontally. Because of this, most emphasis in this analysis has been on the horizon ray.

Simplified models have been used in this analysis, for they illustrate the principles involved, show the magnitudes of the phenomena involved, and yet permit a wide variety of computations based on the relatively meager climatological information available in many parts of the world.

Refraction in the troposphere causes significant variations in the distance to the horizon. The total refraction may be expressed, with moderate error, in terms of the surface value of refractive index. Usually this value is given instead, however, by the refractivity, the deviation of the refractive index from unity expressed in parts per million. Extreme values of refractivity encountered at sea level under normal conditions lie between 270 and 430 N-units.

Since refraction is actually due to the gradient of refractivity, unusual surface conditions result in unusual gradients and unusual refraction. Large negative gradients result in ducts; less-than-normal negative gradients, or positive gradients, result in subrefraction. Although surface ducts and subrefractive layers seldom extend as high as 1 km above the surface, they have a major effect on propagation of the horizon ray because it travels so far in the lowest few hundred meters of the troposphere.

TABLE 11: Summary of Refractive Effects on Range

Conditions	Surface Refractivity Atmospheric Model				Source Figures
	270	350	400	420	
Horizon Distances in km relative to Distance in Vacuum					
Subrefraction					
Lapse rate = -100, $h_g = 1.0$	-22	-8	---	---	Fig. 16 and Fig. 4
$h_g = 0.1$	+39	+58	---	---	
Lapse rate = 0, $h_g = 1.0$	36	53	---	---	
$h_g = 0.1$	62	95	---	---	
Normal refraction $\alpha_0 = 0$	86	143	181	194	Fig. 4
Duct					
Lapse rate = 500, $h_d = 0.1$	---	163	200	---	Fig. 12 and Fig. 4
$h_d = 1.0$	---	177	202	---	
Lapse rate = 200, $h_d = 0.1$	---	208	247	---	
$h_d = 1.0$	---	315	340	---	
Distances in km at 3° Relative to Distance in Vacuum					
Normal refraction	24	34	39	41	Fig. 4

The effects on range of variations in tropospheric properties are summarized in Table 11 where horizon distances are shown relative to the horizon distance in a vacuum for a variety of conditions from subrefraction through ducting.

For the extreme case of subrefraction listed, the range to the horizon is actually 22 km less than the range in a vacuum. For the extreme case of ducting, the horizon range is 340 km more than the range in

a vacuum. Thus, the variation in horizon range for these conditions is over 360 km! Even for normal refraction this variation is shown to be over 100 km. The table also lists the much smaller range extensions for normal refraction for rays making an angle of  $3^\circ$  with the earth's surface. At this angle the effects are much smaller than at the grazing angle; accordingly, duct and subrefraction effects have not been listed for the steeper angle.

Refraction causes rays coming from a transmitter in space to arrive at the surface with steeper angles than they would have had in a vacuum. Since normal refraction ordinarily is due to an atmosphere with a sea-level refractivity of at least 280 N-units, the increased angle of incidence due to refraction is measured with reference to the incident angle for rays in an  $N_s = 280$  atmosphere. Table 12 shows the increased angle of incidence for two cases of normal refraction and for four duct conditions. With normal refraction the maximum increase in incident angle is only a little more than the grazing value of 5.2 milliradians shown. This is so small that normal refraction should have little practical effect.

TABLE 12: Increased Angle of Incidence Due to Refraction (in Milliradians)  
Zero Reference is Angle for  $N_s = 280$

Condition	$N_s = 350$	$N_s = 430$	Source
Normal refraction	2.6	5.2	Fig. 6
Duct Height 0.1 km, Lapse rate 200	7.9		
Lapse rate 500	12.0		Fig. 7
Duct Height 1.0 km, Lapse rate 200	19.5		and Fig. 13
Lapse rate 500	32.0		

This paper is a summary of R.K. Moore, "Tropospheric Propagation Effects on Earth-Space Low Elevation Angle Paths," University of Kansas Bulletin of Engineering No. 61 (1970). The complete report (106 pages) is available from the author for \$4.00 in the U.S. and Canada, \$6.00 in Europe, to cover postage and handling.

#### REFERENCES

- Bean, B.R., B.A. Cahoon, C.A. Samson, and G.D. Thayer, World Atlas of Atmospheric Radio Refractivity, ESSA Monograph 1, U.S. Govt. Print. Off., Washington, (1966).
- Bean, B.R. and E.J. Dutton, Radio Meteorology, National Bureau of Standards Monograph 92, U.S. Gov't. Print. Off., Washington, (1966).
- Kerr, D.E., Propagation of Short Radio Waves, vol. 13, MIT Rad. Lab. Ser., McGraw-Hill Book Co., Inc., New York, (1951).
- Millman, G.H., "Atmospheric Effects on Radio Wave Propagation," in Modern Radar Analysis, Evaluation, and System Design, R.S. Berkowitz, ed., John Wiley & Sons, Inc., N.Y., (1965).
- Millman, G.H., "A Survey of Tropospheric, Ionospheric, and Extraterrestrial Effects on Radio Propagation Between the Earth and Space Vehicles," General Electric Heavy Military Electronics Department, Syracuse, N.Y., Report No. R66EMH1, (January 1966).
- Moore, R.K., "Tropospheric Propagation Effects on Earth-Space Low Elevation Angle Paths," University of Kansas Bulletin of Engineering, No. 61, Lawrence, Kansas, (1970).
- Weisbrod, S. and L.J. Anderson, "Simple Methods for Computing Tropospheric and Ionospheric Refractive Effects on Radio Waves," Proc. IRE, Vol. 47, No. 10, pp. 1770-1777, (October 1959).

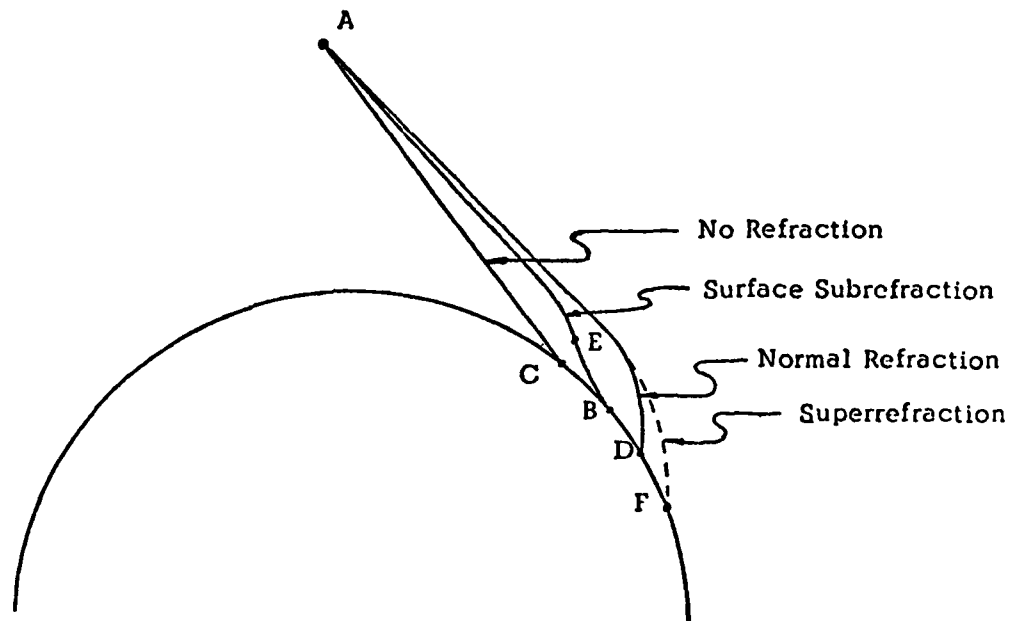


FIGURE 1: Tropospheric Refraction

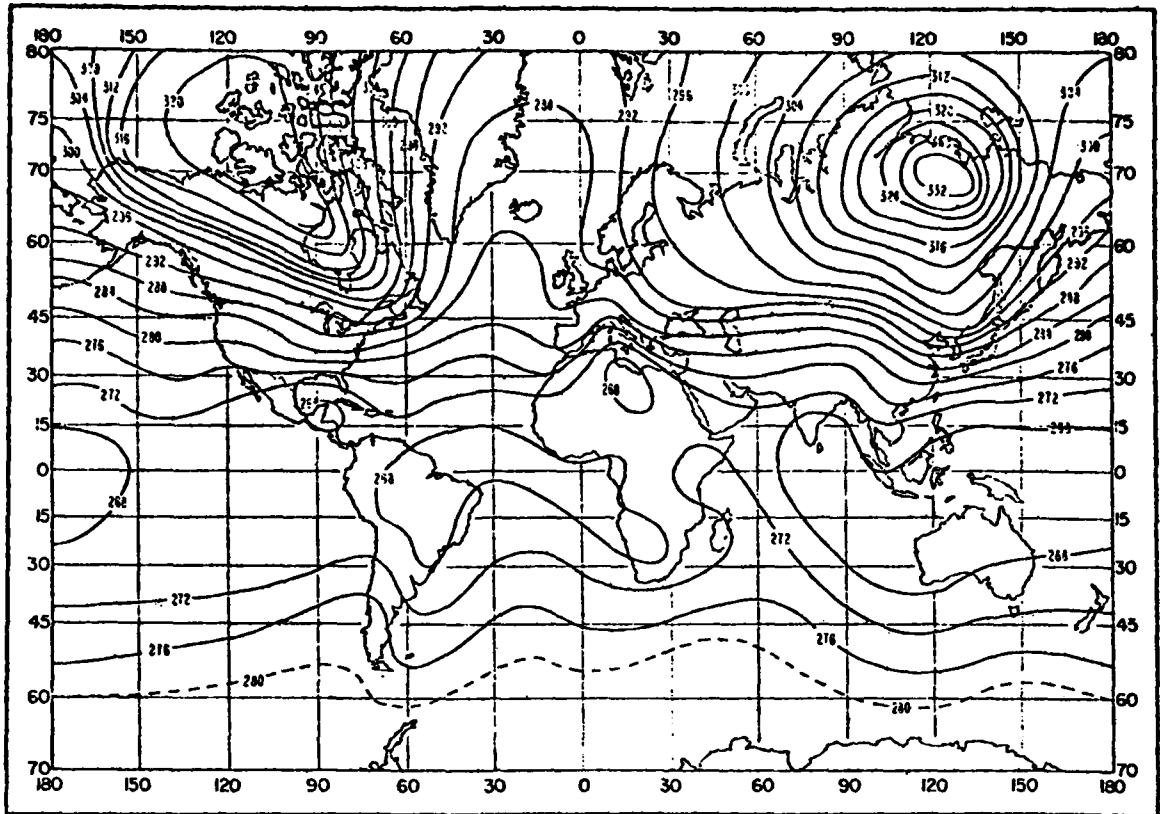


FIGURE A-2. Mean sea-level dry term,  $D_0$ : February.

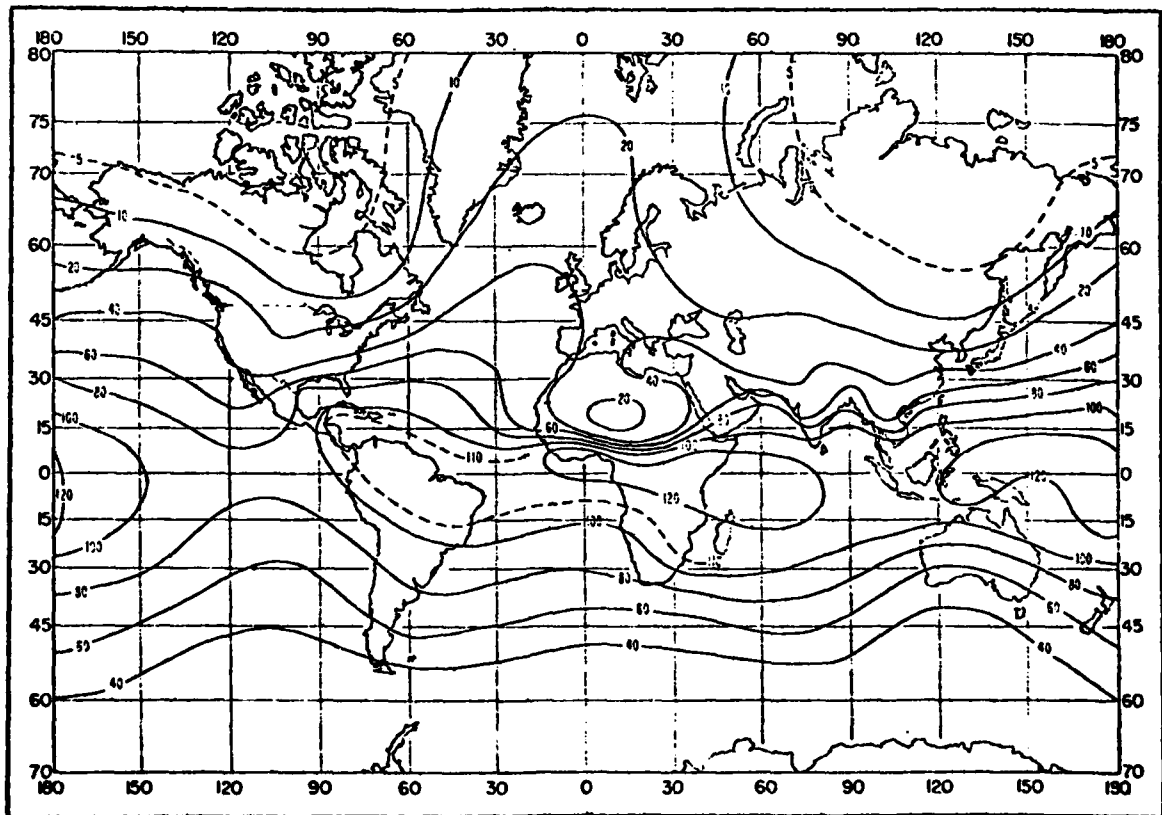


FIGURE A-3. Mean sea-level wet term,  $W_0$ : February.

FIGURE 2: Sample Refractivity Maps (Bean, et al., 1966)

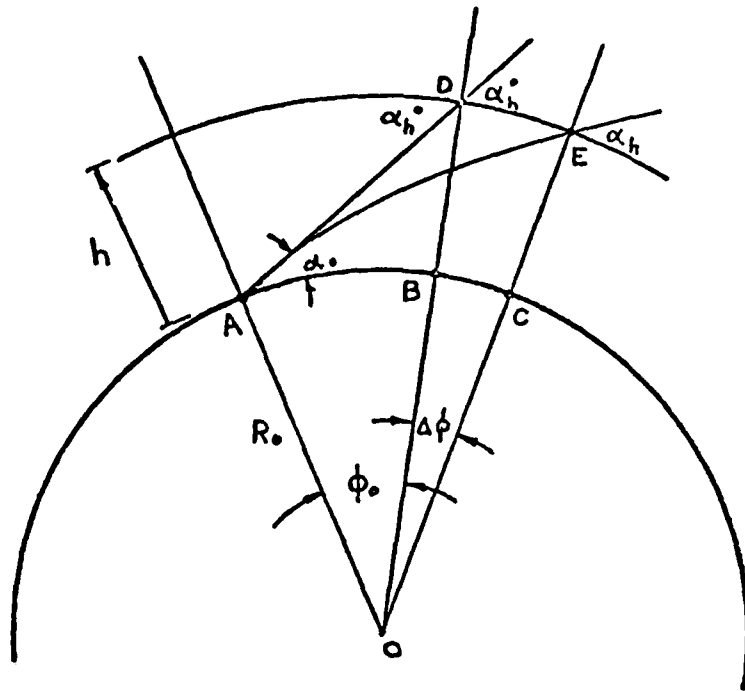


FIGURE 3: Relation of Tropospheric Refraction to Range Extension

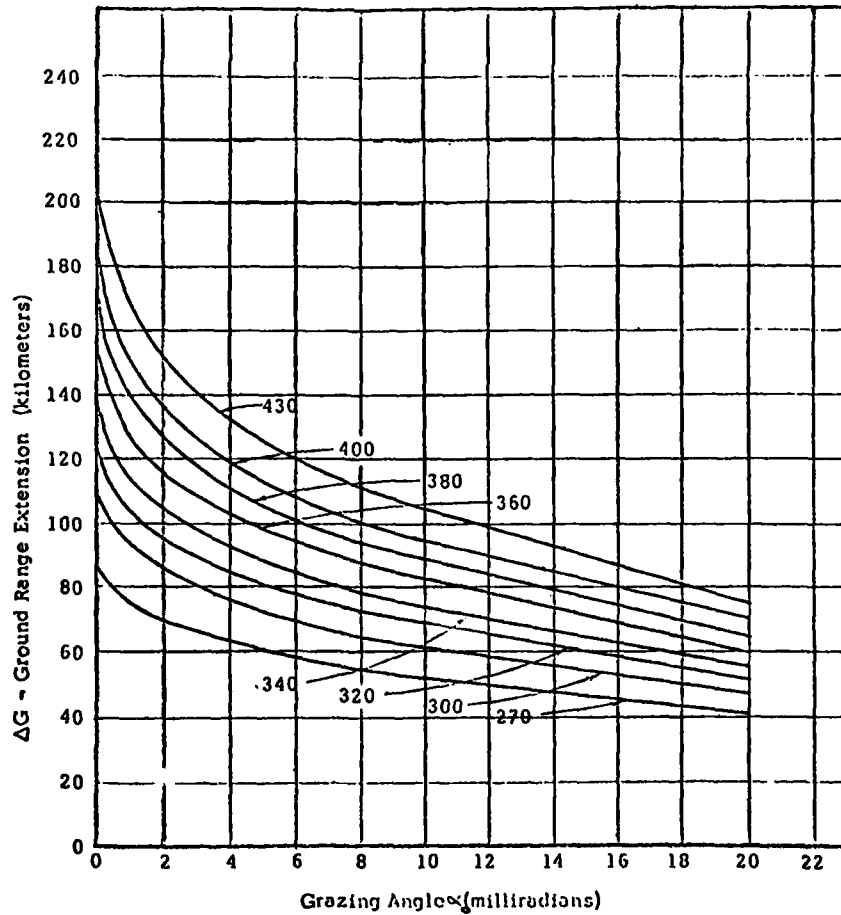


FIGURE 4: Ground Range Extension Due to Tropospheric Refraction -- Parameter is Surface Refractivity in N-units

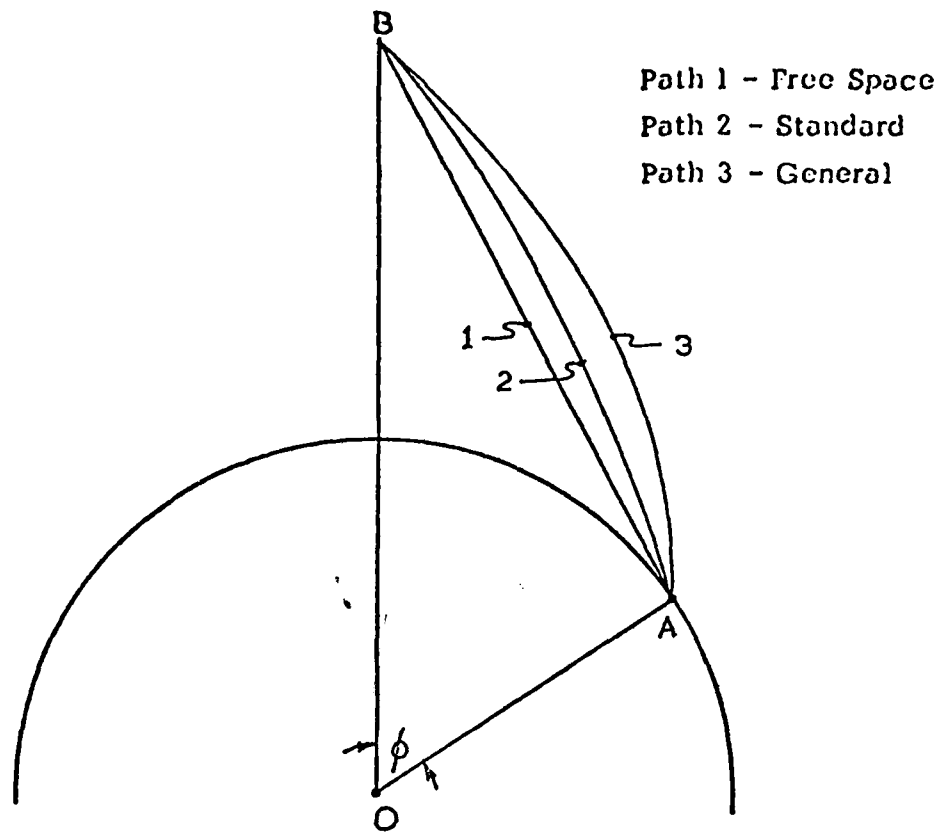


FIGURE 5: Geometry of Fixed-End-Point Error Problem

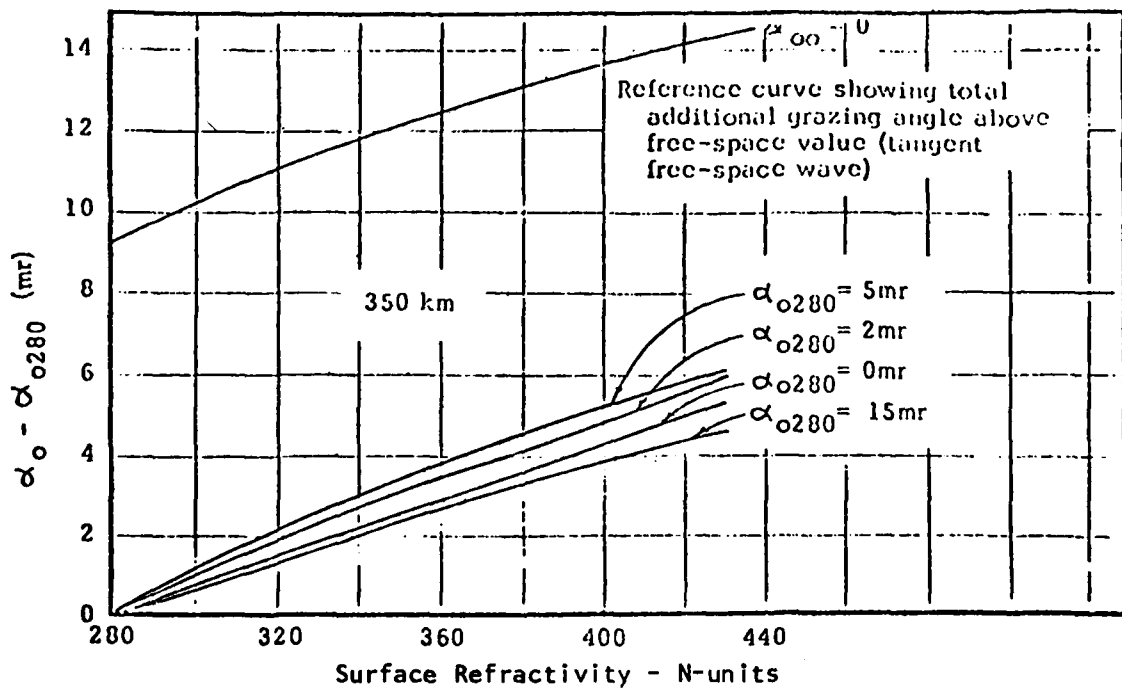


FIGURE 6: Additional Grazing Angle Due to Tropospheric Refraction  
 Reference:  $N_s = 280$  N-units



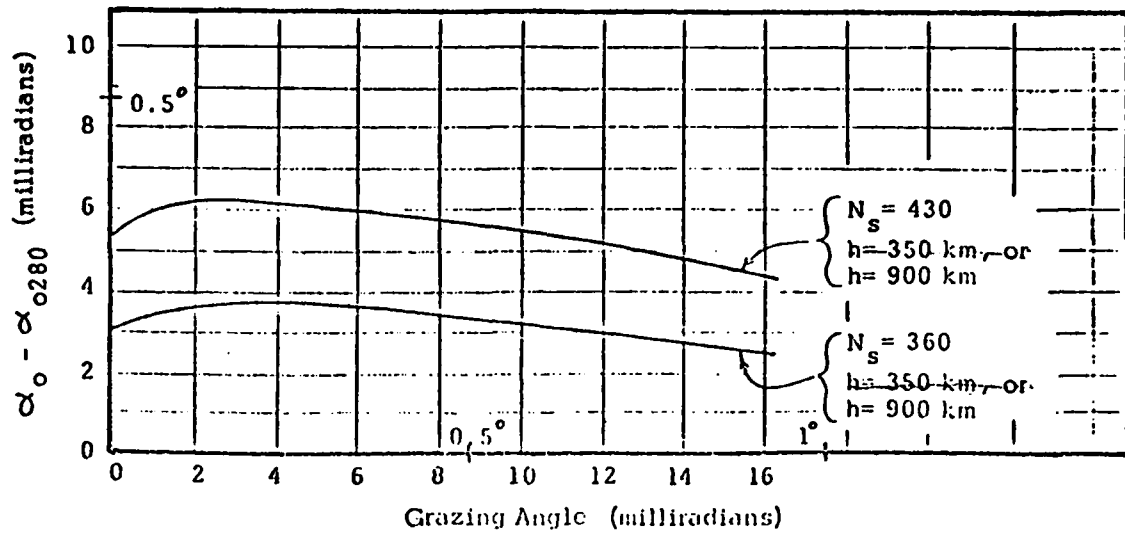


FIGURE 7: Additional Grazing Angle Due to Tropospheric Refraction  
Reference:  $N_s = 280$  N-units

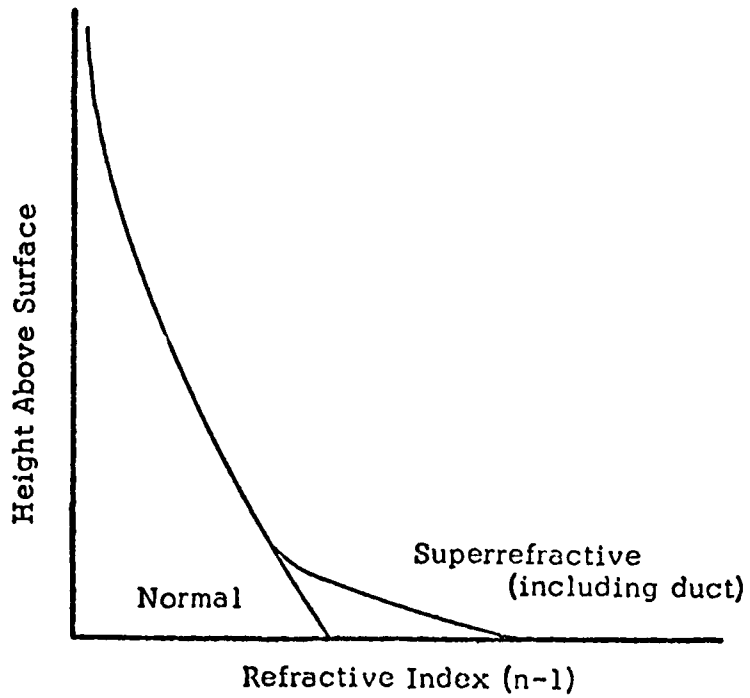


FIGURE 8: Variation of Refractive Index with Height Showing Surface Duct and Superrefraction

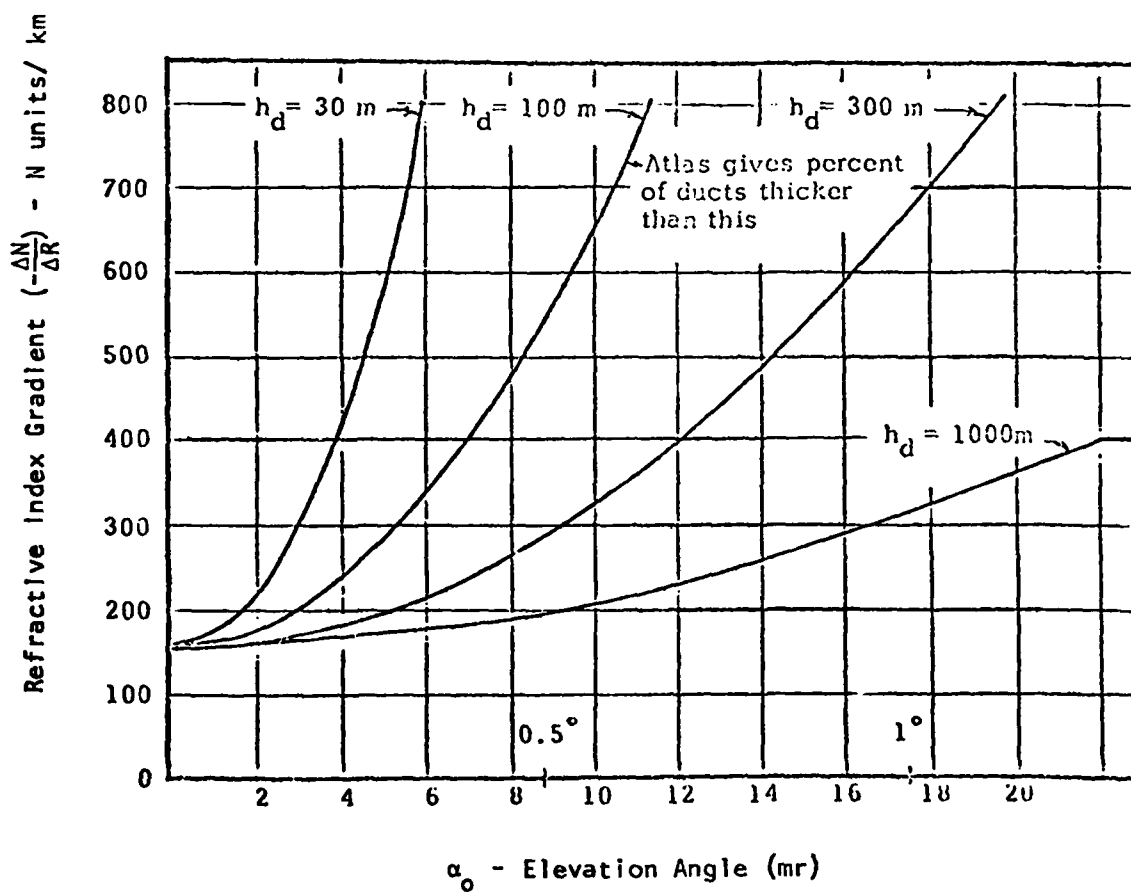


FIGURE 9: Refractive Gradient to Trap Various Elevation Angles

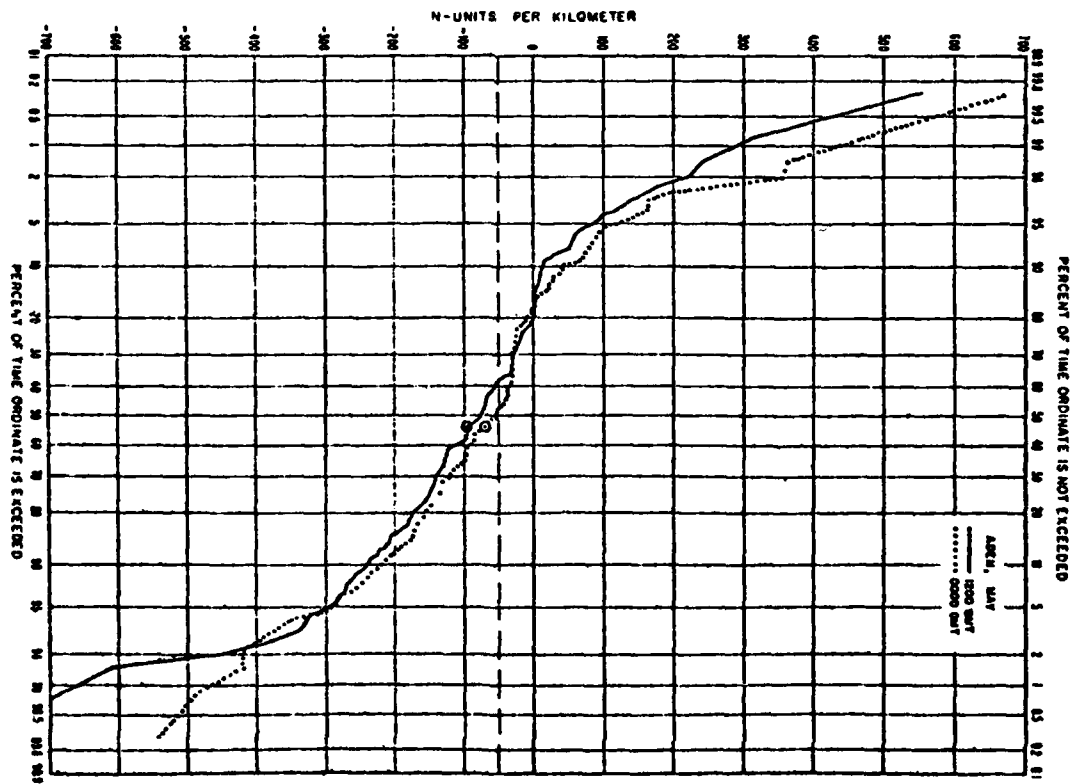
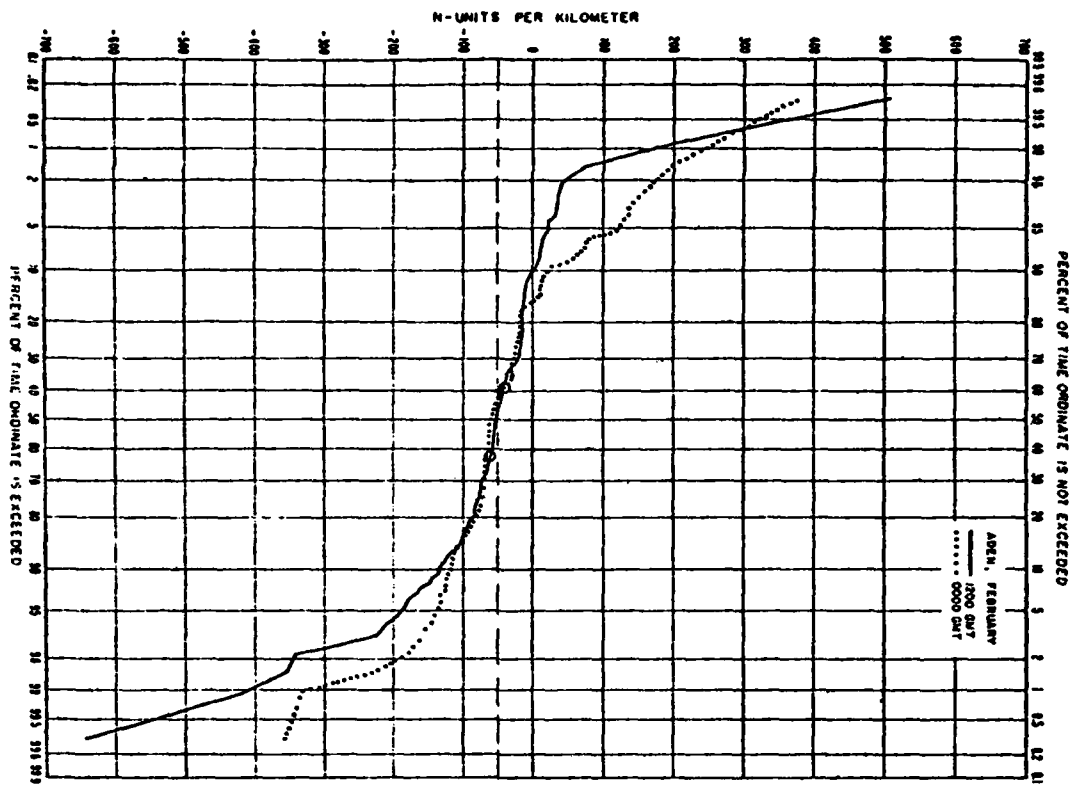


FIGURE 10: Cumulative Probability Distributions of  $dN/dh$  for Ground-Based 100-m layer: Aden, Arabia (February, May).

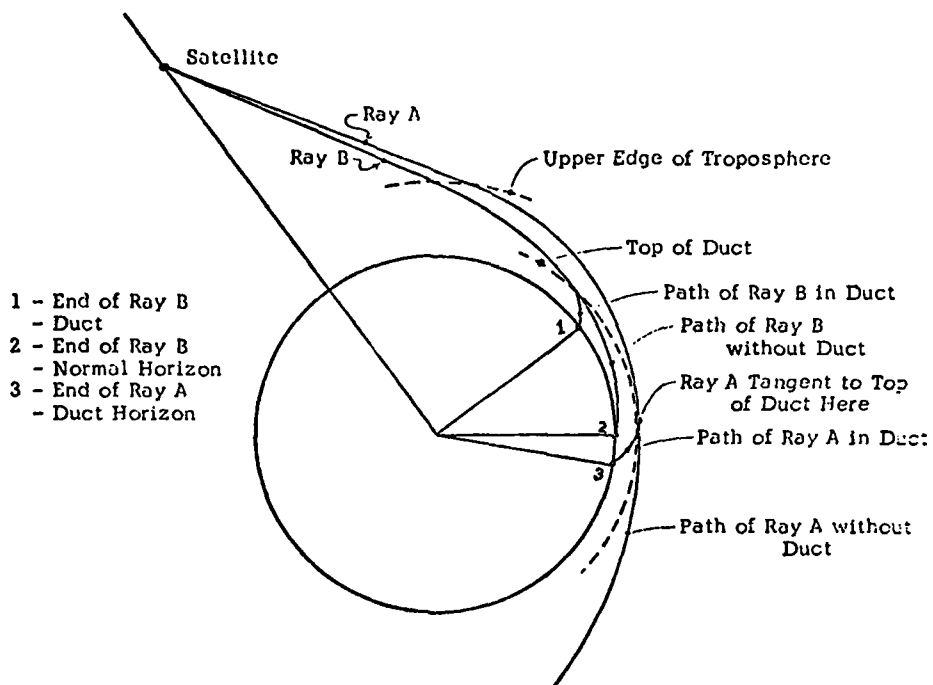


FIGURE 11: Effect of Duct on Maximum Range

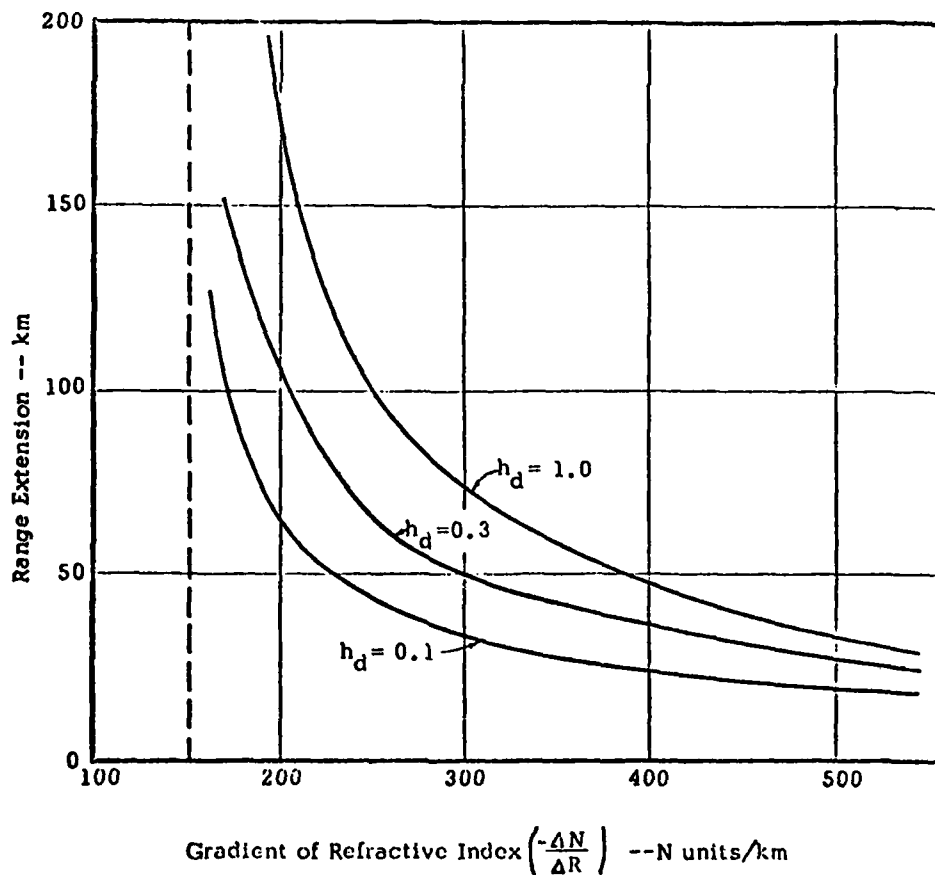


FIGURE 12: Range Extension in Ducts  
CRPL Standard Exponential Atmosphere Above Duct.  
Range Compared with Range for Standard Atmosphere.  
With  $N_s = 350$  Height of 900 km Assumed for Satellite

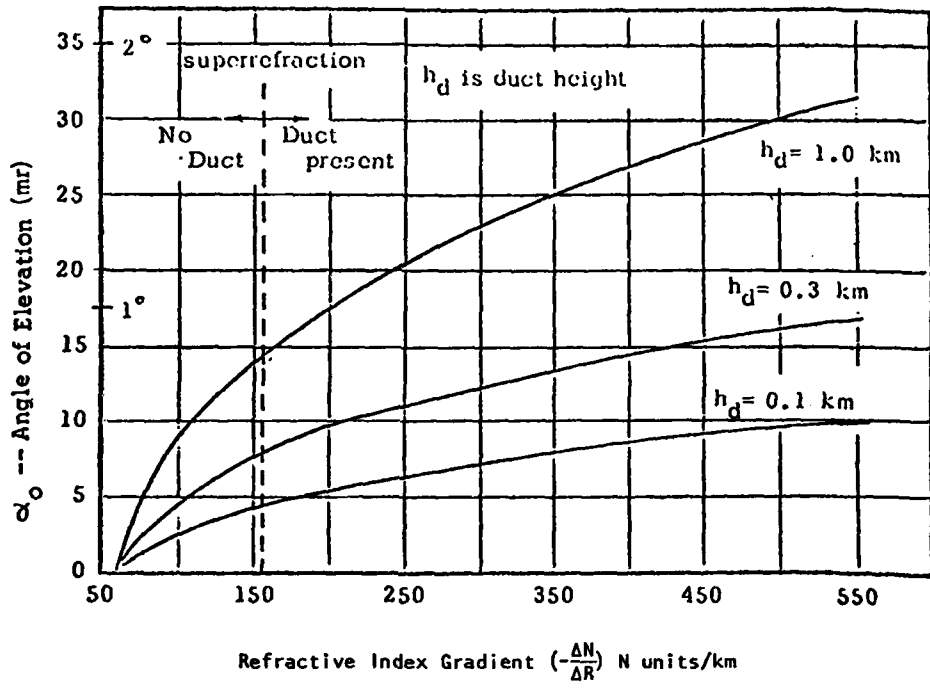


FIGURE 13: Increased Angle of Elevation Due to Ducts  
Incidence Angle for These Rays Would Be Zero for  
CRPL Standard Atmosphere with  $N_s = 350$ .

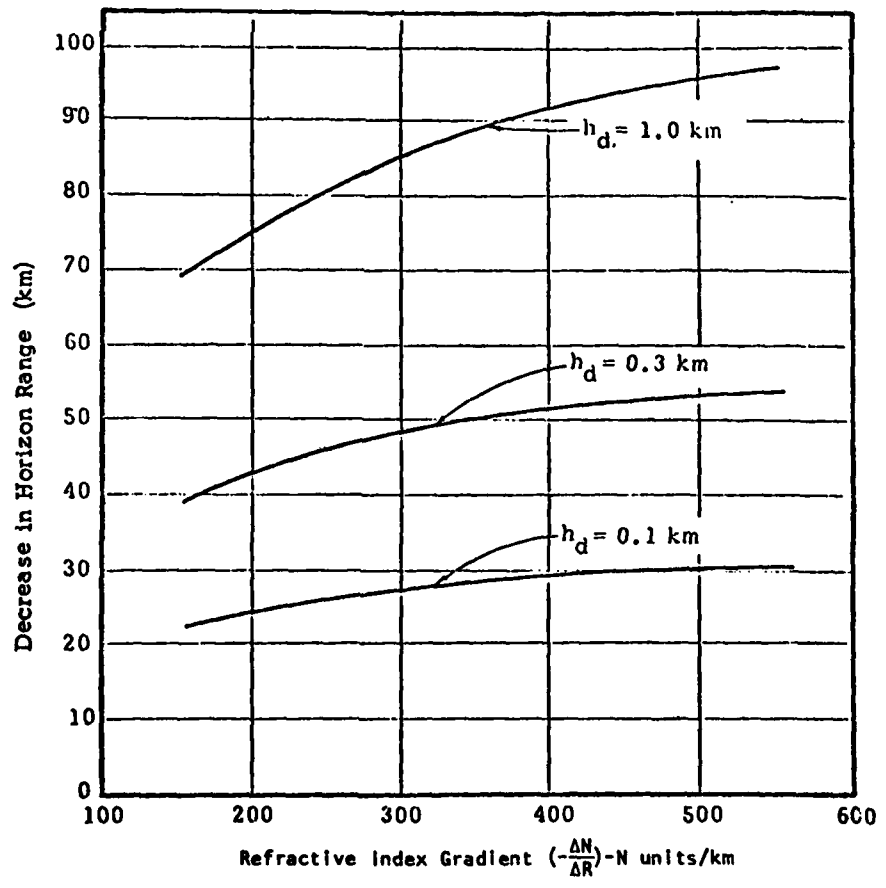


FIGURE 14: Decrease in Range Due to Ducts for Ray That Would Normally  
be Horizon Ray

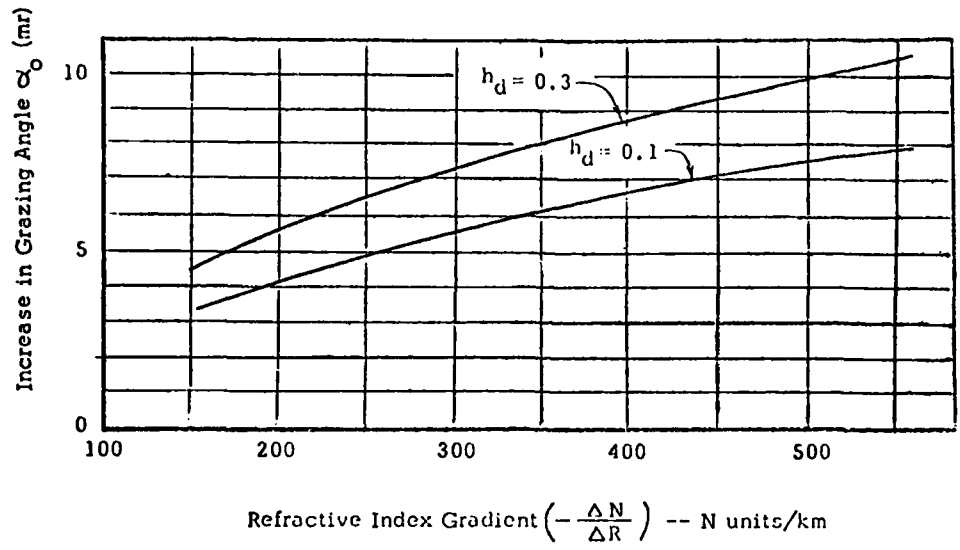


FIGURE 15: Increase in Grazing Angle at the Point Where Rays that Would be Tangent to the Earth in a Normal Atmosphere Strike in a Duct.

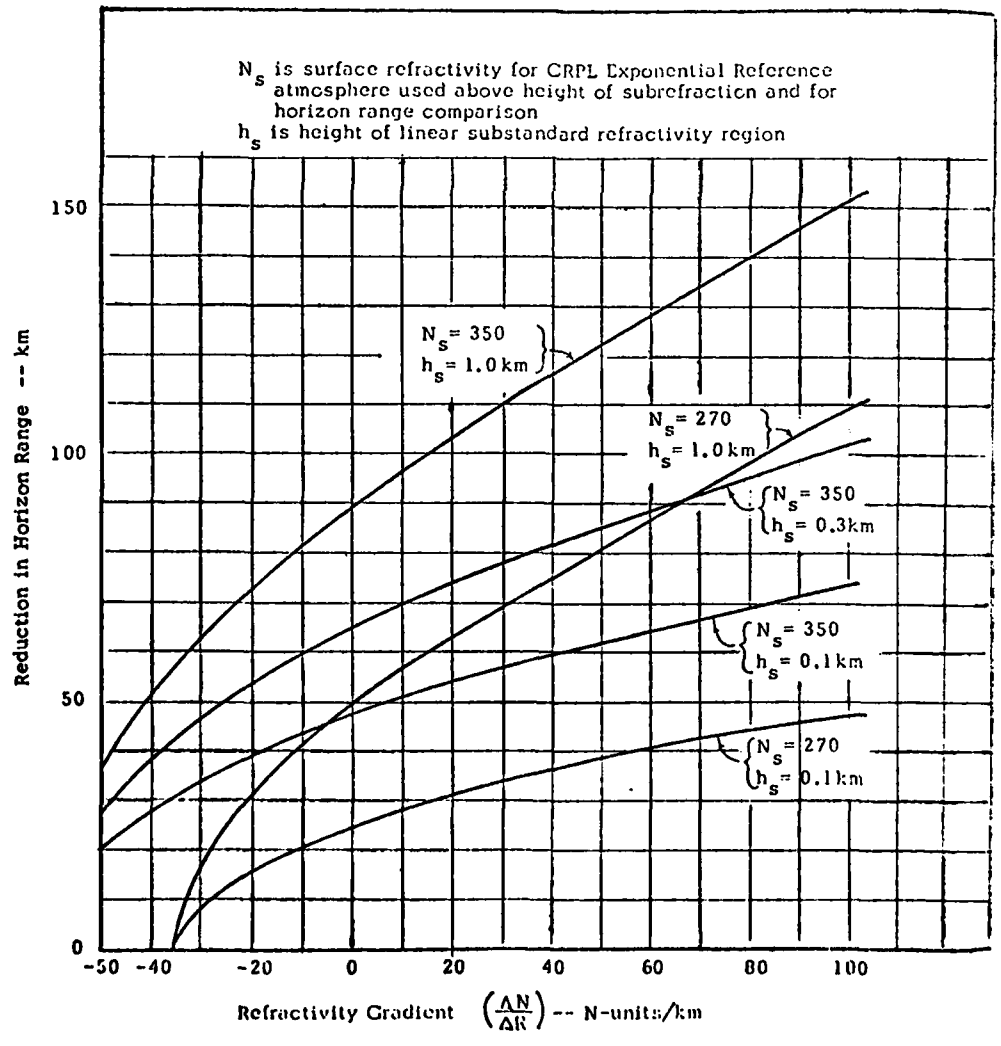


FIGURE 16: Reduction in Horizon Range Due to Substandard Refraction

# A REVIEW OF THEORETICAL PREDICTION TECHNIQUES OF TRANSMISSION

## PARAMETERS FOR SLANT-PATH, EARTH-SPACE COMMUNICATIONS

B.G. Evans and A.R. Holt

University of Essex  
Wivenhoe Park  
Colchester CO4 3SQ

### SUMMARY

A review of the methods needed to calculate transmission parameters such as attenuation and crosspolarisation due to a precipitation filled medium on an earth-space path are given. A comparative view of the electromagnetic techniques associated with single-particle scattering as applied to rain and ice are given. A model which is composed partly of ice and partly of rain is proposed and some interesting results of its application given. The importance of the ice/rain model in determining actual crosspolarisation on a satellite path are discussed. In addition, details of backscattering calculations which have been performed are presented.

We give some results of the extension of the theoretical techniques to millimetre waves and point out some interesting simplifications that can be made in generating scattering data in this region.

### 1. INTRODUCTION

The planning and operation of communications systems between an earth-orbiting satellite and an earth-station necessarily require a knowledge of the propagation of electromagnetic radio waves through the troposphere and ionosphere. In this paper we will be concerned with tropospheric propagation effects on earth-space paths and indeed these will predominate as the frequency of operation moves from the microwave to the millimetre bands. It is possible to segregate tropospheric effects on earth-space paths between those based upon (a) particle scattering e.g. attenuation, dispersion and depolarisation and (b) bulk refractive index variations e.g. scintillation, angle of arrival and multipath. Apart from very low elevation links the effects based upon particle (rain, ice, aerosol) scattering predominate and thus will form the subject of this paper.

Although systems planners place more reliance upon experimental than theoretical determination of propagation phenomena, theoretical prediction is still necessary in order to augment and help interpret experimental results, as well as to supplement them in order to make global planning economic. It might thus be considered sufficient to develop theoretical models for attenuation and depolarisation, being the main system degradations of current concern. However, in the experimental determination of both of these transmission parameters, techniques such as radiometry and radar are often used. In the latter especially, back-scatter as well as forward scatter information is required. With the importance of millimetric radar systems in mind and their operation within the troposphere we include in this paper data on reflectivity and back-scatter cross section which has implications not only on radar systems per-se, but also on the determination of forward transmission parameters.

The problem of predicting propagation through a medium containing precipitation particles has historically been broken down into:

- (i) the single particle scattering problem
- and (ii) the medium modelling problem

The first part of the prediction problem is to evaluate the 'scattering amplitude' of the particles given their shape, size, orientation, refractive index. The latter assumes that we are dealing with homogeneous particles, which need not be the case of course, for ice/water compositions known to exist in the melting region. It is often the lack of precise information about the particles from meteorological sources that makes prediction unsatisfactory, not to mention inaccurate. This stage of the problem relies heavily on classical electromagnetic theory and the use of computers in complex and time-consuming numerical calculation. Here the name of the game is 'efficient computational methods to match the specific scattering problem'.

Having obtained the scattering amplitudes for a range of particles one can then use them as input to the next stage of medium modelling. Here we are interested in the range of size and shapes, distributions of orientations and the use of such information for an assemblage of particles to produce an overall propagation coefficient. Having obtained this propagation coefficient we may derive from it the salient transmission or reflection parameters appropriate to the system being considered.

In the following sections we will review the range of methods available for both single scattering and medium modelling and perhaps most importantly discuss their relative applicability.

## 2. SINGLE-PARTICLE SCATTERING

### 2.1 General Methods

There are four basic techniques that have been applied to the solution of electromagnetic scattering from dielectric precipitation particles and they are in date order:

- (i) Point-matching - Oguchi<sup>(1)</sup> and Morrison and Cross<sup>(2)</sup> (1973-74).
- (ii) T-matrix - Warner<sup>(4)</sup> Barber and Yeh<sup>(5)</sup> (1975)
- (iii) Uni-moment - Chang and Mei<sup>(3)</sup> (1976)
- (iv) Fredholm-Integral method (F.I.M.)- Holt, Uzunoglu and Evans<sup>(6)</sup> (1976)

The dates given are those when the techniques were first applied to precipitation problems. Some methods existed prior to these dates, for instance, Waterman first proposed the T-matrix method for scattering from conducting bodies in 1965<sup>(7)</sup>. In addition and prior to the more exact techniques becoming available perturbation and variational techniques were used<sup>(8,9)</sup> but these have been superseded by the above. In the above mentioned literature tables of scattering amplitude for raindrops, ice and hail particles are to be found for the microwave bands up to 30 GHz or thereabouts. However, relatively few data exists up into the millimetre wave spectrum.

It is with respect to the extension of these techniques, either to higher frequencies (i.e. larger drops with respect to wavelengths) or to different shapes (ice and water/ice crystals and particles), that a comparison is pertinent. As far as oblate spheroidal raindrops are concerned at frequencies up to 30 GHz, the methods have produced comparable results even though efficiencies of production are arguable.

#### Point-matching methods

This involves a modal expansion of the fields interior and exterior to the scatterer. The boundary conditions are matched on the surface of the scatterer. Its main limitations concern large particles and highly eccentric shapes. Not only is the number of matching points required, but the very validity of the modal expansion for the exterior field is open to doubt - it is not clear when the Rayleigh hypothesis holds.

#### T-Matrix method (or Extended Boundary Condition Method)

This was originally formulated in 1965 for perfect conductors but later adapted for perfect dielectrics. The basis of the method is to consider the scattered field as due to a set of surface currents on the particle; for dielectrics the equivalence principle is used, replacing also the field inside the scatterer by an equivalent set of surface currents. Again modal expansions are involved. Application of the surface boundary condition again results in a set of matrix equations (for the expansion coefficients). This method is considered to be superior to the point-matching method, but again as the shape becomes distorted, there are convergence problems - with the number of terms required. Shapes with corners cannot be treated, as essentially the surface current would have a singularity. The method, though, is applicable to many shapes.

#### Uni-moment methods

Consists of a finite element technique which in principle is very adaptable to a wide range of geometries. It can also be used to deal with inhomogeneous scatterers. However, the drawback is in numerical stability and accuracy, particularly for the larger particles.

#### F.I.M

This method employs a volume integral equation formulation and obtains the scattering amplitudes by determining the internal field. The solution is in fact obtained for the Fourier transform of the internal field. The method is stable, and convergence is guaranteed. Part of the calculation is independent of the refractive index of the scatterer, and thus the method can be very efficient in applications. It is, however, in practice limited to regular shapes such as spheroids, ellipsoids, finite circular cylinders, and infinite cylinders of elliptical or rectangular cross-section.

### 2.2 Extended F.I.M.

The volume integral equation describing the scattering of a plane wave, of wave vector  $\underline{k}_0$ , by a scatterer of volume  $V$  and dielectric  $\epsilon(\underline{r})$  is

$$\underline{E}(\underline{r}) = \underline{J}_0 \exp(i\underline{k}_0 \cdot \underline{r}) + \int_V G(\underline{r}, \underline{r}^1) \cdot \gamma(\underline{r}^1) \underline{E}(\underline{r}^1) d\underline{r}^1 \quad (1)$$

where

$$G(\underline{r}, \underline{r}^1) = \left(1 + \frac{1}{2} \frac{VV}{K_0}\right) \exp\left(\frac{iK_0 |\underline{r} - \underline{r}^1|}{4\pi |\underline{r} - \underline{r}^1|}\right) \quad (2)$$

$$\gamma(\underline{r}) = K_0^2 (\epsilon(\underline{r}) - 1) = K_0^2 n_0^2(\underline{r}) \quad (3)$$



$$\mathcal{J}_\lambda = 1 - \bar{K}_\lambda \bar{K}_\lambda \text{ for any subscript } \lambda. \quad (4)$$

$\mathbf{1}$  denotes the unit tensor, and dyadic quantities are in bolder type.

The dyadic scattering amplitude for scattering in the  $\underline{K}_s$  direction is

$$f(\underline{K}_s, \underline{K}_0) = \frac{1}{4\pi} \mathcal{J}_s \cdot \int_V \exp(-i\underline{K}_s \cdot \underline{r}) \mathcal{V}(\underline{r}) \underline{E}(\underline{r}) d\underline{r} \quad (5)$$

The scattering parameters can thus be determined from knowledge of the field inside the scatterer only.

Equation (1) is extremely difficult to solve directly since the Green's function is singular, so in the FIM we iterate the equation and deal with the singularity analytically. This results in a pair of equations.

$$\int d\underline{k} \underline{K}(\underline{K}, \underline{k}) \cdot \underline{C}(\underline{k}, \underline{K}_0) = \mathcal{J}_0 \underline{U}(\underline{K}, \underline{K}_0) \quad (6)$$

$$f(\underline{K}_s, \underline{K}_0) = \frac{1}{4\pi} \mathcal{J}_s \int d\underline{k} \underline{U}(\underline{K}_s, \underline{k}) \underline{C}(\underline{k}, \underline{K}_0) \quad (7)$$

Where  $\underline{C}(\underline{k}, \underline{K}_0)$  is the Fourier transform of the field inside the scatterer,  $\underline{K}$  is a non-singular kernel and  $\underline{U}(\underline{K}, \underline{k})$  is the first Born term (as in the Rayleigh-Gans approximation). Equation (6) is a Fredholm integral equation of the first kind for the transform of the interior field.

We solve these equations by a Galerkin procedure - we approximate the integrations in (6) by numerical quadrature, thus converting this to a matrix equation. The process is very stable since a variational principle is satisfied.

The extension to the method <sup>(10)</sup> consists in expanding  $\underline{C}(\underline{k}, \underline{K}_0)$  as a Fourier series in the azimuthal angle of  $\underline{k}$ . This results for axi-symmetric scatterers in the main matrix becoming block-diagonal and in consequence, not only is the number of matrix elements reduced, but also we have only to solve a number of matrix equations whose dimension is far less than the original matrix equation. Thus the calculation can be extended to much larger values of  $k_0 a$ . The stages are:

- (i) Calculation of a set of basic integrals dependent on  $k_0$  and particle shape parameters - but not on refractive index.
- (ii) Calculation of the matrix elements
- (iii) Solution of a set of matrix equations and calculation of scattering amplitudes.

It is noted that one calculation of the matrix elements in stage (ii) suffices for all scattering amplitudes for any incident direction and/or polarisation. Since also the integrals in stage (i) do not depend on the refractive index of the scatterer, we can perform calculations for a given wavelength, and for a range of refractive indices very economically.

As an example we show the scattering amplitudes  $f_0$ ,  $f_V$ ,  $f_H$  for incidence along the axis of symmetry, and for vertical and horizontal polarisations incident perpendicular to the axis of symmetry of an oblate spheroidal raindrop of equivolumetric radius ( $\bar{a}$ ). Also shown is the Mie amplitudes for spheres of radius  $\bar{a}$  in table 1.

The complexity of the general solutions discussed so far has been necessitated by the large and complex value of refractive index for water in this region, and by the size of raindrops, up to 0.35 cms radius. However, ice (crystals and hail) has a much smaller refractive index which is predominately real (1.78 + i0.0024).

### 2.3 Approximations for ice

Ice occurs in two forms in the troposphere firstly in the form of hail whose sizes and shape are not dissimilar to rain, and secondly, in the forms of very small crystals ( $\leq 1\text{mm}$ ) existing above the melting layer. We have investigated the applicability of several approximations to the exact scattering theory<sup>(11,12)</sup> for these cases:

- (i) Rayleigh ( $k_0 a \ll 1$ ,  $k_0 |n_0| a \ll 1$ )
- (ii) Rayleigh-Gans ( $|n_0 - 1| \ll 1$ ,  $|n_0 - 1| k_0 a \ll 1$ )
- (iii) Van der Hulst ( $|n_0 - 1| \ll 1$ ,  $k_0 a$  large)

We find that the approximations do not yield valid results for hail but that the Rayleigh approximation can be used with reservations for ice crystals. Such high altitude crystals are predominantly needle or plate shaped and in our work we have taken highly eccentric oblate and prolate spheroidal models respectively for these.

The Rayleigh approximation gives a forward scattering amplitude

$$f_{V,H}(\theta) = k_0^2 \bar{V} \cdot g(a/c, n, \theta) \quad (8)$$

Where  $\bar{V}$  is the volume of the spheroid with axes,  $a, c$ ;  $\theta$  is the incidence angle. Evaluation of this together with the exact FIM results indicates good approximation up to 30 GHz for various crystal sizes and eccentricities. However, this does not hold in the backward direction. We make the point here, that this formulation assumes that ice crystal shapes do not affect the scattering significantly. This we consider in section 2.5.

#### 2.4 Elevation angle relationships

In earth-space paths we need to calculate the scattering amplitudes at an arbitrary elevation angle  $\alpha_0$ . This would infer lengthy and expensive calculations for each satellite path. However, we have found that fortunately a simple rule exists relating the three principle calculated amplitudes to those at any angle  $\alpha_0$ .

$$f_{V,H}(\alpha_0, \bar{a}) = f_0(0, \bar{a}) \cos^2 \alpha_0 + f_{V,H}(\pi/2, \bar{a}) \sin^2 \alpha_0 \quad (9)$$

We have found this to be applicable for forward scattering for both rain and ice (including the approximation in 2.3<sup>(11)</sup>) and for values checked, up to 30 GHz. It is not so generally applicable for the backward direction.

#### 2.5 Shape effects of scatterers

##### Rain

In the majority of numerical evaluations conducted the assumption of oblate spheroidal shape is made. Oguchi<sup>(13)</sup> has investigated the validity of this assumption, in particular for the cardioid shapes of the larger real-raindrops as described by Pruppacher and Pitter<sup>(14)</sup>. He finds that the implications of the approximation are negligible.

##### Hail

Barge<sup>(15)</sup> and others have investigated the shapes of hail and whilst these have been found varied, the oblate spheroidal approximation has been found to be representative. Bringi and Seliga<sup>(16)</sup> have investigated the effects of perturbations to hail-stone shapes and found that these can be significant.

##### Ice crystals

There is much more variability to the shape of ice crystals, in which plane faces and corners are known to exist as well as columnar structures<sup>(17)</sup>. We have applied the FIM method to infinite cylindrical scatterers of circular, ellipsoidal and rectangular cross-sections in order to determine shape effects for ice crystals. In fig. 1. we show typical results obtained from the investigation. In general we find shape to be less important in forward than in backward scattering. The direction of maximum scattering intensity can vary with shape and orientation of the scatterer, the relative orientation of faces on a scatterer being of importance in determining pattern, shapes and off-axis peaks. This could be most important in interference calculations. In addition, the scattering pattern and intensity does depend greatly on the incidence direction to the crystal faces and hence, although we only have preliminary data available, there appears to be reason to doubt the formation in section 2.3.

### 3. MEDIUM MODELLING

In the last section the problem of calculating the single particle scattering was addressed. Now, having defined the scattering amplitudes of individual particles we must consider an assemblage of such particles. In fig. 2 we show the regions of consideration in an earth-space path. Taking a layering approximation we might expect to encounter ice crystals in the upper regions and rain in the lower ones. Between these as we have pointed out could be a region containing a number of ice/water inhomogenous particles. Some work has been done on such particles<sup>(16)</sup> but the state of current knowledge is not by any means complete and their inclusion in the model will await further meteorological and scattering determination.

#### 3.1 Bulk propagation coefficients

The method usually applied is to treat the effects of a random medium upon a coherent propagating wave as being characterised by a bulk refractive index, which describes the net transfer properties of the scattering region. Van der Hulst<sup>(18)</sup> and Twersky<sup>(19)</sup> have formulated this problem for the slab of scatterers as shown in fig. 3. The resultant complex propagation coefficient derived is of the form:

$$K_{V,H}(\alpha_0) = K_0 + \frac{\pi}{K_0} \int_0^{\infty} f_{V,H}(0, \alpha_0, \bar{a}) n(\bar{a}) d\bar{a} \quad (10)$$

where  $n(\bar{a}) d\bar{a}$  is the particle distribution per unit volume,  $f_{V,H}$  the scattering amplitudes in the forward direction and  $\alpha_0$  the incidence angle.

There has been some debate concerning (10) recently with Hogg and Chu<sup>(20)</sup> pointing out that the formulation does include all forward multiple scattering effects. Indeed, Twersky<sup>(19)</sup>

shows this in his original paper but it must be pointed out that 'forward multiple scattering' means that each scatterer is involved only once in the scattering chain via single forward components of scattered field. However, the formulation is an exact one and furthermore by successive application of the single scattering to infinitely thin layers will result in all orders of forward multiple scattering being accounted for.

This latter formulation is exact for the coherent wave and includes all multiple scattering. However, it does not represent the incoherent field or the multiple scattering effects upon it. There is some evidence that this may become significant at higher frequencies (21).

For a rain medium the drop size distribution  $n(\bar{a})d\bar{a}$  has been extensively investigated and representative distributions such as Laws and Parsons(22) and Marshall and Palmer(23) and Joss et al(24) used. It must be stressed again that their use may yield good agreement with long term data but considerable variations must be expected for individual events.

In the case of ice crystals equation (10) can be simplified, due to the applicability of the Rayleigh theory. We have shown(25) that the Rayleigh scattering amplitudes of ice models remain constant within the region of applicability up to 30 GHz. Thus if one ignores the shape effects, one can define a bulk propagation coefficient as proposed by Haworth et al(26)

$$K_{V,H} = \frac{2\pi}{\lambda} + \frac{3\pi V}{\lambda} A_{V,H} \quad (11)$$

where  $V$  is the total volume of ice in unit volume of cloud and the Rayleigh scattering amplitudes are

	Prolates (needles)	Oblates (plates)
$A_V (m^{-3})$	0.7228 - j0.00285	0.22813 - j0.0009
$A_H (m^{-3})$	0.3468 - j0.00137	0.72280 - j0.00285

Rayleigh scattering amplitudes for  $\alpha_0 = 0$  incidence

#### 4. TRANSMISSION PARAMETERS FOR EARTH-SPACE PATHS

##### 4.1 The general model

In the latter section we have defined the propagation coefficients  $K_{V,H}(\alpha)$  in the two principle polarisation planes as a function of the incidence angle (in our case the elevation angle) into a region containing particle scatterers. Let us now consider the transmission model applicable to the earth-space path. We propose that this be treated as a stratified region as shown in fig. 2 which in its simplest form will degenerate to a two region model containing (i) ice crystals and (ii) raindrops. The model, however, is quite general and can be made more complex if additional meteorological data is available on the particle populations. We will herein consider the simple model.

The major transmission parameters of interest on an earth-space satellite link are (i) attenuation (ii) phase delay and hence dispersion and (iii) depolarisation. The former two characteristics may be determined directly from the propagation coefficients as

$$A_{V,H} = 8.686 \operatorname{Im} (K_{V,H}(\alpha)) \times 10^5 \text{ dB/km} \quad (12)$$

$$\phi_{V,H} = \frac{180}{\pi} \operatorname{Re} (K_{V,H}(\alpha)) \times 10^5 \text{ }^\circ/\text{km}$$

In the case of attenuation this formulation is fairly accurate as particle orientation is relatively insensitive. However, for phase this is not necessarily the case and we need to investigate orientations further. It is worth mentioning that attenuation is sensitive to temperature changes which affect the refractive index of the particle scatterer and care should be taken in using the model in this respect.

##### 4.2 Particle orientations

This is particularly important in determining the depolarisation of waves, where the angle between the incident polarisation vector ( $K_i$ ) and the axis of symmetry of the particle scatterer ( $N$ ) is the important parameter. We have already considered the case for raindrops in the literature(28) and Bostian and Allnut(29) have considered ice crystals. We will herein adopt a unified definition of particle orientation in terms of two angles  $\chi, \theta$  which is consistent with our earlier raindrop model.

In fig. 4 we show the orientation geometry. The angle between the particle axis of symmetry when projected into the plane containing the incident polarisation vectors ( $E_V, E_H$ ) and the vertical polarisation is  $\theta$ , given by:

$$\cos \theta = \frac{\cos \chi - \cos \alpha_0 \cos \alpha}{\sin \alpha_0 \sin \alpha} \quad (13)$$

$$\text{where } \cos \alpha = \cos \alpha_0 \cos \chi + \sin \alpha_0 \sin \chi \cos \phi \quad (14)$$

The angle  $\theta$  is the so-called canting angle for raindrops. Notice that it is a function of  $(\chi, \phi)$  and the elevation angle  $\alpha_0$ .

Thus if one is to apply the scattering data generated in sections 2 and 3, which is defined in terms of characteristics along the principle axes of the scatterers one must rotate the incident polarisation onto these axes via the rotation matrix:

$$R = \begin{pmatrix} \cos \theta & \sin \theta \\ -\sin \theta & \cos \theta \end{pmatrix} \quad (15)$$

and thence back again into the incident polarisations after scattering by  $R^{-1}$  (the inverse of R).

In general one can take a distribution  $P(\chi)$  and  $P^1(\phi)$  of orientation angles for the particles in which case these should be included in the propagation equations (10) and integrations performed over  $\chi$  and  $\phi$  as well as size distributions. For raindrops it has been the usual case for authors to assume the 'worst case' situation in which  $\phi = 90^\circ$  and the drops are considered 'canted' ( $\chi$ ) in a plane perpendicular to the propagation direction. Whence one can either take an all-aligned rain-drop model ( $P(\chi) \rightarrow \delta(\chi - \chi_0)$ ) or as in the case of terrestrial links make use of canting angle distributions which have been found to fit experimental data<sup>(27)</sup>. These may not be applicable to earth-space paths though.

The above geometry applies equally well for ice crystals which fall into two categories

(i) Plates

which we model as oblate spheroids (i.e. same as raindrops) falling with their axis of symmetry horizontal. This corresponds to a raindrop with  $\chi = 0$ , see fig. 5. Such particles can rotate in the horizontal plane but because of the symmetry of the crystals in this plane the distribution in terms of  $\phi$  is unimportant.

(ii) Needles

we model as prolate spheroids, which fall with their long axis horizontal. As shown in fig. 5 we can consider this as an oblate with  $\chi = 90^\circ$ . Now, however, the movement in the horizontal plane ( $\phi$ ) is important as the crystals are non-symmetrical in this plane. So that we must consider a distribution  $P(\phi)$  for these crystals. Note that Haworth et al<sup>(26)</sup> have assumed that this may be modelled by a degree of alignment factor plus a preferred orientation.

#### 4.3 System Propagation characteristics

In fig. 6 we show the system description of an earth-space path for both circular and linear polarisation transmission. We are interested in both the attenuation and cross-polarisation of the transmission. The definitions of crosspolarisation are given in the figures.

(a) Circular polarisation:

Consider a general circularly polarised wave with components  $E_R$  and  $E_L$  transmitted from the satellite. The received components  $E_R^1$  and  $E_L^1$  are given by:

$$\begin{pmatrix} E_R^1 \\ E_L^1 \end{pmatrix} = C^{-1} R^{-1} T.R.C. \begin{pmatrix} E_R \\ E_L \end{pmatrix} \quad (16)$$

where  $C, C^{-1}$  are the transformation matrices from circular to linear (V,H) and linear (V,H) to circular polarisations

$$C = \frac{1}{\sqrt{2}} \begin{pmatrix} 1 & 1 \\ i & -i \end{pmatrix}, \quad C^{-1} = \frac{1}{\sqrt{2}} \begin{pmatrix} 1 & -i \\ 1 & i \end{pmatrix} \quad (17)$$

$R, R^{-1}$  are the rotation matrices onto the particle principle axes from linear (V,H) and back again, for canting angle  $\theta$  (function  $\alpha_0, P(\chi), P(\phi)$ )

$$R = \begin{pmatrix} \cos \theta & \sin \theta \\ -\sin \theta & \cos \theta \end{pmatrix}, \quad R^{-1} = \begin{pmatrix} \cos \theta & -\sin \theta \\ \sin \theta & \cos \theta \end{pmatrix} \quad (18)$$

T is the linear polarisation propagation matrix through the medium of length L.

$$T = \begin{pmatrix} e^{iKv(\alpha)L} & 0 \\ 0 & e^{iKH(\alpha)L} \end{pmatrix} \quad (19)$$

This may be evaluated for a perfectly R.H or L.H circular transmitted wave, where

$$\begin{pmatrix} E_R \\ E_L \end{pmatrix}_R = \begin{pmatrix} 1 \\ 0 \end{pmatrix}, \quad \begin{pmatrix} E_R \\ E_L \end{pmatrix}_L = \begin{pmatrix} 0 \\ 1 \end{pmatrix} \quad (20)$$

or alternatively the depolarising effects of the satellite and earth-station antennas may be incorporated via two additional matrices<sup>(30)</sup>

Whence the attenuation and crosspolarisation are given by:

$$A = 20 \log \left| \frac{E_R^1}{E_R} \right| \text{ dB} \quad (21)$$

$$XPD_R = 20 \log \left| \frac{E_R^1}{E_L^1} \right| \text{ dB}$$

and by similar expressions for a L.H. transmitted wave.

(b) Linear polarisation

The formulation is similar to that of (a) except for the transmission of a perfect linear polarised wave at an angle  $\gamma$  and tilted to the vertical. This general situation results from the fact that the local vertical at the satellite as viewed from an earth-station at latitude  $(\alpha)$  and longitude  $(\beta)$  with respect to the sub-satellite point appears tilted by  $\gamma$ , where

$$\gamma = 90^\circ - \tan^{-1} \left\{ \frac{\tan(\beta)}{\sin(\alpha)} \right\}$$

whence for the receiver aligned with satellite transmission we have

$$\begin{pmatrix} E_{Vs}^1 \\ E_{Hs}^1 \end{pmatrix} = G^{-1} R^{-1} T R G \begin{pmatrix} E_{Vs} \\ E_{Hs} \end{pmatrix} \quad (22)$$

$$\text{where } G = \begin{pmatrix} \cos \gamma & \sin \gamma \\ -\sin \gamma & \cos \gamma \end{pmatrix}$$

the rotation from the satellite vertical and horizontal  $E_{Vs}$ ,  $E_{Hs}$  to the absolute vertical and horizontal  $E_V$ ,  $E_H$  attenuation and crosspolarisation are given by similar expressions to (21)

In the foregoing the medium transmission matrix is for either a stratified layer of ice or water. Clearly we can cascade these matrices for successive layers if we take care to ensure continuity of input and output polarisation directions.

(c) Ice/Rain model for circular polarisation

As an example we consider an ice/rain, two layered, model for circularly polarised transmission. We then obtain the following system formulation:

$$\text{up-path} \quad \begin{pmatrix} E_R^1 \\ E_L^1 \end{pmatrix} = C^{-1} R_1^{-1} [T_I] R_1 \cdot R_1^{-1} [T_R] R_1 \cdot C \begin{pmatrix} E_R \\ E_L \end{pmatrix} \quad (23)$$

$$\text{down-path} \quad \begin{pmatrix} E_R^1 \\ E_L^1 \end{pmatrix} = C^{-1} R_2^{-1} [T_R] R_2 \cdot R_1^{-1} [T_I] R_1 C \begin{pmatrix} E_R \\ E_L \end{pmatrix} \quad (24)$$

where  $[T_I]$  and  $[T_R]$  are the propagation matrices of the ice and rain medium respectively and  $R_1$  and  $R_2$  the Orientation matrices relating to ice and rain.

It will be seen clearly from the above that the order of the matrices will produce different results for up-path and down-path transmission if  $R_1$  and  $R_2$  are different. Right and left hand polarisation may be affected differently as well. Similar formulations may be made for linear polarisation.

Such rain/ice models have been investigated for a variety of parameters of these mediums and results are given in section 5.

## 5. SOME SPECIFIC RESULTS

In this section we present a sample of some of the recent results that have been obtained from computations based upon the theoretical prediction work given in the latter sections. We emphasise that we have produced more comprehensive results which have already appeared in the literature and which we will not reproduce here.

### 5.1 Extension to millimetre waves

Using the extended FIM given in section 2 we have performed calculations for raindrops at frequencies up to 137 GHz (31). In fig. 7 we show  $K_O I_m(f_H)$  as a function of  $K_O \bar{a}$  for various frequencies calculated. The striking aspect is that the curve is virtually frequency independent and this would suggest that a simple scaling procedure could be applicable in the millimetre range. It has also been noted that  $K_O I_m(f_m)$ , where  $f_m$  is the Mie sphere scattering amplitude, also lies very close to this curve. This is noteworthy not only for small values of  $K_O \bar{a}$ , but also for large ones where the drop is becoming significantly non-spherical. In the inset to fig. 7 we plot, on a linear scale  $K_O I_m(f_H)$  and  $K_O I_m(f_v)$  and as frequency increases then  $I_m(f_v)$  approaches  $I_m(f_H)$ .

In fig. 8 we plot  $K_O R_e(f_H)$  and here again frequency independence is seen to exist, but the closeness to the Mie sphere amplitudes is not so marked.

We have calculated attenuation and crosspolarisation using these results and found that the Mie-sphere assumptions yield attenuation values which agree quite well with the exact horizontal polarisation results but not with the vertical. At 137 GHz the differences are becoming smaller but are still marked.

In all of the calculations we have found that the closeness of the drop-size interval taken in the attenuation calculation is very important in determining the accuracy of the final result. We have also found, to our surprise, that the larger drops cannot be ignored, for instance drops around 0.2 cm radius at 57 GHz and 0.15 cm at 94 GHz are still contributing significantly to the attenuation.

In fig. 9 we show crosspolarisation against attenuation for 57 and 94 GHz. Crosspolarisation has reduced significantly from that at lower frequencies due to the reduction in both differential amplitude and phase. This reduction continues with frequency for linear polarisation but circular polarisation is still some 20 dB worse on average.

### 5.2 Temperature effects

We have investigated the sensitivity of earth-space path attenuation predicted from theoretical rainfall models to the variation of model parameters e.g. raindrop size distribution, shape, orientation and water temperature (32). We find that temperature of water and drop size distributions affect attenuation greatest in the 11-14 GHz range as shown in table 2. With water temperature being the predominant feature. This has been found to be significant in the interpretation of attenuation ratios as determined by radiometric measurements and by satellite beacon experiments. In fig. 10 we show some measured data from the O.T.S. satellite experiment for 14/11 GHz ratios superimposed upon the theoretical calculations. Not only are the temperature effects in the theoretical prediction seen to be important but also the calculation of scattering at the 'exact' frequency of transmission.

### 5.3 Backscatter effects

We are able to calculate scattering at any angle from the FIM program and particularly the backscatter direction which is relevant to radar measurements of propagation parameters. We have already reported resonances (33) which occur in the backward scattering direction from water and ice and have generally concluded that backward scattering rules are not as universally applicable as those for the forward direction.

We have recently examined the differential backscatter cross-section for water at various frequencies. Here we find a very strong higher-order resonance effect which results in the radar cross-section for rain being greater in vertical than horizontal polarisation, Fig 11 for a value of  $K_O \bar{a} \approx 1.6$  which remarkably is independent of frequency and refractive index. This effect had previously been reported for ice (34) but not for rain.

### 5.4 Water/ice models

Until very recently the theoretical prediction of attenuation and crosspolarisation on earth-space paths due to precipitation had been confined to rainfall modelling. With the ATS-6, and latterly with the O.T.S. satellite experiments the existence of effects due to high altitude ice crystals has been demonstrated (35). In making crosspolarisation measure-

ments with the OTS satellite we have seen a large number of events which do not fall into the water-only or ice-only category. We have thus developed a water/ice model as explained in section 4 in order to explain some of these effects.

In fig. 12 we show a measured event on the OTS circularly polarised beacon. At the start of the event we clearly have an all-ice situation and our model does predict that the phase will be constant, even for quite large crosspolarisation amplitude swings. As the event progresses the proportion of water obviously increases and we find that with a low rainfall region and for varying ice concentrations the ice/water model will predict small phase variation for XPD's less than 30 dB. The ice model predicts quite rapid phase fluctuations in alignment situations which could typically accompany electric field changes as shown in this event. However, when the proportion of water in the ice/water model is increased this has the effect of damping out XPD variations and reducing phase variations to very small quantities as measured in this event. Clearly the intervention of the two scattering media has a large effect even for low ice concentrations or low rainfall rates.

We have shown that using the ice/water model some observed effects can be explained. The model is still very simple and does not truly reproduce the complexity of the actual propagation media. More meteorological data will help us to refine it and the resultant predictions made from it.

## 6. REFERENCES

1. OGUCHI, T. (1973) J. Radio Res. Labs. (Tokyo) Vol. 20
2. MORRISON, J.A., CROSS, M.J. (1974) Bell System Technical Journal, Vol. 53, no. 6.
3. CHANG, S. and MEI, K.K. (1976) I.E.E.E. Trans. A.P. 24 (1)
4. WARNER, C. (1975) Electronics Letters 11
5. BARKER, P., YEH, C. (1975) Applied Optics. Vol. 14
6. UZUNOGLU, N. EVANS, B. and HOLT, A. (1976) Electronics Letters, Vol. 12.
7. WATERMAN, P. (1965) Proc. I.E.E.E. 53
8. OGUCHI, T. (1964) J. Radio Res. Labs. (Tokyo) Vol. 11
9. MORRISON, J.A., CROSS, M.J. (1973) Bell System Technical Journal Vol. 52
10. HOLT, A.R., EVANS, B.G. (1980) URSI. Comm. F. Symp. Canada
11. HOLT, A.R., SHEPHERD, J.W. (1978) J. Phys. A.
12. EVANS, B., HOLT, A., SHEPHERD, J. (1979) I.E.E. Conf. Ant. & Prop. U.K.
13. OGUCHI, T. (1977) Radio Science, Vol. 12, no. 1.
14. PRUPPACHER, H., PITZER, R.L. (1971) J. Atmospheric Sci. Vol. 28
15. BARGE, B.L., ISAACS, G.A. (1973) J. de Res. Atmos. Vol. 1
16. SELIGA, T.A., BRINGI, V.N. (1978) Radio Science Vol. 13.
17. HEYMSFIELD, A.J., KNOLLENBERG, R.G. (1972) J. Atmos. Sci. 29
18. VAN DER HULST, H.C. (1957) Wiley and Sons, New York
19. TWERSKY, V. (1962) J. Math. Phys. 3.
20. HOGG, D.C. and CHU, T.S. (1975) Proc. IEEE 63
21. OGUCHI, T. (1980) URSI Comm. F. Symp. Canada
22. LAWS, J.O. and PARSONS, D.A. (1943) Trans. Am. Geophys. Union 24
23. MARSHALL, J.S. and PALMER, W.M. (1948) J. Meteor. 5
24. JOSS, J. et al (1968) Proc. Int. Conf. Cloud Physics, Toronto, Canada
25. EVANS, B.G. and HOLT, A.R. (1979) Electronics Letters

26. HAWORTH, D., WATSON, P. and McEWAN, N. (1977) Electronics Letters 13.
27. DILWORTH, I.J. EVANS, B.G. (1979) Electronics Letters 15.
28. UZUNOGLU, N., EVANS, B. and HOLT, A. (1977) Proc. IEEE 124 (5)
29. BOSTIAN, C.W., ALLNUTT, J.E. (1979) Proc. IEE 126 (10)
30. KENNEDY, D.J. (1979) Comsat Technical Review 9 (2B)
31. HOLT, A.R., EVANS, B.G. (1980) URSI Comm. F. Symp. Canada
32. UPTON, S., EVANS, B. and HOLT, A. (1980) *ibid.*
33. HOLT, A.R., EVANS, B.G. (1977) Proc. IEE 124 (12)
34. BRINGI, V.N., SELIGA, J.A. (1978) Radio Science 13
35. McEWAN, N.J. et al (1977) Electronics Letters 13

TABLE I

Imaginary Part of the Forward Scattering Amplitude at 94 GHz

$\bar{a}$	$k_0 \bar{a}$	Temperature	$f_0$	$f_V$	$f_H$	$f_M$
.02	0.39	20°	9.36 <sup>-4</sup>	9.04 <sup>-4</sup>	9.41 <sup>-4</sup>	9.27 <sup>-4</sup>
.02	0.39	0°	9.35 <sup>-4</sup>	9.02 <sup>-4</sup>	9.38 <sup>-4</sup>	9.25 <sup>-4</sup>
.08	1.58	20°	9.63 <sup>-2</sup>	8.91 <sup>-2</sup>	9.52 <sup>-2</sup>	9.35 <sup>-2</sup>
.08	1.58	0°	9.82 <sup>-2</sup>	9.21 <sup>-2</sup>	9.73 <sup>-2</sup>	9.58 <sup>-2</sup>
.12	2.36	20°	2.11 <sup>-1</sup>	1.93 <sup>-1</sup>	2.05 <sup>-1</sup>	2.02 <sup>-1</sup>
.12	2.36	0°	2.13 <sup>-1</sup>	1.97 <sup>-1</sup>	2.07 <sup>-1</sup>	2.05 <sup>-1</sup>

The index denotes the power of ten by which the entry is to be multiplied

TABLE II

Temperature Dependence of Attenuation (dB). 6 km Slant Path. Marshall &amp; Palmer Rain. Circular Attenuation

FREQUENCY Ghz.	9.4	11.8	14.5	20	30
RAIN RATE MM/HR					
12.5 0°c	1.2	2.2 (9%)	3.5 (11%)	7.0 (8%)	16.2
20°c	1.2	2.4	3.9	7.6	16.3
25 0°c	2.9 (3%)	4.9 (12%)	7.6 (14%)	15.0 (6%)	32
20°c	3.0	5.5	8.7	15.9	32
50 0°	6.7 (9%)	10.9 (14%)	16.6 (12%)	31.0 (5%)	62
20°	7.3	12.4	18.6	32.5	61
100 0°	15 (13%)	24 (12%)	35 (11%)	62 (2%)	113 (-2%)
20°	17	27	39	63	111
150 0°	24 (12%)	37 (11%)	54 (7%)	89 (2%)	159 (-3%)
20°	27	41	58	91	155



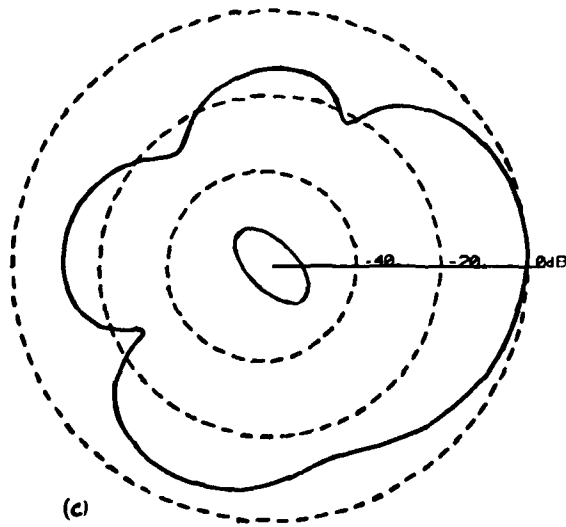
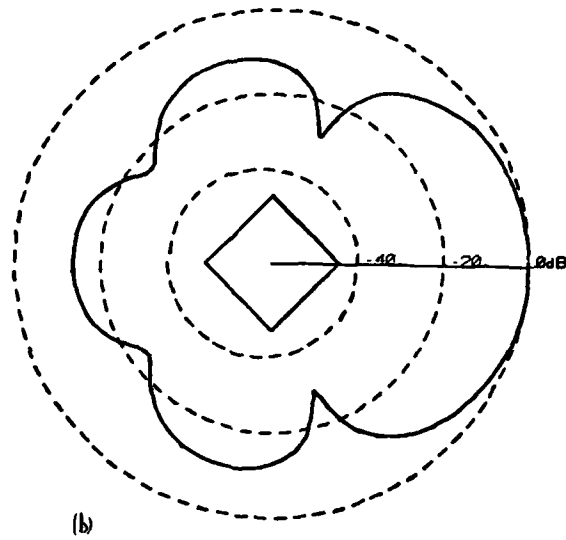
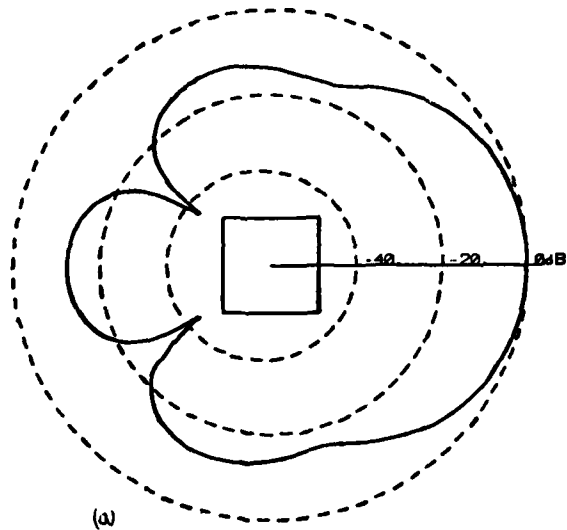


Fig.1 Scattered polar plot for  
 (a) square cylinder with incidence perpendicular to one face  
 (b) square cylinder inclined by  $45^\circ$   
 (c) elliptic cylinder

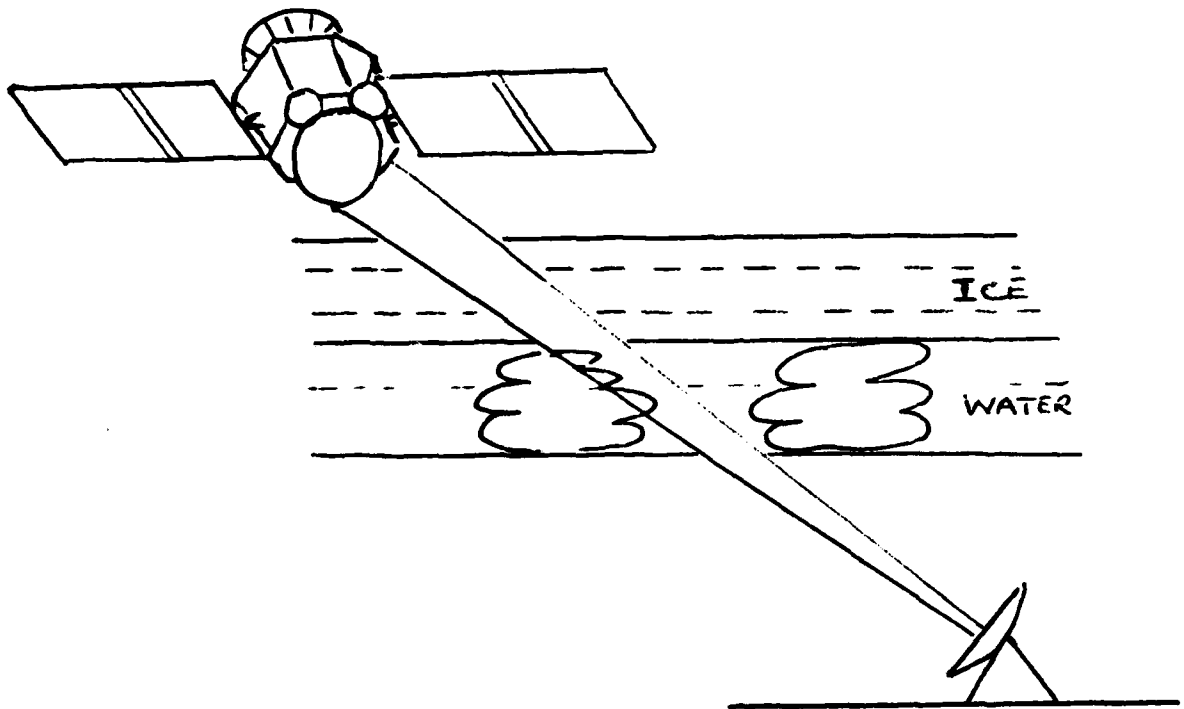


Fig.2 Earth-space path model

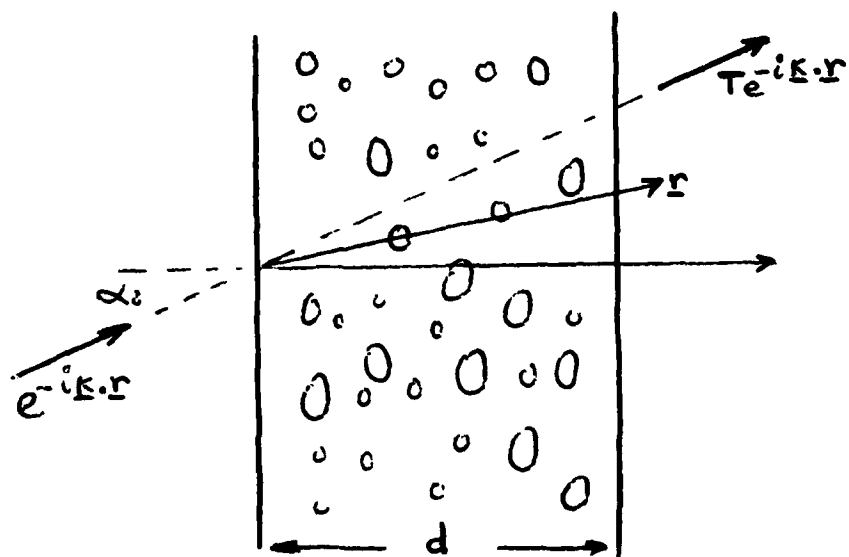


Fig.3 Scattering from slab of particles

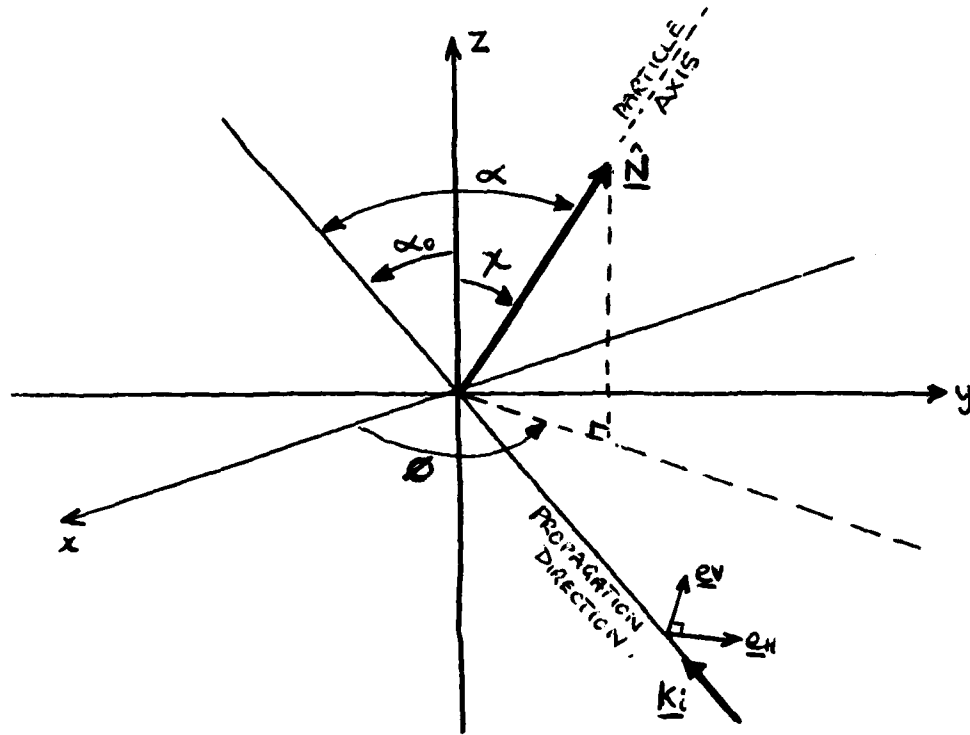


Fig.4 Particle axis geometry

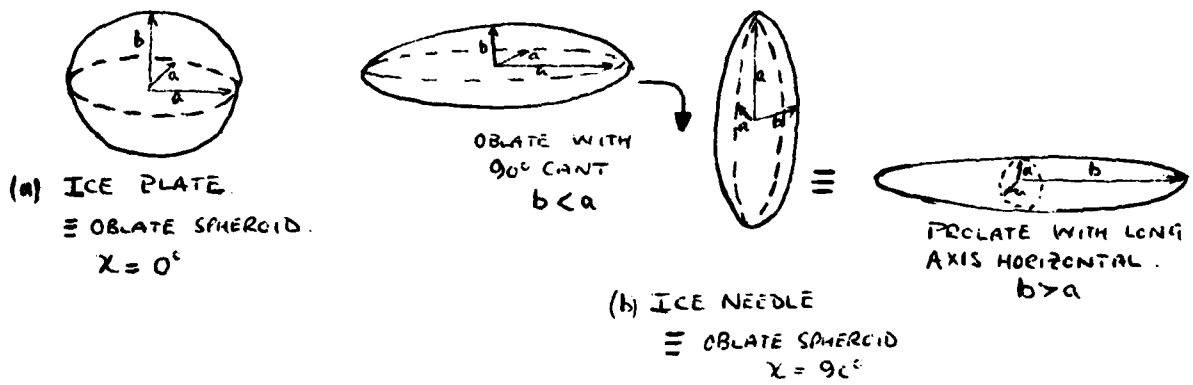
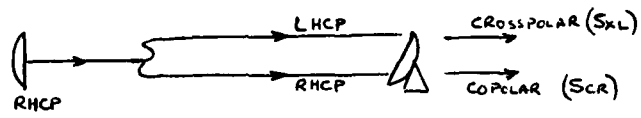


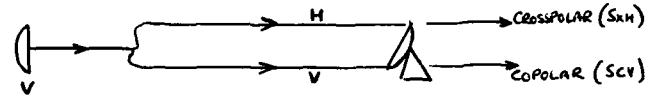
Fig.5 Ice plate and needle geometry



$$XPD_R = 10 \text{Log}_{10} \left( \frac{S_{CR}}{S_{XL}} \right) \text{ dB}$$

$$XPD_L = 10 \text{Log}_{10} \left( \frac{S_{CL}}{S_{XR}} \right) \text{ dB}$$

(a) CIRCULAR POLARISATION



$$XPD_V = 10 \text{Log}_{10} \left( \frac{S_{CV}}{S_{xH}} \right) \text{ dB}$$

$$XPD_H = 10 \text{Log}_{10} \left( \frac{S_{CH}}{S_{xV}} \right) \text{ dB}$$

(b) LINEAR POLARISATION

Fig.6 System crosspolarisation definition

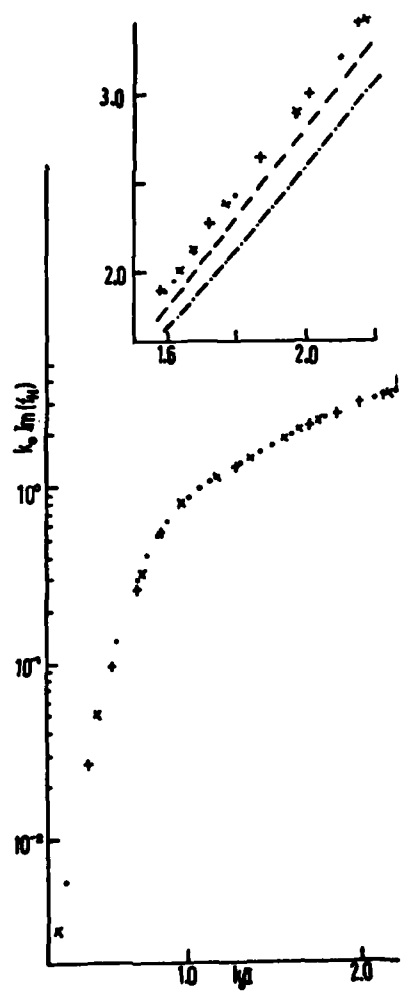


Fig.7  $k_0 \text{Im}(f_H)$  as a function of  $k_0 a$ . . 57.3 GHz  
 x 94 GHz + 137 GHz. Inset shows in addition  
 $k_0 \text{Im}(f_V)$ . - 94 GHz --. 57.3 GHz

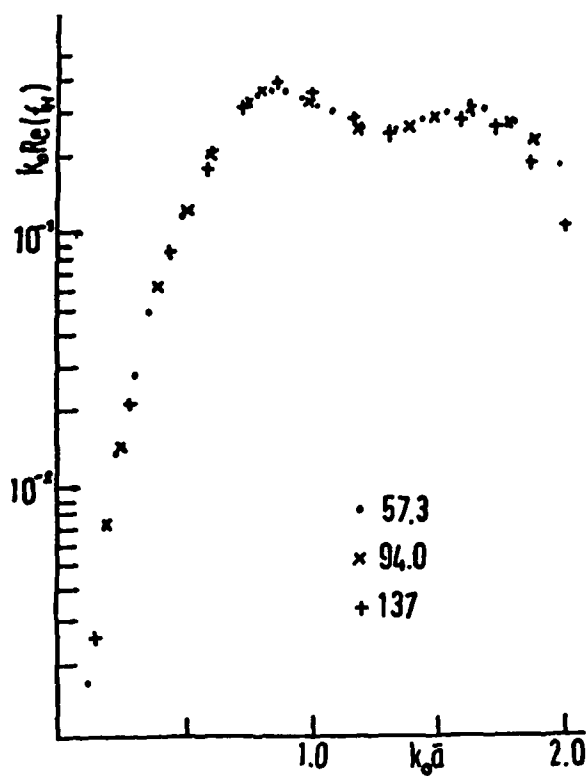


Fig.8  $k_0 \text{Re}(f_{II})$  as a function of  $k_0 \bar{a}$ . ..57.3 GHz x 94 GHz + 137 GHz

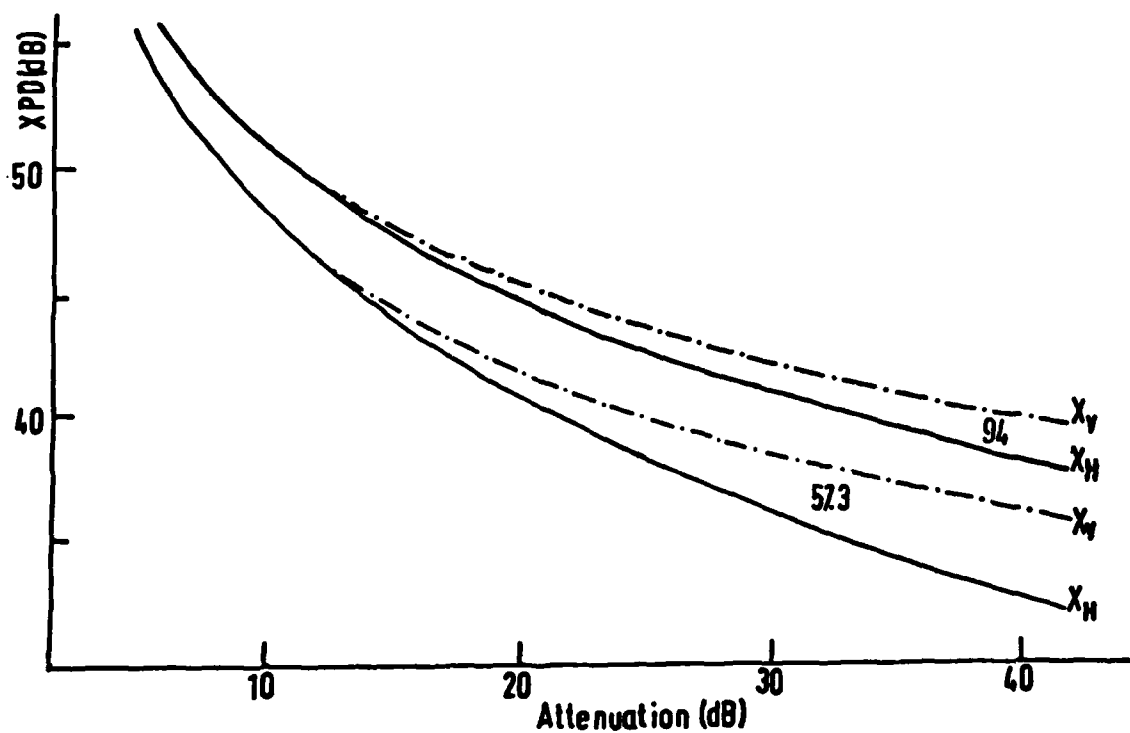


Fig.9 Cross-polar discrimination plotted against attenuation for horizontal and vertically polarised waves at 57.3, 94 GHz

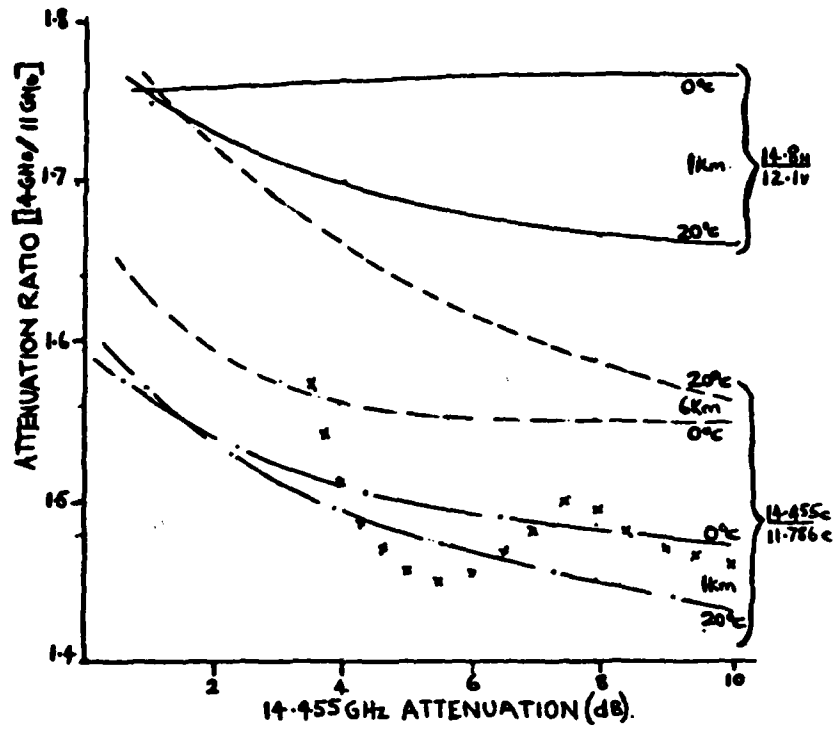


Fig.10 Attenuation ratios 14 GHz/11 GHz (xxx - experimental measurements)

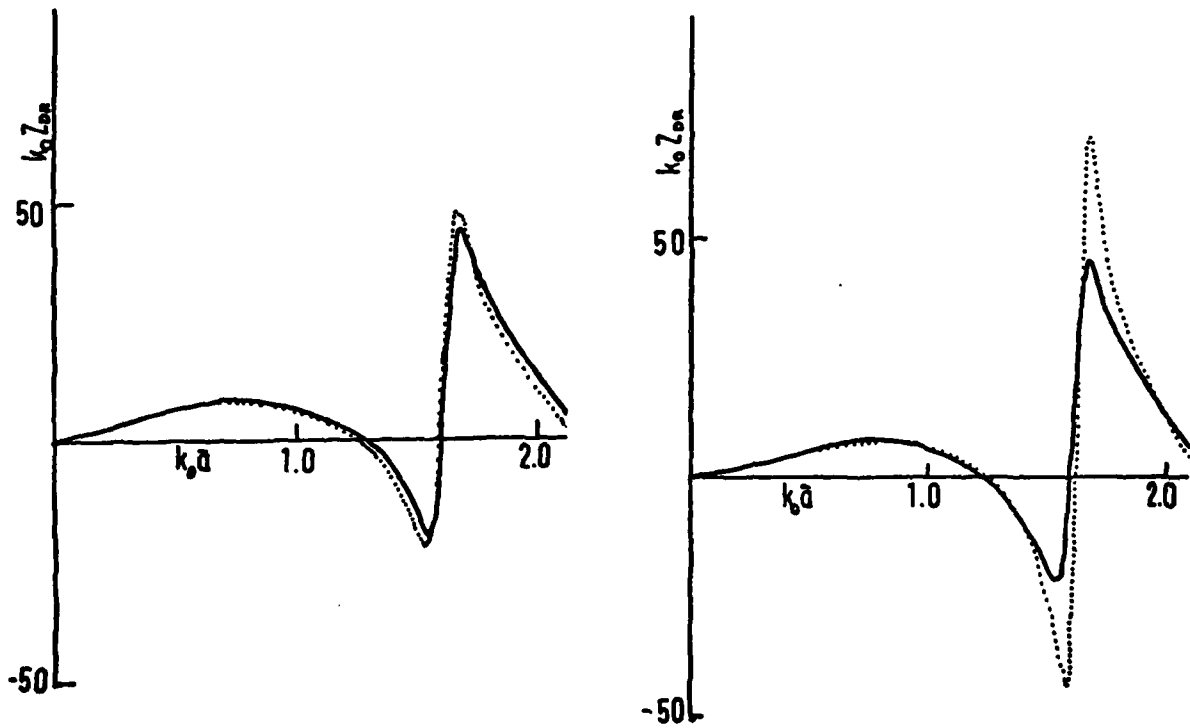


Figure 11

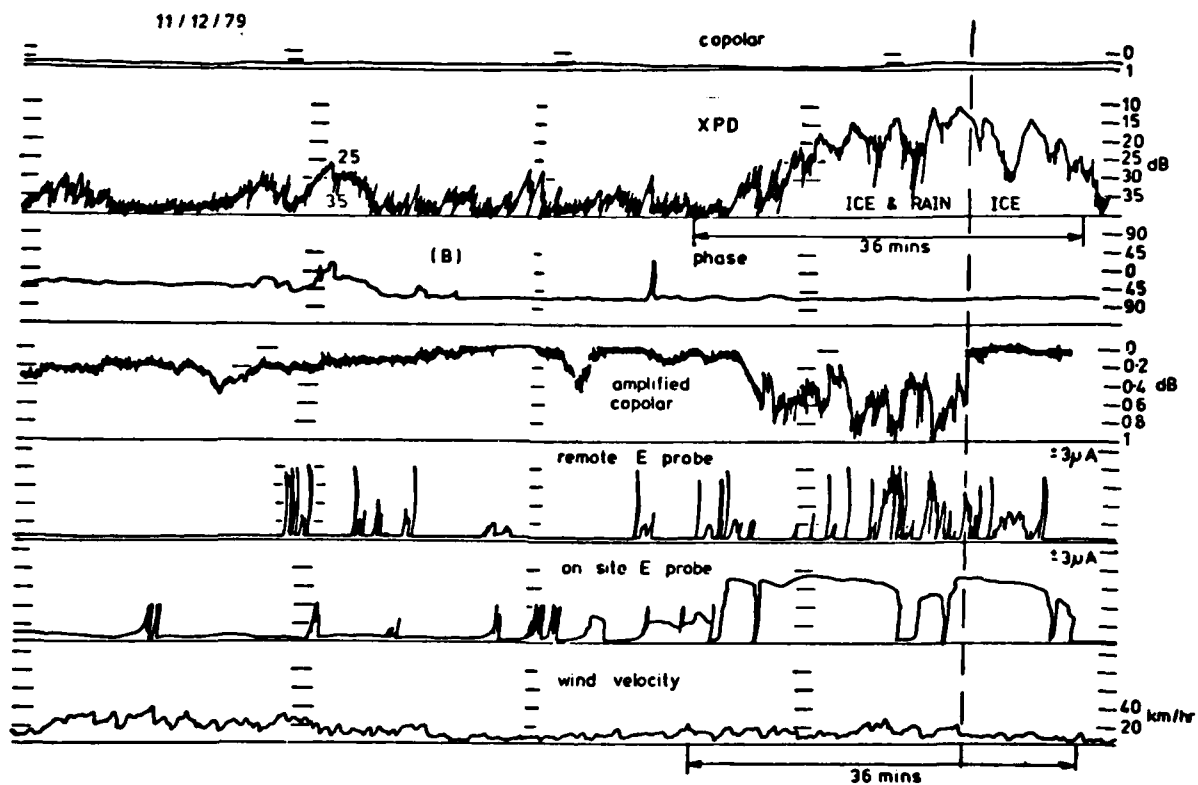


Figure 12

PLANE WAVE SPECTRUM TREATMENT OF MICROWAVE  
SCATTERING BY HYDROMETEORS ON AN EARTH-SATELLITE LINK

Dr. D. P. Haworth\*

University of Bradford, Bradford, West Yorkshire, UK

For satellites operating at frequencies above 10 GHz, the effects of propagation through atmospheric hydrometeors are of major importance. In particular, the hydrometeors attenuate, cross-polarize and scatter signals causing respectively: a loss in signal level, a decrease in the efficiency of dual-polarized channels and station-to-station interference. For large Earth Station antennas operating at high frequencies, the near or Fresnel region of the antenna can extend several kilometres from the antenna and consequently, during disturbed weather, a significant proportion of the hydrometeors affecting propagation are in the near or Fresnel region of the antenna. Previous treatment of propagation through hydrometeors in the Fresnel region of an antenna has proved unsatisfactory and it is the objective of this paper to use the plane wave spectrum technique to accurately characterize antenna-scatterer interaction in both the near and far fields of an antenna. As examples, the Van de Hulst refractive formula for the coherent propagation and the basis of the Radiative Transfer Equation for the incoherent scattering are derived in a rigorous and straightforward manner.

## 1. INTRODUCTION

Propagation through hydrometeors (i.e. rain, hail, snow ice etc.) on a satellite/Earth path can cause significant attenuation, cross-polarization and scattering of the received signal from the satellite and there has been much investigation of the interaction of the satellite signal with hydrometeors on the path<sup>1,2,3</sup>.

With increasing use of higher frequencies, the ability to predict the effects of hydrometeors in both the near and far fields of an antenna is important, particularly in the case of very large Earth station antennas whose near field can extend several kilometres from the antenna. If we consider, for example, a 6m diameter Earth station antenna operating at a frequency of 30 GHz and having an elevation angle of  $27^\circ$  then, using the Rayleigh criterion for the minimum far field distance ( $2D^2/\lambda$  where  $D$  is the diameter of the antenna and  $\lambda$  is the wavelength) we find that, up to 7.2 km along the path or up to an altitude of 3.3 km, the hydrometeors present are in the near field of the receive antenna.

It is now generally accepted that most of the attenuation observed in excess of free space on Earth/satellite links comes from hydrometeors up to and including the melting band, which, in temperate climates for the summer months, is around 3-4 km high<sup>4</sup>. Consequently it is possible, in some cases, that the hydrometeors causing most of the observed excess attenuation on an Earth/satellite link are in the near field of the Earth station antenna.

Present treatments of propagation through hydrometeors on an Earth/satellite path use the equivalent refractive index of Van de Hulst<sup>6</sup> to treat attenuation and cross-polarization and the Radiative Transfer equation<sup>5</sup> to treat incoherent scattering effects (the Radiative Transfer equation also describes coherent propagation effects but these are more easily described by the Van de Hulst equivalent refractive index). Previous work, however, has indicated that conventional descriptions must be modified for scattering from hydrometeors located in the near field of an antenna such as the receive antenna on an satellite-Earth link. To be specific, Crane<sup>7</sup> concluded from the Rain Range experiment results that, "rain in the near field of large antenna systems may cause different values of attenuation than predicted on the basis of the standard theory", and Delogne et al.<sup>8</sup>, treating propagation through hydrometeors with the Radiative Transfer equation, state that their



Radiative Transfer approach is only valid for drops located in the far field region of the antenna.

It is the aim of this paper to show, using the plane wave spectrum theory, that standard techniques of describing propagation through hydrometeors (i.e. the Van de Hulst equivalent refractive index and the Radiative Transfer equation) are equally valid for hydrometeors located in the near or far field of an antenna. To do this we will analyse the case of a plane wave incident normally onto a thin slab of hydrometeors (the slab is thin so that only single scattering by the hydrometeors is important) located at an arbitrary distance from a receive antenna. The model assumed is a reasonable representation of a satellite-Earth path for the purposes of this analysis since the hydrometeors are located relatively very close to the Earth station antenna and occupy a small part of the 35,800 km path length. In practise, hydrometeors present on the path often produce significant multiple scattering effects (indicated, for example, by attenuations of more than 1 to 2 dB in the case of rain on the path) however these effects are not anticipated to affect near-field/far field propagation differences.

## 2. PLANE WAVE SPECTRUM FORMULATION

The plane wave spectrum formulation has been much used in the treatment of near field antenna radiation problems<sup>9,10</sup> and provides a useful formulation of hydrometeor-antenna interaction that is independent, in form, of whether the hydrometeors are located in the near or far field of the antenna.

### 2.1 Interaction between antennas

As a basis, we will consider power transmission between two antennas separated by less than the far field distance of the larger antenna. For a matched load across the receive antenna terminals we find, with reference to figure 1,<sup>10</sup>

$$T = -(1/2Z_0) \int \underline{E}_R(-\underline{u}) \cdot \underline{E}_T(\underline{u}) e^{-ik_0 \underline{u} \cdot (\underline{r}_2 - \underline{r}_1)} d\Omega \quad (1)$$

where:

$T$  is called the 'transmission coefficient' and is defined so that  $|T|^2$  is the power dissipated by a matched load attached to the receiver,

$\underline{E}_R$  is the plane wave spectral component for the receive antenna alone behaving as a transmitter and transmitting a unit total power,

$d\Omega$  denotes the elementary solid angle about the direction vector  $\underline{u}$ . In cartesian coordinates,  $d\Omega = du_x du_y / u_z$ .

A stationary phase evaluation of (1) for a large separation of the transmit and receive antennas gives as  $|\underline{r}_2 - \underline{r}_1| \rightarrow \infty$ :

$$T \sim (\pi / ik_0 Z_0) \underline{E}_R(-\underline{u}_r) \cdot \underline{E}_T(\underline{u}_r) \frac{e^{-ik_0 |\underline{r}_2 - \underline{r}_1|}}{|\underline{r}_2 - \underline{r}_1|} \quad (2)$$

where  $\underline{u}_r$  is the direction vector along  $\underline{r}_2 - \underline{r}_1$ . For matched polarizations:

$$|T|^2 \sim (\pi / k_0 Z_0 |\underline{r}_2 - \underline{r}_1|)^2 |\underline{E}_R(-\underline{u}_r)|^2 |\underline{E}_T(\underline{u}_r)|^2 \quad (3)$$

Noting that, for example,  $|\underline{E}_T|^2/2Z_0$  gives the power density from the transmit antenna per unit solid angle, we have:

$$|T|^2 \sim P G_T(\underline{u}_T) G_R(-\underline{u}_R) (\lambda/4\pi|\underline{r}_2-\underline{r}_1|)^2 \quad (4)$$

where:

P is the total power transmitted,  
 $G_T$  is the gain of the transmit antenna,  
 $G_R$  is the gain of the receive antenna.

Equation (4) can be recognized as the classical Friis transmission formula<sup>11</sup> for the received power on a line of sight microwave link with matched polarizations at the transmitter and the receiver.

It is interesting to note that we can revert from the asymptotic representation of the antenna interaction in equation (2) to the full plane wave expansion in (1) by using the Weyl angular decomposition formula<sup>13</sup>. We have:

$$\frac{e^{-ik_0|\underline{r}_2-\underline{r}_1|}}{|\underline{r}_2-\underline{r}_1|} = (k_0/2\pi i) \int e^{-ik_0\underline{u} \cdot (\underline{r}_2-\underline{r}_1)} d\Omega \quad (5)$$

Substituting from (5) into (2) and including the angular variations of  $\underline{F}_T$  and  $\underline{F}_R$  within the angular integral, equation (1) immediately follows. We note that the plane wave decomposition in (5) and (1) is defined in a half space and, if rectangular coordinates are taken for  $\underline{u}$ ,  $u_x$  and  $u_y$  are real and have limits at  $\pm\infty$  whilst  $u_z$  is real or imaginary depending on whether  $u_x^2 + u_y^2$  is greater or less than unity since  $u_z = (1-u_x^2-u_y^2)^{1/2}$ . The sign of  $u_z$  is chosen opposite to that of  $(z_2-z_1)$  to ensure a decaying evanescent wave at infinity. Angular component waves for which  $u_z$  is real are termed real or propagating waves whilst angular component waves for which  $u_z$  is purely imaginary are termed evanescent or surface waves. In an angular spectrum decomposition of the radiation from an antenna, the evanescent waves represent stored energy in the field whilst the propagating waves represent the radiated energy in the field.

## 2.2 Interaction of a receive antenna with the scattered signal from a hydrometeor illuminated by a plane wave

If a hydrometeor is illuminated by a plane wave having a field  $\underline{E}^i$  at the phase centre of the hydrometeor (denoted by  $\underline{r}_1$ ) and propagating in a direction  $\underline{u}_0$  (as in figure 2) then the scattered field at the point  $\underline{r}_2$  is, using the Van de Hulst asymptotic scattering definition:

$$\underline{E}^s(\underline{r}_2) \sim \frac{\tilde{S}(\underline{u}, \underline{u}_0)}{ik_0} \cdot \underline{E}^i \frac{e^{-ik_0|\underline{r}_2-\underline{r}_1|}}{|\underline{r}_2-\underline{r}_1|} \quad (6)$$

where the  $\sim$  on top of S denotes the tensor characteristic in changing the polarization of  $\underline{E}^s$ . More explicitly we can consider the incident and scattered components as in figure 3. Here we have:

$$\underline{E}^S \sim \begin{bmatrix} S_{11}(\theta, \phi) & S_{12}(\theta, \phi) \\ S_{21}(\theta, \phi) & S_{22}(\theta, \phi) \end{bmatrix} \begin{bmatrix} E_1^i \\ E_2^i \end{bmatrix} \frac{e^{-ik_0 |\underline{r}_2 - \underline{r}_1|}}{ik_0 |\underline{r}_2 - \underline{r}_1|} \quad (7)$$

where  $\underline{E}^S = E_1^S \underline{e}_\theta + E_2^S \underline{e}_\phi$  and  $\underline{E}^i = E_1^i \underline{e}_\theta^0 + E_2^i \underline{e}_\phi^0$

From the angular decomposition formula in (5) we can induce that equation (6) is an asymptotic representation of:

$$\underline{E}^S(\underline{r}_2) = (k_0/2\pi i) \int \frac{\tilde{S}(\underline{u}, \underline{u}_0) \cdot \underline{E}^i}{ik_0} e^{-ik_0 \underline{u} \cdot (\underline{r}_2 - \underline{r}_1)} d\Omega \quad (8)$$

and we can see that the interaction with a receive antenna centred at  $\underline{r}_2$  gives a transmission coefficient:

$$T^S = -(1/2Z_0) \int \frac{\underline{E}_R(-\underline{u}) \cdot \tilde{S}(\underline{u}, \underline{u}_0) \cdot \underline{E}^i}{ik_0} e^{-ik_0 \underline{u} \cdot (\underline{r}_2 - \underline{r}_1)} d\Omega \quad (9)$$

It can be shown that the angular spectral representation of the plane wave is:

$$\underline{E}^i(\underline{u}) = (2\pi i/k_0) \underline{E}^i \delta(\underline{u} - \underline{u}_0) \quad (10)$$

where the  $\delta$  is the Dirac delta function. Substitution into equation (1) gives for a plane wave reception:

$$T^d = (\pi/ik_0 Z_0) \underline{E}_R(-\underline{u}_0) \cdot \underline{E}^i e^{-ik_0 (z_2 - z_1)} \quad (11)$$

Equation (9) and (11) define the transmission coefficient at the receive antenna due to the incident plane wave and scattering from a single hydrometeor.

### 3. APPLICATIONS

In this section, the plane wave spectrum technique will be applied to the analysis of coherent and incoherent effects due to propagation of a plane wave through a thin slab of hydrometeors.

#### 3.1 The Van de Hulst refractive index formula

The Van de Hulst refractive index formula for coherent propagation through a thin slab of hydrometeors as derived by Van de Hulst<sup>6</sup> uses a stationary phase approximation which, whilst producing exact results for the propagation of a plane wave through a plane slab of scatterers, is confusing when the interaction with a receive antenna is considered and can lead to misinterpretation<sup>7</sup>. The use of the plane wave spectrum technique allows the Van de Hulst refractive index to be derived without the use of a stationary phase approximation.

We consider a thin, infinite slab of scatterers with a plane wave incident normally onto the slab as in figure 4. The transmission coefficient  $T$  is, in the single scattering approximation, a linear superposition of the contribution from each scatterer and a directly received signal component i.e.:

$$T = (\pi/ik_0 Z_0) \underline{E}_R(-\underline{u}_0) \cdot \underline{E}^i + \sum_{\underline{m}} (-1/2Z_0) \int \underline{E}_R(-\underline{u}) \cdot \frac{\tilde{\underline{S}}_{\underline{m}}(\underline{u}, \underline{u}_0) \cdot \underline{E}^i}{ik_0} e^{-ik_0(\underline{u}-\underline{u}_0) \cdot (\underline{r}_2 - \underline{r}_1^{\underline{m}})} d\Omega \quad (12)$$

where the phase has been normalised to the directly received signal phase. To evaluate the average or coherent received signal component, we consider each hydrometeor to have a random position within the slab and to move randomly independently of the positions of the other hydrometeors. We also assume, for simplicity, that the hydrometeors have the same physical shape, size and orientation. For a number density 'N' per unit volume, we find:

$$\langle T \rangle = (\pi/ik_0 Z_0) \underline{E}_R(-\underline{u}_0) \cdot \underline{E}^i - (N/2Z_0) \int \underline{E}_R(-\underline{u}) \cdot \frac{\tilde{\underline{S}}(\underline{u}, \underline{u}_0) \cdot \underline{E}^i}{ik_0} e^{-ik_0(\underline{u}-\underline{u}_0) \cdot (\underline{r}_2 - \underline{r}_1)} d\Omega dV \quad (13)$$

where dV is an elementary volume within the slab. The volume integral can be partially evaluated by integrating with respect to  $x_1$  and  $y_1$  and, since the only function that depends on  $x_1$  and  $y_1$  is the exponential, we have:

$$\langle T \rangle = (\pi/ik_0 Z_0) \underline{E}_R(-\underline{u}_0) \cdot \underline{E}^i - (N/2Z_0) \int \underline{E}_R(-\underline{u}) \cdot \frac{\tilde{\underline{S}}(\underline{u}, \underline{u}_0) \cdot \underline{E}^i (2\pi/k_0)^2 \delta(\underline{u}-\underline{u}_0)}{ik_0} dz_1 d\Omega \quad (14)$$

where we have twice used the identity:

$$\int_{-\infty}^{\infty} e^{-ix} dx = 2\pi \delta(x) \quad (15)$$

The angular integration in (14) is now degenerate and, since the integrand in (14) is independent of  $z$ , we have:

$$\langle T \rangle = (\pi/ik_0 Z_0) \underline{E}_R(-\underline{u}_0) \cdot \left[ 1 + \frac{2\pi}{ik_0} N \Delta z \frac{\tilde{\underline{S}}(\underline{u}, \underline{u}_0)}{ik_0} \right] \cdot \underline{E}^i \quad (16)$$

As pointed out by Van de Hulst, the bracketed term in equation (16) can be recognised as the first two terms of an exponential describing a wave having an equivalent refractive index  $\tilde{m}$  with:

$$\tilde{m} = 1 + (2\pi/ik_0^3) N \tilde{\underline{S}}(\underline{u}_0, \underline{u}_0) \quad (17)$$

In arriving at expressions (16) and (17), no account was taken of the distance of the hydrometeor slab from the receive antenna and thus the result is independent of whether the slab is located in the near or far field of the receive antenna.

### 3.2 Incoherent scattering from a thin slab of hydrometeors

For the same thin slab of hydrometeors, the incoherent signal power can also be determined using the plane wave spectrum technique.

Because of the discreteness and random location of the hydrometeors their instantaneous contribution to the received signal will fluctuate about its mean value and, in the case of a uniformly random distribution of hydrometeors, the fluctuation will have an independent contribution from each scatterer which is then termed incoherent.

The incoherent signal is contributed entirely by the hydrometeors (in contrast to the coherent signal which still exists in the absence of the hydrometeors) and can thus be viewed as a scattered signal. We denote this signal average power by  $\langle T^s T^{s*} \rangle_i$  where the superscript 's' denotes a signal scattered from the hydrometeors and the subscript 'i' indicates that the signal is incoherent. Under the assumption of an independent location for each scatterer within the slab, the total incoherent scattered signal power becomes:

$$\langle T^s T^{s*} \rangle_i = (1/4Z_0^2) \left\langle \sum_n \int_H H^* e^{-ik_0(\underline{u}-\underline{u}')} \cdot (\underline{r}_2 - \underline{r}_1^n) d\Omega d\Omega' \right\rangle \quad (18)$$

where we have written:

$$\frac{\underline{E}_R(-\underline{u}) \cdot \tilde{\underline{S}}(\underline{u}, \underline{u}_0) \cdot \underline{E}^i}{ik_0} = H \quad (19)$$

For a uniform number density within the slab and a single scatterer size, equation (18) becomes:

$$\langle T^s T^{s*} \rangle_i = (N/4Z_0^2) \int_H H^* e^{-ik_0(\underline{u}-\underline{u}')} \cdot (\underline{r}_2 - \underline{r}_1) d\Omega d\Omega' dV \quad (20)$$

Carrying out the integration with respect to  $x_1$  and  $y_1$  gives:

$$\begin{aligned} \langle T^s T^{s*} \rangle_i &= (2\pi/k_0)^2 (N\Delta z/4Z_0^2) \int_H H^* \delta(\underline{u}-\underline{u}') d\Omega d\Omega' \\ &= (2\pi/k_0)^2 (N\Delta z/4Z_0^2) \int_H H^* d\Omega dz \end{aligned} \quad (21)$$

Equation (21) shows that there are independent contributions to the received signal power from every elementary angular sector  $d\Omega$ . This is fundamental to the Radiative Transfer <sup>14</sup> formulation and has again been derived independently of the distance of the hydrometeor slab from the receive antenna.

## 4. CONCLUSIONS

In the preceding examples, we have shown, using the plane wave spectrum technique, that, for a thin slab, fundamental equations for the coherent and incoherent signals at a receive antenna due to a plane wave incident on a plane slab of hydrometeors can be derived

independently of the distance of the slab from the receive antenna. This indicates that the Van de Hulst equivalent refractive index description of the propagation of the coherent field and the Radiative Transfer description of the propagation of the incoherent field are, in fact, applicable to propagation through hydrometeors in the near field of an antenna.

A basic assumption in the derivations using the plane wave spectrum technique was that the transverse dimensions of the slab are infinite. It can be seen that, practically, for both coherent and incoherent propagation, the dimensions of the slab must be greater than the illumination region of the antenna so that 'reflections' from the slab boundaries cannot be seen by the antenna.

#### ACKNOWLEDGEMENTS

The author would very much like to thank Drs. P A Watson and N J McEwan for their help and encouragement during this work.

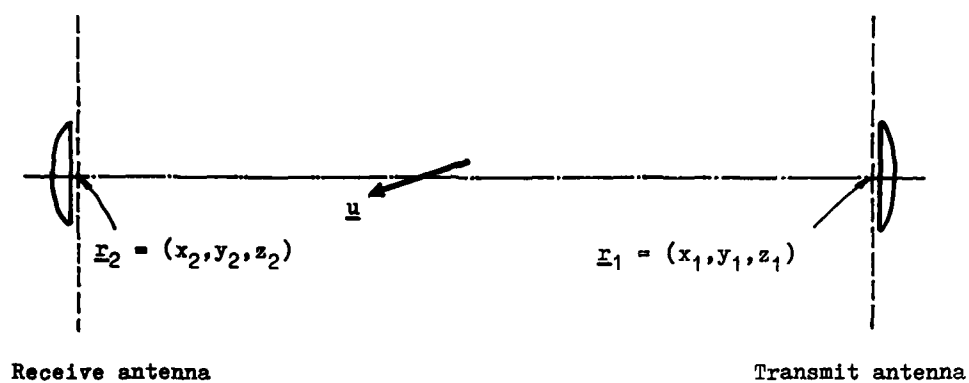
#### REFERENCES

1. WATSON P A  
 "Propagation Factors in the Design of 20 and 30 GHz Telecommunication Satellite Systems", In IEE Conf. Pub. no. 169, pp 130-134.
2. CRANE R K  
 "Prediction of the Effects of Rain on Satellite Communication Systems",  
 Proc. IEEE, 1977, 65, 3, pp 456-476.
3. BOSTIAN C W, ALLNUTT J E  
 "Ice Crystal Depolarization on Satellite-Earth Microwave Radio Paths," Proc. IEE,  
126, 10, pp 951-960.
4. MCEWAN N J, et al.  
 "Cross-Polarization from High Altitude Hydrometeors on a 20 GHz Satellite Radio Path",  
 Electron. Lett., 1977, 13, 1, pp 13-14.
5. CRANE R K  
 "Propagation Phenomena Affecting Satellite Communication Systems Operating in the  
 Centimeter and Millimeter Wavelength Bands", Proc. IEEE, 1971, 59, 2, pp 173-188.
6. VAN DE HULST H C  
 "Light Scattering by Small Particles" (Wiley New York, 1957).
7. CRANE R K  
 "The Rain Range Experiment-Propagation Through a Simulated Rain Environment", IEEE  
 Trans., 1974, AP-22, 2, pp 321-328.
8. DELOGNE P, et al.  
 "Theory and Experimental Study of Microwave Depolarization due to Rain", In 18th  
 General Assembly of URSI, Commission 2, Lima, Peru, August 1975.
9. RHODES D R  
 "Synthesis of Planar Antenna Sources" (Oxford 1974)

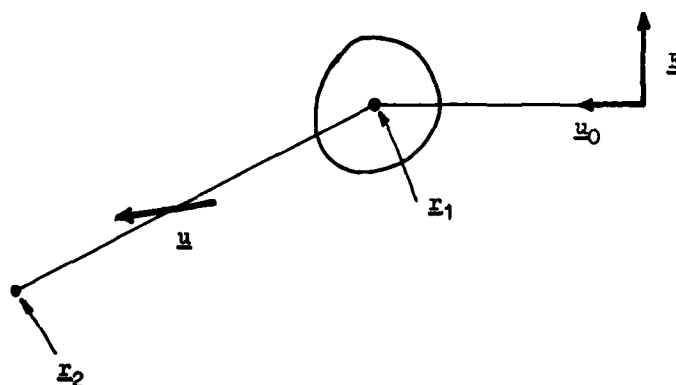
10. BROWN J  
"A Theoretical Analysis of Some Errors in Aerial Measurements", Proc. IEE, 1958, 105C, pp 343-351.
11. PRIIS H T  
"A Note on a Simple Transmission Formula", Proc. IRE, 1946, 34, pp 254-256.
12. HAWORTH D P, PhD Thesis, University of Bradford, 1980, ch 2.
13. DEVANEY A J. WOLF E  
"Multipole Expansions and Plane Wave Representations", J Math. Phys., 1974, 15, 2, pp 234-244.
14. ISHIMARU A  
"Wave Propagation and Scattering in Random Media" (Academic Press, Vol.I, ch 8).

\* Now at:

Ministry of Defence (Procurement Executive),  
Royal Signals and Radar Establishment,  
Defford,  
Dunstall,  
Earls Croome,  
Worcester.

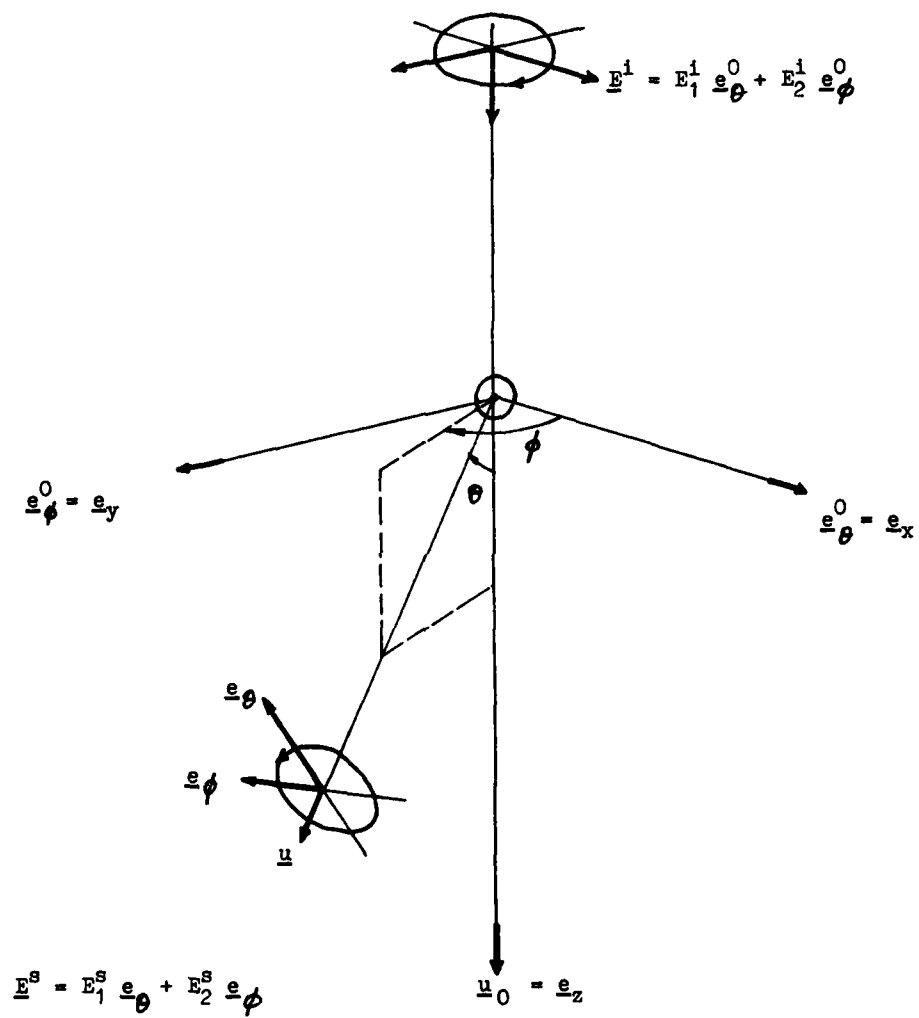
FIGURE 1

Coordinates for interaction of transmit and receive antennas

FIGURE 2

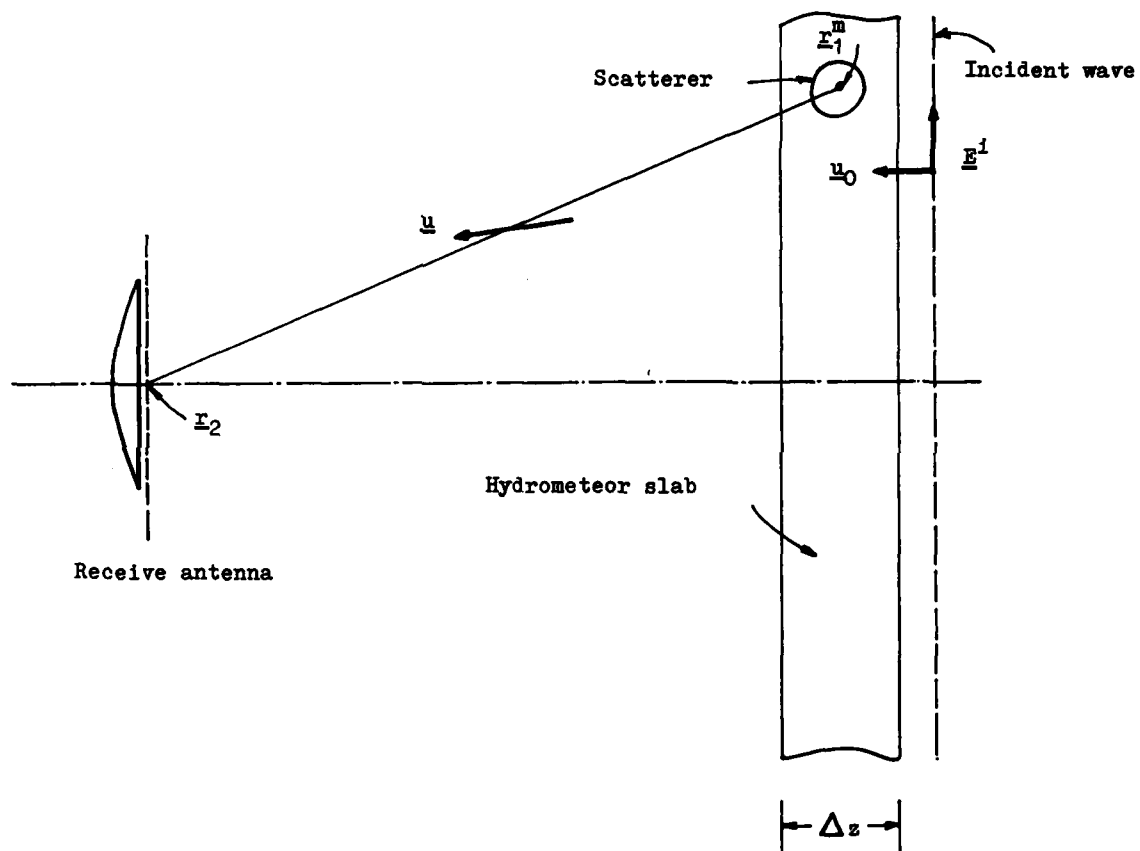
Scattering of a plane wave by a hydrometeor



FIGURE 3

Coordinate system for defining the components of the incident and scattered fields

FIGURE 4



Propagation of a plane wave through a thin slab of hydrometeors

THE FREQUENCY DEPENDANCE OF MICROWAVE PROPAGATION THROUGH RAINFALL

P.T. THOMPSON,  
SHAPE Technical Centre,  
The Hague,  
Netherlands.

A.W. DISSANAYAKE,  
P.A. WATSON,  
University of Bradford,  
United Kingdom.

1. INTRODUCTION

Much interest is being shown in the prediction of rainfall induced attenuation and depolarization at various microwave frequencies and several experiments are being conducted to evaluate such effects on both terrestrial and satellite paths.

This paper addresses the sensitivity of the prediction of rainfall induced attenuation and depolarization to various meteorological parameters.

In addition, regression analysis of the resulting predicted propagation factors leads to a simple formulation of such effects. For attenuation in particular the implications of scaling in frequency from one band to another are presented with respect to the use of such regression techniques and it is pointed out that such frequency scaling is not straight forward.

2. PREDICTION METHOD ADOPTED

Radio wave propagation through rain can be characterized by the transmission matrix (1)

$$T_{11} = \cos^2(\phi_0 + \theta) P [1 + Q \tan^2(\phi_0 + \theta)] \quad (1)$$

$$T_{22} = \cos^2(\phi_0 + \theta) P [Q + \tan^2(\phi_0 + \theta)] \quad (2)$$

$$T_{12} = T_{21} = \cos^2(\phi_0 + \theta) P (1-Q) \tan(\phi_0 + \theta) \quad (3)$$

$$P = \exp \left[ \frac{\ell}{2} (\gamma_1 + \gamma_2) + \frac{\ell}{2} (\gamma_1 - \gamma_2) e^{-2\sigma^2} \right] \quad (4)$$

$$Q = \exp(\Delta\gamma\ell) = \exp \left[ \frac{\ell}{2} (\gamma_2 - \gamma_1) e^{-2\sigma^2} \right] \quad (5)$$

$$\gamma_{1,2} = \frac{2\pi}{k_0} \int_{1,2} S^{(\alpha,0)} n(a) da \quad (6)$$

$S_{1,2}^{(\alpha,0)}$  are the forward scattering amplitudes of a raindrop of radius  $a$  in planes parallel and perpendicular to the symmetry of the drop and at an incidence angle of  $\alpha$  with respect to the major axis; in here  $n(a)da$  is the raindrop size distribution,  $\phi_0$  is the mean canting angle of raindrops in a plane perpendicular to the direction of propagation;  $\sigma$  is the standard deviation of the canting angle distribution, which is assumed to be Gaussian;  $\theta$  is the polarisation tilt angle with respect to the vertical;  $\ell$  is the effective rain path and  $k_0$  is the free space propagation constant.

2.1 Specific attenuation and phase shift

Evaluation of the transmission matrix requires a knowledge of the attenuation and phase shift along the planes parallel and perpendicular to the symmetry axes of raindrops, viz:

$$A_{1,2}^{(\alpha)} = 8.686 \operatorname{Re} \gamma_{1,2} \text{ dBs} \quad (7)$$

$$\phi(\alpha) = \frac{180}{\pi} \operatorname{Im} \gamma_{1,2} \text{ degrees} \quad (8)$$

Invoking the relationship(2)

$$S_{1,2}^{(\alpha,0)} = S_{1,2}^{(0)} \cos^2 \alpha + S_3^{(0)} \sin^2 \alpha \quad (9)$$

where  $S_{1,2}^{(0)}$  are the forward scattering amplitudes with  $\alpha=0^\circ$  incidence and  $S_3^{(0)}$  is that with  $\alpha=90^\circ$ .

$$A_{1,2}^{(\alpha)} = X_{1,2} \cos^2 \alpha + X_3 \sin^2 \alpha \quad (10)$$

$$\phi(\alpha) = Y_{1,2} \cos^2 \alpha + Y_3 \sin^2 \alpha \quad (11)$$

$$\text{where } X = 8.686 \cdot \frac{2\pi}{k_0^2} \int \operatorname{Re} S^{(0)} n(a) da \quad (12)$$

$$\text{where } Y = \frac{180}{\pi} \cdot \frac{2\pi}{k_0^2} \int \operatorname{Im} S^{(0)} n(a) da \quad (13)$$

The forward scattering amplitudes  $S_{1,2,3}^{(0)}$  were calculated using a point matching technique (3) over the frequency range 2 to 30 GHz, for various raindrop temperatures. The refractive index of water for these calculations were obtained by using the data of RAY (4).

The drop shape assumed is that of oblate spheroidal drops with a linear ratio of semimajor to semiminor axes with dropsize.

Use of the forward scattering amplitudes in equations 10, 11, 12 and 13 results in the prediction of attenuation and phase shift for the planes parallel and perpendicular to the axes of the raindrops for any given elevation angle.

This procedure requires the use of numerical integration over the specified raindrop size distribution and checks on this integration have indicated that the interval adopted (13 dropsizes) gives numerical results accurate to better than 1% over the range of interest which is considered adequate for the present considerations.

### 3. SENSITIVITY STUDIES AND RESULTS

Equations 10 and 11 have been evaluated over a range of conditions relating to drop temperature and dropsizes distributions for a 1 Km path length and rainfall rates up to 150 mm/hr.

Most tabulated scattering coefficients appearing in the literature are presented for a drop temperature of 20°C, an unrealistic temperature for earth-space paths.

The relative percentage difference between predicted attenuations at 20°C and 0°C is given in figure 1. It can be seen that differences as large as 15% can exist.

In addition the influence of variations in dropsizes distribution upon attenuation has been evaluated. This feature, which has received considerable attention in the literature, is examined here for one case only for the sake of brevity.

A comparison is made between the Laws and Parsons (5) and Marshall and Palmer (6) dropsizes distributions. The results are shown in figure 2 where it can be seen that relative percentage differences up to 10% can exist between these distributions. Larger differences are expected for the extreme dropsizes distributions present in widespread rain or thunderstorm rain.

When the polarization of the incident signal is taken into account the shape of the drops becomes an important parameter. In order to get an appreciation of the magnitude of such effects relative percentage differences in attenuations for vertical, horizontal and circular polarised signals have been evaluated referenced to the attenuation of spherical drops.

The results are shown in figure 3 where again differences of up to 15% can be seen. Thus it can be seen that drop temperature, drop shape and dropsizes distribution can all have significant influence on the prediction of attenuation and that their effects are not simply related to frequency.

### 4. REGRESSION ANALYSIS

In order to proceed further with the prediction of propagation effects a regression analysis of the previously computed attenuation data was carried out for one raindrop distribution class.

For the Laws-Parson dropsizes distribution, X and Y can be approximately related to rain rate with the following exponential relations.

$$X = aR^b \quad (14)$$

$$Y = cR^d \quad (15)$$

where R is the rain rate in mm/hr.

Regression fits for X and Y as a function of rain rate were found at various frequencies. For rain rates ranging from 5 to 150 mm/hr these regression fits resulted in less than 5% error in X and Y, over the frequency range 9 - 30 GHz. After calculating a, b, c and d at different frequencies, frequency dependant relations for these coefficients were derived by a further regression. We find that;

$$\begin{aligned} a(f) &= 10^{(p+q/f)} & 9 < f < 16 & \quad (16) \\ &= 10^{(p+qf^r)} & 16 < f < 30 & \end{aligned}$$

$$\begin{aligned} b(f) &= s+t \log f & 9 < f < 16 & \\ &= s+tf^u & 16 < f < 30 & \quad (17) \end{aligned}$$

$$c(f) = vf^v \quad 9 < f < 30 \quad (18)$$

$$d(f) = xf^{(y+z \log f)} \quad 9 < f < 30 \quad (19)$$

where f is the frequency in GHz. Regression coefficients for the above relations are given in Table 1 for temperature 0°C and 20°C.

With the above relations, at 20°C, the maximum percentage errors for predicted attenuation and phase shift are at most 6% for the entire frequency range. At 0°C, the maximum errors for attenuation and phase shift are 5%, except for frequencies above 28 GHz, where the respective values increase from 5% to 12% and 7% at 30 GHz. Accurate a, b, c and d values for 30 GHz are at 0°C are shown separately.

It is noted the regression relationships given by Damosso (7) did not include calculations for  $X_2$  and  $Y_2$  and hence will not facilitate predictions for arbitrary elevation angles. Also we have included the effects of temperature on the scattering coefficients, which effects are particularly important in the range 9 to 15 GHz.

Figures 4 and 5 illustrate the variation of  $a_2$  and  $b_2$  with frequency and drop temperature for  $0^\circ$  elevation. The effects of variation in elevation angle from  $0^\circ$  to  $30^\circ$  upon  $a$  and  $b$  have considerably less influence than the drop temperature.

#### 5. FREQUENCY-SCALING OF ATTENUATION

The dependence of specific attenuation on drop temperature and drop-size has been described and parameterised in terms of regression analysis, for the frequency range 9-30 GHz. Evidently such dependence must have a bearing on any theoretical frequency-scaling that may be attempted. However, if one wishes to scale statistics of attenuation considerable caution must be exercised. This point will now be discussed.

Log-normal statistics may be taken as a satisfactory representation for the statistics of ground point rainfall intensity (8-10). In addition the statistics of attenuation on earth-space paths over a long period appear to approximate closely to log-normal (8,11). Frequency scaling of attenuation statistics should thus be in terms of statistical transformations.

Now for any given frequency attenuation-point-rainfall relationships of the form  $\alpha(l) = AR^B$  dB may be derived, provided that a realistic rain cell model or spatial profile  $R(x)$ , is available (12) viz:

$$\alpha(l) = A^1 \int R^{B^1}(x) dx = AR^B \text{ dB} \quad (20)$$

where  $A^1$  and  $B^1$  can be taken for a given temperature and drop-size distribution from the regression relationships given earlier. However, for at least two reasons, it must be noted that it is incorrect to use such relationships directly for frequency scaling. Firstly, and most importantly the statistics of attenuation determined at one frequency relate to the probability of occurrence of various combinations of cell sizes, rain intensities, drop sizes and drop temperatures. At any other frequency, for the same percentage time, other combinations of these factors may be equally important and as statistically significant. Hence it is incorrect to take a deterministic population of drops and base a frequency scaling on that population. The statistics of attenuation at each frequency must be thought of as a convolution of many terms each with a unique frequency dependence. The overall result of the convolution at each frequency (the conditional probability of a fade being exceeded) appears to be adequately described by a logarithmic normal distribution, but the parameters of the distribution, mean and deviation may vary with frequency (see Watson 13). Deterministic transformations using  $\alpha = AR^B$  relationships may of course be used for a variety of extreme drop-size populations, temperatures, cell sizes, etc. in order to determine the physical upper and lower bounds within which the statistical scalings must lie. However, since  $B$  is not unity, such transformations will not be log-normal and should be used with caution. To carry out the complete convolution, we require further statistical data on rainfall spatial structure for intensity and drop-size. As an indication of purely deterministic frequency scaling factors Table 2 gives the ratio between the up and down path frequencies employed with the OTS satellite for various rainfall conditions.

Secondly, for a slant path, contributions from the bright band and ice particles can affect scaling factors quite considerably (13). For example fig. 6 shows the expected attenuation ratios at 30/20 GHz for water and ice particles as a function of particle radius. A small contribution to attenuation ( $\approx 0.5$  dB) from frozen hydrometers at 30 GHz can thus radically change the attenuation ratio. A further factor affecting attenuation ratio at low attenuations is that of the background water vapour content. Frequency scaling uncertainties introduced by ice and water vapour effects are illustrated on fig. 7 using data collected by the UK Post Office during the ATS-6 programme (14).

Both the previous aspects, that is the inappropriateness of taking frequency scalings of statistics from fixed populations of particles and the neglect of ice particle effects, must be raised in argument against the over-simplistic approach to frequency scaling using equivalent radio path length (15). For example if we use the data given in fig. 7 and interpret this in terms of Laws-Parsons rainfall an equivalent radio path length of 14 km must be inferred. Much more reasonable radio-path lengths through rain for this particle path geometry ( $\approx 8$  km) are inferred with just 0.5 dB contributed at 30 GHz from frozen hydrometers.

#### 6. CONCLUSIONS

The effect of temperature and drop-size distribution on rainfall attenuation in the frequency range 2-30 GHz have been illustrated and regression relationships given for attenuation and phase shift in the 9-30 GHz range. These relationships should be directly useful in checking frequency scaling bounds for attenuation. Also with the correct use of statistical techniques and the inclusion of ice-particle and water vapour effects, these relationships represent an essential first step towards the frequency scaling of attenuation statistics.

REFERENCES

1. BRUSSARD, G. "A Meteorological model for rain induced crosspolarisation", IEEE TRANS. AP-24, pp 5-11, 1976.
2. UZUNOGLU, N.  
EVANS, B.G.  
HOLT, A.R. "Scattering of electromagnetic radiation by precipitation particles and propagation characteristics of terrestrial and space communications systems", Proc. IEE, Vol. 124, pp 417-424, 1977.
3. MORRISON, J.A.  
CROSS, N.J. "Scattering of a plane electromagnetic wave by axisymmetric raindrops", B.S.T.J., Vol. 53, pp 935-1019, 1974.
4. RAY, P.S. "Broadband complex refractive indices of ice and water", Appl. Opt., 11, pp 1836-1844, 1972.
5. LAWS, J.O.  
PARSONS, D.A. "The relation of raindrop-size to intensity", Trans. Am. Geophysical Union, Vol. 24, pp 432-460, 1943.
6. MARSHALL, J.S.  
PALMER, W. McK. "The distribution of raindrops with size", J. Meteor., No. 5, pp 165-166, 1948.
7. DAMOSSO, E. "Dependence of specific rain attenuation and phase shift on electrical meteorological and geometric parameters", ESA SP-138, pp 219-225, 1978.
8. LIN, S.H. "A method for calculating rain attenuation distributions on microwave paths" BSTJ 54 No. 6, Aug. 1975, p. 1051-1086
9. HANSEN, L. "General characteristics of rain intensity statistics in the Stockholm area" Report URS 74 092, Central Administration of Swedish Telecommunications, Sept. 1974
10. MISMÉ, P. "Experimental results about rain induced attenuation and improvement of calculation methods" IEE Conf. on "Antennas and Propagation", London, Nov. 1978, Part 2 "Propagation", p. 102-106.
11. BRUSSARD, G.  
WATSON, P.A. "Annual and annual-worst-month statistics of fading on earth-satellite paths at 11.5 GHz" Elec. Letts. 14 No. 9 April 1978 pp 278-280.
12. WATSON, P.A.  
PAPAIOANNOU, G.  
AHMED, H.J. "Long-term prediction of attenuation of terrestrial radio links from rainfall data", IEE Conf. on "Antennas and propagation" London, Nov. 1978, Part 2 "Propagation", pp 92-96.
13. WATSON, P.A. "Propagation factors in the design of 20 and 30 GHz telecommunications satellite systems". i.b.i.d. p. 130-134.
14. HOWELL, et al. "20 and 30 GHz attenuation measurements using the ATS-6 satellite" ESA publication, ESA SP1 131, Sept. 1977, pp. 55-68.
15. HOGG, D.C. "Intensity and extent of rain on earth-space paths" Nature 243 No. 5 June 1973 pp 337-338.

TABLE 1. REGRESSION COEFFICIENTS FOR SPECIFIC ATTENUATION AND PHASE SHIFT

	p	q
$a_1(0^\circ\text{C})$	-0.5556	-14.106
$a_1(20^\circ\text{C})$	-0.2101	-18.18
$a_2(0^\circ\text{C})$	-0.5419	-13.704
$a_2(20^\circ\text{C})$	-0.2389	-17.205
$a_3(0^\circ\text{C})$	-0.5781	-13.671
$a_3(20^\circ\text{C})$	-0.2513	-17.642

$$a(f) = 10^{(p+q/f)} \quad 9 < f < 16$$

	p	q	r
$a_1(0^\circ\text{C})$	12.515	-17.296	-0.07768
$a_1(20^\circ\text{C})$	0.3999	-11.433	-0.6761
$a_2(0^\circ\text{C})$	20.242	-24.9	-0.05085
$a_2(20^\circ\text{C})$	1.2294	-9.0055	-0.4547
$a_3(0^\circ\text{C})$	32.819	-37.483	-0.03271
$a_3(20^\circ\text{C})$	1.3527	-9.204	-0.4403

$$a(f) = 10^{(p+qf^r)} \quad 16 < f < 30$$

	s	t
$b_1(0^\circ\text{C})$	1.5996	-0.4215
$b_1(20^\circ\text{C})$	2.1939	-0.9437
$b_2(0^\circ\text{C})$	1.5415	-0.3384
$b_2(20^\circ\text{C})$	2.0969	-0.8347
$b_3(0^\circ\text{C})$	1.4473	-0.2513
$b_3(20^\circ\text{C})$	2.0283	-0.7644

$$b(f) = s+t \log f \quad 9 < f < 16$$

	s	t	u
$b_1(0^\circ\text{C})$	-0.1468	1.7707	-0.1271
$b_1(20^\circ\text{C})$	0.8973	7.5503	-1.3381
$b_2(0^\circ\text{C})$	-0.6714	2.3674	-0.09755
$b_2(20^\circ\text{C})$	0.307	1.6694	-0.2584
$b_3(0^\circ\text{C})$	-0.6734	2.3291	-0.08972
$b_3(20^\circ\text{C})$	0.08198	1.7897	-0.1909

$$b(f) = s+tf^u \quad 16 < f < 30$$

	v	w
$c_1(0^\circ\text{C})$	0.08827	1.106
$c_1(20^\circ\text{C})$	0.0907	1.1015
$c_2(0^\circ\text{C})$	0.08719	1.1386
$c_2(20^\circ\text{C})$	0.09005	1.1309
$c_3(0^\circ\text{C})$	0.08634	1.1362
$c_3(20^\circ\text{C})$	0.08908	1.1314

$$c(f) = vf^w \quad 9 < f < 30$$

	x	y	z
$d_1(0^\circ\text{C})$	0.7456	0.2145	-0.1395
$d_1(20^\circ\text{C})$	0.8027	0.1585	-0.1195
$d_2(0^\circ\text{C})$	0.7068	0.2988	-0.1886
$d_2(20^\circ\text{C})$	0.7472	0.2595	-0.1755
$d_3(0^\circ\text{C})$	0.6783	0.3308	-0.1989
$d_3(20^\circ\text{C})$	0.7061	0.3052	-0.192

$$d(f) = xf^{(y+z \log f)} \quad 9 < f < 30$$

At 30 GHz and at  $0^\circ\text{C}$ , the coefficients a,b,c and d are as follows:

$a_1$	0.1751	$b_1$	0.9904	$c_1$	3.853	$d_1$	0.7577
$a_2$	0.2044	$b_2$	1.0071	$c_2$	4.3221	$d_2$	0.7409
$a_3$	0.1973	$b_3$	1.02	$c_3$	4.3202	$d_3$	0.7514

TABLE 2.

PREDICTED RATIO OF ATTENUATION 14.455 GHz to 11.786 GHz (DETERMINISTIC)

(Frequencies employed by the OTS satellite)

Rainfall Rate mm/hr	Temperature of Raindrops		
	$0^\circ\text{C}$	$10^\circ\text{C}$	$20^\circ\text{C}$
<b>LAWS &amp; PARSONS</b>			
150	1.464	1.414	1.414
100	1.481	1.434	1.444
50	1.517	1.489	1.532
<b>MARSHALL &amp; PALMER</b>			
150	1.482	1.448	1.472
100	1.498	1.468	1.501
50	1.526	1.507	1.560

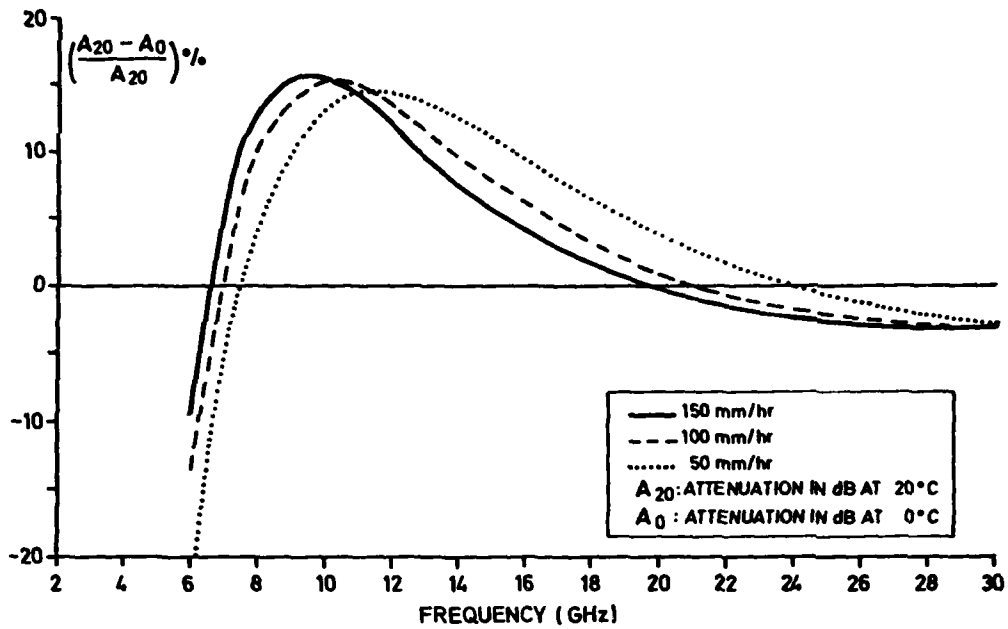


FIGURE 1 INFLUENCE OF RAINDROP TEMPERATURE ON ATTENUATION

(LAWS AND PARSONS DROPSIZE DISTRIBUTION WITH CIRCULAR POLARISATION)

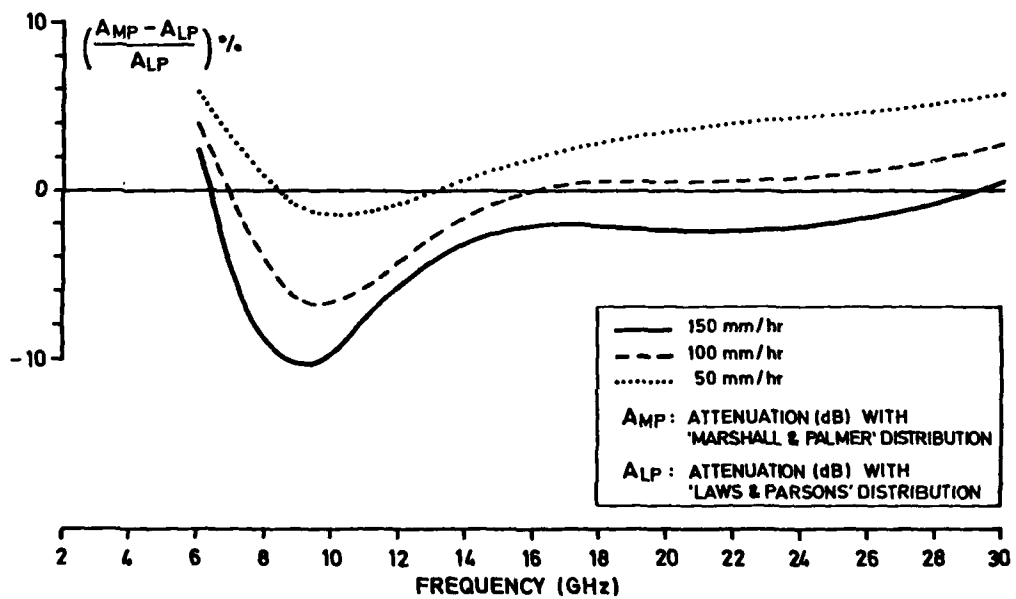


FIGURE 2 INFLUENCE OF RAINDROP SIZE DISTRIBUTION ON ATTENUATION

(CIRCULAR POLARISATION, 0°C)



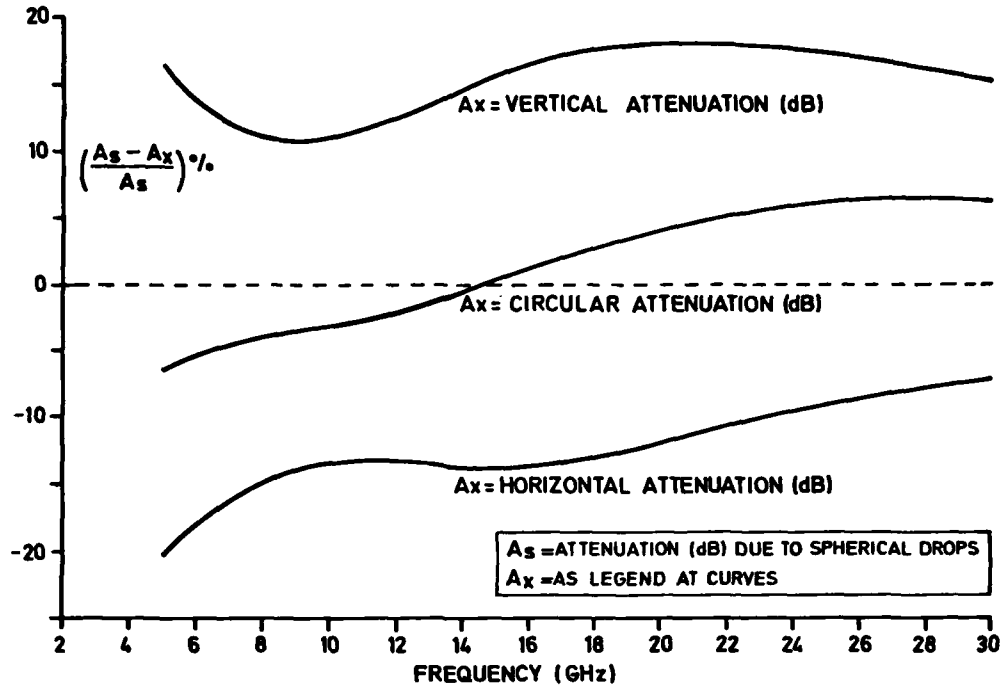


FIGURE 3 INFLUENCE OF DROP SHAPE AND POLARISATION ON ATTENUATION (LAWS AND PARSONS, 0°C, 0° ELEVATION)

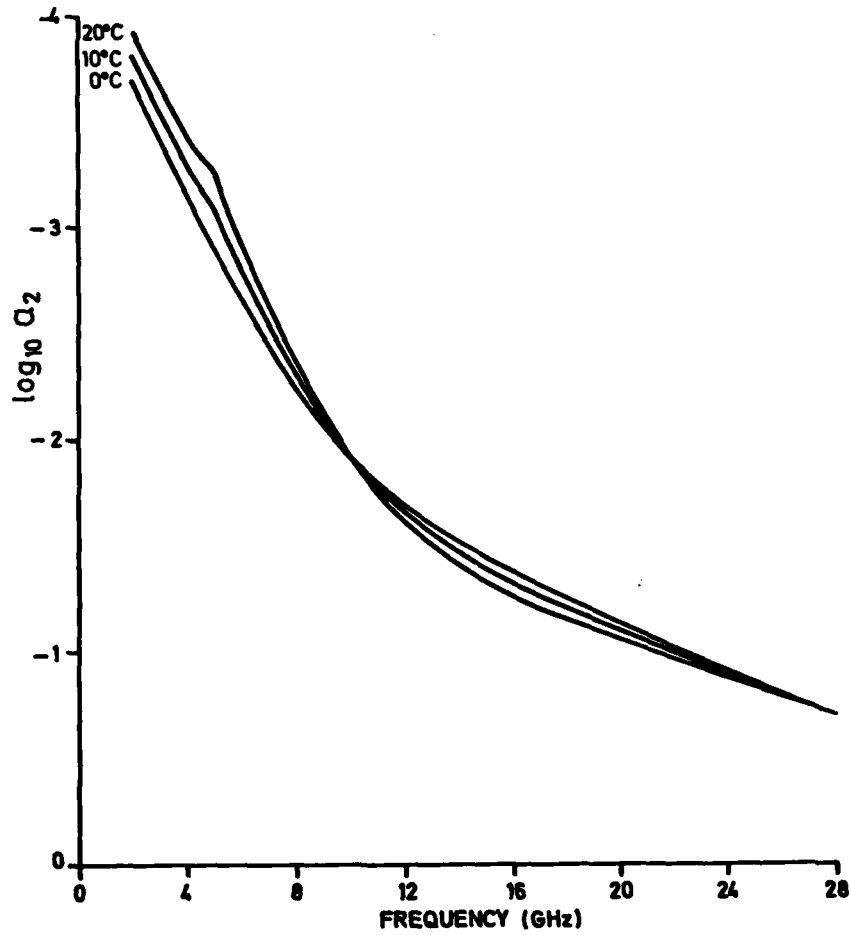


FIGURE 4 VARIATION OF  $\log_{10} Q_2$  WITH FREQUENCY

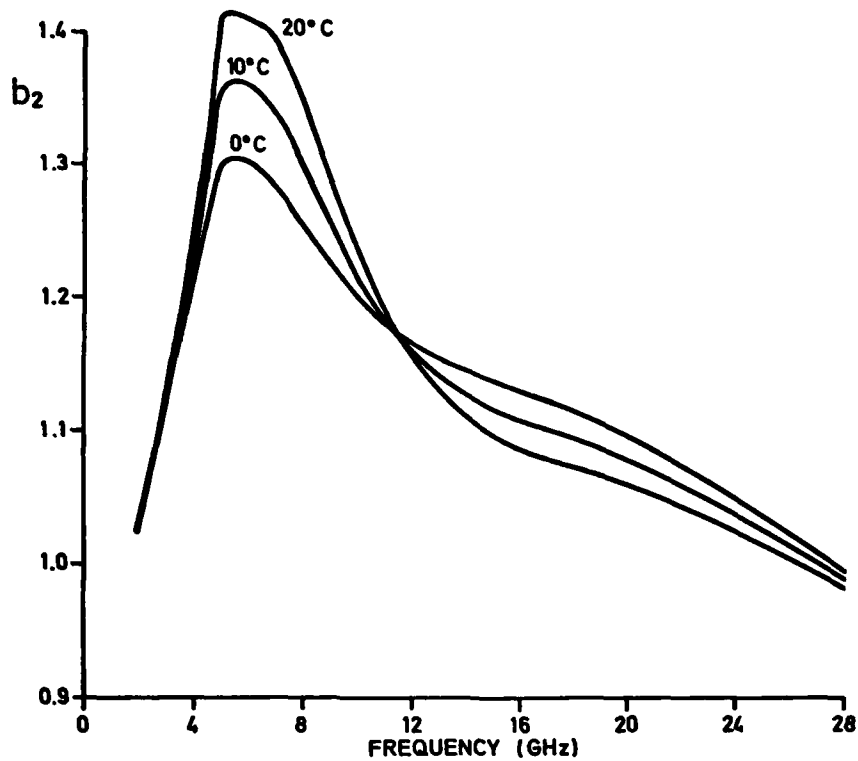


FIGURE 5 VARIATION OF  $b_2$  WITH FREQUENCY

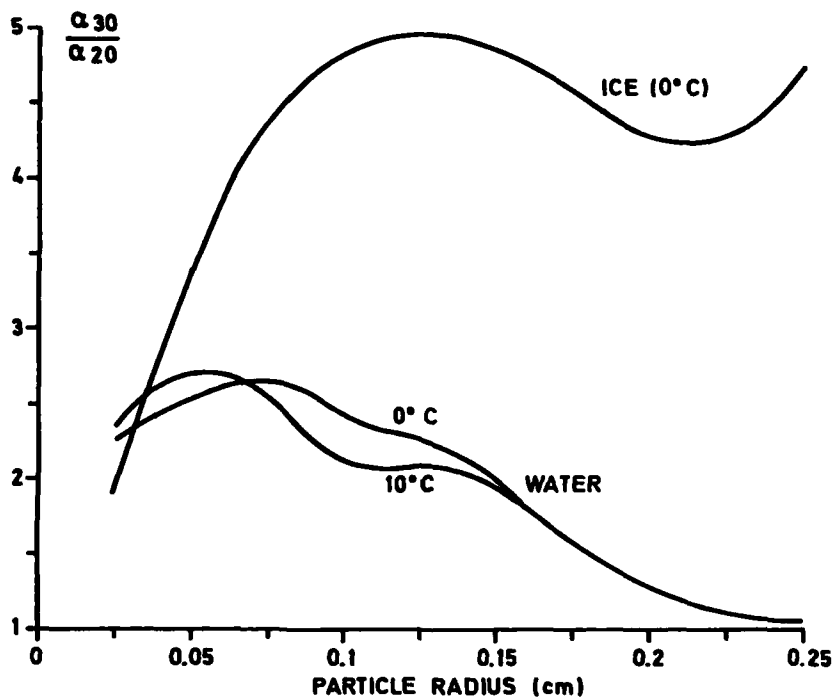


FIGURE 6 RATIOS OF ATTENUATION AT 30/20 GHz FOR ICE AND WATER PARTICLES

VERTICAL POLARISATION

POINT-MATCHING CALCULATIONS FOR OBLATE SPHEROIDS

PARTICLE RADIUS IS THAT OF EQUI-VOLUMETRIC SPHERE

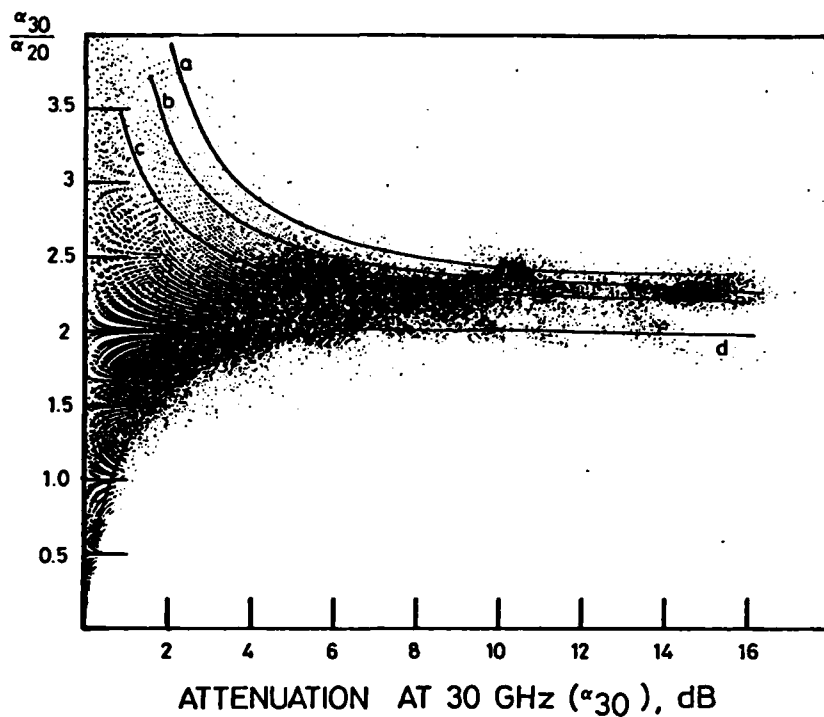


FIGURE 7 RATIO OF ATTENUATION 30/20 GHz VERSUS ATTENUATION AT 30 GHz  
(U.K. P.O. ATS-6 DATA)

ALL THEORETICAL CURVES (a-d) ARE FOR AN 8 KM RAINCELL.

USE OF A SMALLER RAINCELL IMPLIES EVEN LOWER VALUES OF ATTENUATION RATIO.

- a; NO ADDED WATER VAPOUR DURING RAIN, 1 DB ICE ATTENUATION AT 30 GHz, - 0.1 DB RESIDUAL ERROR AT 20 GHz.
- b; DITTO, BUT 0.5 DB ICE ATTENUATION AT 30 GHz.
- c; NO ADDED WATER VAPOUR DURING RAIN OR ICE ATTENUATION, - 0.1 DB RESIDUAL ERROR AT 20 GHz.
- d; SATURATED WATER VAPOUR CONTENT WHEN RAINING FOR GROUND TEMPERATURE OF 15°C (4.5 g/m<sup>3</sup> EXTRA TO a-c) + 0.1 DB RESIDUAL ERROR AT 20 GHz.

## SIMULATION OF EHF PROPAGATION THROUGH THE ATMOSPHERE

J. D. Hopponen

Lockheed Missiles and Space Company  
Sunnyvale, California 94086 USA

### SUMMARY

It is possible to predict the effect of the clear, nonturbulent air mass on the propagation of EHF (10 to 300 GHz) radio waves at various slant path angles. Molecular absorption spectra (principally of O<sub>2</sub> and H<sub>2</sub>O) cause frequency dependent signal attenuation, phase delay, ray bending, and medium noise. The interaction between the physical environment and the traversing radiation is expressed by a complex refractivity N<sub>c</sub>, which is a function of frequency f, total pressure p, partial water vapor pressure p<sub>w</sub>, and temperature T. The Earth's magnetic field strength, which enters into Zeeman splitting of the absorption lines at high altitudes, is regarded as a nearly negligible background parameter. The means of calculating N<sub>c</sub> utilizes a recent spectroscopic data base for the 60 GHz oxygen band and the 22.235 GHz water vapor line. In addition to the 183 GHz water vapor line, 6 higher frequency lines plus a nonresonant term are included. A distribution of the gas variables p, p<sub>w</sub>, and T for the neutral air (surface to 80 km) leads to a profile of N<sub>c</sub> which provides the basis for calculating the various propagation effects along a specified radio path (ground-to-ground, -aircraft, or -spacecraft). The distribution of atmospheric data may be obtained from in situ soundings (e.g., radiosonde) or from standard atmospheric models.

The computer model presented assumes a symmetric, spherically stratified atmosphere in which the layers need not be regarded as homogeneous, as a consequence of the interpolation methods developed for N<sub>c</sub>. The main problems center on the evaluation of integral expressions for radio range, cumulative attenuation, and noise temperature. Lacking closed-form solutions, these integrals are best handled with special numerical methods which are amenable to the adaptive Romberg integration algorithm. Particular detail is given to the treatment of the noise integrals. Various aspects of EHF propagation phenomena which are given by this computer model are exemplified.

### 1.0 INTRODUCTION

The clear, nonturbulent air mass up to an altitude of 80 kilometers acts as a unique filter over the EHF (10 to 300 GHz) band with transfer, shielding, and emission characteristics not found at lower frequencies. The selective absorption of microwave energy by molecular oxygen and water vapor results in frequency-dependent attenuation phase delay, range error, signal-to-noise ratio and offers special remote sensing features. All of these effects are functions of the climatology assumed for the earth-space path of interest and may show considerable diurnal and seasonal variation. Therefore, although standard reference values may be available for the phenomena of interest, the careful assessment of propagation effects along a ground-to-satellite link requires a means of obtaining accurate predictions for any set of meteorological data. One approach to this problem is the computer modelling of electromagnetic wave propagation through the atmosphere.

The coupling of the physical environment and the propagation equations is through the complex index of refraction n<sub>c</sub> of air. In the EHF band, the dispersive components of n<sub>c</sub> are primarily due to the absorption spectra of molecular oxygen and water vapor, and are indicative of attenuation and frequency-selective ray bending and phase delay. Recent laboratory efforts have produced analytic expressions for the calculation of n<sub>c</sub>, and these are used to generate a profile of n<sub>c</sub> from a height distribution of basic atmospheric data. By using the refractive index profile in a ray tracing methodology, characteristics of EHF systems may be simulated to aid in design and analysis. In order to employ such a tool in an optimum manner, it is important to consider the speed and accuracy of the algorithms used in ray tracing.

### 2.0 ATMOSPHERIC INTERACTION WITH RADIATION

#### 2.1 Complex Refractivity

Simulation of electromagnetic wave propagation through the lower 80 km of the air mass begins with specification of the atmospheric conditions. For the clear, nonturbulent atmosphere, it is sufficient to give a height distribution of temperature T, pressure P, and water vapor content P<sub>w</sub>. The calculations which employ these parameters to obtain a height profile of the complex index of refraction require the mks units of kelvins (T) and Pascals (P and P<sub>w</sub>). Since water vapor content is often specified in a variety of ways, (e.g., relative humidity (percent), absolute humidity (grams per cubic meter)), some conversion may be necessary. Also, the heights given in standard reference atmospheres as well as in many radiosonde profiles are in geopotential meters, so an additional conversion, which introduces a dependence on the geographic latitude, is called for. The requisite transformations are given succinctly by List (1958) and the general approach is that of Levine, et al (1973).

Properties of the propagation medium enter into a solution of Maxwell's equations through the complex index of refraction n<sub>c</sub>, which is often reduced to a complex refractivity N<sub>c</sub> by

$$N_c = (\text{Re}(n_c) - 1) \times 10^6 + j \text{Im}(n_c) \times 10^6$$

Re denotes 'real part of' and Im denotes the 'imaginary part of'. For frequencies below 300 GHz,

$$N_c = N_0 + \sum_i (S_i F_i') + N_w' + j \left\{ \sum_i (S_i F_i'') + N_w'' \right\}$$

$N_0$ , the only frequency-independent term, is given by Thayer (1974) as

$$N_0 = K_1 \frac{P}{T} z_d^{-1} + K_2 \frac{P_w}{T} z_w^{-1} + K_3 \frac{P_w}{T^2} z_w^{-1}$$

with pressure in millibars, temperature in Kelvins, and  $K_1 = 77.6$ ,  $K_2 = 64.8$ ,  $K_3 = 3.776 \times 10^5$ . The inverse compressibility factors  $z_d$  and  $z_w$  account for departure from ideal gas behavior.

The frequency-dependent terms are due to the rotational spectra of molecular oxygen and water vapor plus background terms from outside the EHF band. At the low end, the background is from 'nonresonant' absorption at 0 Hz, while resonance lines above 300 GHz form a background which increases with frequency across the band. Additionally, the so-called anomalous absorption by water vapor may enter via the  $N_w''$  and  $N_w'$  terms. The line strength functions  $S_j$ , the modified Van Vleck-Weisskopf shape functions  $F''$  and  $F'$ , and the individual frequencies which correspond to the summations, and the requisite spectroscopic parameters are given by Liebe, et al (1977), who conducted a three laboratory study of the 60 GHz oxygen band and obtained experimental confirmation of the Rosenkranz line overlap theory (Rosenkranz 1975). Although the Rosenkranz formulation and the underlying assumptions are receiving careful scrutiny (Smith 1980), Liebe's methods appear best in terms of a balance between speed and accuracy versus physical theory. Furthermore, Liebe's model includes not only attenuation but also phase effects, allows for the nonlinear interaction between oxygen and water vapor through the foreign gas broadening of the individual lines, and approximates Zeeman and Doppler broadening at high altitudes (above 20 km). It is this model, together with the results of Thayer, which is employed to calculate the complex index of refraction of the atmosphere for a given temperature, pressure, and water vapor content.

## 2.2 $N_C$ Profiles

In terms of  $N_C$ , power attenuation and phase delay are given by

$$\begin{aligned} \alpha &= 20 \log e \times 0.0209 \times f_{\text{GHz}} \times \text{Im}(N_C) \quad (\text{dB/km}) \\ \phi &= 0.0209 \times f_{\text{GHz}} \times \text{Re}(N_C) \quad (\text{Radians/km}) \end{aligned}$$

where  $f_{\text{GHz}}$  is frequency in gigahertz and 0.0209 comes from  $2 \pi/c$  and some adjustment of units. These relatively simple expressions may suffice for predicting certain EHF channel characteristics along short horizontal paths through a homogeneous atmosphere. For the more general case of a slant path through a non-homogeneous clear air mass (e.g., satellite-to-ground links, radar tracking, remote sensing) a height profile of atmospheric data is used to generate a corresponding profile of  $N_C$  for use in a ray tracing methodology. When a  $N_C$  profile is calculated, it is often advisable to store it on computer disk file (or whatever is available) if ray tracing is to be performed by several program executions. This affords some economy as then only the ray tracing with new parameters, say elevation angle, need be run. Furthermore, a separate main program for the complex index of refraction reduces the overall (compiled) size of the ray tracing program and permits future development work on one module from impacting the other. If more than one frequency is to be run, it is advisable to calculate  $N_0$  first and then proceed with the dispersive calculations.

It often happens that the profile of atmospheric data is so coarse (i.e., the data heights are relatively far apart) that the derived  $N_C$  profile is of questionable value in ray tracing. Thus, interpolation on either the basic data or the  $N_C$  profile is required. Although working with temperature, pressure, and water vapor is, in a sense, more fundamental, there are clear advantages in adding additional points directly to the  $N_C$  profile. Generation of new values of  $N_C$  by first interpolating the data entails three interpolations (one for each atmospheric variable) followed by the evaluation of the expression for the complex refractive index. This is not only time consuming but also supposes that the ray tracing program has the code to calculate  $N_C$ , contrary to the philosophy expressed earlier. Furthermore, it is the ray tracing program which will require the interpolated values, and the 'closeness' of points will be seen to be a function of the ray elevation angle and a convergence criterion, discussed below. In view of these considerations, the  $N_C$  values, not the atmospheric data, receive the manipulations.

## 2.3 $N_C$ Interpolation

For interpolation of the real part of  $N_C$  we follow Hopfield (1969). Thus, assuming a linear variation of temperature across a layer with the scaled height  $h$  varying between 0 and  $h_1$ , the hydrostatic equation and the gas law yield

$$\text{Re}(N(h)) = \text{Re}(N(0)) \left[ 1 - mh/T_0 \right]^\mu$$

Here  $h$  lies between 0 and  $h_1$ ,

$$T = T_0 - mh,$$

and the exponent

$$\mu = g/Rm - 1,$$

where  $g$  is the acceleration due to gravity (which varies with height and latitude) and  $R$  is the gas constant given by  $(1.30 \times 10^{-23}) \times (6.02 \times 10^{23})$ .

The imaginary part of  $N_C$  is conveniently treated with linear interpolation, and for layers of 2 km or less the agreement between interpolated values of  $\text{Im}(N_C)$  and those calculated by interpolating the data is quite good. When the input atmosphere has layers larger than 2 km some other method, such as exponential interpolation,

may be more appropriate. The nonlinear behavior is a consequence of the nontrivial temperature-pressure-water vapor pressure dependence of the quantum mechanical expression for  $\text{Im}(N_c)$ .

By virtue of the means to interpolate  $N_c$ , the spherically symmetric shells defined by the height profile of  $N_c$  need not be regarded as homogeneous. This intrinsically satisfying feature has important ramifications in the evaluation of the ray trace integrals.

### 3.0 RAY TRACING

#### 3.1 Path Differential

A 'ray' is an imagined curve generated by successive normals to surfaces of constant phase. For a nonhomogeneous atmosphere the phase velocity may vary from point to point, resulting in ray bending. Using the spherical form of Snell's Law, a differential of curved ray path is given as

$$ds = \left( 1 - \left[ \frac{n_0(h_0) \cos \theta_0}{n_0(h) \left( 1 + \frac{h-h_0}{r_0+h_0} \right)} \right]^2 \right)^{-1/2} dh .$$

In this expression  $dh$  is the differential of height,  $r_0$  is the standard earth radius (6371.23 km) and  $\theta_0$  is the ray elevation angle at the initial height  $h_0$  (usually the earth's surface). For angles less than  $1^\circ$ , the expression for  $ds$  is numerically unstable, particularly when  $h$  is near  $h_0$ . This difficulty is circumvented by expanding both  $n^{-2}$  and  $(1 + (h-h_0)/(r_0+h_0))^{-2}$  as power series and retaining only terms of degree less than three. The resulting quadratic yields an integral which may be obtained in closed form and is similar to the form given by Blake (1968) but takes cognizance of the novel form of interpolation for refractivity ( $\text{Re}(N_c)$ ).

#### 3.2 Adaptive Integration

The path differential  $ds$  is used to formulate several integrals of interest. These integrals resist attempts at closed-form solution and so must be evaluated by numerical methods. Owing to the methodology adopted to treat the input data and also to the nature of the integrands, adaptive Romberg numerical integration (Bauer 1961) is found to be quite satisfactory. Beginning with the trapezoidal rule, the Romberg method shifts to higher order schemes through the use of a relation of the sort

$$R_n^{(k+1)} = \frac{4^{k+1} R_{2n}^{(k)} - R_n^{(k)}}{4^{k+1} - 1}$$

Thus, the Romberg method not only adaptively inserts addition points but also uses the new information in a very prudent manner to accelerate convergence of the algorithm. This is an especially desirable feature since the number of points required to evaluate an integral across an atmospheric layer is not known in advance and may vary considerably with layer size and elevation angle. The lowest layer in the atmosphere, where refraction is most pronounced, is always subdivided into groups of ten intervals of thickness 0.5, 5.0, 50.0, etc., meters up from the surface to the next reporting point, so at low elevation angles the adaptive integration is exercised quite heavily.

#### 3.3 Radio Range and Attenuation

Among the integrals of interest, the easiest to evaluate is radio range,

$$R = \int_0^H n(h) ds$$

where  $n(h)$  is the real part of the refractive index as a function of height. This integral is clearly sensitive to variations in  $n(h)$ , and in particular shows the effect of dispersion. By tracing rays with and without dispersion at several frequencies on either side of the 60 GHz absorption band (where standard resonance considerations indicate dispersion peaks), a difference of nearly 0.4 meters is observed at 63 GHz. Compared to the wavelength of approximately 5 mm, this is substantial. The results are shown in Figure 1.

The imaginary part of  $n_c$  yields another integral, namely cumulative attenuation along the ray path,

$$A = \int_0^H \alpha(h) ds$$

where  $\alpha(h)$  is power attenuation as a function of height. Total attenuation may show considerable variations with season, as depicted in Figure 2. Here attenuation was calculated across the EHF band first using a cool, dry midlatitude winter atmosphere and then a warm, moist summer atmosphere. The fine structure resulting from the complex of lines about 60 GHz is not shown, but a cross-over of the two curves is indicated. This is primarily a result of the complicated temperature dependence in the quantum mechanical expressions for absorption.

### 3.4 Noise Temperature

When the Rayleigh-Jeans approximation to the Planck blackbody function is substituted into the radiative transfer equation for a nonscattering atmosphere, two solutions for equivalent blackbody temperature are obtained (Chandrasekar 1950). In the first case, radiation is upwelling (i.e., impinging from below, as with a nadir viewing satellite-borne antenna), and

$$N_{\text{up}} = \int_{h_0}^H \alpha T \exp\left(-\int_h^H \alpha ds\right) ds .$$

Here  $T$  is air temperature as a function of height,  $H$  is the height up to which the radiation is flowing, and  $h_0$  is the height of the earth's surface. For radiation downwelling to height  $h_0$  (which is not necessarily the earth's surface height in this case), the noise temperature is

$$N_{\text{DN}} = \int_{h_0}^{\infty} \alpha T_{\text{air}} \exp\left(-\int_{h_0}^h \alpha ds\right) ds .$$

In both integrals  $ds$  is a differential of curved ray path and includes refractive bending.

In either integral, the factor  $\alpha T_{\text{air}}$  is, by the Rayleigh-Jeans approximation, proportional to the emission from an infinitesimal volume of the air mass. The exponential factor, called the transmittance, gives the power loss from a point at height  $h$  to the reference point at height  $H$  or  $h_0$ .

Figure 3 shows atmospheric contribution to noise temperature due to vertical radiation upwelling to a satellite through atmospheres representing extreme environmental conditions. The warm, moist tropical atmosphere generally yields higher noise temperatures than the cool, dry subarctic winter atmosphere, although in the bands of high absorption the values are more nearly equal; the actual behavior is dependent on the exact frequency studied as well as the conditions between 0 and 80 kilometers.

Figure 4 compares the atmospheric contribution to upwelling and downwelling noise temperature through a vertical path from a mid-latitude winter atmosphere. Except for regions of strong absorption, where the ground-based sensor receives radiation only from the immediate vicinity, the curves are nearly coincident across the EHF band.

The variation of noise temperature with elevation angle at 58.825 GHz is shown in Figure 5. A midlatitude winter atmosphere was used, and surface contributions ( $T_{\text{surface}} = 280.0$ , emissivity = 0.4) typical of ocean conditions were included. At this frequency there is less than 2 degrees (Kelvin) variation, (so the earth appears as a nearly uniform noise source), but at other frequencies this is not the case.

The variation of noise temperature with elevation angle is a result of the angle dependence of the weighting function (the product of the factors which multiply temperature  $T$  in the noise integral). Figure 6 shows the 58.825 weighting functions for elevation angles of  $0^\circ$ ,  $40^\circ$  and  $90^\circ$  (vertical) as a function of height. Although all three functions peak in an isothermal layer (18 to 25 km), there is a temperature increase above 25 km (the  $0^\circ$  peak) which yields the relatively large noise temperature at  $0^\circ$  shown in Figure 5. The atmosphere also warms below 18 km, accounting for the increase in noise from  $40^\circ$  to  $90^\circ$ , also shown in Figure 5. It follows that noise temperature depends not only upon ray elevation angle but also upon the height distribution of atmospheric data  $T$ ,  $p$ , and  $p_w$ .

### 3.5 Recursion Relations

The ray tracing methodology which is employed to compute the noise temperatures above begins with the specification of atmospheric data at heights

$$h_0 < h_1 < h_2 < \dots .$$

The noise temperature integrals can then be written as

$$N_{\text{up}} = \sum_{i=0}^N \exp\left(-\int_{h_{i+1}}^H \alpha ds\right) \int_{h_i}^{h_{i+1}} \alpha T \exp\left(-\int_h^{h_{i+1}} \alpha ds\right) ds$$

and

$$N_{\text{DN}} = \sum_{i=0}^M \exp\left(-\int_{h_0}^{h_i} \alpha ds\right) \int_{h_i}^{h_{i+1}} \alpha T \exp\left(-\int_{h_i}^h \alpha ds\right) ds .$$

In the expression for the upwelling noise temperature, the index  $N$  is such that  $h_N = H$ , while for the downwelling case,  $M$  is such that  $h_M$  is a suitable replacement for the infinite limit of integration which appears in the equation for  $N_{\text{DN}}$ . This is not only convenient but also physically meaningful since above approximately 80 kilometers the absorption is nearly nonexistent and the assumption of thermodynamic equilibrium begins to break down.

Although the summands in the equations for upwelling and downwelling noise temperature can be calculated and summed by the ray tracing program, a pair of recursion relations which actually yield noise temperatures at not only  $h_0$  and  $H$  but also at all other heights  $h_i$  are preferable to direct summation. For noise temperature due to radiation flowing along a ray up to height  $h_{k+1}$ , it follows that

$$N_{\text{up}}(h_{k+1}) = \int_{h_k}^{h_{k+1}} \alpha T \exp\left(-\int_h^{h_{k+1}} \alpha ds\right) ds + \exp\left(-\int_{h_k}^{h_{k+1}} \alpha ds\right) N_{\text{up}}(h_k) .$$

Similarly, for downwelling radiation,

$$N_{\text{DN}}(h_k) = \int_{h_k}^{h_{k+1}} \alpha T \exp\left(-\int_{h_k}^h \alpha ds\right) ds + \exp\left(-\int_{h_k}^{h_{k+1}} \alpha ds\right) N_{\text{DN}}(h_{k+1}) .$$

Heuristically, the recursion relations show that the noise temperature at one side of a layer is the sum of the emission of that layer plus the noise temperature at the opposite side diminished by a transmission factor.

In view of these equations, it is sufficient, in the course of a surface-to-space ray trace, to compute and store the quantities

$$\int_{h_k}^{h_{k+1}} \alpha ds, \quad \int_{h_k}^{h_{k+1}} \alpha T \exp\left(-\int_h^{h_{k+1}} \alpha ds\right) ds, \quad \text{and} \quad \int_{h_k}^{h_{k+1}} \alpha T \exp\left(-\int_{h_k}^h \alpha ds\right) ds$$

and afterwards to combine them as indicated above.

If the temperature  $T_i$  at the height  $h_i$  is perturbed, as is the case when obtaining the Jacobian matrix of partial derivatives in the Backus-Gilbert inversion method, only those integrals with  $h_i$  as an upper or lower limit need be recomputed, and the recursion relation then applied.

### 3.6 Noise Integrals

The calculation of cumulative attenuation across a layer is easily accomplished by means of numerical integration (adaptive Romberg integration is used). In the development of numerical methods to evaluate the other two integrals, it is assumed that the attenuation integral has been computed. In principle, the noise temperature integrals across the layer from  $h_k$  to  $h_{k+1}$  may be evaluated by the use of the numerical routine employed for the attenuation calculations. However, the integrands are not assumed to vary linearly, but rather are given explicitly in the integral. Therefore, a straight forward approach requires the evaluation of the integrands

$$\alpha(h) T(h) \exp\left(-\int_h^{h_{k+1}} \alpha ds\right) \quad \text{and} \quad \alpha(h) T(h) \exp\left(-\int_{h_k}^h \alpha ds\right)$$

at a number of intermediate heights between  $h_k$  and  $h_{k+1}$ . The exact number of intermediate heights is determined as a function of the convergence criterion in the adaptive Romberg integration routine.

Since the evaluation of each integrand involves the computation of attenuation across a sublayer of the original layer, such a computation is, in a sense, redundant. Furthermore, computing time increases (and so does expense) as the number of calls to the integration routine increases. Finally, the exponential factors in the noise integrands are nearly the same, except that one goes from the top of the layer downward, while the other goes from the bottom up, thereby introducing yet another apparent redundancy. Therefore, in the interest of more efficient computation, several numerical methods have been devised.

It is first noted that if the temperature  $T$  is constant between two successive heights  $a$  and  $b$  (which may lie between  $h_k$  and  $h_{k+1}$ ) then

$$\int_a^b \alpha T \exp\left(-\int_h^b \alpha ds\right) ds = T \left\{ 1 - \exp\left(-\int_a^b \alpha ds\right) \right\} .$$



and also

$$\int_a^b \alpha T \exp\left(-\int_a^h \alpha ds\right) ds = T \left\{ 1 - \exp\left(-\int_a^b \alpha ds\right) \right\} .$$

These equations provide a simple means of evaluating the noise integrals across an isothermal layer, as is often postulated or measured in the upper air mass. When the temperature between  $h_k$  and  $h_{k+1}$  is not constant, the layer may be subdivided into smaller subintervals such that the temperature over each is nearly constant. In that case, the noise integrals across the layer are approximated as

$$\int_{h_k}^{h_{k+1}} \alpha T \exp\left(-\int_h^{h_{k+1}} \alpha ds\right) ds \doteq \sum_{i=0}^L \exp\left(-\int_{a_{i+1}}^{h_{k+1}} \alpha ds\right) T_i \left\{ 1 - \exp\left(-\int_{a_i}^{a_{i+1}} \alpha ds\right) \right\}$$

and

$$\int_{h_k}^{h_{k+1}} \alpha T \exp\left(-\int_{h_k}^h \alpha ds\right) ds \doteq \sum_{i=0}^L \exp\left(-\int_{h_k}^{a_i} \alpha ds\right) T_i \left\{ 1 - \exp\left(-\int_{a_i}^{a_{i+1}} \alpha ds\right) \right\} .$$

Here the points  $a_0 = h_k < a_1 < a_2 < \dots < a_{L+1} = h_{k+1}$  define the subintervals of the layer between  $h_k$  and  $h_{k+1}$  is assumed to be linear and the number of points  $a_i$  is chosen so that the temperature is nearly constant between  $a_i$  and  $a_{i+1}$  for all  $i = 0, 1, \dots, L$ . Each summand is readily computed once the integrals

$$\int_{a_i}^{a_{i+1}} \alpha ds, \quad i = 0, 1, 2, \dots, L$$

are available. Although these may be calculated by calling the integration subroutine, a more efficient approach can be devised.

Between heights  $h_k$  and  $h_{k+1}$  a curved ray path has length

$$P = \int_{h_k}^{h_{k+1}} ds, \quad ,$$

where  $ds$ , the differential of path length, includes the effects of refraction. If the layer is partitioned into  $L+1$  subintervals, as above, then a differential of path length across the interval from  $a_i$  to  $a_{i+1}$  is approximately

$$dP = \frac{P}{L+1} ,$$

and if there is no ray bending then each subsegment has length equal to  $dP$ .

When the ray elevation angle  $\theta$  is assumed constant and the attenuation varies linearly between  $h_k$  and  $h_{k+1}$  then

$$ds = dh / \sin \theta$$

and

$$\begin{aligned} \int_{a_i}^{a_{i+1}} \alpha(h) ds &= \frac{\alpha(a_{i+1}) + \alpha(a_i)}{2} \frac{a_{i+1} - a_i}{\sin \theta} \\ &= \frac{\alpha(a_{i+1}) + \alpha(a_i)}{2} \int_{a_i}^{a_{i+1}} ds \end{aligned}$$

Let  $\alpha_i$  denote the average value of  $\alpha(h)$  between  $a_i$  and  $a_{i+1}$ , so that, if  $\theta$  is constant, it follows from the definition of  $dP$  that

$$\int_{a_i}^{a_{i+1}} ds = \alpha_i dP$$

and if  $\theta$  is not constant then this is an approximation. Consequently, the difference

$$\Delta = \int_{h_k}^{h_{k+1}} \alpha ds - \sum_{i=0}^L \alpha_i dP$$

may not equal zero. To retain the simplicity of the summation of a correction term for the attenuation values is defined as

$$\delta = \frac{\Delta}{(L+1) dP} .$$

Then

$$\begin{aligned} & \int_{h_k}^{h_{k+1}} \alpha ds - \sum_{i=0}^L (\alpha_i + \delta) dP \\ &= \Delta - \sum_{i=0}^L \frac{\Delta}{(L+1) dP} dP = 0 , \end{aligned}$$

as desired.

#### 4.0 CONCLUSIONS

Computer simulation of propagation effects is essential to the design of atmospheric EHF systems. Molecular absorption varies across the 10 to 300 GHz band and poses constraints for transmission and shielding applications. Transfer properties are strongly dependent upon radio path length and elevation angle, and also on meteorological conditions. Methods have been presented to model these properties based on physical principles, algorithm stability and efficiency, and computing philosophy. The noise temperature algorithms not only afford a means of obtaining noise temperatures at many points along a ray (only at the expense of the time required to print the additional information) but also an elementary method for obtaining the elements of the Jacobian matrix used in temperature inversion. The major limitations of the model result from the great variability of the atmosphere and the sporadic occurrence of clouds and rain, which were not addressed.

#### Acknowledgment

Much of the basic development work on the ray tracing program was accomplished under the direction of Dr. D. Levine, Lockheed Missiles and Space Company. Scientists who contributed to the algorithms and program structure include D. Levine, W. Uplinger, T. Bjorn, J. Cromack, W. Futterman, and D. Paul.

## REFERENCES

- BAUER, F. L., 1961, "La Methode d'Integration Numerique de Romberg", Colloque sur L'Analyse Numerique, held at Mons on March 22-24, 119-129.
- BLAKE, L. V., 1968, "Ray Height Computations For a Continuous Non-linear Refractive Index Profile", Radio Science 3(1), 85-95.
- CHANDRASEKAR, S., 1950, "Radiative Transfer", Oxford University Press.
- HOPFIELD, H. A., 1969, "Low Quartic Tropospheric Refractivity Profile For Correcting Satellite Data", J. Geophys. Res. 74, 4487-4499.
- LEVINE, D., CROMACK, J., and BJORN, T., 1973, "Increase of Error in Range Correction with Elapsed Time. Evaluated by Ray Tracing through Radiosonde-generated Atmospheric Models", Radio Science, Vol. 8 No. 7, 633-639.
- LIEBE, H. J., GIMMESTAD, G. G., and HOPPONEN, J. D., 1977, "Atmospheric Oxygen Microwave Spectrum-Experiment Versus Theory", IEEE Trans. Antennas Propagat. AP-25(3), 336-345.
- LIST, R. J., 1958, "Smithsonian Meteorological Tables", Sixth revised edition, Smithsonian Institution, Washington, D.C.
- ROSENKRANZ, P. W., 1975, "Shape of the 5mm Oxygen Band in the Atmosphere", IEEE Trans. Antennas Propagat. AP-23(4), 498-506.
- SMITH, E. W., 1980, "Absorption and Dispersion in the  $O_2$  Microwave Spectrum at Atmospheric Pressures", National Bureau of Standards, Boulder, Colorado, preliminary draft of paper.

- US STANDARD ATMOSPHERE
- ELEVATION ANGLE = 0°
- RANGE DIFFERENCE = RANGE (DISPERSION) - RANGE (NO DISPERSION)
- RANGE ERROR AT 80 KM = 103.174 M (NO DISPERSION)

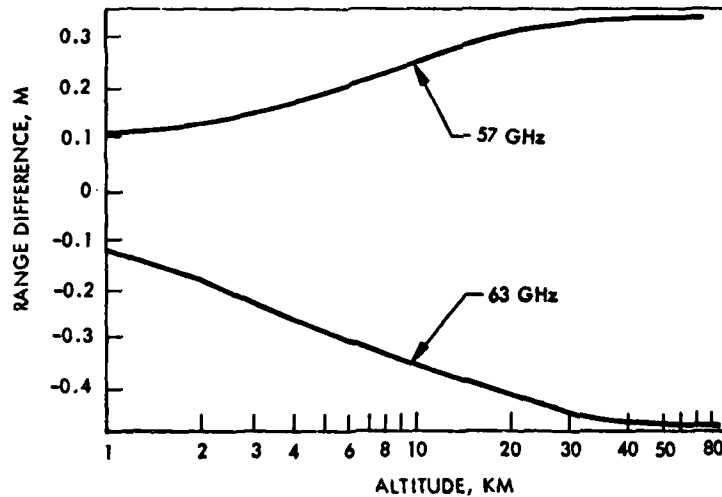


Fig.1 Tropospheric dispersion effects.  
 Shown are radio range errors due to atmospheric dispersion, for frequencies of 57 and 63 GHz, where elevation angle is 0°, error is the range with dispersion minus the range with no dispersion  
 The range error at 80Km is 103.74 with no dispersion

- VERTICAL EARTH-SPACE PATH
- OXYGEN AND WATER VAPOR EFFECTS

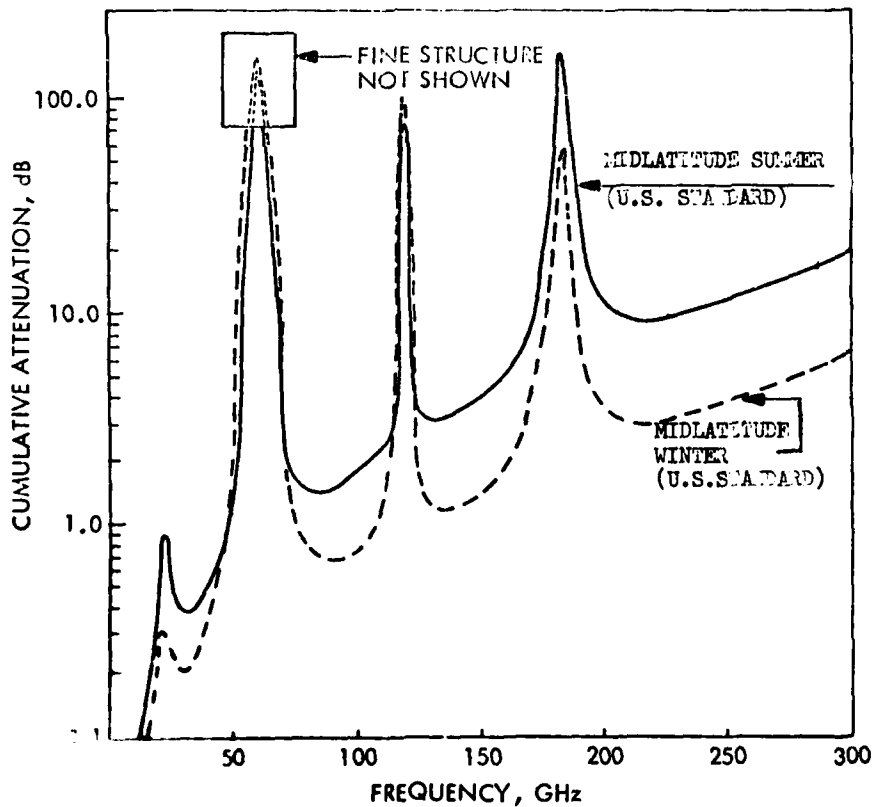


Fig. Seasonal variation of atmospheric attenuation.  
 Solid line is for a cool, dry mid-latitude winter atmosphere and a warm, humid mid-latitude summer atmosphere along a vertical earth to space path

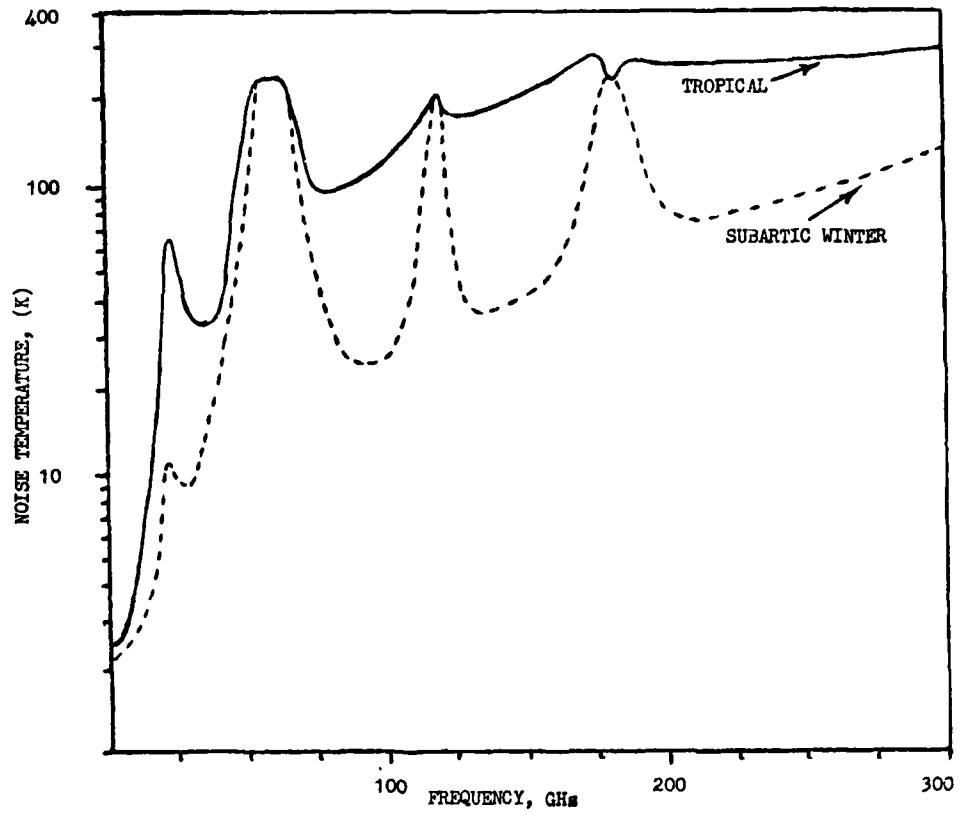


Fig.3 Atmospheric contribution to noise temperatures for environmental extremes. The two curves give noise temperatures due only to the atmosphere from tropical and sub-artic atmospheres representing some environmental extreme conditions for a vertical earth to space path

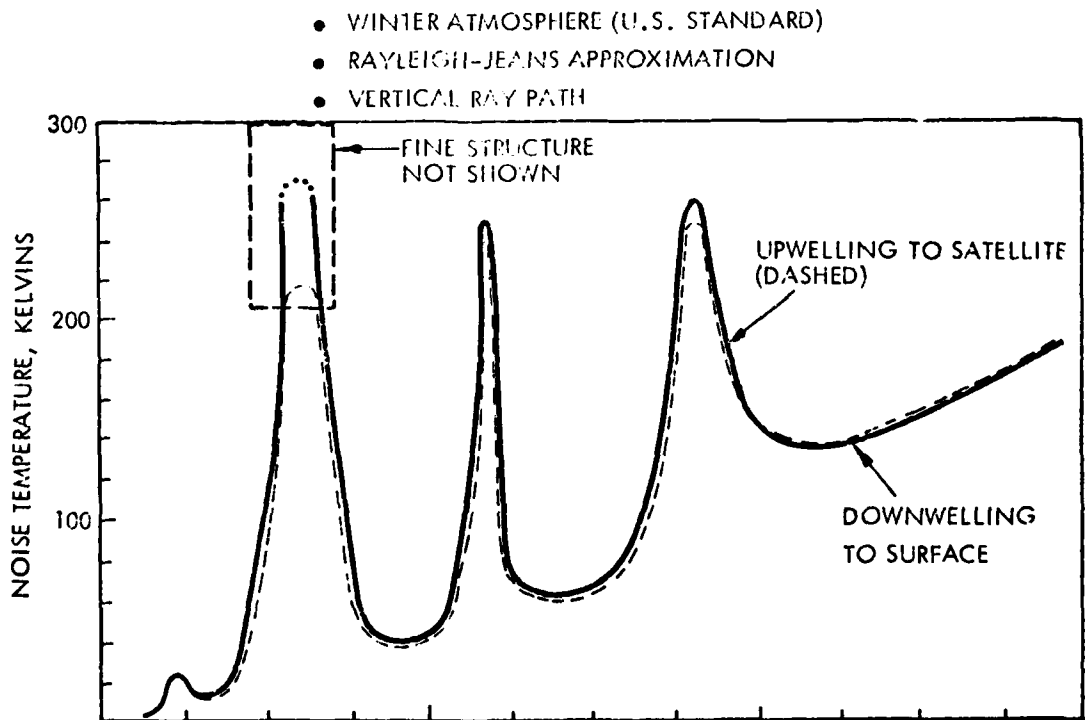


Fig.4 Noise temperature due to the atmosphere. The curves compared the atmospheric contribution to upwelling (no earth's surface contribution) and downwelling noise temperature along a vertical path from a mid-latitude winter atmosphere

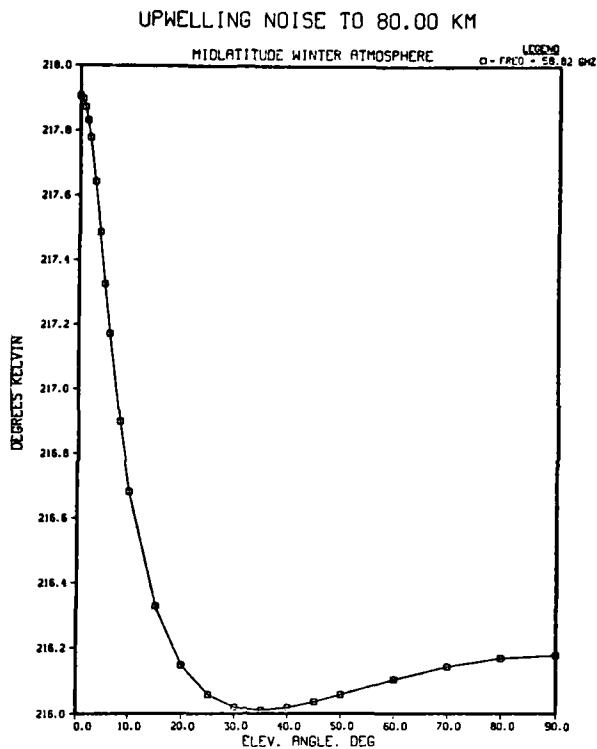


Fig.5 Upwelling noise temperature versus elevation angle. The curve gives the total upwelling noise temperature for elevation angles from zero to 90 degrees. The atmosphere used is mid-latitude winter atmosphere with a smooth ocean surface whose temperature is 280K and has an emissivity of 0.4, for a frequency of 58.825 GHz

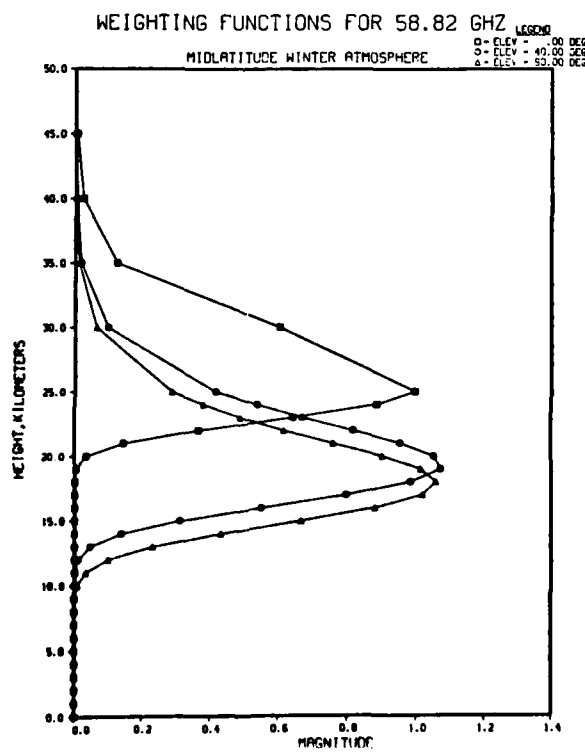


Fig.6 Weighting function at three elevation angles. The three curves give weighting functions for elevation angles of 0, 40 and 90 degrees (90° is vertical) as function of height. The mid-latitude winter atmosphere was used for a frequency of 58.825 GHz

RADAR ESTIMATION OF SLANT PATH RAIN ATTENUATION  
AT FREQUENCIES ABOVE 10 GHz AND COMPARISONS  
WITH MEASURED MULTI-SEASON RESULTS

Julius Goldhirsh  
Applied Physics Laboratory  
The Johns Hopkins University  
Laurel, Maryland

Summary

This paper consists of two parts, the first of which reviews the techniques and results pertaining to estimating earth-satellite path rain attenuation events and statistics using radar at non-attenuating wavelengths. The radar formulation and beam scanning methods are described and the procedure for relating the radar measured Rayleigh reflectivity to the high frequency Mie attenuation coefficient are given. Examples of radar derived single terminal statistics and estimation criteria as they relate to path angle and frequency are reviewed. Also described are radar derived space diversity statistics and their dependence on terminal spacing and frequency. Site diversity performance curves obtained by various investigators using radar and radiometry are compared with each other demonstrating the utility of radar methods.

In the second part of the paper we describe the results of a multi-year experiment at Wallops Island, Virginia. The aims are to test, refine, and establish accuracies of radar methods for arriving at estimates of rain attenuation along an earth-satellite path. The experimental configuration consists of a receiver system which monitors a geosynchronous beacon signal (COMSTAR) at 28.56 GHz down to approximately 30 dB below free space level during periods of rain. A nearby S-band radar ( $f = 2.84$  GHz, beamwidth =  $0.4^\circ$ , peak power = 1 megawatt) simultaneously monitors the reflectivity along the earth-satellite path. These radar data are subsequently injected into a computer program and estimates of slant path attenuation are derived and compared with the directly measured levels on a case by case basis and statistically. Additional inputs to the estimation technique are the nearby simultaneous drop size distribution measurements as well as rain structure data obtained with the radar. Comparisons of measured and radar estimated fade events are presented and found to be generally good. Comparisons of cumulative fade distributions show agreement to be excellent giving an rms deviation of 1 dB.

## 1. INTRODUCTION

The use of experimental geosynchronous satellites with ground receiving or transmitting systems has represented a major means for acquiring information on slant path rain attenuation statistics and space diversity performance. This method, in general, is expensive and inefficient, and often requires many years to arrive at an adequate data base for each frequency, path angle, and location.

An alternate type of measurement coupled with predictive techniques involves the use of radar operating at non-attenuating wavelengths. Radar has the advantage that it could scan in three dimensional space, record regions of rain, and acquire a quasi-photograph of the precipitation structure itself. By modeling paths through the precipitation environment "frozen" on digital tape, a significantly larger data base is amassed than acquired directly for an earth-satellite path configuration which must wait for the rain to intersect it. To exemplify the ability to acquire a large sampling of data using radar, it has been demonstrated by Drufuca and Pawline (1976) that a summer's data base of radar reflectivity enabled the prediction of a rain rate distribution which agreed in shape with the distribution acquired using 10 years of continuous raingage data for the Montreal area. It has been maintained that only radar observations are currently capable of amassing the required number of rain cell observations to produce adequate rain attenuation statistics for model analysis (Crane, 1977).

The first part of this paper represents a mini-review of methods used for estimating path attenuation events and statistics using radar. A more complete review is given by Goldhirsh (1979a). In the second part, we examine an experiment designed to establish the accuracies involved in radar modeling by comparing estimated levels with beacon measured ones. Hitherto we have arrived at a combined data base of five rain days during the summer of 1977 and five rain days during the fall-winter 1978-79, which give a total of 1019 minutes of simultaneous radar, beacon, and disdrometer data.

## 2. RADAR MODELING TECHNIQUE

### 2.1 The Reflectivity Factor, $Z$

Frequencies in S-band (2 to 4 GHz) are optimum for measuring rain reflectivity as they satisfy the assumption of Rayleigh scattering from raindrops ( $\pi D/\lambda \ll 1$ ), negligible rain attenuation of the radar echoes result, and good beam resolution may be achieved. Radars that operate at higher frequencies (e.g., above 10 GHz) give rise to the intractable condition related to the inability of accurately extracting the reflectivity from the attenuated echo (Hitachfeld and Bordan, 1954). Hence we presume in the following paragraphs that the radar operates at a frequency in S band.

In Using radar for rain attenuation modeling, the reflectivity factor,  $Z$ , is the desired

quantity to be estimated from the received echoes. This quantity is given by (Goldhirsh, 1979a),

$$Z(r) = C_0 r^2 P_r(r) \quad (\text{mm})^6/\text{m}^3 \quad (1)$$

where,

$$Z(r) = \int_{D_{\min}}^{D_{\max}} D^6 N(D) dD \quad (2)$$

and where  $C_0$  is a constant containing fixed radar parameters such as transmitter power, pulsewidth, wavelength, antenna gain, vertical and horizontal beamwidths, and line losses. In Eq. (1),  $P(r)$  is the received echo power from a pulse volume centered at the range,  $r$ . The reflectivity factor,  $Z$ , is theoretically given by Eq. (2) where  $N(D)dD$  is the rain-drop size distribution which is defined as the number of drops per unit volume between diameter sizes,  $D$  and  $D+dD$ , and  $D_{\max}$ ,  $D_{\min}$  are the maximum and minimum drop diameters in the pulse volume. We thus note that a radar power measurement defines the quantity  $Z$  which is totally dependent on the rain particle sizes, independent of the wavelength.

The expression for  $Z(r)$  as given by Eq. (1) assumes a conical beam shape whose cross section is an ellipse with major and minor axes defined by their beamwidths, and Gaussian distributions are assumed over the principal axes of the main lobe (Probert-Jones, 1962). In addition, Rayleigh scattering is assumed and the influence of rain and cloud attenuation have been neglected.

Since rain is a noise-like scatterer, a number of independent samples of power must be averaged to achieve a reliable estimate of the true average (Marshall and Hitschfeld, 1953; Wallace, 1953). Various methods for achieving statistical power estimates are reviewed by Goldhirsh (1979a).

## 2.2 Data Acquisition Modes for Estimating Path Attenuation

Two basic methods which have been used for modeling path attenuation at frequencies above 10 GHz are depicted by cases 1 and 2 in Fig. 1. In case 1 the radar beam simulates the earth-satellite path. Each of the shaded regions represents a contiguous pulse volume whose range resolution is  $\Delta r_i = c\tau/2$ ;  $c$  and  $\tau$  being the velocity of light and pulse width, respectively. The reflectivity factor,  $Z$ , corresponding to the  $i^{\text{th}}$  pulse volume along the beam ( $i = 1, 2, \dots, N$ ) may be determined using Eq. (1) and is subsequently converted to an attenuation coefficient,  $k_i$ , through the empirical relation (Goldhirsh, 1979b),

$$k_i = aZ_i^b \quad (\text{dB/km}) \quad (3)$$

where  $a$  and  $b$  are parameters dependent on rain drop size distribution, frequency, and temperature (the extent of which is frequency related).

The attenuation coefficient,  $k$ , is theoretically given by,

$$k = \int_{D_{\min}}^{D_{\max}} C_{\text{ext}}(D) N(D) dD \quad (\text{dB/km}) \quad (4)$$

where  $C_{\text{ext}}(D)$  is called the extinction factor with units of  $(\text{dB/km})\text{cm}^3$  and is a Mie related quantity proportional to the absorption cross section. This quantity, which gives a measure of the attenuation due to a spherical drop of diameter,  $D$ , at a specific frequency and temperature, is tabulated by Medhurst (1965) and Setzer (1970).

The total attenuation along the path is given by

$$A = \sum_{i=1}^N k_i \Delta r_i \quad (5)$$

Path attenuation has been arrived at using these procedures by a number of investigators (Strickland, 1974; Rogers, 1972; Rogers, 1977; Goldhirsh, 1979b). In Eq. (5),  $N$  defines the path length over which the summation is carried out. The extent in which  $N$  is considered is dependent upon the nature of the rain (i.e., widespread versus convective). If the rain is widespread, a well defined melting layer several hundreds of meters thick usually exists in the vicinity of the  $0^\circ\text{C}$  isotherm height. Radar reflections from these regions are enhanced and gives rise to a "bright band" on an RHI (range-height-indicator).

At altitudes above and below this region a predominance of ice (above) and water (below) exists. Hence for a widespread rain, the path length is taken up to the "base" of the melting layer which may be identified by examining the reflectivity factor-height profile along the path (Goldhirsh, 1979c). The base of the bright band has been defined as that height near and below the zero degree isotherm where the reflectivity slope changes abruptly to values of at least 10 dBZ/km and greater with increasing altitude.



On the other hand, convective type rains appear on an RHI as long cellular columns of intense reflectivity extending well above the 0°C isotherm height. Such a rain type implies the presence of water in the supercooled state carried by updrafts above the 0°C isotherm height. For such a rain type, the summation in Eq. (5) is considered along the entire path through precipitation (Goldhirsh, 1976, 1979b,c).

Another possible technique for modeling is depicted in case 2 (Fig. 1) where a scanning beam intersects a predefined shifted path in space. The attenuation coefficient contributions,  $k_1$ , associated with the intersecting pulse volumes (shaded regions-case 2) are summed as given by Eq. (5). Again,  $k_1$  is related to the average reflectivity factor,  $Z_1$ , through the empirical relation given by Eq. (3). For this case, however,  $\Delta r_1$  is the geometric distance between contiguous pulse volumes along the shifted path. This technique of path attenuation modeling is particularly suitable for the determination of space diversity statistics through the consideration of the joint probabilities associated with parallel paths separated given distances (Goldhirsh, 1975; Hodge, 1978).

Both of the above-described methods carry with them the inability to make measurements close to the antenna or the ground due to both echo clutter and near field effects. For example, Austin and Austin (1975) used an inner cutoff range of 8 km to reduce the effect of ground echoes. For case 1, a near field correction formulation was employed by Goldhirsh (1979b) to allow reflectivity contributions to be estimated as close in as 600 m from the 18.3 m diameter S-band antenna (0.4° beamwidth). Since the attenuation was being monitored at elevation angles above 40°, the effect of ground echoes were, in general, negligible beyond this range. At low elevation angles (e.g., 0.4°), a 9 km cut-off range has been used to eliminate ground clutter problems.

### 3. EXAMPLES OF RADAR DERIVED STATISTICS

#### 3.1 Single and Joint Terminal Statistics

Employing previously described methods to a system of parallel paths intersecting the radar beam (case 2, Fig. 1), conditional statistics as well as single terminal and space diversity criteria have been developed (Hodge, 1978; Goldhirsh, 1975). The technique employed by Goldhirsh (1975) assumes an ergodic type characteristic; namely the replacing of attenuation samples in time along a fixed path with samples along an array of paths in space. An example of a set of radar derived conditional statistics is given in Fig. 2 (Goldhirsh, 1975), for the frequency of 100 GHz and path angle of 45°. The ordinate represents the probability that the attenuation exceeds the abscissa value conditioned on the existence of an attenuation event. The curve labeled  $d = 0$  represents the single terminal distribution and the other labeled curves are the joint probability distributions. By systematically sampling the attenuation along parallel paths separated a fixed distance,  $d$ , the joint probability curves given in Fig. 2 were established. The curve labeled "optimum spacing" is derived by squaring the single terminal probability curve values and theoretically represents the joint probability distribution for two decorrelated paths under the assumed condition for which the data base was extracted (i.e., the existence of the given attenuation event). In arriving at this decorrelated distribution, it is tacitly assumed that the single terminal probability is independent of location within the radar observation region. The significance of the joint probability curves in Fig. 2 are elaborated on in Section 3.2.

Although the curves depicted in Fig. 2 are of a conditional nature, a significant amount of information may be acquired from them. For example, to make these curves absolute would require multiplying them by a fixed quantity; namely the probability of an attenuation event. Although this probability is not easily achievable, it is useful to recognize that multiplication of these curves by such a given value in no way alters the relative shapes of these distributions; it merely shifts the logarithmic scale values by a fixed amount. Hence, criteria may be derived from such curves pertaining to path angle and frequency dependence for both single terminal and space diversity statistics (Goldhirsh, 1975).

##### 3.1.1 Angle Dependence

By generating single terminal conditional probability curves of the type given in Fig. 2 for elevation angles ranging from 20° to 90°, Goldhirsh (1975) found these curves follow CSC  $\theta$  variations for fixed-probability levels over effective rain rates between 1 and 20 mm/hr. An illustration demonstrating these results is depicted in Fig. 3, where the solid curves represent independent fade distributions arrived at through individual analysis of the radar derived path attenuations at the given angles. The circled points are the predicted levels using the CSC  $\theta$  variation at each fixed-probability level and assumes a knowledge only of the  $\theta = 45^\circ$  curves;  $\theta$  representing the angle between the path and the local horizon. The predicted curves are found to be within 1-dB rms of the respective radar derived distributions. Rogers (1977), at the McGill University Radar Weather Observatory, Quebec, Canada, corroborated this angle dependence for  $f = 13$  GHz and for elevations as low as 10°.

The above results do not at all imply that rain regions are uniform on a case by case basis. In fact, the above examples are derived from summer data bases. The Wallops Island rains were specifically found to be generally convective resulting in highly non-uniform reflectivities along the individual paths. When considered statistically, however, the rain regions do appear to take on an effective uniform appearance.

Using sun tracker data, Kinase and Kinpara (1973) examined 11.7 GHz attenuations as a function of path angle and their results are found to fluctuate around the CSC  $\theta$  function for path angles greater than  $20^\circ$ . Although their data are statistically noisy, rms deviations of 32% and 24% relative to the CSC  $\theta$  were found at rain rates of 20 and 10 mm/hr percentage times (where data points at  $10^\circ$  intervals were considered from  $20^\circ$  to  $90^\circ$ ). A recent global model by Crane (1979) for rain attenuation prediction which is also in the form of an input document to the C.C.I.R. assumes an angle variation very close to the CSC  $\theta$  for values above  $20^\circ$ . His results show rms deviations from CSC  $\theta$  of 12% and 9%, at rain rates of 20 and 10 mm/hr rains, respectively, considering the same angle interval and sample points as described above.

### 3.1.2 Frequency Dependence

Through the generation of single terminal conditional fade statistics of the type shown in Fig. 2 at a variety of frequencies, Goldhirsh (1975) demonstrated the capability of predicting fade distributions at a third frequency in the range between 13 and 100 GHz given a knowledge of the distributions at two other frequencies. These given distributions allow for the determination of the effective rain rate,  $R_0$  and path length,  $l_0$ , at a given exceedance time through the solution of the simultaneous equations given by

$$A_1 = a_1 R_0^{b_1} l_0 \quad (6)$$

$$A_2 = a_2 R_0^{b_2} l_0 \quad (7)$$

The attenuation at the third frequency  $A_3$  at the same probability may be determined using,

$$A_3 = a_3 R_0^{b_3} l_0 \quad (8)$$

where  $R_0$  and  $l_0$  are now known and where the values of  $a$  and  $b$  are calculated for the given DSD and frequency.

An illustration of these results is given in Fig. 4 where the solid curves represent the individual radar-derived distributions and the circled points the predicted levels, using only a knowledge of 13- and 30-GHz distributions. We note agreement between the predicted points and the radar-derived curves to be generally within 1-dB rms. The two-frequency method employed here is identical to that previously described by Hogg (1973), and successfully tested by Henry (1975) at 13, 19, and 30 GHz using suntracker data, and by Bergman (1978) using beacon signals (19 and 28 GHz) and radiometer (13 GHz) data assuming a Laws and Parsons (1943) distribution.

### 3.1.3 Generation of Absolute Fade Statistics and Extrapolation to Other Locations

Statistics of the type depicted in Fig. 2 were obtained from a conditional data base. Specifically, attenuations were sampled along parallel paths for only those vertical planes possessing at least one path with an attenuation of 2 dB or more. The probability of such an "attenuation event" is difficult to obtain. In hindsight, a more appropriate procedure would have been to select only those paths for which the ground rain rate exceeds a predetermined threshold.

The rain rates could be established by converting the measured reflectivity factors at the base of the respective paths to ground rain rates using an appropriate empirical form,

$$R = az^b \quad (9)$$

This form could, for example, be derived from simultaneous disdrometer measurements made either in the given storm or in a similar type rain (Goldhirsh, 1979b). The absolute probability which gives the number of minutes given fade levels are exceeded might then be established using long term raingage data. That is,

$$P\{A > A_q, R > R_{TH}\} = P\{A > A_q | R > R_{TH}\} P\{R > R_{TH}\} \quad (10)$$

where the left hand side of Eq. (10) represents the fraction of the total time the joint conditions exist that the attenuation,  $A$ , is greater than a level,  $A_q$ , and the rain rate,  $R$ , is greater than a threshold value,  $R_{TH}$ . The first factor on the right hand side of Eq. (10) is the radar derived fraction of time that the attenuation exceeds  $A_q$ , given the condition that a threshold rain  $R_{TH}$  is exceeded on the ground. The second factor is the fraction of the time the threshold rain rate is exceeded; a quantity which may be determined using long term raingage data. The first factor may be considered approximately invariant with location if it is presumed that the characteristics of thunderstorms are similar at the different locations, a contention in part supported by raingage and radar measurements (Konrad, 1978; Goldhirsh and Katz, 1979). The major characteristic differences associated with thunderstorms at the various locations deal with their frequency of occurrence, namely, the second factor in the right

hand side of (10). The value of this factor may be obtained using long term rain-gage data. In this manner a data base of conditional fade statistic obtained at one location might be carried to another place and converted to an absolute distribution using rain-gage data at the second location.

Actually, the desired probability is  $P\{A > A_q\}$  regardless of the ground threshold rain rate. However, it is likely that if  $R_{TH}$  is appropriately selected,  $A > A_q$  implies  $R > R_{TH}$  with a high confidence level over the long run and the left hand side of Eq. (10) equals  $P\{A > A_q\}$ .

### 3.2 Space Diversity Criteria

Because of the variability of rain intensity, especially in the lateral directions in convective storms, it may be useful to employ a space diversity configuration. This involves the utilization of two ground stations spaced a given distance apart. When the fades reach levels in excess of a predefined threshold along one earth-satellite path, transmissions are switched to the alternate ground station where because of the variability of rain intensity, the simultaneous fade levels are likely to be less along this second earth-satellite path. A useful concept for characterizing space diversity is the "diversity gain" which was originally introduced by Hodge (1973). This is defined as the dB difference between the single terminal fade distribution curve (labeled  $d = 0$  in Fig. 2) and the joint probability curve for a given spacing,  $d$ , at a fixed probability level or fixed single terminal attenuation. This characteristic gives a measure of fade margin reduction for a space diversity configuration compared to the single terminal case at any fixed probability levels.

Goldhirsh (1975) and more recently Hodge (1978) analyzed the diversity gain dependence on terminal spacing with radar data. Goldhirsh's results (Wallops Island, Va.) were restricted to the case in which the diversity paths were in the same vertical plane as the satellite and the baseline connecting the paths, whereas Hodge's results (McGill radar, Que.) considered various baseline orientations and path directions. In Fig. 5 is an example of radar derived diversity-gain variations as a function of terminal separation for different single-terminal fades at  $f=30$  GHz (Goldhirsh, 1975). The horizontal lines represent the diversity gains between the single-terminal curve and the conditionally decorrelated case (curve labeled optimum) in Fig. 2. We note that all the curves appear to asymptotically reach the decorrelated case levels. Dividing the diversity gain levels of Fig. 5 by their respective optima, and multiplying by 100, we arrive at a family of curves referred to as "percentage of diversity gain relative to optimum" versus separation distance. These curves are, in general, within 5 percent of one another for any given separation at the various fade levels, and hence may be represented by a single curve by taking their average at fixed separation distances. The resultant curves are plotted in Fig. 6 for frequencies ranging from 13 to 100 GHz. We note that all the curves lie within a +2.5-percent band which demonstrates the frequency independence of these relative diversity gains. The curves also show that at 20 km and beyond, more than 90 percent of the conditionally decorrelated level is achieved making questionable the desirability of increased separation distances beyond this limit.

In Fig. 7 is plotted the average (solid curve) along with the peak deviations (vertical extensions) of the four curves in Fig. 6. Also shown plotted are curves deduced from the experimental results presented by Hodge (1973) (dashed curve). This data represents a composite of the results of several experiments performed in Ohio by Ohio State University and in New Jersey by Bell Telephone Laboratories (Wilson, 1970; Hodge, 1972; Wilson and Mammel, 1973). The system parameters in all cases were approximately the same; namely, frequency = 15 GHz, azimuth angle =  $220^\circ$ , elevation angle =  $35^\circ$ , and terminal baseline orientations from NW to SE. The diversity gain results plotted in Fig. 7 were deduced by first taking the ratio of Hodge's diversity gain at each separation distance to the decorrelated level (assumed to be the value of diversity gain at 31 km). This was done for four curves; namely those with single terminal fades of 4, 6, 8, and 10 dB. The relative diversity gains were then averaged (at each separation distance) to establish the plotted levels. In carrying out the above operations, the average deviation from the mean curve was found to be less than 4%. It is interesting to note from Fig. 7 that the radar derived levels represent a worst case condition for distances smaller than 12 km and for greater distances, the data points of Hodge lie within the computed results of Goldhirsh.

Also shown plotted in Fig. 7 are the percentage diversity gain results of Hodge (1978) (dot-dashed curve) arrived at from radar modeling (McGill University Radar Weather Observatory, Quebec, Canada). In arriving at these results, four cases were averaged pertaining to different pointing directions, and the diversity gain at 40 km was presumed to represent the decorrelated distance. The average deviation of the individual cases relative to the overall mean was found to be less than 5%. We observe that the radar results deduced from Hodge's radar data are very close to those derived by Goldhirsh.

In all the three cases considered (Goldhirsh, 1975; Hodge, 1973; and Hodge, 1978), small deviations were noted of the "relative" diversity gain curves associated with the various single terminal fades or single terminal probability levels. The concurrence of the various results supports the view that the family of curves as depicted in Fig. 5 may be represented by a single curve, namely, the average diversity gain relative to optimum.

#### 4. TESTING OF THE RADAR ESTIMATION METHOD USING THE COMSTAR 28.56 GHz BEACON AT WALLOPS ISLAND, VA

##### 4.1 Experimental Configuration

Since the spring of 1977, a receiving station has been located at Wallops Island, Va., for receiving a 28.56 GHz beacon signal emanating from one of the COMSTAR (Cox, 1978) geosynchronous satellites. The overall experimental configuration (Fig. 8) consists of a nearby S-band radar system ( $f = 2.84$  GHz, beamwidth =  $0.4^\circ$ , pulsewidth = 1  $\mu$ sec, peak power = 1 megawatt) located approximately 30 m away and a system of raingages and disdrometers for measuring rain rate and drop size distributions, respectively. Both the receiver and radar antennas are fixed in direction and point toward the satellite. Up to September 1, 1978, signals from satellite  $D_2$  were received (elevation angle =  $41.6^\circ$ , azimuth =  $210.1^\circ$ ) and subsequently satellite  $D_3$  (elevation angle =  $44.5^\circ$ , azimuth =  $198.3^\circ$ ) was monitored. During selected periods of rain, the radar measures the reflectivity (case 1, Fig. 1) along the parallel earth-satellite path for purposes of testing previously described radar methods for estimating path attenuation at 28.56 GHz (Goldhirsh, 1979b; 1979c). The disdrometer data are used as inputs in these estimation methods for arriving at best fit values of  $a$  and  $b$  given in Eq. (3).

##### 4.2 Comparison of Radar Estimated and Directly Measured Fades

During the summer of 1977 and the fall-winter of 1978-79, a total of 1019 minutes of simultaneous radar data was accumulated covering five rain days in 1977 (304 minutes) and five rain days in 1978-79 (715 minutes). For each rain day, a separate set of values of  $a$  and  $b$  were determined from the disdrometer sampling of measured raindrop spectra. Examples depicting comparison of radar estimated attenuations versus beacon fades for the fall-winter of 1978 are given in Figs. 9 and 10. The flat intervals in Fig. 10 denotes the receiver loss of lock condition (approximately 30 dB). We note relatively good agreement between measured and radar estimated fades for the examples shown. Although most days show similar good agreement, some show only fair agreement. The question that must be answered, therefore, is "does radar provide a sufficiently good estimation of rain attenuation for the user over the long run?" This question is in part answered by comparing the cumulative fade distribution arrived at by radar with that directly measured for all the simultaneous days. These results are shown in Fig. 11. The ordinate represents the fraction of the total simultaneous time (1019 minutes) the abscissa value of fade is exceeded. The thick solid curve corresponds to the beacon results and the thin and dashed curves represent two radar estimation cases. The thin curve gives the estimation where the values of  $a$  and  $b$  are arrived at for each rain period using the disdrometer results (DSD) and the dashed curve is determined from the well known Marshall-Palmer (M-P) (1948) drop size distribution, respectively. The indicated distributions combine the summer (1977) and a fall-winter (1978-79) data bases. Quantitative comparisons between DSD-beacon and the M-P-beacon cases are given (for fades up to 25 dB) in the indicated table in Fig. 11. In Table 1 are itemized a breakdown showing the summer 1977, the fall-winter 1978-79 and the overall data base results. The average probability ratio is obtained by averaging the larger probability value to the smaller one for a series of fade levels (out to 25 dB). We note the radar predicted results for the DSD case consistently resulted in excellent agreement whereas the M-P agreement although close for the fall-winter of 1978 was poor during the summer of 1977. The close agreement during the fall-winter 1978-79 is consistent with the notion that the M-P distribution is more applicable for wide-spread rain conditions which are more prevalent in the winter time.

The above results represent further evidence of the validity of using single frequency non-attenuating radars for the determination of fade statistics.

Table 1: COMPARISON OF CUMULATIVE DISTRIBUTION CURVES

Period	Type	rms dB Deviation	Avg dB Deviation	Avg Prob Ratio	No of Minutes
1977 (summer)	DSD	1.2	1.0	1.09	304
	MP	5.6	5.0	1.37	
1978-79 (fall-winter)	DSD	0.9	0.7	1.10	715
	MP	1.1	0.8	1.11	
Overall	DSD	1.2	1.0	1.10	1019
	MP	3.6	3.1	1.28	

##### 5. CONCLUSIONS

Based upon the large body of radar results described or alluded to in this work, including the more recent COMSTAR beacon-radar attenuation comparisons, we conclude that radar represents a useful tool for establishing single and joint terminal statistics. These derived statistics have already been used to establish criteria associated with the behavior of cumulative fade distributions with path angle and frequency. In addition, path diversity criteria have also been established from radar derived joint probability distributions.

Although radar has hitherto provided the ability for establishing only conditional fade statistics due to the impracticality of continuous operation, a method has been suggested for converting these statistics to absolute values at various locations. These absolute levels may be obtained by conditioning the probabilities with a threshold rain rate and multiplying them by the probability of exceeding such a rain rate, the latter being obtained using long term or measured raingage data at the locality in question.

#### 6. ACKNOWLEDGEMENT

This work was performed under contract with NASA/Goddard Space Flight Center (NASA NDPR S40113B; Radar Prediction of Rain for Earth Satellite Paths).

#### 7. REFERENCES

Austin, L. B. and G. L. Austin, 1975, "Techniques for the Calculation of Attenuation from Precipitation for Single Station and Path Diversity Satellite Communication Systems from Digital Radar Data", Radio Science, Vol. 10, No. 12, pp 1019-1024.

Bergmann, H. J., "A MM Wave Propagation Experiment in Georgia and Illinois Utilizing COMSTAR Beacon Signals", Proc. 1978 International IEEE/AP-S Symposium, USNC/URSI Spring Meeting, Washington, D. C., 15-19 May.

Cox, D. C., 1978, "An Overview of the Bell Laboratories 19 and 28 GHz COMSTAR Beacon Propagation Experiments", The Bell System Technical Journal, Vol. 57, No. 55, pp 1231-1255.

Crane, R. K., 1977, "Precipitation of the Effects of Rain on Satellite Communication Systems", Proc. IEEE, Vol. 65, No. 3, pp 456-474.

Crane, R. K. and D. W. Blood, 1979, "Handbook for the Estimations of Microwave Propagation Effects - Link Calculations for Earth-Space Paths", Technical Report No 1, Document No. P-7376-TR1, Contract No. NAS 5-25341, June. Environmental Research and Technology, Inc., Concord, Mass.

Drufuca, G. and A. Pawline, 1976, "Some Statistics of Radar Precipitation Patterns", Proc. 17th Conf. on Radar Meteorology, Seattle, Washington, AMS, pp 438-447, October.

Goldhirsh, J., 1979a, "A Review on the Application of Non-Attenuating Frequency Radars for Estimating Rain Attenuation and Space Diversity Performance", IEEE Trans. Geoscience Electronics, Vol. GE-17, No. 4, October.

Goldhirsh, J., 1979b, "Predictive Methods for Rain Attenuation Using Radar and In-Situ Measurements Tested Against the 28 GHz COMSTAR Beacon Signal", IEEE Trans. on Antennas and Propagation, Vol. AP-27, No. 3, May.

Goldhirsh, J., 1979c, "Comparison of Radar Derived Rain Attenuation with the COMSTAR Beacon at 28.56 GHz for Summer and Winter Periods", APL Technical Report S1R79U-016, Applied Physics Laboratory/The Johns Hopkins University, Laurel, Maryland, July.

Goldhirsh, J., 1976, "Attenuation of Propagation Through Rain for an Earth-Satellite Path Correlated with Predicted Values Using Radar", IEEE Trans. on Antennas and Propagation, Vol. AP-24, No. 6, pp 786-791.

Goldhirsh, J., 1975, "Prediction Methods for Rain Attenuation Statistics at Variable Path Angles and Carrier Frequencies Between 13 and 100 GHz", IEEE Trans. on Antennas and Propagation, Vol. AP-23, No. 6, pp 786-791.

Goldhirsh, J., and I. Katz, 1979, "Useful Experimental Results for Earth-Satellite Rain Attenuation Modeling", IEEE Trans. on Antennas and Propagation, Vol. AP-27, No. 3, pp 413-415, May.

Henry, P. S., 1975, "Measurement and Frequency Extrapolation of Microwave Attenuation Statistics on the Earth-Space Path at 13, 19, and 30 GHz", IEEE Trans. Antennas and Propagation, Vol. AP-23, pp 271-274.

Hitschfeld, W. and J. Bordan, 1954, "Errors Inherent in the Radar Measurement of Rainfall at Attenuating Wavelengths", J. Meteor., Vol. II, pp 58-67.

Hodge, D. B., 1978, "Path Diversity for Earth-Space Communication Links", Radio Science, Vol. 13, No. 3, pp 481-487, May-June.

Hodge, D. B., 1973, "Space Diversity for Reception of Satellite Signals", Dept. of Electrical Engineering, Ohio State Univ., Columbus, Ohio, Technical Report 2374-16, October.

Hodge, D. B., 1972, "A 15.3 GHz Satellite-to-Ground Diversity Experiment Utilizing the ATS-5 Satellite", Report 2374-11, October, Electroscience Laboratory, Dept. of E. E., The Ohio State University prepared under grant No. NGR36-008-080 for NASA.

Hogg, D. C., 1973, "Intensity and Extent of Rain on Earth-Space Paths", Nature, Vol. 243, pp 337-338, June.

Kinase, A., and A. Kinpara, 1973, "Statistics of Attenuation Due to Precipitation of Radio Waves in 12 GHz Band at Higher Angles of Elevation", Note 101, NHK Tech. Res. Labs., Tokyo, Japan.

Konrad, T. G., 1978, "Statistical Models of Summer Rainshowers Derived from Fine-Scale Radar Observations", Journal of Applied Meteorology, Vol. 17, No. 2, pp 172-188, February.

Laws, J. O. and D. A. Parsons, 1943, "The relation of Raindrop Size to Intensity", Trans. Amer. Geophys. Union, Vol. 22, pp 709-721.

Marshall, J. S. and W. Hitschfeld, 1953, "Interpretation of the Fluctuating Echo from Randomly Distributed Scatterers - Part I", Canadian Journal of Physics, Vol. 31, pp 962-964.

Marshall, J. S. and W. McK. Palmer, 1948, "The Distribution of Raindrops with Size", J. Meteor., Vol. 5, pp 165-166.

Medhurst, R. G., 1965, "Rainfall Attenuation of Centimeter Waves: Comparison of Theory and Measurement", IEEE Trans. on Antennas and Propagation, Vol. AP-13, pp 550-564.

Probert-Jones, J. R., 1962, "The Radar Equation in Meteorology", Quarterly J. Roy. Meteor. Soc., Vol. 88, pp 485-495.

Rogers, R. R., 1977, "Attenuation Due to Rain at Low Elevation Angles", Electronic Letters, Vol. 13, No. 15, July, pp 427-428.

Rogers, R. R., 1972, "Radar Derived Statistics on Slant-Path Attenuation at 10 GHz", Radio Science, Vol. 7, No. 6, pp 631-643.

Setzer, D. E., 1970, "Computed Transmission Through Rain at Microwave and Visible Frequencies", B.S.T.J., Vol. 49, pp 1873-1892.

Strickland, J. I., 1974, "The Measurement of Slant Path Attenuation Using Radar, Radiometers, and Satellite Beacons", Journal De Recherches Atmospheriques, Colloque De L'IUCRM, Vol. VIII, pp 347-358, Janvier-June.

Wallace, P. R., 1953, "Interpretation of the Fluctuating Echo from Randomly Distributed Scatterers - Part II", Canadian Journal of Physics, Vol. 31, pp 995-1009.

Wilson, R. W., 1970, "A Three-Radiometer Path-Diversity Experiment", Bell System Technical Journal, Vol. 49, p 1239.

Wilson, R. W., W. L. Mammel, 1973, "Results from a Three Radiometer Path Diversity Experiment", Proc. Conf. on Propog. of Radiowaves at Frequencies above 10 GHz, London, April, p 23.

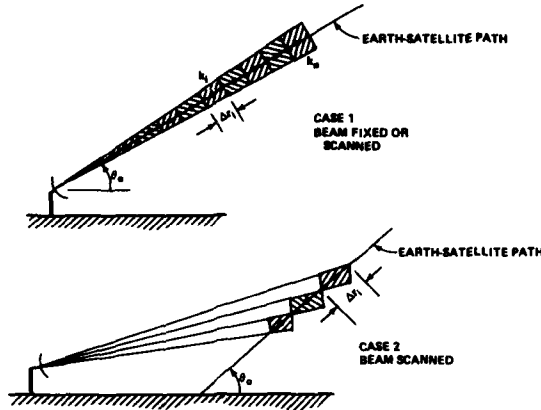


Fig. 1. Configuration for modeling path attenuation with radar. In case 1 the earth-satellite path coincides with radar beam and in case 2 the origin of the earth-satellite path is displaced from the radar location.

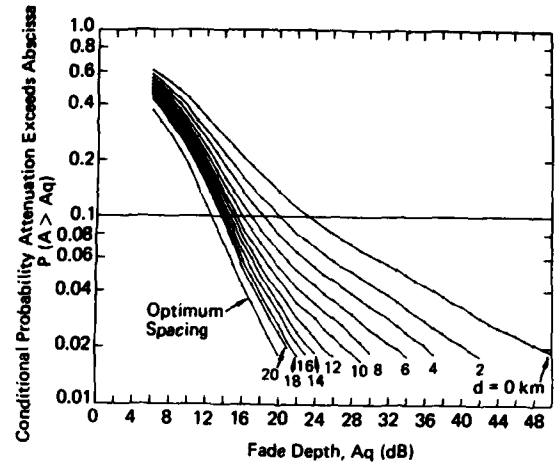


Fig. 2. Radar derived conditional probability for Wallops Island, Va., that the attenuations along two paths separated by a distance,  $d$ , jointly exceed the abscissa attenuations for  $f=100$  GHz and  $\theta = 45^\circ$ . The curved labeled  $d = 0$  is the single terminal probability (Goldhirsh, 1975).

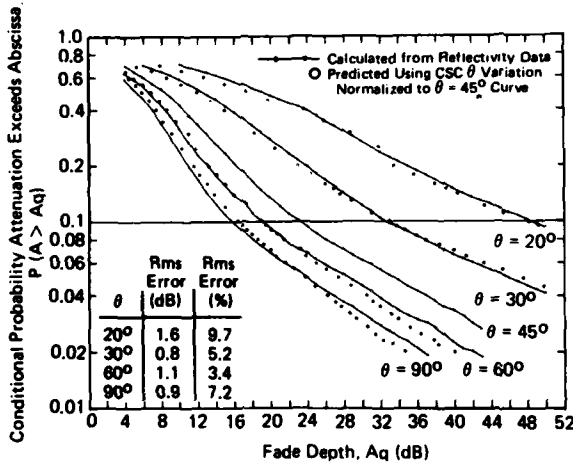


Fig. 3. Prediction of fade distributions (circled points) at other path angles using the  $\theta=45^\circ$  radar derived curve at  $f=100$  GHz and the CSC  $\theta$  approximation. The solid curves represent radar derived distributions (Goldhirsh, 1975).

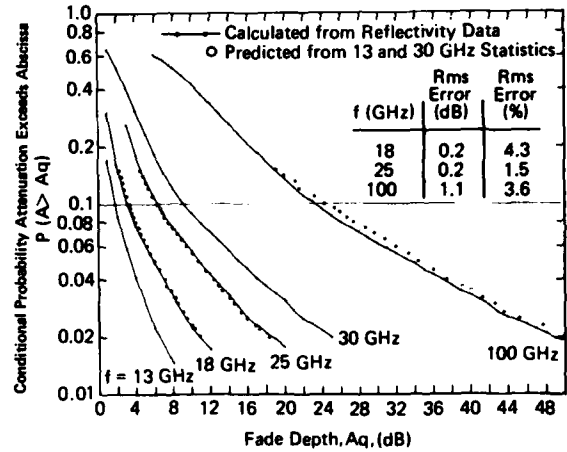


Fig. 4. Prediction of fade distribution (Circled points) at other frequencies using a knowledge of the 13 and 30 GHz curves (see text). The solid curves represent radar derived distributions (Goldhirsh, 1975).

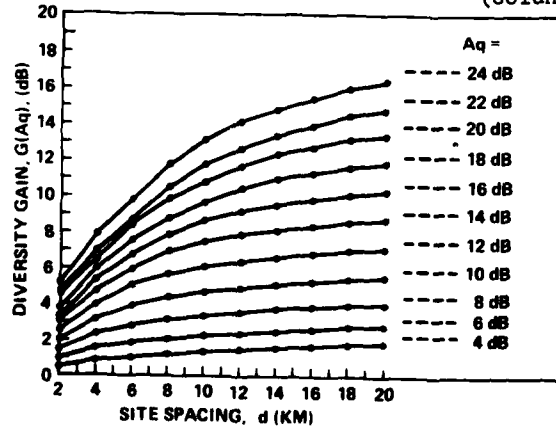


Fig. 5. Family of diversity gain curves at 30 GHz derived from distributions of the type shown in Fig. 2. The horizontal dashed lines are the decorrelated case levels at the corresponding single terminal fades (Goldhirsh, 1975).

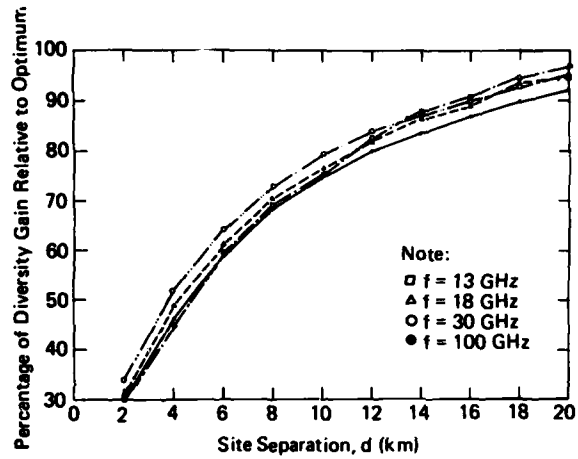


Fig. 6. The average percentage of diversity gains relative to the respective decorrelated levels as a function of site separation at the indicated spacings (Goldhirsh, 1975).

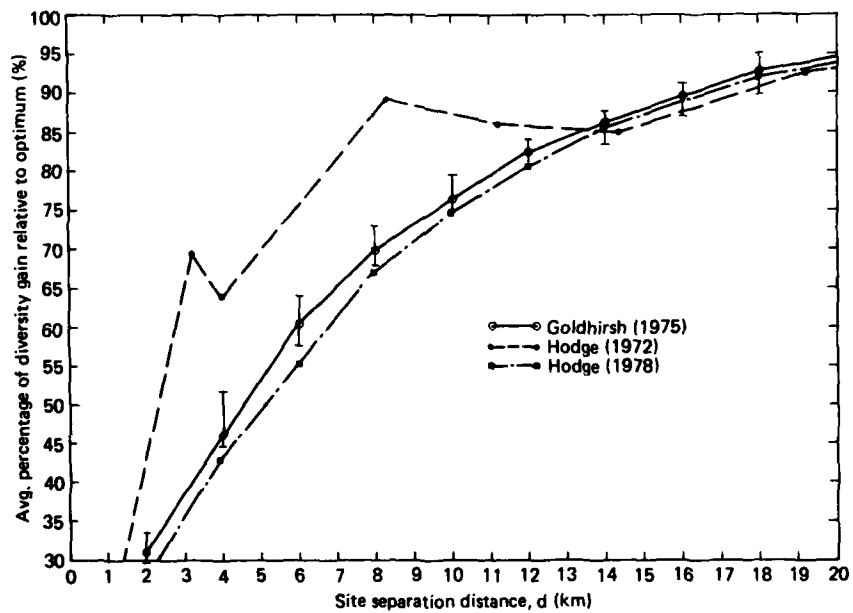


Fig. 7. Comparison of the average relative diversity gains (average of curves in Fig. 6) with those deduced by others (Hodge, 1972; 1978).



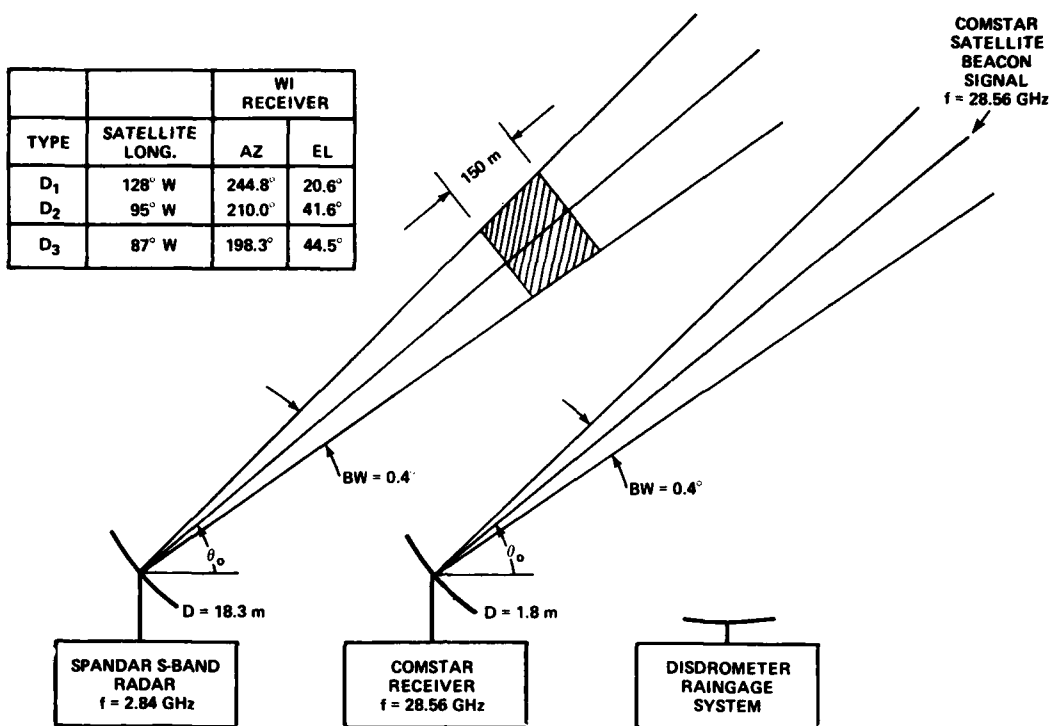


Fig. 8. Experimental configuration at Wallops Island, Va. USA, for monitoring COMSTAR beacon signals and correlating it with radar (Goldhirsh, 1979b, c).

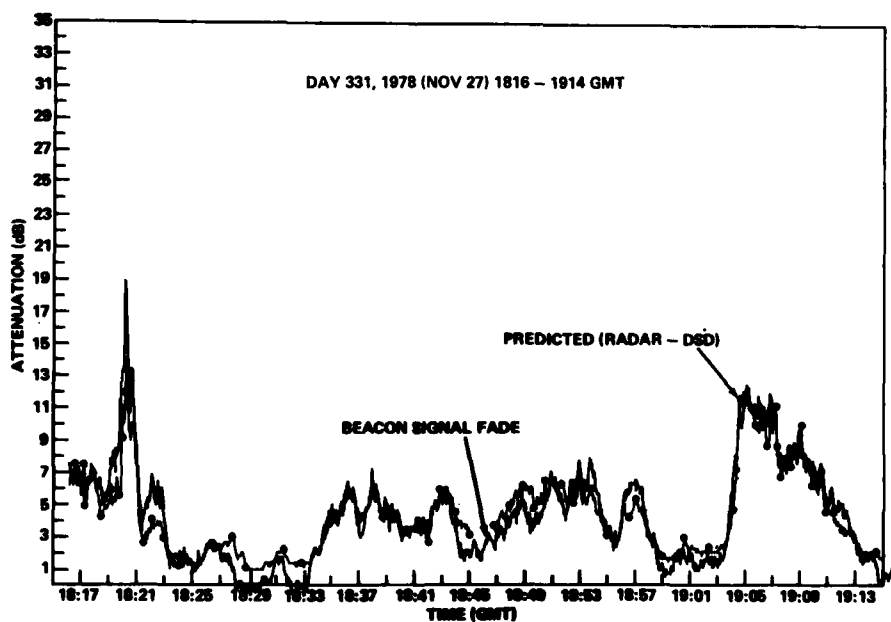


Fig. 9. Comparison of beacon measured fade with radar derived attenuation, for 27 November 1978 (Goldhirsh, 1979c).

AD-A090 850

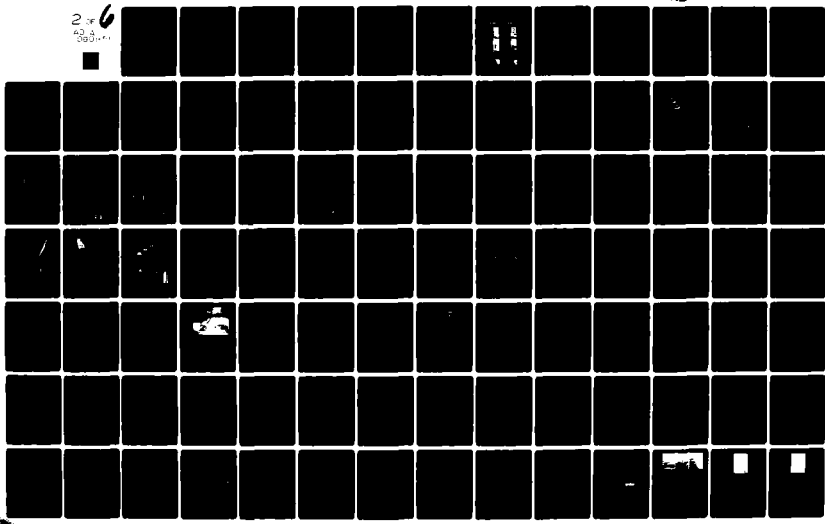
ADVISORY GROUP FOR AEROSPACE RESEARCH AND DEVELOPMENT--ETC F/6 20/14  
PROPAGATION EFFECTS IN SPACE/EARTH PATHS. (U)  
AUG 80 H J ALBRECHT

UNCLASSIFIED

AGARD-CP-284

NL

2 of 6  
62-2  
000...



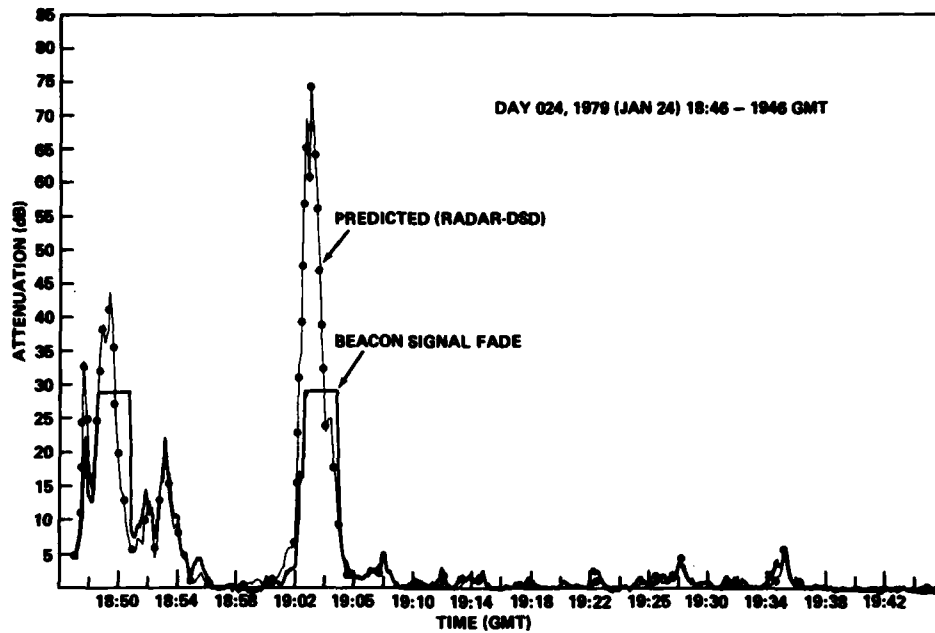


Fig. 10. Comparison of beacon measured fade with the radar derived attenuation event for 24 January 1979 (Goldhirsh, 1979c)

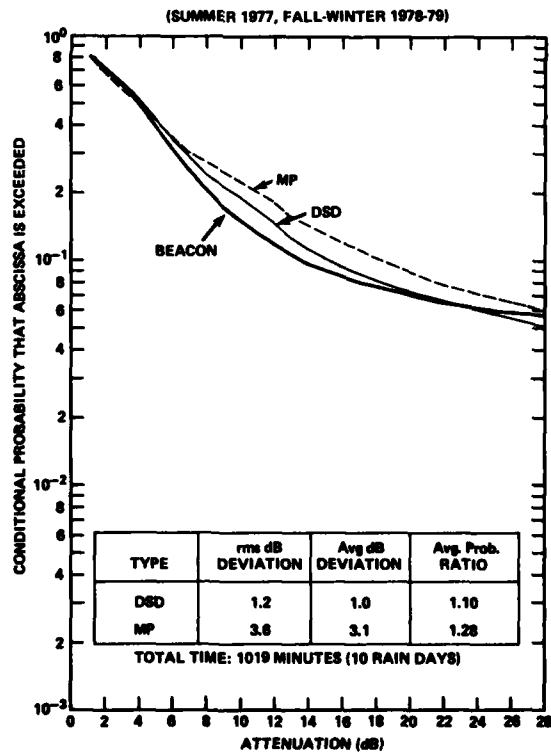


Fig. 11. Comparison of conditional fade distributions for beacon measured case, radar derived using disdrometer measurements case, and radar derived case using MP measurements over summer and winter periods (Goldhirsh, 1979c).

DUAL-POLARISATION RADAR DATA FOR EVALUATION OF  
EARTH-SPACE RADIO LINK ATTENUATION

M. P. M. Hall, S. M. Cherry and J. W. F. Goddard  
S.R.C., Rutherford and Appleton Laboratories, Ditton Park, Slough, Berks., U.K.

SUMMARY

Using conventional (single-polarisation) radar data to assess attenuation due to rain on Earth-space paths requires the assumptions that the drops have a particular statistical distribution of sizes, and that the drops are of water. In the very localised regions of intense rain which influence such paths most severely, these assumptions can lead to large errors. This paper presents comparisons between direct measurements of attenuation and those computed using data from a dual-polarisation radar technique. This technique can considerably reduce the errors of radar-derived estimates of attenuation. It also gives a clear distinction between ice and water. By contrast, estimation of attenuation using raingauge data is seen to be of very much less value.

1. INTRODUCTION

Radar is potentially a valuable tool to investigate the effect of rain on microwave radio links. The ability to observe rain extending over large areas, and at heights especially relevant to satellite-to-Earth paths, gives radar an immediate advantage over ground-based instruments. However, prediction of the attenuation due to rain along a path using back-scatter data obtained by conventional radar involves an assumption of the size distribution of the rain drops. Furthermore, the data are likely to be misinterpreted if hydrometeors other than rain are present. Knowing the drop size distribution is particularly important since it exhibits rapid spatial changes. Only rain within a few tens of metres from the boresight line of transmission contributes to any attenuation, and consequently short-lived deep fades are produced by relatively small-scale intense features in the structure of the rain. By contrast, for estimating average rainfall over a large area, it is less necessary to know the drop size distribution accurately.

A radar system used to obtain accurate estimates of the attenuation on satellite-to-Earth paths should (a) have high spatial resolution, (b) operate on a relatively long wavelength to minimise attenuation along the radar path, which would cause the intensity of distant rain to be underestimated in the presence of close rain, (c) be able to discriminate between rain and other hydrometeors and (d) not need any assumption to be made as to the drop size distribution. The present paper describes the use of such a radar. The characteristics of the drop size distribution and discrimination between water and ice hydrometeors are estimated by measuring the radar reflectivity on both horizontal and vertical polarisations. The technique is employed at 10 cm wavelength on a 25 m diameter antenna which gives a  $0.25^\circ$  beamwidth. Attenuation predictions computed from the radar data are compared with excess attenuation measurements made 5 km away at an Earth terminal receiving the 11.6 GHz TM beacon transmission from the ESA geostationary satellite OTS. This terminal is operated by the U.K. Independent Broadcasting Authority.

Apart from using dual-polarisation radar data for deriving attenuation on Earth-space paths, the technique may offer the possibility of distinguishing hydrometeor types above the melting layer (CHERRY, et al., 1980). This is likely to have application in studies of the important problem of "anomalous" depolarisation, that is the change of the polarisation of radio energy from that in which it is transmitted to some other polarisation.

2. DUAL-POLARISATION RADAR

Falling raindrops take up approximately oblate spheroidal shapes, with the axis of symmetry near vertical. The larger drops are more oblate than the smaller ones, and consequently the ratio of the energy scattered from a vertically-polarised wave to that scattered from a horizontally-polarised one can be used as a measure of the drop size. The ratio of the scatter on the two polarisations as a function of the median volume raindrop size has been deduced by SELIGA and BRINGI, 1976. The distribution of drop-sizes is found experimentally to be of the exponential form (BATTAN, 1973)

$$N(D) = N_0 \exp(-3.67 D/D_0) \quad (1)$$

where  $N(D) \text{ mm}^{-1} \text{ m}^{-3}$  is the number of drops per cubic metre per millimetre range of  $D$ ,  $D$  mm is the diameter of the volume equal to the oblate drop, and  $N_0 D_0/3.67$  is the total number of drops per cubic metre. The definitions are true provided the maximum drop diameter,  $D_{\text{max}}$ , is much greater than  $D_0$ , but  $N_0$  and  $D_0$  are still regarded as parameters which characterise a distribution even if this condition is not met.

The dual-polarisation technique uses measurements of effective radar reflectivity factor  $Z_H, Z_V \text{ mm}^6 \text{ m}^{-3}$  on horizontal and vertical polarisations. The differential reflectivity factor  $Z_{DR} \text{ dB}$  is defined as

$$Z_{DR} = 10 \log_{10} (Z_H/Z_V) \quad (2)$$

$D_0$  can be directly related to  $Z_{DR}$ , and  $N_0$  can be deduced from  $D_0$  and  $Z_H$ . These relationships are derived from exact solutions for the scattering cross sections of oblate spheroids, and have been described by HALL et al. (1980).

The radar used in the present study is located at Chilbolton, in Southern England. A description of the system has been given elsewhere (HALL et al. 1980). The p.r.f. was 610 Hz, and alternate pulses were transmitted on vertical and horizontal polarisations. There were 256 range gates, each 300 m long, and the standard deviations of the random errors in measuring  $Z_{DR}$  and  $Z$  were 0.05 - 0.1 dB and 0.75 dB,

respectively. The systematic errors in  $Z_{DR}$  and  $Z$  were estimated to be less than 0.1 dB and 1 dB, respectively.

### 3. DETERMINATION OF SPECIFIC ATTENUATION FROM $N_0$ AND $D_0$

The specific attenuation,  $\gamma$  dB  $\text{km}^{-1}$ , is given by

$$\gamma = 4.34 \times 10^{-3} \int_0^{D_{\max}} N(D) Q(D) dD = 4.34 \times 10^{-3} N_0 \int_0^{D_{\max}} \exp(-3.67 D/D_0) Q(D) dD \quad (3)$$

Here  $Q(D)$   $\text{mm}^2$  is the total scattering cross-section for a spherical drop of diameter  $D$  (GOLDSTEIN, 1951), and is computed for the OTS transmission frequency using Mie's method (STRATTON, 1941).  $Q(D)$  is a function of the complex refractive index of water which is temperature dependent, assumed here to be  $5^\circ\text{C}$ . Equation 3, together with the rigorous derivation of  $N_0$  and  $D_0$  mentioned in Section 2, is the main basis for computing the specific attenuation in this paper.

In order to examine the way in which analytic forms of  $\gamma$ - $Z$  relationships depend on  $N_0$ , it is useful to assume Rayleigh scattering from spherical drops at the 10 cm radar wavelength, rather than using the approach based on rigorous relationships between  $N_0$ ,  $D_0$  and reflectivity, as considered in the paragraph above. Again it is assumed that  $D_0 \ll D_{\max}$ . Then

$$Z = \int_0^{\infty} N(D) D^6 dD = 720 N_0 (D_0/3.67)^7 \quad (4)$$

and so

$$D_0 = 3.67 (Z/720 N_0)^{1/7} \quad (5)$$

A regression relationship between  $\gamma/N_0$  and  $D_0$ , determined from equation 3, gives

$$\gamma = 5.0 \times 10^{-6} N_0 D_0^{5.12} \quad (6)$$

Substituting  $D_0$  from equation 5 in equation 6 gives

$$\gamma = 3.2 \times 10^{-5} N_0^{0.269} Z^{0.731} \quad (7)$$

A special case of this equation is

$$\gamma = 3.6 \times 10^{-4} Z^{0.731} \quad (8)$$

for which  $N_0 = 8000 \text{ mm}^{-1} \text{ m}^{-3}$ , the value in the Marshall-Palmer distribution (BATTAN, 1973). Equation 7 may be applied where  $N_0$  is known, and indeed it forms a good approximation to the rigorous method indicated above except for very high or very low values of  $D_0$ . Figure 1 shows equation 7 plotted for each decade of  $N_0$  from  $10^2$  to  $10^6 \text{ mm}^{-1} \text{ m}^{-3}$ , the range of values measured to date by the present technique (CHERRY et al. 1979 and 1980), and for the Marshall-Palmer value of  $8000 \text{ mm}^{-1} \text{ m}^{-3}$ . The dependence on temperature of relationships between  $\gamma$  and  $Z$  for the OTS frequency is relatively small,  $\gamma$  being about - 1% per  $^\circ\text{C}$  in the vicinity of  $5^\circ\text{C}$ .

Table 1 shows, for a nominal value of  $D_0 = 1 \text{ mm}$ , the errors in estimating  $\gamma$  for various errors in measuring  $Z_{DR}$ . The errors in  $D_0$  and  $N_0$  are derived from the relationships for  $Z_{DR}$ ,  $Z_H/N_0$  and  $D_0$  and from equation (6). Generally, larger values of  $D_0$  result in smaller errors in  $\gamma$ . For  $D_0 = 0.75 \text{ mm}$ , the percentage error in  $\gamma$  shown in Table 1 should be multiplied by a factor of 1.4, whereas for  $D_0 = 2 \text{ mm}$  the factor becomes 0.45. Since, for a given  $D_0$ ,  $Z_H \propto N_0$  and  $N_0 \propto \gamma$ , errors in measuring  $Z_H$  will result in the same fractional errors in both  $N_0$  and  $\gamma$ . For the Chilbolton radar, the random error in estimating  $Z_{DR}$  and  $Z$ , as given in Section 2, would result in a standard deviation of 25% for  $\gamma$  for a  $D_0$  of 1 mm. The systematic errors in  $Z$  and  $Z_{DR}$  result in a worst-case error in  $\gamma$  of 40% for a  $D_0$  of 1 mm. These systematic errors may be allowed for by comparison with direct measurements, as discussed in Section 4.

TABLE 1

$\Delta Z_{DR}$ (dB)	$\Delta \gamma$ (%)
0.2	- 24
0.1	- 13
0.05	- 7
- 0.05	8
- 0.1	16
- 0.2	39

### 4. DATA FROM THE OTS PATH

Before describing the comparison of directly-measured attenuation with that computed from radar data, it is useful to examine the form of radar data available. Figure 2 shows the distribution of  $Z$  and  $Z_{DR}$  in a vertical section through rain. Distinctive features are the pillars of high  $Z$  and  $Z_{DR}$  between 20 and 45 km from Chilbolton, and the 'bright-band' (high  $Z$ ) region between about 3 and 3.5 km height. A radio sonde ascent 55 km east from Chilbolton at about this time showed the  $0^\circ\text{C}$  isotherm to be at 3.2 km height. As in this case, all examples seen to date have shown the peak of  $Z_{DR}$  to be just below the peak of  $Z$  (HALL, et al. 1980, CHERRY, et al., 1979 and 1980), and a tentative explanation of this has been put forward (CHERRY, et al., 1979). At very low elevation angles,  $Z$  appears to decrease abruptly due to diffraction losses from

hills near to the radar site. However,  $Z_{DR}$  does not change with  $Z$  in this region since the diffraction loss is independent of polarisation.  $Z_{DR}$  and  $Z$  are not plotted at all when  $Z$  is less than 22 dB. (Here the reflectivity factor is expressed in  $\text{dB} > 1 \text{ mm}^6 \text{ m}^{-3}$ , i.e.  $10 \log_{10} Z$ .) Although Figure 2 relates to data discussed later, it is not typical of examples examined to date in that it portrays relatively weak rain falling below the melting layer, and only small regions of medium intensity  $Z$  above this height. Other examples studied have shown high values of  $Z$  extending well above the melting layer, and distinctive changes in  $Z_{DR}$  have been the only indication of the boundary between ice clouds and regions of rainfall (CHERRY, et al., 1979 and 1980; HALL, et al., 1980).

Figure 3 shows the variability of  $N_0$  and  $D_0$  in the rain seen in Figure 2 extending from 20 to 45 km from the radar, and from 1 to 2 km in height. The axes chosen are  $Z$ , the prime radar characteristic, and the rainfall rate,  $R$ , which may be derived from  $N_0$  and  $D_0$  (CHERRY, et al., 1979). The large variability in  $N_0$  and  $D_0$  is clear, but Figure 3 is not typical of data examined to date in that  $N_0$  is usually more uniformly distributed about the Marshall-Palmer (M-P) value of  $8000 \text{ mm}^{-1} \text{ m}^{-3}$  (CHERRY, et al., 1979 and 1980). Figure 3, taken in conjunction with Figure 1, indicates how the range of  $N_0$  values will produce  $\gamma$ - $Z$  relationships differing from that for an M-P drop size distribution.

Figure 4 gives a schematic indication of the way in which data were extracted from the radar scans in order to compute the attenuation along the bottom end of the OTS-to-ground path. The ground terminal is situated at Crawley Court, near Winchester, and the path is elevated at  $30^\circ$  above horizontal. At a typical range of 6 km from the radar (and 1.5 km from the ground terminal), the radar beam width was 30 m, i.e. one tenth of the range gate length. For each of the data cells lying along the ground-to-OTS path, the specific attenuation and range increment,  $\delta r$ , were evaluated, multiplied together and added to the cumulative attenuation,  $A_c = \sum \gamma(r) \delta r$  at the range,  $r$ .

Figure 5 shows five examples of this cumulative attenuation,  $A_c$ , as a function of the height,  $h$ , above the horizontal plane containing the ground terminal (i.e.  $h = r/2$  since the elevation angle is  $30^\circ$ ).  $A_c$  was derived from  $N_0$  and  $D_0$  using the rigorous method mentioned in Section 3. Each example also shows  $Z$  (for horizontal polarisation),  $Z_{DR}$  (which is almost linearly related to  $D_0$ ) and  $N_0$ . Example (a) shows a characteristically marked rise in  $Z_{DR}$  (i.e. in  $D_0$ ) with height at the bottom of the melting layer (2.1 km height). Below this height,  $N_0$  is somewhat higher than the Marshall-Palmer (M-P) value, and  $A_c$  increases steadily with height to reach 0.44 dB at the melting layer. Above 2.1 km, drops cannot be assumed to be of water alone, and so  $D_0$ ,  $N_0$  and  $A_c$  cannot be evaluated from  $Z$  and  $Z_{DR}$ . The apparent rapid rise in  $A_c$  at about 2.5 km is not meaningful. Example (b) shows values of  $N_0$  much closer to the M-P value, and lower  $Z$  values. Above 0.5 km height,  $D_0$  is relatively constant (about 1 mm) up to the melting layer. The total attenuation is only 0.17 dB at the melting layer. Example (c) again shows high values of  $N_0$ , and a region of high reflectivity at about 2 km height which is largely responsible for  $A_c$  reaching 0.61 dB by the bottom of the melting layer. In this case the presence of the melting layer would not have been apparent from a record of  $Z$  alone, but it is clear from the rapid rise in  $D_0$ . Marked variability in  $D_0$  and  $N_0$  with distance along the path is particularly evident in example (d), in which the rate of increase in  $A_c$  with height is quite high, giving a value of 1.96 dB at the melting layer.

Figure 6 shows as a function of time a comparison of attenuation measured directly on the OTS-to-ground path (curve a) and that derived from radar measurements, during a total of 70 minutes on 6 and 8 October, whilst shallow fades occurred due to weak rain of the type indicated in Figure 2. The directly-measured data were read off chart recordings for which the times were checked using ranging test data. Curve b shows the cumulative attenuation,  $A_c$ , along the path from ground level to the bottom of the melting layer using the same method as produced  $A_c$  in Figure 5, apart from one small difference.  $A_c$  in Figure 5 does not assume any data in the first 250 m (slant range) from the ground terminal, since no radar data were available at these low heights. But, for completeness,  $A_c$  in Figure 6 assumes the  $Z$  and  $Z_{DR}$  characteristics in this 250 m interval to be the same as that in the first data sample. In all cases this correction was less than 0.1 dB. The bottom of the melting layer was taken to be the height at which  $D_0$  started to rise rapidly with height.

In the height regions where it may be assumed that ice crystals from greater heights were melting, i.e. the region for which  $D_0$  is generally large and the region for which  $Z$  is large,  $\gamma$  was calculated from a relationship based on

$$\gamma = 2.9 \times 10^{-4} Z^{0.716} \quad (9)$$

since this has been shown by DISSANAYEKE and McEWAN (1978) to apply to such regions. This value was scaled by the factor  $(N_0/8000)^{0.284}$  using the known mean value,  $N_0$ , of  $N_0$  in the 500 m slant range (250 m height interval) below the bottom of the melting layer. Although this has considerably improved the estimates of  $\gamma$  in the melting layer, it is still not entirely satisfactory since there may not have been the one-to-one correspondence of drops within and below the melting layer which is assumed in equation 9 and in the scaling factor used to modify that equation. Vertical-section plots such as Figure 2 suggest that, for the data considered here, the region of melting extended over a height interval of about 0.5 km, even though quite high values of  $Z$  (probably due to ice crystal clouds) were sometimes seen above this region. In the interests of uniformity, the melting layer was always taken to extend over a height interval of 0.5 km, with a lower boundary at the bottom of the region of high  $D_0$  values.

In Figure 6, curve c represents the sum of  $A_c$  up to the melting layer (curve b) added to  $\sum \gamma(r) \delta r$  through the melting layer, as computed from equation 9. Predictions are correct where  $c = a$ . Usually the attenuation in the melting layer was much less than that in the rain below the melting layer, but this was not always so. In a few cases the attenuation due to the melting layer was considerably more than that due to the rain. Because of the associated much smaller complex permittivity, clouds of dry ice particles give negligible attenuation at the frequency of OTS. For example, assuming

$$\gamma = 3.8 \times 10^{-7} Z + 1.9 \times 10^{-5} Z^{0.5} \quad (10)$$

at this frequency (BATTAN, 1973), then even a reflectivity of 30 dB  $> 1 \text{ mm}^6 \text{ m}^{-3}$  (which would be high for the conditions considered in this paper) would produce a specific attenuation of only  $10^{-3} \text{ dB km}^{-1}$ .

Curve d shows the equivalent to curve c, but using the Marshall-Palmer model (equation 8) in place of using the  $N_0$  and  $D_0$  data. Predictions would be correct where  $d = a$ , but for the data discussed here, the M-P values are generally about half those measured directly, and half those computed using  $N_0$  and  $D_0$ . This is entirely consistent with the fact that the  $N_0$  values seen in Figure 5 were generally higher by about a decade than the M-P value, since reference to Figure 1 shows that this increases the specific attenuation (and so the cumulative attenuation  $A_c$ ) by a factor of nearly two. Vertical sections are not available at the time periods indicated in Figure 6, but plan-position information confirms that weak rain of the type indicated in Figure 2 caused these particular fades. Again Figure 3 emphasises the high values of  $N_0$ .

Figure 7 shows a comparison of the data points in Figure 6 for direct measurements,  $A_D$ , (curve a) and for those derived from radar data,  $A_R$  (curve c). A distinction has been made when the attenuation in the melting layer was at least one half of the total attenuation, but it can be seen that these points are not untypical; i.e. the model used for the melting layer does not seem to be a cause of the spread of data points. For all but five of the data points,  $A_R$  differs from  $A_D$  by less than 0.5 dB, and the standard deviation of  $A_R - A_D$  is 0.3 dB. With the few samples available, and because of the large variability of the possible random error associated with the small values of  $D_0$  measured in the present data, it is not practical to comment further on the spread of data points in relation to the random errors discussed in Section 3. However, it does seem that the 40% possible systematic error referred to in Section 3 was pessimistic. Unlike the random error, any systematic error in measuring  $\gamma$  should be readily apparent in Figure 7. Further comparisons should enable this to be allowed for.

During the collection of data previously referred to in this paper, a rapid-response raingauge (of a type described by NORBURY and WHITE, 1971) was sited 9 km from Chilbolton and 0.15 km off the OTS path, as shown in Figure 4. Figure 8 shows a comparison of directly-measured attenuation,  $A_D$ , averaged over 4 minutes, and values derived from the raingauge data,  $A_R$ , assuming a uniform rainfall rate,  $R$  mm h<sup>-1</sup>, up to the melting layer. Equation 8 was used together with

$$Z = 250 R^{1.42} \quad (11)$$

Equation 11 is derived using the fall-speeds given by BEST (1950). It assumes that  $N_0 = 8000 \text{ mm}^{-1} \text{ m}^{-3}$  and that  $Z$  and  $D_0$  are related by equation 5. In addition, Figure 8 shows the values of  $A_R$  supplemented by the attenuation due to the melting layer, as deduced from the radar data (i.e. values equivalent to the differences between curves b and c in Figure 6). Clearly these data would not be available when using raingauge data alone, and the significant improvement that they yield in estimating time-averaged attenuation underlines one major disadvantage of using raingauge data alone for this purpose.

Additional uncertainty arises through the use of measurements at one point to predict conditions over the length of the OTS-to-ground path. Figure 2 shows much variation in raincell structure, even though the overall rainfall rate is low, and although the time-averaging of the raingauge data smoothed out some of these irregularities, this would conceal the important short-lived peaks in attenuation caused by small cells of intense rain associated with thunderstorms. In such conditions the correlation of raingauge-derived and directly-measured attenuation would be less.

## 5. CONCLUSIONS

This paper has described the use of a dual-polarisation radar to derive the attenuation on a slant radio path. This has been tested against direct measurements at 11.6 GHz on an Earth-space link. Data were available for only weak rain, where the technique is least accurate, but almost all radar-derived attenuation values were within 0.5 dB of directly-measured values (standard deviation 0.3 dB). Some parts of the observed rain showed very low values of  $D_0$ , and the estimation of attenuation by the dual-polarisation technique is least accurate for these conditions. In the small intense cells of rain which are associated with thunderstorms and cause highest attenuation,  $D_0$  is usually higher, and the accuracy would then be greater.

For the rain examined, estimation of the attenuation using the reflectivity factor alone, but assuming a Marshall-Palmer drop size distribution, produced an error factor of about two. In local regions of the rain, the error factor in computing the specific attenuation was four. Attempts to predict attenuation using data from a raingauge in the path were much less satisfactory.

Clearly the present paper has made only a start in using dual-polarisation radar for studies of this kind, though it has shown that such a radar can give a much better estimate of attenuation than conventional radar could offer when the distribution of drop sizes is markedly different from that of the Marshall-Palmer model. More study of the problem is necessary, particularly in the region of the melting layer. Subsequently, it is expected that the technique will have value in modelling attenuation through rain over a range of frequencies, and in predicting the performance of diversity operation at 20 and 30 GHz.

## ACKNOWLEDGEMENTS

The radar work described in this paper formed part of the research programme of the Rutherford and Appleton Laboratories of the U.K. Science Research Council. Many colleagues contributed to the success of the radar measurements, G. R. Kennedy and N. W. Whitehead in particular. The directly-measured data for the OTS-to-ground path were made available by the U.K. Independent Broadcasting Authority.

## REFERENCES

- BATTAN, L. J., 1973, "Radar observations of the atmosphere", Univ. of Chicago Press, Chicago and London.  
 BEST, A. C., 1950, "Empirical formulae for the terminal velocity of water drops falling through the atmosphere", Q. J. Roy. Met. Soc., 76, 302-311.

- CHERRY, S. M., GODDARD, J. W. F., HALL, M. P. M. and KENNEDY, G. R., 1979, "Measurement of rain-drop-size distributions using dual-polarisation radar", Proc. 5th Int. Conf. on Erosion by Solid and Liquid Impact, Cambridge, U.K.
- CHERRY, S. M., GODDARD, J. W. F. and HALL, M. P. M., 1980, "Examination of rain drop sizes using a dual-polarisation radar", Proc. Am. Met. Soc. 19th Conf. on Radar Meteorology, Florida, U.S.A.
- DISSANAYEKE, A. W. and McEWAN, N. J., 1978, "Radar and attenuation properties of rain and bright band", IEE Conf. Publn. No. 169 : "Antennas and Propagation", Part 2, 125-129.
- GOLDSTEIN, H., 1951, "Attenuation by condensed water" in 'Propagation of short radio waves', Edited by Kerr, D. E., Rad. Lab. Series, Vol. 13, McGraw-Hill Book Co. Inc., New York, 671-673.
- HALL, M. P. M., CHERRY, S. M. and GODDARD, J. W. F., 1980, "Use of dual-polarisation radar to measure rainfall rates and distinguish rain from ice particles", Proc. IEEE Int. Radar Conf., Washington, U.S.A.
- NORBURY, J. R., and WHITE, W. J. K., 1971, "A rapid response raingauge", *Jl. Phys. E.*, 4, 601-602.
- SELIGA, T. A. and BRINGI, V. N., 1976, "Potential use of radar differential reflectivity measurements at orthogonal polarizations for measuring precipitation", *J. Appl. Meteor.*, 15, 69-76.
- STRATTON, J. A., 1941, "Electromagnetic theory", McGraw-Hill Book Co. Inc., New York, 569.

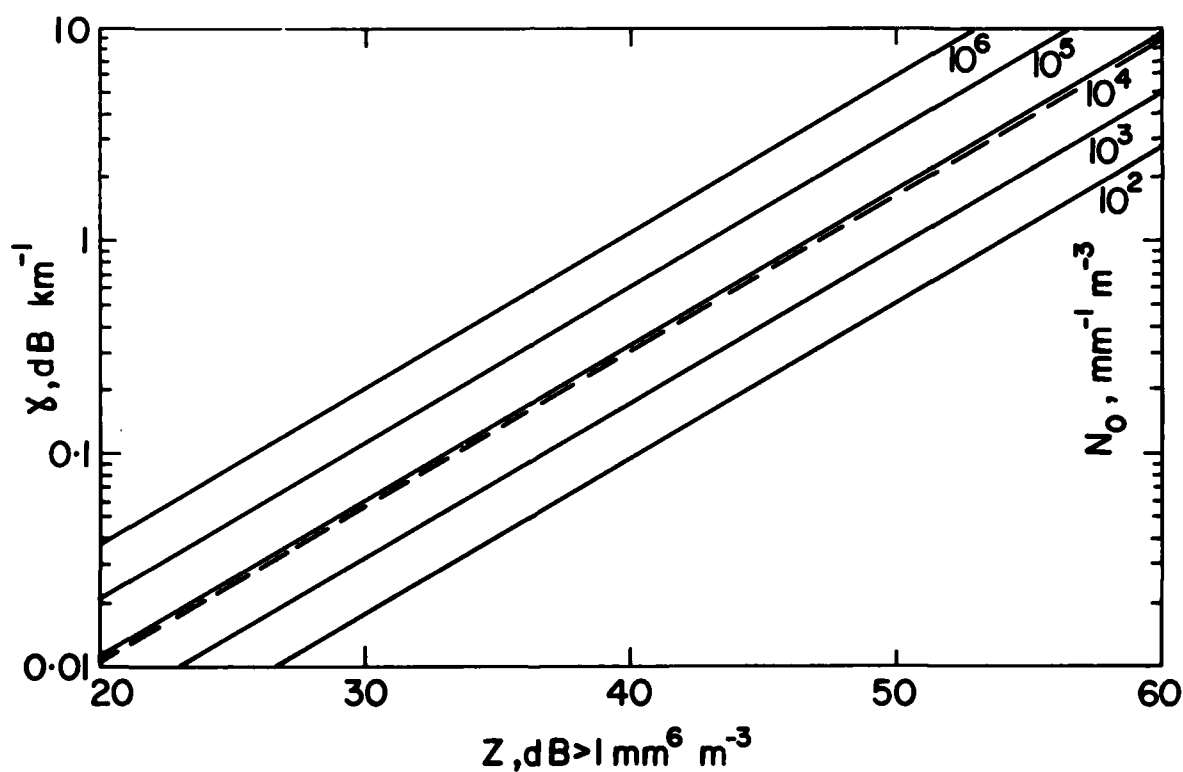


**Figure 1** Dependence on  $N_0$   $\text{mm}^{-1} \text{m}^{-3}$  of relationships between specific attenuation,  $\gamma$   $\text{dB km}^{-1}$ , and reflectivity factor,  $Z$   $\text{dB} > 1 \text{mm}^6 \text{m}^{-3}$ , for a temperature of  $5^\circ\text{C}$ .



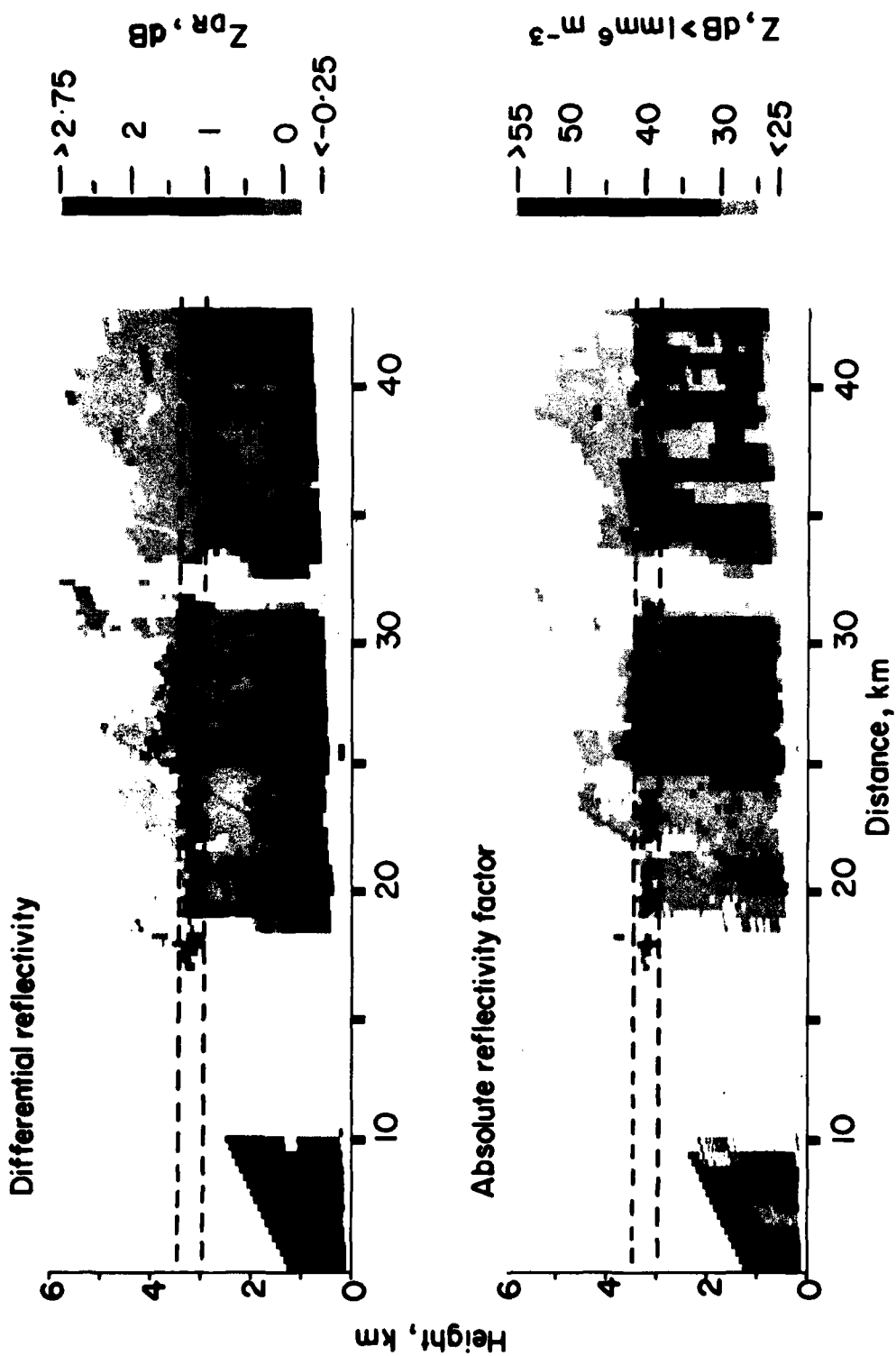


**Figure 2** Spatial distribution of radar reflectivity factor,  $Z$ , (for horizontal polarisation) and differential reflectivity,  $Z_{DR}$ , (horizontal/vertical polarisation) in a vertical plane (azimuth  $152.5^\circ$ ) at 1818 UT on 8 October 1979.

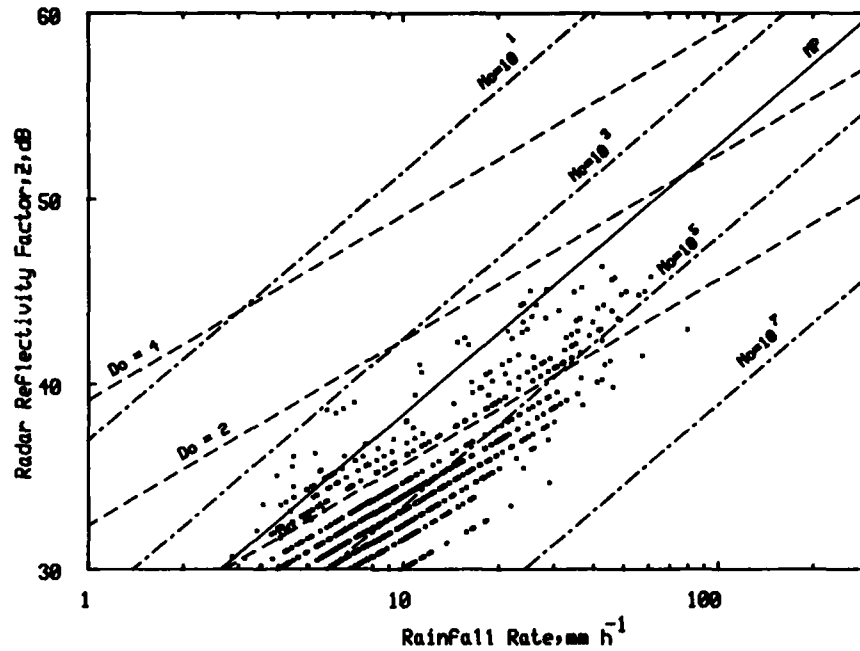


**Figure 3**

Distribution of data samples of  $Z \text{ dB} > 1 \text{ mm}^6 \text{ m}^{-3}$ ,  $R \text{ mm h}^{-1}$ ,  $N_0 \text{ mm}^{-1} \text{ m}^{-3}$  and  $D_0 \text{ mm}$  from data shown in Figure 2 for distances of 20 to 45 km from radar and heights of 1 to 2 km. Each point represents one 300 m long range gate averaged for 0.2s during a vertical scan at  $0.9^\circ \text{ s}^{-1}$ . The solid line labelled MP represents the Marshall-Palmer distribution, i.e.  $N_0 = 8000 \text{ mm}^{-1} \text{ m}^{-3}$ .

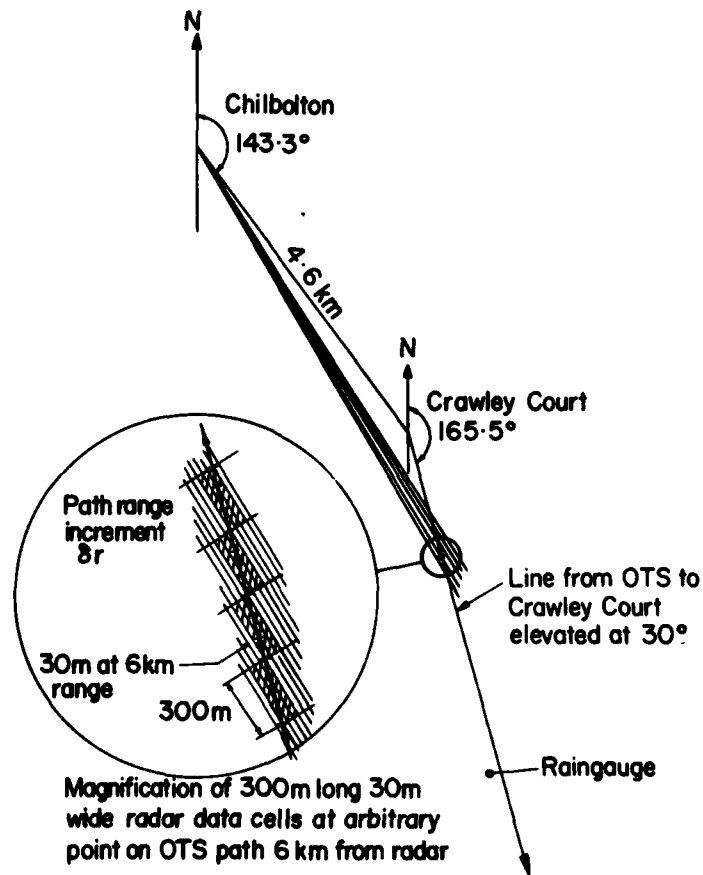


**Figure 4**

Schematic of radar scan in plane containing line from ground terminal to satellite.

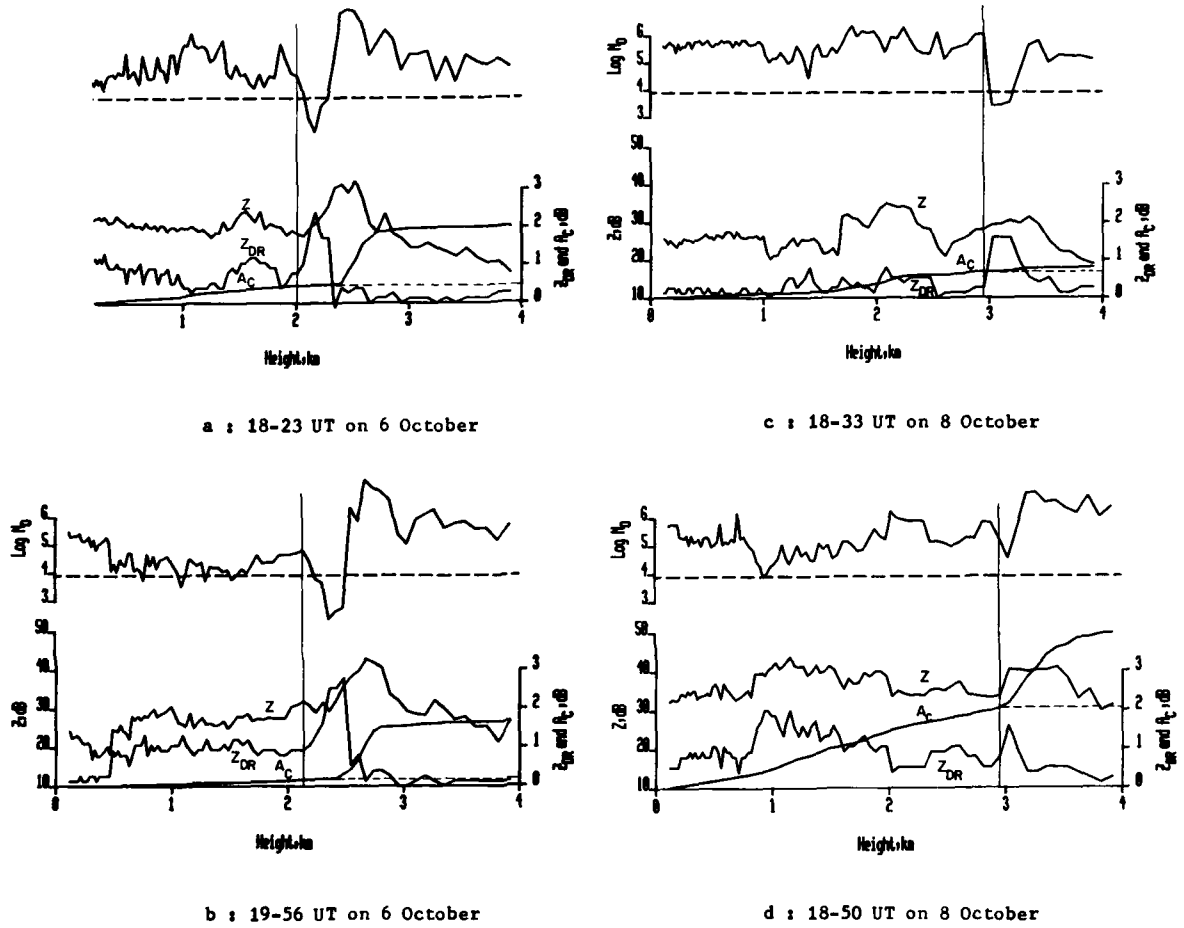


**Figure 5**

Examples of radar-derived parameters  $Z$  and  $Z_{DR}$ , and computed values of  $N_0$  and cumulative attenuation,  $A_c$  dB, as functions of height on ground-to-satellite path. The broken line at  $N_0 = 8000$  corresponds to the M-P drop size distribution.

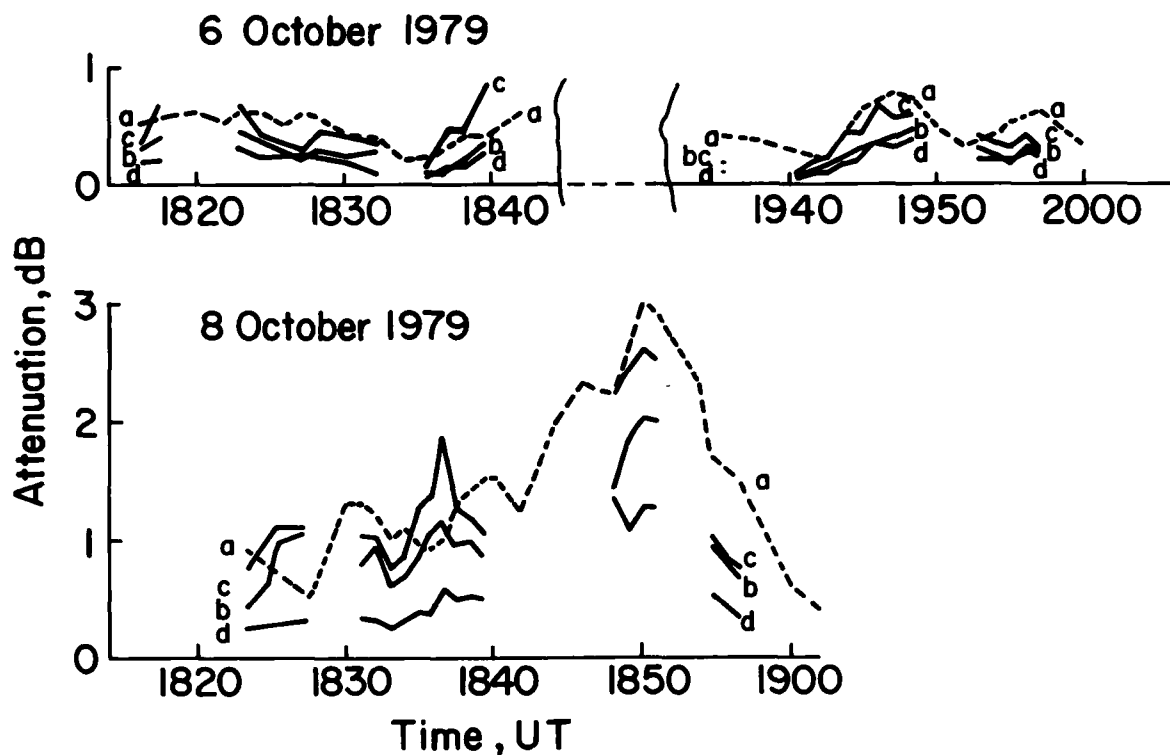


**Figure 6**

Time sequences for periods during 6 and 8 October, 1979, comparing directly-measured values of attenuation on satellite-to-ground path (curve a) and radar-derived values. The latter are plotted for the attenuation up to the melting layer (curve b), assuming  $N_0$  and  $D_0$  as computed from equation 3, and then added to that in the melting layer (curve c) as computed from equation 9, i.e. that for the whole path. Predictions are correct where  $c = a$ . Also shown (curve d) is the attenuation computed for an M-P drop size distribution, from equation 8, added to that in the melting layer, computed from equation 9. These predictions are correct where  $d = a$ .

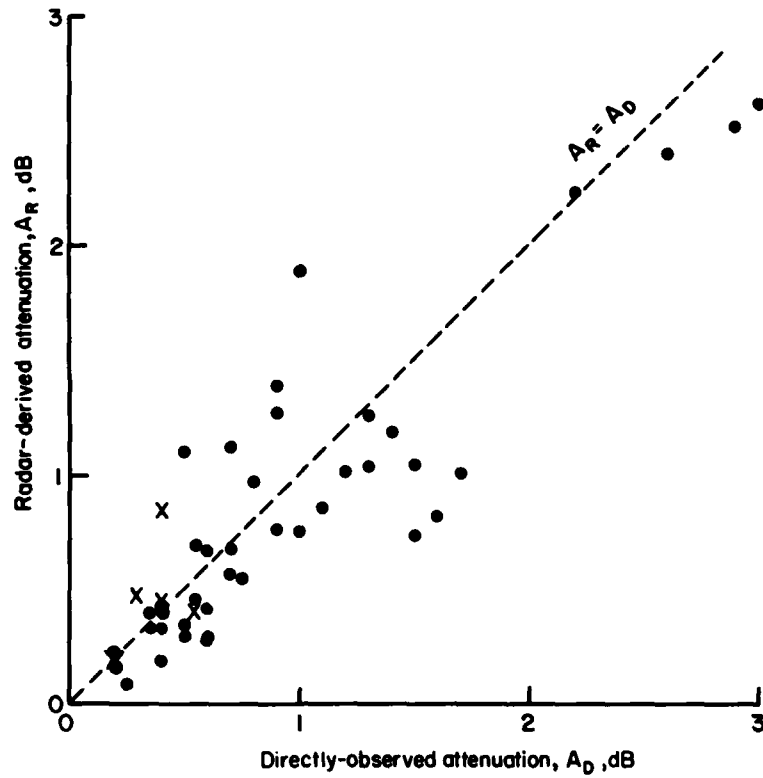


Figure 7

Comparison of directly-measured attenuation,  $A_D$ , and those computed from radar data,  $A_R$ , using all data pairs (curves a and c) shown in Figure 6. x points for which attenuation due to the melting layer was at least half the total,  $A_T$ . o other points.

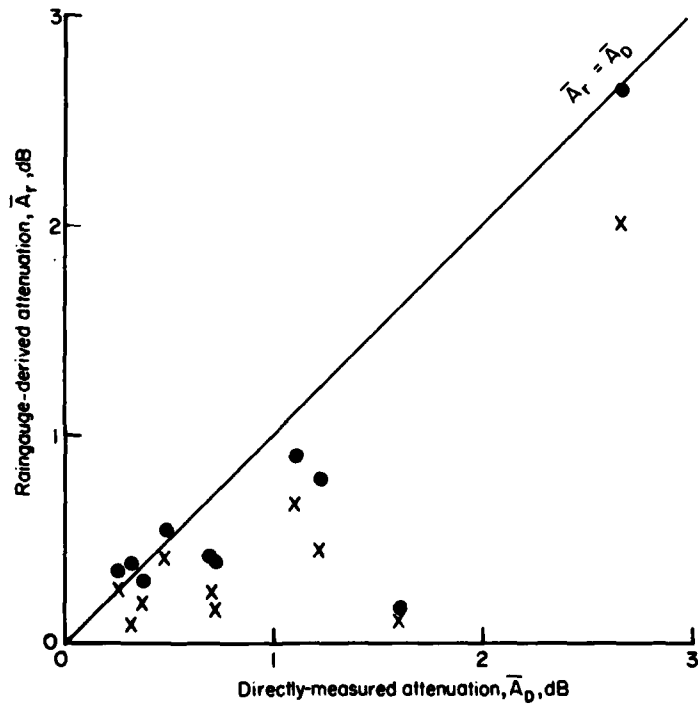


Figure 8

Comparison of time-averaged directly-measured attenuation,  $\bar{A}_D$ , and that computed from raingauge data,  $\bar{A}_R$ .  
 x without allowance for melting layer.  
 o with allowance for melting layer using radar data.

## SUMMARY OF SESSION II – EXPERIMENTAL DATA OF SHF/EHF PATHS

by R. Viddeleer (Session Chairman)

In Session II a total of 11 papers on experimental data of propagation on slant paths at frequencies above 10 GHz were presented. These data were either obtained by using beacon signals of a satellite (e.g. OTS, SIRIO, ATS-6, CTS or COMSTAR) or by measurement of sky noise (fixed mounted radiometers) or attenuation of solar noise (sun-tracking radiometers). A relatively new and promising tool is described in two papers and consists of a radar, which can, apart from giving the total attenuation on a slant path, also give extra information of propagation anomalies as a function of the distance along a path. The use of radar (preferably of the dual-polarised type) could therefore assist in the interpretation of measurement results obtained otherwise and give propagation information in frequency bands and/or at sites where satellites are not available.

From the systems point of view one can draw the following conclusions from the papers that were presented:

- the influence of rain on systems operating above about 10 GHz will be of paramount importance, in particular with respect to attenuation. Even in moderate climates attenuations of 12 dB at 20 GHz and 20 dB at 30 GHz can be expected for 0.01% of a year. The spread in these values from year to year is high.
- the influence of rain on depolarisation depends on the type of polarisation used (linear vs circular) and in the case of linear polarisation also on the tilt angle. In the optimum case (linear polarisation, vertical or horizontal) the depolarisation is about 10 dB less severe than for circular polarisation.
- strong depolarisation can occur without significant attenuation and is likely to be caused by ice crystals. These crystals are likely to be subject to orientation along the field lines in the strong electrostatic fields of thunderstorms.
- systems with frequency reuse by means of polarisation diversity will show degraded performance due to extra attenuation as well as to depolarisation effects. To describe the system performance the joint probability of these two parameters is required. Some papers give data on this joint probability. The conclusion is, that in most systems the attenuation will be the governing factor in the quality criteria of the system.
- with regard to dispersive effects (frequency-dependant attenuation and phase) which are important with regard to wideband systems, the presented measurement results are not conclusive. One author measured no noticeable difference between the measured data and the theoretical bulk frequency dependance, whereas a second author measured significant differences, especially in the phase (two orders of magnitude higher than expected). Until further evidence is provided one has to be careful to draw conclusions.

REVIEW OF SLANT PATH PROPAGATION MEASUREMENTS MADE AT  
THE APPLETON LABORATORY, SLOUGH (UK)

P. G. Davies and E. C. Mackenzie

(S.R.C., Rutherford and Appleton Laboratories, Ditton Park, Slough SL3 9JX, Berks., U.K.)

SUMMARY

This paper reviews slant path measurements made at the Appleton Laboratory since 1968, with particular emphasis on recent measurements using transmissions from the OTS and SIRIO satellites. The following gives an indication of the types of measurement which have been made and the data which have become available during the last ten years :-

- (i) Attenuation measurements using sun-tracking radiometers at 19, 37 and 71 GHz for data collected over periods of 52, 45 and 6 months respectively. The results are available in the form of histograms of the number vs duration of individual events, cumulative distributions for ranges of elevation angle, variability from year-to-year and comparisons of simultaneous measurements at different frequencies.
- (ii) Diversity measurements at 37 GHz using sun-tracking radiometers in a three-site network.
- (iii) Diversity measurements using fixed-pointing 12 GHz radiometers.
- (iv) Measurements of co-polar attenuation, cross-polar discrimination (XPD) and diversity at 30 GHz using the ATS-6 satellite transmissions, and comparisons with radiometric data.
- (v) Apart from measurements of diversity, measurements similar to those in (iv) above have also been carried out using the OTS and SIRIO satellite transmissions. At its Slough site, the Appleton Laboratory operates two receiving stations for microwave satellite transmissions, namely, the main station and a sub-station, separated by 0.35 km. The main station is equipped with a 3 m diameter tracking antenna and is capable of receiving either the SIRIO (carrier and side-band) or the OTS ( $B_0/B_1$ ) transmissions, while the sub-station has a 1 m diameter fixed antenna and can receive only the SIRIO carrier transmission. The main station was used to observe SIRIO between September 1977 and June 1978 when it was repointed and adjusted for OTS reception. The sub-station has monitored the SIRIO carrier transmission almost continuously since September 1977. Details of the systems and a description of the first year of measurements using SIRIO have been published in the June 1979 issue of *Alta Frequenza*. Cumulative distributions of attenuation for both OTS and SIRIO observations indicate that, at Slough, more severe rainfall conditions occurred during 1979 than during 1978. Comparisons with earlier on-site radiometric data indicate that, apart from snowfalls and two large rainfall events, the 1979 conditions appear near to normal. No cancellation is used in the cross-polar measurements and the best XPD recorded is about 26 dB. Strong depolarisation has been observed to be coincident with heavy rainfalls.

1. INTRODUCTION AND GENERAL OVERVIEW

During the 1960's it became apparent that the demands from the rapidly expanding services involved with communications traffic would soon exceed their available frequency allocations below 10 GHz. Attention was therefore turned towards the possibility of exploiting higher frequency bands for both terrestrial and satellite communications links. To achieve the same high reliabilities (~ 99.999 per cent) which were nominally provided in the existing links operated at lower frequencies required

- (i) the technological development of equipment with equivalent or superior reliability for the higher frequency bands, and
- (ii) an evaluation of the degradation of system performance caused by the atmosphere since both the clear atmosphere and atmospheric hydrometeors (cloud, rain, hail, etc.) are not transparent to radiowaves at frequencies above 10 GHz. Also, the various effects are frequency dependent and can impose severe limitations on system performance. In particular, the attenuating effects of rain along paths through the atmosphere needed to be quantified in order to compute, relative to clear sky conditions, how much additional transmitting power or receiver gain should be made available to provide an adequate fade margin for operational systems.

The studies therefore divided naturally into studies of hardware and associated techniques and into studies of radiowave propagation effects. A third aspect enters later relating to the establishment of an operational system. This needs to be designed taking into account the available technology with estimates of the predicted degradations which could be introduced by the atmosphere to provide an adequate, cost-effective service to the customer. The required quality and reliability of the service will depend to a considerable extent on the type of service involved, e.g. good quality and high reliability are essential for an 'on-line' type service such as TV distribution. Possibly however, these criteria can be relaxed for those services in which 'lost' data can be re-transmitted at a later time without causing significant inconvenience.

With regard to the studies mentioned in (i) above, the availability of much larger bandwidths than had been used hitherto provided an opportunity to consider afresh the best methods to employ for the transmission of large quantities of data, either from a single source, or multiplexed on to the carrier from many sources. Hence, new modulation and time-sharing techniques could be employed, and new, better services could be provided for the transmission of both analogue and digital information.

However, these are not the aspects with which the Appleton Laboratory has been primarily concerned hitherto, although it is now becoming more actively involved. During the last ten years, the Laboratory has concentrated on item (ii) above, i.e. characterising the properties of the transmission medium along space-to-Earth and Earth-to-space paths. In the absence of suitable satellite transmissions, initial measurements were obtained over a broad frequency band, from about 10 to 100 GHz, by means of radiometers. These were of several types depending upon the application, as outlined in Section 2. Single-site measurements were made using radiometers located within the grounds of the Laboratory at Slough (latitude  $51^{\circ} 29' N$ ,  $00^{\circ} 34' W$ ). These provided a very extensive collection of data amounting to many site years of observation. In addition, several 'site-diversity' experiments were carried out. These involved co-ordinated arrays of fixed 11.6 GHz radiometers, sun-trackers at 37 GHz, and also fixed 30 GHz radiometers associated with stations receiving the ATS-6 satellite beacon transmissions at 30 GHz. All were located in an area around Slough. The main objective of these experiments was to derive information on how two or more spaced receivers, with separations of not more than about 25 km, can be used to improve the overall performance of a satellite link, particularly when rainfall causes severe attenuation at one of the stations in the network. The improvement obtained using the combined receiving system is evaluated with respect to the performances of the space-to-Earth links associated with individual Earth stations.

In 1970, it was envisaged that the first satellite transmissions to become available would be in the 11 GHz band from the Italian satellite SIRIO which was then planned for launch in 1972. Appleton Laboratory decided to participate in the SIRIO project and constructed the mainstation receiving system at Slough. This comprised a 3 m diameter tracking aerial and receivers for the 11.597 GHz carrier transmission and the side-band transmissions at  $11.597 \text{ GHz} \pm 265 \text{ MHz}$ . In addition, five substations with fixed 1 m diameter aeriels to receive only the SIRIO carrier transmissions were also constructed. Total power radiometers at 11.6 GHz to monitor sky-noise emission over a 6 MHz bandwidth were installed in the mainstation and substation receiving equipment to enable comparisons to be made between the direct measurements of attenuation using the satellite transmissions and the indirect measurements using the radiometers. The intention was to use the SIRIO signals to carry out a space diversity experiment. The substations were therefore located along a line containing the mainstation and covered a range of spacings between 0.4 and 24 km.

However, changes to the mainstation equipment and to the experimental programme involving the substations were made between 1972 and August 1977 when SIRIO was launched. For example, the diversity experiment originally intended as a satellite transmission experiment was instead carried out using the radiometer channels, and this experiment was completed before the satellite was launched. Also, the front-end of the mainstation equipment was temporarily modified to enable the co-polar and cross-polar signals from ATS-6 at 30 GHz to be received. Two of the substations were also modified to receive the ATS-6 co-polar signals, and 30 GHz radiometer channels were added. These radiometers were operated as a diversity pair both during and after the period of ATS-6 transmissions.

When the mainstation was subsequently reconverted back for use with frequencies near 12 GHz, provision was made for it to be capable of receiving the circularly-polarised signals from either the SIRIO satellite or the Orbital Test Satellite (OTS), and a further channel was added so that measurements of the cross-polar signals could be made. Only two of the six stations, namely the mainstation and the nearest substation, have actually been used to receive signals from SIRIO. The substation has monitored the carrier transmissions since launch. The mainstation received the carrier and side-band signals until June 1978 when it became dedicated for use with OTS.

## 2. TYPES OF MEASUREMENT MADE UP TO 1976 AND THEIR PERIODS OF OBSERVATION

Table 1 summarises the single-site and diversity measurements made prior to December 1976. The multi-site systems identify the diversity experiments. The sun-trackers were equipped with antennas giving half-power beam-widths of about  $1^{\circ}$ , approximately twice the angular diameter of the sun.

The procedures and basic equations from which values for the atmospheric attenuation can be derived in conjunction with radiometric measurements of emissions from the sun and atmosphere are outlined as follows. Let the equivalent black body temperature of the sun at the wavelength of interest be  $T_s$ . For the same wavelength, let the instantaneous value of the fractional absorption of the radiation along the path be  $a$ , and let the average, or effective, kinetic temperature of the atmosphere along the path be  $T_{at}$ . For microwave frequencies, the basic equation relating these quantities (see for example DAVIES, P. G., 1974) is

$$T_{ANT} = T_{sun} = (1 - a) T_s + a T_{at} \quad (1)$$

where  $T_{ANT}$  is the antenna temperature of the received signal for an ideal, very narrow beam, antenna. For directions away from the sun

$$T_{ANT} = T_{sky} = a T_{at} \quad (2)$$

Hence, the latter term in equation (1) is the sky emission term which increases in presence of atmospheric absorption. The first term represents the true attenuation of the solar signal. In a given bandwidth  $B$ , the power received is  $k T_{ANT} B$ , where  $k$  is Boltzmann's constant. If no absorption occurred along the path, the corresponding antenna temperature would be  $T_s$ . This must be compared with the value  $(1 - a) T_s$  to derive the attenuation along the path, and leads to the result

$$\text{Attenuation (dB)} = 10 \log_{10} \frac{k T_s B}{k (1 - a) T_s B} = 10 \log_{10} \frac{1}{(1 - a)} \quad (3)$$

In practice, two methods can be used to derive the attenuation :

- (1) the direct method, which compares the attenuated solar signal with the unattenuated signal as



Table 1. Summary of Single-Site and Diversity Measurements up to December 1976

Type of Measurement	Frequency (GHz)	Period of Observation	Reference for Further Details
Sun-Tracker Radiometer	12 (Post Office)	May 1969 to April 1972	Gilroy and Smith (1973)
"	19	June 1968 to September 1972	Davies (1973b, 1975)
"	37 (Three systems with spacings of 10.3, 12.7 and 18 km)	May 1970 to October 1974	Davies (1975)
"	71	March to August 1973	Davies (1975)
Fixed-Pointing Radiometer (29.5° Elevation)	11.6 (Six systems with spacings of between 0.4 and 23.6 km)	June 1973 to June 1975 6682h at Mainstation	Allnutt (1976)
Fixed-Pointing Radiometer (6° Elevation)	11.6 (Two systems with a spacing of 7.1 km)	April 1976 to December 1976 Total observation time 6422h	Allnutt (1977)
Fixed-Pointing Radiometer (90° Elevation)	110	December 1970 to May 1971 November 1971 to July 1972 Total observation Time 5700h	Gibbins (1974)
Reception of ATS-6 Satellite Transmissions (22° Elevation)	30 (Three systems with spacings of 2, 10.3 and 12.3 km)	July 1975 to August 1976 Total transmission time 1743h	Allnutt and Shutie (1977)
Fixed-Pointing Radiometer (22° Elevation)	30 (Two systems with a spacing of 12.3 km)	July 1975 to August 1976 Observation time 9528h at each site [NB This experiment has continued after the period of ATS-6 observations - See Figure 5d]	Allnutt and Shutie (1977)

described by DAVIES, P. G., 1971b. Since the clear atmosphere always imposes some residual attenuation, most measurements of this kind refer to the values of attenuation in excess of the clear air value.

- (ii) the indirect method, which involves only the measurement of the sky signal  $T_{sky} = a T_{at}$  from which the fractional absorption,  $a$ , can be computed if an appropriate value for  $T_{at}$  is chosen, e.g. 275 K. Thus, equation (3) becomes

$$\text{Attenuation (dB)} = 10 \log_{10} \frac{T_{at}}{T_{at} - T_{sky}}$$

If the value used for  $T_{sky}$  is the increase in the sky emission temperature with respect to the clear sky value, the above equation also relates to the excess attenuation.

Several types of radiometer have been employed during the course of the various investigations at the Appleton Laboratory. Dicke-type radiometers were used both for the sun-trackers and for the measurements at 110 GHz whereas total power radiometers were used at 11.6 and 30 GHz. The dynamic range of the measurement of attenuation derived from sky emission data is limited to about 10 dB. The sun-tracker measurements at 19 GHz were also limited to a range of about 10 dB since only a single-feed system was available, and corrections for the background sky emission had to be applied (DAVIES, P. G., 1971b). Some of the initial measurements at 37 GHz were obtained with a 'nodding' radiometer to provide consecutive measurements of the sun and sky signals (DAVIES, P. G., 1973a). However, most of the measurements at 37 GHz and all measurements at 71 GHz were obtained with fast response dual-feed, beam-switching radiometers (DAVIES, P. G., 1976) which enabled the difference between the sun and sky signals to be recorded directly. The nodding and beam-switching techniques resulted in an improved dynamic range of about 15 dB for the attenuation measurement. In principle, if a narrow beam ( $< 0.5^\circ$ ) antenna is used, the dynamic range of the measurement of attenuation obtained with sun-trackers can be much larger than that obtained from sky emission measurements. This stems from the fact that the sun radiates at a much higher temperature ( $\sim 10000$  K at 12 GHz) than the maximum radiation temperature ( $\sim 300$  K) of the atmosphere.

An advantage of the sky emission technique is that it allows the derivation of continuous data at fixed angles of elevation, but it becomes unreliable for attenuations greater than 8 to 10 dB, and at frequencies higher than 15 GHz, is subject to errors due to scattering (ZAVODY, A. M., 1974). On occasions the

assumption of an effective kinetic temperature of the atmosphere near 275 K can lead to large errors (CROOM, D. L., DAVIES, P. G. and POWELL, R. J., 1972). Sun-tracker data suffer from the disadvantage of not being continuous, and the analysis is complicated by the changing angle of elevation. However, the method does afford a direct measurement over a larger dynamic range and takes into account the effects of both absorption and scattering. Satellite techniques are potentially capable of providing precise data relating to both co-polar and cross-polar behaviour, but involve large expense and provide transmissions at a limited number of frequencies. However, this method has gained precedence in recent years as more satellite transmissions have become available, which are less affected by satellite scheduling arrangements.

### 3. SUMMARY OF RESULTS OBTAINED IN THE PERIOD 1968 TO 1976

#### 3.1 Single-Site and Diversity Measurements using Sun-Tracker Radiometers

Observations on emissions from the sun at centimetre and millimetre wavelengths began at the Appleton Laboratory in 1965. The prime objective at that time was to monitor the solar noise signals continuously during the daytime in order to study their variability and frequency dependence, and to complement and extend the measurements of solar emissions being made by other observatories at different longitudes. In particular, interest was centred on the solar radio burst phenomena which normally occur infrequently at wavelengths less than 3 cm (10 GHz), although the number of such events increases at times of solar maximum. However, accurate measurements of the solar flux variations were possible only during periods of clear weather, since, as the wavelength decreases, the signals become increasingly attenuated by atmospheric hydrometeors, particularly rain.

In 1968, when it became apparent that future communications systems would initially need to make more use of the s.h.f. (3 to 30 GHz) band, and, later on, to use the e.h.f. (30 to 300 GHz) band, it was decided to analyse the recorded solar radio signals to extract data on atmospheric absorption. To obtain the best results, it was necessary to take into account the variations of the solar flux and the changing position of the sun in the sky. A detailed analysis of the solar emission effects relevant to studies of tropospheric attenuation was carried out by CROOM, D. L., (1973). It concluded that, provided care is taken in the interpretation of the data, the sun provides a useful, and considerably cheaper, alternative to satellite-borne sources, and is capable of providing much of the information that can be obtained from the latter, with the exception of phase data. Also measurements can be made over a broad frequency range.

##### 3.1.1 Single-Site Measurements

As indicated in Table 1, observations by the Appleton Laboratory at the frequencies 19, 37 and 71 GHz were obtained at the Slough site within the period 1968 to 1975. In addition, the Post Office operated a 12 GHz radiometer at the same site (GILROY, D. L. and SMITH, B. B., 1973). Details of the measurements at 19 and 37 GHz covering different periods of observation have been described by DAVIES, P. G. and LANE, J. A. (1970), DAVIES, P. G. (1971a, 1971b, 1973a, 1973b, 1973c). A summary of these measurements at 19 and 37 GHz together with a presentation of new data at 71 GHz is also available (DAVIES, P. G., 1975). Results have been published in the form of :-

- (i) Cumulative distributions which depict the percentages of observation time for which the attenuation exceeds given values. These were computed, and updated, monthly for data obtained within  $10^\circ$  ranges of elevation and also for data obtained at all possible angles of elevation, i.e. 0 to  $62^\circ$  for sun-trackers at Slough. The annual cumulative distributions illustrate the variability of the weather from year-to-year, and particularly reflect the variability in the very high rainfall rates which occur for very small percentages ( $\sim 0.001$  to 0.01) of the time.
- (ii) Histograms showing the number against duration of individual events which exceeded given values of attenuation.
- (iii) Comparisons of simultaneous measurements at two or more frequencies.

Figure 1 gives examples of some of the results from sun-tracker radiometers. Figure 1a shows that, at 19 GHz, the percentage of time for which the attenuation exceeds 10 dB in the worst month is almost an order of magnitude larger than the corresponding mean value for the four-year period. Also these results demonstrate that there is considerable variability from year-to-year such that the extreme distributions give values of attenuation which differ by a factor of 2. At 37 GHz, a factor of 1.3 was derived from three annual distributions.

Figure 1b depicts attenuation statistics at 37 GHz for  $10^\circ$  ranges of elevation angle. The distributions are well separated for the three ranges up to  $35^\circ$ , but overlap to some extent at higher elevations. The angular dependence of data at 71 GHz for  $10^\circ$  ranges is similar in behaviour to that at 37 GHz. However, this separation of curves, for angles up to  $35^\circ$  contrasts with similar measurements at 19 GHz, over a 52 month period, which showed no appreciable variation with angle. The explanation of this probably lies in the fact that moderate, stratified rainfall produces significant attenuation at frequencies of 37 GHz and above, particularly at the lower angles of elevation, but produces little attenuation at 19 GHz. When large attenuation occurs at 19 GHz, it is produced by heavy rainfall, often associated with a localised, cellular structure.

Figure 1c contains histograms of the number against duration of individual events at 37 and 71 GHz for fade levels of 10 and 15 dB. Individual 10 dB events can persist for over an hour at 37 GHz and for over three hours at 71 GHz. Histograms of fades at 19 GHz over a four-year period are also available (DAVIES, P. G., 1973b, 1973c). For those data, no 10 dB fades lasting more than 8 minutes were recorded.

Figure 1d summarises the attenuation statistics derived from sun-tracker radiometers at Slough. It includes the result obtained from the 12 GHz radiometer owned by the British Post Office. The distributions refer to measurements made at all possible angles of elevation and to a mean annual observing angle of about  $2^\circ$  (refer to Table 1 in the paper by DAVIES, P. G., 1973a). For system applications, this figure clearly demonstrates the importance of attenuation as a function of frequency. For example, for a

fade margin of 6 dB, this level of attenuation was exceeded for about 0.65 per cent of the time (57 hours per year) at 37 GHz and for 0.001 per cent of the time (6 minutes per year) at 12 GHz, i.e. for times which differ by over two orders of magnitude. [NB. More recent measurements at 11.8 GHz using the transmissions from OTS during 1979, when two very severe rainfall events occurred, gave the result that the attenuation exceeded 10 dB for a total of about 15 minutes - see Section 4.3.]

### 3.1.2 Diversity Measurements

The initial diversity measurements at 37 GHz involved sun-tracker radiometers at two sites (DAVIES, P. G. and CROOM, D. L., 1974). Later, this was extended into a three-site network (DAVIES, P. G., 1976). All measurements were carried out between September 1972 and October 1974. Figure 2 summarises the main results. The diversity statistics for site pairs were derived by taking the lower of the two instantaneous values of attenuation at each site and then processing the data in the same way as for single site data. Figure 2 illustrates the general layout of the sites, diversity statistics for site pairs, histograms of the individual fades which produced these statistics, and the diversity advantage factor for each site pair for the three-site network. The diversity advantage factor is defined as the ratio of the time for which the attenuation exceeds a particular value at the single site to the time for which the same value is exceeded simultaneously at both sites. Another parameter which is sometimes used is the diversity gain, defined, for a given percentage of time, as the difference between the diversity signal and the median of the single-site signals (ALLNUTT, J. E., 1978). Values for the diversity can also be derived from the cumulative distributions of Figure 2, which shows, for example, that the diversity gain for the Hurley and Hurley-Winkfield data is large, whereas the diversity advantage is small.

The most important result to emerge from these measurements was that the site separation is not the only factor which determines the diversity improvement. For a two-site system operating at frequencies of 37 GHz, or higher, the diversity advantage factor can depend critically upon the orientation of the sites with respect to the prevailing wind direction. Significant attenuation is produced by widespread, moderate rainfall. During the sun-tracker measurements, many frontal-type storms approached the network from the South-West and produced almost simultaneous fading at Hurley and Winkfield, although these were separated by almost 13 km. For 15 dB fades, the Hurley-Winkfield pair produced a diversity advantage factor of only 2, compared with a factor of 8.5 for the Slough-Hurley pair.

As a bi-product of the diversity measurements at 37 GHz together with the simultaneous single-site measurements at 19 and 37 GHz and at 37 and 71 GHz, a method was developed to predict the diversity characteristics at 19 and 71 GHz (DAVIES, P. G., 1976).

### 3.2 Single-site and Diversity Measurements using Fixed Radiometers

Various sets of data derived from radiometers monitoring sky emission at fixed angles of elevation have also been obtained. Single-site observations were made at 110 GHz, while, at 12 GHz, single-site and diversity measurements have been made at elevation angles near 30° and 6°.

#### 3.2.1 Single-site Measurements at 110 GHz

Results have been reported by GIBBINS, C. J., (1974), and refer to observations of the sky emission from the direction of the zenith. These measurements yielded values of attenuation which exceeded 6 dB and 13 dB for 5 and 0.5 per cent of the time, respectively. The effects of scattering, computed in accordance with the theoretical predictions of ZAVODY, A. M., (1974), were also applied as a correction to the measured data.

#### 3.2.2 Single-site and Diversity Measurements near 12 GHz

These measurements have been described by ALLNUTT, J. E. (1976), and the main results are contained in Figure 3. The site plan also indicates the three sites involved in the diversity measurements associated with the ATS-6 satellite (see Section 3.3). These three sites are identified by triangles at the main-station (M), Langley (L) and Winkfield (W). The mainstation site is common to the diversity measurements at 11.6 and 30 GHz. For the single-site measurements near 30° elevation shown in Figure 3b, the six radiometers were pointed towards the proposed geostationary position of the SIRIO satellite at longitude 15°W.

At the 10 dB level, no site produced cumulative fading which persisted for more than 0.001 per cent of the observation time, equivalent to about 6 minutes per year. With regard to the diversity operation, depicted in Figure 3c, it was concluded that site spacings of about 7 km would be optimum for a working system. However, it must be pointed out that the characteristics of diversity operation near 12 GHz will differ very considerably from those at higher frequencies, e.g. at 30 GHz and above. At 12 GHz, significant attenuation will be caused by only the highest and least frequent rainfall rates, normally associated with very localised cells. This contrasts with the situation at higher frequencies where significant attenuation occurs in the presence of widespread, moderate rainfall.

Figure 3d gives a comparison between the diversity characteristics at the elevation angle of 29.5°, as already described, with other similar measurements made at the low elevation angle of 6°. These latter measurements have been reported by ALLNUTT, J. E., (1977). Use was made of the 11.6 GHz radiometers at sites 2 and 4 of Figure 3a when the higher angle measurements had been completed. The results from the low angle measurements agree fairly well with those extrapolated from the earlier 29.5° results. However, the limit to the diversity gain achievable at low angles may be determined by the attenuation produced by widespread cloud.

### 3.3 Single-site and Diversity Measurements at 30 GHz using the ATS-6 Satellite Transmissions and Ground-Based Radiometers

The Appleton Laboratory participated in experiments associated with the ATS-6 satellite during the period July 1975 to August 1976, while the satellite was geostationary at the longitude 35°. As indicated in

Figure 3a, receiving stations were established at Winkfield (W), the mainstation (M) at Slough and at Langley (L). The mainstation was equipped with a 3m diameter aerial and with a second receiving channel to monitor the cross-polar signal; those measurements are reported in Section 3.4. The substations at Winkfield and Langley were equipped with 1 m diameter aerials and with receivers which also included a radiometer channel. These two radiometers were operated throughout the period when the satellite transmissions were available and were also kept in operation subsequently in order to extend the data base. Data collected after the period of the ATS-6 transmissions are contained in Figure 5d. The range of variation between the single-site curves is similar to that measured during the sun-tracker diversity experiment and illustrated in Figure 2b.

The elevation angles of the paths to the satellite were near  $22^\circ$ , and the three sites gave ground spacings of 2, 10.3 and 12.3 km. Transmissions from the 30 GHz satellite beacon were available only on a scheduled basis and provided an average of between four and five hours of observation per day. ALLNUTT, J. E. and SHUTIE, P. F. (1977) have published details of the results, some of which have been reproduced in Figures 4 and 5. An example of the way in which diversity operation can improve system performance is illustrated in Figure 4a. A storm approached from the SSW along the line containing the three stations which were adversely affected in turn.

For much of 1976, abnormally severe drought conditions existed in the UK and in many other parts of Europe, and little attenuation was recorded. However, during the latter part of 1975 several storms which produced long-lasting (> 30 min) 10 dB fades were recorded by the radiometers (reference Figure 5b). Unfortunately, these did not coincide with the periods when the satellite transmissions were available as can be seen by comparison of the data in Figures 4c and 5b.

Cumulative distributions relating to the satellite measurements, the radiometer measurements and to comparisons between the two for periods of common observation are shown in Figures 4b, 5a and 5c. The satellite transmission data cover a dynamic range of 30 dB, whereas measurements associated with radiometers are limited to a range of about 10 dB. Figure 5c also shows that the statistical data derived from the satellite and radiometer measurements agree fairly well, but ALLNUTT, J. E. and SHUTIE, P. F. have pointed out that analysis of individual events illustrates that the instantaneous measurements do not always agree.

With regard to use of the data for systems applications, Figure 4d presents the diversity gain characteristics for the site pairs. ALLNUTT, J. E. and SHUTIE, P. F. used diversity gain in preference to diversity advantage since the former is considered to be less sensitive to year-to-year variations in statistics and therefore allows a valid comparison to be made between sets of results obtained over different observation periods. The diversity gains are similar for site spacings of 10.3 and 12.3 km, but the diversity gain is only 2 dB lower for the site spacing of 2 km. The differences between the single-site cumulative distributions in Figure 4b indicate that micro-climate effects also occur. A judicious choice of sites in a particular region, rather than use of widely separated sites, can produce a significant improvement in diversity performance.

### 3.4 Depolarisation Measurements using the ATS-6 Satellite Transmissions

Details of these measurements have been published by SHUTIE, P. F., MACKENZIE, E. C. and ALLNUTT, J. E. (1977a, 1977b, 1978), SHUTIE, P. F., ALLNUTT, J. E. and MACKENZIE, E. C. (1977) and by MACKENZIE, E. C. and ALLNUTT, J. E. (1977). The mainstation at Slough received the linearly-polarised co-polar and cross-polar signals at 30 GHz from the ATS-6 satellite during those periods between 1 July 1975 and 2 August 1976 when transmissions were available. In addition, the relative phase between the co-polar and cross-polar signals was recorded and a 9.4 GHz fixed-pointing radar was operated along the path towards ATS-6.

Measurements of the cross-polar discrimination or XPD, defined as the ratio in dB of the wanted co-polar signal to the unwanted cross-polar signal are relevant to systems applications in which signals at the same frequency are simultaneously transmitted with orthogonal polarisations. This is a frequency re-use technique which effectively doubles the channel capacity. Measurements are required to quantify the cross-polar interference caused by the atmosphere, and particularly by rain.

Figure 6 summarises some of the results. Figure 6a refers to a rain event which caused an attenuation of the co-polar signal and an enhancement of the cross-polar signal (or a reduction in the XPD). The relative phase remained essentially constant throughout the event. Figure 6b is an example of a new effect which was observed during the ATS-6 experiments, whereby depolarisation occurs in the absence of any significant co-polar fade. The event shown occurred during the passage of a cumulo-nimbus cloud through the beam. This so-called 'anomalous' depolarisation was the subject of much study during the ATS-6 investigations. Its origin was attributed to the presence of ice clouds. Other interesting effects associated with the cross-polar signal have also been recorded. Figure 6c illustrates the changes in signal strength which occurred during the passage of several thunderstorms, and Figure 6d shows the corresponding radar returns. The first event (period A) is mainly an ice event since the radar gives returns at altitudes well above the freezing layer. The two other periods of attenuation (E and F) are caused by rain. However, during the period A, when intense electrical activity was present, abrupt changes in the XPD level, coincident with lightning strikes, were recorded. The cause of the rapid fluctuation in XPD is considered to be due to re-alignment of the ice particles through the build-up and collapse of electrostatic fields.

A review of ice-crystal depolarisation along satellite-to-Earth paths has been published by BOSTIAN, C. W. and ALLNUTT, J. E. (1979).

## 4. SUMMARY OF RECENT MEASUREMENTS USING TRANSMISSIONS FROM THE ORBITAL TEST SATELLITE AND THE SIRIO SATELLITE

The Italian satellite SIRIO was launched on 25 August 1977 and is geostationary at the longitude  $15^\circ\text{W}$ . The European Space Agency satellite OTS was launched on 11 May 1978 and is geostationary at  $10^\circ\text{E}$ . Apart from other transmissions which will not be considered here, both satellites provide circularly-polarised beacon signals in the 11 to 12 GHz band. These test transmissions are particularly relevant to the task of predicting the performances of the first European operational geostationary satellites, which are

currently being constructed, and which will employ uplink transmissions in the 14 GHz band and downlink transmissions near 12 GHz. For this reason, there has been extensive European interest and participation in the propagation measurements associated with both OTS and SIRIO. The Appleton Laboratory commenced observation on these transmissions shortly after the launch of each satellite.

#### 4.1 Description of the Receiving Systems and Observing Programme

##### 4.1.1 Receiving Equipment

The mainstation at the Appleton Laboratory is equipped with a 3 m diameter aerial attached to a mount which allows for limited steerability over a range of about  $\pm 6^\circ$  in both azimuth and elevation. Motors are programmed to provide the azimuth and elevation motions necessary to track the satellite. The mainstation can monitor the co-polar and cross-polar signals from either SIRIO (carrier and side bands) or OTS, whereas the substation situated at a distance of 0.35 km from the mainstation can monitor only the SIRIO carrier transmissions. The relative locations of these stations and the viewing directions to the satellites are illustrated in Figure 7a.

The basic elements of the mainstation receiving equipment are shown in Figure 7b which is the four-channel configuration appropriate to reception of the SIRIO carrier, side-band and cross-polar signals. Two phase-locked loops are incorporated in the receiver to enable the frequency excursions of the carrier and side-band signals to be accurately followed. These phase-locked loops use a common 10.7 MHz internal oscillator to provide a stable reference signal. When the signal is locked in the loop, the second stage intermediate frequency (i.f.) must be nearly equal to that of the reference signal. The small differences in frequency between the i.f. and the reference frequency are detected in the phase sensitive detector (P.S.D.) which produces an output error voltage signal proportional to the frequency difference. The error signal in turn drives a voltage controlled crystal oscillator (V.C.X.O.) which alters the local oscillator frequency such that when it is mixed with the incoming signal, the resultant i.f. will approach the reference frequency. In practice, the carrier signal must be acquired first, after which the subsidiary phase-locked loop for the side-bands can be brought into operation. Further details of this mainstation equipment, calibration procedures and also a description of the equipment at the substation have been given in a paper by DAVIES, P. G., MACKENZIE, E. C. and HARRIS, G. P., (1979).

For operation with OTS, only the carrier and cross-polar channels are used, and an additional mixing section, not shown in Figure 7b, is brought into operation to take account of the difference in frequency ( $\sim 200$  MHz) between the SIRIO and OTS carrier frequencies. Also, it may be noted that a general description of satellite receiving systems has been published by ALLNUTT, J. E. and GOODYER, J. E. (1977).

##### 4.1.2 Observation Programme

Table 2 depicts the observation programme and ancillary measurements associated with both SIRIO and OTS.

Table 2. SIRIO and OTS Observation Programmes

Nature of Observation	Station	Period of Observation	Types of Measurement
Circularly-polarised signals from SIRIO	Mainstation (3 m diameter aerial)	September 1977 to June 1978	Reception of carrier and side-band signals at 11.596 GHz and 11.596 GHz $\pm$ 265 MHz. Also reception of the cross-polar signal at the carrier frequency.
	Substation (1 m diameter aerial)	September 1977 onward	Reception of SIRIO carrier transmission.
Circularly-polarised signals from OTS-2	Mainstation	June 1978 onward	Reception of either the $B_0$ or $B_1$ transmissions at 11.786 GHz. Also, reception of the cross-polar signal.
Ancillary measurements	The ancillary equipment comprises raingauges, an 11.6 GHz radiometer associated with SIRIO observations, an 11.8 GHz radiometer associated with OTS observations and a 9.4 GHz radar directed along the same path as the mainstation aerial.		

#### 4.2 Results from Measurements of SIRIO Transmissions

The results from the first year of measurements have already been published (DAVIES, P. G., MACKENZIE, E. C. and HARRIS, G. P., 1979) and results from the second year of observation are in course of publication (DAVIES, P. G., MACKENZIE, E. C. and COURTHOLD, M. J., 1980). Following the failure at launch, in September 1977, of the OTS-1 spacecraft, both the mainstation and the substation were used to monitor the SIRIO transmissions until June 1978. In principle, the mainstation enabled several types of measurement to be carried out, i.e. the attenuation at the carrier and side-band frequencies (and hence also the differential attenuation across the band), the cross-polar discrimination, the relative phase between the co-polar and cross-polar signals, and, lastly, the phase distortion, defined as the difference between the phase shifts, induced by the atmosphere, across the two 265 MHz bands on each side of the carrier.

The intention was to investigate the variations in these parameters induced by the atmosphere in general, and by heavy rain in particular. Unfortunately, in common with many other places in Europe, the period

up to June 1978 was very dry and produced a maximum attenuation of only about 3.5 dB. No measurable changes in the phase distortion function were detected in this period. However, an interesting event was recorded on 21 October 1977, as shown in Figure 8a. The cross-polar signal remained above the clear-sky value of -19 dB with respect to the co-polar signal for about three hours. Figure 8a also shows the attenuations computed from the upper and lower side-band signals and from the substation receiver. The cross-polar discrimination (XPD) was reduced to a minimum of only 12 dB, but this was not coincident with the maximum of the co-polar attenuation. During this event, the 9.4 GHz fixed radar was being operated in a visual display mode, but the radar data were not logged. The display indicated strong returns at altitudes above the freezing layer. This event is thought to be the first example of ice/rain depolarisation recorded in the United Kingdom using satellite transmissions near 12 GHz. At the time of the event there was a slight rain drizzle, but the rain-rate was less than 6 mm/hr and insufficient to trigger the recording system of an on-site rain gauge.

Events producing attenuations in excess of 10 dB have been recorded at the substation since June 1978. One such event, recorded on 30 May 1979, is shown in Figure 8b which compares the attenuation measured directly from the satellite signal with that derived indirectly from the radiometer and with the rainfall rate recorded by a rain gauge at the substation. Analyses of such events have yielded histograms of the number against duration of events exceeding various levels of attenuation. Figure 9a shows histograms for all events exceeding 3 dB which were recorded at the substation and also identifies, in lighter shading, those events recorded during the first year of observation (1978). It is apparent that considerably more heavy rainfall occurred in 1979 than during 1978. Figure 9b contains the cumulative statistics for measurements made at the substation between September 1977 and November 1978. The left-hand scale refers only to the satellite data collected over an observing period of 8870 h. Also shown are sun-tracker data and earlier radiometric data obtained along the same path (reference the data of Figure 3b for site 3).

#### 4.3 Results from Measurements of OTS Transmissions

The data obtained during the period of the OTS transmissions have provided information on snow effects and on the effects of heavy rainfall. They are considered to be particularly relevant to the planning and operation of systems which will use the 11 and 12 GHz bands.

Most winters during the last decade have yielded little or no significant snowfalls in the Slough area of the UK. However, in common with many other parts of Europe, the winter of 1978/9 was particularly severe and several periods of prolonged snowfall occurred. The mainstation, monitoring OTS transmissions was operated without an aerial heater while the substation, monitoring SIRIO carrier transmissions, was operated with an aerial heating system. Measurements at the substation showed that snowfalls, both wet and dry, introduced only very small attenuations (< 0.5 dB) along the path to SIRIO. However, on several occasions the mainstation experienced large fading, in excess of 10 dB, and severe depolarisation for several hours. This was due to the build-up of snow in the aerial. An example of these effects, which would very seriously degrade the performance of an operational system, is illustrated in Figure 10a.

Histograms relating to individual fade events for rain-induced attenuation greater than 3 dB are shown in Figure 10b. It will be noted that in an observation period of 9760 hours, the attenuation exceeded 3 dB on sixteen occasions and 10 dB twice. The cumulative distribution associated with these measurements together with details concerning the largest event which was recorded are described in the next Section, in comparison with data from measurements of SIRIO transmissions. Analysis of data relating to the cross-polar measurements is incomplete and will be reported elsewhere. However, it may be stated that the periods of strong depolarisation caused by the atmosphere are coincident with periods of heavy rainfall.

#### 4.4 Comparison of Data derived from SIRIO and OTS Transmissions

From June 1978 it was possible to obtain simultaneous recordings of events along the paths to SIRIO and OTS. The receiving sites were spaced by 0.35 km as illustrated in Figure 7a which indicates that the elevations of these paths were both near 30° but separated in azimuth by about 30°. The largest event which has been observed is shown in Figure 11a. The mainstation receiver monitoring OTS transmissions lost lock when the attenuation exceeded about 25 dB. The attenuation in the direction of SIRIO was smaller than that along the OTS path and the relative intensities of the two peaks in the cell structure were reversed. The peak rainfall rate recorded near the mainstation exceeded 160 mm/hr which indicates that this was a rare type of event. Annual cumulative distributions of rainfall rate for the seven years 1970 to 1976 derived from measurements made on-site by the Appleton Laboratory using rain gauges with a 10s response time have been published by HARDEN, B. N., NORBURY, J. R. and WHITE, W. J. K., (1977). On only one occasion did the rainfall rate just reach 160 mm/hr for those data, and therefore confirms that the event of 15 June 1979 is indeed a very rare event, of a type which may well occur once in a period of five to ten years.

Cumulative distributions derived from OTS and SIRIO measurements are depicted in Figure 11b. Much less heavy rainfall occurred in 1978 than during 1979. The cumulative distribution from the SIRIO transmission measurements for the overall period therefore give values of attenuation lower than those for 1979. The cumulative distribution for the OTS data which include two large rainfall events represents the most severe conditions recorded at the Slough site in comparison with all other observations in the 11 GHz band. Even so, for an elevation angle of 30°, an operational system with a fade margin of 10 dB would not have been affected by signal attenuation for more than about 15 minutes during the year.

### 5. OVERALL EVALUATION OF THE VARIOUS DATA AND THEIR RELEVANCE TO FUTURE OPERATIONAL SATELLITE SYSTEMS

The measurements made at the Appleton Laboratory over the last ten years, to gather data relevant to future satellite systems applications, cover the frequency range 11.6 to 110 GHz. The radiometer measurements at 11.6, 19, 30, 37, 71 and 110 GHz provide data on slant path attenuation and sky noise emission. Diversity data based on radiometer measurements are available at 11.6, 30 and 37 GHz. Results from satellite beacon transmission tests are available at 11.6, 11.8 and 30 GHz; these provide information on slant path attenuation and cross-polar signal behaviour, including phase shift effects together with diversity data at 30 GHz. The papers which are considered to be of particular relevance to the systems designer are: DAVIES, P. G., (1975, 1976); ALLNUTT, J. E. and SHUTIE, P. F., (1977); SHUTIE, P. F., MACKENZIE, E. C. and

ALLNUTT, J. E., (1977a); ALLNUTT, J. E., (1978); DAVIES, P. G., MACKENZIE, E. C. and HARRIS, G. P., (1979) and DAVIES, P. G., MACKENZIE, E. C. and COURTHOLD, M. J., (1980).

The following general statements attempt to summarise the main conclusions :-

- (i) The sun-tracker data of Figure 1d demonstrate the relative importance of attenuation as a function of frequency; the strong frequency dependence can have a severe impact on systems design, particularly when up and down-links use widely separated frequencies, e.g. at 20 and 30 GHz.
- (ii) A large variability of the attenuation characteristics can occur from year-to-year, as indicated in Figure 1a. The variability is more apparent at the lower frequencies (< 20 GHz) where the distributions are dominated by a few individual very intense rainfall events which produce attenuations within the measuring range of the receiver.
- (iii) Over a range of about 10 dB, and within the envelope of the variability which can occur from year-to-year, sun-trackers and fixed radiometers produce very similar results particularly for frequencies below 20 GHz, e.g. compare curve A of Figure 1d with curve M of Figure 3b. The effects of scattering should be considered at higher frequencies, but fixed radiometers calibrated against a set of direct measurements involving a satellite can provide useful long-term information.
- (iv) With reference to the future operational use of the 11 and 12 GHz bands, the Slough area of the UK could provide a good site for an Earth station. The UK is subject to less severe weather conditions than those which can occur at other places in Europe (see, for example, CCIR Report 564). Hence the attenuation characteristics applicable to the UK will not be a prime factor in the design of a European communications satellite. However, the data are relevant to the task of providing efficient, cost-effective Earth stations in the UK.

For an elevation angle of  $30^{\circ}$ , the worst conditions encountered in several years of measurement indicate that a system with a fade margin of 10 dB would not have been affected for more than about 15 minutes per year. It is considered unlikely that these conditions would warrant diversity operation, but this may not be the case for systems operating at very low angles of elevation. The cross-polar measurements at 12 GHz have not been fully analysed. However, the large depolarisations were observed to be coincident with heavy rainfalls. It would seem therefore that these depolarisation events would not degrade the system reliability much beyond that already caused by signal attenuation. The effects of snow accumulating on the aerial and feed are most important and can far outweigh the effects of heavy rainfall. Means must be provided to prevent the build-up of wet snow.

- (v) The cumulative times of occurrence of attenuation for fade levels of between 6 and 10 dB, typical of system fade margins, are about two orders of magnitude greater at 37 GHz than at 12 GHz. Hence the use of site diversity, or other adaptive methods, may become necessary in many future systems applications. Individual 10 dB fades at 30 and 37 GHz can exist for over two hours as indicated in Figures 5b and 2c. Diversity systems can provide a substantial overall improvement as demonstrated in Figures 2a, 3d and 4d. Diversity operation is most effective for intense short duration fades. Very similar results on diversity gain were obtained from the sun-trackers and from the direct satellite measurements (ALLNUTT, J. E., 1978).
- (vi) The establishment of an optimum diversity network is not a simple matter since it does not depend solely upon site separation. The diversity characteristics are frequency dependent; for example, at 12 GHz significant attenuation will be caused only by the highest and least frequent rainfall rates associated with localised cells, whereas moderate, widespread rainfall causes significant attenuation at 30 GHz. Important factors which need to be taken into account are the prevailing wind direction with respect to the orientation of the sites (see Figure 2), and the effects of local topography and microclimate which produce different characteristics at sites not widely separated. These effects are evident in Figure 2b, 3b and 4b.
- (vii) Based on the single-site and diversity measurements in the multi-frequency sun-tracker experiments, a method was devised to extrapolate diversity data from one frequency to another.
- (viii) Satellite tests relevant to systems which will employ frequency re-use by means of signal transmissions at the same frequency but on orthogonal polarisations were carried out at 30 GHz; both rain and ice clouds can cause significant depolarisation which in turn could cause cross-talk.
- (ix) For the future, further propagation experiments involving satellite beacon transmissions at frequencies of 20 GHz and greater are required to provide a wider and longer-term acquisition of data across Europe. However, since the technology for satellite communications systems using the 20 and 30 GHz bands is developing rapidly, particularly in Japan, Italy and the U.S.A., it would seem important to carry out propagation tests alongside communications experiments associated with the transmissions of high-speed data and with various modulation techniques.

## 6. ACKNOWLEDGEMENTS

This review was carried out at the Appleton site of the Rutherford and Appleton Laboratories. The authors acknowledge the contributions of their many colleagues at Slough to the studies summarised in this paper.

## 7. REFERENCES

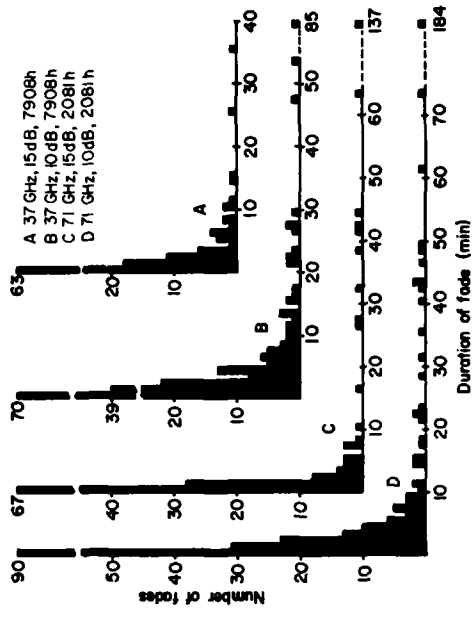
- ALLNUTT, J. E., 1976, "Slant-Path Attenuation and Space-Diversity Results using 11.6 GHz Radiometers", Proc. IEE., 123, pp. 1197-1200.
- ALLNUTT, J. E., 1977, "Variation of Attenuation and Space Diversity with Elevation Angle on 12 GHz Satellite-to-Ground Radio Paths", Electron. Lett., 13, pp. 346-7.

- ALLNUTT, J. E. and SHUTIE, P. F., 1977, "Slant-Path Attenuation and Space-Diversity Results at 30 GHz using Radiometer and Satellite-Beacon Receivers", Paper presented at the ESA Colloquium on ATS-6 Propagation Experiments in Europe, ESA SP-131 October 1977, pp. 69-77.
- ALLNUTT, J. E. and GOODYER, J. E., 1977, "Design of Receiving Stations for Satellite-to-Ground Propagation Research at Frequencies above 10 GHz", *Microwaves, Optics and Acoustics*, 1, pp. 157-164.
- ALLNUTT, J. E., 1978, "Nature of Space Diversity in Microwave Communications via Satellites : A Review", *Proc. IEE*, 125, pp. 369-376.
- BOSTIAN, C. W. and ALLNUTT, J. E., 1979, "Ice-crystal Depolarisation on Satellite-Earth Microwave Radio Paths", *Proc. IEE*, 126, pp. 951-960.
- CROOM, D. L., 1973, "Sun as a Broadband Source for Tropospheric Attenuation Measurements at Millimetre Wavelengths", *Proc. IEE*, 120, pp. 1200-1206.
- CROOM, D. L., DAVIES, P. G. and POWELL, R. J., 1972, "Anomalies in Attenuation and Emission by Rain at 37 GHz (8.1 mm)", *Electron. Lett.*, 8, pp. 189-191.
- DAVIES, P. G. and LANE, J. A., 1970, "Statistics of Tropospheric Attenuation at 19.0 GHz from Observations of Solar Noise", *Electron. Lett.*, 6, pp. 522-3.
- DAVIES, P. G., 1971a, "Comparison of Attenuation Statistics at 19 and 37 GHz for Sun-Earth Paths", *Electron. Lett.*, 7, pp. 51-2.
- DAVIES, P. G., 1971b, "Radiometer Studies of Atmospheric Attenuation of Solar Emission at 19 GHz", *Proc. IEE*, 118, pp. 737-741.
- DAVIES, P. G., 1973a, "Radiometer Measurements of Atmospheric Attenuation at 19 and 37 GHz along Sun-Earth Paths", *Proc. IEE*, 120, pp. 159-164.
- DAVIES, P. G., 1973b, "Slant Path Attenuation at Frequencies above 10 GHz", *IEE. Conf. Publ. No. 98 on Propagation of Radio Waves at Frequencies above 10 GHz*, pp. 141-149.
- DAVIES, P. G., 1973c, "Slant Path Attenuation at Frequencies above 10 GHz", Paper 19 in *AGARD Conf. Proc. No. 107 on Telecommunications Aspects on Frequencies between 10 and 100 GHz*. [NB. The title of the paper is the same as in the previous reference, but the content is different.]
- DAVIES, P. G. and CROOM, D. L., 1974, "Diversity Measurements of Attenuation at 37 GHz with Solar-Tracking Radiometers", *Electron. Lett.*, 10, pp. 482-483.
- DAVIES, P. G., 1974, "Land, Sea and Atmospheric Thermal Noise", Paper 5 in *AGARD Conf. Proc. No. 159 on Electromagnetic Noise Interference and Compatibility, Paris, October 1974*.
- DAVIES, P. G., 1975, "Attenuation by Cloud and Rain on Earth-Sun Paths at 12 to 71 GHz", *Electron. Lett.*, 11, pp. 547-548.
- DAVIES, P. G., 1976, "Diversity Measurements of Attenuation at 37 GHz with Sun-Tracking Radiometers in a 3-Site Network", *Proc. IEE*, 123, pp. 765-9.
- DAVIES, P. G., MACKENZIE, E. C. and HARRIS, G. P., 1979, "Measurements of SIRIO Transmissions near 11.6 GHz at Slough (UK)", *Alta Frequenza*, XLVIII, pp. 158-164, Special Issue (English).
- DAVIES, P. G., MACKENZIE, E. C. and COURTHOLD, M. J., 1980, "Propagation Measurements at the Appleton Laboratory (UK) Using SIRIO Carrier Transmissions Near 11.6 GHz", Paper submitted for publication in a special English issue of *Alta Frequenza*.
- GIBBINS, C. J., 1974, "Tropospheric Emission and Attenuation Statistics at 110 GHz", *Electron. Lett.*, 10, pp. 241-243.
- GILROY, D. L. and SMITH, B. B., 1973, "Atmospheric Attenuation using a 12 GHz Solar Radiometer", *IEE. Conf. Publ. No. 98 on Propagation of Radio Waves at Frequencies above 10 GHz*, pp. 150-154.
- HARDEN, B. N., NORBURY, J. R. and WHITE, W. J. K., 1977, "Measurements of Rainfall for Studies of Millimetric Radio Attenuation", *Microwaves, Optics and Acoustics*, 1, pp. 197-202.
- MACKENZIE, E. C. and ALLNUTT, J. E., 1977, "Effect of Squall-line Direction on Space-Diversity Improvement obtainable with mm-wave Satellite Radio-Communications Systems", *Electron. Lett.*, 13, pp. 571-573.
- SHUTIE, P. F., MACKENZIE, E. C. and ALLNUTT, J. E., 1977a, "Depolarisation Measurements at 30 GHz using Transmissions from ATS-6", Paper presented at the ESA Colloquium on ATS-6 Propagation Experiments in Europe. ESA SP-131, Oct. 1977, pp. 127-134.
- SHUTIE, P. F., MACKENZIE, E. C. and ALLNUTT, J. E., 1977b, "Satellite-ground Signal Depolarisation at mm-wavelengths through Thunderstorms", *Electron. Lett.*, 13, pp. 556-558.
- SHUTIE, P. F., MACKENZIE, E. C. and ALLNUTT, J. E., 1978, "Relative Phase Measurements between Co-polar and Induced Cross-polar Signals Produced by Ice Particles on a Satellite to Ground Link", *Electron. Lett.*, 14, pp. 105-107.

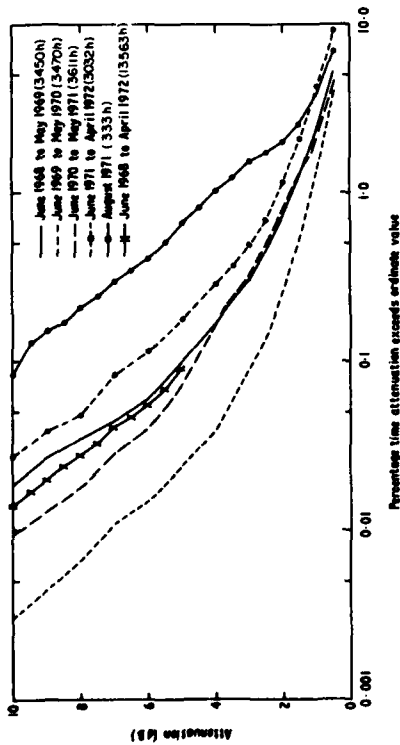


SHUTIE, P. F., ALLNUTT, J. E. and MACKENZIE, E. C., 1977, "Satellite-Earth Signal Depolarisation at 30 GHz in the Absence of Significant Fading", Electron. Lett., 13, pp. 1-2.

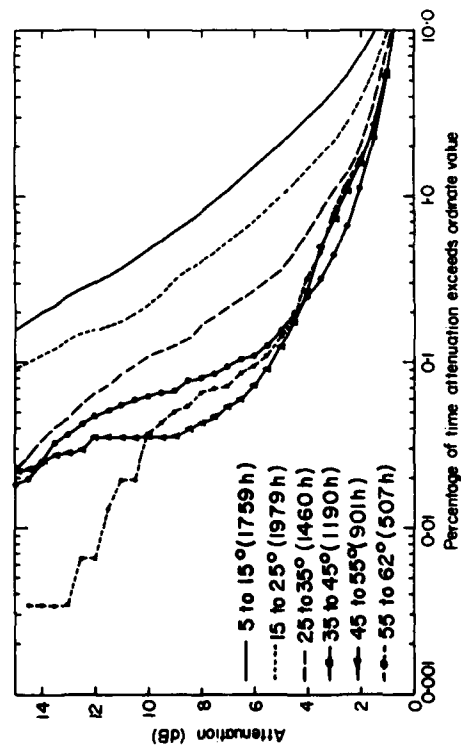
ZAVODY, A. M., 1974, "The Effect of Scattering on Radiometer Measurements at Millimetre Wavelengths", Proc. IEE., 121, pp. 257-263.



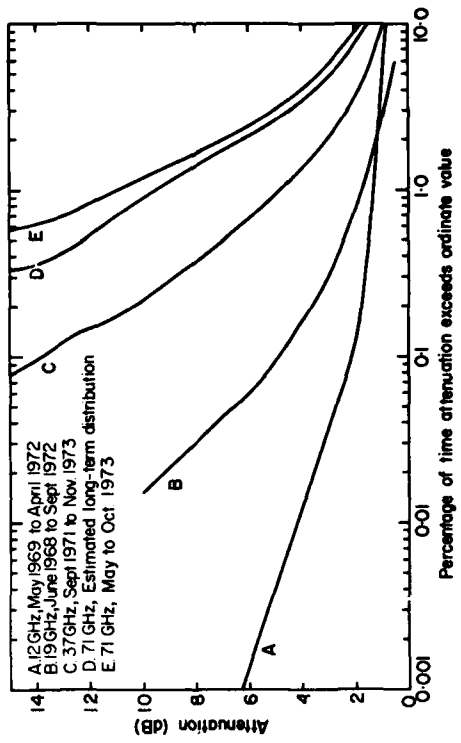
1 c Histograms Showing Number Against Duration of 10 and 15dB Fades at 37 and 71 GHz for the Periods Shown.



1 a Attenuation Statistics at 19 GHz for the Period June 1968 to April 1972

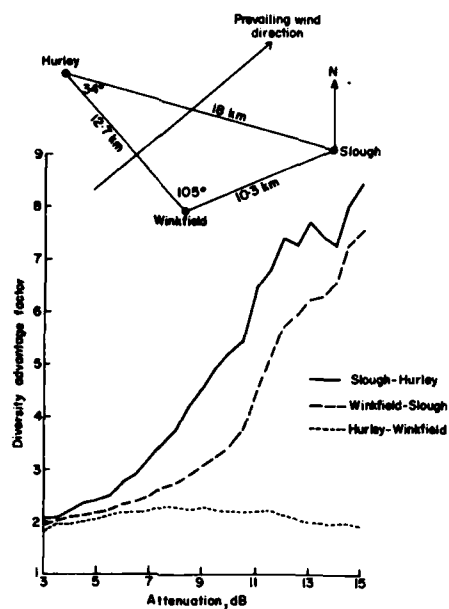


1 b Attenuation Statistics at 37 GHz for 10° Ranges of Elevation Angle (Sept 1971 to Nov 1973)

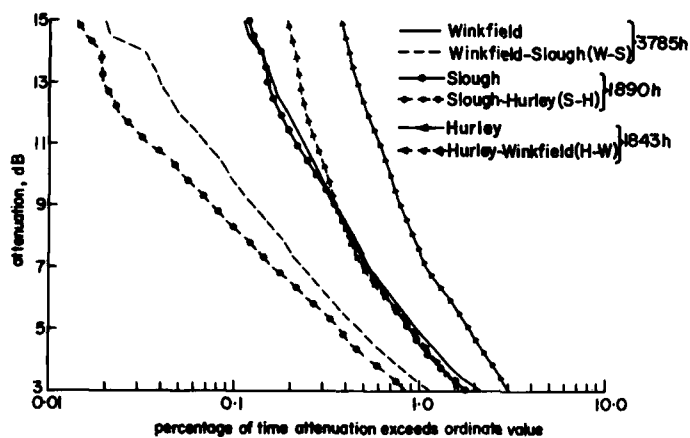


1 d Summary of Attenuation Statistics for Sun-Earth Paths (0 to 62° elevation)

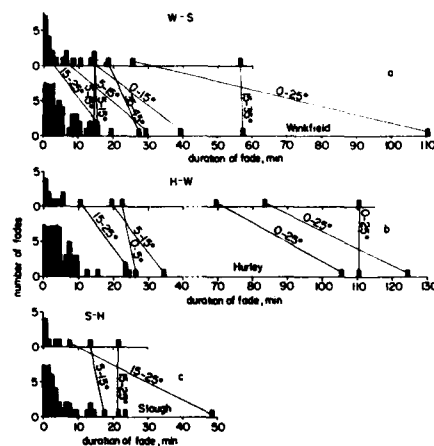
Fig. 1 Examples of single-site measurements obtained with sun-tracker radiometers at Slough



2a Layout of Sites and Diversity Advantage Factor for Site Pairs

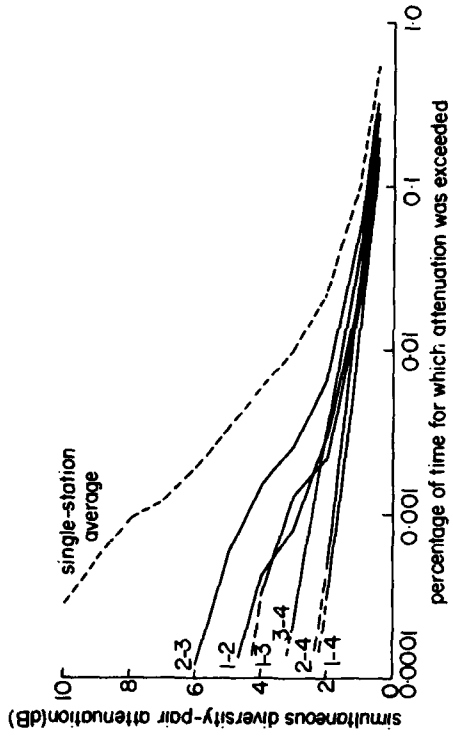


2b Comparison of 1-Site with 2-Site Diversity Statistics for Common Observations Obtained to 31 October 1974.

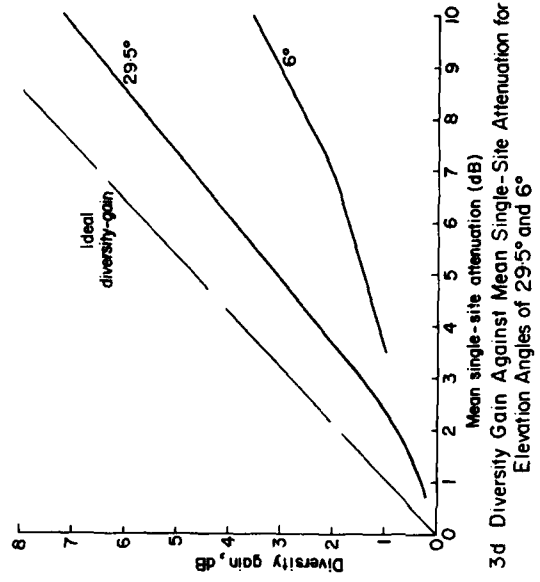


2c Numbers of 10dB Fades for Single-Site and Diversity Operation at 37 GHz.

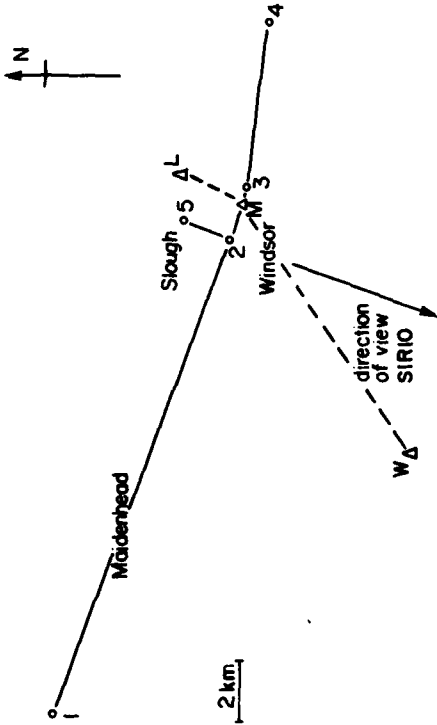
Fig.2 Diversity measurements at 37 GHz from sun-tracker radiometers in a three-site network



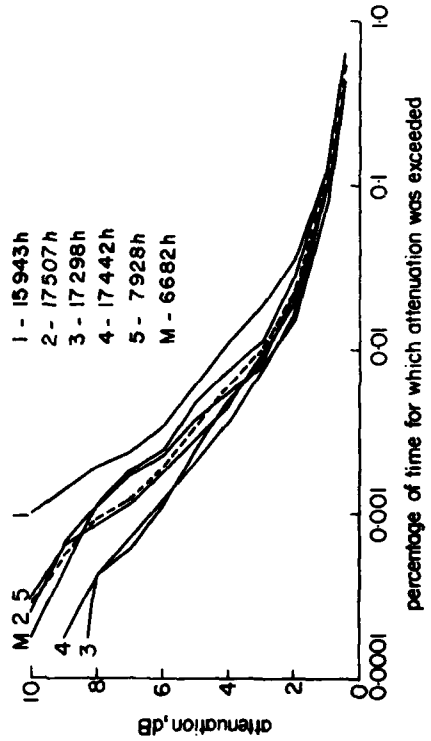
3 c Diversity-Pair Cumulative Attenuation



3 d Diversity Gain Against Mean Single-Site Attenuation for Elevation Angles of 29.5° and 6°

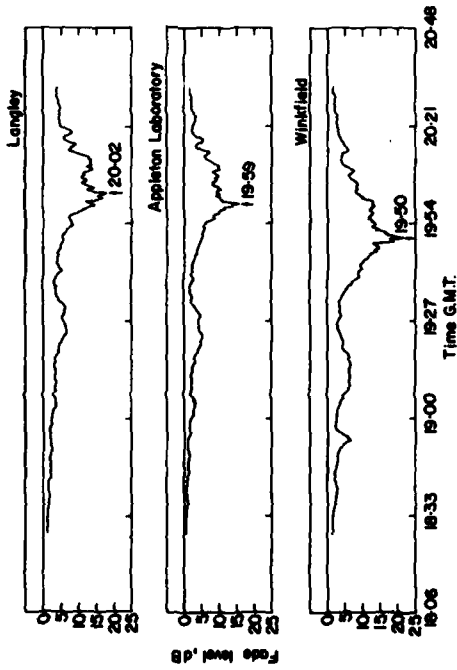


3 a Diversity Networks

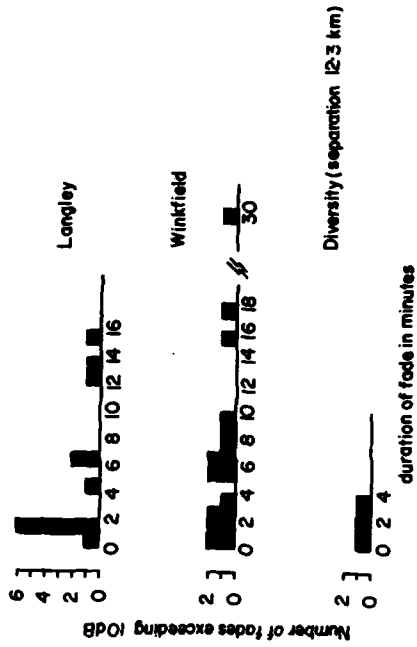


3 b Single Station Cumulative Attenuation Between June 73 - 75

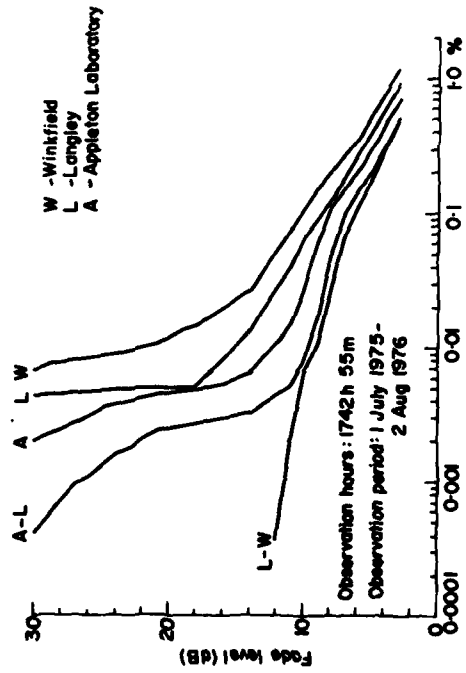
Fig.3 Single-site and diversity measurements obtained with fixed-pointing radiometers at 11.6 GHz



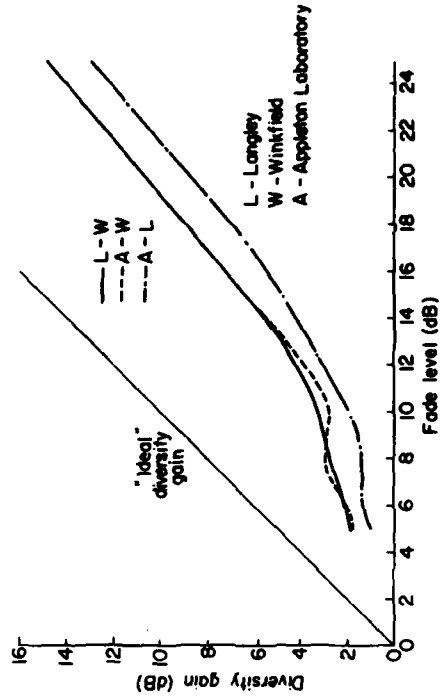
4 a Event on 15 August 1975 (Satellite beacon)



4 c Histogram of Satellite Signal Fades Above 10dB 1 July 1975-2 Aug 1976

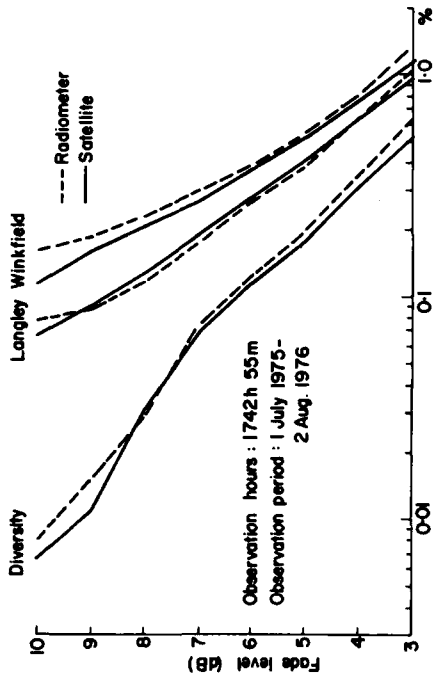


4 b Satellite Cumulative Attenuation (Single - Site and Diversity)

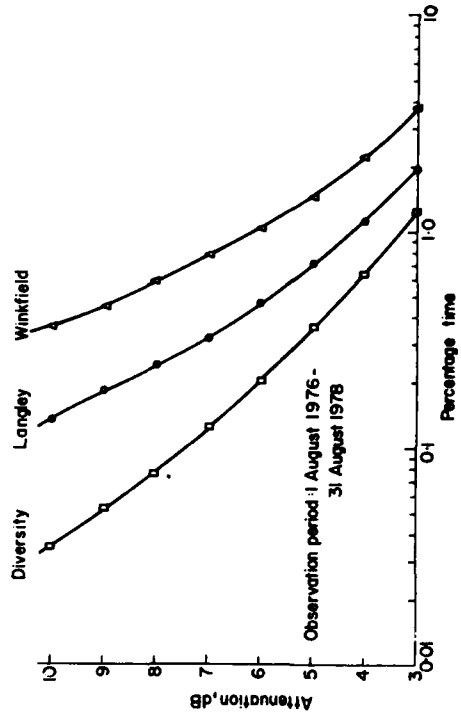


4 d Satellite Beacon Diversity Gain v Fade Level

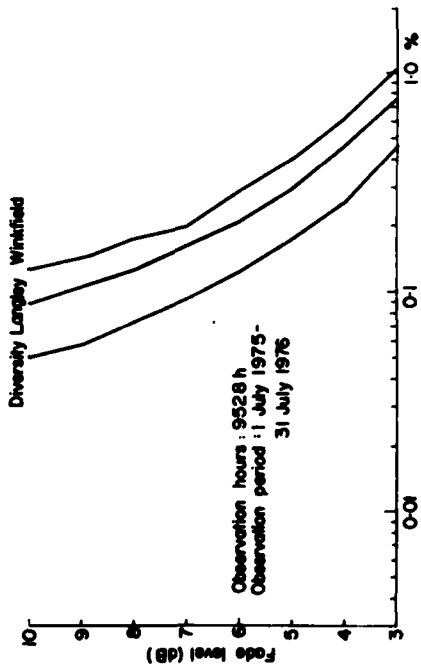
Fig.4 Single-site and diversity measurements using the ATS-6 transmissions at 30 GHz



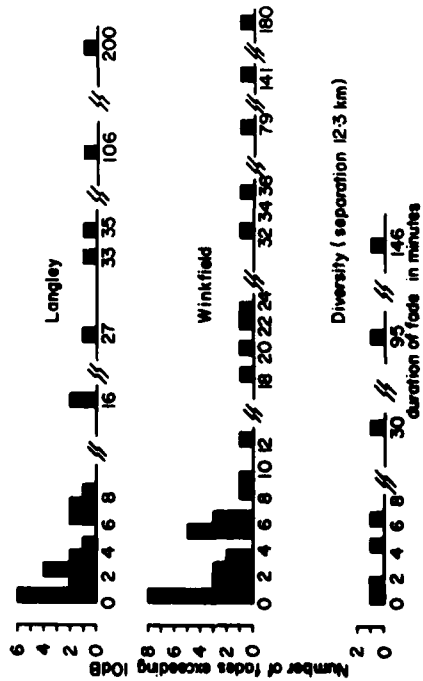
5c Cumulative Statistics of Simultaneous Observations



5d Radiometer Cumulative Attenuation (Single-Site and Diversity)

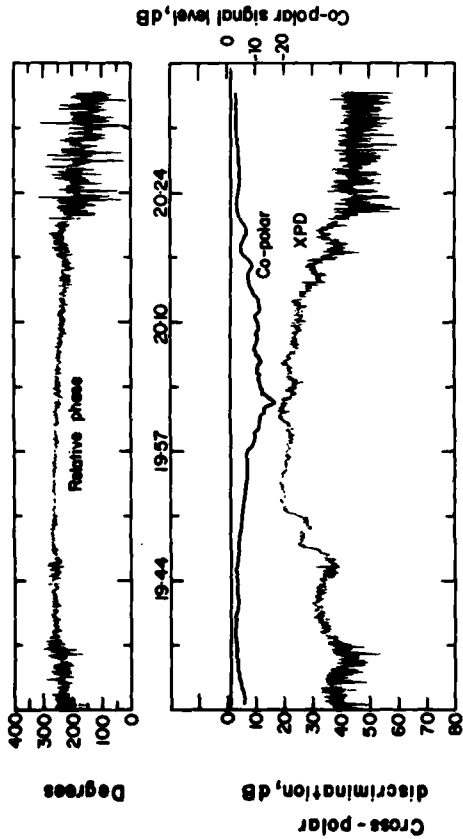


5a Radiometer Cumulative Attenuation (Single-Site and Diversity)

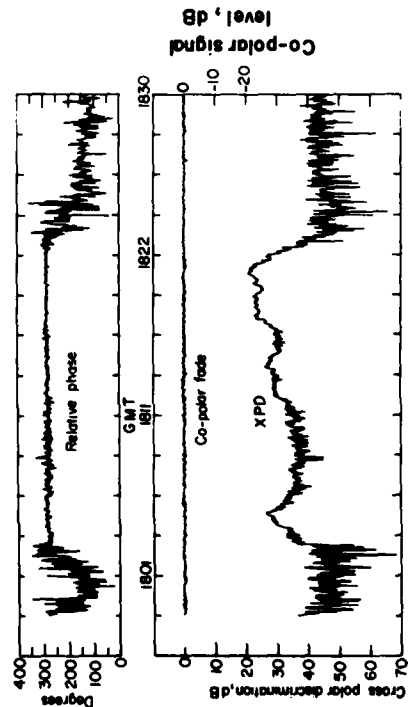


5b Histogram of Radiometer Fades Above 10dB 1 July 1975-2 Aug 1976

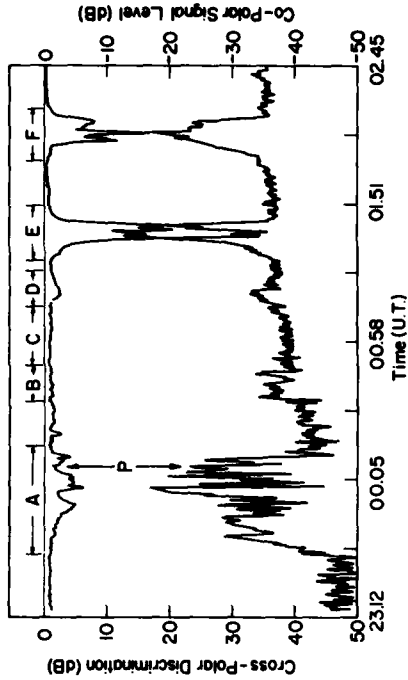
Fig.5 Radiometer measurements of diversity; at 30 GHz and comparison with the satellite transmission data



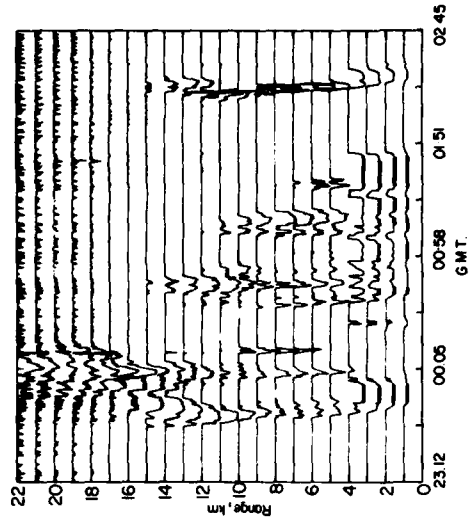
6a Variation of Co-Polar Signal Level, Cross Polar Discrimination and Relative Phase on 15 Aug. 1975



6b Variation of Co-Polar Signal Level, Cross Polar Discrimination and Relative Phase on 20 Aug 1975

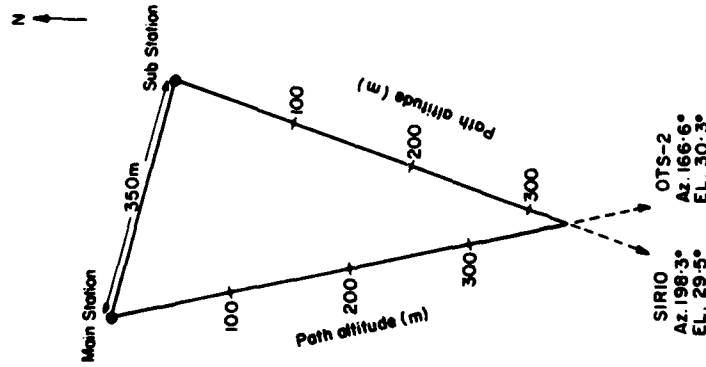


6c Variation of Co-Polar Signal Level (Upper Trace) and Cross-Polar Discrimination (Lower Trace) on 15/16 July 1976

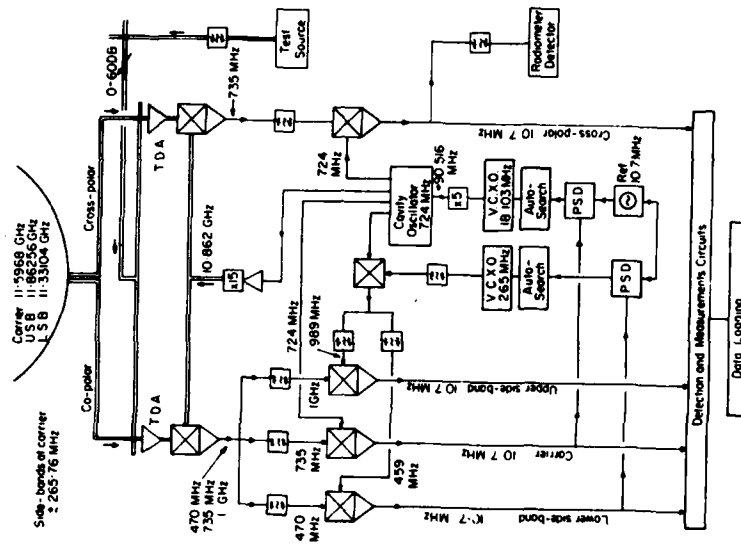


6d Range Radar Output for 15/16 July 1976

Fig. 6 Examples of depolarisation effects at 30 GHz and associated radar data



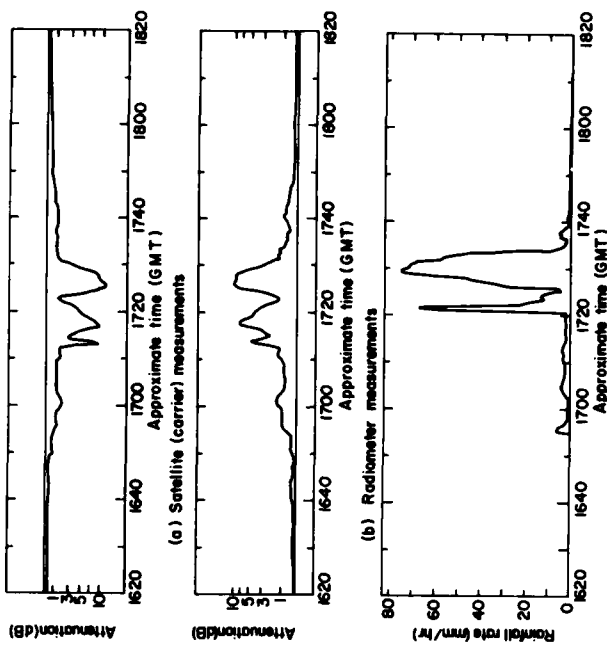
7a Site Locations of the Main Station and Sub Station, Observing Azimuths and Altitudes Along the Paths to OTS and SIRIO



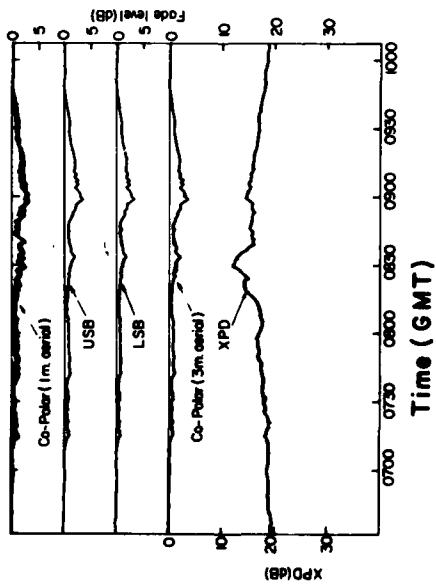
7b Schematic Layout of Mainstation Receiver for SIRIO Transmissions Near 12 GHz

Fig.7 Site locations and layout of mainstation receiver



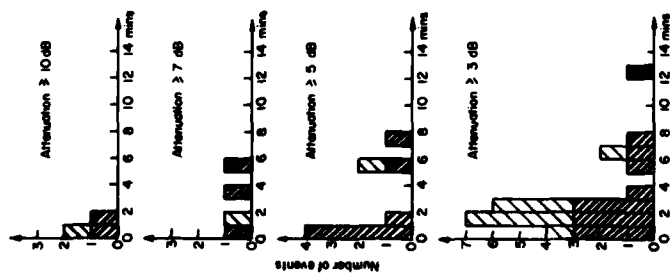


8b Comparison of the Direct and Indirect Measurements of Attenuation Together with Rainfall Rate Measurements for the Event of 30 May 1979

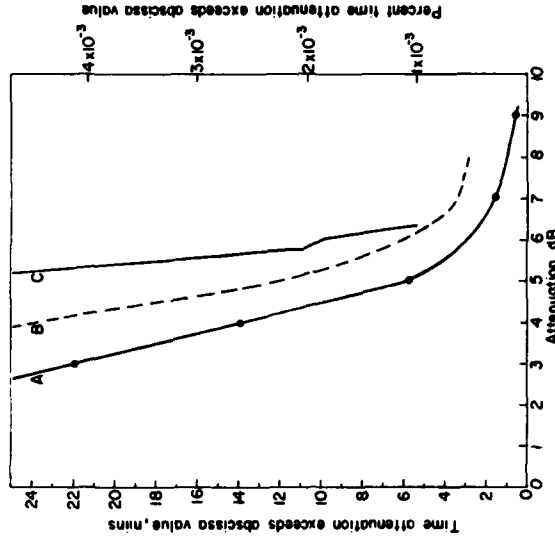


8a Co-Polar, XPD, USB and LSB Levels for 21 October 1977

Fig.8 Examples of measurements associated with transmissions from SIRIO



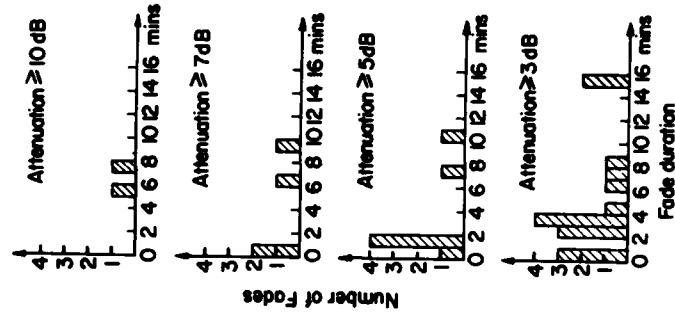
9a Histograms Showing the Number Against Duration of Individual Events Exceeding Various Levels of Attenuation Recorded (i) during 17835h of observation in the period September 1977 to January 1980 (all events), and (ii) during 8968h of observation in the period December 1978 to January 1980 (darkest shaded events)



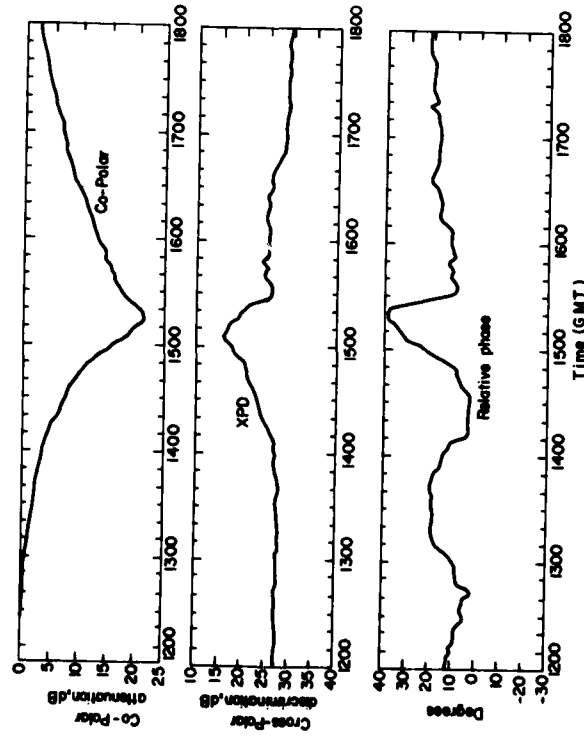
9b Comparison of Cumulative Statistics Derived from SIRIO Measurements with those from Previous Measurements at Slough near 12 GHz

- A SIRIO substation measurements: September 1977-November 1978 (8870h)
- B Substation radiometer measurements: June 1973-June 1975 (17258h)
- C Sun-tracker measurements: May 1969 - April 1972

Fig.9 Histograms and cumulative distributions relating mainly to measurements along the SIRIO path

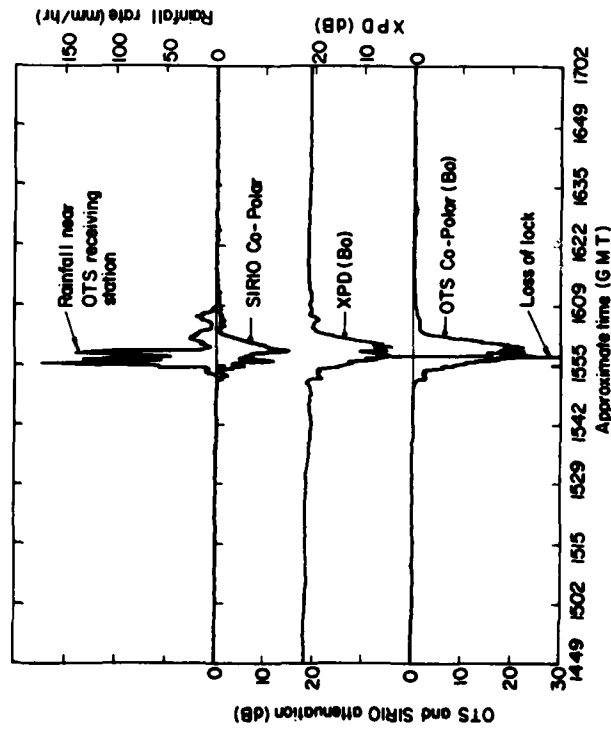


10b Histograms Showing the Number VS Duration of Individual Fades Exceeding Various Levels Attenuation for Events Recorded Over a Period of 9760 Hours

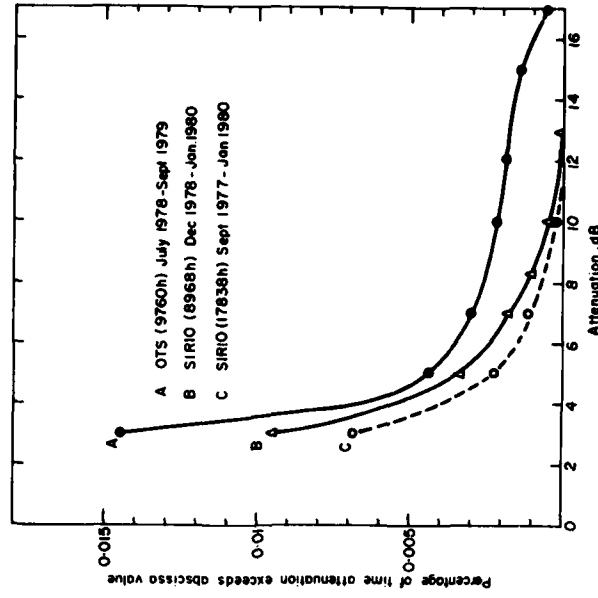


10a Co-Polar, Cross-Polar Discrimination and Relative Phase Variations During a Snow Event on 19 January 1979

Fig.10 A snow event and histograms of rain events from measurements of OTS transmissions



11a. Event Recorded on 15 June 1979



11b Cumulative Distributions Associated with OTS and SIRIO Transmissions

Fig.11 Comparisons of data derived from SIRIO and OTS transmissions

20 AND 30 GHZ SLANT-PATH PROPAGATION MEASUREMENTS  
AT MARTLESHAM HEATH, U.K.

J. Thirlwell and R.G. Howell,  
Post Office Research Centre,  
Martlesham Heath,  
Ipswich,  
IP5 7RE,  
England.

SUMMARY

This paper is a summary of some of the measurements carried out at the Post Office Research Centre during 1975/6 using the 20 and 30 GHz linearly polarised transmissions from the ATS-6 satellite. The studies included the measurement of attenuation ratio between the two frequencies and depolarisation measurements at 20 GHz. Calibration of 20 and 30 GHz radiometers directed along the slant-path was also carried out. The results of these measurements are compared with a theoretical model and the CCIR depolarisation equation. Also the statistical data for depolarisation and attenuation is presented. The need to present depolarisation/attenuation data in the joint probability of occurrence form is emphasised. This is because, due to non-attenuating ice depolarisation effects, there is no simple relationship between depolarisation and attenuation. The long-term radiometer derived attenuation data is also presented and comments on scintillation at elevation angles from 30° down to the horizon are made.

1. INTRODUCTION

This paper is mainly a summary of results which have been presented in detail elsewhere (HOWELL, R.G. et al., 1977a, 1977b; BELL, R.R. et al., 1977, 1979). However, the attenuation/depolarisation data is presented here in a new form, that of joint probability of occurrence, which should be of practical use to system designers. Also the theoretical depolarisation curves presented are based on new data provided by Essex University (UPTON, S.A.J., 1979) using a model (UZUNOGLU, N.K. et al., 1977) and method of calculating scattering parameters (EVANS, B.G. et al., 1977) developed there. The results are also compared with the CCIR (CCIR, 1978) depolarisation equation.

Frequency bands in the region of 20 and 30 GHz have been allocated for future satellite systems. A major factor in the design of such systems will be the slant-path attenuation and depolarisation caused by hydrometeors (HOGG, D.C. and CHU, T., 1975; WATSON, P.A., 1978; VANDER VORST, A.S., 1978). The latter being of importance because of limitations it may impose on systems using dual orthogonal polarisation to increase system capacity. The linearly polarised 20 and 30 GHz beacons transmitted by the ATS-6 satellite, when it was stationed at 35°E during 1975/6, enabled European experiments to carry out such propagation measurements. At the Post Office Research Centre, Martlesham Heath (1.29°E, 52.06°N), the elevation and azimuth bearings of the satellite were 22.7° and 139.8° respectively. The polarisation tilt angle of the beacon transmissions was 23.6° anticlockwise from vertical. While the satellite was geostationary at 35°E (4/8/75-1/8/76) the following measurements were made:-

- i) 20 and 30 GHz attenuation.
- ii) 20 GHz depolarisation.
- iii) 20 and 30 GHz sky noise along the satellite slant-path.

Subsequently, during the drift phase of the satellite to a position 130°W, measurements were made of 30 GHz attenuation and depolarisation until the satellite disappeared below the horizon on 18 Oct 1976, during which time the polarisation tilt angle changed from 23.6° anticlockwise, through zero, to 38° clockwise.

In the following the measure of depolarisation is the crosspolar discrimination (XPD) which is defined as

$$\text{XPD (dB)} = 10 \log_{10} \left| \frac{\text{received power in the copolar channel}}{\text{received power in crosspolar channel}} \right|$$

power being transmitted only in the copolar channel.

2. EQUIPMENT

A 6.1 m diameter steerable off-set Cassegrain aerial, programme tracked to an accuracy of ±0.01°, was used to receive the satellite transmissions. The 3 dB beamwidth of the aerial was 0.18° and 0.13° at 20 and 30 GHz respectively. An air blower was used to prevent the accumulation of water or snow on the aerial feed window and static crosspolar cancellation (EVANS, B.G. & THOMPSON, P.T., 1977) was used to improve the on-axis XPD of the system from 35 dB to better than 45 dB under clear sky conditions. Narrow band (200 Hz) phase-locked receivers with low-noise mixer front-ends were used to measure the copolar and crosspolar levels and the relative phase between these signals. The time constants of the copolar and crosspolar channels were 0.05s and 1s respectively. The 20 and 30 GHz radiometers were of the unbalanced Dicke switching type and their 0.6m diameter front-fed aeriels had 3 dB beamwidths of 1.8° and 1.2° respectively. Each had a bandwidth of about 600 MHz, minimum detectable input temperature increment of 1K and a time constant of 1s.

All data channels were logged at a rate of 2 Hz on a minicomputer. Rain rate data from a fast response (10 sec) drop-counting rain gauge located on site was logged at a rate of 0.1 Hz.

### 3. RESULTS

#### 3.1 General

During the ATS-6 experiment in Europe it was found that not only rain along the satellite slant-path but also high altitude ice crystals cause depolarisation of the transmitted satellite signals (WATSON, P.A., 1978). In the former case the depolarisation is associated with a fade in the received copolar signal, whereas in the latter case there is little copolar fading associated with the depolarisation. An example of a rain event is shown in Fig 1 showing good correlation between the XPD and copolar fade and also between the copolar fade and the 20 and 30 GHz radiometer recordings. In this case the depolarisation results from a combination of differential attenuation and differential phase between the principal planes of the anisotropic rain medium in the propagation path. An example of an ice depolarisation event is shown in Fig 2 where it is seen that a peak depolarisation comparable with that of Fig 1 is reached for a copolar fade level of about 1.5 dB, compared with 7 dB for the rain event. In this case the depolarisation is principally due to differential phase, the attenuation due to ice being insignificant. Some events observed could not be clearly defined as due to either rain or ice but showed behaviour characteristic of both effects, and combination of these effects, at different times (HOWELL, R.G. et al., 1977b). In general the residual clear sky system XPD before and after all events recorded was 45 dB, or better, thus limiting the uncertainty in the XPD measured during an event to  $\pm 1$  dB at the 25 dB level (EVANS, B.G. & THOMPSON, P.T., 1977).

In the following the copolar attenuation was measured relative to the clear sky level closest in time to the event and is therefore referred to as the co-polar fade level. It is estimated that the maximum errors in the attenuation measurements are  $\pm 0.4$  dB at 20 GHz and  $\pm 0.6$  dB at 30 GHz.

In the scattergrams which are presented here every half-second of data is plotted, but it should be noted that existing data points are not overprinted, thus the density distribution of the data points which can be clearly seen in the earlier publications (HOWELL, R.G., et al., 1977a, 1977b) is not apparent here.

#### 3.2 Copolar Fade Ratio

An example of a 30/20 GHz fade ratio scattergram is given in Fig 3 for the rain event shown in Fig 1. Also plotted in Fig 3 are theoretical curves for 1 Km and 6 Km path lengths provided by Essex University (UPTON, S.A.J., 1979) using a model developed there (UZUNOGLU, N.K. et al., 1977, EVANS, B.G. et al., 1977). The theoretical curves are based on a uniform rainfall rate along the slant-path, a Marshall and Palmer dropsize distribution, and take into account the slant-path elevation angle and polarisation tilt angle. A raindrop canting angle of  $4^\circ$  and a wind direction at  $90^\circ$  to the vertical plane of the slant-path are also assumed, but these parameters are of more relevance to the crosspolar predictions and have little effect on the attenuation curves. It is seen from the theoretical curves in Fig 3 that the attenuation ratio is not only path length dependent but also significantly raindrop temperature dependent. The best fit slope to the data in Fig 3 gives an attenuation ratio of 2.09. However the attenuation ratio varied slightly from event to event, and also during events, and a scattergram showing the results from the seventeen most severe events (a total of 24.64 hrs of data) is given in Fig 4. The best fit straight line to this data over the range of 4 dB to 14 dB 30 GHz fade depth gave an attenuation ratio of  $2.20 \pm 0.13$  (standard deviation).

The best fit straight line is not obvious from the data in Fig 4 since this data only shows the extreme spread of nearly 89,000 data points, existing points not being overprinted by the computer. The data is consistent with a path length in the region of 3 Km to 10 Km.

#### 3.3 Depolarisation

It was pointed out in Sect 3.1 that depolarisation is caused both by rain and also by high altitude ice particles and Figs 1 and 2 are illustrations of such types of events. It should also be recalled that the polarisation tilt angle at Martlesham was  $23.6^\circ$  anti-clockwise from vertical and the path elevation angle  $22.7^\circ$ . In Fig 5 the scattergram of XPD versus copolar fade is plotted for the 20 GHz rain event shown in Fig 1. The theoretical curves for rain induced depolarisation presented in Fig 5 were again provided by Essex University and assume uniformly canted drops at  $4^\circ$  and a wind direction of  $90^\circ$  to the vertical plane through the slant-path (worst case). There is no strong dependence on path length, as can be seen from the 6 Km and 1 Km curves. Also the corresponding curves for 1 Km,  $0^\circ\text{C}$  raindrop temperature, and 6 Km,  $20^\circ\text{C}$  raindrop temperature, fall within the bounds of the two curves presented. Also plotted in Fig 5 is a semi-empirical formula relating XPD to fade depth for rain taken from CCIR Report 564 (CCIR, 1978). The data points show a tendency towards the type of behaviour of all the prediction curves plotted on Fig 5. In comparison the data for the ice depolarisation event shown in Fig 2 is plotted in Fig 6, where it is seen that there is no correlation between the measured data and the theoretical rain depolarisation curves because of the absence of significant fading associated with the XPD degradation.

Events were not always as clearly categorised as those of Figs 5 and 6, as can be seen in Fig 7, which is a scattergram produced from the seventeen most severe events recorded. There it is seen that at the higher fade levels the data is tending to be bounded by the CCIR curve and theoretical curves for rain depolarisation with, as expected, the theoretical curves giving the lower bound to the data. At the lower fade levels there is no clear pattern of behaviour, the region between the ice and rain depolarisation regions being filled with data points representing events which must include both rain and ice effects. Thus it is seen that there is a region in which no generalised relationship exists between XPD and copolar fade and there is a wide range of possible XPD values for a given fade depth. In such a situation it is necessary to resort to a statistical relationship between the two parameters.

One method of presenting the XPD and fading data is in the cumulative distribution (CD) form. This has been done in Fig 8 for the seventeen events contributing to the data presented in Fig 7. The total data amounts to 24.64 hrs and the percentages are expressed in terms of the total recording time of the experiment (1156 hrs).

A relationship between XPD and fade can be derived from the CD's of Fig 8 by taking the pairs of values of XPD and fade for given percentage times and this curve has been plotted on Fig 7. However, it should be noted that the fraction of the time that a given pair of XPD and fade data derived in this manner were simultaneously exceeded does not equal the percentage time on the individual CD's from which the data were derived. This is clearly seen by plotting the XPD and fade data in a joint probability form and this has been done in Fig 9. Figure 9 shows equipercantage time contours for which XPD and fade values were simultaneously exceeded. Thus at the 0.3% time exceeded level of the CD's of Fig 8 values of about 24 dB and 3 dB are obtained for XPD and fade respectively. These values correspond to the intersection of the 0.3% contour with the axes of Fig 9 and it is seen from the shape of the contour that the percentage time that 24 dB XPD and 3 dB fade were simultaneously exceeded must lie at a lower percentage level than 0.3%, and, in fact, these levels intersect very close to the 0.1% contour, as shown in Fig 9.

From the above it is seen that to attempt to derive statistically useful data for outage time of a system due to simultaneous fades and XPD degradations it is not sufficient to deal with equipercantage values obtained from concurrent CD's. However, such a method does have the advantage that it errs on the pessimistic, rather than the optimistic, side. It is suggested that the presentation in terms of joint probability should be of more practical use to system designers, since a system may fail from excessive fade, excessive XPD degradation, or a combination of both of these factors.

### 3.4 Long-term Radiometer derived Attenuation Statistics

The statistical data presented in Fig 8 has to be treated with great caution because of the very small data base used - ATS-6 was only available for 1156 hrs during the 12 month period covered. To overcome this problem for the copolar fade data 20 and 30 GHz sky noise radiometers directed along the ATS-6 slant-path were calibrated against the received satellite beacon levels (BELL, R.R. et al, 1977). Once calibrated the radiometers allowed the data base for the 20 and 30 GHz attenuation statistics to be increased to over 6000 hrs. Calibration of the radiometers was carried out by plotting each half-second sample of aerial noise temperature against the corresponding copolar level for rain fade events such as illustrated in Fig 1. From such plots an effective atmospheric absorber temperature was obtained which allowed the conversion of aerial noise temperature to the corresponding copolar attenuation within an accuracy of  $\pm 1.0$  dB up to the 13 dB attenuation level. The data obtained in this manner is true total slant-path attenuation as opposed to copolar fade level such as presented in Fig 8.

The radiometer derived attenuation statistics are presented in Fig 10, which shows the yearly and worst month CD's for 20 GHz and 30 GHz attenuation and for the on-site rainfall rate. The worst month statistics are defined by the envelope of the highest monthly probability values of all the monthly CD's from the year. Thus different months define the envelope at different percentage time exceeded levels. In the present case the envelopes are determined by the months of August and September 1975 and July 1976 ie the summer months, as expected, when the incidence of heavy rain due to convective storms is greatest.

Attenuation duration histograms were also derived from the radiometer data. Five aerial noise temperature thresholds were selected prior to the experiment, namely, 175K, 210K, 230K, 250K and 260K. Following calibration of the radiometers these thresholds were converted to attenuation levels of 4.4 dB, 6.3 dB, 7.9 dB, 10.4 dB and 12.6 dB and the resulting data is presented in Fig 11. Attenuation durations  $> 5s$  but  $< 30s$  are classified in 5s intervals,  $> 30s$  but  $< 60s$  in 10s intervals and  $> 60s$  in 60s intervals. This data shows that significant attenuation ( $> 10$  dB) occurred along the 23° elevated paths for periods in excess of 20 mins. Further information is presented elsewhere (BELL, R.R and THIRLWELL, J., 1979).

### 3.5 Scintillation

Throughout the experiment amplitude scintillation was generally present on the 20 and 30 GHz received copolar signals (HOWELL, R.G., et al, 1977a). This was typically in the range of 0.5 to 1.0 dB, peak-to-peak at 30 GHz and a factor of between 1.4 to 1.8 smaller than this at 20 GHz when the satellite was at 22.7° elevation. The scintillation at the two frequencies was highly correlated and was at a minimum of around 0.2 dB during calm, dry, frosty conditions and during fog. The most pronounced bursts of scintillation were

produced by cumulus and cumulonimbus clouds during summer and autumn and were not associated with precipitation. These bursts were between 2 dB and 6 dB p-p amplitude at 30 GHz and persisted for 5 to 20 minutes.

Spectral analysis of the scintillations was not performed but it was apparent from the recorded data that the sampling rate of 2 Hz was not sufficiently fast to capture the higher frequency components.

Only 30 GHz measurements were possible as the satellite drifted down towards the horizon and during this period the scintillation increased in both amplitude and frequency of occurrence. An indication of the scintillation amplitude for elevation angles below  $8^\circ$  is given in Fig 12 for the last nine transmission sessions, together with the measured and predicted elevation angles of the satellite. An interesting feature occurred when the satellite elevation was  $1.9^\circ$  in that a peak-to-peak amplitude variation of about 6 dB with a period of about 1 min occurred for almost the whole of a two hour transmission session. No explanation of this behaviour could be found but a similar phenomenon has also been reported by Stutzman et al (STUTZMAN, W.L., et al 1975). The very large amplitude scintillations on the 17th and 18th October 1976 (Fig 12) were almost certainly caused by multiple path propagation, which tends to a Rayleigh fading characteristic with rapid, deep, nulls in received signal level occurring - at this time the satellite elevation angle was less than  $1^\circ$ .

#### 4. CONCLUSIONS

The rain fade ratio between 30 GHz and 20 GHz has been measured using the beacons from the ATS-6 satellite and found to be  $2.2 \pm 0.13$  over the range of 4 to 14 dB 30 GHz fade depth on a slant path elevated at  $22.7^\circ$ . The results are in reasonable agreement with a theoretical model indicating an effective rain path length of between 3 and 10 Km. It should also be noted that the ratio is dependent on the temperature of the raindrops causing the attenuation. The theory is also in good agreement with the 20 GHz rain depolarisation measurements which were made but a CCIR semi-empirical rain depolarisation equation may be a little optimistic in terms of predicted depolarisation, however, insufficient deep fades were observed to draw positive conclusions on this matter. Neither the theoretical model nor the CCIR equation account for the severe depolarisation due to high altitude ice particles and which has insignificant associated copolar fade. Thus there is no simple general model to relate XPD to copolar fade on a one-to-one basis, and the use of statistical comparisons using concurrent cumulative distributions should be treated with caution. It is suggested that it is statistically more relevant, and practically more useful, to present XPD and fade data in a joint probability of occurrence form and this has been illustrated.

Long-term attenuation data derived from over 6000 hrs of radiometer measurements has been presented both as cumulative distribution and attenuation duration histograms for both 20 and 30 GHz.

Finally, some general comments on the nature of scintillations on the copolar signals received from ATS-6 have been made.

#### 5. ACKNOWLEDGEMENTS

Acknowledgement is made to the Director of the British Post Office for permission to publish this paper.

#### REFERENCES

- BELL, R.R. et al., 1977, "The Calibration of 20 and 30 GHz Radiometers by using the ATS-6 Satellite Beacons", Proceedings of ATS-6 Meeting, ESTEC, Noordwijk, 6-7 Sept. 1977 pp 135-148. (ESA SP-131, Oct 1977).
- BELL, R.R. and THIRLWELL, J., 1979, "Satellite Slant-Path Attenuation Statistics obtained using 20 and 30 GHz Passive Radiometers at Martlesham Heath" Electronics Letts Vol 15, No. 6, pp 181-3.
- CCIR, 1978, CCIR Kyoto, Green Book, Vol. V, Report 564-1.
- EVANS, B.G. et al; 1977, "Two new Approaches to the Calculation of Rain induced Attenuation and Cross Polarisation", Proc. URSI Commission F Open Symposium, La Baule, France, pp 175-179.
- EVANS, B.G. and THOMPSON, P.T., 1977, "Use of Cancellation Techniques in the Measurement of Atmospheric Crosspolarisation", Electron. Lett., 2, pp 447-448.
- HOWELL, R.G. et al., 1977a, "20 and 30 GHz Attenuation Measurements using the ATS-6 Satellite", Proceedings of ATS-6 Meeting, ESTEC, Noordwijk, 6-7 Sept. 1977, pp 55-68. (ESA SP-131, Oct. 1977).
- HOWELL, R.G. et al., 1977b, "20 and 30 GHz Cross-Polarisation Measurements using the ATS-6 Satellite" *ibid*, pp 85-102.
- HOGG, D.C. and CHU, T., 1975, "The Role of Rain in Satellite Communications", Proc IEEE, Vol. 63, pp 1308-1331.



STUTZMAN, W.L. et al., 1975, "ATS-6 Satellite 20 GHz Propagation Measurements at Low Elevation Angles" Electron Letts., 11, pp 635-636.

UPTON, S.A.J., 1979, Essex University, Private Communication.

UZUNOGLU, N.K. et al., 1977, "Scattering of Electromagnetic Radiation by Precipitation Particles and Propagation Characteristics of Terrestrial and Space Communication Systems", Proc. IEE, 124, No 5. pp 417-424.

VANDER VORST, A.S., 1978, "A Survey of Atmospheric Propagation Research Experiments on Slant Paths, in the Band 15-40 GHz" AGARD Conf. Proc. No 245.

WATSON, P.A., 1978, "A Summary and Assessment of the 20/30 GHz ATS-6 Propagation Data collected during the European Phase" Proc. of Symp. on Advanced Satellite Communications Systems, Genoa, Italy, 14-16 Dec. 1977 (ESA SP-138, Jan. 1978).

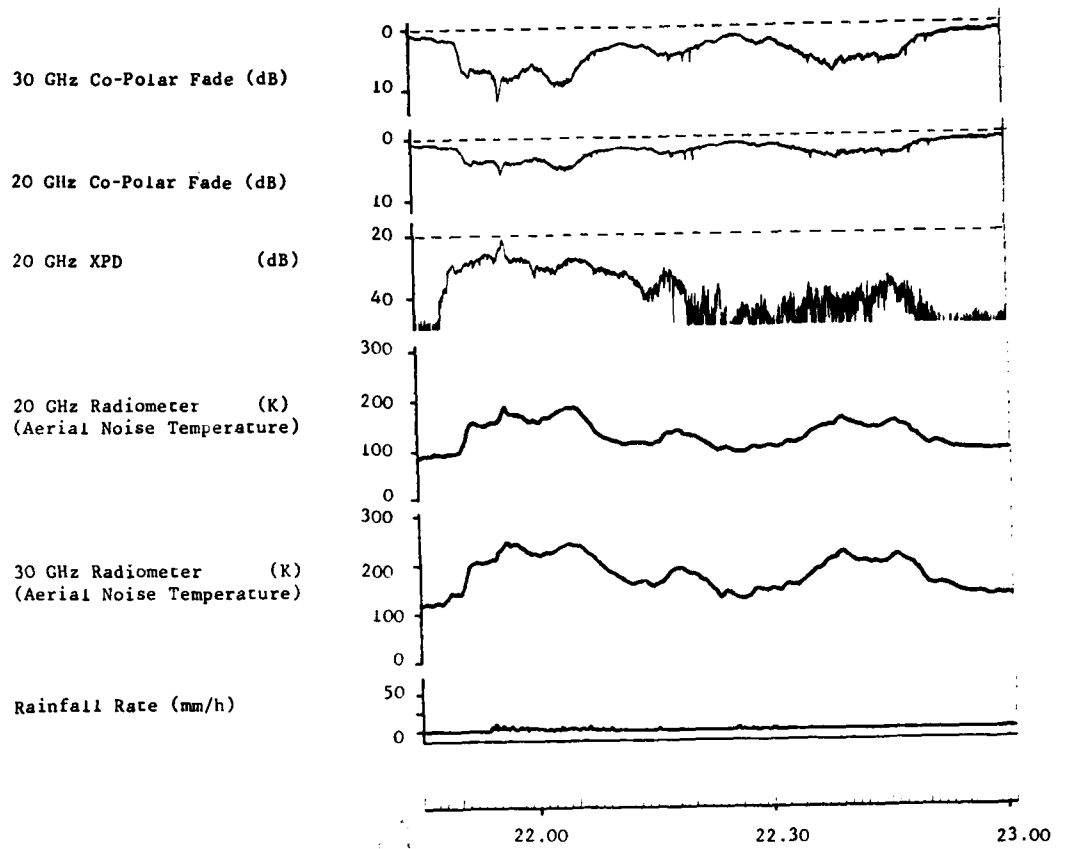


FIG 1

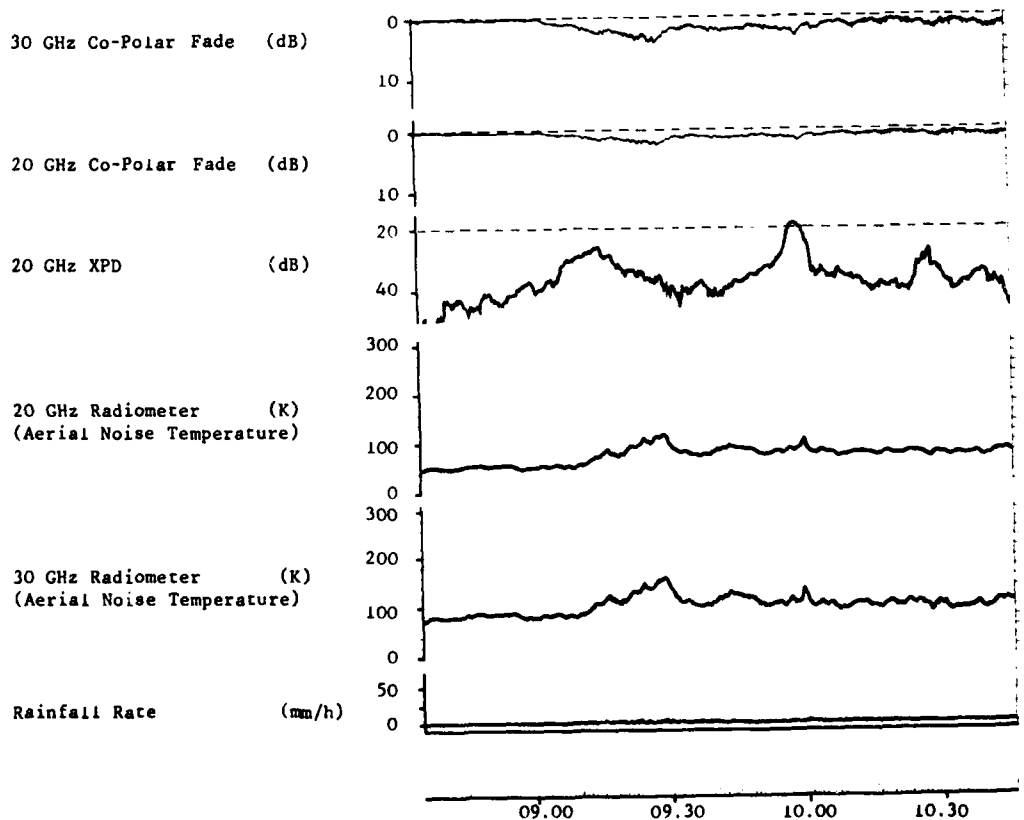


FIG 2

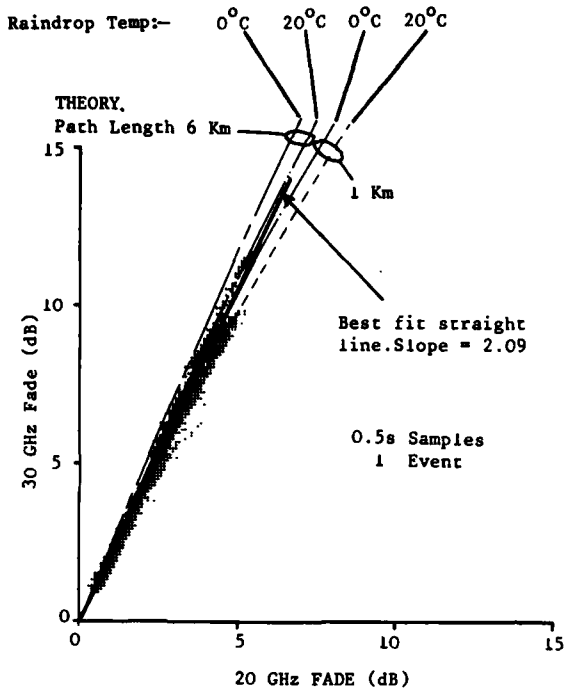


FIG 3 30 GHz Fade v 20 GHz Fade for a Single Rain Event (15/8/75 21.45-23.00)

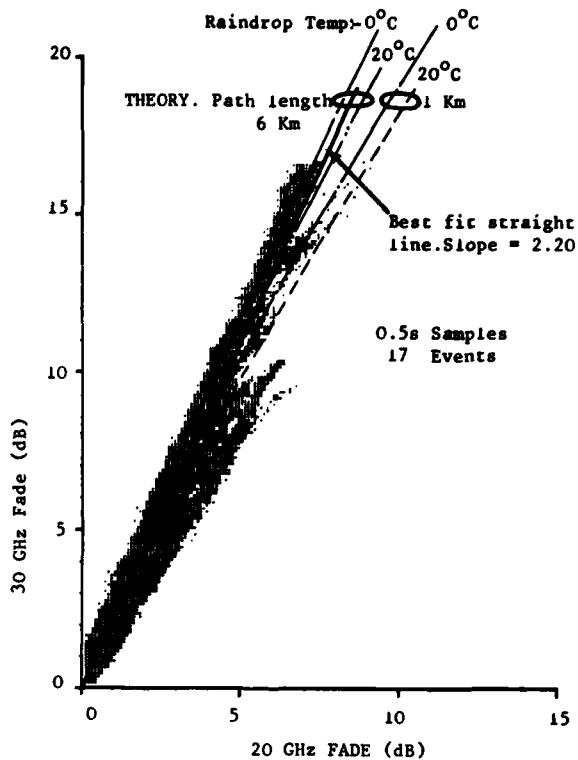


FIG 4 Composite Scattergram of 30 GHz Fade v 20 GHz for 17 Events (11/8/75-19/6/76)

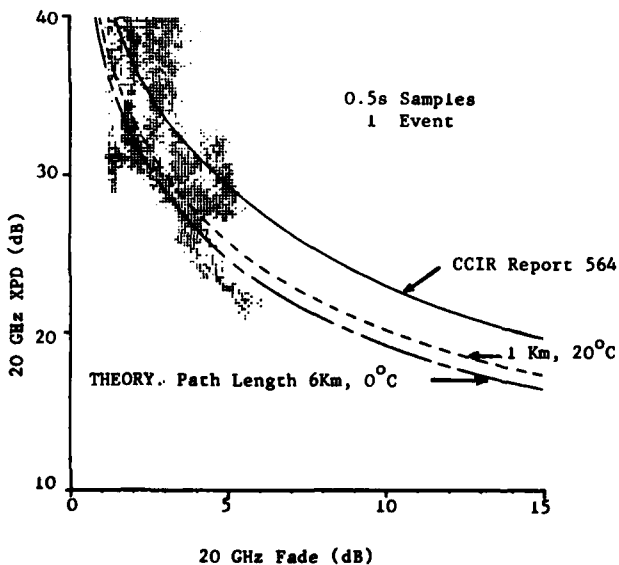


FIG 5 20 GHz XPD v 20 GHz Fade for a Single Rain Event (15/8/75 21.45-23.00)

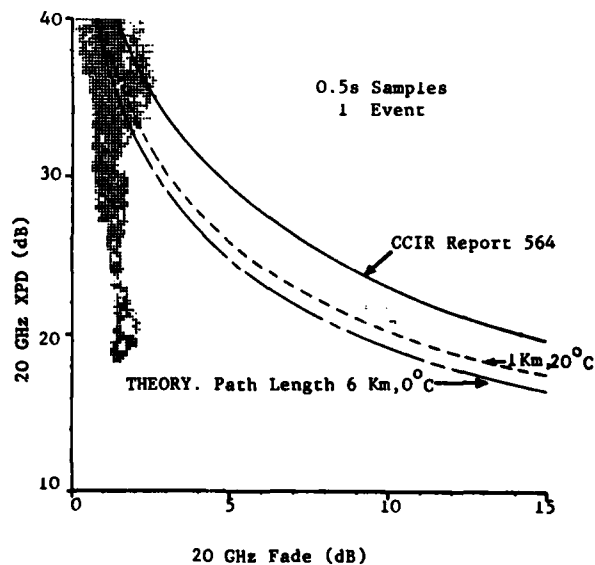


FIG 6 20 GHz XPD v 20 GHz Fade for a Single Ice Event (27/11/75 08.35-10.45)

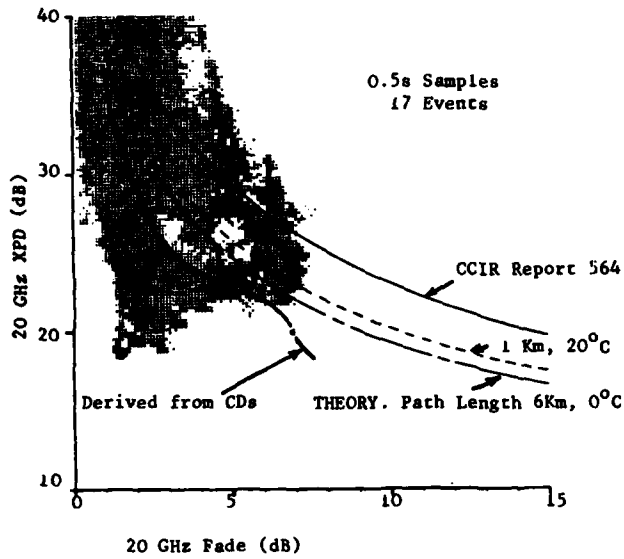


FIG 7 Composite Scattergram of 20 GHz XPD v 20 GHz Fade for 17 Events (11/8/75-19/6/76)

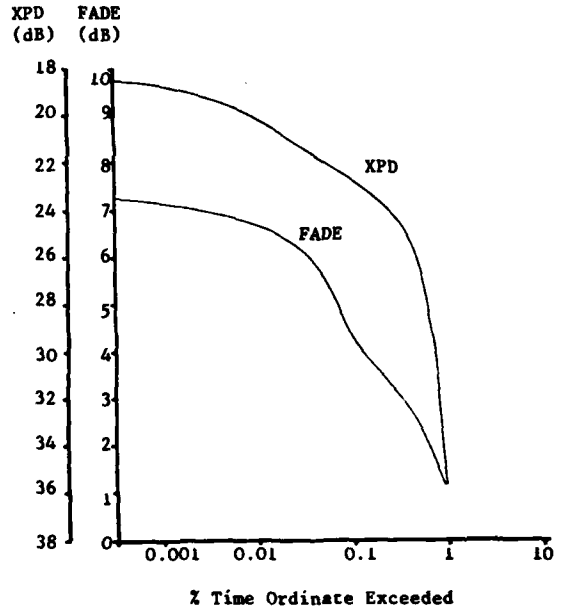


FIG 8 20 GHz Cumulative Statistics of XPD and Fading (11/8/75-19/6/76)

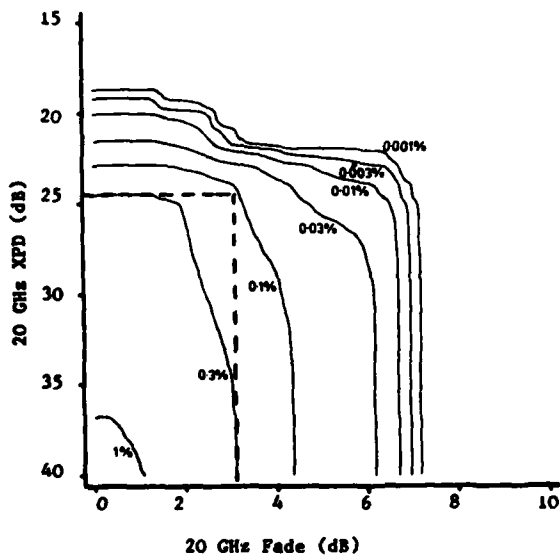
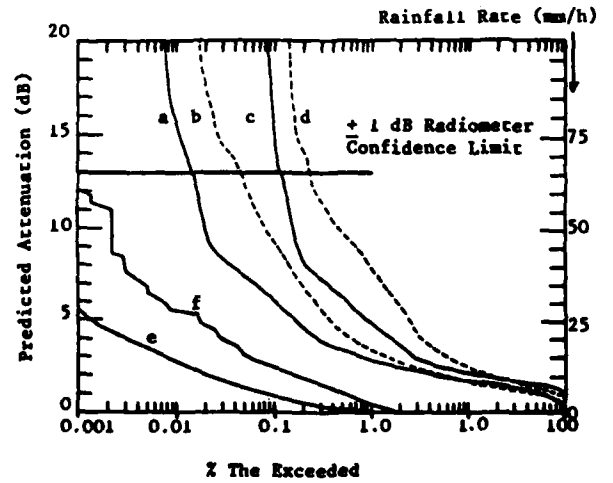


FIG 9 Joint Probability Distribution of XPD and Fading



- a) Yearly CD of 20 GHz attenuation (6096 h)
- b) Yearly CD of 30 GHz attenuation (6569 h)
- c) Worst-month CD of 20 GHz attenuation
- d) Worst-month CD of 30 GHz attenuation
- e) Yearly CD of rainfall rate (6218 h)
- f) Worst-month CD of rainfall rate

FIG 10 Cumulative Distributions of 20 GHz and 30 GHz Radiometrically Derived Attenuations and Rainfall Rate

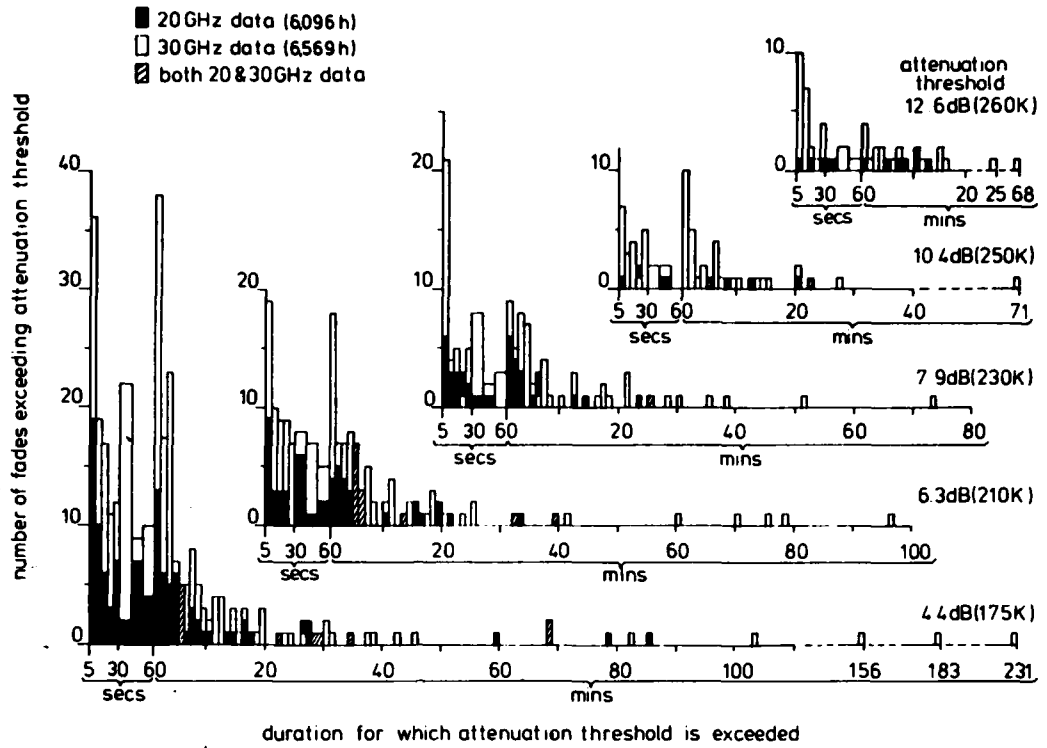


FIG 11 Fade Duration Histograms of 20 and 30 GHz Radiometrically Derived Attenuation

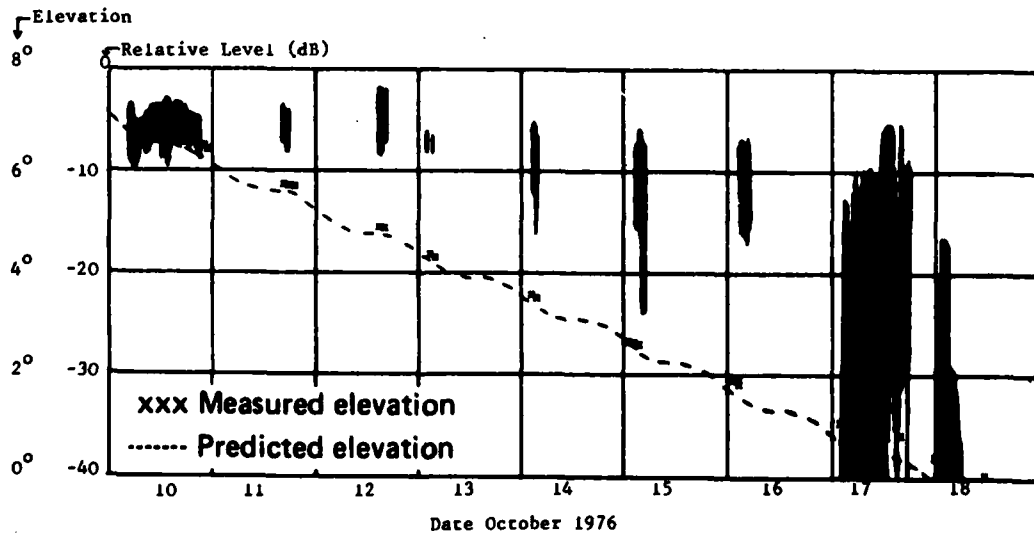


FIG 12 Signal Level and Typical Peak to Peak Scintillation Amplitude During the Final Stages of the Drift Phase

A REVIEW OF SOME CROSS-POLARIZATION EFFECTS  
ON SLANT PATHS IN THE 11-30 GHz FREQUENCY RANGE

T. Pratt

Department of Electronic and Electrical Engineering,  
 University of Birmingham, P.O. Box 363, Birmingham B15 2TT, U.K.

SUMMARY

This paper summarises the results of experimental observations of fading and cross-polarization at 30 GHz on a slant path to central England, and examines the wide variation in cross-polarization caused by ice particles in the propagation path which has been observed at sites in the UK and USA. Some results for propagation on slant paths at low elevation angles are presented showing reliable conditions at angles as low as  $2^\circ$ .

Several events in which cross-polarization has been caused by ice clouds are discussed, for a number of frequencies and sites, and one event showing cross-polarization in clear air is presented. The performance of typical analogue and digital satellite communication links using the 20 and 30 GHz bands is examined, and it is shown that atmospheric cross-polarization does not seriously degrade the performance of the link, particularly at 30 GHz, when frequency reuse by orthogonal polarizations is employed.

1. INTRODUCTION

Measurements of attenuation and cross-polarization at 30 GHz and 11 GHz have been carried out at the University of Birmingham since 1975 using the beacon transmissions from the ATS-6 and OTS satellites. In the ATS-6 measurement programme, carried out during 1975-76, approximately 1100 hours of data were recorded, (1,5). For most of this period the spacecraft had an elevation angle of  $21^\circ$ , but during the period August-October 1976 ATS-6 was drifted westbound in geostationary orbit, permitting observations at angles from a maximum of  $29^\circ$  to a minimum of  $0.5^\circ$ , (3). Measurements of fading, cross-polarization and scintillation were made with the linearly polarized 30 GHz beacon transmission of ATS-6, (4,5). When the satellite had an elevation angle of  $21^\circ$ , the incident polarization vector was at an angle of  $23^\circ$  to the local vertical. A 6m offset Cassegrain antenna was used for reception of the 30 GHz signal, with a dual polarized feed and two channel receiver, (1).

The OTS measurement programme commenced in October 1979 and is continuing at the present time. The 11.786 GHz circularly polarized beacon (B1) and the 11.575 GHz linearly polarized beacon (TM) of OTS are received with two fixed front-fed paraboloidal antennas with diameters of 1.8m (B1) and 2.4m (TM). A four channel receiver is used to measure the copolar and cross-polar outputs from the dual-polarized antennas. The measurement system operates continuously, unattended, and collects data 24 hours/day. The reception of both B1 and TM beacons enables direct comparison of cross-polarization of circularly and linearly polarized signals on the same path. The elevation angle of OTS, as viewed from Birmingham, is  $29^\circ$ .

This paper reviews some of the results obtained at 30 GHz during the ATS-6 programme, with particular emphasis on the cross-polarization observed on this path. Some results for low elevation angle paths are also included. Cross-polarization is frequently observed on space-earth paths without significant copolar attenuation. This effect has been attributed to the presence of ice crystals in the path, (7), and cross-polarization due to this cause has been observed at 30 GHz and at 11 GHz at Birmingham. A model for an ice cloud which can produce cross-polarization is examined against data obtained at Birmingham and at Virginia Polytechnic Institute and State University, Blacksburg, VA, USA, (6). It is apparent that ice depolarization occurs much less often in some locations than others, suggesting that a geographical factor is present in the formation of the conditions in which ice depolarization occurs.

The effect of cross-polarization on a typical dual polarization frequency re-use communications link operating at 20 and 30 GHz can be shown to be small, based on the data collected during the ATS-6 programme in Europe. This is because the signal to noise degradation due to fading exceeds that caused by cross-polarization and occurs more frequently. The effect of co-channel interference by cross-polarization in the atmosphere is more marked at 20 GHz and 11 GHz than at 30 GHz, since the attenuation is lower at the lower frequencies whereas the cross-polar statistics are less frequency dependent.

2. SLANT PATH PROPAGATION AT 30 GHz

2.1 Attenuation and Scintillation

During the period August 1975 - July 1976, when the ATS-6 satellite was transmitting from a geostationary position at  $35^\circ\text{E}$ , approximately 861 hours of data were recorded with the 30 GHz measurement system. 32 fades in excess of 3dB were recorded, with a total duration of 31 hours 53 mins. The time for which a fade depth of 10dB was exceeded was 109 mins, of which 63 mins occurred in a single event in July 1976. The deepest fade occurred on 28/08/76, with a peak attenuation of 33dB (Fig.1). All the events with attenuation exceeding 10dB occurred in the summer months (June - September). Scintillation was found to be typically 0.5dB peak-peak in clear air, often below 0.2dB in winter, but larger when cumulo-nimbus clouds passed through the slant path. A particularly intense scintillation event occurred in clear air in July 1976; this is discussed in the next section.

2.2 Cross-polarization

Cross-polarization of the 30 GHz linearly polarized signal was observed during heavy rain. The measurement system normally maintained a cross-polar discrimination, or XPD, (defined as the ratio of copolar signal to cross-polar signal) of greater than 35 dB; occasionally, tracking errors caused the XPD to fall below this level. Data recorded during these periods were either discarded or re-processed to remove the residual component. Relatively few events caused the XPD to fall below 25dB: only four were observed in the period August 1975 - July 1976, with a total duration of six minutes. For the heavy rain events, where the attenuation exceeded 8dB, the cross-polarization in rain generally followed that predicted by

theory based on drop oblateness and size distribution.

Cross-polarization accompanied by low attenuation was observed on a number of occasions. During two events in May and July 1976, the XPD fell below 21dB with less than 1dB attenuation, indicating that an ice cloud was present in the path. However, cross-polarization due to ice occurred much less frequently at Birmingham, and with less severity, than at the Appleton Laboratory site in S.E.England,(8).

Enhanced cross-polarization with low attenuation was recorded on one occasion in clear air, in July 1976. In this event, of which part is shown in Fig.2, the XPD reached a peak of 22dB with 1dB copolar attenuation. No clouds were visible at the time, suggesting that refraction of the incident beam was the cause. The 6m offset Cassegrain antenna which was used for reception of the 30 GHz signal had a cross-polar antenna pattern with two major lobes in the elevation plane when orientated to receive the ATS-6 transmissions,(5). (The offset Cassegrain reflector is mounted on non-orthogonal axes; for a beam elevation angle of  $21^\circ$ , the plane of asymmetry of the reflector system is close to the vertical plane.) The solid line in Fig.2 plots the antenna XPD in the vertical plane. The clustering of the measured XPD points around this line suggests that the incident signal was varying its angle of arrival in the elevation plane, corresponding to an apparent movement of the source in this plane. For the peak XPD recorded, 22dB, the apparent displacement of the source was  $0.05^\circ$ . Because the antenna had particularly high cross-polar lobes in the elevation plane, the effect was well marked; with a larger antenna than 6m diameter, even greater copolar scintillation would be observed, but the cross-polar enhancement would be kept to a reasonable level with a reflector system on a conventional mount (alt-az), since the cross-polar lobes then occur in the  $45^\circ$  planes.

In the case of the Birmingham system, this event, in clear air, gave rise to an XPD as large as that attributed to ice depolarization. The reasons for the variation in angle of arrival are not clear. The effect occurred only once in some 1100 hours of recorded observations, and is attributed to unusually intense variations in refractive index in the troposphere.

### 2.3 Low angle measurements

The ATS-6 satellite drifted round the geosynchronous orbit from  $35^\circ\text{E}$  to  $140^\circ\text{W}$  during the period August-November 1976. The elevation angle reached  $0^\circ$ , as viewed from Birmingham, on 19/10/76. Regular transmissions of the 30 GHz beacon signal were made during this period, and measurements of attenuation and cross-polarization continued at Birmingham until the satellite set on 19/10/76. The excess attenuation of the copolar signal, relative to its level at  $21^\circ$  elevation angle, followed closely a cosecant law until the elevation angle reached  $2^\circ$ , after elimination of periods when rain was known to have been present in the path. Below  $2^\circ$  elevation, additional attenuation occurred relative to the cosecant law, as might be expected since the cosecant law assumes a planar atmosphere.

The fading of the copolar signal increased in magnitude as the elevation angle decreased, changing in character from a fast scintillation towards scintillation plus Rayleigh fading, with occasional deep fades. However, for a period of several hours on 17/10/76, when the elevation angle was  $2.3^\circ$ , a very steady signal with almost no fading was observed. Fig.3 compares the signals received on 17/10/76 in the early morning, and in the afternoon. Rayleigh fading is evident in the morning record. The cross-polar discrimination remained better than 25dB for most of this period, and did not degrade noticeably as the elevation angle was reduced.

At an elevation angle of  $0.5^\circ$ , the received signal was broken up by deep fades exceeding 20dB, and also had enhancement periods when the level exceeded that expected in clear air by several dB. An explanation for this behaviour, based on a multi-layered model of the atmosphere, has recently been proposed by Strickland (9). In general, one can conclude that useful signals can be obtained at 30 GHz on slant paths with elevation angles as low as  $2^\circ$ , but with increasing Rayleigh fading and high attenuation when there is rain in the path as the elevation angle decreases. No statistical data was derived from the measurements reported here due to the intermittent nature of the transmissions and the relatively small number of hours of data which was obtained.

## 3. DEPOLARIZATION BY ICE CLOUDS

Cross-polarization due to the presence of ice clouds in the slant path has been widely reported in the literature (7,8,10). Various models for the depolarizing medium have been proposed (7,11); the major feature of these models is the postulation of a field of partially aligned ice particles with marked asymmetry. When viewed obliquely along the slant path, the particles present a different scattering cross section to orthogonal polarizations, introducing a differential phase shift and thus causing cross-polarization. The effect is more marked with circular polarization than with linear polarization, since the rotating vector of the circularly polarized signal is at some time aligned with the axis of asymmetry of the particles, resulting in maximum cross-polarization at that instant. Averaged over time, the circularly polarized signal tends to be more affected than the linearly polarized signal, although a linear polarization aligned with the particle axis will be equally affected.

In the model for ice depolarization proposed by Bostian and Allnutt (7), ice particles with needle-like shapes are aligned by the electric field in a thunderstorm, or a large cumulo-nimbus cloud. Some evidence to support the electric field alignment hypothesis comes from correlation of sudden changes in cross-polarization with changes in the ambient atmospheric electric field measured at the earth's surface (12), and by radar measurements (13). Additional evidence for this model has been obtained from simultaneous observations on two slant paths with a small angular separation (6).

### 3.1 Experimental Evidence

Figure 4 shows the records for part of an ice depolarization event which occurred on 10th August 1978, at Virginia Polytechnic Institute and State University's earth station at Blacksburg, Va, USA. Fading and cross-polarization of signals from the CTS spacecraft beacon at 11.7 GHz and the 19.04 GHz beacon of Comstar D2 were made from 1977 to 1979. The CTS signal was circularly polarized, and the path elevation was  $33^\circ$  at an azimuth angle of  $203^\circ$ . The Comstar signal was switched between two orthogonal linear

polarizations (termed 'V' and 'H', but orientated at  $37.5^\circ$  to local vertical and horizontal), and the path elevation was  $44^\circ$  at an azimuth of  $230^\circ$ .

The event shown in Fig.4 illustrates ice depolarization occurring on both the CTS and COMSTAR paths as a thunderstorm drifted through the beam. The attenuation during the event shown in Fig.4 was less than 2 dB, indicating that ice was the major depolarizing agent. There is a time separation of approximately five minutes between the peaks of cross-polarization on the two spatially separated paths, suggesting that a volume of aligned ice particles drifted through the two paths sequentially. The angular separation of the paths was  $23^\circ$  in azimuth and  $11^\circ$  in elevation. If we postulate a volume of ice at an altitude of 5 km, the separation of the paths is approximately 3 km at this height, and a five minute delay between events would result from a horizontal drift velocity of 36 km/hr. normal to the slant paths. The volume of aligned particles would appear to be about 3 km diameter from the width of the major cross-polarization peaks.

In Figure 5 another event is shown which occurred on 8th Aug.1978. In this event, depolarization occurred on the two paths simultaneously, with a peak XPD value of 22 dB on the CTS path at 20.08 GMT. The interesting feature of this event is the sudden fall and subsequent rise in XPD at the points marked 'a' and 'b' in Fig.5. The mechanism which caused the sudden change in XPD affected paths separated by several km at the same instant. This suggests that a large volume of ice, at least 3 km in diameter, was intersecting both paths, and the ice particles were aligned by an intense electric field within the cloud. At point 'a' a lightning discharge occurred, neutralising the electric charge and reducing the field. This caused a near-instantaneous fall in the cross-polarization on both paths. Only an electric field discontinuity could affect regions separated by 3 km. After the sudden drop in cross-polarization, the electric field slowly built up again causing realignment of the particles and increased cross-polarization. A similar sequence of events occurred at point 'b', although less dramatically.

### 3.2 Radar Observations

Figure 6 shows an ice-depolarization event recorded on 26th March 1980, at the University of Birmingham, U.K., with the 11 GHz beacons of OTS. On this occasion, there were large cumulo-nimbus clouds drifting eastwards with heavy showers beneath, but no thunder or lightning was observed. The depolarization event shown in Fig.6 occurred in the late afternoon when a cumulo-nimbus cloud passed through the slant path at a range of 11 km. The position of the cloud was identified both visually and by an X-band PPI radar, which indicated an area of rain approximately 2 km long by 1 km wide at this range. The elevation angle of OTS at Birmingham is  $29^\circ$ , so the slant path intersected the cloud at approximately 5.5 km altitude, well above the  $0^\circ\text{C}$  isotherm in March. Ice depolarization was clearly the cause of this event, in which the attenuation never exceeded 0.5 dB. There is approximately 5 dB less cross-polarization of the linearly polarized TM signal than of the circularly polarized B1 signal; this is consistent with theoretical models for partially aligned ice particles, with a mean alignment of  $45^\circ$  and a standard deviation of alignment angle of  $35^\circ$ , (6).

Radar has considerable potential for analysing the type and orientation of hydrometeors on a slant path, since it is possible to resolve the radar echoes in range. A dual polarization radar with pulse to pulse switching between two linear orthogonal polarizations is currently under development at the University of Birmingham. With this system, it will be possible to make both differential reflectivity measurements on the orthogonal copolar returns, and cross-polarization measurements of scattered energy. Dual polarization radars have already been used successfully in the U.K. to improve the modelling of rain showers in a slant path and in Canada to detect aligned ice particles at high altitudes in thunderstorms, (13).

## 4. SYSTEM PERFORMANCE OF 20/30 GHz COMMUNICATION LINKS

The successful exploitation of the 20/30 GHz, and higher, frequency bands requires an understanding of the influence that the propagation medium has on the performance of a communication link. Very little attenuation and cross-polarization data are available for these frequencies; approximately 7000 hours of data were collected in Europe during the ATS-6 experiment. The results for attenuation are summarized in a paper by Watson (15), and some statistics for cross-polarization at 20 and 30 GHz have been published (16). The data sample is too small to be entirely reliable, but can be used to illustrate the performance which might be expected with single and dual polarized links operating in the 20/30 GHz bands.

Attenuation at 20 GHz reaches 12 dB typically for 0.01% of time, and 20 dB at 30 GHz. It is not possible to design economic satellite communication links with 20 dB margins, so a higher outage time must be tolerated. However, with high gain regional coverage antennas, a margin of 13 dB above a C/N threshold of 12 dB is feasible, and corresponds closely to the performance of INTELSAT standard A systems using regional beams at 4/6 GHz. Using the fading statistics in reference (15) for 20 and 30 GHz, the S/N performance of a typical FM system and a typical 4-phase coherent psk system has been calculated. In each case, a clear air C/N ratio of 25 dB was assumed for a dual polarized system with a clear air isolation of 30 dB. The cross-polarization statistics for 20 and 30 GHz which were published following the ATS-6 experiment show a very wide variation; at Birmingham the worst XPD recorded was 20 dB, at Appleton Laboratories 12 dB (19). The 0.1% statistic for XPD varies between 25 dB and 14 dB for different locations. As a typical case, XPD figures of 15 dB for 0.01%, 20 dB for 0.1% and 25 dB for 1% of a year have been assumed.

Figure 7 shows the S/N ratio as a percentage of time for an analogue modulation system using FM with a 25 dB improvement factor. The curves show S/N for single polarization and dual polarization (frequency re-use) systems at 20 GHz and 30 GHz, using the parameters given above, and assuming a -32 dB interference contribution from miscellaneous causes such as intermodulation. Allowing a 3 dB margin for degradations other than propagation fades, the 12 dB C/N threshold is reached in a single polarized 20 GHz link for less than 0.01% of time, 0.02% for dual poln. At 30 GHz the outage would be 0.04% with single polarization and 0.05% for dual polarization. It is interesting to note that the reduction in S/N when using dual polarization remains nearly constant for all percentages of time, at about 2 dB for the 30 GHz system and 3 to 4 dB for the 20 GHz system. This is because the reduction in S/N ratio due to fading always dominates that due to cross-polarization. (Worst case conditions were assumed, in which fading and XPD were assumed to be completely correlated. In practice, XPD degradation will occur in the absence of fading and vice-versa, but the assumption of completely independent fading and XPD alters the S/N curve for the dual polarized case by less than 0.5 dB.)



Figure 8 shows a calculation of bit error rate for digital links using four phase coherent psk modulation, based on the performance curves published by Prabhu (17). The same clear air conditions were assumed as with the fm link: 25 dB C/N for the copolar signal with 30 dB cross-polar channel isolation. If we take a bit error rate (BER) of  $10^{-4}$  as the threshold for the system, the outage times are slightly lower than for the fm system. The degradation caused by use of a second polarization is even smaller in the digital system, and the overall performance is much better for most of the time. The very low BER for percentage times greater than 0.1 shown in Fig.8 would not be achieved in practice, but the graph illustrates the sudden drop in system performance as threshold is approached.

#### 5. CONCLUSIONS

Some results from propagation measurements on slant paths at 20 and 30 GHz have been presented, illustrating the variation in fading and cross-polarization which can occur on different slant paths and at different times. In attempting to assess the likely cross-polarization on a particular path, one finds a wide variation in XPD statistics for different measurement sites. Ice-depolarization shows the greatest variation, being frequent at some sites and rare at others. The data presented in Figs.4 and 5 show the most severe ice depolarization experienced on the VPI and SU slant paths during the years 1977 and 1978. The XPD reached a minimum of 20 dB for only a few minutes in some 15,000 hours of recording, including many thunderstorms and severe fades. By contrast, sites in the U.K. with slant paths to OTS, at similar elevation angles to the CTS path at VPI and SU, have experienced 20 dB XPD levels in excess of 0.3% of time (18), although some of this time was in the months of November and December when ice on the antenna could have been the cause. Nevertheless, there does appear to be a geographical factor in the occurrence of ice depolarization, possible associated with the presence, or absence, of maritime effects. In continental locations it is possible that the conditions under which needle-like ice crystals can grow in thunderstorms do not often occur, so alignment of the crystals under strong electric fields is less likely.

The system performance calculations for 20 and 30 GHz links show that the outage times as low as 0.01% are theoretically possible in a 20 GHz digital link employing frequency re-use by orthogonal polarizations, given a clear air C/N of 25 dB. The performance of fm links is slightly poorer, but outage times of 0.05% (4 hours per year) appear feasible, even at 30 GHz with frequency re-use. The results are applicable to Western Europe; in the UK, where heavy rain and thunderstorms are infrequent, the performance would be better than is indicated in Figs.7 and 8. The exploitation of these higher frequency bands should not be neglected on the grounds of an unreliable propagation path.

#### 6. ACKNOWLEDGEMENTS

The author wishes to acknowledge the contribution of Dr.D.J.Browning in making the measurements with ATS-6 at Birmingham University, Dr.R.V.Gelsthorpe and Mr.R.W.Parry, in the construction of the OTS receiving system, and the Satellite Communication Group at Virginia Polytechnic Institute and State University, who provided the data for CTS and COMSTAR paths. Part of the work reported here was supported by grants from the U.K. Science Research Council, and part by a NATO grant, No.1282.

#### 7. REFERENCES

1. D.J.Browning and T.Pratt: 'The ATS-6 propagation measurement system at the University of Birmingham, U.K.' ESA Special Publication No.SP 131, 'ATS-6 Propagation experiments in Europe', ESTEC, Noordwijk, Netherlands, 1977, pp 5-14.
2. T.Pratt and D.J.Browning: 'Copolar attenuation and radiometer measurements at 30 GHz for a slant path to central England', Ibid, pp 15-20.
3. T.Pratt and D.J.Browning: 'Cross-polarization measurements for a slant path to Central UK' Ibid, pp 103-110
4. D.J.Browning and T.Pratt: 'Low angle propagation from ATS-6 at 30 GHz', Ibid, pp 149-154.
5. T.Pratt and D.J.Browning: 'Attenuation and cross-polarization measurements at 30 GHz using the ATS-6 satellite: Memorandum No.469, Department of Electronic and Electrical Engineering, University of Birmingham.
6. C.W.Bostian, T.Pratt and A.Tsolakis: 'Ice depolarization at 11.7 and 19 GHz on slant paths in Virginia, U.S.A.', Proceedings of URSI Open Symposium, Lennoxville, Quebec, Canada, May 1980, pp 691-695.
7. C.W.Bostian and J.E.Allnutt: 'Ice crystal depolarization on satellite-earth microwave radio paths', Proc.IEE, Vol.126, No.10, October 1979, pp 951-960.
8. P.F.Shutie, J.E.Allnutt and E.C.MacKenzie: 'Satellite-earth signal depolarization at 30 GHz in the absence of significant fading' Electronic Lett., Vol.13, 1977, pp 1-2.
9. J.I.Strickland: 'Site-diversity measurements of low angle-fading and comparison with a theoretical model', Proceedings of URSI Open Symposium, Lennoxville, Quebec, Canada, May 1980, pp 381-386.
10. N.J.McEwan, P.A.Watson, A.W.Dissanayake, D.P.Haworth and V.T.Vakili: 'Cross-polarization from high altitude hydrometeors on a 20 GHz satellite radio path', Electronic Lett., Vol.13, 1977, pp 13-14.
11. B.G.Evans and A.R.Holt: 'Cross-polarization phase due to ice crystals on microwave satellite paths', Electronic Lett., Vol.13, 1977, pp 664-666.
12. D.P.Haworth, N.J.McEwan and P.A.Watson: 'Relationship between atmospheric electricity and microwave radio propagation', Nature, Vol.266, 1977, pp 703-704.
13. A.Hendry and G.E.McCormick: 'Radar observations of the alignment of precipitation particles by electrostatic fields in thunderstorms', Geophys.Res., Vol.81, 1976, pp 5353-5357.
14. S.M.Cherry, J.W.F.Goddard and M.P.M.Hall: 'Use of dual-polarization radar to assess attenuation on an OTS satellite to ground path', Proceedings of URSI Open Symposium, Lennoxville, Quebec, Canada, May 1980, pp 451-456.

15. P.A.Watson: 'Propagation factors in the design of 20 and 30 GHz telecommunication satellite systems', IEE Conference Publication No.169, Antennas and Propagation, Part 2., IEE, London, 1978, pp 130-134.
16. ESA Special Publication SP131, 'ATS-6 propagation experiments in Europe', ESTEC, Noordwijk, Netherlands, October 1977.
17. V.K.Prabhu: 'Error rate considerations for coherent phase shift keyed systems with co-channel interference', Bell Systems Tech.Journal, Vol.48, 1969, pp 743-767.
18. I.J.Dilworth and B.G.Evans,: 'Propagation measurements due to rain and ice using the OTS satellite', Proceedings of URSI Open Symposium, Lennoxville, Quebec, Canada, May 1980, pp 651-656
19. P.F.Shutie, E.C.Mackenzie and J.E.Allnutt,: 'Depolarization measurements at 30 GHz using transmissions from ATS-6', ESA Publication SP131, ESTEC, Noordwijk, Netherlands, 1977, pp 127-134.

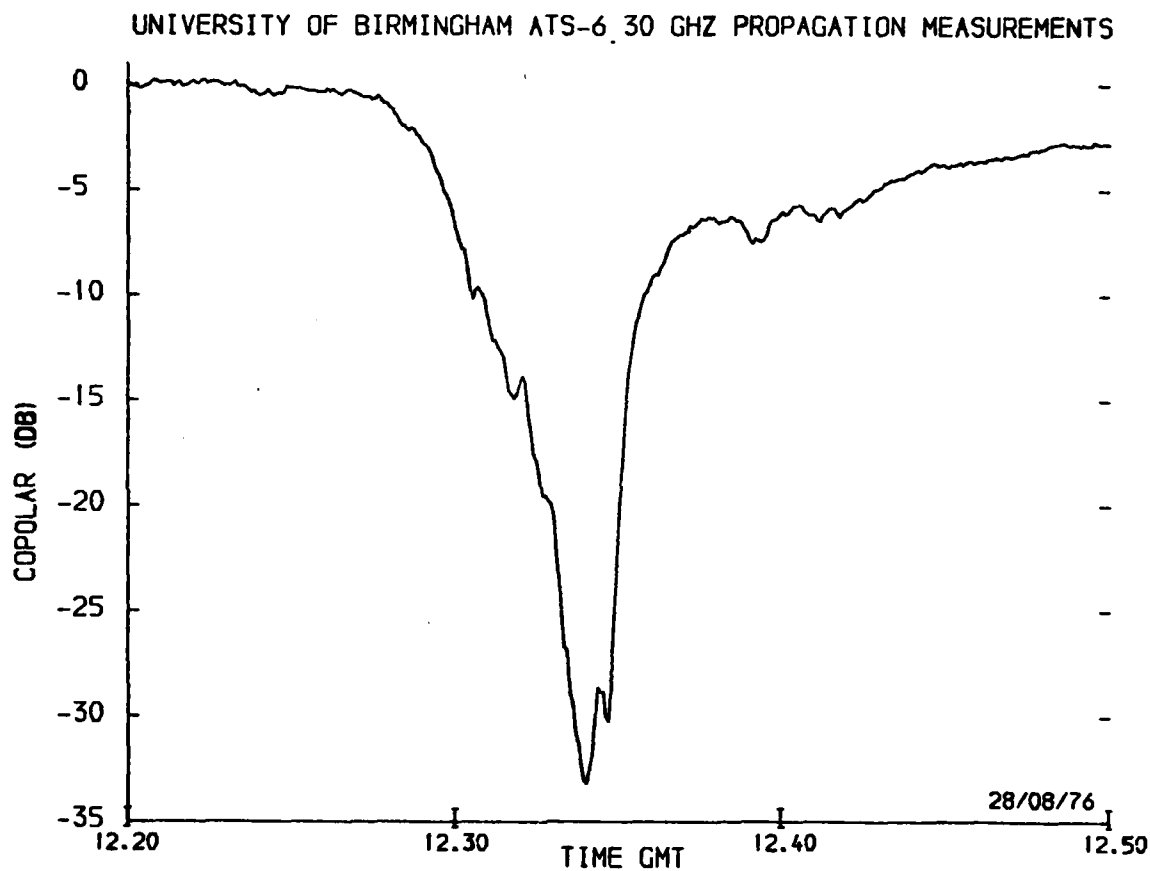


Figure 1 Copolar attenuation at 30 GHz on 28/08/76 due to a brief thunderstorm.

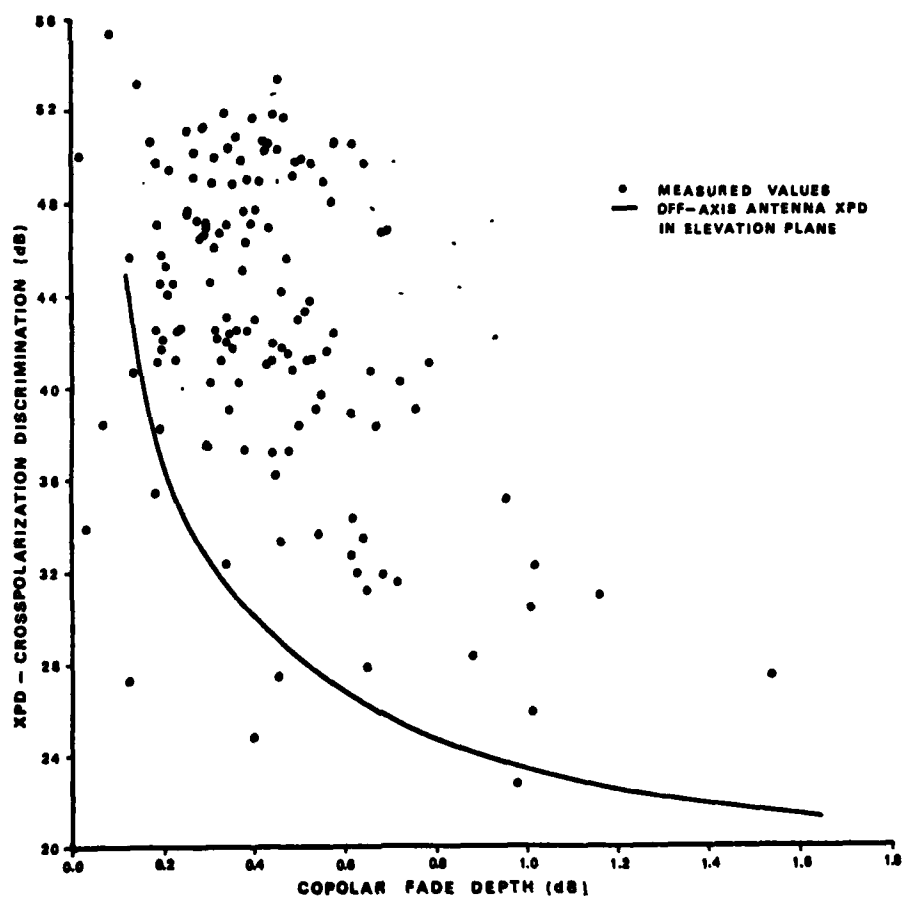
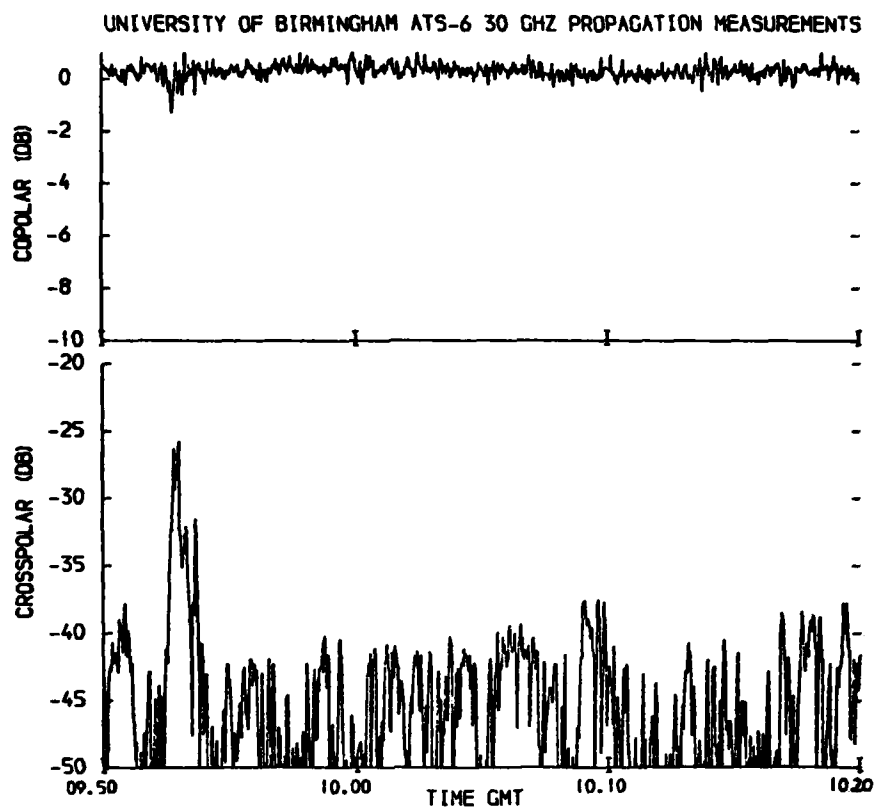


Figure 2 Clear weather cross-polarization at 30 GHz on 6/07/76.

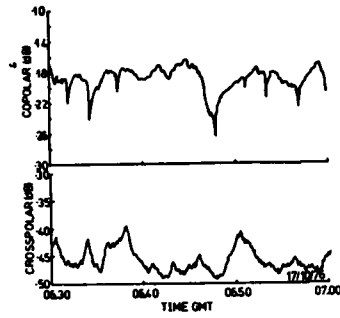


FIG 3a

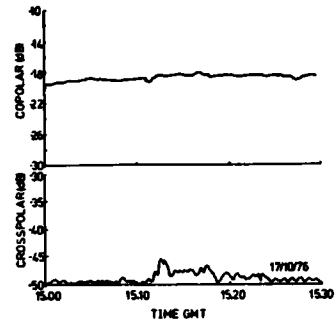


FIG 3b

Figure 3 Clear weather signal behaviour at low elevation angles for 30 GHz transmission from ATS-6.

Elevation angles : Fig.3a, 2.4°, early morning  
Fig.3b, 2.2°, mid afternoon

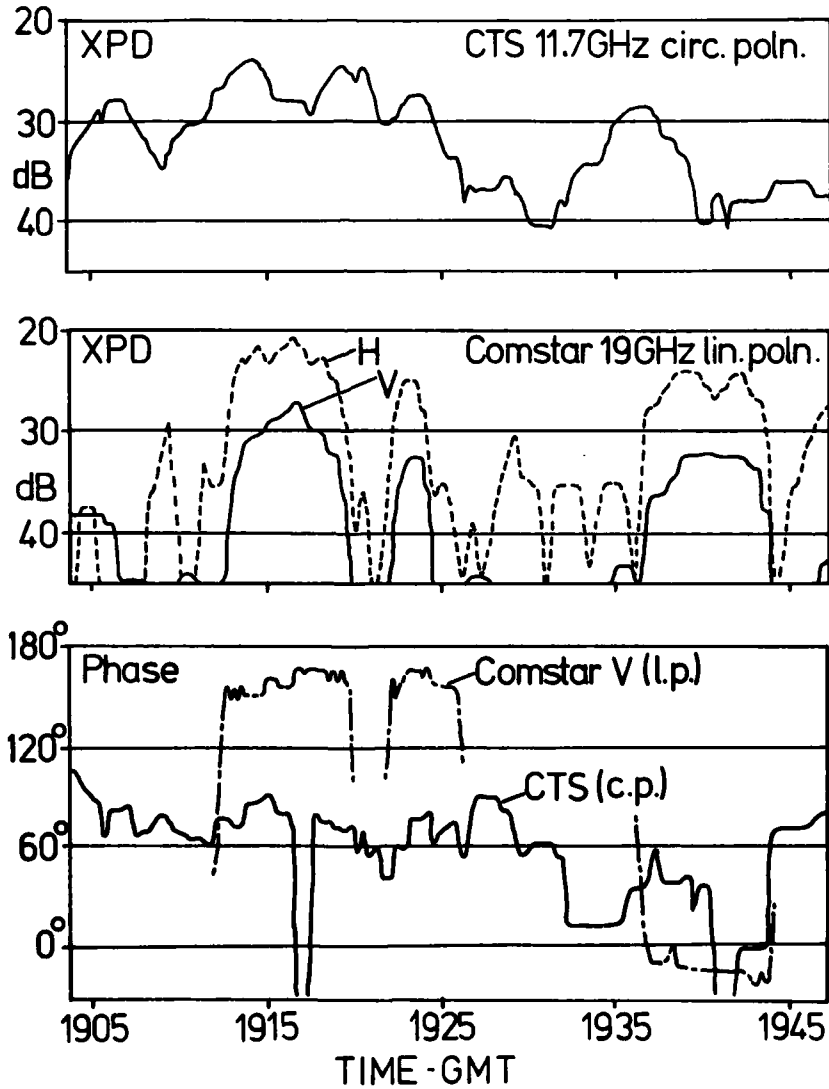


Figure 4 XPD and relative phase of CTS and Comstar signals received at Virginia Polytechnic Institute, U.S.A., on 10th August 1978.

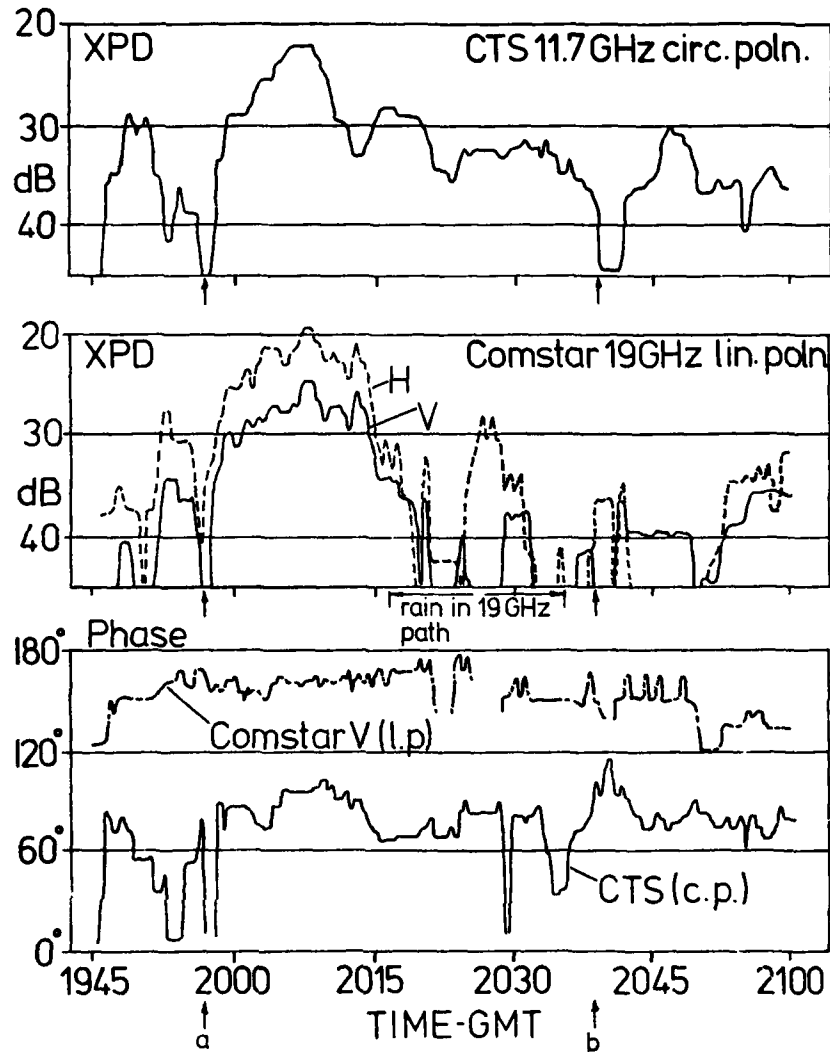


Figure 5 XPD and relative phase of CTS and Comstar signals received at Virginia Polytechnic Institute, U.S.A., on 8th August 1978.

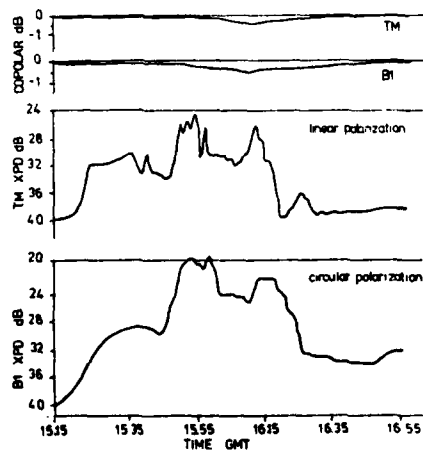


Figure 6 Copolar and XPD records for 11.6 GHz linearly polarized (TM) beacon and 11.8 GHz circularly polarized (B1) beacon signals received at University of Birmingham on 25/03/80, showing strong ice depolarization.

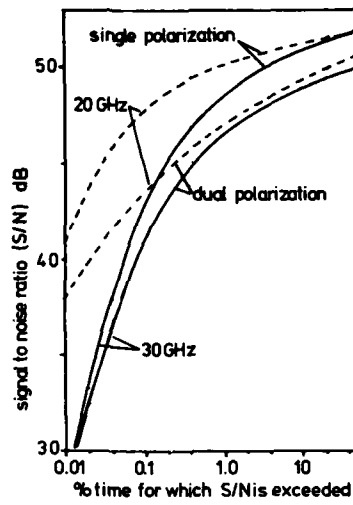


Figure 7 Theoretical performance of single and dual polarized f.m. communications links operating at 20 and 30 GHz in Europe.

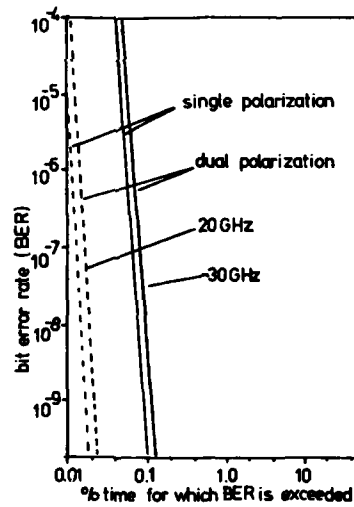


Figure 8 Theoretical performance of single and dual polarized 4 phase cpsk links operating at 20 and 30 GHz in Europe.

ATTENUATION, DEPOLARIZATION AND DISPERSION BY ATMOSPHERIC  
HYDROMETEORS ALONG A 19 AND 28 GHz EARTH-SPACE RADIO PATH

by

D. C. Cox  
H. W. Arnold  
H. H. Hoffman  
R. P. Leck

Bell Laboratories  
Crawford Hill Laboratory  
Holmdel, New Jersey, USA 07733

ABSTRACT

Quantitative relationships are presented relating attenuation, depolarization and dispersion measured at 19 and 28 GHz along an earth-space path to a COMSTAR satellite. Median rain and ice depolarization is minimized for linear polarizations oriented horizontally and vertically at the earth terminals. Median depolarization is maximized for 45° linear polarization and circular polarizations. Maximum depolarization is at least 10 dB to 20 dB greater than the minimum. Phase and amplitude dispersion due to rain and other atmospheric processes is minimal and should not affect the performance of wide bandwidth satellite communication systems.

I. INTRODUCTION

Future satellite communication systems operating at frequencies above 10 GHz may use dual orthogonal polarizations to increase transmission capacity and may use digitally multiplexed signals that occupy much wider bandwidths than the signals used in current satellite systems. Isolation between the two polarizations will be limited by the depolarizing effects of ice clouds and rain. (Hogg and Chu, 1975; Cox et al, 1978) Wideband digital signals are sensitive to phase and amplitude dispersion over their entire bandwidth.

The 19 and 28 GHz beacons on synchronous COMSTAR satellites (Cox, 1978) provide in-orbit sources for measuring attenuation, depolarization and dispersion along earth-space paths. This paper presents statistics from a year's measurements made at the Bell Laboratories, Crawford Hill, New Jersey, U.S.A. receiving site using a 7-meter antenna and the COMSTAR satellite at 95°W longitude. (Cox, 1978; Chu, et al, 1978; Arnold, et al, 1978) Other results from the experimental program are in Arnold and Cox (1978 a & b); Arnold, et al (1979 a & b); Cox, et al (1980).

II. THE EXPERIMENT

Parameters of the experiment are summarized in Table I and described in detail in Cox (1978); Chu, et al (1978); and Arnold, et al (1978). The 7-meter antenna and control building at the main receiving facility on Crawford Hill are shown in Figure 1. Rain attenuation (Arnold, et al, 1979b) is measured by comparing received signal amplitudes in clear air with received amplitudes during attenuating propagation events. The polarization switching of the 19 GHz beacon signal allows measurement of the amplitudes and relative phases of the two received signal components copolarized with the transmitted signals and of the two signal components cross-polarized to the transmitted signals. The diurnal variation of the clear air residual cross-polarized signals is repeatable and, since amplitudes and phases are measured, the residuals can be removed from depolarization events by vector subtraction. The complete set of transmission parameters determined from the 19 GHz measurements is used to calculate depolarization\* for signals with polarizations different from those transmitted by the COMSTAR satellite. (Arnold and Cox, 1978b; Arnold, et al, 1979a) The calculations involve decomposing the desired different incident polarizations into components aligned with the measured polarizations, determining the medium effects on the components from the measured amplitudes and phases, and recombining the components back into the desired incident polarizations. The only assumption required for these calculations is that the propagation medium is linear so that superposition is applicable.

Phase and amplitude dispersion (Cox, et al, 1980) over a 528 MHz bandwidth is measured using the 28 GHz carrier and coherent sidebands. An indication of dispersion over a 9.5 GHz bandwidth results from the measurements on the 19 and 28 GHz carriers.

\* Depolarization in dB is defined as  $20 \log_{10} \frac{E_x}{E_c}$ , where  $E_x$  is the amplitude of the E field component of the received signal that is cross-polarized (orthogonal) to the E field of the transmitted signal and  $E_c$  is the amplitude of the E field component of the received signal that is copolarized (aligned) with the transmitted signal.

The data reported here were recorded on digital magnetic tape and span the year May 18, 1977 to May 18, 1978. The overall data base is nearly complete on the digital tape or backup chart recordings; only three propagation events have data missing after lightning-induced failure of the antenna tracking electronics or because of failure of primary ac power toward the end of the three storms. (Arnold, et al, 1979 a&b) These parts of three events spanning < 15 minutes at > 10 dB attenuation are not a significant part of the overall data base since the times are smaller than the yearly variation.

### III. DEPOLARIZATION AND ATTENUATION

#### 3.1 Joint Statistics of Attenuation and Depolarization

Crosstalk from medium-induced depolarization may be a significant problem for satellite communication systems employing dual-polarization frequency reuse. Since system outages occur when specific attenuation OR depolarization levels are exceeded, the experimental data were summed to indicate the amount of time and percentage of time in the year that either one or both of the two levels (one for attenuation and one for depolarization) is exceeded. These results are shown in Figure 2 for the 19 GHz incident polarization oriented 21 degrees from vertical at Crawford Hill. Attenuation is plotted on the abscissa and time on the ordinate with depolarization as a parameter. The bottom curve is for the smallest depolarization level never exceeded and is, then, the cumulative distribution of attenuation. Similar curves\* for 28 GHz are in Arnold, et al (1979a).

The bottom curve in Fig. 2 indicates that attenuation exceeded 20 dB for 64 minutes of the year. A dual-polarization link capable of operating with 20 dB attenuation and -14.5 dB depolarization would experience 67 minutes outage, a small increase over that due to attenuation alone. A system tolerant of only -19.5 dB depolarization, however, would experience 100 minutes outage, almost twice the outage time from attenuation considerations alone. Thus, depolarization could have a significant effect on some dual-polarization systems.

Relationships between measured attenuation and depolarization are illustrated in Figures 3 and 4. Attenuation and depolarization were quantized in 1 dB bins and for each attenuation value the median, 10 percent and 90 percent depolarization values were plotted. Thus, for attenuations within 0.5 dB of the integer values on the figures, 80 percent of the depolarization values lie between the upper and lower curves and half of the values are above and half below the median curve. The irregularities in the curves are statistical fluctuations due to the small amount of time accumulated in each small bin. Data from charts that are included in Figure 2 but not in Figures 3 and 4 were processed similarly and produced essentially the same attenuation-depolarization relationships.\*\* It is evident from Figures 3 and 4 that, for a given attenuation, the depolarization is somewhat lower at 28 GHz than at 19 GHz.

#### 3.2 Statistics of Minimum and Maximum Depolarization Angles

As discussed earlier, depolarization at 19 GHz may be calculated for any incident polarization. This technique was used to examine every data sample in the one-year digital data base to determine those incident linear polarizations yielding instantaneously minimum depolarization. These depolarization minima occur when the incident polarization is aligned with the average symmetry axes of the raindrops or ice crystals along the path. Figure 5 illustrates the relation between the angle of the depolarization minimum and the copolarized signal attenuation. The middle curve indicates the median angle for each attenuation value. Eighty percent of the data falls between the upper and lower curves. These results show that incident polarizations producing minimum depolarization are clustered around the local vertical and horizontal, as seen at the earth terminal. For 19 GHz attenuations exceeding 15 dB, when rain is the dominant source of depolarization, the optimum incident polarizations are within 3 degrees of local vertical and horizontal more than 80 percent of the time. At lower attenuations, when ice depolarization becomes dominant, the spread around local vertical and horizontal increases to nearly  $\pm 10$  degrees.

The greater angular spread of the average symmetry axis at low attenuations is further evident in Figure 6. This figure illustrates the observed angular distribution of the more-nearly-vertical angle of minimum depolarization for several ranges of copolarized attenuation. The three curves illustrate, for each attenuation range, the total time during the year that the angle was within each 2 degree bin. The upper curve shows the angular distribution for copolarized attenuation less than 1.5 dB. Here all significant depolarization is produced by ice, since depolarization from rain is below -40 dB. These ice-dominated data are excluded from Figure 5. The occasional significant deviation from vertical of the average symmetry axis of ice crystals is evident in the tails of the distribution. The two lower curves indicate the angular distributions for copolarized attenuations of 6 to 10 dB and 16 to 30 dB. The decreased spread at higher attenuations is quite evident.

\* Attenuation and depolarization values here are displaced 0.5 dB from those in Arnold, et al (1979a) because of a 0.5 dB error found in the earlier plots.

\*\* The charts contained 71 minutes or about 25 percent of the total data base for attenuation > 10 dB.



Statistics were accumulated relating attenuation and depolarization at 19 GHz for the optimum incident linear polarizations described above, for several fixed linear polarizations, and for the polarizations producing maximum depolarization. The median relations between attenuation and depolarization are shown in Figure 7 for these incident polarizations. The two upper curves indicate the depolarization observed at an incident polarization 45 degrees from vertical and at the polarizations producing maximum depolarization. These two curves are the same within the 1 dB quantization of the data. Results for circular polarization are essentially identical (Arnold, et al, 1979a) to these two results. The next two curves show the actual measured data at incident polarizations 21 degrees from horizontal and vertical. Going downward, the solid and dotted curve pair indicates the depolarization for fixed vertical and horizontal incident polarizations. The solid and dashed curve pair which starts at the lowest depolarization levels illustrates the depolarization seen at the instantaneously-optimized linear polarizations discussed earlier. The depolarization levels are so low for the bottom four curves that the values are limited by the accuracy of the measurements.

The variation in depolarization with incident polarization angle is quite evident in Figure 7. Instantaneous linear polarization optimization has clearly reduced depolarization, often lowering it below -40 dB to the limits of measurement precision. More interesting, perhaps, is the low depolarization (below -35 dB) observed at fixed vertical and horizontal incident polarizations. These results are consistent with the previous observations of the narrow angular distribution of the average symmetry axes of ice and rain. Linear polarization incident at 45 degrees to vertical or circular polarization, however, results in maximum depolarization; e.g., at 20 dB attenuation the median depolarization was -13 dB. These results show the need for careful choice of incident polarizations to all earth terminals.

### 3.3 Ice Depolarization

The cumulative time distribution of ice depolarization for the polarization 21 degrees from vertical is shown in Figure 8. The data were quantized in 1 dB bins. The somewhat arbitrary criterion used to select depolarization events due to ice alone was that the attenuation of the 19 GHz signals not exceed 1.5 dB. Depolarization due to differential attenuation in rain should be less than -40 dB at this attenuation level. The curve labeled "ICE, PARTIAL" represents all of the 1 year data base on magnetic tape, while the "ICE, COMPLETE" curve includes the data reduced from chart recordings. There is clearly some time missing from the partial data base at high depolarization levels, but the two curves agree within 1 dB at equal outage times. These results may be compared with the two curves labeled "ICE + RAIN." These curves indicate the total depolarization observed at all attenuation levels during the year. Depolarization due to ice alone accounts for 8 percent of the total time that depolarization is observed at the -25 dB level, and even more at lower depolarization levels. The curves from the magnetic tape data that are labeled "PARTIAL" represent the data included in Figures 3-7. The curves labeled "COMPLETE" include all the data as in Figure 2.

## IV. DISPERSION

### 4.1 Rain Attenuation Events

Phase measurements were made between three tones (carrier, upper (USB) and lower (LSB) modulation sidebands) spaced over a 528 MHz bandwidth at 28 GHz, and between 28 and 19 GHz carriers. A sample of measurements during a thunderstorm is shown in Figure 9. The four middle traces show the attenuations of each of the three tones at 28 GHz and a carrier at 19 GHz. The two upper traces indicate the phase measured between the three 28 GHz tones. The rapid fluctuations result from the lower signal-to-noise ratio that exists due to attenuation at 28 GHz. Phase dispersion is less than 4 degrees over the 264 MHz tone spacing.

The lower trace indicates the phase between 19 and 28 GHz carriers. This measurement is contaminated by satellite motion, but indicates phase dispersion on the order of 60 degrees at 30 dB attenuation over the 9.5 GHz tone separation. This wideband result is consistent with the narrower bandwidth observation. These results are typical of all observations.

Statistical phase relationships from rain events are shown in Figure 10. The data include 20 events with attenuation exceeding 5 dB. Quantization was 1 dB by 0.5°. The median phase is indicated by the solid lines. The dashed lines indicate the 5 percent and 95 percent bounds of measured phase in each 1 dB bin. The open circles indicate the attenuation vs. phase characteristics of the measuring equipment. The medians appear consistent with the signal behavior in Figure 9. It appears that for the USB channel, the instrumentation characteristics nearly compensate for the median rain dispersion.

Correction of an instrumental error in the lower sideband measurement results in a median given by the solid circles and in 5 percent and 95 percent bounds indicated by +. A large but undeterminable amount of the total spread in the phase fluctuations in Figure 10 is due to equipment. This is supported by the fact that the bounds remain relatively constant for the first 20- to 25-dB attenuation; i.e., the instrumental drift in the collection of events is greater than the phase fluctuations caused by differences in the rain characteristics and by the decreasing signal-to-noise ratios illustrated in the individual events in Figure 9. Even if the measurement uncertainty is ignored and all of the spread in the phase measurements in Figure 10 is attributed to propagation effects, this spread is insignificantly small.

The relative constancy of attenuation dispersion and, thus, probable lack of variable phase dispersion are illustrated in Figure 11. These curves relate attenuation and difference between attenuations, in dB, for the sidebands and carrier as indicated. The attenuation curves contain data from 40 events with attenuation exceeding 5 dB or about twice as many as were included in the sideband phase curves.

The quantization of attenuation difference is 0.2 dB. The overall measurement accuracy of the attenuation differences is about +0.1 dB over the 40 dB attenuation range. The solid line represents the median attenuation for each 1 dB attenuation bin and the dashes indicate the 5 percent and 95 percent bounds. When a dash is missing, the bound is the same as the median; i.e., the difference between the median and the 5 percent or 95 percent value is less than 0.2 dB. The 0 percent and 100 percent bounds (not shown) are essentially the same as the 5 percent and 95 percent bounds from 0 attenuation to about 30 dB. For attenuations between 30 dB and 40 dB the 0 percent and 100 percent bounds spread slightly to values only .2 dB to .4 dB wider than the 5 percent and 95 percent bounds. The small spread in these attenuation ratios for many propagation events is consistent with the lack of significant phase dispersion over the 528 MHz bandwidth. All of the phase and amplitude dispersion measurements indicate an absence of dispersive mechanisms other than the frequency dependent bulk absorption and phase shifting properties of rain.

#### 4.2 Cloud Scintillation Events

In spring and summer, the passage of large cumulus clouds through the earth-space propagation path produces scintillation (fluctuation) of the received signal amplitudes. Clouds that produce strong (> 1 dB) scintillation are undoubtedly quite wet but often are not producing rain while passing through the path. Since the amplitude fluctuates both above and below the steady clear air value, focusing or multipath propagation caused by strong refractive index gradients in the clouds must be a dominant amplitude changing mechanism. The scintillation results from motion of the cloud refractive index structure with the wind.

Because of the suggestion of multipath propagation in cloud scintillation, such events seem to be possible candidates for dispersion. Many scintillation events were investigated and none show any significant dispersion. The example of particularly intense scintillation ( $\approx +1$  dB) in Figure 12 illustrates this lack of dispersion. The traces in Figure 12 represent the same signal parameters as the traces in Figure 9; however, the scales have been expanded in Figure 12 for some parameters.

The phase differences between the 28 GHz carrier and sidebands in Figure 12 show less than 0.5° peak-to-peak fluctuation. The phase difference between 28- and 19-GHz carriers contains satellite-motion related incidental phase fluctuations but these fluctuations do not increase significantly during the strong amplitude scintillation event and the average phase does not change. The lack of significant phase fluctuation is consistent with the high correlation observed among the amplitude fluctuations of the 19- and 28-GHz carriers and the sidebands. The fluctuation intensity appears comparable in all the amplitude traces and even the minute details of the fluctuation in one trace are reproduced in all other traces. For the 1.5 minutes of strongest scintillation in Figure 12, the calculated correlation coefficient between the 19 and 28 GHz carrier amplitudes is 0.95 and between the upper and lower sideband amplitudes is >0.999. These measurements all indicate a very broadband (> 10 GHz) scintillation mechanism such as focusing.

#### V. CONCLUSIONS

In addition to the quantitative relationships provided by the propagation measurements, the following conclusions about the effects of atmospheric phenomena on the performance of satellite communication systems can be drawn:

- 1) Rain and ice depolarization can significantly affect the performance of dual polarized satellite communication systems if the polarizations are not chosen properly.
- 2) The effects of rain and ice depolarization can be minimized by choosing linear polarizations oriented horizontally and vertically at the earth terminals. The resulting minimum depolarization is usually less than -30 dB.
- 3) Rain and ice depolarization are maximized for 45° linear polarization and circular polarizations. The resulting maximum depolarization is at least 10 dB to 20 dB greater than the minimum.
- 4) Phase and amplitude dispersion due to rain and other atmospheric processes is minimal and should not affect the performance of wide bandwidth satellite communication systems.

#### REFERENCES

1. Arnold, H. W. and D. C. Cox, April 27, 1978(a), "Some Results from 19 and 28 GHz COMSTAR Beacon Propagation Experiments," Proceedings of the Seventh AIAA Communications Satellite System Conference, San Diego, California.
2. Arnold, H. W. and D. C. Cox, November 1978(b), "Dependence of Depolarization on Incident Polarization for 19 GHz Satellite Signals," BSTJ, 57, pp. 3267-3276.

## REFERENCES (Cont'd)

3. Arnold, H. W., D. C. Cox, H. H. Hoffman, R. W. Brandt, R. P. Leck and M. F. Wazowicz, May-June 1978, "The 19 and 28 GHz Receiving Electronics for the Crawford Hill COMSTAR Beacon Propagation Experiment," BSTJ, 57, pp. 1289-1329.
4. Arnold, H. W., D. C. Cox, H. H. Hoffman and R. P. Leck, June 10-14, 1979(a), "Characteristics of Rain and Ice Depolarization for a 19 and 28 GHz Propagation Path from a COMSTAR Satellite," IEEE International Conference on Communications (ICC '79), Boston, Massachusetts, and IEEE Trans. Antennas and Propagation, January 1980.
5. Arnold, H. W., D. C. Cox, H. H. Hoffman and R. P. Leck, November 1979(b), "Rain Attenuation Statistics from a 19 and 28 GHz COMSTAR Beacon Propagation Experiment: One Year Cumulative Distributions and Relationships Between the Two Frequencies," IEEE Trans. on Communications, pp. 1725-1728.
6. Chu, T. S., R. W. Wilson, R. W. England, D. A. Gray and W. E. Legg, May-June 1978, "The Crawford Hill 7-Meter Millimeter Wave Antenna," BSTJ, 57, pp. 1257-1288.
7. Cox, D. C., H. W. Arnold and H. H. Hoffman, May-June 1978, "Depolarization of 19 and 28 GHz Earth-Space Signals by Ice Particles," Radio Science, 13, pp. 511-517.
8. Cox, D. C., May-June 1978, "An Overview of the Bell Laboratories 19 and 28 GHz COMSTAR Beacon Propagation Experiments," BSTJ, 57, pp. 1231-1255.
9. Cox, D. C., H. W. Arnold and R. P. Leck, 1980, "Phase and Amplitude Dispersion for Earth-Space Propagation in the 20 to 30 GHz Frequency Range," to be published in IEEE Trans. on Antennas and Propagation.
10. Hogg, D. C. and T. S. Chu, September 1975, "The Role of Rain in Satellite Communications," Proc. IEEE, 63, pp. 1308-1331.

TABLE I

Parameters of this ExperimentCOMSTAR Satellite Beacon - 95 Degrees W Longitude

Frequencies	19.04 GHz	28.56 GHz
Polarization	Switched between two orthog. linear	Linear (aligned with one 19 GHz)
Modulation	1 kHz Polarization Switching	264.4 MHz Phase (coherent with carrier)

Crawford Hill Receiving Facility - 40.39 Degrees N Latitude,  
74.19 Degrees W Longitude

Altitude	115 Meters	
Climate	Continental Maritime	
Antenna	7-Meter Parabola	
Polarization	Dual Linear	Dual Linear
Beamwidth	0.15 Degrees	0.1 Degrees
Path Azimuth	210.5 Degrees	
Path Elevation	38.6 Degrees	
Path Polarizations	Rotated 21 Degrees from Vertical and Horizontal	Rotated 21 Degrees from Vertical
Receiver Channels	Two Copol Two Xpol	One Copol Carrier Two Copol Sidebands One Xpol Carrier
Received S/N in Clear Air		
Copol Carrier Channels	>60 dB	>60 dB
Copol Sideband Channels	-	>53 dB
Xpol Carrier Channels	>70 dB	>70 dB
Residual Received Xpol due to Beacon and Receiving Antennas (over entire -3 dB beamwidth)	<-35 dB	<-35 dB

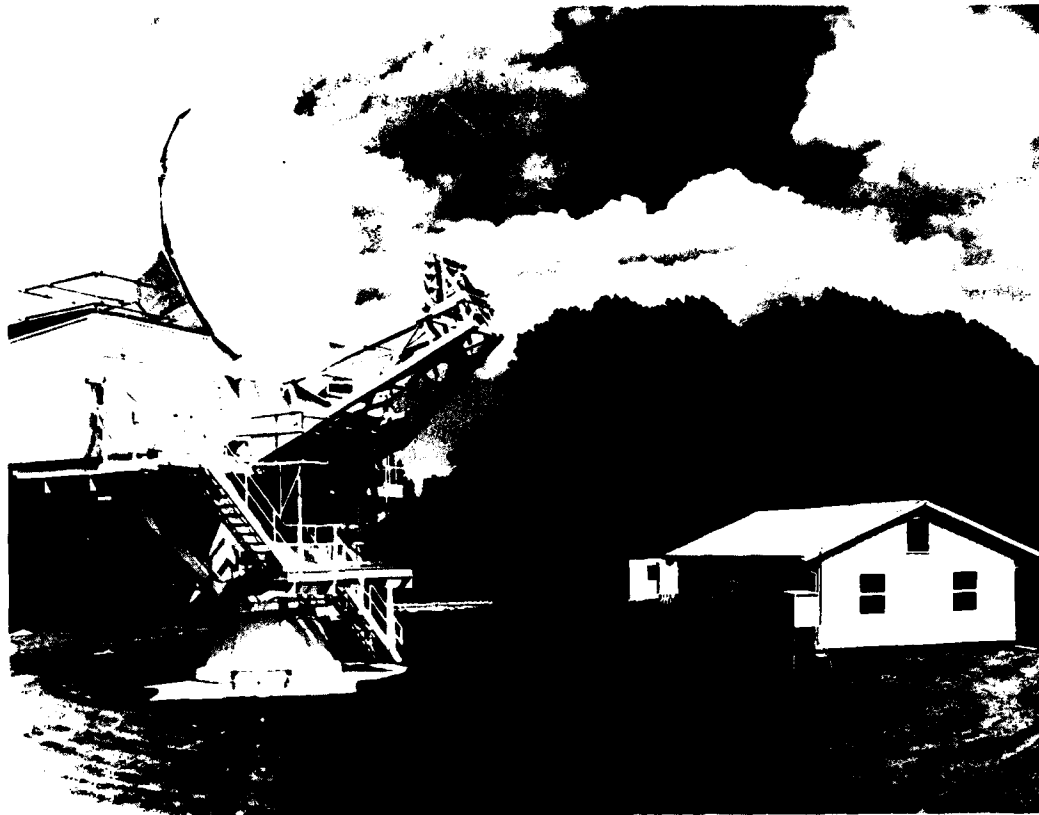


Figure 1 - Receiving facility at Crawford Hill, New Jersey, USA, about 50 Km south-south-east of New York City, showing 7-meter diameter antenna and control building.

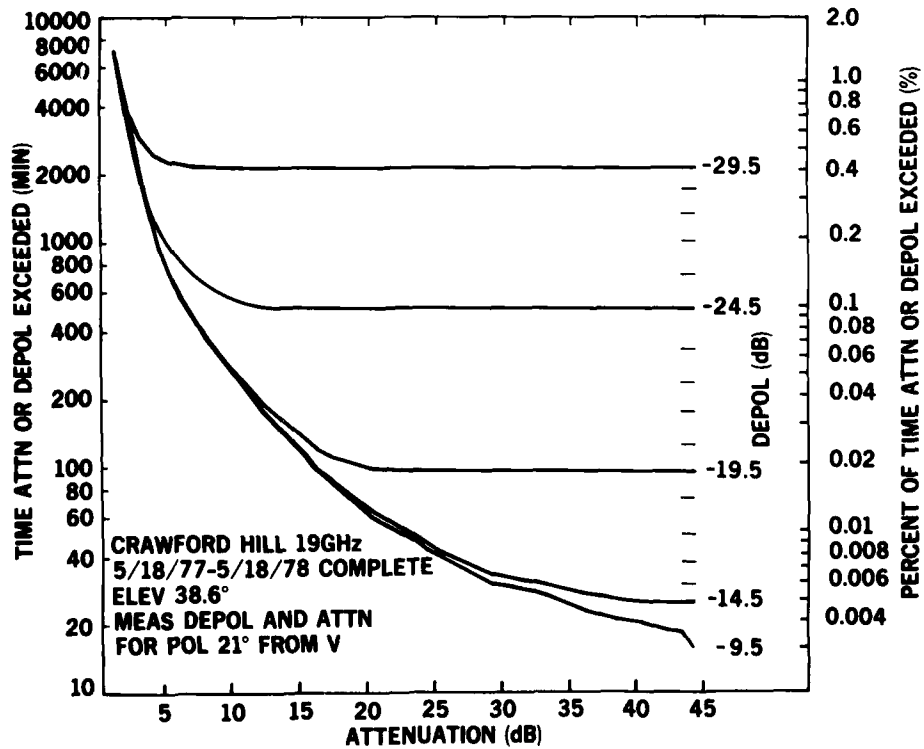


Figure 2 - Joint 19 GHz attenuation-depolarization cumulative distributions from complete data base.

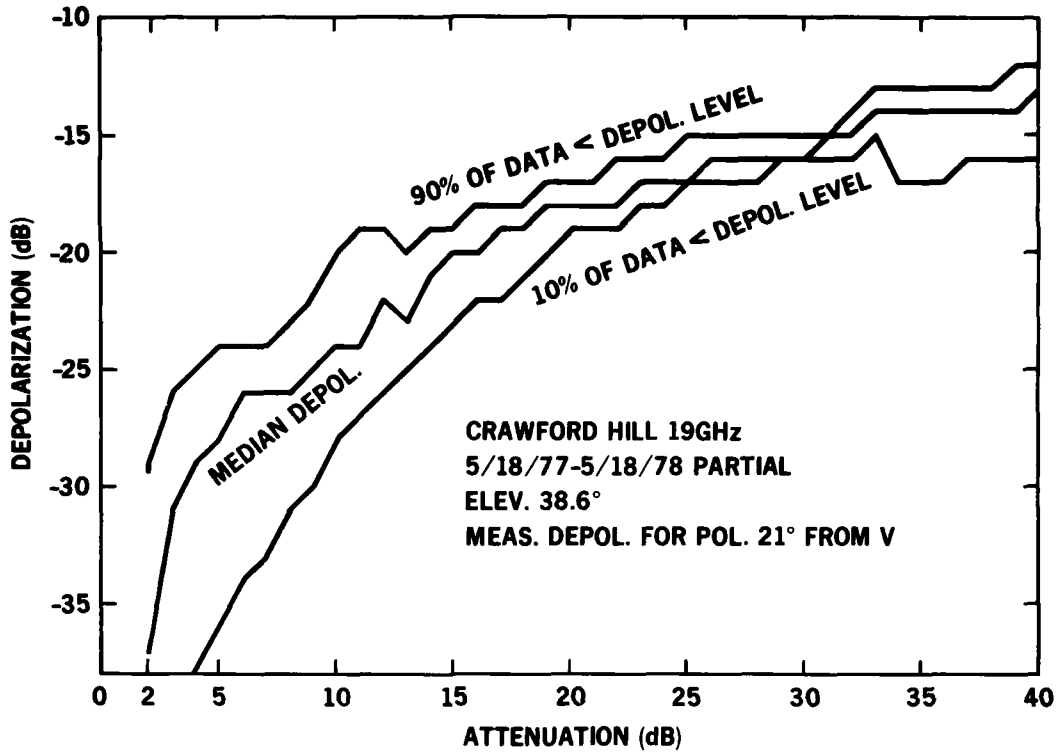


Figure 3 - Statistical relationships between copolarized signal attenuation and depolarization at 19 GHz.

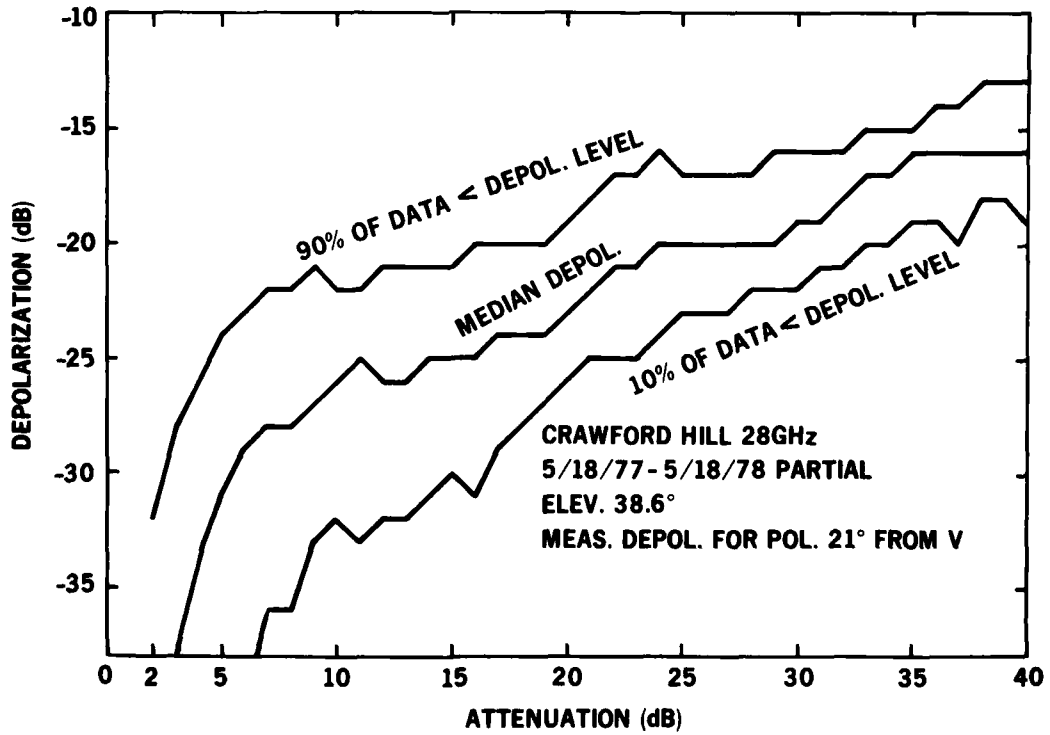


Figure 4 - Statistical relationships between copolarized signal attenuation and depolarization at 28 GHz.

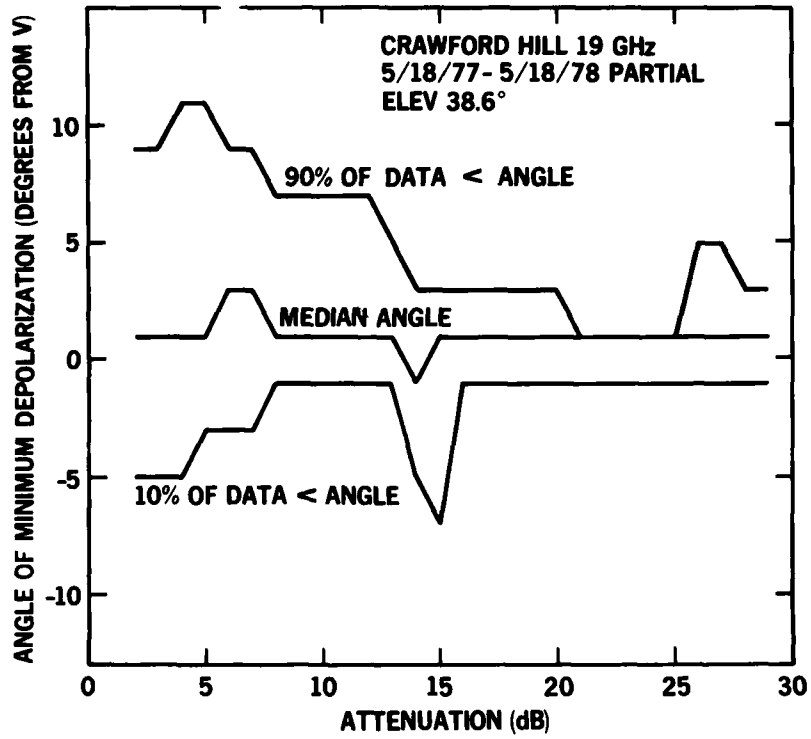


Figure 5 - Statistical relationships between 19 GHz signal attenuation and the polarization angle of minimum depolarization.

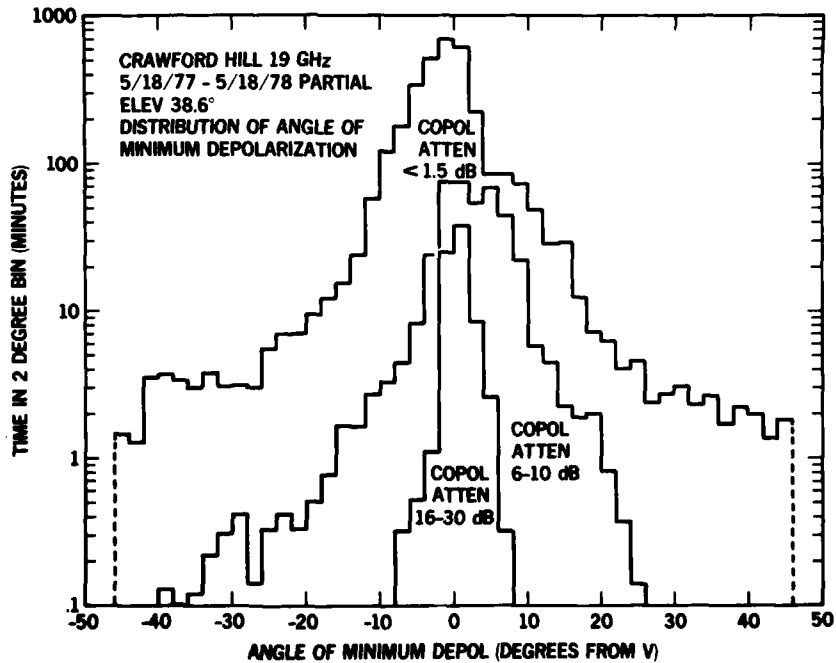


Figure 6 - Distributions of the more-nearly-vertical angle of minimum 19 GHz depolarization.

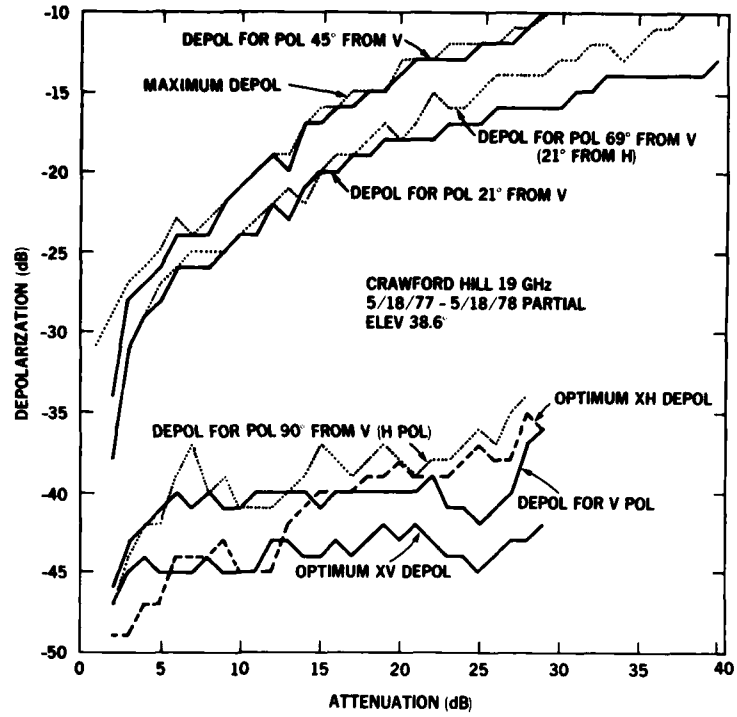


Figure 7 - Statistical relationships between 19 GHz copolarized signal attenuation and median depolarization for different linear polarization angles.

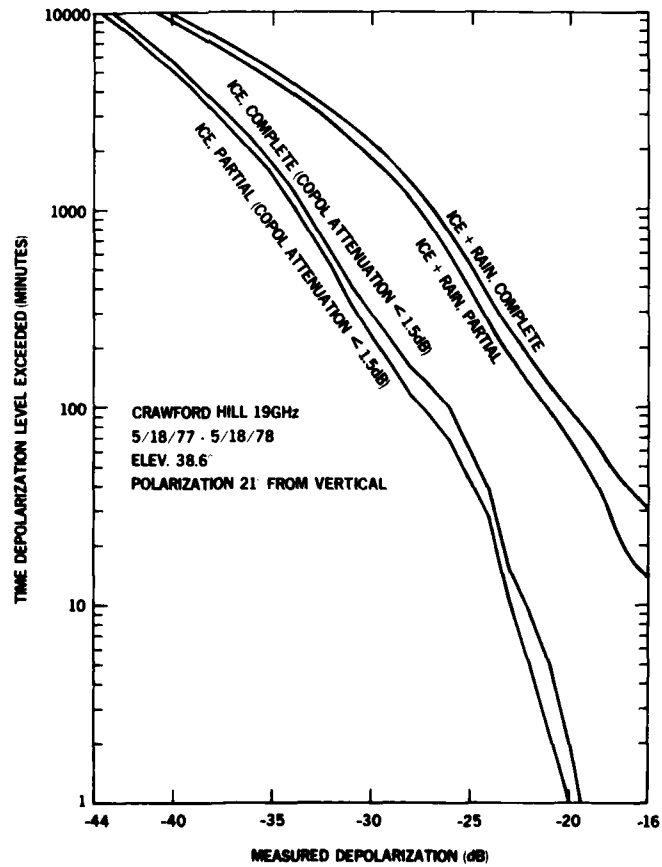


Figure 8 - Cumulative time distributions of 19 GHz rain and ice depolarization.

CRAWFORD HILL 9-26-77 ELEV. 38.6°

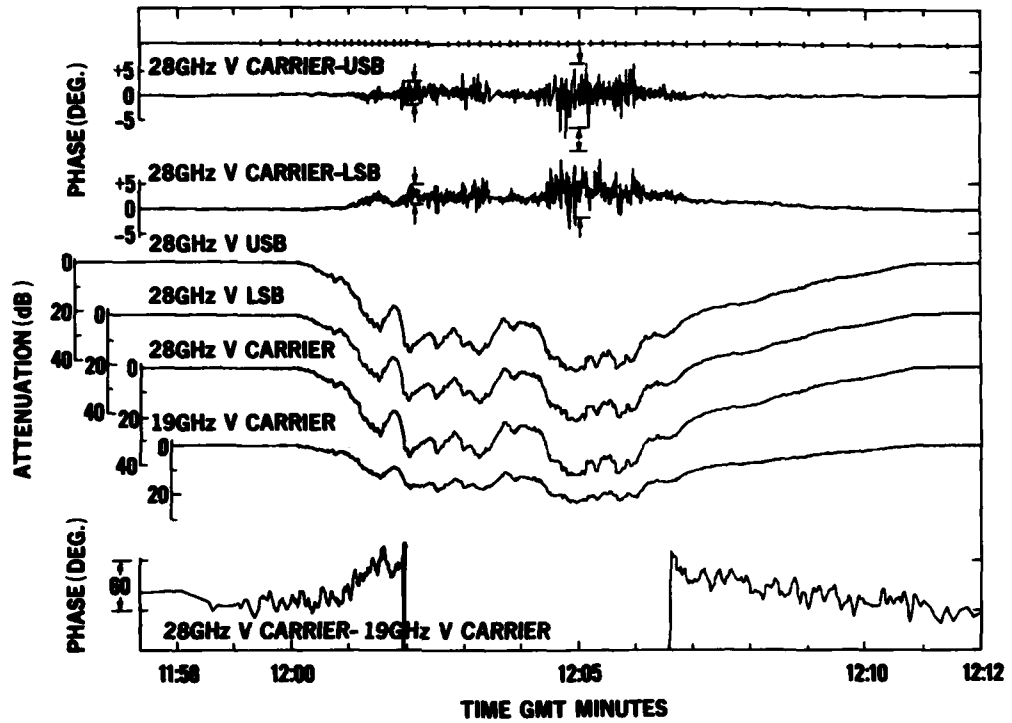


Figure 9 - Time history of signal parameters as a thunderstorm passes through the propagation path.

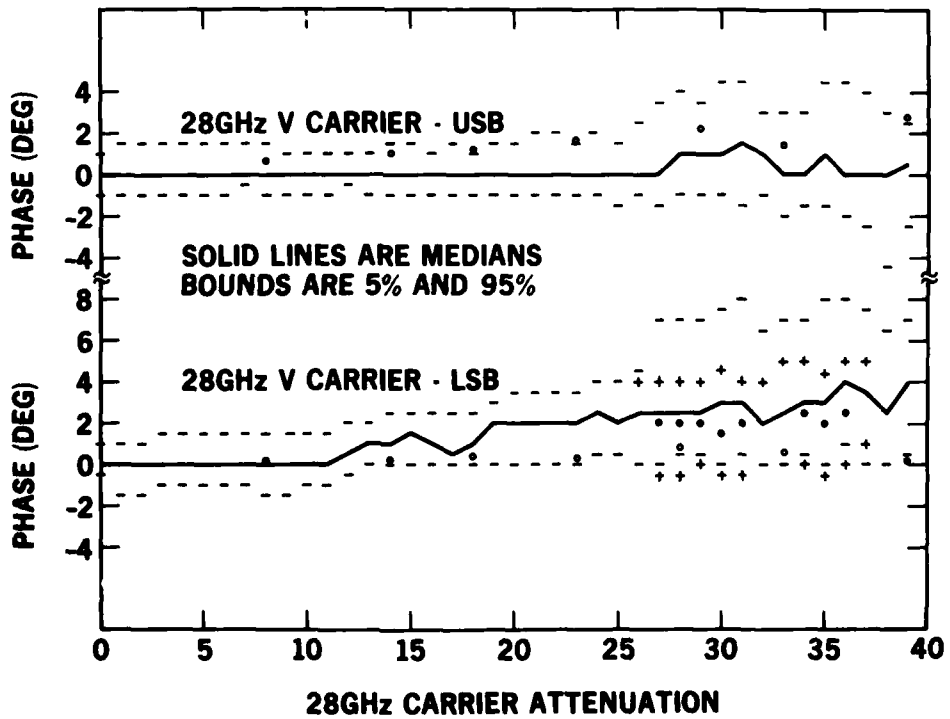


Figure 10 - Statistical relationships between 28 GHz carrier attenuation and the phase differences between the carrier, upper (USB), and lower (LSB) modulation sidebands.



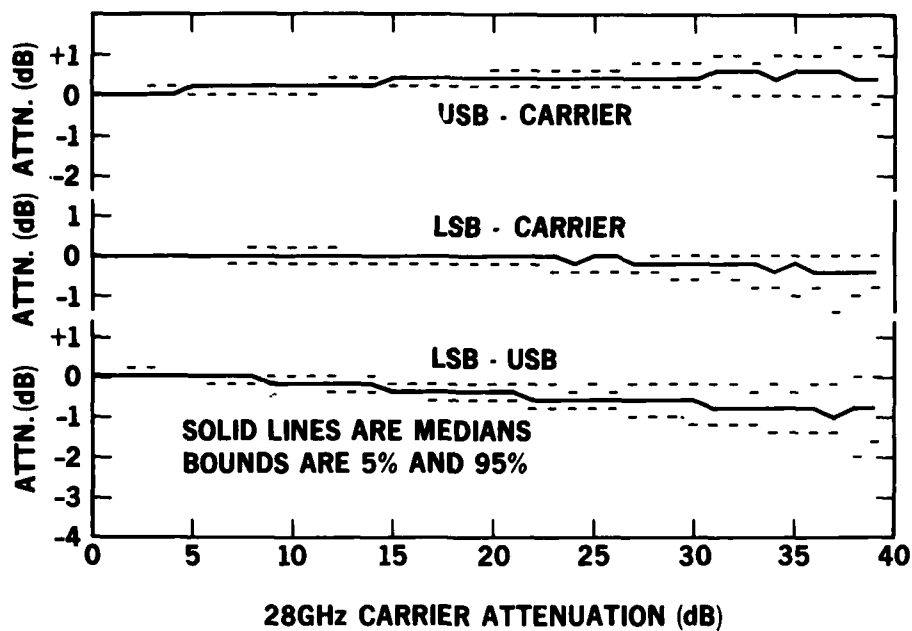


Figure 11 - Statistical relationships between 28 GHz carrier attenuation and the attenuation differences in dB between carrier and modulation sidebands.

CRAWFORD HILL 8-1-77 ELEV. 38.6°

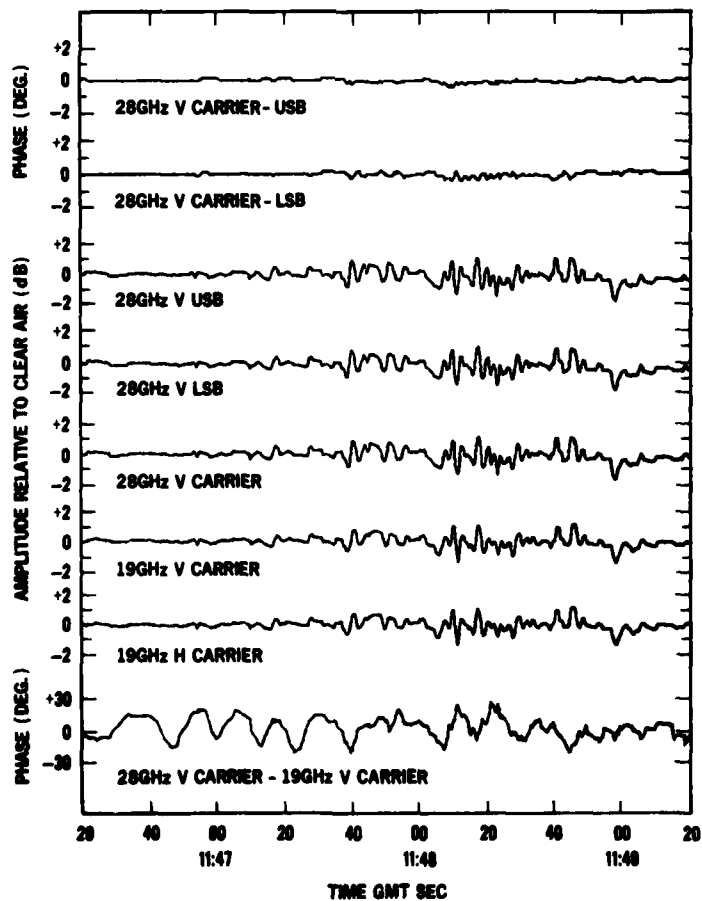


Figure 12 - Time history of signal parameters for a cloud scintillation event.

## RESULTS OF PROPAGATION EXPERIMENTS AT ITALIAN TERMINALS USING THE SIRIO SATELLITE

F. Carassa, M. Mauri, A. Paraboni  
 Centro di Studio per le Telecomunicazioni Spaziali of CNR, Politecnico di Milano (Italy)

### 1. Summary

The Italian satellite SIRIO is operating since September 1977; it allows attenuation measurements in the 11.12 (down link) and 17.18 GHz (up-link) bands. Three stations perform measurements in Italy: two of these, located in the northern and central part of Italy (Lario and Fucino respectively) are equipped with large antennas and have both transmitting and receiving capability; the third one, operating at Spino d' Adda (near Milan) is equipped with a medium size antenna and can only receive.

Attenuation data in the two bands, acquired throughout two years of experiment, are here presented and compared to each other. Preliminary data about fade duration and fade rate of variation are also presented.

### 2. Introduction

The Italian SIRIO satellite was launched in August 1977 to perform propagation and communication experiments in the 11-12 (down-link) and 17-18 (up-link) GHz bands.

The three Italian stations involved in the experiments are located respectively at Fucino (near Rome), Gera Lario (lake Como), and Spino d' Adda (near Milan). The stations of Fucino and Lario are equipped for the whole set of propagation and communication measurements, while Spino d' Adda performs only down-link attenuation and sky noise temperature measurements. Wide information about the satellite and the earth stations can be found in /1/.

In Table I the main characteristics of the three stations are summarized while Table II shows the list of propagation measurements.

Table I  
 Station characteristics

	Fucino, Lario	Spino d'Adda
Antenna diameter	17 m	4 m
Transmitted power	1 kW	-
Receiver noise temperature	180K	1500 K
G/T (dB/K)	40	15.2
EIRP (dBW)	96	-

Table II  
 List of measurements

1. Absolute attenuation	17.8 GHz
2. Differential attenuation	17.4±0.4 GHz
3. Absolute attenuation	11.6 GHz
4. Differential attenuation	11.6±0.26GHz
5. Phase distortion	11.6±0.26GHz
6. Sky noise temperature	11.6 GHz
7. Depolarization (circular polarization)	11.6, 11.86GHz

The data acquired in all the three stations are collected by the Centro Studi Telecomunicazioni Spaziali (CSTS) of the Consiglio Nazionale delle Ricerche (CNR) at the Politecnico di Milano; CSTS has the complete responsibility of the experiments programme, of the processing of all the SIRIO data and of their scientific interpretation.

All the data are recorded on magnetic tape. In processing the data CSTS is supported by the computing facilities of the CNR (CNUCE) and of the Politecnico (CILEA).

In this paper the main statistical results concerning the absolute attenuation are presented. It was found that deep fade occurred only during heavy rain events: as a consequence a significant year-to-year and site-to-site variability was observed because of the remarkable time and space non-uniformity of the climatology existing throughout Italy.

In order to improve the statistical significance of the results and considering the good status of health of the satellite, the experiment has been extended of one year.

### 3. Cumulative distribution

The cumulative probability distributions of 11.6 GHz absolute attenuation for the three stations are shown in fig. 1. Notice that the statistics regarding Spino d' Adda cover only one year instead of two having this station initiated the acquisition in September 1978. The number on the curves indicates how many rainy events contributed to that probability level. It is possible to see that the attenuation values of the same probability levels for Lario are about twice the Fucino ones, whereas the curve for Spino d' Adda is between the previous two in the probability range  $10^{-3}$  +  $10^{-4}$ . However the number of events at the same probability level is almost the same in the various stations.

In fig. 2 the probability distributions of the 17.8 GHz attenuation for the Fucino and Lario stations are shown. They are plotted for comparison together with the cumulative distributions at 11.6 GHz. The lower part of the curve representing the 17.8 GHz attenuation for Lario has been drawn with a dotted line because of a failure in the acquisition system (during July and August 1979) which prevented in this period the measurements at the highest attenuation levels. In this range the up-link attenuation has been extrapolated from 11.6 attenuation data.

Notice that the attenuation statistics for Fucino are substantially unchanged with respect to those obtained during the first year of experiment, while Lario worsens heavily.

#### 4. The relationship between up and down link attenuations

The joint analysis of the attenuation in the 11.6 and 17.8 GHz bands showed a very tight correlation between them. Then a relationship can be easily found out simply by joining couples of values having the same probability level. By applying this procedure the diagrams of fig. 3 have been obtained.

The best fit lines turn out to be:

$$A_{17.8} = 2.19 A_{11.6} - 0.9 \quad \text{Fucino}$$

$$A_{17.8} = 2.28 A_{11.6} - 0.9 \quad \text{Lario}$$

where  $A_{11.6}$  and  $A_{17.8}$  are the attenuations in the related bands.

#### 5. Fade duration

The duration of fade is a relevant parameter in designing earth-to-satellite segments in the future applications.

It has been investigated using the 11.6 GHz attenuation data base, which is wide enough to allow this kind of studies with good confidence margins. In figs. 4 and 5 four curves related to the attenuation levels of 3.5, 6.5, 9.5, 12.5 dB are shown: each curve gives the probability of exceedance of the indicated attenuation level, subjected to the condition that only fade intervals longer than the value indicated in abscissa are considered.

These curves intercept the ordinate axis in points corresponding to the probability levels given in fig. 1.

It appears that the slope of the various curves is almost the same for attenuation higher than 3.5 dB both at Fucino and Lario. If confirmed, this property could allow a simple mathematical model for its description and perhaps be assumed as characteristic of the rain profiles regardless to the site.

#### 6. Fade gradients

The time gradients have been studied by picking up and classifying the time which was taken by the attenuation to cross two successive thresholds 1 dB apart. The results are shown in figs. 6 and 7, where histograms representing this variable have been drawn. Negative values stand for negative gradients (descent) and viceversa.

It can be appreciated that the maximum probability classes are close to the zero ( $\pm 16$  secs) therefore indicating the presence of very steep gradients.

#### 7. Conclusions

Attenuation statistics at 11.6 and 17.8 GHz obtained by means of SIRIO data are given; they refer to two years of experiment. A relationship between the attenuation at the two frequencies has been found: it indicates that the two variables can be considered almost proportional with a ratio about 2.2.

Fade durations and gradients have been calculated. The possibility of building a simple mathematical model of characterizing the statistical behaviour of the duration for attenuation higher than 3.5 dB appears to exist.

Steep gradients have been found to be the most probable ones. Rise and descent times confined between 0-16 sec can be considered the rule.

#### Bibliography

/1/ Alta Frequenza - Special Issue on the SIRIO Programme - Vol. XLVII N. 4 April 1978.

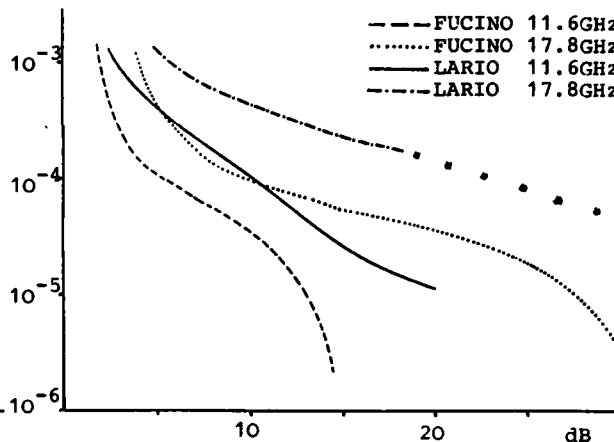
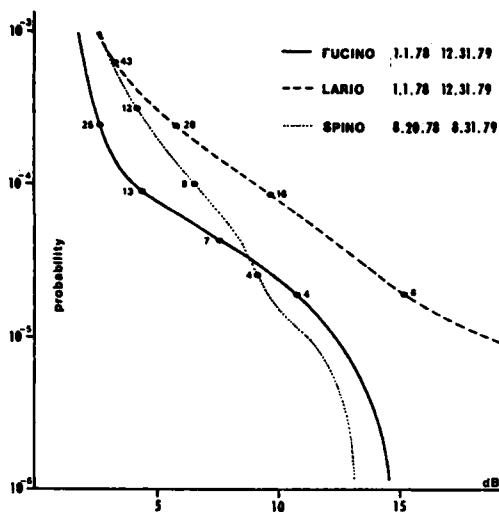


Fig. 1 - Cumulative probability distributions of the 11.6 GHz attenuation. Ordinate gives the fraction of total time during which abscissa was exceeded

Fig. 2 - Cumulative probability distributions of the 11.6 and 17.8 GHz attenuations. Reference period 3.15.78-9.15.79

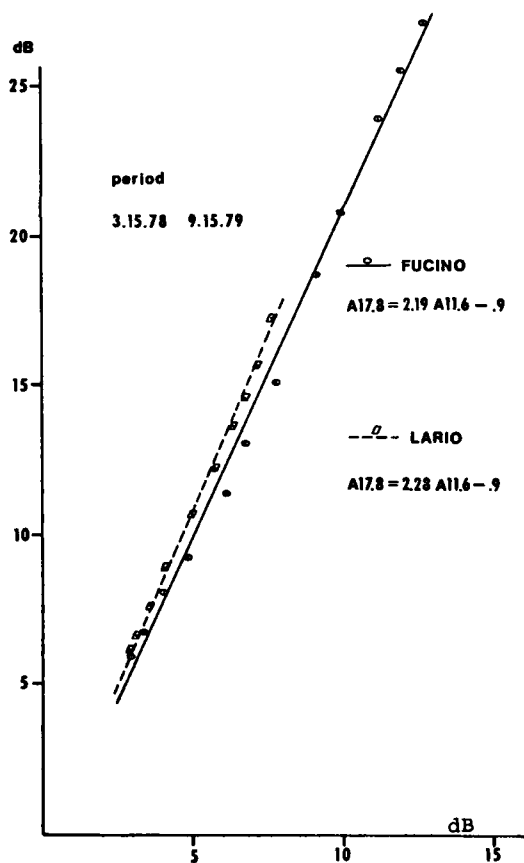
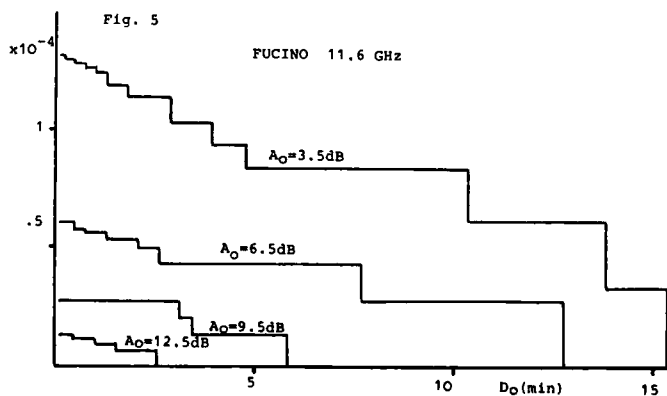
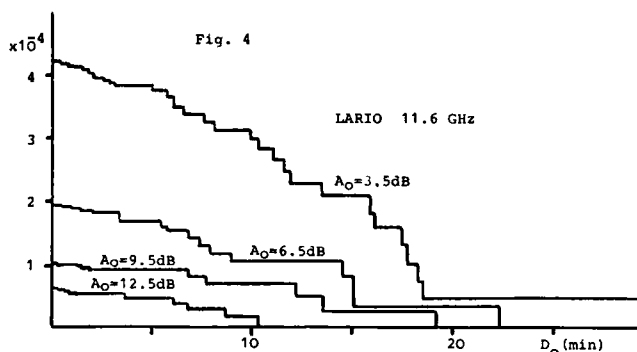


Fig. 3 - Relationship between attenuations measured at 11.6 and 17.8 GHz. Dots represents pairs of values having the same probability level.



Figs. 4-5 - Probability that the attenuation level A is exceeded, considering only fade intervals longer than the value given in abscissa.

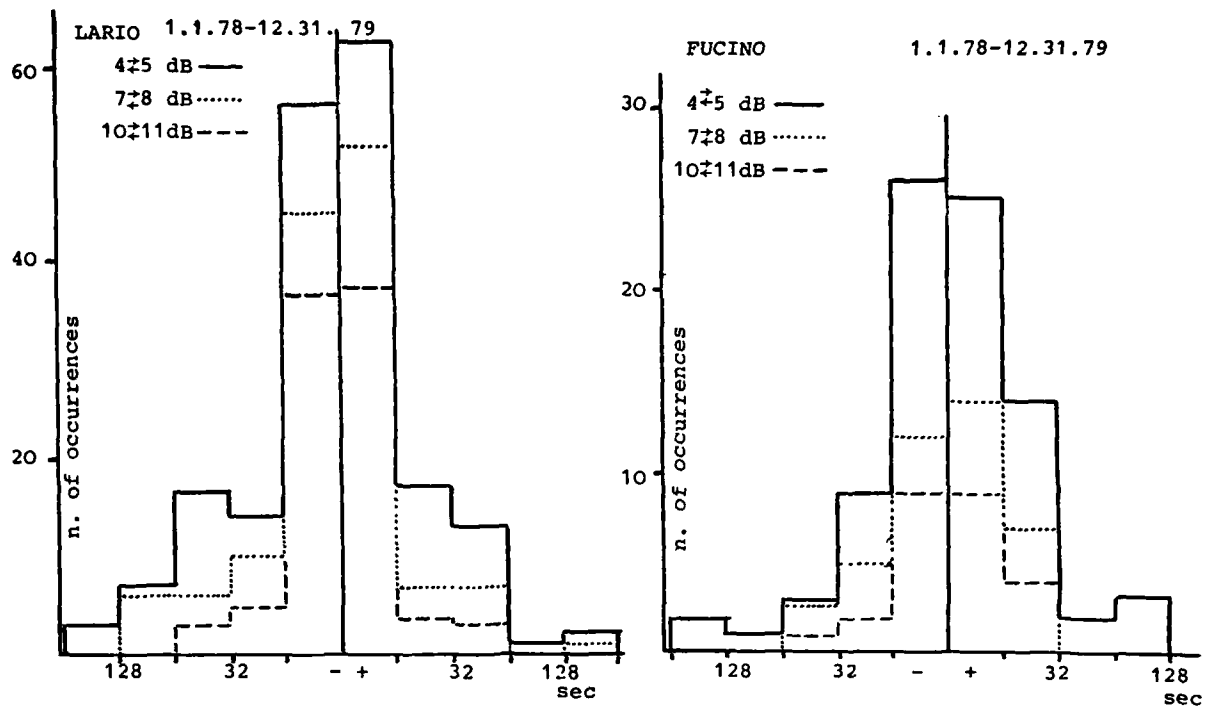


Fig. 6 - Histogram of attenuation gradients: abscissa gives the time taken to cross successive thresholds 1dB apart.

Fig. 7 - Histogram of attenuation gradients: abscissa gives the time taken to cross successive thresholds 1 dB apart.

UTILISATION D'UN RADAR POUR ETUDIER L'ATTENUATION ET LA DEPOLARISATION

DES HYPERFREQUENCES OBSERVEES SUR UN TRAJET OBLIQUE

P. GOLE, J.P. MON et P. RAMAT  
Centre National d'Etudes des Télécommunications  
38-40, rue du Général Leclerc  
92131 ISSY-les-MOULINEAUX - FRANCE -

RESUME

Après avoir rappelé l'intérêt que présentent les radars pour l'étude de la propagation (prévision de l'atténuation, de la dépolarisation, évaluation des performances de la réception en diversité d'emplacement,...) nous décrivons une des expériences effectuées au cours des mois d'Avril et Mai 1979 dans la région parisienne. Ces expériences associaient les mesures de réflectivité effectuées à l'aide d'un des radars du système RONSARD et les données obtenues dans la bande des 11 GHz à l'aide du satellite O.T.S. et enregistrées à la station spatiale expérimentale du Centre National d'Etudes des Télécommunications.

En déterminant les paramètres a et b de la relation empirique  $A = az^b$  liant l'atténuation A observée et la réflectivité Z mesurée, nous avons pu étalonner le radar dans le cas de précipitations convectives.

Des mesures complémentaires sont nécessaires pour établir une corrélation satisfaisante entre découplage de polarisation et réflectivité.

1. INTRODUCTION

Le taux de croissance élevé du nombre de communications téléphoniques acheminées par satellite ainsi que le développement prévisible de nouveaux services (transmission de données, téléconférence, vidéophone,...) conduisent à envisager l'utilisation de bandes de fréquence de plus en plus élevées (CARASSA, F. 1977 ; BRUSSAARD, G. 1979). Qui plus est, afin d'utiliser le plus efficacement possible les bandes de fréquence allouées aux divers services, on envisage de développer des systèmes de réutilisation de fréquence fonctionnant sur deux polarisations orthogonales.

Si la mise en oeuvre technique de tels systèmes fonctionnant à des fréquences élevées ne semble pas poser de gros problèmes, leur utilisation pour acheminer un trafic commercial peut par contre se heurter à des difficultés créées essentiellement par la dégradation des conditions de propagation dans l'atmosphère. Il est donc indispensable, avant de développer ces dispositifs, de parvenir à une connaissance approfondie des caractéristiques du milieu de propagation. Parmi les techniques permettant cette caractérisation, le radar occupe une position privilégiée qui tient essentiellement à sa capacité à explorer un secteur quelconque de l'espace : les radiomètres ou les liaisons expérimentales satellite - Terre ne donnent en effet que des mesures intégrées dans une direction fixée une fois pour toutes.

Fournissant des données dans des portes de largeur bien définie, le radar permet de déterminer avec une grande précision la position et les dimensions des cellules de diffuseurs et de caractériser les hydrométéores (eau, glace, neige...) présents sur la liaison ou dans une direction voisine. On peut, grâce à cette dernière possibilité, évaluer l'amélioration qu'apporte la diversité d'emplacement aux performances d'une liaison (HODGE, D.B. 1973).

Le radar permet aussi de prévoir l'atténuation due à la pluie pour un faisceau d'angle d'élévation quelconque (GOLDHIRSH, J. 1975).

Le choix des sites sur lesquels on se propose de construire des stations terriennes est conditionné par la connaissance de la pluviosité de la région considérée. Or, les données pluviométriques, qui sont souvent disponibles depuis de nombreuses années et qui peuvent donc constituer une base solide pour établir des statistiques d'affaiblissement fiables, doivent être corrigées pour tenir compte de l'existence d'hydrométéores non précipitants et tout particulièrement de la bande brillante (AUSTIN, P.M. 1950). Le radar est pratiquement le seul instrument permettant la caractérisation de la bande brillante et donc la correction des données pluviométriques obtenues au sol.

Enfin, on peut espérer obtenir, grâce au radar, l'explication des phénomènes de dépolarisation sans atténuation observés au cours d'expériences précédentes et qui semblent être dus à la présence de particules de glace à très haute altitude (SHUTIE, P.F...1977 ; Mc EWAN, N.J... 1977 ; COX, D.C... 1977 ; ...).

Dans l'optique considérée, un radar ne peut devenir opérationnel que s'il a été convenablement "étaloné". Pour effectuer cet étalonnage, il est nécessaire de disposer de mesures d'atténuation et de dépolarisation obtenues à partir d'une balise placée à bord d'un satellite.

Après un bref rappel de la théorie sur laquelle nous nous sommes appuyés, nous décrivons la procédure d'étalonnage que nous avons mise en oeuvre et les résultats que nous avons obtenus lors de la campagne de mesures que nous avons effectuée dans la région parisienne au cours des mois d'Avril et Mai 1979.

## 2. RAPPELS THEORIQUES

Dans la plupart des cas considérés les dimensions des diffuseurs sont telles que l'on peut appliquer l'approximation de Rayleigh. Dans ces conditions la réflectivité  $\sigma_i$  mesurée dans un volume diffusant situé à la distance  $r_i$  du radar est donnée par

$$\sigma_i = \frac{\pi^5}{\lambda^4} |K|^2 z_i$$

où  $\lambda$  désigne la longueur des ondes émises par le radar,  $|K|^2$  un paramètre lié à l'indice de réfraction  $m$  et que l'on peut prendre égal à 0.93 dans le cas de l'eau et à 0.20 dans le cas de la glace (BATTAN, L.J. 1973).

$z_i$  est le facteur de réflectivité du volume diffusant

$$z_i = \int_{D_{\min}}^{D_{\max}} N(D) D^6 dD$$

où  $N(D)dD$  représente le nombre par unité de volume de diffuseurs dont les diamètres sont compris entre  $D$  et  $D + dD$ .

$z_i$  s'exprime en  $[(\text{mm})^6/\text{m}^3]$  ou en dBZ.

On détermine  $z_i$  à partir de la puissance retrodiffusée  $P_{ri}$  par le volume diffusant considéré

$$z_i = \frac{r_i^2 P_{ri}}{C_R}$$

où  $C_R$ , constante du radar, est donnée par

$$C_R = C |K|^2$$

$C$  désignant une constante caractéristique de la structure du radar utilisé.

Connaissant  $z_i$ , il est possible de calculer l'atténuation instantanée  $A_R(t)$  subie par une onde électromagnétique, à l'aide de la relation

$$A_R(t) = \sum_{i=1}^N a z_i^b \Delta r_i$$

où  $\Delta r_i$  est la largeur des "portes" de distance utilisées, et  $N$  le nombre de portes explorées le long du faisceau hertzien.

$a$  et  $b$  sont les deux paramètres à déterminer pour étalonner le radar. Ils dépendent de la fréquence de la liaison et du type de précipitation responsable de l'atténuation.

Leur détermination se fait en minimisant l'expression

$$F = \sum_{j=1}^M (A_j - A_{Rj})^2$$

où  $A_j$  désigne l'atténuation effectivement mesurée sur le trajet satellite-Terre,  $M$  le nombre d'échantillons temporels et

$$\text{où } A_{Rj} = \sum_{i=1}^N a z_{ij}^b \Delta r_{ij}$$

Cette minimisation est effectuée à l'aide d'une méthode de régression non linéaire.

Il faut noter qu'on ne peut avoir pour l'atténuation mesurée que l'atténuation moyenne sur la distance Satellite-Terre.

### 3. DISPOSITIF EXPERIMENTAL

La géométrie de l'expérience est schématisée sur la figure 1, le radar est situé en T à 14 kilomètres de la station de réception G. Le satellite O.T.S. est vu de la station de réception sous un angle d'élévation de  $33^{\circ}6$  et un azimut de  $169^{\circ}$ .

#### 3.1. Le radar

Le radar utilisé est l'un des radars du système RONSARD (NUTTEN, B. 1979).

Il peut recevoir alternativement sur deux polarisations orthogonales et comporte un dispositif de contrôle de gain automatique qui confère au récepteur linéaire une dynamique supérieure à 110 dB. Le radar est en outre équipé d'un étalon interne et d'un dispositif supprimeur d'échos fixes.

Ses principales caractéristiques sont données dans le tableau suivant.

Emetteur	Fréquence (MHZ)	5600 ou 5630
	Puissance de crête (KW)	250
	Fréquence de répétition (HZ)	2928 - 1464 - 732
	Largeur des impulsions ( $\mu$ S)	0,34 - 0,68 - 1,36
	Portée (Km)	50,4 - 101,6 - 204,0
Antenne	Diamètre (m)	4
	Largeur du faisceau	$0,9^{\circ}$
	Gain (dB)	44,4
	Précision de pointage	$0,1^{\circ}$
Récepteur	Température de bruit ( $^{\circ}$ K)	45 $^{\circ}$
	Facteur de bruit (dB)	4

#### 3.2. La station de réception

La station expérimentale de Gometz-la-Ville est équipée d'une antenne avec optique Cassegrain qui se compose d'un réflecteur principal de 9 m de diamètre et d'un réflecteur auxiliaire de 1 m de diamètre. L'aérien est supporté par une monture azimut-élévation dont les débattements sont de  $0-90^{\circ}$  en élévation et de  $\pm 270^{\circ}$  en azimut. La source primaire est constituée par un cornet réflecteur illuminant le réflecteur auxiliaire en zone de Rayleigh. Par ce procédé, l'antenne garde des caractéristiques correctes dans une gamme de fréquences comprise entre 10 et 35 GHz, et l'optimisation, pour certaines bandes de fréquences particulières, est obtenue par le changement du cornet d'excitation et des éléments non rayonnants.

La source primaire, permet d'émettre et de recevoir sur deux polarisations circulaires inverses ou sur deux polarisations linéaires orthogonales. L'optimisation des éléments non-rayonnants est faite pour la bande de fréquences des 14 à 14,5 GHz à l'émission et la bande de fréquences des 10,95 à 11,8 GHz à la réception, en polarisation circulaire. Une tête d'écartométrie utilisant le principe de couplage des modes supérieurs permet d'assurer une poursuite automatique des satellites quel que soit le type de polarisation.

Les chaînes de réception connectées aux accès "polarisation directe" et "polarisation croisée" sont composées d'un amplificateur paramétrique et d'un double changement de fréquence qui permet de transposer dans la bande de fréquences des 60 MHz, les signaux reçus du satellite dans les bandes de fréquences des 11 GHz. Si ces deux chaînes sont identiques, dans leur principe, elles diffèrent par le fait que les amplificateurs paramétriques ne sont pas du même type. Sur une chaîne on utilise un amplificateur paramétrique refroidi à l'hélium gazeux qui présente une température de bruit de 33 K à 11,6 GHz. Cet amplificateur peut être incorporé dans un système de mesure des températures de



bruit fonctionnant en radiométrie dans la direction du satellite. En l'absence de satellites, la station expérimentale peut ainsi participer à des campagnes de radiométrie solaire puisque la dynamique de mesure du radiomètre est comprise entre 60 et 12 000 K. Par beau temps, la température du bruit du système de réception est de 125 K ce qui donne un G/T de la station de réception de 37,5 dBK. L'autre chaîne de réception est équipée d'un amplificateur paramétrique non refroidi qui présente une température de bruit de 160 K à 11,3 GHz.

La chaîne émission comprend deux changements de fréquence suivis d'un étage de puissance constitué par un amplificateur à tube à onde progressive de 20 W.

Des récepteurs d'analyse de très bonne stabilité, à verrouillage de phase et à contrôle automatique de gain permettent d'effectuer les mesures d'affaiblissement et de dépolarisation par double démodulation synchrone du signal de polarisation croisée par le signal de polarisation directe. Le récepteur est schématisé sur la figure 2.

L'acquisition des données des différents paramètres mesurés est faite par l'intermédiaire d'un mini-calculateur fonctionnant en temps réel. Ce dernier échantillonne les voies de mesure toutes les 50 ms, opère une moyenne toutes les deux secondes et transfère un bloc de données sur bande magnétique toutes les minutes. Un programme de traitement en temps réel permet la supervision et le calibrage des installations de la station, ainsi que le pré-traitement des données. Un programme de traitement en temps différé permet d'analyser chaque événement de propagation. Tous les dépouillements sont effectués en prenant comme référence les valeurs mesurées par beau temps, soit avant l'événement considéré, soit après. Il faut noter que les dépouillements ont été rendus très difficiles par le fait que le satellite OTS présente des instabilités de la puissance émise ainsi que des variations importantes du signal émis en polarisation croisée au cours du temps.

#### 4. MESURES ET RESULTATS EXPERIMENTAUX

. La station de réception reçoit du satellite OTS les signaux suivants :

$B_0$  : 11.786 GHz polarisé circulairement

$B_1$  : 11.575 GHz polarisé linéairement

$B_8$  : 14.455 GHz polarisé circulairement

(signal émis par Gometz et retransmis par le satellite).

Elle effectue des mesures d'affaiblissement absolu et de découplage de polarisation sur les signaux  $B_0$  et  $B_1$ , des mesures d'affaiblissement absolu sur le signal  $B_8$  et des mesures de température de bruit du ciel dans la direction du satellite avec une largeur de bande de 1 MHz à 11,33 GHz.

En outre, l'intensité des précipitations, la vitesse et la direction du vent sont enregistrés en permanence à la station tandis que des radiosondages quotidiens sont effectués au voisinage du radar.

Nous avons analysé les événements observés à la station de Gometz-la-Ville le 3 Mai 1979 entre 13 H 29 et 14 H 03 (GMT).

Les affaiblissements en polarisation linéaire et circulaire, le découplage de polarisation en polarisation circulaire, la température de bruit du ciel et le taux de précipitation sont représentés sur la figure 3.

On remarque entre 13 H 30 et 14 H, deux diminutions du découplage de polarisation du même ordre (environ 26 dB) mais d'origines différentes puisque la première se produit en l'absence d'atténuation significative alors que la deuxième est accompagnée d'une atténuation de 6 dB et correspond à un accroissement de la température de bruit du ciel et de l'intensité des précipitations.

La figure 4 fournit le profil de température obtenu par radio-sondage à proximité du radar. L'isotherme 0° se trouve à environ 500 mètres d'altitude.

. Simultanément le radar explorait le faisceau radioélectrique par balayages sectoriels successifs couvrant chacun un azimut de 20°. (L'exploration jusqu'à une altitude de 10 kms est faite en un peu moins de 2 minutes).

. L'azimut du point d'intersection du faisceau Satellite-Terre et du faisceau radar étant déterminé avec une précision de  $\pm 1,5^\circ$ , on prend la valeur moyenne des réflectivités mesurées dans chacun de ces intervalles de  $3^\circ$ . D'autre part, afin de réduire l'influence des fluctuations de réflectivité entre deux points d'intersection successifs, seules ont été utilisées les valeurs moyennes des réflectivités mesurées dans trois portes adjacentes.

La figure 5 représente les variations le long du faisceau des réflectivités ainsi calculées lors de l'événement considéré.

Un moyen commode pour suivre l'évolution du phénomène consiste à donner une représentation tridimensionnelle (réflectivité, temps, distance). La figure 6 représente un tel tracé pour 34 minutes de données sur une longueur de 9 kms le long du faisceau. Les réflectivités  $\gamma$  sont données en dBZ. On a aussi représenté sur la figure l'atténuation mesurée à la station de réception et l'atténuation calculée à partir des réflectivités à l'aide de la relation  $A = az^b$ . Afin de ne pas masquer certains détails de la carte des réflectivités nous avons représenté la même séquence en permutant les axes des temps et des distances (figure 7).

#### 5. INTERPRETATION DES RESULTATS

Nous avons tout d'abord calculé les valeurs des paramètres  $a$  et  $b$  de la relation

$$A = az^b$$

en considérant que les diffuseurs étaient de la glace, puisque l'isotherme  $0^\circ\text{C}$  se trouvait à 500 m d'altitude et qu'il neigeait ou grêlait pendant l'expérience. Nous étions en présence d'une situation essentiellement convective.

Le calcul donne  $a = 0,88 \times 10^{-3}$   
 $b = 0,624$

Ces valeurs sont du même ordre de grandeur que celles calculées par GOLDHIRSH (1979), les différences observées pouvant être expliquées par le fait que ses calculs ont été effectués pour une fréquence très différente (28 GHz au lieu de 11,8 GHz) et dans d'autres conditions météorologiques.

La figure 8 représente les atténuations mesurées et calculées à l'aide de ces valeurs. On constate un bon accord.

Nous avons aussi essayé de corrélérer les variations du découplage de polarisation et les réflectivités. La figure 9 montre que la corrélation est très mauvaise, surtout pour la première moitié de l'événement qui correspond à une dépolarisation sans atténuation.

On peut penser que ce phénomène est du à la présence, à très haute altitude, de particules de glace que nous n'avons pas pu déceler à l'aide du radar.

#### Conclusion

Après avoir rappelé tout l'intérêt que présente l'utilisation de radars dans les études de propagation, nous avons décrit une des expériences effectuées au cours des mois d'Avril et Mai 1979, dans les environs de Paris.

Nous avons étalonné notre radar pour des situations convectives en présence de neige.

La méthode présentée permet de prévoir les atténuations avec une assez bonne précision, puisque pour une atténuation de 6 dB l'erreur maximale est de  $\pm 1,9$  dB pour des fluctuations de réflectivité de  $\pm 2$  dBz.

Par contre, la méthode de prévision doit être améliorée si l'on veut prévoir les variations du découplage de polarisation. Elle doit prendre en compte de nouveaux paramètres tels que les angles d'inclinaison des hydrométéores. Afin de déterminer ces angles, nous allons entreprendre des mesures à l'aide des deux radars du système RONSARD en utilisant deux polarisations orthogonales à l'émission et à la réception.

## REFERENCES

- AUSTIN, P.M. and BEMIS, A.C., 1950,  
"A quantitative study of the Bright band in radar precipitation echoes", Journal of Meteorology, vol. 7, p. 145.
- BATTAN, L.J., 1973,  
"Radar observation of the atmosphere", The University of Chicago Press.
- BRUSSAARD, G., 1979,  
Radio propagation research by the European Space Agency", ESA journal, vol. 3, p. 253.
- CARASSA, F., 1977,  
"Application of the 20/30 GHz band to satellite communication systems", Symposium on advanced satellite communication systems, Genova.
- COX, D.C., ARNOLD, H.W. and RUSTAKO, A.J., 1977,  
"Some observations of anomalous depolarization on 19 and 12 GHz earth-space propagation paths", Radio Sci., vol. 12, n° 3, p. 435.
- GOLDBIRSH, J., 1975,  
"Prediction methods for rain attenuation statistics at variable path angles and carrier frequencies between 13 and 100 GHz", I.E.E.E. Trans. on Antennas and Propagation, vol. AP-23, n° 6, p. 786.
- GOLDBIRSH, J., 1979,  
"Predictive methods for rain attenuation using radar and in-situ measurements tested against the 28 GHz Comstar Beacon signal", I.E.E.E. Trans. on Antennas and Propagation, vol. AP-27, n° 3, p. 398.
- HODGE, D.B., 1973,  
"The characteristics of millimeter wave length satellite-to-ground-space diversity links", I.E.E.E. Conference LONDON, p. 28.
- Mc EWAN, N.J., WATSON, P.A., DISSANAYAKE, A.W., HAWORTH, D.R. and WAKILI, V.T., 1977,  
"Cross-polarization from high altitude hydrometeors on a 20 GHz satellite radio path", Electronics letters, vol. 13, n° 14, p. 405.
- NUTTEN, B., AMAYENC, P., CHONG, M, HAUSER, D., ROUX, F. and TESTUD, J., 1979,  
"The RONSARD Radars : a versatile C-band dual doppler facility", I.E.E.E. Trans. on Geoscience Electronics, vol. GE-17, n° 4, p. 281.
- NUTTEN, B., HAUSER, D., ROUX, F. and SCIALOM, G., 1979,  
"The RONSARD Radars : internal Calibration techniques using coherent and noise sources", I.E.E.E. Trans. on Geoscience Electronics, vol. GE-17, n° 4, p. 288.
- SHUTIE, P.F., ALLNUTT, J.E., MACKENSIE, E.G., 1977,  
"Satellite-earth signal depolarization at 30 GHz in the absence of significant fading", Electronics letters, vol. 13, n° 1, p. 1.

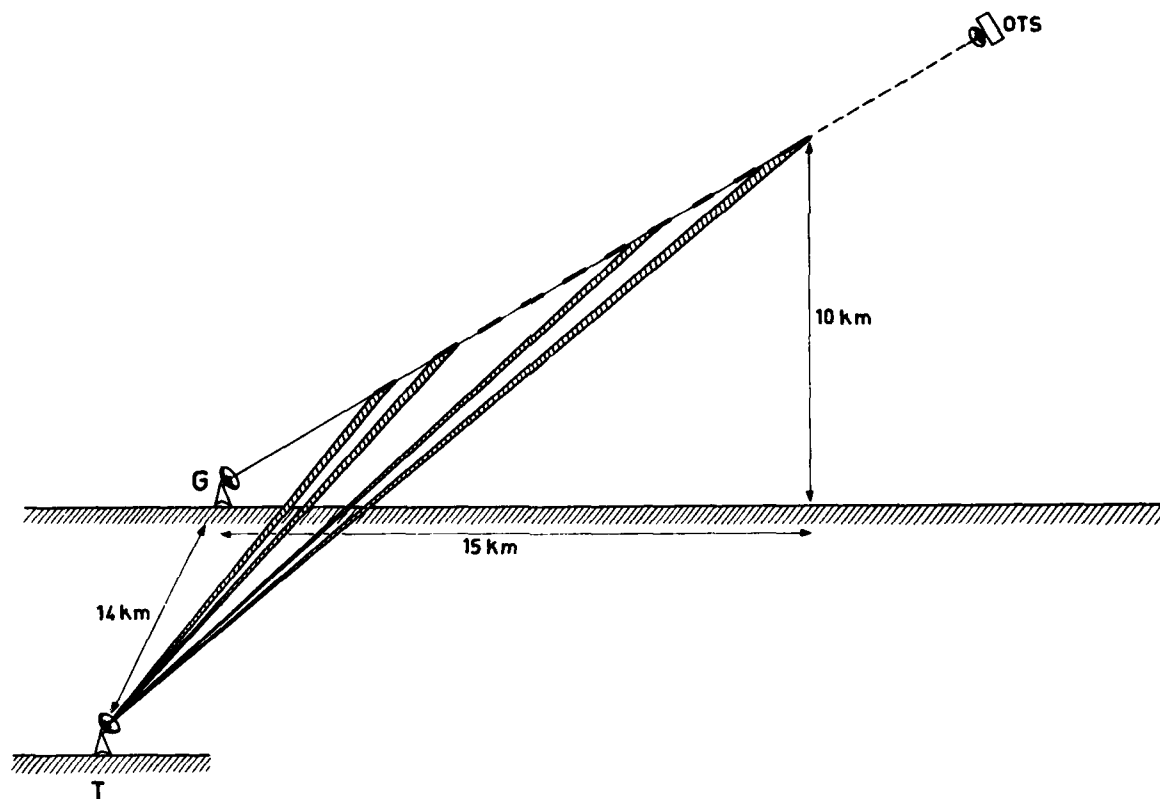


Figure 1 - Géométrie de l'expérience.

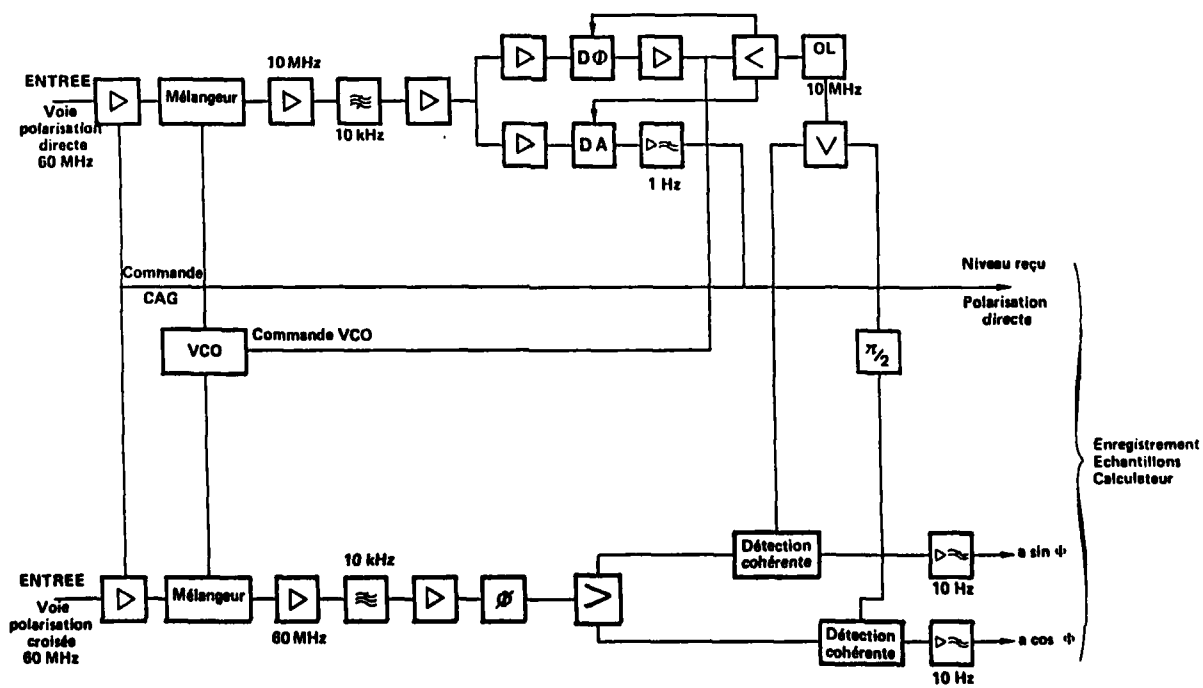


Figure 2 - Récepteur de mesure.

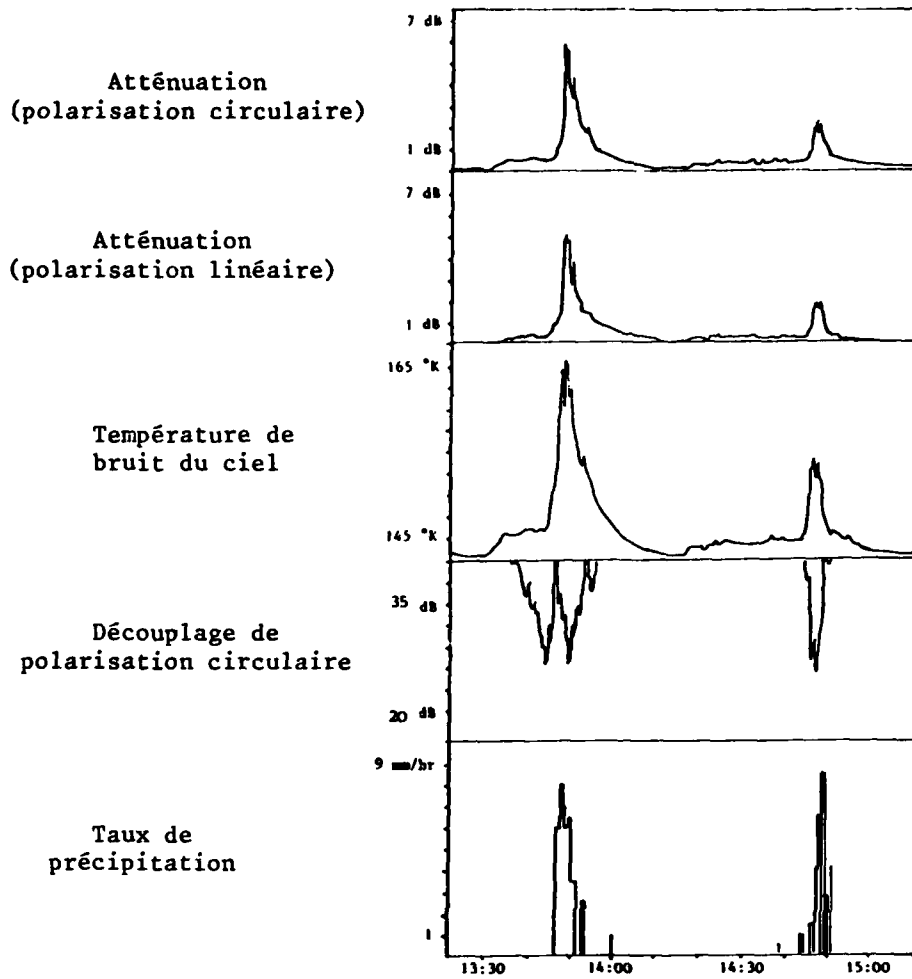


Figure 3 - Atténuations, découplage de polarisation, température de bruit du ciel et intensité des précipitations mesurées le 3 Mai 1979 entre 13 H 30 et 15 H GMT.

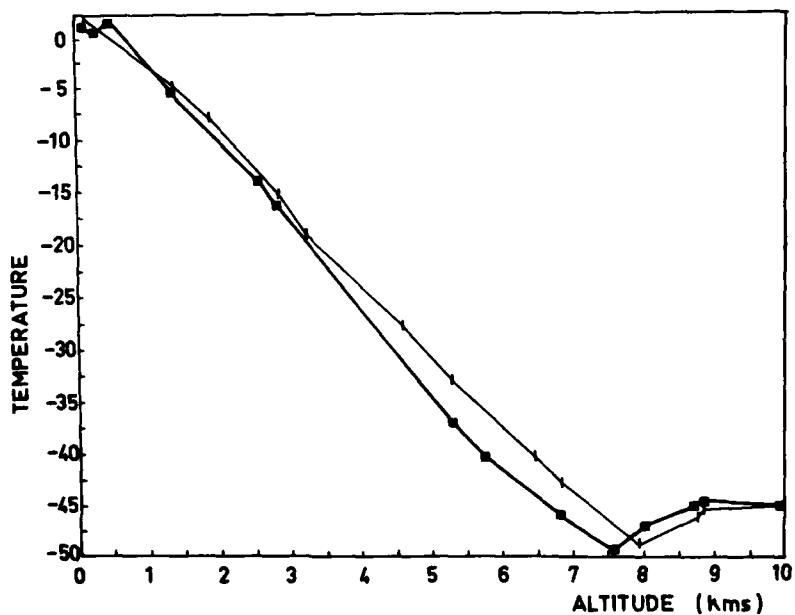


Figure 4 - Profils de température obtenus par radio-sondage à midi (I) et minuit (°).

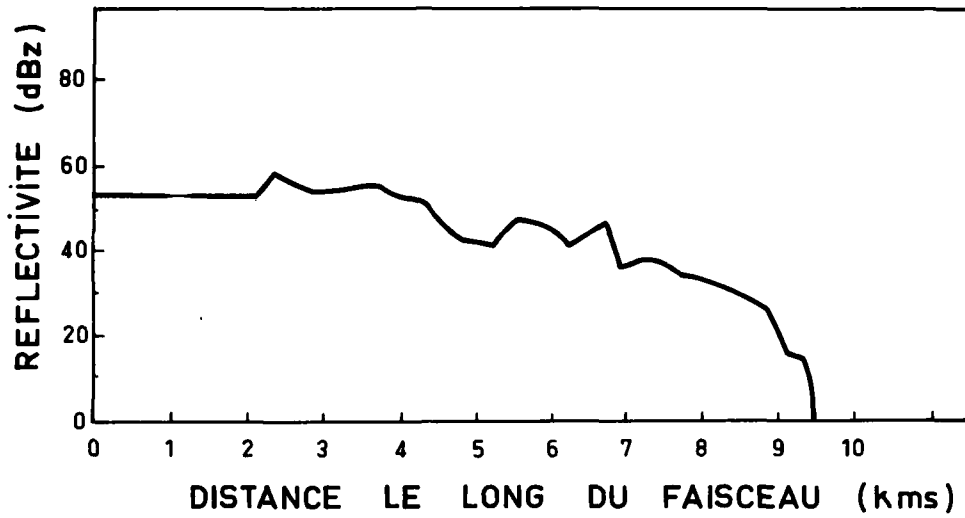


Figure 5 - Profil des réflectivités mesurées le long du trajet Satellite-Terre.

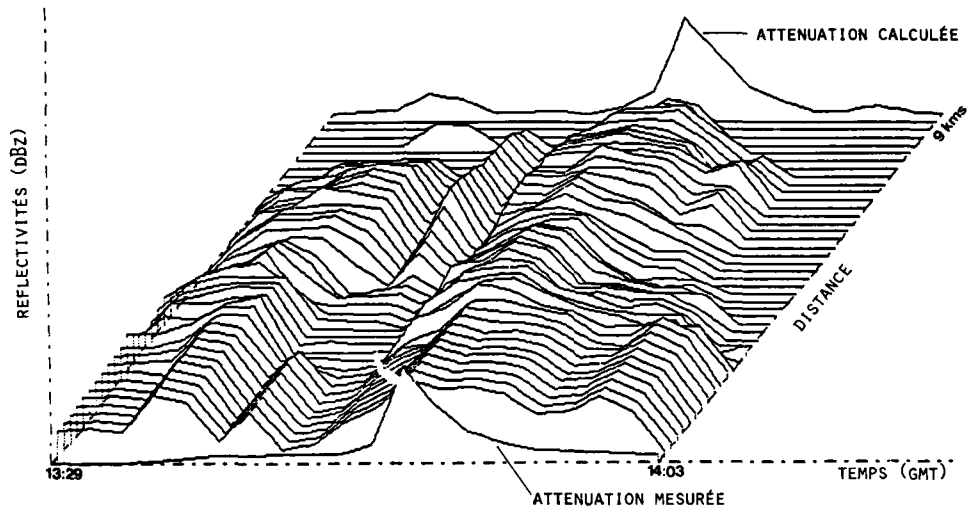


Figure 6 - Représentation tridimensionnelle de l'évolution des réflectivités. (temps - distance - réflectivité).

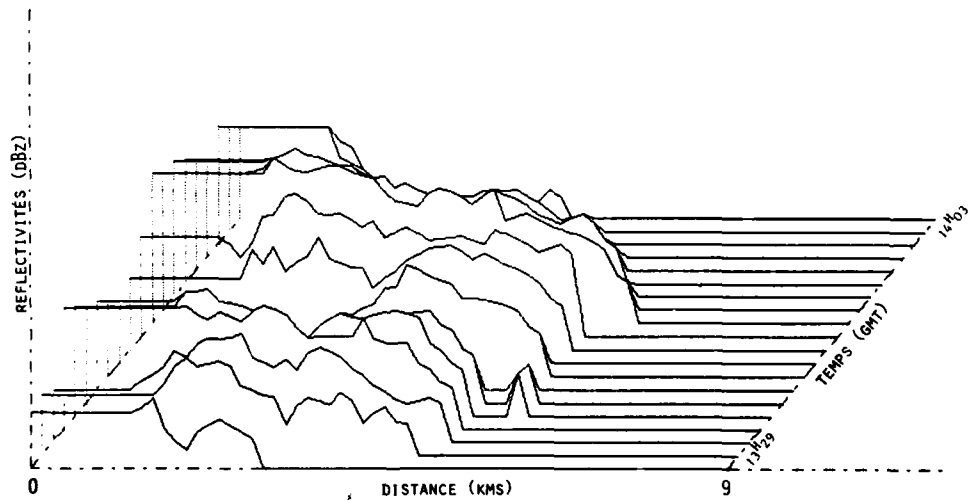


Figure 7 - Représentation tridimensionnelle de l'évolution des réflectivités. (distance - temps - réflectivité).

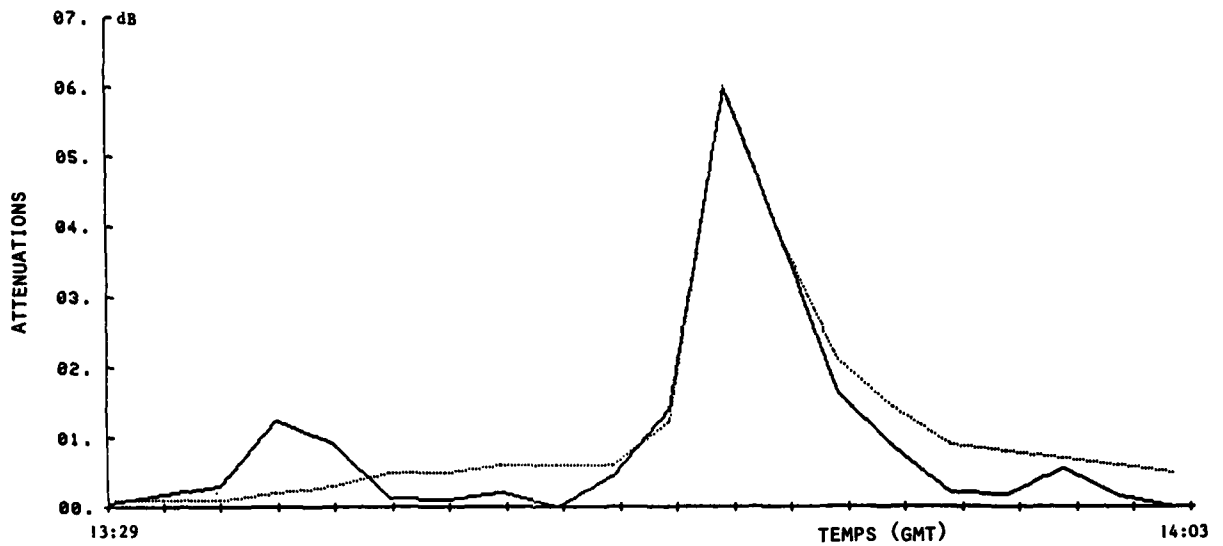


Figure 8 - Comparaison des atténuations mesurée (pointillés) et calculée (traits pleins).

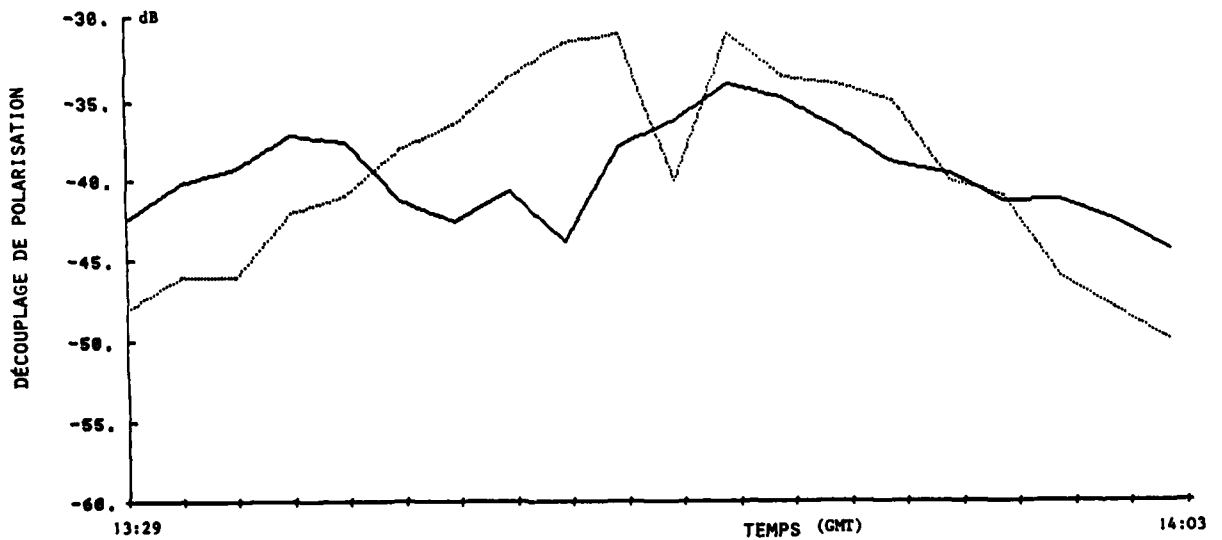


Figure 9 - Comparaison des découplages de polarisation mesuré (pointillés) et calculé (traits pleins).

JOINT STATISTICS OF ATTENUATION AND  
CROSS-POLARIZATION MEASURED WITH THE  
OTS SATELLITE

J. van Cappellen, A.Mawira, J.Neessen  
and F.Zelders

Transmission Division  
Dr. Neher Laboratories (PTT)  
The Netherlands

SUMMARY

This paper deals with some methods, which can be applied to the calculation of the fading margin in satellite communication systems using orthogonally polarized radio channels. A transmission model is introduced and it is discussed whether the joint statistics or the separate statistics of XPD and attenuation can be used for the determination of the fading margin. Propagation data are presented, which were collected with the experimental earth station at Nederhorst den Berg by measurements on OTS beacons. The measured data are used for the evaluation of the methods, which are presented for the calculation of the fading margin.

1. INTRODUCTION

After the launch of the OTS-2 satellite propagation measurements were performed with the experimental earth station at Nederhorst den Berg. Data on attenuation and cross-polarization discrimination ratio XPD were collected by reception of the linearly and circularly polarized signals of the OTS beacons.

In a previous paper (NEESSEN, J e.a.,1980) the impact of cross-polarization phenomena on the fading margin in satellite communication systems has been discussed. Three methods for the calculation of the fading margin were presented. Only a relatively small number of rain events - registered during the measurements on the circularly polarized beacon of the SIRIO satellite - were available for the evaluation. During the registration period with the OTS-2 satellite a much larger amount of propagation data was collected, including events due to rain and ice-particles. In addition data on XPD are available for both linear and circular polarization.

It is common to calculate the fading margin in dual polarized satellite systems by the use of a fixed relation between XPD and attenuation. Such a relation may be given by the values of XPD and attenuation, which are exceeded by the same time percentage. It was felt that the assumption of a fixed relation could have a limited value because of the weak correlation between the measured XPD and attenuation.

The joint statistics of XPD and attenuation are considered as the most appropriate way for the calculation of the fading margin. Measured data on the joint statistics of XPD and attenuation have been presented (MAWIRA, A e.a.,1979). In this paper the use of the joint statistics is evaluated with respect to the calculation of the fading margin in dual polarized satellite communication systems.

2. MEASURING SYSTEM

The experimental earth station is located at Nederhorst den Berg, 20 km south-east from Amsterdam. The earth station has been used for propagation measurements with the SIRIO satellite and since July 1978 for propagation measurements with the OTS-2 satellite. An extensive overview of the measuring system has been presented (OEI, W e.a.,1979) and in this paper only the main characteristics are mentioned. A general block-diagram of the system is shown in fig.1 and some typical data of the receiving system are summarized in TABLE 1.

All microwave equipment used for the propagation experiments is installed at the back of the antenna and connected to the output flange of the primary feed. For the reception of the linearly polarized beacon it was necessary to make the whole microwave part rotatable.



TABLE 1

Technical characteristics of the receiving system

Beacon	TM/TM	TM'/TM'	B0/B1	B0'/B1'
Frequency (GHz)	11.575	11.575	11.786	11.786
Polarization	LINEAR	LINEAR	CIRCULAR	CIRCULAR
Antenna XPD (dB)	-	44	-	36
Nominal signal level (dBm) (input terminal of mixer)	- 91	- 135	- 89	- 125
Noise figure (dB)	7	7	7	7
Detection bandwidth (Hz)	20	1	20	1
S/N (dB)	64	33	65	40

Automatic tracking is done on both the linear and circular beacon by utilization of the  $TE_{21}/TM_{01}$  and  $TM_{01}$  tracking modes respectively. The selection of the tracking beacon is made on frequency base.

The transmitter unit consists of two phase locked oscillators with varactor multipliers providing the up-link frequencies. The required power is obtained by a varactor tuned Gunn oscillator or by a travelling wave tube amplifier. Output EIRP is stabilized by a power regulating loop.

Solid state noise sources are used as reference sources for a daily calibration of the receiver. They were preferred because of their high output power stability.

The one-second samples of the received signals are stored on magnetic tape. Further data processing is done at the Dr. Neher Laboratories. Selection of propagation events has been done by the utilization of strip-chart recordings and data from radiometers, weather radar and a rain gauge network along the azimuth line to the OTS-2 satellite.

### 3. TRANSMISSION MODEL

The impact of propagation phenomena is analysed under the assumption of a simplified transmission model. The model implies a satellite-earth link with a transmission system, using two orthogonally polarized radio channels. The receiving part consists of an antenna with an ortho-mode transducer, to which two receivers are connected. It is assumed that the receiver noise temperature is high compared with the antenna noise temperature.

An important transmission parameter of a communication system is the carrier to noise power ratio. In this paper the carrier to noise power ratio is defined at the output terminal of the ortho-mode transducer. The carrier to noise power ratio of channel 1 is given by the following expression :

$$\left(\frac{C}{N}\right)_1 = \left(\frac{C}{N}\right)_1^{\text{nom}} - A_1 - 10 \cdot \log \left( 1 + \frac{n_1^{\text{eq}}}{n_1^{\text{nom}}} \right) \quad \text{dB} \quad (3.1)$$

with :

- $\left(\frac{C}{N}\right)_1^{\text{nom}}$  the carrier to noise power ratio (dB) of channel 1 during nominal conditions ( channel 2 switched off )
- $A_1$  atmospheric attenuation (dB) in excess of the atmospheric attenuation during nominal conditions ( channel 1 )
- $n_1^{\text{nom}}$  noise power (Watt) in channel 1 during nominal conditions ( channel 2 switched off )

The quantity  $n_1^{\text{eq}}$  is the thermic noise power, which is equivalent - causing the same effects on the system - to the cross-polar signal power originating from channel 2. The value of  $n_1^{\text{eq}}$  follows from :

$$n_1^{\text{eq}} = k \cdot 10^{\frac{C_2^{\text{nom}} - A_2 - \text{XPD}_2}{10}} \quad \text{Watt} \quad (3.2)$$

with :  $C_2^{\text{nom}}$  the carrier power (dBW) of channel 2 received during nominal conditions  
 $A_2$  atmospheric attenuation (dB) in excess of the atmospheric attenuation during nominal conditions (channel 2)  
 $XPD_2$  cross-polarization discrimination ratio (dB) of channel 2

The proportional constant  $k$  includes the allowance for thermic noise and different frequency allocations of the two channels. Combining (3.1) and (3.2) gives the following expression for the carrier to noise power ratio of channel 1 :

$$\left(\frac{C}{N}\right)_1 = \left(\frac{C}{N}\right)_1^{\text{nom}} - F_1 \quad \text{dB}$$

$$F_1 = A_1 + 10 \cdot \log \left( 1 + 10^{\frac{Y_1 - A_1 - XPD_1}{10}} \right) \quad \text{dB} \quad (3.3)$$

$$Y_1 = \left(\frac{C}{N}\right)_1^{\text{nom}} + \left( C_2^{\text{nom}} - C_1^{\text{nom}} \right) + 10 \cdot \log (k) \quad \text{dB}$$

under the realistic assumption that the equality  $A_1 + XPD_1 = A_2 + XPD_2$  is valid. For an actual communication system the statistics of the carrier to noise power ratio have to meet defined requirements, which put constraints on the fading margin  $F_1$ . The value of the fading margin  $F_1$  depends on the propagation parameters and also on the system parameters.

#### 4. THEORETICAL BACKGROUND FOR THE DETERMINATION OF THE STATISTICS OF F

For system design the statistics of the fading-margin  $F$  is required. For propagation experiments it is more interesting to measure  $A$  and  $XPD$  since these quantities relate directly to the transmission properties of the atmospheric medium. However, as can be seen from equation (3.3),  $F$  is a direct function of  $A$ ,  $XPD$  and the system-parameter  $Y$  so that the cumulative distribution of the fading-margin  $F$  exceeding threshold  $F_0$ ,

$$P_F(F_0, Y) = \text{Probability}(F \geq F_0) \quad (4.1)$$

can be determined from the joint-probability function of  $A$  and  $XPD$ , viz.  $f_{AX}(A, XPD)$ , by an integration of  $f_{AX}$  through the  $A$ - $XPD$  surface bounded by the curve

$$XPD = H(A; F_0, Y) \quad , \quad (4.2)$$

where

$$H(A; F_0, Y) = Y - A - 10 \log \left( 10^{\frac{(F_0 - A)/10}{10}} - 1 \right) \quad , \quad (4.3)$$

see Fig. 2. The above expression is the inverse of equation (3.3). From Fig. 2 can be seen that  $P_F(F_0, Y)$  may be expressed as the sum

$$P_F(F_0, Y) = P_1 + P_2 \quad , \quad (4.4)$$

where  $P_1$  represents the integrated probabilities over the subsurface  $C_1$ , Fig. 2, in the  $A$ - $XPD$  plane,

$$P_1 = \iint_{C_1} dA' dX' f_{AX}(A', X') \quad . \quad (4.5)$$

The probability  $P_2$  can be readily seen to be the cumulative distribution of  $A$ , viz.  $P_A(F_0)$ , exceeding threshold  $A = F_0$

$$P_2 = \int_{F_0}^{\infty} dA' \int_{-\infty}^{\infty} dX' f_{AX}(A', X') \quad . \quad (4.6)$$

The probability  $P_1$  represents the extra contribution,  $\Delta P_F(F_0, Y)$ , to the cumulative distribution of the fading margin due to frequency-reuse as compared to single channel use of the communication link

$$P_1 = \Delta P_F(F_0, Y) = \int_{-\infty}^{F_0} dA' \int_{-\infty}^{\infty} dx' f_{AX}(A', X') H(A'; F_0, Y) \quad (4.7)$$

The cumulative distribution of the fading-margin exceeding threshold  $F_0$  can therefore be written as

$$P_F(F_0, Y) = P_A(F_0) + \Delta P_F(F_0, Y) \quad (4.8)$$

In the above considerations the determination of  $P_F(F_0, Y)$  is done by using the joint-probability density function  $f_{AX}$  of A and XPD. In the case that XPD is deterministically related to A, ie.

$$XPD = G(A), \quad (4.9)$$

with G a fixed function, the cumulative distribution  $P_F$  can be directly derived from the cumulative distribution of attenuation  $P_A$

$$P_F(F_0, Y) = \bar{P}_F(F_0, Y) = P_A(A_{DT}(F_0)) \quad (4.10)$$

where the function  $A_{DT}(F_0)$  is derived at by substituting relation (4.9) in equation (3.3) leading to the implicit form

$$F_0 = A_{DT} + 10 \log \left( 1 + 10^{\frac{Y - A_{DT} - G(A_{DT})}{10}} \right) \quad (4.11)$$

As can be seen from fig.2  $A_{DT}(F_0)$  gives the common point between the curve H, equation (4.3), and the curve G, equation (4.9).

Note: in the above derivation was assumed that the function G is such that the value of  $F_0$  increases with increasing value of  $A_{DT}$ . This condition is fulfilled if G is a monotonously non-increasing function of A.

In general the relation between A and XPD is of a statistical nature. Measurements have shown that at any value of A the observed values of XPD may vary considerably, so that the exact determination of the cumulative distribution of F requires the use of the joint probability of A and XPD. In cases when A and XPD are not completely correlated to each other the use of assumed fixed relation between A and XPD will lead to values of  $\bar{P}_F(F_0, Y)$  which might not be equal to  $P_F(F_0, Y)$ . The difference between  $P_F(F_0, Y)$  and  $\bar{P}_F(F_0, Y)$  is given by

$$P_F(F_0, Y) - \bar{P}_F(F_0, Y) = \Delta P_F(F_0, Y) - P_A(A_{DT}(F_0, Y)) + P_A(F_0) \quad (4.12)$$

or alternatively

$$P_F(F_0, Y) - \bar{P}_F(F_0, Y) = P_{11} - P_3 \quad (4.13)$$

The probabilities  $P_{11}$  and  $P_3$  are the integrations of equation (4.5) over the surfaces  $C_{11}$  and  $C_3$ , fig.2. The use of assumed fixed relation of A and XPD to predict the cumulative distribution of F is therefore only warranted if  $P_{11} \approx P_3$ .

## 5. RELATIONS BETWEEN XPD AND ATTENUATION

In Report 564-1 (CCIR, 1978) a prediction method for cross-polarisation due to rain has presented. The following relation between XPD and A for linear and circular polarization is reported :

$$\text{XPD} = G_c(A) = 30.\log(f) - 40.\log(\cos(\epsilon)) - 20.\log(\sin 2\tau) - 20.\log(A) \quad (5.1)$$

with :  $f$  frequency (GHz)  
 $\epsilon$  elevation angle (degree)  
 $\tau$  polarization tilt angle (degree)  
(circular polarization  $\tau = 45^\circ$ )

This expression is based on theoretical calculations, assuming certain raindrop and canting angle distributions. Expression (5.1) may represent an "average" relation between XPD and A. However the statistical meaning of this "average" relation is not sufficiently clear. Data on XPD and A have been collected during the summer periods of 1978 and 1979, which include all events of interest. A typical event - including propagation phenomena due to rain and ice-particles - is shown in fig.5. The following statistics are derived from the available data :

- The cumulative distribution function of A :  $P_A(A)$
- The cumulative distribution function of the XPD :  $P_X(\text{XPD})$
- The probability density function of the XPD under the condition A :  $f_X(\text{XPD}|A)$

The cumulative distribution function of the XPD under the condition A is drawn in fig.3 and fig.4 for linear respectively circular polarization. These figures show the large spread of XPD around their median values. From a statistical point of view it is evident that low values of XPD occur for both high and low attenuation values.

From statistics mentioned above the following relations between XPD and A are calculated :

$$\text{XPD} = G_{eq}(A) \quad \text{from} \quad P_A(A) = P_X(\text{XPD}) \quad (5.2.a)$$

$$\text{XPD} = G_{av}(A) \quad \text{from} \quad \text{XPD} = \int_{-\infty}^{+\infty} dX' X' f_X(X'|A) \quad (5.2.b)$$

$$\text{XPD} = G_{med}(A) \quad \text{from} \quad 0.5 = \int_{-\infty}^{+\infty} dX' f_X(X'|A) \quad (5.2.c)$$

No significant difference exists between  $G_{av}(A)$  and  $G_{med}(A)$  as has been shown in a previous paper (MAWIRA, A e.a., 1979). The relations obtained are plotted in fig.6 and fig.7.

The relation  $G_c(A)$  is calculated from equation (5.1) using the values of the frequency  $f$  and the elevation angle  $\epsilon$  from TABLE 1. The polarization tilt angle for linear polarization is rather small and so the influence of the effective canting angle  $\tau_c$  of the raindrops may be of importance. Therefore  $G_c(A)$  is calculated for  $\tau = 8.3^\circ$  and  $\tau = 12.3^\circ$  ( $\tau_c = 4^\circ$ ). According to fig.6 and fig.7 the CCIR relation  $G_c(A)$  corresponds quite well with  $G_{med}(A)$  in the region, where the effect of the system XPD is negligible. For linear polarization the value of the effective canting angle of the raindrops can be chosen to be zero.

A remarkable difference exists between  $G_c(A)$  and  $G_{eq}(A)$ . It is caused by the large spread of XPD values, in particular at small values of attenuation where low values of XPD are encountered.

The effect of the polarization on XPD is shown in fig.8, where the XPD values for linear and circular polarization are compared as derived from the expressions (5.1) and (5.2). A close agreement is found for the relations concerned in the region, where the effect of the system XPD is negligible.

## 6. MEASURED STATISTICS OF THE FADING MARGIN

In section 3 the fading margin  $F$  was introduced by expression (3.3). From the available data the statistics of  $F$  are determined for defined values of the system parameter  $Y$ . The cumulative distribution function of  $F$  follows from equation (4.4).

From the cumulative distribution functions of  $F$  and  $A$  the values are selected, which are exceeded at the same probability level. It is more convenient to consider  $F-A$ , which gives the fading margin of the dual polarized system in excess of the fading margin of the single polarized system. The results are shown in fig.9, fig.10 and fig.11 for different values of the system parameter  $Y$ .

In addition some approximated relations between F-A and A are calculated. The CCIR relation  $G_c(A)$  of equation (5.1) and the measured relation  $G_{eq}(A)$  of equation (5.2.a) are substituted in equations (4.10) and (4.11). These approximated relations between F-A and A are also shown in fig.9 , fig.10 and fig.11 for different values of the system parameter Y. The presented figures show clearly that the use of the CCIR relation gives too low values of F-A , in particular for low values of A. So caution has to be exercised in the application of this relation for the determination of the statistics of the fading margin in dual polarized systems. The use of the equal probability relation  $G_{eq}(A)$  gives results, which are in reasonable agreement with the measured statistics of F.

As expected the fading margin for circularly polarized systems is larger than that for linearly polarized systems, using the same value of the system parameter Y. However the difference between these two fading margins depends on the value of Y. This difference increases markedly with increasing value of the system parameter Y.

## 7. CONCLUSIONS

The joint statistics of XPD and A are used for the investigation of the impact of cross-polarization phenomena on the fading margin in satellite communication systems using dual polarization. From the analysis and the data obtained from measurements with the OTS-2 satellite the following conclusions are drawn :

1. The CCIR relation between XPD and A corresponds well with the measured median XPD values, derived from the probability of XPD under the condition A.
2. The relation between XPD and A , derived from the separate cumulative distribution functions of XPD and A through equiprobability matching , differs markedly from the CCIR relation. This can be explained by the observed occurrence of depolarization effects due to ice-particles.
3. The difference between the XPD values for linear and circular polarization are predicted well by all relations considered.
4. The measured statistics of the fading margin are approximated well by those following from the equiprobability relation between XPD and A.
5. Caution has to be exercised in the application of the CCIR relation between XPD and A for the determination of the fading margin in dual polarized systems.
6. The fading margin of dual polarized systems in excess of the fading margin of single polarized systems can be large, even for low attenuation values. This effect is quite severe in circularly polarized systems.

## 8. ACKNOWLEDGEMENT

The authors are indebted to their colleagues of the Dr. Neher Laboratories for their contribution to the propagation experiments with the OTS-2 satellite.

## REFERENCES

- 1) CCIR , 1978 , "Propagation data required for space telecommunication systems" , vol.5
- 2) MAWIRA, A. e.a. , 1979, "Some results from propagation experiments using OTS in the summers of 1978 & 1979", Proceedings of the 4th OTS propagation experimenters meeting , Stockholm , Interim Eutelsat
- 3) NEESSEN, J. e.a. , 1980, "The impact of cross-polarization phenomena on the fading margin in satellite communication systems", to be published in Alta Frequenza , 1980
- 4) OEI, W.S. e.a. , 1979 , "System overview of the Dr. Neher Laboratory's experiment in the 11 GHz and 14 GHz bands with the Orbital Test satellite", Proceedings of the 2th OTS propagation experimenters meeting Paris , Interim Eutelsat

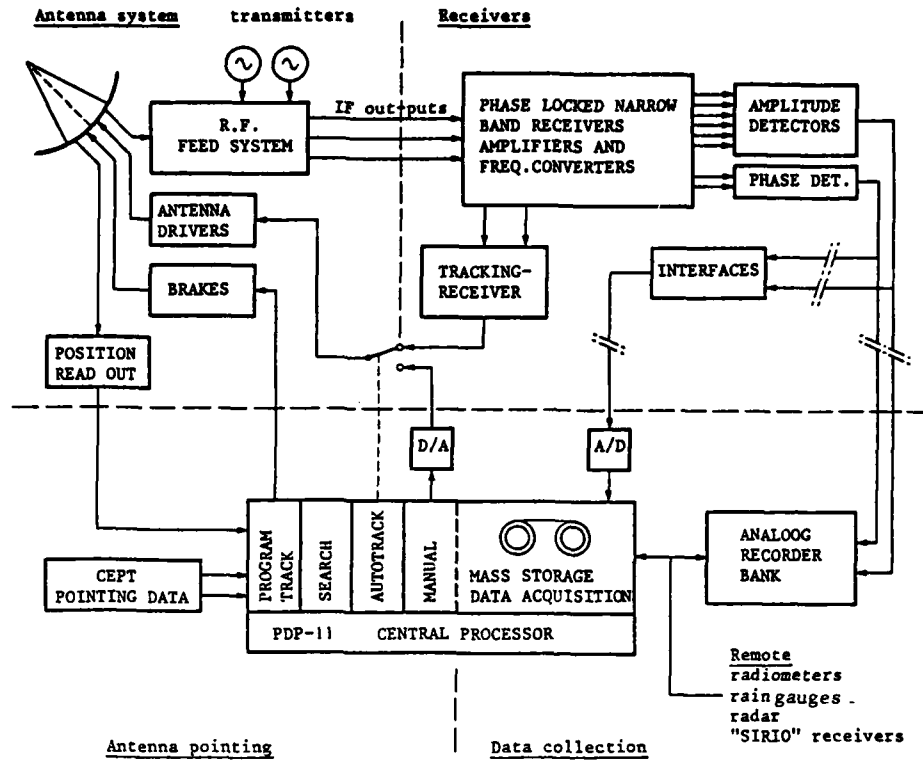


fig.1 : General block-diagram of the measuring system

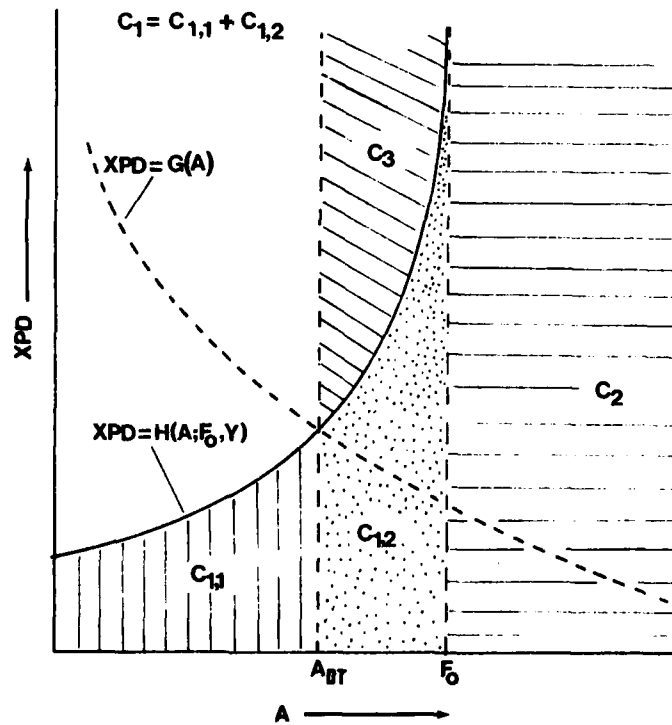


fig.2 : Integration areas in the XPD-A plane

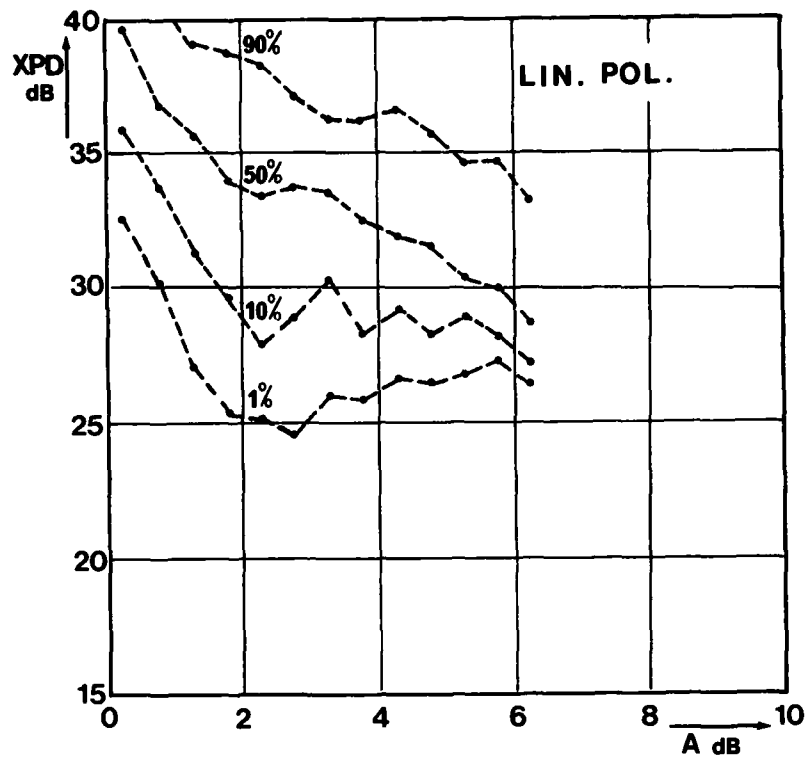


fig.3 : The cumulative distribution function of XPD under the condition A for linear polarization

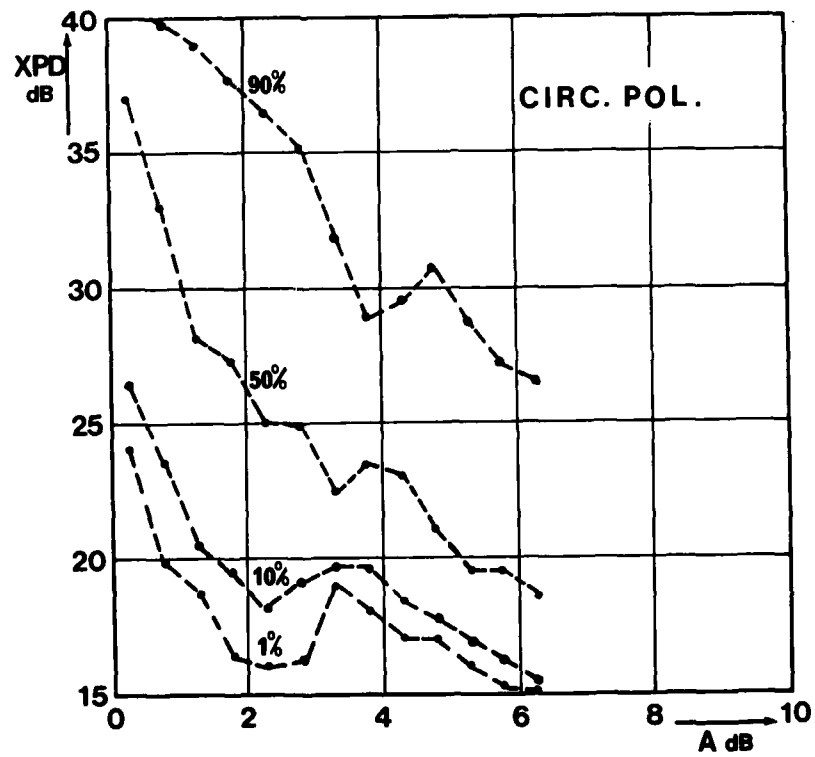


fig.4 : The cumulative distribution function of XPD under the condition A for circular polarization

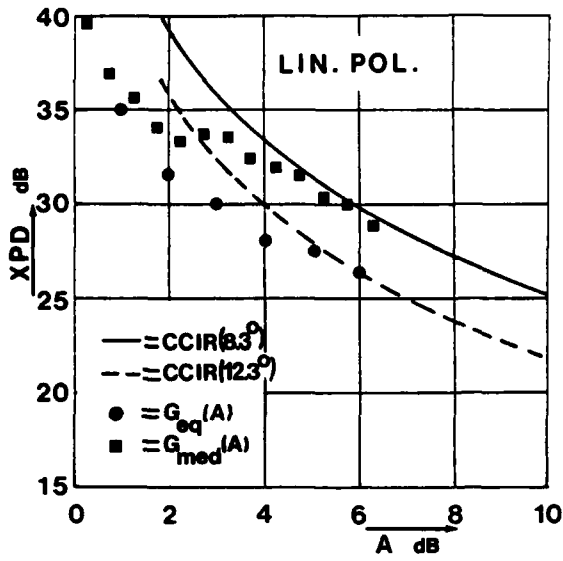


fig. 6 : XPD versus A for linear polarization

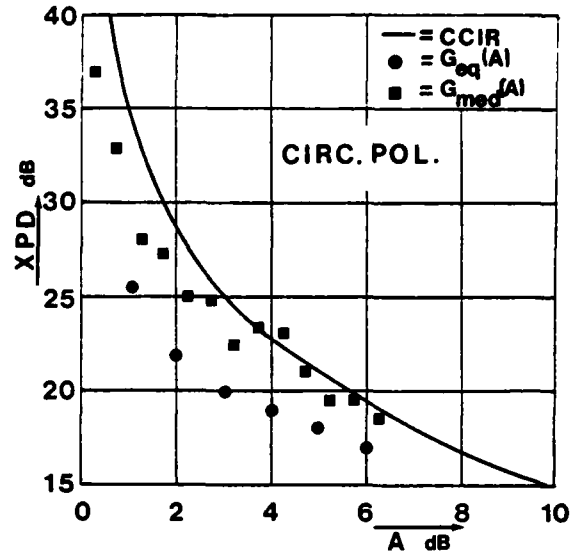


fig. 7 : XPD versus A for circular polarization

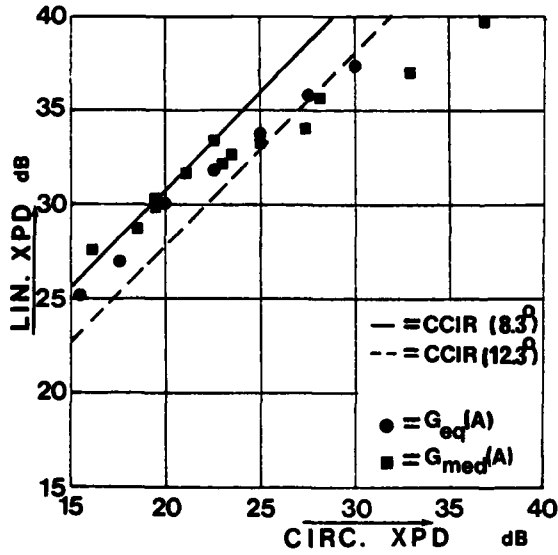


fig. 8 : Linear XPD versus circular XPD

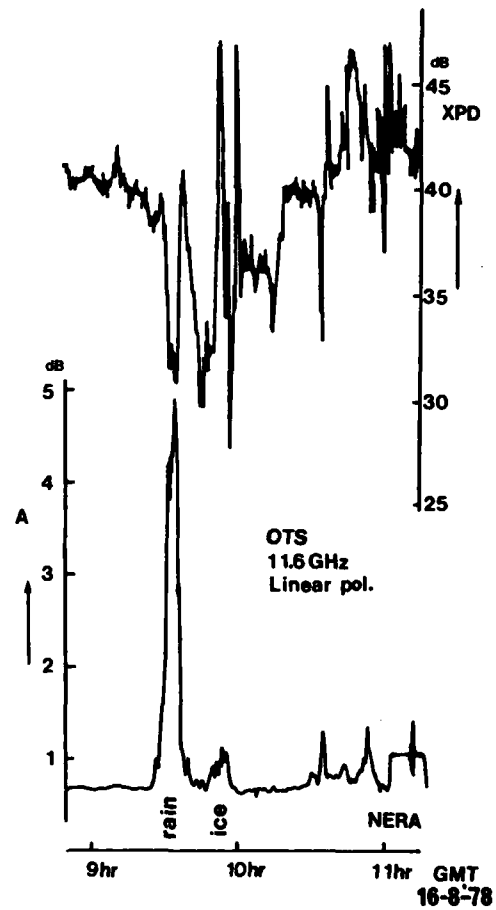


fig. 5 : Typical event including effects of rain and ice-particles



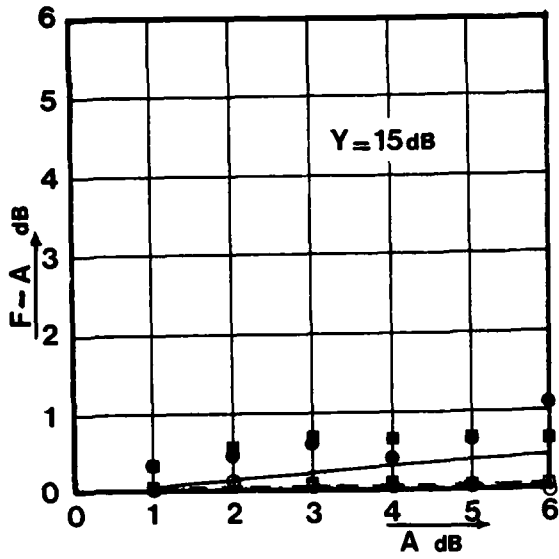


fig. 9 : Degradation of the fading margin for Y = 15 dB

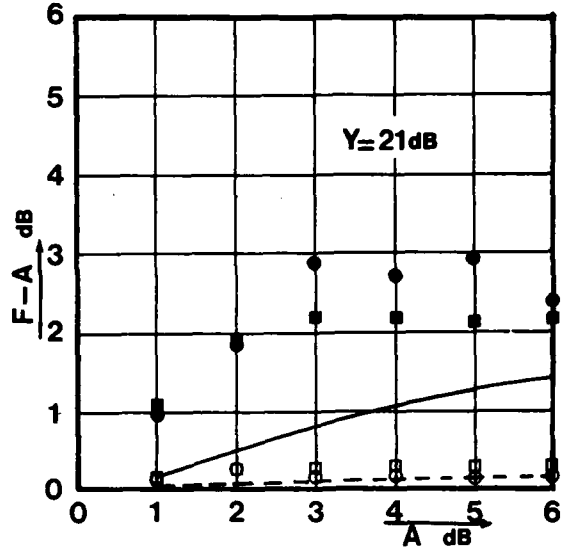


fig. 10 : Degradation of the fading margin for Y = 21 dB

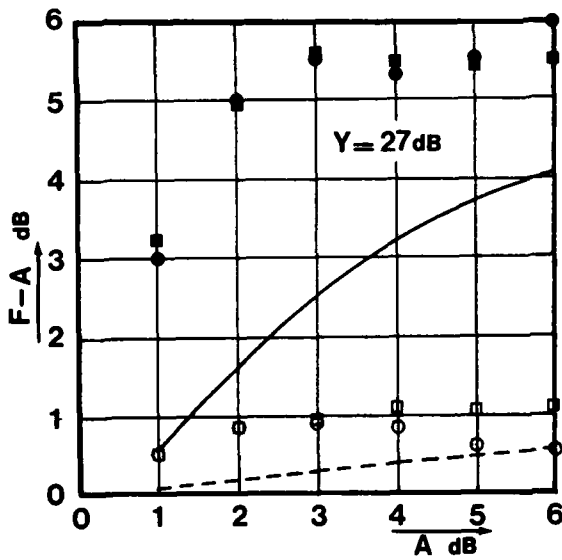


fig. 11 : Degradation of the fading margin for Y = 27 dB

Legend to fig.9 , fig.10 and fig.11

LINEAR POLARIZATION

- CCIR
- measured
- G<sub>eq</sub>(A)

CIRCULAR POLARIZATION

- CCIR
- measured
- G<sub>eq</sub>(A)

RAIN ATTENUATION PREDICTION AT THE NETHERLANDS OTS/SIRIO  
RECEIVING SITE USING INEXPENSIVE X-BAND RADAR

ir. E.P.W. Attema  
Delft University of Technology  
Dept. of Electrical Engineering  
Microwave Laboratory  
Mekelweg 4  
Delft  
The Netherlands

ir. H.J.M. Heemskerck  
Dutch Post Office  
Dr. Neher Laboratory  
Leidschendam  
The Netherlands

SUMMARY

Concomitant with OTS propagation experiments at The Netherlands experimental groundstation, radar reflectivity profiles along the slant path to the satellite were recorded at X-band using an inexpensive mass-produced ship's navigation radar transceiver, slightly modified to produce accurate reflectivity data at X-band. Based on the system parameters, the radar equation for distributed targets is derived, expressing the average reflected power in terms of a radar calibration factor, radar range and reflectivity. Using Laws and Parsons dropsize distribution the theoretical relation between reflectivity and attenuation at the radar frequency (9.4 GHz) and the satellite beacon frequency (11 GHz) were calculated. Following a discussion of some hardware aspects and the residual uncertainties in the attenuation estimates selected precipitation events are examined. Overall correlations are given between radar derived attenuation values and those actually measured. Finally radar derived attenuation statistics are compared to radiometer derived statistics and direct measured results using the OTS beacon.

1. INTRODUCTION

In anticipation of the availability of the experimental geosynchronous satellites SIRIO and OTS the Dutch Post Office (PTT) designed and built a groundstation for propagation and communication experiments at frequencies between 10 and 40 GHz [1]. In order to more fully exploit these experiments for data gathering pertinent to the design of future satellite communication links operating at frequencies above 10 GHz it was decided to supplement the direct measurements of attenuation and depolarization effects on the satellite path by indirect measurements using radiometers and rain gauges. In addition, the Microwave Laboratory of the Delft University of Technology carried out simultaneous radar reflectivity measurements at the same site using X-band radar directed along the satellite-to-earth path. The objective of this experiment was determination of the capability of an inexpensive radar to predict attenuation. If successful such a radar would offer an alternative or supplement to radiometric measurements for continuously gathering attenuation statistics on single satellite paths or in path diversity arrangements. Rather than estimating path attenuation from integral path emission the radar measures reflectivity profiles along the satellite path which provide much more insight into the physical processes causing attenuation and depolarization. Thus the radar provides an additional tool for the interpretation of acquired propagation data and for the extrapolation to other frequencies and/or locations. The Delft University of Technology's involvement constitutes a part of its radar research program that includes radar signature studies of land and sea for remote sensing applications and tropospheric research on turbulence and hydrometeors using its own S-band FM-CW radar facility (DARR) [2]. This paper presents X-band radar derived attenuation prediction in comparison with simultaneous attenuation recordings of the 11 GHz OTS TM-beacon. The first section summarizes the theory, the models and the calculations required to arrive at attenuation predictions from reflectivity data. In the second section the instrumentation is described and an estimate of residual uncertainties is given. The last section is devoted to the evaluation of the experimental results. Individual events are analysed, overall correlations between predictions and direct measurements are calculated and finally radar derived and radiometer-derived cumulative distributions are compared to the direct measured one using the satellite 11 GHz beacon.

2. PATH ATTENUATION ESTIMATION FROM RADAR PRECIPITATION RETURNS

Attenuation estimations using radar echoes from precipitation rely on the simultaneous scattering and attenuation by hydrometeors. Both phenomena arise from the frequency dependent interaction of electromagnetic waves and hydrometeors. Electromagnetic scattering theories and empirical models for precipitation have been advanced to the point, where both attenuation and radar backscattering can be expressed in terms of particle

parameters and wavelength.

For a single particle the attenuation can be expressed as:

$$A_s[\text{dB}] = .4343 Q_t(a, \lambda, T)$$

where

$A_s[\text{dB}]$  is the attenuation per particle

$Q_t[\text{cm}^2]$  is the attenuation cross section, defined as the surface that represents the total power removed from the electromagnetic wave when multiplied by the incident intensity

For a spherical water droplet  $Q_t$  is a function of diameter ( $a$ ), wavelength ( $\lambda$ ) and temperature ( $T$ ).

Neglecting multiple scattering effects the attenuation per unit pathlength for a precipitation cloud comprising of spherical water droplets of various diameters is simply the summation of the attenuation contributions [in dB] of the individual droplets and consequently:

$$A[\text{dB/km}] = 0.4343 \int_0^{\infty} Q_t(a, \lambda, T) n(a) da$$

where  $n(a)$  is the droplet size distribution per unit volume in  $\text{cm}^{-1}$  per cubic meter.

Radar backscattering from a single drop can be expressed using the well-known radar equation [3]:

$$P_r = \frac{P_t G^2 \lambda^2 \sigma}{(4\pi)^3 R^4} L \quad (1)$$

where

$P_t$  peak power transmitted

$P_r$  peak power received

$G$  antennagain

$\lambda$  wavelength

$R$  radarrange

$L$  loss factor

$\sigma$  radar cross section per particle

For a spherical water droplet the radar cross section  $\sigma$  is a function of diameter, wavelength and temperature. The loss factor  $L$  accounts for the attenuation in the medium between the radar and the particle location. For a particle cloud the returns of individual drops arriving at the radar receiver within one pulse duration period add vectorially and produce a random fluctuation echo. This process is schematically indicated in Figure 1. The simulated output signal for a logarithmic receiver is also shown. The ensemble average of this random signal is of interest to attenuation estimation.

Based on the assumptions listed in table I, this average can be expressed in radar parameters and particle cross sections using the radar equation for distributed targets [4]:

$$\langle P_r \rangle = \frac{P_t \lambda^2 G^2 \theta \phi c \tau \eta}{1024 \ln 2 \pi^2 R^2} L \quad (2)$$

where

$\theta$  is the azimuth half power beamwidth

$\phi$  is the elevation half power beamwidth

$\tau$  is the pulse duration

$c$  is the velocity of light

$\eta$  is the radar cross section per unit volume

All other quantities have been defined previously (eq. 1). The radar cross section per unit volume is the summation of the radar cross section of individual droplets and it can be expressed as

$$\eta = \int_0^{\infty} \sigma(a, \lambda, T) n(a) da$$

Instead of  $\eta$  the effective reflectivity factor  $Z_e$  is commonly used. It is defined as

$$Z_e = (\lambda^4 \eta) / (\pi^5 |K|^2)$$

where

$K$  represents the temperature dependent dielectric properties of the water drops

Using the above equations the attenuation in dB per unit length for a given frequency

can be calculated from the reflectivity factor measured at the same or any other frequency. However, in order to do so attenuation cross sections and radar cross sections must be calculated using Mie theory [5] and measured data or models must be applied for particle shape, composition, size distribution and velocity. Using the assumptions listed in Table I attenuation and reflectivity values were calculated numerically and from these A-Ze relations of the form  $A = az_e^b$  were fitted to the calculated values:

$$\begin{aligned} A_{9.4} &= 7.5 \cdot 10^{-5} z_e^{0.82} \text{ dB/km at } 20^\circ\text{C} \\ A_{9.4} &= 9.4 \cdot 10^{-5} z_e^{0.80} \text{ dB/km at } 10^\circ\text{C} \\ A_{9.4} &= 13.5 \cdot 10^{-5} z_e^{0.76} \text{ dB/km at } 0^\circ\text{C} \end{aligned} \quad (3)$$

Similar calculations lead to attenuation values at 11 GHz as a function of  $Z_e$  at 9.4 GHz

$$\begin{aligned} A_{11} &= 15.0 \cdot 10^{-5} z_e^{.80} \text{ dB/km at } 20^\circ\text{C} \\ A_{11} &= 18.7 \cdot 10^{-5} z_e^{.78} \text{ dB/km at } 10^\circ\text{C} \\ A_{11} &= 26.5 \cdot 10^{-5} z_e^{.74} \text{ db/km at } 0^\circ\text{C} \end{aligned} \quad (4)$$

At X-band the loss factor L is of particular concern. In principle L can be determined using the above relations, but some inherent errors in the relations as well as the measurement of  $Z_e$  can very seriously affect the attenuation accuracy. This problem will be discussed in the last section.

Table I Assumptions associated with attenuation and reflectivity calculations in this study

Dropsizes	Spherical
Dropsizes distribution	Laws and Parsons
Spatial particle distribution	Uniformly throughout the pulse volume according to a Poisson Process
Particle composition	Water
Particle temperature	20° Centigrade

### 3. INSTRUMENTATION ASPECTS

For the experiment reported herein an X-band transceiverbox used in mass-produced ship's navigation radar was made available. The most important characteristics of this system are summarized in Table II.

Table II Radar Characteristics

Peak Power	7 KW
Frequency	9.445 GHz
Pulse Duration	50 ns
Pulse repetition frequency	3200 Hz
Receiver	logarithmic, 80 dB dynamic range
Antenna	2 meter diameter disc
Azimuth beamwidth	1.5 degrees
Elevation beamwidth	1.3 degrees
Polarization	vertical

The small transceiverbox was mounted directly to a 2-meter steerable parabolic reflector antenna with a corrugated horn focal feed system optimized for low sidelobes and low cross-polarization. In this construction long waveguide runs and rotating joints can be avoided. The whole system runs on 28 volts DC. Radar equipment of this type has been designed for reliable detection and ranging rather than for accurate echo strength registration, which is of prime importance here. Therefore, a few modifications had to be applied to the original equipment. The receiver subsystem as supplied by DECCA included an integrated intermediate frequency logarithmic amplifier/detector module with AC-coupled video output amplifier, hindering absolute registration. It was, therefore, replaced by a similar unit with DC-coupled temperature compensated video amplifier. Cluttersuppression and electronic gain control circuits were disconnected

where possible. These circuits are the main causes of temperature induced gain variation. For on-line data processing and storage a 50 Hz sample rate and a single 10 bit word per second storage capacity were available. To match this low sample rate to the 16 MHz video output of the radar an analog average and time expansion unit was developed. Consistent with the available storage capacity the radar data were compressed through combined range averaging and time averaging. Finally, every two minutes one range scan consisting of 128 range cells of 150 meter length is registered on magnetic tape, using 10 bit words for the system's 80 dB dynamic range. An example of a raw data record is shown in Figure 2. As can be seen from this figure the random fluctuations of the radarecho have been effectively averaged out. Since every datapoint consists of an average of 640 independent measurements the residual fluctuation is 0.17 dB.

As can be seen in the figure, sampling starts before the radar pulse is transmitted. The receiver noise level and transmitter-receiver leakage may thus be observed prior to the actual precipitation echoes. Unfortunately the two minute time averaging interval obscures significantly the fine structure of the rain storm. To illustrate this some measurement results from the high resolution S-band DARR system (Delft Atmospheric Research Radar) are shown in Figure 3. For the 4 minute examples shown the antenna system was fixed pointed to the zenith. Clearly the bright band can be recognized separating the frozen particles above from the rain below the 0° isotherm. By inverting the radar equation for distributed targets and plugging in the best estimate of the system parameters  $Z_e$  can be determined from the raw data. For the present system the following expression is calculated:

$$10\log Z_e = \langle 10\log P \rangle + 20\log R + 29.3 \quad (5)$$

In this equation the loss factor L has been deleted. In accordance with a recent review [6] the various correctable and incorrectable errors will be discussed. The logarithmic receiver is responsible for 2.5 dB processing loss. Since the major part of the signal averaging is done in analog form the quantization bias is negligible. An additional 2.3 dB processing loss results from processing the rectangular pulses by a matched filter [7]. In equation (5)  $\langle 10\log P \rangle$  is defined at the receiver output thus a net receiver gain of 14 dB had to be taken into account. Uncertainty in the calibration constant 29.3 may be subdivided into two classes: processing errors and system errors. The main processing error is the accuracy of the 80 dB dynamic range logarithmic receiver, specified to be within  $\pm 1$  dB. Compared to this the residual random fluctuations (0.17 dB) and the quantization error (0.08 dB) are insignificant. Quantitative data for specifying error bounds for the system transfer function is lacking for the present system. The number quoted represents the best available estimate. A fair guess of the absolute accuracy would be  $\pm 2$  dB.

System absolute accuracy as well as drift of the transfer function is of particular concern because it follows from equation (4) that an error as small as 1 dB can offset the attenuation prediction by as much as 20%. As will be discussed in the last section, evaluation of the prediction results revealed that the estimated transfer function had to be shifted slightly to match the predicted attenuation values to those actually measured using the satellite beacon. Similar discrepancies have occurred reportedly in similar experiments [6]. In addition to the hardware uncertainties discussed it may be noted that the radar beam even if pointed exactly along the satellite path covers a larger volume than the main contributing region of the satellite path. Considering that the averaging interval of two minutes is somewhat larger than desirable, the discrepancies turned out to be surprisingly small.

#### 4. EXPERIMENTAL RESULTS

During the first measurement period in the summer and fall of 1979 radarreflectivity was continuously recorded in parallel with OTS signal registration. Several interesting rain events took place during that interval. Figure 4 shows attenuation encountered by the 11 GHz beacon signal and rain intensity recorded at the receiving site on September 2, 1979. In the same figure radar derived attenuation values and cross polar discrimination recordings are shown. All data were averaged over a two minute interval. As a first approximation a simple prediction algorithm has been used. From equation (5) (offset by 2.5 dB) the effective reflectivity factor was determined for each range cell. Using equation (4) the corresponding attenuation values were calculated and added to yield total path attenuation. Throughout the measurement period the same calibration factor has been used. As can be concluded from the figure radar derived attenuation values compare favourably with direct measurements. There seems to be a fair correlation with rain-intensity as well. The reflectivity record of Figure 5 reveals that the rain mainly occurred below the 0° isotherm and filled the path rather uniformly. On August 17th the situation was quite different. Two consecutive rain events took place. The first one started to contribute to the upper tropospheric layers and consequently the groundstation recorded rainintensity at the very end of the attenuation occurrence on the path (Figure 6 and 7). Radar attenuation prediction showed fair agreement with the actual attenuation. The last example of an event has been depicted in the Figures 8 and 9. Of special interest is the extra attenuation peak predicted by radar that is absent in the actual attenuation record. The explanation can be found by examining the reflectivity records. Since a straightforward prediction algorithm has been applied that utilizes the A-Z<sub>e</sub> relation for rain regardless of the hydrometeor type a dramatic overestimation is expected in case of elevated layers filled with frozen particles. In the presence of a distinct bright band an overestimation of attenuation occurs as well. Different prediction algorithms were therefore applied to the data that only take into account reflectivity up to the 0° isotherm including or excluding the bright band. The underestimation of attenuation that one would expect for these algorithms was not apparent in the data, because during the experiment period in all cases the bright band

attenuation constituted only a minor portion of the total path attenuation. An attempt was made to apply attenuation corrections. For the majority of cases, however, the attenuation was distributed along the path in such a way that the correction did not have a significant effect on the prediction. For a few cases the iterative correction procedure applied did not yield a stable reflectivity estimate. Further analysis, however, has been postponed until a larger database is available. Table III summarizes the results obtained to date using the prediction algorithms indicated. The figure for radiometer derived results are added in comparison. From Table III it may be concluded that even for very coarse algorithms radar prediction at X-band performs quite well. The residual spread can be attributed to a variety of errors the major sources being drops size distribution variations and system drift.

Table III Correlation between direct measured attenuation and values derived from radar reflectivity and radiometric measurements

Model	Upper layers included	bright band included	attenuation correction	correlation coefficient
1	+	+	-	.883
2	-	+	-	.924
3	-	-	-	.947
		radiometer		.956

Assuming Laws and Parsons drops size distribution to be perfectly adequate in all cases, system drift can be inferred by recalibrating the radar data for each individual event and inspecting the variation of the radar calibration factor. These variations are shown in Figure 10. The overall correlation coefficient in this case raises to .972. In the same figure the radar calibration factor calculated using the best estimate of system parameters is shown in comparison. This number would slightly underestimate the reflectivity factor  $Z_e$  compared to the one required to yield the highest correlation between predicted and measured attenuation values.

Another way to present the results of this experiment is to derive cumulative attenuation statistics from the dataset. The results are shown in Figure 11. In Figure 12 the statistics of direct measured and radiometer derived attenuation levels are compared.

## 5. CONCLUSIONS

Radar derived attenuation predictions based on reflectivity data acquired at X-band using inexpensive mass produced equipment compare surprisingly well with direct measured values. In spite of residual uncertainties correlations were obtained as high as .95 percent using straightforward prediction algorithms. Information concerning the  $0^\circ$  isotherm height has proved essential for accurate results. Attenuation at the radar frequency does not appear to be the main source of error for the events described. The radar derived statistics compare well with similar results from radiometric measurements.

## REFERENCES

- [1] Silva Curiél, A. da, Reinders, M.A.: "The characteristics of an earth station antenna for experimental satellites operating at frequencies above 10 GHz", IEE International Conference on Satellite Communications System Technology, London, April 7-10, 1975
- [2] Lighthart, L.P.: "System considerations of the FM-CW Delft Atmospheric Research Radar (DARR)", IEEE International Radar Conference, Washington DC, April 28-30, 1980
- [3] Skolnik, M.E.: "Radar Handbook", New York, McGraw-Hill, 1970
- [4] Probert-Jones, J.R.: "The radar equation in meteorology", Quarterly Journal of the Royal Meteorological Society, Vol. 88, 1962, pp. 485-495
- [5] Mie, G.: "Contribution to the optics of suspended media, specifically colloidal metal suspensions", Ann. Phys., Vol. 25, 1908, pp. 377-445
- [6] Goldhirsh, J.: "A review on the application of non-attenuating frequency radars for estimating rain attenuation and space diversity performance", IEEE Transactions on geoscience electronics, Vol GE-17 no. 4, October 1979
- [7] Doviak, R.J., Zrnic, D.: "Receiver bandwidth effect on reflectivity and doppler velocity estimates", J. Appl. Meteorology, Vol. 18 no. 1, pp. 70-76, January 1979 (quoted in [6]).

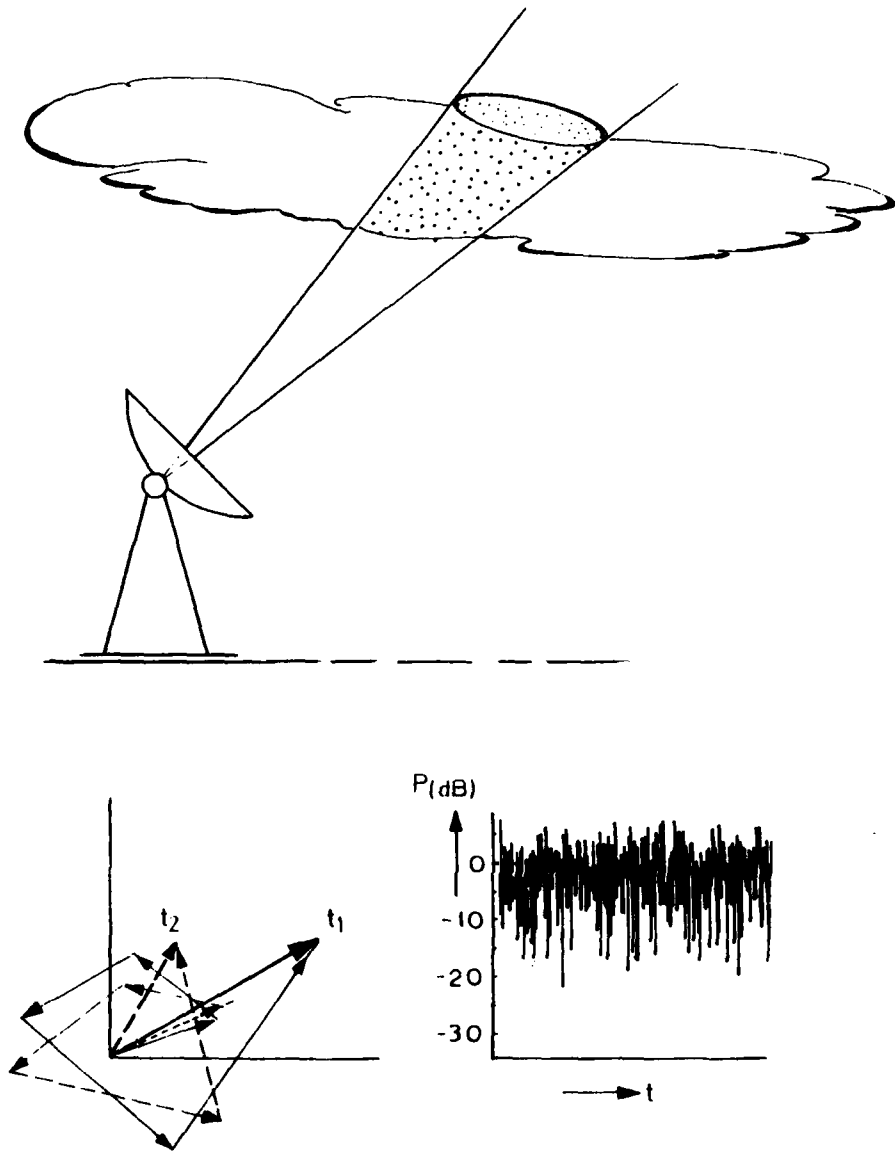


Figure 1 Fluctuating echo from precipitation by mutual interference of individual scatterers.



Figure 2 Raw radar data sample recorded August 2, 1979, 11.08 GMT. Horizontal scale slant range; vertical echo intensity in dB.

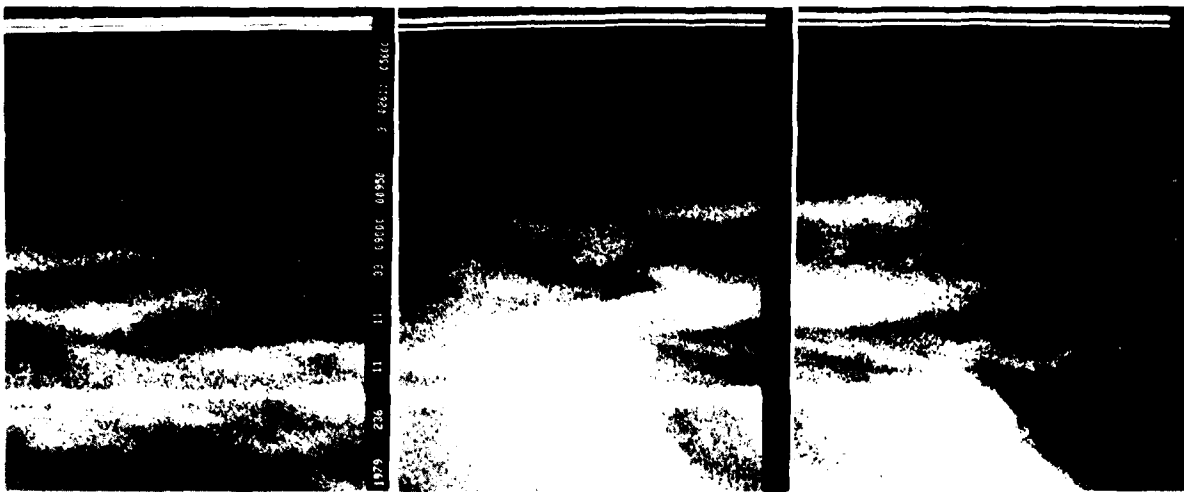


Figure 3 Reflectivity measurements of a rainstorm recorded by high resolution S-band radar pointed vertically. Horizontal range: 4 minutes; vertical range: 7.5 km.

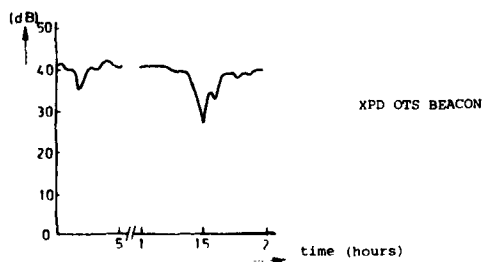
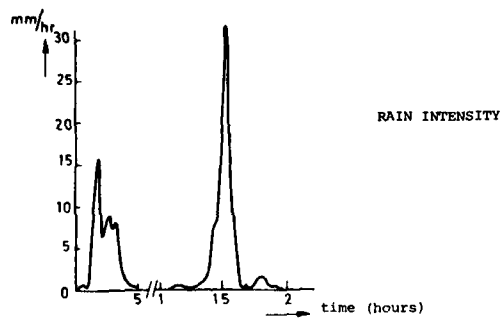
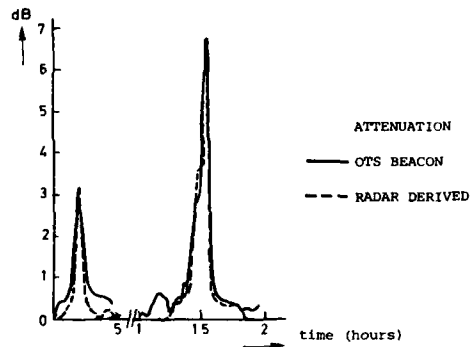


Figure 4 Registration records of PTT groundstation equipment and radar derived attenuation prediction. Date: September 2, 1979



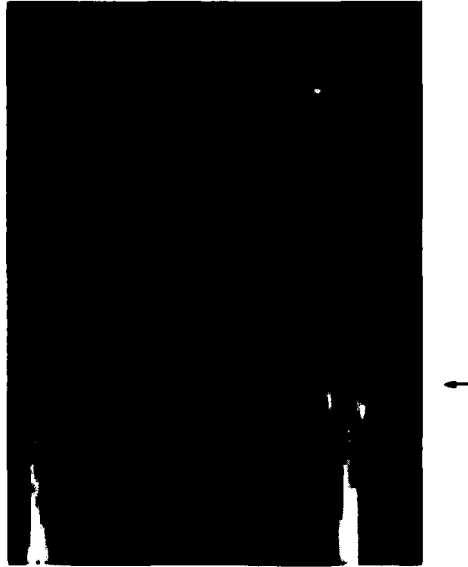


Figure 5 Radarreflectivity along the satellite path on September 2, 1979. Horizontal range: 180 minutes; vertical range: 18.5 km slant range. Zero degree centigrade isotherm indicated by arrow

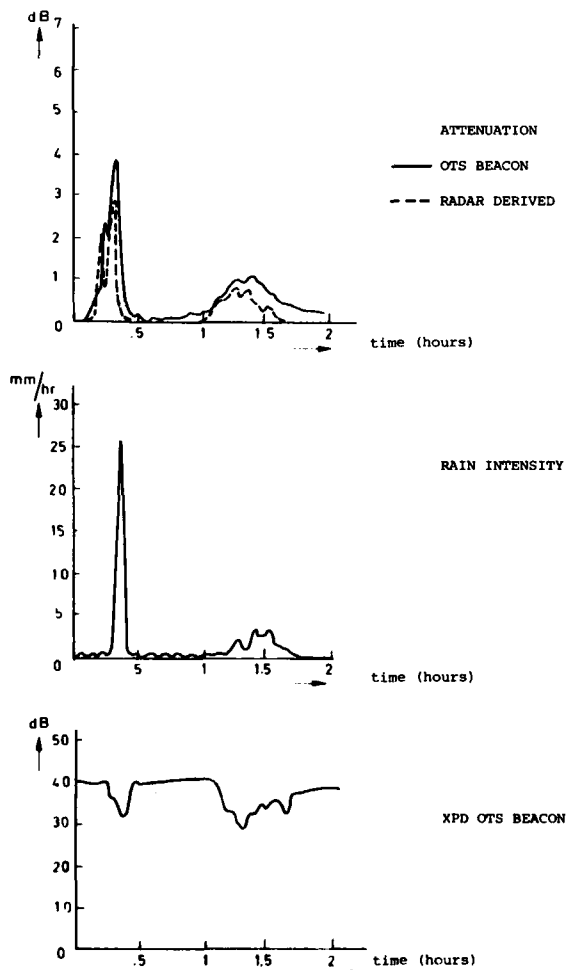


Figure 6 Registration records of PTT groundstation equipment and radar derived attenuation prediction. Date: August 17, 1979

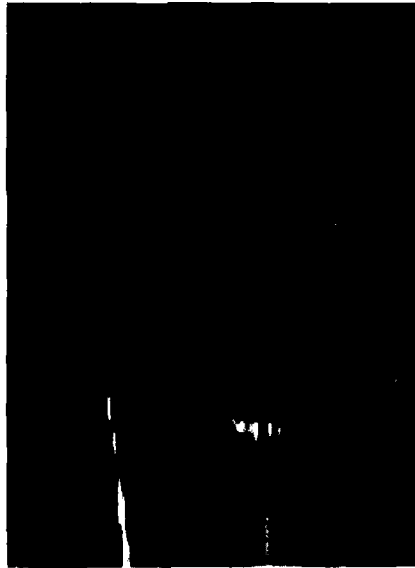


Figure 7 Radarreflectivity along the satellite path on August 17, 1979. Horizontal range: 180 minutes; vertical range: 18.5 km slant range. Zero degree centigrade isotherm indicated by arrow

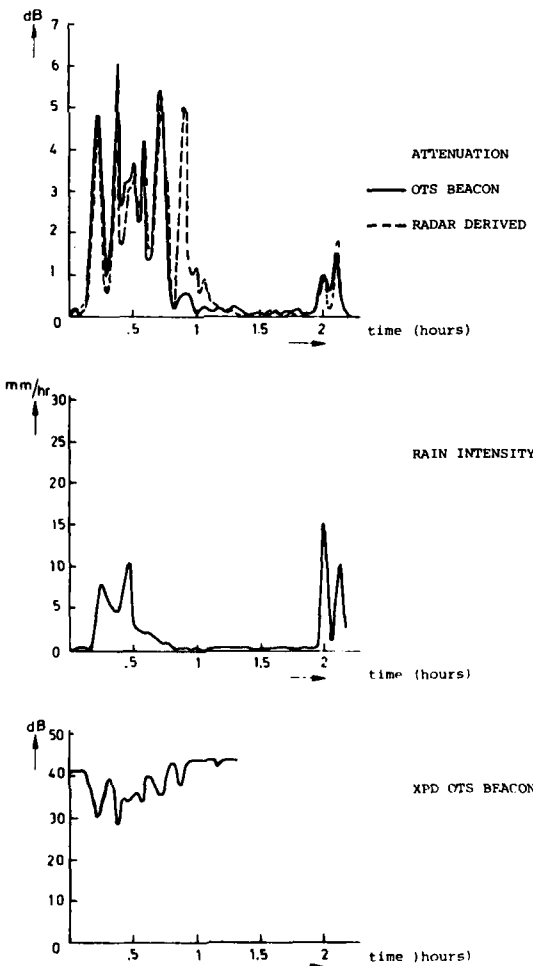


Figure 8 Registration records of PTT groundstation equipment and radar derived attenuation prediction. Date: August 3, 1979

AD-A090 850

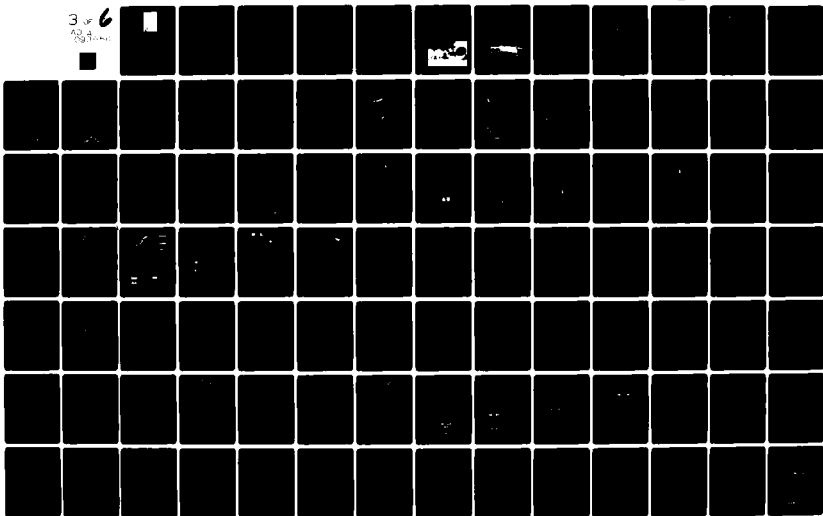
ADVISORY GROUP FOR AEROSPACE RESEARCH AND DEVELOPMENT--ETC F/G 20/14  
PROPAGATION EFFECTS IN SPACE/EARTH PATHS. (U)  
AUG 80 H J ALBRECHT  
AGARD-CP-284

UNCLASSIFIED

NL

3 of 6

2511



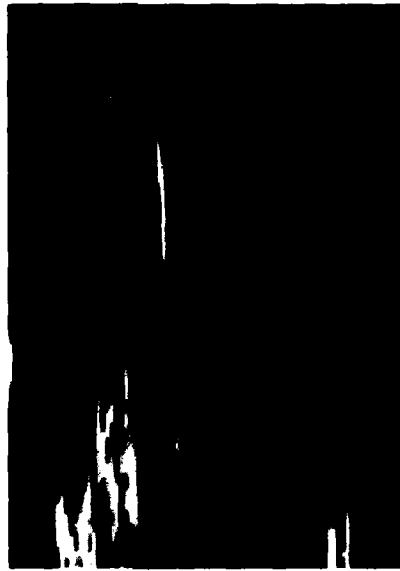


Figure 9 Radarreflectivity along the satellite path on August 3, 1979.  
Horizontal range: 180 minutes; vertical range: 18.5 km slant range.  
Zero degree centigrade isotherm indicated by arrow

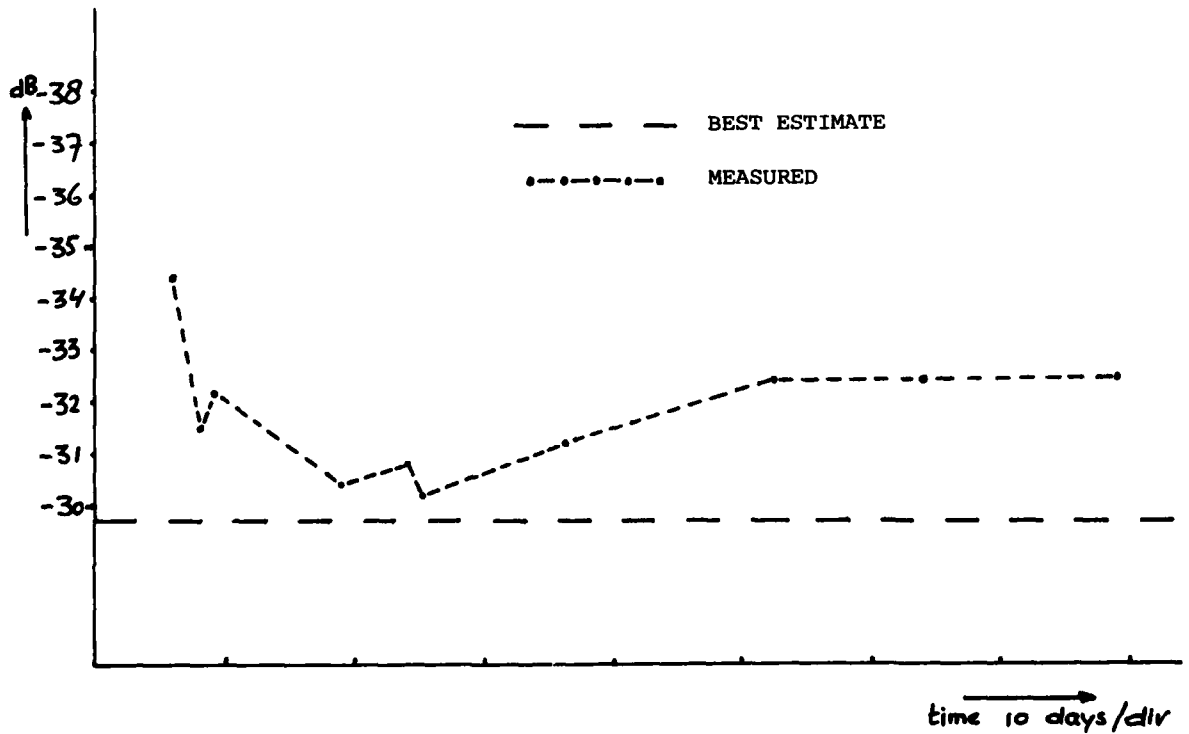


Figure 10 Radar calibration variation throughout the experiment period assuming theoretical models to be perfect. Best estimate of calibration factor indicated by broken line

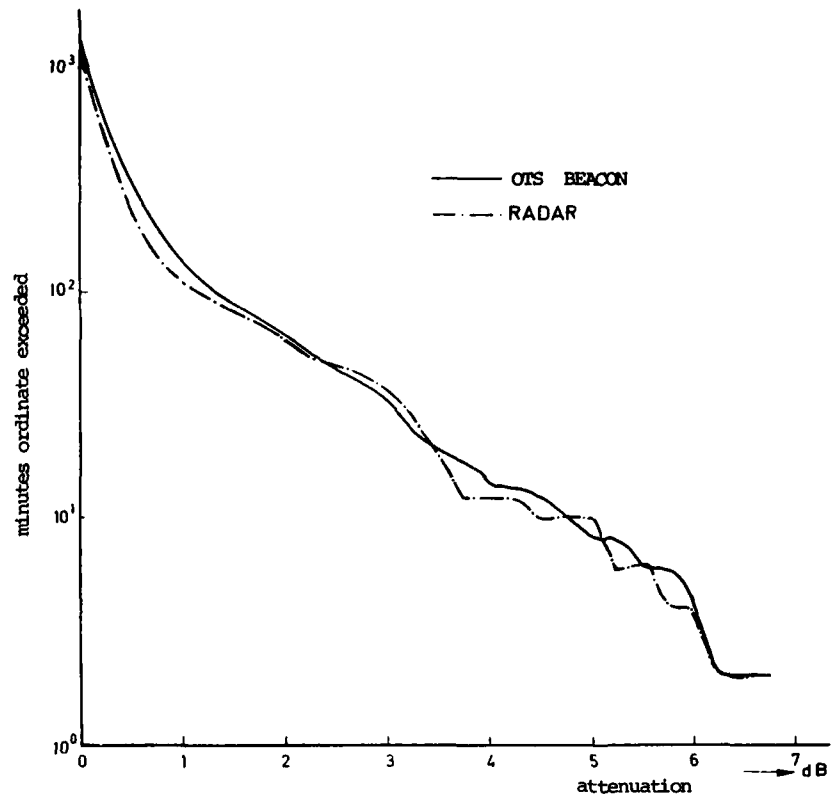


Figure 11 Comparison between radar derived and directly measured cumulative attenuation statistics. All data averaged over two minute interval

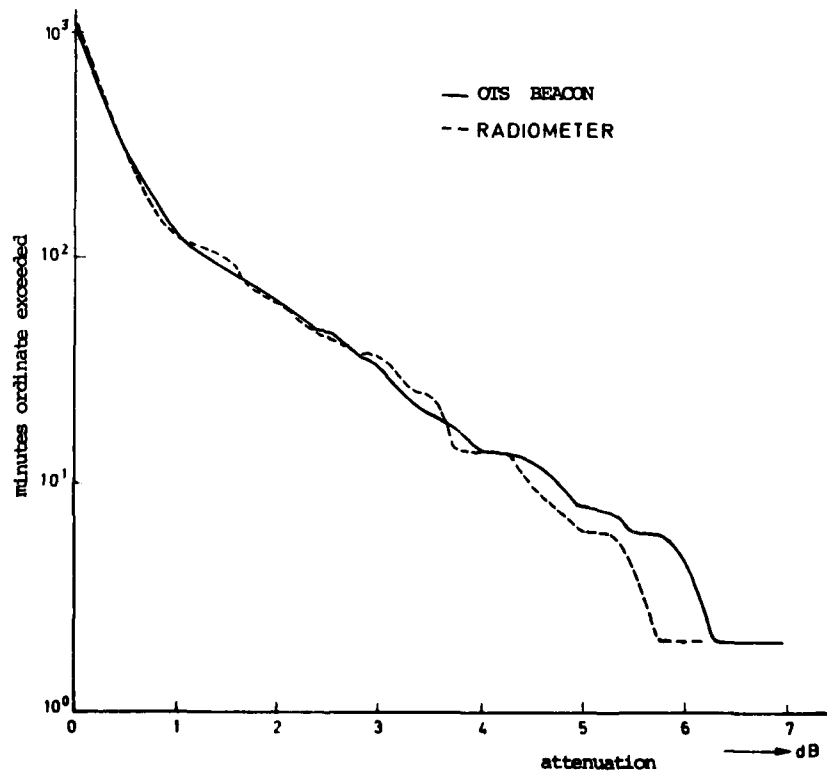


Figure 12 Comparison between radiometer derived and directly measured cumulative attenuation statistics. All data averaged over two minute interval

## OTS PROPAGATION MEASUREMENTS AT EINDHOVEN UNIVERSITY, NETHERLANDS

J. Dijk, C.N.F. Hansen and E.J. Maanders

Eindhoven University, Netherlands.

## ABSTRACT

Since the launch of O.T.S.-2 in May 1978 nearly permanent reception in Eindhoven has taken place of the  $\overline{TM}$  and  $B_0/B_1$  beacon, with respect to attenuation on the path satellite-ground-station. A large amount of fades could be registered, the largest of about 15 dB lasting nearly 10 minutes.

Daily variations of the  $\overline{TM}$  beacon of 500 Hz and long time variations over a period from June 1978 to October 1979 of more than 5000 Hz have been recorded. The  $B_0$  beacon showed very large frequency variations of 20 - 30 kHz per day and long time variations of about 130 kHz over the same period as the  $\overline{TM}$  variations. Statistical material, inclusive cumulative distributions has become available over the entire period of measurements.

## 1. Introduction

After having finished the ATS-6 project (1,2,3), the radio group of Eindhoven University decided to participate in the OTS propagation experiments, to collect knowledge regarding the propagation of electromagnetic waves between earth and satellite in the 11 and 14 GHz frequency bands under local weather conditions. Special attention has to be paid to the measurement of attenuation, depolarisation, and the phase behaviour of linear and circularly polarised waves. By comparing the main and crosspolarisation of the signals an insight can be obtained in the polarisation isolation, being important with respect to frequency re-use plans. The OTS satellite offers the possibility of receiving two beacons viz. the linear beacon ( $\overline{TM}/\overline{TM}$ ) and the circular beacon ( $B_0/B_1$ ) both in the 11 GHz frequency band. To carry out measurements in the 14 GHz frequency band two beacons ( $B_{20}$  and  $B_{21}$ ) have been allocated to Eindhoven University. These signals can be transmitted to the satellite and via the transponder in module B retransmitted to earth in the 11 GHz frequency band.

For this project a groundstation (Fig. 1) has been built to receive and transmit the signals, and a weather station to measure weather data. The experiments are supported by radiometer measurements. Two microcomputers and a minicomputer are used for signal processing of the satellite and other data (4).

In the course of 1978 the 3 meter precision Cassegrain antenna of the groundstation showed serious surface degradation and had to be replaced. For this purpose a smaller 1.5 meter antenna could be found and consequently the number of experiments had to be reduced to reception of the beacons in the 11 GHz band (5). A new 8 meter antenna is expected to be operational in the second quarter of 1980.

## 2. The receiving system

A simplified block diagram of the receiving system is given in Fig. 2. The beacons are down converted by a mixer with local frequency of 11,520 MHz and amplified afterwards. In this way, the IF frequency for the  $\overline{TM}$  beacon will be 55 MHz and that of the  $B_0$  beacon 266 MHz. These two signals are inserted into two separate channels, amplified and down converted to 10 MHz. The final reception takes place in phase locked loop receivers (6). The phase locked loop receiver DC output is amplified in such a way that the final signal is strong enough for digital processing. The amplitude of this signal is recorded and is a measure for the variations or attenuation of the beacon signals in respect to free space attenuation.

All frequencies have been derived from very stable frequency sources (1 and 5 MHz). This offers the possibility to find the frequency of the beacon signals by measuring the controlling voltage of the VCO. These voltages are also recorded on the x-t recorder. At the same time the signals are presented to an A/D converter, being part of the minicomputers (4).

## 3. The location of the satellite

The location of the OTS satellite is  $10^\circ$  East. This position will be maintained within  $\pm 0.1^\circ$  with respect to its north-south and east-west direction. Seen from the ground-station in Eindhoven the satellite is located at azimuth =  $174.25^\circ$  and elevation  $30.97^\circ$ . In general a geostationary satellite does not move in respect to an observer on earth. However, there are several forces which will cause the satellite to drift. These forces are:

- The attractive force of the earth. This force is not uniform and depends upon the longitude and latitude.
- The attractive force of sun and moon, depending upon the position of sun and moon with respect to earth; the influence of the moon is about three times that of the sun.
- The radiation pressure of the sun; depending on the size, orientation and reflectivity of the satellite.

To keep the satellite in the correct position course corrections have to be performed from time to time. In September 1978 such a correction went wrong causing the satellite to oscillate ( $\pm 1^\circ$ ) which has been noticed recording the received signal (Fig. 3). The maximum pointing error due to the satellite movements is about  $0.2^\circ$  (7). Measurements have shown that long term variations in azimuth have not exceeded these  $0.2^\circ$  (Fig. 4). The variation in elevation was much smaller and less than one hundredth of a degree. The small variations in elevation and azimuth had no influence on the measuring results.

#### 4. Variations of the OTS beacons

##### 4.1. Power variations of the beacons $\overline{TM}$ and $B_0$

Fig. 5 shows the amplitude variations of  $\overline{TM}$  in 24 hours. It appears that the variation amounts 0,53 dB p.p. in this period and only caused by the satellite when measurements have been carried out on a day under clear sky conditions. Similar plots of the  $\overline{TM}$  beacon showed variations of 0.5 - 0.7 dB p.p.

The needles in the  $\overline{TM}$  beacon (Fig. 6) are caused by the ranging operations. These ranging operations take place several times a day, where from the earth the position of the satellite is checked with a special signal which influences the power of the beacon; the distance in time of the operations, the number of times per day, and the time of each operation differs from time to time. The variations due to ranging operations and the "normal" variations of the satellite power are factors making an automatic signal investigation nearly impossible especially when the variations take place during fading, which has to be processed digitally.

If analog recording of the received signal is carried out, correction is possible by the human eye, especially if registrations of the  $B_0$  beacon take place at the same time.

Digital processing of the signals is possible if events take place and the daily variations may be neglected; usually, events (thunderstorms) are limited in time.

The amplitude stability of the  $B_0$  beacon is even worse than that of the  $\overline{TM}$  beacon, the daily variations are about 1.2 - 1.5 dB p.p.

##### 4.2. Frequency variations of the $\overline{TM}$ and $B_0$ beacon

The frequencies of the  $\overline{TM}$  and  $B_0$  beacons show also variations. These variations are caused by temperature variations in the satellite (7). The variations of the  $B_0$  beacon are caused by the temperature dependence of the Impatt-diode oscillator. Frequency measurements show this dependence clearly (Fig. 7). The temperature in the satellite near the oscillator was announced by so-called "circular letters". The frequency was known by measuring the VCO controlling voltage of the PLL receiver which was recorded on an x-t recorder. The correlation was very satisfactory ( $r = -0,97$ ).

Linear regression yields the following relationship

$$f(B_0) = 19.22 - 3.23 T \quad (\text{kHz}),$$

where T is the temperature in degrees Celsius near the beacon oscillator.

The daily variations of  $f(\overline{TM})$  are smaller (Fig. 8), about 500 Hz. This is much lower than the original specifications being + 10 kHz per day and long term variations of + 130 kHz. The daily variations of  $f(B_0)$  are about 20 - 25 kHz per day, in agreement with the specification of + 25 kHz per day (Fig. 9). The long term variations of  $f(B_0)$  also satisfy the specification (+ 350 kHz).

##### 4.3. Eclipse phenomena

All geostationary satellites suffer in spring-time and autumn from eclipses as in these periods the earth is in a position between sun and satellite (Fig. 10). Temporarily batteries take care for the energy supply. During 46 successive days the eclipse phenomena are present during a part of the day. It starts 23 days before equinox and ends 23 days after equinox. The eclipse duration varies from 10 minutes in the beginning until 72 minutes at equinox (Fig. 11). During eclipse the satellite is in the shadow of the earth causing strong temperature variations inside and outside the satellite, resulting in extra variations of the transmitted power and the beacon frequencies.

The level of  $B_0$  shows between 23.00 and 24.00 GMT strange jumps and the level of  $\overline{TM}$  increases with 0.5 dB during this period (Figs. 12 and 13).

The variations are probably caused by inaccuracies in the satellite subsystem near the OMT. The  $B_0$  beacon shows further since the spring-time eclipse of 1979 two small jumps one between 20.00 and 21.00 GMT and one between 3.00 and 4.00 GMT.

During eclipse the frequency variation of the  $B_0$  beacon increases and is larger than 25 kHz (Fig. 14). The largest variation, 36 kHz in 3 hours, has been measured on September 18, 1979.

The frequency variation of  $\overline{TM}$  shows jumps of about 1.5 kHz (Fig. 15).

#### 5. Propagation measurements

As explained in the introduction the number of experiments has to be reduced to attenuation measurements only due to a breakdown of the 3 meter Cassegrain antenna. This section gives a detailed survey of the measurements carried out.

##### 5.1. Scintillation or spikes

Amplitude scintillation has been noticed although no further analysis has been undertaken. During cold winter-weather scintillation was most not present or very small. During the wet summer months of 1979 the effect was very often noticeable. The amplitude mostly varied between 1 dB p.p. and the largest variation measured 3 dB p.p. During the winter 1978-1979 and during spring-time 1979 the level of  $\overline{TM}$  beacon showed serious disturbances with sudden variations in the form of spikes (Fig. 16). All spikes decrease the signal level. It is remarkable that this phenomenon was not recorded by all experimenters and that since spring-time 1979 it disappeared. No explanation is available at the moment.

##### 5.2. Attenuation by snow

At a frequency of 11 GHz the attenuation of electromagnetic waves is mainly caused by

rain. Fog has practically no influence; also rain-clouds cause only small attenuations (< 0,2 dB), however, very dark clouds sometimes 0,7 dB. The influence of snow is limited as long as the snow is not melting. Wet snow may cause some attenuation. A wet snow shower, in March 1979, increased the attenuation 2,6 dB. The influence of snow on the antenna surface will be considerable if the snow starts melting (Fig. 17). In the beginning dry snow came down on the antenna surface without any attenuation noticeable. At 8.40 GMT the temperature increased above the freezing-point and the snow started to melt. The signal level dropped 7.5 dB and returned to the old level when the snow became water which flowed down from the antenna surface. The inhomogeneous layer of snow on the surface of the antenna changing the radiation pattern of the antenna may also have formed a contribution to the value of 7.5 dB. A possible solution would be the use of anti-icing systems, although this is not ideal. Large power is required for heating (the new 8 meter antenna would require 48 kW). Moreover, dry snow is very often blown away from the antenna surface by wind giving no attenuation at all. If the surface is heated dry snow turns into wet snow resulting in attenuation (7).

### 5.3. Attenuation by rain

In general, rain is responsible for large attenuations. The attenuation depends upon the quantity of water per unit volume (Fig. 18). Therefore, the showers in the summer will show more attenuation than drizzle. On the other hand, the probability of drizzle is larger than summer showers.

Cumulative distributions are now available for the largest part of 1979. From Fig. 19 it may be noticed that May was the worst month. This was caused by an enormous thunderstorm on May 30. The PLL receiver fell out of lock at an attenuation of 15 dB and started to operate again after about 10 minutes.

Further, the distributions show that from January until May the attenuation is low. The attenuation is very well noticeable from May until October. The results of 1978 confirm this picture.

From the cumulative distributions it is possible to determine the percentage of time that the attenuation is larger than a given value. The percentages deserving special attention are 20%, 1%, 0.3% and 0.1% of a certain month and 0.01% of a certain year (Tables 1 and 2).

Table 1 : Percentage of time in a certain month that the given value of attenuation is exceeded.

1979 % of the months	attenuation value exceeded (dB)								
	1	2	3	4	5	6	7	8	9
20%	-	-	-	-	-	-	-	-	-
1%	0,5	0,7	0,9	0,7	0,9	0,9	0,7	0,9	0,7
0,3%	0,6	0,9	1,2	0,9	1,6	1,4	1,3	1,3	1,4
0,1%	0,6	1,1	2,0	1,1	3,2	2,3	2,4	2,0	2,4

Table 2 : Percentage of time of the year that a given attenuation is exceeded.

% of the year	attenuation value exceeded (dB)		
	1978	1979	'78+'79
0,01%	3,5	6,4	4,8

Fig. 20 shows the cumulative distributions of 1979. The large influence of the 30 May shower is worth mentioning. In Fig. 21 the results obtained in 1978 (June 1 - Dec. 31) are compared with the year 1979. It appears that in 1979 more and longer attenuations have been reported than in 1978. In Table 3 a survey is given of the number of attenuations more than 3 dB.

Table 3 : Fades in 1978 and 1979

number of fades	1978	1979
3 dB	18	24
4	16	15
5	9	13
6	7	8
7	4	6
8	4	5
9	3	5
10	-	4
11		4
12		4
13		2
14		2
15		1



Attenuation measurements by means of radiometers started in August 1979. The two events noticed from time showed good correlation between radiometer measurements and signals from the satellite.

#### 5.4. Conclusions

At a frequency of 11.6 GHz attenuation of more than 3 dB are caused by rain. This 3 dB value is exceeded in less than 0,1% of the time every month (in May 1979 3,2 dB). The attenuation measured is sometimes more than 10 dB; 15 dB has been noticed and a figure of 20 dB seems possible. Conclusions from one year measurements should be drawn with care as large differences may occur from year to year.

#### References

1. J. Dijk, J.P. van der Fluit, E.J. Maanders, P.J. Roelandschap, P.J. de Winter and F. Zelders: "ATS-6 propagation experiments at Eindhoven University", Proceedings of ESTEC Meeting, pp. 37-54, September 1977.
2. J. Dijk and E.J. Maanders: "Copolar and crosspolar signals received at 30 GHz from ATS-6", Paper presented at URSI Symposium Propagation in non-ionized media, La Baule, France, 28 April - 6 May 1977, Annales des Telecommunications nrs. 11-12, pp. 502-506, 1977.
3. J. Dijk, E.J. Maanders and P. de Winter: "Scintillation effects receiving ATS-6 at 30 GHz", Paper presented at URSI Symposium Propagation in non-ionized media, La Baule, France, 28 April - 6 May 1977, Annales des Telecommunications nrs. 11-12, pp. 506-513, 1977.
4. K.G. Holleboom and J.M.H. Wagemans: "Signal processing of orbital test satellite data", Paper presented at the Spacecad Conference, Bologna, Italy, September 18-21, 1979.
5. C.N.F. Hansen and E.J. Maanders: "System overview of earth station nr. 11", Paper presented at the second OTS Experimenters Meeting, Paris, 15-16 March 1979.
6. J. Dijk and J.M.G.A. Ouderling: "A receiving system for experimental geostationary satellites with very accurate phase detection", Paper presented at the symposium on Advanced Satellite Communications Systems using the 20-30 GHz bands, pp. 237-245, Genoa, Italy, December 1977, ESA (European Space Agency) Report SP 138, January 1978.
7. Proceedings of the second OTS Experimenters Meeting, Paris, March 15-16, 1979.
8. J. Spilker: "Digital communications by satellite", Prentice Hall, 1977.



Fig. 1 : A view of the groundstation at the university terrain

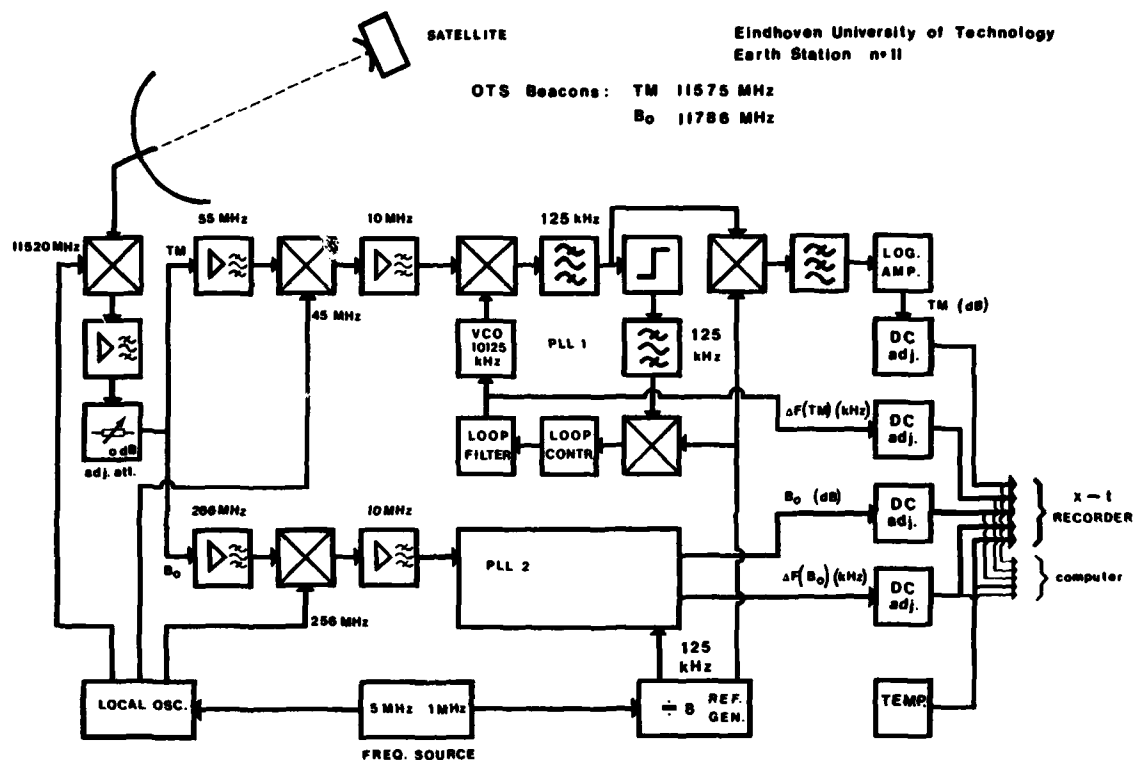


Fig. 2 : A simplified block diagram of the receiving system

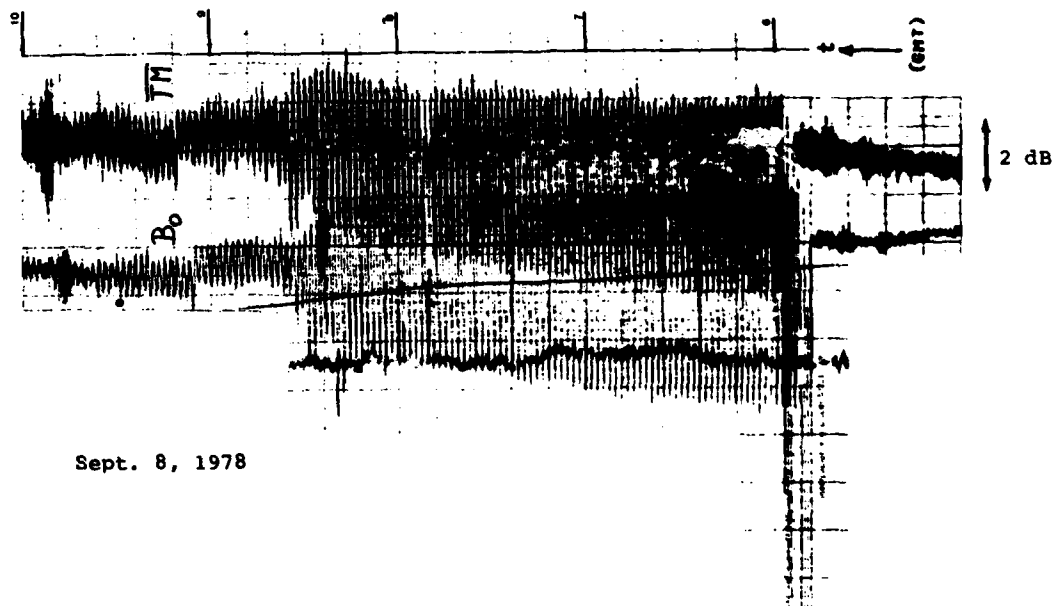


Fig. 3 : Wrong course correction causing the signal to oscillate for about 2 minutes period time, 2 - 2.3 dB p.p.

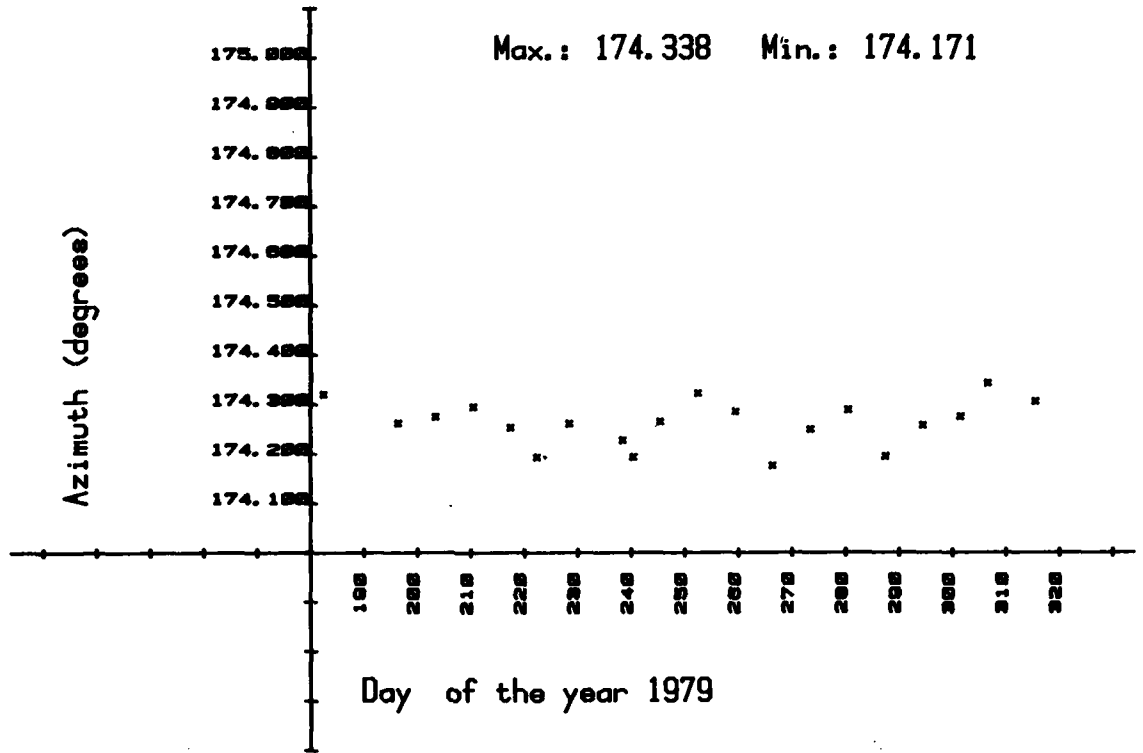


Fig. 4 : Long term variation of the azimuth position of OTS.

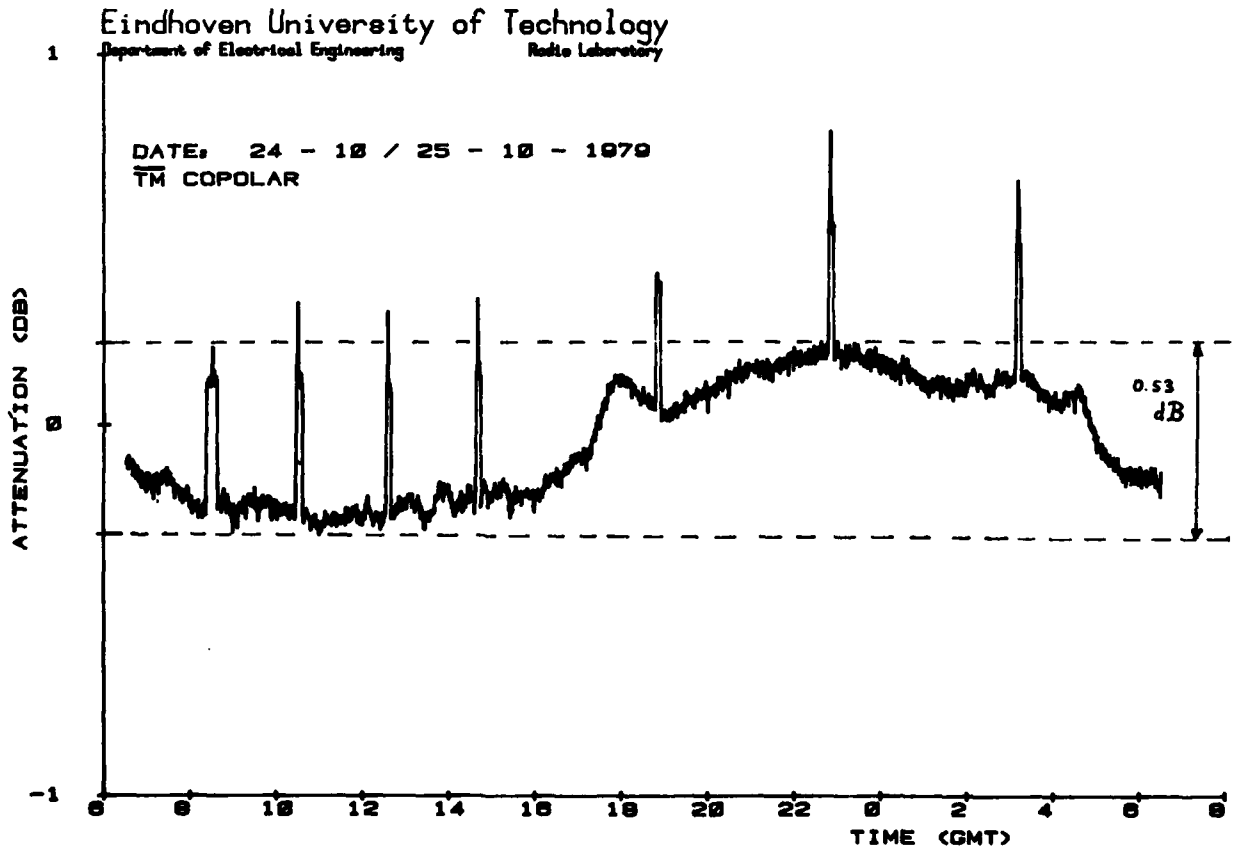


Fig. 5 : Amplitude variations of  $\overline{TM}$  over 24 hours. Sampling rate 2 Hz. Averaging time 100 seconds.

Eindhoven University of Technology  
 Department of Electrical Engineering  
 Radio Laboratory

DATE: 18 - 8 - 1978  
 TM COPOLAR

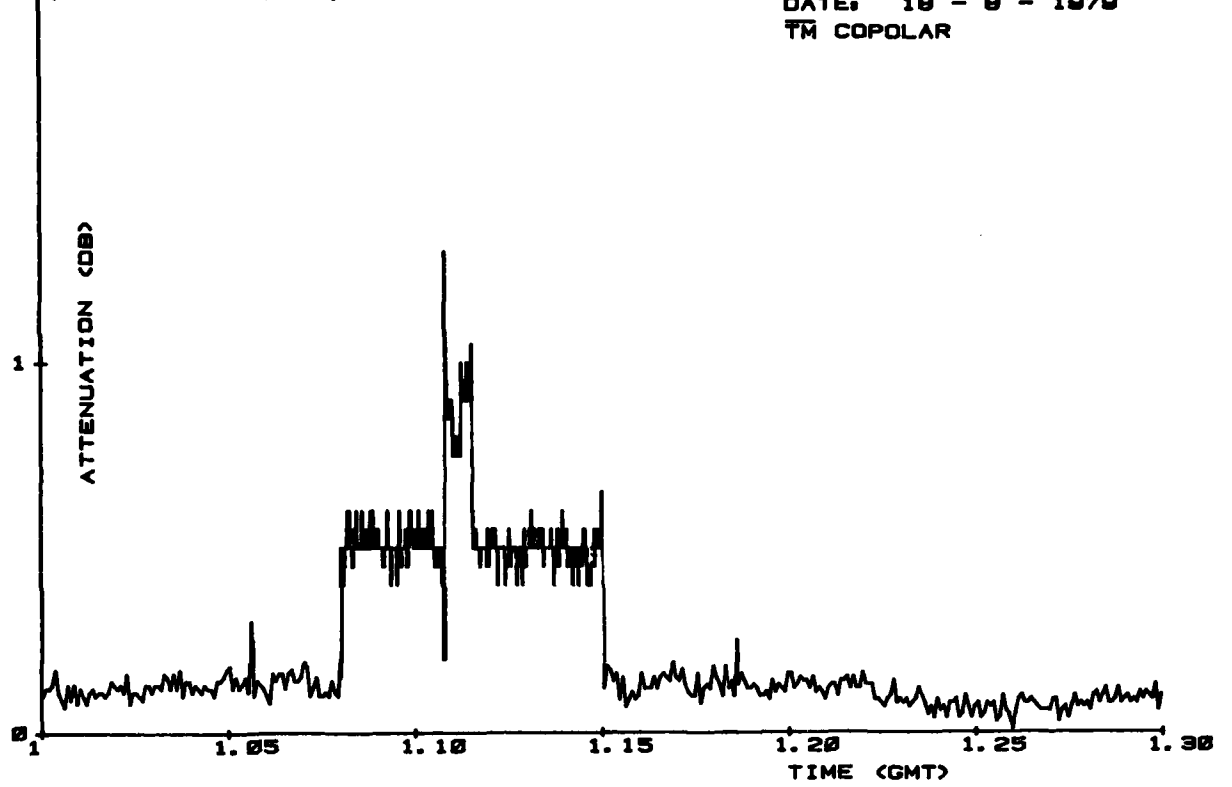


Fig. 6 : Ranging operation. Sample rate 2 Hz. Averaging time 5 secs (1 sec)

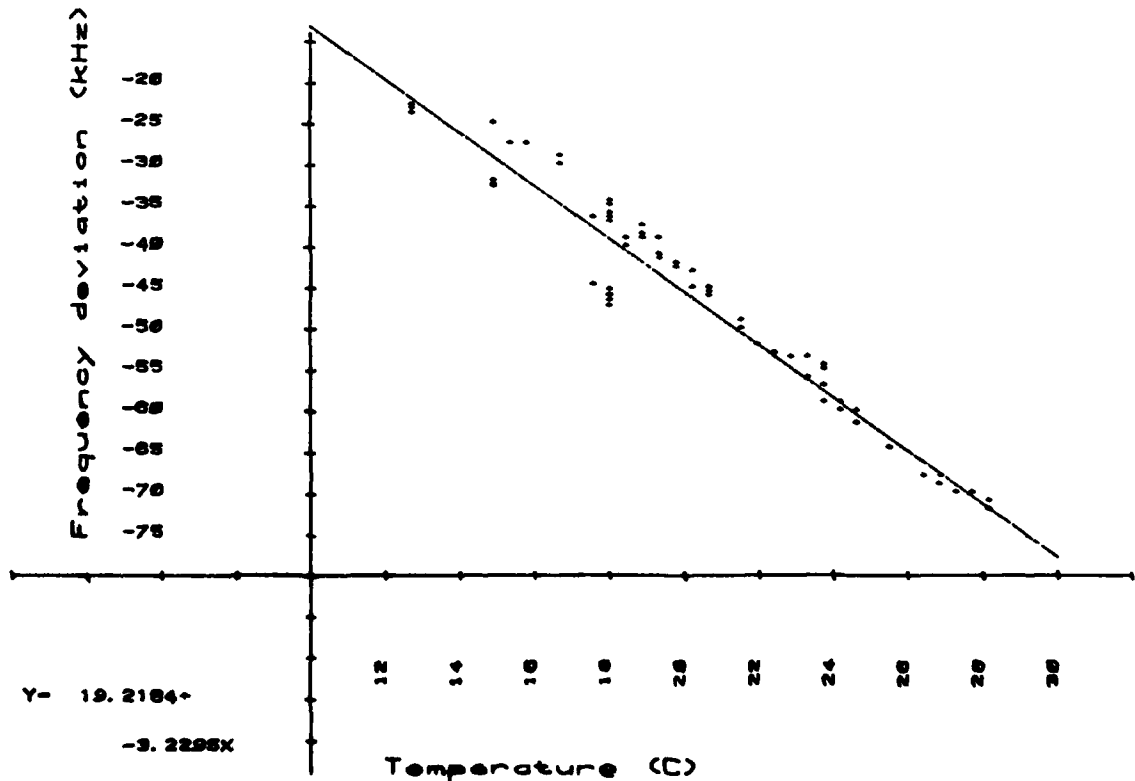


Fig. 7 : Temperature dependence of  $f(B_0)$

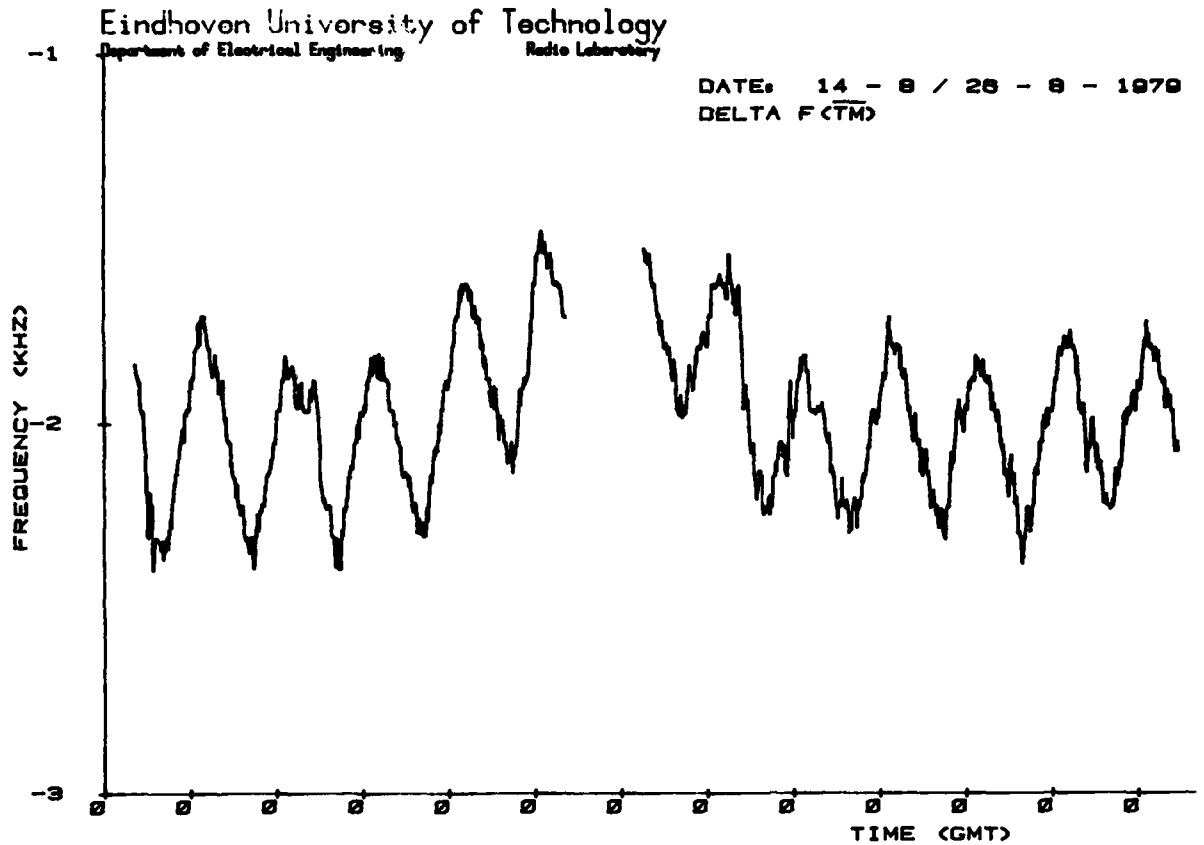


Fig. 8 : Variation of  $f(\overline{T_M})$  over a period of 13 days. Sampling rate 0.1 Hz. Averaging time 100 sec.

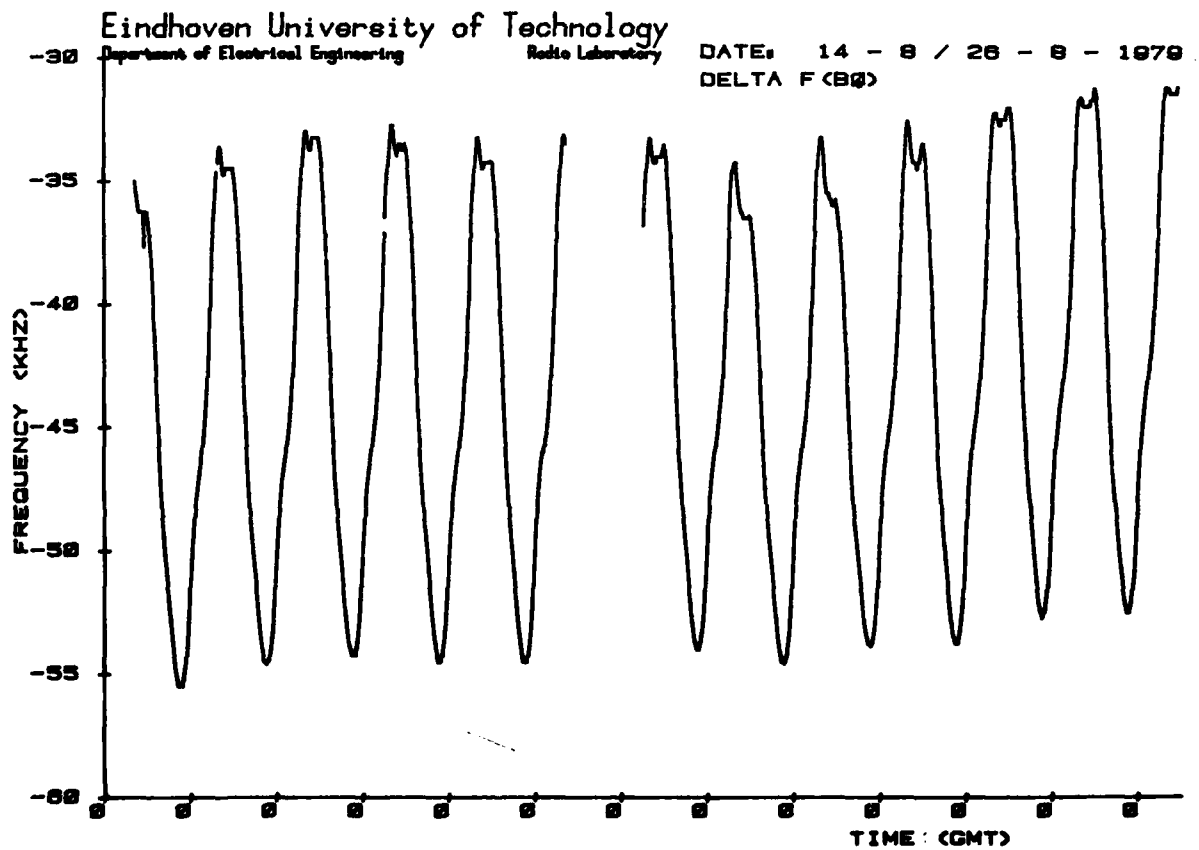


Fig. 9 : Variation of  $f(B_0)$  over a period of 13 days. Sampling rate 1/60 Hz. Averaging time 10 min.

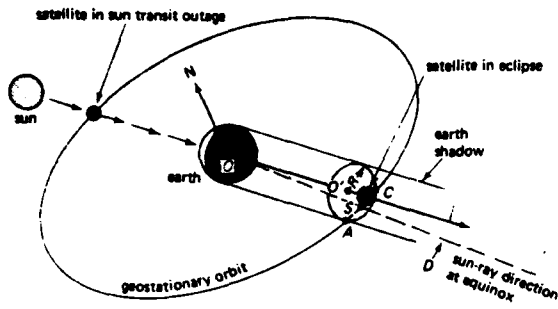


Fig. 10 : Satellite eclipse (8)

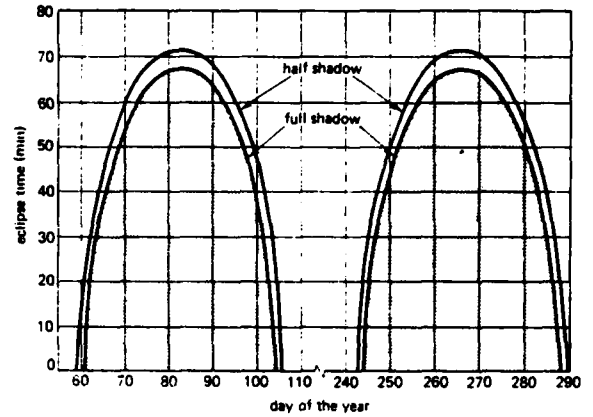


Fig. 11 : Satellite eclipse as a function of the day of the year (8)

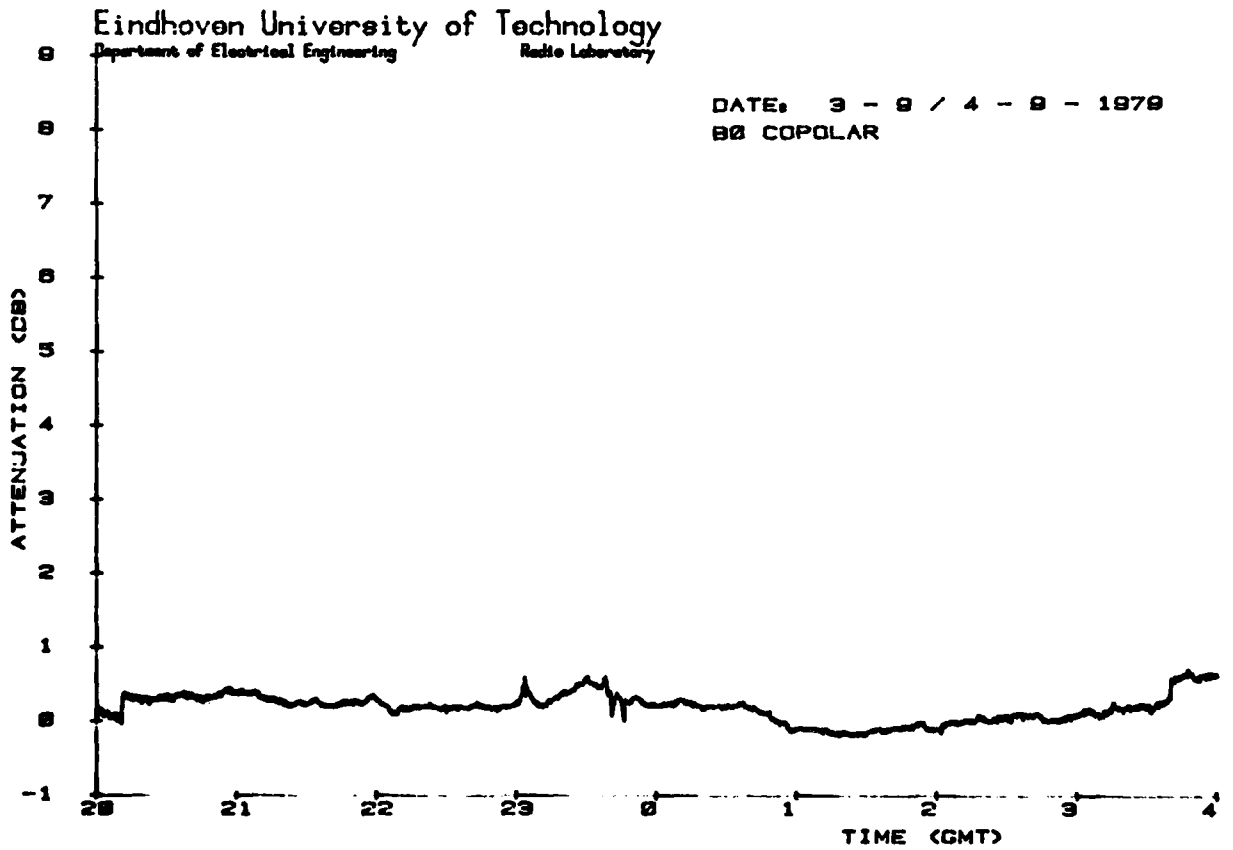


Fig. 12 : B<sub>0</sub> copolar level during eclipse. Sampling rate 2 Hz. Averaging time 12.5 secs.

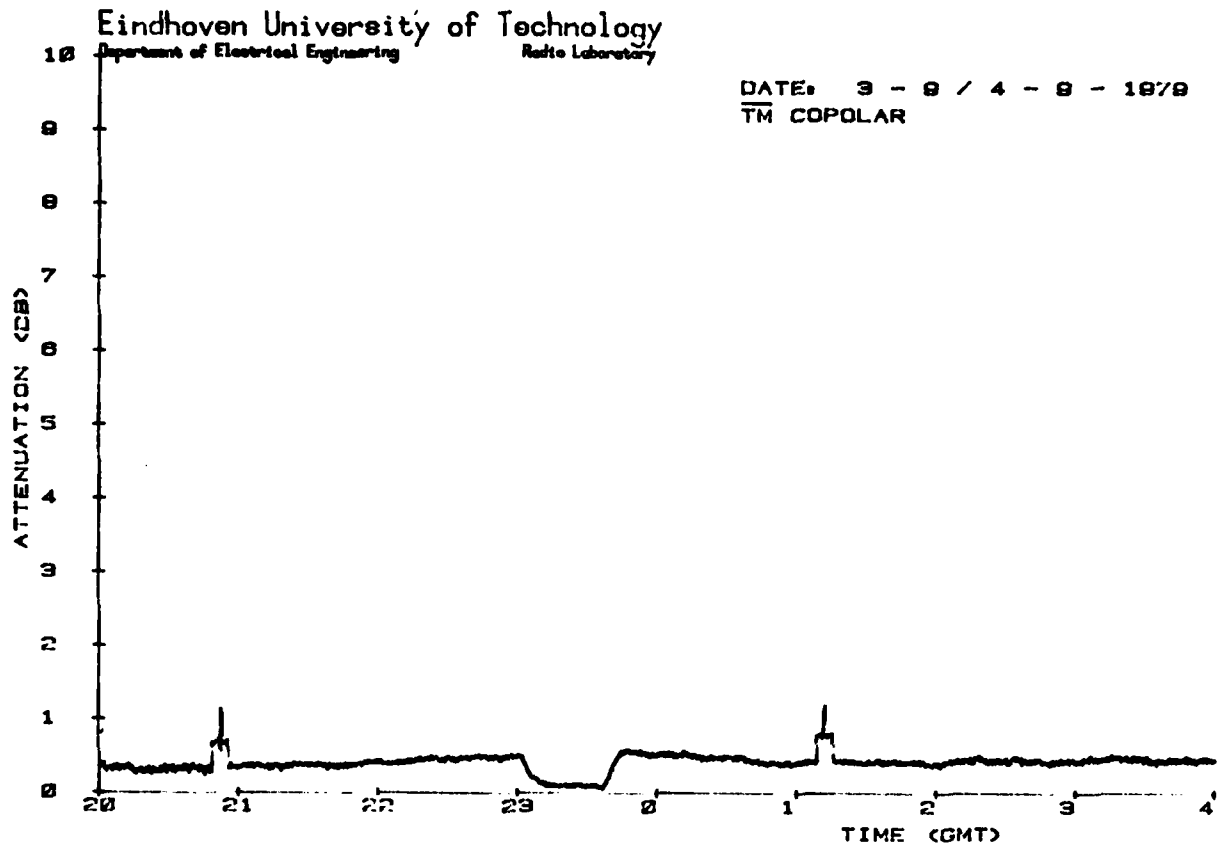


Fig. 13 : TM copolar level during eclipse. Sampling rate 2 Hz. Averaging time 12.5 secs.

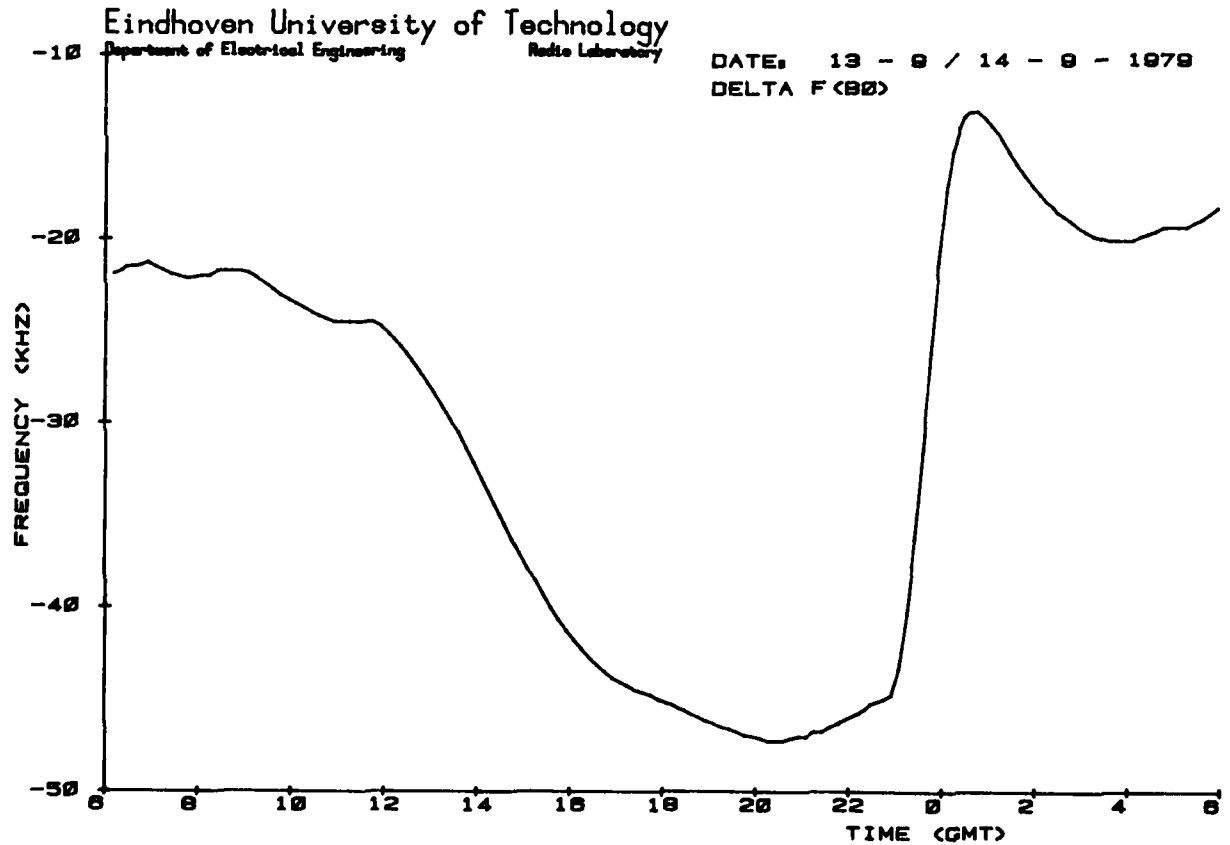


Fig. 14 : Frequency deviation of the B<sub>0</sub> beacon during eclipse. Sampling rate 1/60 Hz. Averaging time 10 min.

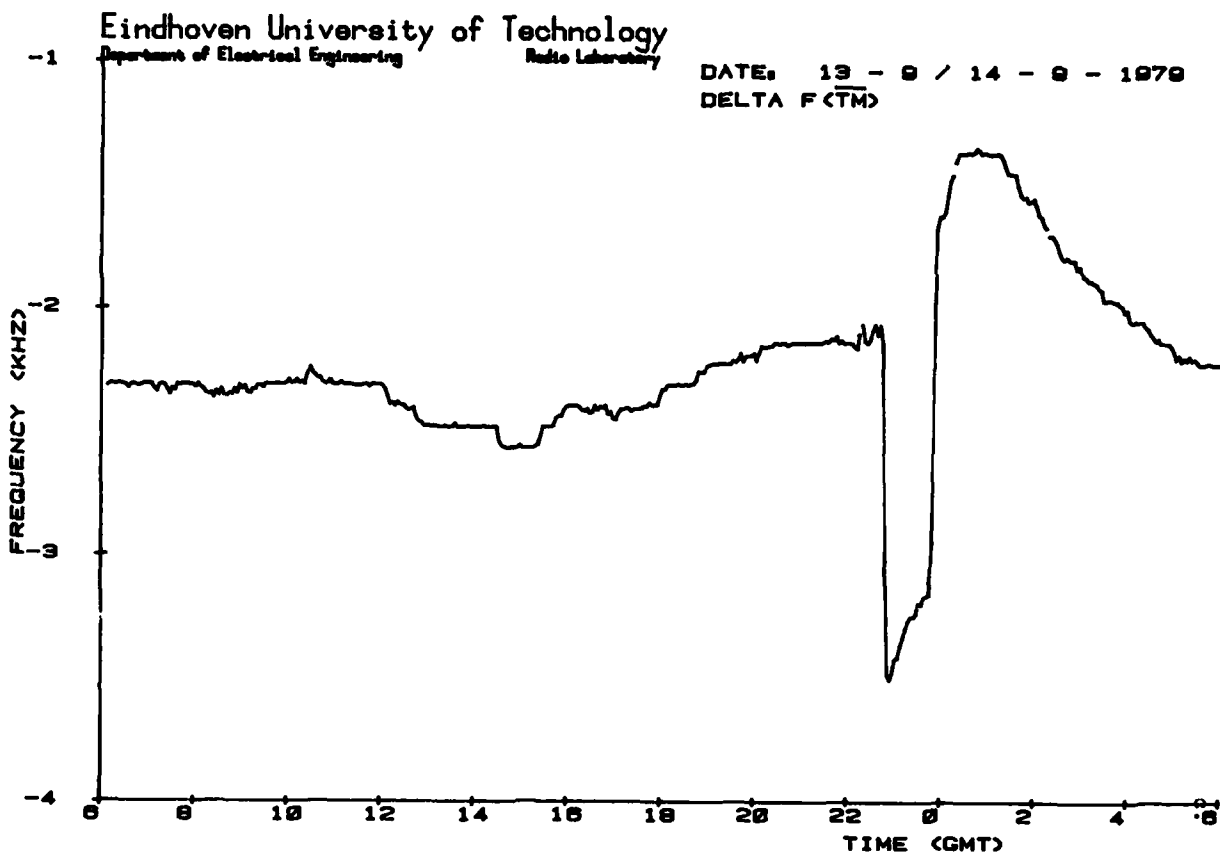


Fig. 15 : Frequency deviation of the  $\overline{TM}$  beacon during eclipse. Sampling rate 0.1 Hz. Averaging time 100 sec.

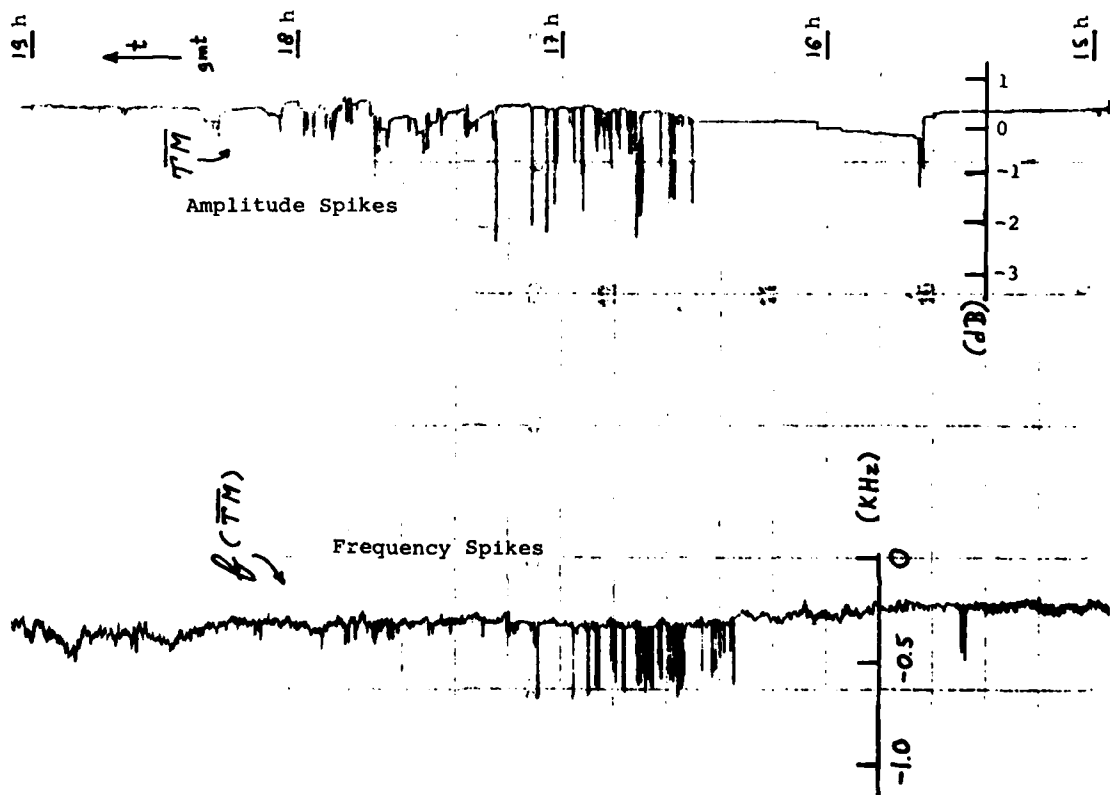


Fig. 16 : Amplitude and frequency "Spikes", February 8, 1979



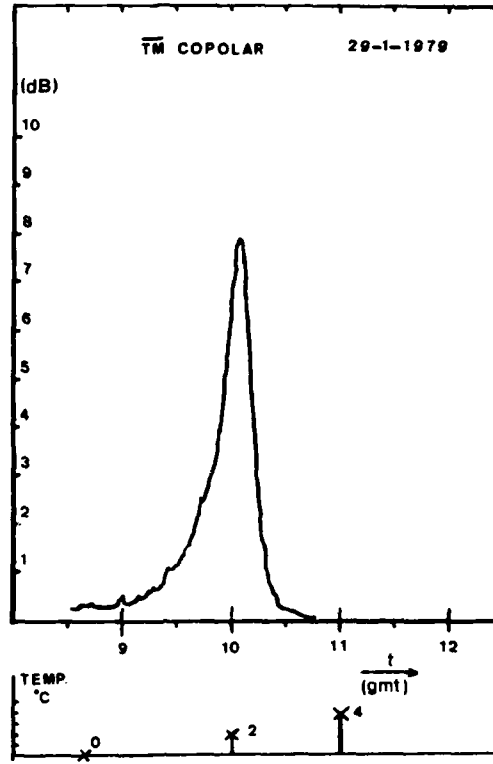


Fig. 17 : "Attenuation" by melting snow on the antenna surface

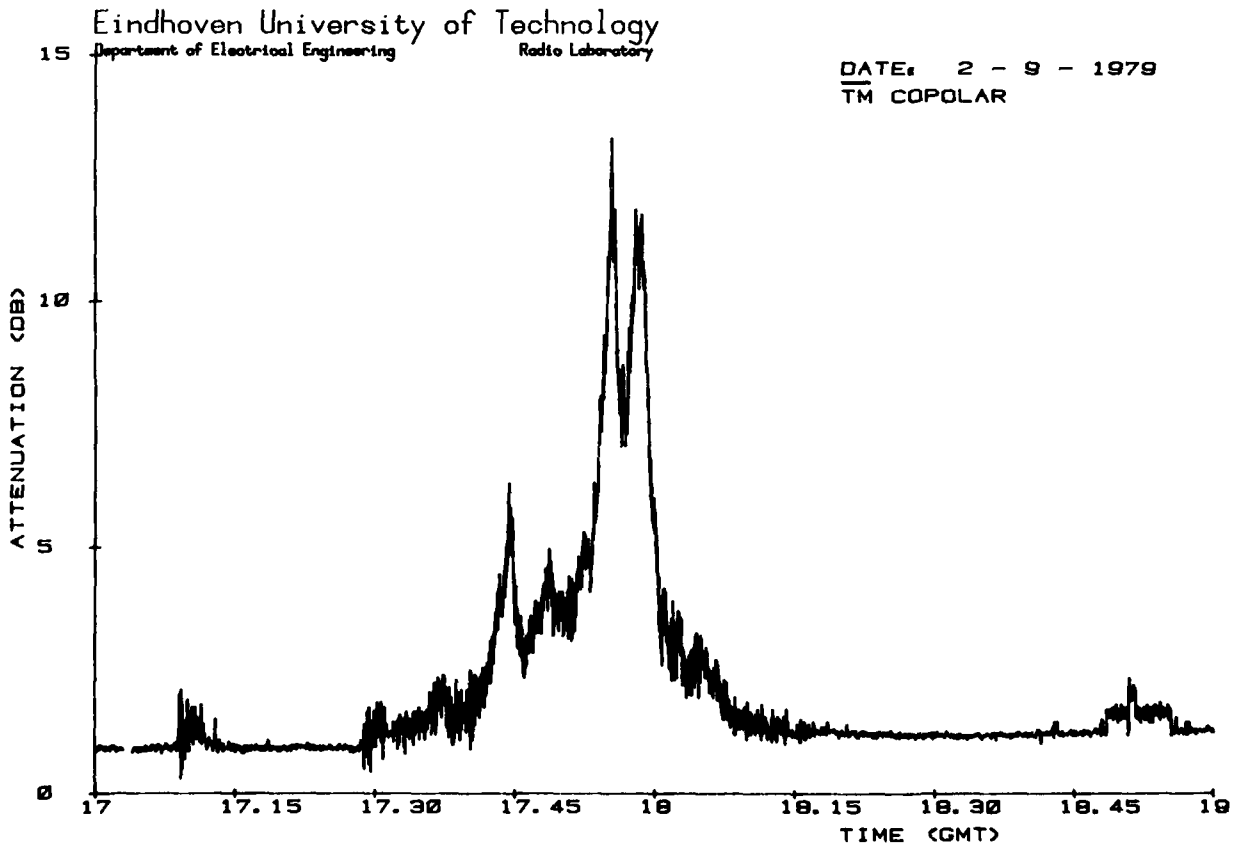


Fig. 18 : Attenuation due to summer shower. Sampling rate 2 Hz. Averaging time 5 sec.

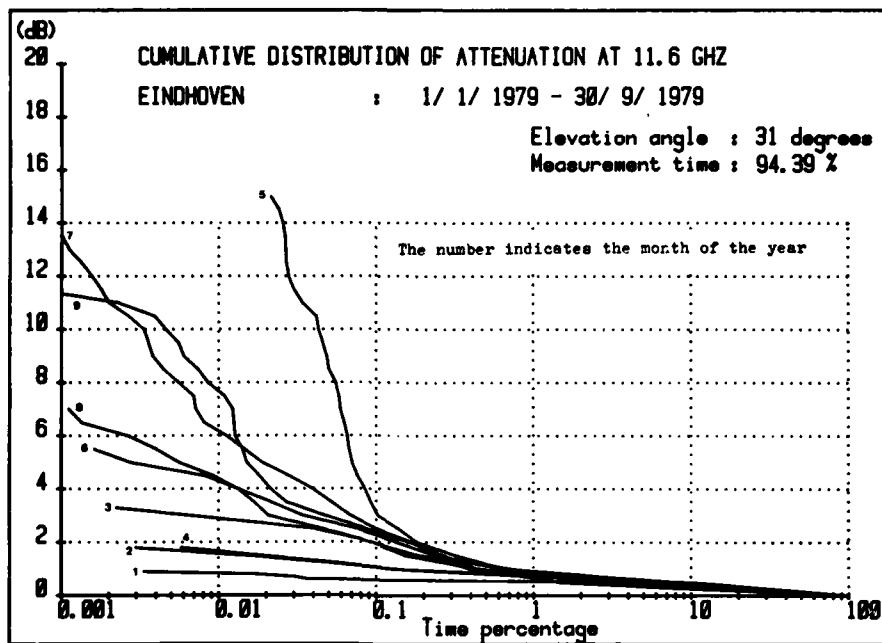


Fig. 19 : Monthly cumulative distributions of attenuation at 11,6 GHz. (Jan. 1 - Sept. 30, 1979).

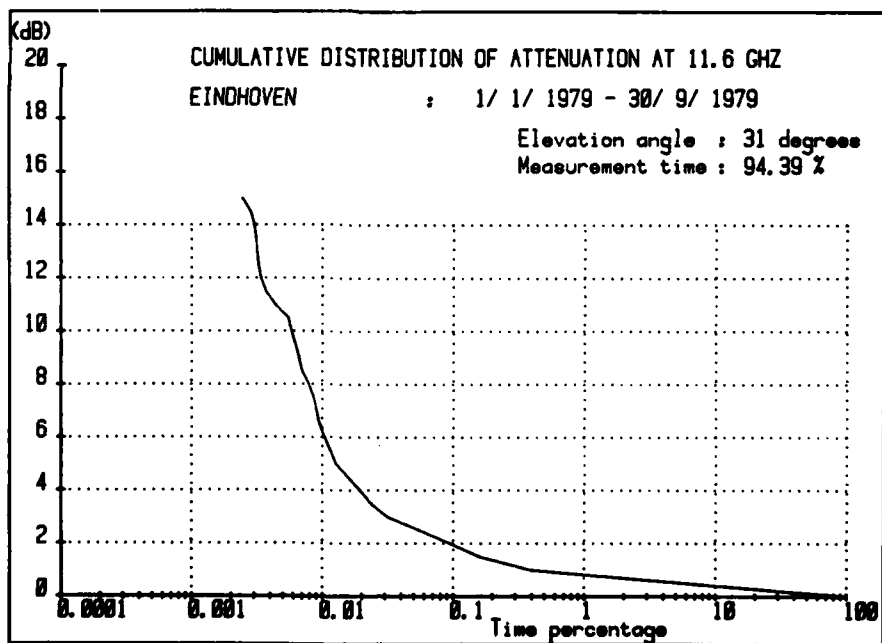


Fig. 20 : Cumulative distribution Jan. 1 - Sept. 30, 1979

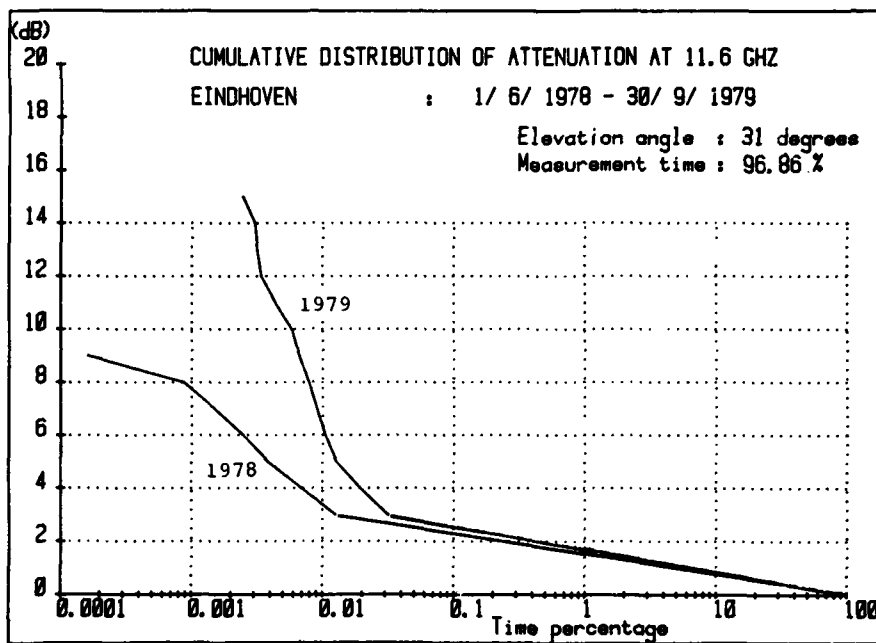


Fig. 21 : Comparison of cumulative distributions 1978 - 1979.

## 11-GHZ PROPAGATION MEASUREMENTS ON SATELLITE LINKS IN THE FEDERAL REPUBLIC OF GERMANY

Fritz Dintelmann and Friedrich W. Rücker

Research Institute of the Deutsche Bundespost D 6100 Darmstadt

### Summary

The growing demand for satellite communications has led to a saturation of the 4/6-GHz bands on the major paths. To cope with the apparent shortage in capacity, the frequency bands above 10 GHz, especially the 11- and 19-GHz bands, are envisaged for use by satellite services in the near future.

Other than in the 4/6-GHz region, communications satellite performance in the bands above 10 GHz may be considerably impaired by rain attenuation, depolarization and scattering. It is for these reasons why intensive research programmes on wave propagation above 10 GHz along earth-space paths have been under way throughout Europe prior to the introduction of operational satellite systems designed for services in these frequency bands.

With the launch of the Italian SIRIO satellite in autumn 1977 and that of OTS II in spring 1978, European propagation experimenters have found nearly ideal conditions for their research work.

The Research Institute of the Deutsche Bundespost at Darmstadt participates, with its Leeheim ground station, in both satellite programmes although in a receive-only mode only. Both, attenuation and depolarization measurements are carried out. Since the SIRIO satellite provides a coherent three-line spectrum in a 532-MHz band, the attenuation characteristic and differential phase effects can be studied. OTS, on the other hand, allows meaningful polarization measurements because its telemetry signal is transmitted in linear polarization and its other emissions in the band are circularly polarized. Hence, the performance of linear polarization can be judged against that of circular polarization on the same link. In addition to these measurements, point rainfall intensities are recorded at various locations in the vicinity of the ground station.

### 1 Introduction

Owing to a growing demand for satellite communications, the 4/6-GHz bands have reached the saturation point on the major paths. To overcome this shortage in capacity, the bands above 10 GHz especially the 11- and 19-GHz bands are envisaged for use by satellite services in the near future. In the INTELSAT system, for instance, INTELSAT V will operate in the 11/14-GHz region and the European ECS is designed for the same frequency band.

Other than in the 4/6-GHz band, satellite links being operated in the 11/14-GHz region or at even higher frequencies may be impaired considerably by rain attenuation, depolarization and scattering.

Although the study of rain fades along earth-space paths does not necessarily require satellites because attenuation in the atmosphere can also be inferred from radiometer recordings, satellite measurements are preferable for a number of reasons. First of all, the dynamic range of the attenuation measurements then is superior to that of radiometers since narrow-bandwidth detection can be utilized. Secondly, the defined state of polarization of satellite emissions allows the depolarization to be studied and thirdly, because of the coherence of a satellite beacon signal, phase measurement can be performed.

It is for these reasons, why intensive research programmes on wave propagation above 10 GHz along earth-space links have been carried out throughout Europe prior to the introduction of operational communications satellites designed for the 11/14-GHz bands.

With the successful launch of the Italian SIRIO satellite in autumn 1977 and the availability of OTS II (a forerunner of ECS) in spring 1978, European propagation experimenters have found nearly ideal conditions for their research work.

SIRIO transmits a phase-coherent three-line spectrum in circular polarization centered around 11.6 GHz whereas OTS emits a circularly polarized beacon signal at 11.786 GHz and a telemetry carrier at 11.575 GHz in linear polarization.

The Research Institute of the Deutsche Bundespost at Darmstadt participates in both satellite programmes with its Leeheim experimental ground station. Both, attenuation and polarization measurements are carried out. In addition, point rain rates at various locations in the vicinity of the ground station are recorded. In this article, the measurements and the results obtained so far are reviewed.

### 2 Attenuation measurements

#### 2.1 Total attenuation

Total attenuation of the circularly polarized signals of SIRIO and OTS at 11.597 GHz and 11.786 GHz, respectively, has been measured from the beginning of the two satellite experiments. In addition, the attenuation of the linearly polarized telemetry carrier of OTS has been recorded. Although the two circularly polarized signals have nearly the same

frequency and the elevations of the radio paths are nearly equal, their cumulative distributions of attenuation exhibit considerable differences. These were unambiguously traced back to differences in the rain intensity distributions under the SIRIO and OTS propagation paths (Rücker, 1980) although they have an azimuth difference of  $30^\circ$  only.

The 1979 cumulative distributions of attenuation for the two circularly polarized beacon signals are shown on Fig. 1.

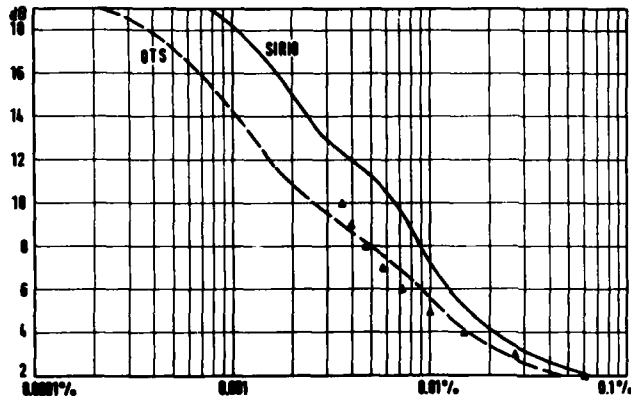


Fig. 1: Time percentage for which rain attenuation (ordinate) is exceeded (1979)

Fig. 1 also includes the results of 11.4-GHz radiometer measurements which had been carried out at the Leeheim station from 1974 until 1976 (Dintelmann and Rücker, 1977). The differences observed between the two links, however, are within the year-to-year variations of one link.

When examining the distributions for the worst month of the year (which in 1979 was August) we find even greater differences between the two links, especially for higher attenuations (Fig. 2).

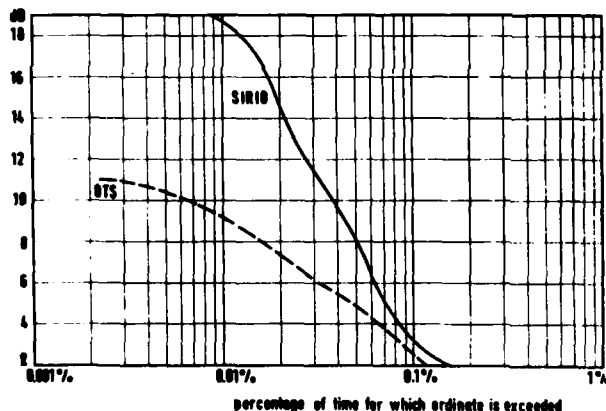


Fig. 2: Time percentage for which rain attenuation (ordinate) is exceeded during the worst month (August 1979)

The worst month in this case is defined as that month of the year for which 7 dB were exceeded with the highest probability. It should be pointed out, however, that the worst month statistics for the SIRIO link is dominated by a single event and therefore these results should be used with due caution.

## 2.2 Frequency-dependence of attenuation in the 11-GHz band

If the frequency dependence of the attenuation is known, attenuation at an adjacent frequency can be predicted. This may be an interesting point for the up-link power control of a ground station as for instance in the INTELSAT system (Allnutt, 1979).

With its three-line spectrum at 11.331, 11.597 and 11.863 GHz, SIRIO offers the opportunity to gather data relating to this problem. A number of papers dealing with this aspect are already available (Olsen et al., 1978; C.C.I.R., 1978). The two following scattergrams (Figs. 3-4) may serve to demonstrate the variability of the frequency dependence of the attenuation in the SIRIO band (i.e.  $a(11.863 \text{ GHz}) - a(11.331 \text{ GHz})$ ) which possibly is due to variations in drop-size distributions and in rain temperature. Fig. 4 indicates a hysteresis-like behaviour which suggests that in the course of a rain fade drop-size distributions and/or rain temperature may change considerably. Such variations are much more likely to occur during heavy rainstorms (causing deep fades) than during moderate rain events. Hence, an extrapolation of the attenuation to another frequency might be wrong if a constant ratio were used.

Fig. 5 shows a cumulative distribution of the attenuation difference  $\Delta A$  as derived from the SIRIO attenuation measurements of 1979. From this distribution all those events have

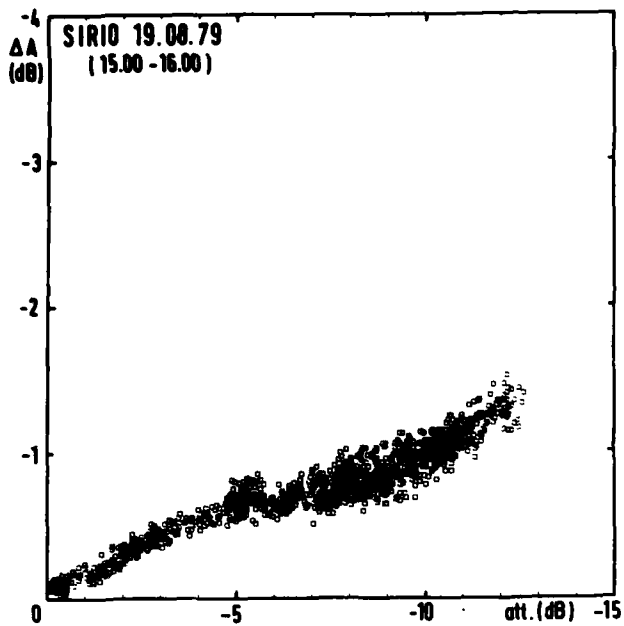


Fig. 3: Scattergram of the attenuation difference  
 $\Delta A = a(11.863 \text{ GHz}) - a(11.331 \text{ GHz})$   
 vs. carrier attenuation  
 $a(11.597 \text{ GHz})$

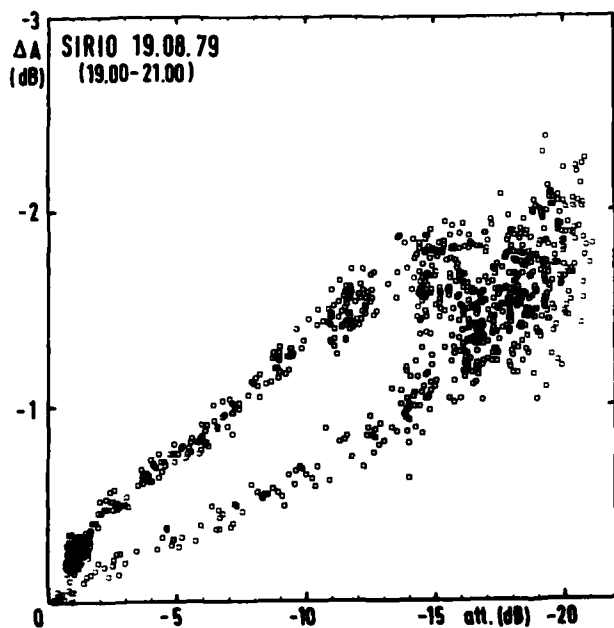


Fig. 4: Scattergram of the attenuation difference  
 $\Delta A = a(11.863 \text{ GHz}) - a(11.331 \text{ GHz})$   
 vs. carrier attenuation  
 $a(11.597 \text{ GHz})$

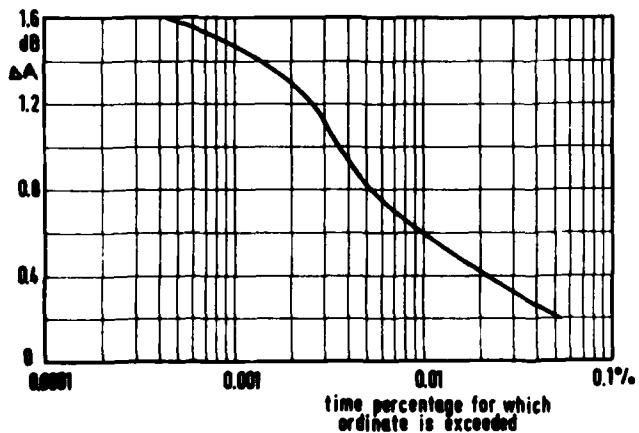


Fig. 5: Cumulative distribution of the attenuation difference  
 $\Delta A = a(11.863 \text{ GHz}) - a(11.331 \text{ GHz})$   
 for 1979

been omitted whose corresponding carrier attenuation was less than 2 dB. This implies the time percentage for 0.2 dB or less to be slightly higher than indicated in Fig. 5.

### 2.3 Attenuation difference between linearly and circularly polarized signals

OTS offers the possibility of measuring the attenuation difference between the linearly polarized  $\overline{TM}$  signal at 11.575 GHz and the circularly polarized B1 beacon at 11.786 GHz. The polarization tilt angle for  $\overline{TM}$  at the Leehelm station is about  $1.4^\circ$  relative to the horizontal. In general, attenuation of a horizontally polarized signal is stronger than that of a vertically polarized one or of a signal transmitted in circular polarization. In Fig. 6, a scattergram of the attenuation of  $\overline{TM}$  vs. that of B1 is shown.

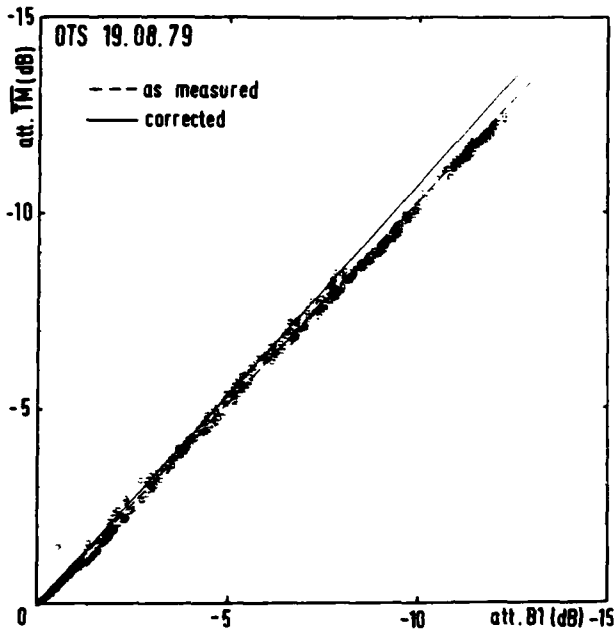


Fig. 6: Scattergram of  $\overline{TM}$ -attenuation vs. B1-attenuation

Although the frequency of  $\overline{TM}$  is lower than that of B1, the rain attenuation is stronger on  $\overline{TM}$  than on B1.

For a comparison of experimental results, however, the various signals should have the same frequency. For the OTS B1- and  $\overline{TM}$ -carriers, the frequency difference is approximately 211 MHz. With the aid of the frequency dependence obtained from the SIRIO measurements the attenuation of the circularly polarized B1 carrier can be scaled to the frequency of  $\overline{TM}$ . The procedure has been outlined elsewhere (Rücker and Dintelmann, 1978). The result is indicated in Fig. 6 by a straight line. The relationship obtained can be used to calculate the attenuation difference between a horizontally and a vertically polarized signal. This difference is essential for the description of rain depolarization (Dintelmann, 1980).

### 3 Rain depolarization

Depolarization measurements on satellite propagation paths have become of major interest to most propagation experimenters since depolarization in the atmosphere has a considerable bearing on the economy of satellite communications.

There has been some discussion whether it is better to use linear or circular polarization in satellite communications. Circular polarization can be easily implemented but has the disadvantage of being more affected by rain. Linear polarization, in general, is preferable in terms of crosspolarization but requires a careful adjustment of the polarization tilt angle.

Rain depolarization is associated with moderate to severe fading. However, there is still some controversy in the question of modelling rain depolarization adequately. In a recent C.C.I.R. report (C.C.I.R., Report 564-1, Kyoto 1978), an attempt is made at provisionally describing crosspolar discrimination in terms of copolar attenuation. Besides the frequency, the elevation of the propagation path and the polarization tilt angle are the parameters in this process.

In addition to depolarization by hydrometeors, ice-clouds are another source for depolarization on slant propagation paths (Watson et al., 1977). This type of depolarization is often referred to as anomalous since it occurs without significant rain attenuation.

With the linearly polarized  $\overline{TM}$  carrier and the circularly polarized B1 beacon signal of OTS, depolarization in the atmosphere can be studied comprehensively. Unfortunately, unlike attenuation, depolarization cannot be investigated without taking account of the properties of the antennae involved. This is because both the receiving and transmitting antennae contribute to the overall crosspolar signal. If the antenna contributions are

small compared with the effects introduced by meteorological conditions, the former may be neglected. Otherwise, however, they can be cancelled by a specially designed compensation network and the effects occurring in the troposphere can be assessed properly (Dintelmann, 1980).

At the Leeheim experimental ground station, the crosspolar components of  $\overline{TM}$ , B1 and of the SIRIO carrier have been received. The phase differences between these components and the corresponding copolar signals have been measured, as well. From a number of tests it was established that the 8.5-m antenna used for the reception of the SIRIO transmissions has a crosspolar isolation of the order of 35 dB or better. The receiving antenna contribution to the crosspolar signal can therefore be neglected in this case. The SIRIO (transmitter-) antenna, however, has a much lower crosspolar isolation which must be taken into account in the data analysis.

Fig. 7 shows a scattergram of the measured crosspolar discrimination (XPD) vs. the copolar attenuation for a rain event measured along the SIRIO propagation path.

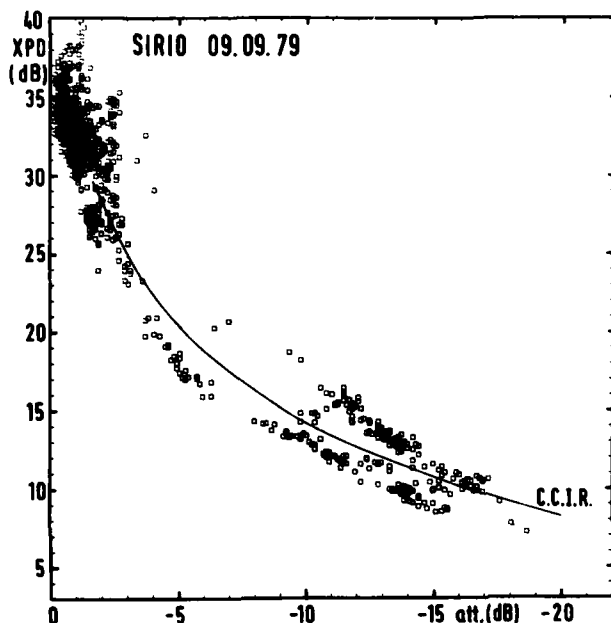


Fig. 7: Scattergram of crosspolar discrimination vs. copolar attenuation

It should be pointed out that for this measurement the antenna contributions were not cancelled. The measured characteristic roughly follows the C.C.I.R. curve (C.C.I.R., 1978). This, however, is not always true as is apparent from another event shown in Fig. 8a.

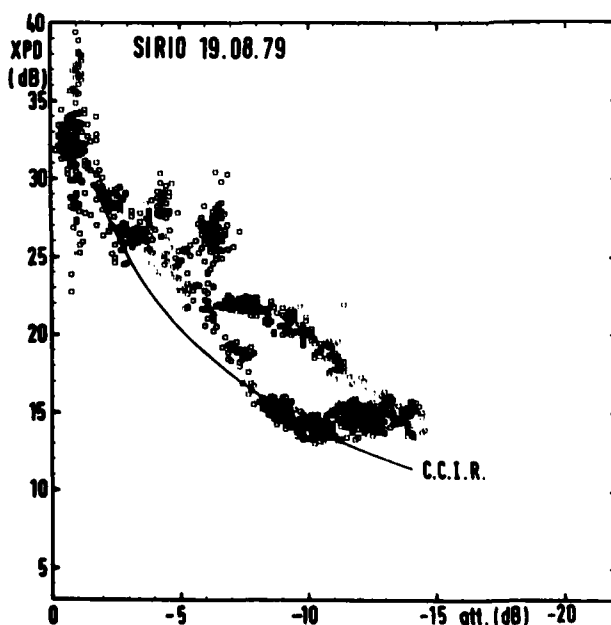


Fig. 8a: Scattergram of crosspolar discrimination vs. copolar attenuation



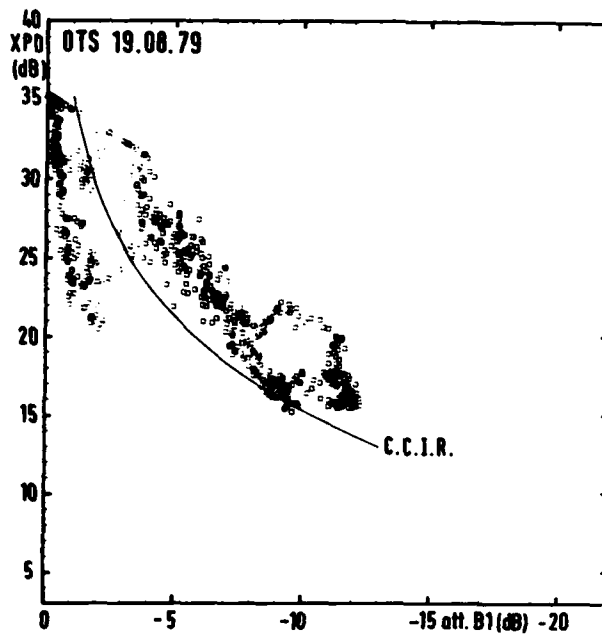


Fig. 8b: Scattergram of crosspolar discrimination vs. attenuation of the B1 signal

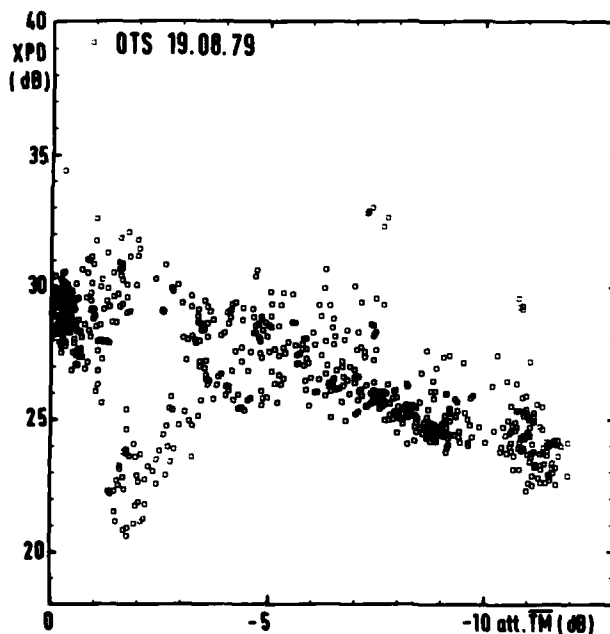


Fig. 8c: Scattergram of crosspolar discrimination vs. attenuation of the TM signal

In the course of this event the crosspolar discrimination mostly is above the C.C.I.R. curve. For low attenuation, anomalous depolarization is observed in this latter event. This tendency is much more pronounced on the OTS link where, in principle, the same behaviour is recorded for the B1 beacon signal (Fig. 8b). While for the SIRIO measurements static cancellation of the antenna contributions was not applied, it was in the case of OTS, however, for the B1 signal only. The dynamic range for the crosspolar signals is limited to about 35 dB below the clear sky copolar signal. Looking at the behaviour of TM (Fig. 8c) we again notice that anomalous depolarization is pronounced. The initial value of XPD at zero attenuation is about 30 dB. This relatively low value is due to the uncompensated operation of the OTS receiver for the telemetry carrier. Nevertheless, it becomes evident from this event that in cases where rain is the predominant source of depolarization, the crosspolarization decoupling for the linearly polarized telemetry carrier is superior to that of the circularly polarized B1 signal.

From the data obtained so far it can be concluded that refinements of the models describing depolarization are urgently required for two reasons: Firstly, a large fraction of depolarization is anomalous and hence cannot be correlated with rain attenuation. Although the physical process for this type of depolarization is reasonably well understood one should try to correlate the governing parameters with meteorological phenomena. Secondly, it seems as if the antenna effects are not sufficiently considered in the present models. When correlating rain attenuation with crosspolarization this aspect deserves some

consideration.

#### 4 Phase shift in the 11-GHz band

The phase-coherent three-line spectrum transmitted by SIRIO allows for the investigation of phase effects in the 11-GHz band (Rücker, 1979). However, only the second-order difference of the phase is measured between the three lines, i.e.  $\Delta^2\psi = [\psi(11.8625 \text{ GHz}) - \psi(11.5968 \text{ GHz})] - [\psi(11.5968 \text{ GHz}) - \psi(11.3310 \text{ GHz})]$ , which is a measure of the slope of the group delay.

The absolute phase shifts at the various frequencies caused by rain can be calculated from scattering theory and the dropsize distribution functions. Numerical data for a variety of dropsize distributions were published by Damosso (Damosso, 1978) and Valentin (Valentin, 1980) and others. From these data we can compile the second-order phase differences  $\Delta^2\phi$  as a function of rain rate (Tab. 1). Although some spread is observed in these data, the specific second-order phase shifts  $\Delta^2\phi$  for the 532-MHz band range from about  $10^{-3}$  deg/km for rain rates of 5mm/h to approximately  $5 \cdot 10^{-2}$  deg/km for a 100mm/h-rain intensity.

Table 1

Second-order phase shift  $\Delta^2\phi$  for the SIRIO band and for horizontal polarization

R mm / h	$10^3 \cdot \Delta^2\phi$ deg / km	
	Damosso	Valentin
5	- 1.0	-
10	- 3.0	- 2.06
20	- 7.2	- 4.14
30	-11.8	- 5.91
50	-21.5	- 8.87
100	-47.1	- 9.51

The discrepancies apparent from Table 1 are due to a number of causes the most important ones being the choice of dropsize distributions, rain temperatures and the accuracy to which the scattering functions (Damosso, 1978; Valentin, 1980) are calculated. Nevertheless, Table 1 shows that for actual rain events  $\Delta^2\psi$  should certainly not exceed  $0.3^\circ$  for the SIRIO link. This result, however, is in contradiction to the experimental data, which may exceed the quoted data by nearly two orders of magnitude. This, however, is certainly not attributable to our equipment since it has been observed elsewhere, too (Ramat, 1979). In addition, rain attenuation and second-order phase shift are correlated as is expected from theoretical considerations. To give an idea of the type of correlation obtained between attenuation and  $\Delta^2\psi$ , Fig. 9 shows a scattergram of  $\Delta^2\psi$  vs. attenuation for a rain event recorded on 29 July 1979.

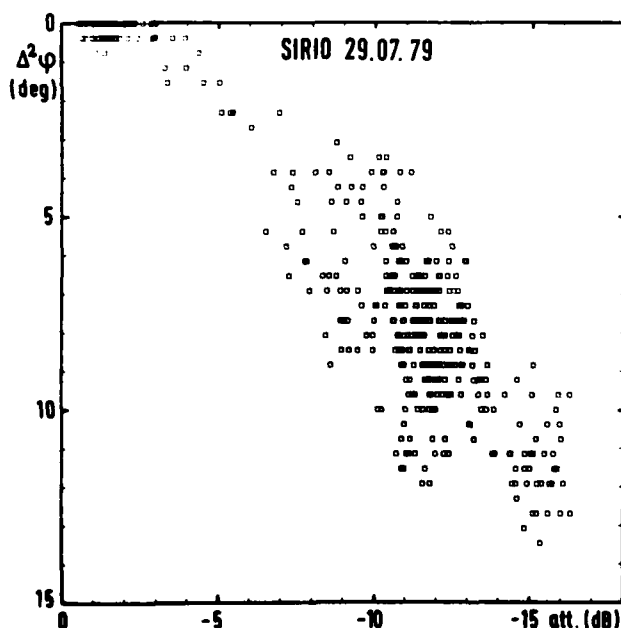


Fig. 9: Scattergram of  $\Delta^2\psi$  vs. attenuation

The spread in the data is real since the long term stability of the phase measurements is better than 30/24 h. The short term stability is by far better.

On the basis of these findings two questions arise:  
 Firstly, is the  $\Delta^2 \psi$  - effect adequately described by scattering theory?  
 Secondly, are there other mechanisms responsible for the observed effects?

There is no evidence for the assumption that the scattering functions and/or dropsize distribution functions are too inaccurate to allow for this effect. At least the real part of the scattering functions seems to be sufficiently accurate to allow a reasonable description of the attenuation measurements. As to mechanisms other than scattering, we have no explanation, yet.

## 5 Conclusions

The propagation measurements carried out by the Research Institute of the Deutsche Bundespost within the SIRIO and OTS programmes yielded some interesting results:

- 1) Attenuation statistics for the same site obtained from two satellites spaced at some degrees in the geostationary orbit and operating in the same frequency band, may differ considerably.
- 2) The attenuation characteristic in the 11-GHz band showed significant variation on an event basis. This fact may be of some importance to up-link power control for operational communications satellites.
- 3) The attenuation difference between a horizontally and a vertically polarized signal can be calculated. This difference is of some relevance to the description of crosspolarization.
- 4) The C.C.I.R. curve describing depolarization in terms of attenuation (C.C.I.R., 1978) requires some refinement.
- 5) The linear group delay variation obtained from the SIRIO measurements is about two orders of magnitude greater than expected from theory.

The statistical results of the 1979 measurements can be probably best summarized by Fig. 10.

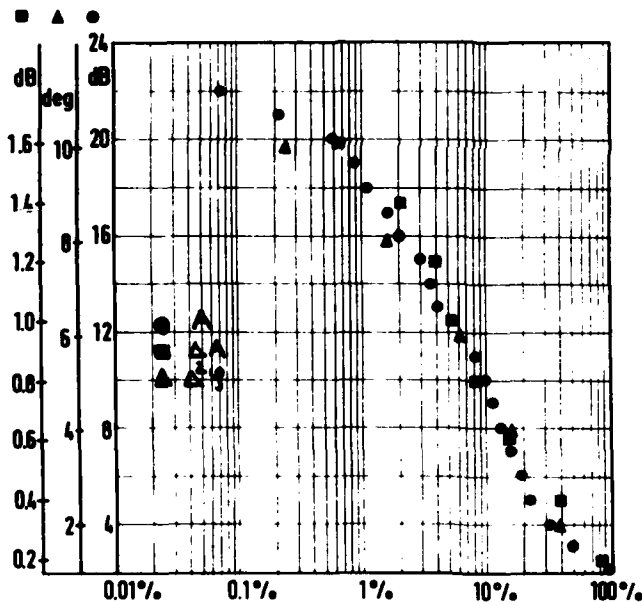


Fig. 10: Cumulative distributions of attenuation (●), of the attenuation difference in the band (■) and of the second-order phase difference (▲) for 1979

This figure shows the cumulative distributions of carrier attenuation, the attenuation difference in the 532-MHz band and the second-order phase difference. Fade events for which attenuation was less than 2 dB and for which the attenuation difference in the band was less than 0.2 dB were omitted from the statistics. Hence, 100 % of the abscissa refers to the total of all events which met these conditions. As shown by Fig. 10, the attenuation difference in the band and the second-order phase difference correlate strongly on a statistical basis.

## 6 References

- Allnutt, J. E., 1979, private communication
- C.C.I.R., 1978, "Attenuation and scattering by precipitation and other atmospheric particles", Report 721, Kyoto, 1978
- C.C.I.R., 1978, "Propagation data required for space telecommunication systems", Report 564-1, Kyoto, 1978

- Damosso, E., 1978, "Dependence of specific rain attenuation and phase shift on electrical, meteorological and geometrical parameters", ESA SP-138 (1978), 219-226
- Dintelmann, F. and Rücker, F., 1977, "Attenuation statistics at 30 GHz derived from measurements with ATS-6 and simultaneous radiometric observations at 11.4 GHz", ESA SP-131 (1977), 31-35
- Dintelmann, F., 1980, "12-GHz slant-path propagation studies with OTS: Polarization measurements", Proc. of the URSI Commission-F open symposium, Lennoxville, May 1980
- Olsen, R. L., Rogers, D. V. and Hodge, D. B., 1978, "The  $aR^b$  relation in the calculation of rain attenuation", IEEE Trans. Ant. Prop. AP-26 (1978)2, 318-329
- Ramat, P., 1979, "Mesures de propagation en polarisation circulaire sur un trajet satellite-terre à partir du satellite expérimental SIRIO", Note Technique NT/TCR/EFT/585, Février 1979
- Rücker, F. and Dintelmann, F., 1978, "Propagation measurements at 11.6 GHz using the SIRIO satellite and simultaneous scatter investigations", Proc. of the International Conference on Antennas and Propagation, London 1978
- Rücker, F., 1979, "Receive facilities for the SIRIO propagation experiment performed at the Deutsche Bundespost experimental ground station at Leeheim", Alta Frequenza 48(1976)6, 176E-180E
- Rücker, F., 1980, "Simultaneous propagation measurements in the 12-GHz band on the SIRIO and OTS satellite links", Proc. of the URSI Commission-F open symposium, Lennoxville, May 1980
- Valentin, R., 1980, private communication
- Watson, P.A. et al., 1977, "Attenuation and crosspolarization measurements at 20 GHz using the ATS-6 satellite with simultaneous radar observations", Proc. of the URSI Commission-F open symposium, La Baule 1977

**EDITOR'S BRIEF SUMMARY OF SESSION III – REMOTE SENSING**

The applicational area of remote sensing was dealt with by this session which was rather short but nonetheless complete as far as coverage is concerned. Apart from a review on the present state of the art in this area and the predicted future development, problems of adaptive radar systems were discussed in detail. In this regard, particular emphasis was directed at influences produced by the propagation medium, as well as by other sources of disturbance and also at multi-frequency radiometric measurements as a means of determining limitations of satellite-radar performance. In the purely passive area of remote sensing, effects of tropospheric turbidity were taken into account.

With regard to the present state of the art, a possible conclusion seems to indicate that medium-dependent effects may be taken into account approximately, whereas a further intensification of relevant research projects would enable the necessary system adaptation to the technological progress.

TARGET ADAPTIVE RADAR, PROPAGATION MEDIUM ADAPTIVE  
COMMUNICATION SYSTEMS, PRESENT DAY METHODOLOGY  
AND FUTURE PERSPECTIVES. A REVIEW

by

Dag T Gjessing  
Chief Scientist  
Royal Norwegian Council for Scientific and Industrial Research  
Environmental Surveillance Technology Programme  
P O Box 25 - N-2007 Kjeller, Norway

SUMMARY

With recent advances in radio science and growing interest in environmental monitoring, remote sensing based on electromagnetic waves has become an important field of study. Using a radar system in which the illuminating frequency can be controlled by a computer system and likewise the receiving system can be "matched" to the backscattered signal, a system which adapts itself both to the transmission medium and to a target of special interest can be designed.

From information theory it is well known that the more information one requires, the wider must the bandwidth of the communication channel be. In terms of radar terminology, what it means, is that the more information we require about the target, the more widebanded must the illuminating radar wave be, and as a consequence of this, we must make use of a transmission medium with sufficient bandwidth capability. We must therefore "code" or "pretailor" the radar wave, so as to allow it to pass through the intervening propagation medium with a minimum of distortion, and at the same time, upon reflection by the object of interest give optimum information about this object.

1 INTRODUCTION

New technology opens a new set of avenues in regard to surveillance of the environment and in regard to detection and identification of targets in general. The progress both as regards technology and also as regards concepts has largely been stimulated by interest in radio communications and by military requirements. In the search for better and more reliable communication channels, a wide spectrum of geophysical and biological factors which affect the propagation of electromagnetic waves has been considered.

The great challenge for radio scientists today, is one of matching new technological achievements to the particular detection/identification problem. In order to achieve this and bridge the scientific gap between the radio scientist and the broad field of applications, a detailed understanding is needed of the interaction mechanisms between electromagnetic waves and the intervening transmission medium (the atmosphere with obstacles) and likewise with targets of interest viewed against a background.

The problem at hand is, as nature in general, very complex. We can not hope to describe every facet of the environment involved in the general target detection/identification problem. We shall have to focus our interest in a pragmatic manner on a set of parameters which adequately describes the particular target in relation to the intervening transmission medium, and the background against which the target is viewed. To achieve this, we shall need a mission oriented (selective) methodology, which will be able to filter out the "target of interest" against a background in which we are not interested. The more detailed information we require about a particular target per unit time, the more wide-banded must our radar illuminator be, and the larger must the usable bandwidth of the propagation medium between the scene to be investigated, and the observation platform be. We must therefore tailor the illuminating waveform, so as to obtain maximum information about the object of interest, and at the same time ensure minimum adverse influence of the intervening transmission medium, and of the background in which the object is concealed.

The key concept in this context is adaptivity:

- Change relevant transmission parameters (carrier frequency, shape of wavefront, receiver configuration etc) so as to increase the usable bandwidth.
- Adjust the information rate of the communication channel (waveform in time and space of radar illumination) so as to match the bandwidth of the propagation medium taking into consideration the ambient noise level.
- Use all the *a priori* information available about the target of interest so as to simplify (minimize effective bandwidth) the detection/identification process.
- Apply optimum estimation methods of target parameters against a background of interferences and through the intervening medium.

In order to present these concepts in a systematic manner, we shall treat the propagation aspects (transfer of wide-banded electromagnetic waves undistorted through the atmo-

sphere) in one section. Next, we shall discuss the interaction of these electromagnetic waves with surfaces (targets). Organizing the material in this way, the chapter on the communication aspects will stand on its own feet in that it will be of interest to the communication engineer separated from the chapter of the radar concepts. The two chapters in combination will be directed towards the radar application. Before we present this chapter on adaption techniques in relation to communications, it may serve a purpose to summarize the radio propagation fundamentals with reference to earlier contributions.

## 2 RADIO PROPAGATION FUNDAMENTALS

It is the purpose of this brief chapter to offer a unified set of theoretical expressions based on simple first principle physics. The aim is to present theoretical expressions which lend themselves to further analysis so as to form the basis for adaptive manipulations, and thus maximize system performance.

### 2.1 Line-of-site propagation

Figure 1 shows the distance dependence of a radio field for various propagation mechanisms. Within line-of-site, the power density decreases with distance as  $R^2$  and in

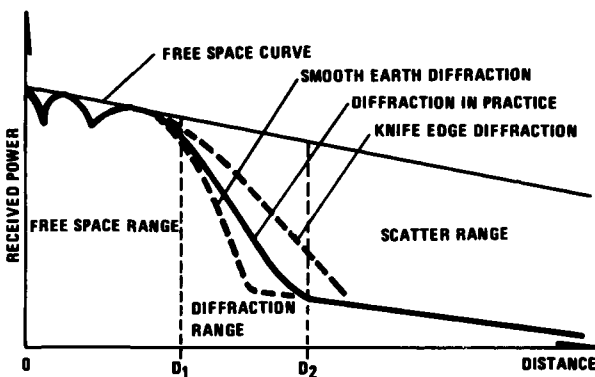


Figure 1 Factors determining the path loss in tropospheric propagation

terms of transmitted power  $P_T$ , gain of transmitting antenna  $G_T$ , area of receiving aperture  $A$ , and distance between transmitter and receiver  $R$  the received power  $P_R$  is given by:

$$\frac{P_R}{P_T} = \frac{G}{4\pi R^2} A \quad (2.1)$$

The received power decreases gradually as the distances increases, there is no radio parameter which can be altered in order to improve the situation.

Then let us consider what happens if part of the transmitted energy is illuminating the ground surface and reflected into the direct wave. If now  $H_T$  is the height above the reflecting surface of the transmitting antenna, and  $H_R$  is the corresponding height of the receiving antenna, then the difference in path-

length of the direct wave relative to that of the reflected wave, is given by

$$\Delta = \frac{2H_T H_R}{R}$$

Phase angle  $\phi$  between the two waves is therefore

$$\phi = \frac{4\pi H_T H_R}{\lambda R}$$

Such that when  $\phi = \pi$  the two waves appear in antiphase giving rise to a minimum in the plot of received power versus distance, as shown in figure 1. Similarly, if the phase angle is equal to  $2\pi$ , we have constructive interference and we get a maximum. Accordingly, in order to change a maximum to a minimum without altering the geometry i.e. the position of the transmitter and the receiver, the wavelength will have to be changed by a factor 2. This, obviously, is within reach in an adaptive communication system (see later).

Now let us assume that we will like to adjust the height of the receiving antenna in such a way so as to achieve constructive interference. As seen from the above expression, this is achieved by shifting the receiving antenna vertically through a distance

$$\Delta H_R = \frac{\lambda R}{4H_T} \quad (2.2)$$

Then let us consider the properties of a propagation circuit involving ground reflections in terms of bandwidth. Having already calculated the delay function related to our transmission circuit, the bandwidth is readily obtained as a function which is proportional to the inverse of delay. Specifically, if the delay function, as in our case, consists of two  $\delta$ -functions with separation

$$\Delta = \frac{2H_T H_R}{R}$$

the correlation properties in the frequency domain of the reflected signal is given by the Fourier transform of the delay function. The Fourier transform of two  $\delta$ -functions is a cosine relationship. The half power bandwidth of the first order is therefore given by

$$\Delta F = 0.25 \frac{c}{\Delta} \quad (2.3)$$

Introducing the geometrical expression for  $\Delta$  above, we find that the bandwidth is given by

$$\Delta F = \frac{c \cdot R}{8H_T H_R} \quad (2.4)$$

For details, the reader is referred to ref (1,2,3).

Then let us consider what happens to a radio wave transmitted through an atmosphere which is not, as in the previous cases, homogeneous in regard to the refractive index, but such that the rays are being bent by refraction and arrive at the receiving antenna with different phase causing constructive and destructive interference. This subject was treated in some detail in an earlier AGARD contribution (ref (4)). It was shown that severe irregularities in the refractive index structure gives rise to a bandwidth reduction. Specifically, by approximate calculations, it was shown that the bandwidth  $\Delta F$  is given by

$$\Delta F = \frac{2c}{\lambda} \quad (2.5)$$

This simple expression is based on the assumption that most of the refracted energy that eventually will reach the receiving antenna propagates through an area within the first Fresnel zone. By similar arguments, it was shown that the spatial correlation distance of fieldstrength  $L$  along a direction normal to the direction of propagation is given by

$$L = 0.62 \sqrt{\lambda R} \quad (2.6)$$

In this context, it should also be mentioned that if the atmosphere is very inhomogeneous in regard to refractive index, a radio duct may be formed. In that case a multi-path situation, very similar to that discussed above will develop whereby an interference pattern will appear at the receiving site. The distance in space between maxima and minima is again determined by the geometry. The reader is here in particular referred to ref (5).

## 2.2 Propagation mechanisms involving reflection and scattering

In an earlier AGARD contribution (ref (4)), the influence of irregularities in the atmosphere on the various properties of radio waves scattered/reflected from these irregularities were discussed in some detail. We shall here limit ourselves to giving the highlights of this AGARD paper in the form of summarized results. In this context, it may be appropriate to make a distinction between the various types of atmospheric structures.

### a) Scattering from "turbulent" irregularities in the atmosphere

The work dealing with the effect of turbulent irregularities on electromagnetic waves is based on a statistical description of the refractive index field. The refractive index structure is described by a three-dimensional irregularity spectrum. One has considered various types of anisotropy in the refractive index structure, and functions describing the lack of homogeneity has been introduced. When dealing with propagation over large distances in the troposphere, what matters is the refractive index variation along a vertical direction. The time dependence of the refractive index spectrum measured vertically gives rise to signal fluctuations. In earlier contributions such as ref (3,4) the refractive index structure along a given direction in space, such as the vertical one, is described by the spatial spectrum

$$\phi(\vec{K}) \sim K^{-n}$$

It is on this  $\phi(\vec{K})$  function that most of the radio circuit parameters rely. The variation in time of the exponent  $n$  is the key to establish the probability functions for the various circuit parameters. It is also shown in ref (9) that the exponent  $n$  (or slope of refractive index spectrum) is controlled by the dynamics of the atmosphere. Specifically, it is shown that there exists a good empirical relationship, and also a theoretical justification, relating  $n$  to a dynamical parameter describing the stability of the atmosphere (Väisälä-Brunt frequency). This stability parameter, which again is related to the Richardson number, another stability parameter, can be determined from measurement of vertical temperature profiles. Based on such measurements, supplied with supporting evidence from radio measurements, the probability distribution of the spectrum slope parameter  $n$  is obtained. An example of this is given in figure 2 (see ref (9)).

In conclusion note that the atmospheric parameter  $n$  gives us information about the capability of atmosphere in regard to scattering of radio waves.



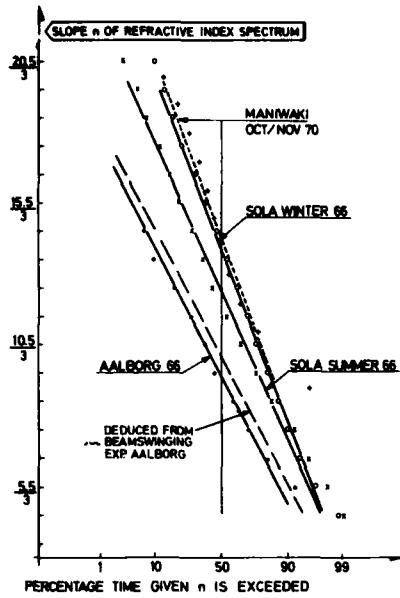


Figure 2 Distributions of the slope of the spectrum of refractive index irregularities as deduced from radiosonde observations and beam-swinging experiments

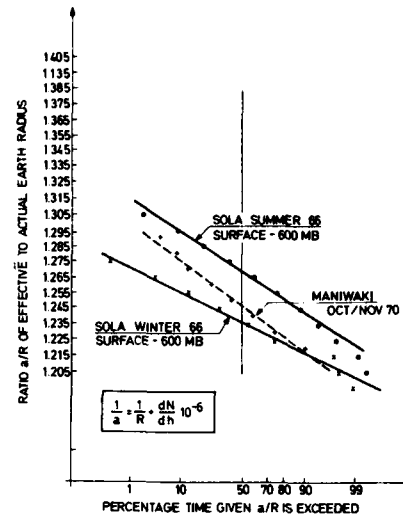


Figure 3 Distributions of the ratio of the effective to the actual earth radius, based on radiosonde observations at Sola, Norway and Maniwaki, Canada

It is further well known that the refractive index normally decreases with height, thus giving rise to bending. The refractive index is directly determined (from observation about temperature and humidity in the atmosphere) by the well-known Debye relationship

$$N = 77.6 \frac{P}{T} + 3.73 \times 10^5 \frac{e}{T^2}$$

where P is the total pressure in mbar, T the absolute temperature, and e the water vapour pressure in mbar. Thus the vertical profile of refractivity N can be determined from conventional radio sonde observations. Note that the refractivity  $N = (n - 1) \times 10^6$ , n being the refractive index. It is customary to express the bending parameter in terms of an effective earth radius. If the refractivity gradient  $dN/dz$  is constant through the height interval involved (from ground to the scattering volume) then the effective earth radius is given by the simple relationship

$$\frac{1}{a} = \frac{1}{R} + \frac{dN}{dz} \times 10^{-6}$$

To illustrate the variability of this bending parameter figure 3 is presented.

COMMUNICATION CIRCUIT PARAMETER	RELATION BETWEEN CIRCUIT PARAMETER AND RADIOMET PARAMETER
WIDTH OF DELAY SPECTRUM	$\Delta\gamma = \frac{d^3}{8a^2c} (e^{2/n} - 1)$
BANDWIDTH	$\Delta\omega = \frac{8a^2c}{d^3} (e^{4/n} - 1)^{-1}$
GAIN LOSS	$G_L = \frac{5Ad^2}{\lambda a^2} (2^{1/n} - 1) (4^{1/n} - 1)^{\frac{1}{2}}$
HORIZONTAL FIELDSTRENGTH CORRELATION DISTANCE	$L_H = \frac{0.44\lambda a}{d(4^{1/n} - 1)^{\frac{1}{2}}}$
VERTICAL FIELDSTRENGTH CORRELATION DISTANCE	$L_V = \frac{0.44\lambda}{d(2^{1/n} - 1)}$
WAVELENGTH DEPENDENCE	$\frac{P(\lambda_1)}{P(\lambda_2)} = \left(\frac{\lambda_1}{\lambda_2}\right)^{n-1}$

Table 1 Some relationships characterizing a communication channel

Based on the atmospheric parameters  $n$  and  $a$  the radio circuit parameters of interest to the communications engineer, can be calculated. For details the reader is here referred to ref (3,4).

Table 1 lists the mathematical expressions for a set of circuit parameters, namely width of the delay spectrum, bandwidth, gain loss, fieldstrength correlation distance and wavelength dependence. In these expressions  $d$  refers to distance between transmitter and receiver,  $c$  is the velocity of light,  $\lambda$  is the wavelength, and as indicated above,  $n$  describes the refractive index irregularity structure, and  $a$  describes the bending action of the refractive index field. Figure 4 shows how these circuit parameters varies with atmospheric conditions.

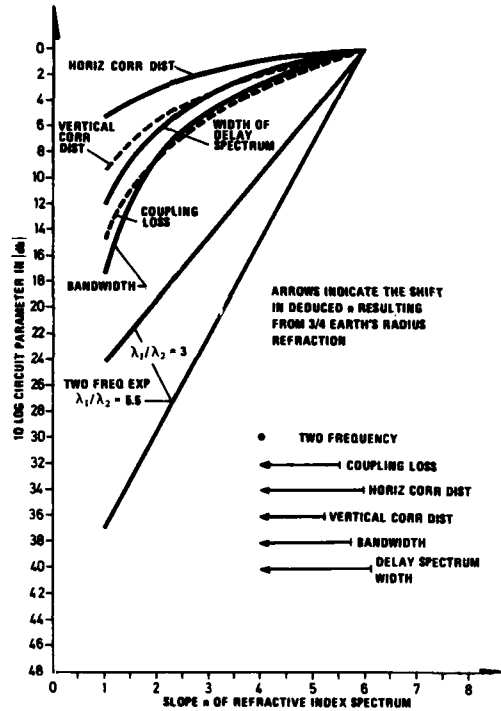


Figure 4 The theoretical relationship between the circuit parameter and the slope  $n$  of the refractive-index spectrum ( $\phi(K) \sim K^{-n}$ ). The curves show the degree to which the spectrum slope affects the circuit parameter.

b) Scattering from atmospheric layers (waves)

In the previous chapter, the theory was based on the assumption that the refractive index irregularities were distributed randomly in the atmosphere, and superimposed on a gradual decrease of refractive index with height. We shall now consider another extreme case where the scattering/reflection largely is a result of a thin strata through which the refractive index varies drastically. For the purpose of illustrating the physics and the fundamental principles of the problem at hand, we shall explicitly present three different idealized atmospheric structures. These are shown in figure 5 and the reader is referred to ref (6) for details. In figure 5 the first

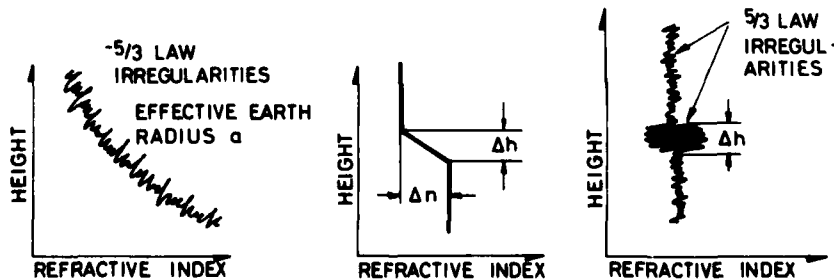


Figure 5 The categories of atmospheric structures under consideration

sketch (a) refers to the case we have just discussed above. Sketch (b) will now be considered. Here we assume an irregular refractive index profile characterized by a layer of thickness  $\Delta h$ , through which refractive index varies linearly by total amount  $\Delta n$ .

As we have already inferred above, and treated in detail in ref (1,3,4), the angular power spectrum of the scattered (reflected) wave is obtained by a simple Fourier transformation of the refractive index profile within the scattering volume. This procedure has been substantiated by several authors i e J Wait, see ref (7).

$$|\rho|^2 = \left| \frac{\Delta n}{2 \sin^2(\frac{\theta}{2})} \left( \frac{\sin X}{X} \right) \right|^2$$

Here  $X$  is a function of the geometry as follows

$$X = \frac{2\pi \Delta h}{\lambda} \sin \theta/2$$

where  $\theta$  is the scattering angle.

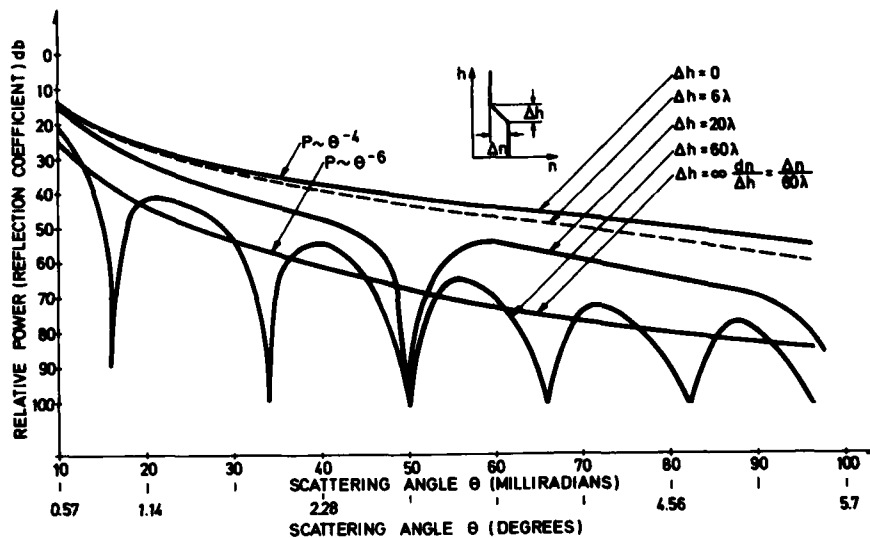


Figure 6 Angular power spectrum of a scattered wave resulting from a layer of thickness  $\Delta h$

This function is plotted to the basis of scattering angle for various layer thicknesses in figure 6. Note that for a layer which is infinitesimally thin, the angular power spectrum is on the form

$$P \sim \theta^{-4}$$

which is very close to that which will be obtained from an homogeneous isotropic turbulence field where the refractive index structure

$$\phi(K) \sim K^{-11/3}$$

Note also that if the layer is very thick, then the angular spectrum approaches

$$P \sim \theta^{-6}$$

Then let us consider the case where the refractive index irregularities are confined to a very thin strata as depicted in figure 5c. In order to simplify the mathematical computations, we shall assume that the variance of the refractive index irregularities through the turbulent stratum is given by a  $\sin X/X$  relationship, and that the spectrum of irregularities can be written in the form  $K^{-n}$ . The resultant spectrum is a convolution integral where the  $K^{-n}$  spectrum is convolved with the spectrum of  $\sin X/X$  filter function. The spectrum of the  $\sin X/X$  filter is a rectangular function. The width of this rectangular filter spectrum is taken to be  $2 \times K'$  and the density  $A$  is taken as  $K'/2$  such that the integral of the filter spectrum becomes unity. The power spectrum of such a turbulent stratum then becomes

$$E(K) = \int_{K-K'}^{K+K'} ACK^{-n} dK$$

Solving this integral for a particular value of  $n = 4$ , we get

$$E(K) = K^{-4} \left( 1 + 10/3 \left( \frac{K}{KT} \right)^{-2} + 7 \left( \frac{K}{KT} \right)^{-4} + \dots \right)$$

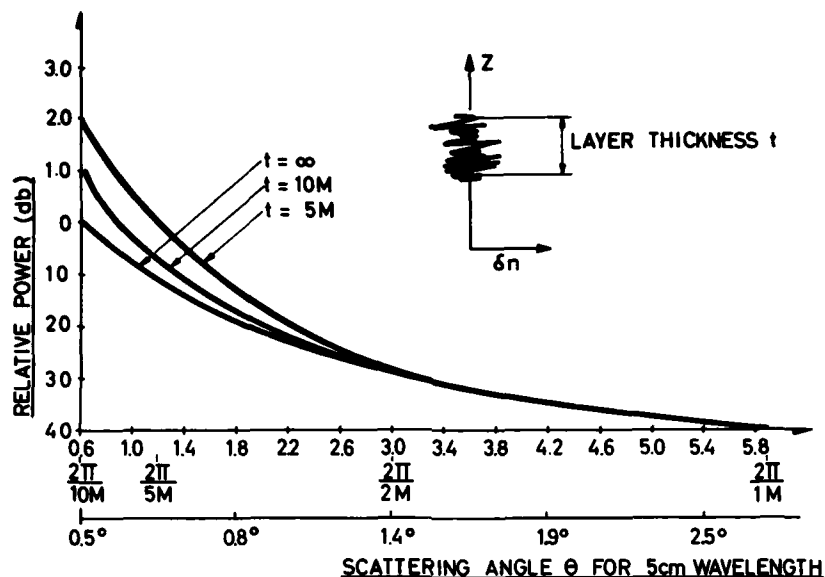


Figure 7 Angular power spectrum of a scattered wave resulting from a thin stratum of intense turbulence

This function is plotted in figure 7. We see that unless the thickness of the stratum is less than two or three-times the projected wavelength ( $\lambda/\sin \theta/2$ ), the spatial intermittancy of the refractive index irregularities has no influence on the angular spectrum of the scattered wave. Finally, in conclusion, table 2 is presented. This shows some theoretical relationships pertaining to forward scattering from turbulence and from stratified layers respectively.

	Type of structure	Background turbulence	Thin layer
Type of experiment			
Measure angular power spectrum of scattered wave	Beamswinging	$\frac{P(\theta)}{P(\theta_0)} = \left( 1 + \frac{\theta}{d/a} \right)^{-11/3+1}$	$\frac{P(\theta)}{P(\theta_0)} = \left( 1 + \frac{\theta}{d/a} \right)^{-4}$
	Multifrequency	$\frac{P(\lambda_1)}{P(\lambda_2)} = \left( \frac{\lambda_1}{\lambda_2} \right)^{11/3-2}$	$\frac{P(\lambda_1)}{P(\lambda_2)} = \left( \frac{\lambda_1}{\lambda_2} \right)^{4-2}$
Vertical E-correlation		$L_r = \frac{0.44 a}{\lambda} = \frac{0.44 a}{d(2^{2/11} - 1)}$	$L_r = \frac{0.44 a}{\lambda} = \frac{0.44 a}{d(2^{1/4} - 1)}$
	Horizontal E-correlation	$L_h = \frac{0.44 a}{\lambda} = \frac{0.44 a}{d(4^{2/11} - 1)^{1/2}}$	$L_h = \frac{0.44 a}{\lambda} = \frac{0.44 a}{d(4^{1/4} - 1)^{1/2}}$
Coupling loss		$G_L = \frac{5A(2^{2/11} - 1)(4^{2/11} - 1)^{1/2}}{(a/d)^2 \lambda^2}$	$G_L = \frac{5A(2^{1/4} - 1)(4^{1/4} - 1)^{1/2}}{(a/d)^2 \lambda^2}$
Measure vertical distribution of scatterers	Pulse delay	$\Delta \tau = \frac{d^3}{8a^2 c} (e^{4/11} - 1)$ 200-km path $\Delta \tau = 60$ ns	$\Delta \tau = \frac{2d}{ac} dh$ 200-km path, $dh = 10$ m $\Delta \tau = 2$ ns
	Bandwidth	$\Delta f = \frac{8a^2 c}{2ad^2(e^{12/11} - 1)}$ 200-km path $\Delta f = 1.2$ MHz	$\Delta f = \frac{ac}{2dh}$ 200-km path, $h = 10$ m $\Delta f = 500$ MHz

Table 2 Some theoretical relationships pertaining to forward scattering from turbulence and stratified layers

### c) Scattering from terrain irregularities

In this section of the review we shall with reference to (1) focus our attention on the earth's surface, this acting as a reflector of electromagnetic waves. There are several applications of such an investigation:

- The ground can be used constructively in reflecting a radio beam in a desired direction
- Ground reflections can give undesired multipath and reduced bandwidth on satellite and terrestrial radio circuits
- Ground reflections can give undesirable interference between different radio systems
- The earth surface can constitute a background against which a target should be detected.

With these applications in mind and emphasizing the communication aspects, we shall perform basic calculations for the purpose of obtaining information about the interaction of electromagnetic waves with the earth surface.

In order to simplify the geometry, let us first consider the backscatter case involving a monostatic situation with both the transmitter and the receiver at the same location viewing the same geographical area.

The geometry is sketched in Figure 8; our aim now is to calculate the bandwidth of the reflecting surface. We have shown in the chapter above that this bandwidth is calculated from the delay spectrum of the reflector. Specifically, if  $\sigma(z)$  is the distribution in depth of the scatterers such that the delay spectrum is  $\sigma(z/c)$  where  $c$  is the wave velocity, then the following relationships hold:

$$F(\omega) = \text{Fourier transform of } \sigma\left(\frac{z}{c}\right)$$

$$\text{Power spectrum } W(\omega) = F(\omega) F^*(\omega)$$

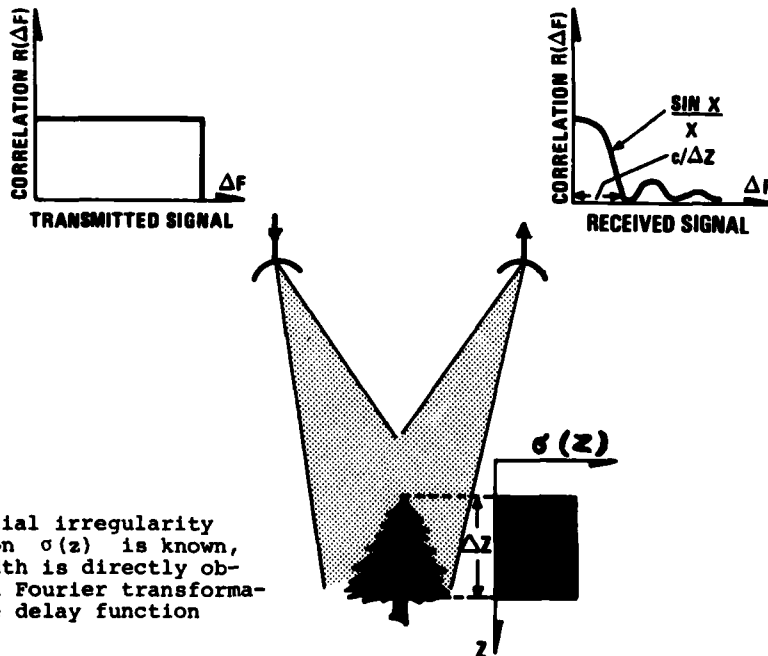


Figure 8

If the spatial irregularity distribution  $\sigma(z)$  is known, the bandwidth is directly obtained by a Fourier transformation of the delay function  $\sigma(z)$

The bandwidth of the reflecting surface is the half-power width of  $W(\omega)$ .

Essentially there are two different approaches to the problem:

- A deterministic procedure in which the scattered field is derived from the geometry of the scattering object using Maxwell's equation and the appropriate boundary conditions, by calculation of the complex reflection coefficient from the sum of a often large but finite number of discrete scattering centres
- A statistical procedure in which representative properties of the scattered wave are calculated on the basis of statistical information about the scattering object.

The relative merits of these two procedures depend on the nature of the problem at hand. If the scattering object (scattering surface) is a complex one describable only in terms of statistical functions, a statistical approach has to be used.

For this reason, and also in order to be able to use the expressions developed above in the next chapter where we shall deal with targets and terrain backgrounds, we shall also here apply statistical methods.

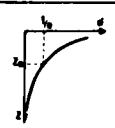
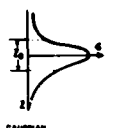
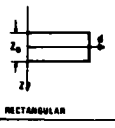
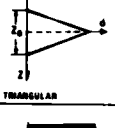

DISTRIBUTION IN DEPTH OF SCATTERERS	FREQUENCY DEPENDENCE OF REFLECTING SURFACE	HALF POWER BANDWIDTH
 <p>EXPONENTIAL</p>	$W(\omega) = \frac{\sigma_0^2}{\left(\frac{c}{z_0}\right)^2 + \omega^2}$	$\Delta F_{1,2} = 0.16 \frac{c}{z_0} \text{ Hz}$
 <p>GAUSSIAN</p>	$W(\omega) = \frac{\sigma_0^2}{4} \frac{e^{-\frac{\omega^2 z_0^2}{8 c^2}}}{\left(\frac{c}{z_0}\right)^2}$	$\Delta F_{1,2} = 0.37 \frac{c}{z_0} \text{ Hz}$
 <p>RECTANGULAR</p>	$W(\omega) = 4\sigma_0^2 \left(\frac{\sin \frac{z_0 \omega}{2c}}{\omega}\right)^2$	$\Delta F_{1,2} = 0.44 \frac{c}{z_0} \text{ Hz}$
 <p>TRIANGULAR</p>	$W(\omega) = \frac{64 \sigma_0^2}{\left(\frac{z_0}{c}\right)^2} \left(\frac{\sin \frac{z_0 \omega}{4c}}{\omega}\right)^4$	$\Delta F_{1,2} = 0.64 \frac{c}{z_0} \text{ Hz}$
	$W(\omega) = 4 \sigma_0^2 \left(\cos \frac{z_0 \omega}{2c}\right)^2$	$\Delta F_{1,2} = 0.25 \frac{c}{z_0} \text{ Hz}$

Table 3

Referring again to figure 8 we express the distribution in depth of the scatterers (along the direction of propagation) in terms of a depth distribution function (a delay-spectrum)  $\sigma(z/c)$ . Note that this depth distribution refers to the area on the ground illuminated by the transmitter and "seen" by the receiver.

Table 3 gives the results of calculations based on a set of such  $\sigma(z/c)$  functions. The resulting  $w(f)$  functions are plotted in a normalized form in figure 9. The depth distribution parameter  $z_0$  is taken as 100 m in all cases. Since the wave by reflection passes twice through the scattering medium, this implies that the scattering strata is 50 m thick.

Note that the particular shape of the depth distribution function  $\sigma(z/c)$  has a pronounced influence on bandwidth. Note also that if the structure is periodic, the "bandwidth" is not centered around zero frequency (ref (8)).

We see that if the scatterers are distributed in a gaussian manner over 50 m in depth, the bandwidth of the reflector is approximately 1 MHz.

From a radar probing point of view this is an ideal situation; by the use of a simple experiment involving the measurement of bandwidth, detailed information about the topography, or about the vegetation, can be obtained.

The example based on a backscatter monostatic situation is not a very realistic one from the point of view of communication.

Now let us discuss the bistatic situation in which the transmitter and the receiver are widely separated.

From simple geometrical considerations, with reference to ref (4), we find that the difference in path length  $\Delta l$  can be expressed in terms of depth  $z$  as follow:

$$\Delta l = z \left( \alpha + \frac{z}{d} \right)$$

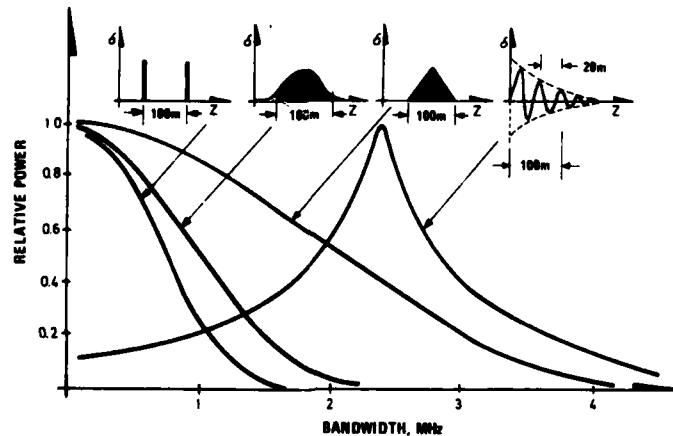


Figure 9 Knowing the geometrical shape of an object (spatial distribution of scatterers) we can calculate the radar signature. If the target manifests itself as a limited number of discrete scattering centers, the radar signature will be the sum of cosinus relationships as illustrated in the figure

where  $\alpha$  is half the scattering angle and  $d$  is the distance between transmitter and receiver.

Thus, if the distribution in depth of the scatterers is  $z_0$  and if the path length as an example is 50 km and the angle  $\alpha$  is 500/50 000 (implying that the vertical distance from the line between transmitter and receiver to the scattering area is 500 m), then the resulting delay  $\Delta l$  is approximately  $z_0/100$ .

The bandwidth of this reflector configuration is thus increased by a factor 100 relative to the pure backscatter case.

If, however, some of the transmitted power reaches the receiver directly through the line of sight path, then the spread in path length  $\Delta l$  is given by

$$\Delta l = \frac{2H_1H_2}{d}$$

where, as before,  $d$  is the path length.  $H_1$  and  $H_2$  are the height above the reflecting surface of the transmitter and receiver respectively.

In the example considered above  $H_1 = H_2 = 500$  m and  $d$  is 50 km.

Under such multipath conditions the difference in path length is some 10 m, and the bandwidth is reduced by a factor 1000 relative to the case discussed above with forward scatter and no direct line of sight path.

### 2.3 Diffraction of radio waves by terrain obstacles

Our problem is the following:

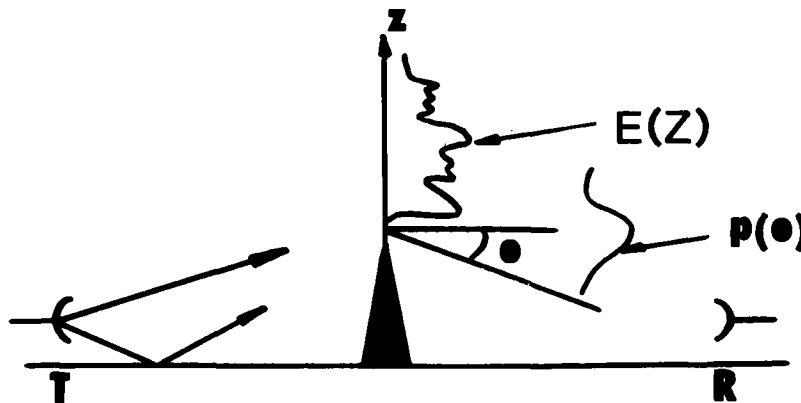


Figure 10 Geometry of the diffraction problem

The transmitter at point  $T$  illuminates a region above the obstacle. This gives rise to a distribution of field strength along a vertical direction above the obstacle. This distribution is determined by multipath effects, by the ground reflection coefficient, and by the radiation properties of the antenna. On the basis of knowledge about  $E(z)$ , we want to calculate the angular power spectrum  $P(\theta)$  of the diffracted wave.

We now use exactly the same approach as for scatter propagation (see e.g. ref (1)) and derive the following expression for the secondary field  $E_s$ , (scattered field or diffracted field as the case may be):

$$E_s = \frac{k^2}{4\pi R} \int E_0(z) \epsilon(z) e^{-jkz} dz$$

where

$R$  = distance between receiver and diffraction element (distance from obstacle)

$k$  =  $\frac{2\pi}{\lambda}$  where  $\lambda$  is the wavelength

$\epsilon(z)$  = distribution of permittivity above the obstacle

$E_0(z)$  = distribution of field strength above the obstacle

$\theta$  = essentially the direction of the diffracted wave under consideration.

Thus the secondary field is the Fourier transform of the  $E_0(z) \epsilon(z)$  product.

Two limiting cases are of interest:

- a) If the field  $E_0$  incident on the plane above the obstacle varies far more rapidly with height  $z$  than does  $\epsilon(z)$ , then  $\epsilon(z)$  does not contribute to the convolution and we can put  $\epsilon(z)$  outside the Fourier integral. We thus have an important relation. The angular distribution of diffracted wave is the Fourier transform of the fieldstrength distribution measured in a plane above the obstacle giving rise to diffraction.
- b) Conversely, if  $\epsilon(z)$  varies rapidly in relation to  $E_0(z)$ , then  $E_0(z)$  does not contribute to the convolution and we have an expression for the scattered wave. The angular distribution of the scattered waves is the Fourier transform of the permittivity (refractive index) distribution.

Thus, if we want to calculate the transmission loss resulting from a given obstacle, the procedure is in short the following:

#### Step 1

Calculate the fieldstrength distribution along a vertical direction over the obstacle, considering the influence of ground reflections, etc. Note that if the obstacle cannot be considered as a knife edge, then reflection from the obstacle itself may contribute to the fieldstrength distribution over the ridge.

#### Step 2

Having obtained an expression for  $E_0(z)$ , we compute the Fourier transform of  $E_0(z)$ , thus obtaining the angular fieldstrength distribution  $E_s(\theta)$  of the diffracted wave. In order to obtain the angular power distribution  $P(\theta)$ , we shall have to multiply  $E_s(\theta)$  with its complex conjugate  $E_s^*(\theta)$ .

Note that in order for this Fourier transformation to be dimensionally meaningful, the space coordinate will have to be normalized with respect to wavelength. The direction  $\theta$  is then to be expressed in terms of  $\sin \theta$ .

#### Step 3

Having obtained the angular power spectrum  $P(\theta)$ , we shall essentially have to repeat step number one in order to obtain the desired expression for the power received at a given point in the diffraction zone behind the obstacle.

We shall now consider this procedure in some degree of detail.

#### Let us first calculate the fieldstrength distribution above obstacle

In order to obtain simple, comparatively general and in particular physically interpretable expressions for the fieldstrength distribution above the obstacle (first step in the procedure) we shall have to idealize the problem and in doing so make certain approximations.

Inspecting the numerical results in relation to interference pattern from ground reflections, we see that the most striking feature of the vertical fieldstrength distribution is the periodicity. We clearly have a component of fieldstrength which varies in a sinusoidal fashion with height.

From knowledge about the reflection properties of the sea surface under various degrees of roughness, one would expect the influence of multipath on the vertical fieldstrength profile to diminish with height. Hence one would expect the sinusoidal fieldstrength oscillation to be damped in some manner. This too is evident in some of the line of sight ducting results. Lastly, we see that the DC level of the  $E_0(z)$  profile is a parameter of some importance.

Our diffraction problem will therefore be based on the following fieldstrength profile:

- a constant term  $E_1$
- a damped sinusoidal term given by  $E_2(z) = E_2 e^{-\alpha z \lambda} \sin \frac{2\pi}{L} \lambda z$ .

Note that the vertical coordinate  $z$  is measured in terms of number of wavelengths.

#### Then let us consider the angular spectrum of diffracted field

The next step in the calculation involves a Fourier transformation of the vertical fieldstrength profile.

- a) The first term in the expression for the field is a step function

$$E_1(z) = \begin{cases} 0 & \text{for } z < 0 \\ 1 & \text{for } z > 0 \end{cases}$$

The Fourier transform of this is the following



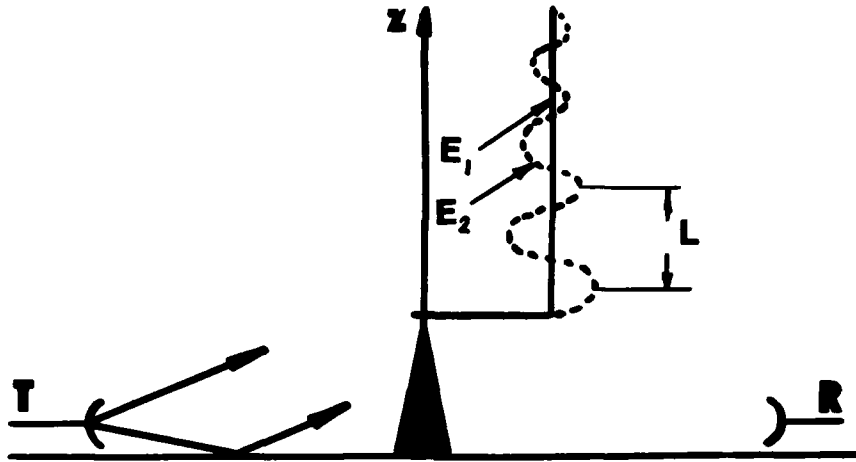


Figure 11 Vertical fieldstrength distribution with ground reflections

$$F_1(\theta) = \delta(\theta) + \frac{1}{j\theta}$$

This assumes small angles  $\theta$  such that  $\theta \approx \sin \theta$ . Note that  $\delta$  is a Dirac delta function.

b) For simplicity we write the second term as follows

$$E_2(z) = E_2(e^{-\alpha z} \sin \beta z)$$

such that  $\beta = \lambda/L$ .

This function gives a comparatively simple Fourier transform, namely

$$F_2(\theta) = \frac{\beta}{\alpha^2 + \beta^2 - \theta^2 + 2j\alpha\theta}$$

such that the resultant angular spectrum is given by

$$\begin{aligned} F(\theta) &= F_2(\theta) + F_1(\theta) \\ &= \frac{\beta E_2}{\alpha^2 + \beta^2 - \theta^2 + 2j\alpha\theta} + \frac{E_1}{j\theta} \end{aligned}$$

The angular power spectrum is then obtained from the following

$$P(\theta) = F(\theta) \cdot F^*(\theta)$$

This function has a pronounced maximum for a certain direction, namely the direction corresponding to

$$\theta = \pm \sqrt{\beta^2 + \alpha^2}$$

If we have no damping, i.e. if  $\alpha = 0$ , then we have a Dirac delta function for  $F_2(\theta)$  centered at

$$\theta = \beta \quad \text{i.e. at} \quad \theta = \frac{\lambda}{L}$$

This is the same as the results obtained using the Bragg scattering relationship in connection with the scattering from sinusoidal variations with height of the refractive index. From Bragg we have the following.

Maximum scatter in a direction  $\theta$  given by

$$K = \frac{4\pi}{\lambda} \sin \theta/2$$

where  $K = 2\pi/L$ . As in the diffraction case above,  $L$  is the period in space of the sinusoidal variations, i.e.

$$\frac{2\pi}{L} = \frac{4\pi}{\lambda} \theta/2$$

i.e.  $\theta = \lambda/L$

as we obtained directly from equation above.

We know that a single ground reflected component interfering with the direct wave will give a fieldstrength distribution above the obstacle of the form given in equation above. The damping factor  $\alpha$  will then be determined by the rate at which the ground reflection coefficient decreases with increasing angle of incidence to the ground. The period of oscillation,  $L$ , is given by the geometry as shown in chapter 2.1.

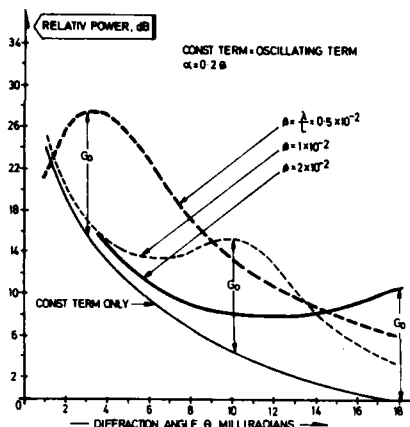
$$L = \frac{\lambda R}{2h}$$

Thus, in this case, we will have maximum energy diffracted in a direction given by

$$\theta = \frac{2h}{R}$$

Thus, by adjusting the height,  $h$ , of the transmitting antenna, we can beam the diffracted wave in a desired direction. We see that ground reflection (leading to an oscillating vertical profile of fieldstrength) actually increases the power received at a given

Figure 12 Angular diffraction spectrum  
For various periods of field-  
strength oscillations



point behind the obstacle. This increase is known as obstacle gain. Note that we shall have to transform the coordinate system such that  $\theta$  is measured relative to the line joining the top of the knife-edge obstacle and the transmitter and not relative to the horizontal line through the obstacle top. See figure 12.

### 3 THE POTENTIAL OF GENERAL ADAPTION TECHNIQUES IN RELATION TO THE VARIOUS PROPAGATION MECHANISMS

A communication circuit should ideally adapt itself to allow for maximum information transfer. This means that at any given time the information rate (bandwidth) should make full use of the instantaneous bandwidth of the transmission medium. To achieve this one has to use the results of the chapter above, where we have characterized the propagation medium in a way which is meaningful in relation to information transfer. If our task is to transmit a certain amount of information from point A to point B, we shall need a buffer store at A and one at B. Between A and B a set of "pilot tones" is transmitted. By the aid of these, the channel parameters of the communication medium are measured continuously. Information about the communication medium is returned to the transmitter, and the system is coded in order to transmit the message at an optimum rate, and in a manner which makes optimum use of the available bandwidth. Figure 13 illustrates the general scheme.

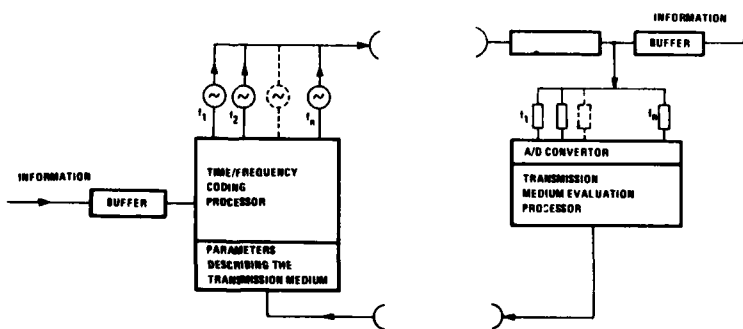


Figure 13 A schematic diagram of a propagation medium adaptive communication system. A set of pilot frequencies is transmitted through the propagation medium. The characteristic properties of the transmission medium is assessed by a processor. Information regarding the propagation medium is used to program the time/frequency coding processor of the transmitting system in an adaptive manner

Note that this scheme is passive in the sense that it only adjusts the information rate so as to be harmonized to the prevailing conditions. We use the same radio carrier frequency, and we confine ourselves to an adjustment of the rate at which the message is transferred on this carrier.

As we have inferred from the chapter 2 above, however, we can also improve the propagation conditions by e g changing the carrier frequency.

To illustrate this, we shall confine ourselves to a very specific and well defined transmission mode. Namely, one which is based on the spread spectrum concept. This is visualized in figure 13. For this application there are two propagation parameters which are of dominating importance. The first is, obviously, the instantaneous bandwidth of the propagation medium. A definition of "bandwidth" would help to avoid the confusion, that even arises when the term is used in relation to scattering processes. Consider the case in which several radiowaves, each having different frequencies, are transmitted simultaneously. At the receiver, the voltage at each of these frequencies is measured as a function of time (i e we measure  $V_{F_1}(t)$ ,  $V_{F_2}(t)$ ). If we take the instantaneous ratio of the power at the various frequencies, and integrate the ratio we form

$$\int \frac{(V_{F_1}(t))^2}{(V_{F_2}(t))^2}$$

We then obtain information about bandwidth. On the other hand, if we integrate the signal at either frequency over the appropriate time interval, by forming

$$\frac{\int (V_{F_1}(t))^2}{\int (V_{F_2}(t))^2}$$

we do not obtain information about bandwidth but rather about "the wavelength dependence propagation circuit".

Forming the ratio of the instantaneous voltage at each of the two frequencies is one way of obtaining information about bandwidth. Another way is to transmit a set of radiowaves having different frequencies as in the first case, and at the receiving end correlate the fieldstrength at one frequency with that of the other by forming the cross-correlation  $R_{12}(\gamma)$ . The more narrow-banded the transmission channel, the poorer the correlation for a given frequency spacing. Transmitting then many correlated waves spread over a frequency band enables us to find the complete autocorrelation function  $R(\Delta F)$  in the frequency domain. We then define bandwidth as the frequency spacing for a correlation coefficient of  $1/e$ .

Another important parameter describing the propagation medium is the correlation distance in space. We transmit a single wave at point A. At the receiving point B we have a set of vertically spaced receiving antennas. We measure the complex fieldstrength (amplitude and phase) and we compute the spatial autocorrelation function. The antenna separation corresponding to a  $1/e$  correlation coefficient, we define as the spatial correlation distance. In the general case where we want both to match to the available bandwidth and take the spatial correlation properties of the propagation medium into consideration, we need a set of transmitters which is capable of transmitting a set of electromagnetic waves with different frequencies in an adaptive manner as illustrated in figure 13, and this set of electromagnetic waves carrying the information to be transferred, should be passed through a computer controlled array element antenna, capable of shaping the wavefront (directing the antenna beam) adaptively, so as to minimize the adverse effect of the propagation medium. By means of such a system, we can do more than merely adjusting our information transfer rate to match the available bandwidth. We can adjust our system parameters so as to, at any one given instant, improve the usable bandwidth conditions.

In this brief review, we shall confine ourselves to the frequency domain (spread spectrum application), and we shall bear in mind that the concepts developed are directly applicable to the spaced antenna case. We shall now discuss such a spread spectrum adaptive system with reference to the various propagation modes discussed in chapter 2.

### 3.1 Adaption techniques in relation to scatter propagation

We shall now consider two properties of a communication channel involving scatter propagation. The first is bandwidth, the second is spatial field strength correlation. In terms of the two parameters characterizing the tropospheric transmission medium, namely effective radius of the earth  $a$  and the slope  $n$  of the refractive index irregularity spectrum, the bandwidth  $\Delta f$  is given by

$$\Delta f = \frac{8a^2 c}{2\pi D^3} (e^{4/n} - 1)^{-1}$$

$D$  is the distance between transmitter and receiver and  $c$  is the velocity of light. From knowledge about the probability distribution of  $n$  and the probability distribution of  $a$ , we can calculate the probability distribution of bandwidth  $\Delta f$ . Note that such a simple approach assumes that there is no direct correlation between the parameters  $a$  and  $n$ . This assumption has been verified both experimentally and theoretically. On the basis of the probability distribution of  $n$ , shown in figure 2 above, and that of the effective earth radius  $a$ , shown in figure 3 above, the bandwidth probability function is shown in

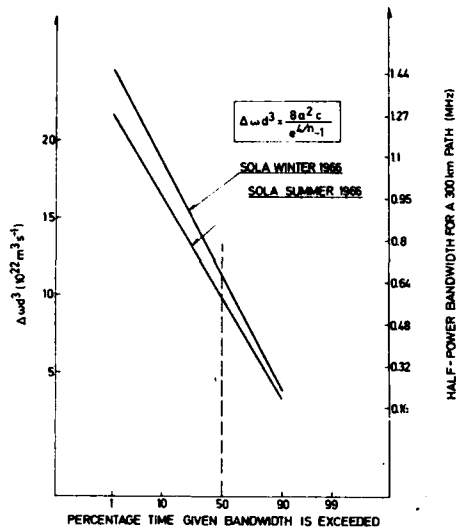


Figure 14 Distributions of the half-power bandwidth  $\Delta\omega$

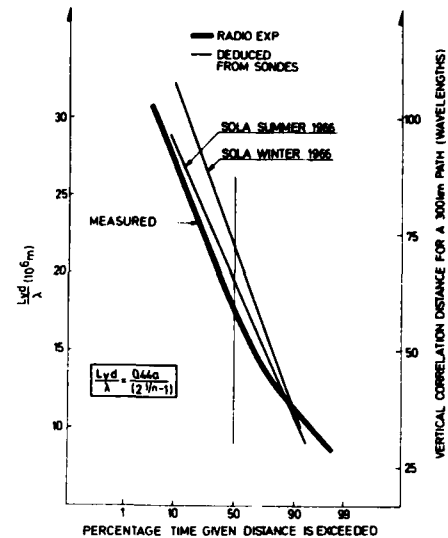


Figure 15 Distributions of vertical field-strength correlation distance. The solid lines are based on the Sola radiosonde measurements. The dashed line was measured by Grosskopf (10)

figure 14. Note that this is plotted on gaussian probability paper. We note from this figure that the bandwidth varies drastically; over a pathlength of 300 km, a bandwidth of something like 0.16 MHz is exceeded in 90% of the time whereas a bandwidth of 1.5 MHz is exceeded in only 1% of the time. Accordingly, if we were to make use of a static non-adaptive communication system, and satisfy the CCIR requirements, (satisfactory conditions in 99.98% of the time), our communication bandwidth to which our system should be adjusted, is very low indeed. However, since the total amount of information which can be transferred over a communication channel is the integral of the bandwidth versus time function, we see from figure 14 that by use of an adaptive system, the information transfer capability of the scatter circuit is considerable. It is also evident, however, that there is no parameter we can control to improve the bandwidth of the communication channel for a fixed spacing  $D$  between transmitter and receiver.

Then let us briefly discuss the spatial correlation properties of the scattered wave for the purpose of investigating to what extent we can improve the channel performance by space diversity. With reference to chapter 2, we see that the vertical correlation distance is given by

$$\frac{L_v}{\lambda} = \frac{0.44a}{D(2^{1/n} - 1)}$$

Again, based on the probability distributions for the two atmospheric parameters  $a$  and  $n$ , respectively, the probability distribution for vertical correlation distance is given in figure 15. Note that the correlation distance varies considerably, and that a substantial improvement in system performance may be obtained with space diversity. This, of course, is well known.

In conclusion: if we possess information about the probability distribution of a given parameter characterizing the communication channel, we can design an adaptive system which optimizes the conditions. The efficiency of such a system, however, is determined by several factors of which two should be mentioned:

- The bandwidth required to transmit information about the atmospheric state-variables. This is determined by the rate at which the atmospheric conditions changes and also by the amount of *a priori* information we already have about the atmospheric processes.
- Secondly, the buffer requirements must be considered. If the atmospheric processes are slow, we shall need a buffer with a large storing capacity. If, on the other hand, the atmosphere is such that the state-variables (e.g. the bandwidth) changes rapidly, we shall need a buffer with quick response (quick reading and writing capability).

### 3.2 Adaptivity requirements in relation to line-of-site propagation with added ground reflections

In chapter 2 we established some simple relationships in connection with line-of-site propagation. We saw that, by altering the height of the receiving antenna, relative to the reflecting plane, a considerable improvement in signal strength is achieved. We also saw that, by changing the frequency of the carrier wave, the propagation loss can likewise be minimized. What we want, therefore, is a communication channel which first changes

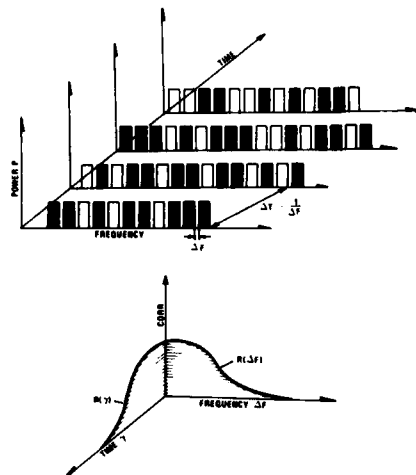


Figure 16 A simple schematic coding diagram of a frequency-time adaptive communication system. The information is coded in both frequency and time domain in a manner determined by the propagation medium (the  $R(\Delta F)$  and the  $R(\tau)$  functions)

$$\Delta T > \frac{1}{\Delta F}$$

(See figure 16).

Then let us assume that the ambient noise level increases such that the noise intensity within each of the  $N$  frequency channels exceeds the signal level. To improve this signal-to-noise situation, we must know something about the correlation properties both in frequency and in time of this noise. If the correlation distance in time of the noise is  $\gamma_0$ , and we can integrate the signal in each frequency slot over a period  $T$ , and we receive a signal/noise enhancement proportional to  $\sqrt{T/\gamma_0}$ . This is the same as repeating the  $N$ -bit information frame  $n$  times, where  $n = T/\Delta T$ . We have thus obtained an  $n$ -fold redundancy in the time domain.

Then let us do the same in the frequency domain. Let us reduce the information content in our information frame by a factor  $r$  such that the information is contained in  $N/r$  frequency slots. We have then the possibility of transmitting the same message at the same time in other portions of our available frequency spectrum. With this ratio  $r$  between the message bandwidth, we obtain an  $r$ -fold redundancy, and the corresponding processing gain. This means that we can increase the ambient noise level correspondingly without altering the error rate of our circuit.

If now the bandwidth of the communication channel decreases whereas the ambient noise-level remains constant, then we must confine our "spread spectrum message" to a set of frequency slots within which we have correlated conditions. This reduces our redundancy potential, and also correspondingly our processing gain.

Not note that we cannot always treat the frequency domain and the time domain separately. When we have "frequency selective fading" resulting from multipath phenomena, then there is a direct relationship between the correlation distance in the frequency domain, and the correlation distance in the time domain (Fourier-transforms). For a given coding in the frequency domain, therefore there is a corresponding one in the time domain. In the general case, however, with "power fading" as well as multipath fading, some improvements in system performance can apparently be achieved by coding both in the frequency domain and the time domain as indicated in figure 16.

To visualize this, figure 17 is presented. This is a sketch of an adaptive communication system which adapts itself both to bandwidth and to center frequency for maximum field-strength. This system can adapt itself from a digital large bandwidth spread spectrum to a "single frequency" low data-rate channel.

Finally, figure 18 illustrates a composite system involving a tropospheric scatter channel, a terrestrial link based on reflections from terrain obstacles, and a path involving a two-ray system. Practical examples are also listed.

the carrier frequency so as to optimize the conditions from the point of view of transmission loss, and thereafter adjusts the bandwidth for maximum information transfer rate. As an example, with reference to the schematic diagram of figure 13, we shall consider a "spread spectrum" communication channel. Let us assume that we have to our disposal a large number  $N$  of discrete frequency generators on the transmitting end, and these can be switched on and off by a microprocessor. Let us assume that the information word is composed in a binary fashion by switching the frequency generators on and off such that  $N$  frequency generators give us an  $N$ -bit word as depicted in figure 16. At the receiver, there are  $N$  narrow-band filters, which are tuned to the corresponding set of transmitting generators. If now the bandwidth of the transmission medium is large enough so as to take care of all the  $N$  frequency lines simultaneously, our "message frame" can contain  $N$ -bits of information. If now the frequency spacing between the channels is  $\Delta F$ , then we can transmit another  $N$ -bit frame after a time-interval

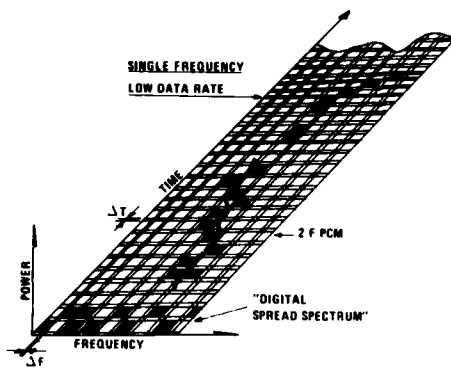


Figure 17 Frequency-time-power plot of a self-adaptable communication system. The system adapts itself from wide band spread spectrum through two frequency PCM to a single frequency low data rate system. The total information transfer is proportional to the time-frequency integral

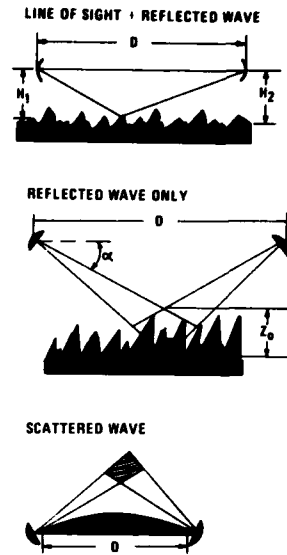


Figure 18 Some typical propagation modes related to terrestrial communication circuits illustrating the bandwidth variability

4 FUNDAMENTALS OF RADIO WAVE SCATTERING FROM TARGETS/SURFACES IN RELATION TO ADAPTIVE TECHNIQUES

In chapter 2.2, we introduced some general concepts in relation to scattering from rough surfaces. Specifically we have shown that if the scatterers are distributed in depth as  $\sigma(z)$  such that the delay function becomes  $\sigma(z/c)$ , the autocorrelation function in the frequency domain (bandwidth of reflector) is obtained directly as the Fourier transform of the function  $\sigma(z/c)$ . Furthermore, we presented a table giving this frequency dependence for a set geometrical structures. We also presented a graphical representation of some of these surface structures. We have concluded that the more detailed information we require about a given surface, the larger the bandwidth of our illuminator has to be.

To illustrate the basic physical principles involved, let us first consider the simplest of all targets, consisting of two reflection points spaced  $\Delta z$  longitudinally along the direction of wave propagation (see figure 19). A wide spectrum of frequencies is transmitted on to this object, and the set of interfering waves received is analyzed. As the

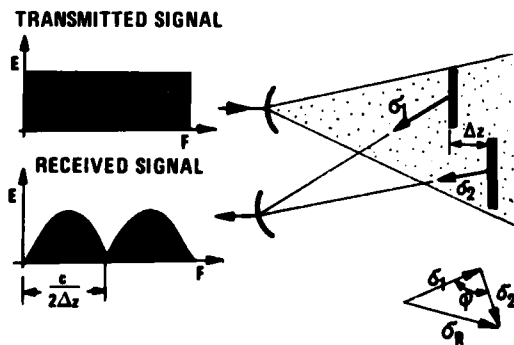


Figure 19 Determination of distribution in distance of the scattering elements in a target. Basic principle

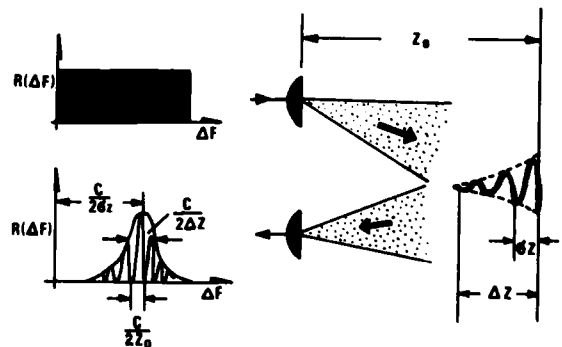


Figure 20 The correlation function in the frequency domain of the reflected wave gives information about the distance to the object, the size of the object and its shape

difference in frequency of the two waves is changed, the waves arrive in antiphase at the receiving site, causing a minimum in the frequency spectrum. If the distance in depth between the two reflecting elements is  $\Delta z$ , the phase angle between the wave reflected from the two reflectors is given by

$$\phi = 2\pi \frac{2\Delta z}{\lambda_1} = 2\pi \frac{2\Delta z F_1}{c}$$

for frequency  $F_1$ . To change the phase angle  $\phi$  through  $180^\circ$ , so as to move from constructive interference to destructive interference, requires a frequency change to  $F_2$  such that

$$2\pi + \phi = 2\pi \left( \frac{2\Delta z F_2}{c} \right)$$

The frequency difference between two successive interference minima, is thus given by

$$F_2 - F_1 = \Delta F = \frac{c}{2\Delta z}$$

Now, consider the more general situation with an object in the form of a periodic structure (e.g. a tree with a set of equally spaced branches) where the scatterers are distributed according to some probability distribution  $\sigma(z)$ . The size of the object is now  $\Delta z$ , and the fine scale structure  $\delta z$  (exponentially damped sinusoidal oscillation). The object is at a distance  $z_0$  from the transmitter and is illuminated with a set of correlated frequencies, i.e. derived from a common source. When this set of electromagnetic waves is coupled to the object shown, the reflected wave is decorrelated with respect to frequency as shown in figure 20; the maximum of the correlation envelope is shifted a distance  $(c/2\delta z)$  and the width of the correlation envelope is determined by  $(c/2\Delta z)$ . Finally, under the envelope of the correlation function there are periodic oscillations stemming from the fact that the system delay function is nonsymmetrical, resulting in a complex autocorrelation function in the frequency domain. In analysing the fine scale oscillation of the correlation function, a period can be found which is given by  $(c/2z_0)$ , where  $z_0$  is the distance to the target.

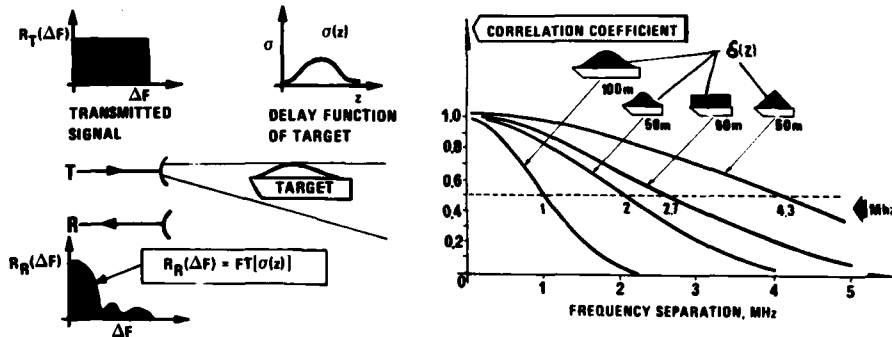


Figure 21 Shining a set of radio-waves having different frequency on to a reflecting target, information about shape and size is obtained

For details regarding these questions, the reader is referred to (1, 8, 11). To summarize this section, figure 21 is presented. Note that by shining a set of radiowaves having different frequency on to a scattering object, we obtain information about the statistical properties of a scattering surface. Specifically, we obtain information about shape and size of target.

Then to the question of adaptivity. From the pioneers of information theory, such as Shannon, we know that it takes zero bandwidth to detect a sinewave when we know its frequency, and sufficient observation time is provided. This means that the more *a priori* information we have about the target of interest, the more we can pretailor the illumination to "match" the particular target of interest. In doing so, we achieve maximum detection capability and at the same time we obtain minimum interference from the background. As we have seen from the chapter on the communication aspects above, however, it is important also to know the characteristic properties of the intervening transmission medium. Whereas the background gives rise to additive noise, the intervening medium gives rise to multiplicative noise (distortion). There are different techniques available for noise suppression whether the noise is adaptive or multiplicative. See reference (1).

The concept of tailored (matched filter) illumination is illustrated in figure 22. Note that if a matched filter illumination is provided, it takes zero bandwidth of the receiver to detect an object of known size and shape.

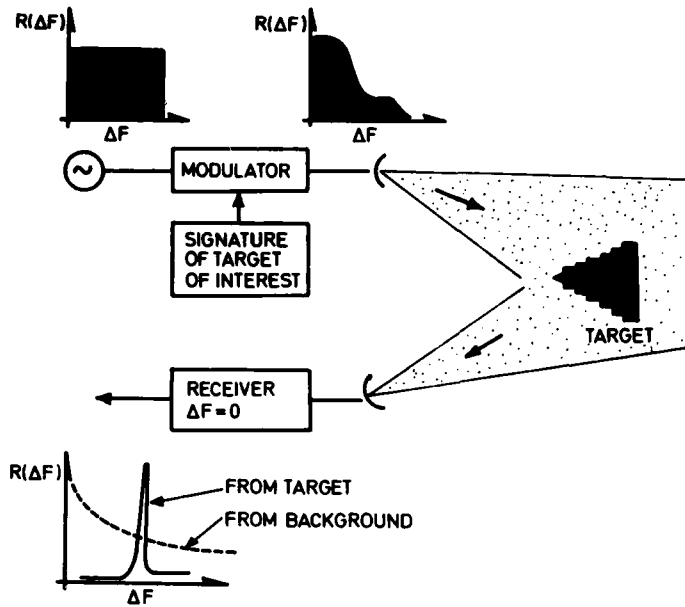


Figure 22 Illumination function for optimum detection sensitivity and identification potential

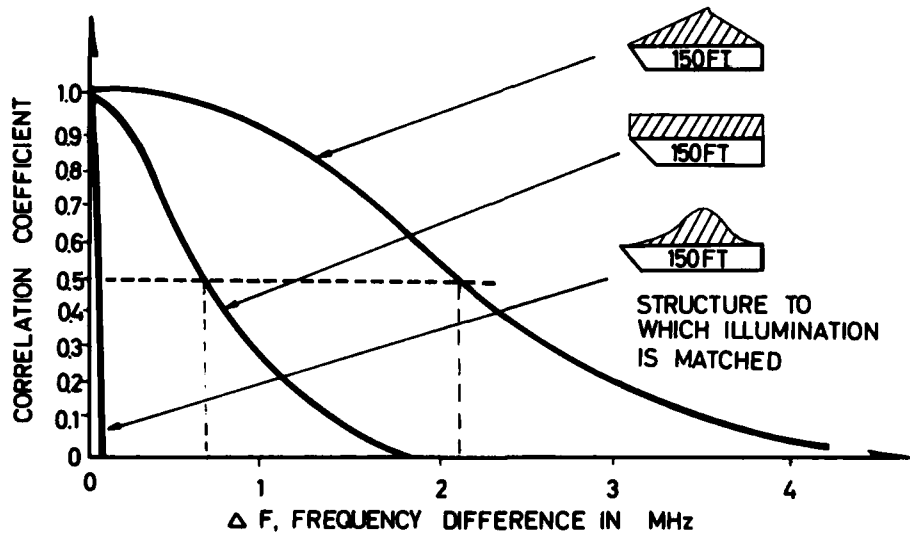


Figure 23 Theoretical results of "method illumination"

Finally, figure 23 gives the theoretical results of such a tailored illumination. If the structure to which the illumination is matched is a 150 feet ship with statistically gaussian distributed scattering elements, we will receive a signal with zero bandwidth from this target whereas a target in the form of a ship with rectangular scattering distribution requires a bandwidth of some 0.6 MHz. A triangular target requires a bandwidth of some 2.2 MHz. Finally, figure 24 shows a practical adaptive radar arrangement developed by the authors organization. Note that here the target is illuminated in such a way so as to obtain 15 different separations between the radio frequencies. This is achieved with 6 carrier waves with different frequency spacing. By means of this system, the illumination can be matched to ship signatures in such a way so as to minimize the influence of sea-clutter. Conversely, the radar can be matched to the sea-surface in such a way so as to provide information about waveheight, wavelength, wave-velocity and wave-direction.

The results of such investigations are in the process of being analyzed at the authors institution.



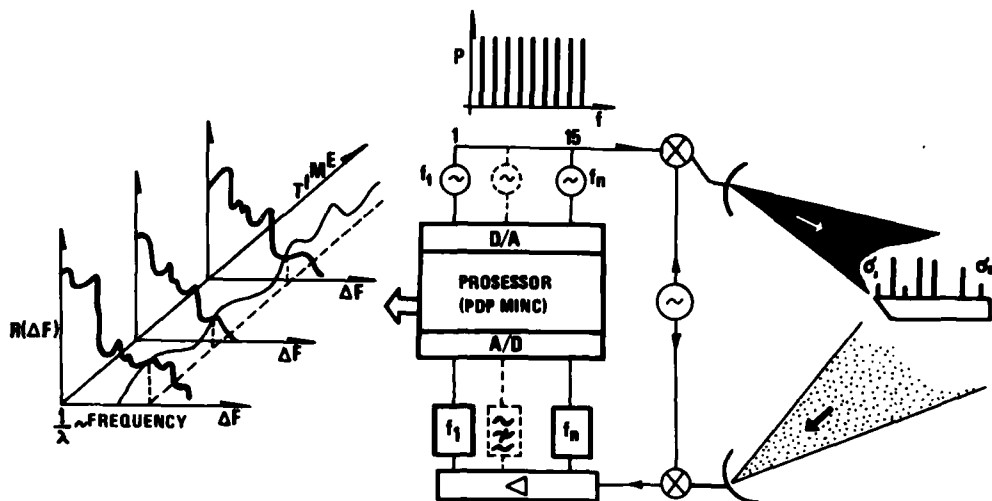


Figure 24 Schematic diagram of a target-adaptive radar system which, in its simplest form, is being developed by the author's organization

## 5 CONCLUSIONS

Advanced technology opens a new set of avenues in regard to detection and identification of objects with hitherto unidentifiable properties if a detailed adaption system is used. To achieve this, however, we shall need correspondingly detailed information about the target of interest, about the background against which this target is viewed, and about the intervening propagation medium. It has been the endeavour of the current contribution to summarize some of the factors involved to illustrate the potential of modern adaption techniques.

## Acknowledgements

I wish especially to express my appreciation to my secretary Mrs Eva Rødsrud who so tolerantly and very ably handled the arduous task of typing and editing the manuscript. Likewise I wish to thank my colleague, Terje Lund, for his conscientious proofreading of the manuscript, and for his many helpful suggestions.

## References

- (1) Gjessing, Dag T: Remote Surveillance by electromagnetic waves for air-water-land, Ann Arbor Science Publishers Inc, Ann Arbor, Michigan, USA (1978)
- (2) Gjessing, Dag T: Scattering of radio waves from regular and irregular time varying refractive index structures in the atmosphere, AGARD conference Proceedings no 37, (August 1968)
- (3) Gjessing, Dag T, K S McKormick: On the prediction of the characteristic parameters of long distance tropospheric communication links, IEEE Transactions on communications Vol COM-22, no 9 (September 1974)
- (4) Gjessing, Dag T: Scattering mechanisms and channel characterization in relation to broadband radio communication systems, AGARD conference Proceedings no 244 (October 1977)
- (5) Früchtenicht, H W: Characteristics and applications of line-of-site duct propagation, NATO Advanced Study Institute Series, Modern topics in microwave propagation and air sea interaction, ed A Zancla (1973)
- (6) Gjessing, Dag T: On the use of forward scatter techniques in the study of turbulent stratified layers in the troposphere, Boundary-layer Meteorology 4 (1973) 377-396
- (7) Wait, J R: A note on VHF reflection from a tropospheric layer, Radio Science 7, 847-848 (1964)
- (8) Gjessing, Dag T: The potential of general adaption techniques in relation to radar detection and identification of objects in an ocean environment, Submitted for publication
- (9) Gjessing, Dag T, A G Kjelaas, J Nordø: Spectral measurements and atmospheric stability, Journal of atmospheric sciences Vol 26, no 3, pp 462-468 (May 1969)

- (10) Grosskopf, J: Investigation of receiving field for scatter propagation, AGARD conference Proceedings Vol 37, pp 22.1 - 22.11 (1968)
- (11) Gjessing, Dag T: Environmental remote sensing, Part I: Methods based on scattering and diffraction of radio waves, Physics in Technology, Vol 10, pp 266-271 (December 1979)

USE OF A SATELLITE MULTI-FREQUENCY RADIOMETER TO DETERMINE  
ATTENUATION SUFFERED BY A SATELLITE RADAR

G.J. Dome, R.K. Moore, I.J. Birrer and K. Van Sickle  
Remote Sensing Laboratory  
The University of Kansas Center for Research, Inc.  
Lawrence, Kansas 66045 U.S.A.

SUMMARY

The Seasat Active Scatterometer System (SASS) is a multibeam radar designed to measure two radar backscatter signals from the sea and from them determine the wind vector. When condensed water is present in clouds and rain, the return signal is attenuated by the atmosphere and must be corrected before a wind determination can be made. The Seasat Scanning Multifrequency Microwave Radiometer (SMMR) provided the opportunity to measure the attenuation.

The antenna temperature of the radiometer observing the sea without attenuation can be calculated, for vertical polarization and at SMMR's 49° angle of incidence, if the surface temperature is known. Thus, an increase in the observed value above this value is an excess temperature caused by attenuation in the atmosphere. The amount of this excess temperature has been determined for various model cloud and rain conditions, as has the attenuation. An empirical relation was determined between excess temperature at 37 GHz and 18 GHz, and the attenuation at 14.6 GHz (SASS frequency). An algorithm was then developed to use the 37 GHz radiometer to establish small attenuations and the 18 GHz radiometer to establish moderate attenuations and large attenuations. This method has been tested against some of the early Seasat observations, and has been shown to be reasonably successful, within limitations posed by poor knowledge of the actual attenuation with which the results for the algorithm must be compared.

1. INTRODUCTION

The first discussion of the advantage of combining joint radar and radiometer measurements was presented by Moore and Ulaby (1969). This concept was further developed and a satellite system was later proposed by Moore and Pierson (1971) for worldwide ocean wind and wave predictions. Using a combined sensor system to view the ocean allows estimates of the wind speed to be made by both sensors during clear sky conditions. The radiometer portion, however, is more severely affected by the intervening atmosphere. When heavy wet cloud cover or precipitation is present, measurements by the radiometer may only consist of contributions from the intervening atmosphere. Use of a radiometer, therefore, allows regions of cloud cover and precipitation to be located. Furthermore, information from the radiometer can be used to estimate the attenuation seen by the radar, and thus, allow meaningful estimation of the wind speed even under these conditions.

An analysis by Wu and Fung (1973) demonstrated how a downward-looking radiometer could be used to estimate attenuation. In calculating the apparent temperature, that which would be measured by the radiometer, for a given atmospheric condition, several assumptions were imposed: (1) contributions arising from scattering by precipitation particles were ignored, (2) a simplified expression was used for the sky temperature (Peake, 1959),

$$T_{\text{SKY}}(\theta) = (1.12 T_{\text{air}}(0) - 50) (1-L)$$

and (3) the radiometer was assumed to be located sufficiently high enough so that the atmospheric temperature was equal to the sky temperature. The primary feature of this portion of their analysis was defining an appropriately-named quantity, the excess brightness temperature, which was the difference between the total apparent temperature and the brightness temperature of the sea. A unique relation was found between the atmospheric attenuation and the excess brightness temperature.

The first application of a satellite-borne radiometer-scatterometer (RADSCAT) system was SKYLAB. An algorithm to correct the radar portion of the RADSCAT using the radiometer portion was developed by Komen (1975). To derive the key relation between attenuation and excess brightness temperature, soundings taken by a NIMBUS satellite were incorporated in an analytical analysis. This approach serves as a forerunner to the present effort since (1) a relation between excess brightness and attenuation was used; and (2) a heavy reliance was placed on vertically polarized radiometer measurements taken at an incidence angle of 50°.

2. SEASAT SASS AND SMMR

On 26 June 1978, the SEASAT-A satellite was launched by NASA, carrying an array of sensors to prove the concept that meteorological and oceanographic parameters could be monitored from space. Two of the sensors were a microwave radar scatterometer and a microwave radiometer. These sensors, however, operated independently, unlike a true RADSCAT system.

A fan-beam scatterometer system, described by Grantham et al. (1977) was selected as most suitable to meet user requirements. This system, the SEASAT-A Scatterometer System (SASS), had an operating frequency of 14.6 GHz to provide maximum wind sensitivity, while minimizing atmospheric effects. Four antennas were squinted at angles of 45° from satellite sub-track providing a 'star-like' illumination pattern on the surface so that orthogonal measurements were possible to estimate the wind vector.

The Scanning Multi-Frequency Microwave Radiometer (SMMR), meanwhile, provided both vertically and horizontally polarized measurements at 6.63, 10.69, 18.0, 21.0, and 37.0 GHz as described by Gloersen and Barath (1977). A rotating reflector system about a fixed feed horn provided a conical scan pattern at a constant incidence angle of 49° from normal. The field of view of the SMMR extended from behind the

satellite along a 50° arc on the right of the subtrack. The coverage of these two sensors is illustrated in Figure 1.

### 3. MODELING

An algorithm to correct the SASS for atmospheric effects requires the determination of a relation between atmospheric attenuation at 14.6 GHz and excess brightness temperature at the SMRM frequencies and look angle. However, the modeling problem in our case may be simplified since neither the 21.0, 10.69 or 6.63 GHz frequencies are suitable for this application. The 21.0 GHz channel exhibits a strong dependence on water vapor unlike the SASS. This channel is also located reasonably near the one at 18.0 GHz, and therefore, inclusion of information from this channel would offer little or no advantage. Neither the 10.69 or 6.63 GHz channels have fine enough resolution, ~ 85 km x 85 km and ~ 150 km x 150 km, respectively, to use in correcting a 50 km x 50 km SASS resolution cell. Furthermore, the 6.63 GHz channel exhibits a strong dependence on sea surface temperature while offering only limited sensitivity to atmospheric conditions. For these reasons, modeling efforts were undertaken using only the SMRM frequencies of 18.0 and 37.0 GHz at an incidence angle of 49°.

#### 3.1 Radiative Transfer

When the majority of radiation is thermal, as in the case of a downward-looking microwave radiometer, use of the radiative transfer equation is indicated. The total radiation measured by the radiometer will be called the apparent temperature,  $T_A$ , and consists of contributions from both the surface and the intervening atmosphere. Formulation of such problems has been previously discussed by Chandrasekhar (1960). If the contributions arising from scattering by particles in the atmosphere is ignored, as in this study, the radiative transfer is governed by

$$\cos \theta \frac{dT_{Aj}(z, \theta)}{dz} + \alpha_T(z) T_{Aj}(z, \theta) = \alpha_T(z) T_{AIR}(z) \quad (1)$$

The solution of this expression takes the form

$$T_{Aj}(z, \theta) = L(z, \theta) [\epsilon_j(\theta) T_s + T_{Rj}(\theta)] + T_{ATM}(z, \theta) \quad (2)$$

where:

$j$  = polarization,  $j = h$  or  $v$

$L(z, \theta)$  = transmittance of the atmosphere in terms of the attenuation,  $\alpha$ , at an incidence angle,  $\theta$ ,

$$= \exp \{-\sec \theta \int_0^z \alpha(z) dz\} \quad (3)$$

$\epsilon_j(\theta)$  = emissivity of the surface

$T_s$  = temperature of the surface

$T_{Rj}(\theta)$  = reflected sky temperature

$$= (1 - \epsilon_j(\theta)) \int_z^0 \alpha(z') T_{AIR}(z') \exp \{-\sec \theta \int_{z'}^0 \alpha(u) du\} dz' \quad (4)$$

$T_{ATM}(z, \theta)$  = atmospheric temperature

$$= \sec \theta \int_0^z \alpha(z') T_{AIR}(z') \exp \{-\sec \theta \int_{z'}^z \alpha(u) du\} dz' \quad (5)$$

This study, like Komen's, elected to use only vertically polarized results to minimize wind speed effects. Experimental data from Hollinger (1971) and theoretical modeling by Stogryn (1967), both considering only roughness effects, suggest vertically polarized measurements at the SMRM incidence angle are insensitive to surface roughness caused by wind speed. However, an increase in the surface emissivity should occur due to the generation of foam for wind speeds greater than 7.5  $\text{ms}^{-1}$  since the emissivity of foam is in the range 0.94 - 0.99 (Droppleman, 1972). The magnitude of these combined wind speed effects, roughness and foam generation, have been studied at other incidence angles by Cardone and Ross (1970) and Webster et al. (1976).

Initially, these effects from wind speed will be ignored and a recent model by Klein and Swift (1977) will be used to describe the emissivity of the sea surface. A method to reduce errors arising from wind speed effects will be presented later.

In this manner, the brightness temperature of the sea surface,  $T_{Bj}$ , may be determined:

$$T_{Bj}(\theta) = \epsilon_j(\theta) T_s \quad (6)$$

This result, along with expressions (3) - (5), allows calculations of the apparent temperature, (2), which would be measured by the SMRM viewing different homogeneous atmospheric conditions. The excess brightness temperature for these conditions may be established using the relation

$$T_{Exj}(\theta) = T_{Aj}(\theta) - T_{Bj}(\theta) \quad (7)$$

### 3.2 Absorption Models

Absorption of energy by the Earth's atmosphere arises from several sources. In clear sky conditions, absorption at microwave frequencies occurs due to water vapor and molecular oxygen. Under cloudy conditions, additional absorption arises from the liquid water content of the clouds. When precipitation occurs, the total absorption is further increased. Consequently, the total absorption,  $\alpha_T$ , may be expressed as

$$\alpha_T = \alpha_{H_2O} + \alpha_{O_2} + \alpha_{CLOUD} + \alpha_{RAIN} \quad (8)$$

where the constituents are written in ascending orders.

The effects of water vapor and molecular oxygen have been extensively studied. Expressions from Ulaby (1973), developed through a comprehensive study of literature, were selected to describe these effects. In this work the formulation of water vapor absorption was derived based on an expression by Van Vleck and Welsskopf (1945) and a consistent set of empirical relations from numerous authors. In a like manner, the absorption coefficient for molecular oxygen was developed following the development proposed by Meeks and Lilley (1963).

Possible severe attenuation of satellite radar signals, such as those from SASS, occurs when the intervening atmosphere consists of non-precipitating cloud cover. The first effort to develop theoretical expressions for the absorption coefficients for these cases was by Ryde and Ryde (1944). Their results were later summarized by Gunn and East (1954) who added separate expressions for the cloud absorption coefficient based on the composition of the clouds. Using these later theoretical results, Benoit (1968) proposed the following empirical model for the cloud absorption:

$$\alpha_{CLOUD}(z) = Mf^b \exp(a), \text{ dB(km)}^{-1} \quad (9)$$

where  $M$  = liquid water content of the cloud,  $\text{gm(m)}^{-3}$   
 $f$  = propagating frequency, GHz  
 $b$  = frequency index (water clouds = 1.95, ice clouds = 1.006)  
 $a$  = temperature coefficient  
 = -6.866 [1 + 0.0045 ( $T_{AIR}(z) - 273$ )] for water clouds  
 = -8.26 [1 - 0.01767 ( $T_{AIR}(z) - 273$ ) - 0.0004374 ( $T_{AIR}(z) - 273$ )<sup>2</sup>]  
 for ice clouds

For simplicity, this model was selected to describe the attenuation resulting from non-precipitating cloud cover. In this case and for the clear sky absorptions, a lapse rate of  $6.5^\circ\text{K (km)}^{-1}$  was used to describe the air temperature profile.

Similarly, the absorption coefficient of rain follows results developed by Gunn and East. In this case, the absorption coefficient is described by the empirical model

$$\alpha_{RAIN}(z) = ar^b(z) \quad \text{dB (km)}^{-1} \quad (10)$$

where  $r(z)$  = rainfall rate at point  $z$  along the path,  $\text{mm(hr)}^{-1}$   
 $a, b$  = empirical coefficients

Defining the proper set of coefficients to use in this expression is more difficult. Initially, these coefficients were determined theoretically using either droplet-size distributions from Laws and Parsons (1943) or Marshall and Palmer (1948). However, Medhurst (1965) concluded actual observed attenuation between microwave links during 1946-1962 exceeded the theoretical maximum. Further experimental programs continued and de Bettencourt (1974), like Medhurst, summarized these data. This latter study showed better agreement with theoretical results. Better agreement possibly occurred because the rainfall rate was more accurately measured along the attenuation path. For this reason, the empirical coefficients from de Bettencourt are used to describe the loss during precipitation.

### 3.3 Results

In the two previous sections, necessary relations have been formulated for the calculation of the attenuation and apparent temperature at microwave frequencies. To provide the best results, realistic models for non-precipitating and precipitating clouds are necessary. Models chosen for this purpose are portions of those proposed by Valley (1965), Porter (1969), Levine (1965), and Kreiss (1969).

Through the use of varying atmosphere profiles, Table 1, relations between the attenuation at 14.6 GHz and the excess brightness temperature at the selected SMHR frequencies were found. These results for the two-way nadir attenuation are illustrated in Figures 2 and 3 for 18.0 and 37.0 GHz, respectively, at a sea surface temperature of  $290^\circ\text{K}$ . A nearly unique relation between the attenuation and excess brightness is observed. However, a value of excess brightness temperature does exist beyond which the attenuation cannot be uniquely determined. When the excess brightness is greater than this level, the emissions measured by the radiometer arise only from a portion of the atmosphere. In these instances, the excess brightness is only a function of the temperature and moisture near the cloud top as illustrated by Figure 3.

In practice, the relationship between attenuation and excess brightness temperature, at  $\theta = 49^\circ$ , may be modeled as

$$\alpha(\theta=49^\circ) = A_1 T_{EX}(\theta=49^\circ) + A_2 T_{EX}^2(\theta=49^\circ) + A_3 T_{EX}^3(\theta=49^\circ) \quad (11)$$

where  $A_1$ ,  $A_2$ , and  $A_3$  are empirical coefficients. This result is illustrated for the 18.0 GHz case in Figure 3. For computational convenience, inclusion of the first order term of this expression is sufficiently accurate to describe this behavior for the 37.0 GHz channel prior to saturation as seen in Figure 4.

#### 4. ALGORITHM

Attenuation observed by the SASS is estimated using information obtained from overlapping SMRR vertically polarized measurements at 18.0 and 37.0 GHz. A problem exists in co-locating these measurements since the coverage of these sensors is greatly different as illustrated previously by Figure 1. In a true RADSCAT system, such a problem would not exist since both sensors would use the same antenna. For this case, however, the problem has been greatly reduced since the apparent temperature is determined during processing at JPL using a series of four overlapping 600 km x 600 km grids using an algorithm developed by Njoku (1979). These four grids are defined in Table 2.

##### 4.1 Co-Location

An operational algorithm to co-locate SASS and overlapping SMRR measurements has been developed by Birrer and Dome (1980). This approach passes the SASS data scans through a SMRR vector space generated by forming two data matrices containing three consecutive 600 km x 600 km SMRR data blocks. Separate matrices are used for 18.0 and 37.0 GHz data to eliminate unnecessary computer storage. These matrices are referenced through (I,J,K) coordinates. The I-index corresponds to grid rows in the along-track direction of the data vector. Cross-track elements of the data vector are referenced through the J-index, and the K-index contains the data elements: latitude, longitude and apparent temperature.

The co-location process begins once a SASS data scan is known to overlap the SMRR space by comparing the SASS and SMRR time tags. At this point, a search is initiated to locate the best 37.0 GHz cell, grid 4, referenced as  $(i_{15}, j_{15})$ , which is a minimum distance from the nadir SASS cell.

For the remaining SASS cells, distance,  $d$ , is computed from the nadir SASS cell to a specific cell, cell  $n$ . This distance and an angle,  $\psi$ , formed between satellite subtrack and SASS beam are used to estimate the 37.0 GHz cell,  $(i_n, j_n)$ , nearest the center of the desired SASS cell, by the relations:

$$i_n = i_{15} + d \cos \psi / r_{37} \quad (12a)$$

$$j_n = j_{15} + d \cos \psi / r_{37} \quad (12b)$$

where  $r_{37}$  is the resolution cell size at 37.0 GHz. The geometry used to determine the other SASS cells is illustrated in Figure 4. Since the 37.0 GHz resolution cell is  $\sim 27$  km x 27 km, a 3 x 3 submatrix of 37.0 GHz measurements is specified to insure complete overlap of the SASS cell.

To guarantee that the coordinates  $(i_n, j_n)$  are the best match to the SASS cell, a 3 x 3 submatrix is selected about these coordinates. This submatrix is then searched to locate the 37.0 GHz cell nearest the SASS cell center. If the initial guess is incorrect, a new center point is designated,  $(i_{n,best}, j_{n,best})$  and the final 3 x 3 submatrix is formed.

Since the SMRR grids for different frequencies cover the same 600 km x 600 km surface, the overlapping submatrix for the 18.0 GHz channel, or any other channel, may be determined without searching. Two opposite corner points of the 37.0 GHz submatrix designated as  $(i_4, j_4)$ , can be simply decoded into two potential corner points for any frequency,  $(i_\ell, j_\ell)$  as follows:

$$i_\ell = (i_4 - 1)n_\ell / 22 + 1 \quad (13a)$$

$$j_\ell = (j_4 - 1)n_\ell / 22 + 1 \quad (13b)$$

where  $\ell$  is the finest grid code for a specific frequency and  $n_\ell$  is the number of rows (or columns) for the frequency grid. This decoding will specify at most a 2 x 2 submatrix at other frequencies. However due to the larger resolution cells, these potential submatrices may degenerate into either 2 x 1, 1 x 2, or 1 x 1 submatrices.

##### 4.2 Attenuation Estimate

In the previous section, a technique to locate SMRR measurements which encompass a given SASS cell has been described. A best estimate of the apparent temperature at a given SASS cell was chosen to be the distance-weighted average of the measurements in the previously-described submatrix. Recalling expression (7), the excess brightness is defined for the SEASAT case as

$$T_{EXV,f}(\theta=49^\circ) = T_{AV,f}(\theta=49^\circ) - \epsilon_{v,f}(\theta=49^\circ) T_s \quad (14)$$

where  $f$  refers to the frequencies of 18.0 and 37.0 GHz. To determine this quantity, the only necessary input remaining is a value for the sea surface temperature.

Two options exist to determine the sea surface temperature. Methods have been developed using SMRR measurements to estimate this quantity, and several other oceanographic and meteorological parameters by Wilheit

(1979) and Wentz (1979). Portions of these methods could be incorporated in an attenuation algorithm to estimate the sea surface temperature. The accuracy of the above methods, while encouraging, is currently degraded because of problems arising from the relatively poor efficiency of the SMMR's antenna at the lower frequencies. Until a radiometer system is developed which employs a higher antenna efficiency, such as planned for the upcoming National Ocean Survey System (NOSS), the best estimate for the surface temperature may be a look-up table upgraded periodically. Such a table could best be developed using global results provided by a center such as the U.S. Navy's Fleet Numerical Weather Central.

Since the SEASAT satellite was operational only for slightly longer than three months, a simpler approach was selected. A single look-up table was developed by F.J. Wentz, of Remote Sensing Systems, Inc., using climatology data. This table provides reasonably accurate estimates of the sea surface temperature during the operational period of this satellite. This result, coupled with the limited sensitivity of the algorithm to errors in sea surface temperatures, allows adequate operation of the algorithm without using a more complex approach.

On the assumption that this simple approach yields a suitable estimate of the sea surface temperature, the attenuation observed by the SASS is estimated based on the excess brightness temperature at an optimal SMMR frequency. This optimal frequency is selected through a simple decision tree process. The first decision is based on the level of the one-way attenuation estimate (one-way at  $\theta=49^\circ$ ) using the 37.0 GHz channel. If this estimate does not exceed 0.4 dB, a linear relation exists between the attenuation at 14.6 GHz and the excess brightness at 37.0 GHz. This condition insures that the measurements from the 37.0 GHz channel have not saturated, and consequently, arise from emissions from the total atmospheric layer. Therefore, results using this channel are chosen to provide the estimate of the attenuation seen by the SASS, since over this range of values it offers the greatest sensitivity.

If the one-way attenuation estimate from the 37.0 GHz channel exceeds 0.4 dB, a new value for the attenuation is selected using the 18.0 GHz channel. When this value is below 3.0 dB, this channel is selected as providing the optimal attenuation estimate. For values exceeding this limit, no attempt is made to estimate the attenuation for two reasons. First, this channel begins to lose sensitivity at these higher attenuation values since measurements in this region are rapidly approaching the saturation level. Second, for this large value of attenuation to exist over the entire resolution cell, precipitation must be occurring. In these instances, measurements using the 18.0 GHz channel must be severely affected by scattering arising from the precipitation. This scattering effect would be more severe than that experienced by the radar since the scattering from rain droplets (Mie, 1908) is proportional to the frequency to the fourth power,  $f^4$ .

To use these estimates,  $\alpha_{EST}(\theta=49^\circ)$ , to remove atmospheric effects observed by the SASS, the estimates must be corrected to reflect the two-way path loss experienced. This correction may be obtained using the relation

$$\alpha_{SASS}(\theta) = 2 \alpha_{EST}(\theta=49^\circ) \left[ \frac{\cos(49^\circ)}{\cos(\theta)} \right] \quad (15)$$

#### 4.3 Improvements

From the previous discussions, a possible source of error in the attenuation estimates is wind speed effects, since only a specular surface was assumed. Increasing wind speed leads to increasing surface roughness, generation of foam, and then to larger patches of foam coverage. These changes in the composition of the sea surface can be characterized as an increase in the surface emissivity. A nominal value of  $0.0015^\circ\text{K}/(\text{ms}^{-1})$  has been reported over the frequency range of interest by F.J. Wentz, in private communication, for vertical polarization at an incidence angle of  $49^\circ$ .

Intuitively, any errors in the attenuation estimate arising from wind speed effects should be minimal at 37.0 GHz, since a relatively large change in excess brightness is needed for a small change in attenuation as seen by Figure 3. Sizable errors, if they exist, would only occur using the 18.0 GHz channel. To explore these possible errors, the previously discussed simulation was used to determine values for the apparent temperature using values of emissivities corresponding to wind speeds of 0, 10, 20, and  $30 \text{ ms}^{-1}$ . From these values of apparent temperature, an excess brightness was calculated using the brightness temperature of a specular surface as initially proposed. These values of excess brightness at different wind speeds are plotted in Figure 5 at a surface temperature of  $290^\circ\text{K}$  versus the true excess brightness for a specular surface. The absolute error in excess brightness diminishes as the excess brightness temperature increases. This behavior is expected since less of the surface contribution is observed by the radiometer as the transmittance of the atmosphere becomes less. To illustrate how this error affects the attenuation, Figure 5 has a double scale the one-way attenuation at  $\theta=49^\circ$ . The error in the attenuation estimate, however, will increase with increasing excess brightness.

To reduce the observed errors, the sea surface can be described for a  $10 \text{ ms}^{-1}$  wind speed instead of assuming a purely specular sea surface. Employing this idea, the excess brightness may be expressed as

$$T_{EXV,f}(\theta=49^\circ) = T_{AV,f}(\theta=49^\circ) - [\epsilon_{SPV}(\theta=49^\circ) + 0.015] T_s \quad (16)$$

Like the previous specular case, a relation between the attenuation at 14.6 GHz and this excess brightness may be determined. Values for the  $A_1, A_2$ , and  $A_3$  coefficients needed to explain this relation at 18.0 GHz as a function of sea surface temperature are shown in Figures 6-8. Similarly, the temperature dependence of the first order coefficient for 37.0 GHz is shown in Figure 9. Using the values of apparent temperature at 0, 10, 20 and  $30 \text{ ms}^{-1}$  previously discussed, the excess brightness was computed via expression (16). These values at different wind speeds are displayed in Figure 10 versus the true excess brightness for a  $10 \text{ ms}^{-1}$  surface at a sea surface temperature at  $290^\circ\text{K}$ . As in the previous example, a double scale is included on this figure to illustrate the errors arising from neglecting wind speed variations. Through use of the  $10 \text{ ms}^{-1}$  bias, the errors can be considerably reduced.

TABLE 1  
A. Cloud Models

Bottom (km)	Top (km)	Water Content gm(m) <sup>3</sup>	Source
0.5	3.20	1.00	Porter
0.4	0.90	0.67	Porter
0.3	0.65	0.33	Porter
0.46	3.81	1.25	Levine
0.46	2.59	1.00	Levine
0.46	1.07	0.50	Levine
0.63	7.18	0.25, 0.50, 0.75, 1.00, 2.00	Kreiss
0.63	3.01	0.25, 0.50, 0.75, 1.00, 1.50, 2.00	Kreiss
0.63	1.95	0.25, 0.50, 0.75, 1.00, 1.50, 2.00	Kreiss
0.63	1.46	0.25, 0.50, 0.75, 1.00, 1.50	Kreiss

B. Rain Models

Rain Parameters			Cloud Parameters		Source
Altitude Extent (km)	Rain Rate mm(hr) <sup>-1</sup>	Altitude Extent (km)	Water Content gm(m) <sup>-3</sup>		
0.-3.1	10.3	3.1-7.0	0.30	Valley	
0.-3.2	7.9	3.2-7.0	0.25	Valley	
0.-3.3	5.2	3.3-7.0	0.15	Valley	
0.-3.5	2.8	3.5-7.0	0.10	Valley	
0.-3.1	9.1	3.1-7.0	0.30		
0.-3.2	6.5	3.2-7.0	0.25		
0.-3.3	4.0	3.3-7.0	0.15		
0.-3.5	1.4	3.5-7.0	0.10		

TABLE 2  
SMMR Data Grids

Grid	Columns & Rows In ~ 600 km x 600 km	Radiometric Measurements (GHz)	
		Vertical Polarization	Horizontal Polarization
4*	22	37.0	37.0
3**	11	37.0, 21.0, 18.0	37.0, 21.0, 18.0
2	7	37.0, 21.0, 18.0, 10.69	37.0, 21.0, 18.0, 10.69
1	4	37.0, 21.0, 18.0, 10.69, 6.63	37.0, 21.0, 18.0, 10.69, 6.63

\* Grid 4 is used for 37.0 GHz

\*\* Grid 3 is used for 18.0 GHz

#### REFERENCES

- BENOIT, A., "Signal Attenuation Due to Neutral Oxygen, Water Vapor, Rain and Cloud," Microwave Journal, Vol. 11, November 1968, pp. 73-80.
- BIRNER, I.J., and G.J. DOME, "SASS/SMR Co-Location Algorithm," Remote Sensing Laboratory, The University of Kansas Center for Research, Inc., Technical Memorandum TM 343-3, February 1980.
- CARDONE, V. and D.B. ROSS, "Observations of Oceanic Whitecaps and Their Relation to Remote Measurements of Surface Wind Speed," J. Geophys. Res., Vol. 79, January 1974.
- CHANDRASEKHAR, S., Radiative Transfer, New York: Dover Publications, 1960.
- de BETTENCOURT, J.T., "Statistics of Millimeter-Wave Rainfall Attenuation," Jour. de Recherches Atmospheriques, Vol. 8, June 1974, pp. 89-119.
- DROPPELMAN, J.D., "Apparent Microwave Emissivity of Sea Foam," J. Geophys. Res., Vol. 75, January 1972.



- GLOERSEN, P. and F.T. BARATH, "The SEASAT-A Scanning Multichannel Microwave Radiometer," IEEE J. Oceanic Eng., Vol. OE-2, April 1977, pp. 172-178.
- GRANTHAM, W.L., E.M. BRACALENTE, W.L. JONES, and J.W. JOHNSON, "The SEASAT-A Satellite Scatterometer," IEEE J. Oceanic Eng., Vol. OE-2, April 1977, pp. 200-206.
- GUNN, K.L.S. and T.W.R. EAST, "The Microwave Properties of Precipitation Particles," Quarterly J. of the Royal Meteor. Soc., Vol. 80, October 1954, pp. 522-545.
- HOLLINGER, J.P., "Passive Microwave Measurements at the Sea Surface Roughness," IEEE Trans., Vol. GE-9, July 1971, pp. 165-169.
- KLEIN, L.A. and C.T. SWIFT, "An Improved Model for the Dielectric Constant of Sea Water at Microwave Frequencies," IEEE Trans., Vol. AP-25, January 1977, pp. 104-111.
- KOMEN, M.J., "Methods for Correcting Microwave Scattering and Emission Measurements for Atmospheric Effects," Remote Sensing Laboratory, The University of Kansas Center for Research, Inc., Technical Memorandum TM 254-6, August 1975.
- KREISS, W.T., "The influence of Clouds on Microwave Brightness Temperatures Viewing Downward Over Open Seas," Proc. of IEEE, Vol. 57, April 1969, pp. 440-446.
- LAWS, J.D. and D.A. PARSONS, "The Relation of Drop Size to Intensity," Trans. Am. Geographers Union, 1943, p. 452.
- LEVINE, J., "The Dynamics of Cumulus Convections in the Trades: A Combined Observational and Theoretical Study," Woods Hole Oceanographic Institution, Ref. 65-43, 1965.
- MARSHALL, J.S. and J.W. PALMER, "The Distribution of Raindrops with Size," Jour. of Meteor., Vol. 5, 1948, pp. 165-168.
- MEDHURST, R.G., "Rainfall Attenuation of Centimeter Waves: Comparison of the Theory and Measurements," IEEE Trans., Vol. AP-13, July 1965, pp. 550-564.
- MEEKS, M.L. and A.E. LILLEY, "The Microwave Spectrum of Oxygen in the Earth's Atmosphere," Jour. of Geophysical Res., Vol. 68, March 1963, pp. 1683-1703.
- MIE, G., "Beitrag zur Optik truber Medien, Speziell Kolloidale Metallosungen," Ann. Phys., Vol. 25, 1908, pp. 345-377.
- MOORE, R.K. and W.J. PIERSON (Jr.), "Worldwide Oceanic Wind and Wave Predictions Using a Satellite Radar Radiometer," J. Hydronaut., Vol. 5, April 1971, pp. 52-60.
- MOORE, R.K. and F.T. ULABY, "The Radar Radiometer," Proc. IEEE, Vol. 57, April 1969, pp. 587-590.
- NJOKU, E.G., "Antenna Pattern Correction Procedures for the Scanning Multichannel Microwave Radiometer (SMMR)," to be published in Bdy. Layer Met., 1979.
- PEAKE, W.H., "Interaction of Electromagnetic Waves with Some Natural Surfaces," IRE Trans. (Special Supplement), Vol. AP07, December 1959, pp. 5324-5329.
- PORTER, R.A., "An Analytical Study of Measured Radiometric Data, Vol. 1," Radiometric Technology, Inc., December 1969.
- RYDE, J.W. and D. RYDE, "Attenuation of Centimeter Waves by Rain, Hail, and Clouds," G.E. Company Res. Labs. Report 8516, Wembley, England, August 1944.
- STOGRYN, A., "The Apparent Temperature of the Sea at Microwave Frequencies," IEEE Trans., Vol. AP-15, March 1967, pp. 278-286.
- ULABY, F.T., "Clear Sky Atmospheric Absorption and Emission at 13.9 GHz," Remote Sensing Laboratory The University of Kansas Center for Research, Inc., Technical Report TR 243-1, June 1973.
- VALLEY, S.L., Handbook of Geophysics and Space Environment, McGraw-Hill, 1965.
- VAN VLECK, J.H. and V.F. WEISSKOPF, "On the Shape of Collision Broadened Lines," Reviews of Modern Physics, Vol. 17, 1945, pp. 227-236.
- WEBSTER, W.J., T.T. WILHEIT, D.B. ROSS, and P. GLOERSEN, "Spectral Characteristics of the Microwave Emission from a Wind-Driven Foam-Covered Surface," J. Geophys. Res., Vol. 81, June 1976.
- WENTZ, F.J., "SEASAT Gulf of Alaska Workshop Report," Jet Propulsion Laboratory, February 1979.
- WILHEIT, T.T. (Jr.), "SEASAT Gulf of Alaska Workshop Report," Jet Propulsion Laboratory, February 1979.
- WU, S.T. and A.K. FUNG, "A Theory of Microwave Apparent Temperature Over the Ocean," NASA Contractor Report, CR-2329, November 1973.

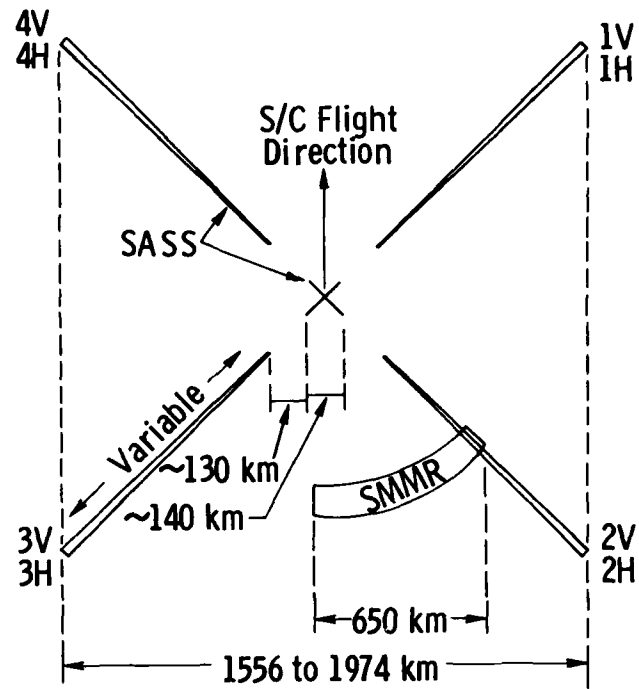


Fig.1 SEASAT-A SASS and SMMR instrument coverage

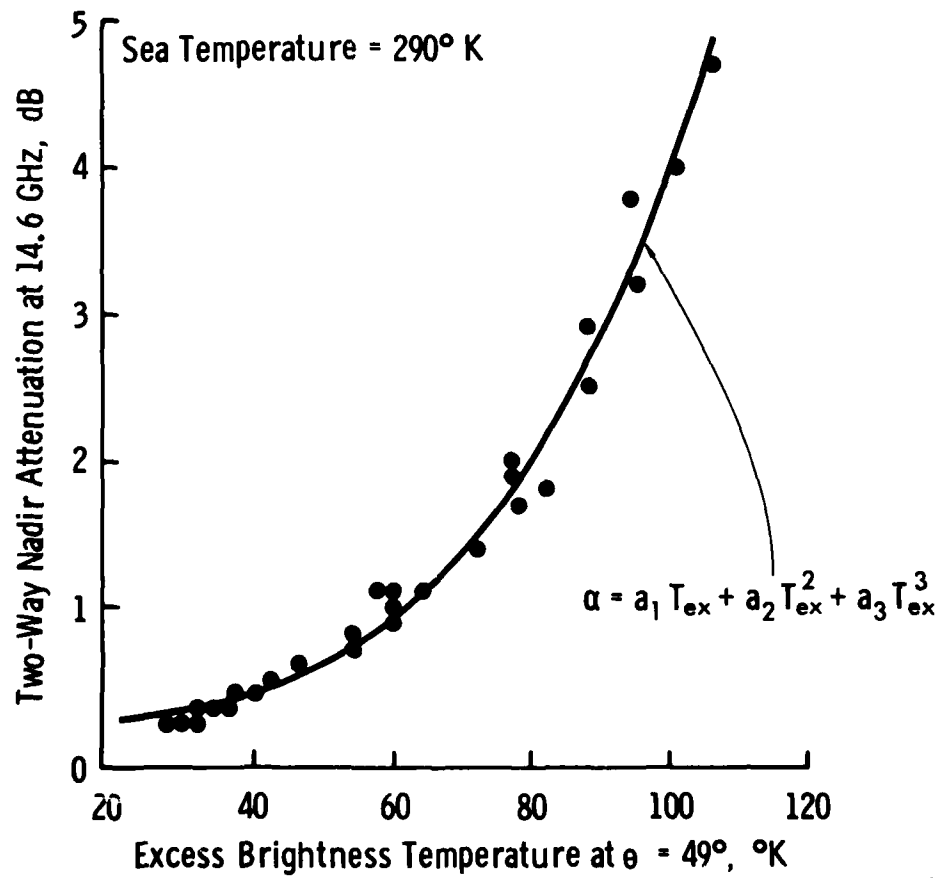


Fig.2 Two-way Nadir attenuation at 14.6 GHz vs. excess brightness temperature at  $18\text{ GHz}$

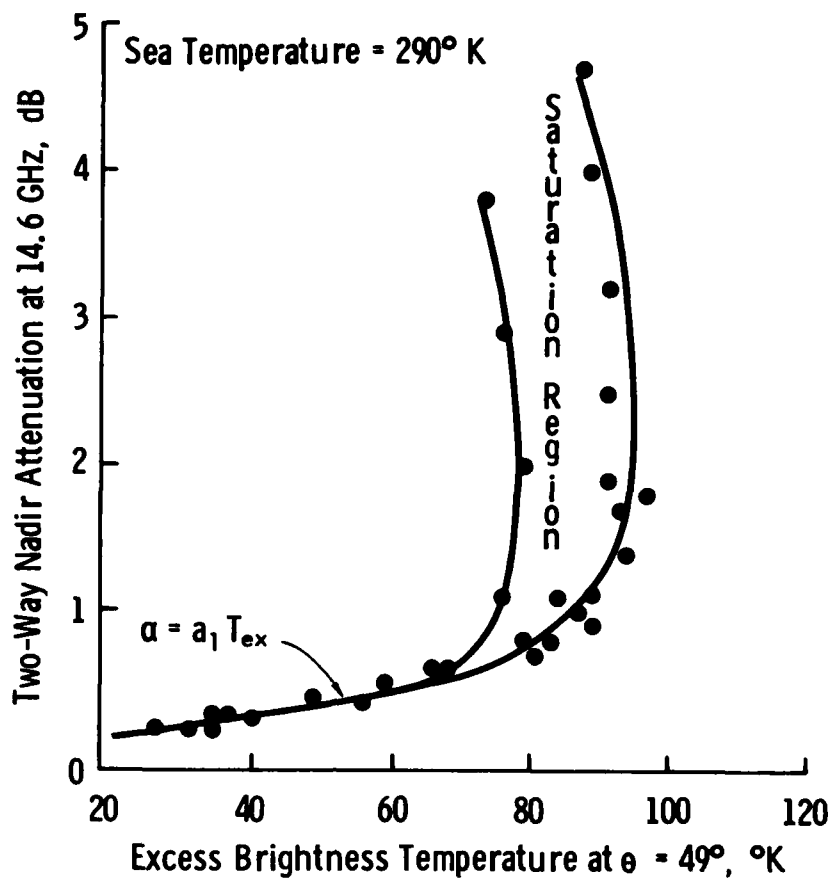


Fig.3 Two-way Nadir attenuation at 14.6 GHz vs. excess brightness temperature at 37 GHz

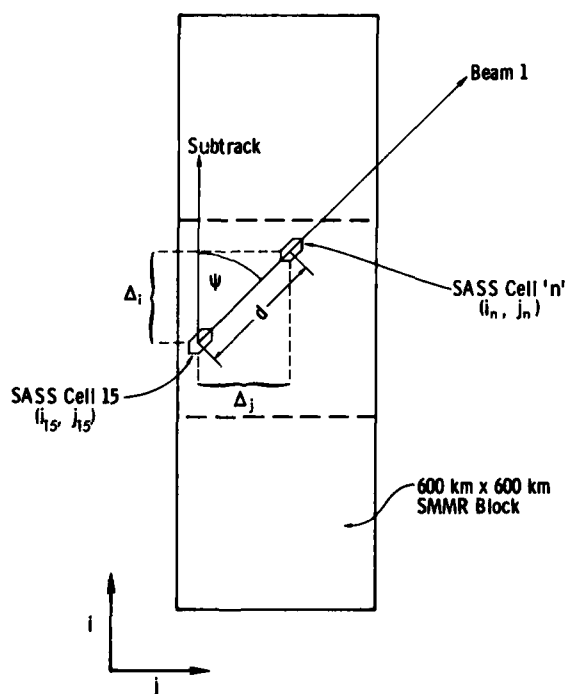


Fig.4 Illustration of SASS cell positioning in SMMR vector space

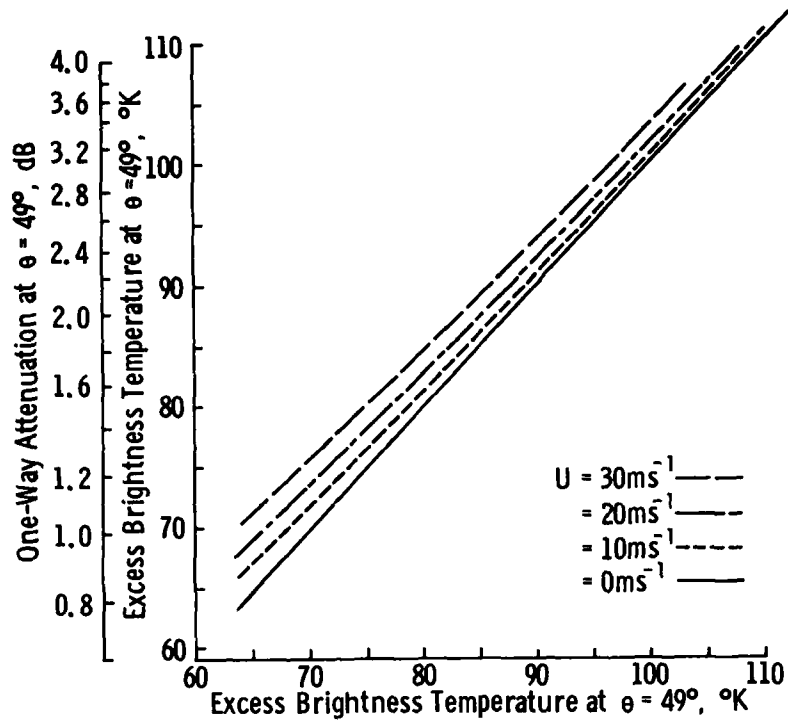


Fig.5 Error in attenuation and excess brightness temperature if  $0 \text{ ms}^{-1}$  surface is assumed

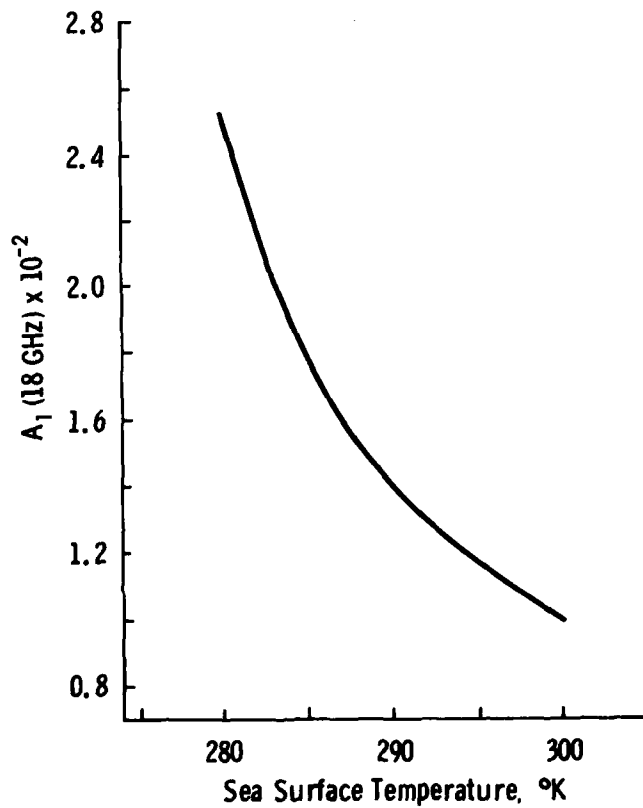
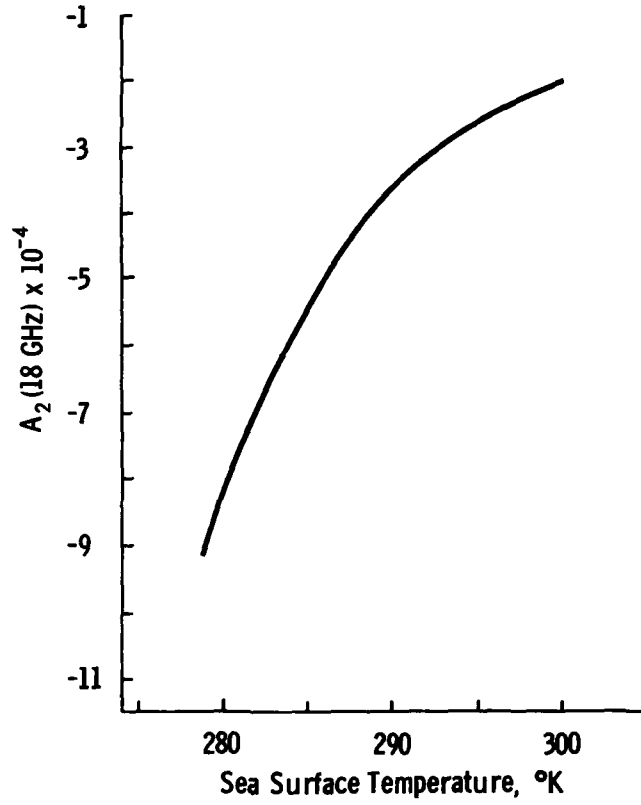
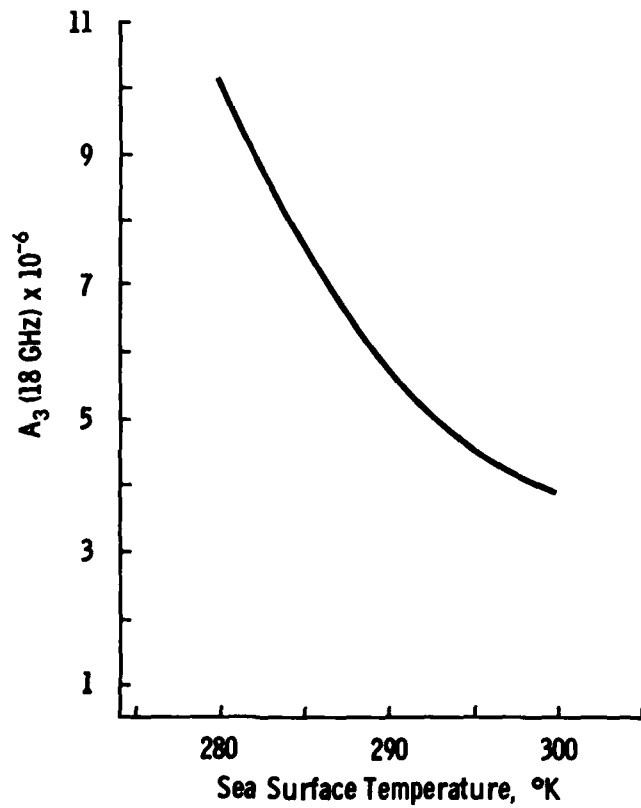


Fig.6 Temperature dependence of  $A_1$  coefficient for 18.0 GHz

Fig.7 Temperature dependence of  $A_2$  coefficient for 18.0 GHzFig.8 Temperature dependence of  $A_3$  coefficient for 18.0 GHz

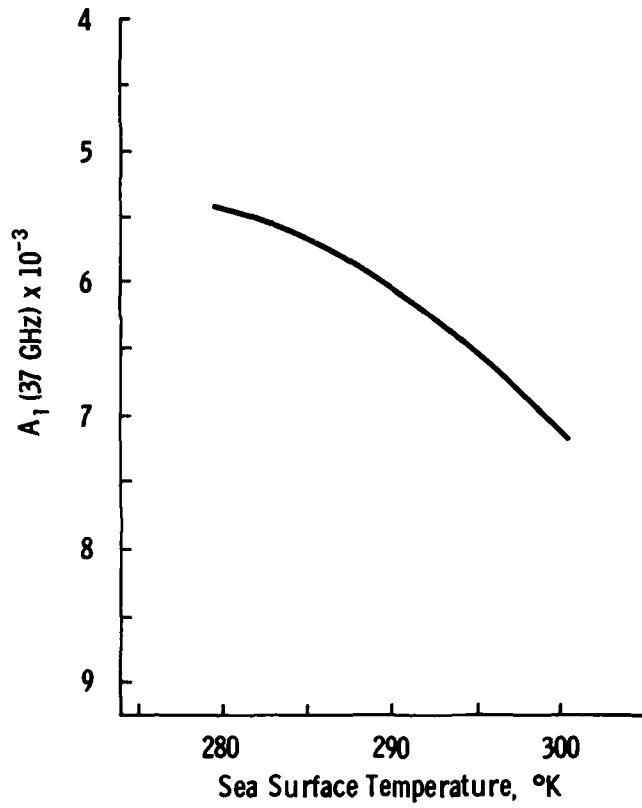


Fig.9 Temperature dependence of  $A_1$  coefficient for 37.0 GHz

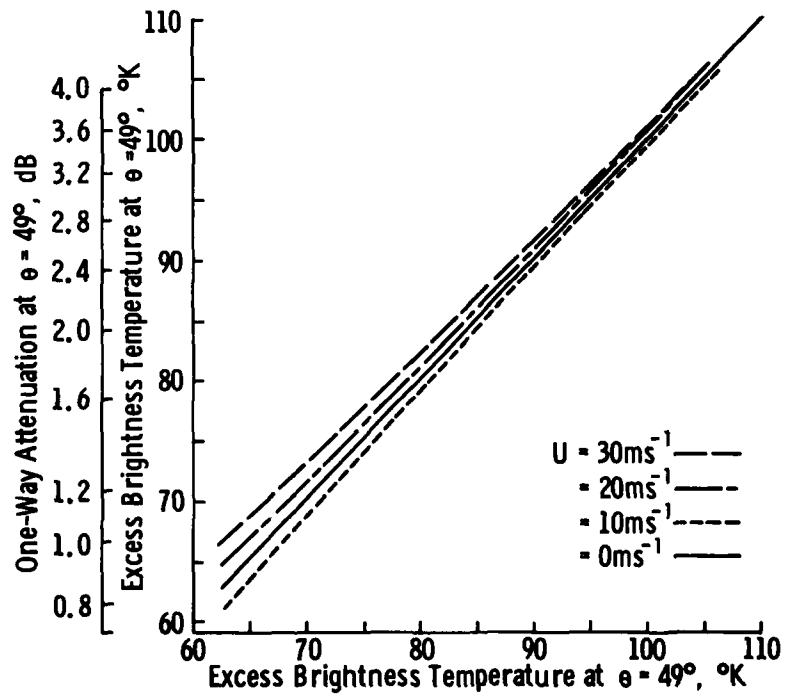


Fig.10 Error in attenuation and excess brightness temperature if 10 ms<sup>-1</sup> surface is assumed

The Effect of Turbidity on Remote Sensing  
of Ocean Color

G. Metzger, E. Raschke  
Institut für Geophysik und Meteorologie  
der Universität zu Köln, FRG

SUMMARY

Multispectral satellite measurements of the solar radiation reflected from the earth to space open the possibility to monitor the dynamics of phytoplankton but also the transport of various inorganic materials in the coastal zones of oceans. The quantitative interpretation of such measurements requires in particular an accurate correction for the atmospheric effects on the backscattered radiation, which even in clear and rather clean cases may completely diminish the weak signals of the radiation penetrating from the subsurface layers of the water up to space.

This paper describes a series of theoretical investigations of this problem with a one-dimensional radiative transfer model for the atmosphere-ocean system. This model consists of two components: a two-stream approximation for the ocean and an iterative radiance model for the atmosphere.

1. INTRODUCTION

The availability of multispectral satellite measurements of reflected solar radiation, such as those provided from the Nimbus 7 "Coastal Zone Colour Scanner (CZCS)" since October 1978, stimulate a variety of theoretical investigations for the quantitative interpretation of such data in terms of soil properties or the amount of particular organic and anorganic material suspended in the upper ocean layers. In principle, these informations can be obtained only if reliable methods are available to correct the multiple scattering of solar radiation in the atmosphere, primarily by aerosols. But also the specular reflection and the polarization of radiation at the sea surface needs to be taken into account.

Sturm (1979), Gordon (1977), Quenzel and Kästner (1978), Plass and Kattawar (1969) and many others began thorough investigations of this problem. The authors of this paper could begin with earlier work by Raschke (1971), who made multiple scattering calculations of non-polarized radiation in one-dimensional models of the atmosphere-ocean system.

2. THE METHOD

A retrieval method to derive quantitative data on the amount or concentration of plankton or other material in the subsurface layers of the oceans has not yet been developed. Unlike for remote sensing of stratospheric ozone with multiply scattered ultra violet radiation one has to consider here also the transfer of radiation through the rough air-water interface. Furthermore, calculations have shown, that there was no possibility to identify those layers contributing significantly to the upward radiation, as in the case of vertical temperature soundings from satellites.

Therefore the estimation of the concentration will primarily be used to link comparisons of measured with calculated radiances, where the results may carefully be tuned to in-situ measurements at various selected spots. Such control experiments have already been carried out in the Gulf of Mexico and the Mediterranean Sea. Our work is entirely based on model calculation.

The computational algorithm, developed for this purpose, consists of two parts. Since the field of upward scattered radiation underneath the air-water interface is almost isotropic (Fig.1, taken from (7)) it can be calculated easily with the time-saving two stream approximations, of which ours has been developed by Kerschgens et al. (4). Both models are coupled at the air-sea interface, whose reflection and transmission characteristics have been calculated for a Gaussian-distribution of the sea-surface slopes, as described analytically in dependence on the wind speed and direction by the Cox-Munk model (COX, C., MUNK, W., 1956). This coupling is illustrated in Fig.2, where all involved radiation fluxes are indicated schematically.

These calculations take into account multiple scattering by atmospheric molecules and aerosols and relevant parameters for ocean water and phytoplankton (JERLOV, N.G., 1968). Also the absorption by atmospheric ozone, water vapour and aerosols and the water and its hydrosols are taken into account (KERSCHGENS, M. et al., 1978).

3. RESULTS

All calculations shown here were made for a zenith angle of the sun of  $37,5^\circ$ . The spectrum between 0.3 and 0.76  $\mu\text{m}$  has been divided into 15 intervals to study the contribution of underlight in these spectral intervals for a refinement of a later evaluation

technique. Unlike in Gordon's technique, we consider simultaneous measurements in both, the blue region and the near infrared region, where almost no light from underneath the water surface can be measured from space, to contain more informations on the atmospheric aerosol content, than only measurements in one spectral range. These data will later be used to correct the atmospheric effects in all other simultaneous measurements in these spectral ranges containing informations on the water properties, i.e. where there is a significant contribution from the underlight. These are created in the spectral range between about 0.45 and 0.7  $\mu\text{m}$ , where water is most transparent for solar radiation. In Fig.3 are shown curves of the depth, where the solar spectrum is diminished to  $1/e$  of its incident value, i.e. the skin depth.

Several results of our calculations are shown in Figs 4 to 8. These are calculated radiances to be observed immediately above the ocean surface (Fig.4) and at the top of the atmosphere (Figs 5 to 8). In the latter case for better clearness one of the input parameters is constant. This is done for the two wave lengths,  $\lambda=0,45\mu\text{m}$  and  $\lambda=0,55\mu\text{m}$ , the optical depth of the atmosphere, and the chlorophyll content of the sea-water. For comparison also the radiance of the diffuse radiation is plotted, to demonstrate the overwhelming contribution of the sun's glint. We see, that over the ocean at the wave length of  $\lambda=0,55\mu\text{m}$  a strong signal can be observed due to the chlorophyll at all angular ranges outside the sun's glint. The scattering in the atmosphere reduces the relative contributions of the underlight. At the wave length of  $\lambda=0,45\mu\text{m}$  the radiances at the top of the atmosphere are mainly influenced by the turbidity of the atmosphere. Therefore this wave length might be good to correct satellite data from atmospheric signals. In our examples, we selected a rather turbid atmosphere with a mean turbidity of about 2.5 and 5 respectively. Due to pure molecular scattering the optical thickness at that wave length amounts to about 0.1. Further results computed for other wave lengths will be shown during the oral presentation.

#### 4. CONCLUSIVE REMARKS

Our calculations repeat the well-known effect, that ever flying aircraft can observe much stronger signals of the underlight, than satellites. However, careful selection of the spectral ranges for simultaneous multispectral measurements from space will provide adequate means to correct for the contribution of atmospheric scattering. The present and also future earthresources mission will provide enough data to check this hypothesis. Miller (private communication) has demonstrated this already with the data of the Nimbus 7 CZCS-data. If possible, in the oral presentation of this paper, we will show similar results, too.

#### 5. REFERENCES

- COX, C., MUNK, W., 1956, "Slopes of the Sea Surface deduced from Photographs of Sun glitter", Bulletin of the Scripps (1956), p. 401-488.
- GORDON, H.R., 1977, "A Possible Scheme for Correcting CZCS Imagery for Atmospheric Effects", paper submitted to the Nimbus 7, CZCS NET.
- JERLOV, N.G., 1968, "Optical Oceanography", Elsevier Publ. Comp. Amsterdam-London-New York.
- KERSCHGENS, M. et al., 1978, (4) "A modified two-stream approximation for computations of the solar radiation budget in a cloudy atmosphere", Tellus 30, 1978, p. 418-429.
- PLASS, G.H., KATTAWAR, G.W., 1969, "Radiative Transfer in an Atmosphere-Ocean System", Appl. Optics 8, p. 455-466.
- QUENZEL, H., KÄSTNER, M., 1978, "Remote Sensing of Chlorophyll in the Ocean: Masking Effects of the Atmosphere", EEG Contract No. 798-77-10 SISP D, Universität München, Meteorologisches Institut.
- RASCHKE, E., 1971, (7) "Berechnung des durch Mehrfachstreuung entstehenden Feldes solarer Strahlung in einem System Ozean-Atmosphäre", Abt. f. Phys. u. Astr. d. Ruhr-Universität Bochum, BMBW-FB 71-20.
- STURM, E., 1979, "Biological Applications Including Pollution Monitoring", paper presented at the EURASEP-WORKSHOP in ISPRA 1979, Joint Research Centre, Ispra-Establishment, Italy.



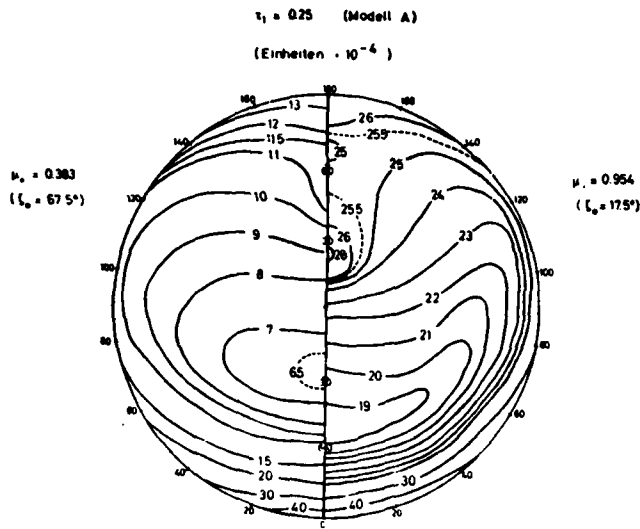


Fig.1 : Diffuse underlight below the water surface at two different Sun's zenith distances.

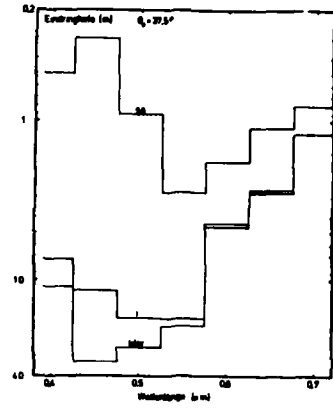


Fig.3 : The spectral e-folding depth of radiance ( see text ).

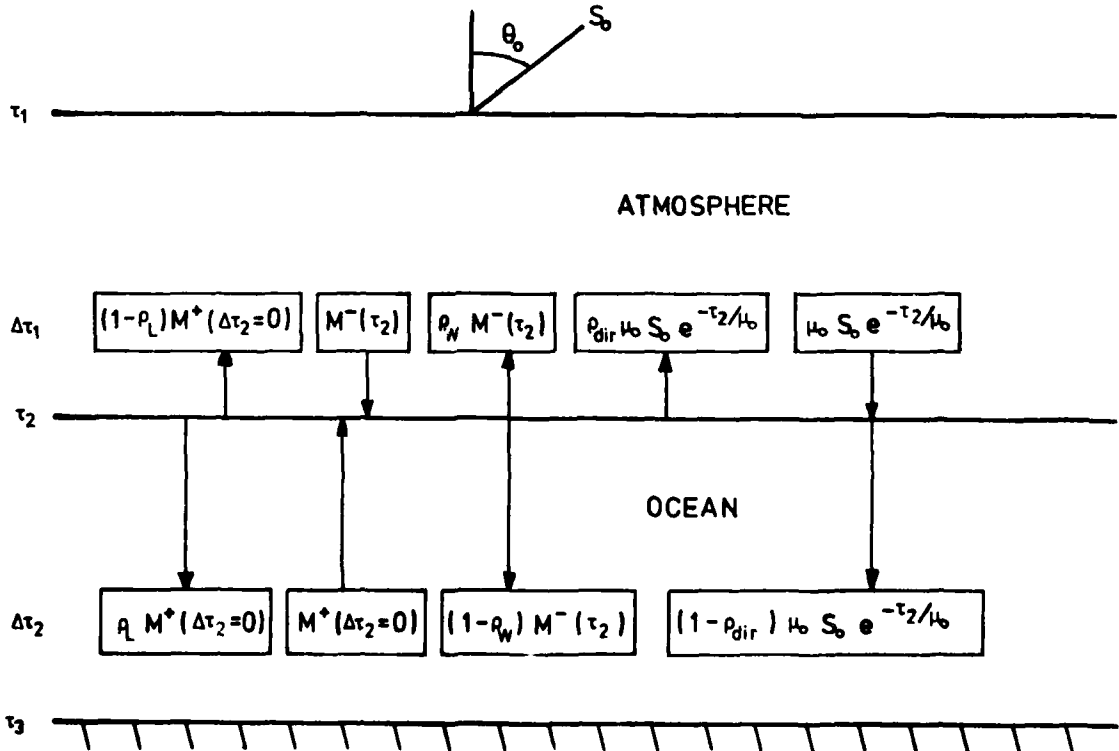


Fig.2 :

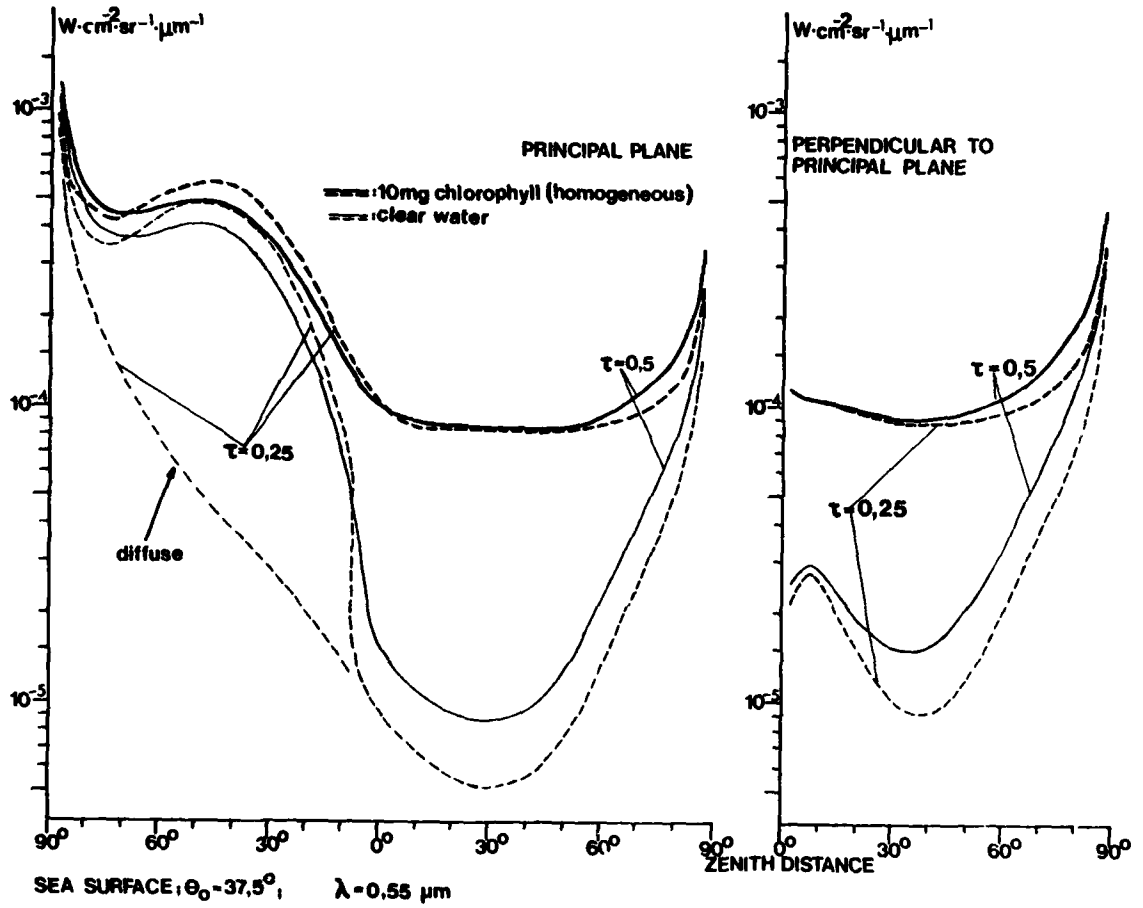


Fig. 4 :

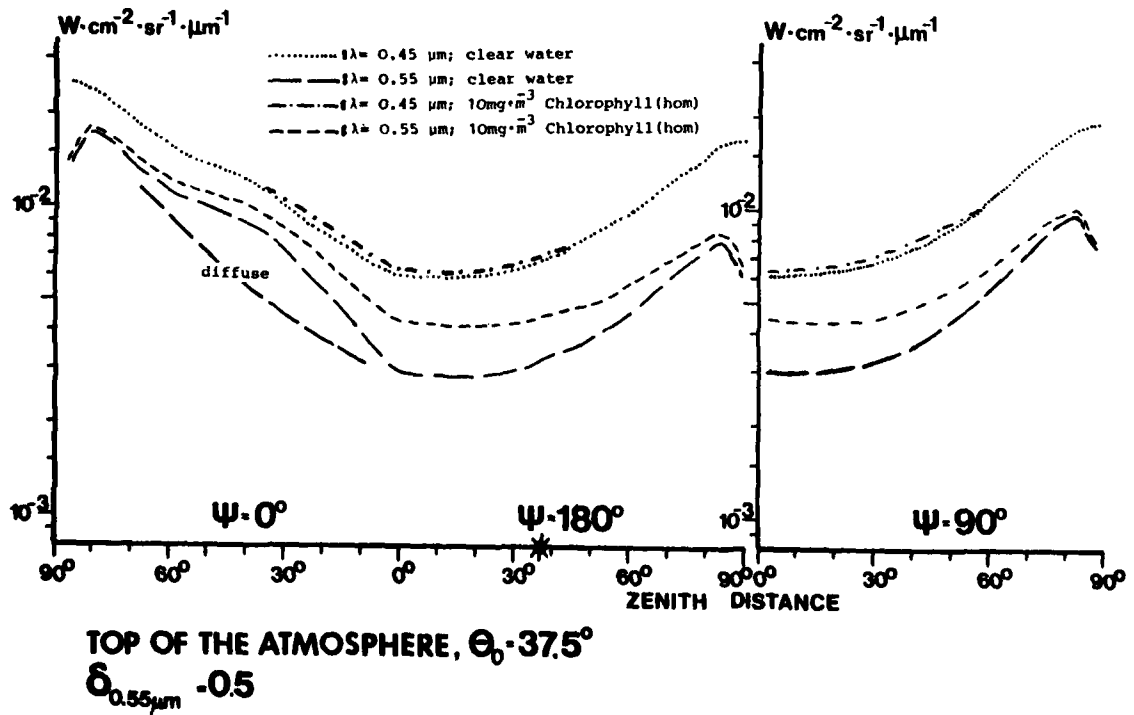
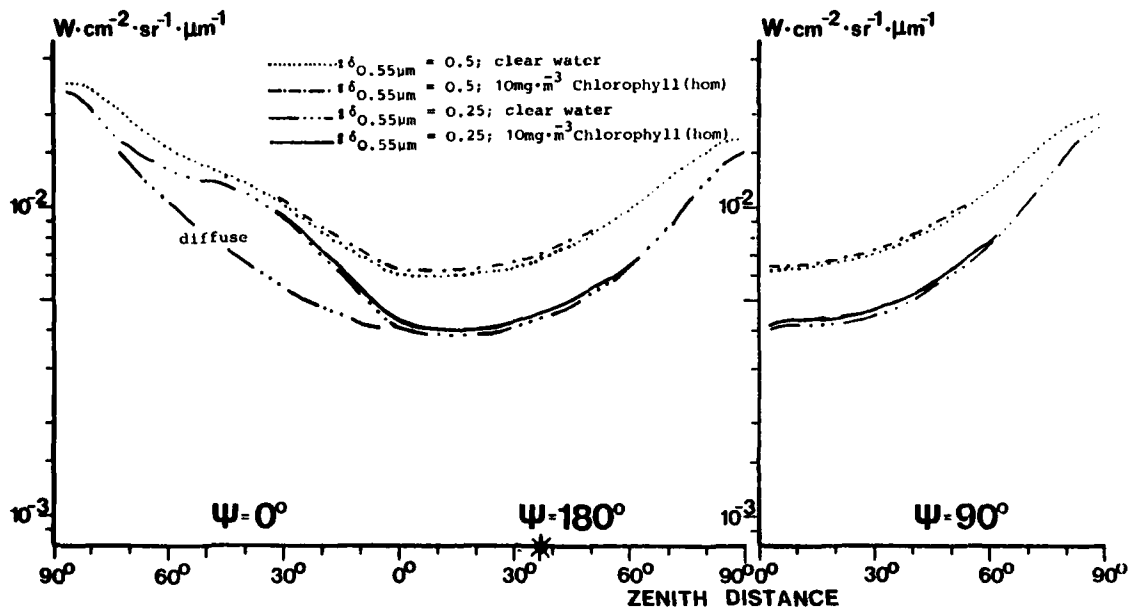
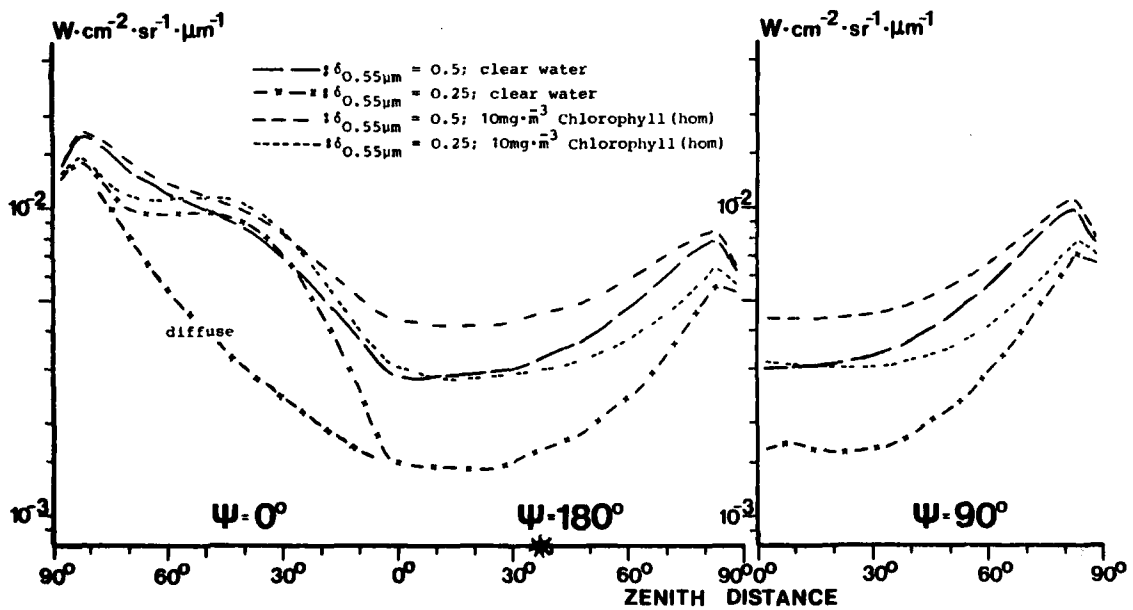


Fig. 5 :



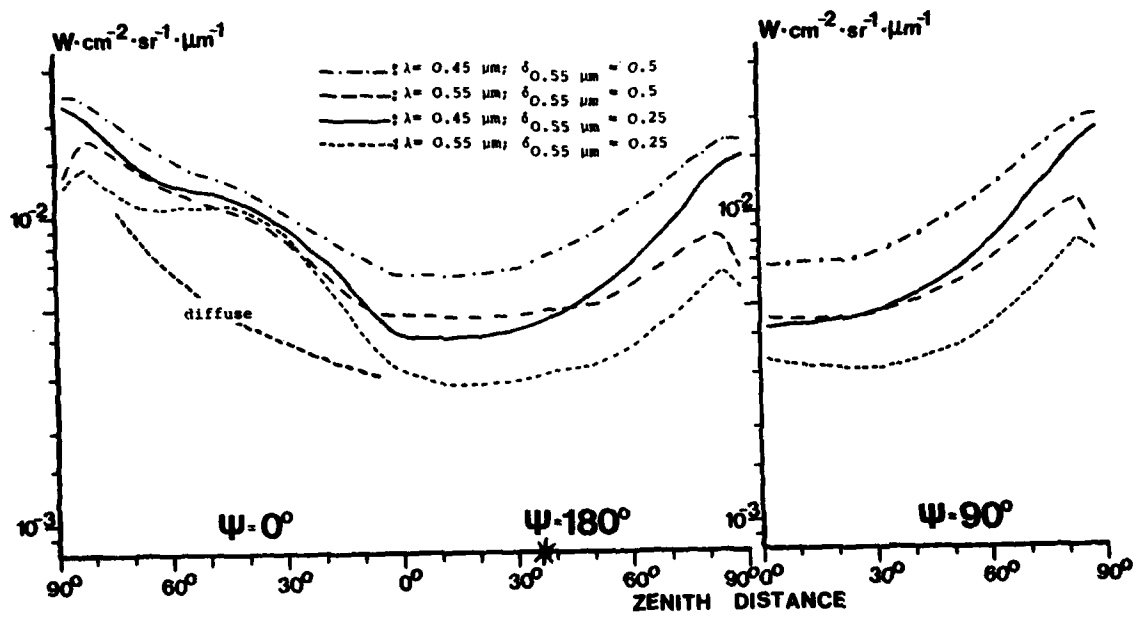
TOP OF THE ATMOSPHERE,  $\Theta_0 = 37.5^\circ$   
 $\lambda = 0.45\mu\text{m}$

Fig. 6 :



TOP OF THE ATMOSPHERE,  $\Theta_0 = 37.5^\circ$   
 $\lambda = 0.55\mu\text{m}$

Fig. 7 :



TOP OF THE ATMOSPHERE,  $\Theta_0 = 37.5^\circ$   
 10mg·m<sup>-3</sup> Chlorophyll (homogeneous)

Fig. 8 :

## SUMMARY OF SESSION IV – GENERAL IONOSPHERIC DISPERSION EFFECTS

by H. Soicher (Session Chairman)

The papers in this session dealt with the dispersive nature of the ionosphere and with its effects on transionospheric propagation. In particular, most papers dealt with the measurements and propagation effects of the total integrated electron content of the ionosphere (TEC) and derived parameters.

**K. Davies** presented results of observations utilizing the beacon sources of the ATS 6 synchronous satellite. Measurements of the total columnar electron content, and the plasmaspheric electron content indicate diurnal, seasonal, latitudinal, solar-cycle, and solar disturbance variability. Maps of electron content also show troughs, ridges, holes, and other irregularities with dimensions from thousands of kilometers to around 100 meters. The propagation effects of such irregularities, as well as their properties, were also discussed.

**L. Kersley** discussed an empirical model of ionospheric slab thickness which is defined as the ratio of TEC to the maximum ionospheric electron concentration. The rationale behind modelling such a quantity is the wide availability and ease of measurement of the maximum concentration (or equivalently, the ionospheric critical frequency) and the application of such a data base to the estimation of the transionospheric time delay (or equivalently the total electron content, TEC). It was shown that the modelled values represent the monthly mean values to within one standard deviation of the individual daily values in most circumstances.

The paper by **E. Bahar** and **B. S. Agrawal** was summarized by **C. L. Rino**. The paper investigated the distortion and depolarization of a 1.5 GHz transient signal as it propagates through the dispersive, inhomogeneous and anisotropic ionospheric medium using the full-wave approach.

**G. H. Millman** and **K. A. Olsen** discussed the propagation effects imposed by the dispersive ionosphere on wideband pulses. The distortion of the pulse amplitude, envelope, pulse length, modulation and phase was examined in terms of various values of TEC along the transmission path and for given signal characteristics.

**E. M. Poulter** and **J. K. Hargreaves** used ionospheric data obtained by the beacon emissions of the ATS 6 satellite to obtain empirical description of the total ionospheric and plasmaspheric electron contents, the slab thickness (defined above) and the shape factor (which is defined in the text).

Harmonic analysis applied to the data provides a description of the median behavior. The daily coefficients vary in a well defined manner enabling a description in terms of annual and semi-annual variations, thus enabling TEC data reconstruction with a typical r.m.s. deviation of one-half TEC units ( $\sim 10-15\%$  of daytime TEC values).

## RADIO BEACON STUDIES OF IONOSPHERIC IRREGULARITIES

by

Kenneth Davies

Space Environment Laboratory  
 NOAA Environmental Research Laboratories  
 Boulder, Colorado 80303

SUMMARY

We discuss satellite beacon observations of ionospheric irregularities with dimensions ranging from thousands of kilometers to around 100 meters. These observations were made using the beacon on board the ATS6 synchronous satellite from which one can obtain the total columnar electron content ( $N_T$ ) and the plasmaspheric columnar electron content ( $N_P$ ). It is found that the European values of  $N_T$  and  $N_P$  are larger than those over the USA. During winter days  $N_P$  has a peak near noon in Europe while over the USA the peak is near 0300 LT. Maps of electron content, obtained by combination of signals from synchronous and polar orbiting satellites show troughs, ridges, holes, etc. in the content structure. Such maps are of use in making corrections for ionospheric refraction. Traveling ionospheric disturbances made in the USA and in India show different directions of travel. Small scale irregularities give rise to radio scintillations which obey an  $f^{-n}$  law where  $f$  is radio frequency. In general  $n$  is near unity but on occasions it can be negative. Multi-frequency observations of Fresnel-type fading by intense irregularities have been used to determine some properties of the irregularities.

1. INTRODUCTION

Satellite radio beacons offer a particularly simple method of monitoring the general state of the ionosphere with high-time resolution. In this paper we shall first consider the general role of radio beacons in ionospheric research and monitoring and then discuss how amplitude scintillation (or fading) can be used to learn something about the physical structure of narrow isolated plasma irregularities in the ionosphere.

Satellite beacon contributions to studies of the structure of the ionosphere have been reviewed recently by Evans (1977) who has pointed out that since the launch of Sputnik I in 1957 satellite beacons have been used for research in two areas: (1) total electron content, (2) small-scale irregularities. Total electron content here means the integral of the electron density along the radio ray path from satellite to receiver. The earliest observations were on moon echoes which showed long period fading due to (Faraday) rotation of the electric vector of the radio wave. These observations showed that about 3/4 of the total content lay above the height of maximum of F2 density.

The earliest beacons were on relatively low orbiting satellites, e.g. Sputnik; these provided information on the horizontal distribution of Faraday content because the speed of the satellite was much larger than movements of the ionosphere. A survey of ionospheric effects on earth-space radio propagation has been published by Lawrence, Little and Chivers (1964) in which they derived the frequency dependence and orders of magnitude of radio effects on frequencies well above the penetration frequency of the ionosphere. These effects included: phase change, group path or time delay, refraction, Doppler shift, polarization rotation and absorption. The early beacon measurements had the advantage that Faraday rotation was relatively easy to measure and, since the beacon was often provided by a telemetry channel, no special transmitters were required. Since the rotation is directly proportional to the component  $B_L$  of the field along the ray path, the conversion of Faraday rotation to Faraday or ionospheric content was hampered by the movement of the ray path with respect to the geomagnetic field. Other difficulties arose from horizontal gradients, from the necessity to track the beacon and having to estimate the integral number of half-rotations along the closest path.

The relative advantages of synchronous satellites (period = 1 day) were quickly recognized (Garriott and Little, 1960). The main advantage is that the satellite's position is fixed relative to an observer; this eliminates the necessity of tracking and insures a constant angle between ray path and the geomagnetic field. Thus a synchronous beacon enables measurements at fixed geographical and geomagnetic configurations with high time resolution.

However, the Faraday rotation  $\Omega$  is proportional to the integral along the ray path of  $NB_L$  where  $N$  is electron density. Various workers (Yeh and Gonzales, 1960; Titheridge, 1972)<sup>L</sup> have shown that for a given ray path and geomagnetic field model it is possible to express the relation between  $\Omega$  and Faraday content  $N_F$  in the following form:

$$\Omega = 1.35 \times 10^6 \bar{B}_L N_F$$

where  $\bar{B}_L$  is a suitably weighted average of  $B_L$  along the ray path and is determined by averaging values for a number of electron density profiles and an appropriate model of

the geomagnetic field, i.e. averaged in space and time. Since the value of  $\bar{B}_T$  for a given ray path geometry depends on the electron density profile it will vary with time of day, season, sunspot number, etc., so that some error is present in  $N_F$  or, from an alternative point of view, the height  $h_F$ , to which  $N_F$  is the electron content, is in error. On the average, however, these errors are relatively small ( $\sim 5\%$ ).

The difficulty of accurately determining  $N_F$  was recognized early in beacon studies and an alternative method was suggested that depended on the relative phase change between two (or more) harmonically related and coherent radio signals (Evans, 1977). This is independent of the geomagnetic field and gives directly the total electron content  $N_T$  along the entire ray path. A slight modification of this technique (e.g., Davies et al., 1975) uses two closely spaced frequencies such as is used on the ATS6 radio beacon.

The difference between the total and Faraday contents

$$N_P = N_T - N_F \quad (2)$$

is the plasmaspheric content between a height of about 2000 km and the satellite. The other measurement of value is the received signal strength the fluctuations of which often reveal the presence of plasma blobs, i.e. radio lenses, in the ionosphere.

We shall proceed to discuss some aspects of ionospheric structure, as revealed by satellite beacon techniques, starting with large scale sizes ( $> 1000$  km), through medium scale traveling ionospheric disturbances ( $\sim 100$  km) to small ( $< 1$  km) irregularities. For illustration of these phenomena we shall consider observations made with the ATS6 geostationary radio beacon which is the first beacon to be designed specifically for the simultaneous measurement of total content and Faraday content.

## 2. LARGE SCALE DIFFERENCES

The ATS6 radio beacon, which has operated since July 1974 (A) at  $94^\circ\text{W}$  from June 1974 to May 1975, (B) at  $35^\circ\text{E}$  from September 1975 through July 1976 and (C) at  $140^\circ\text{W}$  from late 1976 to the present (see Figure 1) has enabled the continuous measurement of the absolute total and Faraday contents. Comparison of total contents in America (1974-1975) and in Europe (1975-1976) show intercontinental differences (e.g., Kersley and Klobuchar, 1978) as seen in Figure 2. At Boulder both noon and midnight  $N_T$  are larger in winter than in summer which contrasts with the Aberystwyth, Wales, values (Kersley et al., 1977) which are smaller in winter. The midnight values at Aberystwyth are, on the average, about twice those at Boulder of which only about 1.5 is caused by the greater obliquity of the Aberystwyth path. This greater content at Aberystwyth is in spite of the larger solar zenith angle there and the smaller sunspot numbers, i.e., the difference does not appear to be a temporal one.

The noon plasmaspheric content  $N_p$  over North America is about half that in Europe, (Figure 3) although the radio paths above 2000 km differ by only about 3%. Furthermore, while there is relatively little seasonal variation in noon  $N_p$  at Boulder, there is a marked seasonal change at Aberystwyth.

Turning to diurnal variations of  $N_T$  and  $N_F$ , we find that while they are similar in the American and European sectors there is a marked difference in the diurnal variations of  $N_p$  in the winter as shown in Figure 4. Whereas in Aberystwyth the peak occurs during the day, in Boulder the peak occurs in the middle of the night ( $\sim 03$  LT). Kersley and Klobuchar (1978) have suggested that the difference is caused by a combination of plasma fluxes from the conjugate and local ionospheres. Although the ATS6-Aberystwyth path terminates in a higher geographical latitude than does the Boulder path, the geomagnetic configurations are reversed, as depicted in Figure 5; the Aberystwyth path penetrates to a magnetic L shell of about 1.7 compared with about 2 for the Boulder path. The night peak in  $N_p$  at Boulder occurs about the same time as  $N_m F_2$  in the conjugate F2 region attains its diurnal maximum.

Latitudinal and longitudinal differences in  $N_F$  in the two sectors have been pointed out by Soicher (1976) who has compared values at São Paulo, Brazil; Fort Monmouth, New Jersey and Richmond, Florida during May 1975 and February 1975 as shown in Figure 6. The day vertical content is much higher in equatorial regions than in middle latitudes which shows the importance of the equatorial anomaly, i.e., peaks in  $N_m F_2$  on both sides of the equator. The small content at Kiruna compared with that at Haifa is caused partly by differences in solar zenith angles and partly by the passage of the Kiruna path through a midlatitude trough.

## 3. INTRA-CONTINENTAL IRREGULARITIES

Contour maps of Faraday content have been constructed from orbiting beacons by several workers (e.g., Bertin and Papet-Lepine, 1970; Liska, 1967). An example in Figure 7, shows night minima near  $50^\circ$  geographic latitude. Leitinger (see Davies, Hartmann and Leitinger, 1977) has constructed contour maps by combination of polar orbiting NNSS beacons (that give good latitudinal resolution) with a synchronous beacon (ATS6) and one of his maps (Fig. 8) shows large scale features such as troughs or holes and ridges in the content structure. These maps are of use to radio astronomers who need to allow for refraction of signals from radio stars.

#### 4. TRAVELING IONOSPHERIC DISTURBANCES

Synchronous beacons provide a very convenient method of studying traveling disturbances by measuring the time differences seen at spaced receivers (see Davis and da Rosa, 1969). The technique preferentially selects disturbances moving in certain directions so the results tend to be biased in respect to azimuth of propagation. Nevertheless, the observations confirm that during magnetic disturbances, large traveling waves move to lower latitudes from the auroral oval.

Observations near Boulder over a triangle with sides about 125 km sometimes showed good correlation which indicated the presence of a single wave. More often, however, the correlation was not good at all three receivers (even when it was high at two of them) and this is taken to indicate that more than one wave was present. Two winter night maxima at Boulder were found to move roughly from east to west with speeds near  $70 \text{ m s}^{-1}$ . To measure the horizontal velocities of TIDs at Boulder, Davies, Degenhardt, Hartmann and Leitinger (1977) filtered the Faraday data and from the resulting cross correlations derived the velocities shown in Figure 9. Somewhat similar measurements in India using the ATS6 beacon Lakha Singh et al. (1977) have measured drift velocities and they find that the directions of travel of isolated irregularities are quite different from those in the U.S.A., for while at Boulder the TIDs travelled predominantly towards the south-east, in India no daytime velocities were in this direction.

#### 5. SMALL SCALE IRREGULARITIES OR LENSES

##### 5.1 Scintillations

The term scintillation is normally used to describe irregular fluctuations in the amplitude (and sometimes the phase) of radio signals. They are caused by the motion over the ground of an irregular (diffraction) pattern produced by interference of waves refracted and diffracted by the blobs or holes in the ionospheric plasma with sizes of the order of 1 km (Ratcliffe, 1956). When the phase change suffered by a wave in traversing an irregularity is smaller than about one radian the diffraction pattern on the ground has a one-to-one relationship with irregularities in the ionosphere, e.g., three blobs of plasma in the ionosphere produce three minima in signal amplitude on the ground. The theory underlying this case is referred to as "thin screen" or "weak scatter" and, because the interpretation is relatively straightforward, experimental records are often interpreted on this basis. When the phase change in the diffracting screen is many radians the situation is different and, as will be shown later, a single ionospheric irregularity can produce a number of maxima and minima on the ground. Thus, in the absence of information on the type of scintillation, i.e., thin screen or thick screen (also called multiple scatter), an observer would interpret the data as indicating the presence of a patch containing a number of small, weak irregularities when in reality there is only one.

In the case of weak scintillations the scintillation index (i.e., depth of scintillation) decreases with increasing frequency ( $\propto f^{-n}$ , where  $n \sim 1$ ). As the scintillations become stronger  $n$  decreases in magnitude and under some circumstances changes sign so that the scintillation depth increases with increase of frequency (Rastogi et al., 1977). Scintillation theory is discussed by Yeh et al. (1975).

##### 5.2 Lenses in the Ionosphere

Scintillation is often considered in statistical terms, e.g., scintillation index (rms value), frequency exponent, spectral slope, etc. We shall now consider the case of individual events and use them to infer some physical properties of the causative irregularity in the ionosphere. Consider, for example, the rather extreme case depicted in Figure 10 where the amplitude fading has a deep central minimum and Fresnel-type fading that increases in frequency away from the center (Basu et al., 1976; Davies and Whitehead, 1977; Elkins and Slack, 1969; Heron, 1976). The amplitude of the fading pattern usually decreases away from the center, however, when the lens is sufficiently strong, there is a modulation of the fading envelope as seen in Figure 10, note also the subsidiary maximum in the central minimum.

A model to explain these events has been advanced by Heron (1976) and by Davies and Whitehead (1977) in terms of isolated dense cylinders of plasma with gaussian radial distributions of electron density and widths of the order of a few hundreds of meters. The relevant geometry is given in Figure 11. When the lens is weak there is slight defocusing at the center of the pattern giving a single minimum (Fig. 11a) but there is no strong interference at the ground between a direct and refracted ray as occurs with a relatively strong lens (Fig. 11b). With a sufficiently strong lens there is interference between three rays that produces the envelope modulation. Titheridge (1971) has shown that for a given irregularity the depth of fading is largest when the radio frequency is such that the situation in Figure 11b holds. The frequency of maximum fading is near  $0.6 f_T$  where  $f_T$  is a frequency, for a given irregularity, above which geometrical optics are applicable and below which physical optics (interference) must be used (Heron, 1979).

A remarkable feature of these diffraction patterns is that the width of the central minimum is much greater than the width of the gaussian lens. For example, in the case cited by Davies and Whitehead (1977) the half width of the lens is about 100 m (if the lens is in the E region) while the corresponding size of the ground diffraction pattern



to the first maximum is 1100 m. The transition frequency for this irregularity is 1064 MHz at which the phase change through the center of the lens is 5.3 radians (Heron, 1978).

For a given isolated cylindrical lens the diffraction patterns on the ground for four different frequencies are presented in Figure 12. The deepest amplitude fading is on 62.5 MHz whereas  $f_T = 104$  MHz and the frequency variation of the scintillation index is as shown in Figure 13.

One can see from Figure 12 that with observations on a single frequency (say 30 MHz) one might conclude, on the basis of a thin screen model, that the pattern was generated by a large number of ionospheric irregularities. It could be argued that no astute observer would be deceived by these characteristic patterns. This may well be so, but can an average observer looking at one of the patterns in Figure 14 detect that it is produced by three quite similar irregularities juxtaposed with axes parallel at 400 km as shown in Figure 15? Identification is rendered more difficult because in practice the diffraction patterns are quite asymmetric. The mean value ( $\bar{f}$ ) of  $f_T$  for this configuration of 3 lenses is 97 MHz and the frequency variation of the  $S_4$  scintillation index is given in Figure 16; it has a peak in scintillation near 75 MHz which is  $0.77 \bar{f}_T$ . On frequencies below 50 MHz the pattern on the ground spreads out, the scintillation becomes faster and shallower, and all resemblance to the causative structure is lost. On frequencies above 97 MHz the diffraction pattern bears a simple correspondence to the ionosphere structure, i.e., each deep fade corresponds to a local electron density enhancement in the ionosphere. An important point to notice in Figure 16 is that, for a range of frequencies below about 75 MHz, the scintillation depth increases with increase of frequency, which is the reverse of the frequency dependence for weak scintillations. Such a frequency dependence has been observed by Rastogi et al. (1977) and by Crane (1976). The latter found on several occasions an increase in received spectral power density above 10 Hz that require ionospheric irregularities in the scale size range from 200 to 700 m be more dense than given by a monotonic power law.

## 6. CONCLUSION

In this talk I have tried to illustrate, by a few examples, the ways in which satellite radio beacons have been used in recent years to study ionospheric irregularities. The technique, although providing only data integrated along the path, is one of very few that can provide continuous data with high time resolution on such phenomena as plasmasphere and ionosphere content and effects of solar-geomagnetic disturbances.

The use of multifrequency observations is very important in the interpretation of data, especially those concerned with scintillation by small intense irregularities.

## 7. REFERENCES

- Basu, S., B. K. Guhathakurte, G. N. Bhattacharyya and A. Das Gupta (1976), VHF scintillation observations at Calcutta with orbiting and geostationary satellites, The Geophysical Use of Satellite Beacon Observations, 295-300, ed. M. Mendillo, Boston University.
- Bertin, F. and J. Papet-Lepine (1970), Latitudinal variation of total electron content in the winter at middle latitudes, *Radio Sci.*, 5, (6), 899-906.
- Crane, R. K. (1976), Spectra of ionospheric scintillation, *J. Geophys. Res.*, 81, (13), 2041-2050.
- Davies, K., W. Degenhardt, G. K. Hartmann and R. Leitinger (1977), Electron content measurements over the U.S., Joint Radio Beacon Program, NOAA/MPAE/Graz, Max-Planck-Institute for Aeronomy, Lindau, Germany.
- Davies, K., R. B. Fritz, R. N. Grubb and J. E. Jones (1975a), Some early results from the ATS6 radio beacon experiment, *Radio Sci.*, 10, (8 and 9), 785-799.
- Davies, K., G. K. Hartmann and R. Leitinger (1977), A comparison of several methods of estimating the columnar electron content of the plasmasphere, *J. Atmos. Terr. Phys.*, 39, 571-580.
- Davies, K. and J. D. Whitehead (1977), A radio lens in the ionosphere, *J. Atmos. Terr. Phys.*, 39, 383-387.
- Davis, M. J. and A. V. da Rosa (1969), Traveling ionospheric disturbances originating in the auroral oval during polar substorms, *J. Geophys. Res.*, 74, 5721-5735.
- Elkins, T. J. and F. F. Slack (1969), Observations of travelling ionospheric disturbances using stationary satellites, *J. Atmos. Terr. Phys.*, 31, 421-439.
- Evans, J. V. (1977), Satellite beacon contributions to studies of the structure of the ionosphere, *Rev. Geophys. Space Phys.*, 15, (3), 325-350.

- Garriott, O. K. and C. G. Little (1960), The use of geostationary satellites for the study of ionospheric electron content and ionospheric radio-wave propagation, *J. Geophys. Res.*, 65, (7), 2025-2027.
- Heron, M. L. (1976), On the modelling of ionospheric irregularities from Fresnel diffraction patterns, *J. Atmos. Terr. Phys.*, 38, 1027-1031.
- Heron, M. L. (1979), Diffraction from discrete and homogeneously structured ionospheric irregularities, *Radio Sci.*, 14, (1), 97-102.
- Kersley, L., H. Hajeb-Hosseini and K. J. Edwards (1977), ATS-6 observations of ionospheric/protonospheric electron content and flux, University of Wales, Aberystwyth.
- Kersley, L. and J. A. Klobuchar (1978), Comparison of protonospheric electron content measurements from the American and European sectors, *Geophys. Res. Letters*, 5, (2), 123-135.
- Lakha Singh, P. N. Vijayakumar, S. C. Garg, T. R. Tyagi, R. K. Bhardwaj, R. S. Dabas, O. P. Nagpal and A. Sen Gupta (1977), Study of large and medium scale irregularities using 140 MHz ATS-6 Faraday rotation records from three stations, *Indian J. Radio Space Phys.*, 6, (3), 245-249.
- Lawrence, R. S., C. G. Little and H. J. A. Chivers (1964), A survey of ionospheric effects upon earth-space radio propagation, *Proc. IEEE*, 52, (1), 4-27.
- Liska, L. (1967), The high-latitude trough in the ionospheric electron content, *J. Atmos. Terr. Phys.*, 29, (10), 1243-1259.
- Rastogi, R. G., M. R. Deshpande, Hari Om Vats, K. Davies, R. N. Grubb and J. E. Jones (1977a), Amplitude scintillations of ATS6 radio beacon signals within the equatorial electrojet region (Ootacamund, dip 4°N), *Pramana*, 8, (1), 1-13.
- Ratcliffe, J. A. (1956), Some aspects of diffraction theory and their application to the ionosphere, *Reports on Progress in Physics*, Vol. XIX, 188-267, ed. A. C. Stickland, London, The Physical Society.
- Titheridge, J. E. (1971), The diffraction of satellite signals by isolated ionospheric irregularities, *J. Atmos. Terr. Phys.*, 33, (1), 47-69.
- Titheridge, J. E. (1972), Determination of ionospheric electron content from the Faraday rotation of geostationary satellite signals, *Planet. Space Sci.*, 20, 353-369.
- Soicher, H. (1976), Comparative ionospheric and plasmaspheric electron contents from three world regions, *Nature*, 264, 46-48.
- Yeh, K. C., C. H. Liu and M. Y. Youakim (1975), A theoretical study of the ionospheric scintillation behavior caused by multiple scattering, *Radio Sci.*, 10, 97-106.

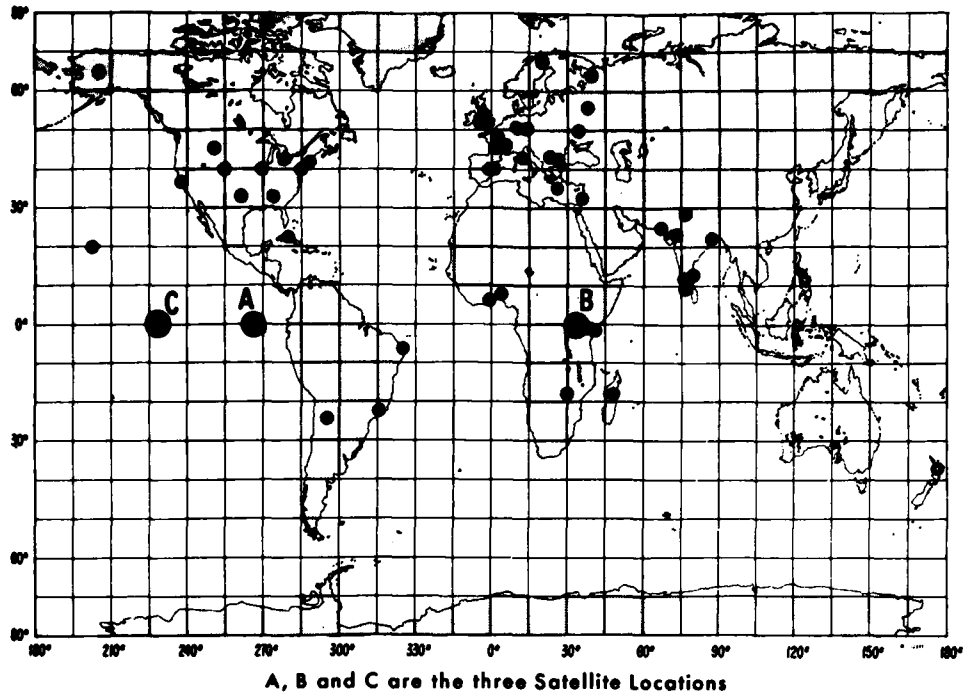


Fig. 1 Map showing ATS6 beacon and receiver locations.

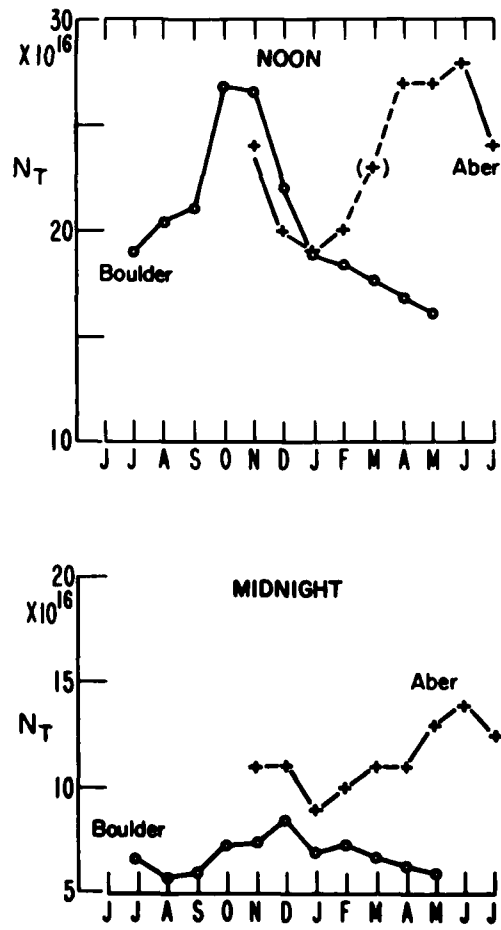


Fig. 2 Monthly medians of slant total content ATS6 to Boulder and ATS6 to Aberystwyth.

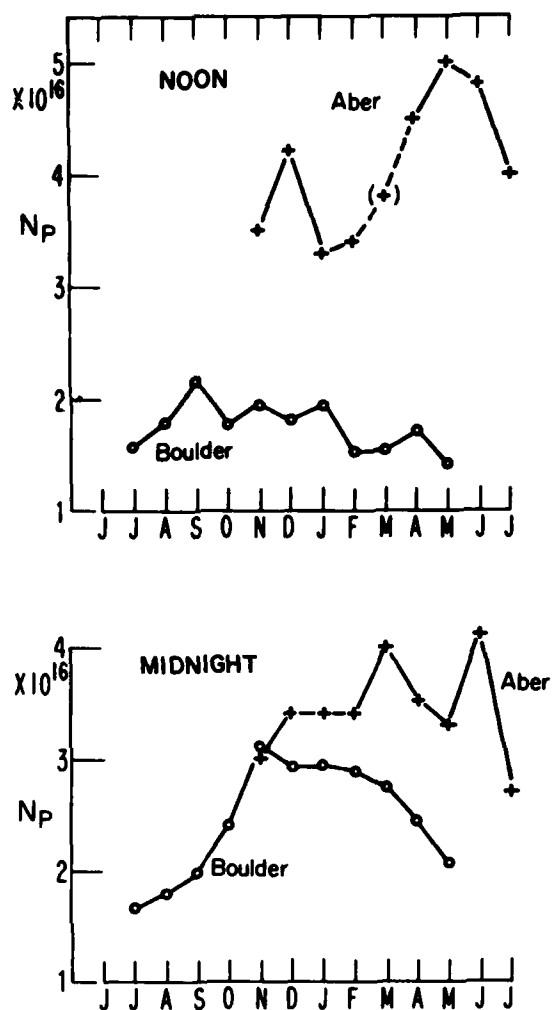


Fig. 3 Monthly medians of plasmaspheric content ATS6 to Boulder and ATS6 to Aberystwyth.

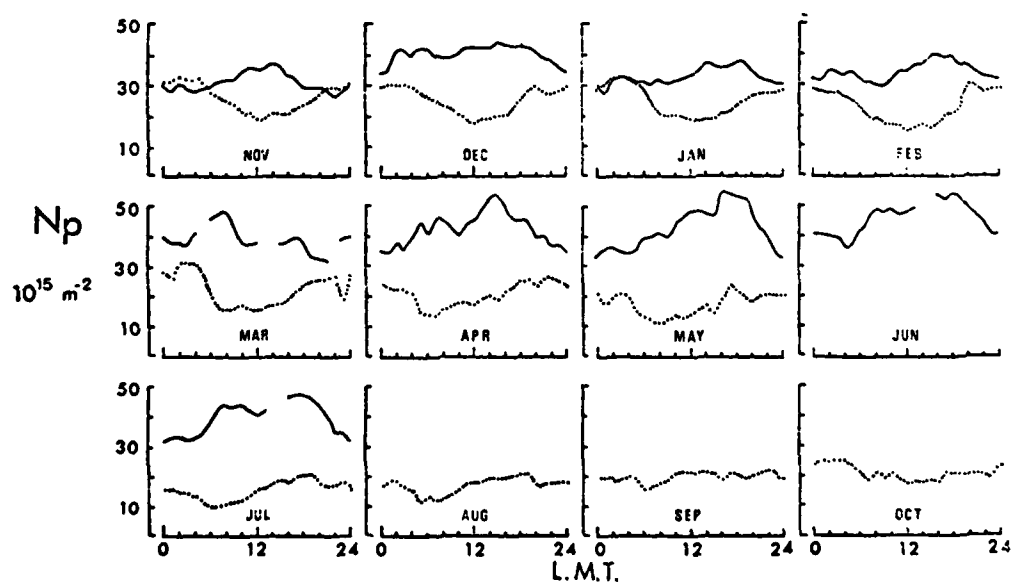


Fig. 4 Diurnal variations of  $N_p$  at Boulder and at Aberystwyth (from Kersley et al., 1977).

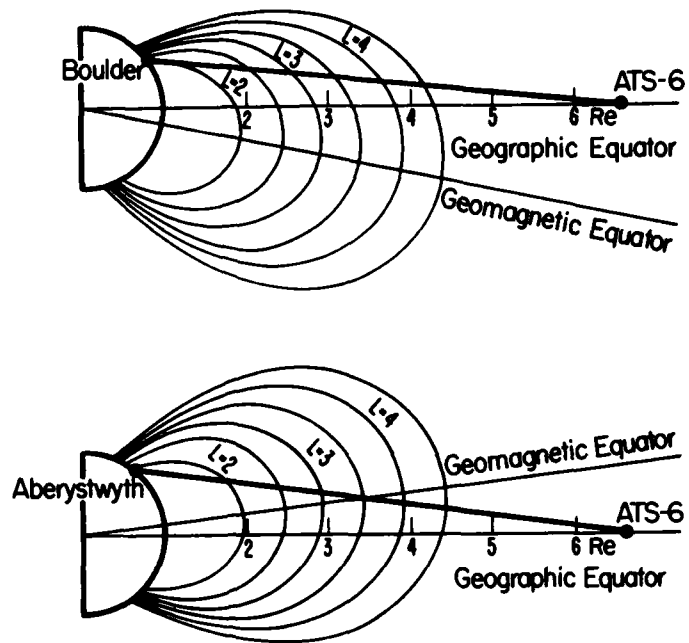


Fig. 5 Geomagnetic configurations of the ATS6 to Boulder and the ATS6 to Aberystwyth paths.

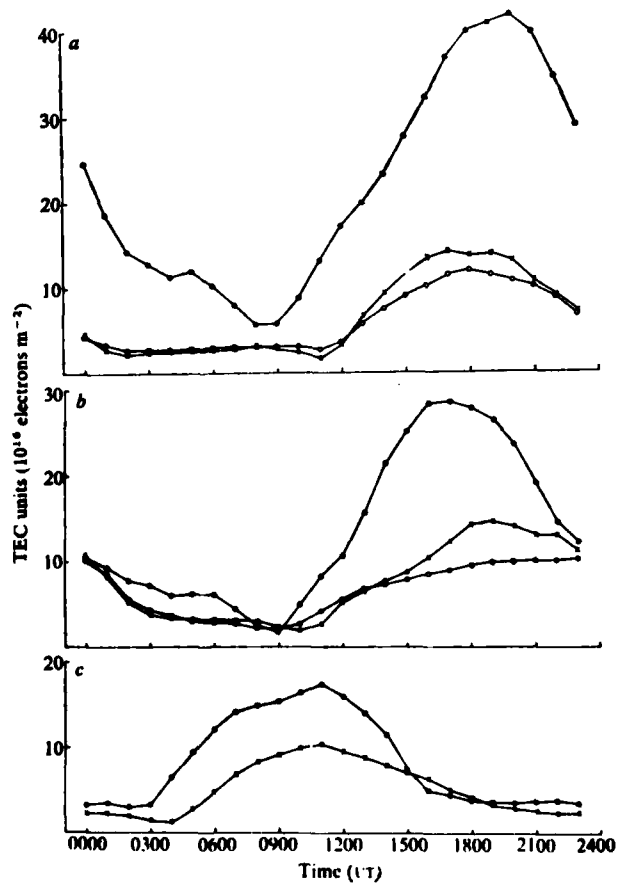


Fig. 6 Monthly medians of  $N_p$  at Sao Paulo (●) (LT = UT-3), Fort Monmouth (O) (LT = UT-5) and at Richmond (X) (LT = UT-5) during February 1975 (a) and May 1975 (b). Also at Kiruna (X) (LT = UT+1) and Haifa (O) (UT = LT+2) in October 1975 (c).

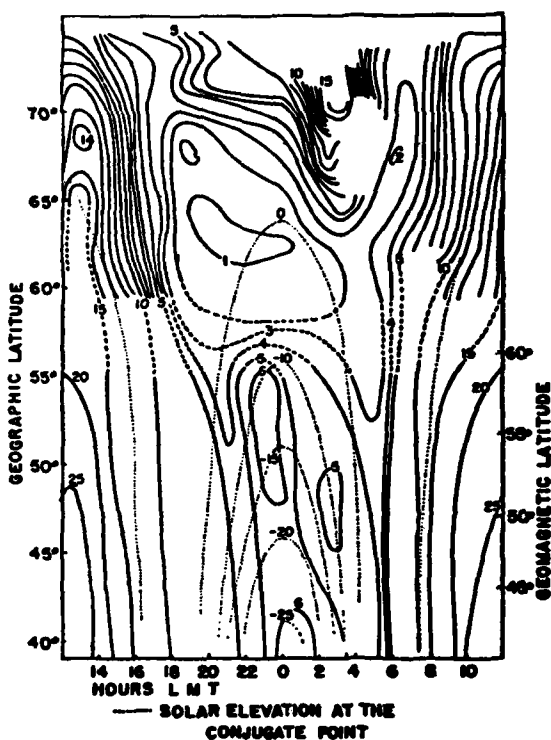


Fig. 7 Lines of constant Faraday content  $\times 10^{16}$  elect  $m^{-2}$  for winter 1966-1967 (from Bertin and Papet-Lepine, 1970, Fig. 3).

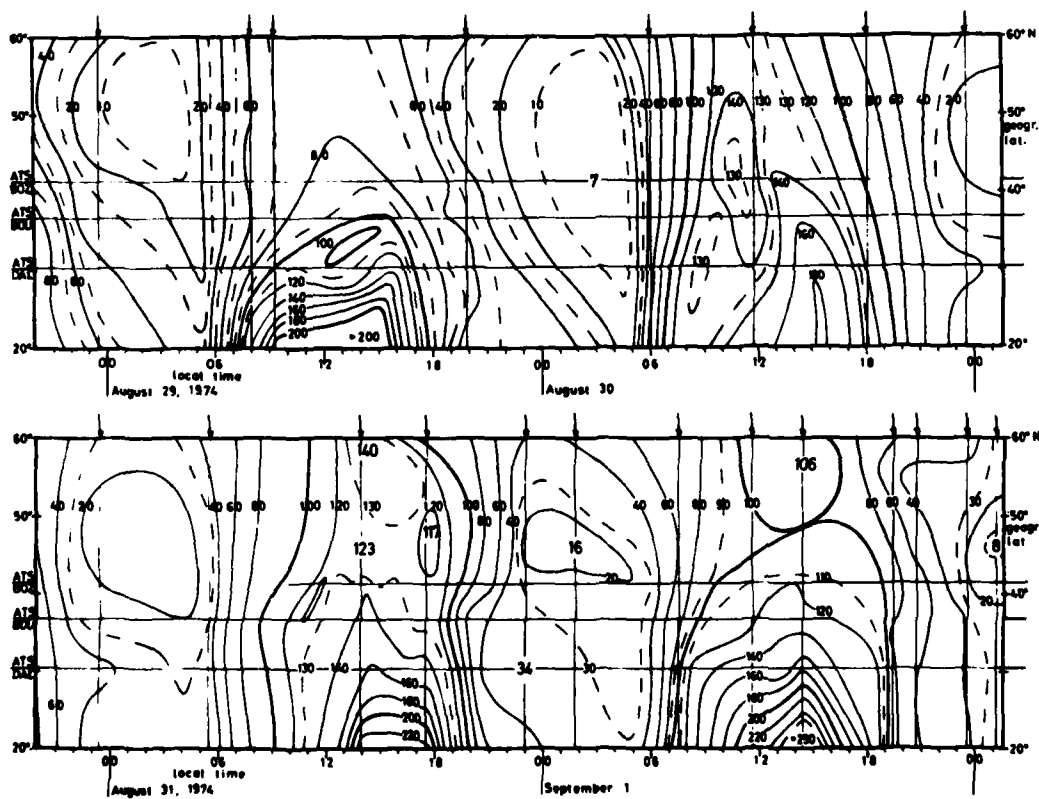
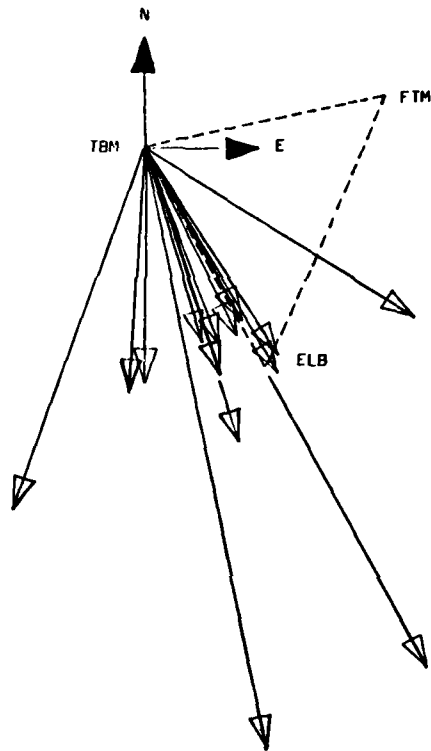


Fig. 8 Contours of electron content in a local time versus latitude grid. Vertical content is in units of  $10^{15} m^{-2}$ . Separation of solid lines  $\sim 20 \times 10^{15} m^{-2}$ . Obtained by combination of ATS6 beacon data with NNSS orbiting beacon data.



Phase velocities of horizontal movements (plane waves, 300 km height) deduced from Faraday measurements at TBM, FTM, ELB on December 06, 09, 14, 1974; between 0700 and 1400 LT

Fig. 9 Horizontal velocities of TIDs at Boulder.

#### ATS6 RBE Amplitude Irregularities, Boulder, 1-2 July 1974

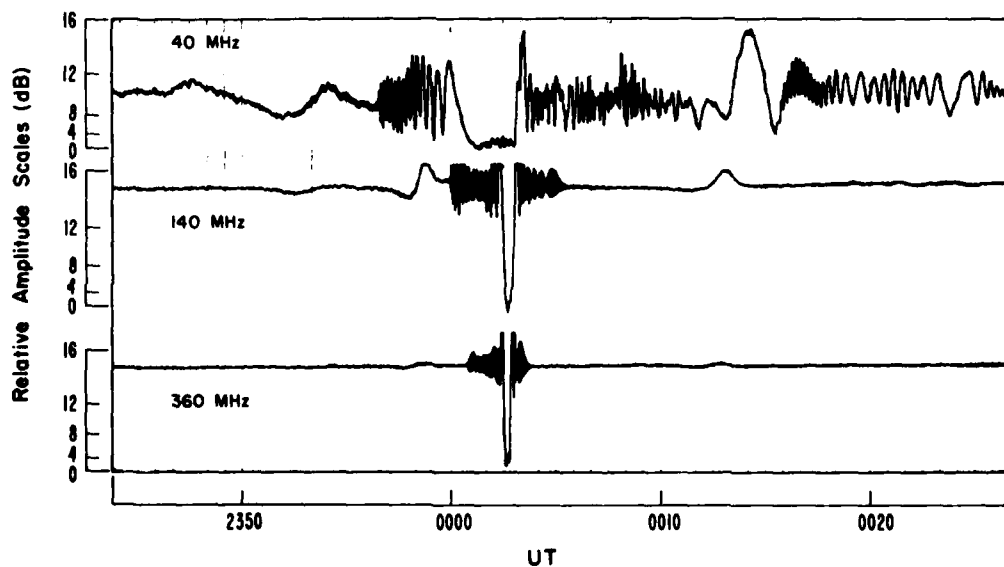
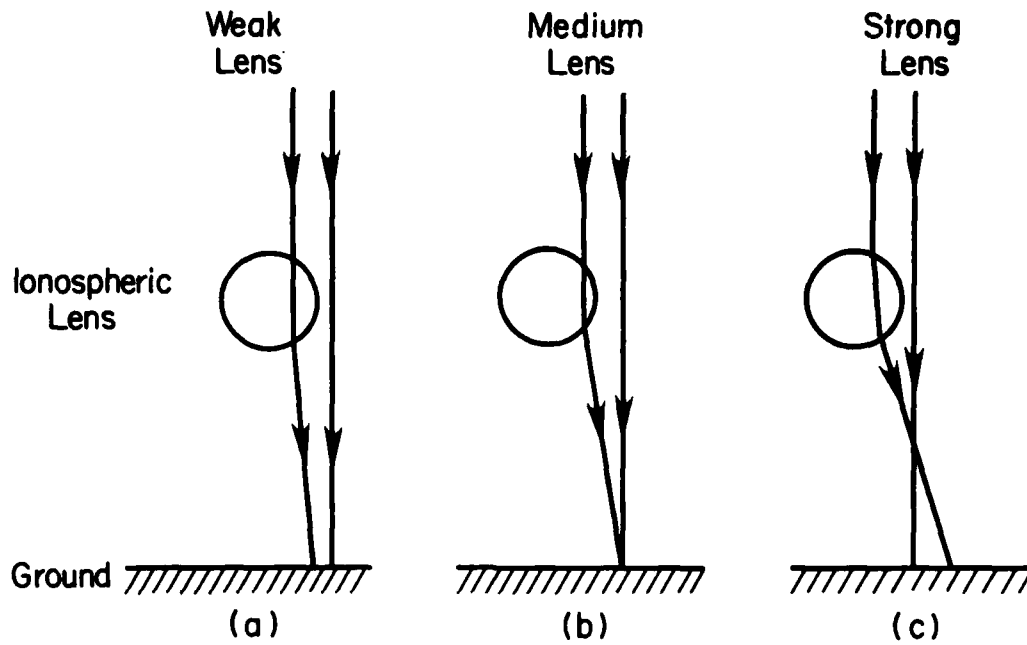


Fig. 10 Amplitude scintillations of ATS6 radio signals at Boulder.



Ray Refraction from Distant Beacon

Fig. 11 Geometry of diffraction by cylindrical lens. (a) Weak lens, (b) strong lens, and (c) intense lens.

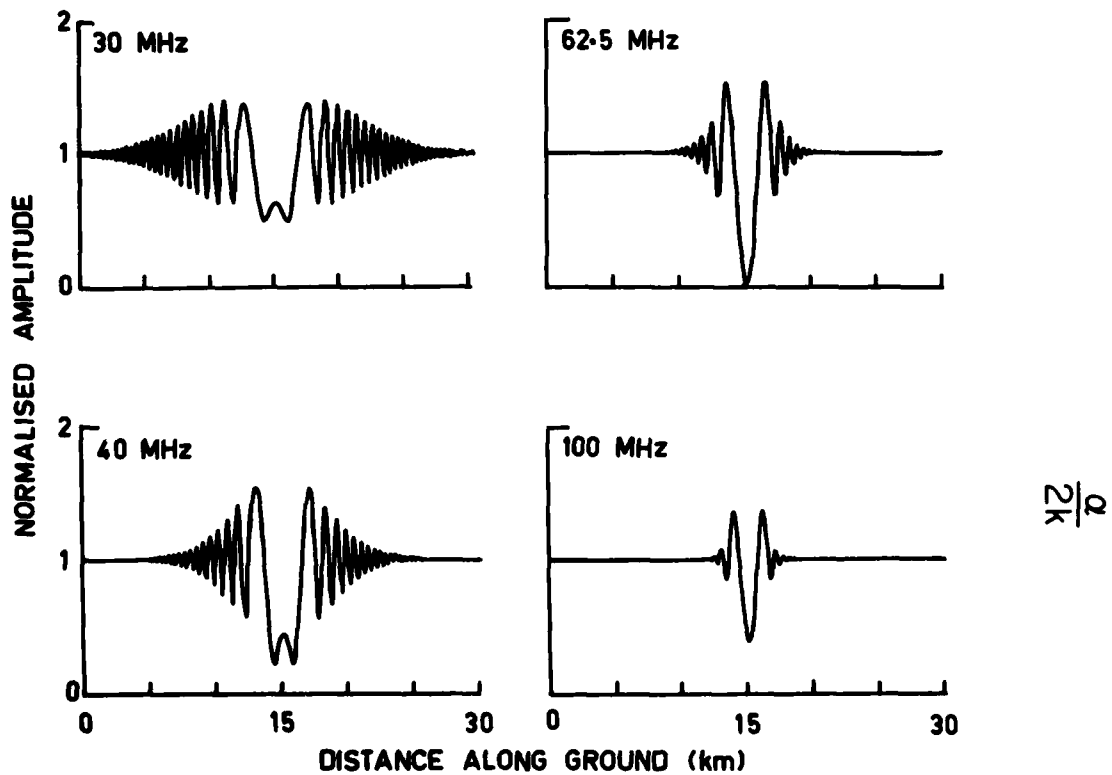


Fig. 12 Diffraction pattern on the ground produced by a single elongated gaussian enhancement in electron density at 400 km

$$\phi = \phi_0 \exp \left[ -\frac{x^2}{d^2} \right]$$

$\phi_0 = 1.2$  radian on 140 MHz,  $d = 0.41$  km, and  $f_T = 104$  MHz.



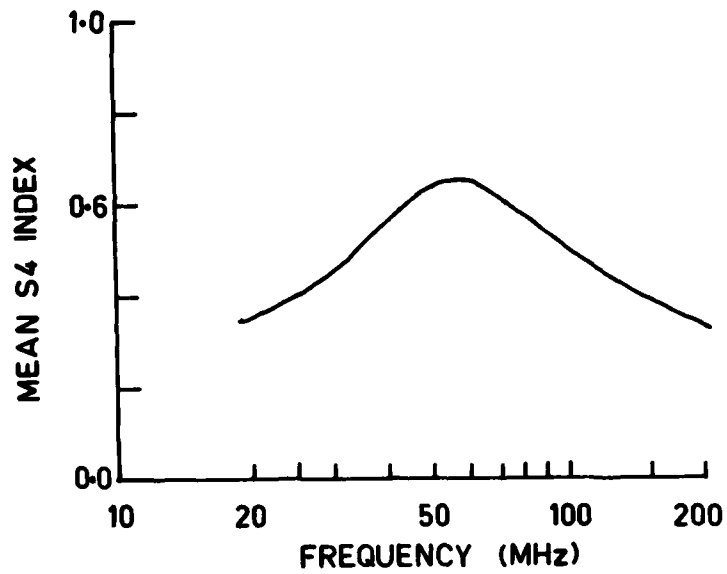


Fig. 13 Mean scintillation indices ( $S_4$ ) for the patterns in Figure 12.

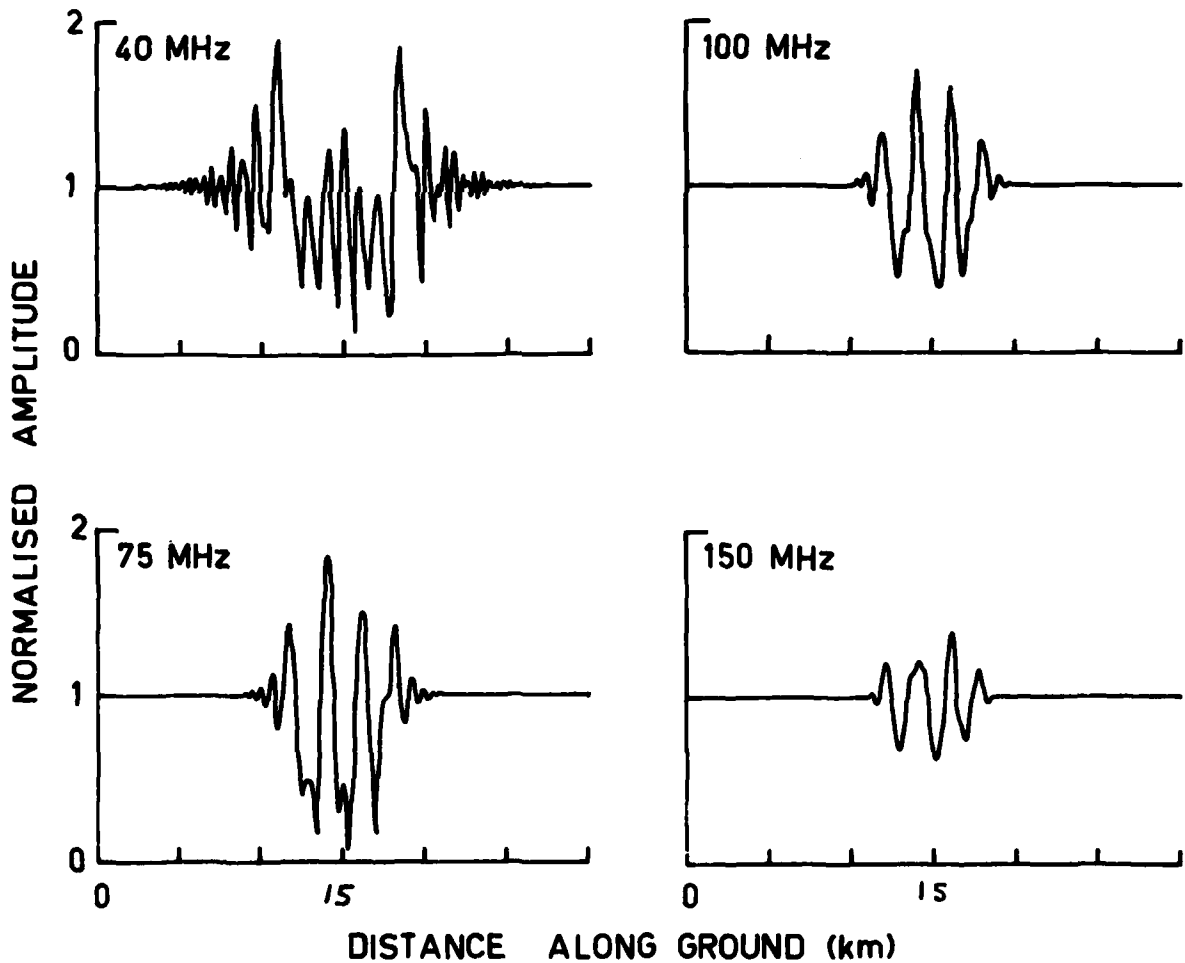


Fig. 14 Diffraction patterns produced on the ground by three quite similar irregularities juxtaposed in the ionosphere at a height of 400 km. Where  $\phi_0$  on 140 MHz are 1.0, 1.2 and 0.8 radians,  $d = 0.40, 0.41$  and  $0.39$  km and the separations of the centers are 1.1 km and 0.9 km.

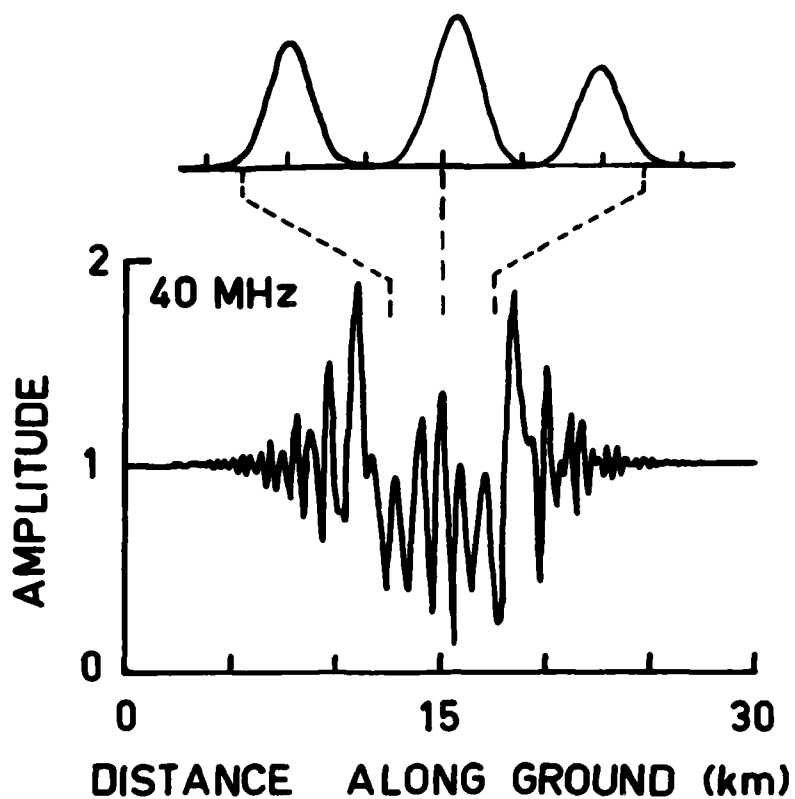


Fig. 15 Arrangement of three irregularities used to calculate the diffraction pattern in Figure 14.

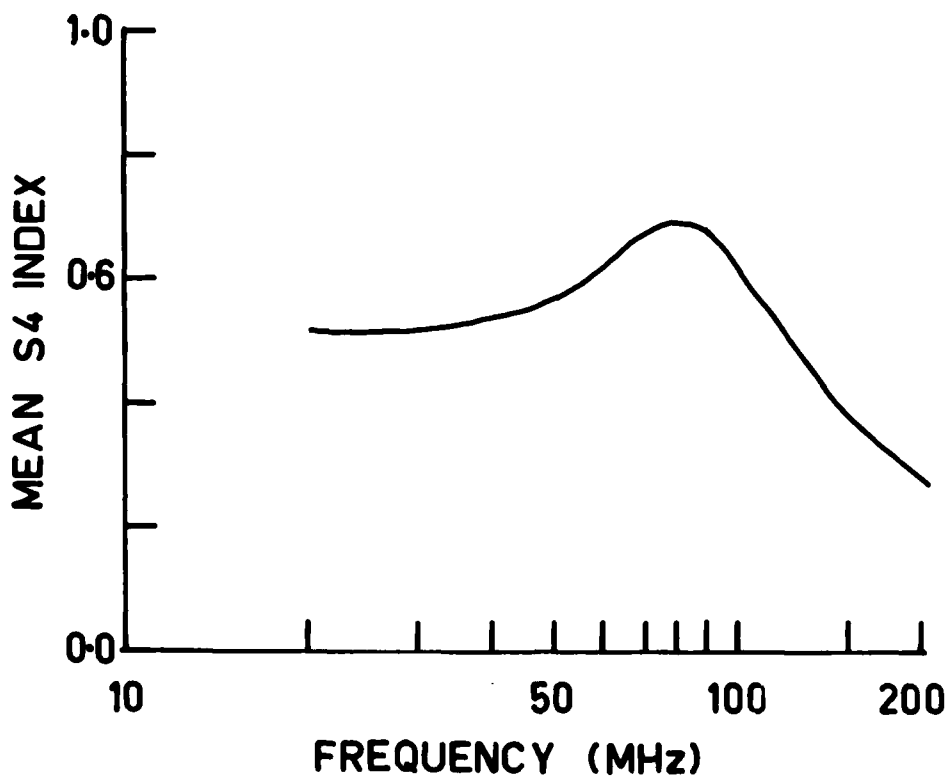


Fig. 16 Frequency variation of scintillation index ( $S_4$ ) for the 3 lens model used in Figure 14.

AN EMPIRICAL MODEL OF IONOSPHERIC SLAB THICKNESS

L KERSLEY

Department of Physics  
University College of Wales  
Aberystwyth, U.K.

ABSTRACT

In timing and positioning systems involving satellites and radars, as well as in some radio astronomical applications, the effect of the earth's ionosphere can represent a major source of error. Certain advanced navigational systems make group delay corrections in real time, however other systems rely on ionospheric models which may or may not be updated with current information on the state of the ionosphere. Ionospheric group delay is dependent on the so-called total electron content so that knowledge of the variability of this parameter is of importance in assessing time delay errors. The wide availability and ease of measurement of F2-layer critical frequency is exploited in the present approach to estimating total electron content which is based on slab thickness, a parameter defined as the ratio of equivalent vertical total electron content to peak electron density. In the work described here an empirical model of slab thickness is developed which can be combined with foF2 to estimate total electron content and hence group delay for prevailing conditions.

The data for this study comprise monthly mean values of slab thickness for the period October 1967 to September 1974, years covering solar maximum, for a station in the mid-latitude European sector. The slab thickness is shown to be dependent on both geomagnetic and solar activity as well as having diurnal and annual variations. These individual variations have been isolated and formulated into an empirical model in terms of linear and harmonic functions.

To develop the model the data have been normalized to a common level of geomagnetic activity by means of a linear function of  $A_p$  and then the diurnal variation for each month described by an harmonic series, with three harmonics giving representation of the original data to better than ten percent in the worst case. It is found that the solar activity dependence is contained almost exclusively in the zero order terms from which two coefficients are obtained by linear regression allowing the terms to be normalized to a uniform solar flux. The annual variation is now held in twelve monthly values of each of eight coefficients, these being the intercept and solar flux gradient of the zero order term and average values of each of three amplitudes and phases of the harmonic coefficients of the diurnal series. The annual variation of each of these eight coefficients is now represented by a second order harmonic series giving a total of forty coefficients.

The model has been tested against the hourly values of slab thickness and it is found that the value computed from the model is within the standard deviation of the individual daily values for all cases except near sunrise in winter when the slab thickness changes rapidly. A table of the coefficients and a step by step procedure for use of the model are presented.

1. INTRODUCTION

The slab thickness of the ionosphere is defined as the equivalent thickness of a rectangular slab of unit cross-sectional area containing a total number of electrons equal to the vertical columnar total electron content (TEC) and a constant electron density equal to the electron concentration at the F2-layer peak ( $N_m$ ), that is  $S = \text{TEC}/N_m$ .

Slab thickness has significance as an ionospheric parameter in that, for an assumed electron density profile, the slab thickness can be related directly to the scale height of the ionisable constituent. In addition, from an applications standpoint, knowledge of slab thickness and its variations has importance in applications involving the transionospheric passage of radio signals where corrections must be made for ionospheric effects. Use is made here of the wide availability of values of peak electron density a parameter readily obtained from ground based ionospheric sounding or prediction models of F2-layer critical frequency. Combining slab thickness and peak density yields total electron content which is directly related to ionospheric group delay and polarization rotation, factors for which allowance must be made in applications involving navigational, radar and radio astronomical systems. While certain systems use the dispersive nature of the ionosphere or updated models to make ionospheric corrections in actual or near real time, nevertheless there is another class of user whose needs can be satisfied by post facto information on the state of the ionosphere. It is for the benefit of this group that the current empirical model of slab thickness is presented.

KLOBUCHAR and ALLEN (1970) using data from the American sector developed a slab thickness model using analytic functions to describe diurnal and seasonal variations, work which was extended by KLOBUCHAR and HAJEB-HOSSEINIEH (1974) to include solar flux dependence. In the work described here the geomagnetic dependence has been added to the diurnal, annual and solar activity variations in an empirical model applicable to the European mid-latitude sector.

## 2. EXPERIMENTAL DATA BASE

The data used in the present study result from the monitoring of the ionospheric polarization rotation of VHF transmissions from various synchronous satellites at Aberystwyth (52.42°N, 4.05°W) during the period from October 1967 to September 1974 inclusive. The Faraday rotation angles have been converted to total electron content for an assumed mean ionospheric height of 420km and hourly slab thickness values obtained using F2-layer critical frequency data from Slough (51.5°N, 0.6°W).

Although large day to day variability is found in the slab thickness data attention has been concentrated in the present study on monthly average values with a view to modelling the variations of the mean data to better than the limits set by a departure of one standard deviation of the individual daily values from the average. Figure 1 is included to show the form of the diurnal variations of mean slab thickness for different months at solar maximum.

## 3. DEVELOPMENT OF THE MODEL

### 3.1 Geomagnetic variation and the framework for the model

The original slab thickness data were first normalized to a uniform level of geomagnetic activity using the technique described by KERSLEY and HAJEB-HOSSEINIEH (1976) involving a linear function based on the monthly mean geomagnetic index  $\bar{A}_p$  of the form

$$S_{\text{norm}} = S - 2.9 (\bar{A}_p - 12.9) \text{ km} \quad (1)$$

The diurnal effects for each month can then be represented by an harmonic series. The resulting amplitude and phase coefficients display an annual variation which can be described by another harmonic series while the d.c. term contains additional information on the solar flux dependence which can be represented by a linear function.

### 3.2 Fourier analysis of diurnal variations

A standard harmonic analysis was performed on the 24 hourly values for each month to obtain coefficients for a series function of the form

$$S_{\text{norm}} = S_0 + \sum_{n=1}^{11} S_n \cos \left[ \frac{2\pi (nt - P_n)}{24} \right] \quad (2)$$

where  $t$  is the time of day in hours.  $S_0$  is the d.c. component or mean of the 24 hourly values for each month and  $S_1, S_2, \dots$  and  $P_1, P_2, \dots$  represent the amplitudes and phases respectively of the diurnal, semi-diurnal, etc. terms. Studies showed that three orders ( $n = 1, 2, 3$ ) were adequate to model the actual data in most circumstances with inclusion of higher harmonics not yielding significant improvement in the fit.

### 3.3 Zero order components and solar flux dependence

The mean diurnal component of the Fourier series ( $S_0$ ) is usually larger than the corresponding amplitude of the first harmonic ( $S_1$ ) by about an order of magnitude. In fact the mean of the ratio ( $S_1/S_0$ ) works out to be 14 per cent for the entire data set. It is thus to be expected that the contribution to slab thickness variations associated with solar activity and annual behaviour will be found in the zero order component ( $S_0$ ) rather than the sinusoidal components represented by the harmonic coefficients. The mean diurnal components ( $S_0$ ) computed from the Fourier analysis are plotted against monthly mean solar flux index in Figure 2 with the data grouped according to month. A clear solar activity dependence of  $S_0$  with good correlation is apparent from the graphs, so that the zero order component of Equation 2 can be expressed in terms of solar flux index by a linear regression of the form

$$S_0 = a \bar{F} + b \quad (3)$$

where the gradient  $a$  and intercept  $b$  are functions of the months of the year.

Similar regression analyses were performed on the first and second harmonic amplitudes ( $S_1$  and  $S_2$ ) and their corresponding phases ( $P_1$  and  $P_2$ ). The correlation coefficients were in general low and no clear solar activity dependence could be deduced for these harmonics. It was thus decided to assign to each harmonic coefficient ( $S_1, S_2, S_3$  and  $P_1, P_2, P_3$ ) a mean value for each month averaged from all the corresponding coefficients associated with that month throughout the data. That is, there are twelve values, one for each month, for each of the six harmonic coefficients from which the annual dependent relations have been constructed.

### 3.4 Annual dependence

The coefficients  $a$  and  $b$  representing the gradient and intercept respectively of Equation 3 are plotted as functions of month in Figure 3. An appreciable annual change in the gradient can be seen, but the range of intercepts is small. The intercept represents the value of  $S_0$  for zero solar flux index which has little practical reality. A more meaningful approach is to use a normalised intercept for a mean solar flux index. A solar flux value of 120 units (1 unit =  $10^{-22} \text{ Wm}^{-2} \text{ Hz}^{-1}$ ) was chosen since this was close to the average during the period of the data. Thus Equation 3 has been rewritten in the form

$$S_0 = a (\bar{F} - 120) + S_0(120) \quad (4)$$

where  $S_0(120)$  is the intercept at  $\bar{F} = 120$  units. The normalized intercept ( $S_0(120)$ ) is plotted as a function of month in Figure 4 where a clear annual dependence is apparent.

There are thus eight coefficients,  $S_0$  (120),  $a$ ,  $S_1$ ,  $S_2$ ,  $S_3$ ,  $P_1$ ,  $P_2$ ,  $P_3$  which now contain only information on the annual variation. These coefficients are plotted as functions of month in Figures 3 to 6, and again the importance of the zero order term  $S_0$  (120) is clear.

A twelve point harmonic analysis has been performed on each of the eight coefficients. It was found that two harmonics representing the annual and semi-annual cycles gave adequate representation of the seasonal changes in the coefficients. Thus the series function representing the annual dependence can be written

$$A = A_0 + \sum_{n=1}^2 A_n \cos \left[ \frac{2\pi (nM - \phi_n)}{12} \right] \quad (5)$$

where  $A$  represents each of the eight coefficients listed above and  $M$  is the month number. The coefficients  $A_0$  together with the harmonic amplitudes ( $A_1$  and  $A_2$ ) and phases ( $\phi_1$  and  $\phi_2$ ) are tabulated in Table 1. The curves of Figures 3 to 6 show the functions represented by Equation 5 which are in general a good representation of the data points except for the phase of the third harmonic where the individual monthly values present no clear pattern themselves.

The coefficients of Table 1 together with Equations 1, 2, 4 and 5 thus form the basis for the empirical slab thickness model.

Table 1 Amplitude and phase coefficients for the annual harmonic analysis performed on the coefficients of the daily analysis

Coefficient analysed	Amplitude			Phase	
	$A_0$	$A_1$	$A_2$	$\phi_1$	$\phi_2$
$S_0$ (120)	283	37.7	14.0	6.7	0.5
$a = \partial S_0 / \partial \bar{F}$	0.37	0.16	0.08	5.4	2.2
$S_1$	42.0	16.0	14.0	0.3	11.8
$S_2$	16.0	2.5	6.0	7.9	1.1
$S_3$	10.0	6.0	1.0	0.7	10.0
$P_1$	5.7	6.0	1.7	6.2	0.5
$P_2$	12.1	3.6	1.0	0.9	2.0
$P_3$	15.8	4.7	3.0	0.0	3.0

The units of the coefficients are:

Amplitude :  $S_0$ ,  $S_1$ ,  $S_2$  and  $S_3$  (km)  
 $a$  (km per solar flux unit)  
 $P_1$  (hr),  $P_2$  (2 hr) and  $P_3$  (3 hr)  
Phase :  $\phi$ , (month) and  $\phi_2$  (2 months)

#### 4. TEST OF CONFIDENCE IN THE MODEL

Having developed an empirical model for slab thickness based on analytic functions it is important to test how well the model values represent the actual observed data. To do this the model has been used to compute monthly mean slab thickness values for twenty four hours of the day for each month throughout the seven years of observation using the actual monthly mean values of solar flux and geomagnetic indices as input parameters. The percentage deviations of the computed from the observed values show that the overall agreement is good, with errors in the daytime hours of less than 10 per cent for most months. The largest errors are generally around dawn and sunset, particularly in the winter months when the model fails to reproduce completely the strong gradients found in the original data. The overall root mean square deviation for each month calculated from the hourly values ranges from 4 to 18 per cent, although only 9 months have a standard deviation greater than 12 per cent, and the mean value is 8.6 per cent.

Figure 7 shows a comparison between computed and observed values of monthly slab thickness for four selected months representing the four seasons. Figure 7a is for high solar activity ( $\bar{F} > 150$ ), with Figure 7b for low solar activity ( $\bar{F} \leq 100$ ). The error bars about the observed mean values represent plus and minus one standard deviation computed from the individual daily observations. It can be seen that with only a few exceptions the predicted values represent the actual values to well within one standard deviation from the mean of the day to day fluctuations. Agreement is best in daytime, particularly in summer and autumn and poorest around sunrise in winter.

Figure 7 shows that the modelled slab thickness is, in general, in agreement with the observed monthly mean value to within less than one standard deviation of the individual daily values. Thus, since for an assumed normal distribution of daily values about the mean, some 70 per cent will be within this range, it may be concluded that the model provides a reasonable representation of an individual daily value.

## 5. CONCLUSION

An empirical model of ionospheric slab thickness has been developed for users who require to make first order estimates of ionospheric total electron content for post facto corrections for the effects of ionospheric group delay or polarization rotation. It has been shown that the modelled values represent the monthly mean values to within one standard deviation of the individual daily values in most circumstances.

A step by step guide to use of the slab thickness model is given in Appendix 1.

## 6. ACKNOWLEDGEMENTS

The sponsorship of Air Force Geophysics Laboratory under Grant AFOSR 72-2267 in support of this work is gratefully acknowledged.

Thanks are also due to Mr. K.J. Edwards for invaluable assistance with experimental aspects of the satellite recording and to Dr. H. Hajeb-Hosseinih for help in formulation of the model.

## 7. REFERENCES

KERSLEY, L. and HAJEB-HOSSEINIEH, H. (1976) The dependence of ionospheric slab thickness on geomagnetic activity. *J. Atmos. Terr. Phys.*, 38, 1357-60.

KLOBUCHAR, J.A. and ALLEN, R.S. (1970) A first order prediction model of total electron content group delay for a mid-latitude ionosphere. AFCRL-TR-70-0403.

KLOBUCHAR, J.A. and HAJEB-HOSSEINIEH, H. (1974) Seasonal and solar flux dependence of mid-latitude slab thickness. Presented at URSI Meeting, Boulder, Colorado, U.S.A., October 1974.

APPENDIX 1

## STEP BY STEP GUIDE TO USE OF SLAB THICKNESS MODEL

1. Select month (M) and calculate  $S_o(120)$  using

$$A = A_o + \sum_{n=1}^2 A_n \cos \left[ \frac{2\pi (nM - \phi_n)}{12} \right] \quad [ = S_o(120) ]$$

with appropriate coefficients from line 1 of Table 1.

2. Repeat step 1 calculating in turn a,  $S_1, S_2, S_3, P_1, P_2, P_3$  using appropriate coefficients from Table 1.  
 3. Determine mean solar flux index ( $\bar{F}$ ) for month selected and calculate  $S_o$  from  $S_o = a(\bar{F} - 120) + S_o(120)$ .  
 4. Select hour (t) and calculate  $S_{norm}$  from

$$S_{norm} = S_o + \sum_{n=1}^3 S_n \cos \left[ \frac{2\pi (nt - P_n)}{24} \right].$$

5. Determine mean geomagnetic index ( $\bar{A}_p$ ) for month selected and calculate final slab thickness (S) from

$$S = S_{norm} + 2.9 (\bar{A}_p - 12.9) \text{ (km)}.$$

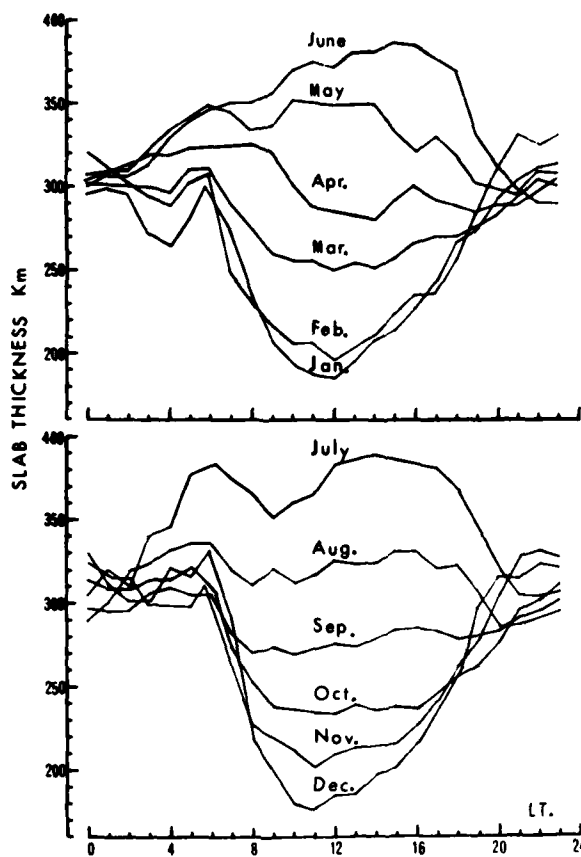


Figure 1 Diurnal variations of monthly mean slab thickness at solar maximum (1968-70).

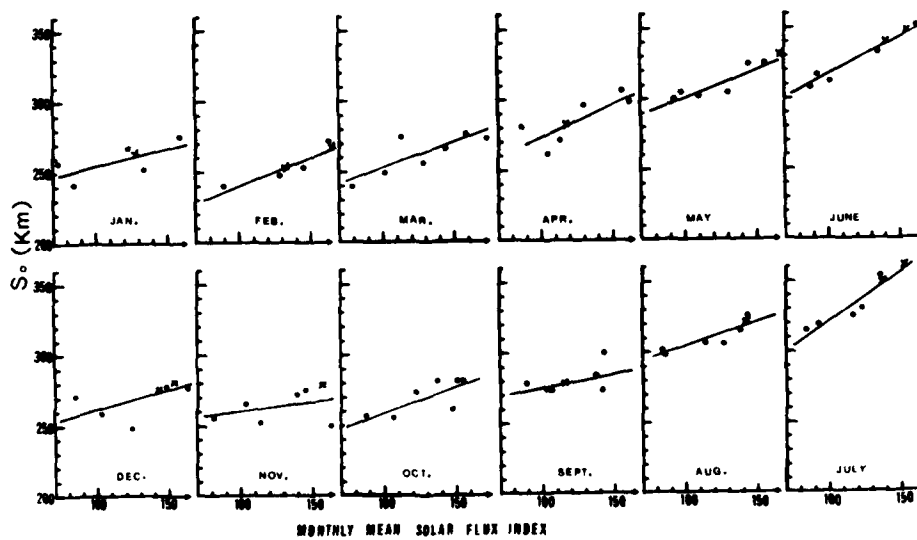


Figure 2 Solar flux dependence of the d.c. component of the diurnal Fourier analysis ( $S_0$ ) by month.

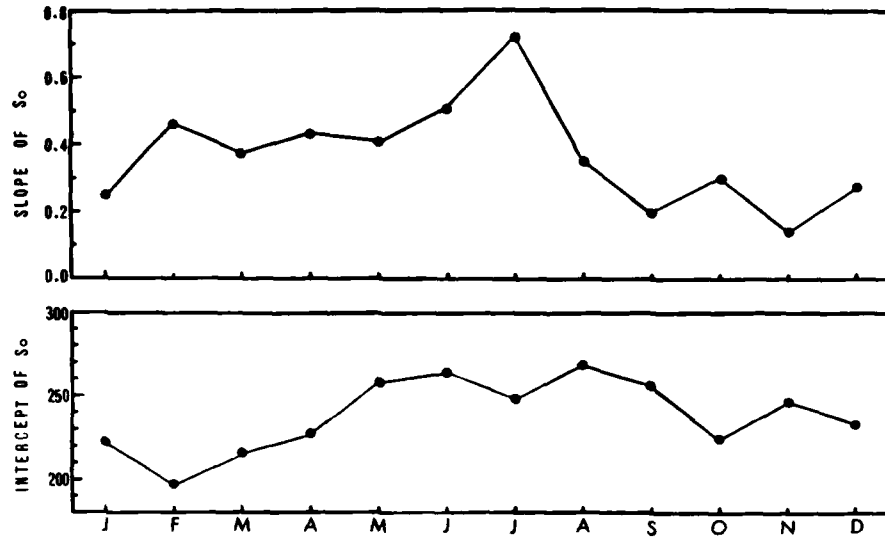


Figure 3 Annual variations of the gradient and intercept of the d.c. component of the diurnal Fourier analysis ( $S_0$ ).

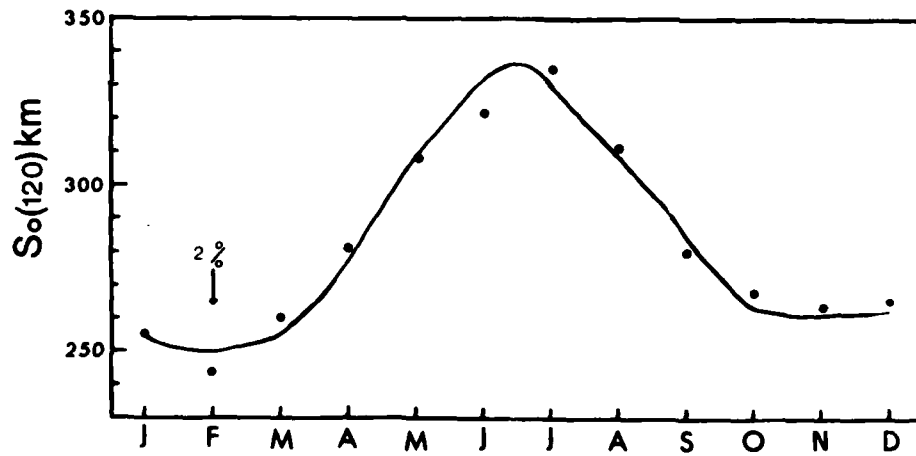


Figure 4 Annual variation of  $S_0(120)$ .



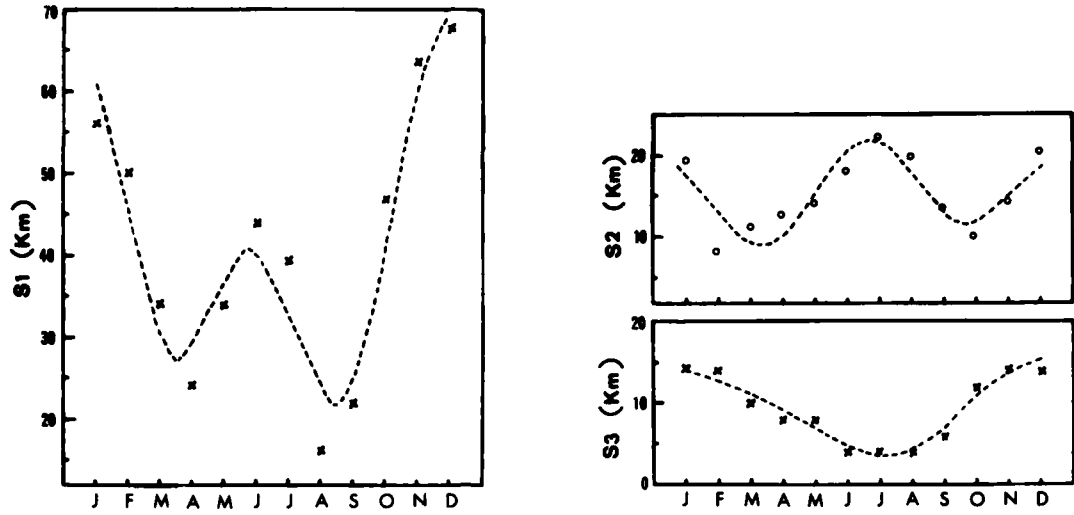


Figure 5 Annual variations of the first three Fourier harmonic amplitudes of the diurnal variations of the normalized slab thickness.

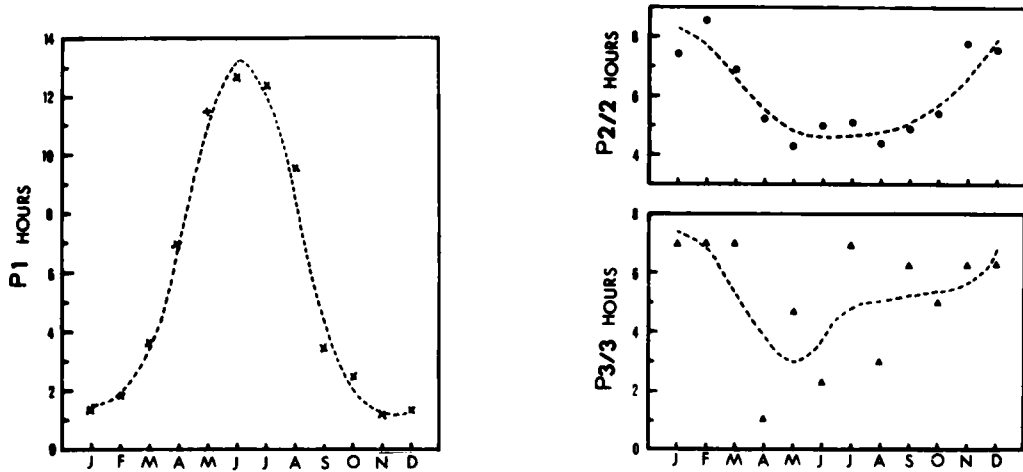


Figure 6 Annual variation of the first three Fourier harmonic phases of the diurnal variations of the normalized slab thickness.

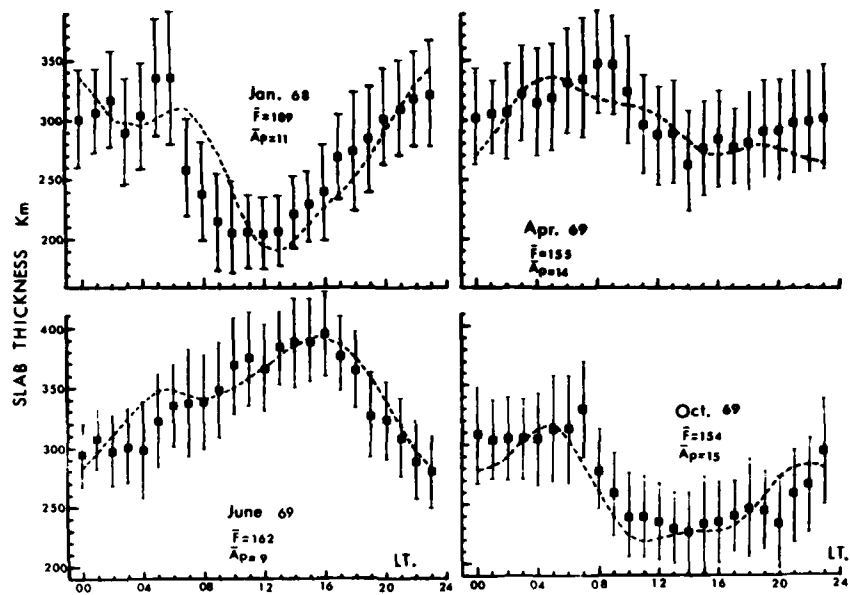


Figure 7a The modelled and observed monthly mean diurnal variations of slab thickness for selected months at high solar activity. The error bars show one standard deviation from the mean of the individual daily values.

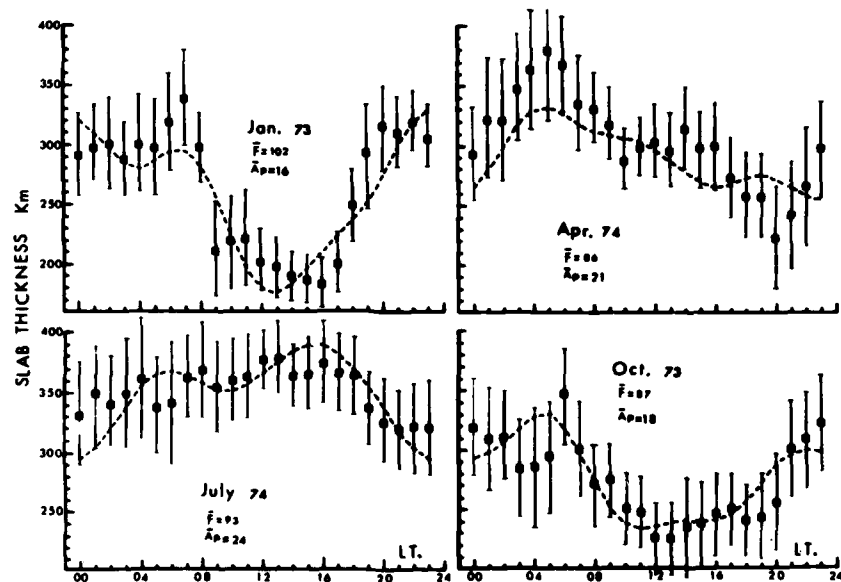


Figure 7b As Figure 7a but for lower solar activity.

ANISOTROPIC MEDIUM EFFECTS ON THE PROPAGATION OF 1.5 GHz  
SIGNALS CODED BY PHASE REVERSALS: FULL-WAVE SOLUTIONS

E. Bahar and B. S. Agrawal  
Electrical Engineering Department  
University of Nebraska--Lincoln, Nebraska 68588

ABSTRACT

The distortion and depolarization of 1.5 GHz transient signals that propagate through an inhomogeneous anisotropic model of the ionosphere are investigated using a full-wave approach. The dispersive and anisotropic properties of the ionosphere impede the decoding at the receiver of the two orthogonally polarized signals which are independently coded at the transmitter. Thus, in addition to determining the signal delays and the phase shifts of the transmitted signals, features that distinguish between the depolarized and nondepolarized signals are also identified.

1. Introduction

Satellite signals coded by phase reversals undergo dispersion and depolarization on transmission through the ionosphere. Since the signals of the two polarizations (vertical and horizontal linear polarizations or right and left circular polarizations) are independently coded, the dispersion and the depolarization of the signal by the ionosphere impede the decoding of the signal at the receiver. These two effects of the ionosphere on the L-Band coded signal are therefore investigated in detail.

The steady state solutions for the four transmission coefficients (and the four reflection coefficients) are obtained numerically using a full-wave approach. This approach employs generalized characteristic vectors (up to rank four) to represent the electromagnetic fields in terms of four linearly independent wave amplitudes even for regions of critical coupling. (BAHAR 1976). Since the propagation path through the ionosphere (measured in free space wavelengths) is very large, a set of recursive formulas is derived to solve the wave amplitudes. The full-wave solutions satisfy the reciprocity and realizability relations in electromagnetic theory.

It is found convenient in this work to represent the coded transient signals by an excitation which is a complex function of time. The relationship between the transforms and the inverse transforms for these complex signals and for the corresponding real signals are presented. In addition to the transient response, the envelope and the instantaneous phase of the response are evaluated. An analytic expression for an undistorted coded signal transmitted through a medium without the dispersive properties of the ionosphere is also derived. To limit the bandwidth of the transmitted signal a fourth-order Butterworth band pass filter is used. Fast Fourier Transform techniques as well as a direct integration method are used to determine the transient response for the illustrative examples presented. These examples show the distortion of the coded signals due to the dispersive property of the ionosphere and identify any distinguishing features between the depolarized and nondepolarized signals.

2. Steady State Solutions for the Transmission Coefficients at L Band

In this section we present the basic formulas that are suitable to compute the transmission coefficients  $T_{PQ}(\omega)$  (P and Q = V or H) at L band frequencies. Both vertically and horizontally polarized incident plane waves are considered. The inhomogeneous, anisotropic medium is characterized by the plasma frequency  $\omega_p$ , the collision frequency  $\nu$ , and gyrofrequency  $\omega_H$ . Thus for instance,  $T_{VV}(\omega)$  is the transmission coefficient for vertically polarized waves when the incident plane wave is also vertically polarized and  $T_{VH}(\omega)$  is the transmission coefficient for the vertically polarized wave (first subscript V) when the incident plane wave is horizontally polarized (second subscript H). The medium is assumed to be horizontally stratified and for simplicity the incident wave normal in free space,  $\bar{n}$ , is assumed to be in the x, z plane (see Fig. 1)

$$\bar{n} = (s\bar{a}_x + c\bar{a}_y) \quad (2.1)$$

where

$$s = \sin\theta \text{ and } c = \cos\theta \quad (2.2)$$

and  $\theta$  is the angle of incidence. Thus there are no field variations in the y direction. To obtain the steady state solutions for the transmission coefficients an  $\exp(i\omega t)$  time dependence is assumed. All the electromagnetic field components are proportional to the factor  $\exp(-ikx) \cdot \exp(i\omega t)$  which is suppressed throughout this work. Thus Maxwell's equations for the transverse components  $E_x$  and  $E_y$  of the electric field  $\vec{E}$  and the transverse components  $H_x$  and  $H_y$  of the normalized magnetic field  $\vec{H}$  ( $\eta = (\mu_0/\epsilon_0)^{1/2}$  is the free space wave impedance) can be written as (BUDDEN 1962, BAHAR 1976).

$$de/dz = e' = -ikTe \quad (2.3)$$

in which  $k = \omega \sqrt{\mu_0 \epsilon_0}$  is the free space wave number

$$e = \begin{pmatrix} E_x \\ -E_y \\ H_x \\ H_y \end{pmatrix} \quad (2.4)$$

and the elements of the 4 x 4 matrix T can be expressed in terms of the susceptibility matrix M and the direction cosines of the incident wave normal in free space. To facilitate the solution of (2.3), the transverse field components e are expressed in terms of four linearly independent wave amplitudes f, through the transformation

$$e = Sf \quad (2.5)$$

On substituting (2.5) into (2.3), it transforms into

$$f' = -iks^{-1}(TS - S')f \equiv Cf \quad (2.6)$$

When the four characteristic values  $q_i$  of the matrix  $T$  are distinct, the four wave amplitudes are the upward and downward propagating ordinary and extra-ordinary waves. In this case four linearly independent characteristic vectors can be found such that

$$T_c S^i = q_i S^i \quad (2.7)$$

where  $T_c = T(z_c)$  and the elements  $S_{ij}$  of the column matrix  $S^i$  are the elements of the  $i$ th column of the constant matrix  $S$ . Thus at  $z = z_c$  the matrix  $C$  in (2.6) is a diagonal matrix whose elements are  $q_i$ .

If however, the characteristic values  $q_i$  merge (for instance at grazing incidence  $c \rightarrow 0$ ), the transformation matrix  $S$  defined by (2.7) becomes singular. In the vicinity of such turning points of the differential equation it has been shown recently (BAHAR 1976) that generalized characteristic vectors of rank  $r$  ( $r \geq 2$ ) can be used to determine the elements of a nonsingular transformation matrix  $S$  such that

$$T_c S - S' = S \Delta_c \quad (2.8)$$

where the elements of the diagonal matrix  $\Delta_c$  are the generalized characteristic values. Thus even for regions of critical coupling between the four characteristic waves, the matrix  $C$  is a diagonal matrix at the level  $z = z_c$  where the characteristic values merge. To obtain rigorous solutions to (2.6) we define the  $4 \times 2$  matrix  $F$  as follows

$$F = (f^H \ f^V) \quad (2.9)$$

where  $f^H$  and  $f^V$  are the solutions to (2.6) for incident horizontally and vertically polarized waves respectively. The differential equation and the mixed boundary conditions for  $F$ , for waves incident from below the horizontally stratified medium ( $z < 0$ ) are

$$F' = CF \quad (2.10)$$

and

$$F(0) = \begin{pmatrix} 1 & 0 \\ R_{HH} & R_{HV} \\ 0 & 1 \\ R_{VH} & R_{VV} \end{pmatrix} \quad \text{and} \quad F(L) = \begin{pmatrix} T_{HH} & T_{HV} \\ 0 & 0 \\ T_{VH} & T_{VV} \\ 0 & 0 \end{pmatrix} \quad (2.11)$$

where the transformation matrix for free space is

$$S = \begin{pmatrix} 0 & 0 & c & -c \\ 1 & 1 & 0 & 0 \\ c & -c & 0 & 0 \\ 0 & 0 & 1 & 1 \end{pmatrix} \quad (2.12)$$

Since neither the reflection nor the transmission coefficients  $R_{PQ}$  and  $T_{PQ}$  respectively, are known prior to solving (2.6), the matrix  $F$  is expressed as follows:

$$F(z) = G(z)T \quad (2.13)$$

where

$$T = \begin{pmatrix} T_{HH} & T_{HV} \\ T_{VH} & T_{VV} \end{pmatrix} \quad (2.14)$$

and at  $z = L$  the  $4 \times 2$  matrix  $G$  is defined as

$$G(L) = \begin{pmatrix} 1 & 0 \\ 0 & 0 \\ 0 & 1 \\ 0 & 0 \end{pmatrix} \quad (2.15)$$

In view of (2.10) and (2.13)

$$G' = CG \quad (2.16)$$

Thus instead of solving (2.10) subject to the mixed boundary conditions (2.11), we solve (2.16) subject to the unmixed boundary condition (2.15). The values of the transmission matrix  $T$  (2.14) and the reflection matrix  $R$

$$R = \begin{pmatrix} R_{HH} & R_{HV} \\ R_{VH} & R_{VV} \end{pmatrix} \quad (2.17)$$

are obtained directly from the elements  $G_{ij}$  of the matrix  $G$  at  $z = 0$ . Thus

$$T = G_1^{-1} \quad \text{and} \quad R = G_2 T \quad (2.18)$$

where

$$G_1 = \begin{pmatrix} \epsilon_{11} & \epsilon_{12} \\ \epsilon_{31} & \epsilon_{32} \end{pmatrix} \quad G_2 = \begin{pmatrix} \epsilon_{21} & \epsilon_{22} \\ \epsilon_{41} & \epsilon_{42} \end{pmatrix} \quad (2.19)$$

For very low frequencies, the width,  $L$  of the inhomogeneous anisotropic region ( $0 < z < L$ ) is comparable to the wavelength in free space  $\lambda$ , and equation (2.16) in conjunction with the continuity conditions for the transverse field components can be solved using standard numerical techniques such as the Runge-Kutta method (BAHAR and AGRAWAL 1978). However, for frequencies in the L-band this method is not suitable since  $L \gg \lambda$ . For this case, a recursive formula is derived for  $g_m(z)$  after converting the coupled differential equations (2.6) into coupled integral equations (see Appendix A). As a check these recursive formulae have shown to yield results that are in very good agreement with the Runge-Kutta method at very low frequencies. In addition, for frequencies in the L-band they are found to satisfy the adjoint reciprocity relationships in electromagnetic theory (KERNS 1976).

### 3. Transient Response for L-Band Signals Coded by Phase Reversals

In this work it is convenient to express the L-band signals coded by phase reversals  $f(t)$  in terms of the complex function  $f_s(t)$ . Thus

$$\begin{aligned} f(t) &= \text{Re } f_s(t) = \text{Re } \exp[i\omega_c(t-\tau)] [-H(t) + 2H(t-\tau) - H(t-T)] \\ &= \cos[\omega_c(t-\tau)] [-H(t) + 2H(t-\tau) - H(t-T)] \\ &\equiv \cos[\omega_c(t-\tau)] g(t) \end{aligned} \quad (3.1)$$

in which  $H(t)$  is the unit step function,  $g(t)$  is the envelope of the signal,  $\omega_c = 2\pi f_c$  is the carrier frequency,  $T$  is the duration of the pulse ( $0 < t < T$ ) and the phase reversal occurs at  $t = \tau = T/2$ . Denoting the Fourier transforms of  $f(t)$  and  $f_s(t)$  by  $F(\omega)$  and  $F_s(\omega)$  respectively, it can be shown that

$$F(\omega) = [F_s(\omega) + F_s^*(-\omega)]/2 \quad (3.2)$$

where the symbol (\*) denotes the complex conjugate. In general since  $f(t)$  is real,  $F(\omega) = F^*(-\omega)$ , however,  $F_s(\omega) \neq F_s^*(-\omega)$  unless  $f_s(t)$  is also real. Thus

$$\begin{aligned} F_s(\omega) &= \int_{-\infty}^{\infty} f_s(t) \exp(-i\omega t) dt = \frac{4i \exp[-i\omega T/2] \sin^2[(\omega - \omega_c)T/4]}{\omega - \omega_c} \\ &= \exp[-i\omega T/2] G(\omega - \omega_c) \neq F_s^*(-\omega). \end{aligned}$$

where  $G(\omega)$  is the Fourier Transform of  $g(t)$ . Since all the transfer functions (the transmission coefficients) satisfy the relationship

$$T(\omega) = T^*(-\omega) \quad (3.3)$$

the transmitted signal can be expressed in terms of the inverse Fourier Transform of  $F_s(\omega)T_{PQ}(\omega)$ .

$$\begin{aligned} e(t) &= F^{-1}[F(\omega)T(\omega)] \equiv \frac{1}{2\pi} \int_{-\infty}^{\infty} F(\omega)T(\omega) \exp(i\omega t) d\omega \\ &= \text{Re}\{F^{-1}[F_s(\omega)T(\omega)]\} \\ &= \text{Re } e_s(t) = \text{Re}[e_R(t) + i e_I(t)] = e_R(t) \end{aligned} \quad (3.4)$$

The envelope and the instantaneous phase of the transient signal are defined as

$$e_E(t) = |e_s(t)| \quad (3.5)$$

and

$$\phi(t) = \tan^{-1}[e_I(t)/e_R(t)] \quad (3.6a)$$

thus

$$\Delta\phi(t) = \phi(t) - \omega_c t \quad (3.6b)$$

is the deviation of the instantaneous phase from its steady state value. In a narrow band around the carrier frequency the transfer function can be expressed approximately as

$$T(\omega) = |T(\omega)| \exp[i\psi_T(\omega)] \approx T(\omega_c) \exp[-i(\omega - \omega_c)\tau_T] \quad (3.7a)$$

in which the delay at the carrier frequency is given by

$$\tau_T = -(d\psi_T(\omega)/d\omega)_{\omega=\omega_c} \quad (3.7b)$$

Defining the new time variable  $t'$  by

$$t' = t - \tau_T \quad (3.8)$$

we get

$$e(t') = \text{Re}\{F^{-1}[F_s(\omega)T(\omega) \exp(i\omega\tau_T)]\} \quad (3.9)$$

and using (3.7), the approximate, undistorted, transmitted signal is

$$\begin{aligned} e_A(t') &= \text{Re}\{F^{-1}[F_S(\omega)T(\omega_c)\exp[i\omega_c\tau_T]]\} \\ &= \text{Re}\{T(\omega_c)\exp[i\omega_c\tau_T]f_S(t')\} \\ &= |T(\omega_c)|\cos[\omega_c(t'+\tau_T-\tau) + \psi_T(\omega_c)]g(t') \end{aligned} \quad (3.10)$$

To restrict the bandwidth of the signal it is convenient to use a fourth order band pass Butterworth filter with the transfer function  $F_F(\omega)$

$$F_F(\omega) = [p^4 + 2.6131 p^3 + 3.4142 p^2 + 2.6131 p + 1]^{-1} \quad (3.11a)$$

in which

$$p = \frac{\omega_c^2 - \omega^2}{i\omega B_w} \quad (3.11b)$$

and  $B_w$  is the bandwidth. Expressing (3.11a) approximately as

$$F_F(\omega) = |F_F(\omega)|\exp[i\psi_F] \approx F_F(\omega_c)\exp[-i(\omega-\omega_c)\tau_F] \quad (3.12a)$$

in which

$$\tau_F = -(d\psi_F/d\omega)_{\omega=\omega_c} \text{ and } F_F(\omega_c) = 1 \quad (3.12b)$$

the band limited transmitted signal  $e(t')$  and the undistorted signal  $e_A(t')$  are

$$e(t') = \text{Re}\{F^{-1}[F_S(\omega)F_F(\omega)T(\omega)\exp(i\omega\tau_m)]\} \quad (3.13a)$$

$$\begin{aligned} e_A(t') &= \text{Re}\{T(\omega_c)F_F(\omega_c)\exp[i\omega_c(\tau_T+\tau_F)]f_S(t'-\tau_F)\} \\ &= |T(\omega_c)|\cos[\omega_c(t'+\tau_T-\tau) + \psi_T(\omega_c)]g(t'-\tau_F) \end{aligned} \quad (3.13b)$$

For convenience the transient response  $e(t)$  and  $e_A(t)$  are normalized in this work on dividing by  $T(\omega_c)$ . Thus

$$e_N(t) = e(t)/|T(\omega_c)| \quad (3.14)$$

In addition to presenting plots of  $e(t')$  and  $e_A(t')$  the difference  $\Delta e(t')$  is also plotted.

$$\begin{aligned} \Delta e(t') &\equiv e(t') - e_A(t') = F^{-1}\{F_S(\omega)\{F_F(\omega)T(\omega)\exp(i\omega\tau_T) \\ &\quad - F_F(\omega_c)\exp[i(\omega_c-\omega)\tau_F]T(\omega_c)\exp[i\omega_c\tau_T]\}\} \end{aligned} \quad (3.15)$$

The function  $\Delta e(t')$  which vanishes for  $(t'-\tau)f_c \gg 1$  represents the dispersive effects of the transfer functions.

Since the transfer function  $T_{RO}$  is solved numerically as a function of frequency, the Fast Fourier Transform Technique (FFT) is used to evaluate the inverse Fourier Transform,  $F^{-1}$  (BRIGHAM 1974). Thus for

$$0 \leq t = (k-1)\Delta t \leq N\Delta t = T = 1/\Delta f, \quad k = 1 \dots N+1, \quad f_{\max} = N\Delta f/2 \quad (3.16)$$

the inverse transform of

$$E_S(\omega) = F_S(\omega)F_F(\omega)T(\omega)\exp(i\omega\tau_T) \quad (3.17)$$

is given by the complex conjugate of  $e_S^*(t) = e_S^*(k\Delta t)$  where (BRIGHAM and ORAN 1974)

$$e_S^*(k) = \frac{1}{T} \sum_{n=1}^N E_S^*(n) \exp[-2i\pi(n-1)(k-1)/N] \quad (3.18)$$

In (3.17)  $E_S(n)$  corresponds to  $E_S[(n-1)\Delta\omega]$  for  $n=1, 2, \dots, N/2$ , to

$[E_S(\omega_{\max}) + E_S(-\omega_{\max})]/2$  for  $n = N/2+1$  and to  $E_S[(n-1-N)\Delta\omega]$  for  $n = N/2+2, \dots, N$ .

Since, in this work it is sufficient to evaluate the transient signal for times,  $t$  very close to the occurrence of a phase reversal ( $t' \approx \tau$ ) and since  $E(\omega)$  is significant only in a very narrow band about  $\omega_c$ ,  $|\omega-\omega_c| \leq \omega_o$  (3.18) can also be approximated by

$$\begin{aligned} e_S(t) &= \int_{\omega_1}^{\omega_2} E_S(\omega)\exp(-i\omega t)d\omega = \exp(i\omega_o t) \int_{-\omega_o}^{\omega_o} E_S(\omega')\exp(i\omega' t)d\omega' \\ &\equiv \exp(i\omega_c t)h_S(t) \end{aligned} \quad (3.19)$$

where

$$-\omega_o \leq \omega' = \omega - \omega_c \leq \omega_o, \quad \omega_1 = \omega_c - \omega_o, \quad \omega_2 = \omega_c + \omega_o$$

and

$$\frac{k_1}{f_c} \leq t' = t - \tau_T \leq \frac{k_2}{f_c} \quad (3.20)$$

Recall that since the signal is represented by a complex function  $f_S(t)$ ,  $|E(-\omega_c)| \ll |E(\omega_c)|$  and by neglecting the contribution about  $-\omega_c$  only a small error is introduced. Thus  $h_S(t)$  corresponds to the envelope of the transient response processed by a low pass filter.

When  $\omega_2 \ll \omega_{\max}$  and  $(k_1+k_2)/f_c \ll T$ , (3.19) is evaluated by direct summation. Hence

$$e_s^*(k) = \frac{1}{T} \sum_{n=n_1}^{n_2} E_s^*(n) \exp[-2i\pi(n-1)(k-1)/N] \quad (3.21a)$$

where

$$\omega_1 = (n_1-1)\Delta\omega \quad \text{and} \quad \omega_2 = (n_2-1)\Delta\omega \quad (3.21b)$$

#### 4. Illustrative Examples

For all the illustrative examples presented here, the carrier frequency is  $f_c = \frac{c}{\lambda} = 1.5$  GHz ( $\lambda = 0.2$  m is the free space wavelength). The inhomogeneous anisotropic ionosphere is characterized by the plasma, collision and gyrofrequencies  $\omega_p, \nu$  and  $\omega_H$  respectively. The variable plasma frequency is given by

$$X(z) = (f_p(z)/f)^2 = \frac{X_1}{2} [1 - \cos 2\pi z/L] \quad 0 \leq z \leq L \quad (4.1a)$$

where

$$X_1 = X(L) = (f_p(L)/\omega)^2 = (\lambda/\lambda_p(L))^2$$

The variable collision frequency is given by

$$Z(z) = \nu(z)/\omega = Z_1 \exp(-\gamma z) \quad 0 \leq z \leq L \quad (4.2a)$$

where

$$Z_1 = Z(0) = \nu(0)/\omega = \lambda/\lambda_\nu(0) \quad (4.2b)$$

and

$$\lambda_\nu(0) = 30\text{m}, \quad \gamma = 8.10^5 \text{m}^{-1} \quad (4.2c)$$

The gyrofrequency is given by

$$Y(z) = f_H/f = \lambda/\lambda_H \quad (4.3a)$$

where

$$\lambda_H = 300\text{m} \quad (4.3b)$$

The direction of the earth's magnetic field  $\bar{a}_H$  is given by

$$\bar{Y} = \bar{a}_H Y = (0.7 \bar{a}_x + 0.7 \bar{a}_y + 0.1414 \bar{a}_z) Y \quad (4.4)$$

In Figures 2 through 7,  $\lambda_p = 75$  m,  $L = 150$  km and the angle of incidence is  $\theta = 0$  ( $s=0$ ). The duration of the signal is  $T = 40/f_c$  and the bandwidth of the filter is  $0.4 f_c$ . For the evaluation of the FFT,  $N = 512$  (3.16).

In Figures 2 through 4, the horizontally polarized transmitted signal excited by a horizontally polarized incident signal is presented and in Figures 5 through 7 the vertically polarized transmitted signal excited by a horizontally polarized incident signal is presented. Figures 2 and 5 are plots of the normalized transient signals (FFT)  $e(t'-\tau)$  and (analytical)  $e_A(t'\tau)$  ((3.13a) and (3.13b) respectively). Figures 3 and 6 are plots of the difference  $\Delta e(t')$ , (3.15) and Figures 4 and 7 are plots of the instantaneous phase deviation (3.6b). Note that for the unpolarized signals  $\Delta\phi(t)$  increases continuously by  $\pi$  radians at  $t' = \tau$  while  $\Delta\phi(t)$  decreases continuously by  $\pi$  radians at  $t' = T$  for the depolarized signals. This is a principal distinguishing feature between the depolarized and unpolarized signals. Since the circularly polarized signals are superpositions of the linearly polarized signals presented here, the same conclusions hold for the circularly polarized waves.

In Figures 8 through 13,  $\lambda_p = 25$  m,  $L = 500$  km. The duration of the pulse is  $T = 2^{13}/6.4f_c = 8.533 \times 10^{-7}$  s,  $4/f_c < t' - \tau < 50/f_c$  and the bandwidth of the filter is  $0.05 f_c$ . For the evaluation of the inverse transform, (3.18),  $N = 2.0^{14}$ . In Figures 8-11,  $\theta = 45^\circ$  and contributions from outside the two bands  $-\omega_c < \omega \mp \omega_c < \omega_0$  are neglected, and in Figures 12 and 13,  $\theta = 0^\circ$  and contributions from outside the single band  $-\omega_1 < \omega - \omega_c < \omega_1$  are neglected (3.21). In view of the bandwidth of the filter, in these computations  $2\omega_0 = 0.125 \omega_c$ . In Figures 8, 9 and 12 the incident and transmitted waves are vertically polarized and in Figures 10, 11 and 13 the incident wave is vertically polarized but the transmitted wave is horizontally polarized. In Figures 8 and 10, the normalized transient response is plotted and in Figures 9, 11, 12 and 13 the envelope (3.5) and the instantaneous phase (3.6) are plotted. These plots of  $\phi(t)$  show the same distinguishing feature between the depolarized and nondepolarized waves as noted before. Except for the small ripples, the envelopes in Figures 9 and 11 are the same as the envelope of the transient response processed by a low pass filter. These small ripples do not exist in Figures 12 and 13 where contributions from outside the single band  $-\omega_1 < \omega - \omega_c < \omega_1$  are neglected (3.21).

In all the illustrative examples the transfer functions  $T_{PQ}(\omega)$  are evaluated using the recursion formula (4.6) with partition size  $\Delta z = L/M = L/40$ . In Table 1 the values of  $|T(\omega_c)|$ ,  $\psi_T(\omega_c)$  and the delay  $\tau_T$  (3.7) are given for all four transmission coefficients  $T_{PQ}(\omega)$ . The shift in the phase reversal caused by the filter  $\tau_P$  (3.12) is also given in the Table.

## 5. Concluding Remarks

To illustrate the ionosphere effects on L-band signals coded by phase reversals, several examples are presented in Section 4. An analytic expression for an undistorted coded signal through a medium characterized by the same phase shift, attenuation and delay as the transmitted signal but without the dispersive properties of the ionosphere is also derived. The difference between the transient response and this "undistorted" signal illustrates the dispersive effects of the ionosphere on the coded signals. The envelope of the received signal is approximately the envelope of the transient response processed by a low pass filter. An interesting feature that distinguishes between the depolarized and nondepolarized signals is the instantaneous phase as shown by the plots of  $\Delta\phi(t)$ , (3.6).

## 6. Acknowledgments

This work was supported by the National Science Foundation, the U. S. Army Research Office and the Engineering Research Center of the University of Nebraska. The full paper will be published in Radio Science.

TABLE 1  
TRANSMISSION COEFFICIENTS  $T_{PQ}(\omega_c)$ , TRANSMISSION DELAYS  $\tau_T$   
AND FILTER DELAY  $\tau_F$

Angle of incidence  $\theta = 45^\circ$  and  $\tau_F = 1.1096 \times 10^{-8}$  s

Polarization	HH	VH	HV	VV
$ T(\omega_c) $	0.98829	0.14027	0.14027	0.98829
$\psi_T(\omega_c)$ (rad)	-2.4068	0.73451	-2.4064	-2.4067
$\tau_T(\omega_c) \times 10^8$ s	9.5713	9.5713	9.5713	9.5713

## APPENDIX A

Equation (2.16) is reformulated as the following integral equation:

$$g_m(z) = g_m(z_T) \exp\left\{ \int_{z_T}^z C_{mm}(v) dv \right\} + \sum_{n \neq m} C_{mn}(z') g_n(z') \exp\left\{ \int_{z'}^z C_{mm}(v) dv \right\} dz' \quad (A.1)$$

in which the symbol  $\sum_{n \neq m}$  implies that the summation does not include the term  $n = m$ . The first term in (A.1) constitutes the phase memory type solution. By virtue of the transformations discussed in Section 2 even in critical coupling regions where  $\frac{\omega_p}{\omega} \approx c = \cos \theta$ ,  $|C_{nm}| \ll 1$  for  $n \neq m$ . Applying (A.1) to an inhomogeneous slab of width  $\Delta z$  where

$$\Delta z = L/M \quad (A.2)$$

the expression for  $g_n(z')$  in the coupling term is replaced by the first order iterative solution

$$g_n(z) = f_n(z_T) \exp\left\{ \int_{z_T}^z C_{nn}(v) dv \right\} \quad (A.3)$$

and the coupling term  $C_{mn}(z')$ , ( $n \neq m$ ) is replaced by the first three terms of its Taylor series expansion

$$C_{mn}(z) \approx C_{mn}(z_c) + C'_{mn}(z_c)(z-z_c) + C''_{mn}(z_c) \frac{(z-z_c)^2}{2} \quad (A.4)$$

where  $z = z_c$  at the center of the partition of width  $\Delta z$ . Thus we set

$$z_T = L - p\Delta z, \quad z_B = L - (p+1)\Delta z, \quad z_c = L - (p+1/2)\Delta z \quad (A.5)$$

for  $p = 0, 1, 2, \dots, M$ , and integrate with respect to  $z'$  ( $z_T < z' < z_B$ ) to obtain the following recurrence formula for the wave amplitudes  $g_m(z_B) \equiv g_m(p+1)$  in terms of  $g_m(z_T) \equiv g_m(p)$  and the coupling terms

$$C_{mn}(z_c) \equiv C_{mn}(p+1/2)$$

$$g_m(p+1) = P_m^-(p+1/2) \left[ g_m(p) P_m^+(p+1/2) + \sum_{n \neq m} D_{mn}(p+1/2) g_n(p) P_n^+(p+1/2) \right] \quad (A.6)$$

$$P_m^\pm(p+1/2) = \exp\left[ -\frac{\Delta z}{2} \left\{ C_{mn}(p+1/2) \pm \frac{\Delta z}{4} C'_{mn}(p+1/2) + \frac{(\Delta z)^2}{24} C''_{mn}(p+1/2) \right\} \right] \quad (A.7)$$



$$D_{mn}(p+1/2) \equiv -\Delta z \operatorname{sinc} \theta_{mn} \left[ C_{mn}(p+1/2) + \frac{i\Delta z}{2} C'_{mn}(p+1/2) \left[ \frac{1-\theta_{mn} \cot \theta_{mn}}{\theta_{mn}} \right] + \frac{(\Delta z)^2}{8} C''_{mn}(p+1/2) \left\{ 1 - \frac{2(1-\theta_{mn} \cot \theta_{mn})}{\theta_{mn}^2} \right\} \right] \quad (\text{A.8})$$

and

$$\theta_{mn} = \frac{i\Delta z}{2} [C_{mm}(p+1/2) - C_{nn}(p+1/2)] \quad (\text{A.9})$$

The derivatives of the coupling coefficients  $C_{mn}(q+1/2)$  are

$$C'_{mn}(p+1/2) = [C_{mn}(p) - C_{mn}(p+1)]/\Delta z \quad (\text{A.10})$$

and

$$C''_{mn}(p+1/2) = [C_{mn}(p+1) + C_{mn}(p) - 2C_{mn}(p+1/2)](2/\Delta z)^2 \quad (\text{A.11})$$

## References

BAHAR, E., 1976, "Generalized Characteristic Functions for Simultaneous Linear Differential Equations with Variable Coefficients Applied to Propagation in Inhomogeneous Anisotropic Media," *Can. J. Phys.*, **54**, pp. 301-316.

BAHAR, E. and B. S. AGRAWAL, 1978, "Ionosphere Effects on Navigational and Positioning Signals--Full-Wave Solutions," *IEEE Transactions on Antennas and Propagation* (in press).

BRIGHAM, E. Oran, 1974, "The Fast Fourier Transform," Prentice-Hall, Inc., Englewood Cliffs, NJ.

BUDDEN, K. G., 1961, "Radio Waves in the Ionosphere," Cambridge University Press, London.

KERNS, D. M., 1976, "Plane-Wave Scattering-Matrix Theory of Antennas and Antenna-Antenna Interactions: Formulation and Applications," NBSIR 75-824, National Technical Information Service (NTIS), Springfield, VA 22151.

## ILLUSTRATIONS

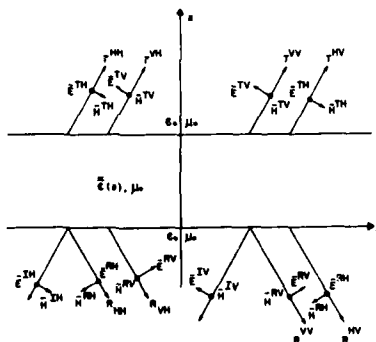


Fig. 1 Propagation of horizontally and vertically polarized waves through inhomogeneous magnetoionic media.

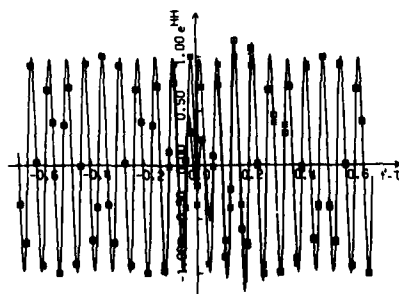


Fig. 2 Transient response for horizontally polarized transmitted signal excited by horizontally polarized incident waves,

$$e^{HH}(t'-\tau)\text{FFT} (\square); e_A^{HH}(t'-\tau) \text{ analytical} (*).$$

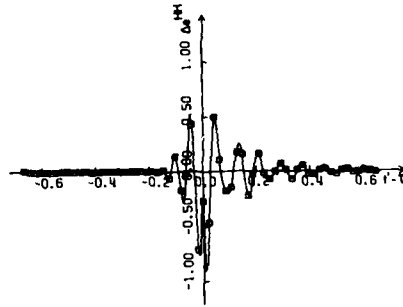


Fig. 3 The difference between the FFT and analytical solutions  $\Delta e^{HH}(t'-\tau)$ .

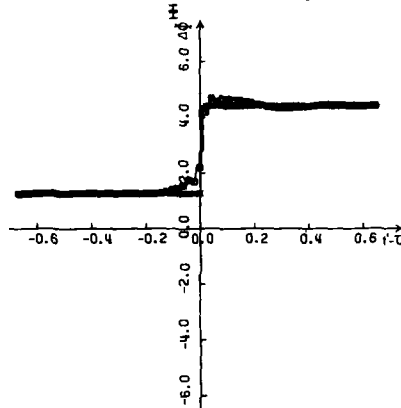


Fig. 4 Instantaneous phase deviation  $\Delta \phi^{HH}(t'-\tau)$  FFT(n); analytical (\*).

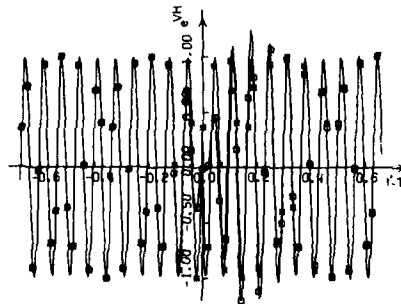


Fig. 5 Transient response for vertically polarized transmitted signal excited by horizontally polarized incident wave  $e^{VH}(t'-\tau)$  FFT(n);  $e_A^{VH}(t'-\tau)$  analytical(\*).

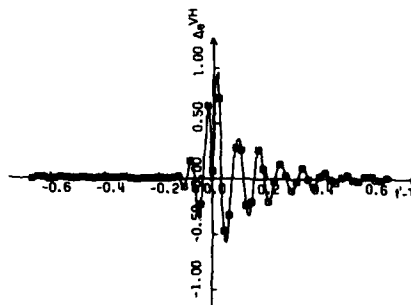


Fig. 6 The difference between the FFT and analytical solutions;  $\Delta e^{VH}(t'-\tau)$

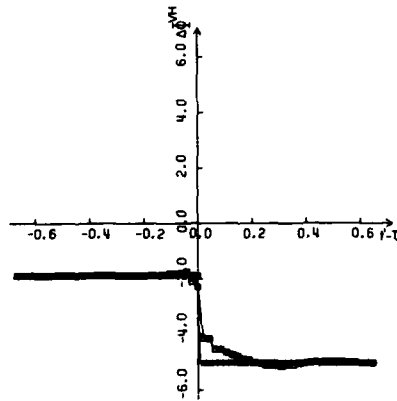


Fig. 7 Instantaneous phase deviation  $\Delta\phi^{VH}(t'-\tau)$  FFT( $\square$ ); Analytical (\*).

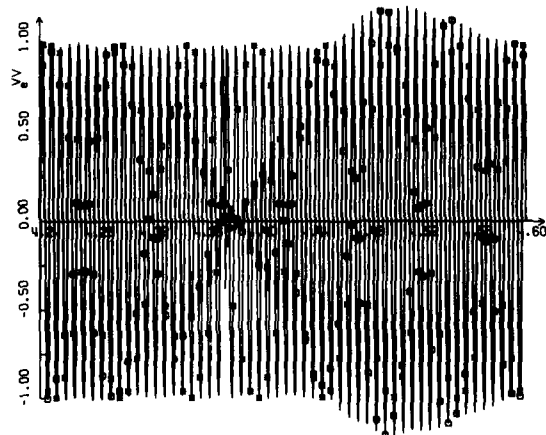


Fig. 8 Transient response for vertically polarized transmitted signal excited by vertically polarized incident wave  $e^{VV}(t')$  FFT( $\square$ );  $e_A^{VV}(t')$  analytical (\*).

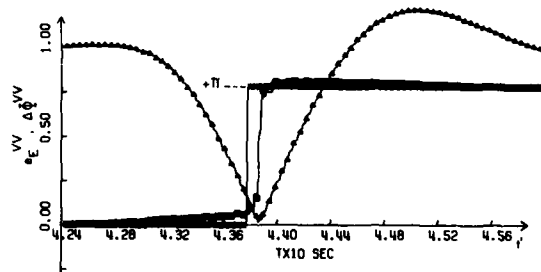


Fig. 9 Instantaneous phase deviation  $\Delta\phi^{VV}(t')$ ; FFT( $\square$ ), analytical (\*). Envelope  $e_E^{VV}(t')$  ( $\Delta$ ).

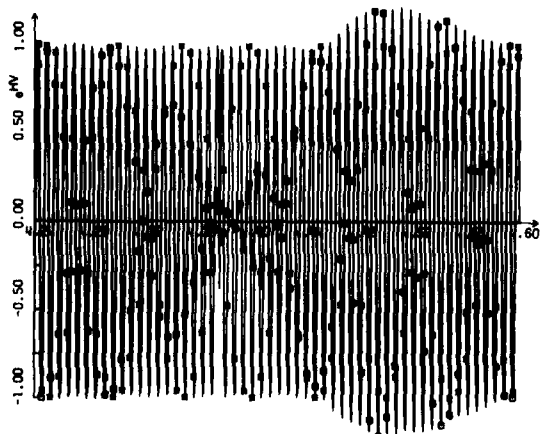


Fig. 10 Transient response for horizontally polarized transmitted signal excited by vertically polarized incident wave.  $e^{HV}(t')$  FFT( $\square$ );  $e_A^{HV}(t')$  analytical (\*).

AD-A090 850

ADVISORY GROUP FOR AEROSPACE RESEARCH AND DEVELOPMENT--ETC F/G 20/14  
PROPAGATION EFFECTS IN SPACE/EARTH PATHS.(U)

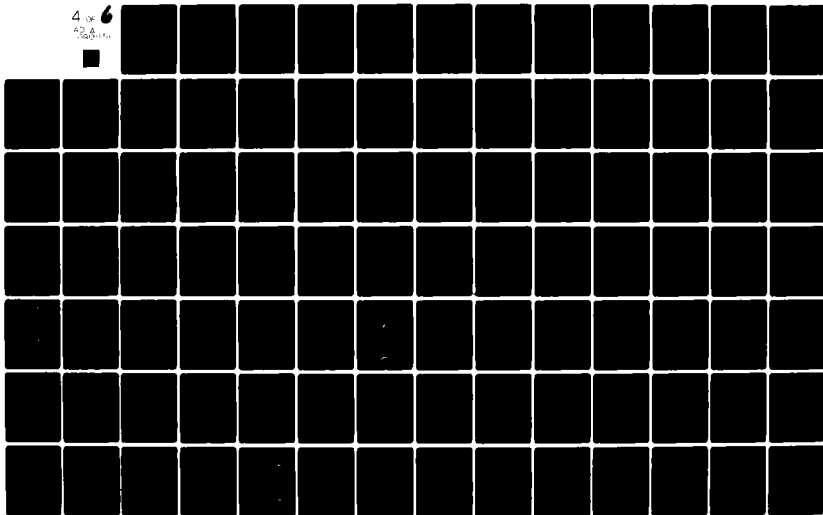
AUG 80 H J ALBRECHT

AGARD-CP-284

NL

UNCLASSIFIED

4 x 6  
42.6  
100.0



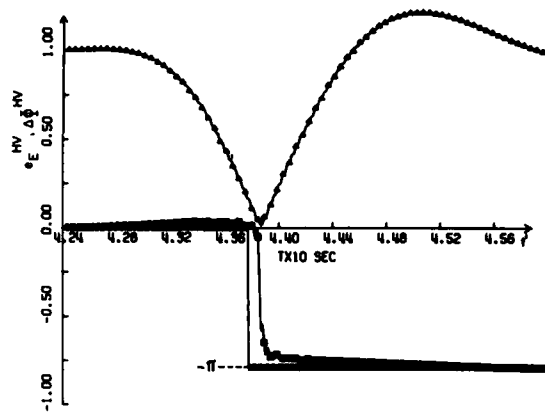


Fig. 11 Instantaneous phase deviation  $\Delta\phi^{HV}(t')$ ; FFT( $\square$ ), analytical (\*).  
Envelope  $e_E^{HV}(t')$  ( $\Delta$ ).

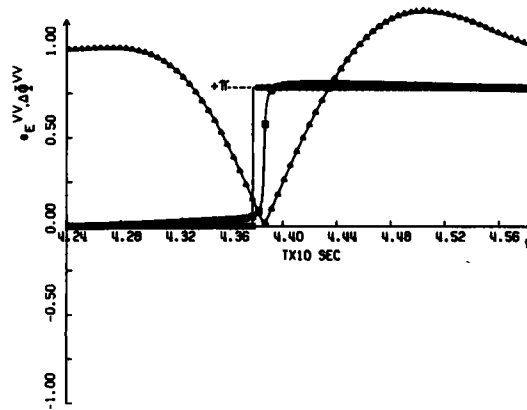


Fig. 12 Instantaneous phase deviation  $\Delta\phi^{VV}(t')$ ; FFT( $\square$ ), analytical (\*).  
Envelope  $e_E^{VV}(t')$  ( $\Delta$ ) Contributions only from single band  $-\omega_0 < \omega - \omega_c < \omega_0$ .

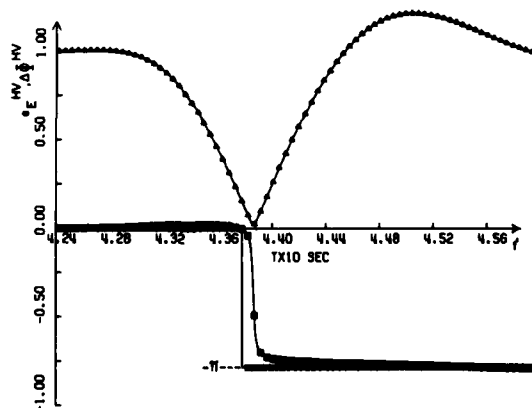


Fig. 13 Instantaneous phase deviation  $\Delta\phi^{HV}(t')$  FFT( $\square$ ), analytical (\*).  
Envelope  $e_E^{HV}(t')$  ( $\Delta$ ). Contributions only from single band  $-\omega_0 < \omega - \omega_c < \omega_0$ .

1979-1980 DATA PROCESSING AND RESULTS FROM THE  
OTS BEACONS BO/B1 AND TM, AND RADIOMETRY AT 11.4 AND 35 GHz

A. VANDER VORST, P. SOBIESKI

Laboratoire de Télécommunications et d'Hyperfréquences  
Université Catholique de Louvain

Louvain-la-Neuve, BELGIUM

ABSTRACT

*Measurements are described, on the beacons BO/B1 and TM/TM of the satellite OTS of E.S.A., as well as by a dually polarised radiometer at 12 GHz and by a radiometer at 35 GHz. This yields the simultaneous recording of the copolar and the crosspolar components of the beacon, two sky temperatures at 12 GHz in orthogonal linear polarisation as well as the differential sky temperature at the same frequency, and the sky temperature at 35 GHz.*

*Data processing has been improved to compensate for regular (for instance, daily) variations of the clear sky level of the copolar signal, the crosspolar discrimination and its phase. Ranging operation on TM is also processed. This yields compensated data which can be more readily processed and understood.*

*Typical examples are given.*

INTRODUCTION

Measurements on atmospheric microwave propagation are carried out since about ten years at the Telecommunications and Microwaves Laboratory of the University of Louvain, Belgium. The present experiments involve two earth-stations, respectively with a 5 m and a 3 m dish, and two radiometers, respectively at 11.4 and 35 GHz (this last one can be used as a sun-tracker). There is also a mobile station with a 1.2 m dish; it will not be mentioned in this presentation, however.

The basic equipment and the basic data processing system have already been described (Laloux et al., 1979).

The main dish is located at Louvain-la-Neuve. Linearly polarised, it is able to receive the TM/TM beacons, as well as to transmit and to receive a color television signal. This paper only covers experiments on TM. The 3 m dish is located at Lessive. Circularly polarised, it receives the BO/B1 beacons. The 12 GHz radiometer has a dual linear polarisation feeder, hence it delivers two temperatures as well as the temperature difference. The 35 GHz radiometer has one linear polarisation.

This paper shows how measurements on the copolar and the crosspolar signals, as well as their relative phase, are compensated for clear-sky diurnal variations, which include all effects except the atmospheric ones (level of the beacon and attitude of the antennas at the satellite and at the earth station). The effect of the compensation is illustrated by various examples. A correction for the ranging operation on TM is also used and illustrated. Finally, several examples are given of simultaneous measurements on TM, copolar and crosspolar, and on the 35 and 12 GHz radiometer, this last one with the three temperature outputs. One of the samples shows an important temperature difference between the two channels of the 12 GHz radiometer, of the order of 50°K (1.5 dB), which cannot be explained by the classical radiative transfer theory.

COMPENSATION FOR THE CLEAR-SKY DIURNAL VARIATION

There are diurnal and seasonal variations of the amplitude of the copolar and crosspolar signals, as well as of their relative phase, due to the satellite (position, antennas, influence of the sun) and to the earth-station (antennas). They can be important for a non-tracking system. They make it more difficult to analyze the data due to meteorological events, especially those of rather small amplitude.

Hence a procedure has been developed to extract regular variations from the daily data. The principle of the numerical cancellation has already been presented (Delogne et al., 1977) as well as an example of application (Vander Vorst, 1980).

The first compensation acts on the values of the copolar and of the discrimination. Every period of one day is divided into 96 periods of 15 minutes. In each of these subperiods, and only if there is no meteorological event, a temporal mean value is calculated separately on the value of the copolar signal, as well as on the cartesian complex components of the crosspolar discrimination (hence not on the crosspolar signal). The procedure takes into account the values reached by those components at about the same time (within a

period of 15 minutes) for 3 to 5 consecutive days. It produces for every day the mean "clear-sky" diurnal behavior of the copolar signal, and of the crosspolar discrimination as a set of 96 complex quantities. This mean value is then vectorially subtracted from the recorded data, which yields the set of corrected copolar and crosspolar discrimination data.

Figure 1 shows the calculated mean value on  $B_0$  for the period extending from July 5 to July 12, 1979. The figure shows the value calculated from five samples (hence, five days) for every period of 15 minutes; the samples are represented by dots. The example illustrates the diurnal "clear-sky" variation of the link for a non-tracking 3 m antenna. Figure 2 shows the comparison on  $B_0$  between a set of rough recorded data for 10 days (non compensated) and the set of compensated data in the copolar case. Figure 3 illustrates the same comparison for the crosspolar discrimination. It is quite obvious that the meteorological events are much more apparent in the compensated data. A small difficulty arises from the fact that, due to the procedure, the average level of the copolar signal is about zero, which yields negative values for the "attenuation". On the other hand, the average level of the crosspolar discrimination is of course much higher after the compensation : there is a difference of more than 15 dB.

Finally, figure 4 shows the comparison of a monthly diagram of the rain rate, copolar signal, crosspolar discrimination and relative phase, before and after compensation.

Such a compensation is useful not only to produce monthly diagrams and statistics, but also to analyse particular events. A polar diagram of the crosspolar discrimination, indeed, may lead to important mis-interpretation if no correction has been made. It is mainly the relative phase between the copolar and the crosspolar signals, hence the phase of the discrimination, that yields such wrong interpretation.

To illustrate this, figures 5 and 6 show two typical examples. Each figure shows six diagrams. The first four diagrams pertain to non-compensated data : the copolar signal, the crosspolar signal, their relative phase, and a "polar" diagram of the crosspolar discrimination; this last diagram has a radial scale in decibels (from 35 dB at the center to 20 dB at the external limit). The last two diagrams show compensated data : the crosspolar level and the "polar" diagram; in this last one, the radial scale is not the same as in the first one, it now extends from 50 dB at the center to 20 dB at the external limit.

Figure 5 clearly shows an event where there is a definite phase behavior of  $90^\circ$ , which is apparent only after compensation. Figure 6, on the other hand, shows a more "clear-sky" behavior with small events for which there is no definite behavior for the phase : after compensation, the relative phase takes different values for the various events.

Those figures definitely show that, using non-tracking antennas, which will be the case in direct or semi-direct television or data transmission systems, one has to be very careful about the interpretation - hence the possible automatic cancellation - of non-compensated data.

#### CORRECTION FOR $TM/TM$ RANGING OPERATION

Ranging steps are present in the  $TM/TM$  beacon operation. Figure 7 shows what is a ranging step and how its presence does affect a daily record. Its influence is not negligible : there is a peak of about 1.5 dB and steps of a certain duration. To compensate for the ranging steps, the beginning and the end of the copolar thresholds are detected and the whole duration of the step, a new value is introduced which is at the level of the data before the perturbation starts. This procedure is presently in use, acting satisfactorily under clear sky conditions as well as during not too heavy rainy events. For important events, the correction has to be applied very carefully, in a manual mode, and sometimes completely avoided whenever impossible. Figure 8 shows the same data after compensation (October 6, 1979).

#### SIMULTANEOUS ANALOG RECORDS OF $TM$ AND 12 AND 35 GHz RADIOMETERS

The equipment presently in operation at Louvain-la-Neuve yields the following simultaneous analog records :

- one linear polarisation by radiometry at 11.4 GHz (V)
- the orthogonal linear polarisation by radiometers at the same frequency (H)
- the difference between the two corresponding temperatures ( $T_v - T_h$ )
- one linear polarisation by radiometry at 35 GHz (RAD 35)
- the copolar level of the  $DTS$  beacon  $TM/TM$  at 11.6 GHz (COPOLAIRE)
- the crosspolar level of  $TM/TM$  (CONTRAPOLAIRE)

The radiometers are oriented very near to the satellite direction. They are both linearly polarised : "vertical" at 35 GHz, and "vertical" and "horizontal" at 11.4 GHz. This last one radiometer is dually polarised which yields "vertical" and "horizontal" temperatures of the sky as well as the differential temperature between those.

Figure 9, 10 and 11 show three typical records. The scales are calibrated for the radiometers either in  $^\circ K$  or in dB, accounting for the attenuation calculated with an assumed atmosphere temperature equal to  $275^\circ K$ .

Figure 9 illustrates the fact that clouds are visible by 35 GHz radiometry even if they induce practically no attenuation on the beacon at 12 GHz. They may induce, however, important depolarisation phenomena, as is shown by the figure (February 25, 1980).

Figure 10 represents important events. The correlation between radiometry at 12 GHz and attenuation measured on the copolar beacon signal is quite obvious. The depolarisation, however, is rather small. There are distinct radiometric differences between 12 and 35 GHz, essentially due to clouds. There is practically no differential radiometric effect at 12 GHz, however (March 29, 1980).

Figure 11 represents a remarkable differential temperature effect at 12 GHz : there is a peak of 50°K difference between the two orthogonal polarisations, which is confirmed by a difference of about 1.5 dB between the two channels V and H. Such an effect is not explained by the classical radiative transfer theory. It coincides with absorption peaks at 12 GHz measured by radiometry (V and H), on the beacon at 12 GHz, and at 35 GHz (RAD 35). It clearly does not coincide with a peak on the crosspolar component of the beacon, which occurs about 5 minutes earlier. This last peak coincides with an intermediate absorption peak at 35 GHz, which does not appear at 12 GHz.

From the simultaneous recording on the various channels, it can be induced that there are events for which the sky temperature is lower at 35 GHz than at 12 GHz. It also seems that there is some correlation between the sky temperature at 35 GHz and the occurrence of beacon depolarisation. It is too early however, to make definite statements about these observations.

## CONCLUSIONS

Measurements on OTS (BO/B1 and TM/TM) are in progress, simultaneously with dual-polarisation radiometry at 12 GHz and radiometry at 35 GHz.

Data processing has been improved to compensate for regular variations of the clear-sky level of the copolar signal, the crosspolar discrimination and their relative phase. Ranging operation on TM beacon has also been processed.

This yields compensated data which can be more readily processed and understood.

The simultaneous recording of various channels will soon lead to a more detailed numerical analysis of typical events.

## ACKNOWLEDGMENTS

Acknowledgments are due to Professor A. Laloux for useful advice on numerical processing and for taking care of the processing management, to S. Jaspers for taking care of the earth station, to L. Collard who developed software and C. Maudoux for radiometric measurements.

## REFERENCES

- DELOGNE, P., SOBIESKI, P., "Fine structure of microwave cross-polarisation due to precipitation", Ann. Télécom., 32, 11-12, 1977, pp. 377-385.
- LALOUX, A., LOBELLE, M., SOBIESKI, P., VANHOENACKER, D., VANDER VORST, A., "Processing and preliminary conclusions on OTS-propagation data in Belgium", Proc. Telecom. 79, pp. 2.3.8.1 to 8.
- VANDER VORST, A., "Slant-path propagation research in Belgium", Tijdschrift N.E.R.G., 45, 2, 1980, pp. 105-111.



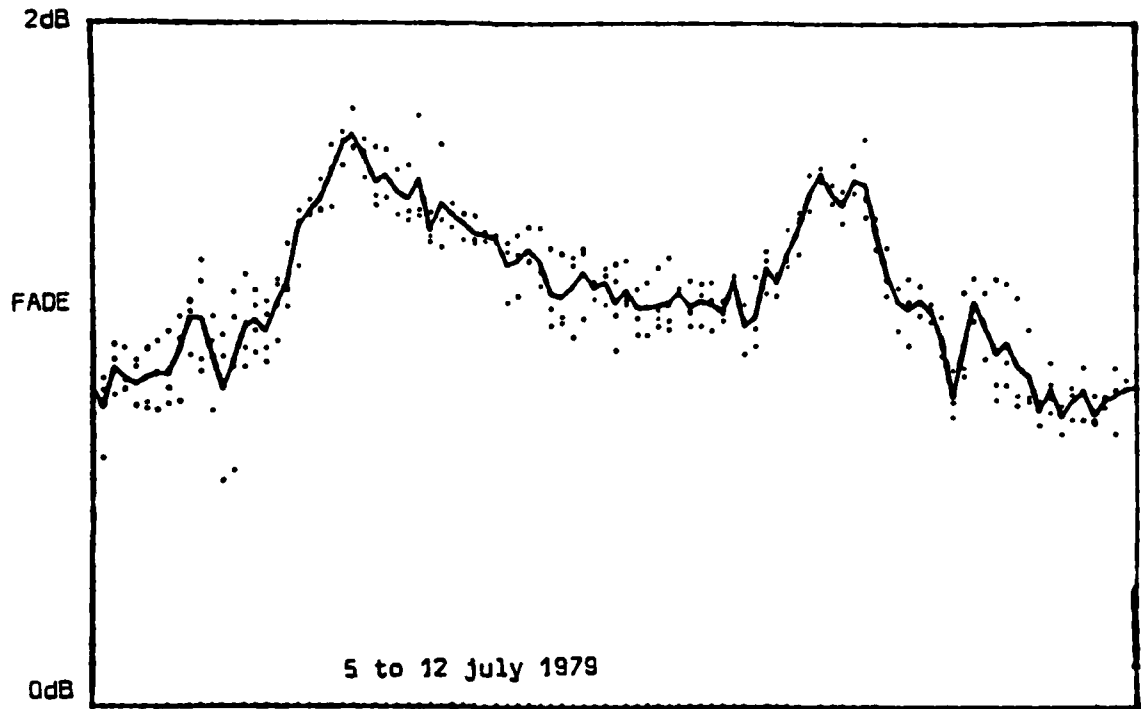


Figure 1. Diurnal mean variation on B0, averaged on five days.

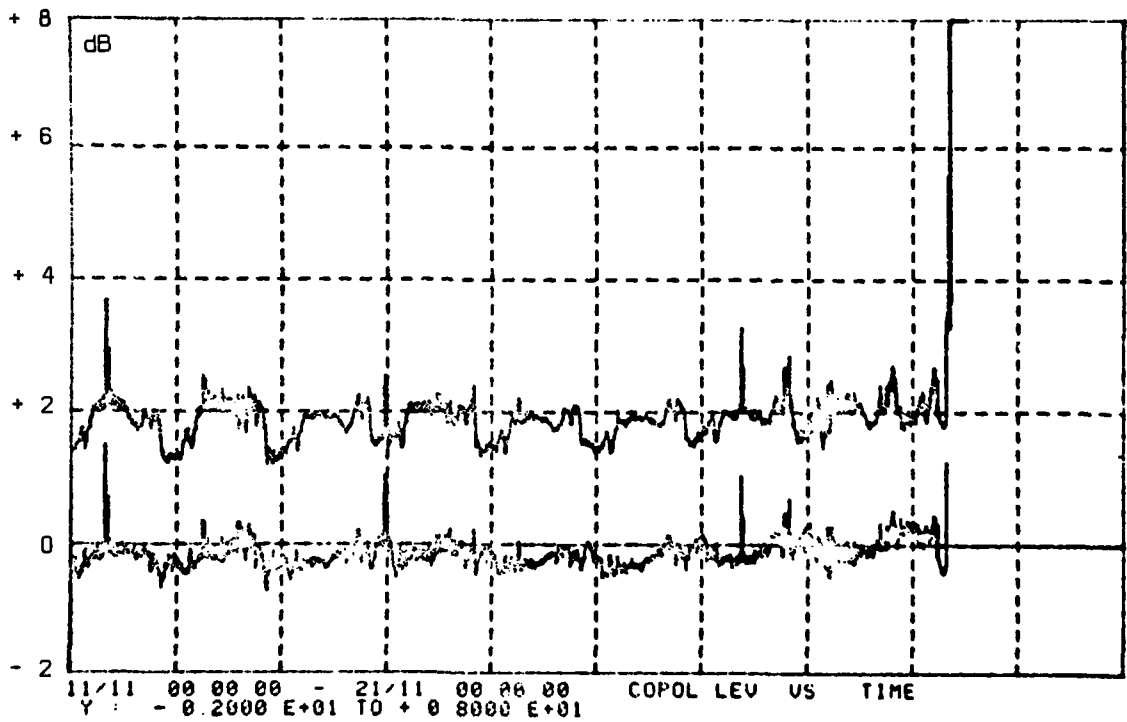


Figure 2. "Clear sky" correction on the copolar component of B0 (November 11 to 21, 1979).

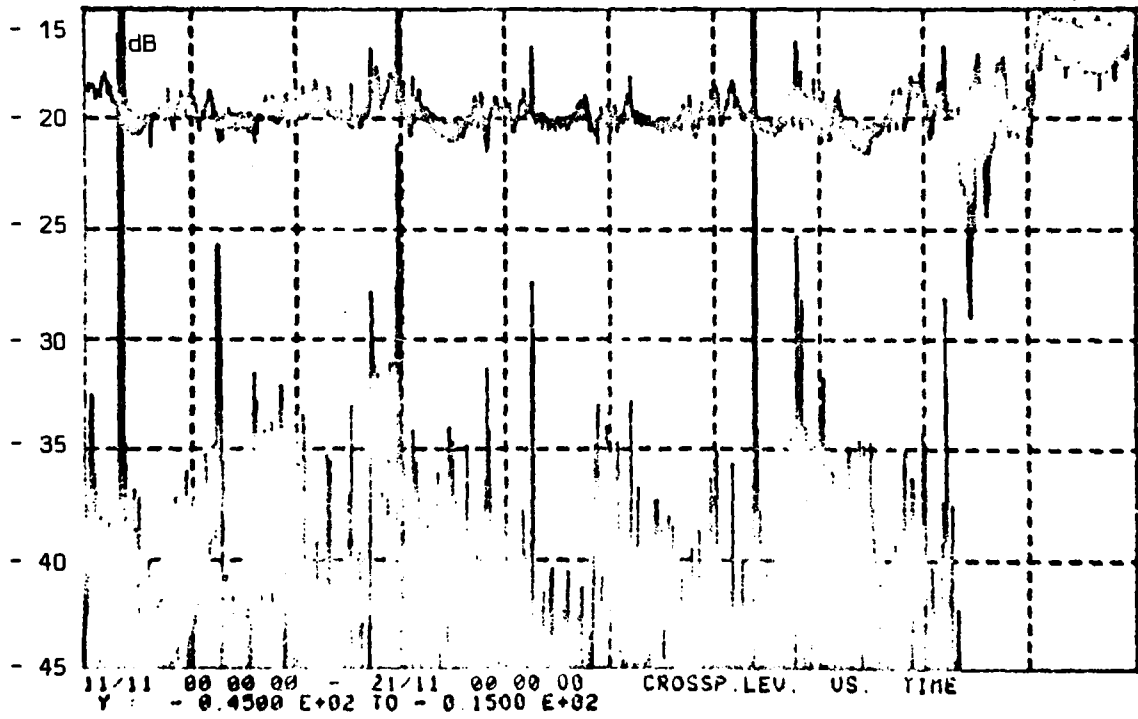


Figure 3. "Clear sky" correction on the crosspolar component of B0  
(November 11 to 21, 1979).

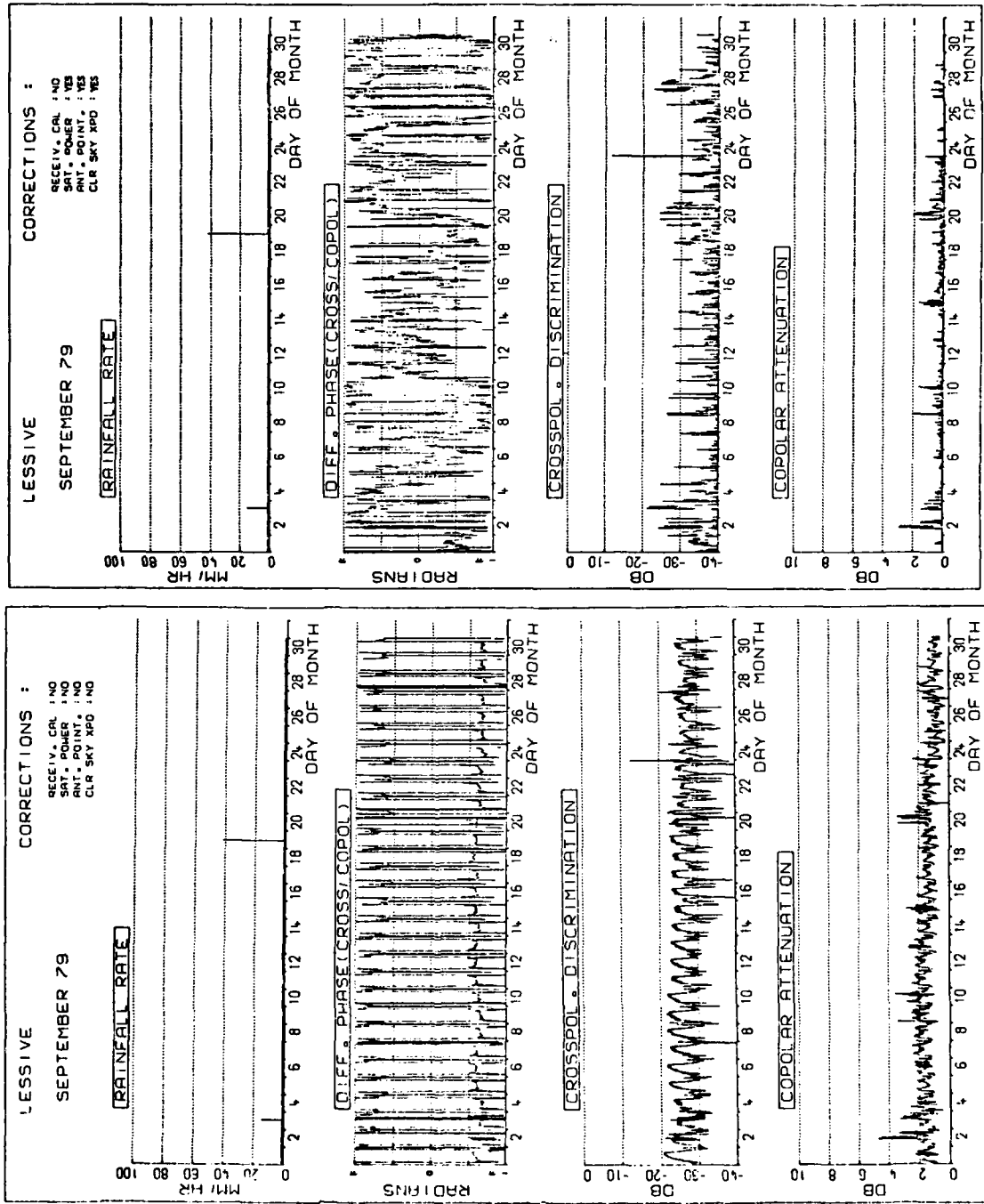


Figure 4. Comparison of monthly data, without and with compensation.

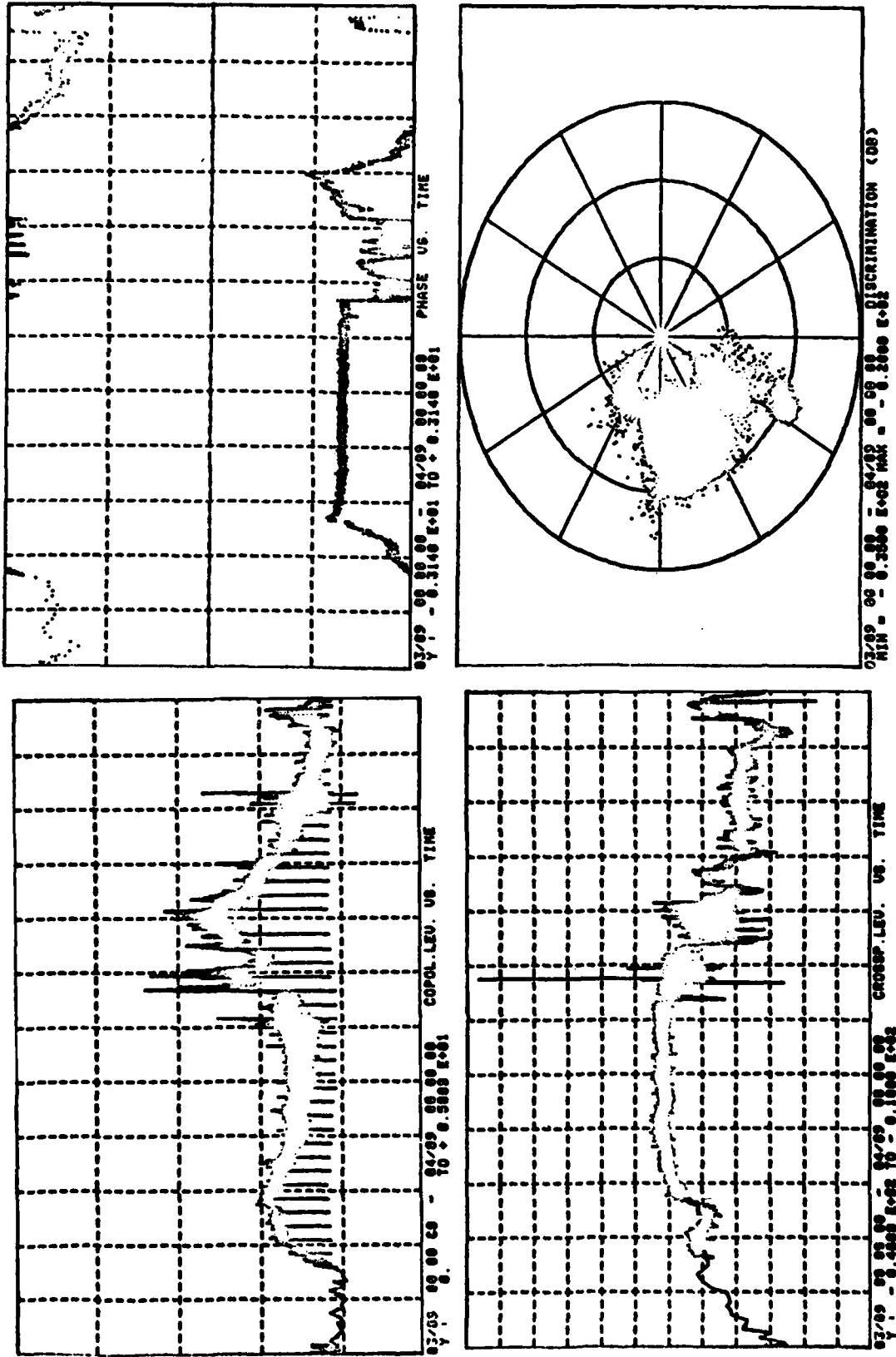
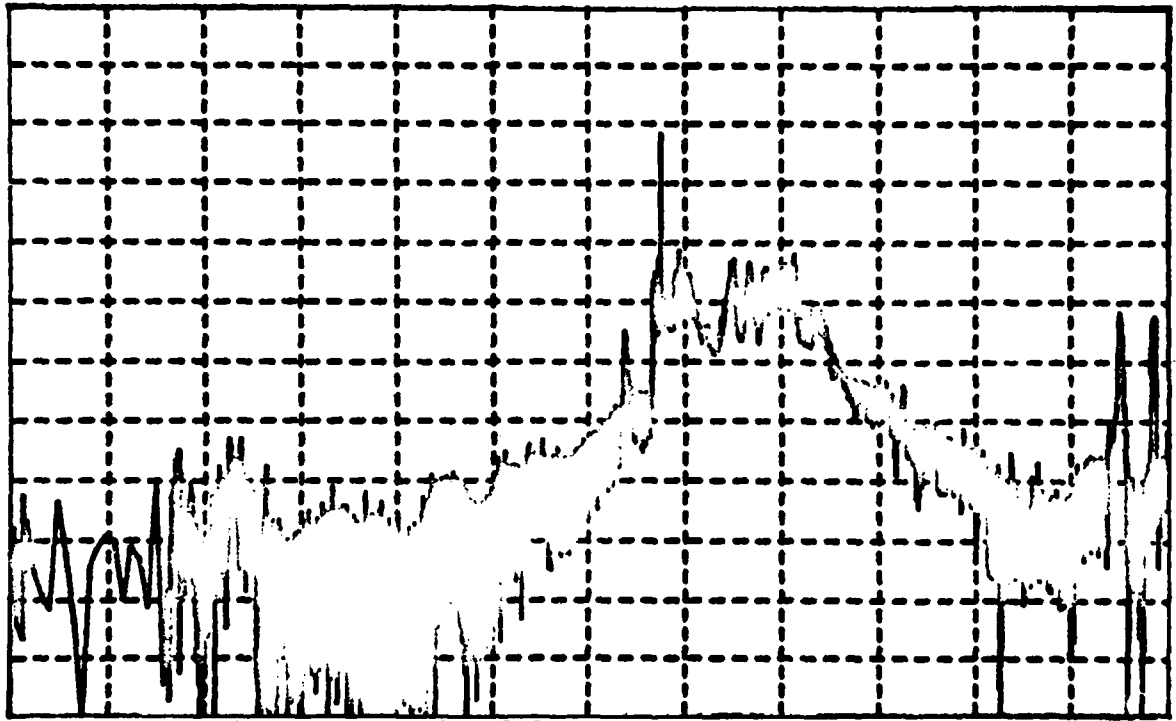
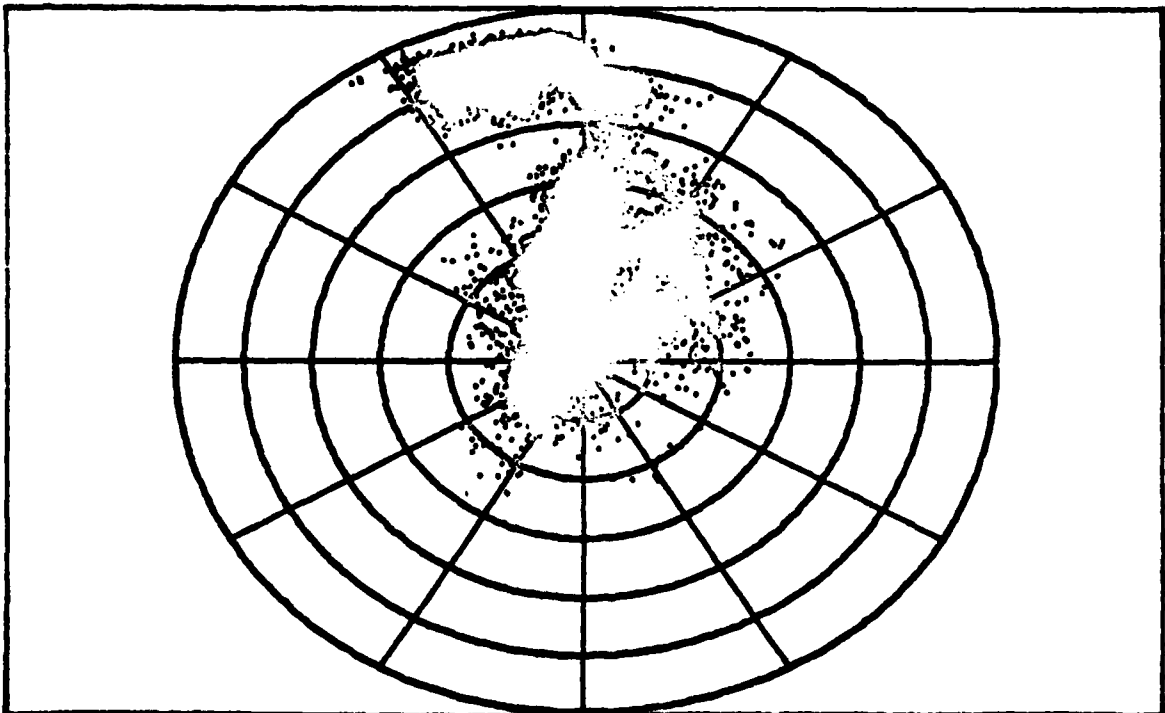


Figure 5.a. Copolar and crosspolar levels, phase and discrimination, before correction (September 3, 1979).



03/09 00 00 00 - 04/09 00 00 00 CROSSP.LEV. US. TIME  
Y 1 - 0.5000 E+02 TO 0.



03/09 00 00 00 - 04/09 00 00 00 DISCRIMINATION (DB)  
MIN = - 0.5000 E+02 MAX = - 0.2000 E+02

Figure 5.b. Crosspolar level and discrimination, after correction  
(September 3, 1979).

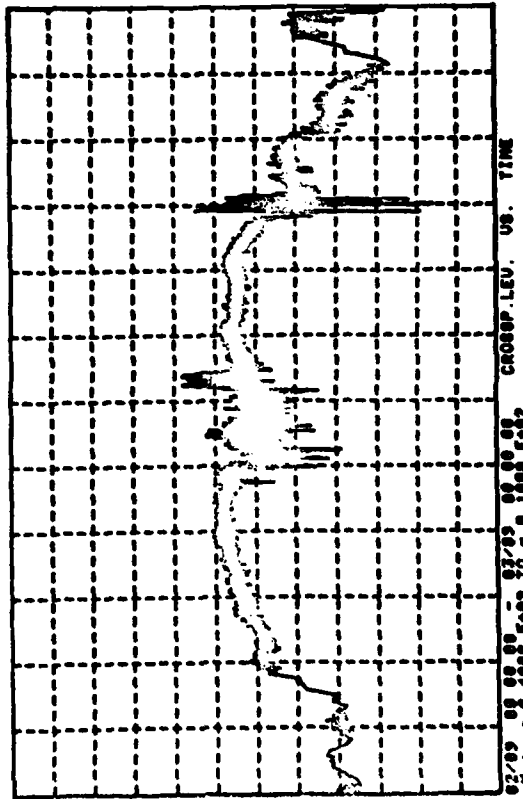
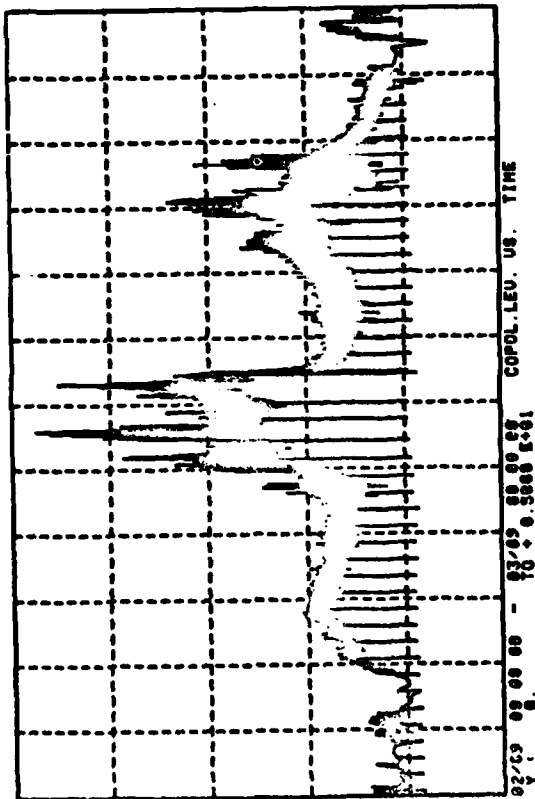
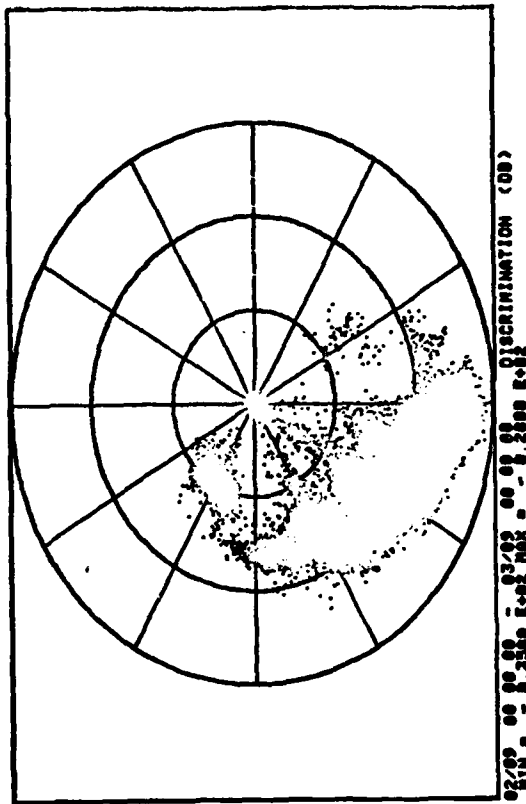
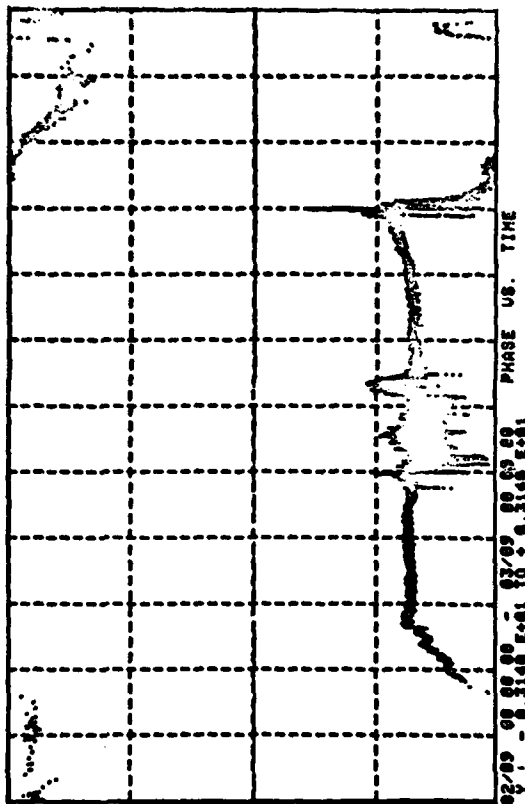
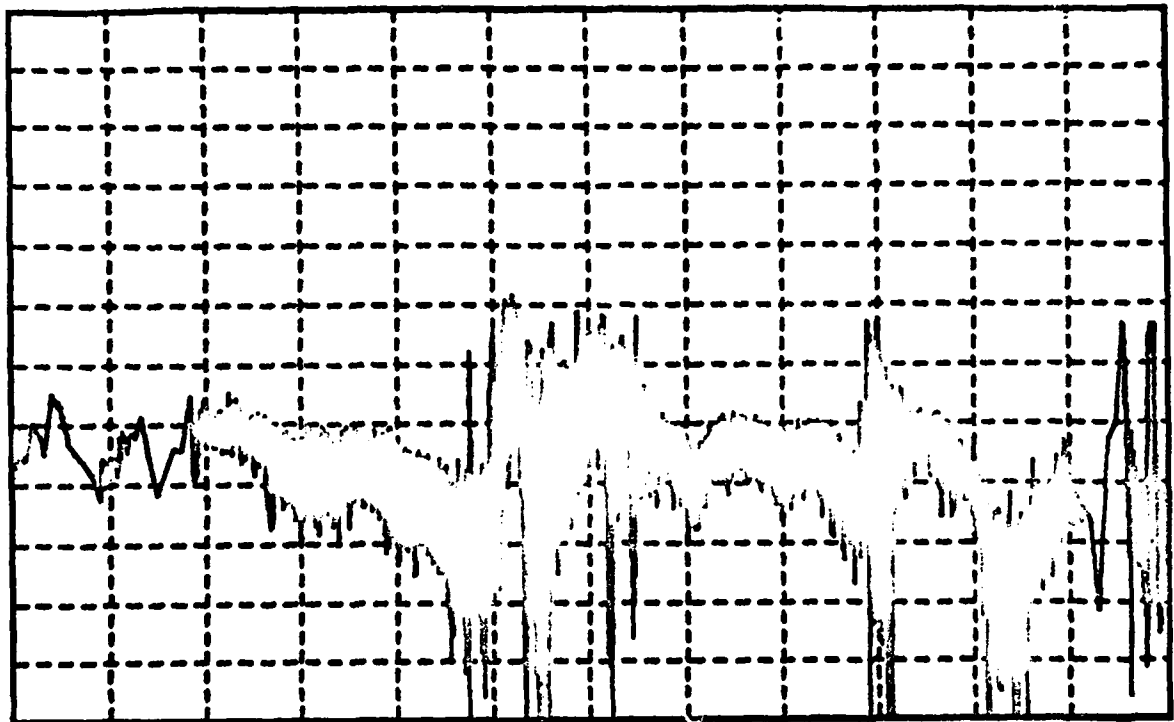
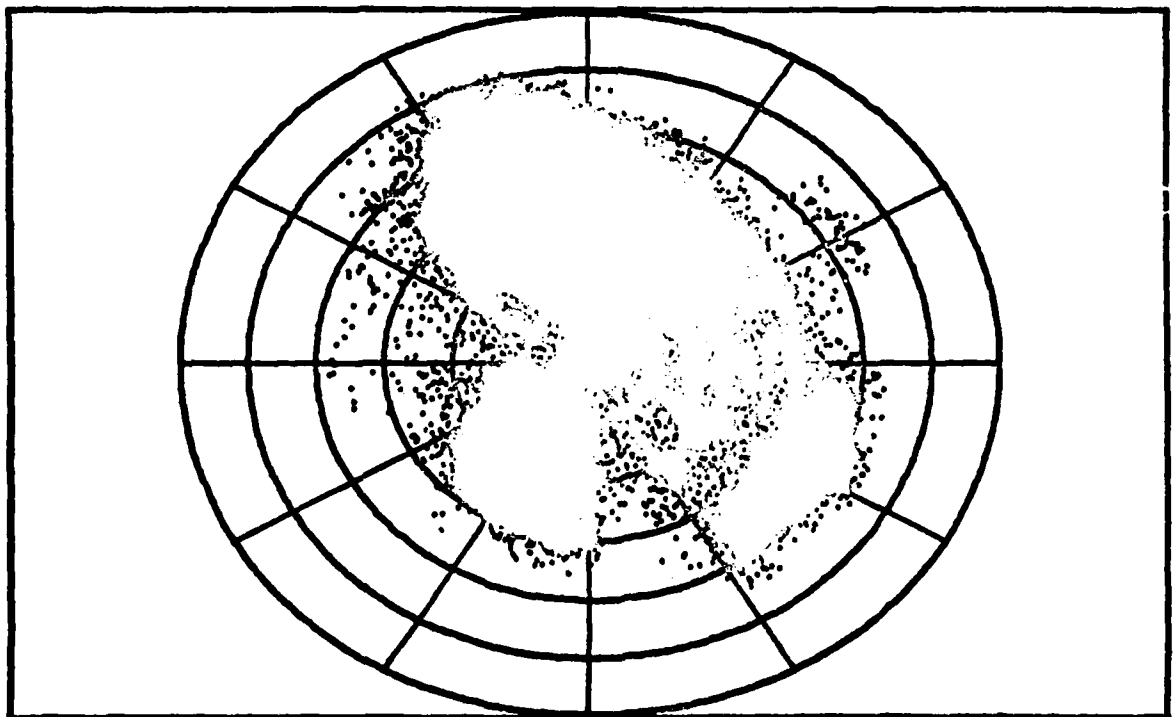


Figure 6.a. Copolar and crosspolar levels, phase and discrimination, before correction (September 2, 1979).



02/09 00 00 00 - 03/09 00 00 00 CROSSP.LEV. US. TIME  
 Y : - 0.6000 E+02 TO 0.



02/09 00 00 00 - 03/09 00 00 00 DISCRIMINATION (DB)  
 MIN = - 0.5000 E+02 MAX = - 0.2000 E+02

Figure 6.b. Crosspolar level and discrimination, after correction  
 (September 2, 1979).

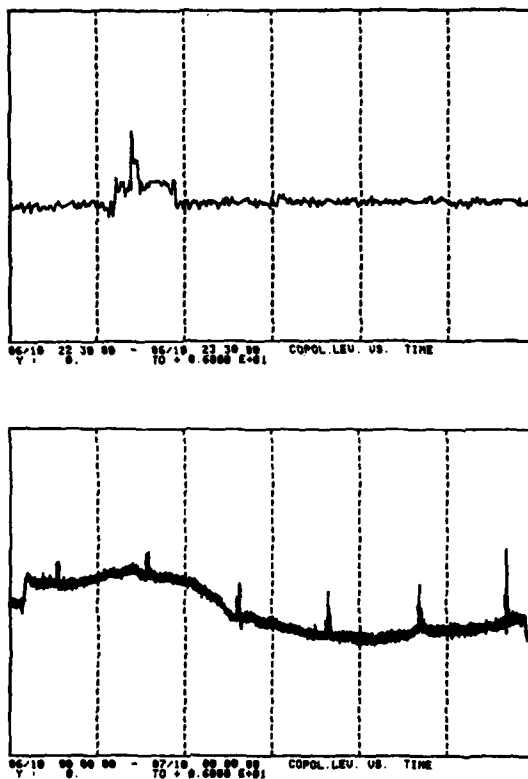


Figure 7. Ranging step (half-an-hour scale) and daily variation, before correction.

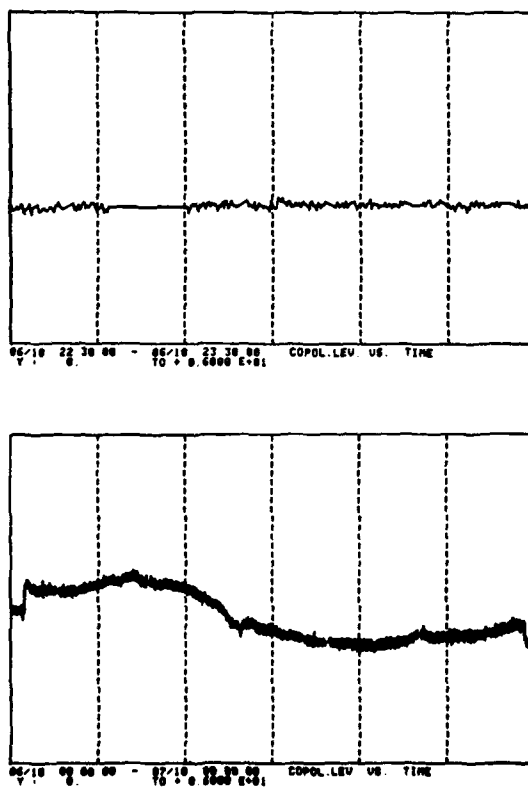


Figure 8. Ranging step (half-an-hour scale) and daily variation, after correction.



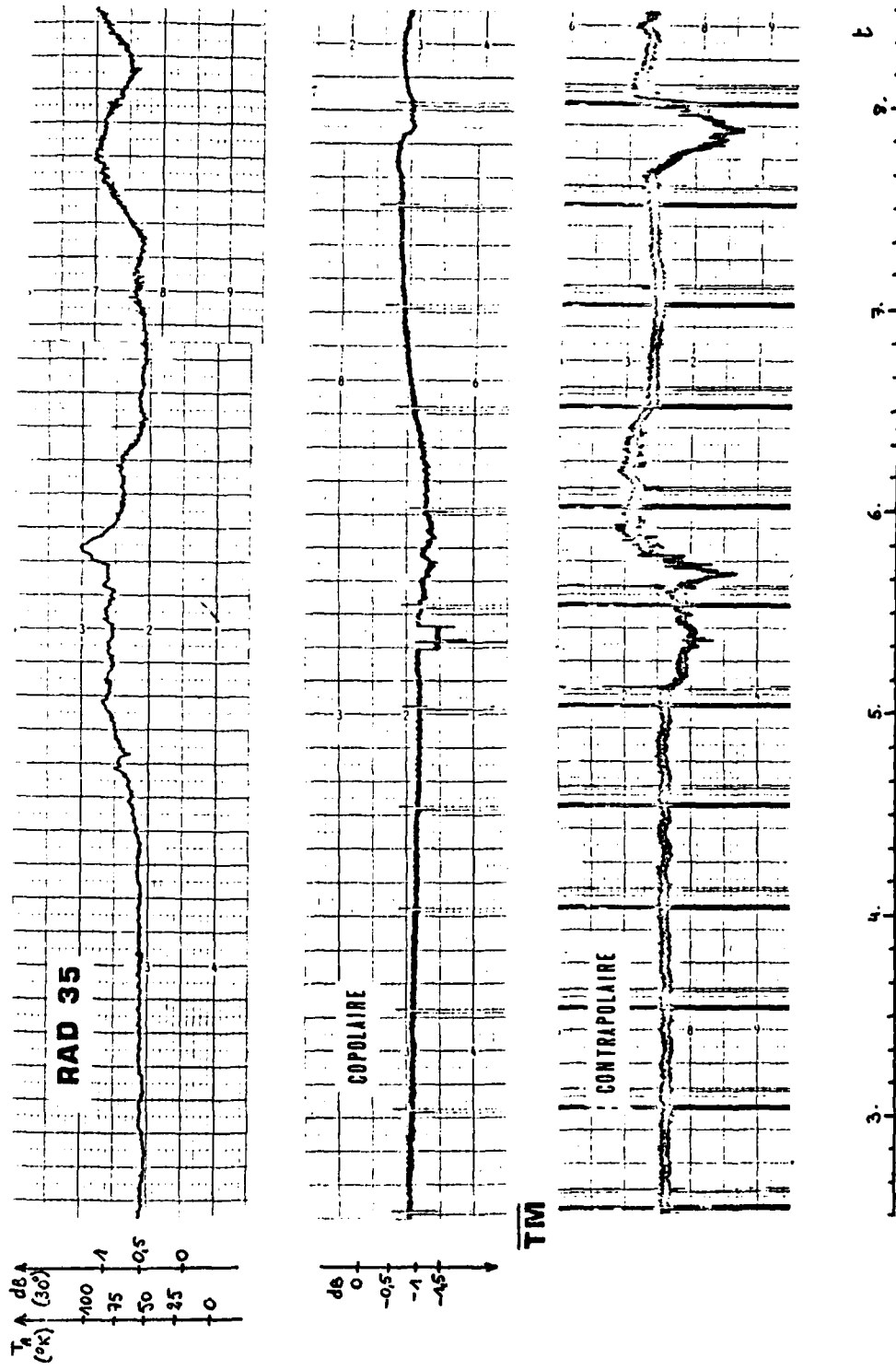


Figure 9. Simultaneous recording (February 28, 1980).

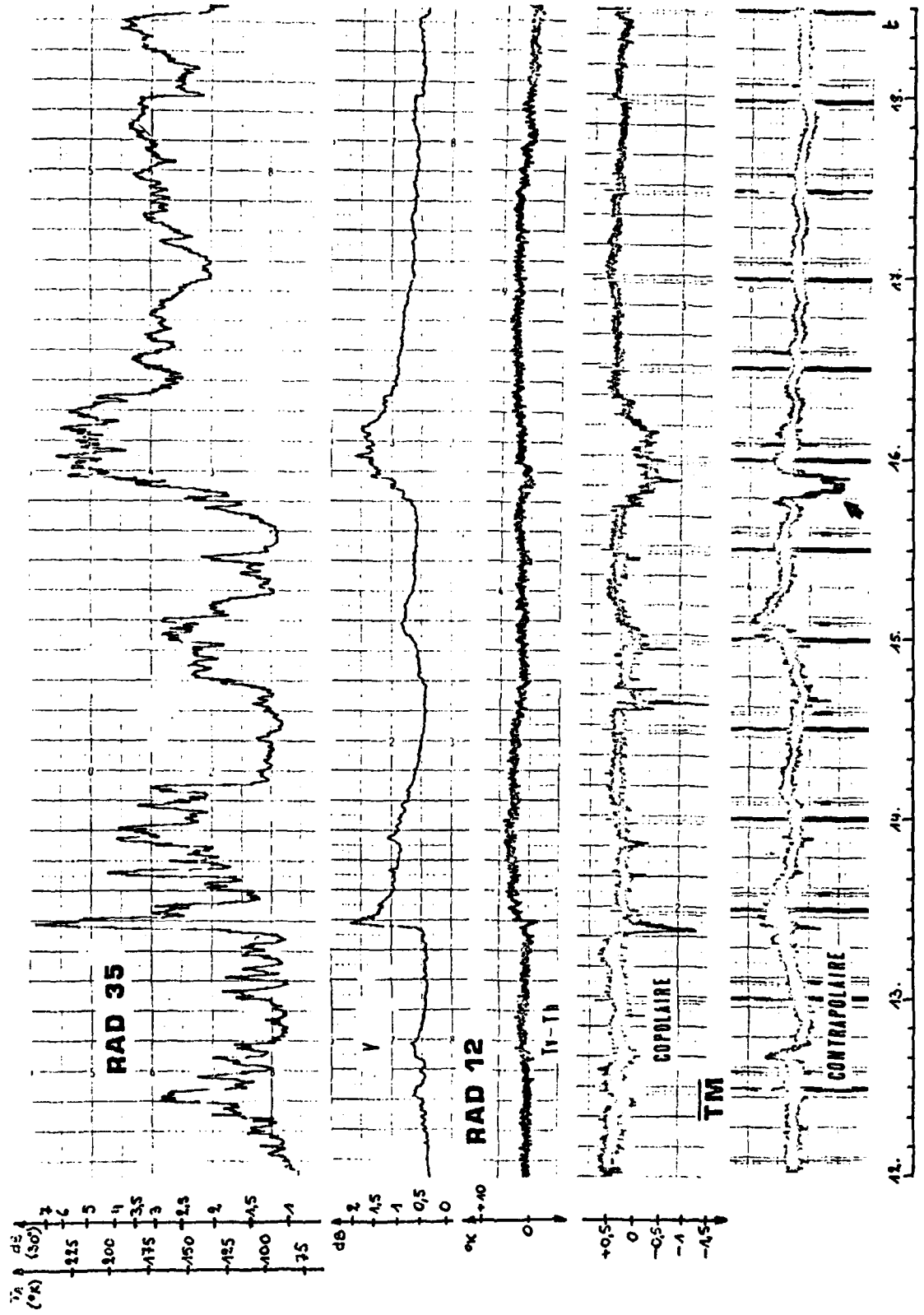


Figure 10. Simultaneous recording (March 29, 1980).

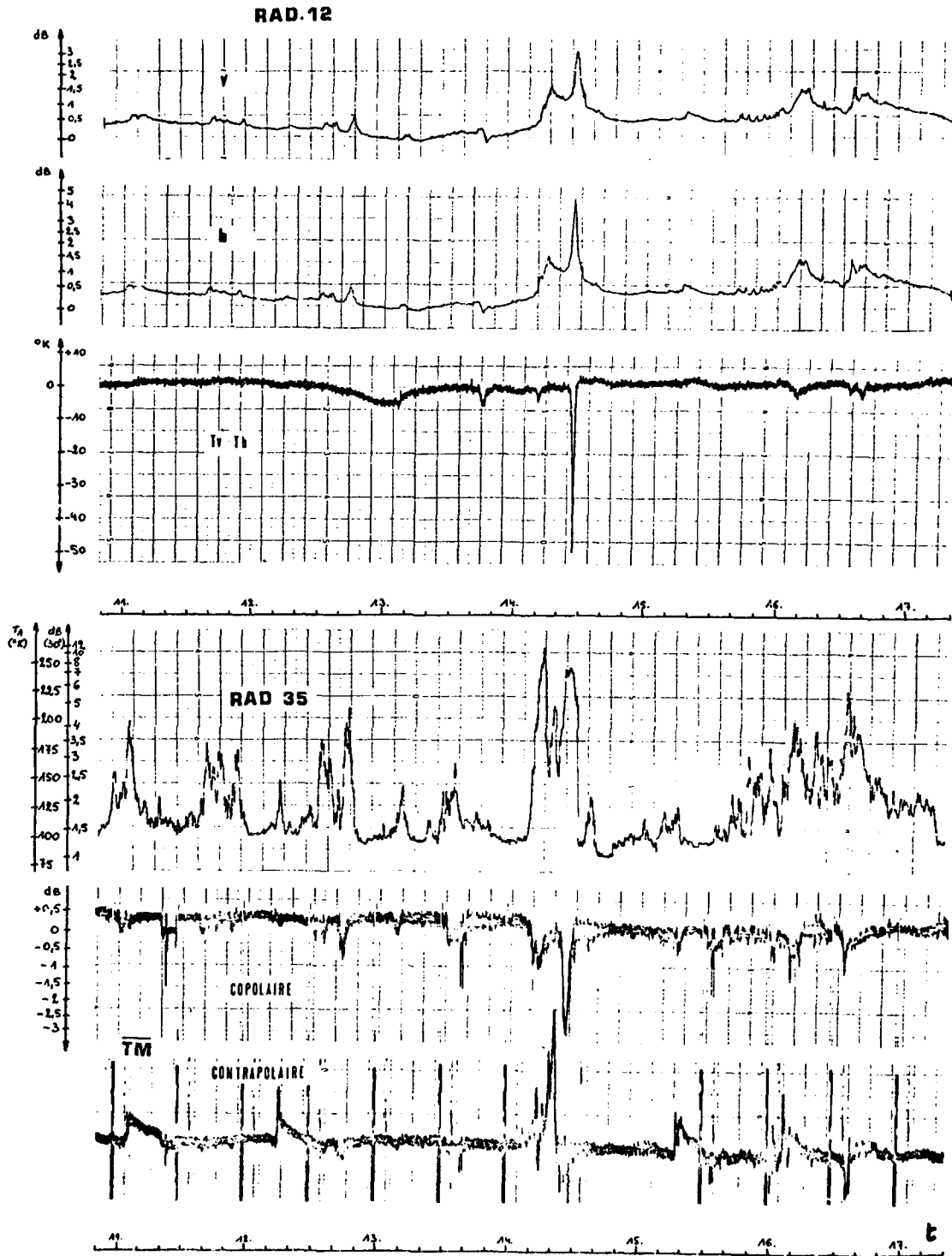


Figure 11. Simultaneous recording (March 28, 1980).

## IONOSPHERIC DISPERSION EFFECTS ON WIDEBAND TRANSMISSIONS

by

George H. Millman and Kurt A. Olsen  
General Electric Company  
Syracuse, New York 13221, USA

### SUMMARY

An evaluation is made of the effects of the dispersive characteristics of the ionosphere on a frequency-modulated and an unmodulated, i. e., no frequency modulation, Gaussian-shaped pulse. The distortion of the signal amplitude, envelope, pulse length, modulation and phase caused by the ionosphere is examined in terms of the integrated electron density of  $10^{17}$  and  $10^{18}$  electrons/m<sup>2</sup> along the transmission path, signal bandwidths of 5, 10 and 15 percent, pulse compression ratios of 100 and 1000 and carrier frequencies ranging between 100 MHz and 10 GHz.

### 1. INTRODUCTION

The ability of a radar to detect an object in space is basically limited by the receiver noise, i. e., noise which either is internally generated within the receiver, or enters the receiver through the antenna. The detection capability of a radar which is peak-power limited can be improved by employing long pulses. With pulses of long duration, however, the ability of a radar to resolve two or more targets, and to determine accurately the spatial location of a target, could be impaired. When system requirements specify a high degree of resolution and accuracy, short pulses are necessary. This implies that the radar must be capable of transmitting wideband signals.

A technique which can be used to achieve simultaneously an improvement in resolution, accuracy and detection is frequency modulation (FM) pulse compression. This involves the modulation of long transmitted pulses. On reception, the pulses are demodulated and compressed into pulses of short duration.

Since the ionosphere is a dispersive medium, i. e., the index of refraction is a function of frequency, the frequency components in the spectrum of a pulsed electromagnetic wave propagating through the medium undergo different phase shifts. This phenomenon can cause pulse distortion, the magnitude of the effect being dependent upon the radar characteristics and ionospheric conditions.

The effects of a dispersive medium on an unmodulated electromagnetic signal have been theoretically investigated by Budden (1961), Ginzburg (1961), Knop (1964), Wait (1964), Bek (1966) and Kozaki and Mushiaki (1969). Dispersion effects on FM signals have been examined by Millman and Bell (1971), Millman et al. (1972), El-Khamy and McIntosh (1973) and Brookner (1973, 1978).

In this paper, an evaluation is made of the distortion of an FM and an unmodulated Gaussian-shaped and rectangular-shaped pulse due to ionospheric dispersion.

### 2. THEORETICAL CONSIDERATIONS

#### 2.1 Gaussian Pulse

The transmitted waveform of a linear FM Gaussian pulse can be expressed as

$$f(t) = A_0 \exp(-t^2/2\sigma^2) \exp j(\omega_0 t + mt^2/2) \quad (1)$$

where  $\omega_0$  is the carrier frequency,  $A_0$  is the pulse amplitude, and  $\sigma$  is the standard deviation of the Gaussian distribution. The parameter  $m$  is the rate of frequency sweep given by  $m = (\Delta\omega/T)$  where  $\Delta\omega$  is the swept spectrum angular bandwidth. For convenience, the uncompressed pulse length,  $T$ , is defined in terms of the standard deviation as  $T = 4\sigma$ .

The frequency-domain representation of the pulse is obtained from the Fourier transform

$$f(\omega) = \int_{-\infty}^{\infty} f(t) \exp(-j\omega t) dt \quad (2)$$

which evaluates to

$$f(\omega) = A_0 \sigma \left[ \frac{2\pi}{1 - jm\sigma^2} \right]^{1/2} \exp \left[ - \frac{(\omega - \omega_0)^2 \sigma^2}{2(1 - jm\sigma^2)} \right] \quad (3)$$

After traversing the ionosphere, the time function of the emerging signal can be expressed by

$$F(t) = \frac{1}{2\pi} \int_{-\infty}^{\infty} f(\omega) \exp[-j\phi(\omega)] \exp[j\omega t] d\omega \quad (4)$$

where  $\exp[-j\phi(\omega)]$  is the transfer function of the ionosphere and where  $\phi(\omega)$  is the frequency-dependent phase shift introduced by the medium.

Expanding the phase function,  $\phi(\omega)$ , in a Taylor series about the angular carrier frequency,  $\omega_0$ , there results

$$\phi(\omega) = \phi(\omega_0) + (\omega - \omega_0) \phi'(\omega_0) + \frac{(\omega - \omega_0)^2}{2} \phi''(\omega_0) + \dots \quad (5)$$

where the primes signify the derivative of  $\phi(\omega)$  with respect to  $\omega$  and  $\phi'(\omega_0)$  is the group time delay.

It can be readily shown that, on substituting Equations (3) and (5) in Equation (4), the time function  $F(t)$  evaluates to

$$F(\tau) = A_m \exp \left[ j \frac{1}{2} \tan^{-1} \left( - \frac{\phi''(\omega_0)}{\sigma^2(1 + m\phi''(\omega_0))} \right) \right] \exp \left[ j \left( \omega_0 \tau + \omega_0 \phi'(\omega_0) - \phi(\omega_0) + m \frac{\tau^2}{2} \right) \right] \exp \left[ \frac{-\tau^2}{2\sigma_m^2} \right] \quad (6)$$

where  $\tau = t - \phi'(\omega_0)$  and the subscript  $m$  signifies the parameter modification with respect to the input FM Gaussian pulse.

A comparison of Equation (6) with the transmitted waveform, Equation (1), reveals that the envelope of the signal emerging from the ionosphere is also Gaussian in shape and that the output signal amplitude,  $A_m$ , standard deviation (pulse length),  $\sigma_m$ , and rate of frequency sweep,  $m_m$ , are given by

$$A_m = \frac{A_0}{\left[ \left( 1 + m\phi''(\omega_0) \right)^2 + \left( \phi''(\omega_0)/\sigma^2 \right)^2 \right]^{1/4}} \quad (7)$$

$$\sigma_m = \sigma \left[ \left( 1 + m\phi''(\omega_0) \right)^2 + \left( \phi''(\omega_0)/\sigma^2 \right)^2 \right]^{1/2} \quad (8)$$

$$m_m = \frac{m \left( 1 + m\phi''(\omega_0) \right) + \phi''(\omega_0)/\sigma^4}{\left( 1 + m\phi''(\omega_0) \right)^2 + \left( \phi''(\omega_0)/\sigma^2 \right)^2} \quad (9)$$

According to Equations (7), (8) and (9), when an unmodulated Gaussian waveform ( $m = 0$ ) is transmitted through a dispersive medium, the emergent signal has the following characteristics: the amplitude is decreased by a factor of  $1/[1 + (\phi''(\omega_0)/\sigma^2)^2]^{1/4}$ ; the pulse length is increased by a factor of  $[1 + (\phi''(\omega_0)/\sigma^2)^2]^{1/2}$ ; and linear frequency modulation of the form  $[\phi''(\omega_0)/\sigma^4]/[1 + (\phi''(\omega_0)/\sigma^2)^2]$  is present. These results are in agreement with Bek's (1966) analysis of dispersion effects on an unmodulated Gaussian pulse.

## 2.2 Rectangular Pulse

The transmitted waveform of a linear FM rectangular pulse can be described by the function

$$f(t) = A_0 \exp \left[ j \left( \omega_0 t + \frac{m t^2}{2} \right) \right] \quad (10)$$

in the interval  $-(T/2) \leq t \leq (T/2)$ , while  $f(t) = 0$  for  $t$  elsewhere.

Substituting Equations (2), (5) and (10) in Equation (4), it follows that the time waveform of an FM pulse emerging from a dispersive medium is expressed by the function

$$F(t) = \frac{A_0}{[2\pi |\beta''(\omega_0)|]^{1/2}} \exp \left[ j \left\{ \omega_0 t - \beta(\omega_0) - \frac{\pi}{4} \text{sgn} [\beta''(\omega_0)] \right\} \right] \int_{-(T/2)}^{(T/2)} \exp \left[ j \left\{ \frac{m\xi^2}{2} + \frac{[\xi + \beta'(\omega_0) - t]^2}{2\beta''(\omega_0)} \right\} \right] d\xi \quad (11)$$

where  $\xi$  is a dummy variable and  $\text{sgn}$  denotes the signum function (i. e.,  $\text{sgn} [\beta''(\omega_0)] = 1$  when  $\beta''(\omega_0) > 0$ ,  $\text{sgn} [\beta''(\omega_0)] = -1$  when  $\beta''(\omega_0) < 0$ , and  $\text{sgn} [\beta''(\omega_0)] = 0$  when  $\beta''(\omega_0) = 0$ ). [Bracewell, 1965].

For the case in which  $m\beta''(\omega_0) \neq -1$ , Equation (11) evaluates to

$$F(\tau) = A_m \exp \left[ j \tan^{-1} \left\{ \frac{S(x_m) + S(y_m)}{C(x_m) + C(y_m)} \right\} \right] \exp \left[ j \left\{ \omega_0 [\tau + \beta'(\omega_0)] - \beta(\omega_0) - \frac{\pi}{4} \text{sgn} [\beta''(\omega_0)] + \frac{m_m \tau^2}{2} \right\} \right] \quad (12)$$

where  $C(x_m)$ ,  $C(y_m)$  and  $S(x_m)$ ,  $S(y_m)$  represent the Fresnel cosine and sine integrals, respectively, and

$$x_m = \frac{(1/2) + (\tau/T_m)}{(k_m/2)^{1/2}} \quad (13)$$

$$y_m = \frac{(1/2) - (\tau/T_m)}{(k_m/2)^{1/2}} \quad (14)$$

$$k_m = \left| \frac{2\pi\beta''(\omega_0)[1 + m\beta''(\omega_0)]}{T_m^2} \right| \quad (15)$$

The output signal amplitude,  $A_m$  (which is time dependent), pulse width,  $T_m$ , and angular frequency sweep rate,  $m_m$ , are given by

$$A_m = \frac{A_0}{[2|1 + m\beta''(\omega_0)|]^{1/2}} \left\{ [C(x_m) + C(y_m)]^2 + [S(x_m) + S(y_m)]^2 \right\}^{1/2} \quad (16)$$

$$T_m = T |1 + m\beta''(\omega_0)| \quad (17)$$

$$m_m = \frac{m}{1 + m\beta''(\omega_0)} \quad (18)$$

When  $m = 0$ , Equation (11) simplifies to an expression which is identical to Ginzburg's (1961) result for the effects of a dispersive medium on an unmodulated rectangular pulse. The parameter  $k_m$ , Equation (15), becomes  $k$  which is, in terms of Bek's (1966) terminology, the magnitude of the coefficient of dispersion of the pulse.

For the special case of  $m\beta''(\omega_0) = -1$ , Equation (11) integrates to

$$F(\tau) = A_0 \left[ \frac{|m|T^2}{2\pi} \right]^{1/2} \frac{\sin(mT\tau/2)}{(mT\tau/2)} \exp \left[ j \left\{ \omega_0 [\tau + \beta'(\omega_0)] - \beta(\omega_0) + \frac{\pi}{4} \text{sgn}(m) - \frac{m\tau^2}{2} \right\} \right] \quad (19)$$

This expression is similar to the result obtained by Cook (1960) for the output of a matched filter excited by a linear FM rectangular pulse.

### 3. DISCUSSION

The frequency-dependent phase shift introduced by the ionosphere for a one-way transmission path is defined by

$$\phi(\omega) = \frac{\omega}{c} \int_0^s n \, ds \quad (20)$$

where  $c$  is the free space velocity ( $3 \times 10^8$  m/s) and  $ds$  is the element of path length.

To a first approximation, the index of refraction,  $n$ , can be defined by the relationship

$$n = \left[ 1 - \frac{N_e e^2}{\epsilon_0 m_e \omega^2} \right]^{1/2} \approx 1 - \frac{N_e e^2}{2 \epsilon_0 m_e \omega^2} \quad (21)$$

where  $N_e$  is the electron density (electrons/m<sup>3</sup>),  $e$  is the electron charge ( $1.6 \times 10^{-19}$  C),  $m_e$  is the electron mass ( $9.1 \times 10^{-31}$  kg),  $\epsilon_0$  is the electric permittivity of free space ( $10^{-9}/36\pi$  F/m), and  $\omega$  is the angular frequency of the incident wave (rad/s). It should be noted that the ionospheric refractive index is also a function of both the earth's magnetic field and the electron collision frequency. However, for frequencies in the VHF band and above, it is valid to disregard both parameters.

In evaluating the effects of ionospheric dispersion on FM electromagnetic transmissions, pulses having the following characteristics were considered: signal bandwidths of 5, 10, and 15 percent of the carrier frequency which ranged between 100 MHz and 10 GHz; and pulse compression ratios (i. e., dispersion factor,  $D$ ) of 100 and 1000 where  $D = T\Delta f = (2\pi(\Delta f^2/m))$ . The integrated electron density (i. e., electron content) along the transmission path in the ionosphere was assumed to be  $10^{17}$  and  $10^{18}$  electrons/m<sup>2</sup>. The former is applicable to nighttime propagation at vertical incidence and the latter to daytime propagation along the horizon. Both values are appropriate for the midlatitude ionosphere for altitudes up through approximately 1000-2000 km.

The effect of ionospheric dispersion on the angular sweep frequency rate of an FM Gaussian pulse with 100- and 1000-pulse compression ratio are shown in Figures 1 and 2, respectively. It is seen that, at a fixed frequency, the rate change is directly proportional to the signal bandwidth and the integrated electron density along the path, and inversely proportional to the pulse compression ratio. As the frequency increases, the percent variation in the angular sweep frequency rate decreases. According to Figure 1, the rate change at 400 MHz, under normal ionospheric conditions, should be less than approximately 7 percent for pulse compression ratios greater than 100 and signal bandwidths less than 10 percent.

The modification of the amplitude and pulse length (which is proportional to the standard deviation) induced by the ionospheric on FM Gaussian pulse transmissions is presented in Figures 3 and 4, the calculations being based on a positive sweep frequency ramp (i. e., frequency increasing with time). It is evident that there is a slight decrease in the pulse length with a corresponding increase in the signal amplitude, the effect being predominant at the low end of the frequency band. When utilizing a negative ramp, pulse stretching and amplitude decay would occur. According to Figure 4, at a frequency of 400 MHz and electron content of  $10^{18}$  electrons/m<sup>2</sup>, the maximum amplitude change for a signal bandwidth of 15 percent is on the order of 0.7 dB while, for a 5-percent signal bandwidth, the amplification is less than 0.1 dB. By increasing the pulse compression ratio to 1000, the amplitude and pulse length modification become quite insignificant. For example, the amplitude and pulse length changes for a pulse compression of 1000 and electron content of  $10^{18}$  electrons/m<sup>2</sup> are identical to those illustrated in Figure 3. It is of interest to note that the distortion effects caused by the ionosphere are indicative that this medium behaves like a dispersive delay line normally used in pulse compression systems.

In the case of an unmodulated Gaussian pulse traversing the ionosphere, pulse spreading prevails in contrast to a reduction in the signal amplitude, as depicted in Figures 5 and 6. It is seen in Figure 5 that the decrease in amplitude for a signal bandwidth of 5 percent and 10 percent at 400 MHz could be as high as 6.4 dB and 12.3 dB, respectively, while, at 5000 MHz, the decay could be on the order of 0.2 dB and 2.3 dB, respectively.

An unmodulated Gaussian pulse transmitted through the ionosphere will also experience a frequency modulation. According to Figure 7, an increase in the signal bandwidth results in an increase in the depth of frequency modulation.

It can be readily shown from Equation (6) that the phase shift experienced by an unmodulated Gaussian pulse traversing the ionosphere can be expressed by the function

$$\phi = \frac{1}{2} \tan^{-1} \{-X\} - \frac{\omega_0^2 \sigma^2 X}{2} \left[ 1 - \frac{X^2}{4(1+X^2)} \right] \quad (22)$$

where  $X = (\phi'(\omega_0)/\sigma^2)$ . It is interesting to note that the ionospheric phase shift, plotted in Figure 8, is somewhat insensitive to signal bandwidth and is approximately directly proportional to the electron content in the path of propagation and inversely proportional to the transmission frequency.

The effects of ionospheric dispersion on a linear FM and an unmodulated rectangular pulse at carrier frequencies of 100 MHz and 10 GHz are shown in Figures 9 through 12.

It can be seen that, for a fixed percent bandwidth, the unmodulated pulse is more severely distorted than the linear FM pulse. The FM pulse distortion is characterized by the dimensionless parameter  $k_m$ , as defined by Equation (15) and contained in the Fresnel integrals of Equations (12), (13) and (14). Table 1 lists the values of  $k_m$  deduced on the basis of the system and environmental parameters employed in this analysis.

An examination of Figures 9 through 12 reveals that for  $k_m < 10^{-4}$ , the output FM pulse is approximately rectangular in shape, with a slight rounding at the corners. For  $k_m > 10^{-4}$ , the Fresnel integrals produce oscillations in the pulse amplitude, the maximum oscillation being on the order of 16 percent as depicted in the 100-MHz calculations.

The effects of dispersion on an unmodulated rectangular pulse are dependent on the parameter  $k$  which is defined by  $k_m$  when  $m = 0$ . The values of  $k$  used in this analysis are presented in Table 2.

According to Figures 9 through 12, the output pulse undergoes severe distortion for  $k$  less than approximately 0.5. It is evident that the pulse envelope tends to resemble a  $(\sin x)/x$  type function for  $k > 0.5$ , the period being directly proportional to the magnitude of  $k$ .

#### 4. CONCLUSIONS

The effects of the dispersive characteristics of the ionosphere on wide band-pulse transmissions are dependent on the carrier frequency, the signal bandwidth, the pulse compression ratio and the integrated electron density along the propagation path.

The results of this analysis indicate that for a given fractional bandwidth, the distortion introduced by the ionosphere on an FM Gaussian and rectangular pulse is less than that for an unmodulated pulse.

The signal amplitude, pulse length, modulation, phase and envelope degradation effects described in this paper pertain to propagation in the normal ionosphere. In a nuclear-disturbed environment, where the integrated electron density could be an order of magnitude greater than that encountered under normal ionospheric conditions, the dispersive distortion effects could be correspondingly more severe.

#### 5. REFERENCES

- Bek, S. S., "A Method of Analyzing the Dispersive Distortions of a Short Pulse in the Ionosphere," Proceedings 22nd All-Union Scientific Session Devoted to Radio Day (Theory and Techniques of Transmitting Discrete Signals Section), Moscow, 1966.
- Bracewell, R. N., "The Fourier Transform and Its Applications," McGraw-Hill Book Company, New York, 1965.
- Brookner, E., "Ionospheric Dispersion of Electromagnetic Pulses," IEEE Transactions on Antennas and Propagation, Vol. AP-21, pp 402-405, May 1973.
- Brookner, E., "Ionospheric Pulse Time Dispersion Including Effects of Earth's Magnetic Field," IEEE Transactions on Antennas and Propagation, Vol. AP-26, pp 307-311, March 1978.
- Budden, K. G., "Radio Waves in the Ionosphere," Cambridge University Press, London, 1961.
- Cook, C. E., "Pulse Compression -- Key to More Efficient Radar Transmission," Proceedings IRE, Vol. 48, pp 310-316, March 1960.
- El-Khomy, S. E. and R. E. McIntosh, "Optimum Transionospheric Pulse Transmissions," IEEE Transactions on Antennas and Propagation, Vol. AP-21, pp 269-273, March 1973.



Ginzburg, V. L., "Propagation of Electromagnetic Waves in Plasma," Gordon and Breach, Science Publishers Inc., New York, 1961.

Knop, C. M., "Pulsed Electromagnetic Wave Propagation in Dispersive Media," IEEE Transactions on Antennas and Propagation, Vol. AP-12, pp 494-496, July 1964.

Kozaki, S., and Y. Mushiake, "Propagation of the Electromagnetic Pulse with Gaussian Envelope in Inhomogeneous Ionized Media," IEEE Transactions on Antennas and Propagation, Vol. AP-17, pp 686-688, September 1969.

Millman, G. H., and C. D. Bell, "Ionospheric Dispersion of an FM Electromagnetic Pulse," IEEE Transactions on Antennas and Propagation, Vol. AP-19, pp 152-155, January 1971.

Millman, G. H., K. A. Olsen and C. D. Bell, "The Effects of a Dispersive Medium on an Electromagnetic Pulse," General Electric Technical Information Series Report No. R72EMH4, April 1972.

Wait, J. R., "Propagation of Pulses in Dispersive Media," Radio Science, Vol. 69D, pp 1387-1401, November 1965.

TABLE 1  
PARAMETER  $k_m$  FOR AN FM RECTANGULAR PULSE

Frequency (MHz)	Electron Content (Electrons/m <sup>2</sup> )	Signal Bandwidth (Percent)	
		5	15
100	10 <sup>17</sup>	6.64 x 10 <sup>-5</sup>	5.96 x 10 <sup>-4</sup>
	10 <sup>18</sup>	6.64 x 10 <sup>-4</sup>	5.96 x 10 <sup>-3</sup>
10,000	10 <sup>17</sup>	6.64 x 10 <sup>-7</sup>	5.96 x 10 <sup>-6</sup>
	10 <sup>18</sup>	6.64 x 10 <sup>-6</sup>	5.96 x 10 <sup>-5</sup>

TABLE 2  
PARAMETER  $k$  FOR AN UNMODULATED RECTANGULAR PULSE

Frequency (MHz)	Electron Content (Electrons/m <sup>2</sup> )	Signal Bandwidth (Percent)	
		5	15
100	10 <sup>17</sup>	6.64 x 10 <sup>-1</sup>	5.96
	10 <sup>18</sup>	6.64	59.64
10,000	10 <sup>17</sup>	6.64 x 10 <sup>-3</sup>	5.96 x 10 <sup>-2</sup>
	10 <sup>18</sup>	6.64 x 10 <sup>-2</sup>	5.96 x 10 <sup>-1</sup>

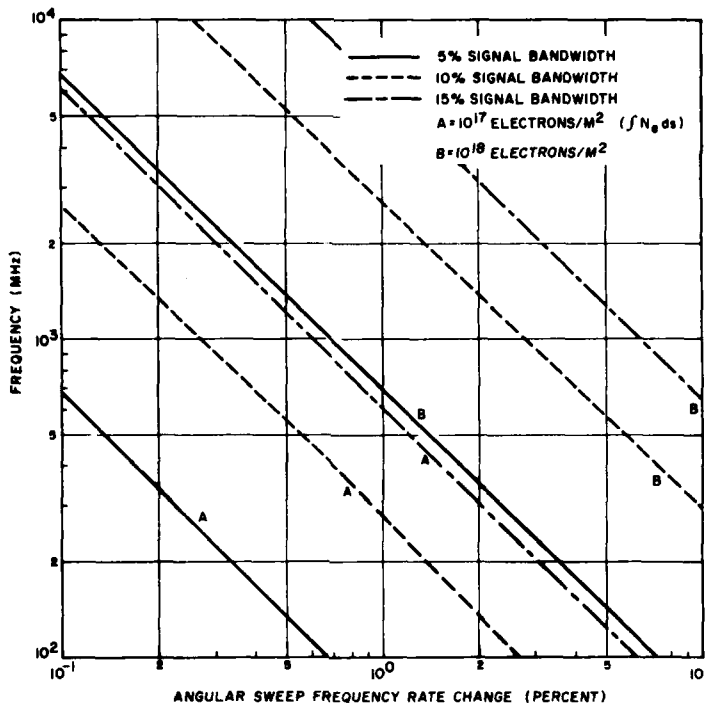


Figure 1. Variation in the Angular Sweep Frequency Rate of an FM Gaussian Pulse with 100-Pulse Compression Ratio Traversing the Ionosphere

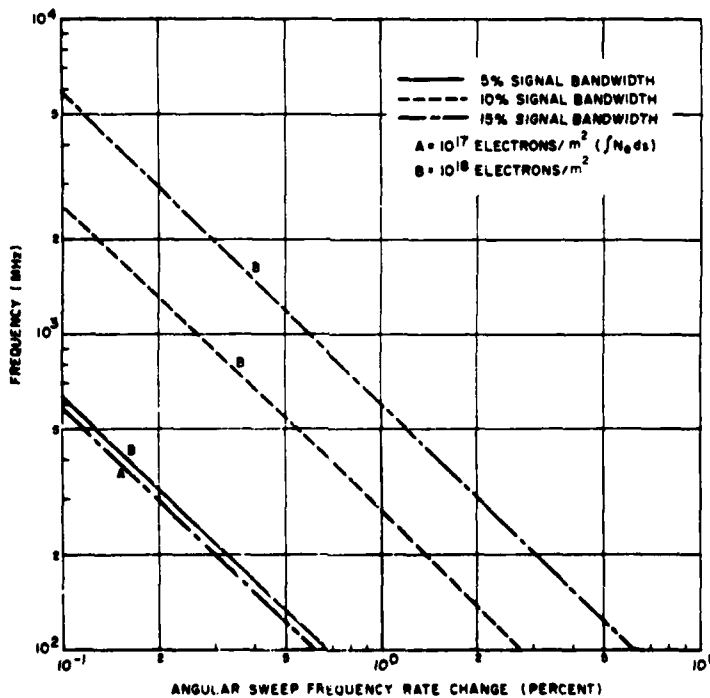


Figure 2. Variation in the Angular Sweep Frequency Rate of an FM Gaussian Pulse with 1000-Pulse Compression Ratio Traversing the Ionosphere

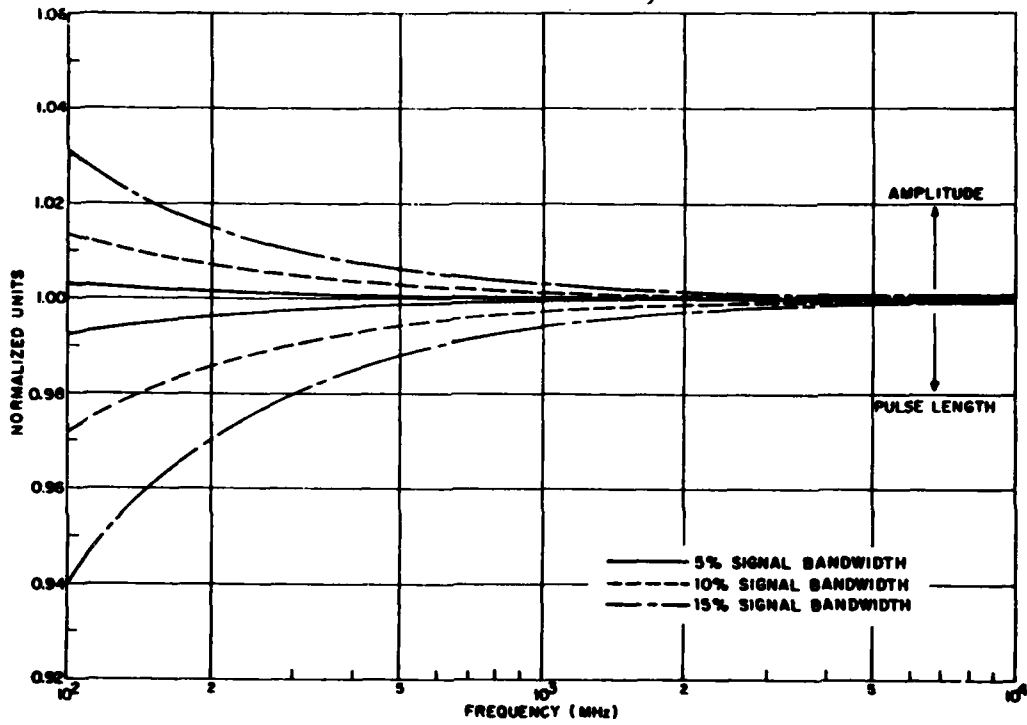


Figure 3. Amplitude and Pulse-Length Modification of an FM Gaussian Pulse with 100-Pulse Compression Ratio Traversing the Ionosphere with an Electron Content of  $10^{17}$  Electrons/ $m^2$

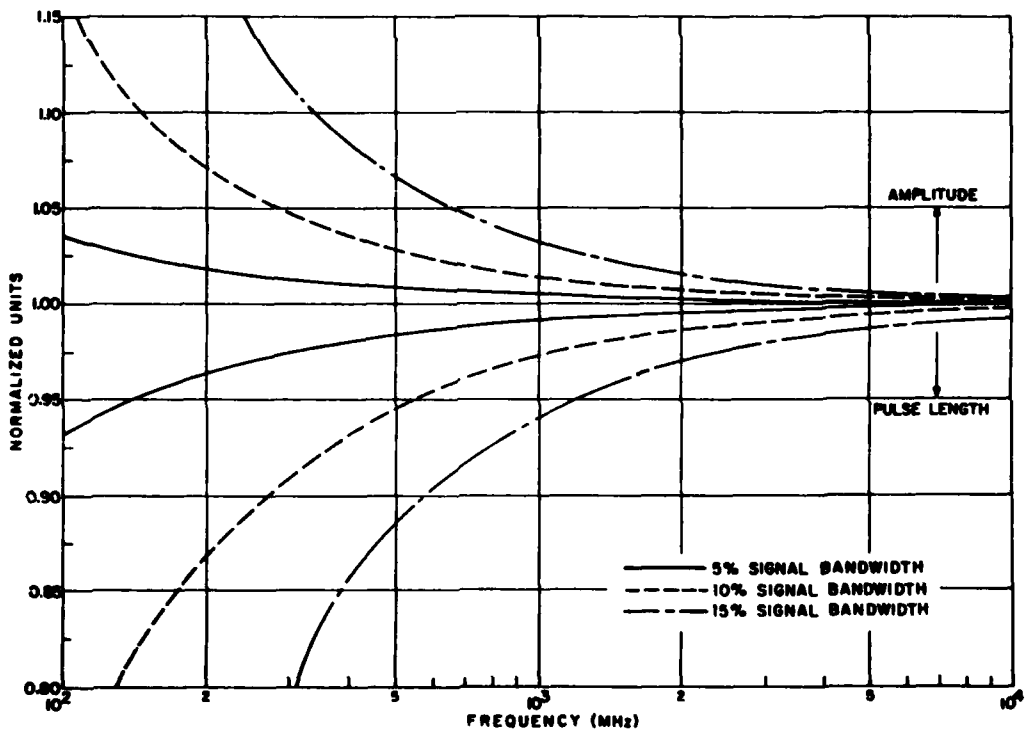


Figure 4. Amplitude and Pulse-Length Modification of an FM Gaussian Pulse with 100-Pulse Compression Ratio Traversing the Ionosphere with an Electron Content of  $10^{18}$  Electrons/ $m^2$

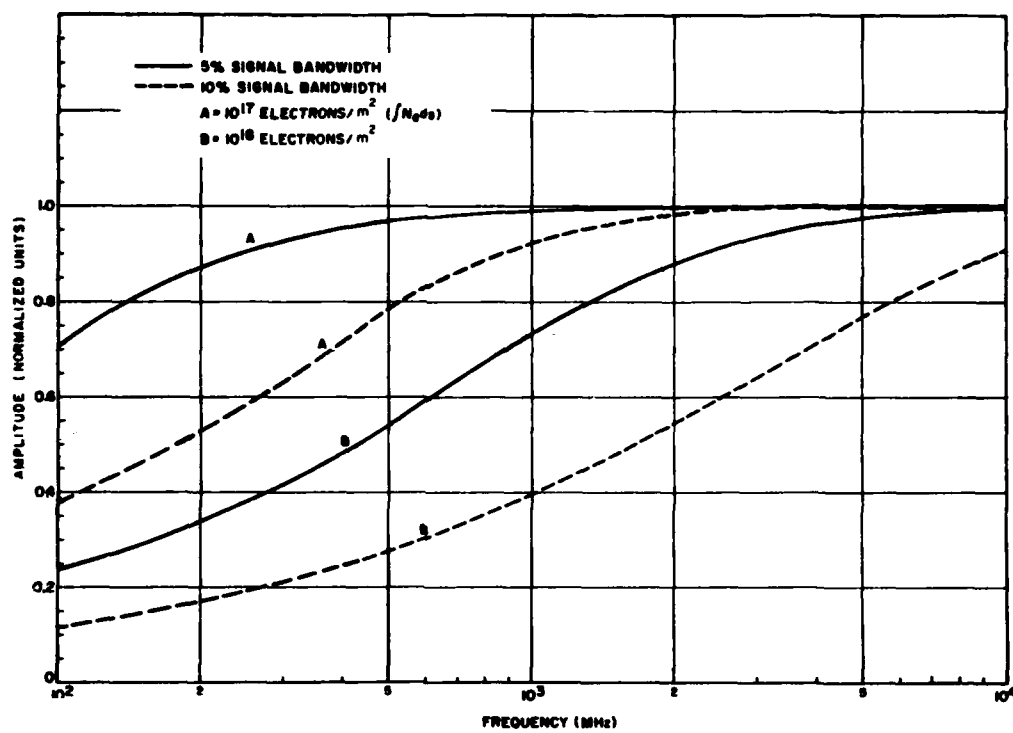


Figure 5. Amplitude Modification of an Unmodulated Gaussian Pulse Traversing the Ionosphere

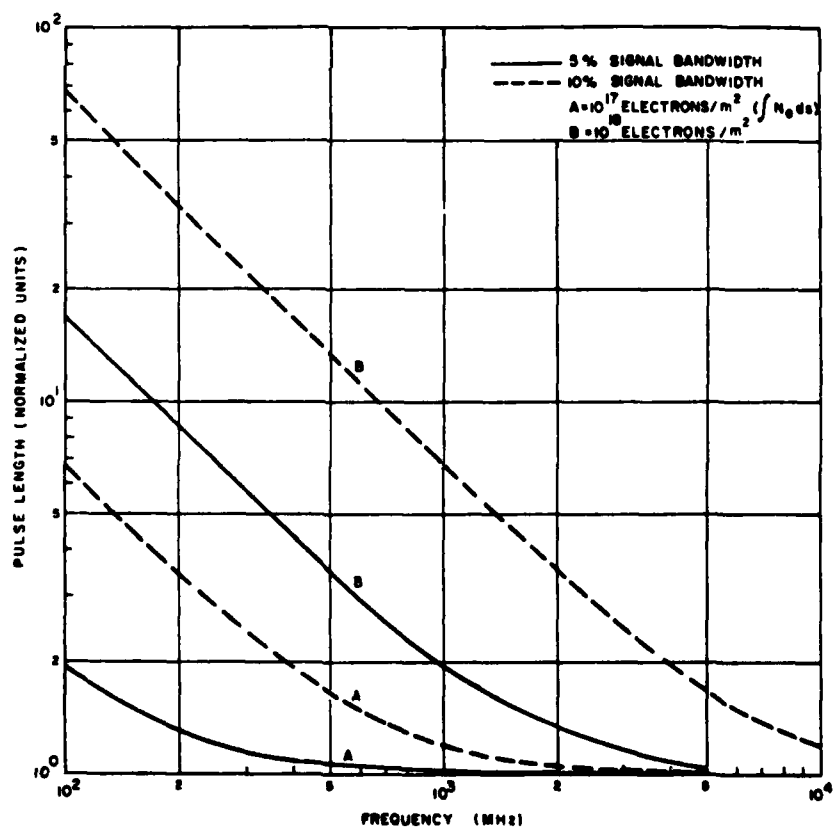


Figure 6. Pulse-Length Modification of an Unmodulated Gaussian Pulse Traversing the Ionosphere

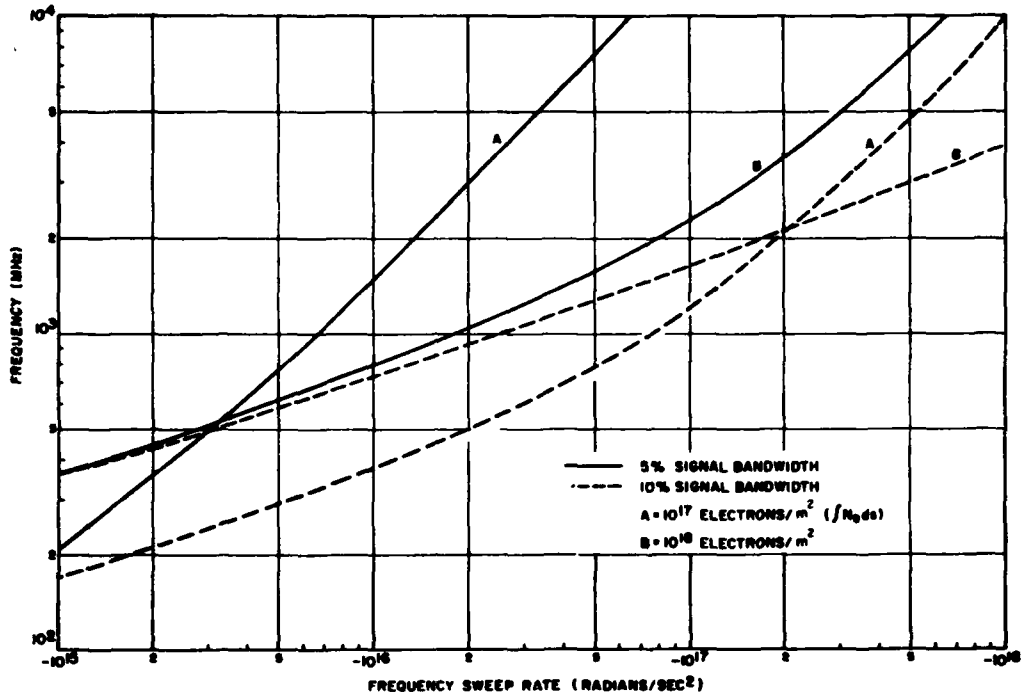


Figure 7. Frequency Modulation Induced in an Unmodulated Gaussian Pulse Traversing the Ionosphere

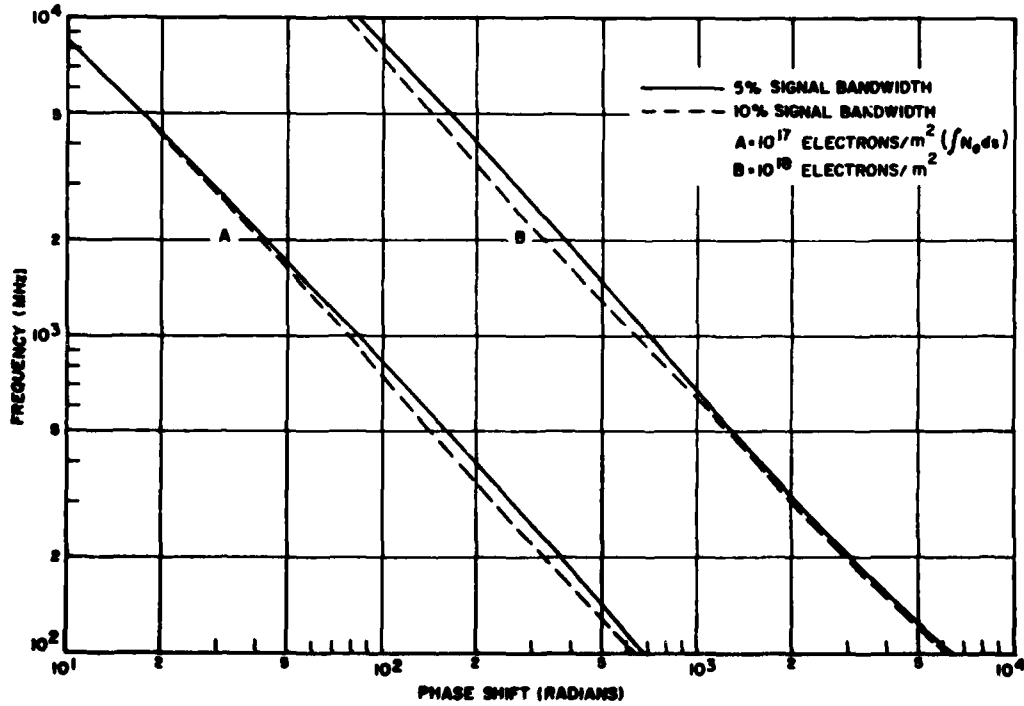


Figure 8. Phase Shift of an Unmodulated Gaussian Pulse Traversing the Ionosphere

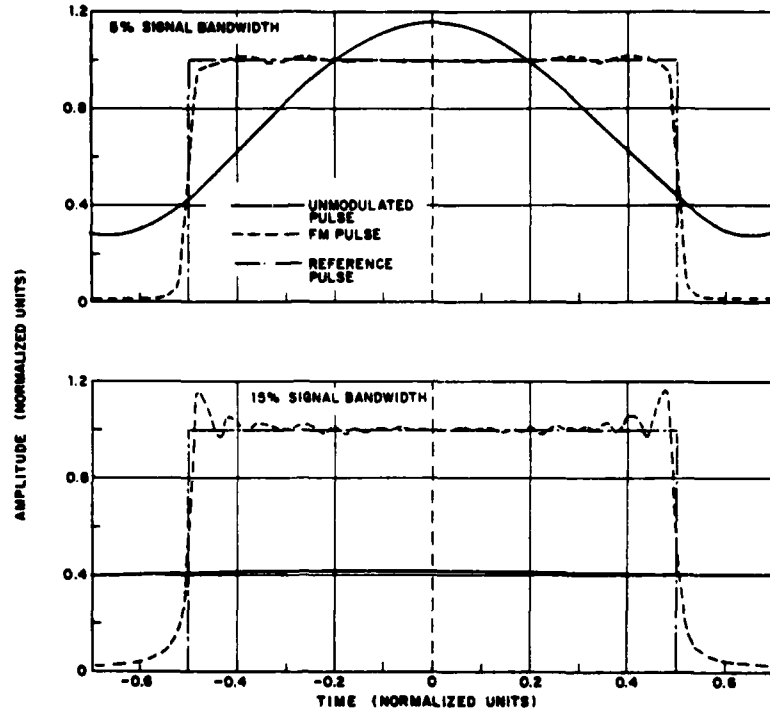


Figure 9. Envelope of a 100 MHz — FM and Unmodulated Rectangular Pulse Traversing the Ionosphere with Electron Content of  $10^{17}$  Electrons/ $m^2$

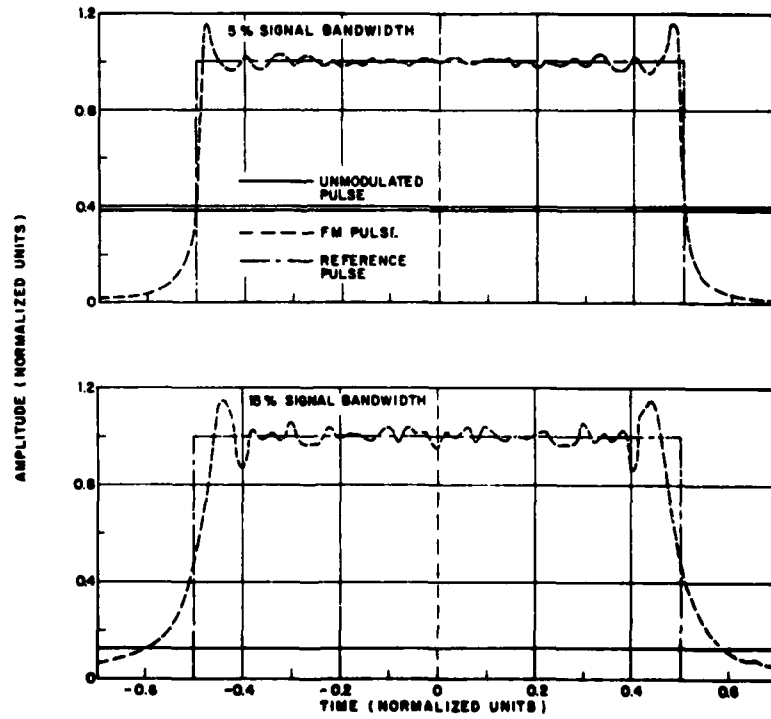


Figure 10. Envelope of a 100 MHz — FM and Unmodulated Rectangular Pulse Traversing the Ionosphere with Electron Content of  $10^{18}$  Electrons/ $m^2$

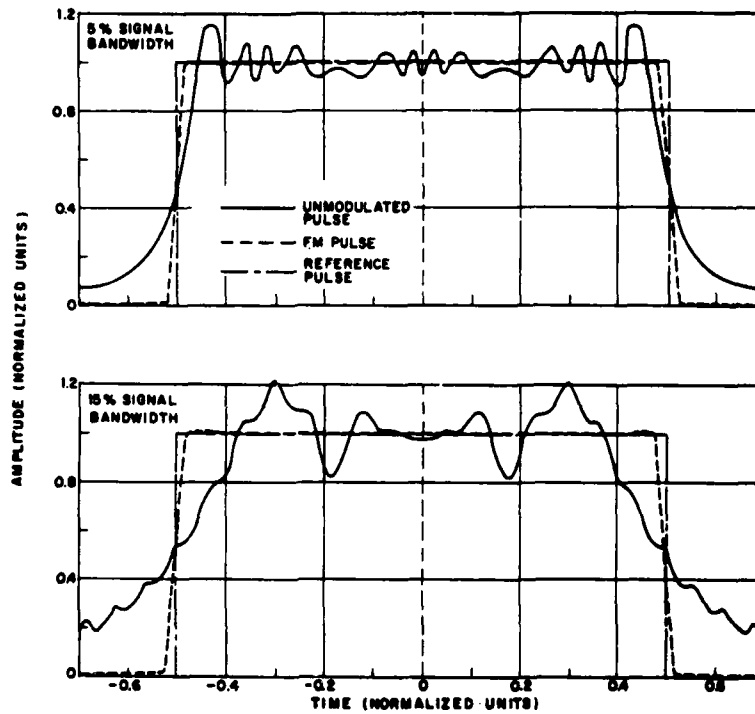


Figure 11. Envelope of a 10 GHz - FM and Unmodulated Rectangular Pulse Traversing the Ionosphere with Electron Content of  $10^{17}$  Electrons/m<sup>2</sup>

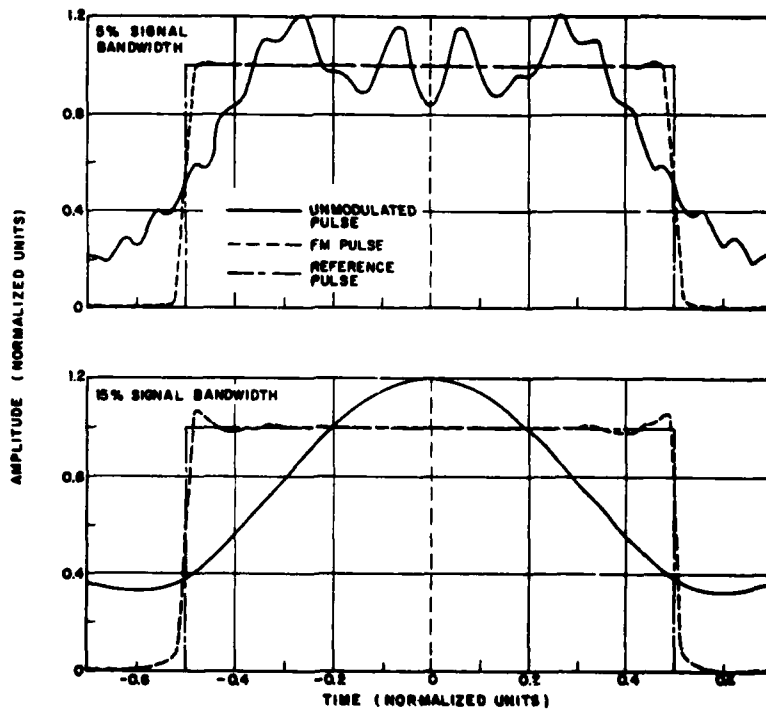


Figure 12. Envelope of a 10 GHz - FM and Unmodulated Rectangular Pulse Traversing the Ionosphere with Electron Content of  $10^{18}$  Electrons/m<sup>2</sup>

ELECTRON CONTENT MEASUREMENTS AT LANCASTER: HARMONIC ANALYSIS OF  
ATS-6 MEASUREMENTS

E. M. Poulter and J. K. Hargreaves  
Department of Environmental Sciences  
University of Lancaster  
Lancaster, England

ABSTRACT

The radio beacon experiment carried on the ATS-6 satellite has allowed the measurement of the signal group delay and hence the electron content ( $N_T$ ) along the ray path. The more usual electron content measurement, the Faraday rotation angle, could also be obtained independently. Since this latter quantity represents the electron content weighted by the geomagnetic field, it provides an additional parameter relating to the shape of the electron density profile. Alternatively it may be used to separate the total electron content into ionospheric and protonospheric components during periods of geomagnetic quiet. For the period July 1975 to July 1976, the satellite was positioned at longitude  $35^\circ\text{E}$ , enabling measurements of the group delay and Faraday rotation to be routinely performed at Lancaster. Additional information on the ionospheric layer shape was obtained from concurrent ionosonde data:  $N_{\text{max}}$  from Dourbes, and occasional profiles from the topside sounders aboard ISIS satellites. These data cover a range of seasonal variations and changing conditions of geomagnetic activity. For consideration of the gross features, the data have been reduced to 30-minute mean values, comprising the electron content, shape factor  $F$  and slant slab thickness ( $N_T/N_{\text{max}}$ ). An adequate empirical description of these parameters is supplied by harmonic analysis. This reveals the variation of the harmonic coefficients with solar and geomagnetic variations. These will be compared with available empirical models evaluated for the appropriate conditions and applied to the local ray path geometry. In addition, preliminary results will be presented from a theoretical approach using a physically realistic plasmaspheric model.

1. INTRODUCTION

The passage of a modulated radio frequency signal between a satellite and ground is both retarded and refracted by the intervening ionized medium. The delay is directly proportional to the number of free electrons encountered along the path, and the dispersive nature of the medium may be exploited to deduce the electron content from multi-frequency observations. These may be used as a real time correction for the propagation delay, or for scientific studies of the ionized medium. Electron content studies have been carried out at Lancaster using transmissions from the ATS-6 satellite for the period September 1975 to July 1976. Most ionospheric parameters, including electron content, depend on the sun's declination (diurnal and seasonal variations) and on the solar activity. Because of the cyclic nature of these variations it is possible to produce empirical descriptions of the electron content data. Such a description in terms of harmonic coefficients will be presented for the ray path from Lancaster ( $54^\circ\text{N}$ ,  $3^\circ\text{W}$ ) to ATS-6 ( $35^\circ\text{E}$ ). The median electron content behaviour will also be compared with two global empirical models, namely the Bent model (Llewellyn and Bent, 1973) and the International Reference Ionosphere (Rawer et. al., 1978). Recently, work has begun on applying a generalized plasmaspheric model (Murphy et. al., 1976) to the Lancaster ray path. At present this is being evaluated for a variety of ionospheric/plasmaspheric conditions in order to simulate the Lancaster data; preliminary results will be presented.

2. OBSERVATIONS

The coherent signals from ATS-6 allowed the measurement of the group delay or modulation phase ( $\phi$ ) from the 1 MHz amplitude modulation of 360 MHz and 140 MHz carriers. This quantity is simply related to the electron content by

$$N_T \text{ (m}^{-2}\text{)} = 4.89 \times 10^{14} \phi^\circ$$

In addition, the Faraday rotation of the plane of polarization after passage through the ionosphere could be determined. The rotation ( $\Omega$ ) is also dependent on the electron content, weighted however by the longitudinal component of the geomagnetic field, or equivalently, the longitudinal component of the electron gyrofrequency  $f_1$

$$\Omega = \frac{K}{f^2} \int_s N f_1 ds$$

with  $N$  the electron density,  $f$  the radio frequency and  $K$  a constant. Studies using empirical electron density profiles have shown that a constant value  $F_1$  may be found such that  $\Omega$  is proportional to the electron content up to an altitude near 2500 km for a variety of profile shapes (Titheridge, 1972). The 140 MHz and 40 MHz emissions from ATS-6 also enabled this quantity  $N_F$ , usually called the Faraday or ionospheric content, to be estimated. It was measured using the 140 MHz signals received at Lancaster. ( $\Omega$  and  $N_F$  are related by  $\Omega = \frac{K}{f^2} F_1 N_F$ )



The electron content derived from group delay measurements may be split into Faraday and residual (or protonospheric) components

$$N_T = N_F + N_P$$

allowing monitoring of the more distant ionization represented by  $N_P$ . During periods of geomagnetic disturbance this might not be an appropriate separation because  $F_1$  depends on profile shape. An alternative is to calculate a shape factor  $F$  defined by

$$F = \frac{\int_s N f_1 ds}{\int_s N ds} = \Omega / \phi$$

$F$  then represents the actual value of  $F_1$  required to equate the two independent measures of electron content. It is an indicator of the ionization profile shape and altitude, large values of  $F$  representing profiles dominated by low altitude contributions.

A further shape parameter is provided by the slab thickness, defined as

$$\tau = N_T / N_{\max}$$

with  $N_{\max}$  in the present case obtained from routine ionosonde measurements at Dourbes (50°N, 5°E), approximately the crossing point at the ionospheric peak of the Lancaster to ATS-6 ray path. All of the above measured quantities refer to this slant path and are for solar minimum conditions.

Measurements of both  $\phi$  and  $\Omega$  were digitized at 1 second intervals and then reduced to 1 minute averages, appropriate calibrations being included. For study of the coarse features, 30-minute averages have been produced and the following results refer to this data set. The slab thickness is limited to hourly values by the operating schedule of the Dourbes ionosonde.

### 3. DATA REPRESENTATION

To demonstrate the typical variations of the recorded quantities, a sample day (November 19th, 1975) is shown in Fig. 1. The electron content increases rapidly after sunrise, reaching peak values of approximately  $30 \times 10^{16} \text{ m}^{-2}$  shortly after mid-day. Large variations not removed by the 30-minute averaging are due to the presence of large scale travelling disturbances. During the night the electron content is held approximately constant after an initial decay. This probably results from the combination of an equatorward neutral wind, raising the layer to regions of lower loss, and by an influx of ionization from the more distant protonosphere.

The shape factor  $F$  generally has a similar diurnal behaviour to  $N_T$ . The production of electron-ion pairs by solar ultra-violet radiation proceeds most rapidly at altitudes below the ionization peak, increasing  $F$  since it biases the layer to lower levels. The increase at sunrise is more rapid than that for  $N_T$  indicating that the layer shape is relatively unchanged during most of the daylight hours. This implies that the net rate of production at lower levels is approximately balanced by an increase in the upper levels due to diffusive processes. It is also usual for the evening decay of  $F$  to be more rapid than that of  $N_T$ , consistent with greater loss rate at low altitudes, effectively raising the layer.

Although a noisy parameter, due mainly to its origin in  $f_oF_2$ , the slab thickness consistently exhibits a large sunrise peak, minimum values during the day, and a second, smaller, increase near sunset.

The residual or protonospheric content ( $N_P$ ) is the difference between two quantities of similar magnitude,  $N_T$  and  $N_F$ , and so is subject to relatively large uncertainties. A diurnal variation is seen in  $N_P$ , with the peak value lagging the corresponding peak in  $N_T$ . The relative values of  $N_P$  and  $N_F$  indicate that the ionization above 2500 km may account for up to 50% of the electron content by night.

The empirical description of these data requires a simple representation capable of approximating these types of behaviour. Previous approaches considered representing the diurnal variation in  $N_T$  by a positive half cosine variation and by a Gaussian function (Klobuchar, 1975). In mid-latitudes, however, electron content often exhibits a pronounced mid-day bite out and neither of these representations is faithful to this feature. The essentially diurnal nature of the variations suggests a harmonic analysis approach.

Spectra of the electron content variations have been obtained using the maximum entropy method (M.E.M.). These are shown for groups of four days for winter, equinox and summer periods in Fig. 2. Mean values and a linear trend have been removed prior to the spectral analysis. As expected, the diurnal term dominates the spectrum, but there is also a substantial semi-diurnal component, especially during summer. These spectra are similar to those reported by Titheridge (1971) for southern hemisphere data obtained from Faraday rotation measurements. The resolution and stability of the M.E.M. depends on the length of the prediction error filter, which in these examples was 2% of the time series length, well within the safe margin suggested by Chen and Stegun (1974). Except for the semi-diurnal

component, all other spectral features are more than 20 dB below the diurnal component. The magnitudes of these residuals are approximately the size of the standard deviations of the individual 30-minute averages and so are not considered significant. The spectra for the protonospheric contents during these periods also reveal a peak near 24 hours but very little at 12 hours, indicating that different physical processes govern the ionospheric and protonospheric behaviour.

A harmonic analysis comprising a mean value, and 24-hour and 12-hour components, a total of 5 coefficients, is therefore sufficient for a description of the daily electron content behaviour:

$$N_T = N_0 + N_{24} \cos \left( \frac{2\pi}{24} (t - t_{24}) \right) + N_{12} \cos \left( \frac{2\pi}{12} (t - t_{12}) \right)$$

Ideally, a multiple regression including solar and geomagnetic activity indices should be carried out. This, however, requires a priori knowledge of the dependence of the experimental quantities on such quantized indices. Although certain features are common to large changes in geomagnetic activity, uniform behaviour for individual days is not as well defined. For this reason, the harmonic functions alone have been fitted to 24-hour periods of data without any selection, using a weighted least squares approach. The weighting simply allows gaps in the data to be dealt with. An 8-hour component was also included in trial sections of the data, but this was of the same order as the r.m.s. deviation of the fitted coefficients, typically  $1.3 \times 10^{16} \text{ m}^{-2}$  for  $N_T$ , 0.03 MHz for  $F$ , 80 km for  $\tau$  and  $5 \times 10^{15} \text{ m}^{-2}$  for  $N_p$ . Examples of the harmonic functions fitted to the data are included in Fig. 1 as solid lines. The fit appears to be good except for a short period at sunrise.

#### 4. THE HARMONIC COEFFICIENTS

##### 4.1 Mean values

The daily mean values for  $N_T$ ,  $F$ ,  $\tau$  and  $N_p$  are shown in Fig. 3 along with the annual and semi-annual variations, also determined in a least squares approach. In the case of  $N_T$  the seasonal variation is apparent, with values ranging from approximately  $10$  to  $25 \times 10^{16} \text{ m}^{-2}$ . The minimum value occurs 28 days after the winter solstice. The maximum, however, occurs in early summer, and the July values ( $\sim$  day 200) are relatively small, contributing to the semi-annual coefficient, which at  $2.15 \times 10^{16} \text{ m}^{-2}$  is approximately half the annual term of  $4.96 \times 10^{16} \text{ m}^{-2}$ . This July period was subject to little geomagnetic activity ( $\Sigma K_p < 17$ ), and the measured values of  $N_T$  show little variation. Increased activity generally leads to depressed electron content values, and so this mid-summer decrease is a real feature of the mean values. In the period immediately preceding (days 90-180), a regular variation with apparent period near 27 days is observed. During this interval, the geomagnetic activity revealed a similar periodic variation, presumably linked to the solar rotation. This behaviour is also reflected in the mean  $N_p$  values.

The mean values of  $F$  are dominated by an annual variation with largest values occurring in summer, when the ionization profile is dominated by the lower or ionospheric region. During winter, a larger proportion of the ionization along the ray path resides at higher altitudes and so the mean  $F$  values correspond to profiles that are biased towards higher altitudes. The winter mean  $F$  value is subject to relatively large changes following enhanced geomagnetic activity, and so the winter minimum may not be accurately defined. The large July values suggest a dominance of the lower portion of the ray path, although mean  $N_T$  values are decreased. This implies a correspondingly larger reduction in the protonospheric content.

The protonospheric content is a combination of  $N_T$  and  $F$ , and although the fitted annual and semi-annual variations are shown, neither of these is larger than the r.m.s. deviation of the individual values from the fitted functions. Despite the scatter of the individual points, there is an apparent trend, with the mean  $N_p$  values decreasing throughout the year. There is no evidence for the winter maximum reported in the Boulder data by Davies et. al., (1977). The smoothed observed Zurich sunspot numbers also decreased during this interval, the minimum of the sunspot cycle occurring near June 1976. Although these observations are for a limited period, this trend suggests that the influence of the solar variations on the protonospheric content could be as important as any seasonal variations, either coupled via the diffusive interaction with the underlying ionosphere, or directly induced. In general, depletion of the upper levels follows increased geomagnetic activity, although the lower values of  $N_p$  in summer were during a quiet period.

The mean slab thickness exhibits considerable day to day variability. These data are dominated by a semi-annual variation, with maxima near the solstices.

##### 4.2 Deviations from mean values related to geomagnetic activity

Of the five coefficients describing the electron content behaviour, only the mean values reveal any systematic behaviour with geomagnetic activity. Following large increases in activity,  $N_T$  values are initially depressed while  $F$  is generally increased; both subsequently return to average levels over periods of several days. Abrupt increases in geomagnetic activity ( $\Sigma K_p > 30$ ) are indicated in Fig. 3.

The depletion of  $N_p$  is relatively severe, being up to 75%, compared with 55% maximum depletion for  $N_T$ . During disturbed periods the separation of  $N_T$  into ionospheric and protonospheric components may not be appropriate due to severe changes in the shape of the ionization profile. A depletion of the ionization in the topside ionosphere will result in increased F values, which subsequently decay as the upper ionization is replenished from the underlying ionosphere. The storm deviations in F are most obvious in winter, particularly during winter nights, when a considerable proportion of the electron content is at higher altitudes. Kersley and Hajeb-Hosseini (1976) reported that the night slab thickness increases with increasing geomagnetic activity. However, the scatter in the mean slab thickness values masks any such behaviour in the present analysis.

Despite these responses of  $N_T$  and F to geomagnetic activity, the correlation coefficients between the residuals and the geomagnetic indices are small. The best correlation is obtained when the residual mean  $N_T$  is correlated with the  $\Sigma K_p$  index for the previous day (Fig. 4). The regression lines support a negative correlation between these parameters, with a correlation coefficient magnitude of 0.56.

#### 4.3 Diurnal components, amplitudes

Unlike the mean  $N_T$  values, the diurnal components are dominated by a semi-annual variation with largest values near the equinoxes (Fig. 5). The minimum diurnal variation in  $N_T$  occurs approximately 12 days after the solstice. A similar variation is reported by M nther (1975) for the solar minimum years 1965/1966, although the present magnitudes are approximately twice as large. M nther's data also consistently depict the summer values as the smallest for all the ascending sunspot cycle years, in contrast to the present results.

Since the layer shape is dominated by the ionospheric portion in summer, the smallest diurnal variation of F is also expected at this time. The larger relative changes of the layer shape in winter are also revealed in the diurnal component of the slab thickness, which essentially follows an annual variation.

The diurnal component of the protonospheric content does not vary significantly throughout the year, although the July values again show self-consistent behaviour. The diurnal variation averages only 17% of the mean  $N_p$  content, whereas that for  $N_T$  is typically 45%. The effective contribution of  $N_p$  to maintaining the nighttime ionosphere along the ray path is then typically

$$N_p \sim 0.7 \times 10^{16} \cos\left(\frac{2\pi}{24}(t - t_{24})\right)$$

yielding a maximum apparent downward flux of

$$\left.\frac{\Delta N_p}{\Delta t}\right|_{\max} \sim 2 \times 10^{12} \text{ m}^{-2} \text{ s}^{-1}$$

Although this quantity refers to the slant path, this is probably dominated by flux tubes with L values near 2, for which a flux of this magnitude is appropriate (Murphy et al., 1976).

#### 4.4 Diurnal components, phases

The diurnal phases (Fig. 6) are represented as the hour at which the maximum occurs. Due to the solar control over  $N_T$ , little variation is expected in the diurnal phase for this quantity, and the r.m.s. deviation is only 0.69 hours. There is, however, a retarding of the maximum by approximately 1.5 hours during summer, a feature also identified by M nther (1975). In winter the maximum occurs approximately 1 hour after mid-day, a delay that may be associated with the diffusive processes responsible for the F2 region, the major contributor to the electron content. The increased lag in summer might be produced by poleward neutral winds by day, decreasing the electron content during the early part of the day.

Diurnal phases of the F values exhibit more variability than those of  $N_T$ . The annual mean value of 12.8 hours is 0.75 hours ahead of the mean phase for  $N_T$ ; the layer is effectively at its lowest extent before the electron content maximizes. This again is consistent with the production maximum being below the F2 region peak in electron density.

The diurnal phase of slab thickness is near local midnight during most of the year, the slab thickness being largest during night hours (Fig. 1), except for the sunrise peaks. However, during summer this phase is retarded to near 0900 hours.

The diurnal  $N_p$  variations are small and the corresponding phase exhibits considerable scatter. Peaks occur most often in the evening sector. The annual mean value is 14.87 hours, which lags the mean diurnal maximum in  $N_T$  by 1.34 hours.

The protonosphere is commonly thought to provide a reservoir for the underlying ionosphere, supplying ionization at night and being replenished during the day by diffusion along geomagnetic field lines. Although the present ray path intersects many field lines, its ionospheric portion is dominated by L values near 1.8 - 2.0 and so the above phase difference represents the delay in the diffusive process. The maximum value of  $N_p$  occurs when the plasma pressures above and below a height near 2500 km are equal, at times near 1800 LT

at  $L = 3$  according to the equinox model of Murphy et al. (1976). The present ray path geometry is more complicated than this however, and phase differences of  $N_p$  between the European and American sectors have been attributed to coupling with the conjugate ionosphere (Kersley and Klobuchar, (1978)).

#### 4.5 Semi-diurnal components, amplitudes

The semi-diurnal coefficients (Fig. 7) for  $N_T$  confirm the general behaviour indicated by the spectra for short selected periods (Fig. 2), i.e. largest values in summer. Munther (1975) also reported maximum values in summer, with the ratio of semi-diurnal to diurnal amplitudes exceeding unity during sunspot minimum years. The present values of this ratio are no greater than 0.7. Large values of the semi-diurnal component of  $F$  in winter are a result of changes in the layer shape which correspond to the nocturnal increases in  $N_T$ . Slab thickness values also maximize in winter, where the sunrise peak is more pronounced. The coefficients of  $N_p$  are typically of the same magnitude as the r.m.s. deviation of daily values, and consequently they reveal no significant behaviour; neither do their semi-diurnal phases (Fig. 8).

#### 4.6 Semi-diurnal components, phases

During winter the  $N_T$  semi-diurnal phase has a peak near 1200 hours. This contribution results from the nocturnal increases, whereas during summer,  $N_T$  behaviour is dominated by the bite-out near noon and the extended length of daylight. The large summer 12-hour components peak at 0800 (and 2000) to describe these features. Similar behaviour is observed in the  $F$  values. A distinct summer to winter change is also apparent in the slab thickness, the consistent winter phase near 0600 accounting for the sunrise peaks at this time.

### 5. RECONSTITUTION OF THE DATA

The empirical description requires 25 coefficients in all, for example

$$N_T = N_{T0} + N_{24} \cos\left(\frac{2\pi}{24}(t - t_{24})\right) + N_{12} \cos\left(\frac{2\pi}{12}(t - t_{12})\right)$$

with each of the 5 coefficients given by equations such as

$$N_{T0} = N_{00} + N_{365} \cos\left(\frac{2\pi}{365}(d - d_{365})\right) + N_{183} \cos\left(\frac{2\pi}{183}(d - d_{183})\right)$$

The 25 coefficients for  $N_T$  are presented in table 1 of the appendix. The deviations are approximately normally distributed and although the five coefficients are not expected to be strictly independent, there is no significant correlation between them. Summing the variances suggests that the electron content variations can be reconstructed with an r.m.s. deviation of  $5 \times 10^{16} \text{ m}^{-2}$ . Figure 9 shows the reconstructed data for the 15th day of each month and a comparison with the monthly medians, whose r.m.s. deviation is typically  $3 - 4 \times 10^{16} \text{ m}^{-2}$ . During September, data were only recorded on nine days, and those for March were also subject to large gaps. The largest electron content values occur during the equinoctial months, and other features reproduced by the formulae include the noon bite-out during summer and the nocturnal increases in the winter months. Thus, a description using two harmonics is faithful to the most important features in these data.

It has been suggested that the annual variation of slab thickness might be used to predict local electron content values from measured or predicted  $N_{\text{max}}$  or foF2. For example, Klobuchar and Allen (1970) suggest including diurnal and annual variations

$$\tau = 261 + 26 \sin\left(\frac{t-9}{12}\pi\right) + 37 \sin\left(\frac{d-60}{183}\pi\right)$$

The present analysis, however, suggests that the behaviour is not as simple as this, and a reconstitution of  $N_T$  from the slab thickness and  $N_{\text{max}}$  from Dourbes is unable to reproduce the data satisfactorily.

Clearly, the harmonic analysis with only 2 harmonics cannot represent rapid (< 3 hours) variations. Inclusion of an 8-hour component does not, however, improve the reconstruction of the slab thickness, and the 8-hour components are usually of the same order as the r.m.s. deviation. The large variations are an intrinsic feature of the slab thickness parameter and some smoothing prior to a harmonic analysis may be appropriate.

### 6. COMPARISONS WITH GLOBAL MODELS

#### 6.1 The Bent model

The Bent model (Llewellyn and Bent, 1973) is a global empirical description of the ionization profile up to an altitude of 2000 km. It is based on 50,000 topside sounder profiles and describes the topside ionosphere, referred to  $N_{\text{max}}$  from predictions, in three exponentially decreasing sections. The coefficients of these sections have seasonal, latitudinal and solar activity variations derived from the topside data base. The profiles are intended for the calculation of time delay and refractive effects and so some details, notably features of the bottom-side ionosphere, have been sacrificed. Profiles

from the Bent model appropriate to the Lancaster ray path and solar activity conditions (represented by the 10.7 cm solar flux) have been integrated to produce electron contents. Since these refer to altitudes below 2000 km, a comparison with the Faraday content,  $N_F$ , described in section 2 is appropriate (Fig. 10). The extra 500 km or so of ray path which  $N_F$  represents will have the greatest effect during winter nights. Even with this taken into account, the nighttime content of the Bent model is still slightly low according to our data. In that model, increases in the solar activity produce increased content values during the day but leave the night values relatively unchanged. Also during the night, the diurnal change in  $F_1$  will cause  $N_F$  to be underestimated slightly. The summer and equinox behaviour of the Bent calculations is in reasonable agreement with the observed medians.

To convert electron contents from Faraday rotation measurements to total contents, Davies (1978) has suggested

$$N_T = K N_{Fmax} + N_F \quad \text{with } K = 0.1$$

since the diurnal variation in  $N_p$  is typically less than  $10^{16} \text{ m}^{-2}$ . A regression analysis of the Lancaster data supports this expression for summer ( $K = 0.085$ ); however for winter and equinox  $K$  is 0.25.

### 6.2 International reference ionosphere (1978)

This empirical model (Rawer et. al., 1978) is more concerned with the actual profile shapes than is Bent, particularly in the lower ionosphere. The topside, however, is derived from the Bent description but excludes the discontinuities introduced by the three parameter topside profile. This model is limited to an altitude of 1000 km, mainly due to the scarcity of data for higher levels and the fact that it simultaneously produces temperature and positive ion data. The F2 region parameters  $h_{max}$  and  $N_{max}$  may be generated by the model, but the comparison in Fig. 11 has used experimental medians for  $N_{max}$ . In summer and equinox the agreement with  $N_F$  is good despite the extra vertical equivalent of 1500 km of ray path. In winter, although the night values are good, the model profile thickness is too large during the day.

### 6.3 Time-dependent solutions

Work has recently begun on adapting a physically realistic plasmaspheric model (Murphy et. al., 1976) to the Lancaster to ATS-6 ray path. This is a time dependent model, with a plasmasphere consisting of  $O^+$  and  $H^+$  ions embedded in a model neutral atmosphere. The constituent momentum and continuity equations for each ionic species are integrated along given (dipole) magnetic field lines. The resulting densities are interpolated to the Lancaster ray path, corrected for local time variations and subsequently integrated. In the past, electron content models have usually restricted themselves to regions below 1000 km and impose upper boundary conditions of zero flux at this level. The transport of ionization between the ionosphere and protonosphere is important, however, and is a fundamental part of this model. An example, Fig. 12 shows the three parameters relevant to the ATS-6 data:  $N_T$ ,  $F$  and  $\tau$ . The electron content behaviour is typical of a disturbed day with an evening peak. In an attempt to simulate this pattern, the neutral meridional wind, an input to the model, has been given a large equatorward flow at this time (as a possible consequence of auroral zone heating). While this provides a description of  $N_T$ , the other two parameters are clearly at variance with the observations. The large  $F$  values suggest that the topside ionosphere is deficient in the model, i.e. the effective profile is too low down. Changes to the model could include changes to the plasma temperatures, temperature gradients, or neutral hydrogen concentration. These, of course, have consequences for the protonospheric contents and fluxes. It is hoped that simulation of the Lancaster data will provide an insight into the magnitude of these parameters, and the ability of satellite beacon experiments to deduce related quantities. This approach is being pursued at present.

## 7. SUMMARY

Harmonic analysis of the electron content recorded at Lancaster using the ATS-6 transmissions provides a satisfactory description of the median behaviour. The daily coefficients vary in a well defined manner throughout the year, enabling a description in terms of annual and semi-annual variations. These enable the electron content data to be reconstructed with a typical r.m.s. deviation of  $5 \times 10^{16} \text{ m}^{-2}$ . A natural extension of this analysis is to other ray path geometries and solar activity conditions. A comparison with two readily available empirical models considers their success and favours the Bent model for the derivation of integrated content.

Further empirical models are described in the review by K hnlein (1979). These models take the level of solar activity into account, either through the sunspot number of 10.7 cm flux, but they exclude the effects of geomagnetic variations. These effects are in general only predictable for sudden large disturbances. An improvement for predictions including geomagnetic storm behaviour could follow the approach of Mendillo and Lynch (1979) who find that quiet and disturbed days have 'mirrored' deviations from the monthly medians.

The preliminary example of the plasmaspheric model (Fig. 12) shows the difficulty of simulating the data with a time dependent model when more than just the electron content is known. However, when successful, this approach should place well defined limits on the physical parameters involved in several key plasmaspheric processes.

### Acknowledgements

The authors wish to thank G. J. Bailey and R. J. Moffett of the Department of Applied Mathematics and Computing Science, University of Sheffield, for the model data used in section 6.3; R. S. Allen of A.F.G.L. for the Bent model calculations; S. Ganguly for his work during the observational phase and M. G. Berry for assistance in the data reduction. The ionosonde data from Dourbes were supplied by World Data Centre-C1.

### References

- CHEN, W.Y. and STEGUN, G.R., 1974, Experiments with maximum entropy power spectra of sinusoids. *J. Geophys. Res.* **79**, 3019.
- DAVIES, K., 1978, Overview of published research using the ATS-6 radio beacon. In: Proceedings of the symposium on beacon satellite measurements of plasmaspheric and ionospheric properties. (ed. P.F. Checcacci), Firenze, Italy.
- DAVIES, K., DEGENHARDT, W., HARTMAN, G.K. and LEITINGER, R., 1977, Electron content measurements over the U.S. Station report. Max-Planck-Institut für Aeronomie.
- KERSLEY, L. and HAJEB-HOSSEINIEH, H., 1976, The dependence of ionospheric slab thickness on geomagnetic activity. *J. atmos. terr. Phys.*, **38**, 1357.
- KERSLEY, L. and KLOBUCHAR, J.A., 1978, Comparison of protonospheric electron content measurements from the American and European sectors. *Geophys. Res. Lett.*, **5**, 123.
- KLOBUCHAR, J.A., 1975, A first-order, worldwide, ionospheric, time delay algorithm. AFCRL-TR-75-0502. Airforce surveys in geophysics, No. 324.
- KLOBUCHAR, J.A. and ALLEN, R.S., 1970, A first order prediction model of total electron-content group path delay for a mid-latitude ionosphere. AFCRL-70-0403.
- KÖHNLEIN, W., 1978, Electron density models of the ionosphere. *Rev. Geophys. and Space Phys.* **16**, 341.
- LLEWELLYN, S.K. and BENT, R.B., 1973, Documentation and description of the Bent ionospheric model. ARCRL-TR-73-0657.
- MENDILLO, M. and LYNCH, F.X., 1979, The influence of geomagnetic activity on the day-to-day variability of the ionospheric F region. AFGL-TR-79-0074.
- MÜNTHER, C., 1975, Fourier analysis of sequences of total electron content. In: Proceedings on the beacon satellite investigations of the ionosphere structure and ATS-6 data. Moscow 1975.
- MURPHY, J.A., BAILEY, G.J. and MOFFETT, R.J., 1976, Calculated daily variations of  $O^+$  and  $H^+$  at mid-latitudes. *J. atmos. terr. Phys.* **38**, 351.
- RAWER, K., RAMAKRISHNAN, S. and BILITZA, D., 1978, International Reference Ionosphere 1978 U.R.S.I. Brussels.
- TITHERIDGE, J.E., 1971, The spectrum of electron content fluctuations in the ionosphere. *Planet. Space Sci.* **19**, 1593.
- TITHERIDGE, J.E., 1972, Determination of ionospheric electron content from the Faraday rotation of geostationary satellite signals. *Planet. Space Sci.* **20**, 353.

### Appendix

Tables of annual coefficients of  $N_T$ ,  $F$ ,  $\tau$  and  $N_p$ . Daily phases are in radians unless otherwise stated.

Table 1  
Annual Coefficients of  $N_T$  (in units of  $10^{16} \text{ m}^{-2}$ )

	$N_{00}$	$N_{365}$	$d_{365}$	$N_{183}$	$d_{183}$	$\Delta r.m.s.$
$N_{T0}$	17.05	4.96	191	2.15	296	2.27
$N_{24}$	7.86	1.32	203	2.53	279	1.52
$t_{24}$ (hours)	13.53	-0.61	344	-0.38	311	0.69
$\phi_{24}$ (rad.)	2.74	0.16		0.10		0.18
$N_{12}$	2.83	1.05	211	0.75	168	1.02
$t_{12}$ (hours)	10.80	-2.35	151	-0.76	164	1.91
$\phi_{12}$ (rad.)	0.63	1.23		0.40		1.00

Table 2  
Annual Coefficients of F (MHz)

	F <sub>00</sub>	F <sub>365</sub>	d <sub>365</sub>	F <sub>183</sub>	d <sub>183</sub>	Δr.m.s.
F <sub>0</sub>	0.60	0.08	181	0.01	223	0.025
F <sub>24</sub>	0.09	0.04	14	0.02	279	0.017
φ <sub>24</sub> (r)	2.94	0.12	250	0.22	208	0.308
F <sub>12</sub>	0.04	0.01	25	0.01	149	0.016
φ <sub>12</sub> (r)	0.82	1.04	155	0.50	310	1.033

Table 3  
Annual Coefficients of τ (km)

	τ <sub>00</sub>	τ <sub>365</sub>	d <sub>365</sub>	τ <sub>183</sub>	d <sub>183</sub>	Δr.m.s.
τ <sub>0</sub>	771.5	32.4	94	61.9	167	84.4
τ <sub>24</sub>	185.1	74.3	356	23.5	185	71.5
φ <sub>24</sub> (r)	5.39	1.23	361	0.45	269	0.50
τ <sub>12</sub>	118.6	54.8	17	63.2	162	66.2
φ <sub>12</sub> (r)	3.96	0.63	143	0.46	283	0.97

Table 4  
Annual Coefficients of N<sub>p</sub> (in units of 10<sup>16</sup> m<sup>-2</sup>)

	N <sub>p00</sub>	N <sub>p365</sub>	d <sub>365</sub>	N <sub>p183</sub>	d <sub>183</sub>	Δr.m.s.
N <sub>p0</sub>	4.09	0.41	305	0.73	296	0.79
N <sub>p24</sub>	0.69	0.08	184	0.16	223	0.30
φ <sub>24</sub> (r)	2.39	0.11	238	0.40	300	0.92
N <sub>p12</sub>	0.32	0.00	250	0.06	207	0.17
φ <sub>12</sub> (r)	3.20	0.58	264	0.60	250	1.52

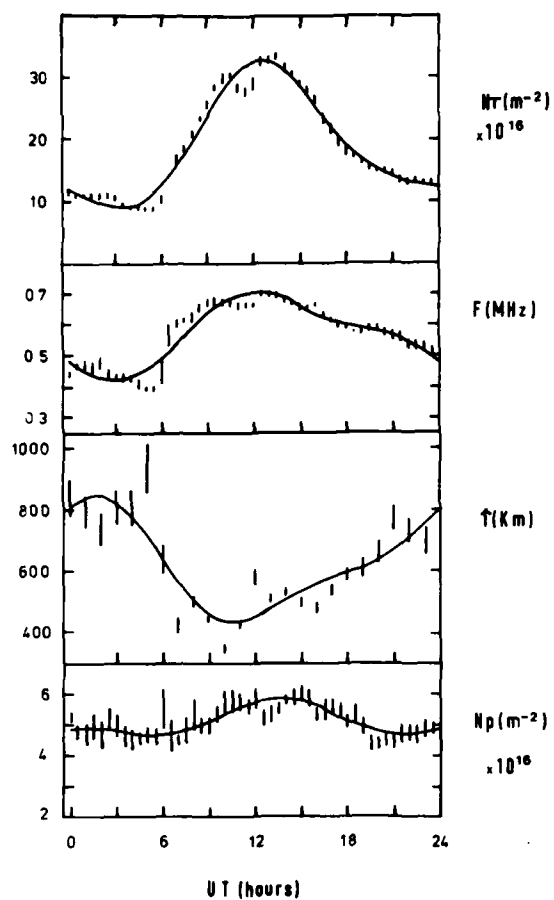


Fig. 1 Typical example of the recorded data (November 19th, 1975). The solid line represents the best fit using mean, diurnal and semi-diurnal components.

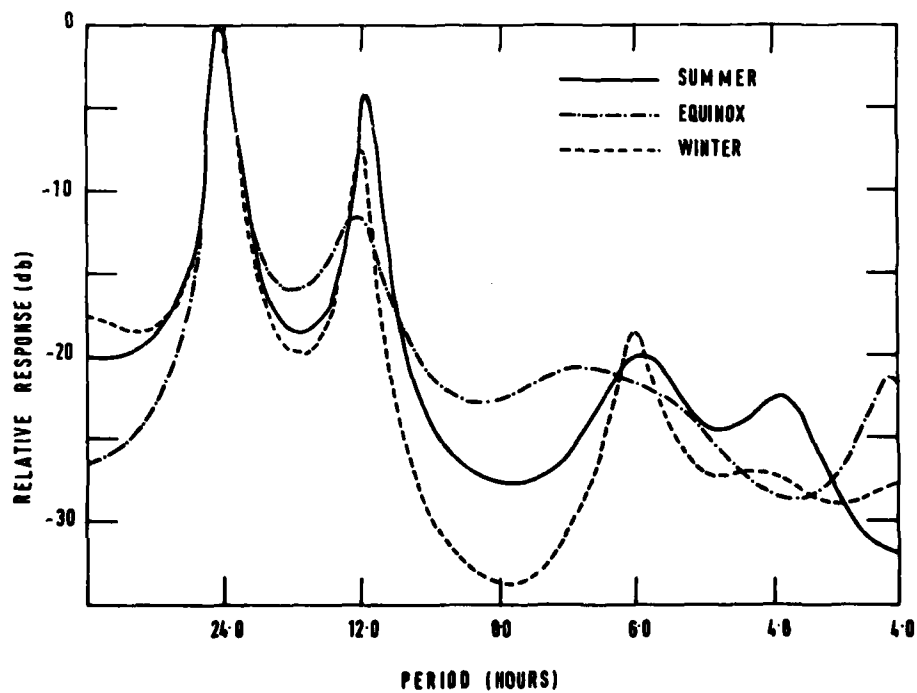


Fig. 2 Maximum entropy method spectra of electron content variations.



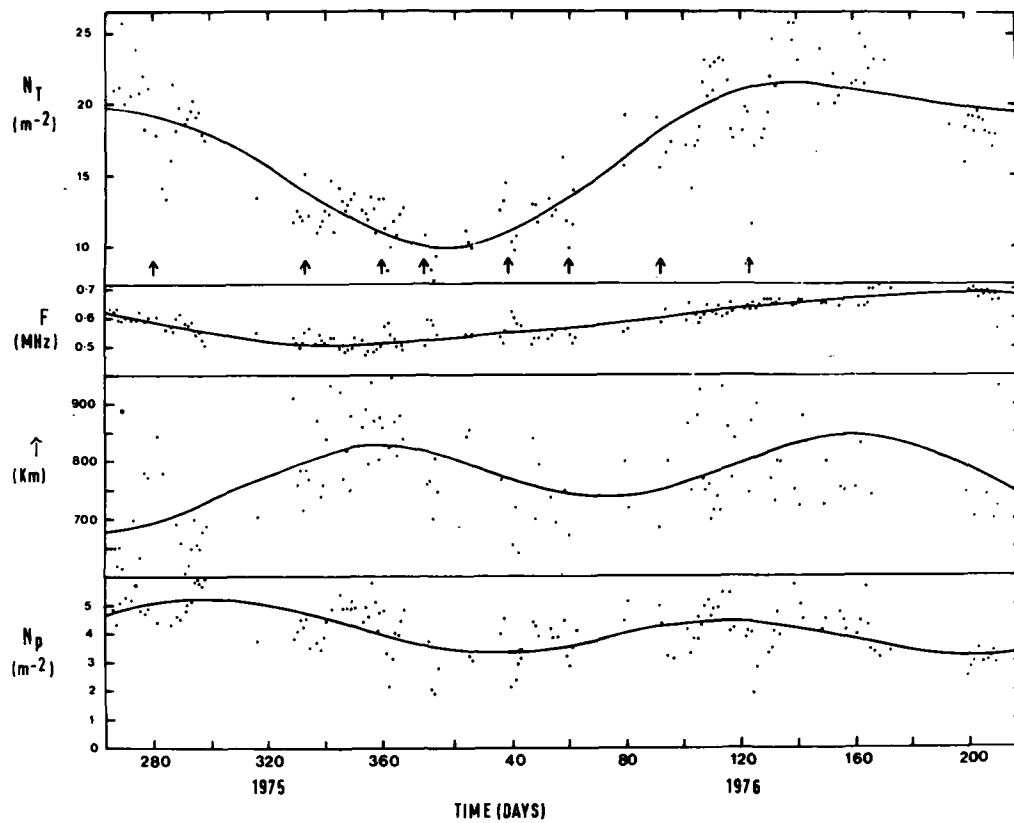


Fig. 3 Daily mean values of  $N_T$ ,  $F$ ,  $\tau$  and  $N_p$ . Arrows indicate days on which large increases in geomagnetic activity ( $\Sigma K_p > 30$ ) occurred. Solstices are days 356 (winter) and 174, equinoxes are days 265 and 82.

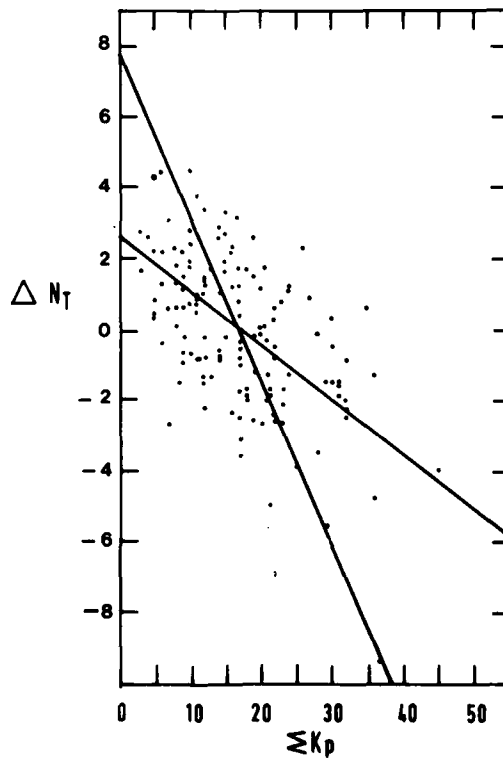


Fig. 4 Residual mean electron content versus  $\Sigma K_p$  for the previous day.

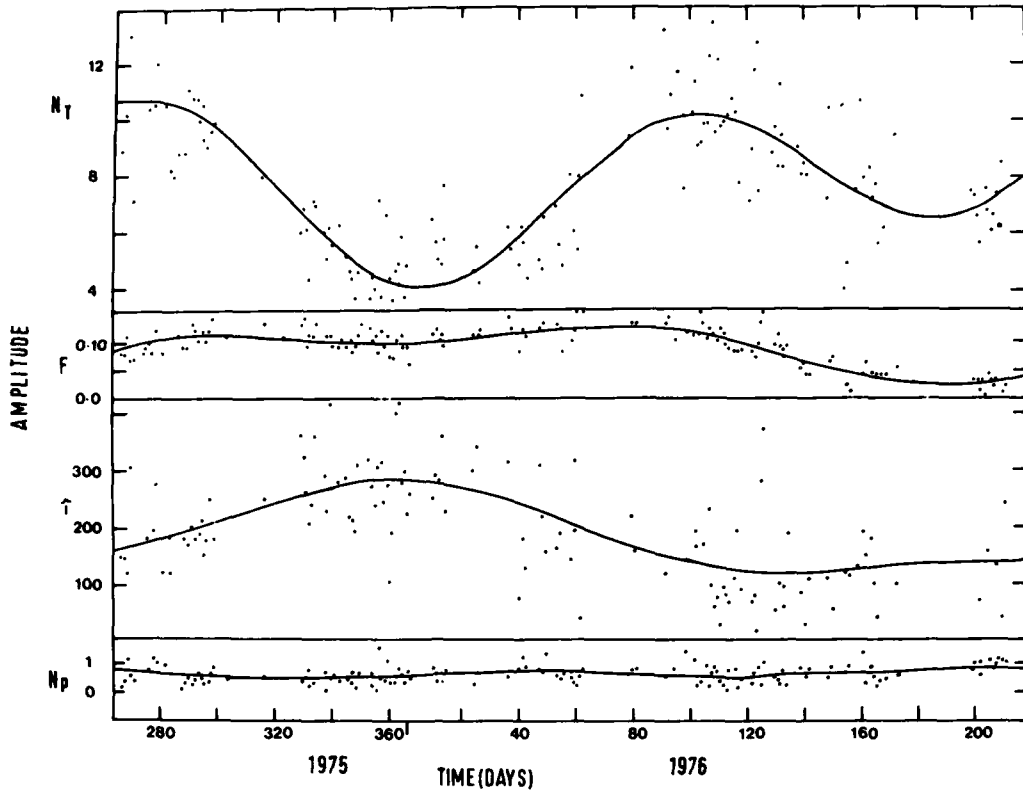


Fig. 5 Diurnal amplitudes for  $N_T$  ( $\times 10^{16} \text{ m}^{-2}$ ),  $F$  (MHz),  $\tau$  (km) and  $N_p$  ( $\times 10^{16} \text{ m}^{-2}$ ).

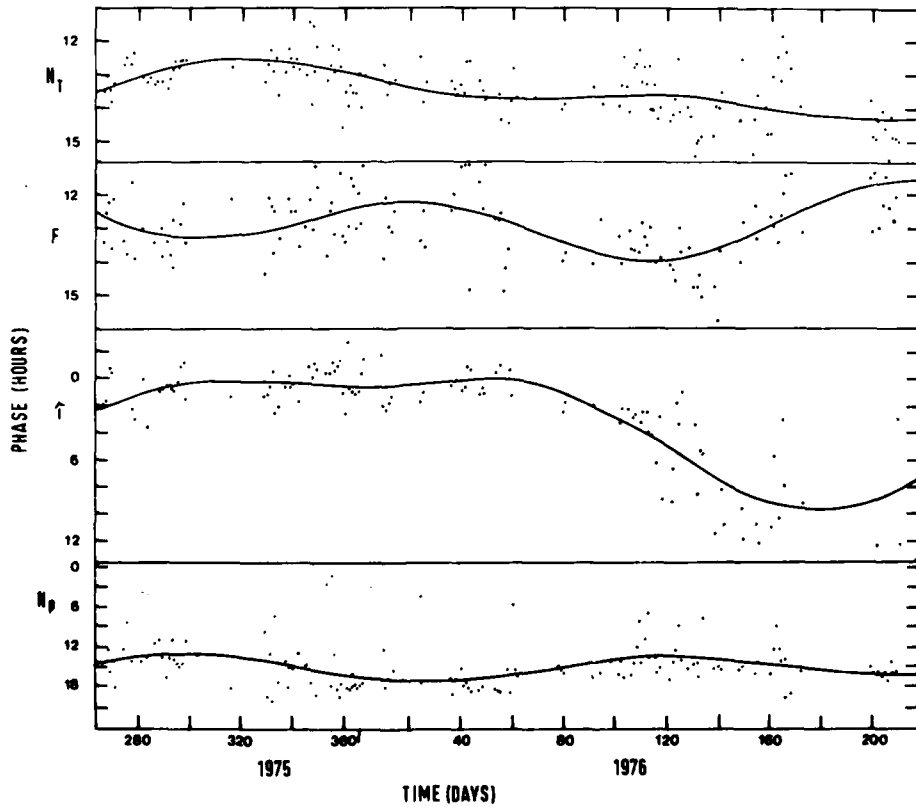


Fig. 6 Diurnal phase (hour of the maximum value) for  $N_T$ ,  $F$ ,  $\tau$  and  $N_p$ .

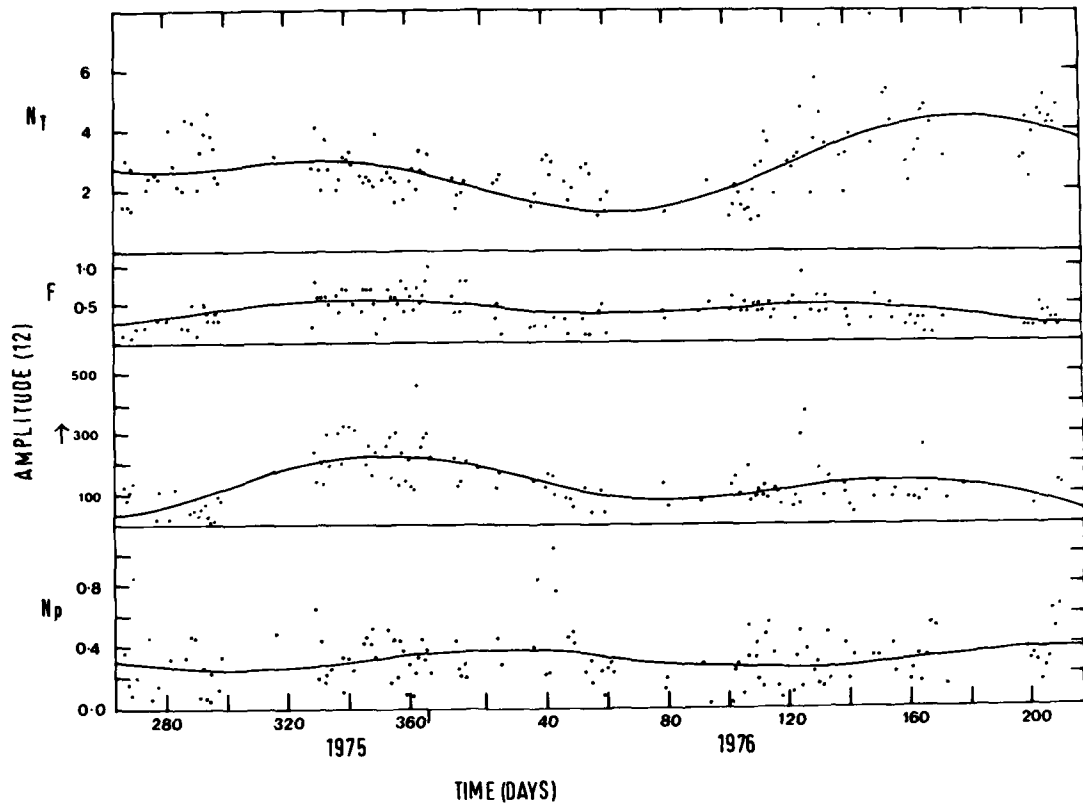


Fig. 7 Semi-diurnal amplitude for  $N_T$  ( $\times 10^{16} \text{ m}^{-2}$ ),  $F$  (MHz),  $\tau$  (km) and  $N_p$  ( $\times 10^{16} \text{ m}^{-2}$ ).

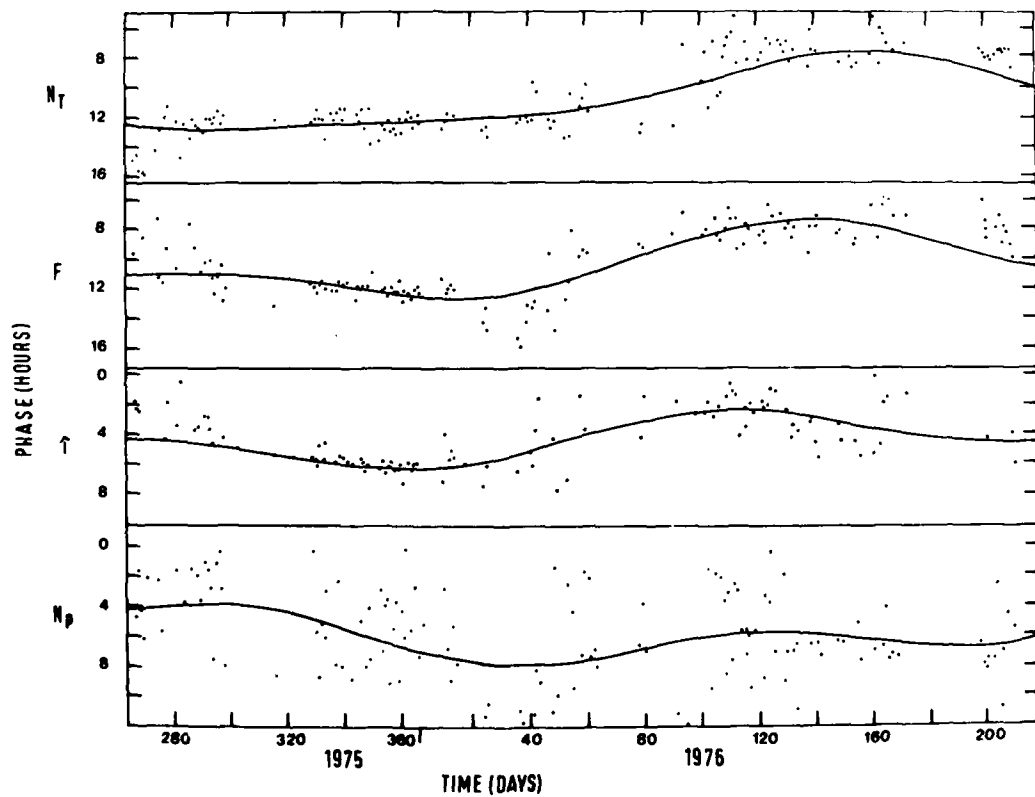


Fig. 8 Semi-diurnal phase (hour of the maximum value) for  $N_T$ ,  $F$ ,  $\tau$  and  $N_p$ .

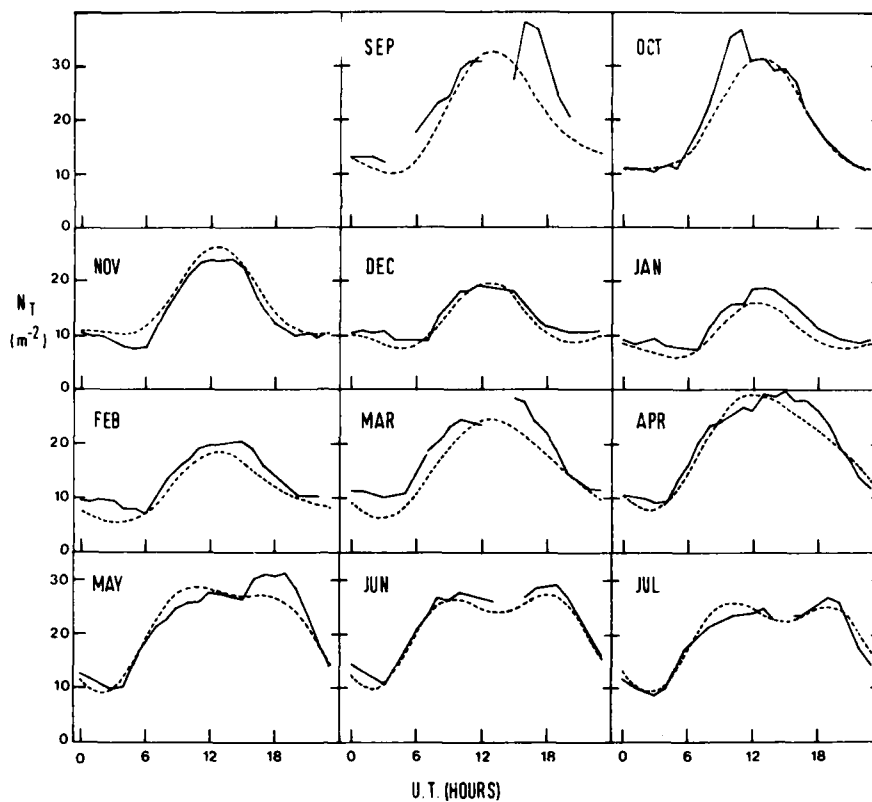


Fig. 9 Reconstitution of the electron content from the harmonic analysis (dashed line) and median observed values (solid line).

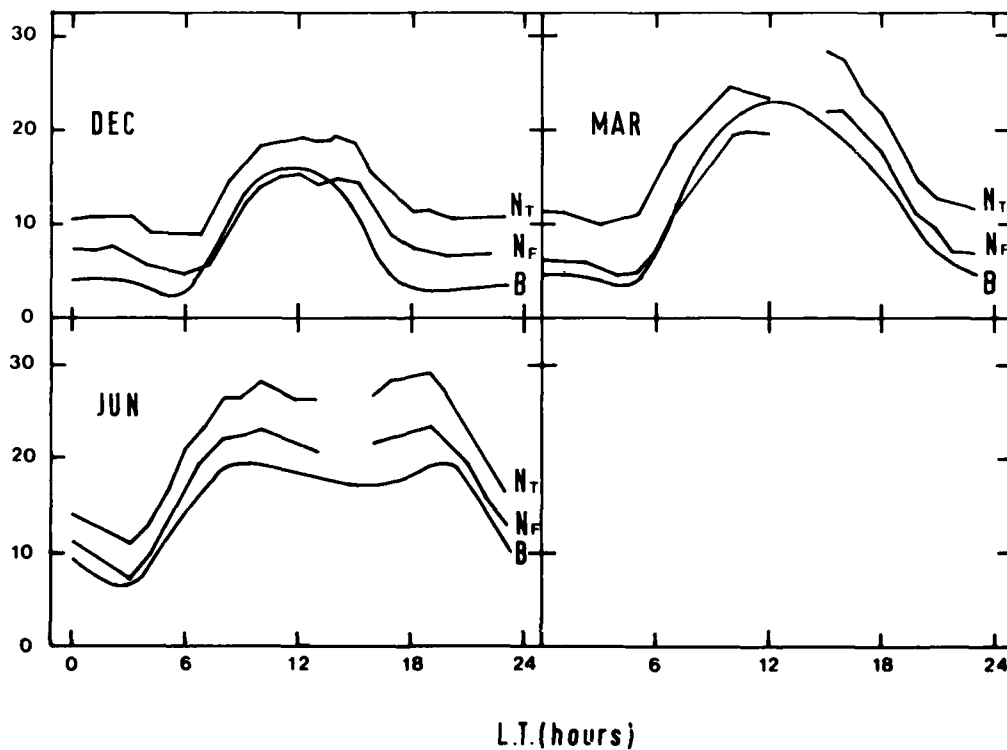


Fig. 10 Comparison of the Bent model (B) with median electron content  $N_T$  and Faraday content  $N_F$  (units  $10^{16} \text{ m}^{-2}$ ).

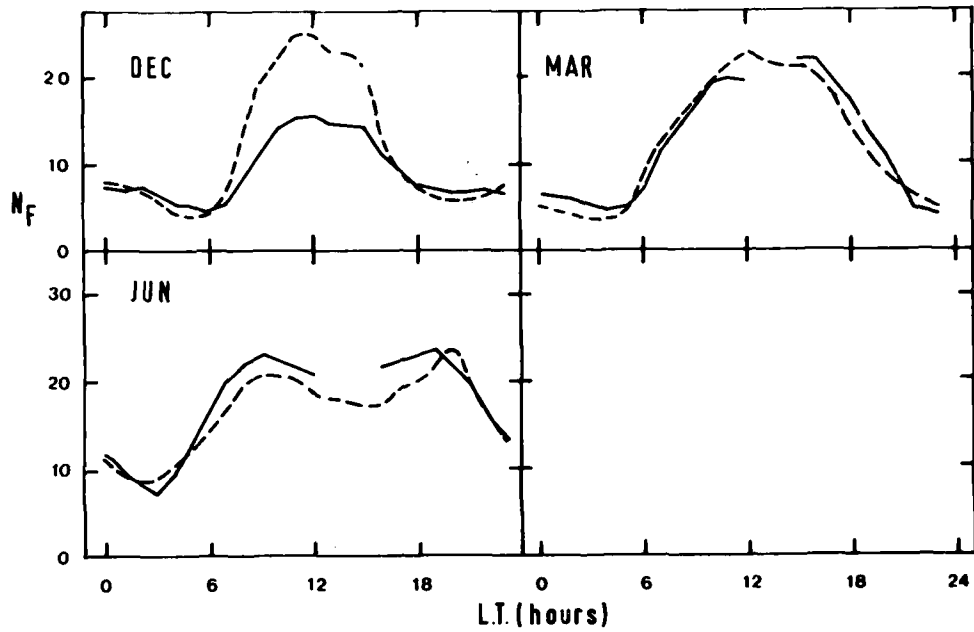


Fig. 11 Comparison of the International Reference Ionosphere (dashed line) with median Faraday content  $N_F$  (solid line) (units  $10^{16} \text{ m}^{-2}$ ).

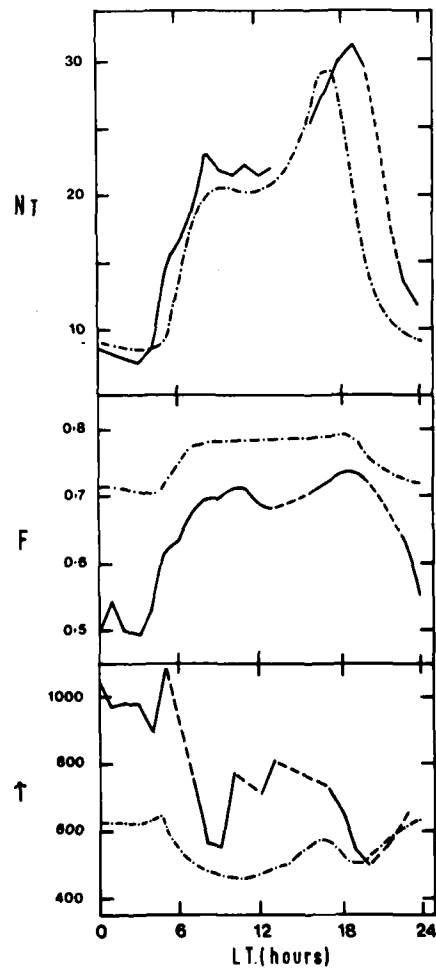


Fig. 12 Comparison of time dependent solutions (dashed line) with experimental parameters for May 9th, 1975 (solid line).

**SUMMARY OF SESSION V – NEW DATA ON IONOSPHERIC IRREGULARITIES**

by **C.L.Rino** (Session Chairman)

The opening summary paper by **C.Rino** reviewed the propagation theory and signal statistics advances that have emerged during the last five or six years together with Wideband satellite data that verify the principal results. **G.Hartmann** took a broad look at the general methodology of scintillation studies in light of new computer and graphic display technology. **C.Liu** presenting the paper by **Yeh** and **Liu** reviewed recent analysis of ATS 6 data that further verified the predicted behavior of the intensity scintillation index and the time structure of scintillating signals.

In a change from theory, **J.Aarons** reviewed some very interesting new observations of equatorial scintillation. **D.Fang** reviewed equatorial scintillation data obtained from the Comsat satellites. Finally, **A.Johnson** reviewed some novel measurements made from the AFAL aircraft. The latter were particularly interesting in light of the demonstrated effectiveness of scintillation mitigants.

Overall, the session showed continued and even increasing progress in the areas of scintillation theory and new data sources and analysis methods.

## TRANSIONOSPHERIC RADIOWAVE PROPAGATION AND SIGNAL STATISTICS

C. L. Rino  
SRI International  
Menlo Park, CA 94025 USA

## ABSTRACT

With the advent of satellites such as NTSS/TRANSIT, ATS-6, and WIDEBAND that carry multifrequency phase-coherent beacons, a large body of phase-scintillation data has been obtained. These data have made important contributions to our overall understanding of scintillation phenomena. New, theoretical results that characterize intense scintillation in power-law environments have also recently emerged. This paper presents a unified review of these developments.

In a power-law environment, the large-scale structures are primarily phase perturbers, whereas the small-scale structures give rise to more fully developed scintillation. This two-component signal structure is a prominent feature of the first-order signal statistics, which are discussed in detail. The theory is reviewed with the aim of producing a set of simple formulas that characterize the onset of amplitude and phase scintillation, the scintillation time structure under weak- and strong-scatter conditions, and the coherence bandwidth.

Amplitude and phase scintillation data that support the theory are presented. As an example of the broad applicability of the theory, a model that characterizes the ionospheric-induced radar coherent integration loss is also described.

These results, together with refinements in morphological models and a rapidly improving comprehension of the instability mechanisms that cause the irregularities, should improve our ability to predict or mitigate the deleterious effects of radiowave scintillation.

## 1. INTRODUCTION

The amplitude scintillation of transionospheric radiowaves has been studied for decades. Only recently, however, with the advent of satellites such as NNSS/TRANSIT, ATS-6, and WIDEBAND that carry multifrequency phase-coherent beacons has the full complex signal structure been measured. Concomitant research in related fields such as optics, radio astronomy, and acoustics has stimulated the development of new theoretical results. This paper presents a unified review of these developments.

As shown in Section 2, the complex signal structure is dominated by large, slowly varying phase excursions. This is a direct consequence of the size distribution of the ionospheric irregularities, which admits a power-law spectral characterization. The power-law continuum evidently extends from scale sizes below a few hundred meters to several tens of kilometers.

Under weak-scatter conditions at frequencies above VHF, the largest and most intense irregularities subtend a Fresnel zone. They are, therefore, mainly phase perturbers. Smaller, less intense irregularities suffer more diffraction, and thereby contribute most of the amplitude structure. Because the signal components exist simultaneously, the full complex-signal structure cannot be characterized by Rician, log-normal, or generalized gaussian statistics, although the latter does reproduce the most rapid scintillation.

For system-analysis and modeling applications, one needs a simple characterization of the onset of amplitude and phase scintillation, and the time structure of the fading, particularly under strong-scatter conditions. In Section 5 an appropriate set of formulas is summarized. To introduce them, however, in Section 3 we review the computation of complex signal moments from the parabolic-wave equation using the "Markov" approximation.

All complex signal moments can, in principle, be computed from the integrated-phase structure function. Because of the central role, the structure function plays in the propagation theory, its power-law form is discussed in detail in Section 4 together with its various approximations. The power-law slope is a critical parameter in this model.

The one-dimensional spectral-density function (SDF) of the signal phase has the power-law form  $Tf^{-p}$  over all significant temporal frequencies. If  $p$  is less than three, the phase structure function can be simply described in terms of a structure constant, and the techniques used to analyze neutral fluid turbulence are applicable. If  $p$  is greater than or equal to three, the situation changes dramatically. Under strong-scatter conditions, for example, the  $S_4$ -scintillation index achieves an asymptotic value greater than unity. Such effects are unique to scattering in power-law environments.

In spite of the elegance of the complex-moment equations derived under the "Markov" approximation, they are very difficult to solve in most cases. Computations using the phase-screen model, however, are comparatively simple. Important recent results have shown that the phase-screen model accurately reproduces all the essential features of propagation in an extended medium (Bramley, 1977; Fante, 1976). The equivalent phase-screen is obtained by integrating the variations in electron density along the propagation path. All the theoretical results presented in this paper have been derived by using the phase-screen model.

In Section 6 data from the Wideband-satellite experiment that support the theory are presented. Analysis of the phase-scintillation data shows that the spectral index of the one-dimensional phase spectrum is generally less than three, in which case simple asymptotic relations that characterize the fade-coherence time can be used. Excellent agreement between theory and experiment has been obtained for the fade-coherence time under strong-scatter conditions. Correlative work, using data from the NNSS satellites and ATS-6, is also discussed in Section 6.

In Section 7 the single-point two-frequency coherence function is described. An approximate analytic form is derived and then applied to obtain simple formulas for the resultant delay jitter and pulse dispersion. The formulas complement the set presented in Section 5, but data to verify the frequency coherence model have not yet been analyzed.

To illustrate the application of the propagation theory to the analysis of coherent systems, in Section 8 a model that characterizes the ionosphere-induced coherent-integration loss in radars is described. The angular spectrum effectively provides a direct measure of the coherent-integration loss.

## 2. FIRST-ORDER SIGNAL STATISTICS

Rice's (1953) model for a random ensemble of discrete scatterers was first applied to characterize the first-order scintillation statistics (Ratcliffe, 1956). In the complex plane, Rice's model predicts uniform scatter about a constant, coherent signal component. The inphase and phase-quadrature signal components are uncorrelated, identically distributed, gaussian processes. The signal phase is uniformly distributed, and the amplitude distribution is given by a simple formula.

To apply Rice's model to the scintillation problem, a large number of independent scatterers within a Fresnel zone must be present. Mercier (1962) proved that in the limit as the propagation distance approaches infinity, the distribution of the amplitude scintillation becomes Rician. Mercier's result applies to weak and strong scattering, but in the latter case the distribution is Rayleigh, a special case of Rice's distribution in which the coherent-signal component is zero.

In a power-law environment, however, there are typically both large and small scale sizes within a Fresnel zone. Only the small-scale structures potentially satisfy the central-limit theorem, and even then the quadrature signal components need not be uncorrelated. It was noted early that the log-normal distribution fits measured amplitude scintillation distributions better than Rice's distribution (Cohen et al., 1967; Ochs and Lawrence, 1969). The Rytov theory, moreover, gave theoretical support to the log-normal model (Tatarski, 1971).

Chytil (1967) first suggested that the general gaussian model is more appropriate than the Rician model. Rino et al. (1976) showed that weak ionospheric amplitude scintillation follows the general gaussian model somewhat better than the log-normal model. Recent analysis of amplitude and phase scintillation data by Fremouw et al. (1980) shows, however, that neither the gaussian nor the log-normal models are strictly applicable.

Fremouw et al. (1980) developed a multiplicative two-component model in which the more rapid amplitude and phase fluctuations are gaussian (the scatter component), and the slower variations are log-normal (the focusing component). The model is illustrated in Figures 1 through 3. Figure 1 shows a typical complex signal structure under weak to moderate scintillation conditions. Large, slow phase variations have been removed by a detrending procedure that effectively extracts the coherent signal component.

If the detrending procedure is reapplied to remove the intermediate phase variations and the associated amplitude variations with comparable time scales, the gaussian "scatter" component shown in Figure 2 results. Figure 3 shows the intermediate component that accounts for most of the phase scintillation. Note that most, but not all, of the amplitude structure is reproduced by the gaussian component, in agreement with the earlier work of Rino et al. (1976).

Figure 4 is a sequence of scatter diagrams showing the progression of the scatter and focus components from weak to strong scattering. Under strong-scatter conditions, the scatter component approximates a Rayleigh distribution. There are, however, large, slowly varying contributions from the focus component. Thus, the complex scintillation statistics do not adhere strictly to the Rayleigh model, even though  $S_4$  is near unity and the amplitude distribution is well approximated by the Rayleigh distribution.

Theoretical studies of scintillation statistics have attempted to establish relations among the various complex signal moments that are consistent with the competing statistics models. The results of these efforts confirm the empirical studies in that no simple model (e.g., log-normal, gaussian, nor Rayleigh) is completely satisfactory (DeWolf, 1969; Wang and Strohbehn, 1974; Wernik, 1976).

The Nakagami distribution fits measured amplitude-scintillation distributions very well over a broad range of scattering conditions. This is illustrated in Figure 5. The Nakagami distribution is completely specified in terms of the  $S_4$ -scintillation index  $[S_4^2 = (\langle I^2 \rangle - \langle I \rangle^2)^{1/2} / \langle I \rangle]$  as

$$P(y) = \frac{m^m y^{m-1}}{\Gamma(m)} \exp\{-my\} \quad (2.1)$$

where  $y$  is the signal intensity and  $m = S_4^2$ . A simple gaussian distribution provides a fair approximation to the phase statistics (Fremouw et al., 1980).

## 3. COMPLEX SIGNAL MOMENTS

A complete treatment of multiple scattering generally proceeds from the parabolic-wave equation

$$\frac{\partial u}{\partial s} = -i \frac{k}{2} \nabla_T^2 u(\vec{\rho}, z) + ir_e \Delta N_e(\vec{\rho}, z) u(\vec{\rho}, z) \quad (3.1)$$

where  $\partial u / \partial s$  is the directional derivative along the propagation direction,  $\nabla_T^2$  is the transverse laplacian operator,  $r_e$  is the classical electron radius,  $\lambda$  is the wavelength ( $k = 2\pi/\lambda$ ), and  $\Delta N_e(\vec{\rho}, z)$  is the local



perturbation to the electron density. A derivation and detailed discussion of Eq. (3.1) can be found in Rino (1978) and in the review papers by Prokhorov et al. (1975), Fante (1975), and Barabanenkov et al. (1971).

By applying the "Markov" approximation, one can derive differential equations from Eq. (3.1) for the complex signal moments of all orders. The references cited show, for example, that the differential equation for the complex-signal mean  $\langle u \rangle$  is

$$\frac{\partial \langle u \rangle}{\partial s} = -i \frac{k}{2} \nabla_T^2 \langle u \rangle - \frac{\partial \langle \delta \phi^2 \rangle}{\partial s} \langle u \rangle \quad (3.2)$$

where

$$\delta \phi = -r_e \lambda \int \Delta N_e(\vec{\rho}, z) ds \quad (3.3)$$

is the integrated-phase increment. Similarly, the differential equation for the mutual-coherence function

$$R_u(\vec{\rho}_1, \vec{\rho}_2; z) = \langle u(\vec{\rho}_1, z) u^*(\vec{\rho}_2, z) \rangle \quad (3.4)$$

is

$$\frac{\partial R_u}{\partial s} = -i \frac{k}{2} \left[ \nabla_{T_1}^2 - \nabla_{T_2}^2 \right] R_u - \frac{1}{2} \frac{\partial D(\vec{\rho}_1, \vec{\rho}_2)}{\partial s} R_u \quad (3.5)$$

where

$$D(\vec{\rho}_1, \vec{\rho}_2) = \langle (\delta \phi(\vec{\rho}_1) - \delta \phi(\vec{\rho}_2))^2 \rangle \quad (3.6)$$

is the integrated-phase structure function. By using the Markov approximation the averages of terms involving  $\Delta N_e$  and  $u$  are put into the simple product forms that appear in the equations.

For an incident plane wave in a medium where  $\langle \delta \phi^2 \rangle$  is independent of  $\vec{\rho}$  and  $D(\vec{\rho}_1, \vec{\rho}_2)$  depends only on  $\Delta \vec{\rho} = \vec{\rho}_2 - \vec{\rho}_1$ , the solutions to Eq. (3.2) and Eq. (3.5) are readily shown to be

$$\langle u \rangle = \exp \left\{ -\frac{1}{2} \langle \delta \phi^2 \rangle \right\} \quad (3.7)$$

and

$$R_u(\Delta \vec{\rho}) = \exp \left\{ -\frac{1}{2} D(\Delta \vec{\rho}) \right\} \quad (3.8)$$

respectively. Equation (3.8) was first derived by Fejer (1953). Bramley (1954) later derived the same equation by using the phase-screen model. The Fourier transform of Eq. (3.8) gives the angular spectrum (Booker et al., 1950).

Equation (3.7) shows that the complex signal mean becomes small as the phase variation increases. This behavior is easily understood from the phasor plots shown in Figures 1 and 4. Once the phase variations exceed  $2\pi$  radians, the signal mean will be small even if the associated amplitude scintillation is negligible.

The equations for higher-order moments cannot be solved directly, and one must resort to iterative or asymptotic methods. Throughout the development of radiowave scintillation theory, the phase-screen model has proven a very powerful tool for obtaining such results (Salpeter, 1967; Singleton, 1970). Rumsey (1975), Taylor (1972), and Gochelashvily and Shishov (1971), for example, have shown that the intensity SDF is given by the integral

$$\Phi_I(\vec{k}) = \iint \exp \left\{ -g(\vec{\xi}, \vec{k} z/k) \right\} \exp \left\{ -i \vec{k} \cdot \vec{\xi} \right\} d\vec{\xi} \quad (3.9)$$

where

$$g(\vec{\xi}, \vec{\eta}) = D(\vec{\xi}) + D(\vec{\eta}) - \frac{1}{2} D(\vec{\xi} + \vec{\eta}) - \frac{1}{2} D(\vec{\xi} - \vec{\eta}) \quad (3.10)$$

The integral itself cannot be evaluated analytically but asymptotic results are easily derived from it. To illustrate this, consider the equivalent form of Eq. (3.10).

$$g(\vec{\xi}, \vec{\eta}) = 8 \iint \phi_{\delta\phi}(\vec{q}) \sin^2(\vec{\eta} \cdot \vec{q}/2) \sin^2(\vec{\xi} \cdot \vec{q}/2) \frac{d\vec{q}}{(2\pi)^2} \quad (3.11)$$

where  $\phi_{\delta\phi}(\vec{q})$  is the phase SDF (Rino, 1979b). If  $|g(\vec{\xi}, \vec{\eta})| \ll 1$ , substituting Eq. (3.11) into Eq. (3.9) readily shows that

$$\phi_I(\vec{k}) \cong (2\pi)^2 \delta(\vec{k}) + 4\phi_{\delta\phi}(\vec{k}) \sin^2(\kappa^2 k/2) \quad (3.12)$$

which is a well known weak-scatter result.

To summarize this section, we have shown that the most important complex signal moments that characterize the scintillation structure can be computed in terms of a single quantity, the integrated-phase structure function. The most general moment equations are difficult to solve, but comparatively simple and accurate results can be derived from the gaussian phase-screen model. We will now describe the form of the phase structure function in power-law environments.

#### 4. THE PHASE STRUCTURE FUNCTION

The structure function was developed by Kolmogorov to characterize a class of nonhomogeneous processes, which he called locally homogeneous (Kolmogorov, 1941). The term is often loosely applied to describe the situation in which the background is slowly changing. For a homogeneous process, the integrated-phase structure function can be expressed in terms of the integrated-phase autocorrelation function as

$$D(\Delta\vec{\rho}) = 2 \left( R_{\delta\phi}(0) - R_{\delta\phi}(\Delta\vec{\rho}) \right) \quad (4.1)$$

A convenient SDF model that is mathematically tractable and accommodates inner- and outer-scale cutoffs is described in Rino (1979b). Within the power-law continuum,  $q_0 < q < q_1$ , the three-dimensional irregularity SDF has the form  $\phi_{\Delta N_e}(q) = C_s q^{-(2\nu+1)}$ . The corresponding two-dimensional phase SDF has the similar form  $\phi_{\delta\phi}(q) = C_p q^{-(2\nu+1)}$  where

$$C_p = r_e^2 \lambda^2 \ell_p C_s \quad (4.2)$$

In Eq. (4.2),  $r_e$  is the classical electron radius,  $\lambda$  is the wavelength, and  $\ell_p$  is the propagation path length. The phase variance has the form

$$\sigma_\phi^2 = C_p \frac{\Gamma(\nu-1/2)}{4\pi^{1/2}(\nu+1/2)} q_0^{-2\nu+1} \quad (4.3)$$

The form of the phase structure function for this model is

$$D(y) = 2\sigma_\phi^2 \mathcal{L}(y) \quad (4.4)$$

where

$$\mathcal{L}(y) = 1 - 2 \sqrt{\epsilon^2 + (q_0 y/2)^2}^{\nu-1/2} K_{\nu-1/2} \left( 2 \sqrt{\epsilon^2 + (q_0 y/2)^2} \right) \Gamma(\nu-1/2) \quad (4.5)$$

$\epsilon = q_0/q_1$ , and  $K_\nu(x)$  is the modified Bessel function.

In Figure 6,  $\mathcal{L}(y)$  is plotted against  $yq$  for  $\nu = 1, 1.5$ , and 2. Changing  $\epsilon$  by an order of magnitude produces no perceptible change over the  $yq_0$  range plotted. The precise value of the inner scale cutoff has very little effect on the overall shape of the structure function, as one should expect.

If the power-law index is not too steep, an asymptotic approximation to  $D(y)$  can be derived that is valid for  $q_0 y \ll 1$ . It is shown in Rino (1979b), for example, that

$$D(y) \sim C_{\delta\phi}^2 |y|^{2\nu-1} \quad (4.6)$$

where

$$C_{\delta\phi}^2 = \frac{C_p}{2\pi} \frac{2\Gamma(1.5-\nu)}{\Gamma(\nu+0.5)(2\nu-1)^{2\nu-1}} \quad 0.5 < \nu < 1.5 \quad (4.7)$$

is the phase structure constant. Note that in the small  $q_0$  approximation  $D(y)$  and  $\phi_{\delta\phi}(q)$  have complementary power-law forms; moreover,  $D(y)$  has no explicit dependence on the outer scale.

To demonstrate the range of validity of the small  $q_0$  approximation, in Figure 7 Eq. (4.6) is superimposed on a plot of  $\mathcal{L}(y)$ . The plot is presented with an expanded scale to emphasize the range of  $y$  values for which  $y < q_0^{-1}$  [i.e.,  $yq_0 < (2\pi)^{-1} = 0.159$ ]. For  $\nu \leq 1.2$ , the small  $q_0$  approximation works over this entire range. As the spectrum steepens ( $1.5 > \nu \geq 1.4$ ), the  $yq_0 \ll 1$  condition becomes more stringent. The Kolmogorov value  $\nu = 4/3 = 1.333$  lies within the range of validity of the small  $q_0$  approximation. Equation (4.10) has been used almost exclusively for studying scintillation induced by neutral turbulence (Tatarski, 1971). In such studies the structure constant for the refractive index is typically modeled directly (see, for example, Van Zandt et al., 1978).

For ionospheric scintillation studies, it is generally assumed that  $\nu$  is near 1.5, which is outside the range of the small  $q_0$  approximation; thus, other approximations must be used. Several researchers have used a Taylor series approximation to  $D(y)$  (Yeh and Liu, 1977; Taylor and Infosino, 1975; Buckley, 1971a,b). Difficulties arise because higher-order moments exist only if the inner-scale cutoff is finite. We shall consider only the quadratic approximation

$$\mathcal{L}(y) \cong D_1 (q_0 y)^2 \quad (4.8)$$

where

$$D_1 = \frac{1}{2} \epsilon^{\nu-3/2} K_{\nu-3/2}(2\epsilon) / \Gamma(\nu-0.5)$$

$$\cong \begin{cases} -\frac{1}{2} \log(2\epsilon) & \nu = 1.5 \\ \frac{\Gamma(\nu-1.5)}{4\Gamma(\nu-0.5)} & \nu > 1.5 \end{cases} \quad (4.9)$$

Note that for  $\nu > 1.5$ ,  $D_1$  does not depend on  $\epsilon$ . Coefficients of higher order terms in the Taylor series will, of course, depend strongly on  $\epsilon$ . The quadratic approximation is shown in Figure 8. Unlike the small  $q_0$  approximation, the quadratic approximation improves as  $\nu$  increases; moreover,

$$D(y) \cong 2\sigma_\phi^2 (q_0 y)^2 D_1 \quad (4.10)$$

retains an explicit dependence on  $q_0$  [see Eq.(4.3)].

To summarize, if  $q_0 y \ll 1$ ,  $D(y)$  can be approximated by Eq. (4.6) if  $0.5 < \nu \leq 1.4$ , and by Eq. (4.10) if  $\nu \geq 1.5$ . In the former case there is no explicit dependence on the outer scale; thus,  $q_0$  need not be explicitly known. For the more steeply sloped spectra ( $\nu \geq 1.5$ ), the outer scale exerts a direct influence on the mutual coherence function [see Eq. (3.8)].

## 5. SUMMARY OF SCINTILLATION FORMULAS

Under conditions of weak to moderate scattering, the measured rms phase can be estimated from the formula

$$\sigma_\phi^2 = \frac{2T}{p-1} \tau_d^{p-1} \quad (5.1)$$

where  $p = 2\nu$  is the power-law index of the temporal phase SDF,  $\tau_d$  is the length of the data interval over which  $\sigma_\phi^2$  is measured, and

$$T = C \frac{G}{P} \frac{\sqrt{\pi} \Gamma(\nu)}{(2\pi)^{2\nu+1} \Gamma(\nu+1/2)} v_{\text{eff}}^{2\nu-1} \quad (5.2)$$

The temporal phase SDF has the power law form  $Tf^{-P}$ .

The derivation of Eq. (5.2) is presented in Rino (1979a). The parameter  $G$  varies between unity and the value of the axial ratio for field-aligned propagation. The effective velocity converts spatial variations along the scan direction to temporal variations. In an isotropic medium or in a one-dimensional medium (highly anisotropic irregularities)  $v_{\text{eff}}$  is equal to the component of the relative scan velocity perpendicular to the line of sight. Note that  $v_{\text{eff}}$  depends critically on the equivalent phase-screen height for moving satellites.

In Figure 9 the rms electron density, obtained by integrating Eq. (4.3) over all spatial wavenumbers with  $k_0 = 2\pi/q_0$ , is plotted against  $C_n$ . The rms electron density, like the rms phase, depends on the interval over which it is measured. Since the rms electron density normalized to the average electron density measured over some interval is most often reported from in-situ measurements. Figure 9 can be used to estimate  $C_n$ . Ideally,  $C_n$  would be measured directly as is done in neutral turbulence studies. Note also that in general  $C_n$  will vary along the propagation path so the  $C_n$  value in Eq. (5.2) should be thought of as an average or effective value.

Under weak scatter conditions, the intensity-scintillation index,  $S_4$ , can be computed from the formula

$$S_4^2 = 4C_p Z^{\nu-1/2} \left[ \frac{\Gamma\left(\frac{2.5-\nu}{2}\right)}{2\sqrt{\pi} \Gamma\left(\frac{\nu+0.5}{2}\right) (\nu-0.5)} \right] \bar{J} \quad (5.3)$$

where

$$Z = \frac{\lambda}{4\pi} \left( \frac{R_1 R_2}{R_1 + R_2} \right) \quad (5.4)$$

is the Fresnel area. In Eq. (5.4)  $R_1$  and  $R_2$  are the respective distances from the equivalent phase screen to the receiver and source. The factor  $\bar{J}$  is defined in Rino (1979a). In an isotropic medium,  $\bar{J} = 1$ , and in a highly anisotropic (one-dimensional) medium,  $\bar{J} \sim \Gamma(\nu) / [\sqrt{\pi} \Gamma(\nu+1/2)]$ .

Equation (5.3) is valid only when  $\sqrt{Z} q_0 \ll 1$ , which is generally a very good approximation for ionospheric conditions. Rufenach (1975) and Costa and Kelley (1977) have used a modified power-law SDF from which an exact form that retains an outer-scale dependence can be derived, but only for  $\nu = 1.5$ . Crane (1976) has presented a general formula equivalent to Eq. (5.3) that accommodates variations along the propagation path, but it must be evaluated numerically. Crane (1976) used the Rytov formula which gives the log-amplitude variance  $\sigma_\chi^2$ . Within the range of validity of the weak-scatter theory, however,

$$S_4^2 \cong 4\sigma_\chi^2 \quad (5.5)$$

From Eq. (5.3) it follows that  $S_4 \propto \lambda^{(\nu+1.5)/2}$ . Figure 10 shows the  $C_p$  levels required to produce gigahertz scintillation. Recall that  $C_p \propto C_g$  [see Eq. (4.2)]. The strict range of validity of Eq. (5.3) is difficult to assess because of the large number of factors involved. In general, if one uses the observed rms phase as a reference level to establish  $C_g$ , Eq. (5.3) gives a result equal to or larger than the observed value of  $S_4$ . This is expected, since the weak-scatter theory does not accommodate saturation effects. For engineering applications, one can simply take the maximum value of Eq. (5.3) or unity.

To formally extend these results to the strong scatter regime, we have used the phase-screen model Eq. (3.9). In a power-law environment the scintillation level depends on the strength parameter

$$U \propto C_p Z^{\nu-0.5} \quad (5.6)$$

times a function of  $\nu$  that is discontinuous at  $\nu = 1.5$ . This is discussed in detail in Rino (1979b). The important point to note here is that  $U$  has the same functional dependence on  $C_p$  and  $Z$  as does the weak-scatter  $S_4^2$  formula in Eq. (5.2). For fixed  $\nu$ , the effects of changing propagation distance or perturbation strength are contained in a single parameter.

Figure 11 shows numerical computations of  $S_4$  for a one-dimensional phase screen (Rino, 1980) for different values of the phase spectral index,  $p$ . When  $p$  is less than 3,  $S_4$  asymptotically approaches unity from below as  $U'$  increases [ $U'$  is the one-dimensional form of  $U$ ]. For  $p \geq 3$ ,  $S_4$  first exceeds unity, then achieves a local maximum [strong focusing], and finally converges to the large  $U'$  asymptote from above. The large  $U'$  asymptote is equal to unity for  $p = 3$ , but greater than unity for  $p > 3$ . Similar behavior occurs for a two-dimensional phase screen. There, however, strong focusing occurs when  $\nu < 1.5$  as well as when  $\nu \geq 1.5$ .

These results show that in a power-law scattering medium with  $\sqrt{Z}q_0 \ll 1$ , the necessary conditions for Rayleigh scattering are strictly achieved only when  $p \leq 3$ . It is instructive to contrast this behavior with that of a medium with a well defined cutoff scale. In Figure 12 we show a schematic representation of  $S_4$  by Singleton (1970) that was originally used by Cohen et al. (1967) to summarize Salpeter's (1967) analysis.

Unlike the power-law case, perturbation strength can be parameterized by the rms phase  $\varphi_0$ . Moreover  $\varphi_0$  and the normalized propagation distance,  $\lambda z/r_0^2$ , are independent variables. If  $\lambda z/r_0^2 > 1$  and  $\varphi_0 < 1$  (Region II),  $S_4 < 1$  and the single scatter theory applies. Where  $\lambda z/r_0^2 \ll 1$  (Region I), ray optics can be used to extend results beyond  $\varphi_0 = 1$ . If  $\varphi_0$  is large enough,  $S_4$  can exceed unity (Region IV), but  $S_4$  ultimately averages to unity in the mixing region (Region III) where Rayleigh statistics are presumed to apply.

Returning now to the power-law model, if  $\nu < 1.5$  ( $p < 3$ ) it can be shown (Rino, 1979b) that

$$\langle II' \rangle - 1 = |R_u(\Delta\phi)|^2 \quad (5.7)$$

which is also a necessary condition for Rayleigh statistics. Under weak-scatter conditions, the intensity coherence time depends on the Fresnel radius. One can take

$$\tau_I \leq \sqrt{z}/v_{\text{eff}} \quad (5.8)$$

as a rough upper bound to the intensity-coherence time. Under strong-scatter conditions Eq. (5.7) can be used together with Eq. (3.8), by which  $\tau_I$  can be determined from the relation

$$D(v_{\text{eff}}\tau_I) = 1 \quad (5.9)$$

Equation (5.9) is easily evaluated by using the small  $q_0$  approximation Eq. (4.6) or the quadratic approximation Eq. (4.8). Under strong-scatter conditions, Eq. (5.9) shows that  $\tau_I$  is independent of  $Z$  and decreases with increasing  $C_p$ . Note, however, that

$$D(v_{\text{eff}}\tau_C) = 2 \quad (5.10)$$

defines the coherence time of complex signal under all scatter conditions.

The formulas presented in this section define the onset of phase and amplitude scintillation Eq. (5.1), Eq. (5.3), and the intensity coherence time  $\tau_I$  under conditions of weak Eq. (5.8) and strong Eq. (5.9) scattering. The coherence time of the complex signal is given by Eq. (5.10) for all scattering conditions. Equations (5.7) and (5.9), however, only apply when  $v < 1.5$ . It must also be kept in mind that  $L_p C_p$  is an average value that sets the perturbation levels for the equivalent phase screen. These formulas are adequate for most engineering and modeling purposes. Indeed, a unity  $S_4$  prediction by Eq. (5.3) will most often overestimate the actual  $S_4$  level.

## 6. AMPLITUDE AND PHASE SCINTILLATION DATA ANALYSIS

The Navy navigation satellites (NNSS/TRANSIT) were first used for intensive amplitude and phase scintillation measurements (Crane, 1976). The NNSS satellites transmit modulated phase-coherent signals at 150 MHz and 400 MHz for precise navigational applications that can also be used for amplitude and differential phase-scintillation measurements. The geosynchronous Applied Technology Satellite ATS-6 carries a 40, 140, and 360 MHz phase-coherent beacon for ionospheric measurements. The 360-MHz signal has sidetones for absolute total electron-content measurements (Davies et al., 1975). The Defense Nuclear Agency Wideband satellite--a modified NNSS satellite--transmitted phase-coherent signals at VHF, UHF, L band and S band for transionospheric propagation studies (Fremouw et al., 1978).

Data from all these sources show that under weak-scatter conditions ( $S_4 < 0.4$ ), the measured phase and intensity SDFs admit a power-law representation of the form  $Tf^{-p}$ . For the phase spectra, the power-law continuum generally extends from the lowest measured frequency to the noise level at the high-frequency end. The intensity spectra, however, show a low-frequency roll-off near the Fresnel frequency  $f_F \approx v_{\text{eff}}/\sqrt{Z}$ , (Crane, 1976; Ott, 1977; Umeki et al., 1977a,b).

As the scintillation increases, the phase spectra retain their power-law form, although diffraction effects may upset the simple mapping between the integrated-phase spectrum and the signal-phase spectrum. The intensity spectra undergo a significant change under strong-scatter conditions. Whitney and Basu (1977) report a continual steepening of the power-law slope as  $S_4$  increases from small values to saturation, reflecting the theoretically predicted change from a power-law to a more nearly gaussian form under strong-scatter conditions.

A value of the integrated-phase spectral index,  $p$ , near 3 is most often reported, although few attempts have been made to measure it systematically. Analyses of the Wideband satellite data have consistently shown  $p$  values smaller than three (Rino 1979a; Rino and Owen, 1980). Figure 13 shows data from an equatorial station. The systematic lowering of the measured  $p$  values for small  $S_4$  levels is due to noise contamination.

To verify the wavelength dependence of the phase scintillation ( $\sigma_\phi \propto \lambda$ ) predicted by Eqs. (5.1) and (5.2), Figure 14 shows scatter diagrams of measured  $\sigma_\phi$  values. At the higher frequencies where weak-scatter conditions generally prevail, the data closely follow the theoretical curve. As the scintillation increases, the  $\sigma_\phi$  data show significantly more scatter with a tendency to fall to the right of the theoretical curve in Figure 14(b), which suggests that saturation may be occurring in the phase data.

Figure 15 shows the corresponding scatter plots for  $S_4$ . In this figure there is a pronounced saturation about the Rayleigh value  $S_4 = 1$ . The scatter in the data values is too large to reveal small departures from the ( $S_4 \propto \lambda^{1.5}$ ) wavelength dependence consistent with  $p = 3$ . For  $p < 3$ , however, the calculations shown in Figure 11, which apply to the highly anisotropic equatorial irregularities, show convergence of  $S_4$  to unity from below. While there are many  $S_4$  values greater than unity, the average behavior seems to be in agreement with the theory for  $p < 3$  [see Figure 11].

In Figure 16 theoretical calculations based on Eq. (5.1), Eq. (5.2), and Eq. (5.3) are shown together with UHF data from a Wideband satellite pass recorded at Ancon, Peru. The measured value of  $T$  together with a median value for  $p = 2v$  were used to calculate  $\sigma_\phi$ . From Eq. (5.2)  $C_p$  was then estimated and used in Eq. (5.3) to calculate  $S_4$ . Figure 16 also shows the corresponding  $C_p$  value for a 200 km scattering layer thickness. The theory does very well as long as  $S_4$  is small ( $S_4 < 0.4$ ).

Figure 17 shows measured values of the intensity coherence time. When  $S_4$  is small,  $\tau_I$  varies as  $\sqrt{Z}$  [see Eq. (5.8)], that is  $\tau_I \propto \sqrt{\lambda}$ . Under strong-scatter conditions,  $\tau_I$  depends only on the perturbation strength [see Eq. (5.9)]. To show the strong-scatter dependence more clearly, in Figure 18  $\tau_I$  is plotted against  $T$ . Under weak-scatter conditions, there is a substantial amount of scatter; however, for strong scatter,  $\tau_I$  approaches the result given by the asymptotic formula

$$\tau_I^{p-1} = T \frac{4\pi^{(p-1/2)} \Gamma(1.5-p/2)}{(p-1) \Gamma(p/2)} \quad (6.1)$$

for  $p = 2.4$ , which was determined by a log-linear least-squares fit to the data. The discrepancy is partly due to the fact that no spherical wave correction was applied to the measured  $\tau_1$  values. The plane-wave theory predicts smaller  $\tau_1$  values than are actually observed [see for example Bowhill (1961)].

To conclude this section, Figure 19 shows preliminary measurements of the mutual coherence function  $\langle uu^* \rangle$ . The data are from the Wideband satellite and they show a progression from strong to weak scattering. Prior to 4 41 22 UT,  $S_4 \sim 1$ . No attempt is made here to perform a detailed comparison to the theoretical predictions from Eq. (3.8) using Eq. (4.8) or Eq. (4.10). The qualitative behavior--short coherence times under strong scatter conditions and very long coherence times under weak scatter conditions--is, nonetheless, as expected.

Overall, the experimental data are in good agreement with the power-law phase-screen theory with  $p \sim 2.5$ . One can predict the onset of scintillation and bound the intensity coherence time under conditions of weak and strong scatter with simple formulas. The mutual coherence function is simply described under all scattering conditions. Finally, the fading statistics can be characterized by using the Nakagami distribution.

There remain, however, a number of important questions that must ultimately be resolved. The theory and data were put together without direct in-situ measurements. In-situ measurements of irregularity structure have existed for some time, but only recently have they been analyzed to reveal the variations that might occur along a typical propagation path. It appears that at least for kilometer sized structures and smaller, a  $\kappa^{-2}$  one-dimensional SDF is observed, which is steeper than a simple mapping of the Wideband satellite data would predict; thus, the relation between the in-situ power-law index and  $p$  remains to be explained.

The effective value of  $C_s$  required to produce gigahertz scintillation, moreover, is quite large. Because of this, questions have been raised as to the strict applicability of the theory (Booker and Ferguson, 1978; Crain et al., 1979). Recent simulations by Wernik (1976) have shown, moreover, that when steep gradients are present inhomogeneities can arise that give artificially large  $S_4$  values. Such effects could explain the large  $C_s$  values, since the theory is based on homogeneous statistics. Current theoretical and experimental efforts are being directed toward answering these questions.

## 7. FREQUENCY COHERENCE

For most applications one can ignore the random frequency dispersion associated with ionospheric scintillation. Under severely disturbed conditions, however, loss of coherence bandwidth does occur. Figure 20 shows an example of the decorrelation of signal intensity over a 70 MHz bandwidth at UHF. The  $S_4$  index was near unity over the entire frequency band.

Loss of coherence bandwidth causes delay jitter and pulse dispersion. Such effects are of concern to precision navigation systems such as the Global Positioning System [GPS] (Spilker, 1978). If the complex signal  $v(t) \langle \hat{v}(f) \rangle$  is transmitted the dispersive effects can be characterized by the temporal moments

$$M_n = \int_{-\infty}^{\infty} t^n \langle |v_o(t)|^2 \rangle dt \quad (7.1)$$

Yeh and Liu (1977) have shown, for example, that

$$\tau_d \triangleq M_1 = \frac{1}{2\pi i} \int_{-F/2}^{F/2} |\hat{v}(f)|^2 \left[ \frac{\partial}{\partial \delta f} R(\delta f; f+f_c) \right]_{\delta f=0} df \quad (7.2)$$

and

$$\begin{aligned} \Omega_d \triangleq M_2 &= \int_{-\infty}^{\infty} t^2 |v(t)|^2 dt \\ &= \frac{1}{2\pi i} \int_{-F/2}^{F/2} |v(f)|^2 \left[ \frac{\partial^2}{\partial \delta f^2} R(\delta f; f+f_c) \right]_{\delta f=0} df \end{aligned} \quad (7.3)$$

where  $F$  is the bandwidth,  $f_c$  is the center frequency, and

$$R(\delta f; f) = \langle u(t; f+\delta f/2) u^*(t; f-\delta f/2) \rangle \quad (7.4)$$

is the single-point, two-frequency coherence function.

To calculate  $R(\delta f; t)$ , we use the Huygens-Fresnel formula

$$u(\vec{\rho}_1, z_1; f_1) = \frac{k_1}{2\pi i z_1} \iint \exp \left\{ -i\frac{k_1}{2z_1} \left( \vec{\rho}_1 - \vec{\rho}_2 \right)^2 \right\} u(\vec{\rho}_2, z_2; f_2) d\vec{\rho}_2 \quad (7.5)$$

from which

$$R(\delta f; f) = \frac{1}{2\pi i} \frac{k_1 k_2}{(k_1 - k_2) z_\ell} \iint \exp \left\{ i \frac{\Delta \xi^2}{2} \frac{k_1 k_2}{(k_1 - k_2) z_\ell} \right\} R_1(\Delta \xi; f_1, f_2) d\Delta \xi \quad (7.6)$$

follows directly. In Eq. (7.6),  $k_1$  and  $k_2$  are the wavenumbers corresponding to  $f_1 = f - \delta f/2$  and  $f_2 = f + \delta f/2$  respectively. To calculate the two-frequency coherence function at  $z = 0$ , the phase-screen model can be used. If  $\epsilon = \delta f/(2f)$  is small, it can be shown that

$$R_u(\Delta \xi; \delta f, f) = \exp \{-D(\Delta \xi)\} \exp \{-2\epsilon \sigma_\phi^2\} \quad (7.7)$$

where  $\sigma_\phi^2$  and  $D(\Delta \xi)$  are evaluated at the mean frequency,  $f$ .

By substituting Eq. (7.7) into Eq. (7.6), making the small  $\epsilon$  approximation and a series of variable changes, it can be shown that

$$R(\delta f; f) = i \sqrt{\beta^2 - \alpha^2} \int_0^\infty J_0(u\gamma) \exp \{-i u \beta\} \exp \{-D([w^2 Z \delta f/f]^{1/2})\} dw \exp \{-\sigma_\phi^2 2\epsilon\} \quad (7.8)$$

where  $\alpha$  and  $\beta$  depend on the propagation geometry and the anisotropy of the irregularities. For isotropic irregularities  $\beta = 1/2$  and  $\alpha = 0$ . For highly anisotropic irregularities ( $a \gg 1$ )  $\alpha \sim \beta \sim \alpha^2 - \beta^2 \sim a^2/4$ .

If the small  $q_0$  approximation is used

$$D([w^2 Z \delta f/f]^{1/2}) \sim C_{\delta\phi}^2 [2Z \delta f/f]^{\nu-0.5} w^{\nu-0.5} \quad (7.9)$$

Unfortunately, Eq. (7.8) cannot be evaluated analytically for arbitrary  $\nu$  values within the admissible range between  $0.5 < \nu < 1.5$ . However, if  $\nu$  in Eq. (7.9) is set equal to 1.5, then Eq. (7.8) can be evaluated giving the result

$$R(\delta f; f) \cong \frac{\sqrt{\beta^2 - \alpha^2} \exp \{-\sigma_\phi^2 2\epsilon\}}{\sqrt{(\beta - iH|\delta f/f|)^2 - \alpha^2}} \quad (7.10a)$$

where

$$H = C_{\delta\phi}^2 2Z \quad (7.10b)$$

If the quadratic approximation is used,

$$D([w^2 Z \delta f/f]^{1/2}) \cong (2\sigma_\phi^2 D_1 q_0^2) 2Z \delta f/f \quad (7.11)$$

This gives rise to a form identical to Eq. (7.10a) but with  $H$  replaced by  $H_q$  where

$$H_q = 2\sigma_\phi^2 D_1 q_0^2 \quad (7.12)$$

The form of Eq. (7.10a), therefore, is exact for the more steeply sloped phase SDFs that retain an explicit dependence on the outer-scale wavenumber  $q_0$ .

In any case, Eq. (7.2) and Eq. (7.3) can be evaluated using Eq. (7.10). If  $\delta f/f \ll 1$ , then

$$\tau_d \cong \frac{H}{2\pi f_c} \frac{\beta}{\beta^2 - \alpha^2} \quad (7.13)$$

and

$$\Omega_d \cong \left( \frac{H}{2\pi f_c} \right)^2 \frac{\beta^2 + \alpha^2}{(\beta^2 - \alpha^2)^2} \quad (7.14)$$

For highly anisotropic irregularities  $\beta/(\beta^2 - \alpha^2) \sim 1$  and  $\Omega_d = 2\tau_d^2$ . Equations (7.13) and (7.14) are simplified forms of similar expressions derived by Fante (1978) and Yeh and Liu (1977). The simplifications arise mainly because the phase screen model was used.

To give some idea of the order of magnitude of the expected delay jitter, in Figure 21,  $\tau_d$  is plotted against  $C_p$  for the same parameter values that were used to generate Figure 10. The quadratic approximation is also plotted for  $f_0 = q_0/2\pi = 10$  km. The results show that under conditions that produce strong gigahertz scintillation, 1 ns to 3 ns of delay jitter can occur, which is in agreement with the calculations of Yeh and Liu (1977).

These results, however, must remain somewhat speculative because they have not yet been tested against real data. Analysis of the Wideband satellite frequency coherence data is not yet complete.

#### 8. THE IONOSPHERIC LIMITATION TO COHERENT INTEGRATION

Coherent integration is used in radar signal processing to improve target detectability. The radar processor forms the FFT spectral estimate

$$\hat{\phi}_n = \left| \frac{1}{N} \sum_{k=0}^{N-1} W_k v_R(k\Delta t - t_r) \exp \{-2\pi i n k / N\} \right|^2 \quad (8.1)$$

where  $W_k$  is a weighting function,  $v_R(t)$  is the complex envelope of the radar echo,  $t_r$  is the time delay for the particular range, and  $\Delta t$  is the subpulse spacing; thus,  $T = N\Delta t$  is the coherent integration time.

For a moving target,

$$v_R(k\Delta t) = \exp \{2\pi i f_d k \Delta t\} \quad (8.2)$$

where  $f_d$  is the Doppler shift. By substituting Eq. (8.2) into Eq. (8.1) with  $W_k = 1$  for all  $k$ , it is easily shown that

$$\hat{\phi}_n = \frac{1}{N^2} \frac{\sin^2 \left\{ \frac{\pi (f_d \Delta t - n/N) N}{2} \right\}}{\sin^2 \left\{ \frac{\pi (f_d \Delta t - n/N)}{2} \right\}} \quad (8.3)$$

If  $f_d = m/N\Delta t$ , then  $\hat{\phi}_n$  achieves its maximum value of unity when  $n = m$ , and a value on the order of  $1/N$  when  $|n-m| > 1/N\Delta t$ . In a background of white noise, it follows that the target detectability is enhanced by  $20 \log_{10} N$  dB.

For transionospheric operation, however, the return pulses suffer an amplitude and phase modulation, which reduces the effectiveness of coherent integration. We define the coherent integration loss,  $L(T)$ , as

$$L(T) = \max_n \{10 \log_{10} \langle \hat{\phi}_n \rangle\} \quad (8.4)$$

It is readily shown that

$$\langle \hat{\phi}_n \rangle = \frac{1}{N} \sum_{m=-N}^N R_u(mv_{\text{eff}} \Delta t) \exp \{-2\pi i m n / N\} \quad (8.5)$$

where  $R_u(y)$  is the mutual coherence function. Formally,  $\langle \hat{\phi}_n \rangle$  is the one-dimensional angular spectrum along the scan direction defined by the irregularity drift and target motion.

Figure 22 shows plots of the coherent integration loss plotted against the phase-turbulent strength  $T$  in Eq. (5.2) for different values of the phase spectral index  $p$ . The small  $q_0$  approximation was used to evaluate  $R_u$ . The results show that under strong-scatter conditions at the radar frequency ( $T \gg -10$  dB), coherent integration times greater than 10 s begin to lose effectiveness. A detailed discussion can be found in Rino et al. (1977).

The example presented in this section shows how measures of performance of coherent systems can be derived in terms of the mutual coherence function. Similar analysis can be applied to assess the performance of satellite-borne synthetic aperture radars.

#### Acknowledgments

The multifrequency beacon aboard the P76-5 (Wideband) satellite ceased operation in August 1979 because of a voltage supply failure. It is timely, therefore, to acknowledge the contributions of Mr. Ray L. Leadbrand, who conceived the Wideband satellite experiment, and Mr. Dow E. Evelyn of the Defense Nuclear Agency, who served as project officer on the program since its inception. Messers Roy A. Long and Boyd C. Fair guided the development of the spacecraft hardware and the three tracking stations. Dr. Michael D. Cousins developed the digital data acquisition system. Mr. Robert C. Livingston developed most of the data analysis software. Dr. Edward J. Fremouw directed the program until 1977.



## REFERENCES

- Barabanenkov, N., A. Kravtsov, S. M. Rytov, and V. I. Tatarskii (1971), "Status of the Theory of Propagation of Waves in a Randomly Inhomogeneous Medium," Sov. Phys. Usp., Vol. 13, p. 551.
- Booker, H. G. and J. A. Ferguson (1978), "A Theoretical Model for Equatorial Ionospheric Spread-F Echoes in the HF and VHF Bands," J. Atmos. Terr. Phys., Vol. 40, p. 803.
- Booker, H. G., J. A. Ratcliffe, and D. H. Shinn (1950), "Diffraction from an Irregular Screen with Applications to Ionospheric Problems," Phil. Trans. Roy. Soc. A., Vol. 242, p. 579.
- Bowhill, S. H. (1961), "Statistics of a Radio Wave Diffracted by a Random Ionosphere," J. Res. Nat. Bur. Stand.--D, Radio Prop., Vol. 65D, p. 275.
- Bramley, E. M. (1977), "The Accuracy of Computing Ionospheric Radio-Wave Scintillation by the Thin-Phase-Screen Approximation," J. Atmos. Terr. Phys., Vol. 39, p. 367.
- Bramley, E. M. (1954), "The Diffraction of Waves by an Irregular Refracting Medium," Proc. Roy. Soc. A., Vol. 225, p. 515.
- Buckley, R. (1971a), "Diffraction by a Random Phase Screen with Very Large R.M.S. Phase Deviation I. One-Dimensional Screen," Aust. J. Phys., Vol. 24, p. 351.
- Buckley, R. (1971b), "Diffraction by a Random Phase Screen with Very Large R.M.S. Phase Deviation II. Two-Dimensional Screen," Aust. J. Phys., Vol. 24, p. 373.
- Chytil, B. (1967), "The Distribution of Amplitude Scintillation and the Conversion of Scintillation Indices," J. Atmos. Terr. Phys., Vol. 29, p. 1175.
- Cohen, M. H., E. J. Gunermann, H. E. Hardebeck, and L. E. Sharp (1957), "Interplanetary Scintillations II. Observations," Astrophys. J., Vol. 147, p. 449.
- Costa, E. and M. C. Kelley (1977), "Ionospheric Scintillation Calculations Based on In Situ Irregularity Spectra," Radio Science, Vol. 12, No. 5, p. 797.
- Crain, C. M., H. G. Booker, J. A. Ferguson (1979), "Use of Refractive Scattering to Explain SHF Scintillations," Radio Science, Vol. 14, p. 125.
- Crane, R. K. (1978), "Variance and Spectra of Angle-of-Arrival and Doppler Fluctuations Caused by Ionospheric Scintillation," J. Geophys. Res., Vol. 83, p. 2091.
- Crane, R. K. (1976), "Spectra of Ionospheric Scintillation," J. Geophys. Res., Vol. 81, p. 2041.
- Davies, K., R. B. Fritz, R. N. Grubb, and J. E. Jones (1975), "Some Early Results from the ATS-6 Radio Beacon Experiment," Radio Science, Vol. 10, p. 785.
- DeWolf, D. A. (1969), "Are Strong Irradiance Fluctuations Log Normal," J. Opt. Soc. Am., Vol. 59, p. 1455.
- Fante, R. L. (1978), "Multiple-Frequency Mutual Coherence Functions for a Beam in a Random Medium," IEEE Trans. Ant. and Prop., Vol. AP-26, No. 4, p. 621.
- Fante, R. L. (1976), "Comparison of Theories for Intensity Fluctuations in Strong Turbulence," Radio Science, Vol. 11, No. 3, p. 215.
- Fante, R. L. (1975), "Electromagnetic Beam Propagation in Turbulent Media," Proc. IEEE, Vol. 63, No. 12, p. 2669.
- Fejer, J. A. (1953), "The Diffraction of Waves in Passing Through an Irregular Refracting Medium," Proc. Roy. Soc. A., Vol. 220, p. 455.
- Fremouw, E. J., R. C. Livingston, and D. A. Miller (1980), "On the Statistics of Scintillating Signals," submitted to J. Atmos. Terr. Phys.
- Fremouw, E. J., R. L. Leadbrand, R. C. Livingston, M. D. Cousins, C. L. Rino, B. C. Fair, and R. A. Long (1978), "Early Results From the DNA Wideband Satellite Experiment--Complex-Signal Scintillation," Radio Science, Vol. 13, p. 167.
- Gochelashvily, K. E. and V. I. Shishov (1971), "Multiple Scattering of Light in a Turbulent Medium," Optica Acta, Vol. 18, No. 10, p. 767.
- Knepp, D. L. (1976), "Variance and Bias of Angle Estimation Radars," IEEE Trans. Ant. Prop., Vol. AP-24, No. 4, p. 518.
- Kolmogorof, A. N. (1941), "The Local Structure of Turbulence in Incompressible Viscous Fluid for Very Large Reynolds Numbers," C. R. Acad. Sci., U.R.S.S., Vol. 30, p. 301.
- Mercier, R. P. (1962), "Diffraction by a Screen Causing Large Random Phase Fluctuations," Proc. Camb. Phil. Soc., Vol. 58, p. 382.
- Ochs, G. R. and R. S. Lawrence (1969), "Saturation of Laser-Beam Scintillation under Conditions of Strong Atmospheric Turbulence," J. Opt. Soc. Am., Vol. 59, p. 226.

- Ott, R. H. (1977), "Observed Temporal Amplitude and Phase Spectra From ATS-6 Radio Beacon Experiment at 40, 140, and 360 MHz," Radio Science, Vol. 12, p. 319.
- Prokhorov, A. M., F. V. Bunkin, K. S. Gochelashvily, and V. I. Shishov (1975), "Laser Irradiance Propagation in Turbulent Media," Proc. IEEE, Vol. 63, p. 790.
- Ratcliffe, J. A. (1956), "Some Aspects of Diffraction Theory and Their Application to the Ionosphere," Report of the Physical Society on Progress in Physics, Vol. 19, p. 188.
- Rice, S. O. (1953), "Statistical Fluctuations of Radio Field Strength Far Beyond the Horizon," Proc. IRE, p. 274.
- Rino, C. L. (1980), "Numerical Computations for a One-Dimensional Power-Law Phase Screen," in press, Radio Science.
- Rino, C. L. (1979a), "A Power-Law Phase Screen Model for Ionospheric Scintillation 1. Weak Scatter," Radio Science, Vol. 14, p. 1135.
- Rino, C. L. (1979b), "A Power-Law Phase Screen Model for Ionospheric Scintillation 2. Strong Scatter," Radio Science, Vol. 14, p. 1147.
- Rino, C. L. (1978), "Iterative Methods for Treating the Multiple Scattering of Radio Waves," J. Atmos. Terr. Phys., Vol. 40, p. 1011.
- Rino, C. L. and E. J. Fremouw (1977), "The Angle Dependence of Singly Scattered Wavefields," J. Atmos. Terr. Phys., Vol. 39, p. 859.
- Rino, C. L. and J. Owen (1980), "The Time Structure of Transionospheric Radiowave Scintillation," accepted for publication Radio Science.
- Rino, C. L., R. C. Livingston, and H. E. Whitney (1976), "Some New Results on the Statistics of Radio Wave Scintillation 1. Empirical Evidence for Gaussian Statistics," J. Geophys. Res., Vol. 81, p. 2051.
- Rino, C. L., J. Petriceks, R. Livingston, and C. Dawson (1977), "Data Reduction and Analysis of Coherent Satellite Transmissions," Final Report, Purchase Order No. 211-275012-40472, SRI Project 6449, SRI International, Menlo Park, CA.
- Rufenach, C. L. (1975), "Ionospheric Scintillation by a Random Phase Screen: Spectral Approach," Radio Science, Vol. 10, p. 155.
- Rumsey, V. H. (1975), "Scintillations Due to a Concentrated Layer with a Power-Law Turbulence Spectrum," Radio Science, Vol. 10, p. 107.
- Salpeter, E. E. (1967), "Interplanetary Scintillations I--Theory," Astrophys. J., Vol. 147, p. 433.
- Singleton, D. G. (1970), "Saturation and Focusing Effects in Radio-Star and Satellite Scintillations," J. Atmos. Terr. Phys., Vol. 32, p. 187.
- Spilker, J. J. Jr. (1978), "GPS Signal Structure and Performance Characteristics," Navigation, Vol. 25, No. 2, p. 121.
- Tatarskii, V. I. (1971), "The Effects of the Turbulent Atmosphere on Wave Propagation," TT-68-50464, National Science Foundation, Washington, D.C.
- Taylor, L. S. (1972), "Scintillation of Randomized Electromagnetic Fields," J. of Mathematical Phys., Vol. 13, p. 590.
- Taylor, L. S. and C. L. Infosino (1975), "Diffraction Theory of Optical Scintillations Due to Turbulent Layers," J. Optical Soc. Am., Vol. 65, p. 78.
- Umeki, R., C. H. Liu, and K. C. Yeh (1977a), "Multifrequency Spectra of Ionospheric Amplitude Scintillations," J. Geophys. Res., Vol. 82, p. 2752.
- Umeki, R., C. H. Liu, and K. C. Yeh (1977b), "Multifrequency Studies of Ionospheric Scintillations," Radio Science, Vol. 12, p. 311.
- Van Zandt, T. E., J. L. Green, K. S. Gage, and W. L. Clark (1978), "Vertical Profiles of Refractivity Turbulence Structure Constant: Comparison of Observations by the Sunset Radar with a New Theoretical Model," Radio Science, Vol. 3, p. 819.
- Wang, T. and J. W. Strohbehn (1974), "Log-Normal Paradox in Atmospheric Scintillation," J. Opt. Soc. Am., Vol. 65, p. 583.
- Wernik, A. W. (1976), "Extinction Effects in the Single Scattering Scintillation Theory," Publ. Inst. Geoph. Pol. Ac. Sci., Vol. E-1(100), p. 43.
- Whitney, H. E. and S. Basu (1977), "The Effect of Ionospheric Scintillation on VHF/UHF Satellite Communications," Radio Science, Vol. 12, p. 123.
- Yeh, K. C. and C. H. Liu (1977), "Diagnosis of the Turbulent Stats of Ionospheric Plasma by Propagation Methods," Radio Science, Vol. 12, p. 1031.

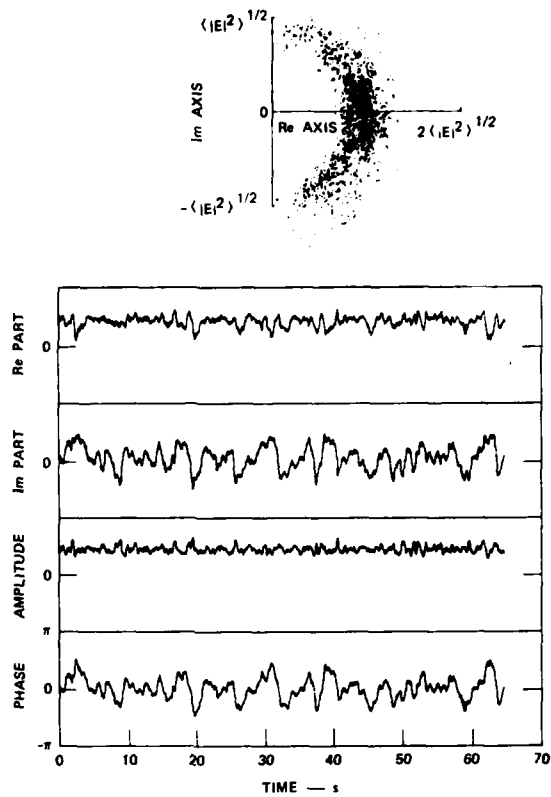


Figure 1 Typical detrended complex signal undergoing weak ionospheric scintillation

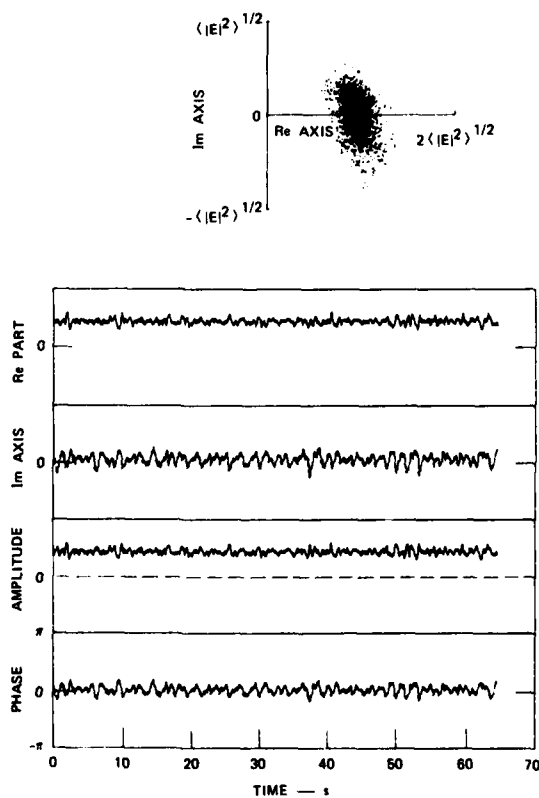


Figure 2 Gaussian "scatter component" of complex signal shown in Figure 1

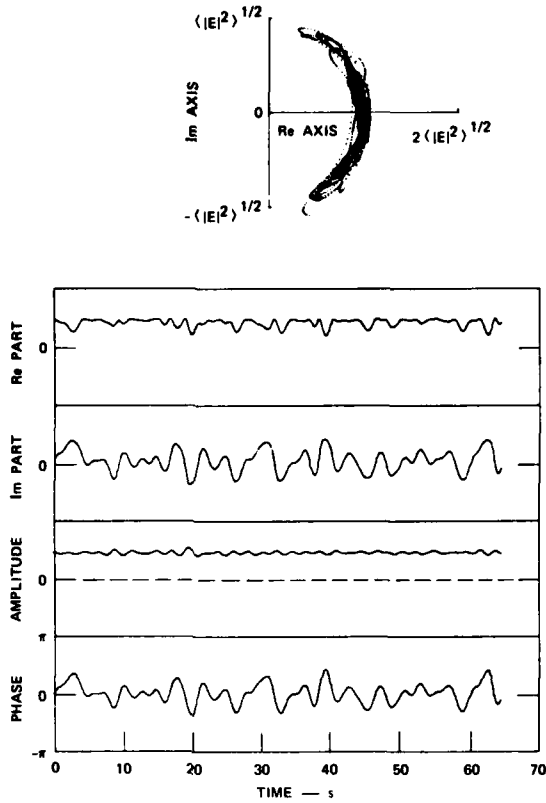


Figure 3 Slowly varying "focus component" of complex signal shown in Figure 1

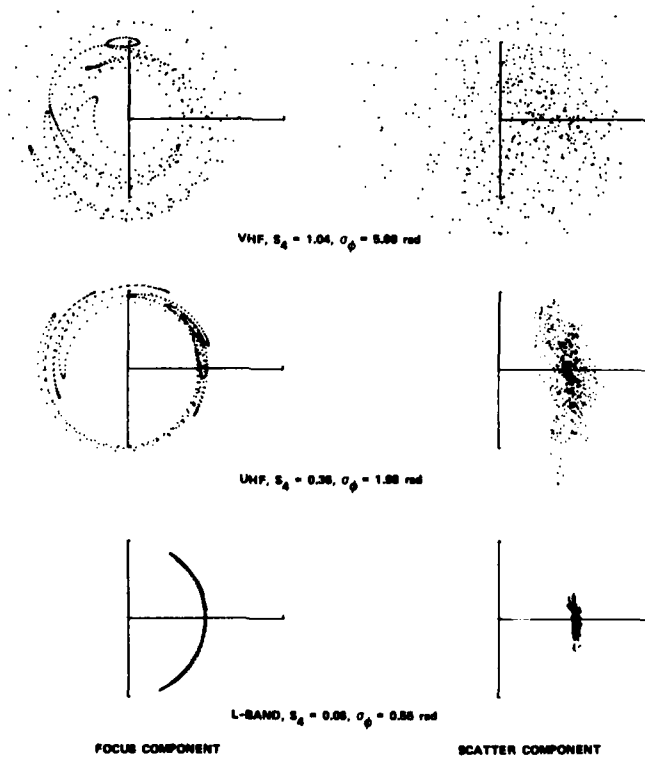


Figure 4 Scatter diagrams of focus (left) and scatter (right) components showing progression from weak to strong scatter

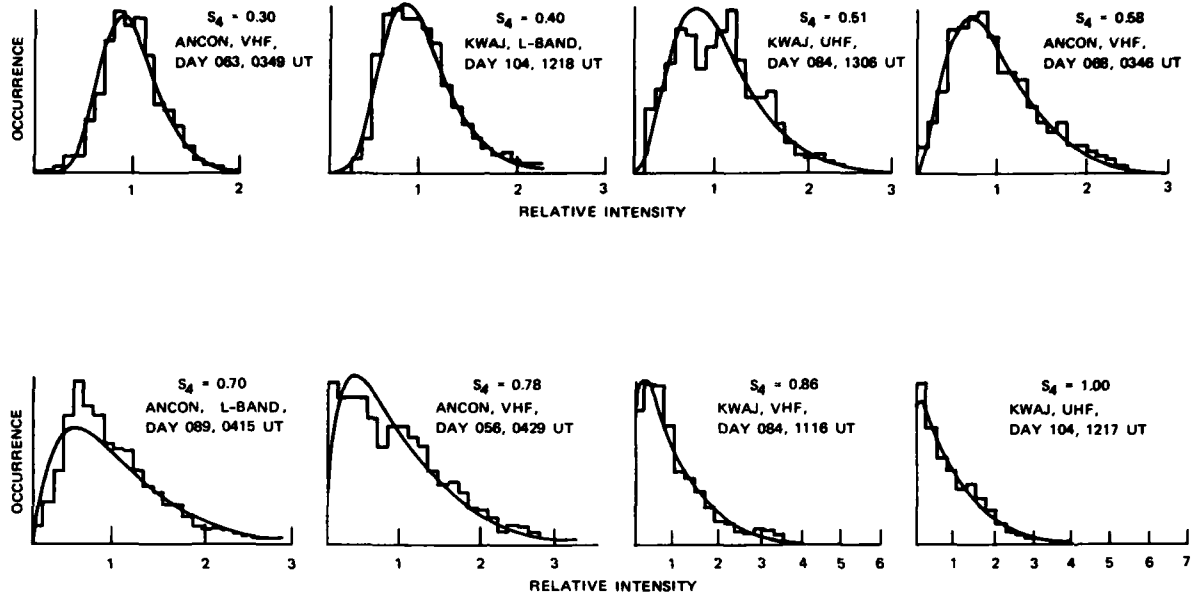


Figure 5 Wideband equatorial intensity scintillation probability distributions and the corresponding Nakagami distributions (solid curves). All data sets correspond to approximately one minute

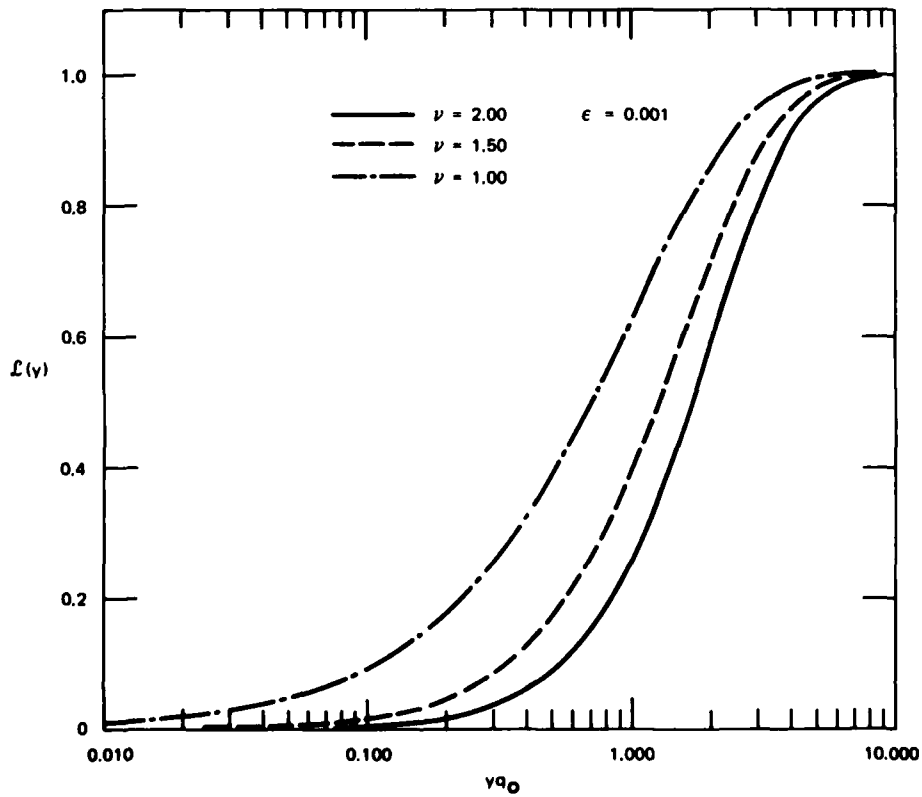


Figure 6 Plot of normalized integrated-phase structure function showing dependence on spectral slope parameter,  $\nu$

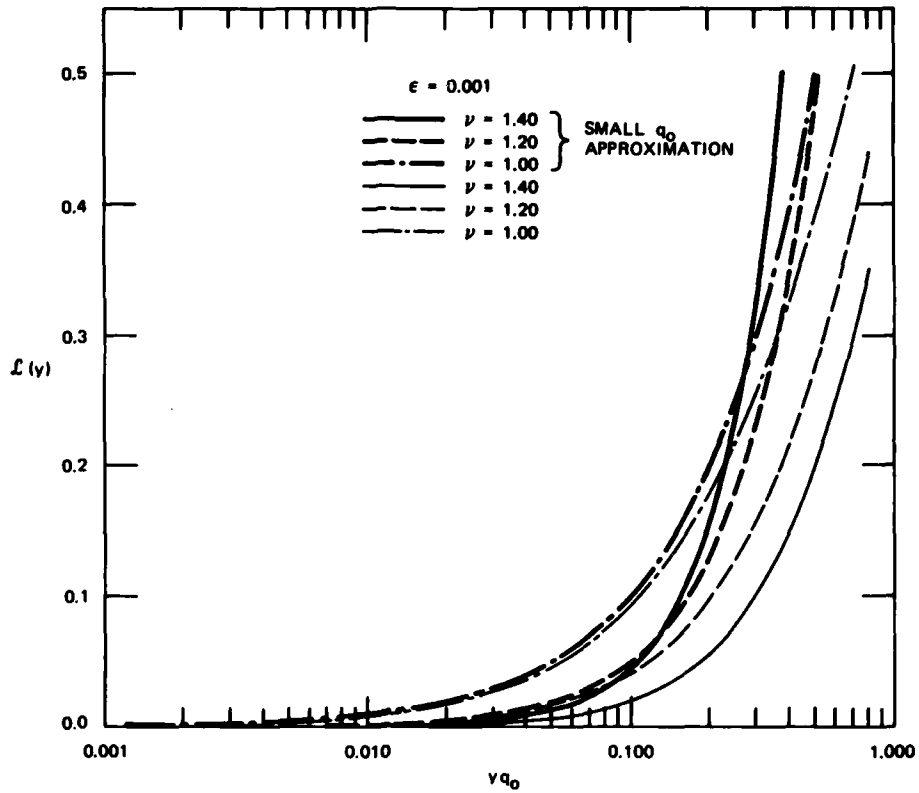


Figure 7 Plot of asymptotic approximation to integrated phase structure function which is valid for  $\nu < 1.5$  and  $q_0 y \ll 1$  superimposed on exact curves

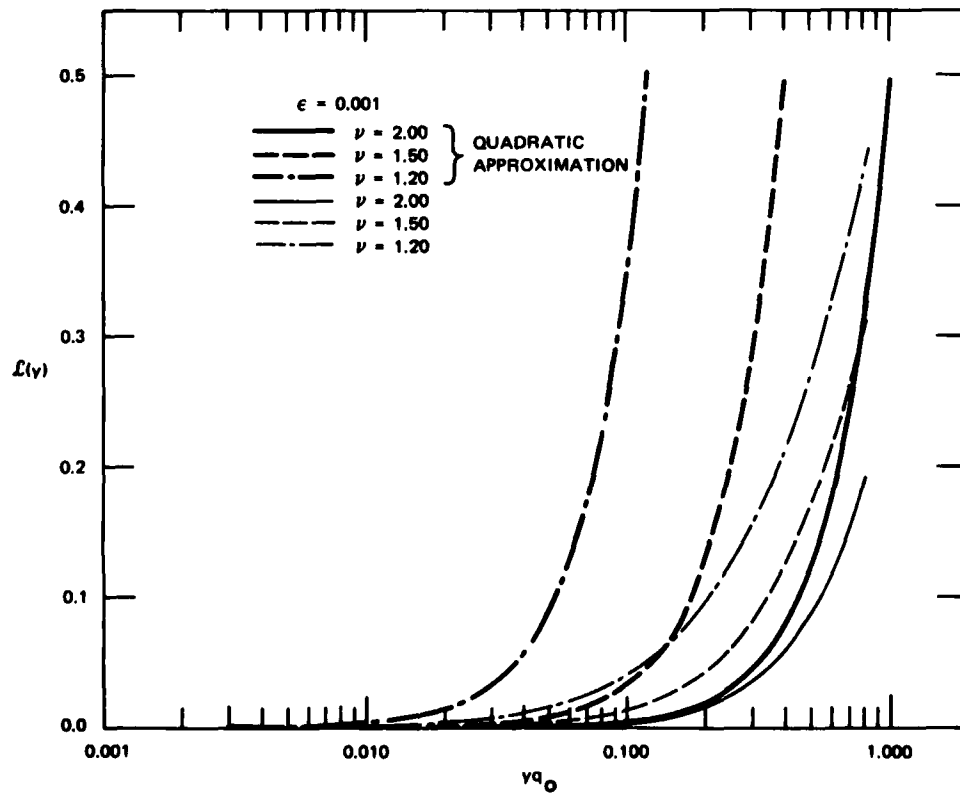


Figure 8 Plot of quadratic approximation to integrated-phase structure function which is valid for  $\nu > 1.5$  and  $q_0 y \ll 1$  superimposed on exact curves

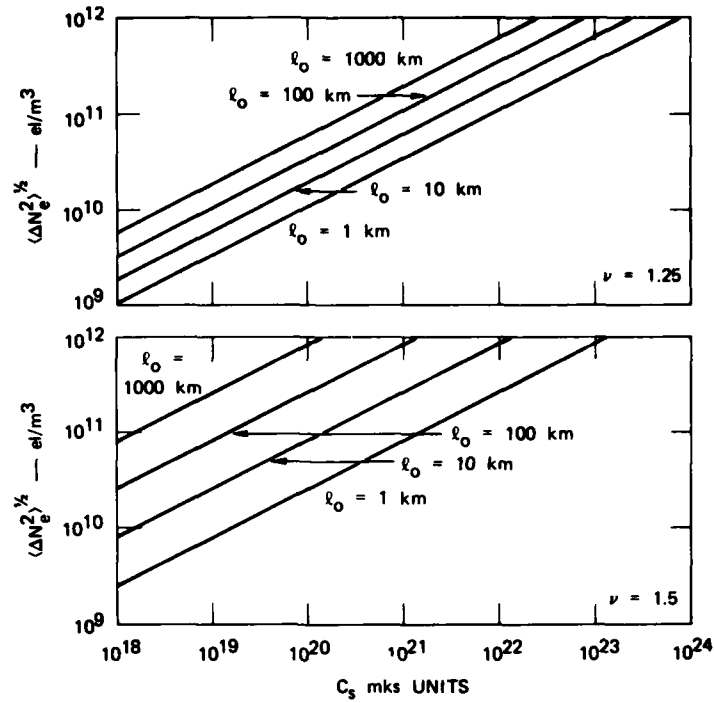


Figure 9 Plot of rms electron density vs  $C_s$  in mks units for different outer-scale cutoffs [ $l_o = 2\pi/q_o$ ]

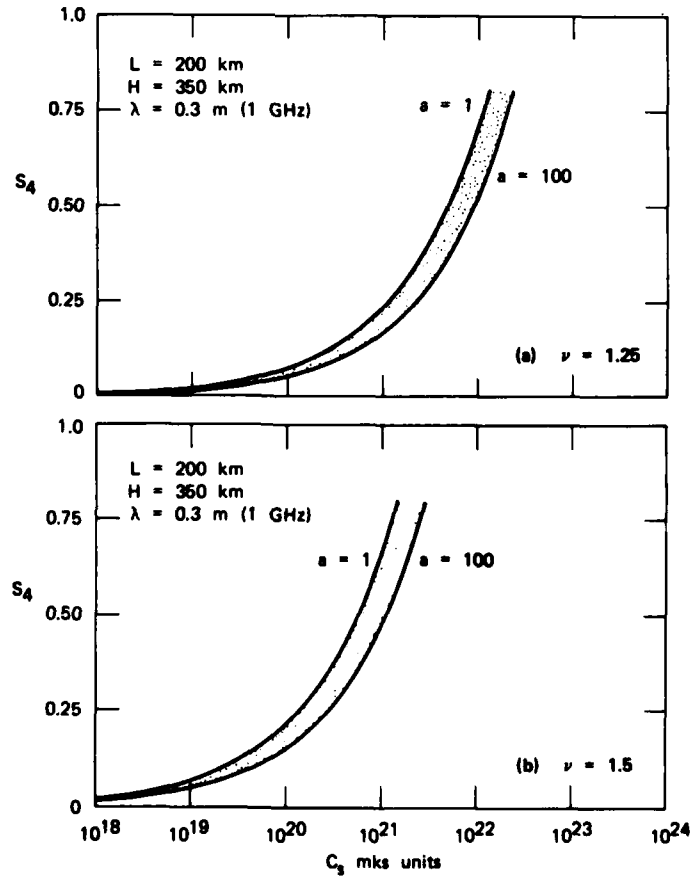


Figure 10 Plots of  $S_4$  vs  $C_s$  for normally incident signal at 1 GHz

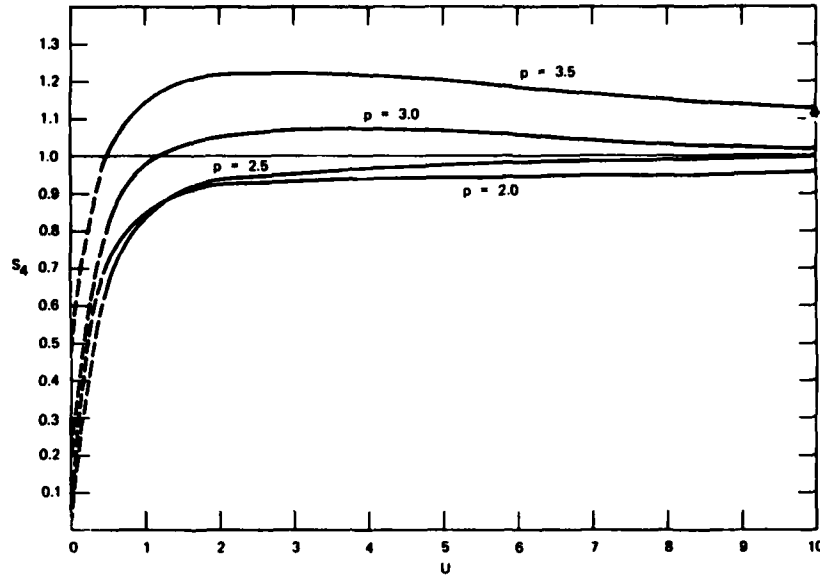


Figure 11 Theoretical calculations of  $S_4$  vs  $U'$  for a one-dimensional phase screen for different  $p$  values. When  $p \geq 3$ ,  $S_4$  achieves a maximum value greater than unity. When  $p > 3$  the large  $U'$  asymptote is larger than unity

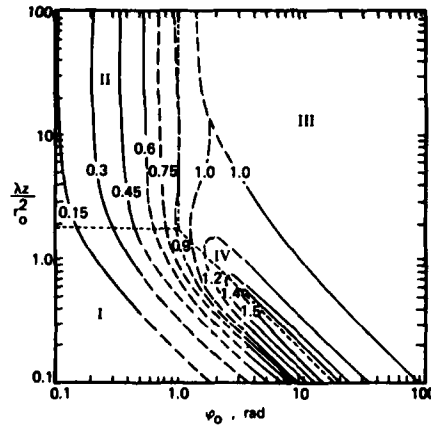


Figure 12 Cohen-Singleton diagram showing dependence of  $S_4$  on propagation distance and rms phase in a scattering medium with a single dominant scale size

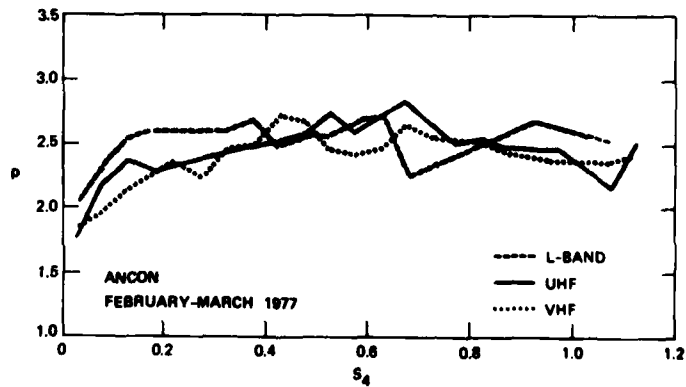


Figure 13 Average of measured  $p$  index for varying levels of intensity scintillation. Shaded region shows the measured standard deviation of the UHF data



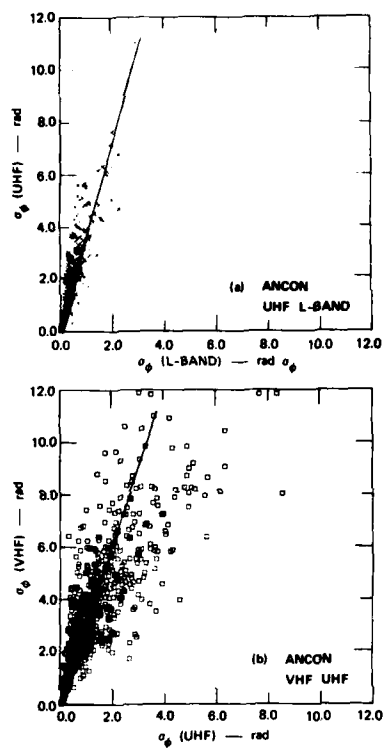


Figure 14 Scatter plots of multifrequency measurements of  $\sigma_\phi$ . The solid lines show the expected theoretical  $\sigma_\phi \propto \lambda$  dependence. a) UHF vs L band; b) VHF vs UHF

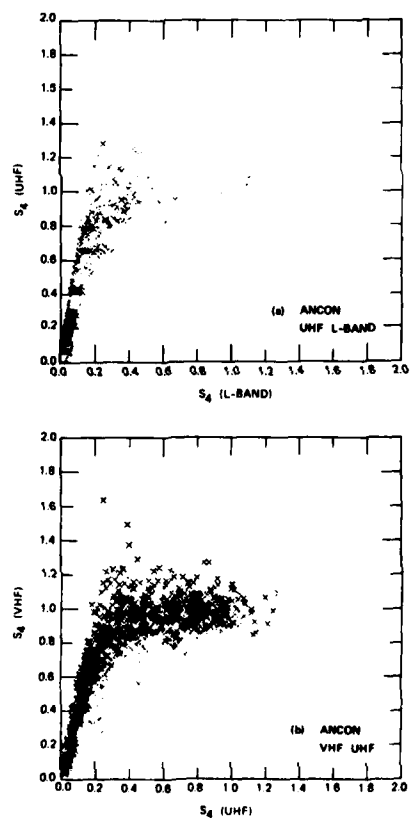


Figure 15 Scatter plots of multifrequency measurements of  $S_4$ . a) UHF vs L band; b) VHF vs UHF

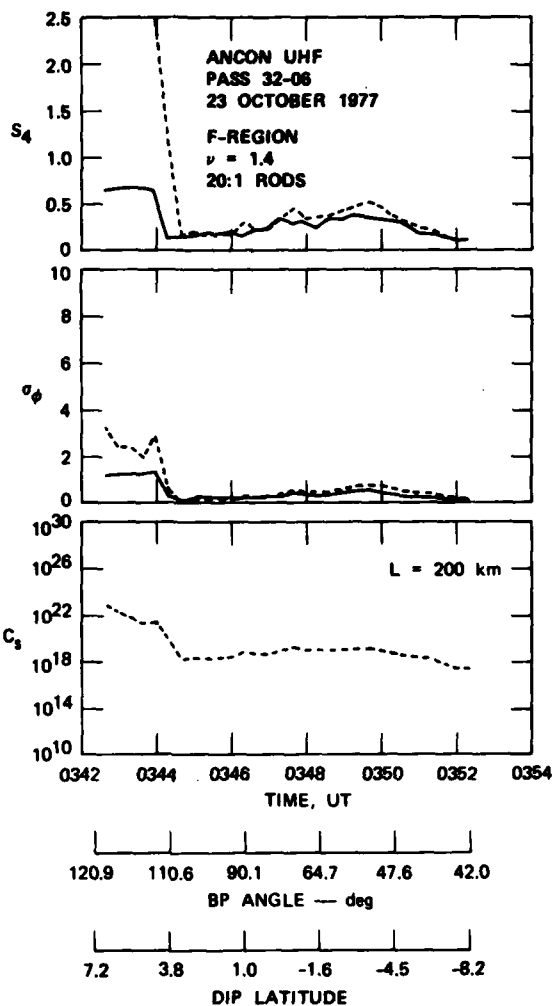


Figure 16 Comparison of weak-scatter theory with equatorial scintillation data

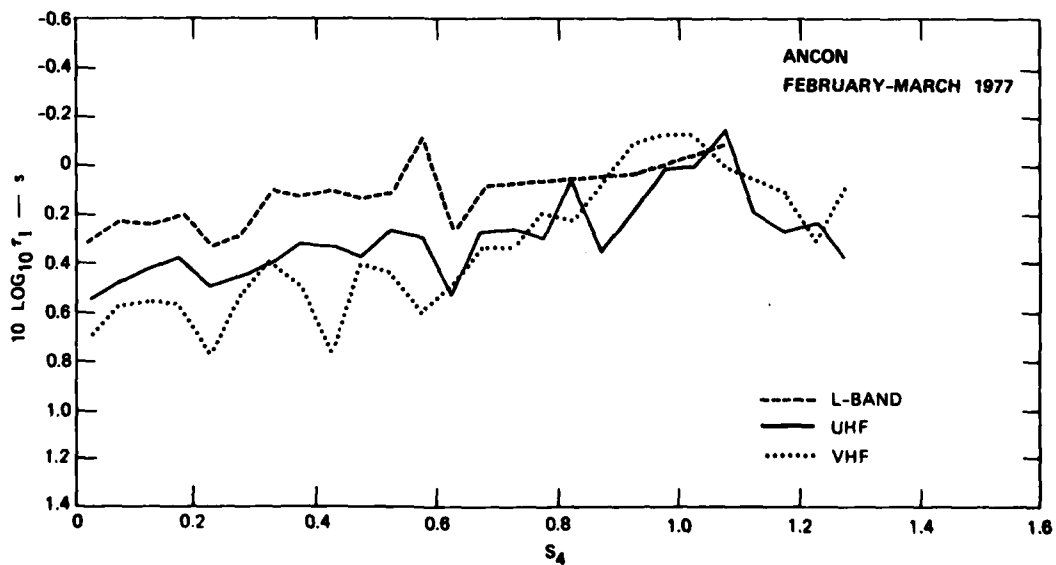


Figure 17 Semi-log plot of measured intensity coherence time plotted against  $S_4$  for VHF, UHF, and L band. Note the transition from Fresnel radius control to perturbation strength control as  $S_4$  increases

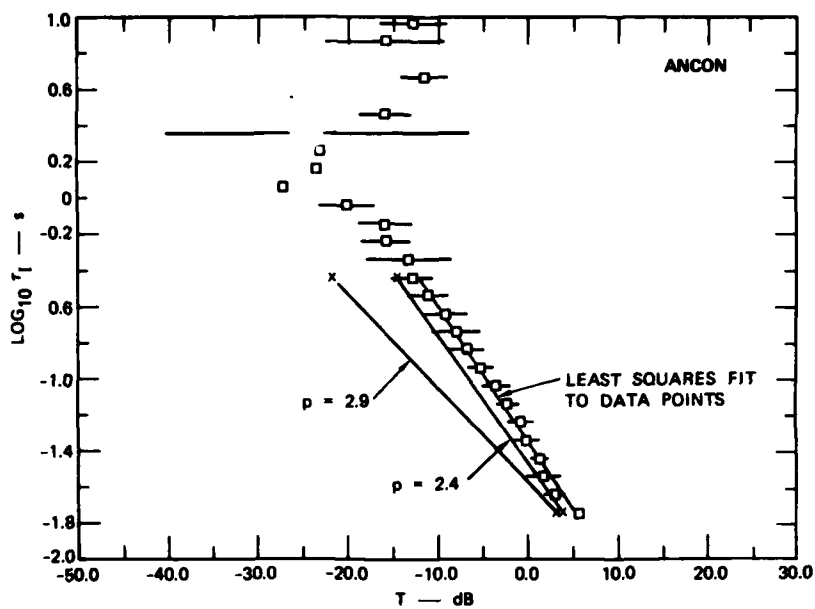


Figure 18 Log-log plot of  $\tau_T$  showing log-linear dependence under strong scatter conditions. The  $\tau_T$  values are not corrected for wavefront curvature

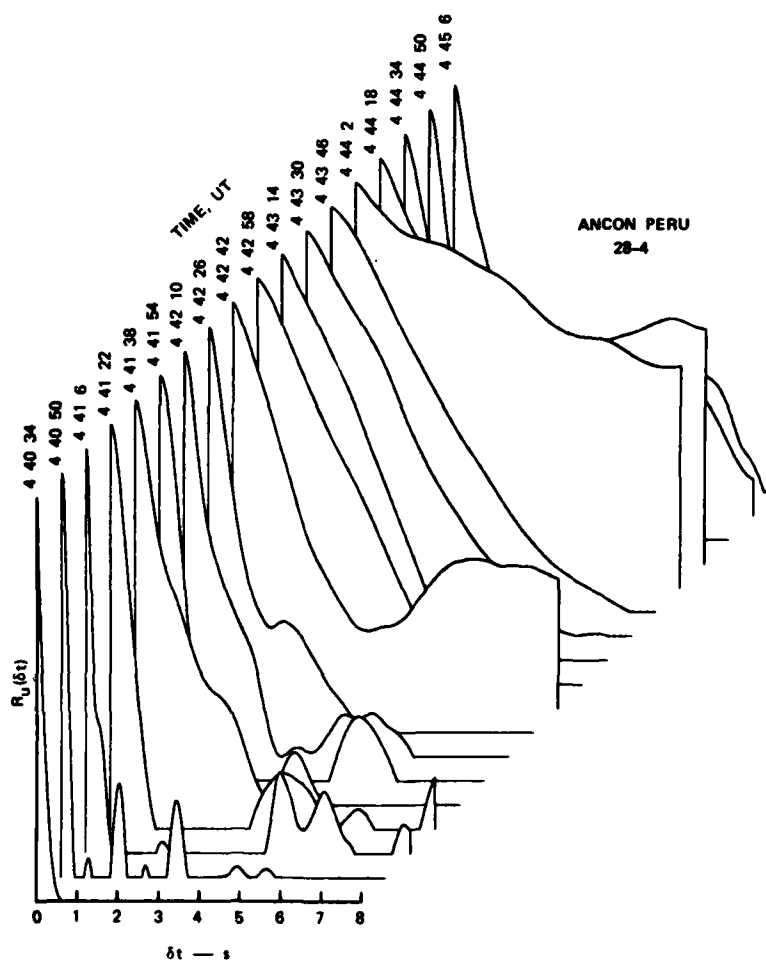


Figure 19 Perspective plot of measured mutual coherence functions through a period of generally decreasing scintillation [4 40 49 to 4 44 2]

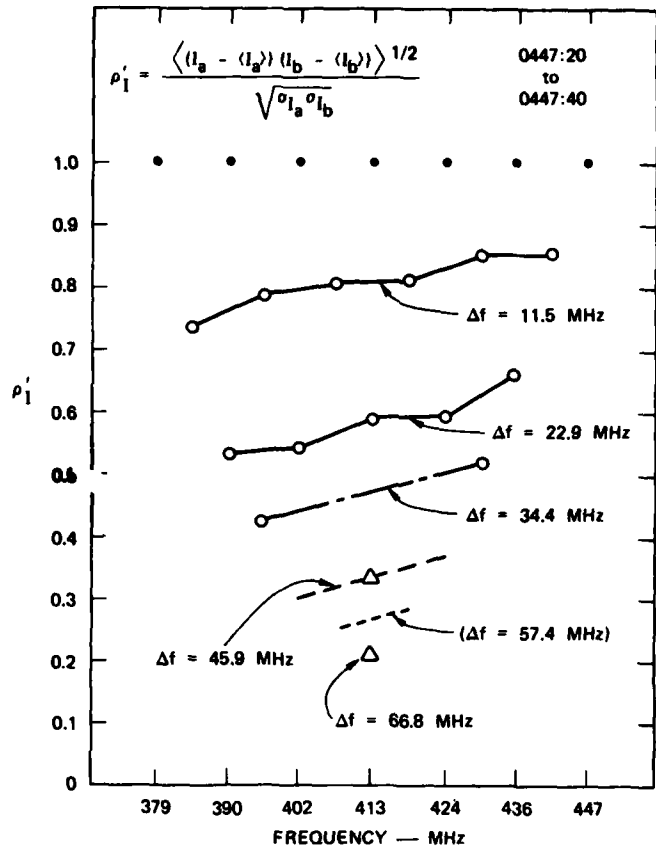


Figure 20 Decorrelation of intensity scintillation under severely disturbed conditions

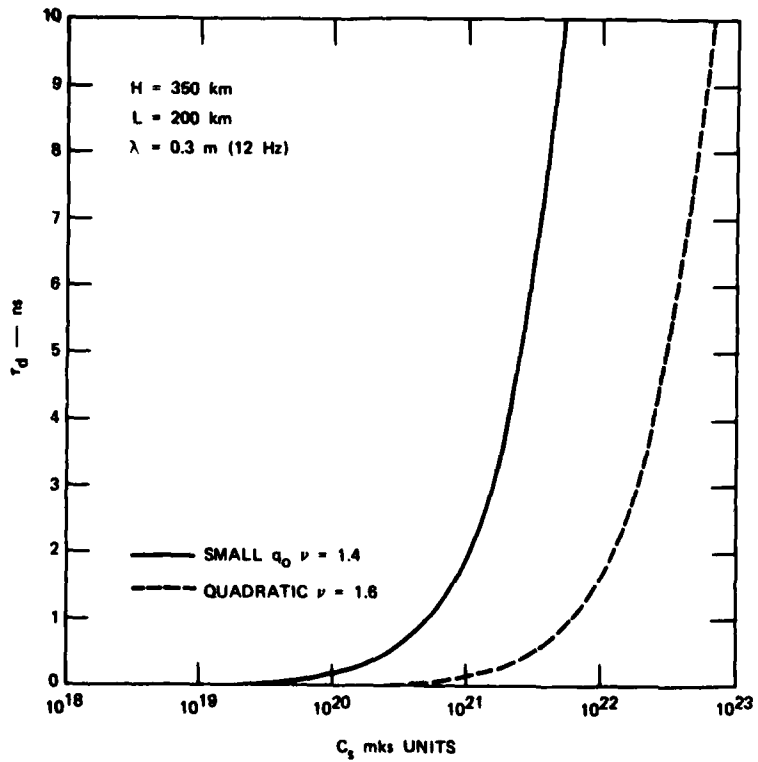


Figure 21 Theoretical calculations of delay jitter caused by loss of coherence bandwidth

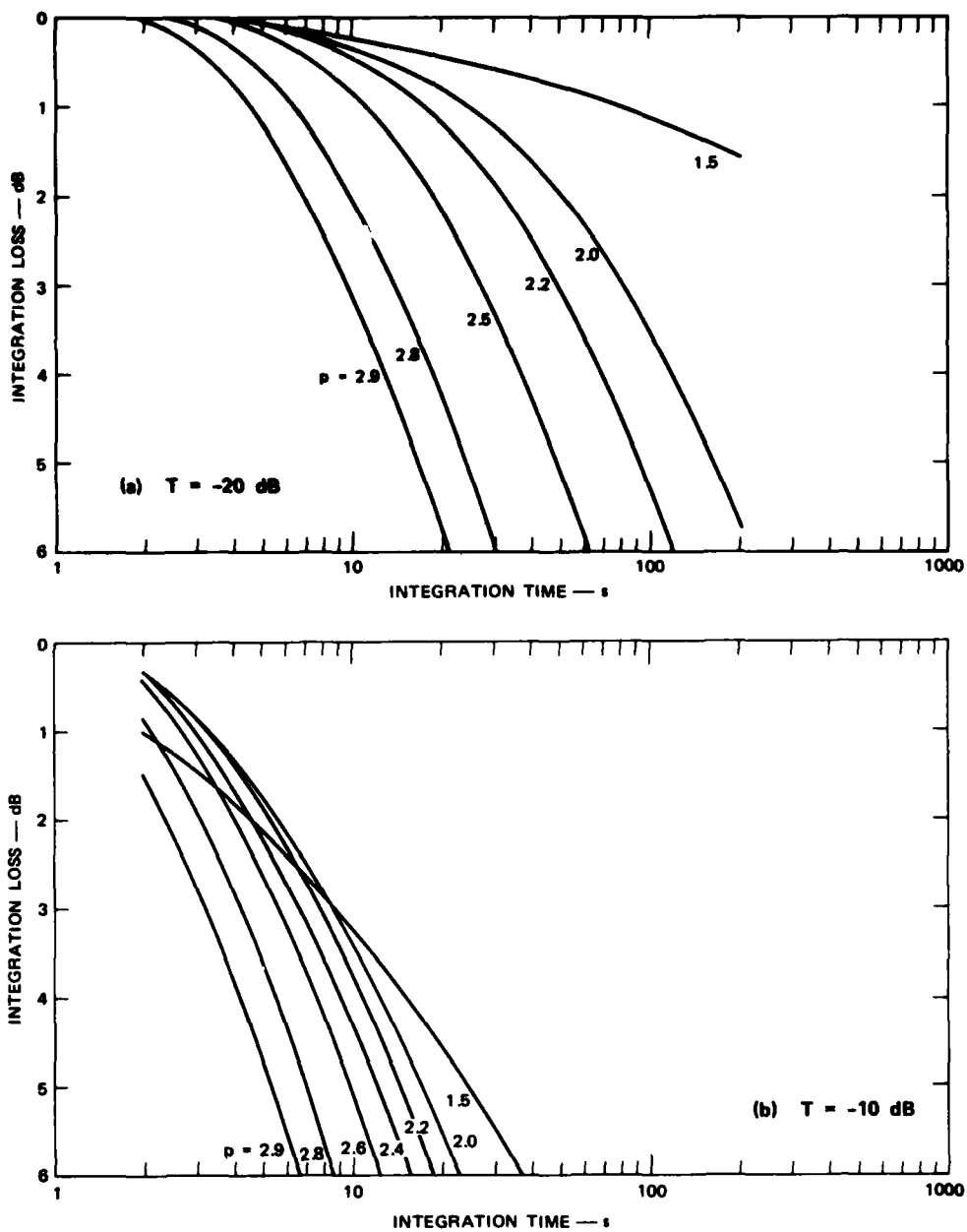


Figure 22 Calculated coherent integration loss for transionospheric radars for different temporal phase turbulence levels  $T$ . a)  $T = -20$  dB; b)  $T = -10$  dB

## RECENT ASPECTS OF IONOSPHERIC SCINTILLATION OBSERVATIONS

G. K. Hartmann  
 Max-Planck-Institut für Aeronomie  
 D-3411 Katlenburg-Lindau 3, P.O.Box 20  
 Germany

## SUMMARY

The propagation of electromagnetic waves through an inhomogeneous, anisotropic atmosphere (e.g. ionosphere) usually results in variations in the amplitude, phase and angle of arrival of the waves at the receiving site which is generally located on the ground but may also be aboard a satellite. These variations were denoted by astronomers as scintillations. (Nuclear physics uses this term in a different context.) Since all types of these variations can disturb - the more, the stronger they are - Radio Communication as well as Radio Navigation and Positioning Systems, the investigation of these scintillations and the possibility of their predictability is very important for many applications. Taking into consideration satellite communication and/or navigation systems the sources for scintillation can be in the upper atmosphere (ionosphere) as well as in the lower atmosphere (troposphere). Scintillation occurrence and scintillation intensity depend upon frequency, location, propagation path geometry, geophysical conditions, receiving equipment characteristics, - such like the receiving antenna beamwidth, the receiver resolution and stability, and the data acquisition facilities - and the measure used to describe scintillation. This causes many problems by comparing data from different sources. After fifty years of ionosphere research and more than twenty years of intensive scintillation measurements future experimental trends might be as much determined by some already visible limitations as by the application of the very recent advanced technologies. Both aspects are mentioned here. There are two principally different methods to investigate the scintillation producing irregularities in the ionosphere. 1. In situ measurements, 2. Remote sensing methods. It is shown that we have at present three different experimental possibilities if we want to improve our knowledge about the scintillation producing irregularities in the ionosphere. The first one, possibly the most important at present is based upon a new experimental technique (VIGRODOS) which possibly will allow a better, faster and easier understandable and more efficient combination of preedited data that stem from radar experiments, satellite radio beacon experiments, aurora and airglow measurements, as well as from in situ experiments.

## I. INTRODUCTION

Increasing efforts for a better understanding of our environment, e.g. the upper atmosphere (ionosphere) during the last years led not only to tremendous growth rates of scientific data [14-20] but also to more new questions than to solutions of old problems. If this continues this will seriously affect any experimental activity. Future experimental trends might be thus as much determined by some already visible limitations - Table 1 - as by the application of the very recent advanced technologies. After more than fifty years of ionosphere research and more than twenty years of very intensive scintillation measurements, supported by the immense technical progress during the last two decades, we have just now such a large variety of experiments in use that measure directly or indirectly scintillations, that in the time allotted for this talk either an uncritical detailed compilation of experiments could be provided or a less detailed but critical review.

## II. WHAT IS SCINTILLATION ?

The propagation of electromagnetic waves (e.g. radio wavelengths) through an inhomogeneous, anisotropic atmosphere (e.g. ionosphere) usually results in variations in the amplitude, phase, and angle of arrival of the waves at the receiving site which is generally located at the ground but may also be aboard a satellite. These variations were denoted by astronomers as scintillations and included not only radio frequencies but also optical frequencies (twinkling stars). Nuclear physics uses this term in a different context. This definition shows that strictly spoken only experiments that use as tools ("sensors") electromagnetic waves can directly measure scintillations. However, there are a fair amount of experiments that measure indirectly scintillations that will be briefly mentioned, too.

Observations of scintillations at radio wavelengths are of great importance not only from an application point of view, since they negatively affect radio navigation and radio communication systems [1, 2, 12, 13] that make use of the ionosphere as communication channel, but also from the point of view of basic physics of the upper atmosphere and recently also the lower atmosphere to a growing extent, however in higher frequency domains (GHz-region). No matter for which of the two fields the experiments are conceived, scintillation measurements are an indirect indication of the presence of irregularities atmosphere e.g. in the electron density distribution of the ionosphere or of turbulences in the solar wind (Interplanetary Scintillations [8]). The intensity of the amplitude scintillations are mostly described by so called scintillation indices, which were firstly reported by H. J. Whitney, in [1].

## III. THE IONOSPHERE

The ionosphere [25, 28] occupies a key position in solar terrestrial physics because, extending up to

now we have to consider to which extent the atmosphere is modified by our experiments, regardless whether we deal with rockets, spacecrafts or just electromagnetic waves as tools for these investigations.

In this context the author feels that the use of the terms "active" and "passive" measurements might be reconsidered. If they are still adequate they might be used in the following context:

- a) Passive: The effect of the experiment on the medium under investigation is negligible, strictly spoken: is much smaller than the instrumental noise.
- b) Active: The effect of the experiment on the medium under investigation is not necessarily negligible. Examples for a) are the investigation of the atmosphere by microwave radiometry, scintillation observations by signals from radio stars and/or radio beacon experiments. An example for b) is the modification experiment of the ionosphere called "Heating".

#### Ad 4.

- a) Any theory of physics makes more physical and philosophical assumptions than the facts (data) alone can give or imply. For this reason, any theory is subject to further modification and reconstruction with advent of new evidence that is incompatible with its basic assumptions. See fig. 1. This might be related to K. Poppers "falsification theorem".
- b) From a scientific point of view the interpretation of the data is the most important topic, since any experiment the data of which cannot be or are not interpreted is useless. Disregarding this, experimental techniques run the risk to develop into a l'art pour l'art. However, this gets extremely complicated when we deal with experiments that are conceived to investigate "Uncontrolled Conditions" or Conscious Ignorance [16] as displayed in fig. 2. Most experiments in laboratory physics fall into the category "Conditions Controlled by Man".  
The interesting relations in ionosphere physics are therefore derived by statistical methods and are based upon large amounts of time series data. We do have two principal statistical methods of treating large amounts of data.  
1. Frequency distribution 2. Descriptive statistical parameters.
- c) Data noise problems  
Due to the data growth rates and because of the large technical progress during the past two decades a subdivision of the experimental techniques and the relevant time series data into three generations (time) is suggested [16].  
Table 3 shows this as an example for atmosphere data.  
The small standard deviations in the third generation represent small fluctuations, that are often called "noise". In order to distinguish it from the instrumental noise the author would prefer to use the term "data noise". The additional term noise is used since data noise contributes like the instrumental noise to the degradation of the signal to noise ratio, however has a different origin and contains actual, however till now hidden, physical information.  
Remark: Noise as it is understood in communication science is the result of a random process, i.e. caused by chance. We have to remember that "Chance" describes an event, the occurrence of which is dependent from several independent processes. Thus there is no word that such a "random fluctuation" is principally indeterminable or incalculable.  
If we want to learn more from this data noise, we have to conceive operational experiments - like in meteorology - (uninterrupted, long-term measurements), and then to apply various filter techniques to the data. The longer the uninterrupted time series, the smaller the bandwidth of any applied filter can be, which improves the signal to noise ratio. Any type of mean value, median value, cross-correlation etc. is the result of a "filtered" data set. Non-operational experiments are a very good means for "case studies" which are most valuable in the first generation of data, e.g. if a new quantity is measured for the first time, but mostly only supplementary in the third generation. It has to be emphasized that at present any type of operational activity is much less attractive than any purely experimental activity. This is true not only from an economical point of view but also from a scientific one, since the latter involves much more hardware activities and is generally less time consuming than we know from "operational experiments".
- d) Data growth rate problems that affect experimental and interpretation activities are treated by the author in: [14 - 20].
- e) Modelling  
Without any doubt this is the ultimate goal. Reviews on this topic are given in [4, 5, 26, 27, 37].

## V. SCINTILLATION MEASURING TECHNIQUES

We can subdivide the experiments for the investigation of the irregularities in the upper atmosphere into two major categories.

- A. In situ methods (Measurement: at the location of the equipment)
- B. Remote sensing methods (Measurement: remote from the equipment)

#### Ad A: In situ methods

By means of retarding-potential analyzers (RPA) [3, 11] and magnetic ion mass spectrometers (MIMS) [21, 24] etc. aboard satellites and rockets [22] the irregularities in the ionization of the upper atmosphere are directly measured, i.e. the cause of the scintillations. Thus these in situ measurements are only indirect scintillation observation experiments while the latter ones give only indirect information about the irregularities. Due to this these in situ measurements will be only briefly mentioned here.

Only about 20 % of the published papers on scintillations at radio wavelengths originating from the upper atmosphere stem from in situ measurements. It is very likely that the ratio between the total number of present in situ experiments and the total number of remote sensing experiments is of the same order of magnitude. In situ measurements generally provide a one dimensional "snapshot" of the electron and/or ion density along the orbit of the spacecraft or along the trajectory of the rocket recent techniques allow very good temporal and spatial resolution despite the fact that an orbiting spacecraft never allows a complete separation between temporal and spatial variations.

the magnetosphere and down to the domain of meteorology it impinges on both. Qualitative understanding of the ionosphere certainly exists, and the ionization and energy balances are probably known quantitatively to within a factor of 2 [23]. Better precision is attainable in some "case studies", but any attempt to achieve greater accuracy everywhere is hampered by the fact that the ionosphere and particularly the F2 layer, shows marked spatial and temporal variability: place to place, hour to hour, day to day. Some features are repeatable, some attributable to magnetic disturbance, some apparently random. This variability has often been studied and commented upon, but never satisfactorily explained. Is it just "noise" resulting from random fluctuations of the many parameters that influence the ionosphere, in which case it is of limited scientific interest? Or does it conceal unrecognized physical processes or linkages between the sun, the magnetosphere, the upper atmosphere, the lower atmosphere and weather, terrestrial and oceanic phenomena?

Hence it is quite obvious that many topical questions need still to be solved [23].

It is known, that the ionosphere frequently exhibits irregularities in the electron concentration which seem to be mostly random type. Their root mean square fluctuations from the mean are usually fairly small, but they can rise to 50 % or even larger at the geomagnetic equator as shown by in situ measurements. There are reported irregular biteouts of up to three orders of magnitude in the ion concentration  $N_i$  in the nighttime equatorial F region [24] associated with small scale inhomogeneities in  $N_i$ . Although it has not yet been demonstrated either experimentally or theoretically - however the latter is planned as the author was recently told - it might be expected that the strong gradients and the steep "fingers" of ionization shown by Mc Clure et al. [24] might give rise to microwave scintillations.

#### IV. LIMITATIONS FOR EMPIRICAL SCIENCES (EXPERIMENTS)

There are four basic types of limitation for each experiment carried out for studying the atmosphere

1. Logistics - distribution of the measurement in space and time
2. Technology - engineering problems
3. Interdependence - influence of the experiment on the investigated object
4. Interpretation - interpreting the data in terms of the final product

Political, economical, and social limitations are disregarded here but they are very important in drawing consequences out of these limitations.

Ad 1. As we already know the ionosphere is a space (x, y, z) and time (t) dependent medium [10], and different from many other domains in physics, time is an actual physical parameter. Thus what we want to measure is generally a function of four parameters  $F = F(x, y, z, t)$ , i.e. we have to deal with five dimensions at a time. This is not only extremely difficult from the experimental point of view, i.e. from the data acquisition side, but also from the view of data processing, which has to be stronger considered in designing future experiments. Data processing - as understood by the author - comprises 1. Data collection and ordering, 2. Data documentation, 3. Data compression. The last might be subdivided again into: 3a. Graphic representation, 3b. Statistical analysis, 3c. Modelling [15, 16, 19].

Remark: The enormous data growth rates implied that we have to insert a new step between data acquisition (production of new data) and data processing. See table 2. This new step is denoted by the author as data preediting [15, 16, 19]. Using holography techniques "moving" three dimensional presentation (acquisition) is possible, i.e. four dimensions. Adding colors to it we finally get five dimensions at a time. If this "colored hologram film" could be expanded and reduced in its time scale, i.e. by slow motion and fast motion techniques, as well as in its spatial coordinates, e.g. by optical magnification and reduction techniques, then we would have reached the optimum goal for studying very efficiently physical phenomena of the upper atmosphere. Referring to experimental aspects of ionospheric scintillation observations this would imply a recording and presentation of the irregularities in the ionospheric electron density distribution in the following manner:

1. Electron density distribution as a function of two space coordinates by a hologram (three dimensions).
2. Electron density distribution also as a function of the third space coordinate by colors.
3. Variations of the electron density distribution in time by a sequence of holograms - "moving" hologram or hologram film.

Apart from some very few experiments from the data processing side, e.g. like those carried out by the Data Management Group of the Lawrence Livermore Laboratory (V. E. Hampel), University of California, Livermore, Ca. 94550, which are steps into this direction, we still are very far away from this goal. At present we are already very satisfied if we can get three dimensional data representation. Due to technical and economical limitations on the data acquisition side we are till now in a much worse position.

Ad 2. Under this heading we include all questions of instrument design, including basic instrumental noise, calibration accuracies and data preediting procedures.

Apart from the preediting, these are "more" technological limitations and by the expenditure of sufficient time and money they can be reduced almost to insignificance. In practice, however, they are very important as they give rise to both random and systematic errors in the final product. See figs 1 and 2. The problem of instrumental noise becomes increasingly important the smaller variations in the data we want to interpret, i.e. when "data noise" - term will be explained later - approaches the level of the instrumental noise.

Ad 3. From Quantum physics it is well known how serious the influence of the experiment on the investigated object can be - see fig. 1. However, it seems surprising that this should play any significant role in the investigations of the upper atmosphere. As long as we dealt with the first and second generation of data - see Table 3 and 3a - e.g. dealt with coarse effects - this influence could be neglected. Now we are dealing in many domains with the third generation of experiments and data, where we want to study fairly small variations of the medium by the application of very sophisticated and high resolution techniques and



In dealing with in situ measurements Telemetry, Telecommand, and Tracking problems have to be considered simultaneously with the data acquisition problems by the sensors.

Ad B: Remote sensing methods

1. General aspects for studies of the upper atmosphere

These experimental techniques are based upon the propagation of electromagnetic waves and they use these waves as a tool ("sensor") for investigating the medium traversed by these waves. Despite the fact that astronomers have used the term scintillation also for describing star twinkling in the optical domain, here we will mainly refer to those experiments that are concerned with radio wavelengths ( $\sim 1 \times 10^6$  Hz to  $3 \times 10^{10}$  Hz). The propagation of those electromagnetic waves through an inhomogeneous, anisotropic ionosphere (and troposphere) results usually in variations in the amplitude, phase, and angle of arrival of the waves at the receiving site. While amplitude measurements are the simplest and most inexpensive ones, phase measurements are much more complicated and expensive. However, the most sophisticated and most expensive ones are angle of arrival measurements. From the present state of the art we may call the first "Simple Technology", the second "Intermediate Technology" - in a sense as E. Schumacher [33] suggests it for world wide application also in the Third World - and the third "Advanced Recent Technology".

By means of dispersion theory absorption measurements can be transformed by a so called Hilbert integral transform into dispersion measurements and vice versa.

Looking at the present experiments they can be grouped due to five different propagation paths (Table 4).

a) Ground - ionosphere - ground

A wave transmitted from a ground station is - depending on the frequency and the state of the ionosphere - reflected and/or scattered or partially absorbed in the ionosphere (and troposphere) and then received by a ground station. This encompasses all bottomside ionosonde sounding studies, radar backscatter studies, and incoherent scatter radar studies.

Due to the very large amount of work accomplished in this field only one statement and two review papers will be given here. Spread F and sporadic E are associated with scintillations [24, 29, 31, 36]. Reviews are given by [14, 28].

b) Satellite (Star) - ionosphere - ground

A wave transmitted by an artificial satellite (or rocket) or by a radio star traverses the ionosphere - if the frequency is high enough - and is received at a ground station, or vice versa. This includes all satellite radio beacon studies and radio star studies, especially problems introduced by the ionosphere and troposphere, into radio navigation systems and/or radio communication systems. Being very precise in terminology only this category allows actual scintillation measurements. Most of the scintillation studies were carried out with various types of radio beacon experiments. Only some review papers will be mentioned here [1, 2, 7, 9, 12, 13, 27, 30, 34].

c) Satellite - ionosphere (ground) - satellite

A wave transmitted from a satellite is - depending on the frequency - reflected and/or scattered or partially absorbed in the ionosphere or at the ground and then received by a satellite receiver. This includes all topside ionosonde sounding studies as well as Sidelooking Radar Experiments (SAR) from spacecrafts. Both methods again enable to detect irregularities in the ionosphere which are mostly associated with scintillations. This holds true for any stronger effect. However, due to different equipment characteristics - sensitivity, noise level etc. - this is mostly not the case for weaker effects. Thus it may occur that radio beacon data show weak scintillations, while topside ionograms show no disturbance. Thus one has to be very careful by comparing data from different sources. If the amplitude, phase, and/or angle of arrival of the electromagnetic waves along these three different propagation paths are used to deduce physical properties of the ionosphere, they were earlier denoted as HF and UHF propagation studies. Recently the term remote sensing replaces the old one.

d) Ionosphere - ground and/or ionosphere - satellite

The ionosphere itself radiates upwards and downwards electromagnetic energy. The most significant portions lie in the optical frequency domain and are known as aurora and airglow phenomena [6]. (However, they get slowly supplemented by infrared and microwave frequencies.) They indicate the presence of irregularities in the upper atmosphere which are mostly associated with scintillations. However, like the in situ measurements, these experiments give indirect evidence of scintillations.

Aurora and airglow are measured with all-sky spectrometric imaging systems. The airglow data [6] is particularly valuable in understanding equatorial scintillations. Ridges of bright and dark bands were observed long ago from Hawaii, and interpreted by Mc Clure et al., [24] as resulting from upward motion of F1 region plasma into the upper F2 region. Weber et al., [35] show that the bright and dark N - S aligned bands drifting eastward along with the ionosphere, lasting for more than three hours, and clearly associated with scintillation, spread F, oblique echoes, a "plume" on a radar map [36, 24] and bubbles.

e) Satellite - satellite or ground - ground

A wave transmitted from a satellite or rocket or aircraft is received by another satellite or rocket or aircraft. This includes all so called "Mother-Daughter" Experiments, based on the propagation of electromagnetic waves.

If transmitter and receiver are located at the ground, we deal with all line of sight measurements.

## VI. BASIC QUANTITIES AND CHARACTERISTICS

From the previous statements it became quite clear that the two basic quantities that can be measured and therefore should be measured are amplitude (e.g. absorption) and phase (e.g. dispersion) of those electromagnetic waves used as a tool ("sensor") in remote sensing experiments. On the receiving side there are two principal possibilities to measure amplitude and phase.

- a) The quadrature components, e.g.  $E_y$  and  $E_x$  as displayed in fig. 3.
- b) The linear amplitude and phase or generally spoken the complex amplitude as it is used for example in radioholography studies [32].

As far as the author knows there are more and better models to infer from the last measurements features of the irregularities than from the first type. Nonetheless both can be used to measure scintillations and each has its inherent technical advantages and disadvantages.

All remote sensing methods are "integrating" over smaller or larger volume elements in the atmosphere. Thus the data set obtained is principally very different from that we know from in situ measurements. Receiving just one frequency at one observing station it is almost impossible to "record" more than a two dimensional picture of the irregularity (time and one space coordinate). With very many assumptions a three dimensional one might be very speculatively obtained. However, this is still far away from the earlier mentioned goal of a five dimensional picture. By the application of frequency [29, 32] diversity and space diversity - like J. Mac Dougall in [27] - e.g. interferometry, one can get information about an additional dimension. Thus we can expect to obtain a three dimensional picture (time and two space coordinates) of the irregularities. At best - again with very many assumptions - a four dimensional picture might be possible.

## VII. CONCLUSIONS

If we want to improve our knowledge about the atmosphere we have at present three principally different experimental possibilities that should be considered simultaneously which supplement each other but do not replace each other.

1. A better, faster and easier understandable and more efficient combination of preedited data that stem from various experiments (sources). At the first moment it does not look like as if any experimental technique apart from computer skill would be involved here. However, due to the tremendous data growth rates and the large difficulties to compare data from various sources a new experimental technique comes into view or has to be developed for this purpose, if we do not want to stay with one or two case studies. The author denotes it VIGRODOS (Video-Graphic-Communication and Documentation System). [15, 16, 19]
2. Expansion of the time series measurements with simultaneous "spatially denser" observation networks. This would involve more of the - less attractive - "operational" experiments rather than experiments for just "case studies".
3. Concepts and designs of new experiments that a) allow to record (data acquisition) a picture of the atmosphere or its constituents with more dimensions at a time than at present (and less assumptions) or b) allow to measure a quantity that could not be measured till now and gives more direct insight into the behaviour of the atmosphere, no matter whether we think only of "case studies" or longer term operational experiments.

Due to various points of view, technical, economical, and scientific the first way seems to be the most promising and rewarding at the moment.

Considering the investigation of scintillations the following statements can be made: No major progress in theory can be expected without these activities as recent studies show [4, 5], since they are still based on almost as many assumptions as 10 years ago.

Recent studies further show - again in context with this first way - that only a combination of radar data, airglow, and aurora data, as well as in situ measurements can lead fairly soon to a significantly better understanding of the complicated physical processes that cause these irregularities in the ionization of the ionosphere. First steps were done by [24, 35, 36].

The third way is very likely the most attractive, involves the most advanced hardware, is highest estimated, and gets the most economic support.

## VIII. ACKNOWLEDGEMENT

The author thanks the Max-Planck-Institut für Aeronomie, represented by Prof. Dr. W. I. Axford for the support of this work.

## IX. REFERENCES

- [1] Aarons, J. (Editor), 1970  
A Survey of Scintillation Data and its Relationship to Satellite Communications  
AFRL Report no. 106, AFRL-70-0053, AFRL, L. G. Hanscom Field, Bedford, Mass., USA

- [2] Aarons, J. (Editor), 1973  
Total electron content and scintillation studies of the ionosphere  
AGARD ograph no. 166
- [3] Basu, Su.; Basu, Sa.; Khan, B. K., 1976  
Model of Equatorial Scintillations from In Situ Measurements  
AFGL-TR-76-0080, AFGL Hanscom AFB, Mass. 01731
- [4] Booker, H. G.; Miller, C. D., 1977  
A theoretical model for ionospheric scintillation caused by weak irregularities of ionization density  
Report: SRI International, Menlo Park, Ca. 94025, USA
- [5] Booker, H. G.; Ferguson, J. A., 1977a  
A theoretical model for equatorial ionospheric spread F echoes in the HF and VHF bands  
Report: University of California, San Diego, La Jolla, Ca. 92093, USA
- [6] Buchau, J.; Weber, E. J.; Mc Clure, J. P., 1978a  
Radio and optical diagnostics applied to an isolated equatorial scintillation event  
Proceedings of Ionospheric Effects Symposium, 24-26 January 1978, Arlington, V.A.
- [7] Buchau, J.; Aarons, J.; Mullen, J. P.; Weber, E. J.; Whalen, J. A.; Whitney, H. E.; Crampton, Jr., E. E., 1978  
Amplitude scintillation studies in the polar region on 250 MHz  
Proceedings of Ionospheric Effects Symposium, 24-26 January 1978, Arlington, V.A.
- [8] Coles, W. A.; Rickett, B. J.; Rumsey, V. H., 1974  
Interplanetary Scintillations Asilomar Solar Wind Conf. 1974  
Dept. of Applied Physics and Information Science, University of California at San Diego, La Jolla, Ca. 92037, USA
- [9] Davies, K.; Degenhardt, W.; Hartmann, G. K.; Leitinger, R., 1977  
Electron Content Measurements over the U.S.  
Joint Radio Beacon Program NOAA / MPAE / Graz, Station Report ATS-6, 94<sup>0</sup> W  
Ed. Max-Planck-Institut für Aeronomie, P.O.Box 20, D-3411 Katlenburg-Lindau 3, Germany
- [10] Dieminger, W., 1975  
Geophysical investigations by scattered radio waves.  
Radio Science, 10, 7, 681-691
- [11] Hanson, W. B.; Zuccaro, D. R.; Lippincott, C.R.; Sanatani, S., 1973  
The retarding potential analyzer on Atmosphere Explorer  
Radio Science, 8, 333
- [12] Hartmann, G. K., 1972  
A brief review of scintillation studies  
Space Research XII, 1221-1228
- [13] Hartmann, G. K., 1975  
HF and UHF propagation studies of the midlatitude ionosphere (Review)  
Ann. Geophys. 31, 1, 39-52
- [14] Hartmann, G. K., 1977  
Why do we need data, what are data, what principal data evaluation problems have to be considered?  
Ed: ZAED Kernforschungszentrum, D-7514 Eggenstein-Leopoldshafen, Federal Republic of Germany
- [15] Hartmann, G. K., 1978  
Numerical Data Growth Rate Problems  
6th International CODATA Conference, May 22-25, 1978, Santa Flavia, Italy, p 413-420
- [16] Hartmann, G. K., 1978  
The information explosion and its consequences for data acquisition, documentation and processing  
Ed: World Data Center A, Solid Earth Geophysics Report SE-11; Solar Terrestrial Physics Report UAG-65, U.S. Dept. of Commerce, NOAA, EDS, Boulder, Colo. 80302, USA
- [17] Hartmann, G. K., 1978  
Betrachtungen über Energie und Information  
ntz, Bd 31, Heft 8, 535-536
- [18] Hartmann, G. K., 1978  
Informationsexplosion - Grenzen, Folgen, Handlungsmöglichkeiten  
Teil 1: Energie und Information; ntz, Bd 31, Heft 3, 568-571  
Teil 2: Probleme des Informationswachstums; ntz, Bd 31, Heft 9, 654-657
- [19] Hartmann, G. K., 1979  
Documentation problems of large amounts of measured data  
Hrsg. Fachinformationszentrum Energie, Physik, Mathematik GmbH Karlsruhe, D-7514 Eggenstein-Leopoldshafen 2, Nr. 1, Sept. 1979, ISSN 0172-2204
- [20] Hartmann, G. K., 1979  
Aspekte der Meßdatendokumentation  
In: Datenbanken, Datenbanken, Netzwerke, S. 155-169; Hrsg. Rainer Kuhlen; K. G. Saur, München, New York, London, Paris
- [21] Hoffman, J. H.; Hanson, W. B.; Lippincott, C. R.; Ferguson, E. E., 1973  
The magnetic ion mass spectrometer on Atmosphere Explorer  
Radio Science, 8, 315
- [22] Kelley, M.C.; Haerendel, G.; Kappler, H.; Valenzuela, A.; Balsley, B.B.; Carter, D.A.; Ecklund, W.L.; Carlson, C.W.; Hausler, B.; Torbert, R., 1976  
Evidence for a Rayleigh-Taylor type instability and upwelling of depleted density regions during equatorial spread F  
Geophys. Res. Lett. 3, 448

- [23] Kohl, H.; Rishbeth, H., 1976  
Topical Questions of Ionospheric Physics: A Working Group Report  
J. Atmos. Terr. Phys. 38, 775
- [24] Mc Clure, J. P.; Hanson, W. B.; Hoffman, J. H., 1977  
Plasma Bubbles and Irregularities in the Equatorial Ionosphere  
J. Geophys. Res. 82, 19, 2650-2656
- [25] Nisbet, J. S., 1975  
Models of the Ionosphere  
In: B. M. Mc Cormac (ed) Atmosphere of Earth and Planets, 245-258, D. Reidel Publishing Company
- [26] Pope, J. H., 1974  
Global Scintillation Model  
NOAA Technical Report ERL308-SEL30, U.S. Dept. of Commerce, NOAA ERL, Boulder, Colo. 80302, USA
- [27] Proceedings, Ed: IROE, 1979  
Proceedings of the COSPAR Symposium on Beacon Satellite Measurements of Plasmaspheric and Ionospheric Properties, 22-25 May 1978, IROE-CNR, Firenze, Italy
- [28] Rawer, K.; Suchy, K., 1967  
Radio observations of the ionosphere  
Geophysics II/2, pp 1-537, In: S. Flügge, Editor: Springer Verlag, Berlin, Göttingen
- [29] Rino, C. L.; Fremouw, E. J., 1977  
The angle dependence of singly scattered wave fields  
J. Atmos. Terr. Phys. 39, 859-868
- [30] Rino, C. L.; Fremouw, E. J.; Livingston, R. C., 1977a  
Wideband Satellite Observations  
(Report DNA 001-75-C-0111) SRI International, 333 Ravenswood Ave., Menlo Park, Ca. 94025, USA
- [31] Röttger, J., 1976  
The macro-scale structure of equatorial spread F irregularities  
J. Atmos. Terr. Phys. 38, 97
- [32] Schmidt, G.; Tauriainen, A., 1975  
The localization of isolated ionospheric irregularities by the holographic method  
J. Geophys. Res. 80, 4313
- [33] Schumacher, E. F., 1973  
Small is beautiful  
Blond and Briggs, London
- [34] Umeki, R.; Liu, C. H.; Yeh, K. C., 1977  
Multifrequency Spectra of Ionospheric Amplitude Scintillations  
J. Geophys. Res. 82, 19, 2752
- [35] Weber, E. J.; Buchau, J.; Eather, R. H.; Mende, S. B., 1978  
North South aligned equatorial airglow depletions  
J. Geophys. Res. 83, no. A2, pp. 712-716
- [36] Woodman, R. F.; La Hoz, C., 1976  
Radar observations of F-region equatorial irregularities  
J. Geophys. Res. 81, 5447
- [37] Yeh, K. C.; Liu, C. H.; Youakim, M. Y., 1975  
A theoretical study of the ionospheric scintillation behaviour caused by multiple scattering  
Radio Science, 10, 97-106

#### X. CAPTIONS OF TABLES AND FIGURES

Table 1 Limitations for empirical sciences (experiments)

Table 2 From Data Acquisition to Data Processing

Table 3 A subdivision of experimental techniques and the relevant time series data into three generations

Table 3a Various steps of empirical, experimental sciences

Table 4 The main five propagation paths for remote sensing of the atmosphere

Figure 1 Fundamental aspects of physics as a science

Figure 2 Elements of empirical science

Figure 3 Phase measurement and preediting

Figure 4 The three basic elements of literature in a broader sense and their major documentation techniques with combinations indicated by arrows, leading possibly to VIGRODOS

## XI. TABLES AND FIGURES

Table 1 Limitations for empirical sciences (experiments)

- |                     |   |  |
|---------------------|---|--|
| 1. Logistics        | - | distribution of the measurement in space and time      |
| 2. Technology       | - | engineering problems                                   |
| 3. Interdependences | - | influence of the experiment on the investigated object |
| 4. Interpretation   | - | interpreting the data in terms of final product        |

Table 2 From Data Acquisition to Data Processing

- I. Data Acquisition
- II. Data Preediting
- III. Data Processing
  1. Data collection and ordering
  2. Data documentation
  3. Data compression
    - a) Graphic representation
    - b) Statistical analysis
    - c) Modelling

Table 3 A subdivision of experimental techniques and the relevant time series data into three generations. Example: Investigations of the atmosphere

1. First generation of experiments and atmospheric data  
(Simple Data Technology: SIDAT)  
+  
Mean behaviour with large standard deviations  
+  
Very coarse scale reference atmosphere  
+
2. Second generation of experiments and atmospheric data  
(Intermediate Data Technology: INDAT)  
+  
Further, additional data + processing  
+  
Mean behaviour with moderate standard deviations  
+  
Coarse scale reference atmosphere  
+
3. Third generation of experiments and atmospheric data  
(Recent Data Technology: REDAT)  
+  
Further, additional data + processing  
+  
Mean behaviour with small standard deviations  
+  
Fine scale reference atmosphere

Table 3a

## Various steps of empirical, experimental sciences

First generation

(Simple Data Technologies, SIDAT)

Data Acquisition (DA), Data Preediting (DP), Data Documentation (DD), Data Processing (DPr), Data Exchange (DE), and Data Handling (DH) are done at the same location and by one institution. Here we deal with a relativ small amount of data and mainly with pure research activities.

Second generation

(Intermediate Data Technologies, INDAT)

The specialisation and "branching" processes due to the organic information growth imply that the steps DA, DP, DD, DPr, DE, and DH are getting complexer and are slowly institutionally and organizingly separated, i.e., they occur generally at several different locations, being accomplished by several different organisations. Here we deal in general with medium amounts of data. We still have more research than service activities. (Service means in this context the foundation of so-called "information systems" for data handling.)

Third generation

(Recent Data Technologies, REDAT)

The above mentioned steps DA, DP, etc. are mostly completely separated, spatially, temporally, and organizingly. Here we deal with a large amount of data. Generally there are more service activities required than research activities. (Service for Research and Application.)

Foundation of Information Analysis Centers (IACs), Data-networks, and Data Base Management Systems (DBMS).

Here we reach at present the limits of the human information processing capabilities and capacities.

Fourth generation ????

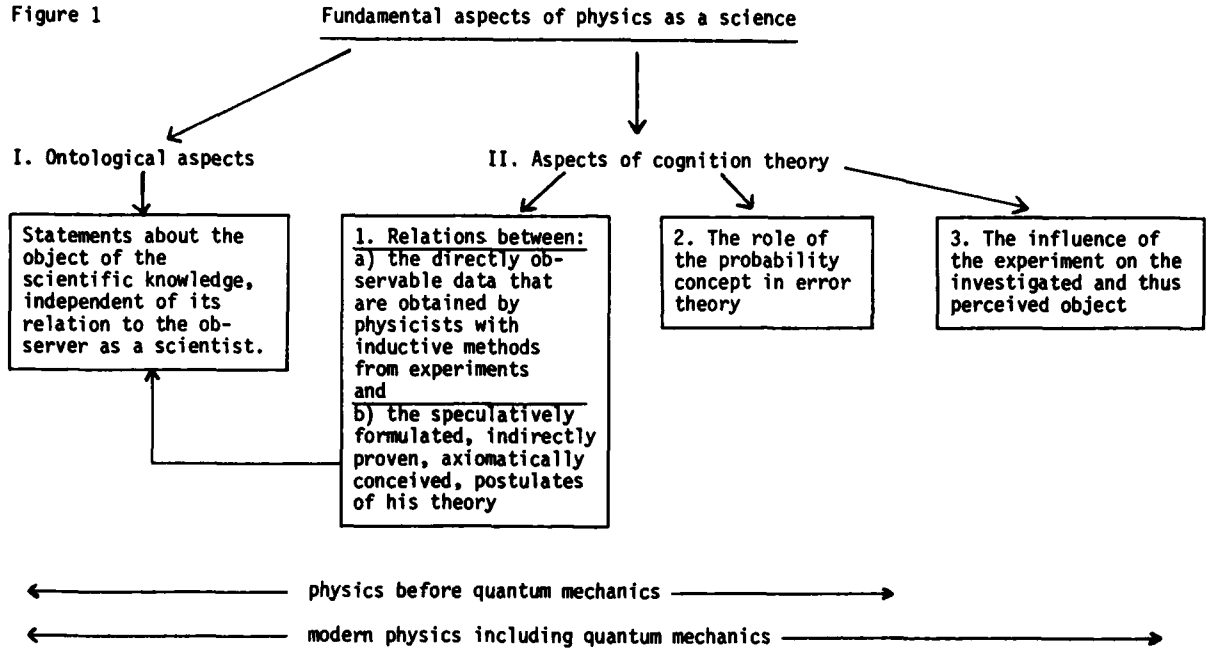
There might later occur a leap across the just mentioned limits, possibly initiated by new ways of information experience and information understanding which amongst others will be supported by VIGRODOS-Systems - Video-Graphic-Communication and Documentation System - term defined by the author.

Table 4

## The main five propagation paths for remote sensing of the atmosphere

- a) Ground → ionosphere → ground  
(Bottomside ionosonde sounding studies, radar backscatter studies, and incoherent scatter radar studies)
- b) Satellite (Star) → ionosphere → ground  
(Radio Star measurements, Satellite Radio Beacon Experiments (RBE))
- c) Satellite → ionosphere (ground) → satellite  
(Topside ionosonde sounding studies, topside radar backscatter studies, Side looking radar (SAR))
- d) Ionosphere → ground and/or ionosphere → satellite  
(Radiation from the upper atmosphere, like aurora, airglow etc. received at a ground station or at a satellite)
- e) Satellite → satellite or ground → ground

Figure 1



**Remarks:** II.1: The last portion b) determines the object of the scientific knowledge and thus leads to the ontology. The relation between a) and b) defines a parameter in cognition theory.

II.2: The role of the probability factor in error theory is the following: With its help the physicists decide how far the results of their experiments can deviate - due to human faults - from the results deduced from the model (theoretical) calculations before they regard this deviation as a disproof of the theory.

general: Any theory of physics makes more physical and philosophical assumptions than the facts alone give or imply. For this reason, any theory is subject to further modification and reconstruction with the advent of new evidence that is incompatible with its basic assumptions.

Figure 2

Elements of empirical science

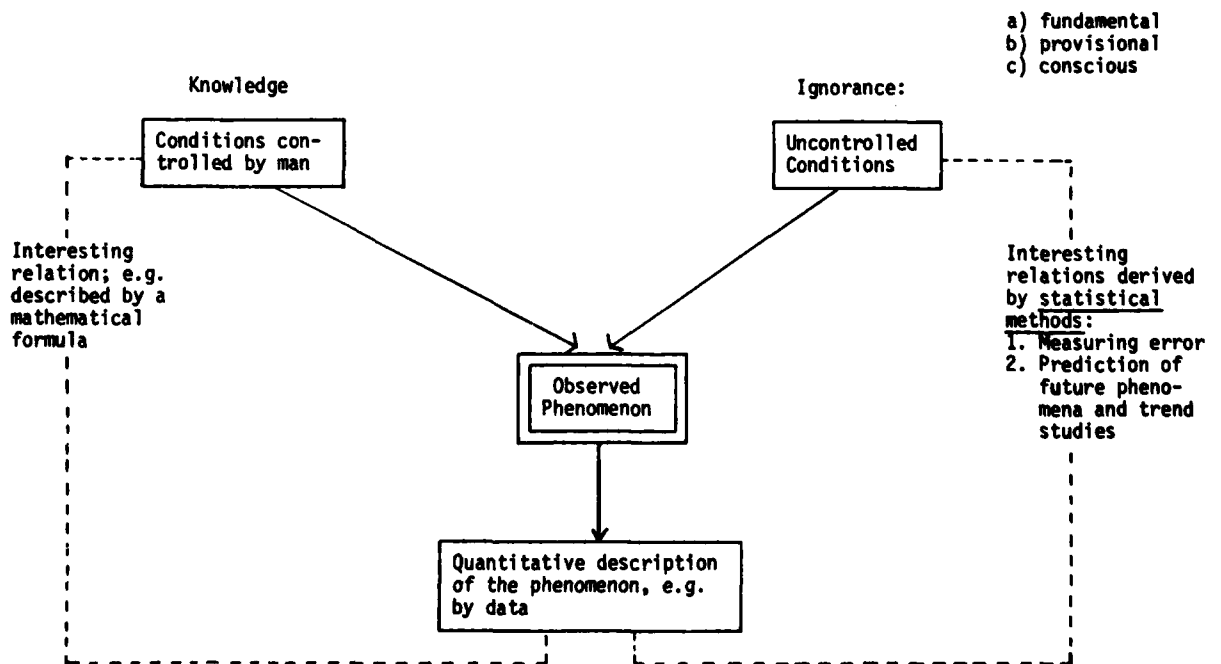


Figure 2 continued

## Remarks:

- A. The ignorance about the uncontrolled conditions can be of three different types a) fundamental type - if for instance the influence of a parameter cannot be determined in principle (time of nuclear splitting); b) provisional type - if we can hope that by the use of new information we can expand the range of controllable conditions; c) conscious type - if we know of the existence of some uncontrolled conditions and disregard them, since regulating them is either of no interest or technically not feasible or too expensive.
- B. There are two principal statistical methods of treating large amounts of data.  
1. Frequency distributions; 2. Descriptive statistical parameters.

Figure 3

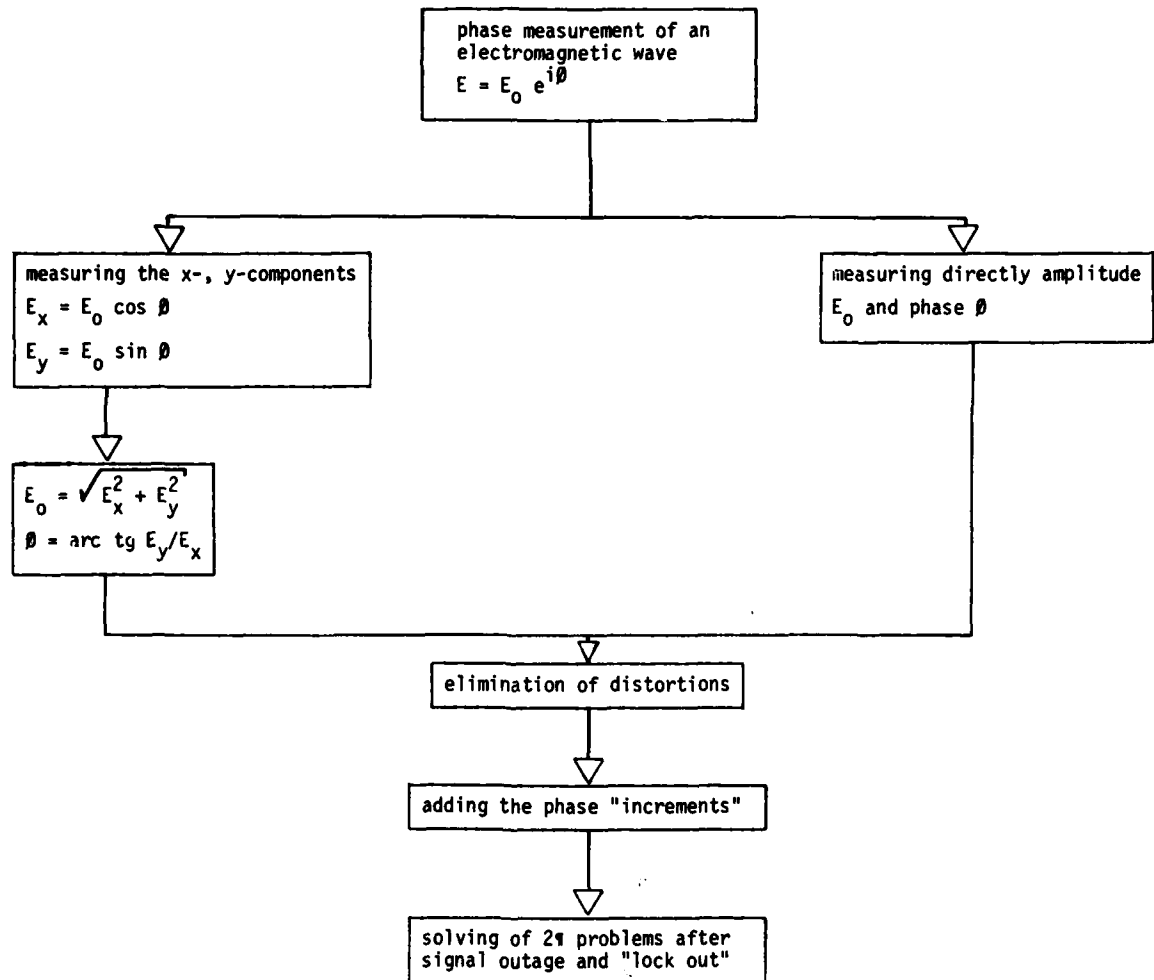
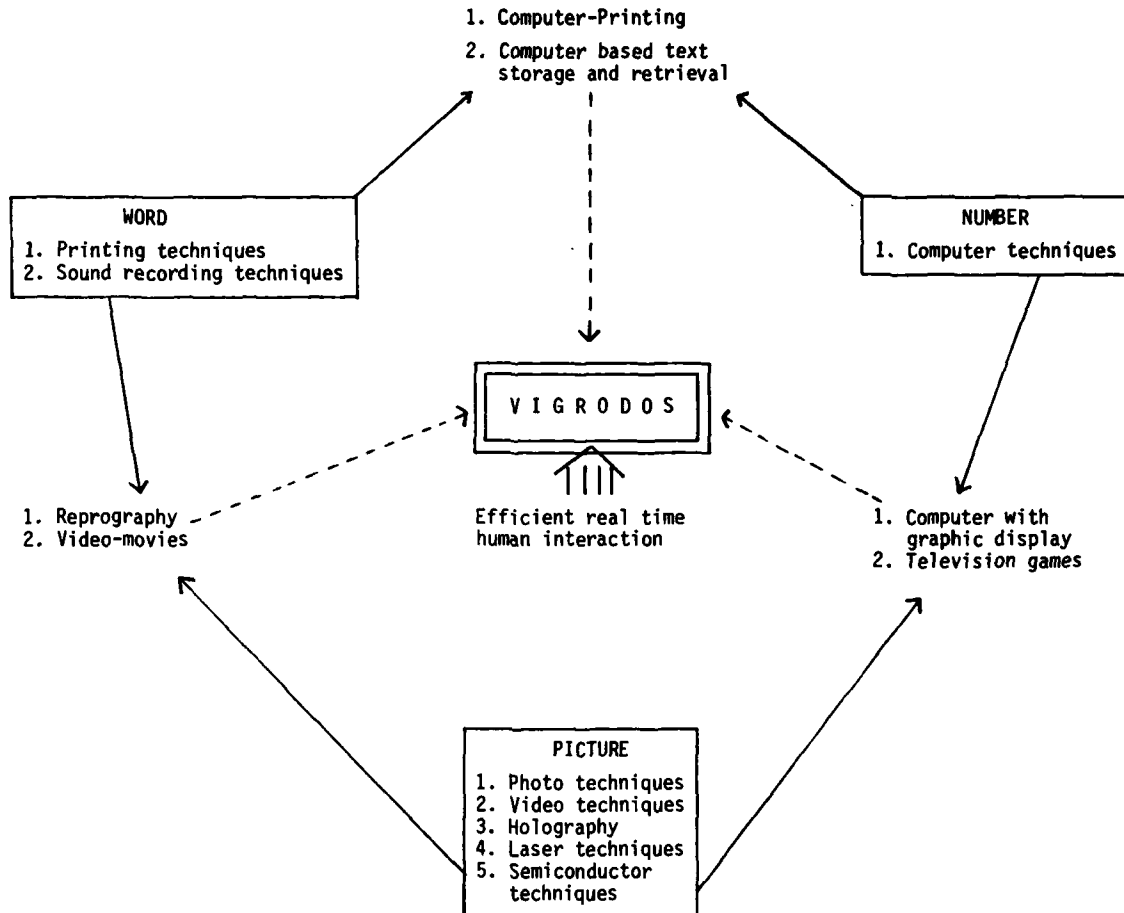
Phase measurement and preediting



Figure 4

The three basic elements of literature in a broader sense and their major documentation techniques with combinations, indicated by arrows, leading possibly to VIGRODOS



The broken arrows indicate the possible future combination of the recent combination techniques, towards a Video-Graphic-Communication and Documentation System (VIGRODOS, term defined by the author)

Statistical Properties of Transionospherically Propagated  
Radio Signals under the Intense Scintillation Conditions

K. C. Yeh and C. H. Liu  
Department of Electrical Engineering  
University of Illinois at Urbana-Champaign

Abstract

Scattering from electron density irregularities is known to be responsible for producing scintillations on radio signals that propagate through the ionosphere. These ionospherically related scintillation effects have been observed up to a frequency as high as the lower end of the SHF band. To characterize such a fading communication channel, one needs to know the statistical properties of the received signals. Extensive studies have been carried out both experimentally and theoretically, especially for amplitude of the signal, under the weak scatter conditions. This paper attempts to review some of the recent results, particularly those which clearly delineates the importance of multiple scattering.

The simplest indicator of scintillation activities is the value of scintillation index. There are several scintillation indices commonly in use, but they are all derived from the amplitude data and they are all related. For precise work the index  $S_4$ , which is defined as the fractional mean square deviation of the received power from the mean power, is recommended. This index has been found to be rather sensitive to radio frequencies in the weak scatter regime, but become increasingly insensitive to radio frequencies in the multiple scatter regime. Such a behavior is also predicted theoretically and has been ascribed to the saturation effects. As for phase, the results are not so consistent possibly because of its sensitivity to the data processing technique. In terms of quadrature components it has been found that most of the power resides in the phase-quadrature component in the weak scatter limit, but gradually becomes equalized among the two components as the scintillation index  $S_4$  increases. Other considerations such as the power spectrum and the correlation interval of the amplitude, phase and quadrature components have also been investigated and reviewed in this paper.

1. INTRODUCTION

In a space-earth propagation path the radio wave may encounter regions of the ionosphere where variations in electron density may have scales ranging from fractions of a meter to many kilometers. These electron density variations are known as irregularities which can scatter radio waves to produce the scintillation phenomenon. In the space-earth geometry such ionospheric irregularities are often confined to a slab region. The radio wave after emerging from the slab has to undergo the diffraction process. Even though the region outside the slab is homogeneous or horizontally stratified, the diffraction process will mix further the phase of the decomposed spectral plane waves. As a result the amplitude fluctuations of the radio wave will grow with the propagation distance. That is, the  $S_4$  scintillation index (defined as the fractional mean square deviation of the received power from the mean power) will increase with distance. However, the increase in  $S_4$  is not unlimited. Computational results show that  $S_4$  actually approaches a constant value asymptotically for large distances in a manner shown in Fig. 1. Because of the manner for which  $S_4$  approaches a constant value, effects connected with the condition that  $S_4$  is nearly unity are called the saturation effects. In the saturation regime the scintillation is intense. When this happens, effects predicted by the weak scintillation theories will break down. The purpose of this paper is to show these saturation effects.

The aforementioned saturation effects can be more lucidly illustrated in a different manner for propagation through the ionosphere. This is because the ionosphere is a dispersive medium and its refractive index is a function of frequency. As a matter of fact the fluctuation of relative permittivity is

$$\Delta\epsilon(\vec{r}) = \frac{-(\omega_p/\omega)^2}{1 - (\omega_p/\omega)^2} \cdot \left( \frac{\Delta N(\vec{r})}{N_0} \right) \quad (1)$$

where  $\omega_p$  is the angular plasma frequency of the background ionosphere,  $\omega$  is the angular radio frequency,  $N_0$  is the background electron density whose corresponding angular plasma frequency is  $\omega_p$ , and  $\Delta N$  is the fluctuating part of the electron density. As given by (1)  $\Delta\epsilon$  is frequency dependent. The value of  $\Delta\epsilon$  decreases to zero as  $\omega$  increases without bound. Consequently, for a given ionosphere and its accompanied irregularities, the scintillation at a reasonably high frequency may be weak; but as the frequency decreases the scintillation is expected to intensify and all effects associated with the saturation phenomenon are expected to reveal themselves. This is clearly demonstrated in Fig. 2. It is seen that the linear dependence of  $S_4$  on  $\langle(\Delta N)^2\rangle^{1/2}$  is valid only when  $S_4$  is less than about 0.2 to 0.3. Substantial departure from this linear relationship occurs when  $S_4$  is larger than 0.5. The F2 region ionosphere has a density of about  $10^{12}$  electrons/m<sup>3</sup> at the peak. If the rms fluctuation in electron density is one percent which corresponds to  $\langle(\Delta N)^2\rangle^{1/2} = 10^{10}$  electrons/m<sup>3</sup>, Fig. 2 shows that the scintillation is weak for frequencies above about 100 MHz. If, however, the rms fluctua-

tion in electron density increases to ten percent (corresponding to  $\langle(\Delta N)^2\rangle^{1/2} = 10^{11}$  electrons/m<sup>3</sup>), there will be some saturation effects even at 500 MHz. Recent measurements made in situ on board the satellites have shown that the rms fluctuation in electron density can be fairly large, even close to 100%. For such large fluctuations the saturation effects can be expected to be important throughout the VHF and UHF bands and may even be felt at the lower end of the SHF band. Some experimental scintillation observations have already demonstrated this to be the case.

## 2. SOME PROPERTIES OF THE SCINTILLATION INDEX AND THE CORRELATION INTERVAL

One of the important properties in characterizing the scintillation signals is the frequency dependence of the scintillation index  $S_4$ . For weak scintillations with an irregularity power spectrum of the form  $\phi_N(\kappa) \propto \kappa^{-p}$ , the theory predicts a frequency dependence  $S_4 \propto f^{-(p+2)/4}$  (Lovelace et al., 1970; Jokipii and Hollweg, 1970). This means that for each doubling of frequency the  $S_4$  index will be reduced by a factor  $2^{(p+2)/4}$ . For  $p=4$  for which curves of Fig. 2 were computed, this factor turns out to have a numerical value of 2.83. Closer examination of Fig. 2 shows that such a frequency relation is approximately valid for  $S_4$  less than about 0.3 within which  $S_4$  depends approximately linearly on  $\langle(\Delta N)^2\rangle^{1/2}$ . Departure from the linear dependence on  $\langle(\Delta N)^2\rangle^{1/2}$  also signifies departure from the frequency dependence law of  $f^{-(p+2)/4}$  valid only under the weak scintillation conditions. In the saturation regime this frequency dependence is much weakened. This point has been made abundantly clear by the numerical results of Yeh et al. (1975) based on multiple scatter theory. Experimentally such a behavior has been demonstrated by Umeki et al. (1977), among others. For this purpose we may define a spectral index  $n$

$$n(f_1/f_2) = -\log[(S_4)_1/(S_4)_2]/\log(f_1/f_2) \quad (2)$$

between  $S_4$  indices at frequencies  $f_1$  and  $f_2$ . When  $n$  is independent of frequency, (2) predicts a frequency law of  $S_4 \propto f^{-n}$  with the value of  $n$  given by  $n=(p+2)/4$ . This is expected only for weak scintillations. Taking the satellite ATS-6 data at 40 and 140 MHz recorded at various times in the year 1974-75 (hence corresponding to various ionospheric conditions), the  $S_4$  indices and the spectral index  $n(140/40)$  defined by (2) have been computed for many data sets. When  $n$  is plotted as a function of  $S_4$  at 140 MHz, we obtain the results shown in Fig. 3. A curve through the data points has been inserted by inspection merely to show the trend. Even with the spread of data points, the results of Fig. 3 clearly show the dependence of  $n$  on  $S_4$ , suggesting the dependence of  $n$  on  $f$ . Only when  $S_4$  at 140 MHz is less than about 0.1, is  $n$  nearly constant with an average value of about 1.6. For this value of  $n$ , the three-dimensional irregularity power spectrum must have the form  $\phi_N(\kappa) \propto \kappa^{-4}$  which is in agreement with other observations. As the scintillation intensifies the spectral index  $n$  reduces, suggesting a weakened dependence on frequency.

In the environment of a power-law irregularity spectrum the concept of Fresnel filtering is very useful in explaining the weak scintillation phenomenon (Wernik and Liu, 1974). Under this concept the major contribution to the amplitude scintillation of a radio signal at frequency  $f$  (or wavelength length  $\lambda$ ) and distance  $z$  comes from irregularities having a size of the order of Fresnel zone  $\lambda_F = \sqrt{\lambda z}$ . These Fresnel irregularities also play a controlling role in determining the scale of spatial fluctuations in amplitude at the receiving plane. If the temporal fading is produced entirely by the horizontal motion of the ionosphere as is the case under the Taylor's frozen-in condition (Tatarskii, 1971) the temporal correlation interval of the fading amplitude should then be proportional to  $\lambda_F/v$ , where  $v$  is the horizontal ionospheric velocity. In other words, if all ionospheric parameters are the same, the temporal correlation interval should decrease with frequency in a manner given by  $f^{-1/2}$ . Starting at a very high frequency so that the amplitude scintillation is weak the correlation interval (inversely proportional to the fading rate) increases as the frequency  $f$  is decreased. As  $f$  continues to decrease  $S_4$  index is expected to increase signifying increased scintillation. When  $S_4$  reaches a value of about 0.3 the weak scintillation theory used above to predict the  $f^{-1/2}$  dependence is no longer valid. What happens to the correlation interval as  $f$  is further decreased requires a theory valid under intense scintillation conditions. Such a theory shows that the randomization effects associated with multiple scattering will modify the trend so that the increase in the correlation interval is gradually slowed down until it reaches a peak, and further reduction in frequency will actually be accompanied by a decrease of correlation interval (Yeh et al., 1975). Experimental support for this behavior has been found by Umeki et al. (1977) in the form of Fig. 4. In order to remove dependence of correlation interval on other ionospheric parameters (especially the horizontal velocity) the correlation intervals at 40 and 140 MHz for the same data set were divided by the correlation interval at 360 MHz. When normalized in this way the correlation interval is found to have a variation very close to  $f^{-1/2}$  when the scintillation is weak (depicted by curve 1 of Fig. 4). As the scintillation intensifies the departure from the  $f^{-1/2}$  dependence occurs as depicted by curve 2. Further intensification of the amplitude scintillation actually brings about a reversed trend, i.e. the increase of correlation interval with frequency as demonstrated by the lower frequency portions of curves 3 and 4 of Fig. 4. This reversed trend has its origin in the randomization brought about by multiple scattering. Based on these observations it is clear that the frequency dependence of the correlation

interval depends on two competing factors: Fresnel filtering effects and multiple scatter effects. When the scintillation is weak so that effects connected with Fresnel filtering dominates, the correlation interval has  $f^{-1/2}$  dependence. On the other hand when the scintillation is strong so that effects connected with decorrelation through multiple scattering dominates, the correlation interval increases with increasing frequency. Therefore, for a given ionospheric and irregularity conditions, as the radio frequency increases from the saturation regime the temporal correlation interval first increases because of the multiple scatter effects, then the correlation interval reaches a maximum when multiple scatter effects diminish in importance. With further increase in frequency the correlation interval begins to decrease and eventually approaches a  $f^{-1/2}$  dependence, when the Fresnel filtering effect dominates as is the case in the weak scintillation case.

### 3. SOME PROPERTIES OF THE POWER SPECTRA

When more details are desired in characterizing the received scintillation signals one often uses the power spectra. In case of weak scintillations, the theory is well developed (Rufenach, 1972; Singleton, 1974; Umeki et al., 1977). The degree of agreement between the experimentally observed spectrum and the spectrum computed theoretically by using an ionospheric and irregularity model is demonstrated in Fig. 5. The  $S_4$  indices computed from the experimental data are  $0.54 \pm 0.04$  at 40 MHz and  $0.076 \pm 0.006$  at 140 MHz, while the corresponding theoretical  $S_4$  indices are 0.59 and 0.077. The agreement is remarkable. The agreement between the experimental and theoretical spectra is also striking as shown in Fig. 5. Both spectra are very flat up to a roll-off frequency known as the Fresnel frequency  $\nu_F$  above which the spectra falls with a power-law dependence. The weak scintillation theory predicts a high frequency asymptote to have a dependence  $\nu^{-3.5}$ . For the example given in Fig. 5 the high frequency asymptote has the dependence  $\nu^{-3.5}$  which yields  $p=4.5$ , a value very close to 4.4 deduced from the consideration of radio frequency dependence of  $S_4$  index in section 2.

The Fresnel frequency  $\nu_F$  at which the roll-off starts has a dependence  $f^{1/2}$ , i.e. quadrupling the radio frequency  $f$  with double  $\nu_F$ . The observed roll-off frequency for the data set shown in Fig. 5 are found to be 0.07 Hz at 360 MHz, 0.045 Hz at 140 MHz and 0.025 Hz at 40 MHz, approximately satisfying the  $f^{1/2}$  dependence. When the spectra are normalized by their respective roll-off frequency the spectral curves on these three radio frequencies fall very closely on top of each other as shown in Fig. 6. The flattening of the spectrum at 360 MHz for  $\nu/\nu_F$  larger than 3 is caused by noise since the scintillation is extremely weak at this frequency ( $S_4=0.016$ ). One observation that can be made at this point is that even though  $S_4$  is equal to 0.54 at 40 MHz the theory developed for the weak scintillation seems to work rather well (See also Fig. 5). In view of our discussion in section 2 in regard to the dependence of the correlation interval on  $S_4$  index, it will be interesting to investigate what change occurs, if any, in the power spectrum when the scintillation saturates. To investigate the saturation effects on spectra a different data set is selected. The results are depicted in Fig. 7. The frequency axis is again normalized by the respective Fresnel frequency. A comparison of Fig. 7 with Fig. 6 shows that for strong scintillations the roll-off is more gradual and the spectrum extends out to contain more high frequency components than the case of weak scintillations. This increased high frequency content during severe scintillations is entirely consistent with the decrease of correlation interval discussed in section 2. It is interesting to observe that even though the data at three radio frequencies have different scintillation indices, the high frequency asymptotes in the spectra have the same power law dependence of  $\nu^{-3.2}$ . Using a thin phase screen model, Rumsey (1975) and Mariani (1975) find that the high frequency asymptote is independent of the scintillation level, in agreement with our observation. However, a more complete theory valid in the multiple scatter case is not yet available at present time.

In all of above discussion about the  $S_4$  index, the correlation interval and the spectrum, the statistical information is derivable from the amplitude of the received signal alone. For some applications it is also desirable to know the behavior of the phase and quadrature components of the scintillating signal. In the weak scatter regime, the phase fluctuations are sensitive to large irregularities, while the amplitude fluctuations are not affected much by irregularities larger than the Fresnel size. Consequently, unlike amplitude, the phase fluctuations are dominated by low frequency components. This is demonstrated in Fig. 8 where the high frequency asymptote of  $\nu^{-3.3}$  dependence is seen extending to the lowest frequency that is limited by the detrending process on phase data. The fact that the phase is dominated by low frequency components poses a practical problem, i.e. the results on statistical analysis of the phase data depend on the cutoff frequency of the detrending process as found by several authors (Crane, 1976, Myers et al., 1979). This is very undesirable since the conclusion may depend on the way that the data is handled. In any interpretation of the phase data, care must therefore be exercised in making sure that whatever conclusions one wishes to draw the detrending process does not play a role.

In addition to decomposing into amplitude and phase, the complex amplitude can also be decomposed into quadrature components defined by

$$X = A \cos \phi \quad Y = A \sin \phi \quad (3)$$

where  $A=A_0 + A_1$  is the detrended amplitude with the mean  $A_0$  restored and  $\phi$  is the detrended phase. Normally  $X$  is referred to as the in-phase component and  $Y$  the phase-

quadrature component. For weak scintillations,  $\phi$  is small. In this case expanding (3) to the second order gives

$$X_1 = A_1 - (A_0/2)\phi^2 \quad Y_1 = A_0\phi + A_1\phi \quad (4)$$

Eq. (4) indicates that the statistics of the in-phase component  $X_1$  should be very similar to that of the amplitude  $A_1$  and the statistics of the phase-quadrature component  $Y_1$  should be very similar to that of the phase  $\phi$  in case of weak scintillations. The confirmation of this observation can be found in Figs. 9 and 10. However, such agreements cannot be extended to strong scintillations as one may deduce by examining (4). As usually is the case under the saturation regime, the amplitude fluctuation is fast owing to the decorrelation effects discussed in section 2 while the phase fluctuation is large but slow owing to domination by large irregularities. When this happens the power contained in the quadrature components become nearly equal. This is supported by Fig. 11 where the spectra of two quadrature components are seen to lay on top of each other. Additionally, the in-phase component and hence also the phase-quadrature component agree with the amplitude spectrum as shown in Fig. 12. These results suggest that under intense scintillation conditions, the power spectra of quadrature components are dominated by the fast fluctuation of the amplitude. The equalization of power between the two quadrature components comes about because of the slow and large phase fluctuations.

#### 4. CONCLUSION

In this paper we have summarized some of the statistical behaviors of transionospherically propagated radio signals under the intense scintillation conditions. Contrast with the weak scintillation behavior is emphasized by comparison. Where possible comparisons with theoretical expectations are also made.

We have shown that

1. For a power law irregularity spectrum of the form  $\phi_N(\kappa) \propto \kappa^{-p}$ , the frequency dependence of the  $S_4$  index follows closely the theoretically expected dependence  $S_4 \propto f^{-(p+2)/4}$  only when  $S_4$  is less than about 0.3. This frequency dependence is much weakened when the scintillation intensifies and practically no frequency dependence is obtained in the saturation regime.
2. The dependence of the correlation interval on radio frequency is subjected to the relative importance of two competing factors: decorrelation due to multiple scattering which is apt to occur at low radio frequencies and Fresnel filtering which is apt to occur at high radio frequencies. At the low frequency end where multiple scattering is important the correlation interval increases with radio frequency. It reaches a peak when the two competing factors are equally important. Further increase in radio frequency is accompanied by the decrease in the correlation interval, as Fresnel filtering becomes the controlling factor. Eventually it approaches a  $f^{-1/2}$  dependence at the high frequency end.
3. The weak scintillation theory predicts a spectrum for scintillating amplitude that is nearly flat to the Fresnel frequency  $\nu_F$ , beyond which the spectrum rolls off and approaches asymptotically to  $\nu^{-1-p}$ . This, together with the  $f^{-1/2}$  dependence of  $\nu_F$ , is verified experimentally. When the scintillation intensifies, the roll-off becomes gradual and the spectrum extends out to contain more high frequency components, but the asymptote  $\nu^{-1-p}$  is apparently kept intact.
4. The phase of scintillating radio signal is sensitive to large irregularities. For weak scintillations, the  $\nu^{-1-p}$  dependence on phase spectrum extends to the lowest frequency permitted by the detrending process. For strong scintillations, the asymptote has a smaller slope.
5. Under weak scintillation conditions, the power is mainly contained in the phase-quadrature component whose spectrum behaves much like the phase spectrum. The weak in-phase component has a spectrum much like the amplitude spectrum. When the scintillation intensifies, the power between the two quadrature components tends to be equalized and their spectra tend to behave very much like each other and both in turn like the spectrum of the amplitude.

#### ACKNOWLEDGEMENT

This research was supported by the Atmospheric Sciences Section of the National Science Foundation under Grant ATM 77-22485.

## References

- Crane, R. K., 1976, "Spectra of ionospheric scintillation," J. Geophys. Res., 81, 2041-2050.
- Jokipii, J. R. and J. V. Hollweg, 1970, "Interplanetary scintillation and the structure of solar-wind fluctuations", Astrophys. J., 160, 745-753.
- Lovelace, R. V. E., E. E. Salpeter and L. E. Sharp, 1970, "Analysis of observations of interplanetary scintillations", Astrophys. J., 159, 1047-1055.
- Marians, M., 1975, "Computer scintillation spectrum for strong turbulence, Radio Sci., 10, 115-120.
- Myers, W. J., R. J. Gjedum, C. H. Liu and K. C. Yeh, 1979, "A study of ionospheric scintillations of phase and quadrature components", J. Geophys. Res., 84, 2039-2048.
- Rufenach, C. L., 1972, "Power law wave number spectra deduced from ionospheric scintillation observations," J. Geophys. Res., 77, 4761-4772.
- Rumsey, V. H., 1975, "Scintillation due to a concentrated layer with a power-law turbulence spectrum", Radio Sci., 10, 107-114.
- Singleton, D. G., 1974, "Power spectra of ionospheric scintillations", J. Atmos. Terr. Phys., 36, 113-134.
- Tatarskii, V. I., 1971, "The effects of the turbulent atmosphere on wave propagation", National Technical Information Service.
- Umeki, R., C. H. Liu and K. C. Yeh, 1977, "Multifrequency studies of ionospheric scintillation", Radio Sci., 12, 311-317.
- Umeki, R., C. H. Liu and K. C. Yeh, 1977, "Multifrequency spectra of ionospheric amplitude scintillations", J. Geophys. Res., 82, 2752-2760.
- Wernik, A. W. and C. H. Liu, 1974, "Ionospheric irregularities causing scintillations of GHz frequency radio signals", J. Atmosph. Terr. Phys., 36, 871-879.
- Yeh, K. C., C. H. Liu and M. Y. Youakim, 1975, "A theoretical study of the ionospheric scintillation behavior caused by multiple scattering", Radio Sci., 10, 97-106.

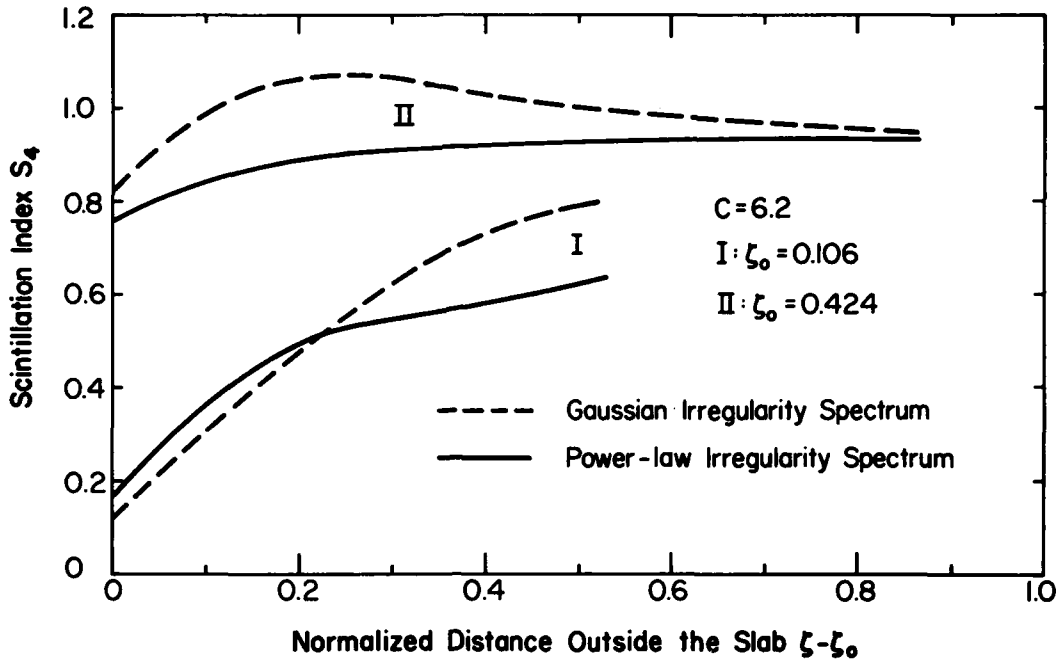


Fig. 1 Computed scintillation index as a function of normalized distance outside the slab of irregularities. The power-law irregularity spectrum has the form  $\phi_N(\kappa)=r_0^3/\pi^2(1+\kappa^2r_0^2)^2$ . The parameter  $C$  is defined by  $C=k^3r_0^3(f^{-4}/f^4)\langle(\Delta N/N_0)^2\rangle/4$  and the normalized distance is defined by  $\zeta=z/kr_0^2$ .

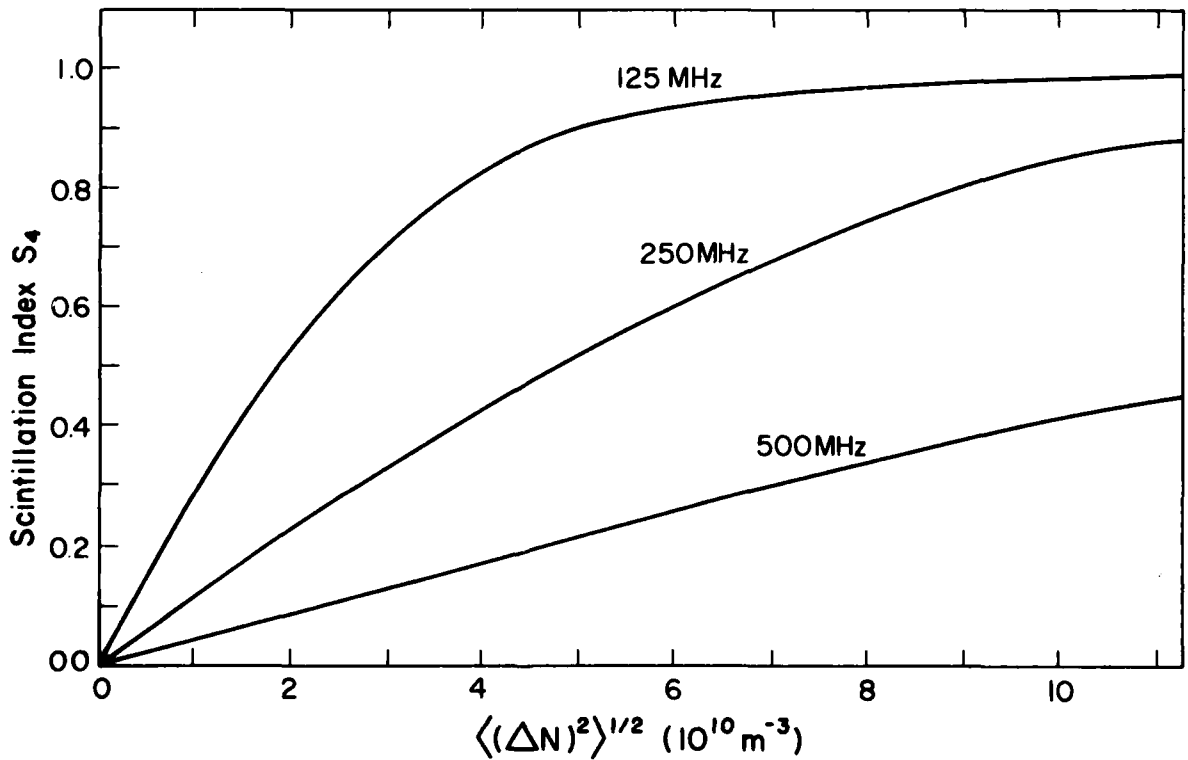


Fig. 2 Scintillation index  $S_4$  as a function of rms  $\Delta N$  computed for frequencies 125 MHz, 250 MHz and 500 MHz. The irregularity slab has a thickness of 50 km. This distance between the bottom of the slab and the observer is 237.5 km.

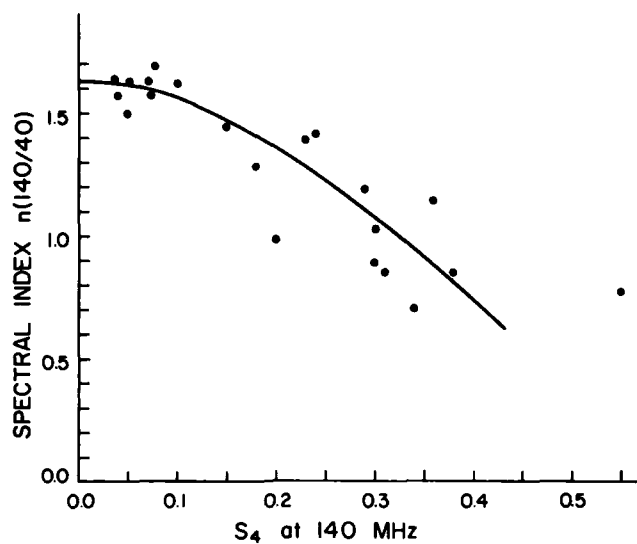


Fig. 3 The dependence of spectral index  $n(140/40)$  defined by eq.(2) as a function of  $S_4$  at 140 MHz. The experimental data were recorded at Boulder, Colorado from radio transmissions of the geostationary satellite ATS-6.

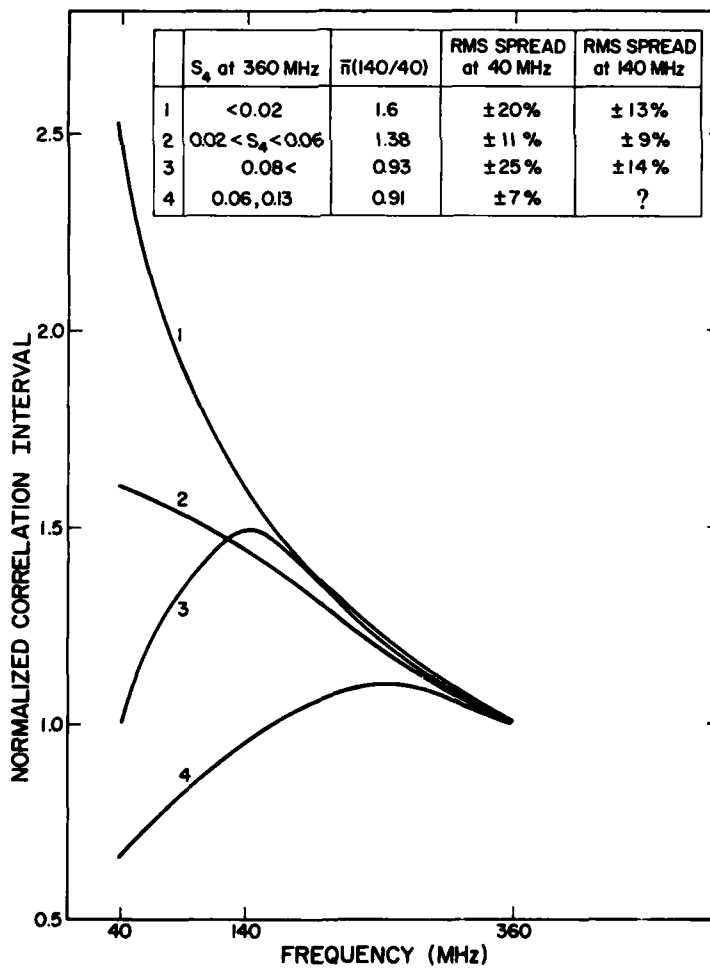


Fig. 4 Normalized correlation intervals as a function of frequency for four scintillation conditions.



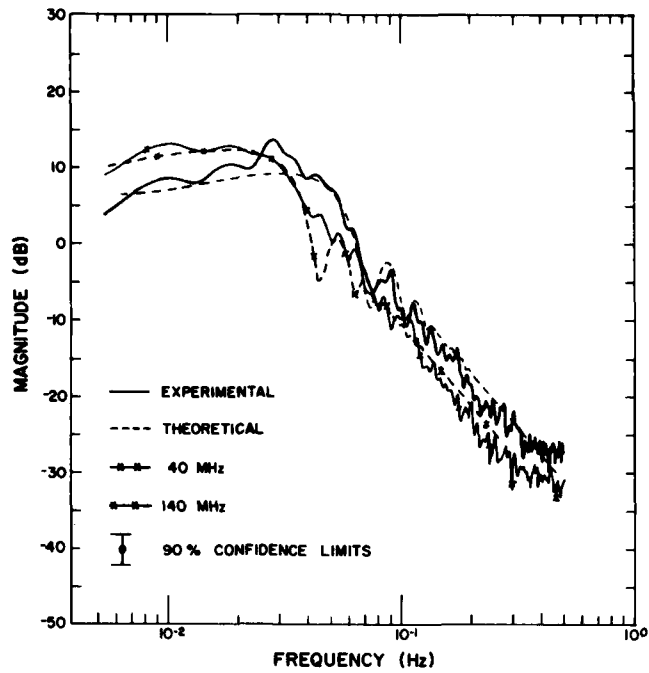


Fig. 5 A comparison of theoretical and experimental power spectra of amplitude data received at Boulder from ATS-6, 0920-1000 UT, Dec. 24, 1974. The ionospheric parameters used for theoretical computations are: background plasma frequency = 5 MHz, irregularity slab thickness = 90 km, distance from the bottom of the irregularity slab to ground receiver = 310 km, irregularity spectral index  $p = 4.5$ , outer scale = 9 km, anisotropic factor = 3, rms electron density fluctuations = 1.6%.

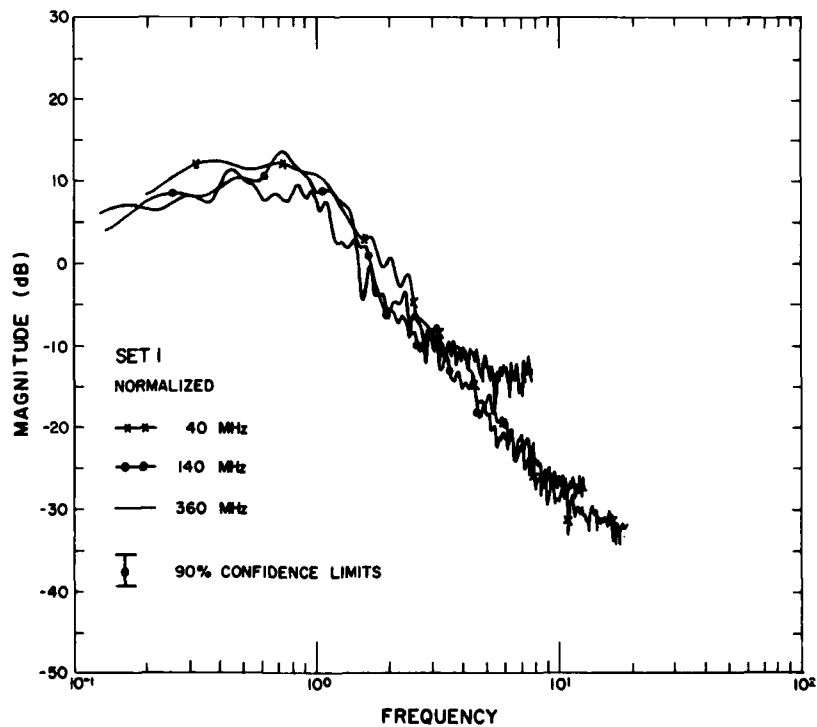


Fig. 6 Power spectra as a function of normalized frequency  $\nu/\nu_F$ , where  $\nu_F$  is the roll-off frequency or the Fresnel frequency. The  $S_4$  scintillation indices are 0.54 at 40 MHz, 0.076 at 140 MHz and 0.016 at 360 MHz. The data set is identical to that shown in Fig. 5.

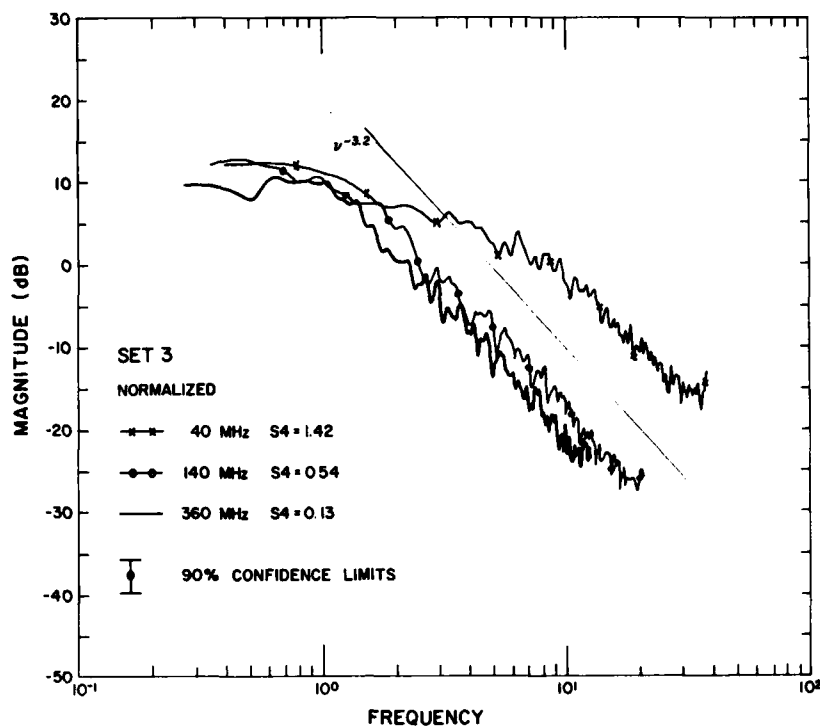


Fig. 7 Power spectra as a function of normalized frequency  $\nu/\nu_F$ . The  $S_4$  scintillation index for each of three radio frequencies is shown in the legend. The ATS-6 data were recorded on January 7, 1975, 0700-0750 UT.

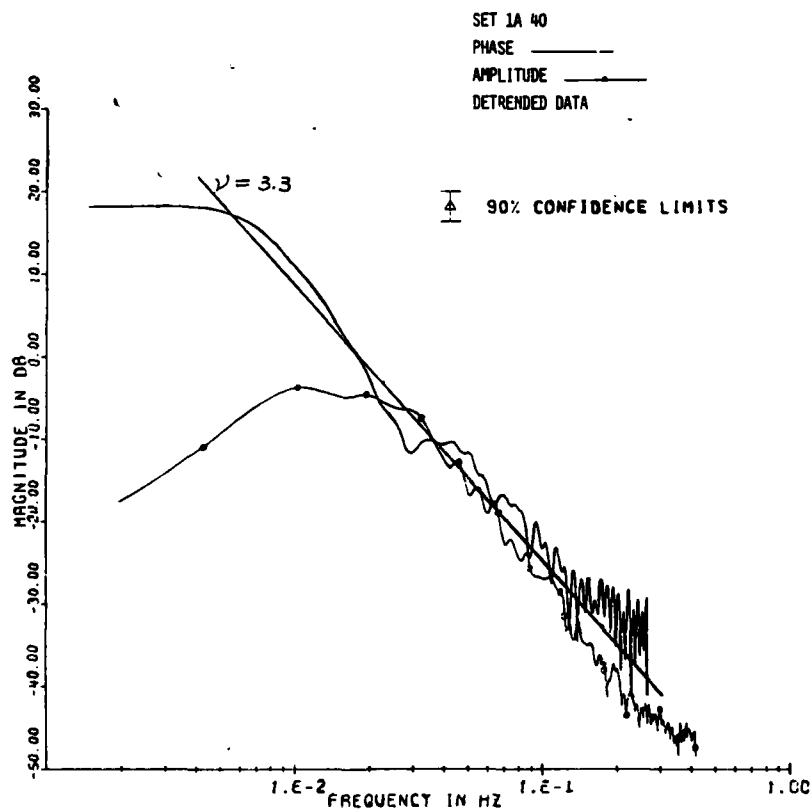


Fig. 8 Power spectra for amplitude and phase at 40 MHz, Dec. 26, 1974, 0921-1000 UT. The scintillation index  $S_4$  is 0.523 and the rms phase fluctuation is 1.628 rad. The cutoff frequency of the detrending process is 0.003 Hz.

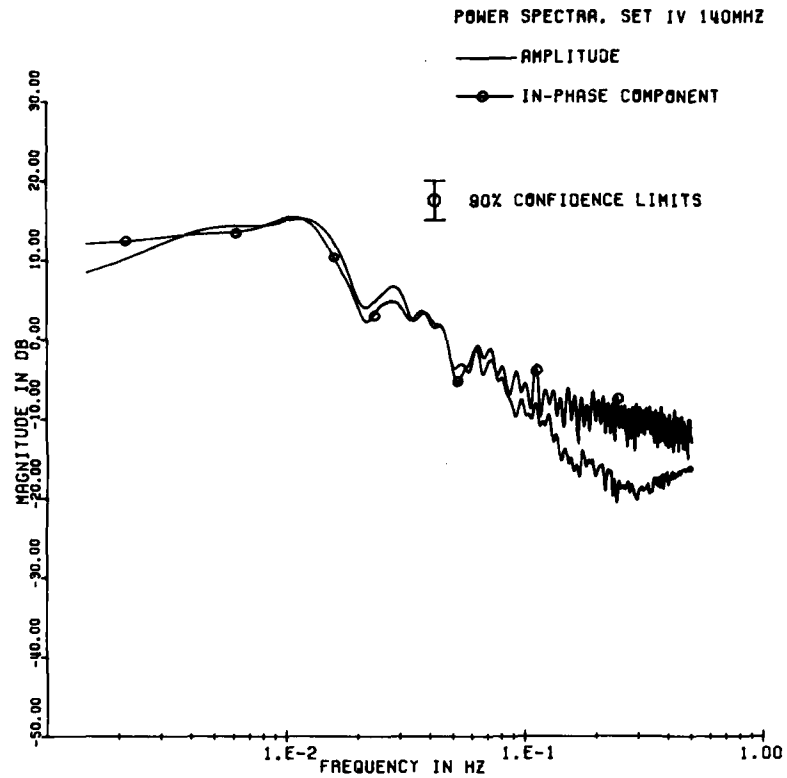


Fig. 9 Comparison of amplitude and in-phase component power spectra for data recorded at 140 MHz, Aug. 25, 1974, 0525-0548 UT. The  $S_4$  scintillation index is 0.522 and the rms phase fluctuation is 1.397.

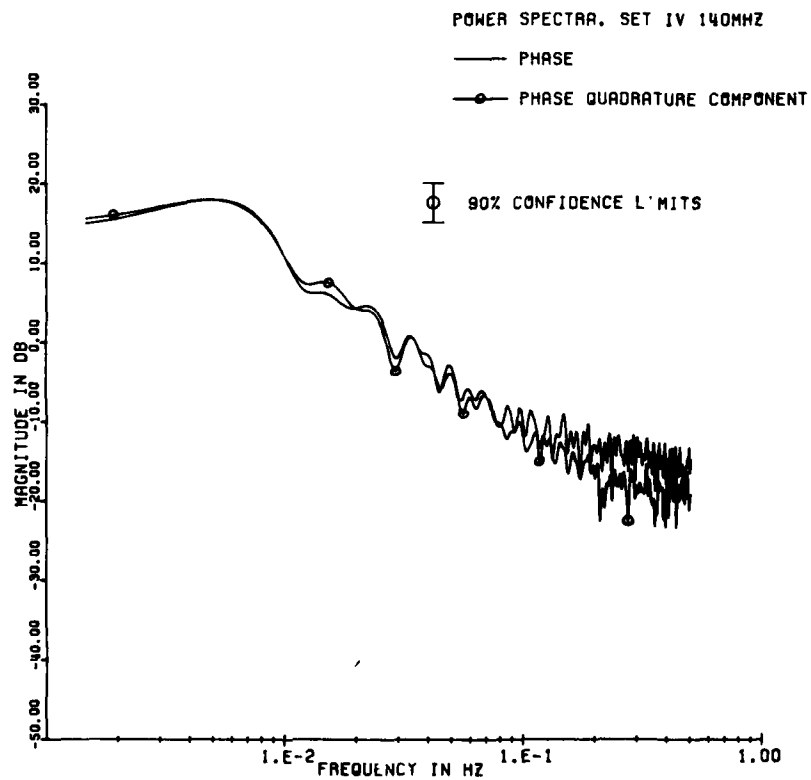


Fig. 10 Comparison of phase and phase-quadrature component power spectra for the same data as those shown in Fig. 9.

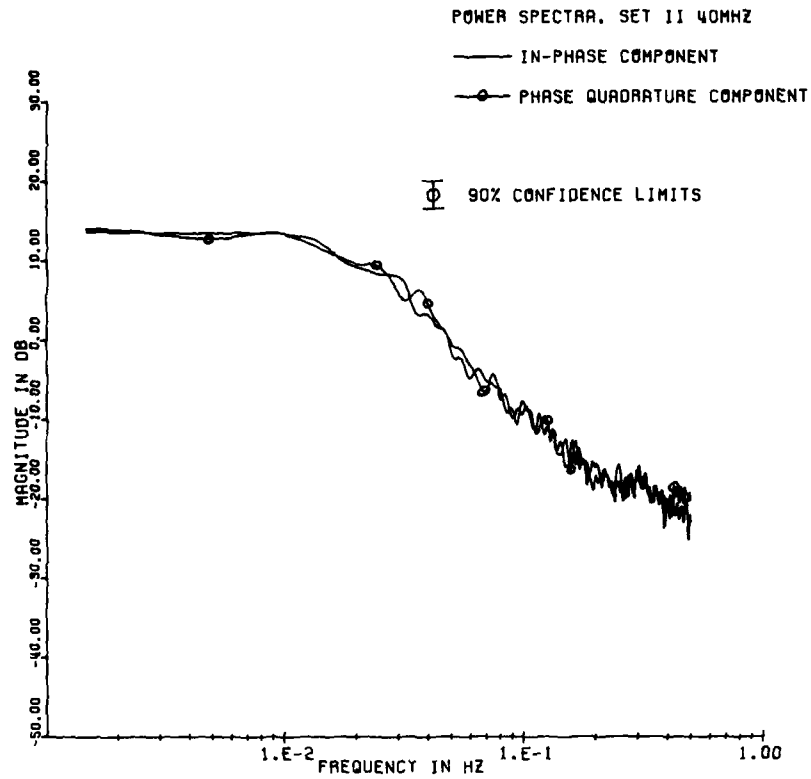


Fig. 11 Comparison of power spectra of two quadrature components of signal at 40 MHz, August 23, 1974, 0505-0558. The scintillation index is 1.30 and the rms phase fluctuation is 2.677 rad.

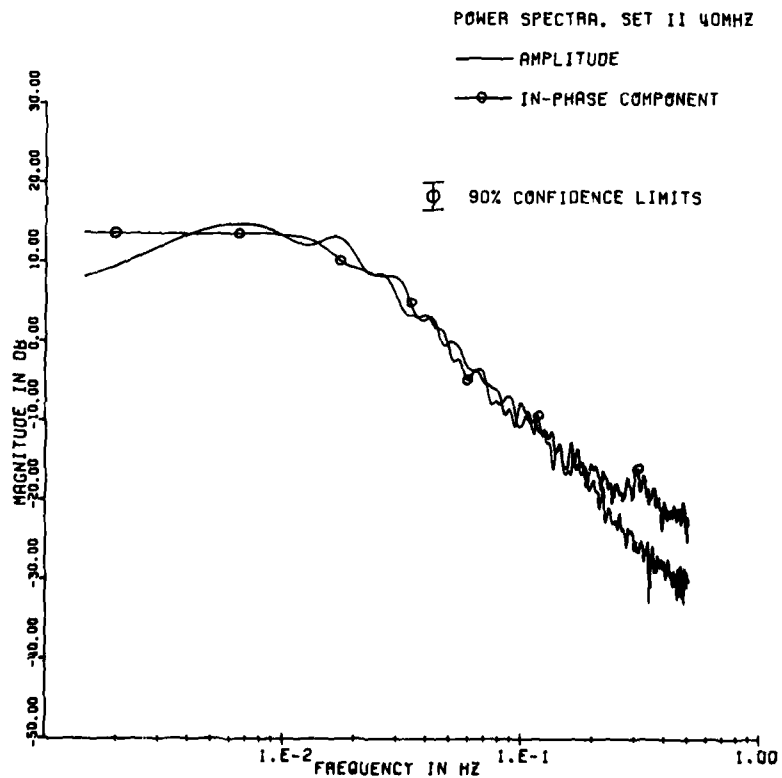


Fig. 12 Same data as Fig. 11 but for amplitude and in-phase component.

RECENT OBSERVATIONS OF EQUATORIAL AND HIGH LATITUDE SCINTILLATIONS

J. Aarons and H.E. Whitney  
Air Force Geophysics Laboratory  
Hanscom AFB, MA 01731

SUMMARY

Within the past few years a combination of factors has caused continued interest in the fading of trans-ionospheric radio signals in the 136 MHz to 4 GHz range. From the systems viewpoint, satellite communication and navigation systems in the range of 200 - 2000 MHz are coming into use or are being developed. The scientific community has become interested in the generating mechanisms of the equatorial irregularity bubbles as well as their maintenance and decay. At auroral and polar latitudes the scientific community has developed an interest in studying E and F layer irregularity formation, ionospheric-magnetospheric coupling, and the relationship of irregularities to precipitation of electrons, convection systems and heating.

AFGL in collaboration with several groups has mounted a series of campaigns of 2-3 weeks duration with a large variety of measurements. These include ground and airborne observations, in-situ studies and radar backscatter observations. A large number of scientists both within and outside of AFGL have contributed to these intensive operations.

At equatorial latitudes, combined airborne and ground measurements of radar backscatter, electron density profiles, scintillations, airglow at 6300 A, and total electron content have yielded data on the development and decay of the irregularity patches containing the hundred meter irregularities responsible for amplitude and phase scintillation. The use of airglow measurements from aircraft has allowed the form of the patch to be deduced.

At auroral latitudes, sheets of irregularities have been observed at Poker Flat, Alaska and at Goose Bay, Labrador using phase fluctuations of the WIDEBAND signals. WIDEBAND phase and amplitude deviations when correlated with DMSP photographs show intense activity over diffuse and discrete aurora.

The increase of intensity of scintillation activity at equatorial and polar latitudes has been noted during 1979 and 1980 when very high solar flux levels were recorded. These increases take place even under quiet magnetic conditions when solar flux is high and take place during the increased number of magnetic storms.

1. INTRODUCTION

One effect of the ionosphere on radio signals transmitted along earth-space paths is that of fading and enhancement of signals i.e. scintillations. Various programs primarily involving simplified airborne and shipborne operations such as the proposed civilian maritime satellite, INMARSAT, have prompted an interest in studies of ionospheric irregularity development, maintenance, and decay and initiated technical programs on the details of morphology and signal statistics.

The aim of this study is to introduce recent results from equatorial and high latitude scintillation programs performed primarily by a group of laboratories associated with the U.S. Air Force Geophysics Laboratory. Reviews of equatorial scintillations are in the literature (Aarons, 1977; Basu and Kelley, 1979) and a recent review of some of the campaign results of the AFGL group are contained in Buchau et al. (1979). The present paper will add to these three papers, briefly outlining new work now being put into journal and report form. The work is the result of a large number of individuals.

The studies are of two types. One is that of the intensive campaign measurements. For the campaigns we have mounted airborne observations (with the assistance of the aircraft from Air Force Avionics Laboratory) and have performed intensive ground measurements. These have been done at both high and equatorial latitudes. To bolster this type of operation, continuous measurements have been made at a series of observatories including sites at Thule, Greenland and Goose Bay, Labrador for the high latitude program and at Ascension Island, Natal, Brazil, Accra, Ghana and Huancaayo, Peru for the equatorial studies.

2. EQUATORIAL SCINTILLATION ACTIVITY

Two regions are of importance for irregularity effects: the equatorial and the high latitudes. In the equatorial region the most significant effects take place between sunset and midnight with activity on occasion continuing beyond midnight.

After sunset, in some seasons and during some nights, a depleted region forms below the F layer (200-300 km) and moves thru the F layer producing irregularities throughout a height from 200 km to over 1000 km. These irregularities spread over lines of force forming a patch which appears somewhat like that in Figure 1. The patch maintains its integrity, moving eastward during the night, then (for the most part) decaying in the

post-midnight to early morning period.

Equatorial campaign measurements have provided information on the development of irregularity patches, particularly those observations noted in Buchau et al. (1979). During some evenings, irregularities develop in a systematic westward motion. In Figure 2, we have illustrated the series of scintillation starting events which took place with a westward motion on March 19-20, 1977. In the top panel, a tracing of a portion of the backscatter observations at 50 MHz is shown (P. McClure, personal communication). A thin layer of relatively weak 3-m irregularities forms at 1935 LST but the plume starts to develop at 1950 LST. Greater values of  $\Delta N$  and increased thickness then occur. Scintillation activity noted at Ancon on the GOES-1 beacon, the path closest to the Jicamarca magnetic meridian, increased sharply at 1950 LST.

The timing of the start of scintillation activity at each of the ionospheric paths is shown in the remaining panels. This timing coupled with the adjacent map indicates clearly a westerly development of the patch. The sequence and direction of starts are shown by arrows (+) and a numerical order of commencements.

Using three VHF observations in order to equalize starting time definition (Huancayo-GOES, Ancon-GOES and Huancayo A-3) a velocity of 200-300 m/sec is determined in the initial westward development. The patch has very large dimensions E-W as borne out by the continuous high level of activity at each of the stations. This relatively continuous activity through the night does not allow us to determine a subsequent eastward velocity by the gross motion of the patch.

Some patches (observed on the propagation paths available during these campaigns) showed evidence of decay. Data from the backscatter radar and the AFGL airborne observatory as well as ground recordings of WIDEBAND and the synchronous satellites illustrate this. Data recorded on March 16-17, 1977 will be described to illustrate the decay of irregularities.

Figure 3 illustrates the backscatter records for March 16-17. Over Jicamarca the irregularities appeared slightly before 2300 LST, maintained medium level intensity in the altitude region 300-600 km until 2330 LST then trailed off in intensity at the higher altitudes until 0030 LST. The trailing off appears to be a decrease in intensity of the 3 meter irregularities.

From WIDEBAND data at Ancon (SRI) and at Huancayo (AFGL-IGP) a patch could be noted nearly over Jicamarca with a sharp eastern front at 76°W at 2318 LST. In Figure 4 data from the aircraft, tracing a route from 3° north to 3° south of Jicamarca but off 3° to the west, indicated scintillations as high as 12 dB across the patch in the time period from 2300 to 2325 LST. Airglow data (Weber, private communication) is available which identifies this patch. The activity on the path from LES-9 to the aircraft decreased after 0020 until low levels were reached at 0100 LST. The Ancon path to LES-9 (also shown in Figure 4) has a maximum of 10 dB fades with a start of some activity at 2350 LST; this position is to the east of the aircraft viewing. The velocity, as determined from spaced receivers at Ancon, however, remained about 90 m/sec; only the irregularity intensity decreased as the patch moved eastward. The Huancayo L-9 maximum excursions (0040-0050 LST) were of the order of 3 dB. Within 1½ hours or less, the scintillation levels decreased from 12 dB to 3 dB at 254 MHz. The MARISAT records, far to the east, showed no scintillation activity after this time. Essentially this illustrates the decay in the intensity of the irregularities of a typical patch noted near the position of the magnetic equator at the Peruvian longitudes.

### 2.1. Irregularities Within The Patch

The irregularities forming the patch run the gamut of sizes. Each type of measurement is dominated by a relatively narrow range of sizes (more accurately a spectral region). In addition to the scintillation and airglow observations noted in the section on equatorial scintillation (Buchau et al., 1979), the data indicates the following:

(1) The large scale dimensions of patches (50 km - several hundred km) are vividly shown by in-situ observations of the high inclination satellite AE-C and the equatorial AE-E; in-situ electron density data have been shown at times to decrease several orders of magnitude in density when the satellite entered the patch (McClure and Hanson, 1973).

(2) The medium scale irregularities of the order of a few kilometers to tens of kilometers are best measured by the total electron content or phase observations, as will be shown in this paper; the phase scintillation measurements of this scale have been illustrated by Fremouw et al. (1978). HF sounder returns are dominated by irregularities of this order.

(3) Irregularities of the order of 100 meters to a few kilometers produce the amplitude scintillations observed at 100 MHz to 4 GHz as shown by spectral studies and by considerations relative to the Fresnel wavelength in this frequency regime.

(4) Smaller scale irregularities of the order of half a meter to three meters are responsible for the backscatter noted on the Jicamarca radar and other units (ALTAIR in Kwajalein). The Jicamarca radar shows returns extending to well over 800 kilometers after initial formation at lower heights.

Although all of these irregularities are associated with the patch region, the formation and decay of the various regimes of sizes may differ considerably as has been shown for two size regimes by Basu et al. (1978). The results of observations to be illustrated show clearly differences between times of appearance of the 100 meter irregularities producing amplitude scintillations and those irregularities producing Total Electron Content fluctuations.

To illustrate Total Electron Content and scintillation observations, Klobuchar (private communication) recorded these two parameters at Ascension Island at a dip latitude of  $\sim 16^\circ$  for the 350 km intersection point. Continuous measurements of the Faraday rotation have been converted to equivalent vertical total electron content (TEC) in a standard manner using the longitudinal magnetic field intensity and zenith angle at a mean height of 420 km. Figure 5 shows an evening period when two clearly evident depletions in TEC occurred. Note that depletions from an assumed quiet background TEC, indicated by a dashed line, are up to 10-15 percent. In addition, the close association with the occurrence of amplitude scintillation is indicated by the start and stop times of amplitude scintillation. Figure 6 shows the intimate association of TEC fluctuations with rapid, severe amplitude scintillations observed along the same path. There are many instances when the TEC fluctuations do not coincide exactly in time of start or end with the rapid severe amplitude scintillations, thereby illustrating that the VHF polarimeter used for the TEC fluctuation measurements is relatively insensitive to amplitude scintillation.

## 2.2. Longitudinal Variations of Scintillation

The larger data base of continuous observations from ground station measurements has been utilized to establish the features of the major scintillating regions. However, this is uneven in longitudinal coverage and unavailable over ocean surfaces. Satellites carrying out in-situ observations of irregularity parameters do provide a mapping technique.

Basu and Basu (1980) have developed a model from in-situ, theoretical, and scintillation studies. In their morphological model of scintillations, measurements of irregularity amplitude,  $\Delta N/N$ , as computed from T sec of data are utilized in conjunction with simultaneous measurement of electron density N. A combination of  $\Delta N/N$  and N data provides the required  $\Delta N$  parameter as a function of position and time. In case the satellite altitude is much lower than the height of maximum ionization, proper allowance should be made in deriving  $\Delta N$  estimates. The in-situ measurements of irregularity spectrum and phase scintillation measurements with WIDEBAND satellite indicate that the outer scale at F region heights is large, probably on the order of tens of km. In view of this, the spatial length corresponding to T sec time interval when projected in the direction of shortest correlation distance of electron density deviation sets the apparent outer scale length  $q_0$ . The outer scale wavenumber is, therefore,  $K_0 = 2\pi/q_0$ . For the equatorial scintillation model that they developed from the OGO-6 in-situ observations, the time interval was T=5 secs and the outer scale length was considered to be 20 km corresponding to an outer scale wave number of  $K_0 = 0.3 \text{ km}^{-1}$ .

## 2.3. Comparison of Seasonal Observations

Using ground observations, a series of measurements of the amplitude scintillations of the UHF beacon on MARISAT has been taken at three locations within the equatorial irregularity region. This makes it possible to compare data for a limited longitudinal sector and to determine seasonal and magnetic dependence over this range. Although the temporal extent of this common data base is only for one year, the data trends have been substantiated through additional observations at the individual stations.

The data bank used consists of 257 MHz observations of the MARISAT satellite as observed at Accra, Ghana, Natal, Brazil and Huancayo, Peru in the period Jan 1977 - March 1978. (Data supplied by J.R. Koster, R.F. daSilva, J.R. Medeiros, R.T. Medeiros, A. Bushby, J. Pantoja and J. Lanat). Jan 1977 - Jan 1978 was a time of moderate level of solar radio flux at 10.7 cm (Ottawa flux  $\sim 75-100$ ), while Feb-Mar 1978 had a high solar flux level ( $S_f \sim 140$ ). Thus there is some caution to be used in the seasonal comparison.

The 15-minute indices used to categorize the diurnal variation of scintillations have been sorted for hourly occurrence during each season with respect to Kp. In Figures 7 and 8, we plot in local time the occurrence of scintillations,  $SI \geq 6$  dB peak-to-peak which corresponds to an  $S_{44}$  of .3. The data for Kp = 0,1 (magnetically quiet conditions) are contrasted with that of Kp  $\geq 3^+$ . The observations for Kp = 2,3, though not shown, are consistent with the trends of change with magnetic index. The data clearly must be divided into pre- and post-midnight time periods, as was shown by Mullen (1973).

Between November and April (Figure 7a and b), in the pre-midnight time period, scintillation activity decreased at all sites with the higher magnetic indices. For the post-midnight time period during these months, scintillation activity increased during magnetically active periods at Huancayo.

For the months of May through July (Figure 8a) activity was minimum. Pre-midnight activity maximized during periods of magnetic activity. Post-midnight scintillation occurrence was low except in Huancayo where magnetic activity increased scintillation occurrence.

For the months of August to October (Figure 8b), pre-midnight scintillation occurrence shows little relationship with magnetic activity. Post-midnight occurrence increased during periods of magnetic activity.

What is quite clear is the minimum in activity in the May-July period. In spite of the  $\sim 70^\circ$  difference in the longitude of the two most distant intersections and the intersections being North or South of either the geographic or the dip equator, the minimum period of activity remains the same.

Maximum activity for Accra and Huancayo was during February to April while maximum for Natal was during November to January. This is not true at the longitudes of Guam (Paulson, 1979) and Kwajalein (Nichols, 1974) where the maximum activity is recorded in May-June.

#### 2.4. 1.5 GHz Measurements

Long term observations are also available at higher frequencies. A carefully calibrated set of long-term (approximately 20 months) observations of 1.54 GHz scintillation from the geostationary satellite MARISAT I at  $15^\circ\text{W}$  have been made from the magnetic equatorial station of Huancayo, Peru ( $12.04^\circ\text{S}$ ,  $75.33^\circ\text{W}$ , dip  $2^\circ\text{N}$ ). The observation period April, 1976 - October, 1977 belongs to the lowest sunspot cycle epoch, the sunspot number varying from 15 to 40.

In Figure 9, Basu and Mullen (private communication) present occurrence of 1.5 GHz scintillations  $\geq 2$  dB (corresponding to  $S_4 = 0.13$ ) for the approximately 20-month period of observation. The times of ionospheric (350 km) sunset and sunrise are marked. An equinoctial maximum of scintillation occurrence is immediately evident. Also evident is the confinement of scintillations to the period between sunset and local midnight. It should be noted that the proximity of the 5 percent occurrence contour to the sunset line is a result of interpolation; individual cases always show a delay of tens of minutes between ionospheric sunset and onset of scintillations. There is a reduction in scintillation occurrence during the December-January period and a total absence of scintillation during May-July. At VHF, there is a diffuse maximum of scintillations from October through April with an absence of activity during the June-July months (Aarons, 1977). Thus the two sets of observations are consistent, it being apparent that the single diffuse maximum at VHF is caused by the saturation effect.

During December, 1979, a period of high solar flux, Ascension Island observations of the 1.5 GHz transmissions of MARISAT showed hour long periods of  $\sim 27$  dB peak to peak scintillations at a period of time when Huancayo records continued a low level of activity. The Ascension Island position relative to the magnetic equator and the high solar flux are thought to account for the difference in irregularity intensity.

#### 2.5. Spread F and Scintillations

Equatorial spread F has been divided into range and frequency spread (Calvert and Cohen, 1961) with range spread correlated with strongly scattering irregularities. Chandra and Rastogi (1972) studying equatorial ionograms showed that spread F echoes at the magnetic equator had the following characteristics: (1) range spread with diffuse echoes at lower frequencies and with clear critical frequencies (2) frequency spread with the intensity of spread increasing with frequency and critical frequencies not definable. During the early stages of development, in the pre-midnight hours, spread F is predominantly of the range type whereas during the post-midnight hours spread F is mostly frequency spread. Range spread F is also associated with scintillation activity.

Rastogi (1980) has studied the occurrence patterns at Huancayo, Peru of both types of spread F. In his analysis, he found that during sunspot maximum years, the occurrence probability of range spread increases very rapidly after 1900 LT, reaches a peak value of 40% at 2100 LT and decreases thereafter and has a value of less than 10% after midnight hours. The occurrence of frequency spread increases after sunset rather slowly to a peak value at midnight and decreases slowly to zero by about 0645 LT (Figure 10).

During minimum sunspot years, the occurrence of range spread increases after sunset reaching a peak value of about 30% at 2100 LT but remains greater than 20% for the most part of the night up to about 0500 LT. The occurrence of frequency spread increases rather slowly after sunset, reaches a rather flat peak between 2300-0200 LT and remains above 20% up to 0530 LT.

Rastogi and Woodman (1978) have shown that in addition to range spread appearing in the post sunset period, it can appear during other times of night following the abnormal reversal of the vertical F region drift.

Vertical drift velocities, measured at Jicamarca on selected days since 1968 (Woodman, 1970) can be taken as a measure of the horizontal electric field (1 mV/m corresponds to approximately 40 m/sec). Velocities are upward (positive) during the day with typical values of the order of 20 m/sec, which corresponds to an eastward electric field of the order of 0.5 mV/m. Velocities are downward during the night with velocities comparable to the daytime values. The reversal of the electric field occurs about 1 to 2 hours after sunset and within 1 hour before or after sunrise. The later nighttime reversals of the electric field were associated with the appearance of spread F



particularly in the post midnight hours (Fejer et al., 1976).

## 2.6. Equatorial Signal Statistics

Whitney (private communication, 1979) has studied various parameters of scintillation activity through the use of spaced receivers at Ancon, Peru. His observations of LES-9 using three spaced antennas (East-West) at distances of 122, 244 and 366 m has revealed the change of velocities over the period of 13 nights in March 1977.

Initial scintillations at the beginning of a patch development are often confused for several reasons: (1) the solar sunset terminator is westward, (2) the wind velocity relative to a fixed intersection is towards the east and (3) the bubble is moving vertically. Thus the velocity measurements shown in Figure 11a between sunset and 2100 are not absolutely defined. Once the patch forms, the correlation coefficient is high and the velocities are consistent.

Velocities appear to increase once the patch has fully developed (in the 2100 time period). During the course of the night the velocities decrease as has been shown by Koster (1972) and as is shown in Figure 11a.

The average scintillation index as determined by these carefully calibrated measurements (with  $S_4$  derived from computer analysis of 1.5 minutes segments of data) appears to increase in the 2100-2200 time period and then decrease through the night. The minimum in  $S_4$  at midnight and the increase again (post midnight) may be due to the sparse data sampling (Figure 11b).

The average correlation interval does not change significantly throughout the night until midnight. Gradually after midnight the correlation interval increases as the velocity slows down and the signals show evidence of weak scatter (Figure 11c).

The shape of the power spectra of ionospheric scintillations is a function of the scintillation amplitude ( $S_4$ ) and the rate of scintillations. Within the illustrations (Figures 12 and 13) several different examples of amplitude and rate are shown with their corresponding power spectrum. In general the spectral shape is characterized by a rising (positive) slope in the low-frequency region, a relatively flat mid-frequency portion and a constant power-law rolloff. Intersections of straight-line fits to the slopes in the three frequency regions determine two cut-off frequencies,  $f_L$  and  $f_H$ . Not all spectra exhibit both cut-off frequencies within the displayed frequency range; sections 3 and 5 are examples of spectra having two cut-off frequencies. The low frequency limit is set by the three minute data sample. The scintillation of the input signal is characterized by three degrees of rate, i.e. SLOW, MEDIUM and FAST and three degrees of amplitude change, i.e. LOW, MEDIUM and HIGH. Table I summarizes the characterization for the six examples. The measured cut-off frequencies and slopes of the spectra are listed against the corresponding input signals. The high frequency cut-off varied from about .06 to .8 Hz; section 8 could not be measured because of the limit on the low frequency resolution. For the two cases #3 and #5 which also exhibited a low-frequency cut-off, it was approximately 1/3 of the high frequency cut-off. Examples #3 and #5 therefore exhibited the three slopes; a positive low-frequency slope of index +1, a mid-frequency slope of approximately -1, and a high frequency slope of -3 to -4. Those spectra that only exhibited mid and high frequency slopes, i.e. #1, #2 and #7, would have the low frequency (positive) slope below the low-frequency limit, .01 Hz.

Theoretical considerations indicate that, for weak amplitude scintillations, the slope of the rolloff portion of the scintillation spectrum is expected to have  $f^{-3}$  slope when the three-dimensional irregularity power spectrum is assumed to have a spectral index of 4. Steeper slopes and an increase in the cutoff frequency arise when strong scattering is encountered.

## 3. AURORAL AND POLAR STUDIES

The initiation of phase measurements on a long term basis at high latitudes began with the launching of WIDEBAND, a 1000 km satellite transmitting a series of coherent frequencies. Morphological studies are still in progress (Fremouw et al., 1979). Their comparisons indicate that auroral irregularities at E and F layers show a diurnal pattern (particularly in winter) strongly affected by the longitude of the observer. Thus during quiet magnetic conditions there is almost no diurnal variation in the winter observing from Narssarsuaq, Greenland; for the same season there is considerable variation observing at Poker Flat, Alaska. The prediction of this effect was made by Basu (1975) and has been borne out by recent observations.

A second contribution of recent studies notably Livingston and Rino (1978) and Martin and Aarons (1977) is that sheet-like irregularities exist at auroral latitudes. The WIDEBAND phase observations indicate that at night sheets of ionization with dimensions 10:10:1 exist; the Martin and Aarons data predict sheet sizes greater than 5:2:1 with the first term  $\alpha$ , elongation of the irregularity along the lines of force of the magnetic field, the second is  $\gamma$ , orthogonal to the elongation along the lines of force, thus being in the magnetic east-west plane; the third term is orthogonal to the other two planes. At high latitudes, this would lie in the north-south meridian.

In January 1979 AFGL in collaboration with SRI International installed equipment at

TABLE I

## Characterization of Power Spectra

Sample Scint. No. Rate/Amp.	Cut-off freq.(Hz)		Slope = $f^p$		
	$f_L$	$f_H$	PL	PM	PH
#1 Slow/Low		.06		$\sim 0$	-1.8
#2 Fast/High		.8		$\sim 0$	-3
#3 Med./High	.1	.3	1	- .8	-3
#4 Med./Med.		.15	1		-2.5
#5 Med./High	.07	.3	<1	-1	-4
#6 Slow/Low		.08	<1		-2.5
#7 Slow/High		.1		$\sim 0$	-3
#8					-2

Goose Bay, Labrador to measure phase and amplitude scintillations from WIDEBAND and from a synchronous satellite. The WIDEBAND data for selected periods has been compared to DMSP (Defense Meteorological Satellite) photographs (primarily green line emission) and from DMSP, measurements of energetic particle flux.

One night's data, that of January 25, 1979, have been chosen to show the extent of the optical aurora, the energetic electron precipitation zone, and the scintillations.

WIDEBAND severe amplitude and phase scintillations at 378 MHz were noted in the area denoted by cross hatching i.e. directly over the aurora in Figure 14. The FLTSATCOM signals at 244 MHz at the southern edge of the auroral region also showed high level scintillation activity. The evidence therefore is that at auroral latitudes, scintillations are very high over discrete and diffuse auroral forms, maximizing for this illustration over discrete forms. Amplitude data taken at Thule of the WIDEBAND satellite shows very high levels at 137 MHz over a region not illuminated by the aurora. The charged particle sensors with observations at 0325 UT indicated little flux over the polar region.

The indications from a series of observations are that there is high correlation between optical green line emission, total flux of precipitating electrons and auroral region scintillations but little correlation between the optical green line emission, precipitating electrons and the general level of polar scintillation activity. Study of very soft electron precipitation, red line emission at F layers, and scintillations in the polar region is in progress (Weber and Buchau, private communication).

The phase information from another pass of WIDEBAND shows a dramatic form as illustrated in Figure 15 where phase fluctuations of one radian outside of the auroral region increase to 16 radians when the satellite path crossed the sheet-like irregularities at a dip latitude of 62°; Kp for this period was 4. The path of this satellite pass where the most dramatic phase scintillations were observed took place over the discrete aurora.

Using observations from Goose Bay, daytime scintillations do not show the sheet-like nature (possibly because of orientation of the site vis a vis the sheets). The sheets show their dramatic effects predominantly when viewed from the same latitude. If sheets exist in the daytime they are expected at higher latitudes. Daytime observations from Goose Bay show a motion of the satellite propagation path into a region of irregularities; this can be illustrated in Figure 16 where a clear boundary exists between strong irregularities (at 137 MHz) and a quiescent ionosphere. In this illustration the boundary was at 66° corrected geomagnetic latitude.

A series of measurements of scintillation activity from Goose Bay, Labrador and from Sagamore Hill, Mass. has been analyzed for 12 magnetic storms during 1971 and 1972 (Houminer et al., 1980) identifying the plasmopause as the seat of irregularities, the trough as a region of low irregularity intensity and the poleward edge of the trough wall as the beginning of increased irregularity intensity.

It now appears in order to refine the scintillation boundary concept of Aarons and Allen (1971). The equatorward edge of the boundary is the plasmopause. Progressing from this region poleward, the trough shows lower levels of irregularity activity. The poleward edge of the trough marks the commencement of the appearance of auroral oval irregularities.

#### 4. CONCLUSIONS

##### 4.1. The Equatorial Region

The experimental results at the equator have succeeded in forming a more solid base for theoretical studies on the development of the patches. In the area of fully explaining the basic origin of the patches, i.e. the conditions under which a patch either forms or fails to form, there is little experimental data. Much remains to be done with the decay of the patches. There are times of the year and periods of the sunspot cycle when patches last only until 0100 LT and other times when patches don't decay until dawn or shortly after; the atmospheric and ionospheric conditions associated with these diverse sets of data have not been clearly delineated.

At the equator, the differences between various longitude regions have not been fully explained. It would appear that lower atmospheric conditions and the neutral atmosphere play important roles in the processes of producing different seasonal patterns at various longitudes; determining the initial conditions necessary for developing a patch will help us understand the longitudinal differences.

##### 4.2. The High Latitudes

At high latitudes, there are two regions with apparently differing patterns of behavior. The auroral oval serves as the seat for the auroral scintillation activity with increasing irregularity intensity. With greater magnetic activity, the strong effect of sheet-like irregularities has been noted.

In the polar cap region, there is a positive (but small) correlation of polar cap scintillation with magnetic index. However, seasonal differences are more dramatic. Perhaps in this area the current concepts of convective electric fields will aid in our understanding of polar cap scintillation activity. High solar flux has increased polar cap irregularity intensity and occurrence. The role of UT versus local time will have to be carefully studied in order to develop clues as to the mechanisms. These are some of the parameters of interest in the coming years.

Experimental and theoretical studies will be continued to determine scintillation characteristics on a global scale and to attempt to understand initiating mechanisms for the patches of irregularities.

#### 5. ACKNOWLEDGEMENTS

The authors would like to thank the various individuals and observatories who have contributed to the studies. We would like to reemphasize that the work reported is a summary of studies which have been performed by individuals both within and outside of Air Force Geophysics Laboratory; their contribution will be reported in the scientific literature and in reports from AFGL and their associated observatories.

#### 6. REFERENCES

- Aarons, J., 1977, Equatorial scintillations: A review, IEEE Trans. Antennas Propagat., AP-25, 729.
- Aarons, J. and R.S. Allen, 1971, Scintillation boundaries during quiet and disturbed magnetic conditions, J. Geophys. Res., 76, 170.
- Basu, Sunanda, 1975, Universal time seasonal variation of auroral zone magnetic activity and VHF scintillation, J. Geophys. Res., 80, 4725.
- Basu, S., Sunanda Basu, J. Aarons, J.P. McClure, and M.D. Cousins, 1978, On the co-existence of km- and m-scale irregularities in the nighttime equatorial F-region, J. Geophys. Res., 83, 4219.
- Basu, Sunanda and M.C. Kelley, 1979, A review of recent observations of equatorial scintillations and their relationship to current theories of F-region irregularity generation, Radio Sci., 14, 471.
- Basu, S. and Sunanda Basu, 1980, Modelling of equatorial phase and amplitude scintillations from OGO-6 and AE irregularity data, To be published in Space Research XX.
- Buchau, J., E.J. Weber and H.E. Whitney, 1979, New insight into ionospheric irregularities and associated VHF/UHF scintillations, Acard Conference Proc. #239 on Digital Communications in Avionics.
- Calvert, W. and R. Cohen, 1961, The interpretation and synthesis of certain spread-F configurations appearing on equatorial ionograms, J. Geophys. Res., 66, 3125.
- Chandra, H. and R.G. Rastogi, 1972, Spread-F at magnetic equatorial station, Thumba, Ann. Geophys., 28, 37.

- Fejer, B.G., D.T. Farley, B.B. Balsley and R.F. Woodman, 1976, Radar studies of anomalous velocity reversals in the equatorial ionosphere, J. Geophys. Res., 81, 4621.
- Fremouw, E.J., R.L. Leadabrand, R.C. Livingston, M.D. Cousins, C.L. Rino, B.C. Fair and R.A. Long, 1978, Early results from the DNA Wideband satellite experiment - Complex signal scintillation, Radio Sci., 13, 167.
- Fremouw, E.J. and J.M. Lansinger, 1979, Continued geophysical analysis of coherent satellite scintillation data, Physical Dynamics, Inc. Annual Report, 30 November.
- Houminer, Z., J. Aarons and E. MacKenzie, 1980, Plasmopause and auroral oval irregularities during magnetic storms, To be presented at URSI, Quebec, Canada, June.
- Koster, J.R., 1972, Equatorial scintillation, Planet. Space Sci., 20, 1999.
- Livingston, R.C. and C.L. Rino, 1978, Ionospheric irregularity anisotropy and drifts at high latitudes, presented at URSI, Boulder, CO.
- Martin, E. and J. Aarons, 1977, F-layer scintillation and the aurora, J. Geophys. Res., 82, 2717.
- McClure, J.P. and W.B. Hanson, 1973, A catalog of ionospheric F region irregularity behavior based on Ogo-6 retarding potential analyzer data, J. Geophys. Res., 78, 7431.
- Mullen, J.P., 1973, Sensitivity of equatorial scintillation to magnetic activity, J. Atmos. Terr. Phys., 35, 1187.
- Nichols, B.E., 1974, UHF fading from a synchronous satellite observed at Kwajalein October 1970 through June 1972, Technical Note of Lincoln Laboratory, 1974-19.
- Paulson, M.R., 1979, Scintillation of UHF Satcom signals: Occurrence at Guam from mid-March 1978 through June 1979, Technical Report 446, Naval Ocean System Center, San Diego, CA, 15 August.
- Rastogi, R.G., 1980, Seasonal and solar cycle variations of equatorial spread-F in the American zone, Submitted to J. Atmos. Terr. Phys.
- Rastogi, R.G. and R.F. Woodman, 1978, VHF radio wave scattering due to range and frequency types of equatorial spread-F, J. Atmos. Terr. Phys., 40, 485.
- Woodman, R.F., 1970, Vertical drift velocities and east-west electric fields at the magnetic equator, J. Geophys. Res., 75, 6249.

AD-A090 850

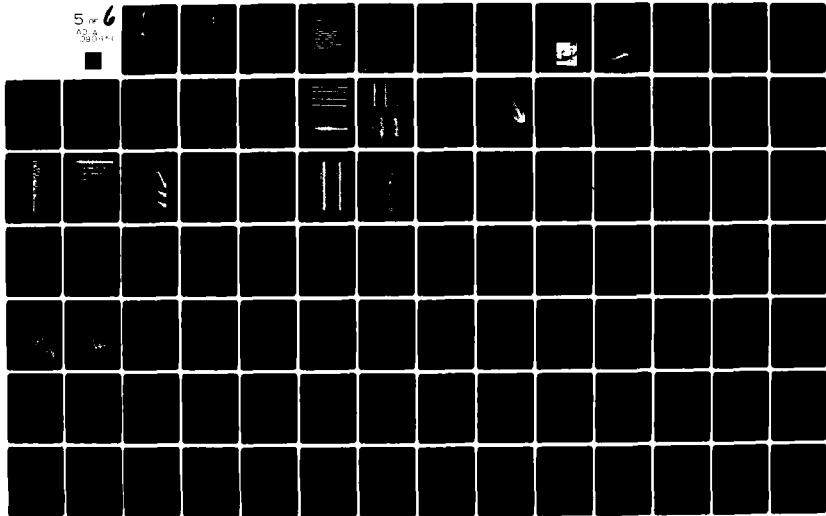
ADVISORY GROUP FOR AEROSPACE RESEARCH AND DEVELOPMENT--ETC F/6 20/14  
PROPAGATION EFFECTS IN SPACE/EARTH PATHS.(U)  
AUG 80 H J ALBRECHT

UNCLASSIFIED

AGARD-CP-284

NL

5 of 6  
090441



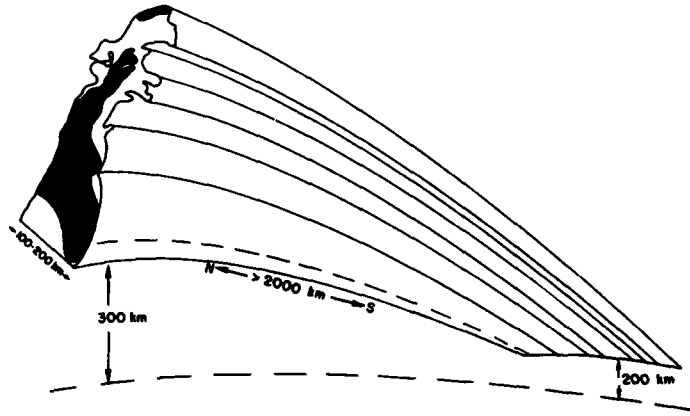


Figure 1. A magnetic equator cut through the general form of the equatorial patch, shown following the contours of the earth's magnetic field. North-south dimensions are typically > 2000 kilometers, while it may measure several hundred kilometers east-west and vary in vertical thickness from 50 to several hundred kilometers.

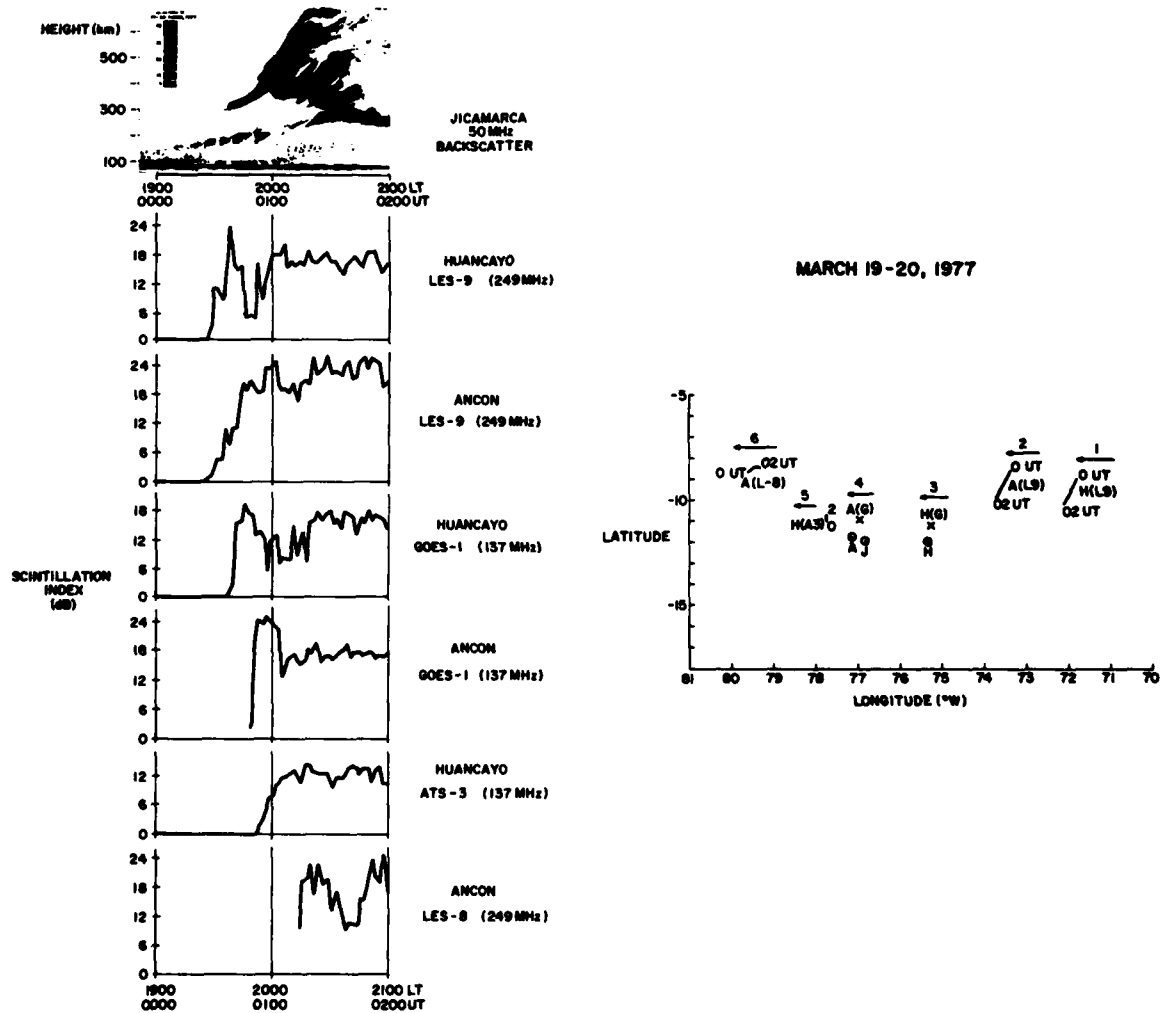


Figure 2. Backscatter and scintillation data recorded on March 19-20, 1977 of several satellites observed from Ancon and Huancayo, Peru. The accompanying map of the 400 km sub-ionospheric points illustrates the westward development of the patch through the use of arrows and the numerical order of commencements.

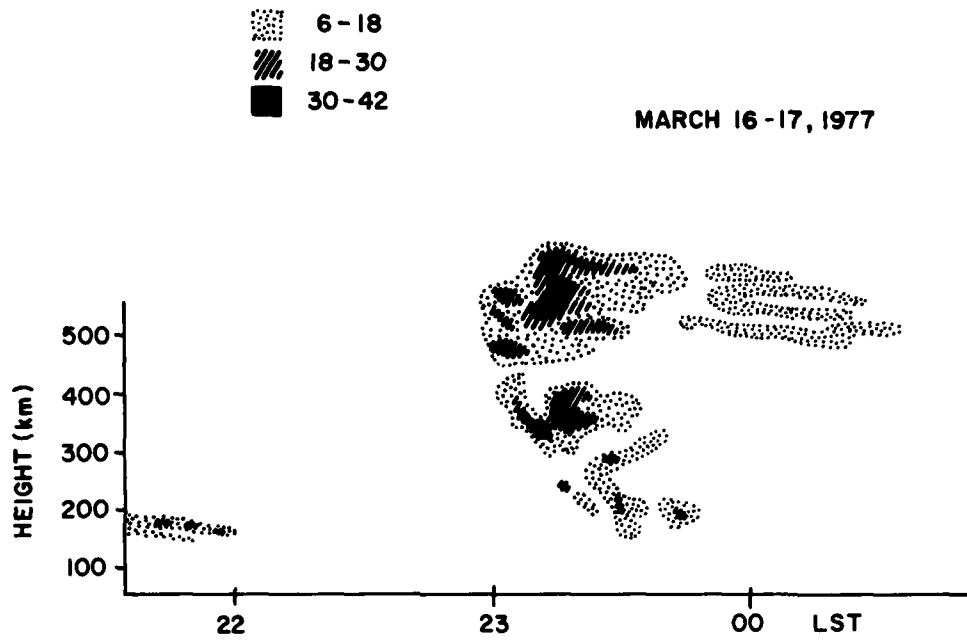


Figure 3. Backscatter records of March 16-17, 1977. The irregularities maintain medium level intensity from  $\approx$  2300-2330 LST, at heights of 300-600 km, then disappear at the lower altitudes and trail off in intensity at the higher altitudes until 0300 LST.

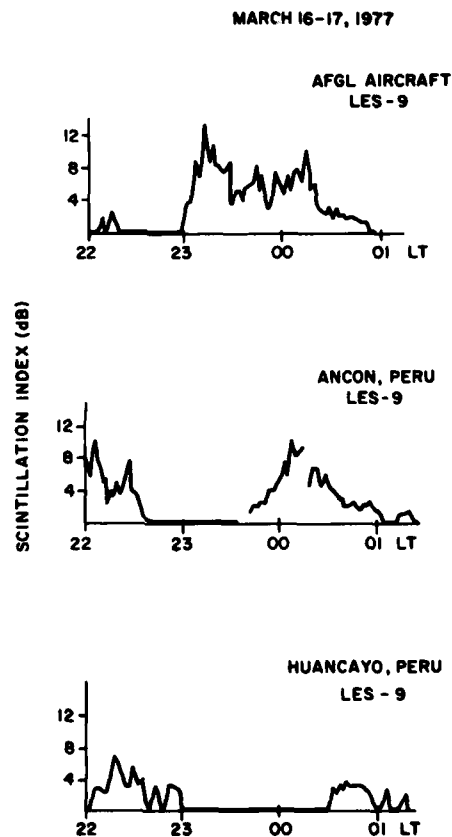


Figure 4. Scintillation observations of the LES-9 beacon seen at Ancon and Huancayo, Peru and by the AFGL aircraft tracing a route over Jicamarca, on the same day as the backscatter records shown in Fig. 3. The eastward movement of the patch is shown with intensity of scintillation falling off corresponding to the drop in intensity of the backscatter.

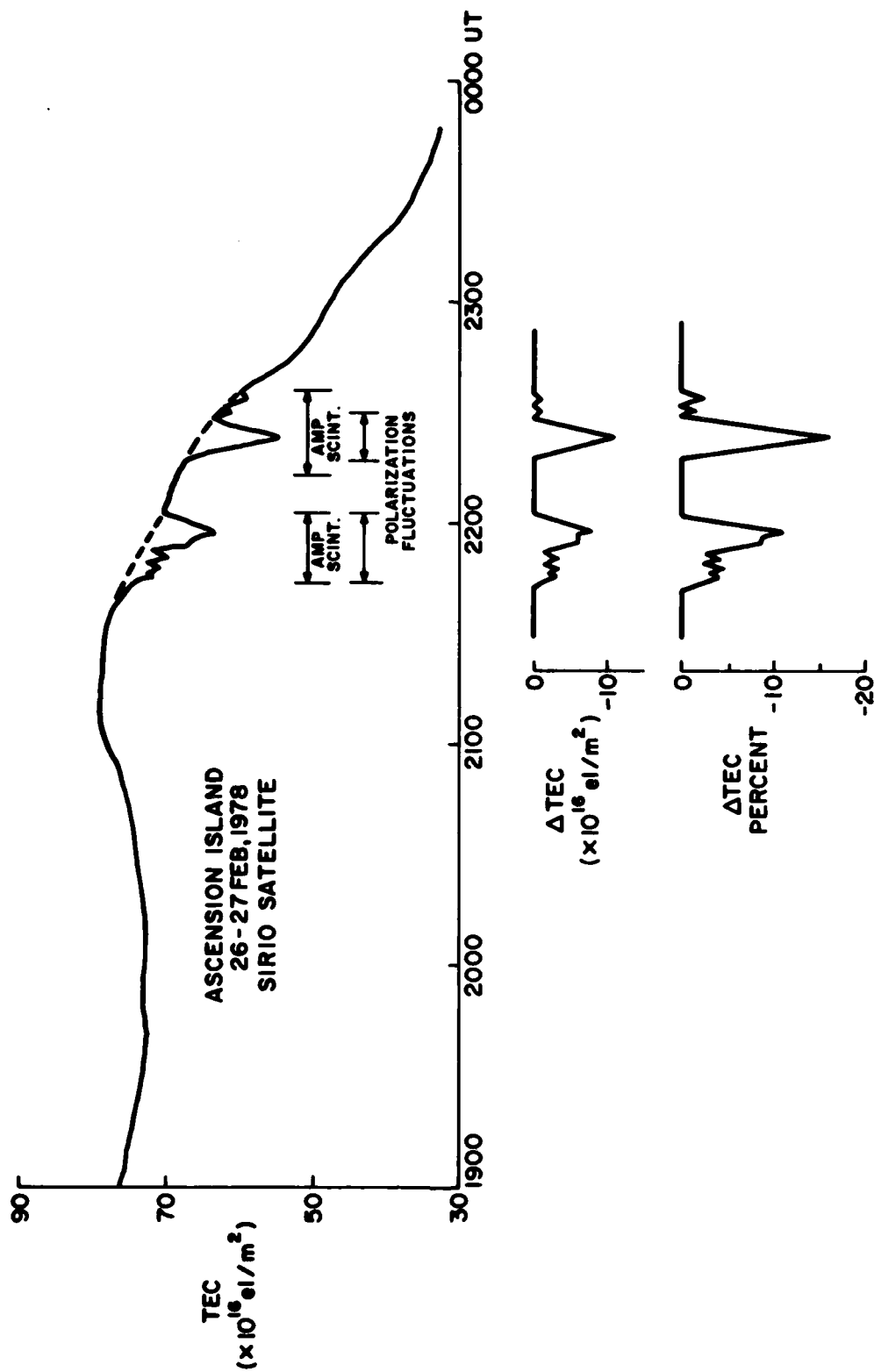


Figure 5. Two depletions in total electron content from an assumed quiet background observed on Feb. 26-27, 1978 at Ascension Island. The close association with the occurrence of amplitude scintillation is noted.



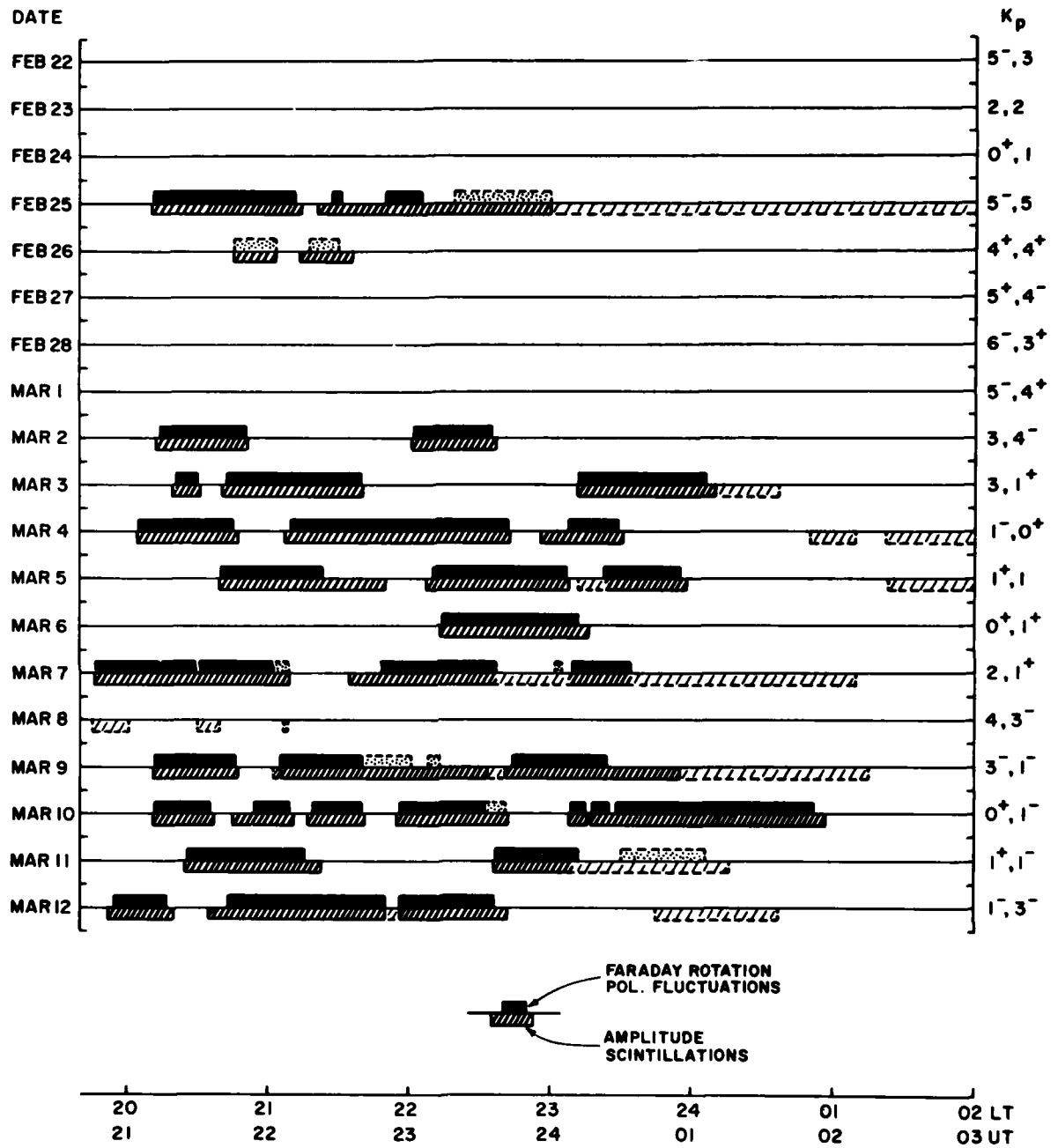


Figure 6. Association of TEC fluctuations with rapid, severe amplitude scintillations at Ascension Island observing the SIRIO beacon during Feb. 22 - March 12, 1978.

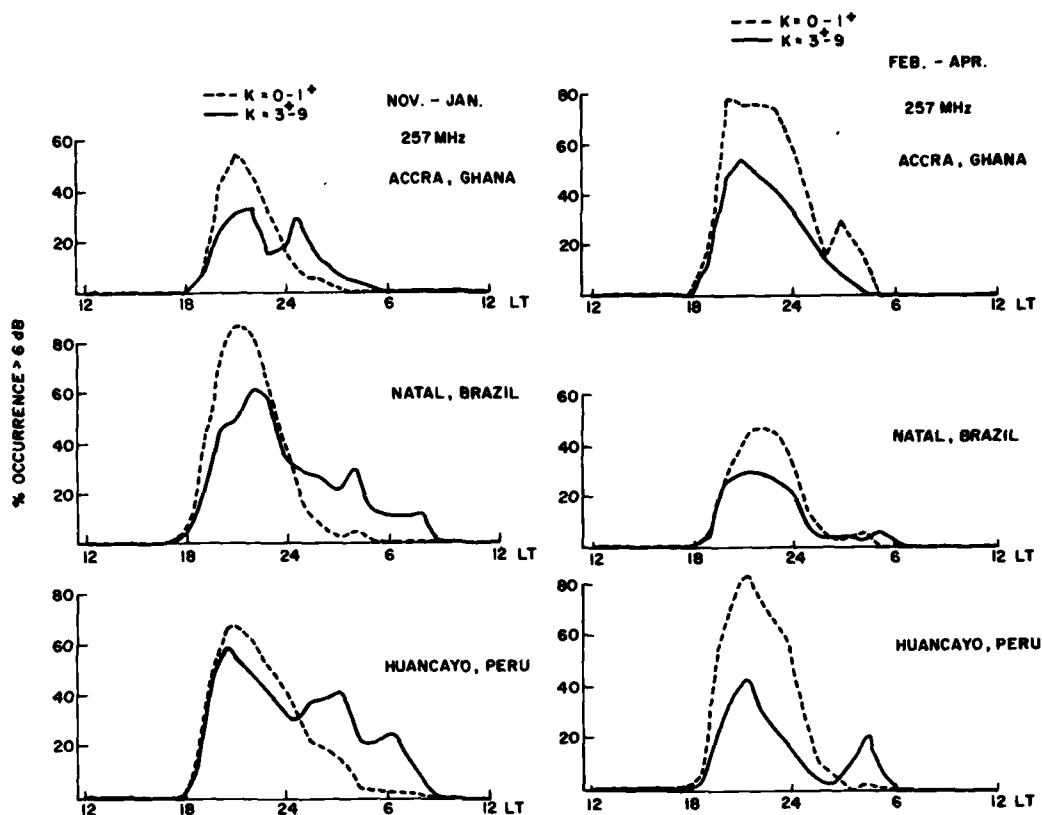


Figure 7. Percentage occurrence of 137 MHz scintillations  $SI \geq 6$  dB peak-to-peak for Nov-Jan and Feb-Apr under quiet and disturbed magnetic conditions.

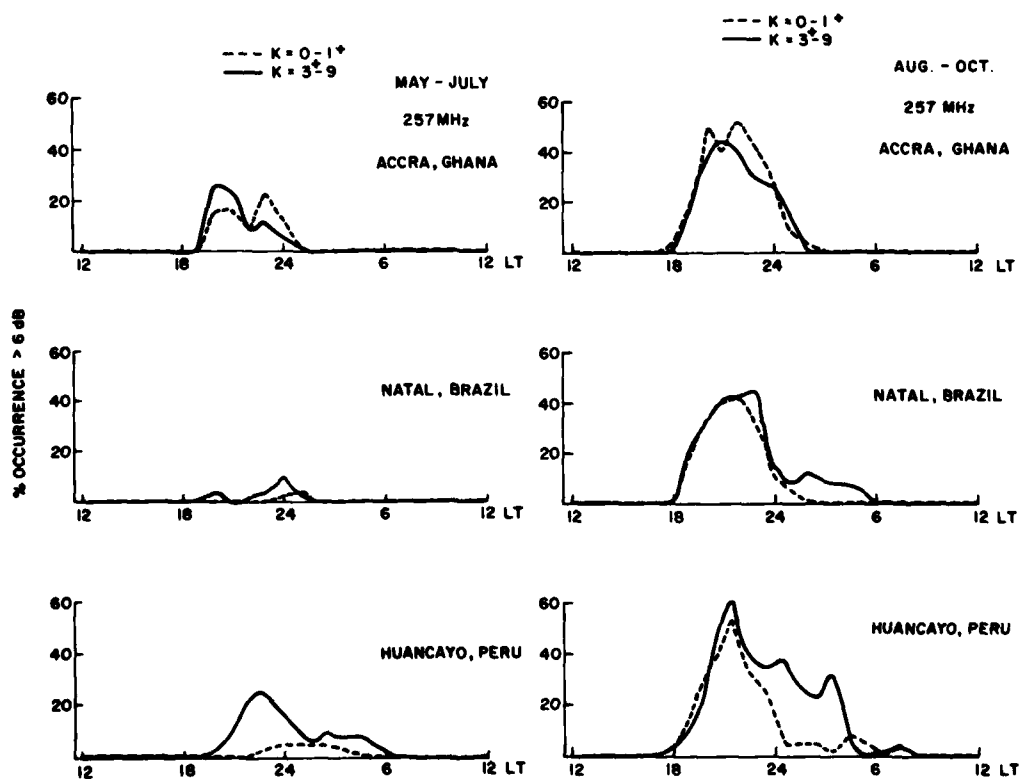


Figure 8. Percentage occurrence of 137 MHz scintillations  $SI \geq 6$  dB peak-to-peak for May-July and Aug-Oct under quiet and disturbed magnetic conditions.

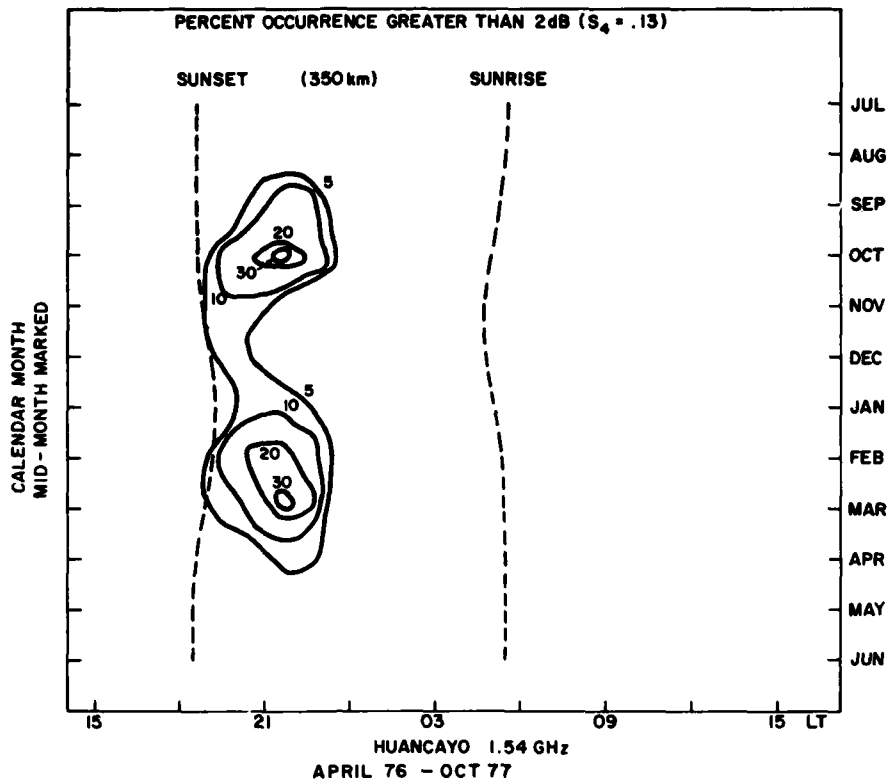


Figure 9. Percentage occurrence of 1.5 GHz scintillations  $\geq 2$  dB during April 1976- Oct 1977.

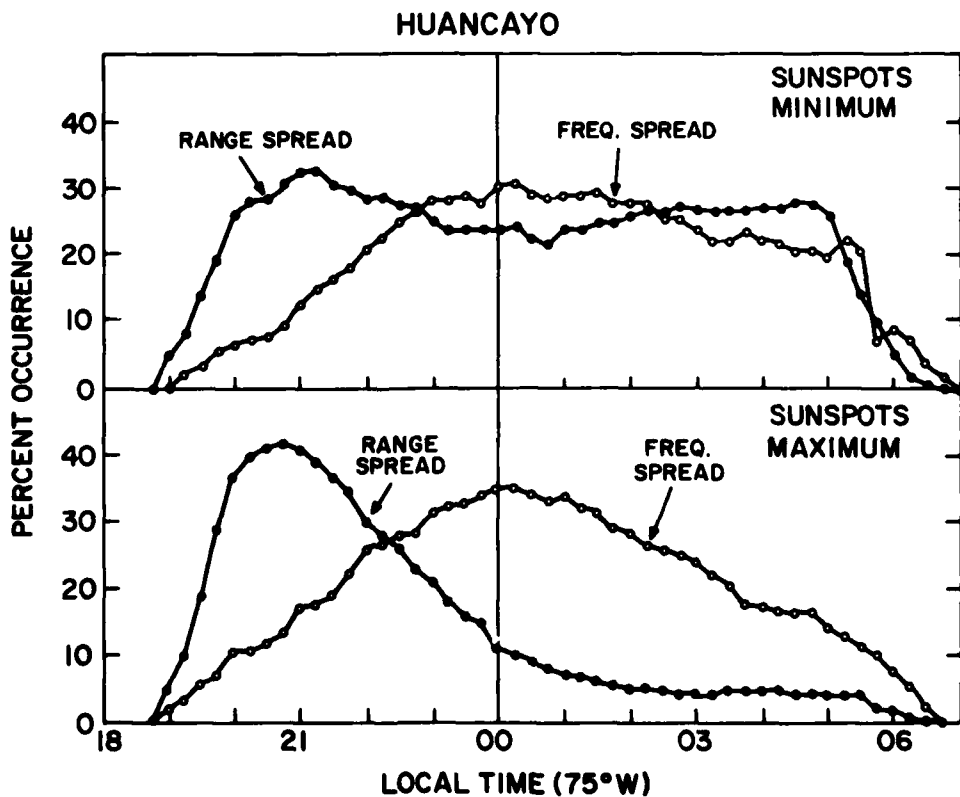


Figure 10. Percentage occurrence of range and frequency spread-F under sunspot maximum and sunspot minimum conditions.

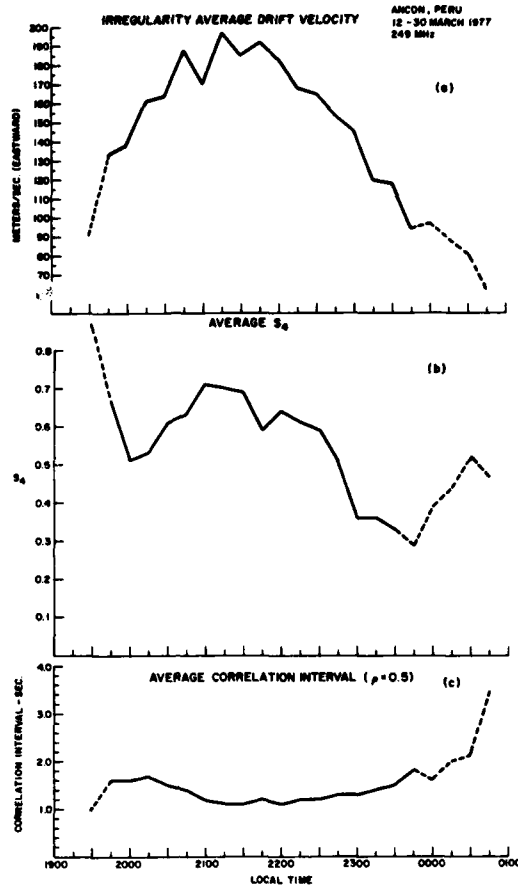


Figure 11. (a) Average velocity measurements of spaced receiver data at Ancon, Peru during March 1977. (b) Average  $S_4$  measured on spaced receiver data at Ancon, Peru during March 1977. (c) Average correlation interval measured on spaced receiver data at Ancon, Peru during March, 1977.

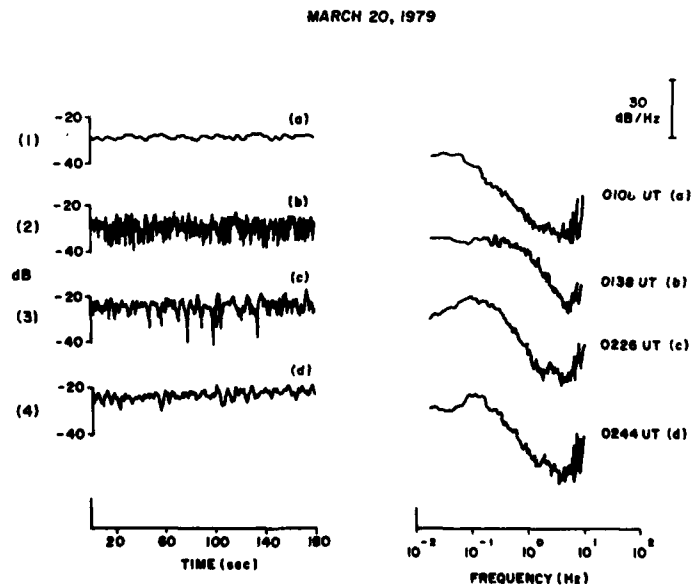


Figure 12. Several illustrations of variations of amplitude ( $S_4$ ) and rate within power spectra on March 20, 1979.

MARCH 21, 1979

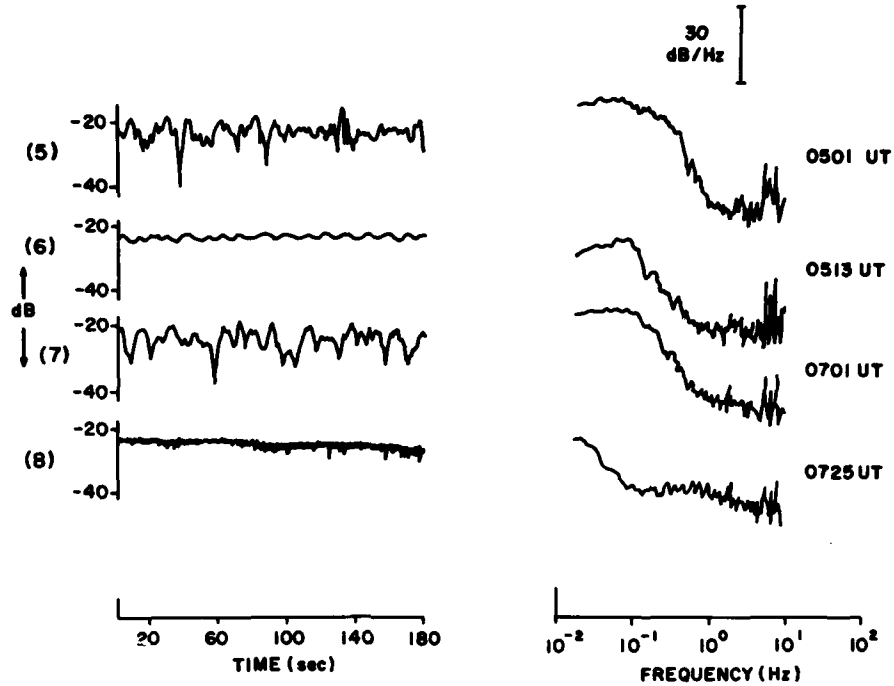


Figure 13. Several illustrations of variations of amplitude ( $S_4$ ) and rate within power spectra on March 21, 1979.

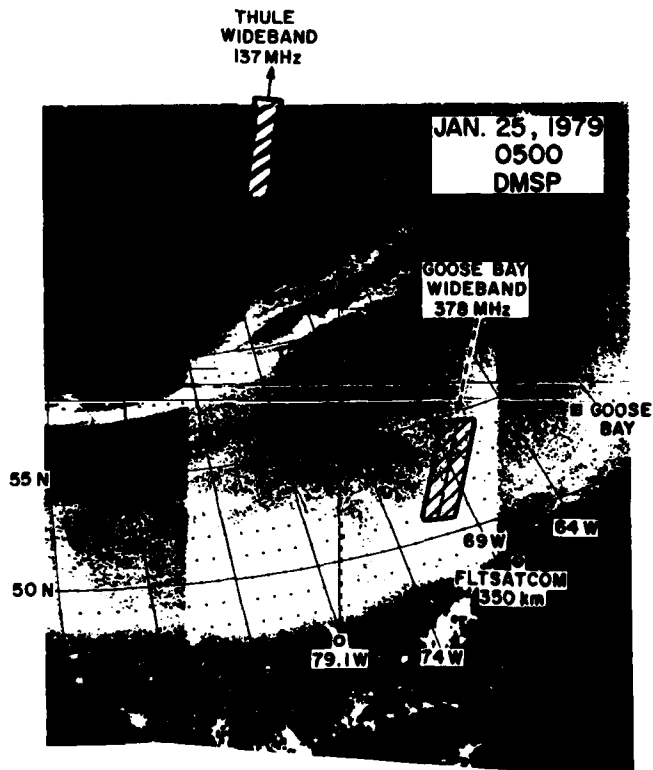


Figure 14. DMSP photo showing aurora at 0500 UT on Jan. 25, 1979 with Goose Bay (378 MHz) and Thule (137 MHz) Wideband passes as well as the position of the Goose Bay station and the 350 km intersection of Goose Bay FLTSATCOM.

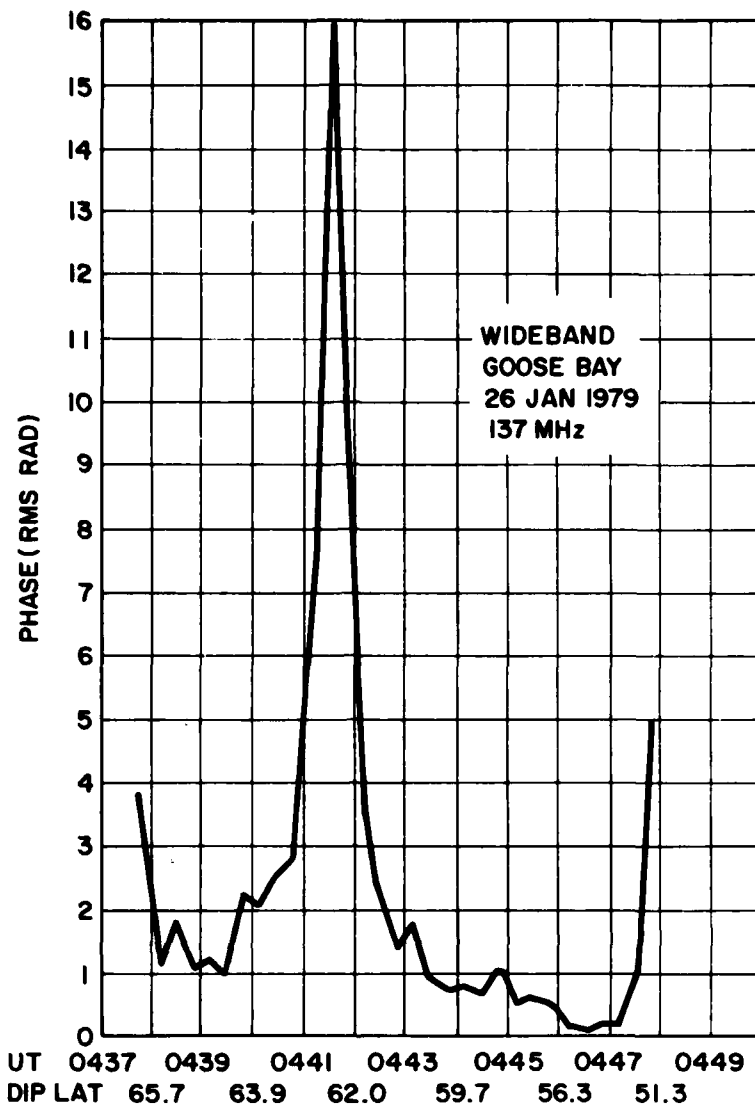


Figure 15. Phase scintillations observed from Goose Bay of the 0437 UT WIDEBAND pass (137 MHz).

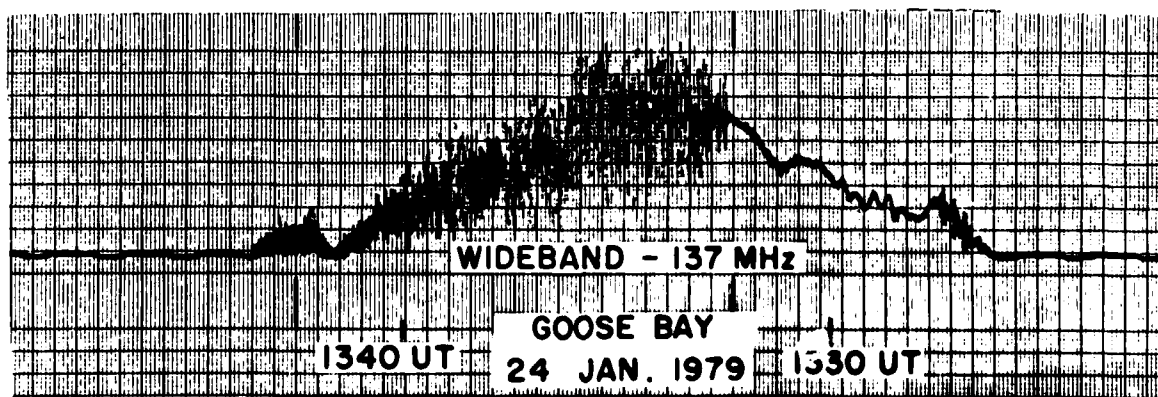


Figure 16. Daytime scintillation pass showing the propagation path from the WIDEBAND satellite to Goose Bay as it moves from a region of strong irregularities into a quiet ionosphere. The boundary is at  $\sim 66^\circ$  corrected geomagnetic latitude.

4/6-GHZ IONOSPHERIC SCINTILLATION MEASUREMENTS

D. J. Fang  
COMSAT Laboratories  
Clarksburg, Maryland 20734

ABSTRACT

Since 1970, COMSAT Laboratories has conducted a 4/6-GHz ionospheric scintillation measurement program, employing INTELSAT earth stations around the world. Early data established the existence of 4- and 6-GHz ionospheric scintillations and gross features such as dependence on local sunset conditions, diurnal and seasonal occurrence patterns, geomagnetic boundaries, and the order of magnitude of the frequency dependence of the scintillation phenomena. Recent data collected during years of different levels of solar activity have provided further insight into the nature of 4- and 6-GHz scintillations. Their gross dependence on annual solar activity was established by comparing the level of scintillation activity over the ten-year period.

Most of the data presented in this paper were collected at the Taipei Earth Station from June 1976 to June 1977, the first year of sunspot cycle 21, during which the low solar activity level began to increase. Annual and worst-month cumulative statistics for ionospheric scintillations were provided for use in system studies and planning. The worst-month statistics varied considerably, depending on the definition of worst-month; therefore, a formal definition for engineering applications was warranted. Power spectral density analyses confirmed an  $f^{-3}$  dependence, indicating that the conventional weak scattering theory for a thick screen with a power law electron density fluctuation spectrum of  $p = 4$  would be adequate to explain the weak gigahertz ionospheric scintillation events observed at Taipei.

## 1. INTRODUCTION

The ionosphere is an ionized region of plasma in the earth's atmosphere extending from about 50 km to approximately 2,000 km above the surface. The principal cause of ionization is electromagnetic radiation from the sun extending over the ultraviolet and x-ray portions of the spectrum. This effect is counterbalanced by ionization-loss processes, essentially the collisional recombination of electrons and positive ions, and the attachment of electrons to neutral gas atoms and molecules. The ionosphere contains relatively uniform and stationary ambient ionization patterns. Some highly localized randomly fluctuating inhomogeneous patterns, known as ionospheric irregularities, also exist.

When radio waves propagate through the ionosphere in the presence of irregularities, the waves will be scattered and/or diffracted. These effects manifest themselves as fluctuations of the amplitude and phase of the waves, i.e., ionospheric scintillations. Numerous experimental and theoretical studies have been performed on such phenomena. Early studies of ionospheric scintillation were in the frequency ranges from HF to UHF (Booker, H. G., and Gordon, W. E., 1950; Bowles, K. L., 1964; Ratcliffe, J. A., 1956; Fremouw, E. J., and Rino, C. L., 1973; Briggs, B. H., and Parkins, I. A., 1963; Rufenach, C. L., 1975; Crane, R. K., 1976; and Basu, S., et al., 1977). Since 1970, experimenters, stimulated by the need for satellite-earth communications, have also observed scintillations at gigahertz frequencies (Taur, R. R., 1976; Liu, C. H., and Yeh, K. C., 1977; Fang, D. J., et al., 1978; Skinner, N. J., et al., 1971; Craft, H. D., and Westerlund, L. H., 1972).

COMSAT Laboratories has been using INTELSAT earth stations around the world and INTELSAT satellites in the three oceanic regions to measure 4/6-GHz ionospheric scintillations for the past ten years. The gross features of gigahertz scintillations can be summarized as follows (Fang, D. J., et al., 1978):

- (a) Scintillations occur near the geomagnetic equator only; the geometric boundaries of scintillation activity were found to be approximately  $30^\circ$  GMN and  $30^\circ$  GMS.
- (b) The frequency of occurrence of scintillation events has strong diurnal peaks. The probability that events will occur is greatest at about one hour after local ionospheric sunset.
- (c) The frequency of occurrence exhibits seasonal variations. Peak activity periods are observed shortly after the vernal and autumnal equinoxes.
- (d) An  $f^{-n}$  relationship with  $n$  between 1.5 to 2.0 appears to exist between the amplitude of scintillation events measured at 4 and 6 GHz.
- (e) Both the frequency of occurrence and the peak-to-peak fluctuation magnitude of ionospheric scintillations in one year appear to be positively correlated with the level of solar activity in that year.

A maximum peak-to-peak fluctuation of 6 dB at 4 GHz was reported (Taur, R. R., 1976) at the Hong Kong Earth Station from 1970 to 1972, when the monthly averaged Zurich sunspot numbers varied from 60 to 110. On the other hand, recent measurements at the same earth station in 1979, when the sunspot numbers varied from 120 to 160, revealed a maximum

peak-to-peak fluctuation near 10 dB at 4 GHz. Furthermore, no significant ionospheric scintillations were observed from the data collected in 1975, a year of minimum solar activity in the 11-year solar cycle, with a monthly averaged Zurich sunspot number less than 30. Thus, an investigation of the dependence of scintillation occurrence on solar activity, which compares data collected over the 10-year period, is warranted.

To illustrate a typical measurement setup used for observing ionospheric scintillations, this paper reports on the measurements made from June 1976 to June 1977, at the Taipei Earth Station in Taiwan. During this period, the monthly averaged sunspot number recovered from a low point of 20 to 70, and as might be anticipated, gigahertz scintillation activity also changed from an insignificant to a moderate level of activity. The results confirm the general relationship between ionospheric scintillations and solar activity.

Cumulative statistics for ionospheric scintillations are derived based on the one year of measurement data. Since CCIR design criteria involve the concept of a 1-minute mean value of signal variation over any month (CCIR Document 4/147, 1976), both the annual and worst-month scintillation statistics are provided. The power spectra for ionospheric scintillations are generated and analyzed. The frequency dependence of the roll-off slope is emphasized, since it helps to explain the physics of SHF scintillations in the ionosphere.

## 2. SYSTEM CONFIGURATION

The Taipei Earth Station is located at 121.55° E and 25.14° N, or approximately 25 km northwest of the city of Taipei. The geomagnetic latitude is 15° GMN. The station has two 30.48-m (diameter) antennas, Taipei 1 and Taipei 2, which point to the Pacific Ocean Regional (POR) satellite at 174° E (26° elevation angle) and the Indian Ocean Regional (IOR) satellite at 61.4° (19° elevation angle), respectively. Table 1 gives the antenna performance characteristics.

Table 1. Antenna Performance Characteristics

f (GHz)	Performance	Taipei 1 (G/T = 41.0 dB/K)	Taipei 2 (G/T = 43.0 dB/K)
4	Gain	59.8 dB	60.8 dB
	3-dB Beamwidth	0.17°	0.16°
6	Gain	61.3 dB*	64.3 dB*
	3-dB Beamwidth	0.13°	0.12°

\*At HPA output flange.

Figure 1 shows the basic measurement configurations for Taipei 1 and Taipei 2. Six signals were monitored by the two antenna receive systems:

- (a) Taipei 1: POR satellite beacon level, azimuthal tracking error, and elevation tracking error.
- (b) Taipei 2: IOR satellite beacon level, azimuthal tracking error, and elevation tracking error.

At the earth station antenna receive system, the satellite beacon signals are received as tracking error and tracking sum voltages based on the monopulse principle. As shown in Figure 1, the system has two inputs from the antenna. The first comes from a mode coupler at the end of the antenna feed assembly, which couples either the TE<sub>01</sub> mode and TM<sub>01</sub> mode signals (for Taipei 1) or the TM<sub>01</sub> mode signal only (for Taipei 2) received from the satellite beacon transmission. These are tracking error signals caused by antenna pointing errors. The second input is the communications signals which pass directly through the mode coupler in the TE<sub>11</sub> mode. These signals are channeled through the polarizer, duplexer, and LNR subsystem before they are down-converted for subsequent communications signal processing. The beacon portion of the signal is sampled at this stage through a coupler and sent through a phase shifter into the tracking receiver as the tracking sum signal, which is at least 15 dB stronger than the tracking error voltages.

The tracking receiver consists of a double down-converter and a phase detector, as shown in Figure 2. The double down-converter converts the tracking error and tracking sum signals separately from 4 GHz to 630 MHz and further to 136.5 MHz. An internally generated 10.7-MHz reference signal is phase locked to the stronger tracking sum signal, after it has been down-converted to 10.7 MHz. The output of the voltage-controlled oscillator (VCO) of the phase-locked loop then provides the precise frequencies needed for mixing not only with the tracking sum signal, but also with the weaker tracking error signal. In the tracking demodulator, the tracking error signal is then processed to provide the appropriate elevation and azimuthal antenna pointing error information. The automatic gain control (AGC) voltage of the phase detector provides information on the instantaneous amplitude fluctuation of the beacon signal received at the earth station.

As shown in Figure 1, the tracking error signals are fed into a servo drive system which controls antenna pointing. The autotrack accuracy is better than one-tenth of the half-power beamwidth, i.e., about 0.01°. The autotrack loop transient settling time is about 1 to 3 seconds, depending on the operating mode.



Two HP 3690A magnetic tape recorders were used to make FM data recordings. The tape width is 1/4 inch, and the reel length is about 2300 ft. Operated at a speed of 15/16 IPS, each reel is capable of continuous recording for about 8 hours. The FM carrier frequency is 1.69 kHz, and the recording passband frequency is 0 to 312 Hz with a signal-to-noise ratio better than 46 dB. In addition, a 4-pen rectilinear strip chart recorder was provided for direct recording of the collected data on the chart paper.

During the measurement period, the system was calibrated at least once a month according to the following procedures:

- (a) Insert precision IF attenuator at the input of the tracking demodulator.
- (b) Vary the attenuator +5 dB in 1-dB steps and adjust the buffer amplifier gain so that a sensitivity of 1 dB/V is obtained.

No RF calibration was performed because of earth station traffic considerations.

### 3. DATA ANALYSIS AND DISCUSSION

#### 3.1 General Signature of Ionospheric Scintillations

Less than 12 ionospheric scintillation events for peak-to-peak fluctuation over 1.0 dB were observed during the Taipei measurements. A typical signature of 4-GHz ionospheric scintillations is illustrated in Figure 3, which is a strip chart record of peak-to-peak fluctuations observed during the evening of April 28, 1977. The scintillations occurred in the Indian Ocean link. Figure 4 shows detailed 10-minute samples of the record. Record A reveals that low-level signal fluctuations were present in the early evening. Diffraction patterns (van de Hulst, H. C., 1957) (signal wiggings between the local peaks of maximum and minimum) due to small-scale weak irregularities which originated in the ionosphere are clearly identifiable. At 2220 local time, intense signal fluctuations erupted suddenly (see record B) and in less than a minute the signal fluctuation reached a maximum level of 2.5 dB or more. The high peak-to-peak level was maintained for more than an hour (record C) before it decreased to a lower level for the next few hours (records D and E). Fluctuations finally became sporadic and gradually disappeared (record F). Subsection 3.4 discusses the power spectral density for each of the records, which indicates how the electromagnetic waves were scattered by the ionosphere in each of the corresponding stages.

Figure 3 also reveals that when the ionospheric scintillation event was in progress on the Indian AGC channel, the two angle-of-arrival channels (INDIAN AZ ERROR and INDIAN EL ERROR) did not register any significant signal level variations. In the 10-minute period starting at 2320 local time, all three channels associated with the Pacific link showed mild but clearly noticeable signal level fluctuations. The pattern of fluctuations in the AGC channel was identical to that of the azimuthal and elevation error channels. This kind of fluctuation was not related to ionospheric scintillations; often, they were also observed in daytime. For the Taipei Earth Station, the fluctuations were observed most frequently in the early afternoon when atmospheric turbulence was most severe.

#### 3.2 Correlation Between Gigahertz Scintillations and Solar Activities

The correlation of occurrence of gigahertz scintillations and solar activities was documented by Taur (Taur, R. R., 1974) when he tabulated and compared the total minutes of scintillations measured in 1970 and in 1972 at Bahrain, Brazil, and Hong Kong. A linear relationship between the occurrence of scintillation and the sunspot number was later postulated (Paulson, M. R., and Hopkins, R. U. F., 1977).

The present study reviewed all scintillation data at 4 GHz collected by COMSAT Laboratories in five previous measurement programs from 1970 to 1979. It was found that the least number of scintillations was observed at the Hong Kong Earth Station in 1975-1976, a year earlier than the Taipei measurement. The data collection configuration at Hong Kong was similar to that at Taipei, except that about 15 carriers transmitted from earth stations located within 20° geomagnetic latitude were monitored. Data analyses revealed that practically no ionospheric scintillation events with signal fluctuations exceeding 1.0 dB peak-to-peak were available. When the Hong Kong results were compared with those from the Taipei measurement, it was obvious that both the number of occurrences and the magnitude of peak-to-peak fluctuations increased significantly from 1975 to 1977. This is a first indication that gigahertz scintillations and the yearly solar activities appear to be positively correlated.

To examine this correlation further, the occurrence of ionospheric scintillations was evaluated in terms of the percentage of time in a year during which peak-to-peak signal fluctuations exceeded 1.0 dB, as a function of the monthly averaged Zurich sunspot numbers for the five past ionospheric scintillation measurement programs. For each measurement program, upper and lower bounds of occurrence are established based on the maximum and minimum percentages of occurrence monitored in the multiple carrier channels. The bounds of the abscissa are the maximum and minimum monthly sunspot numbers observed for the entire program.

Figure 5, which gives a summary plot, suggests a log-linear dependence of the scintillation occurrence on sunspot numbers for the years in which the maximum sunspot number is less than 70. There appears to be a gradual saturation as the sunspot number exceeds 70.

Such a dependence can only be regarded as gross at this time. The actual occurrence of scintillation for any individual link may significantly deviate from that of the dependence curve shown because of the differences in link configuration, geomagnetic location, local ionospheric conditions, elevation angles, and other factors that affect gigahertz ionospheric scintillations.

For UHF scintillation, specific relationships have been found for correlating the scintillations and solar activity parameters. For example, Goodman (Goodman, J. M., 1978) postulated a simple algebraic equation that evaluates the scintillation index ( $S_4$ ) as functions of  $\Sigma Kp$ , the sum of eight 3-hourly planetary magnetic indices following a scintillation event, and  $R_z$ , the daily sunspot number of the day preceding the scintillation event. To determine if similar correlations are possible for the present study, a tabulation of  $R_z$  is given in Table 2, indicating the days during which ionospheric scintillations occurred. The table does not suggest any specific dependence on daily sunspot numbers.

Table 2. Relative Daily Sunspot Numbers for the Entire Experimental Period

Day	1976							1977					
	Jun	Jul	Aug	Sep	Oct	Nov	Dec	Jan	Feb	Mar	Apr	May	Jun
1	0	9	10	17	31	7	0	20	15	0	7	15	44
2	0 <sup>a</sup>	8	18	20	28	0	0	32	19	8	11	14	43
3	0 <sup>a</sup>	14	19	12	30	0	0	25	19	8	10	22 <sup>b</sup>	43
4	0	8	14	11	32	0	0	25	16	8	7	23	49
5	0	8	17	17 <sup>a</sup>	25	0	0 <sup>a</sup>	24	18	8	7	18	40
6	0 <sup>a</sup>	10	15	10	24	0	0	13	7	9	8	16	39
7	0	7 <sup>a</sup>	26	9	30	0	0	0	7	8	7	12	41
8	11	0	30	9	7	0	20 <sup>b</sup>	0	26	20	0	19	38
9	10	0	31	18 <sup>a</sup>	14	0	25	0	21	20	0	25	33
10	7	0	24	22	0 <sup>a</sup>	0	16	0	25 <sup>a</sup>	19	0 <sup>a</sup>	29	29
11	7	0	22	24	0	0 <sup>a</sup>	24	14	28	19	0	34	27
12	8	0	29	20	14	0	16	22	48	14	12	35	22
13	8	0	27	12	17	10	23	23	68	8	16	26	20
14	15	0	16	10	25	0	34	22	61	7	22	33	25
15	18	0	8	16	27	7	34 <sup>a</sup>	24	45	0	29	26	8
16	12	0	15	14	32	7	39 <sup>b</sup>	18	49	0	31	25	8
17	18	0	19	8	36	14	34	30	47	8	32	20	8
18	24	0	23 <sup>b</sup>	8	28	20	18	26	37	0	29	12	21
19	23	0	25	7	21	13	16	7	25	0	22	0	33
20	17	0	19	0	20	12	8	0	14	0	12	11	21
21	30	0	17	0	15	8	9	15	9	0	20	14	28
22	31	0	8	0	18	13	9	24	9	10	19	7	40
23	23 <sup>b</sup>	0	9	7	34	11	9 <sup>b</sup>	34	9	9	18	7	57
24	26	0	17	7	33	10	17	35	8	7	8	7	60 <sup>b</sup>
25	19	0	9	16	32	9	20 <sup>a</sup>	20 <sup>a</sup>	8	14	0	0	74
26	19 <sup>a</sup>	0	14	17	30	9	25	14	8	8	14	7	71
27	9	0	7	18	26	8	16	0	0	9	8	13	74
28	16	0	8	18	21	8	16	13	0	16	11 <sup>b</sup>	16	65
29	11	0	9	25	17	8	19	11		16 <sup>b</sup>	10	20	50
30	10	0	10	31	9	0	19	8		8	9	30	45
31		0	9		0		11	10		8		40	
Mean	12.4	2.1	16.9	13.4	21.8	5.5	15.0	16.4	23.1	8.7	12.9	18.6	38.5

<sup>a</sup>Ionospheric scintillations exceeding 0.5 dB peak to peak were observed along the POR or IOR satellite link at the Taipei Earth Station.

<sup>b</sup>The level exceeds 1.0 dB.

### 3.3 Cumulative Statistics of Scintillations

For communications system applications (Fang, D. J., et al., 1978), the information most needed for link design is the cumulative statistics, i.e., the percentage of time in a year and in a worst month that ionospheric scintillations exceed a given level. Annual statistics are needed to establish the system margins required to ensure the desired quality of a link. In addition, for digital communications systems, outage conditions such as the loss of synchronization and the time required to restore synchronization are also critical. To establish an outage condition, a typical criterion requires that the mean 1-minute value of the bit-error rate should not be worse than  $10^{-4}$  for more than 0.3 percent time of any month (Fang, D. J., et al., 1978; CCIR Document 4/147, 1976). Consequently, the worst-month occurrence statistics for ionospheric scintillations are also essential.

Figure 6 gives both the annual and worst-month cumulative statistics. Yearly statistics cover the period from June 1, 1976, to May 31, 1977. The POR and IOR statistics are comparable for small peak-to-peak fluctuations. However, they are far apart for fluctuations over 1.5 dB peak-to-peak, with the IOR link showing much more severe fluctuations than the POR link. The difference in statistics for fluctuations over 1.5 dB is caused by two scintillation events on the IOR link, which occurred on April 28 and May 3, 1977. The pattern of the May 3 event is very similar to that of the April 28 event shown in Figure 3, except that it has a peak-to-peak fluctuation of 2.8 dB. If the contributions of these two events were removed, the statistics of the IOR and POR links would be comparable.

The worst-month cumulative statistics can be generated without ambiguity only if an adequate sample size is provided (Crane, R. K., and Debrunner, W. E., 1978). For example, in microwave precipitation studies, the worst-month statistics of rainfall are independent of the definition of worst-month (either calendar month or consecutive 30 days) as long as multiyear data are used to derive the statistics (Crane, R. K., and Debrunner, W. E., 1978). Unfortunately, for gigahertz ionospheric scintillations, the sample sizes are generally small because of the 11-year sunspot cycle. As a result, the concept of worst-month is highly subjective.

It appears that at present the worst-month can be defined either as the worst-calendar month or as the worst 30 days. The worst-calendar month is a month during which the maximum minutes of peak-to-peak signal fluctuations are equal to or greater than 0.5 dB, the minimum detectable level of ionospheric scintillation for the present experiment. Based on this definition, the worst month for both the POR and IOR links is December 1976. The worst 30 days is a continuous 30-day period covering major scintillation events with the highest magnitude of peak-to-peak fluctuations in the entire year. Therefore, the worst 30-day period for the IOR was April 10 to May 9, 1977, when 3.2- and 2.9-dB peak-to-peak fluctuation events were recorded on April 28 and May 3, 1977, respectively. Figure 6 presents worst-month cumulative ionospheric scintillation statistics for either definition. The worst-month statistics (IOR link) differ substantially for these two definitions, which would produce substantial differences in assessing the impact on a digital communications system.

Based on the definition, the worst 30-day statistics will be subject to large ranges of year-to-year and link-to-link variations. Since ionospheric scintillations are seasonal phenomena with peak activity around the equinoxes, the worst 30-day statistics are quite useful to physicists and engineers who analyze the trend of changing scintillation activity at peak periods. However, for the purpose of assessing the outage conditions for a digital communications system, the generally accepted threshold value is a bit-error rate of  $10^{-4}$  that is exceeded less than 0.3 percent of the time in a month. It appears that the worst calendar month statistics are more appropriate for this application.

Another advantage of the worst calendar month statistics is that they are more stable in comparison with the worst 30-day statistics, because the maximum peak-to-peak fluctuations of the most severe scintillation event, which are highly volatile from year to year and link to link, are not part of the definition. Researchers in ionospheric scintillations have given little attention to worst-month statistics because the lack of a data base and the need for defining and studying the "worst-month" was not generally recognized until recently. Since digital modulation techniques are being used increasingly in satellite communications, additional studies of monthly and short-duration scintillation statistics are warranted.

#### 3.4 Power Spectral Density

The mathematical derivation and physical interpretation of the power spectral density for ionospheric scintillation studies have been given in detail (Crane, R. K., 1976). It is generally believed that the correlation function for the electron density irregularities that are responsible for medium-to-strong gigahertz ionospheric scintillations must have power law spectra (Rufenach, C. L., 1975; Crane, R. K., 1976) instead of the well-known Gaussian spectra, which have been successfully used in earlier studies for UHF scintillations (Briggs, B. H., and Parkins, I. A., 1963). The main issue to be settled is the index,  $p$ , of the power law spectra. Different values of  $p$  have been reported for different measurements (Crane, R. K., 1976; Dyson, D. L., et al., 1974).

In the present study, power spectral density plots of the ionospheric scintillation signals were generated by a high-precision spectrum analyzer (Ubiquitous, Model 440A) after the data recorded on magnetic tapes were first detrended by a low pass filter. An x-y plotter was used to produce the distribution. Because of equipment limitations, spurious noise contributions attributable to modulation variation and unavoidable radio-frequency interference (RFI) from the earth station environment were not eliminated.

Figure 7 shows the spectra for the six 10-minute records given in Figure 4. Within the dynamic range of the spectrum analyzer, the vertical scale is adjusted so that the spectra of the six records can be illustrated in one plot. Spectra A and F (before and after the intense signal fluctuation period, respectively) are typical of those produced by weak scintillations. The mean square fluctuations of amplitude increase with frequency at the low frequency end until they reach the maximum near the Fresnel frequency. Beyond the Fresnel frequency, the spectra appear to roll off with the characteristics of a Gaussian form. However, during intense signal fluctuations (B, C, D, and E), the characteristics of roll-off change from the Gaussian form to a power law form. For the four

records (B, C, D, and E) the roll-off slope remains the same, yielding a frequency dependence of  $f^{-3}$ . The power spectral density for the major scintillation which occurred May 2, 1977, is similar to the one presented in Figure 7. In particular, the same  $f^{-3}$  frequency dependence is noted.

The  $f^{-3}$  dependence confirms the high-frequency asymptotes based on theoretical calculations of the power spectral density using a power law spectrum index of  $p = 4$  (Rufenach, C. L., 1975). It is in good agreement with the in situ experimental observations made with the Ogo 6 satellite (Dyson, D. L., 1974), and with the results provided by Crane (Crane, R. K., 1976).

The power spectral density information appears to suggest that the weak scattering theory for a thick screen with a 3-dimensional electron density power law spectrum will be adequate to explain the observed gigahertz scintillations. However, the scintillations observed in the present experiment are relatively mild with peak-to-peak fluctuations of 3-dB only. Much stronger scintillations during higher solar activity are expected, which will determine the merit of the weak scattering theory.

### 3.5 Angle of Arrival Measurement

The basic advantage of using an INTELSAT earth station for ionospheric scintillation measurements is that results such as the cumulative scintillation statistics can be readily applied to estimate the performance of INTELSAT communications links without much further assessment. On the other hand, since the operational earth station is not designed as a research tool for measuring ionospheric scintillation, many important features of ionospheric irregularities cannot be obtained.

Azimuthal and elevational tracking errors were monitored in the Taipei experiment with the anticipation of deducing the information regarding the angle-of-arrival variations, or indirectly the phase variations of the signal produced by ionospheric irregularities. In the data analyses, such information could not be retrieved. In the autotrack mode used for regular traffic conditions, automatic pointing adjustments including overshooting and settling were made continuously rather than in specified increments or decrements. Often, the servo system in steady state would not produce a voltage large enough to be registered in the encoder for the evaluation of angle-of-arrival deviations. The autotracking accuracy is capable of better than one-tenth of the half-power beamwidth, about  $0.01^\circ$ . Although this accuracy is more than adequate for the earth station pointing for satellite communications, it is insufficient for the measurement of changes in the angle-of-arrival caused by ionospheric irregularities known to be the order of  $10^{-4}$  degrees. Consequently, the settling times for the correction of tracking overshoot are too long for any meaningful ionospheric scintillation studies. As a result, angle-of-arrival data collected during the measurement have been insignificant.

It may be speculated that phase variations can be determined indirectly by monitoring the frequency fluctuations in the automatic frequency control (AFC) loop of the earth station receiver. Theoretically, the frequency fluctuation is proportional to the Doppler shift produced by drifting ionospheric irregularities. Therefore, the Doppler spectrum should be related to the phase spectrum by an integration factor. This technique remains to be tested.

## 4. CONCLUSIONS

INTELSAT communications satellite signals were used to monitor ionospheric scintillations for one year at the Taipei Earth Station, beginning in June 1976. Less than 12 scintillation events were observed, with peak-to-peak fluctuations over 1.0 dB. When the results were compared with those generated in earlier programs, the dependence of scintillations on the annual level of solar activity became evident and was plotted in Figure 5. The dependence was only of a gross nature. There appeared to be no correlation between scintillations and daily sunspot numbers.

Contrary to earlier observations, correlations of scintillations between the IOR and the POR links appeared to be unrecognizable, based on the results of the Taipei measurement. Most of the events occurred only along one link, i.e., the IOR link. Consequently, the annual cumulative statistics of scintillation for the two links differed considerably. The worst-month cumulative statistics will remain uncertain until an agreed-upon definition of worst-month can be postulated.

Power spectral density analyses indicate an  $f^{-3}$  dependence of the ionospheric scintillation spectra versus frequency, which confirms the high-frequency asymptotes based on theoretical calculations. It suggests that the weak scattering theory for a thick screen with a power-law electron density fluctuation spectrum of  $p = 4$  would be adequate to explain the weak gigahertz scintillations observed at the Taipei Earth Station.

Using an operational INTELSAT earth station to observe angle-of-arrival signals by monitoring the azimuthal and elevational tracking errors appears to be impractical. An alternative approach may be the use of AFC loop frequencies to assess the Doppler information produced by drifting ionospheric irregularities.

## ACKNOWLEDGMENT

This paper is based on work performed under the sponsorship of the International Telecommunications Satellite Organization (INTELSAT). Views expressed are not necessarily those of INTELSAT.

The author wishes to express his sincere appreciation to Taipei Earth Station personnel for their enthusiastic cooperation in performing the experiment. Thanks are due to Mr. F. T. Tseng for his effort in performing the power spectral density analyses. Careful data reduction by Mrs. K. Yeh is also gratefully acknowledged.

## REFERENCES

- Basu, S., et al., 1977, "Preliminary Comparison of VHF Maps of F Region Irregularities with Scintillations in the Equatorial Region," Journal of Atmospheric and Terrestrial Physics, Vol. 39, pp. 1251-1261.
- Booker, H. G., and Gordon, W. E., 1950, "A Theory of Radio Scattering in the Troposphere," Proc. I.R.E., Vol. 38, pp. 401-412.
- Bowles, K. L., 1964, "Radio Scattering in the Ionosphere," Advances in Electronics and Electron Physics, Vol. 19, pp. 55-176.
- Briggs, B. H., and Parkins, I. A., 1963, "On the Variation of Radio Star and Satellite Scintillations with Zenith Angle," Journal of Atmospheric and Terrestrial Physics, Vol. 25, p. 339.
- CCIR Study Group 4A Document 4/147, "Systems in the Fixed-Satellite Service Using PCM for Telephony; Bit Error Rates at the Output of the Hypothetical Reference Circuit," United States Contribution, May 24, 1976.
- Craft, H. D., and Westerlund, L. H., 1972, "Scintillations at 4 and 6 GHz Caused by the Ionosphere," AIAA Tenth Aerospace Sciences Meeting, San Diego, California, January 17-19, 1972, Paper No. 72-179.
- Crane, R. K., 1976, "Spectra of Ionospheric Scintillation," Journal of Geophysical Research, Vol. 81, pp. 2041-2050.
- Crane, R. K., and Debrunner, W. E., 1978, "Worst Month Statistics," Electronics Letters, Vol. 14, pp. 36-40.
- Dyson, D. L., McClure, J. P., and Hanson, W. B., 1974, "In Situ Measurements of the Spectral Characteristics of F Region Ionospheric Irregularities," Journal of Geophysical Research, Vol. 79, pp. 1497-1502.
- Fang, D. J., Kennedy, D. J., and Devieux, C., 1978, "Ionospheric Scintillations at 4/6 GHz and their System Impact," EASCON-78 paper, IEEE Pub. No. CH1352-4/78/0000-0385.
- Fremouw, E. J., and Rino, C. L., 1973, "An Empirical Model for Average F-Layer Scintillation at VHF/UHF," Radio Science, Vol. 8, p. 213.
- Goodman, J. M., 1978, "UHF Scintillation at High Latitudes for a Brief Period During 1976," Effect of the Ionosphere on Space and Terrestrial Systems, U.S. Govt. Printing Office, J. M. Goodman, ed., NRL/ONR.
- Liu, C. H., and Yeh, K. C., 1977, "Model Computations for Ionospheric Scintillations at GHz Frequencies," Journal of Atmospheric and Terrestrial Physics, Vol. 39, pp. 149-156.
- Paulson, M. R., and Hopkins, R. U. F., 1977, "Spatial Distribution Characteristics of Equatorial Scintillation," NOSC-TR-113, Naval Ocean Systems Center, San Diego, California.
- Ratcliffe, J. A., 1956, "Some Aspects of Diffraction Theory and Their Application to the Ionosphere," Report on Progress in Physics, Vol. XIX, pp. 188-267.
- Rufenach, C. L., 1975, "Ionospheric Scintillation by a Random Phase Screen-Spatial Approach," Radio Science, Vol. 10, pp. 155-165.
- Skinner, N. J., Kelleher, R. F., Hacking, J. B., and Benson, C. W., 1971, "Scintillation Fading of Signals in the SHF Band," Nature, Vol. 232, pp. 19-21.
- Taur, R. R., 1974, "Ionospheric Scintillation at Frequencies Above 1 GHz," COMSAT Technical Review, Vol. 4, pp. 461-476.
- Taur, R. R., 1976, "Simultaneous 1.5- and 4-GHz Ionospheric Scintillation Measurements," Radio Science, Vol. 11, pp. 1029-1036.
- van de Hulst, H. C., 1957, Light Scattering by Small Particles, Wiley, New York.

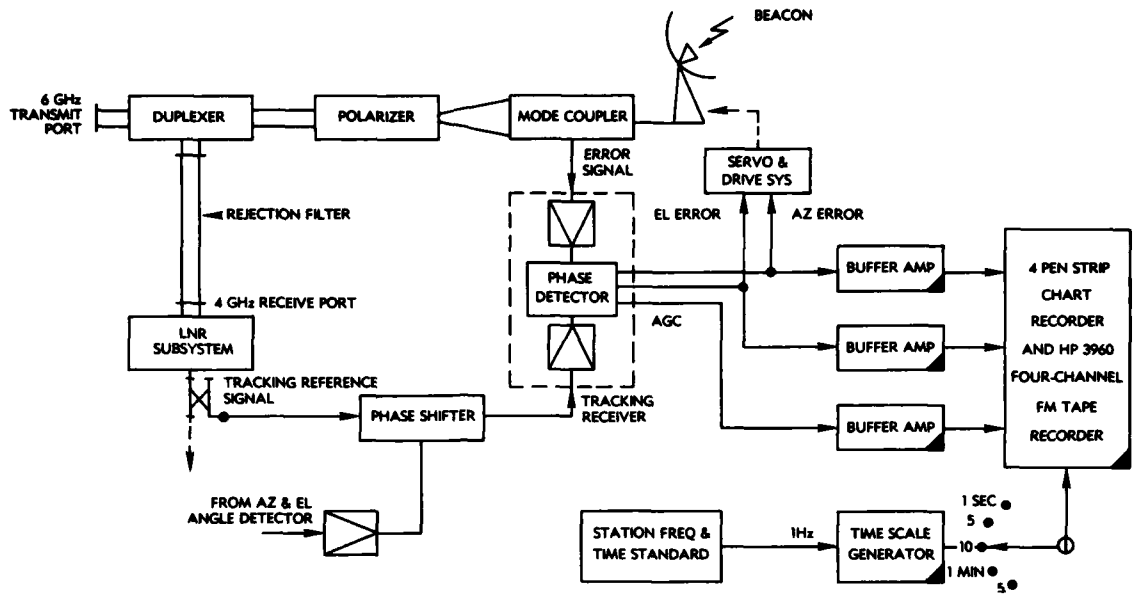


Figure 1. Ionospheric Scintillation Measurement Configuration

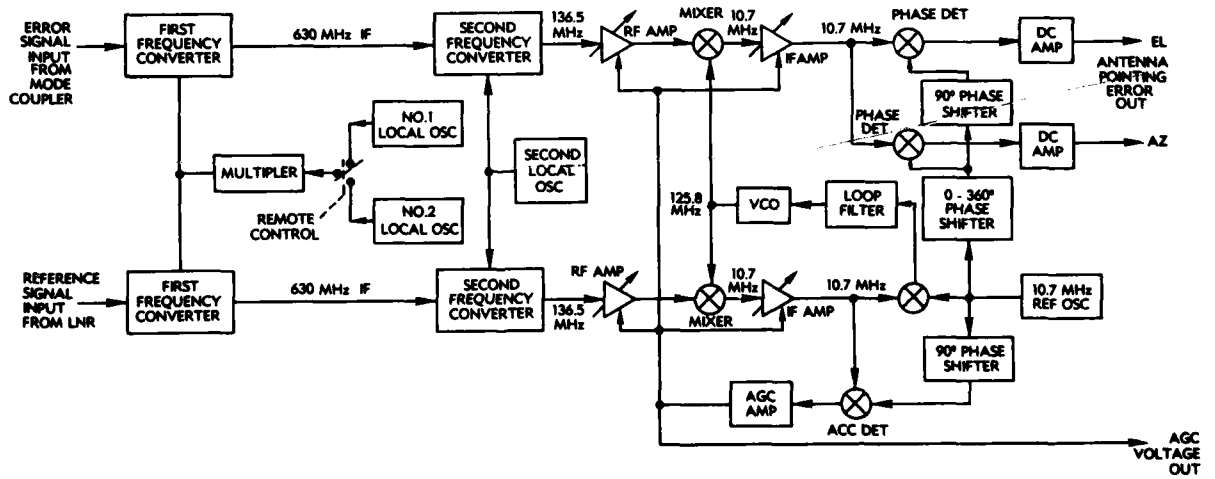


Figure 2. Simplified Block Diagram of Tracking Down-Converter and Demodulator

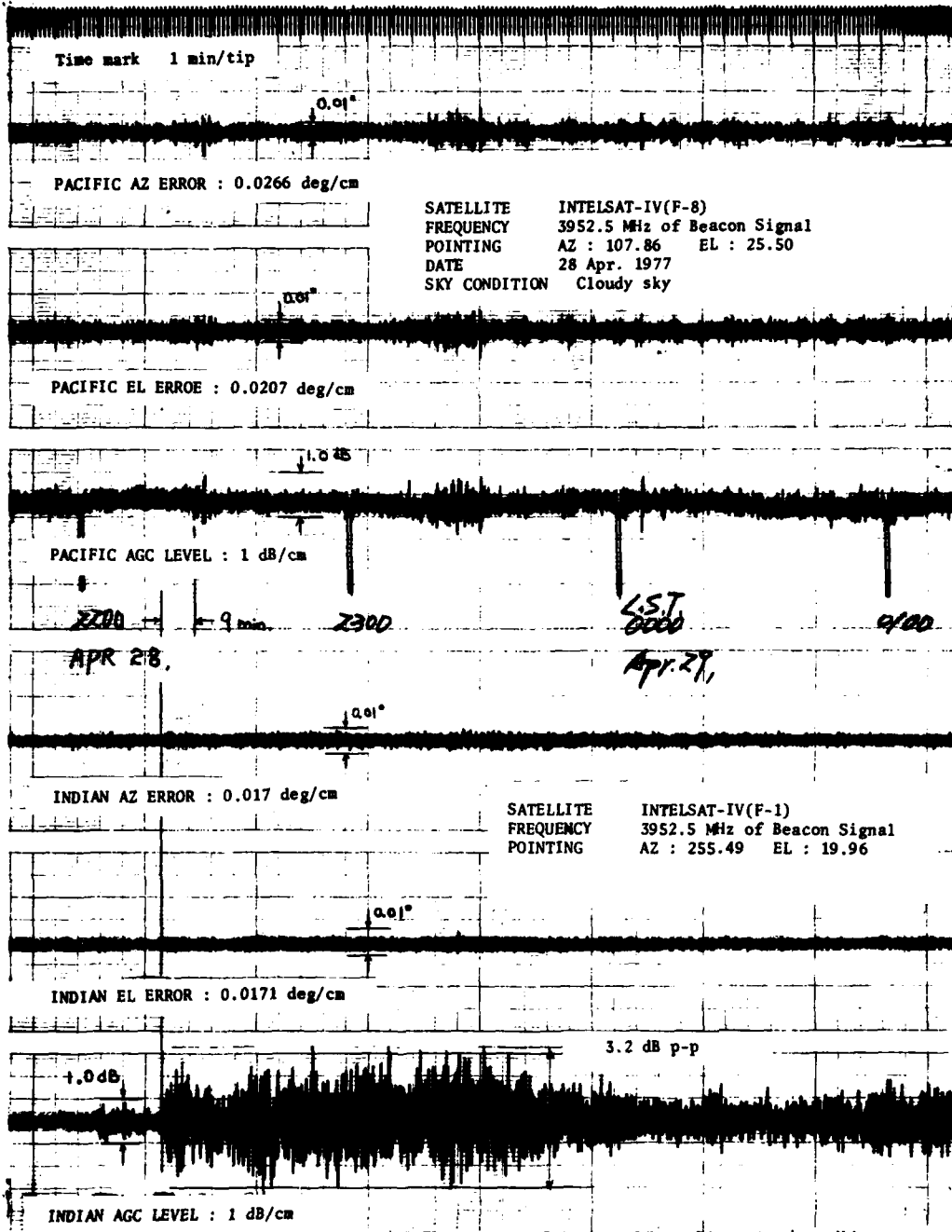
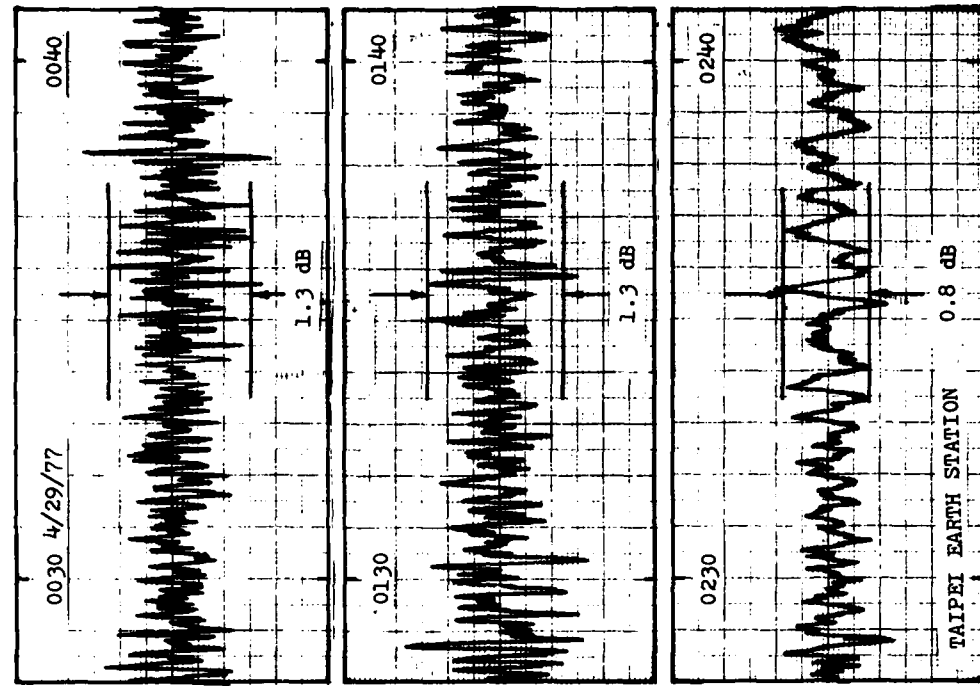


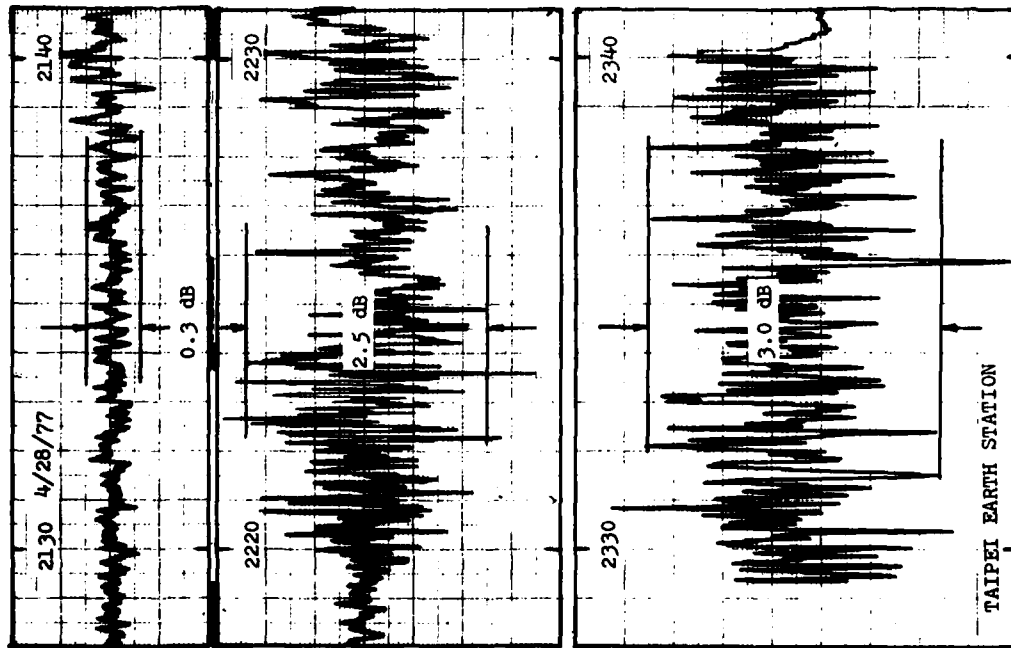
Figure 3. Typical Strip Chart Record of Ionospheric Scintillation on April 28-29, 1977



D: TWO HOURS AFTER

E: THREE HOURS AFTER

F: FOUR HOURS AFTER



A: 30 MINUTES BEFORE

B: AT THE BEGINNING

C: ONE HOUR AFTER

Samples of the Record of Ionospheric Scintillations on April 28-29, 1977

Samples of the Record of Ionospheric Scintillations on April 28-29, 1977

Figure 4. Expanded 10-Minute Samples of the IOR-AGC Record of Ionospheric Scintillations on April 28-29, 1977



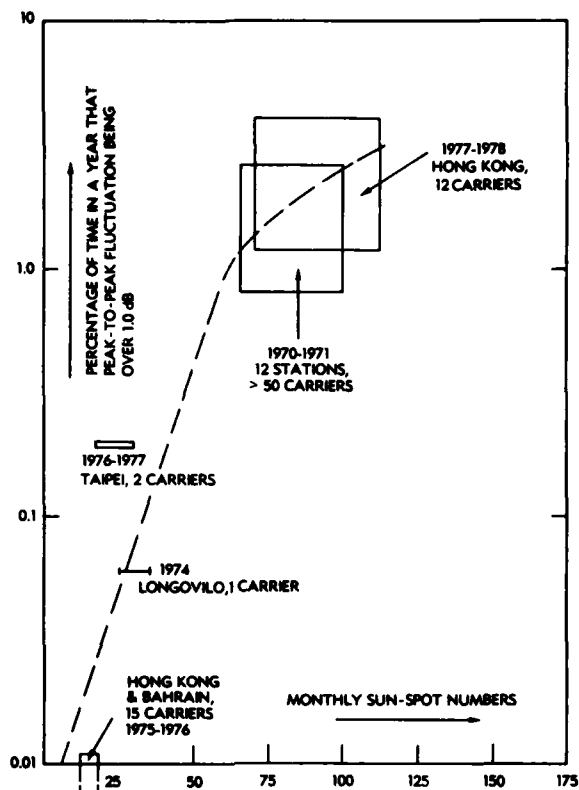


Figure 5. Occurrence of Ionospheric Scintillation vs Sunspot Numbers

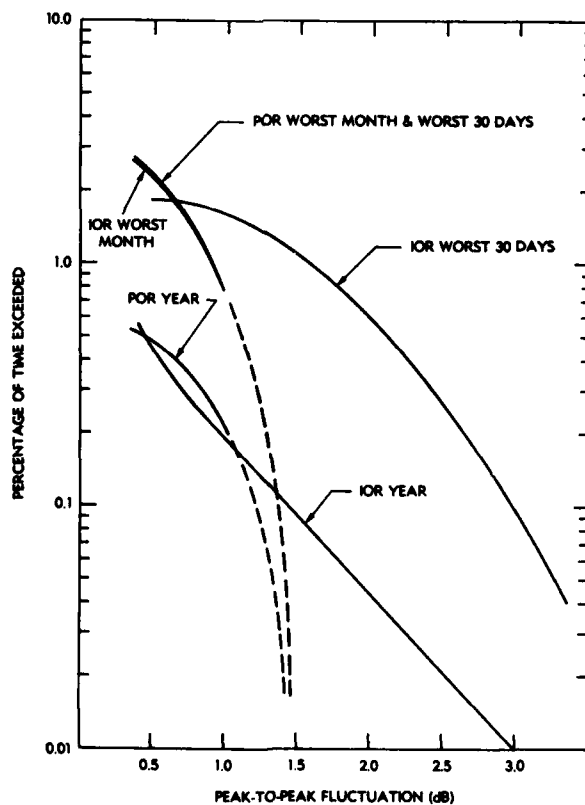


Figure 6. Annual and Worst-Month Cumulative Statistics of Ionospheric Scintillation

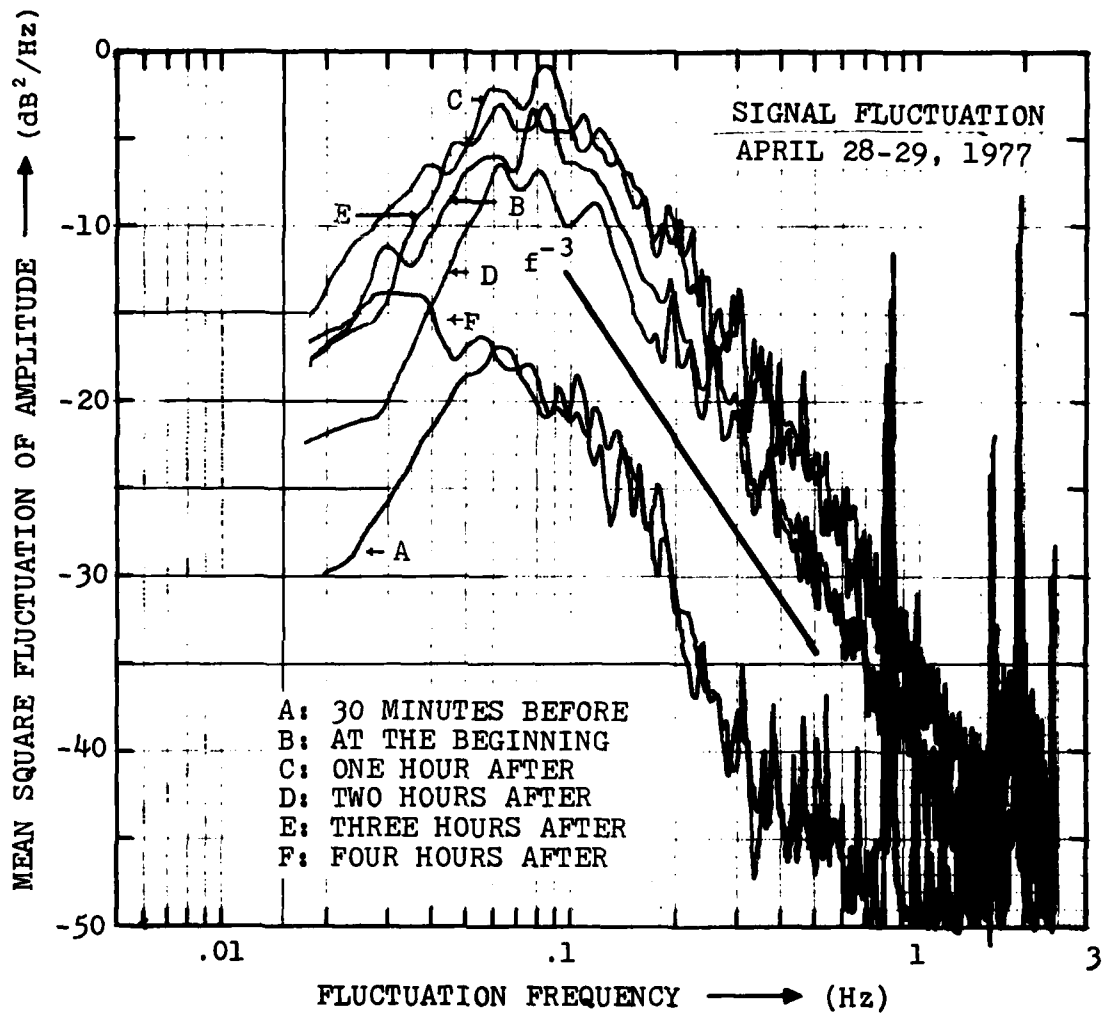


Figure 7. Power Spectral Density for the Six 10-Minute Sample Periods Given in Figure 4

PROPAGATION ANOMALIES AFFECTING AIRBORNE SATELLITE COMMUNICATIONS

Allen L. Johnson  
Air Force Wright Aeronautical Laboratories  
Wright-Patterson AFB, Ohio

SUMMARY

Airborne satellite communication and navigation systems can be disrupted by propagation anomalies. Ionospheric scintillation fading and earth multipath fading can cause 15 to 30 db amplitude fading and over 1000 degree per second phase variations which can reduce message intelligibility and navigation accuracy. The ionospheric scintillation effects are particularly severe in the polar and equatorial regions. The multipath effects are worse over water at low elevation angles to the satellite. Diversity techniques can be used to mitigate the disruptive effects of both the ionospheric scintillation and earth multipath. While frequency, space and time diversity all improve the signal performance against earth multipath fading, only time diversity offers a significant improvement against ionospheric scintillation fading in an airborne environment.

1. INTRODUCTION

The performance of airborne satellite communication and navigation systems can be severely degraded by ionospheric scintillation and multipath fading. This paper reviews the results of airborne equatorial and polar ionospheric scintillation tests and the airborne multipath tests performed during the past twelve years to derive information on the fading characteristics and mitigation techniques which could overcome the detrimental effects of these propagation anomalies on system performance.

2. EQUATORIAL IONOSPHERIC SCINTILLATION

The past decade has seen an extensive multi-nation campaign to quantify and model the equatorial ionospheric scintillation phenomena (Aarons 1976, Ossakow 1979, Koster 1971). A comprehensive picture of the ionospheric irregularity has been developed by theoretical studies, earth terminal-to-satellite observations and in situ measurements along the magnetic equator. The current knowledge indicates that the ionospheric irregularities form in the F region (200 to 400 kilometers altitude) one to two hours after local sunset. The irregularities develop in patches along the equator, developing westward at a velocity approximating the sun terminator velocity. The patches develop with an east-west size of 50 to 200 kilometers (Aarons et al, 1979-1). Following the initial irregularity development an upward velocity occurs causing the patch to extend from its 200 kilometer bottom side with a plume reaching up to approximately 1000 kilometer altitude. During this vertical development there is also a north-south propagation of the irregularity along the magnetic field lines. Recent measurements indicate the north-south propagation to occur at speeds of approximately 400 meters per second (Johnson et al, 1979-1).

The equatorial ionospheric irregularities result from a depletion of electrons compared with the surrounding F region. This depletion results in sharp gradients with abrupt changes in electron content of one to three orders of magnitude. Once formed, the irregularities drift in an easterly direction with velocities of 100 to 200 meters per second. The initial velocities, immediately after formation, appear to be higher than the later velocities. Individual irregularity patches have been tracked for periods of up to three hours using an all-sky photometer at 6300 Å to measure the air glow (Weber et al, 1978). Irregularity patches with a north-south extent of two thousand kilometers have been observed. Irregularities often occur in series with alternating disturbed and undisturbed ionospheric patches. Ground measurements and all-sky photometer measurements often have identified groups of four or five patches more or less uniformly spaced (Weber et al, 1978). Along the magnetic equator the irregularity patches tend to have a thin fabric of irregularities connecting the patches. This thin irregularity structure between patches causes only minor ionospheric scintillation. As one travels away from the magnetic equator, the fabric connecting the irregularities disappears leaving distinct field aligned irregularities separated by undisturbed ionosphere.

The occurrence of equatorial ionospheric disturbances appears to increase during the sun spot maximum. There also appears to be a negative correlation between irregularity formation and magnetic index (Koster 1971, Singleton 1978). During periods of strong magnetic activity scintillation occurrence is minimized. The occurrence of equatorial ionospheric irregularities follows a seasonal pattern which varies, depending upon the observer's location along the magnetic equator. In general, the occurrence peaks up during the equinox periods and remains relatively strong during the local summer. A minimum occurrence is noted during the local winter.

The trigger mechanism which causes the irregularity formation has not been identified. During the scintillation season an observer along the magnetic equator may see several nights of strong irregularity formation interspersed with nights of absolutely no ionospheric disturbances. Correlation with solar flux density or magnetic intensity offers little explanation for the erratic occurrence of the irregularity patches.

The irregularities primarily affect the VHF and UHF bands. Earth terminal-to-satellite links of 100 to 500 MHz are severely affect by the equatorial ionospheric scintillation. When the irregularity patches occur, fading of 20 to 35 db peak-to-peak is regularly encountered (Whitney 1979). Frequencies from 500 MHz up to 2 GHz experience moderate scintillation fading with 2 GHz fades of 3 to 6 db under severe conditions (Taur 1973). Frequencies from 4 to 8 GHz experience only minor scintillation effects of 1 or 2 db fading during severe irregularities (Johnson et al, 1973).

The onset of scintillation is very abrupt, especially for an airborne terminal. The fading often goes from less than 1 db to 30 db in sixty seconds. With aircraft flying in a westerly direction against the eastwardly drift of the irregularity, abrupt onsets of scintillation have been observed in 10 to 20 second periods, Figure 1 (Johnson 1972). The fading rate tends to be greater in the premidnight period

when the velocity of the irregularity is normally greatest. Airborne measurements show that the fading rate is sensitive to aircraft direction. An aircraft flying westwardly against the irregularity drift may record fading rates of 1 Hz or greater, Figure 2 (Johnson 1979-1). An aircraft flying in an eastward direction can effectively synchronize its motion with that of the irregularity patch and may encounter one fade in 60 to 120 seconds. The severe amplitude fading encountered in the equatorial region tends to be Rayleigh distributed. The equatorial ionospheric irregularities do not present an attenuation factor to the satellite-to-earth signal but merely redistribute the energy into enhanced areas and null areas. Enhancements of 6 to 10 db are encountered during severe fading along with fades of 15 to 20 db.

Power spectral density plots of the fading amplitude indicate that the slope has a power law relationship which appears sensitive to aircraft direction. While flying westwardly against the velocity of the patch of the irregularity, slopes of  $f^{-5}$  have been observed, Figure 3. While flying eastwardly with the velocity of the patch, slopes tend to be  $f^{-2}$  or  $f^{-3}$  (Johnson 1979-1, Whitney et al, 1977).

The autocorrelation function of the severe amplitude equatorial fading decreases to one-half its value in a time which varies with aircraft flight direction. While flying in a westward direction, autocorrelation decay times of one-tenth of a second have been recorded. While flying in an easterly direction, autocorrelation times as long as ten seconds have been recorded (Johnson 1979-1).

The strong amplitude scintillation is accompanied by phase scintillation. Measurements made at 250 MHz in the equatorial region showed phase scintillations with abrupt phase changes at a rate of  $2\pi$  to  $16\pi$  radians per second, Figure 4 (Prettie et al, 1977).

### 3. POLAR IONOSPHERIC SCINTILLATION

The development of a polar ionospheric irregularity model is at a state roughly equivalent to the equatorial model development a decade ago. The infancy of the model development is due to the lack of extensive observation stations in the polar region. While the equatorial region is characterized by nearly horizontal, parallel flux tubes, the polar region encounters magnetic flux tubes at a near vertical geometry. The effect of particle precipitation and magnetic storms is severe in the polar region. Polar observation by fixed ground stations and airborne portable terminals has been carried out for the past ten or twelve years. Using extensive ground measurements at 137 MHz Aarons, et al (1979-2) has developed a heuristic, analytical model to which the ground observations were fitted. This model uses the magnetic index  $K_p$ , solar flux  $S_f$ , seasonal period and local time-of-day to describe the scintillation fading expected.

$$\text{Scintillation Index} = f(K_p, S_f, \text{Day-of-Year}, \text{Time-of-Day})$$

The model predicts irregularity maximums during the summer period and minimums during the winter period. Aarons' formula indicates that for southern Greenland the magnetic index tends to have a stronger influence than solar flux density. Aarons indicates that his formula is dependent upon observations made primarily during the sunspot minimum and that the observations were primarily through the auroral oval.

The irregularity formation in the polar region, as in the equatorial region, tends to be elongated along the magnetic field lines. Elongations of five to ten times the irregularity width have been postulated from measurements (Aarons et al, 1979-2). The fact that these irregularities are at steep angles to the horizon make the observations very geometry sensitive. Measurements by Reno, et al (1978) indicate that observations which are L-shell aligned experience more scintillation than non-aligned observations.

A series of observations by the Air Force Avionics Laboratory and the Air Force Geophysics Laboratory using airborne terminals in the polar cap region has provided extensive new scintillation data for that region. A series of joint observations during January 1979 experienced extensive scintillation in the polar cap region (Johnson, et al 1979-2). These flights, made during a high solar flux density period ( $S_f = 250$ ), indicate that scintillation activity in the polar cap may be more strongly dependent on solar flux density than equatorial or auroral scintillation. The first polar cap flight during January resulted in scintillation of 5 db or more being experienced 96% of the flight time. Scintillations greater than 20 db amplitude were experienced about 60% of the flight time. Fading rates varied from 15 to 30 fades per minute.

The scintillation experienced appeared to be patchy with strong scintillation occurring for fifteen to thirty minutes, followed by brief, quiet periods. The second flight in January into the polar cap produced scintillation 68% of the flight time. The third flight showed scintillation occurrences 83% of the flight time. The polar cap scintillation experienced in January was as severe and rapid as strong equatorial scintillation. An autocorrelation function of the amplitude scintillation decreased to one-half of its value in less than 0.4 seconds. The power spectral density of the amplitude fading showed a power law relationship for the slope of  $f^{-3}$  and a corner frequency of approximately 0.2 Hz.

UHF phase scintillations were also measured in the polar region. During the January tests phase scintillations with variations up to  $10\pi$  radians per second were recorded during the extensive amplitude scintillation, Figure 5.

Observations of the polar ionospheric irregularities using an all-sky photometer at 6300 Å showed irregularities drifting away from the noontime auroral oval and drifting across the polar cap (E. J. Weber, private communications). These irregularities appear to be 100 to 300 kilometers in diameter. It is postulated the irregularities drift away from the sun across the polar cap and then reform and rejoin the auroral oval in a two-cell circulation back to the noontime side. Measurements of the ionospheric F layer height using an airborne HF ionosonde showed the F layer undisturbed height to be four or five hundred kilometers prior to the onset of fading (J. Buchau, private communications). The F region height dropped to a few hundred kilometers during the scintillation period and then rose again after the irregularity had passed.

During July 1979 another series of polar cap flights was conducted. Three eight-hour flights into the polar cap during July resulted in zero scintillation observations at 250 MHz (Johnson, et al 1979-3). The solar flux density during July was at a temporary minimum of 150. These observations tend to support the theory that solar flux density plays a prominent role in polar cap irregularity formation.

During December 1979 another joint polar expedition was flown. These flights corresponded to a high solar flux density (250). Extensive amplitude and phase scintillation were recorded approximately 90% of the flight time in the polar cap region (Johnson 1980-1).

#### 4. MULTIPATH FADING

Airborne multipath fading caused by terrain reflections can also severely disrupt communication-navigation system performance. The disruption is caused by the destructive interference of the direct and reflected signal. The severity of the multipath fading is dependent upon the ratio of the amplitude of the direct signal and the reflected signal. The reflected signal consists of a specular or geometrically reflected component and a diffuse, or scattered component. The depth of the two ray multipath fading is determined by the following equation (Reed & Russel, 1953):

$$F \text{ db} = 20 \log [1 - \frac{X_1}{X_2} \times K_t \times K_r \times |R| \times D \times S].$$

where:

- $X_1$  = Direct path length from satellite to aircraft
- $X_2$  = Reflected path length from satellite to aircraft
- $K_t$  = Ratio of transmit antenna gain toward reflection point to transmit antenna gain along direct path (transmit antenna illumination factor)
- $K_r$  = Receive antenna illumination factor
- $R$  = Complex reflection coefficient
- $D$  = Divergence factor (spread or reflected wave from curved earth)
- $S$  = Surface roughness factor

The antenna illumination factor, or antenna pattern, has a major influence on the multipath severity. This is the primary factor over which the system designer has any control. By choosing an antenna that maximizes the gain towards the direct path and minimizes the gain in the direction of the reflection, the system designer can minimize multipath fading depth.

While multipath fading does not have a strong inherent frequency dependence, the practical choice of antennas makes the VHF and UHF frequencies more prone to multipath than microwave frequencies. VHF and UHF airborne antennas tend to be omnidirectional, having nearly equal gain for both the direct and reflected path. Microwave airborne antennas tend to be directive, thereby minimizing the gain in the directions of the reflection. For this reason VHF and UHF aircraft-to-satellite links are most severely affected by multipath fading.

The simplest airborne antennas provide an omnidirectional gain pattern over the upper hemisphere. Antenna illumination factors will vary with antenna placement and with azimuth angle. Variations from .03 to 1.0 have been recorded (Clanton 1974).

The reflection coefficient is modified by the surface roughness factor to account for the specular and diffuse reflections. The reflections coefficient is dependent upon the physical constants of the reflecting surface. Most of the irregular surfaces, such as mountains, forests and broken terrain, have a very low reflection coefficient causing only intermittent, sporadic reflections (Salter 1966). Smooth surfaces with high conductivity such as sea water tend to have very high reflection coefficients (Chinnich 1977). Correspondingly, multipath fading occurs primarily over ocean or large bodies of water. Reflection coefficient is dependent upon polarization as well as surface conditions. Horizontal polarization tends to be reflected more effectively than vertical polarization. The vertically polarized wave goes through a minimum in amplitude and a 180° phase reversal at an angle defined as the Brewster angle. For sea water this occurs in the 5 to 8° elevation angle. This fact gives circular polarization a degree of multipath protection by causing a reversal in the sense of the polarization at reflection angles above the Brewster angle (Jordan 1969).

The other factor affecting multipath fade depth is the divergence of the reflected wave from the curved earth. This factor tends to be unimportant for aircraft-to-satellite communications except for low elevation angles or very high aircraft altitudes (Johnson 1979-2).

A typical multipath fade depth for an airborne terminal operating in the UHF band flying over water ranges from 5 to 15 db, Figure 6. The rate of the fading is dependent upon the geometry between the aircraft flight direction and the satellite motion. For subsonic aircraft flying directly towards the satellite at low elevation angles fade rates of 1 Hz can be experienced. For higher elevation angles or other aircraft directions fade rates of 0.1 to 0.2 Hz are typical. Flights over ice and deep snow have shown strong multipath reflections with fading equivalent to sea water or a large lake (Johnson & Miller 1970).

Recent airborne observations have revealed an unexpected area of strong multipath fading. This fading occurs when an aircraft traverses the coastline of a land mass (Johnson 1978). Apparently the locally smooth ocean surface near the shore causes an unexpected strong multipath reflection. Multipath fading

has been experienced over coastal areas at high elevation angles to the satellite where the antenna discrimination factor between the direct and reflected would normally reduce the multipath to an unnoticeable amplitude. Measurements made at 40 to 80° elevation angles using a directive overhead UHF antenna have shown multipath fading of 2 to 4 db of amplitude, Figure 7 (Johnson 1980-2).

#### 5. MITIGATION TECHNIQUES FOR IONOSPHERIC SCINTILLATION FADING

Ionospheric scintillation fading tends to cover a broad frequency band. For this reason frequency diversity appears to offer little advantage for mitigating ionospheric scintillation fading. At 300 MHz frequency separations of 100 MHz would be required to provide any significant diversity improvement. Measurements of space diversity made by Paulson and Hopkins (1977) showed space diversity requires antenna separations of 500 to 1000 meters to obtain good decorrelation. Obviously, airborne platforms cannot provide this much antenna separation. Polarization diversity offers no improvement for UHF frequencies against ionospheric scintillation.

One space diversity technique which would provide significant improvement at the cost of system complication is the use of two satellites. Spaced satellites would allow the aircraft-to-satellite paths to be spatially separated to decorrelate the fading and offer a diversity improvement. However, such a technique would complicate the system operation.

The technique which appears to offer significant improvement is the use of time diversity. Since ionospheric scintillation fading has no significant attenuation factor associated with it, it should be possible to make use of the periods of normal or enhanced signal amplitude to carry through the periods of degraded signal amplitude. Several systems involving forward error correction coding and interleaving have been built and tested (Fischbach, 1977; White, 1977). These techniques use one-half rate or three-quarter rate forward error correction coding along with bit interleaving to compensate for the fade periods. Since the fading is relatively long, large bursts of errors are periodically generated. The use of bit interleaving randomizes these burst errors providing a more uniform distribution of bit errors. The forward error correction decoder can then operate on the randomly distributed errors providing an error free decoded message. Systems have been tested in both the equatorial and polar scintillation conditions and have shown that error free message copy can be accomplished even during severe scintillation periods.

Another technique which offers a pseudo space diversity approach is the use of the bottom mounted aircraft antenna in conjunction with the upper top mounted antenna. Experimental tests have shown that at relatively high elevation angles sea multipath degrades the signal amplitude only 3 to 6 db (Johnson 1979-3). If the aircraft-to-satellite path is 40° elevation or greater, the direct path and sea reflected path propagate through different parts of the ionosphere, resulting in a space diversity. In addition, the sea multipath reflection area is a large area encompassing the first Fresnel zone and inherently displays a space diversity characteristic. Measurements made in the equatorial region during severe ionospheric scintillation showed the multipath reflected signal to display considerably less amplitude variations than the direct signal received by a top mounted antenna. Therefore, the combination of the sea multipath and direct signal using a diversity combiner or even the use of the multipath signal by itself offers a significant degree of scintillation protection. Measurements made in the equatorial region indicated that the effect of severe ionospheric equatorial scintillation can be reduced significantly using this technique (Johnson 1978).

#### 6. MITIGATION TECHNIQUES FOR MULTIPATH FADING

Multipath fading on the path from an aircraft-to-satellite tends to be very frequency selective. Therefore, a relatively small amount of frequency separation can provide a diversity signal which can significantly reduce the multipath fading effect. Frequency separations of 300 to 500 KHz are sufficient to provide multipath protection down to 2 or 3° elevation angles (Jordan 1969). Antenna space diversity is another technique which can overcome multipath fading. Location of UHF antennas on top and bottom of an aircraft can provide sufficient vertical separation to significantly reduce the multipath fading amplitude (Johnson & Miller 1970). Antenna polarization is another good mitigation technique. The use of circular polarization on the satellite can significantly reduce the multipath fading amplitude. An additional technique which the designer can use to minimize multipath fading is the optimum choice of antenna pattern shape and antenna location to emphasize the gain in the direction of the satellite while minimizing the gain in the direction of the horizon.

#### BIBLIOGRAPHY

1. Aarons, J. (76): Equatorial Scintillation - A Review. Air Force Geophysics Laboratory TR 76-0078; Hanscom AFB, MA; 13 April 1976.
2. Aarons, J., P. Mullens, H. E. Whitney, E. M. MacKenzie (79-1): The Dynamics of Equatorial Irregularity Patch Formation, Motion and Decay. J. Geophys Res 1979.
3. Aarons, J., E. MacKenzie, K. Bhavanani (79-2): High Latitude Analytical Formulas for Scintillation Levels. Radio Science, 1979.
4. Chinnich, J. H. (77): A Report on Low Angle Ocean Scatter Measurements. Communication Research Centre Report; Ottawa, Canada; 29 August 1977.
5. Clanton, S. (74): AFSCS Antenna Patterns on B52-H. Boeing Test Report T-3-1687; Reston, Wash.; 25 April 1974.
6. Fischbach, W. O. (77): Fade Resistant Modem Operation With Ionospheric Scintillation. AFAL Internal Memo 77-40; Wright-Patterson AFB, Ohio; 1 July 1977.
7. Johnson, A. L., M. A. Miller (70): Three Years of Airborne Communication Testing Via Satellite Relay. Air Force Avionics Laboratory Tech Rpt. 70-156; Wright-Patterson AFB, Ohio; November 1970.

## BIBLIOGRAPHY (Cont.)

8. Johnson, A. L. (72): Equatorial Ionospheric Scintillation Flight Testing. Air Force Avionics Laboratory Tech Rpt 72-363; Wright-Patterson AFB, Ohio, Dec. 72.
9. Johnson, A. L., R. C. Beach, T. A. Grizinski (73): UHF/SHF Ionospheric Scintillation Test. AFAL Internal Memo 73-6; Wright-Patterson AFB, Ohio; 8 April 1973.
10. Johnson, A. L. (78): Dual Frequency SATCOM Atlantic Flight Test Report. AFAL Internal Tech Memo 78-34; Wright-Patterson AFB, Ohio; 25 Dec 78.
11. Johnson, A. L. (79-1): The Effect of Ionospheric Scintillation Fading on Air-to-Satellite Communications. Air Force Avionics Laboratory Tech Report AFAL-TR-78-171; Wright-Patterson AFB, Ohio; Feb 79.
12. Johnson, A. L. (79-2): Airborne Measurements of Electromagnetic Wave Reflections from Land and Sea Water. AGARD Symposium; Spatind, Norway, Paper #11; Sept 79.
13. Johnson, A. L. (79-3): UHF Multipath Test. AFAL Internal Tech Memo 79-2; Wright-Patterson AFB, Ohio; 1 March 1979.
14. Johnson, A. L., R. C. Beach, W. O. Fischbach, R. N. Wright (79-1): South American Test Report. AFAL Internal Tech Memo 79-14; Wright-Patterson AFB, Ohio; 9 July 1979.
15. Johnson, A. L., R. Swanson, R. Beach (79-2): 1979 SATCOM Polar Flight Test. Internal Tech Memo 79-1; Wright-Patterson AFB, Ohio; 28 February 1979.
16. Johnson, A. L., R. L. Swanson (79-3): Polar-Pacific Flight Test Report. AFAL Internal Tech Memo 79-21; Wright-Patterson AFB, Ohio; Dec 79.
17. Johnson, A. L. 80-1: Polar-Atlantic Flight Test Report. AFAL Internal Tech Memo 80-1; Wright-Patterson AFB, Ohio; Feb 80.
18. Johnson, A. L. (80-2): Coastal Multipath Fading. Air Force Avionics Laboratory Tech Rpt 80-2; Wright-Patterson AFB, Ohio; Feb 80.
19. Jordan, K. L., Jr. (69): Multipath Characteristics in A Satellite-Aircraft Link at 230 MHz. MIT Lincoln Laboratory Rpt MS2605; Lexington, Mass.; September 1969.
20. Koster, J. R. (71): Ionospheric Research Using Satellites - Equatorial Scintillation. Scientific Report #1; University of Ghana, Accra, Ghana; September 1971.
21. Ossakow, S. L. (79): A Review of Recent Results of Spread F Theory. Naval Research Laboratory; Memo Rpt 2909; Washington D. C.; 9 January 1979.
22. Paulson, M. R., RUF Hopkins (77): Spatial Distribution Characteristics of Equatorial Scintillation. Naval Ocean System Center Tech Rpt. 113; San Diego, CA; 2 May 77.
23. Prettie, Dr. C., A. Johnson, Dr. J. Marshall, T. Grizinski and R. Swanson (77): Project STRESS Satellite Communication Test Results. Air Force Avionics Laboratory Tech Report AFAL-TR-77-158; Wright-Patterson AFB, Ohio; July 1977.
24. Reed, H. R., C. M. Russell (53): Ultra High Frequency Propagation. New York: John Wiley & Son, 1953.
25. Rino, C. L., R. C. Livingston and S. J. Matthews (78): Evidence for Sheetlike Auroral Ionospheric Irregularities. Geophys Res Ltr 5; 1039-1042, 1978.
26. Salter, R. E. (66): An Investigation of Airborne Microwave Communications. System Eng. Group Tech Rpt 66-31; Wright-Patterson AFB, Ohio; 1966.
27. Singleton, D. G. (78): Predicting Transionospheric Propagation Conditions. Electronics Research Laboratory Tech Rpt 0049; Salisbury, South Australia, Nov 78.
28. Taur, R. R. (73): Ionospheric Scintillation at Frequencies Above One GHz. COMSAT Laboratories Tech Memo CL-29-73; Clarksburg, MD; 2 Aug 73.
29. Weber, E. J., J. Buchau, J. G. Moore (78): Airborne All-Sky Imaging of Equatorial Airglw. Air Force Geophysics Laboratory TR-78-0224; Hanscom AFB, MA - 21 Sept 1978.
30. White, D. P. (77): A Time Diversity Coding Experiment for UHF/VHF Satellite Channel with Scintillation. Lincoln Laboratory Tech Note 1977-22; Lexington, MA; 1 Sept 1977.
31. Whitney, H. E., J. Buchau, A. L. Johnson, J. P. Mullen, E. J. Weber (77): Report on Peru Scintillation Tests October 1976 and March 1977. Air Force Geophysics Laboratory Tech Report AFGL TR-77-0282; Hanscom AFB, MA; 8 December 1977.
32. Whitney, H. E. (79): Report on Peru Scintillation Test March 1978. Air Force Geophysics Laboratory Tech Rpt 79-0030; Hanscom AFB, MA; 22 Jan 79.

Airborne Near Saipan 1230Z 21 September 1971

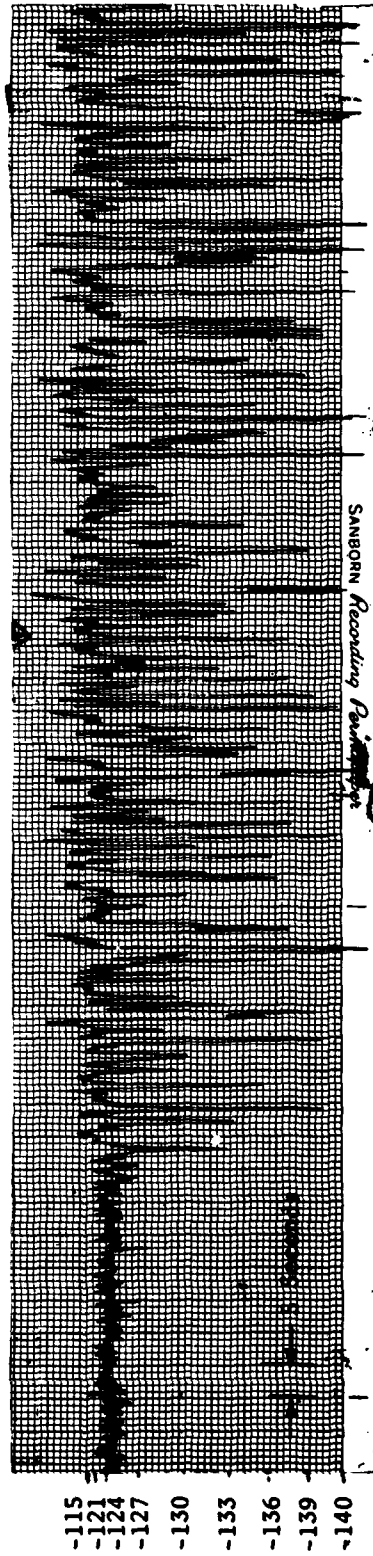


Figure 1 Abrupt Start of UHF Ionospheric Scintillation Fading

RECEIVED BEACON SIGNAL LEVEL in dbm



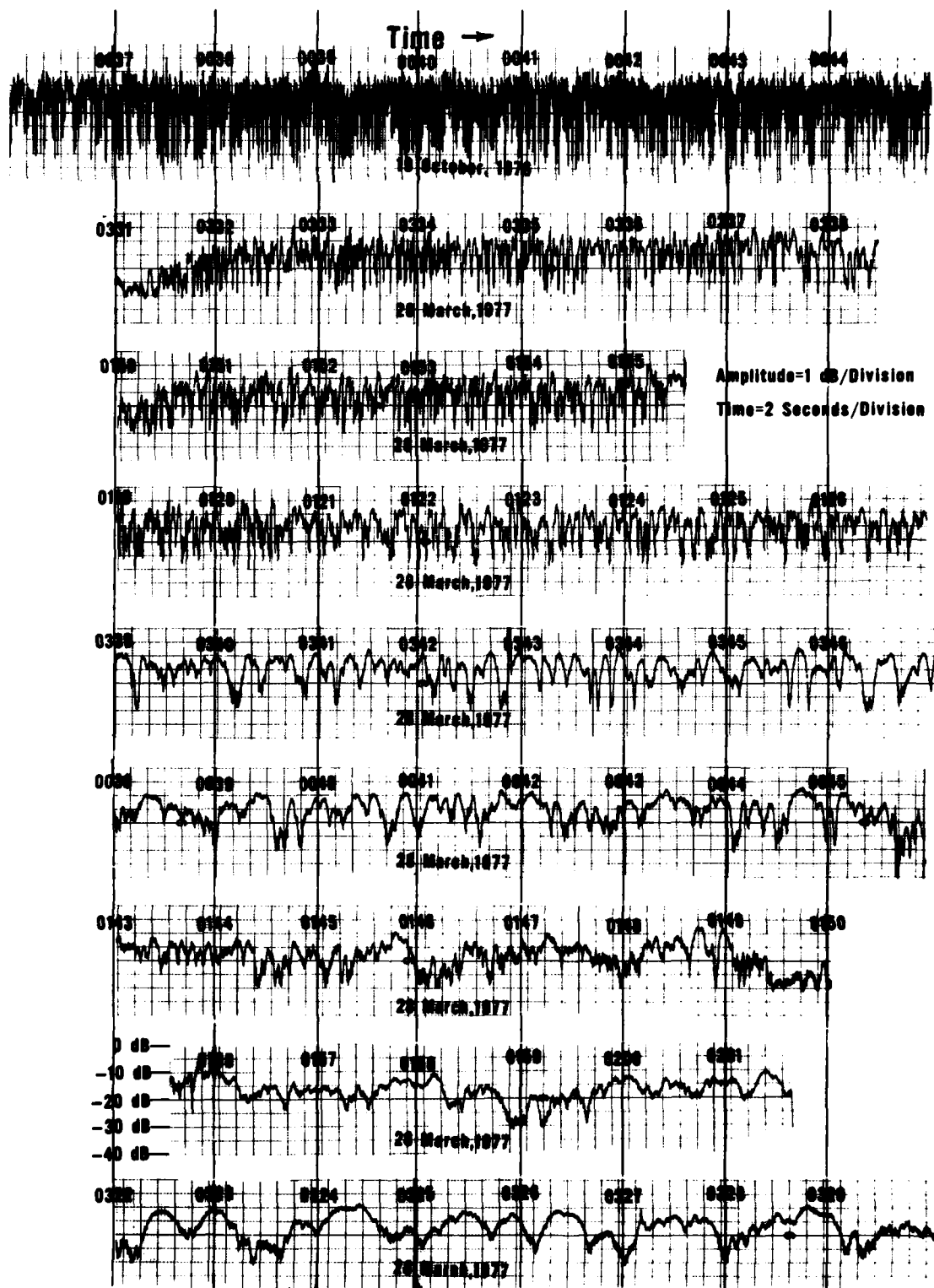


Figure 2 Equatorial UHF Ionospheric Scintillation Fade Variations

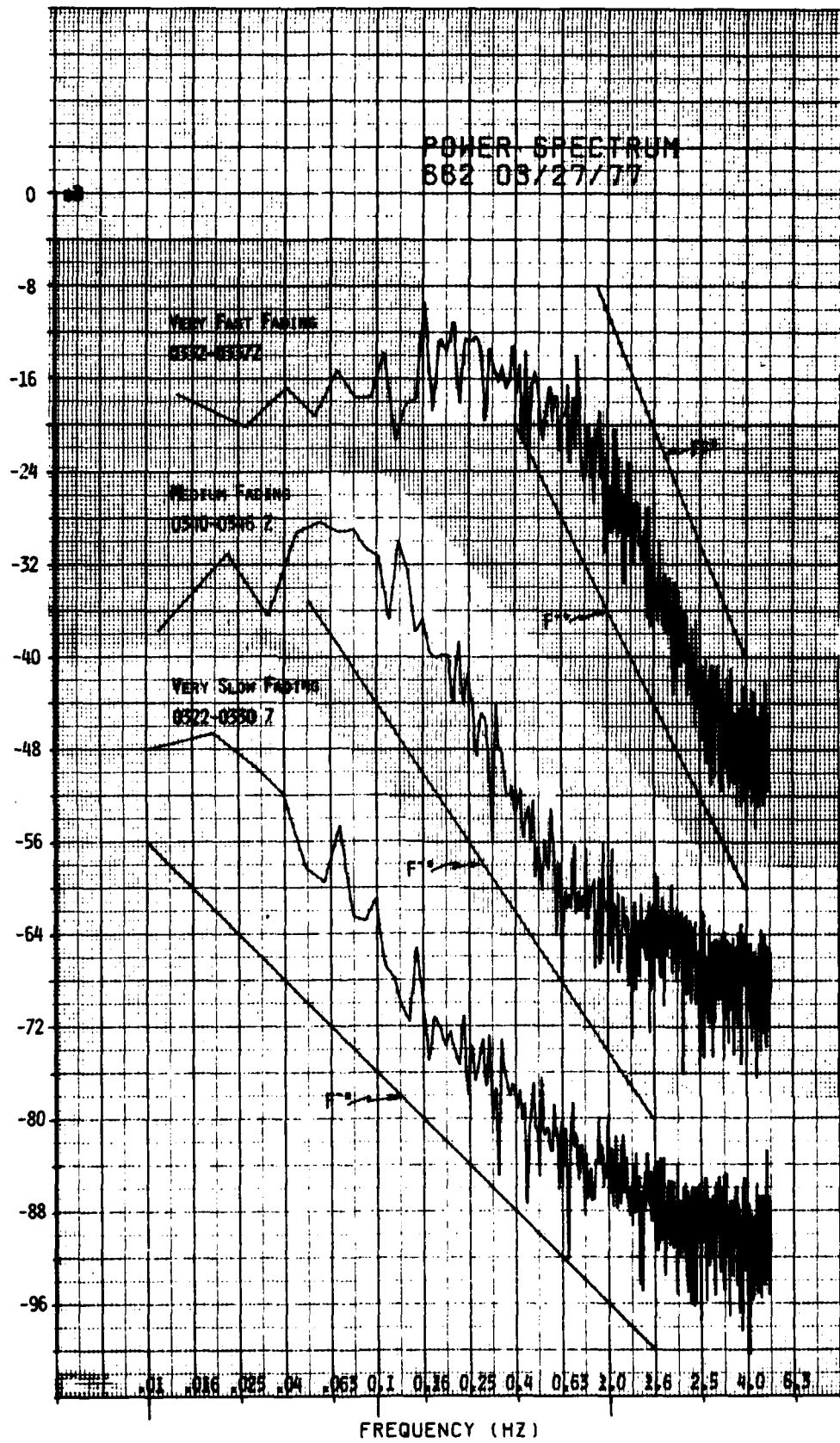


Figure 3 Power Spectral Density Slope Variation With Aircraft Heading

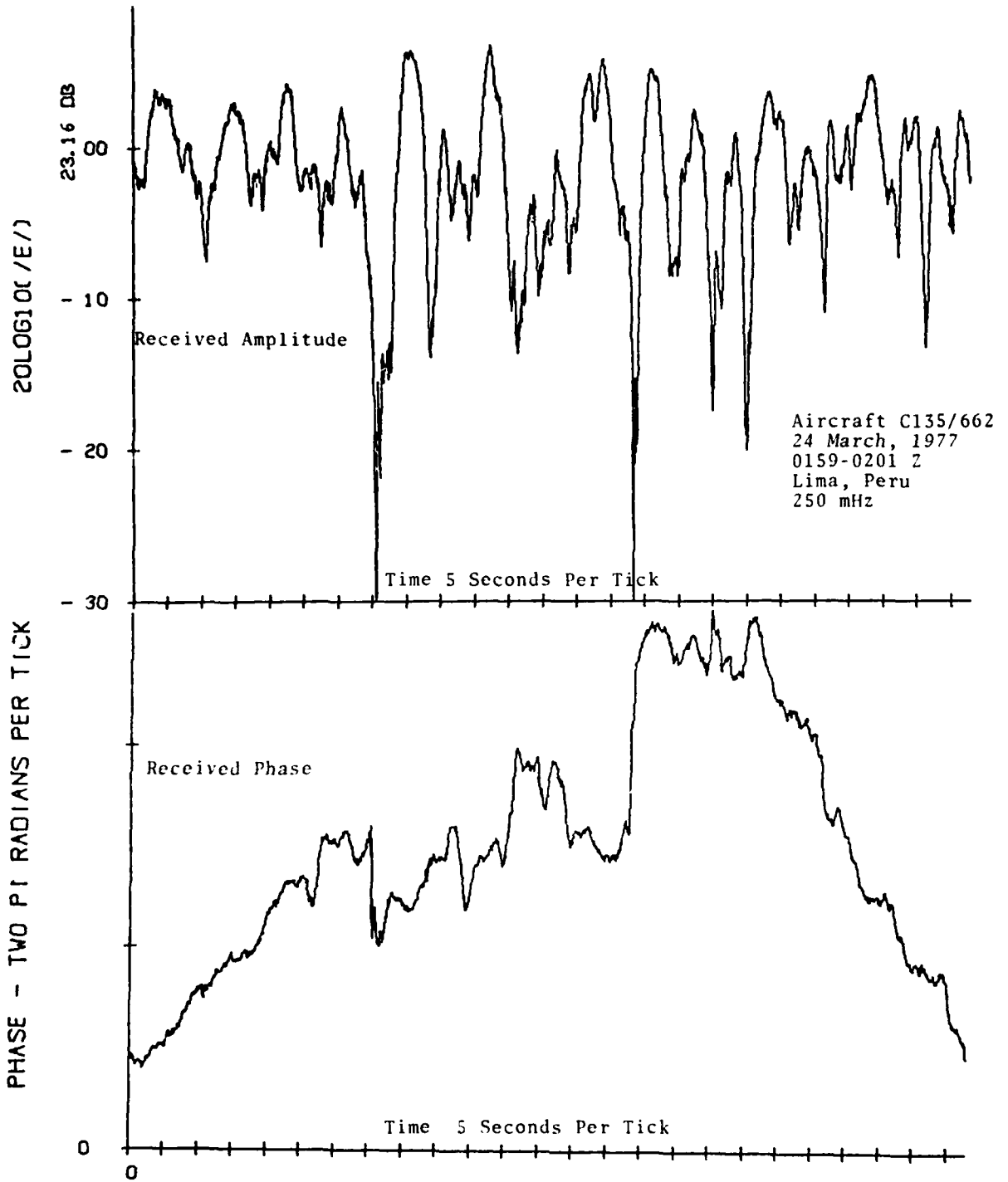


Figure 4 Received Signal Amplitude & Phase for Equatorial Scintillator

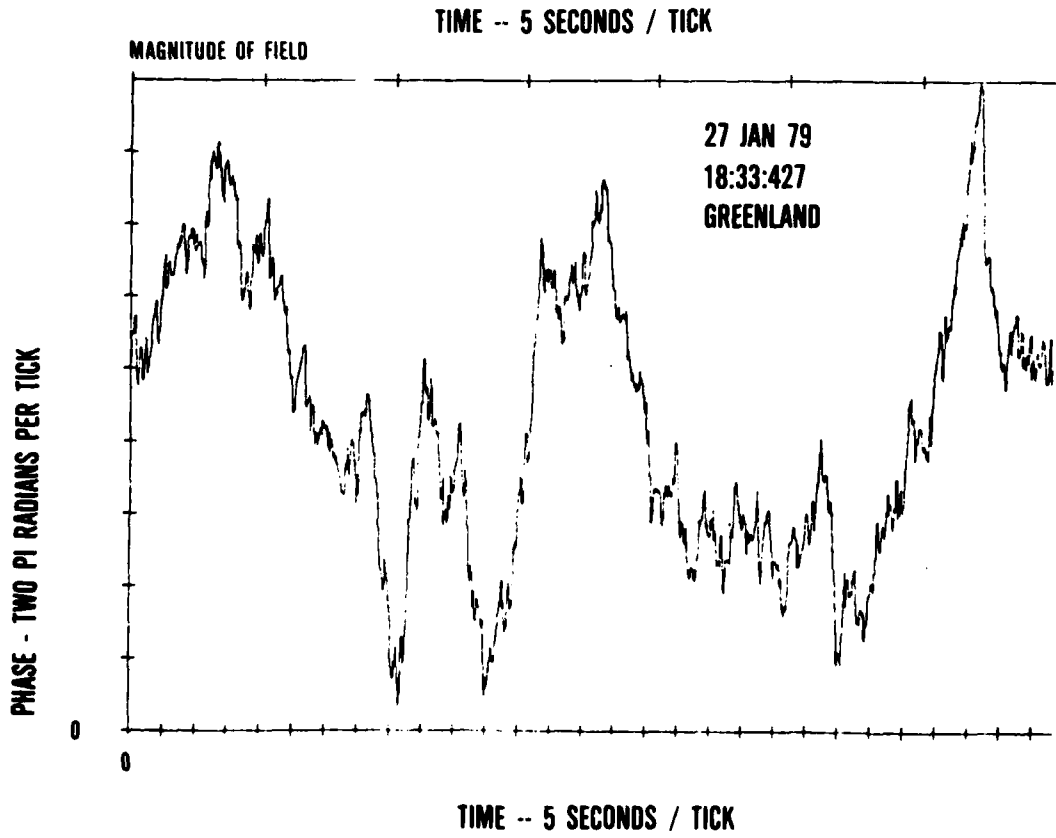
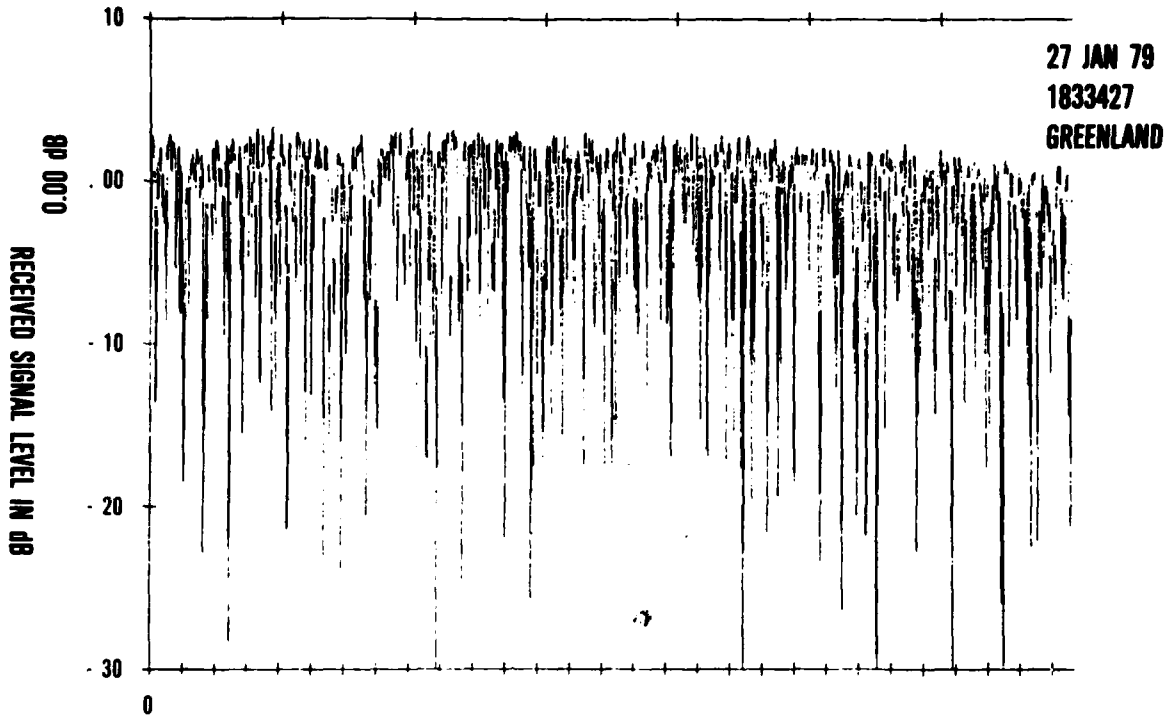


Figure 5 Received Signal Amplitude & Phase for Polar Scintillation

26 JANUARY 1979  
AIRCRAFT C-135/662  
LES 8 UHF  
TOP BLADE ANTENNA  
POLAR CAP

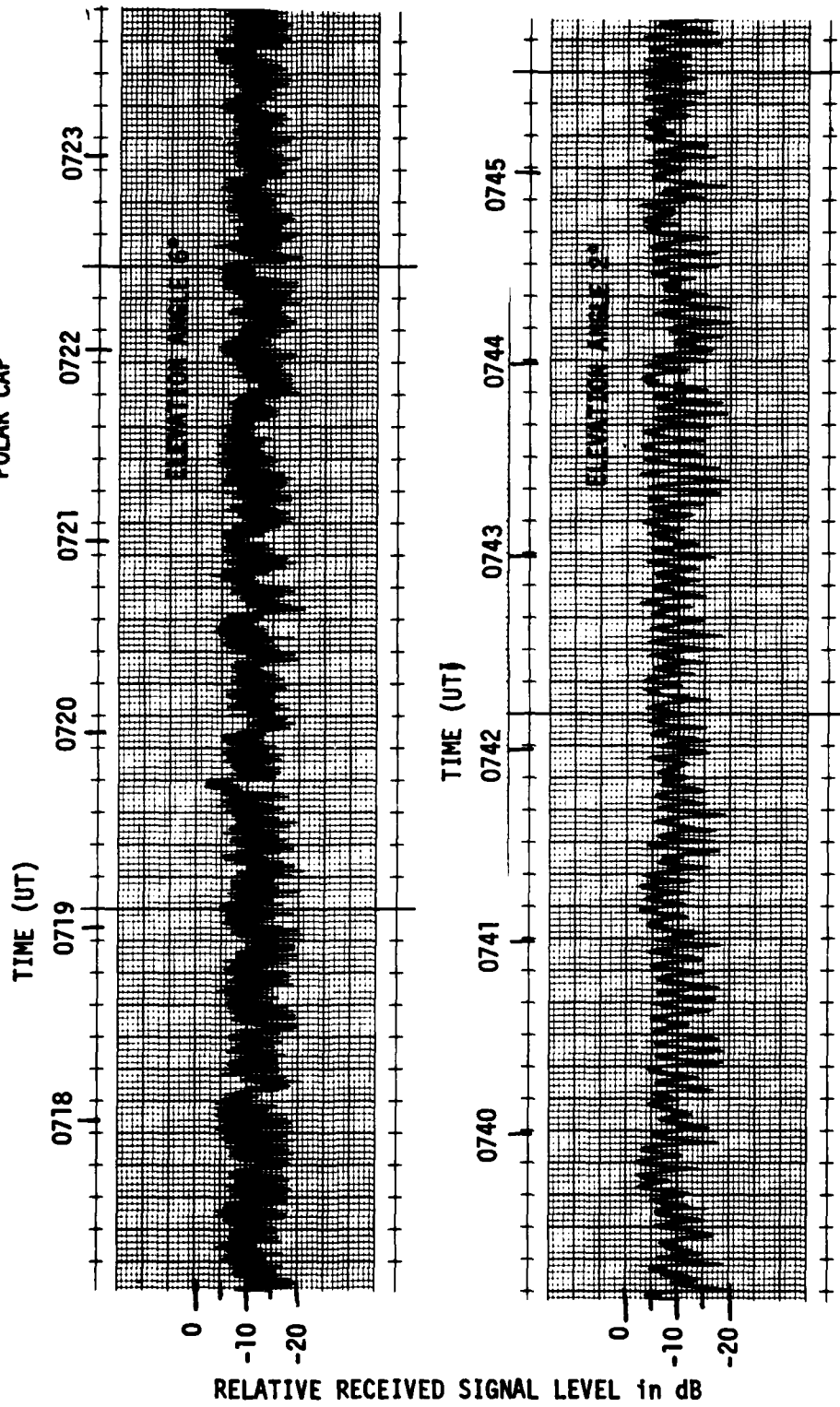


Figure 6 Examples of Low Elevation Angle UHF Multipath Fading

25 Apr 11 1975  
C-141-779  
Labrador  
Elevation Angle 40°

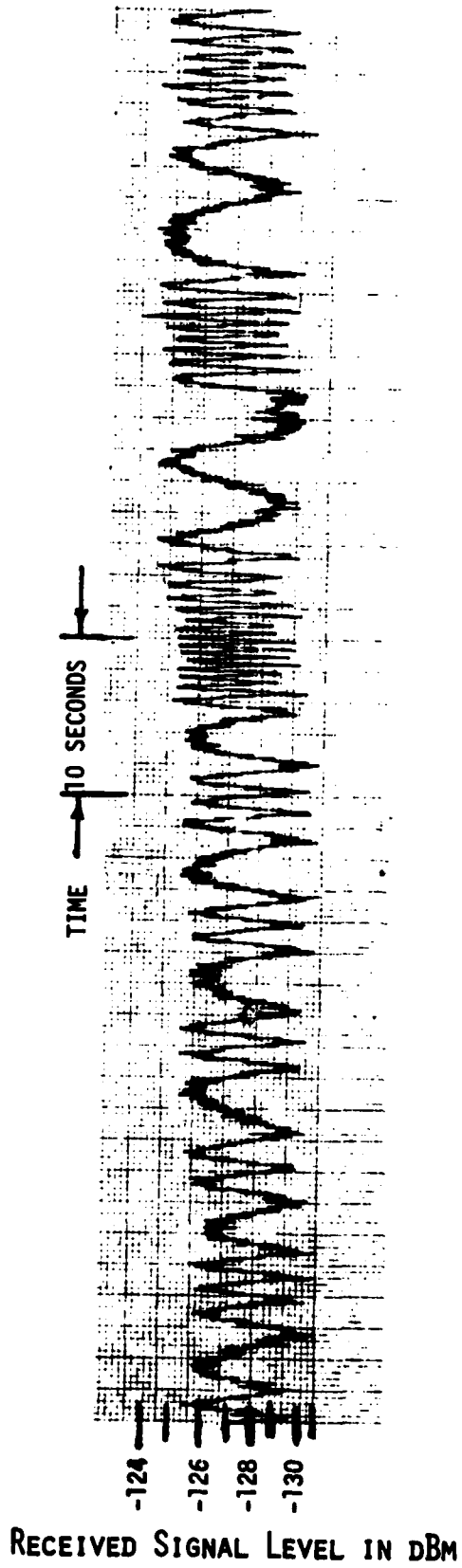


Figure 7 Variable Rate Coastal Multipath

## SUMMARY OF SESSION VI – PROPAGATION LIMITATIONS IN SYSTEMS

by H.J.Albrecht (as Session Chairman)

In the final session of the symposium, particular attention was paid to system applications and limitations caused by electromagnetic wave propagation. Apart from aspects of current and future satellite systems, the concept of solar power satellites was considered an item of sufficient interest for a detailed treatment of propagation-dependent limitations in an undertaking of such dimensions.

A review on the entire subject was presented by J.M.Goodman with his paper entitled "Environmental constraints in earth-space propagation". He stressed the advantages inherent in space systems, i.e. the relative simplicity of maintaining maximum global coverage for applications in communications, in navigation and remote sensing or surveillance. On the other hand, he also pointed to the disadvantages encountered, with propagation effects being of major influence in ionospheric and tropospheric regions of the atmosphere. The importance of such aspects for planning and operation of systems was illustrated by means of appropriate examples.

J.A.Klobuchar and H.Soicher reported on "preliminary evaluation of the two-frequency ionospheric correction for the NAVSTAR Global Positioning System". Concerning the group-path retardation caused by the ionosphere, the appropriate potential error may be larger than allowed in system design specifications. The introduction and proper choice of a second operating frequency enables a direct measurement of the ionospheric time delay and thus an automatic correction of the measured pseudo range for the ionosphere at the system operating frequency. The reported and discussed results are considered very satisfactory.

With a paper on "Studies of the potential impact of the solar power systems on the ionospheric and telecommunications systems", W.Grant, C.Rush, and E.Morrison presented a review on the energy satellite concept which has been under discussion for a number of years, and referred to assessment studies being undertaken to identify problems envisaged with regard to other users of the medium. In detail, possible functional and operational degradation of all electromagnetic systems, e.g. communications, radar, navigation, and environment-sensitive instruments and equipment, e.g. computers, sensors, electronic medical instruments and security devices, have been studied during the last two years. It was mentioned that the satellite power system (SPS) is not expected, on the basis of investigations so far, to adversely impact upon the performance of communication systems operating in the VLF, LF, and MF portions of the spectrum. Effects in other areas are being studied. It was indicated that further theoretical investigations are necessary in order to explain results of the simulation studies on medium modifications and to extrapolate these results to the actual SPS operational scenario. In addition, problems are anticipated in electromagnetic compatibility, particularly within 50 to 100 km of the rectenna site. On the other hand, current studies also concern mitigation recommendations and appropriate design guidelines.

A subsequent paper on "The interactions of a solar power satellite transmission with the ionosphere and troposphere" by K.A.Hughes supplemented the information available on the subject and discussed possible power losses due to mechanisms like scattering, absorption, in atmospheric media.

The treatment of this somewhat futuristic concept of solar power satellites was completed by a paper entitled "On microwave power transmission and the feasibility of power satellites for Europe" by D.Koehn. This contribution discussed briefly the various power satellite concepts documented in past literature and included some preliminary conclusions specific to the use in a European environment. These indicate, at least on the basis of qualitative results, a feasibility which would have to be confirmed by further studies.

Papers and discussions during this session contributed to a proper consideration of system aspects, in accordance with the session objective.

ENVIRONMENTAL CONSTRAINTS IN EARTH-SPACE PROPAGATION  
(A REVIEW PAPER)

John M. Goodman  
Naval Research Laboratory  
Washington, D. C. 20375 USA

SUMMARY

The advantages of utilizing space for telecommunications is well known in both the commercial and military arenas. A small complement of satellites at synchronous orbit, for example, may provide nearly global coverage and may be designed to support small disadvantaged customers as well as those characterized by large antenna structures and sophisticated acquisition and processing capabilities. Modern navigational and timing needs can also be satisfied through exploitation of space platforms and NAVSTAR/GPS is a system which exemplifies the utilization of space for those purposes. Applications of space in surveillance and kindred areas also exist and spaceborne instruments for monitoring the exoatmospheric environment and transmissions from the sun abound. There is an obvious charm in the utilization of space for various purposes, however most applications require the transmission of intelligence or data between space platforms and other space segments or a ground terminal. Thus the channel or the propagation path clearly becomes a part of the total system as a perturbation source. The nuisance value of the propagation path derives from the extent to which it does not duplicate free space at a specified frequency.

This paper reviews the general utilization of space to introduce the importance of earth-space radio propagation with special emphasis directed toward DoD mission areas. An outline of the basic properties of earth-space RF propagation follows and finally an assessment of the major effects is given.

1. INTRODUCTION

Since the advent of the space age, there has been an accelerated awareness of the benefits which might accrue from utilization of orbiting systems for a variety of purposes. Because of the unique vantage point provided by space, the potential for military and commercial communication, navigation, surveillance, earth observation, and space research has been increased significantly. Advanced societies have developed the technologies for the successful launch, orbital maintenance, and operation of highly sophisticated systems over the years since 1958; and currently there are more than 800 payloads in orbit of which approximately 30% are still actively performing their assigned missions. Of these, as reported in a popular military journal, approximately 75 are active communication satellites with the majority being Soviet systems [Schemmer, 1978]. These statistics, whether they be precise or not, do indicate the increased emphasis being placed upon space systems by the major industrial nations to fulfill national objectives in the C<sup>3</sup>I arena.

In order to fully utilize the benefits of space, it is necessary to account for the subtle environmental factors which may continuously interfere with successful operations or may constrain or limit the performance of the system at seemingly random epochs in time. In principle an a-priori knowledge of the full range of problems imposed by nature should lead to the design of robust systems (including both space segments and earth terminals) which are either impervious to disturbances or those which may adapt to the changes in some sense. At the very least the environmental knowledge is a pre-requisite to intelligent system design. Otherwise "band-aid" approaches will be dictated after-the-fact. For the disadvantaged user who is constrained by operational environment, cost, real-estate, or other factors, the entire burden or robustness must be borne by the space segment and this cost may be too large. Techniques of diversity (including frequency, polarization, time or coding, and space) and various resource management schemes involving re-routing and/or gateway scenarios are options which have been explored for mitigation or avoidance of environmental effects. In some cases the implementation of these techniques is either too costly or cumbersome considering the perceived risk.



This paper outlines the various environmental influences on the earth-space path. A brief summary of various systems which use the earth-satellite path is also included to provide the reader with a background of earth-space propagation requirements and a rationale for consideration of this topic.

## 2. THE UTILIZATION OF SPACE

### 2.1 Military Satellite Communications Systems

Trans-ionospheric propagation experiments were performed using the moon as a passive reflector of signals as early as 1946 [i.e., PROJECT "DIANA"] and J. H. Trexler of NRL discovered that UHF voice could be successfully bounced off the moon and returned to earth. It is of interest to note that [Browne et al, 1956] in conducting moon-bounce studies, detected the trans-ionospheric Faraday rotation effect, which was used rather comprehensively in succeeding years in conjunction with artificial earth satellites to study the ionospheric electron content. The U. S. Navy subsequently initiated the first regularly operating satellite telecommunication service in 1960 using the moon-bounce technique. It is understood that this system is still in operation by the U. S. Navy.

The first active link experiments were PROJECT SCORE and PROJECT COURIER. Project SCORE, initiated by the U. S. Air Force, culminated in a 1958 launch of an Atlas-ICBM-Type rocket containing communication equipment which allowed for earth reception and retransmission of voice messages. PROJECT COURIER culminated in two satellite launches in 1961. A logical follow-up to the early moon-bounce experiments was the passive communication ECHO satellite in 1960 and the launch of a large cloud of metallic dipoles (PROJECT WEST FORD) by Lincoln Laboratory in 1963. Both of these initiatives would potentially allow for communication service whenever the moon was not in view.

Other early tests were conducted by NASA (viz; TELSTAR in 1962, EARLY BIRD in 1965, and SYNCOM in 1963) and the Soviet Union (i.e., the MOLNIYA series).

The U. S. Dept of Defense recognized the utility of satellites early in the decade of the sixties and the DoD initiated Project ADVENT, a comprehensive program which was subsequently cancelled as too ambitious, and replaced it by the IDSCP (Initial Defense Satellite Communication Project) which was a phased-approach concept. Since that time the DoD has relied increasingly upon satellites for communications, surveillance, and navigation.

Until the Viet Nam War when IDSCP was initiated, all satellite communications systems were funded out of R&D dollars, were simply demonstration systems, and therefore were used very limitedly. Indeed they lacked the suitable follow-on systems to ensure the requisite continuity of service to potential customers. The first SHF demonstrations were performed with the Lincoln Experimental Satellites LES-3 and LES-4 launched in 1965. The IDSCP, relying heavily on earlier U. S. Army participation in the NASA SYNCOM program, launched 26 satellites between 1966 and 1968 [Miller, 1976] for SHF communications (i.e., 7-8 GHz).

The Military Satellite Communications Systems have evolved along two lines; SHF for long-haul, fixed, point-to-point communications, and UHF for tactical communications. The SHF requirements were initially satisfied by the IDSCP and the follow-up system was the Defense Satellite Communications System (DSCSII) which was a larger system with greater power, bandwidth and link connectivity potential. Launches began in 1971 and two satellites are currently in orbit, one over the Pacific and the second over the Atlantic Ocean. The DSCS SHF requirements include long haul communications, and support to WWMCCS for crisis and conflict management, ground mobile forces, large Naval ships and some non-DoD users.

Unfortunately the constraints of terminal cost, size, and complexity required for connectivity with the SHF-based DSCS systems are too severe for many users, especially the small tactical-mobile forces. The U. S. Navy is a prime example of this category of user which has thousands of individual units under its aegis. Hence the 225-400 MHz band (UHF) has been utilized for this large aggregate of users to limit cost and allow utilization of smaller less constraining terminals. Early tests of UHF for telecommunications were performed by MIT Lincoln Lab with the launch of the LES-5 satellites in 1965, followed by LES-6 in 1968. These satellites studied propagation effects among other things and demonstrated the utility of UHF for tactical use. The result of the UHF research led to the formation of the tri-service Tactical Satellite Program (TACSATCOM). The TACSAT satellite was launched as a result; it had both UHF and SHF capability. Although the TACSAT satellite was successful, it soon emerged that ionospheric scintillation could be a potential problem at UHF [Paulson and Hopkins, 1973]. This was somewhat of a moderate surprise to military designers even though NASA scientists had

recognized the potential problem for VHF links somewhat earlier [Golden, 1968] and vigorous work on radio star and satellite beacon scintillation had been undertaken by AFCL and others for many years previous to the launch of TACSAT. The follow-up to the TACSATCOM program was the two-service UHF satellite communication system called FLTSATCOM. This system contains the U. S. Air Force AFSATCOM subsystem as a separate entity within the main frame while at the same time preserving the identity of a separate UHF satellite for the fleet. The FLTSATCOM is a major component of the Navy SATCOM program and has several advantages over TACSATCOM including reduced dependence upon OCONUS (Outside Continental United States) facilities, provision for a robust Fleet Broadcast (FLTBCST), a ship-to-shore information exchange system, SHF uplink jamming protection for FLTBCST and UHF downlink to exploit simple, low-cost shipboard equipment. Because of the complexity of the FLTSATCOM system, launch schedule delays were necessitated. As an interim step the U. S. Navy contracted with COMSAT General Corporation to lease UHF service on MARISAT, with 2 satellites being launched in 1976 -- one being placed over the Atlantic and one over the Pacific, these satellites are termed GAPPILLER. Subsequently another satellite was placed over the Indian Ocean. The FLTSATCOM satellites were launched in 1978, 1979, and 1980. As noted above, they provide part of the AFSATCOM strategic command and control (C<sup>2</sup>) function. AFSATCOM transponders are also located on other host satellites such as the U. S. Air Force Satellite Data Systems Spacecraft. For the U. S. Navy there are four primary Communication Area Master Stations (CAMS) and one Naval communication station which are configured for GAPPILLER/FLTSATCOM capability. They are Norfolk, Virginia (NAVCAMSLANT), Stockton, California (NAVCOMMSTA), Hawaii (NAVCAMSEASTPAC), Guam (NAVCAMSWESTPAC), and Bagnoli, Italy (NAVCAMSMED). Currently the U. S. Navy has over 416 AN/SSR-1 FLTBCST Receivers and 638 AN/WSC-3 transceivers in place. The United Kingdom and the U. S. participated jointly in the IDCSP test phase and the U. K. and U. S. launched two SKYNET satellites to meet the military needs of the United Kingdom ... specifically long distance point-to-point digital links between Hong Kong and London and selected tactical links [Miller, 1976]. SKYNET I was launched in 1969 and SKYNET II was launched in 1974. The NATO Satellite program was established to improve intra-alliance communications. NATO IIA and IIB were launched in 1970 and 1971, being the same design as SKYNET. NATO IIIA was an evolutionary higher power satellite; the first of three satellites was launched in 1976.

The future Military Satellite Communication System (MILSATCOM) will be comprised of (i) an improved general purpose SHF system (now called DSCS III), (ii) an improved UHF system (now called GPSCS) and (iii) an improved AFSATCOM (now called SSS for Strategic Satellite System). Improvements in the DSCS III will include six identical transponders for user isolation and redundancy, and the use of two independent multibeam antennas with patterns ranging between 3.5° and earth coverage to increase capacity and provide flexible coverage. The GPSCS improvements may include FDMA uplink, a TDM downlink, satellite signal processing, and a large aperture multi-beam antenna. The SSS improvements may include new modulation techniques, satellite-to-satellite cross-link, EHF, and the use of new long-life radioisotope thermoelectric power generation. Some of these ideas have been tested with the LES-8 and LES-9 satellites.

Future generation satellites both in the tactical and strategic arenas may well be designed to operate in the EHF portion of the radio spectrum. There are certain advantages to this including robustness, jam resistance, and increased bandwidth. However the disadvantage lies with higher propagation loss especially during rainfall. According to [Reynolds, 1979] of the U. S. A. F. Space Division, an option for use of SHF/X-Band (i.e. 7-8 GHz) would be included for backup. It is noteworthy that high latitude users may not be too joyful at the prospect of EHF satellites in geostationary orbits because of the low elevation angles resulting in long paths through the atmosphere and enhanced atmospheric absorption. Thus both geostationary and polar orbiting satellites may be required. For connectivity either EHF or laser cross-links between satellites might be explored along with suitably selected earth terminals as gateways [Rosen, 1979].

## 2.2 Military Navigation Systems

The charm of satellite-borne navigation aids is obvious just as it has been for satellite communications for many years. However until recently the existing ground-based systems have been adequate for most purposes. Emitters in space result in expanded system coverage and the space frequency selection process is limited only by propagation loss and measurement error and not by the vagaries of the frequency-dependent terrestrial propagation path as in OMEGA, LORAN and in HF communication systems. On the other hand local region systems may be less susceptible to interference and jamming.

The only operational satellite-based navigation system is the Navy TRANSIT or NNSS system which has been in operation since 1964 but was fully operational in 1968. It is essentially an all-weather passive user system

producing fixes to better than 0.1 n.mi. Timing is synchronized to UTC within 200 microseconds. The constellation consists of 5 satellites in circumpolar orbits at 600 n.mi. and transmitting at 150 and 400 MHz. The position of the user is determined by measuring and examining the doppler shift of the signals. TRANSIT terminals are in use on a variety of Navy platforms including SSN, CV, DD, DE, DLG with the earliest use being for FBM submarines. The accuracy requirements range from 0.1 to 2 km with the former being appropriate for interface with the Shipboard Inertial Navigation System (SINS). The typical terminal consists of an antenna, receivers, processor and display unit. The opportunity for a SATNAV fix is dependent upon the user latitude with intervals being as short as 30 minutes near the poles and as much as 110 minutes near the equator. Over 300 Navy platforms are equipped with TRANSIT terminals.

The Defense Navigation Satellite Time and Ranging System (NAVSTAR) or Global Positioning System is a four service system in which the space segment provides the RF signal, the ground segment provides the satellite ephemeris and clock synchronization, and the user equipment computes position, velocity and time. The attributes of the system are precise 3-D navigation, continuous global coverage, worldwide common grid, passive all-weather operation, high jam resistance, and selective availability [Henderson, 1979]. The total system will comprise 24 satellites with 8 satellites in each of three orbital planes such that each user will have four satellites available within the field of view at any time. There are a myriad of GPS applications. The NAVSTAR program was conceived in the early 70's, the development began in 1974, and full operational capability is scheduled by 1987. The GPS deployment of terminals will consist of at least six categories of equipment to support the varied user environment as well as cost and accuracy requirements. User types may be either ships, aircraft, or manpack. The minimum terminal will consist of an antenna, receivers, data processor, software, control, and display unit. Most users will receive both 1227 and 1575 MHz transmissions but there are also some single frequency users. By the 1990's over 20,000 military users are projected. Of these the U. S. Navy plans approximately 2700 terminals to be installed on submarines, aircraft, and ships [U.S.N. Space Master Plan, 1979]. The advanced GPS will provide 3 meter accuracy for two frequency users. Furthermore it is planned to add special purpose communications and surveillance packages to the GPS. There is some limited concern vis-a-vis environmental effects and GPS. This concern is outlined by [Parkinson et al, 1976] and [Cretcher, 1975].

### 2.3 Satellites Used for Earth Observations

There has been a continuing evolution of earth monitoring satellites launched since the initial TIROS 1 was launched in 1960. Meteorological studies of significance to long and short-term forecasting have been facilitated since that time and techniques have been developed for global mapping of weather systems and atmospheric phenomena with a variety of sensors. The groundwork for future earth-observation from space was paved by the early TIROS, NIMBUS, ATS, AND ESSA series of satellites. The current operational weather satellite system spawned by the NIMBUS and TIROS efforts is the ITOS (Improved Tiros Operational System). The prototype spacecraft TIROS-M, launched in 1970, was followed by satellites dubbed NOAA 1-5 to satisfy needs of the U. S. Weather Bureau. The evolution and launch of a series of Geostationary Operational Environmental Satellites (GOES) was based upon the success of the ATS-1 and ATS-2 in demonstrating the benefit of continuous observations. (These are dubbed SMS/GOES). The first of the Synchronous Meteorological Satellites (SMS) were launched in 1971 and 1973. Others followed in 1975. The SMS/GOES satellites also monitor solar x-ray flux of benefit to solar physicists, ionosphericists, and communication specialists concerned with sudden ionospheric disturbances caused by solar flares. Current and future operational systems include LANDSAT-C, NIMBUS G, TIROS-N, and SEASAT, the latter being the first satellite designed especially for ocean surveillance - having both active and passive microwave sensors on the same spacecraft and having the ability for global observation and quasi-real time data processing and dissemination. Unfortunately SEASAT operated properly for only a few months following its launch. Some of these future systems will produce daily data rates exceeding  $10^{12}$  bits/day. The NASA Tracking and Data Relay Satellite System (TDRSS) will be employed for data relay. This will obviate the use of a cumbersome set of ground stations for tracking and retransmission to a orbital processing facility for ultimate data dissemination. [Garbacz et al, 1976].

Military requirements vis-a-vis satellite meteorological data have been documented [MJCS, 1976] and are generally applicable to all services in the DoD. Ocean surveillance is stressed in the U. S. Navy as would be expected. Operational polar orbiting satellite systems to fulfill these requirements include the DoD 2-satellite system called the Defense Meteorological Satellite Program (DMSP) and the civilian 2-satellite system (NOAA) developed under the ITOS program discussed previously. The two DMSP satellites are in

noon-midnight and dawn-dusk orbits of 845 km respectively. DMSP data is directly available to Air Force and Naval ground terminals and is used to support tactical air, surface, and ASW operations among others. Global synoptic data is also transmitted to the Fleet Numerical Weather Central (FNWC) for use in global weather analysis and forecasting models. DMSP data is transmitted to the Air Force Global Weather Central (AFGWC) for weather analysis, and special sensor data is also used for application in ionospheric modelling, forecasting, and assessment to serve a variety of DoD and civilian customers. Future plans may call for incorporation of an operational topside ionosonde on DMSP to characterize the topside ionosphere to improve the support of various C<sup>3</sup>I functions. The NOAA operational satellites are in polar sun-synchronous orbits and at altitudes of approximately 1500 km. Observation times occur near 0900 LT and 2100 LT. U. S. Navy use of the TIROS-N data is also planned in the future; with data being transmitted to FNWC in Monterey, California.

Geosynchronous satellites which provide environmental data to support DoD requirements include those in the GOES System mentioned above. GOES is part of the Worldwide Geosynchronous Meteorological Satellite System (WGMS), provides visible and IR data, and has an environmental data relay capability.

There is considerable although not unassailable pressure to merge both civilian and military needs into a single national system for meteorological use in the future. The principal justification for a separate military system (such as BLOCK 6 on DMSP) arises from control and security issues and more stringent military requirements.

#### 2.4 Exo-atmospheric Monitoring and Geophysical Forecasting Systems

The U. S. Air Weather Service has responded to the requirements of the U. S. Air Force through a comprehensive development of various categories of support in the space environment arena. The Air Force Global Weather Central (AFGWC) system at Offutt AFB, Nebraska includes a central facility to forecast the state of the sun, the interplanetary medium, the magnetosphere and the ionosphere. The Air Weather Service and the Air Force Geophysics Laboratory have coordinated the establishment of a network of solar optical (SOON) and radio (RSTN) stations to augment the traditional solar monitoring technologies. Other nearly real-time data sets available at AFGWC include x-ray and high energy proton data from GOES, some x-ray and particle data from VELA 5 and 5B, a variety of data from the NOAA/AWS High Latitude Monitoring Station (HLMS), magnetometer data from its magnetometer data network, auroral imagery, in-situ plasma probe and precipitating electron data from DMSP, and various ground-based ionospheric data including that obtained from vertical incidence ionosonde and total electron content monitors.

The U. S. Navy entered into the quasi-operational exo-atmospheric monitoring arena with the launch of SOLRAD HI in 1976. This system which had severely degraded by 1979, was designed to meet two goals: First, to provide continuous real-time solar measurements to the U. S. Navy during FLEET support demonstrations and to the Air Force and NOAA for their environmental forecasting centers; and secondly, to provide data for research. The two satellite system, super-synchronous in nature, carrying a multiplicity of particle and electromagnetic sensors, was a central ingredient in a total system for Environmental Prediction and Assessment (EPAS) for predicting performance variations in communication, radar, and navigation systems. The Navy has no current plan to build a follow-on for SOLRAD HI.

#### 2.5 Other Systems and Activities

##### 2.5.1 The Commercial World

There are, of course, a plethora of commercial communication satellites now in operation and many more are planned. Telecommunications is probably the only commercial use of space technology and it is now a multi-billion dollar industry. A review of the industry is provided by [Gould, 1976].

##### 2.5.2 The Scientific World

The ability to study the earth's environment from the vantage point of space has provided answers to many basic questions while raising some new and interesting ones. Of particular note here are the vigorous programs in solar-terrestrial physics which have been conducted since the launch of the first U. S. earth satellite, Explorer I in 1958. Approximately 90 satellites have been involved in solar-terrestrial research. Studies of solar electro-magnetic and particulate flux, solar features such as auroral holes, the solar wind, the interplanetary magnetic field, the radiation belts, and the electron and ionic populations in the outer atmosphere are just a few noteworthy examples. Satellites have been platforms for synoptic measurements of the ionosphere through use of various in-situ probes and other techniques

which exploit the unique properties associated with radio-wave propagation in an inhomogeneous magneto-ionic medium. Topside ionosonde which operates in the HF band (Canadian Alouette and ISIS spacecraft and the Japanese ISS-B satellite) have provided considerable information about the macroscopic morphology of the topside ionosphere and the F2 maximum whereas direct measurements of electron density (in-situ probes) have been used to deduce inhomogeneity wave number spectra, a parameter of importance in scintillation theory. A number of satellites not specifically designed for scientific use have nevertheless provided a resource by which useful data has been obtained. These include many communication satellites as well as experimental satellites of opportunity. Of particular interest are total electron content studies based upon measurements of the dispersive doppler or Faraday rotation introduced by the ionosphere on the downlinks of various space systems. These data are ultimately of importance to the NAVSTAR/GPS community. Communication satellites are the primary source of amplitude scintillation data; however the necessity to understand the importance of phase scintillation in the operation of advanced communication systems using PSK modulation or its derivatives has led to the launching of a satellite designed to explore this problem (WIDEBAND DNA-002).

Various experimental studies of millimeter wave propagation have been facilitated through use of Applications Technology Satellites (ATS-5/6), the Communications Technology Satellite (CTS), COMSTAR, and SIRIO.

## 2.6 Concluding Remarks to this Section

Clearly the utilization of space is increasing for a variety of purposes serving both the civilian and military communities. Because of this, the intervening environment (including the troposphere and its weather, the ionosphere, the magnetosphere, and the interplanetary medium) is a necessary consideration. As a result, serious basic research efforts have been initiated over the years to ascertain the basic nature of the total environment or at least its statistical climatology with the ultimate goal being to estimate the range and variance of deleterious system effects. This information is utilized for purposes of system design and development but may also be of value in developing forecasting and assessment techniques for use in operational resource management. The next section will outline some of the constraints placed upon space systems which rely upon the earth-space propagation path.

## 3. A RESUME OF EARTH-SPACE RADIO PROPAGATION EFFECTS

### 3.1 Introduction

One of the earlier papers dealing with this topic was due to Millman [1965] who surveyed both tropospheric and ionospheric effects on radio propagation between the earth and space vehicles. A basic paper with special emphasis on the ionospheric aspect of earth-space propagation by Lawrence et al [1964] is also noteworthy although the more recent developments in scintillation morphology have rendered it considerably outdated in that specialty. For background the reader is referred to books by Davies [1965], Kelso [1964], and Buddin [1964] to name a few, and to the excellent library of AGARD publications which have treated various propagation effects over the years. With respect to propagation effects due to the lower atmosphere, texts by Kerr [1951], Battan [1959], and Bean and Dutton [1966] are good introductions. There are numerous papers which have been published over the years dealing with the material covered in this survey. Nevertheless recent papers by Rush [1979] on ionospheric radio propagation, Klobuchar [1977, 1978] on ionospheric time delay, Aarons [1978] on scintillation morphology, Fremouw and Rino [1978] on scintillation modelling and statistics, Crane [1977] on prediction of rainfall effects and Bean and Dutton [1976] as well as Bothias [1976] on tropospheric propagation are worthy of note. A sketch of the ionospheric effects upon earth-space propagation is also available in a CCIR report [1974]. The proceedings of the two previous IES symposia [Goodman, 1975, 1978] and a recent COSPAR symposium [Mendillo, 1976] are also drawn upon in developing the material for this survey. In the section dealing with millimeter wave propagation and hydrometeor effects, the author was fortunate to have lecture material provided by Ippolito [1975].

There are a myriad of radio propagation effects which come to mind as one recalls the nature of media through which rays must propagate between earth and space. The obvious effects of refraction and absorption in the lower atmosphere have their counterparts in the ionized upper atmosphere but there is a greater richness of effects in the ionosphere as a result of the magnetoionic medium. The Faraday rotation of linearly polarized radiowaves and various differential effects resulting from bi-refringence come to mind. Although tropospheric weather (and the propagation effects it generates) is not uncomplicated, the traditional primary concern vis-a-vis earth-space propagation has been the ionosphere and its personality. This is a result

primarily of the fact that space frequencies were lower near the advent of the space age than they are at present or will likely be in the future. The following sections discuss some of the more important RF propagation effects for rays which traverse both the troposphere and the ionosphere.

### 3.2 Refraction in Earth-Space Propagation

Figure 1 depicts both the tropospheric and ionospheric components of bending introduced over an earth-space path. This is due, of course, to the non-vanishing refractivity in the earth-space medium. The earth-space refractivity may be written

$$N(s) = (n-1) \times 10^6 = N_t + N_I$$

$$= \frac{77.6}{T(s)} \left[ p(s) + \frac{4810 \epsilon(s)}{T(s)} \right] - \frac{40.28 \times 10^{-6}}{f^2} N_e(s) \quad (1)$$

where  $N(s)$  is the refractivity,  $n$  is the refractive index,  $N_t$  is the tropospheric component or refractivity,  $N_I$  is the ionospheric component of refractivity,  $T(s)$  is the air temperature ( $^{\circ}\text{K}$ ),  $p(s)$  is the atmospheric pressure (mb),  $\epsilon(s)$  is the partial vapor pressure (mb),  $f$  is the radiofrequency (MHz),  $N_e$  is the electron density ( $\text{M}^{-3}$ ), and  $s$  is the distance parameter.

Figure 2 depicts a typical refractivity profile from ground level through the ionosphere. It is noteworthy that  $N_t(h)$ , where  $h$  replaces  $s$  for zenithal propagation, is independent of  $f$  whereas  $N_I(h)$  is inversely proportional to the square of it. Clearly for the higher space frequencies the tropospheric refractivity dominates the ionospheric component. The immediate implication that ionospheric refractivity effects are to be ignored at higher space frequencies is to be avoided, however.

With respect to gross tropospheric bending Bean and McGavin [1965], Bean and Cahoon [1957], and Bean et al [1971] have shown that surface values of the refractivity  $N$  may be used to approximate the effect. A considerable amount of work has been done by Bean and his colleagues as well as others in recent years. For example the reader should examine material in the NATO/AGARD conference on Tropospheric Radiowave Propagation [Albrecht, 1971] in which a review by Millman [1971] is contained (Also see Bean and Dutton [1976] and Bothias [1976]). Bending through the total neutral atmosphere may be given by the following approximate relation [Bean and McGavin, 1965]:

$$\tau_{\omega}(\theta) = b(\theta) N_s + a(\theta) \quad (2)$$

where  $\theta$  is the initial ray elevation angle,  $N_s$  is the surface refractivity, and  $a$  and  $b$  are constants.

A typical value for  $N_s$  is the order of 334 and the set  $(a,b)$  ranges between  $(-18.0, 0.12)$  at  $\theta = 0^{\circ}$  and  $(-0.14, 0.01)$  at  $\theta = 90^{\circ}$ . The refraction at these extremes amounts to 21 and 3 milliradians respectively. Figure 3 from Bean and McGavin [1965] exhibits the  $\theta$  dependence of  $\tau_{\omega}$  and its standard deviation. It is noteworthy that there does exist a climatology for the surface refractivity and models for  $N_s(h)$  also have been published (See Bean and Dutton [1976]). The simple recipe given by equation 2 above is obviously insufficient under extreme climatic conditions, and in particular the "humid" term (i.e.,  $4810 \epsilon/T$ ) exhibits large variations. It is well known that both the horizontal and vertical details of refractivity are of great importance in radio propagation. If the vertical gradient of  $N$  has a very large negative value (for example  $\frac{dN}{dh} = -157 N$  units per km), then super refraction or ducting will occur. If the vertical gradient is positive (or slightly negative), then super refraction will occur. Such matters, however, are generally of little significance to earth-space links except at very low propagation angles. It is clear from this discussion and also from Figure 2 that the refractivity of the atmosphere is not a pure exponential. Attempts have been made to construct both 2-part and 3-part exponential models [Bean et al, 1966]. Even these sophisticated models are inadequate to explain the situation in the tradewind zones.

The index of refraction is the troposphere is greater than unity and since  $dN/dh$  is negative in that region, non-zenithal rays are bent away from the normal. As a result, the apparent elevation to the space object is higher than its actual value and the radio range to the object is larger than the geometrical distance. The index of refraction in the ionosphere is less than unity. Nevertheless, the net effect of the ionospheric component of refraction is to combine with the tropospheric contribution such that the total refraction is essentially the sum of the two components. Figure 4 [Millman, 1965] shows the total refraction error introduced at radio

frequencies of 100 and 200 MHz as a function of altitude. Limiting tropospheric and ionospheric range errors due to refraction and signal delay are given in Figure 5 as a function of elevation angle. It is noteworthy that the time delay component of range error dominates for elevation angles above 30°. The diurnal variation of the ionospheric component of elevation error at 400 MHz is given in Figure 6 [Evans and Wand, 1975], and Figure 7 shows that the ratio of refractive error to range error is not fixed as a function of local time. Of course the range error results from both a time delay due to an increase in path length (caused by bending) and to a reduction in the radiowave signal velocity, so such behavior is not unanticipated.

In summary we may state that the ionospheric component of refractivity remains quite important in comparison to the tropospheric component in the UHF band provided the elevation angle exceeds a critical value, say 50°. Below this elevation the tropospheric component begins to dominate and other effects such as ducting, atmospheric multi-path, and atmospheric scintillation become increasingly important. Millman [1971] reviews many of these effects. The tropospheric errors are typically less variable at higher elevation angles and the climatology of surface refractivity and its variance exhibits a degree of stability (or may be readily measured). As a result, routine subtraction of the tropospheric effects of bending and range bias may be accomplished with some degree of confidence. Ionospheric errors are not as easy to address since the climatology is not well known and the variances are relatively large and moderately unpredictable. This situation still exists despite the fact that valiant attempts at ionospheric prediction and assessment continue to this day.

### 3.3 Attenuation in Earth Space Paths

The absorption introduced by the ionosphere is of negligible significance at UHF and higher space frequencies. The most enhanced effects would be introduced during polar cap absorption (PCA) and kindred auroral events. At UHF even these extreme events will produce absorption of less than 1 dB at space frequencies above VHF. The interested reader is referred to AGARDOGRAPH No. 53 [Gerson, 1962], Davies [1965], and CCIR Report 263-3 [1974].

The troposphere on the other hand introduces potentially severe attenuation of earth-space signals. Attenuation, including both absorption and scattering, is considerably a function on the various atmospheric constituents and their frequency-dependent characteristics. Figure 8 [Bern, 1979] depicts the specific attenuation for normal absorption, resonance absorption, rain, and fog. Absorption and scattering are typically unimportant for frequencies less than 3 GHz. Figure 9 shows the total attenuation through the atmosphere due to resonance absorption for an elevation angle of 45°. Note that at 61, 119, 183, and 324 GHz the attenuation exceeds 100 dB. Scattering from clouds and hydrometers (rain) will reduce the amount of energy available in the forward direction, will change the polarization of the radiowaves, and will deflect energy back toward the transmitter as well as other directions.

Probably since the resonance absorption peaks of H<sub>2</sub>O and O<sub>2</sub> are well known and can be avoided, the most significant future problem for systems which will use the earth-space propagation path at frequencies between 10 and 100 GHz is likely to be rainfall attenuation. Two types of rain are considered: stratiform and convective. Stratiform rain generally develops in stable masses of air, along frontal surfaces typically, and is characterized by steady and uniform rain over wide areas for hours to days; low rain rates are typical. Convective rainstorms, on the other hand, develop in highly unstable air masses, are limited in extent and duration and are characterized by high rain rates. If rainfall statistics are unavailable for a typical area, it is possible to estimate the rainfall distribution from Figures 10 and 11 due to Bean and Dutton [1976]. Attenuation by hydrometers is given by

$$\alpha \text{ (dB/km)} = 4.343 \int_0^{\infty} Q_T(a) \eta(a, R) da \quad (3)$$

where  $Q_T$  is the attenuation cross section/drop,  
 $\eta$  is the drop size distribution,  $a$  is the drop radius,  
 and  $R$  is the rain rate.

The attenuation function  $Q_T$  is determined from classical Mie and/or Rayleigh scattering theory and for computing a several drop size distributions are available [Laws and Parsons, 1943; Marshall and Palmer, 1948; and Joss et al, 1968]. From the Laws & Parsons distribution, the specific attenuation is given in Figure 12 for various rain rates. An empirical relationship between rain rate  $R$  and  $a$  is due to Ryde and Ryde [1968], and Gunn and East [1954]:

$$a \text{ (dB/km)} = a R^b \quad (4)$$

where  $a$ ,  $b$  are frequency dependent constants.

Curves of the parameters a and b are given in Figure 13 (Beach [1979]). Uniform rain attenuation is proportional to the cosecant of the ray elevation angle since the total attenuation is proportional to the product of the specific attenuation a and the path length L.

The frequency scaling law for rainfall attenuation is approximately.

$$\frac{A(f_2)}{A(f_1)} = \left( \frac{f_2}{f_1} \right)^{1.72} \quad (5)$$

which for uniform rain becomes approximately  $a_2/a_1$ .

It may be shown that water cloud attenuation is equivalent to light rain ( $\leq 5$  mm/Hr) attenuation below 100 GHz. Ice cloud attenuation is at least 2 orders of magnitude less than water cloud attenuation and thus is of little relative practical significance. Figure 14 exhibits cloud attenuation as a function of frequency.

#### 3.4 Polarization Effects in Earth-Space Paths

The Faraday effect is well known to ionosphericists since it is a major technique for measuring the total electron content of the ionosphere. The expression for the amount of Faraday rotation is given by:

$$\Omega = 2.97 \times 10^{-2} f^{-2} \int H \cos \theta \sec x N dh \quad (6)$$

where  $\Omega$  is the amount of rotation of the plane of polarization (radians),  $f$  is the radiofrequency (Hz),  $H$  is the magnetic field strength (Amperes turns/meter),  $x$  is the ray zenith angle,  $N$  is the electron density ( $\#/m^3$ ) and  $h$  is the vertical distance.

Due to the inverse  $f^2$  dependence of  $\Omega$ , the amount of Faraday rotation diminishes rapidly as the space frequency is raised. At 7 GHz, for example, the plane of polarization of the transmitted signal would rotate only 1.4 degrees in transit through the entire ionosphere assuming a value for  $\int N dh$  of  $10^{18}$  electrons/ $m^2$  and  $H \cos \theta \sec x = 40$  amperes turns/meter. Below 1 GHz the amount of rotation begins to become significant and circularly polarized antennas are employed to obviate the effect. However this mitigation scheme disallows the use of polarization as a means for frequency re-use.

The major factors in the transmission path causing depolarization effects are hydrometeors, multi-path, and Faraday rotation. Of these three, the depolarization caused by rain dominates decisively at GHz frequencies. It has been experimentally shown that the polarization isolation is inversely proportional to the signal attenuation (See Figure 15). Ice depolarization also occurs but is less significant.

#### 3.5 Propagation Delay in Earth-Space Propagation Paths

The total excess delay  $\Delta T$  for a signal traversing an earth-space path has two additive components, tropospheric and ionospheric. Thus:

$$\Delta T = \Delta T_t + \Delta T_i = \frac{10^{-6}}{c} \int_0^s N_t(s) ds + \frac{40.3}{cf^2} \int_0^s N_e ds \quad (7)$$

where  $c$  is the free space velocity of light,  $N_t$  is the tropospheric refractivity  $(n-1) \times 10^6$ ,  $f$  is the radiofrequency,  $N_e$  is the electron density,  $s$  is the distance along the ray trajectory, and the integral  $\int_0^s N_e ds$  is the total electron content (TEC) of the ionosphere.

The first term  $\Delta T_t$  is approximated by  $N_s H \sec x$  where  $N_s$  is the surface refractivity,  $H$  is the atmospheric scale height and  $x$  is the ray zenith angle. Taking  $N_s = 300$  and  $H = 7 \times 10^3$  meters, we see that  $\Delta T_t$  is the order of 7 nanoseconds. This term may be easily modelled to leave a residual of less than 1.5 nanoseconds. The second term  $\Delta T_i$  is dependent upon frequency. At the GPS frequency of 1.6 GHz, and taking the integral equal to  $10^{18}$  electrons/ $m^2$ , we find that  $\Delta T_i = 50$  nanoseconds. There is, of course, a considerable variation in this number because of the extreme variability in the total electron content, TEC. Using various models for prediction of  $\Delta T_i$  residuals of between 1 and 13 nanoseconds have been observed [Parkinson et al, 1977]. Various models have been used to predict the TEC [Klobuchar and Allen, 1970; Waldman and daRosa, 1971; Rao et al, 1971; Pisacane et al, 1972; and Bent et al, 1972]. Of particular interest is a model



described by Klobuchar [1977] which predicts the time delay for single frequency users of the NAVSTAR/GPS system. It is written as

$$\Delta T_i = DC + A \cos \frac{(t - \phi) 2\pi}{P} \quad (8)$$

where DC, A,  $\phi$ , and P are parameters which are modelled. The functional dependence of the parameters are given in Figure 16.

In general the ionospheric contribution to time delay is compensated for through use of a two-frequency correction technique intrinsic to the GPS system. Thus only single frequency users need to have concerned with the ionospheric contributions to path delay. It will be seen shortly that by far the most important propagation effect as far as GPS is concerned is not propagation delay but scintillation.

In addition to a delay in the mean arrival time  $\Delta T$  and the well-known pulse distortion effect  $T_i$  [Wong et al, 1978], inhomogeneities in the ionospheric plasma give rise to a time delay spread of the radiowave signal (denoted by  $T_2$ ). The time delay spread is directly related to angular scattering. In general the time required for a signal to traverse a distance s is given by:

$$T = \frac{1}{c} \int ds + \Delta T_t + \Delta T_i + T_1 + T_2 \quad (9)$$

where  $\Delta T_t$  and  $\Delta T_i$  are the delays due to propagation through the troposphere and ionosphere respectively  $T_1$  is due to pulse distortion arising from finite signal bandwidth,  $T_2$  is due to scattering, and  $c^{-1} \int ds$  is the free space transit time.

The term  $\Delta T_i$  has been described previously (see equation 7); it is obviously first order. The term  $T_1$  arises due to the different speeds in which the various Fourier components of the signal travel [See Figure 40, 41 in Millman, 1965]. The term  $T_2$  is due to scattering from ionospheric turbulence. Figure 17 shows the relationship between the two.

### 3.6 Scintillation in Earth-Space Propagation

Fluctuations in signal power and phase often accompany radio wave propagation over earth-space paths as a result of inhomogeneities in the refractivity. This phenomenon, analogous to the twinkling of stars in the visible part of the electromagnetic spectrum, has been the object of research for several decades. Many excellent papers are available on ionospheric scintillation and the limited space provided herein does not allow the author to do justice to this extremely rich and interesting phenomenon. Nevertheless scintillation is probably the single most important deleterious factor in future systems utilizing the earth-space propagation path. Much experimental work has been conducted by Aarons and his coworkers at AFGL over the years and he has recently published a short summary of ionospheric scintillation which will serve as a good starting point for the uninitiated [Aarons, 1978]. A thorough review has been presented by Crane [1974]. The morphology of ionospheric scintillation, which is of major interest here, is now fairly well established although details remain to be clarified. A considerable amount of effort has been directed toward the development of models to describe the effect, ultimately directed toward communication channel modelling. In such approach has been to deduce the morphology from all available scintillation data and to derive the channel properties from the hypothesis of a two component signal statistical model [Fremouw and Rino, 1978]. Alternate schemes for modelling the scintillation morphology based upon strong tendencies for correlation with Spread F [Singleton, 1979a, 1979b] or upon the nature of the observed inhomogeneity wave number spectrum have also been suggested [Basu and Basu, 1976, 1979]. Figure 18 shows the scintillation index in the Pacific zone at 257 MHz based upon Singleton's model. Figure 19 is a sample set of scintillation contours obtained using OGO-6 in-situ irregularity data [Basu and Basu, 1979].

Much of the current attention is directed toward the scintillation cause and effect relationships both in the auroral and the equatorial zones. However, more emphasis is placed on the latter zone where the effect is most intense. Indeed GHz scintillation over very limited regions may sometimes occur following ionospheric sunset near the geomagnetic equator. The most interesting aspects of the current drive to understand the problem stems from the involvement of three seemingly distinct phenomena; viz, radar backscatter of small scale structures, scintillation caused by ionospheric inhomogeneities, and detection of quite large-scale electron content depletions or plumes. Clearly the instabilities which give rise to plume development is of major concern in understanding the equatorial scintillation

problem. Moreover the scintillation which exists at high latitudes is thought to arise from an entirely different instability and the modest scintillation which occurs at midlatitudes has not been fully investigated. Although plumes as such are not observed at high latitudes, large variations in TEC are at least circumstantially related to auroral zone scintillation since scintillation enhancements are conspicuous in the data only when the TEC gradient is exceedingly sharp [Rino, 1979]. A considerable advance in the total understanding of the ionospheric scintillation phenomenology as well as the underlying physical processes involved has been achieved through utilization of data sets (both amplitude and phase) obtained via the WIDEBAND DNA-002 program. It is well known that external factors related to sunspot activity strongly control ionospheric scintillation occurrence and amplitude. Solar activity tends to enhance equatorial scintillation and geomagnetic activity enhances scintillation near the auroral zone.

A considerable effort has been directed toward the elucidation of those parameters of importance to the design of systems which use the earth-space path in order to counter the scintillation problem. Fluctuations in signal power are a major problem to satellite links in the military band (225-400 MHz) unless compensating techniques are implemented. Communication systems may counter the effects of substantial fading by using space diversity. If the paths are of sufficient separation (depending upon the details of the inhomogeneity wave number spectrum) then fading is independent on the two links and diversity gain may be achieved. Separation of the order of a kilometer are involved and these useful minimum separations are certainly larger than ship dimensions at UHF [Paulson and Hopkins, 1973]. One would normally expect that radio links which are sufficiently separated in frequency, polarization, or transmission time would be effective in combating scintillation. Alas, this is not true in the case of polarization diversity, and furthermore frequency separation of up to 100 MHz may be required to obtain an adequate diversity gain. Clearly frequency diversity is not applicable in the UHF band but it may be applicable at higher frequencies where allocation problems are less severe. Consequently time diversity is the only viable procedure for overcoming scintillation at UHF. Coding and interleaving schemes have been investigated by Bucher [1975], White [1977], and Johnson [1975]. A study of ionospheric scintillation and its effect on the UHF Fleetbroadcast of FLEETSATCOM [APL Report, 1976] found that without any mitigation schemes employed

- (i) high latitude (i.e., Norwegian Sea) scintillation will distort message traffic up to 5% of the time.
- (ii) message traffic at midlatitudes will only rarely be distorted.
- (iii) equatorial (South and Central Pacific, South Atlantic, and Indian Ocean) scintillation will distort message traffic as much as 30% of the time following sunset and before midnight.

Alternative mitigation or avoidance schemes besides brute force (increasing antenna gain or transmitter power on the uplink or downlink as appropriate) include utilization of DSCS assets at 7-8 GHz for FLEETBROADCAST. This involves the reception of UHF FLTROADCAST by specified gateway stations that are also equipped with DSCS terminals. These gateways would be located adjacent to virulent scintillation zones but not within the zone themselves. Retransmission of the FLEETBROADCAST to assets in the scintillation zone would be accomplished via DSCS at 7-8 GHz where it is suspected that scintillation is not as severe. It is remarked, however, that selection of the gateway stations is rather a critical function of the known (presumed) morphology of scintillation, and the absence of GHz scintillation in the equatorial zone is by no means clear [Craft and Westerlund, 1972].

In practical terms the most important parameters needed for channel specification include  $S_4$  (the scintillation index),  $T_C$  (the fade coherence time), and a rough measure of the coherence bandwidth [Transionospheric Propagation W G Report, 1979]. The fade coherence time must, of course, be large compared to the baud duration to avoid failure; nevertheless as  $T_C$  decreases the "time diversity coding gain" will typically increase until the baud duration limit is reached. In this regime the  $S_4$  index is appropriate to the Nakagami [1960] distribution which describes the probability of amplitude scintillation adequately. As a result, fading depth statistics can be deduced with a degree of confidence knowing  $S_4$  alone. Further, the system degradation introduced by  $S_4$  can be retrieved through time diversity albeit with some loss in timeliness and throughput. Clearly in a Rayleigh fading environment (i.e.  $S_4 = 1$ ) the scintillation is characterized as "strong" and pulse distortion may arise in some instances given the conditions above. It is of interest to note that a precise description of the channel using complex signal statistics (i.e. amplitude phase) is unnecessary unless the fading is rapid and strong. But in this instance the Rayleigh model, which is well known and understood, may be employed. When  $S_4 = 1$  only a measure of  $T_C$  is needed to specify the performance of a communication channel.

There is presently an increased interest in utilizing the earth-space path

to transmit increasingly higher data rates and as mentioned above, scintillation conditions in some instances may not support such a requirement. Furthermore the need for greater accuracy and availability of precise navigation data only emphasizes the constraint placed on systems by ionospheric inhomogeneities. Techniques for synthesizing large antennas in space by coherent processing and for improving the detection range of space surveillance radars by coherent detection rely heavily on ionospheric smoothness at the frequency involved. Thus the temporal and spatial personality of inhomogeneities in the ionosphere (and the phase and amplitude scintillation which results) is of utmost relevance. The ionospheric limitation to coherent integration in transionospheric radars has been discussed by Rino et al [1978]. These authors find that the time variation of signal phase is given by

$$\phi(t) = \phi_0 + w(t-t_0) + \dot{w}(t-t_0)^2 + \delta\phi(t-t_0) \quad (10)$$

which is defined over a short interval ( $t_0 \leq t \leq t_0+T$ ) and  $\delta\phi$  is a random component of phase defined by a power law probability density function.

The  $\phi_0$  term is a phase bias due to TEC, the linear term  $w(t-t_0)$  is the doppler shift (which causes no problem for target coherent detection), and  $\dot{w}(t-t_0)^2$  gives rise to spectral broadening and may reduce processing gain as will the term  $\delta\phi(t-t_0)$ . For midnight periods both  $\dot{w}$  and  $\delta\phi$  are quite large over the equator limiting integration at VHF to much less than 10 seconds. More striking is that omnipresent non-vanishing  $\dot{w}$  values during the day will limit integration to less than a minute. (See Figure 20).

Tropospheric scintillation is also observed in both a clear air and cloudy environment. However the depth of fading is typically less pronounced than ionospheric scintillation observed at lower frequencies. Ionospheric amplitude and phase scintillation diminishes in proportion to  $f^{-1.5}$  and  $f^{-1}$  respectively, but tropospheric scintillation exhibits little resolvable frequency dependence [Hodge et al, 1976].

Both ionospheric and tropospheric scintillation increase as the zenith angle increases; nevertheless it is found that the obliquity factor for the tropospheric variety of scintillation is much more severe. Near the horizon, tropospheric scintillation will dominate at most earth-space frequencies except under the more virulent conditions. The variance of scintillation (scintillation index) is found to be proportional to  $L^{11/6}$  where L is the tropospheric path length. Scintillation as high as 25 dB has been observed at elevation angles of  $2^\circ$  in the 20-30 GHz band [Hodge et al, 1976].

### 3.7 Doppler Frequency and the Earth-Space Path

The well known expression for ionospheric excess doppler (Hz) is:

$$\Delta f = - \frac{40 \times 10^6}{cf} \frac{d}{dt} \int N_e ds \quad (11)$$

where  $f$  is the transmission radio frequency  $c$  is the speed of light, and  $N_e$  is the electron density.

This number is typically negligible in comparison with the free-space doppler introduced by satellite or target motion.

For geosynchronous satellites, the  $\Delta f$  correction to the transmission frequency is only academic (being only a fraction of a Hertz) and even for orbiting satellites  $\Delta f$  is relatively unimportant at typical space frequencies. Maximum value of the time derivative occurs near the horizon. Even in this extreme case and for  $\int N_e ds = 10^{18}$  electrons/m<sup>2</sup>,  $\Delta f$  will be less than 5 Hz at 1.6 GHz. Typically well-designed  $\phi$  lock tracking loops will encounter no difficulty. Even though the dispersive doppler introduced by the ionosphere is not significant as a system effect in earth-space propagation, it has been quite useful in ionospheric studies.

## 4. CONCLUSION

There are numerous applications for utilization of space in the arenas of communication, navigation, surveillance and related disciplines. The one unique advantage afforded by space is the vantage point it provides. A single satellite, appropriately placed in geosynchronous orbit, can observe and/or serve almost 1/2 the globe. The trend in DoD is for satellite platforms to be the backbone for most strategic and tactical communications, navigation, positioning and overhead surveillance. The virtues of satellites for use in commercial communication and remote sensing of earth resources, weather systems, ocean environment and related areas is well known. Furthermore the use of satellites for relay of data from earth terminals, buoys, and other satellites is of major significance.

Despite the trend toward increased utilization of space, there must be a parallel awareness that over-zealous commitment will not ultimately be an Achilles heel. Factors such as survivability in a strategic environment are being studied since they are obvious considerations. However, system architects should also be aware of the environmental constraints which the use of space will necessarily introduce. The ionospheric parameters of importance in space system design are known but their detailed personalities are not completely understood and most certainly forecasting capability is almost non-existent. Typically ad-hoc climatologies are employed to define the ranges (i.e. margins) over which systems must be made to adapt. Thus ionospheric and tropospheric research has been of great benefit to system designers in specifying to first order the degree of robustness which must be engineered into space systems. Further design constraint reductions would be achieved through use of second order improvements involving some form of environmental monitoring or assessment function. Increasingly the point of view is emerging that the short-term forecasting requirement must be achieved through quasi-real-time environmental remote sensing which is employed in conjunction with algorithms for extrapolation into denied areas.

Not to be ignored is the examination of environmental limitations to earth-space propagation in that such limitations apply to both adversary as well as friendly forces. It is not inconceivable that techniques for exploitation and/or control of the environment may well be components in the hierarchy of future electronic warfare systems. Of special interest in this regard are emerging studies of ionospheric modification using chemical reagents and RF heating. Natural disturbances also have morphologies which might also be exploited although current capability to forecast natural events is probably insufficient. With the increased demands placed upon space systems in terms of accuracy and data rate, the environmental constraints upon the earth-space path may well be a limiting factor in the ability to achieve the design goals. The successful search for "windows" or "doors" in which environmental constraints exhibit extremes should enable enhanced operation in both natural and disturbed environments and more secure operation against a threat. To the extent that natural "doors" and "windows" are non-existent, their creation may be critical and more than justifies continued research in the arena of environmental modification.

#### REFERENCES

- AARONS J., 1978, "Ionospheric Scintillations - An Introduction", in Recent Advances in Radio and Optical Propagation for Modern Communications, Navigation and Detection Systems, edited by J. Aarons, AGARD-LS-93, Tech. Edit. and Reprod. Ltd., London.
- ALBRECHT H. J. (editor), 1971, Tropospheric Radio Propagation (Parts 1 & 2), NATO-AGARD-CP-70-71, Tech. Edit. and Reprod. Ltd., London.
- BASU S., S. BASU, and B. K. KHAN, 1976, "Model of Equatorial Scintillation from In-Situ Measurements", Radio Sci., 11, 821.
- BASU S. and S. BASU, 1979, "Model of Phase and Amplitude Scintillations from In-Situ Data", Paper 129 prepared for STP-PW Conference, Boulder.
- BATTAN L. J., 1959, Radar Meteorology, Univ. of Chicago Press., Chicago.
- BEACH J. B., 1979, "Atmospheric Effects on Radiowave Propagation", Defense Electronics, Dec., pp 95-98.
- BEAN B. R., and B. A. CAHOON, 1957, "Use of Surface Weather Observations to Predict the Total Atmospheric Bending of Radiowaves at Small Angles", Proc. IRE 45, 145-6.
- BEAN B. R. and R. E. MCGAVIN, 1965, "A Review of Refraction Effects on the Apparent Angle of Arrival of Radio Signals", in Propagation Factors in Space Communications, edited by W. T. Blackband, NATO-AGARD Conf. Proc., Technivision, Maidenhead, England.
- BEAN B. R., B. A. CAHOON, C. A. SAMSON, and G. D. THAYER, 1966, "A Worldwide Atlas of Radio Refractive Index", ESSA Monograph 1, U. S. GPO, Washington, D. C.
- BEAN B. R. and E. J. DUTTON, 1966, Radio Meteorology, NBS Manograph 92, Supt. Doc., GPO, Washington, D. C.
- BEAN B. R. and E. J. DUTTON, 1976, "Radio Meteorological Parameters and Climatology", Telecomm. J., 43 (VI), 427-435.
- BEAN B. R., G. D. THAYER, and B. A. HART, 1971, "Worldwide Characteristics of Refractive Index and Climatological Effects", in Tropospheric Radio Propagation (Part 1), edited by H. J. Albrecht, NATO-AGARD-CP-70; Tech. Edit. and Reprod. Ltd., London.

- BEM D. J., 1979 "Propagation Aspects in the Planning of Telecommunication Services", J. Telecomm. 46 (XI).
- BENT R. B., S. K. LLEWELLYN, and M. K. WALLOCK, 1972, "Description and Evaluation of the BENT Ionospheric Model", SAMSO TR-72-239, DDC-AD 753081-6, DBA Systems, Melbourne, Fla.
- BOITHIAS L., 1976, "Structure of the Tropospheric Refractive Index and Propagation", Telecomm. J., 43 (VI), 419-426.
- BROWNE I. C., J. V. EVANS and J. K. HARGREAVES, 1956, "Radio Echoes from the Moon", Proc. Phys. Soc., London, B, 69, 901.
- BUCHER E. A., 1975, "UHF Satellite Communications During Scintillation", Lincoln Lab TN 1975-10.
- BUDDEN K. G., 1964, Lectures on Magnetionic Theory, Gordon and Breach, New York.
- CCIR Report 263-3, 1974, "Ionospheric Effects on Earth-Space Propagation".
- CRAFT H. D. and L. H. WESTERLUND, 1972, "Scintillations at 4 and 6 GHz Caused by the Ionosphere", paper presented at AIAA 10th. Aerospace Sciences Meeting, San Diego.
- CRANE R. K., 1974, "Morphology of Ionospheric Scintillation", Lincoln Lab., TN-1974-29.
- CRANE R. K., 1977, "Prediction of the Effects of Rain on Satellite Communication Systems", Proc. IEEE, Vol. 65, #3.
- CRETCHER C. K., 1975, "Ionospheric Effects in NAVSTAR GPS", in Effect of the Ionosphere on Space Systems and Communications edited by J. M. Goodman, IES '75, U. S. Gov't Printing Office, Washington, D. C.
- DAVIES K., 1965, Ionospheric Radio Propagation, NBS Monograph 80, Supt. Doc. U. S. Gov't Printing Office, Washington, D. C.
- EVANS J. V. and R. H. WAND, 1975, "Ionospheric Limitations on the Angular Accuracy of Satellite Tracking at UHF or VHF", in Radio Systems and the Ionosphere, edited by W. T. Blackband, NATO-AGARD-CP-173, Tech. Edit. and Reprod. Ltd., London.
- FREMOUW E. J. and C. L. RINO, 1978, "A Signal Statistical and Morphological Model of Ionospheric Scintillation", in Operational Modelling of the Aerospace Propagation Environment, edited by H. Soicher, AGARD-CP-238, Tech. Edit. and Reprod. Ltd., London.
- GARBACZ M., H. MANNHEIMER, and W. STONEY, 1976, "Earth Observations Satellites (Past, Present, and Future)", NTC Proceedings, IEEE, New York, 25.4-1 to 4-6.
- GERSON N. C., (editor), 1962, Radiowave Absorption in the Ionosphere, AGARDOGRAPH 53, Pergamon Press, New York.
- GOLDEN T. S., 1968, "Ionospheric Distortion of Minitrack Signals in South America", Goddard SFC Report X-525-68-56.
- GOODMAN J. M., (editor), 1975, Effect of the Ionosphere on Space Systems and Communication, GPO, Washington, D. C.
- GOODMAN J. M., (editor), 1978, Effect of the Ionosphere on Space and Terrestrial Systems, GPO, Washington, D. C.
- GOULD R. G., 1976, "Commercial Communication Satellites: Operational, Experimental and Planned", NTC Proceedings, IEEE, New York, 25.5-1 to 5-8.
- GUNN K. L. S. and T. W. R. EAST, 1954, "The Microwave Properties of Precipitation Particles", Quarterly J. Roy. Met. Soc., 80, 522-545.
- HENDERSON D. W., 1979, "NAVSTAR GPS System and Technology Outlook", in Proc. AIAA Conference, New Directions in C<sup>3</sup> Systems and Technology, Washington, D. C.
- HODGE D. B., D. M. THEOBOLD, and R. C. TAYLOR, 1976, "ATS-6 Millimeter Wavelength Propagation Experiment", Ohio State Univ. Electro Science Lab., Report 3863-6.
- IPPOLITO L. J., 1975, Unpublished lecture notes for GWU Course 501, Millimeter Wave Space Communications.

- JOHNSON A. L., 1975, "Simulation and Implementation of a Modulation System for Overcoming Ionospheric Scintillation Fading" in Radio Systems and the Ionosphere, edited by W. T. Blackband, AGARD-CP-173, Tech. Edit. and Reprod. Ltd., London.
- JOSS J., J. C. THAMS, and A. WALDVOGEL, 1968, "The Variation of Raindrop Size Distributions at Locarno", Proc. Int. Conf. Cloud Physics, Toronto, pp 369-373.
- KELSO, J. M., 1964, Radio Ray Propagation in the Ionosphere, McGraw-Hill, New York.
- KERR D. E., 1951, Propagation of Short Radio Waves, McGraw-Hill, New York (Also Dover Publications, New York, 1965).
- KLOBUCHAR J. and R. ALLEN, 1970, "A First-Order Prediction Model of Total Electron Content for a Midlatitude Ionosphere", AFCL-70-0403.
- KLOBUCHAR J. A., 1977, "Ionosphere Time Delay Corrections for Advanced Satellite Ranging Systems", in Propagation Limitations of Navigation and Positioning Systems, AGARD-CP-209, Tech. Edit. and Reprod. Ltd., London.
- KLOBUCHAR J. A., 1978, "Ionospheric Effects on Satellite Navigation and Air Traffic Control Systems", in Recent Advances in Radio and Optical Propagation for Modern Communications, Navigation and Detection Systems, edited by J. Aarons, AGARD-LS-93, Tech. Edit. and Reprod. Ltd., London.
- KLOBUCHAR J. A., (editor), 1979, Report of the Transionospheric Propagation Working Group", STP-PW Conference, Boulder.
- LAWRENCE R. S., C. G. LITTLE, and H. J. A. CHIVERS, 1964, "A Survey of Ionospheric Effects Upon Earth-Space Radio Propagation", Proc. IEEE, Vol. 52, pp 4-27.
- LAWS J. O. and D. A. Parsons, 1943, "The Relation of Raindrop Size to Intensity", Trans. AGU, 24, 452-460.
- MARSHALL J. S., and W. M. Palmer, 1948, "The Distribution of Raindrops with Size", J. Meteorology 5, 165-166.
- MENDILLO M., (editor), 1976, "The Geophysical Use of Satellite Beacon Observations", Boston University Pub.
- MILLER D. L., 1976, "Military Satellite Communication Systems", NTC Proceedings, IEEE, New York, 25.1-1 to 1-4.
- MILLMAN G. H., 1967, "A Survey of Tropospheric, Ionospheric, and Extra-Terrestrial Effects on Radio Propagation Between the Earth and Space Vehicles", in Propagation Factors in Space Communications, edited by W. T. Blackband, NATO-AGARD Conference Proc., Technivision, Maidenhead, England; also G. E. Report TISR66EMHI, pub. 1965.
- MILLMAN G. H., 1971, "Tropospheric Effects on Space Communications", in Tropospheric Radio Propagation (Part 1), edited by J. J. Albrecht, NATO-AGARD-CP-70, Tech. Edit. and Reprod. Ltd., London.
- MJCS 251-76 of 31 Aug 1976 (Validation of Military Requirements for Meteorological Satellite Data).
- NAKAGAMI M., 1960, "The M-Distribution - A General Formula for Intensity Distribution of Rapid Fading" in Statistical Methods on Radio Wave Propagation, edited by W. C. Hoffman, Pergamon Press, New York.
- PARKINSON B. W., E. M. LASSITER, and C. K. CRETCHER, 1977, "Ionospheric Effects in NAVSTAR/GPS", in Propagation Limitations of Navigation and Positioning Systems, edited by P. Halley, AGARD-CP-209, Tech. Edit. and Reprod. Ltd., London.
- PAULSON M. R. and R. U. F. HOPKINS, 1973, "Effects of Equatorial Scintillation Fading on SATCOM Signals", NELC/TR/1875.
- PISACANE V. L., M. M. FEEN, and M. STURMANIS, 1972, "Prediction Techniques for the Effect of the Ionosphere on Pseudo-Ranging from Synchronous Altitude Satellites", SAMSO TR-72-22, DDC-AD 749486, APL.
- RAO N. N., M. Y. YOREAKIM, and K. C. YEH, 1971, "Feasibility Study of Correcting for the Excess Time Delay of Transionospheric Navigational Ranging Signals", SAMSO TR-71-63, DDC-AD-729797, University of Illinois.
- REYNOLDS J. W., 1979, (quote) appearing in "Shift to Millimeter Wave in Space Scene", by P. L. Klass, Aviation Week and Space Technology, Nov. 5, pp 67-69.

RINO C. L., C. H. HAWSON, R. G. LIVINGSTON, and J. PETRICEKS, 1978, "The Ionospheric Limitation to Coherent Integration in Transionospheric Radars" in Effect of the Ionosphere on Space and Terrestrial Systems, edited by J. M. Goodman, GPO, Washington, D. C.

RINO C. L., 1979, "Some Ramifications of the Wideband Satellite Data for Scintillation Modelling", paper prepared for STP-PW Conference, Boulder.

ROSEN P., 1979, "Military Satellite Communication Systems: Directions for Improvement", Signal, Nov-Dec, pp 33-38.

RUSH C. M., 1979, "Transionospheric Radio Propagation", in Aerospace Propagation Media Modelling and Prediction Schemes for Modern Communications, Navigation, and Surveillance Systems, edited by H. Soicher, AGARD-LS-99, Tech. Edit. and Reprod. Ltd., London.

RYDE J. W. and D. RYDE, 1945, "Attenuation of Centimeter and Millimeter Waves by Rain, Hail, Fog and Clouds", Report 8670, G. E. Research Labs., Wembley, G. B.

SCHEMME B. F., 1978, "Strategic C<sup>3</sup>: The Satellite Arena - 20 Years of the Sputnik", Armed Forces Journal International, February, pp 18-30.

SINGLETON D. G., 1979a, "Predicting Transionospheric Propagation Conditions", paper prepared for STP-PW Conference, Boulder.

SINGLETON D. G., 1979b, "An Improved Ionospheric Irregularity Model", paper 59 prepared for STP-PW Conference, Boulder.

Staff, Space Development Dept., APL, 1976, "The Effect of Ionospheric Scintillation on the Fleet Broadcast of the Fleet Satellite Communication System", SDO-4380.6.

U. S. Navy Space Master Plan, 1979.

WALDMAN H. and A. V. DAROSA, 1971, "Prognostication of Ionospheric Electron Content", SAMSO TR-71-82, DDC-AD 731095/6, Stanford University.

WHITE D. P., 1977, "A Time Diversity Coding Experiment for a UHF/VHF Satellite Channel with Scintillation: Equipment Description", Lincoln Lab TN 1977-22.

WONG Y. K., K. C. YEH, and C. H. LIU, 1978, "Mean Arrival Time and Mean Pulse Width of Signals Propagating Through an Inhomogeneous Ionosphere with Random Irregularities" in Effect of the Ionosphere on Space and Terrestrial Systems, edited by J. M. Goodman, GPO Washington, D. C.

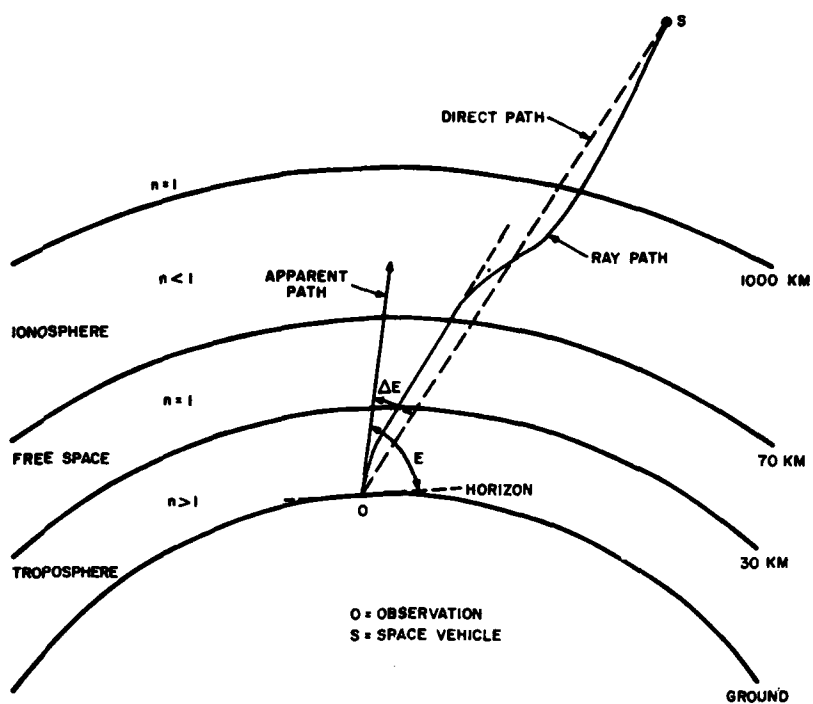


Fig. 1 Radiowave Trajectory through the Troposphere and Ionosphere. (After Millman [1965])

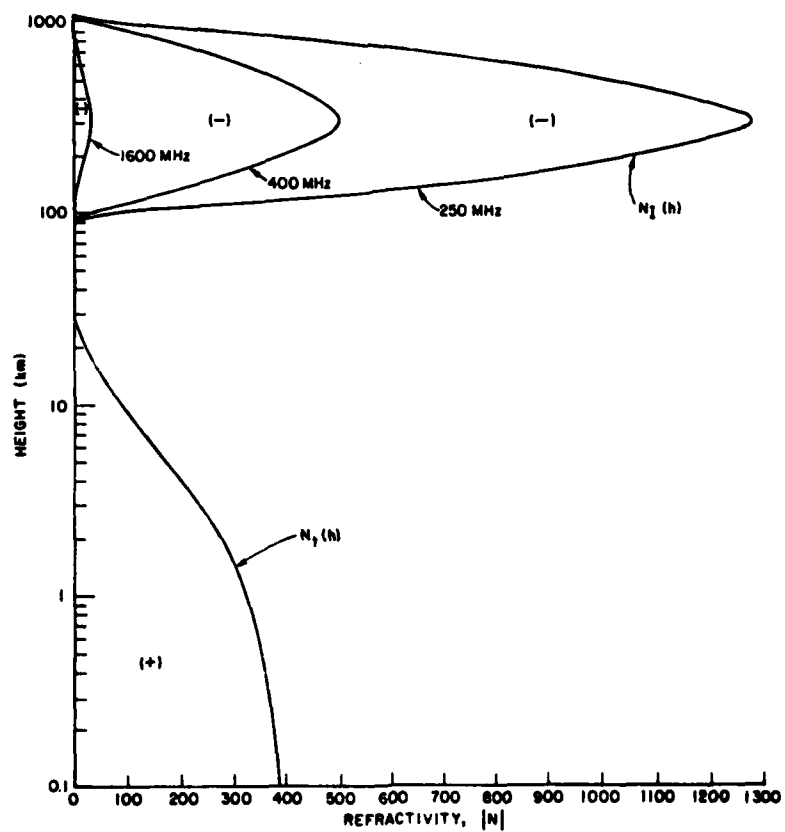


Fig. 2 Radio refractivity versus altitude. Representative ionosphere profiles are shown for 250, 400, and 1600 MHz. The tropospheric refractivity profile is based on data from Bean et al [1971].



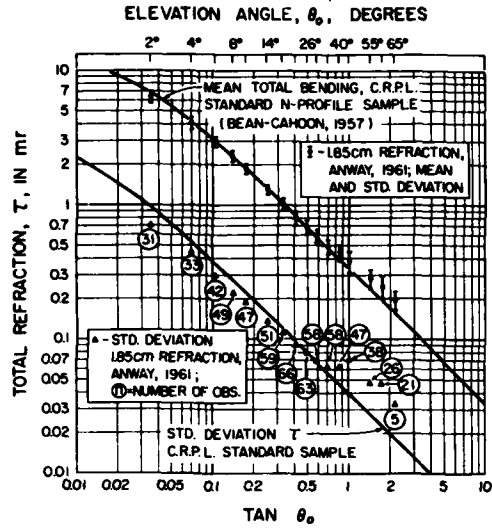


Fig. 3 Total atmospheric refraction  $\tau$  and its standard deviation  $\Delta$  versus elevation angle  $\theta_0$ . Also shown is a comparison with actual measurements at a radio wavelength of 1.85 cm (16.2 GHz). (From Bean and McGavin [1965])

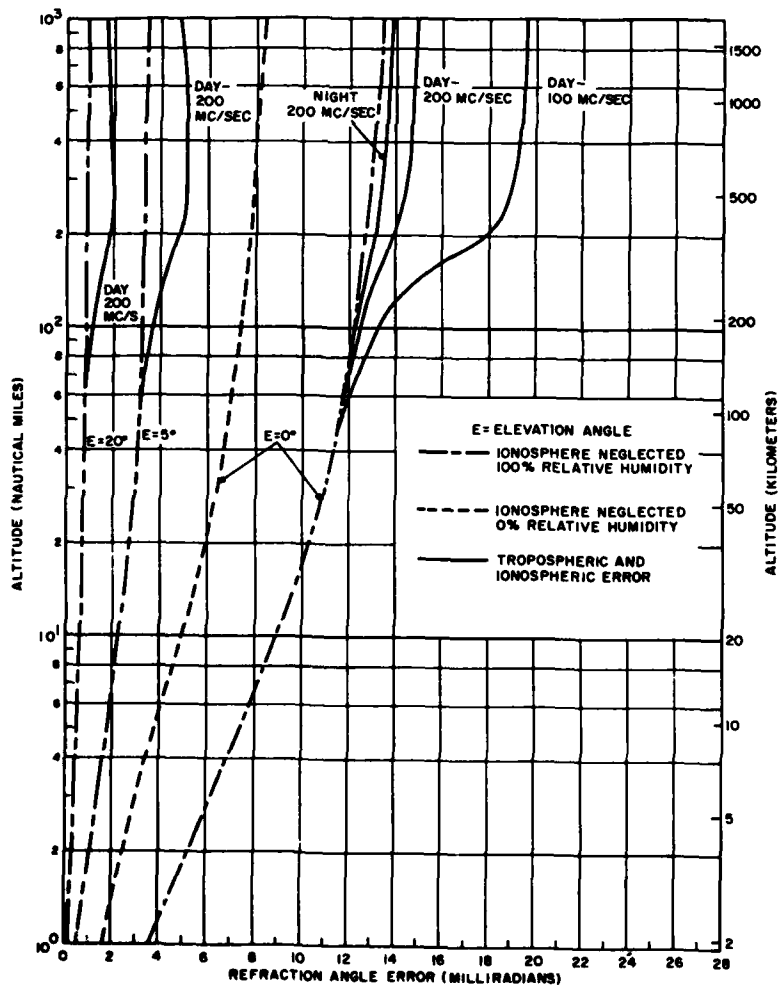


Fig. 4 Total Refraction error at 100 and 200 MHz as a function of altitude. (From Millman [1965])

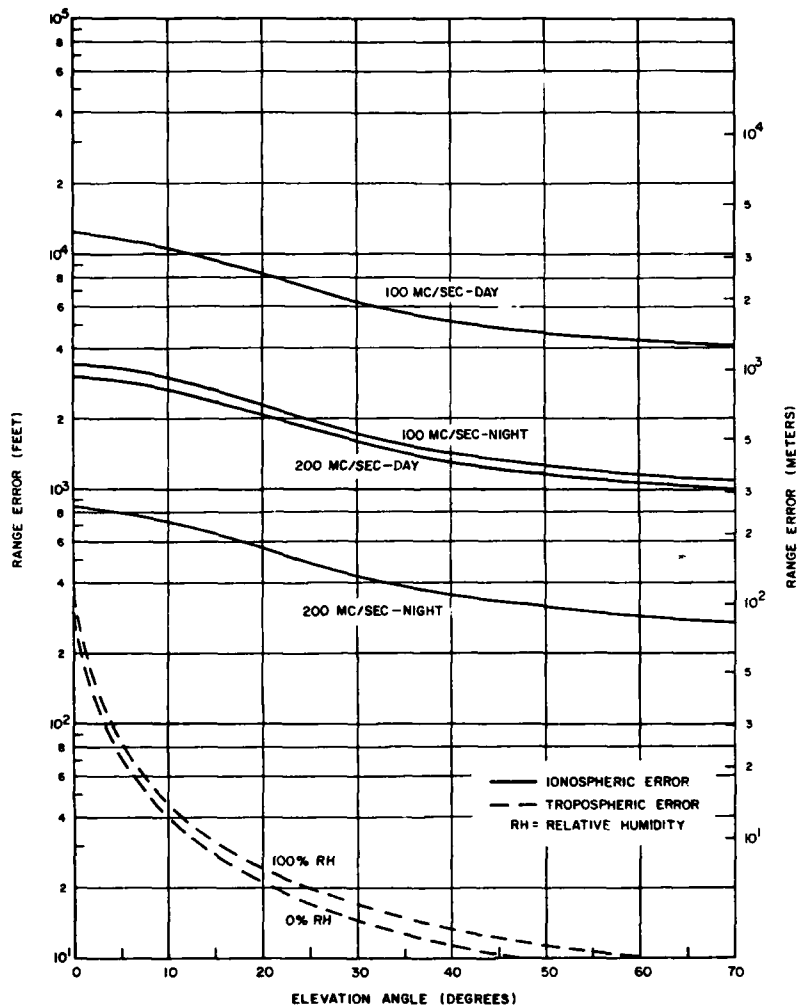


Fig. 5 Limiting tropospheric and ionospheric range error as a function of elevation angle. (From Millman [1965])

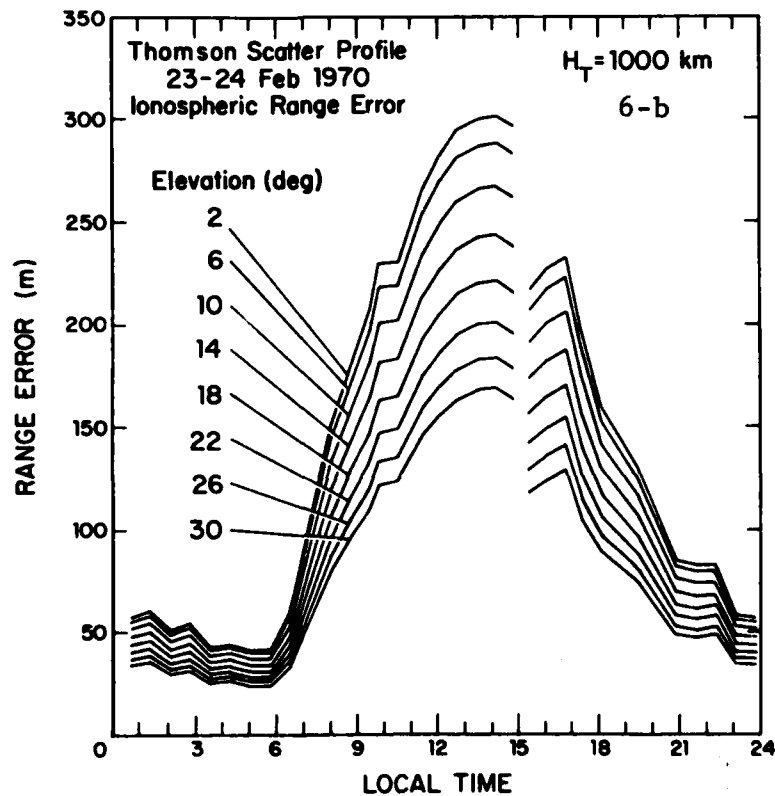
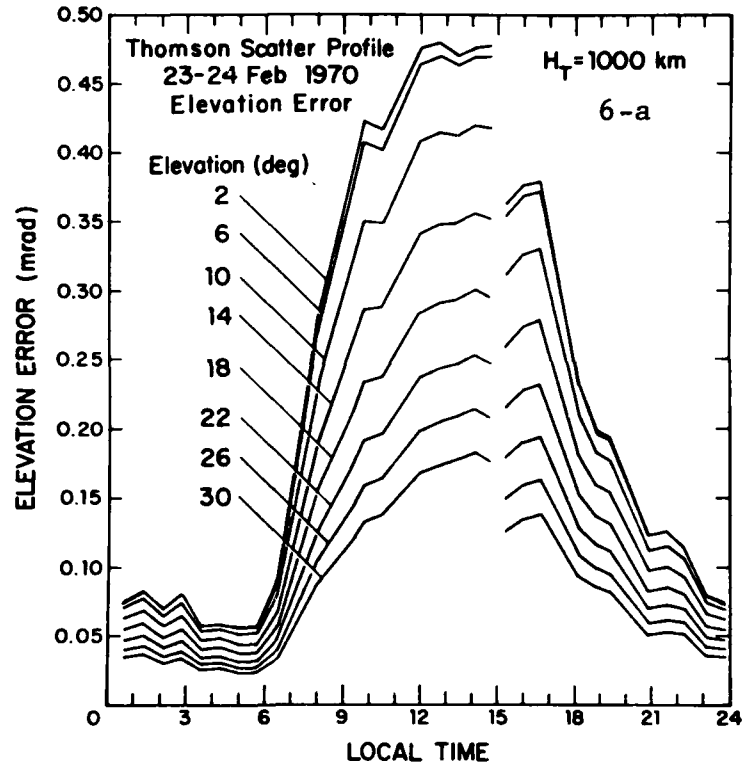


Fig. 6 Ionospheric refraction (a) and range (b) errors at 400 MHz as deduced by ray tracing through Thomson scatter - derived electron density profiles. (From Evans and Wand [1975])

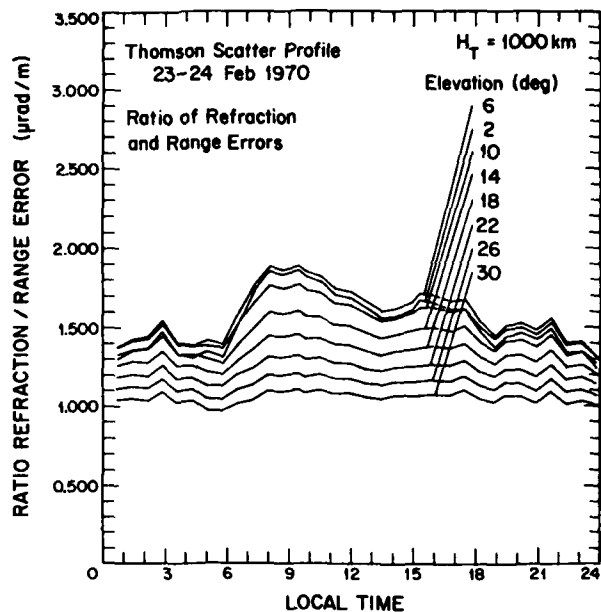


Fig. 7 Ratio of elevation angle to range error at 400 MHz (from Evans and Wand [1975]). Note that the ratio becomes more linear as the launch elevation angle is increased indicating a reduction in delay due to bending. The bending enhancement in range error is most pronounced at sunrise.

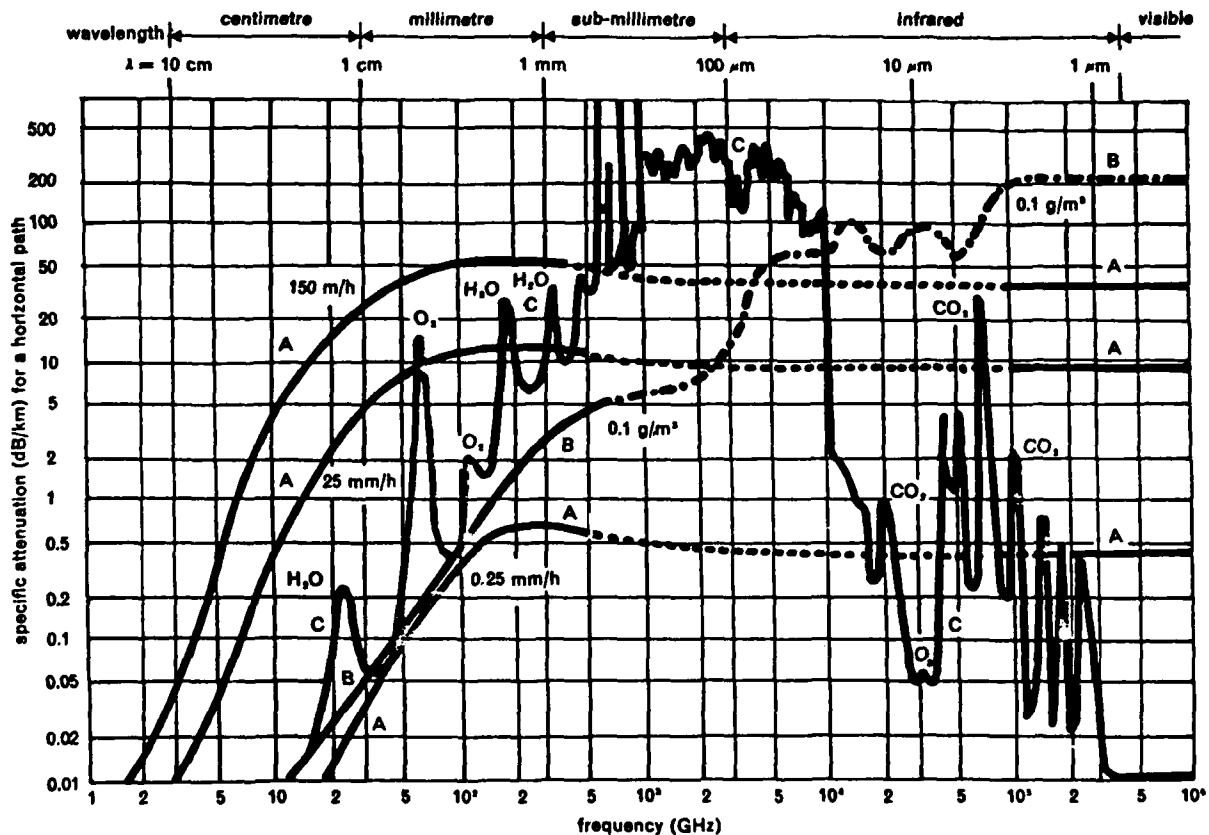


Fig. 8 Specific attenuation of radiowaves, IR, and visible light due to atmospheric constituents. The conditions assumed:  $T = 20^\circ\text{C}$ , vapor pressure =  $7.5 \text{ cm}^3$ . A = rain, B = Fog, C = Gas. (From Bem [1979])

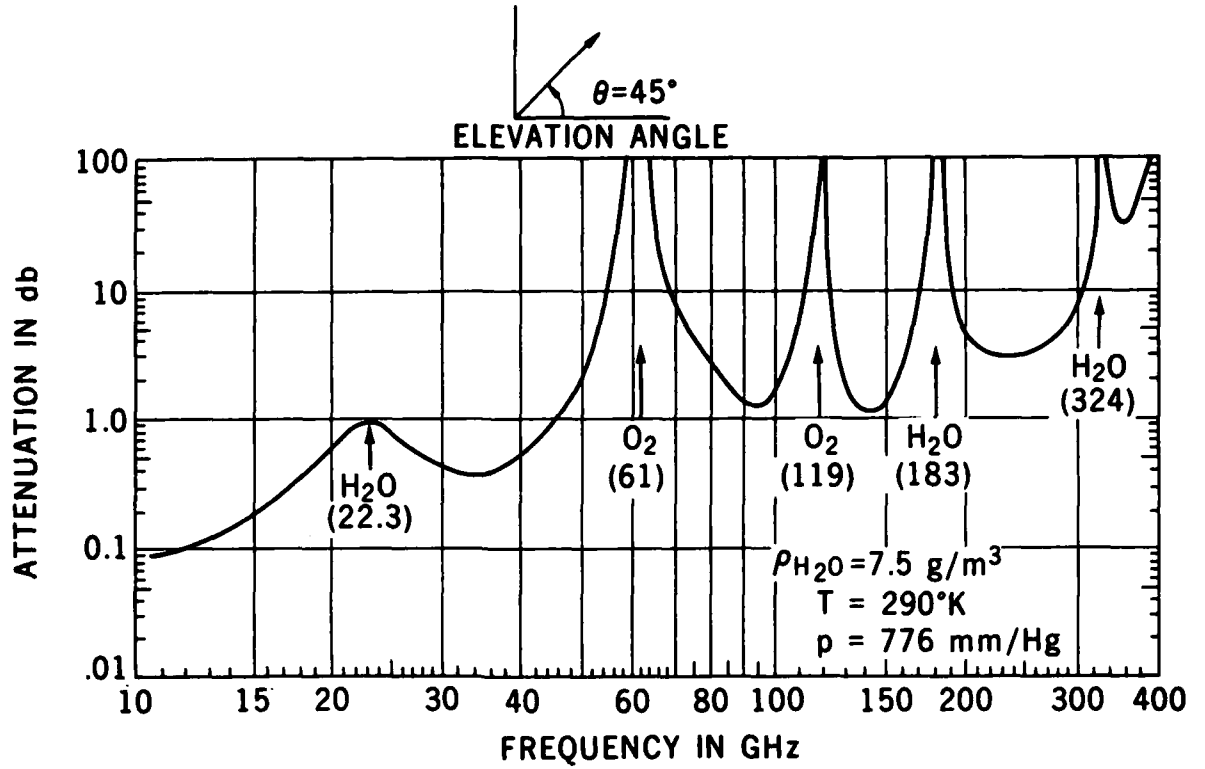


Fig. 9 Total attenuation of the atmosphere due to resonance absorption. (From Ippolito [1978])

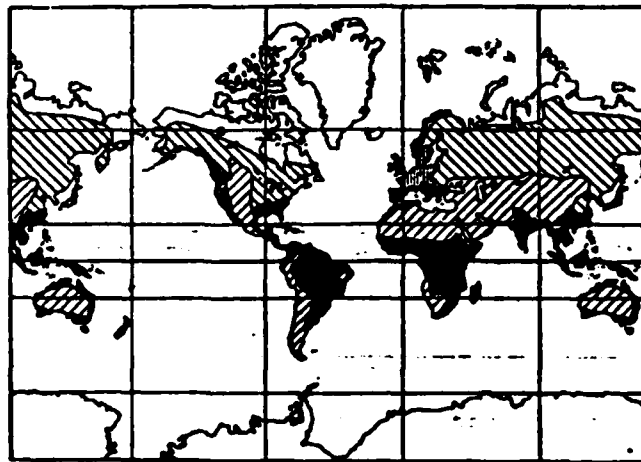


Fig. 10 Rainfall distribution. (See Figure 11 for Rain rate distributions). (From Bean and Dutton [1976])

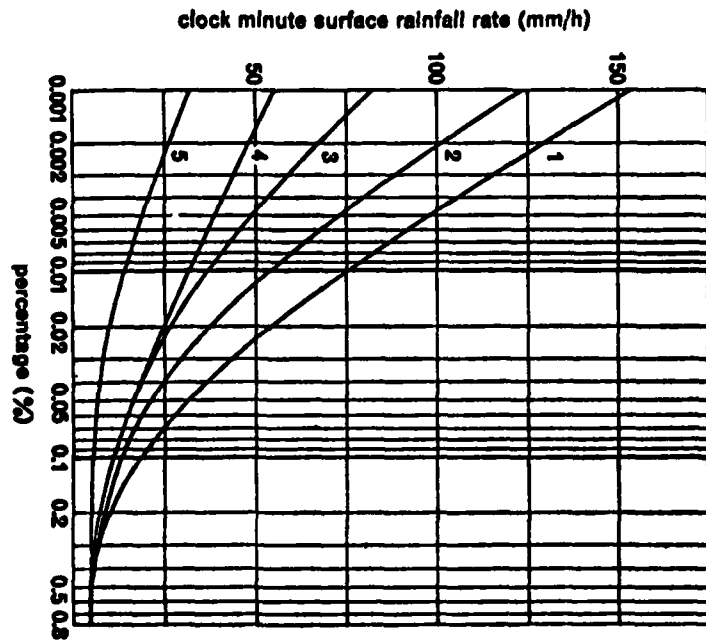


Fig. 11 Average yearly percentage of time specified rain rate is exceeded. (Regions 1-5 are depicted in Figure 10). (From Bean and Dutton [1976])

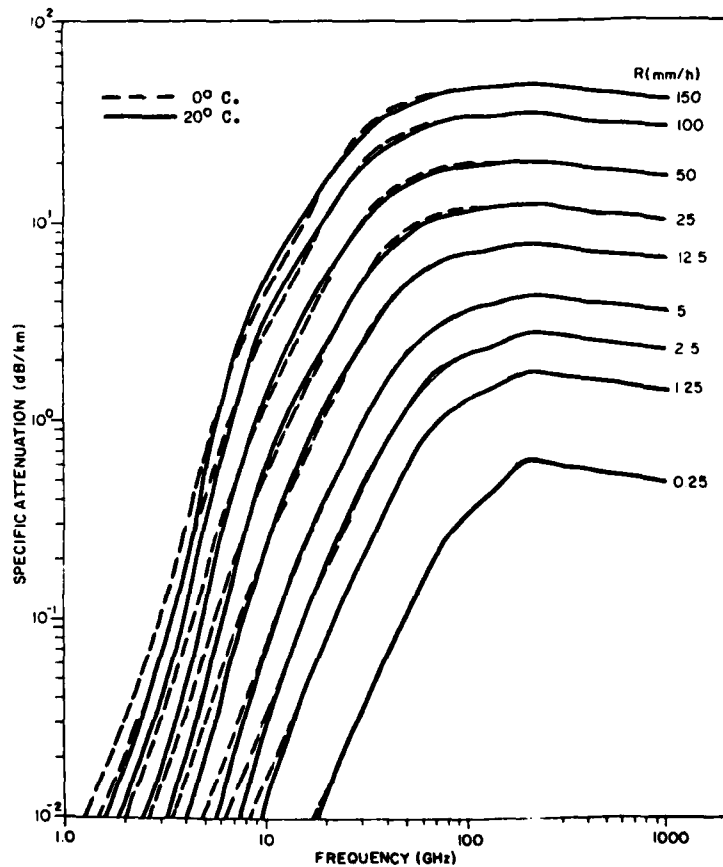


Fig. 12 Predicted specific rainfall attenuation versus frequency (From Ippolito [1978])

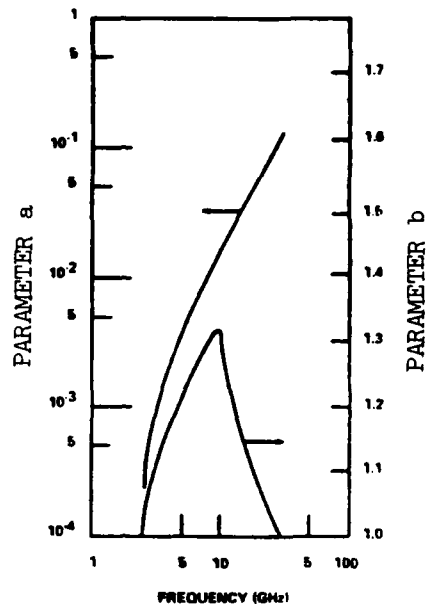


Fig. 13 Frequency - dependent parameters a(f) and b(f). (From Beach [1979])

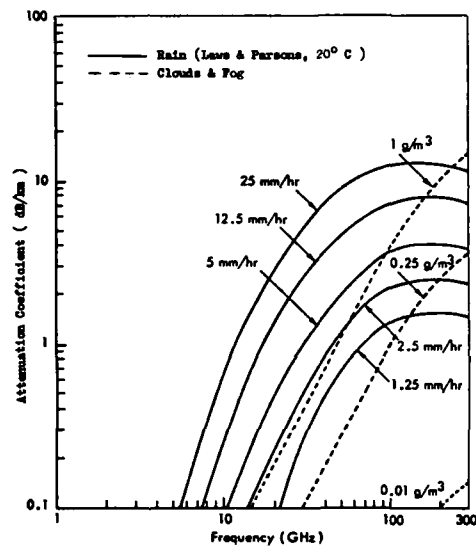


Fig. 14 Comparison of Cloud, Fog, and Rain attenuation. (From Ippolito [1978])

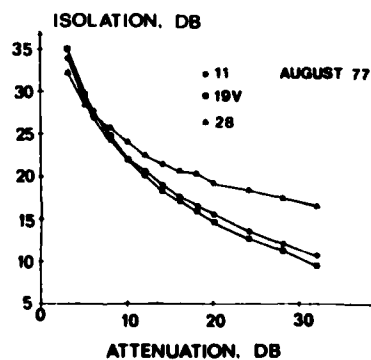


Fig. 15 Polarization isolation (dB) versus signal attenuation (dB). (From Ippolito [1978])

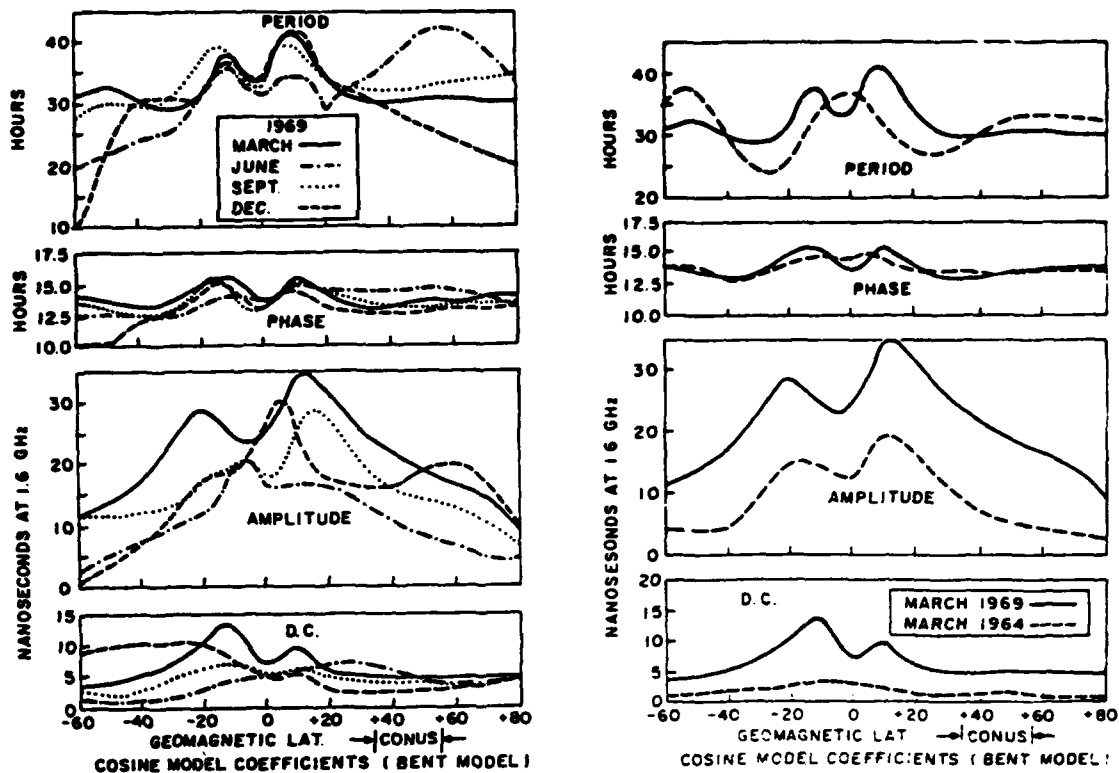


Fig. 16 Latitudinal variation of the coefficients of ionospheric time delay. A: Seasonal effects at solar maximum; B: comparison of solar maximum and solar minimum in March. (From Klobuchar [1977])

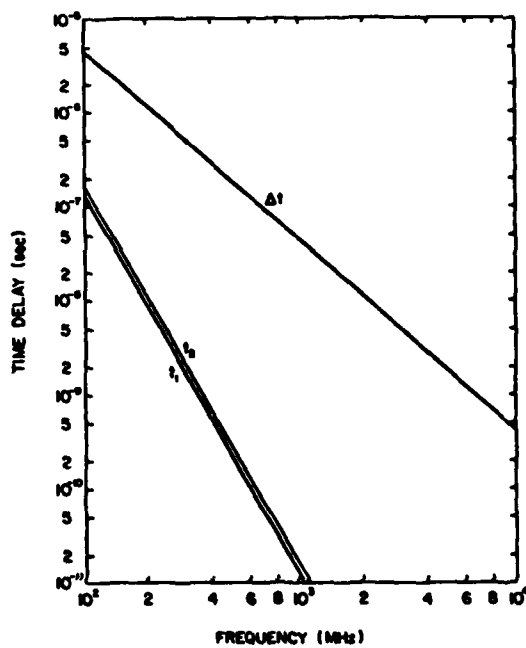


Fig. 17 Time delay parameters  $\Delta T$  (mean delay),  $T_1$  (distortion of the pulse), and  $T_2$  (scattering) as a function of frequency. (From Wong et al [1978])



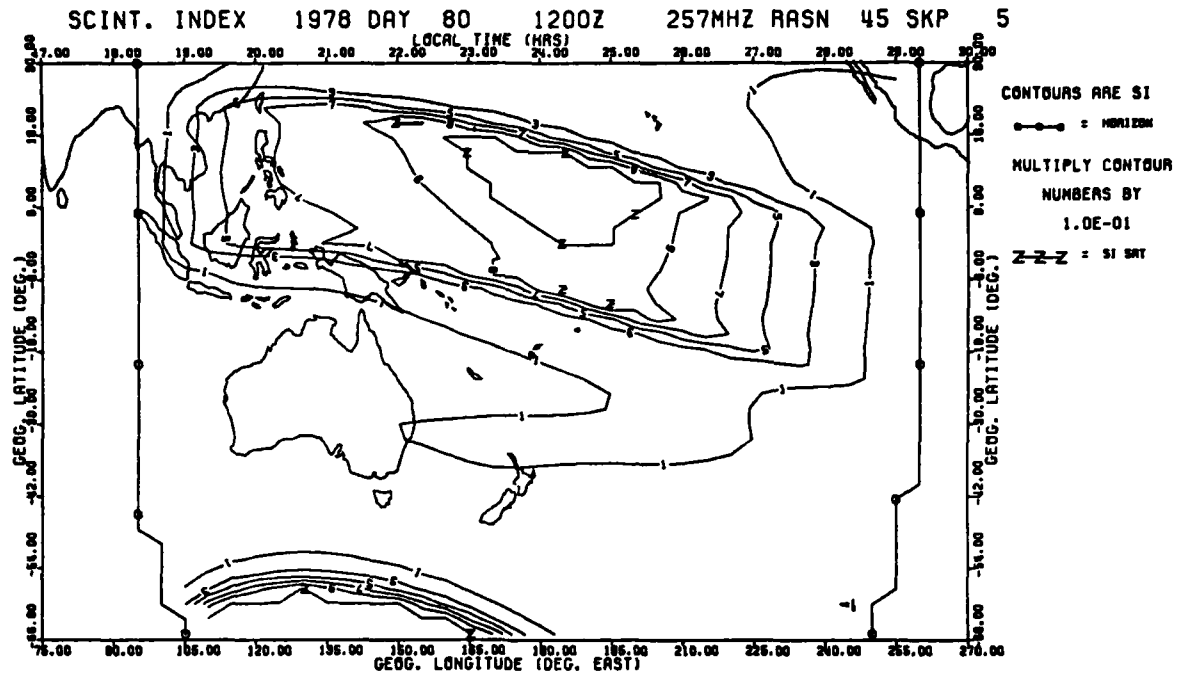


Fig. 18 Scintillation index over the Pacific sector at a frequency of 257 MHz; other parameters are: 1200Z, Spring equinox, sunspot number 45, and  $K_p = 5$ . The satellite is located at  $176.5^\circ\text{E}$ . (From Singleton [1979])

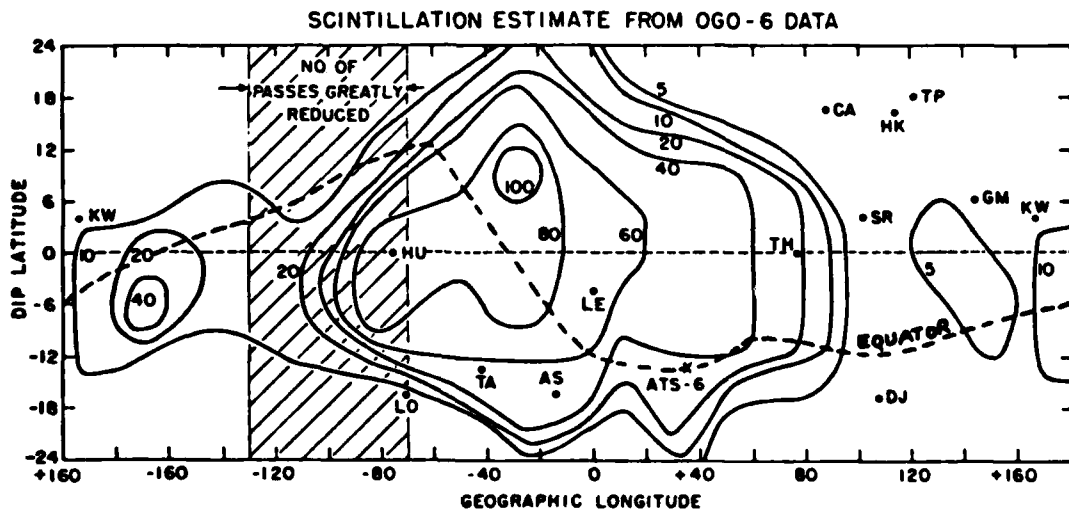


Fig. 19 Percentage occurrence of amplitude scintillation  $> 0.24$  (given by  $S_4$ ) or phase scintillation  $\geq 0.1$  radian at a frequency of 140 MHz. Time period Nov-Dec 1969-70 between 1900 and 2300 Mean local time. (From Basu and Basu [1979])

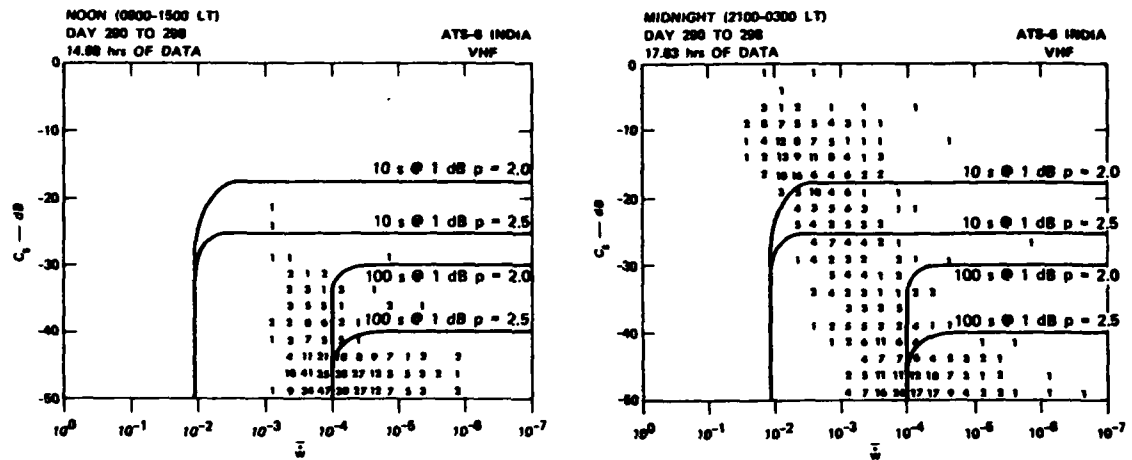


Fig. 20 Histograms of  $C_S$ (dB) and  $\bar{W}$  for both noon (A) and midnight (B) from a set of ATS-6 differential phase data at 165 MHz obtained at an Indian site. The phase spectrum is assessed to have the form  $C_S f^{-p}$  where  $p$  is the power law (After Rino et al [1978])

A PRELIMINARY EVALUATION OF THE TWO-FREQUENCY IONOSPHERIC  
CORRECTION FOR THE NAVSTAR-GLOBAL POSITIONING SYSTEM

J.A. Klobuchar  
Air Force Geophysics Laboratory  
Hanscom AFB, MA 01731

H. Soicher  
U.S. Army Communications Research & Development Command  
Ft. Monmouth, NJ 07703

J.A. Pearson  
Navigation Satellite System Directorate  
The Aerospace Corporation  
Los Angeles, CA 90009

SUMMARY

The Navstar Global Positioning System (GPS) is an advanced worldwide navigation system with a design accuracy of 16 meters spherical error probability for 50%ile in 3 dimensions. The largest potential error source in the navigation system is due to the group path retardation of the earth's ionosphere which can produce range delays of up to 100 meters on a worst case basis. Analytic models can be utilized to reduce the ionospheric error contribution, but the use of a state of the art ionospheric time delay model is expected to reduce the ionospheric range error by not more than 75 percent, still leaving worst case delays of approximately 25 meters, well above the system design specifications.

Fortunately the ionosphere is a dispersive medium with the amount of the ionospheric time delay proportional to the inverse square of the operating frequency. Hence, a second modulated frequency, called L2, was incorporated on the GPS signal structure to allow the system user's receiver to automatically correct for the ionospheric time delay. The initial tests of the correction capability of this dual frequency signal structure was provided by a GPS modulator which was orbited on the NTS-2 satellite in late 1977. In an attempt to evaluate the accuracy of the two frequency ionospheric correction system several days of two frequency navigation data were obtained from the NTS-2 preliminary system tests from the GPS master control facility and from two GPS monitor stations and comparisons were made of the ionospheric time delays measured at these three stations with independent measurements of ionospheric time delay taken at nearby locations by other methods. The results of these comparisons showed excellent agreement indicating successful operation of the two frequency technique, and also showed that careful attention must be paid to the differential receiving system signal delays over the two frequency bandwidth. The effects of multipath at lower elevation angles are clearly seen as increased system noise, though multipath did not affect the two frequency ionospheric correction capability.

1. INTRODUCTION

The Navstar Global Positioning System, GPS, is an advanced navigation system, currently in its advanced development phase, in which a user would determine position by measuring pseudo range from precisely known clock signals transmitted from four, high orbit satellites. The user requires measurements from four satellites to determine his position in three dimensions and to correct for the unknown time reference of his own clock against which the received time information from each satellite is measured. Lassiter and Parkinson (1977) have described the details of the proposed GPS in which the primary navigation frequency is 1,575 MHz. At this frequency the ionosphere can delay the arrival time of radio waves which pass through it over 100 meters in range on a worst case basis. The overall desired accuracy of the GPS navigation is 16 meters spherical error probability for 50%ile in 3 dimensions, therefore the ionospheric range error is clearly unacceptable and can, at times, be the largest single error source in the system.

Fortunately the ionosphere is a dispersive medium, that is, the amount of the time delay effect is proportional, to first order, to the inverse square of the system operating frequency. A suitable choice of two operating frequencies can be used to actually measure the ionospheric time delay directly and automatically correct the measured pseudo range for the ionosphere at the system operating frequency. In fact, the GPS was designed to make exactly this direct measurement of ionospheric time delay and to automatically correct for ionospheric time delay. The desired residual ionospheric error after the two frequency correction is 2 meters r.m.s. It is the purpose of this paper to describe the results of the first tests of the accuracy of the two frequency ionospheric time delay elimination technique, using data taken from transmissions from the GPS modulator placed on board the Navigation Technology Satellite (NTS-2) launched in late 1977.

2. RELATIONSHIP BETWEEN IONOSPHERIC TIME DELAY AND TOTAL ELECTRON CONTENT

The ionospheric time delay is related to the total number of electrons along the slant path to the satellite by

$$\Delta t = \frac{40.3}{cf^2} \text{ TEC}$$

where  $f$  is the system operating frequency, in Hertz,  $c$  is the velocity of light in meters per second and TEC is the Total Electron Content, total number of electrons along the path from the satellite to the receiver in units of electrons per square meter column. For a two frequency system, the differential time delay between the ionospheric delay at frequencies  $L1$  and  $L2$  can be measured, and this differential time delay can be used to determine the total time delay of the ionosphere at the primary system operating frequency,  $L1$ . The differential time delay is

$$\delta(\Delta t) = \frac{\Delta t(L1)}{1.5457}$$

and the total ionospheric time delay at  $L1$  is

$$\Delta t(L1) = 5.415 \times 10^{-26} \times \text{TEC} \quad (\text{seconds})$$

where  $L1$  is 1575 MHz, and  $L2$  is 1227 MHz.

The structure of the GPS transmitted signals consists of pseudo random noise modulation of carriers at both  $L1$  and  $L2$  at a 10.23 MHz rate. The resultant signal is of spectral shape  $(\sin X/X)^2$  with the first nulls at 10.23 MHz either side of the carrier. With the GPS frequencies the total ionospheric time delay at  $L1$  is measured automatically by the differential time delay of the 10.23 MHz modulation envelopes transmitted on the  $L1$  and  $L2$  carriers and is subtracted from the measured pseudo range at  $L1$ .

On the primary frequency,  $L1$ , an additional 1 MHz pseudo random modulation is transmitted, with the modulation containing satellite orbital information, transmitted clock offset, and other information including the coefficients of an algorithm designed for users of the system in a single frequency mode to correct for approximately 50 percent of the r.m.s. ionospheric time delay error (Klobuchar, 1975). Users requiring the full precision capability of the GPS, however, will require a two frequency receiver to enable them to correct for the ionospheric first order time delay error by actual measurements of ionospheric time delay in the direction to each satellite.

### 3. IONOSPHERIC EFFECT ON RANGE RATE MEASUREMENTS

The ionosphere would affect range rate tracking only to the extent that the TEC changes during the time interval required to make the range rate interval measurement. Because of the dispersive nature of the ionosphere, a differential phase measurement can be made of received RF carrier phase on two, coherently derived, frequencies, and the contribution of phase change due to the ionosphere can be separated from that of the geometrical radial velocity. The total phase change,  $\phi$ , due to the ionosphere, at a single frequency,  $L1$ , over a time interval can be related to the differential phase change,  $\Delta\phi$ , at the GPS coherent pair of frequencies,  $L1$  and  $L2$ , by the following:

$$\phi(L1) = 1.5457 \Delta\phi.$$

In any practical case a differential phase measurement at one time has a large ambiguity of  $N$  times 360 degrees so that absolute phase changes, or absolute values of the ionospheric TEC, cannot be made with this system except under very special conditions. The great sensitivity of the differential carrier phase technique lies in its use to correct for range rate errors due to ionospheric TEC changes during the measurement interval, and this is its main use in the GPS system. The differential modulation phase measurement is a correction for the ionospheric time delay, or group delay to the total range measurement, and the differential carrier phase measurement is used to correct for the range rate values observed over an interval of time. In this report we present data only on the capability of the differential modulation phase measurements to measure the true ionospheric time delay.

### 4. DATA AVAILABLE FROM GPS

Data was made available for the comparison of the GPS two frequency group delay ionospheric time delay measurement with independent ionospheric TEC measurements for the period of 1-7 December 1977 from three stations, the GPS master control facility at Vandenberg Air Force Base, California, and two GPS monitor stations, one located on Oahu, Hawaii and the other located near Anchorage, Alaska. Figure 1 summarizes the periods of each day during the seven day period when data was recorded and provided for this study. The NTS-2 satellite was in a 12 hour synchronous orbit at 63 degrees inclination, with visibility times from all three monitor stations occurring in the late period of the UT day which corresponded to the local morning and noon time periods. In addition, from the Vandenberg and Alaska stations a few, short data periods from approximately 0600-0900 UT were available due to the portion of the satellite orbits seen when over the north pole from those two stations.

Figure 2 illustrates the locus of sub-ionospheric locations from the monitor stations viewing the NTS-2 satellite. Note that the Hawaii station has only one sub-ionospheric track. It moves from SSW of the station to north of the station at approximately 1930 UT, then moves SSE of the station at almost 2400 UT. One of the sub-ionospheric tracks for the Vandenberg station passes nearly overhead at 2100 UT while the early morning sub-ionospheric track lies in the Northeastern quadrant from 0520-0715 UT. For the Anchorage station the sub-ionospheric track crosses over the station at approximately 1930 UT while the over-the-pole pass of the other orbit of the day moves from ENE to NW of the Anchorage station in the early morning UT hours.

The circled X's in Figure 2 indicate the locations of the equivalent ionospheric intersection points for the independent TEC data taken from 24 hour geostationary satellite VHF transmissions. Comparisons of the GPS group delay ionospheric values with the independent TEC values from geostationary satellites should be most accurate at times when the NTS-2 satellite most nearly coincided in direction with the geostationary satellite.

During the first seven days of December 1977, there was a variety of activity of the earth's magnetic field with a magnetic storm occurring in the latter part of December 1, and relatively quiet conditions for the 6th and 7th of December. Figure 3 shows the three hour magnetic activity index, Kp, for the first seven days of December 1977. Note that the 2nd and 5th of the month were the highest and fourth highest days of magnetic disturbance, respectively, while the 6th and 7th were classified as magnetically quiet days. The total electron content of the earth's ionosphere generally differs from average conditions by the largest amount during magnetically disturbed conditions; thus, the first seven days of December 1977 provided a variety of ionospheric conditions for initial tests of the two frequency capability of GPS.

#### 5. INDEPENDENT TEC MEASUREMENTS FOR COMPARISON WITH GPS TWO FREQUENCY DATA

Measurements of the Total Electron Content, TEC, of the ionosphere were made independently at three stations near the three GPS monitor stations to provide standards of reference to verify the GPS two frequency correction technique. The independent TEC data was taken by measurements of the Faraday rotation of linearly polarized VHF radio waves transmitted from geostationary satellites in the standard manner described by Titheridge (1972). The TEC obtained by the Faraday rotation technique is a measure of the electron content up to vertical heights of approximately 2500 kilometers, and a correction for the additional contribution of electrons above that height was needed. Electron content above approximately 2500 km heights has been called plasmaspheric or protonospheric electron content. Klobuchar et al. (1978) described the additional contribution of plasmaspheric electron content to TEC measured by the Faraday rotation technique. Measurements of plasmaspheric electron content have been made by Solcher (1976a and 1976b), Fritz (1976), Hajeb-Hosseini (1977), Davies (1975) and others. The magnitude of the plasmaspheric component of electron content not measured by the Faraday effect corresponds to approximately 2 nanoseconds of time delay at L1, the primary GPS navigation frequency, or an error of approximately 2/3 of a meter in range. Figure 4 shows monthly average values of this additional TEC contribution for several stations for the near solar-minimum years of 1974-76. Note that 2 nanoseconds may be somewhat high for the data shown in Figure 4, but may be more appropriate for the latter part of 1977 when the solar activity was higher than in 1974-75.

Measurements of the Faraday contribution of TEC for the first seven days of December 1977 from the three TEC monitoring stations located at White Sands, New Mexico, Palehua, Hawaii and Anchorage, Alaska are shown in Figures 5, 6, and 7, respectively. Note that the ionospheric TEC has a maximum value of over  $55 \times 10^{16}$  el/m<sup>2</sup> vertical column for the Hawaii station, corresponding to a group path delay at L1 of approximately 30 nanoseconds, or 10 meters of range error. Note also in Figures 5, 6, and 7 the large day-to-day variability in TEC values observed at all three stations during the seven day period.

#### 6. COMPARISON OF INDEPENDENT TEC MEASUREMENTS WITH GPS TWO-FREQUENCY TECHNIQUE

The independent TEC data taken from the Faraday rotation measurements was compared with the GPS two frequency group delay measurements in the following manner. First, measured Faraday rotation values were converted to equivalent vertical values of TEC, taking into account the slight non-geostationarity of the satellites from which the VHF observations were made. Then, using a model of average ionospheric gradients developed by Bent (Bent et al., 1978), values of TEC in the changing directions to the NTS-2 satellite were calculated. Finally, the contribution of the plasmaspheric electron content, that not measured by the Faraday effect, was estimated and added to the equivalent vertical TEC. The final slant values of TEC were converted to nanoseconds of time delay at the primary GPS L1 frequency for easy comparison against the GPS group delay measurements. The plotted GPS data are one minute averages of 6 second maximum likelihood estimator values of the two frequency TEC correction.

Results of this comparison are shown in Figures 8, 9 and 10. In these figures the independent TEC values were computed at hourly intervals and are indicated either by circled X's or circled dots. The "X" values represent our best estimate of the TEC correction along the NTS-2 direction based upon actual independent TEC measurements taken at that time, while the circled dots represent estimates of the TEC based only upon the monthly average TEC gradient model, as actual TEC values were not available at that time from a nearby station. Note in Figure 8, for the Vandenberg data for December 1, 1977 that the measurements and estimates of TEC, indicated at hourly intervals, are higher than the actual GPS receiver two frequency data plotted from 1830-2005. There is fair agreement, though no overlapping times for the GPS data from 2315 to 2355 UT. The GPS data for December 2, 1977 from Vandenberg illustrates several things. Note the sudden changes in the GPS representations of TEC which are seen at approximately 1900 and again at 2300 UT. These are due to switching from the low elevation to the high elevation antenna and back again at those times respectively, and it is clear that the differential phase of the high elevation antenna was incorrect for this day. Note the good agreement of the independent TEC values with the GPS data at 1900 and again at 2300 UT.

Vandenberg data for December 5, 1977 shows excellent agreement between the independent

TEC data and the GPS two frequency TEC data, especially at 2200-2300 when the two satellite directions nearly coincide. Also note that the apparent noise of the GPS measure of TEC is greater near the ends of the pass. This is apparently caused by effects of multipath signals received with the lower elevation antenna. Figure 8 also illustrates excellent agreement between the GPS two frequency TEC determination and the independent measurements on Dec 6 and 7 respectively. Note that for the hours 1800, 1900, and 2000 UT, on December 6 only monthly average TEC independent values were available and the agreement between the two sets of data is poor. For 2100, 2200, and 2300 UT when actual values of independent values of TEC were available the agreement is excellent.

Data from the Alaska monitoring station, along with independent TEC monitoring station values from a polarimeter located at the same Air Force installation, is plotted in Figure 9. In this figure actual 6 second maximum likelihood estimator values of the GPS data are plotted. Note the very high noise of the GPS data observed on all 4 days from Alaska. After these observations were made it was discovered that the connections to the low and the high elevation antennas on the GPS monitor receiver were inadvertently reversed. The resultant received signal was very noisy, thus the ionospheric time delay measurement was also noisy. Despite the poor signal to noise ratio the relative ionospheric correction on the 4 days shown in Figure 9 was reasonably good.

Figure 10 shows the comparison of GPS two frequency ionospheric time delay measurements from Hawaii with TEC determined by a polarimeter located nearby. Note the jump in ionospheric time delay values with the GPS data between 2200 and 2300 UT on all the days when data was taken at those times. Again the receiver differential input phase at the two frequencies was not the same for the high elevation antenna as for the low elevation antenna, causing the drop in apparent ionospheric delay. For the Hawaiian station the differential phase of the high elevation antenna was incorrect. The short period of data in Figure 10 on Dec 6, near 1600 UT, was also taken with the low elevation antenna. Note also on Dec 1 and Dec 6 in Figure 10 the large increase in ionospheric time delay from 1900 UT to approximately 2330 UT followed by a small decrease in ionospheric time delay just before the satellite went below the horizon. The increase from 1900 to 2330 UT was due to the increasing slant ionosphere viewed as the satellite changed in direction from nearly overhead slightly north of the station to a low elevation to the SSE. At approximately 2330 UT the downturn in ionospheric time delay near the horizon was likely due to the presence of a latitudinal gradient in ionospheric TEC through which the NTS-2 signal passed at a slightly higher elevation angle.

## 7. CONCLUSIONS

The results of this initial attempt to determine the ability of the dual frequency signal structure of the GPS advanced navigation system to automatically correct for the time delay of the earth's ionosphere are very encouraging. Initial problems with differential receiver phase errors at the two GPS frequencies and reversed antenna connections have been corrected. Our comparisons of the ionospheric time delay error as determined by the dual frequency GPS signals with independent measurements by the Faraday effect showed good agreement on magnetically quiet and disturbed days with both the absolute value of the time delay as well as with the shape of the change as a function of satellite position within the expected error range. Overall dual frequency ionospheric time delay correction is certainly within the 2 meters r.m.s. desired for residual error after correction.

## 8. REFERENCES

- Bent, R.G., S.K. Llewellyn, G. Nesterczuk, and P.E. Schmid, "The Development of a Highly Successful Worldwide Empirical Ionospheric Model and Its Use in Certain Aspects of Space Communications and Worldwide Total Electron Content Investigations", in "Effect of the Ionosphere on Space and Terrestrial Systems", Editor J.M. Goodman, US Government Printing Office, Nr. 008-051-00069-1, 1978.
- Fritz, R.N., "ATS-6 Radio Beacon Electron Content Measurements at Boulder, July 1974 - May 1975", Report USG-58, World Data Center A for Solar-Terrestrial Physics, Boulder, CO, September 1976.
- Hajeb-Hosseini, H., "Ionospheric Studies Using Geostationary Satellites", Thesis Submitted to the University of Wales, Aberystwyth, Wales, June 1977.
- Klobuchar, J.A., M.J. Buonsanto, M.J. Mendillo, and J.M. Johanson, "The Contribution of the Plasmasphere to Total Time Delay", in "Effect of the Ionosphere on Space and Terrestrial Systems", Editor J.M. Goodman, US Government Printing Office, Nr. 008-051-00069-1, 1978.
- Lassiter, E.M., and B. Parkinson, "The Status of the Development of the Navstar-Global Positioning System", Navigation, Volume XXV, Nr. 97, pp. 13-26, January 1977.
- Soicher, H., "Diurnal, Day-to-Day, and Seasonal Variability of  $N_f$ ,  $N_t$ , and  $N_p$  at Fort Monmouth, New Jersey", Cospar Satellite Beacon Symposium, Boston, MA, Boston University, Ed. by M. Mendillo, June 1976.
- Soicher, H., "Comparative Ionospheric and Plasmaspheric Electron Contents from the Three World Regions", Nature, Vol. 264, pp. 46-48, Nov. 4, 1976.

Titheridge, J.E., "Determination of Ionospheric Electron Content from the Faraday Rotation of Geostationary Satellite Signals", Planet. Space Sci., 1972, Vol. 20, pp. 353-369.

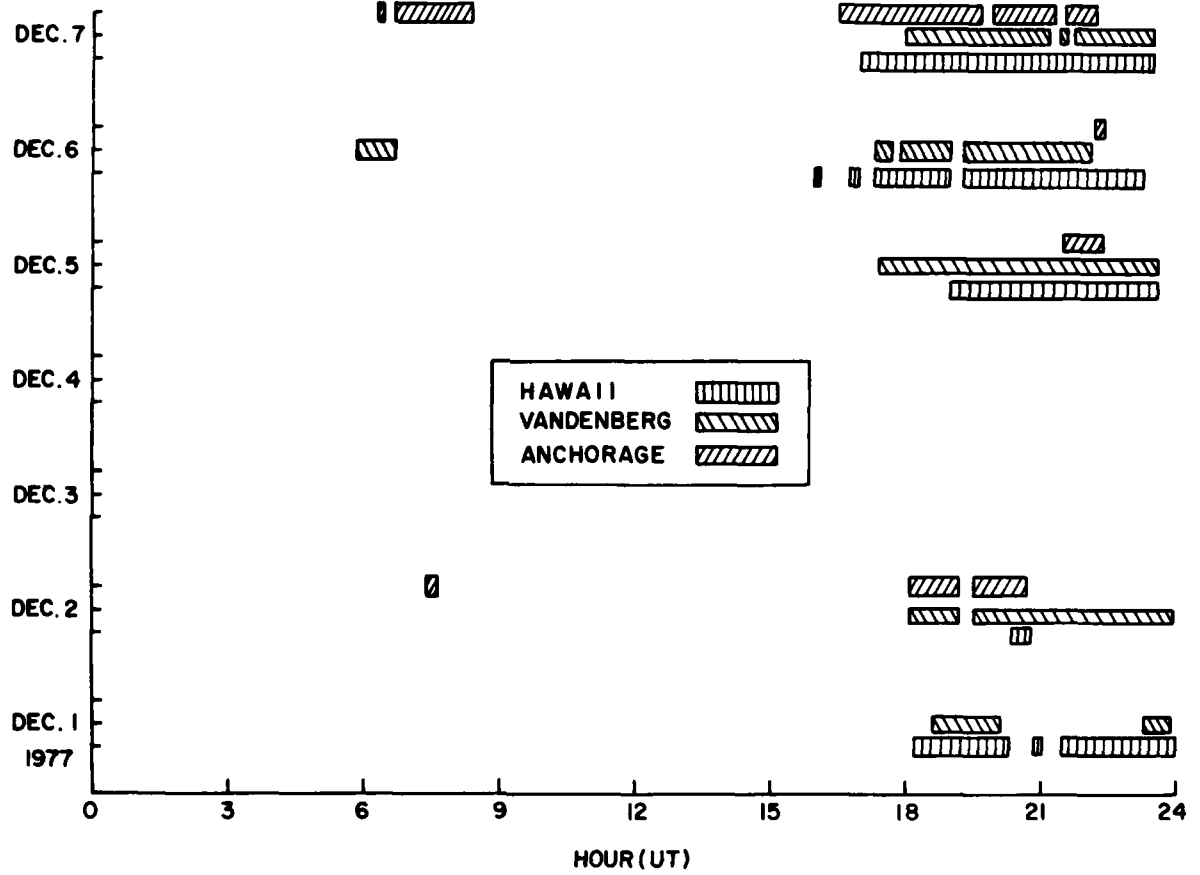


Figure 1. Data provided for absolute ionospheric time delay verification.

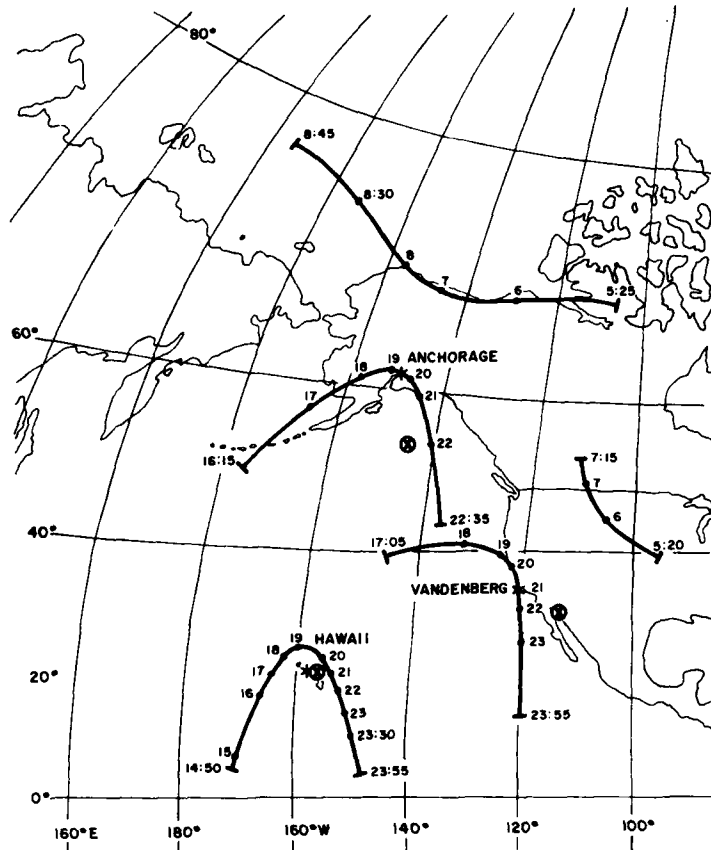


Figure 2. Sub-ionospheric locations from three stations viewing the NTS-2 satellite, December 4, 1977 (420 km ionospheric height used).

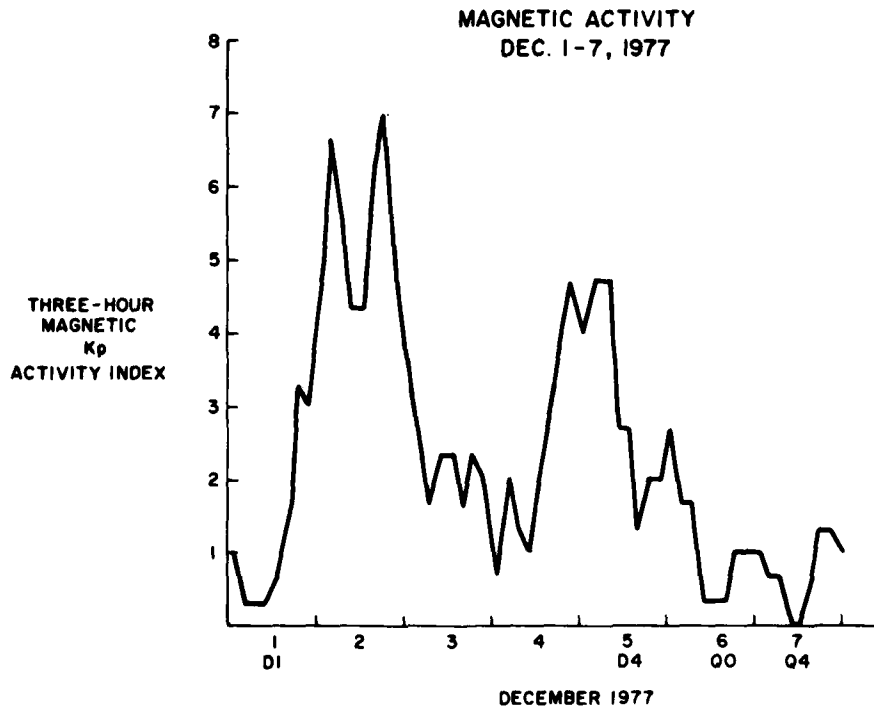


Figure 3. Three hour magnetic activity index, Kp, for the first seven days of December 1977.



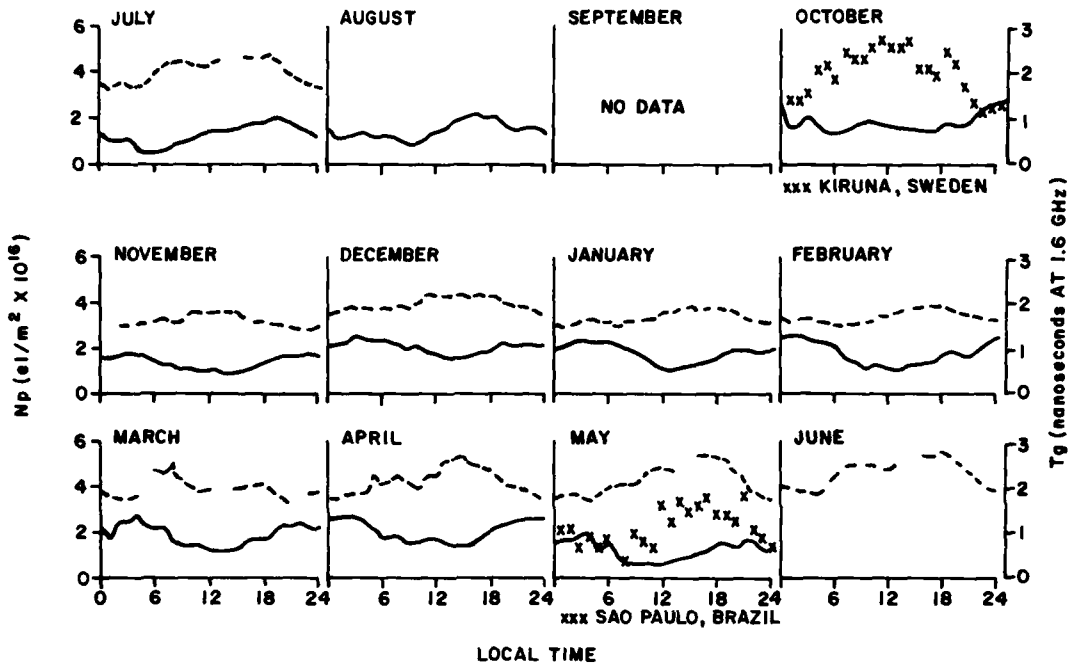


Figure 4. Plasmaspheric electron content during solar minimum period 1974-76 from group delay minus Faraday electron contents measured from the ATS-6 radio beacon. Solid curve data is from Hamilton, Massachusetts. Dashed curve data is from Aberystwyth, Wales.

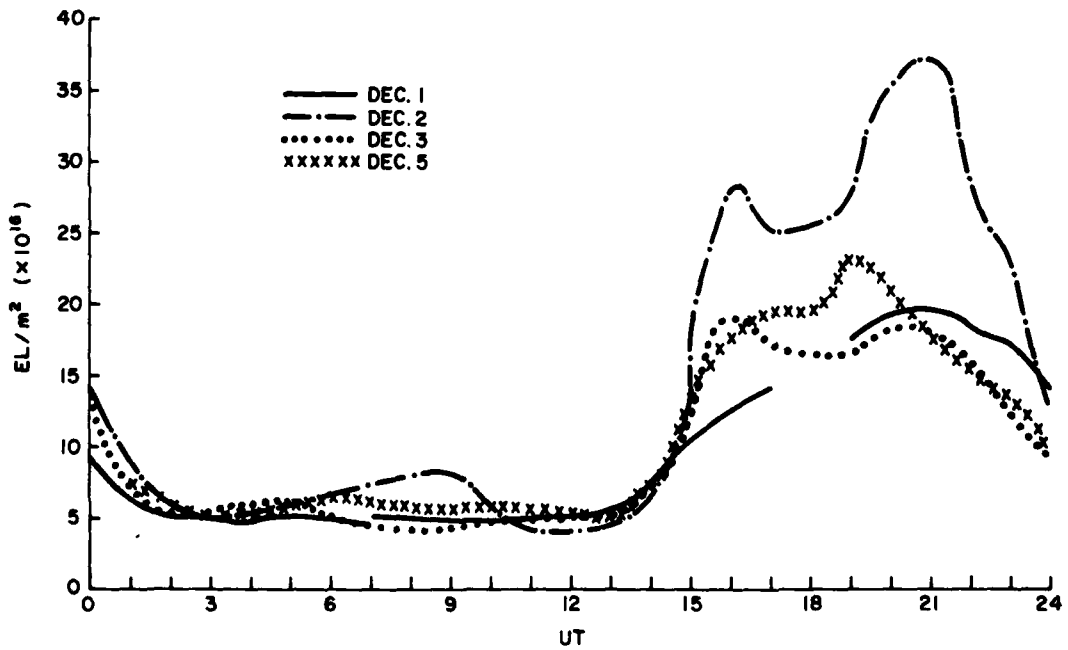


Figure 5. Equivalent vertical ionospheric electron content from White Sands, New Mexico, December 1977.

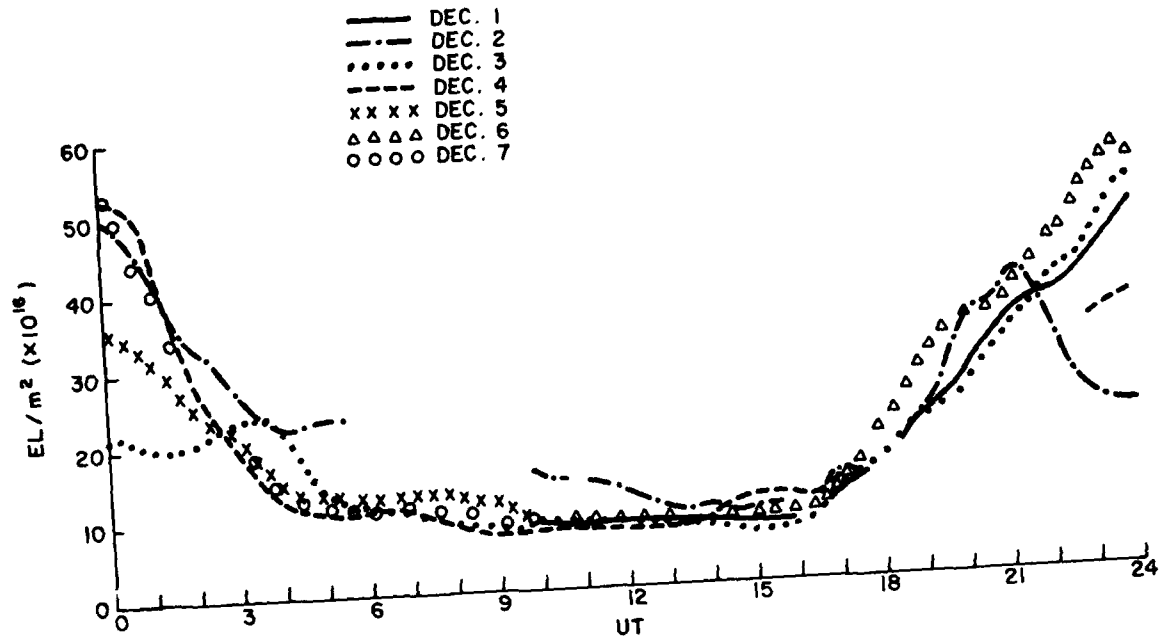


Figure 6. Equivalent vertical ionospheric electron content from Palehua, Hawaii, December 1977.

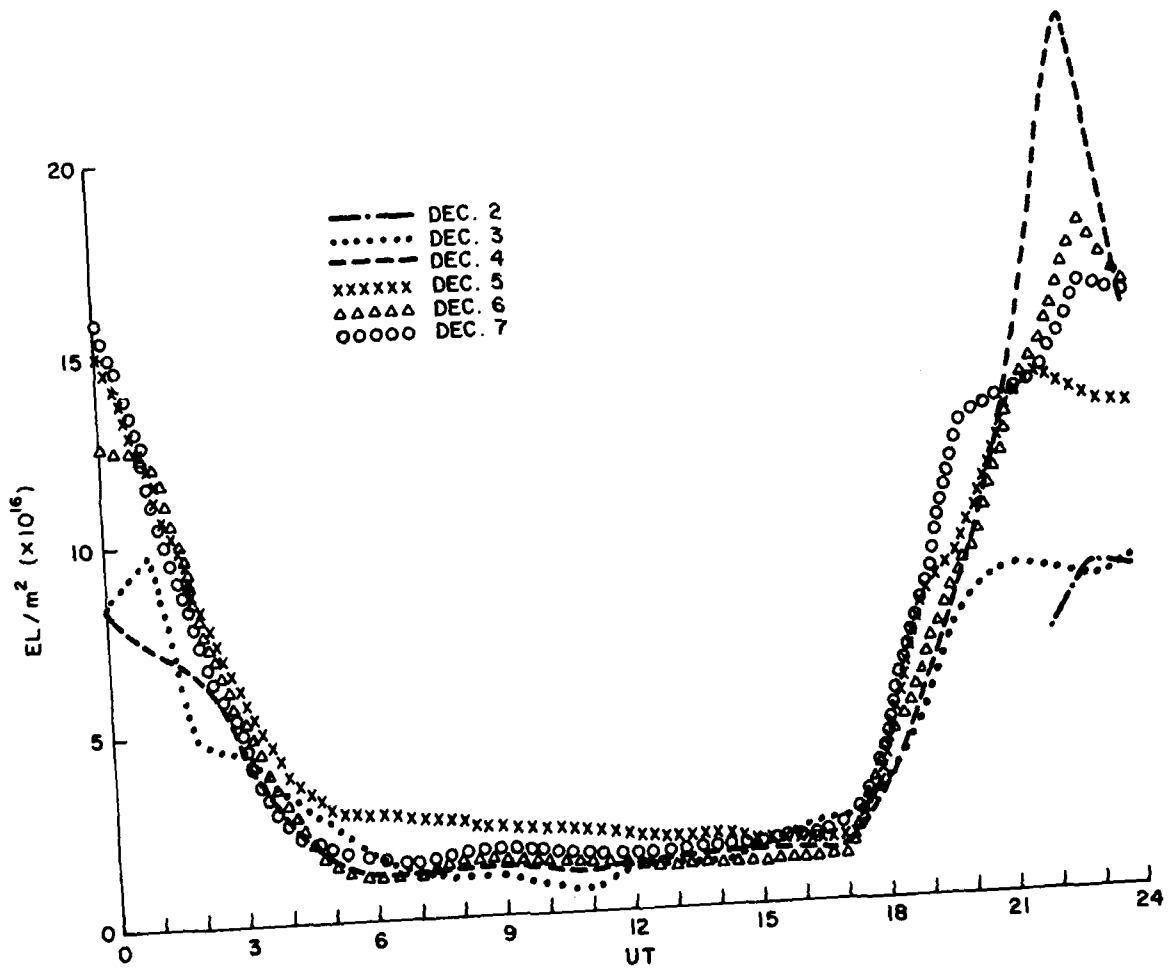


Figure 7. Equivalent vertical ionospheric electron content from Anchorage, Alaska, December 1977.

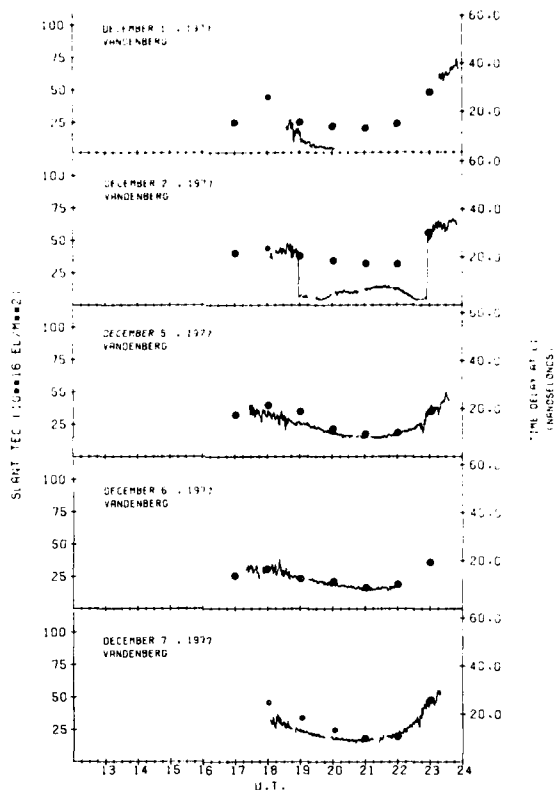


Figure 8. Comparison of ionospheric contribution to time delay from the dual frequency GPS signals with independent ionospheric measurements. The circled x values indicate actual independent ionospheric measurements, while the circled dots represent monthly average ionospheric time delay correction values. GPS data from Vandenberg, CA. Independent ionospheric data from White Sands, New Mexico.

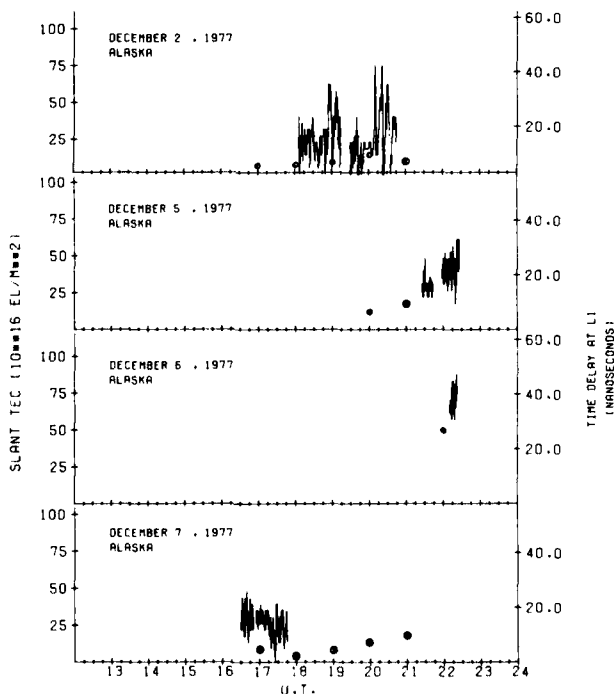


Figure 9. Same as Figure 8 except, GPS data is from Anchorage, Alaska. Independent ionospheric data is also from Anchorage, Alaska.

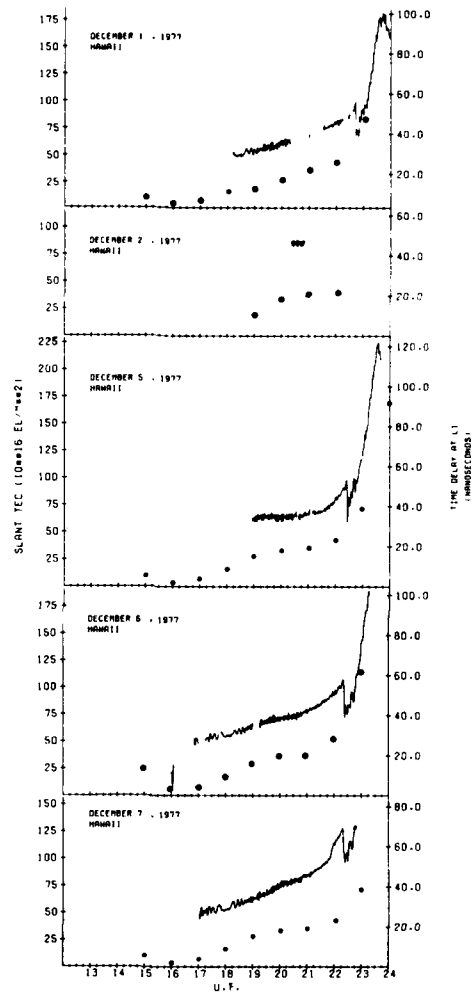


Figure 10. Same as Figure 8, except GPS data is from Hawaii. Independent ionospheric data is also from Hawaii.

## THE INTERACTIONS OF A SOLAR POWER SATELLITE TRANSMISSION WITH THE IONOSPHERE AND TROPOSPHERE

K A Hughes  
Home Office  
Directorate of Radio Technology  
LONDON SE1 8UA

## SUMMARY

A significant contribution towards meeting the Earth's future energy requirements could stem from Solar Power Satellites (SPS). In such systems, solar energy is collected by a large array of solar cells in geostationary orbit, converted to r.f power at microwave frequencies and beamed to Earth for conversion into dc (Glaser, 1977). The propagation of the high power microwave beam through the Earth's atmosphere may initiate interactions in the ionosphere and troposphere that have disruptive effects on existing radio services. In addition, the transmission of the SPS beam may also be affected. Radio interference on the SPS frequency could occur from scattering of the beam in both the ionosphere and troposphere; more serious broad-band interference may arise from ionospheric modification, resulting from intense ohmic heating. The problems associated with these interactions are discussed and where possible, the effects on existing radio services are quantified.

## 1 INTRODUCTION

The proposal to transmit microwave energy from SPS systems introduces a new concept for the use of the radio frequency spectrum. The power level associated with the energy transmission to Earth is far in excess of that usually encountered in radio services and it is important, therefore, to determine the effects the transmission may have on the environment. In particular, the microwave beam will interact with the ionosphere and troposphere which could have serious effects on radio services; in turn the interactions could affect the transmission of the power satellite beam itself.

The construction of SPS systems will require many flights of large rockets called heavy-lift launch vehicles (HLLV). Powered flights of these large hydrogen or hydrocarbon burning rockets may cause temporary removal of ions and electrons from the F region. Severe depletions in the ionospheric density could result, in turn causing serious effects on telecommunications.

Design proposals for an SPS quote a transmitted power level in the range 5-10 GW, giving rise to a power flux density on Earth, at the centre of the transmitted beam, of some  $20 \text{ mW cm}^{-2}$  ( $200 \text{ Wm}^{-2}$ ). The frequency is 2.45 GHz, chosen at a value where the combined effects of the ionosphere and troposphere would tend to be a minimum. Lower frequencies would suffer increased interactions with the ionosphere such as refraction, absorption and Faraday rotation, whilst higher frequencies would be subject to increased absorption by atmospheric gases and hydrometeors. Equally important is the choice of elevation angle for the SPS transmission. Design specifications frequently imply transmission to the equatorial sub-satellite point on Earth. However, this may not be practicable or perhaps desirable if the intended users of the power are located at high latitudes. From a propagation viewpoint, transmission of the beam at high elevation angles may involve the special problems associated with transionospheric propagation at equatorial latitudes, i.e. disturbance by the equatorial scintillation region. At lower elevation angles however, serious problems could arise from refraction and absorption, and therefore in the following discussions, the elevation angle is generally considered as being at least  $25^\circ$ , appropriate for reception of the beam at middle or low latitudes.

The relevant interactions of the power satellite beam with the ionosphere and troposphere are discussed in turn.

## 2 INTERACTIONS WITH THE IONOSPHERE

The ionospheric interactions may be separated broadly into two categories:-

- (i) Passive Interactions, in which the ionospheric plasma influences the propagation of the power satellite beam in some way, and in some instances possibly gives rise to co-channel interference through scattering of the beam;
- (ii) Active Interactions, whereby the ionospheric plasma itself is modified. Strong electron heating from the power satellite beam may produce irregularities in the ionisation, capable of scattering radio waves of lower frequencies, thereby increasing the potential for broadband interference. Ionospheric modification may also result from the emission of exhaust effluents from HLLV's. The associated changes in ionospheric chemistry can lead to depletions in ionisation at F region heights.

2.1 Passive interactions2.1.1 Refraction

Due to electron density gradients in the ionosphere, transionospheric radio propagation undergoes deflection resulting in an apparent change in the elevation angle of the radio source. The effect decreases with increasing elevation angle and frequency. The following table gives values of the apparent horizontal displacement of the power satellite

beam on the Earth as a function of elevation angle for a high mid-latitude daytime value of ionospheric total electron content.

TABLE 1  
APPARENT HORIZONTAL DISPLACEMENT OF SPS BEAM DUE TO  
REFRACTION IN THE IONOSPHERE

Elevation Angle (degrees)	Apparent Displacement (metres)
75	0.9
50	4.6
25'	38.9

The effect becomes far more serious for small elevation angles of  $10^\circ$  or less.

Superimposed on this normal refraction effect could be smaller scale variations in the direction of arrival arising from the passage of ionospheric irregularities across the beam. The effect of these travelling ionospheric disturbances on the power satellite beam would be slight, causing an apparent displacement of less than 1m.

Retrodirective mechanisms incorporated in the SPS system will correct any displacement detected in the received beam.

#### 2.1.2 Faraday rotation

A linearly polarised wave traversing the ionosphere is subject to the Faraday effect resulting from the bi-refrangent property of the ionosphere in the Earth's magnetic field. The amount of rotation is inversely proportional to the square of the frequency and would be only some  $7^\circ$  for a power satellite transmission to mid-latitudes through the daytime ionosphere. There would normally be very little reduction in transmission efficiency due to this effect, therefore.

#### 2.1.3 Naturally occurring F region irregularities

Irregularities of electron density in the ionosphere can cause variations in the amplitude, phase, polarisation and angle of arrival of transionospheric radio signals; the variations are collectively termed scintillation.

At gigahertz frequencies, scintillation is generally a night-time phenomenon, occurring mainly in equatorial and auroral regions; it tends to be more frequent in the equinoxes. At frequencies close to that of the SPS system, the peak to peak amplitude of fading is in general above 4 dB for 0.1 per cent of the time (Taur, 1973).

Scintillation at gigahertz frequencies may be interpreted as variations in signal strength resulting from diffraction effects. Field aligned irregularities in the F region tend to have an approximately regular distribution and their effect on an SPS transmission could be crudely simulated by that of a diffraction grating, giving rise to intensity maxima on the Earth's surface outside of the main beam. Power flux densities associated with the central maximum and three principal maxima of such a diffraction pattern are given in the following table, for strong scintillation of 6 dB peak to peak.

TABLE 2  
DIFFRACTION OF SPS BEAM BY IONOSPHERIC SCINTILLATION IRREGULARITIES

Distance from Central Maximum (km)	Spectral Order	p.f.d ( $\mu\text{W cm}^{-2}$ )
0	0	$33 \times 10^3$
10	56	1.0
50	278	$4.3 \times 10^{-2}$
1900	1592	$3.4 \times 10^{-4}$

The distance of 1900 km corresponds to the principal maximum tangential to the Earth's surface.

To assess the significance of these power levels, comparison may be made with the maximum permitted power flux density on the Earth from a space station in the fixed satellite service operating at 2.5 GHz. The Radio Regulations state this figure as  $2 \times 10^{-12} \mu\text{W cm}^{-2}$  for elevation angles above  $25^\circ$ . The figures in Table 2 indicate that this value would be exceeded by a factor of at least 80 dB at any location of a maximum

on the side of the Earth visible to the SPS beam.

Although it is unlikely for ionospheric irregularities to be sufficiently well-defined and uniformly distributed to comprise a grating capable of producing a stable diffraction pattern, the above result does indicate the serious dispersion that could arise from ideal diffraction conditions, and the potential co-channel interference that could ensue.

Naturally occurring electron density irregularities may also give rise to scattering of the SPS beam. An approach to this problem has been made invoking the scattering theory of Booker (1959), using the same parameters as above. Lower values of power flux density are obtained compared with those calculated in the diffraction case, but nevertheless they still exceed the regulatory fixed satellite service level by several orders of magnitude. Clearly, propagation of the SPS beam through F region irregularities could cause serious problems for co-channel radio services.

## 2.2 Active interactions

### 2.2.1 Electron heating

As a radio wave passes through the ionosphere, the electrons are set in motion by the electric field of the wave. When the electrons collide with ions and neutral particles this motion is destroyed and as a result the radio wave suffers absorption and is attenuated. The energy extracted from the radio wave increases the temperature and velocity of the free electrons, and this ohmic heating of the plasma increases the electron collision frequency which results in further electron heating. Furthermore, in the lower regions of the ionosphere, important cooling mechanisms (by rotational excitation of  $O_2$  and  $N_2$ ) are found to decrease with increasing temperature. Sufficiently strong ohmic heating thus gives rise to considerably enhanced electron temperatures, particularly in the D and E regions of the ionosphere.

Calculations have been undertaken to determine the extent to which the ionosphere will be heated by the SPS beam (Perkins and Roble, 1978) and the results indicate that an approximately four-fold increase of the electron temperature in the D and E regions may occur. In turn, such heating could affect fundamental ionospheric processes such as electron-ion recombination rates, ionospheric densities, or drive secondary non-linear ionosphere-microwave interactions, further disturbing the ambient plasma. All these disturbances could have serious effects on existing telecommunication services.

Since ohmic heating is inversely proportional to the square of the frequency, it is possible to simulate experimentally the ohmic heating which should occur from an SPS transmission by scaling down both the frequency and power of the heating wave. In this manner, attempts are underway to verify experimentally the potential heating effects cited above, using ionospheric heating facilities in the USA.

### 2.2.2 Absorption

The increase in electron collision frequency arising from the propagation of an electromagnetic wave through the ionosphere will cause increased absorption of any other radio wave traversing the same region of the ionosphere as the original wave. Additionally, in the SPS case, a two-fold increase in D region electron density is predicted to occur (Perkins and Roble, 1978), a further factor contributing to an increase in radio wave absorption. It is important therefore, to consider the extent to which a radio wave may be attenuated when propagating through a region of the ionosphere illuminated by the SPS beam. Since the non-deviative absorption of a radio wave is proportional to the product of electron density and collision frequency, an 8-fold increase in absorption may therefore be expected. However, because of the relatively limited area in which the increased absorption would occur, it is thought unlikely that any significant disruption to ionospheric radio circuits would take place.

### 2.2.3 Field-aligned irregularities

A plasma mechanism associated with ohmic heating of the ionosphere is thermal self-focusing. There exist in the ionosphere small natural fluctuations in electron density which cause corresponding variations in the refractive index of the plasma. An electromagnetic wave propagating through the plasma is slightly focused and defocused by these variations and refracted into those regions of lower electron density. Here, the electric field intensity increases causing more plasma to drift away from these focused regions, thereby amplifying the original perturbation. The process continues until hydrodynamic equilibrium is reached, creating large-scale ( $\sim 1$  km wide) electron density irregularities in the F region of the ionosphere.

The formation of these irregularities, or striations, has been observed in ionospheric modification experiments performed over the last decade (Utlaut, 1975). These experiments have purposely set out to modify the electron temperature and density of the ionosphere through ohmic heating by high power HF radio waves. Many unanticipated phenomena have also been observed, perhaps the most important being the discovery that the modified region can act as a significant scatterer to radio frequencies up to UHF. It has been possible to demonstrate a potential usefulness of ionospheric modification for telecommunications purposes, and transmissions at VHF and UHF have been made via the modified region between terminals separated by several thousands of kilometres. However, the potential also exists for the modified region to cause serious interference to radio services at frequencies from HF to UHF. It is important therefore, to consider mechanisms such as thermal self-focusing as a potential interaction arising from the power satellite transmission.

In order for well-defined striations to occur in the F region ionisation, the thermal self-focusing instability must be capable of growing at a sufficiently rapid rate and within a realistic spatial extent. Analysis of the problem for the SPS case has shown that for a given power level, a striation wave length can be predicted for which the spatial growth is a maximum. Furthermore, the geometrical arrangement conducive to maximum growth is one in which the striations are aligned with the geomagnetic field such that the electron density variations occur in a direction normal to the plane of the field and the axis of the microwave beam. The widths and growth lengths of the striations are functions of the angle between the SPS beam and the geomagnetic field. For reception of the beam at mid-latitudes, striation widths of some 200 m are predicted to occur, with growth lengths of approximately 200 km. It is possible that the SPS transmission could produce these irregularities over a wide range of latitudes and current work is aiming to quantify accurately their formation and effects on existing telecommunications services.

Theory indicates that for a given growth length, the threshold power to initiate the thermal self-focusing instability is inversely proportional to the cube of the frequency. Thus, by suitable scaling down of power and frequency, it may be possible to simulate experimentally the SPS conditions predicted to cause the instability.

#### 2.2.4 Further plasma interactions

In addition to large-scale field aligned irregularities, small-scale plasma striations, having dimensions of a few metres, have been observed in HF ionospheric heating experiments. These observations helped in the discovery of a new mode of plasma reaction in which the beating between two high frequency waves, the modifier wave and an electrostatic plasma wave, produces a low frequency plasma wave which travels transversely to the geomagnetic field and causes small-scale ( $\sim 3$  m) field aligned density structures. These irregularities give rise to scattering but at frequencies displaced from the transmitted signal frequency by an amount equal to the heating frequency. This scattering is far less aspect sensitive than that caused by large-scale striations, not being a strong function of the magnetic field geometry. The formation of these small-scale striations therefore provides a further potential for increased interference with consequent disruption of radio services.

At first sight, it would appear unlikely for an SPS transmission to give rise to small-scale striations because the microwave frequency is too far removed from electrostatic plasma frequencies for production of the low frequency component necessary for the formation of the striations. However, certain reasons exist for pursuing studies of the phenomenon in the SPS case:

- (i) The generation of small-scale plasma striations may be the result of secondary instabilities in the presence of thermal self-focusing irregularities and several possible mechanisms are being investigated.
- (ii) The SPS microwave beam is to be controlled by information derived from a pilot signal transmitted from the ground and received at the SPS antenna. The difference in frequency between the uplink pilot signal and the microwave power-beam could fortuitously give rise to plasma reactions by beating with an electrostatic wave and generating the small-scale density structures, as described above. The problem could be avoided by ensuring that the frequency difference always exceeds the highest expected plasma frequency but it must be borne in mind however, that similar effects could occur if other transmissions, on frequencies close to that of the SPS, were incident on the same region of the ionosphere.

A thorough understanding of the generation of these small-scale plasma striations is still required. It is hoped that their full relevance to SPS will become apparent following proposed heating experiments.

#### 2.2.5 SPS constructional effects on the ionosphere

The construction of SPS systems necessitates numerous launches of HLLV's. Ionospheric depletions of electron and ion densities are predicted to occur as a result of these launches, caused by the injection of exhaust products into the F region. At altitudes of approximately 200 km, the normally occurring  $O^+$  ions transfer their charge to combustion products  $H_2O$ ,  $H_2$  and  $CO_2$ , forming polyatomic ions that recombine rapidly with free electrons. An enhancement of the electron-ion recombination rate thus occurs, resulting in depletions of F region ionisation density.

Several observations of this effect have been made from previous rocket launches. A reduction of some 50 per cent in total electron content was measured after the launch of Skylab 1 in May 1973. The depletion extended over a region some 2000 km in diameter and was observed for approximately 4 hours (Mendillo et al, 1975). Fluctuations in



electron density of 5-10 per cent were also observed following the launches of spacecraft; during the disturbances, multiple reflections of HF radio waves occurred (Zasov et al, 1977).

Decreases in electron density will directly affect HF communications and in addition cause changes in the propagation properties of other electromagnetic waves traversing the disturbed region; some further predicted effects include disturbances of the electron temperature profile and electrical conductivities.

### 3 INTERACTIONS WITH THE TROPOSPHERE

#### 3.1 Refraction

An electromagnetic wave passing through the troposphere undergoes bending caused by variations in refractive index. The effect is largely independent of frequency and is greatest for small angles of elevation. In the case of propagation from a satellite to Earth, the effect manifests itself in an apparent change in the position of the satellite. For elevation angles greater than  $25^\circ$  however, the apparent displacement of the SPS beam would be only a few metres. As for the analogous effect due to the ionosphere, suitable compensation mechanisms would take account of the displacement.

#### 3.2 Amplitude fluctuations

In addition to bending the radio wave beam, variations in refractive index can cause fluctuations in the amplitude of the received signal. The magnitude of this scintillation is highly dependent on elevation angle and varies with time of day, season and climate. For elevation angles greater than  $25^\circ$ , the depth of fading should never exceed 1 dB for 0.1 per cent of the time (CCIR Rep 564-1, 1978); for an SPS transmission however, this would amount to a loss of some 1.3 GW of power.

#### 3.3 Absorption by atmospheric gases

Absorption by the clear atmosphere occurs when gaseous molecules with permanent dipole moments couple the electric or magnetic components of the electromagnetic wave field to their rotational energy levels. The atmospheric constituents chiefly responsible for this absorption are molecular oxygen and water vapour. For a wave frequency of 2.45 GHz, the total one-way zenith attenuation is around 0.04 dB in a moderately humid atmosphere (CCIR Report 719, 1978). This figure increases for oblique ray paths, the cosecant of the elevation angle being the appropriate multiplication factor for elevation angles down to  $5^\circ$ . Thus, for an elevation angle not less than  $25^\circ$ , the attenuation due to this mechanism should not exceed 0.1 dB, which for the SPS transmission, corresponds to absorption of some 150 MW of power.

#### 3.4 The effects of hydrometeors

Hydrometeors such as rain, cloud, fog, hail and snow cause attenuation of electromagnetic waves through both absorption and scattering.

##### 3.4.1 Absorption by hydrometeors

The primary hydrometeor of concern is rain and attenuation depends on the size and shape of the drops and the rate of precipitation. At 2.45 GHz, the attenuation due to absorption is relatively small and for a rainfall rate of  $26 \text{ mmh}^{-1}$  (exceeded in the UK for 0.01 per cent of the time) would be  $4 \times 10^{-3} \text{ dB km}^{-1}$ . For a path length through the rain cell of under 10 km, the loss of power from an SPS transmission could amount to some 60 MW.

Only the densest of fog causes attenuation comparable with rain. For a visibility of only 30 m, the specific attenuation may be as high as  $0.01 \text{ dB km}^{-1}$  at  $0^\circ\text{C}$  (Ryde, 1946). Comparable attenuation can be reached from water clouds but ice cloud attenuation is in general some two orders of magnitude smaller.

The effects of hail and snow are usually considered serious only at millimetre wavelengths. However, in the severest of hail storms (associated with approximately 0.001 per cent of the time) the precipitation rate of liquid water produced after melting may be comparable with that of rain and attenuation of some  $0.04 \text{ dB km}^{-1}$  could result at 3 GHz (Ryde, 1946). On the other hand, a high precipitation rate for snow corresponds to only about  $10 \text{ mmh}^{-1}$  and consequently the absorption is usually considerably less than for the other hydrometeors.

Therefore, with the possible exception of time percentages less than 0.01, the maximum attenuation suffered by the SPS beam through hydrometeor absorption would be under 0.05 dB, corresponding to a power loss of 75 MW.

##### 3.4.2 Scattering by hydrometeors

Hydrometeors, in particular rain, are capable of scattering electromagnetic waves and thereby enable a coupling to be made between two antennas on the ground. Alternatively, rain scatter can cause serious interference problems to co-channel services. Consideration must be given therefore to scattering of the SPS beam by hydrometeors in the troposphere.

Since the wavelength of the SPS transmission is considerably greater than the diameter of raindrops, the mechanism can be reasonably described by Rayleigh scattering and the scattered signal can be assumed isotropic. When calculating the scattered power from a rain cell, the important parameter to determine is  $\eta$ , the scatter cross-section per unit volume, which is itself a function of several other parameters including the total variance of the refractive index variations within the scattering volume. By using procedures described in CCIR texts, values of  $\eta$  can be calculated for the particular frequency and rainfall rate considered. The power radiated from a rain cell may then be determined, assuming an average incident power flux density from the SPS of  $10 \text{ mW cm}^{-2}$ . Results are given below in Table 3 for two climate types - one applicable to the US, the other to the UK.

TABLE 3  
RAIN SCATTER OF SPS BEAM

	Rainfall Rate ( $\text{mmh}^{-1}$ )	% time Rainfall Rate is exceeded	Power Radiated from Rain cell (kW)	Pfd at 100 km from Rain cell ( $\mu\text{W cm}^{-2}$ )	Fixed satellite Pfd Limit ( $\mu\text{W cm}^{-2}$ )
Climate 2 (US)	14	0.1	180	$1.4 \times 10^{-4}$	$2 \times 10^{-12}$
	55	0.01	650	$5.2 \times 10^{-4}$	
Climate 4 (UK)	8	0.1	54	$4.3 \times 10^{-5}$	
	26	0.01	190	$1.5 \times 10^{-4}$	

The power flux densities are compared with the regulatory satellite limit used earlier in section 2.1.3 when discussing diffraction from ionospheric irregularities. The figures indicate that serious co-channel interference could ensue at considerable distances from the SPS beam. Rain scatter is clearly a problem therefore, even in moderate rates of precipitation.

Scattering may also occur from sand and dust particles suspended in the atmosphere. Since a desert region may be a possible location for reception of a power satellite transmission, consideration should be given to the potential extent of scatter from dust or sand storms. Unfortunately, very few propagation data are available for these conditions but evidence exists to indicate that the reflectivity from sand or dust would be less than that of moderate rainfall. A need exists however, for propagation studies to be made at microwave frequencies in conditions of high sand and dust content.

#### 4 CONCLUSION

The paper has discussed basic interactions associated with the propagation of electromagnetic radiation through the Earth's atmosphere, quantifying the effects for an SPS transmission. The interactions tend to fall into two categories:

(i) Disturbance of the SPS beam:

- Losses in the power received at the ground arise from - absorption
- scintillation
- scattering

all of which occur in both the ionosphere and troposphere. In addition, these mechanisms may affect the uplink signal used for controlling the power transmission.

(ii) Modification of the propagation environment:

- Processes include - increasing absorption
- disturbance of local ionospheric thermal budget, in turn affecting other ionospheric mechanisms
- generation of large-scale field aligned striations
- initiating other plasma interactions, in turn leading to generation of small-scale striations.

In addition, ionospheric electron density depletions may occur as a result of numerous flights of large rockets used for SPS construction.

Interactions in both categories would cause interference to radio services. Co-channel interference would arise from scattering of the power satellite beam from ionospheric irregularities and hydrometeors in the troposphere. More serious broad-band interference could be caused by radio wave scattering from field aligned striations produced from heating mechanisms initiated by the power satellite transmission. More precise quantification of these effects is required but initially a much improved understanding of the relevant mechanisms must be achieved. A need exists for meaningful heating experiments

in which SPS heating effects are simulated.

#### ACKNOWLEDGEMENT

This paper is published by kind permission of the Director of Radio Technology.

#### REFERENCES

- BOOKER, H.G. (1959), Radio scattering in the lower ionosphere. *J Geophys Res.*, 64, 2164 - 2177.
- CCIR Report 564-1, (1978), Propagation data required for space telecommunication systems.
- CCIR Report 719, (1978), Attenuation by atmospheric gases.
- GLASER, P.E. (1977), The potential of satellite solar power. *Proc. IEEE*, 65, 1162-1176.
- MENDILLO, M, HAWKINS, G.S. and KLOBUCHAR, J.A. (1975), A sudden vanishing of the ionospheric F region due to the launch of Skylab. *J Geophys Res.*, 80, 2217 - 2228.
- PERKINS, F.W. and ROBLE, R.G. (1978), Ionospheric heating by radio waves: Predictions for Arecibo and the Satellite Power Station. *J Geophys Res*, 83, A4, 1611 - 1624.
- RYDE, J.W. (1946), The attenuation and radar echoes produced at centimetre wavelengths by various meteorological phenomena. *Meteorological Factors in Radio-Wave Propagation*, The Physical Society (London), 169 - 188.
- TAUR, R.R. (1973), Ionospheric scintillations at 4 and 6 GHz. *COMSAT Tech. Rev.*, 3, 145 - 163.
- UTLAUT, W.F. (1975), Ionospheric modification induced by high-power hf transmitters - A potential for extended range vhf - uhf communications and plasma physics research. *Proc IEEE*, 63, 1022 - 1043.
- ZASOV, G.F., KARLOV, V.D., ROMANCHUK, T Ye., SOLODOVNIKOV, G.K., TKACHEV, G.N. and TRUKHAN, M.G. (1977), Observations of disturbances in the lower ionosphere during Soyuz-Apollo experiments. *Geomag and Aeronomy*, 17, 234 - 235.

ON MICROWAVE POWER TRANSMISSION AND  
THE FEASIBILITY OF POWER SATELLITES

FOR EUROPE

Diederich Koehn  
AEG-TELEFUNKEN  
D 5300 Bonn

SUMMARY

The forthcoming shortage of primary energy in industrially developed areas has led to conceptual considerations of giant power plants in remote areas (because of the environmental contamination) or even in space. The realisation of such projects suggest or even force a non-cable-bound transmission of power, e.g. by a collimated microwave beam. However, the propagation of microwaves is affected by tropospheric and ionospheric effects (attenuation, diffraction, reflection, decollimation, depolarisation) which degrade the power transmission efficiency.

This paper describes briefly the power satellite concepts discussed hitherto and explains the principles of the proposed microwave power transmission system. The main interfering atmospheric effects are explained and an appraisal of their influence on the transmission path and the overall power transmission system is given. Some of those effects show a latitudinal dependence, and conclusions on the feasibility of power satellite systems for Europe are derived.

1. INTRODUCTION

During the recent years a great number of investigations have been carried out, dealing with the question of how the energy supply for the earth's population could be managed in future when the fossile fuels, now predominantly used, come to an end. This problem will become severe particularly for industrially developed areas where the standard of living is high, e.g. for Europe; and a solution is the more urgently needed the more the energy demand increases with time.

In the first instance the number of conventional power stations using coal or nuclear energy could be increased; however, only at the expense of increased environmental pollution. An alternative would be the placing of such power stations in waste areas of the earth, e.g. in deserts, pole regions or artificial islands in the oceans, but these areas are in the first place not in general subjected to the sovereignty of the industrial countries in question, and in the second place the problem of a highly efficient energy transmission would have to be solved.

To avoid the first mentioned problem suitable power stations (on the basis of nuclear power or solar radiation) could be positioned and operated in space, but the problem of the power transmission would be aggravated then.

Some project proposals for power supply systems, based on the beforementioned thoughts, have been published in the past ten years in form of studies, carried out mainly in the U.S. These studies assume the production of the primary electric power either

1. in space or
2. on the surface of the earth

by means of

- a. nuclear fission or
- b. thermodynamic conversion of solar radiation or
- c. solar (photovoltaic) cells

and the power transmission to be effected by a collimated microwave beam.

All possible combinations of the numbers and letters above have been investigated in the mentioned studies. The spacecraft involved have to be positioned for good reasons in the geostationary orbit (altitude ca. 36,000 km). The problems of transporting the necessary material into space and the mounting of the spacecraft on the spot are considerable; however, an enlargement upon these topics would go beyond the limit of this paper and reference is made to the literature (e.g. AEG-TELEFUNKEN, DORNIER System and the ILR of the TU Berlin, 1975, and Covault, C., 1978). The same remark applies to the fact that satellite solar power stations are apparently not only of civil interest (Ozeroff, M.J., 1978).

But before discussing the principles and problems of microwave power transmission the concepts and some features of the proposed power satellites shall be presented briefly.

## 2. POWER SATELLITE CONCEPTS

### 2.1. Satellite Nuclear Power Station (SNPS)

An orbiting nuclear power station was proposed in 1973 (Williams, J.R., et al., 1973). It should contain a breeder reactor of either a hydrogen-moderated gas core or a colloidal core (NERVA) type; the transformation of thermal into electrical energy should be effected by a magnetohydrodynamic (MHD) converter. The satellite would have a (probably very optimistically) estimated mass of ca. 10,000 t and would produce a primary power of 13 GW.

For mass reasons almost no nuclear radiation shielding is foreseen; maintenance and repairs have therefore to be done by remotely controlled manipulators. But in view of the fact that the operation of nuclear power stations is apparently not unproblematic yet even on earth, the development of a space-qualified nuclear power station seems to be so difficult, costly and risky that the idea of a SNPS is seemingly not pursued further anymore.

### 2.2. Solar Thermo-electric Power Satellite

In 1974 an orbiting power station of the following concept was proposed (Patha, J.T., and Woodcock, G.R., 1974): The solar radiation is focused by means of giant mirrors (parabolic solar concentrators, each ca. 1.5 km in diameter) onto absorbers in which a suitable gas is heated up. The hot gas drives a Brayton-type gas turbine and a linked generator for producing the primary electric power. 40 of such units are mounted together, forming a solar radiation collection area of ca. 65 km<sup>2</sup> and generating an electric energy of some 15 GW. The total mass of the satellite is in the order of 100,000 t according to more recent estimations (Taylor, R.W., 1976).

### 2.3. Photoelectric Power Satellite (Satellite Solar Power Station, SSPS)

Almost precisely ten years ago the concept and the rationale of a solar power satellite using photovoltaic cells to provide for the primary electric energy was published in a series of articles (Stuhlinger, E., 1970, Glaser, P.E., 1970, Goubau, G., 1970, Robinson jr., J., 1970, Brown, W.C., 1970, Falcone jr., V.J., 1970, Brown, W.C., 1970), followed by a feasibility study of the satellite (Glaser, P.E., et al., 1974) and detailed investigations of the related problems.

The advantage of not having to deal with moving parts for the generation of the electric power has to be paid for by a smaller conversion efficiency of the solar cells. The necessary collection area now under discussion is about 100 km<sup>2</sup> in size and the most recent mass estimations of the satellite amount to 100,000 t (Covault, C., 1978). Of all power satellite projects the SSPS is probably the one pursued deepest by studies and investigations until now (Boeing Aerospace Co., 1977; Hanley, G.M., 1978).

### 2.4. Power Relay Satellite (PRS)

Quite different from the satellites mentioned before is the PRS (Ehrlicke, K.A., 1974). The underlying power supply concept assumes the placing of terrestrial primary power stations in remote areas and the transmission of the energy to the consumption sites by a microwave beam which is reflected by a passive orbiting mirror, the PRS. The mass of such a satellite would be much smaller than that of a power-generating satellite (probably in the order of only 500 - 1,000 t), but the requirements on station and attitude keeping are much higher.

Such a satellite could be launched in principle already by the space shuttle of the first generation presently in production. However, some disadvantages of an application of the PRS principle in conjunction with mid- or high-latitude ground installations will be mentioned later.

## 3. MICROWAVE POWER TRANSMISSION

### 3.1. Generation and transmission of microwaves

For a microwave power transmission system the achievable overall efficiency is of crucial importance. The optimum operating frequency for such a system is in the order of 2 - 3 GHz; at lower frequencies the dimensions of the involved antennae would become too big and at higher frequencies the atmospheric absorptions would increase.

The probably most suitable microwave generator at present for the purpose of power transmission is the amplitron, a backward-wave crossfield amplifier which permits DC/AC conversion efficiencies of up to 90 % (Brown, W.C., 1974). At the power levels in question the amplitron can be operated in a cold-cathode mode for the benefit of longevity and reliability. But the use of klystrons is also considered.

The requirement of high transmission efficiency leads to certain requirements on the antennae dimensions and the beam power profile which can be derived conveniently by using analogies and principles of the light optics (Ehrlicke, K.A., 1974). A non-focused collimated electromagnetic beam which is emitted phase-coherently from an extended source stays collimated only within the so-called Fresnel distance  $R_F$ .

$$R_F = \frac{D^2}{\lambda}$$

where  $D$  is the diameter of the source and  $\lambda$  the wavelength of the radiation. At greater distances the so-called Fraunhofer diffraction causes the beam to diverge at an angle  $\Theta$

$$\Theta = 1.22 \frac{\lambda}{D}$$

A further requirement on the electromagnetic beam is that the energy density across the beam follows at least approximately a Gaussian distribution (Brown, W.C., 1971).

A wavelength of 10 cm = 3 GHz and a Fresnel distance according to the geostationary orbit result in transmit and receive antennae diameter of about 2 km. It can nevertheless be shown that one diameter may be varied to the cost of the other; since installations in space are much more expensive than those on ground a spacecraft antenna diameter of only 1 km is generally assumed in the studies, leading to ground antennae dimensions in the order of 5 - 10 km, depending to a certain extent still on the geographical latitude of the ground installation.

Because of the distances involved the angle under which the antennae are seen by each other is very small, typically in the order of 10 arc sec. This requires a very sophisticated beam steering and control system, especially in view of the possible interferences on the transmission path through the atmosphere. For details of the adaptive beam control system reference must be made to the literature (see e.g. Ehrlicke, K.A., 1974; Raytheon Co., 1978; Chic, C.M., 1979).

As mentioned before, the microwave energy has to be emitted phase-coherently from the transmit antenna. For obvious reasons antennae having diameter in the km range and handling energies in the GW range cannot be realized in form of parabolic reflectors - they must be of the phased-array type. The receive antennae (so-called rectennae) consist of arrays of dipoles fitted with rectifying diodes which are interconnected in series and in parallel so that the output power can be processed further conveniently.

The overall DC/DC efficiency of such a microwave power transmission system (neglecting at the moment any interfering influences of the atmospheric path) can be estimated with confidence to at least 60 %; this value is supported already by an experiment (Dickinson, R.M., 1976).

### 3.2. Effects of the transmission path

The microwave beam transporting the energy is subjected to interferences during its path through the ionosphere and the troposphere (the stratospheric contributions are in general small); these interferences depend on the frequency of the microwaves and on the elevation angle under which the satellite is seen from the ground installations. In principle the occurring interferences are known already from terrestrial microwave links and from satellite communications systems; however, the effects differ somewhat in their consequences because of the much greater beam diameter involved and the requirement of high energy transport efficiency.

In particular the following effects have to be considered:

#### a. Attenuation

- Ionospheric attenuation due to the interaction of the microwave beam with free charge carriers (ions, electrons). Since the resonance frequencies are in the MHz region the attenuation in the GHz region is small, typically  $\leq 0.1$  % (Falcone, V.J., 1970).
- Attenuation in the troposphere due to resonance absorption of water vapour and oxygen molecules and absorption in clouds and precipitation areas. These effects are investigated more in detail (see e.g. Falcone, V.J., 1970, Holzer, W., 1965, Medhurst, R.G., 1965). The absorption is dependent on the interaction length, i.e. on the slant of the path; the results indicate possible power absorption values of some %, in unfavourable cases perhaps up to 10 % for elevation angles  $\geq 10^\circ$ .

#### b. Beam diffraction effects

Gradients or local inhomogeneities of the refraction index of the propagation medium may cause beam angle diffraction effects (bending, displacement, defocusing). Such refraction phenomena can occur

- in the ionosphere, caused by horizontal and vertical gradients of the electron density. The angle diffraction and the beam displacement will normally be in the order of 0.1 arc sec and 10 m respectively; however, under adverse conditions (e.g. abnormally increased activity of the sun) these values can become greater by more than one order of magnitude (Goubau, G., 1970, Ehrlicke, K.A., 1974),
- in the undisturbed troposphere because of the vertical change of the atmospheric density. The temporary variations of this diffraction contribution are nevertheless small,

- in clouds and precipitation areas because of the different refraction indices therein. The beam parallel displacement caused by a layer of different refraction index is in principle of the same order of magnitude as that caused within the ionosphere. However, since the dimensions of the antennae are in the order of km the clouds in the beam path can show local inhomogenities which are small compared with the beam cross section. If the correlation distance of these inhomogenities is small compared with the beam diameter a kind of scattering occurs, leading to a widening of the beam opening angle; the beam will not be displaced on the whole anymore (Ruina, D.P., et al., 1963). However, this effect is understood only qualitatively at present.

The following table lists the effects of the beam diffraction phenomena mentioned above and contains some estimated maximum values of the individual contributions (taken from AEG-TELEFUNKEN, DORNIER System and the ILR of the TU Berlin, 1975). The underlying assumptions are given in the last column.

Reason	Beam Angle Deflection max. arcsec	Beam Parallel Displacement max. m	Beam Impact Area Horizontal Displacement max. m	Assumptions
Ionosphere - Undisturbed	0.1	$20 f^2 \frac{\cos \xi}{\sin^2 \xi}$	$\frac{0.1}{\sin^2 \xi} + 20 f^2 \frac{\text{ctg } \xi}{\sin^2 \xi}$	Plasma Frequency $f_N \leq 15$ MHz Height $H \approx 200$ km
- Solar Flares	2	$400 f^2 \frac{\cos \xi}{\sin^2 \xi}$	$\frac{2}{\sin^2 \xi} + 400 f^2 \frac{\text{ctg } \xi}{\sin^2 \xi}$	Electron Area Density normal $N \leq 5 \cdot 10^{13} \text{ cm}^{-2}$ in flares $N \leq 10^{15} \text{ cm}^{-2}$
Undisturbed Troposphere	$60 \text{ ctg } \xi$			Reference Atmosphere after CCIR Doc. IV/1036-E
Clouds	$\frac{80}{\sin \xi}$	$2.6 \frac{\cos \xi}{\sin^2 \xi}$	$\frac{3.5}{\sin^2 \xi} + 2.6 \frac{\text{ctg } \xi}{\sin^2 \xi}$	Difference of Refraction Index $\Delta n \leq 4 \cdot 10^{-4}$ in $H = 2.5 \dots 9$ km
Precipitation	$80 \text{ ctg } \xi$		$1.2 \frac{\text{ctg } \xi}{\sin^2 \xi}$	Difference of Refraction Index $\Delta n \leq 4 \cdot 10^{-4}$ in $H = 0 \dots 3$ km

Table of Refraction Effects within the Atmosphere  
( $f$  = Frequency in MHz,  $\xi$  = Elevation Angle,  $\xi \geq 10^\circ$ )

It follows from the table that for elevation angles  $\xi \geq 20^\circ$  the major beam angle deflections are caused by clouds. The consequences are somewhat different for orbital power stations and the reflector satellite: in the case of the former the deflections take place very close to the receiving site (i.e. the recenna) and the actual interferences are probably negligible. But in the PRS case the power beam is deflected (and probably also scattered to a certain extent) partly already close to the ground-based transmit antenna; it may be remembered that the thus probable upward link angle deflections are almost one order of magnitude bigger than the target area, i.e. the satellite reflector. The virtue of a PRS lies therefore probably more in applications at lower geographical latitudes than European ones.

For a frequency of about 3 GHz the ionosphere and the clouds deliver about equal contributions to the parallel displacement of the power beam. For orbital power stations and for receiving sites at mid latitudes ( $\xi \geq 30^\circ$ ) the total effect remains small - in the order of some 100 m - even under most adverse conditions; however, at elevation angles  $\xi = 10^\circ$  values of up to 10 km can be reached at abnormal high sun activity.

#### c. Rotation of the polarization plane

- in the ionosphere because of the Faraday-effect,
- in the troposphere due to clouds and precipitation.

Estimations yield a probable value of the total polarization rotation to be expected of some degrees, under most adverse conditions perhaps up to  $15^\circ$ . A detrimental effect on the power transmission efficiency could be avoided by using circular polarisation; however, the cost for the antenna systems would almost be duplicated.

#### d. Reflection.

If the microwave power beam hits a layer of different refraction index on its way from the transmit to the receive antenna a part of the power will be reflected. But because of the very small refraction index differences the power attenuation effect will be small - perhaps only some ppm will be lost. However, in the case of a PRS system some EMI-effects may well be experienced even at sites distant from the transmit antenna because of the high emitted power (in the order of 10 GW), especially when ducts are formed because of certain weather conditions.

The - however preliminary - conclusion of summarizing all the transmission path effects is that power satellite systems are feasible for most of the European area from that point of view, at least orbiting power stations; it should be emphasized nevertheless again that most of the effects are indeed understood qualitatively, but not yet quantitatively to all sufficiency. The requirements on the transmission system differ after all somewhat from those of conventional communications systems: e.g. dispersion effects causing phase delays during the propagation of the waves have almost no influence because of their monochromatism; at the other hand all effects which reduce the power transmission efficiency in any way even by small amounts are of much higher importance than in communications systems (where normally link budget margins of some db are reserved). Thus quite a lot of pertinent investigations are still necessary before a power satellite project could be started.

It should finally be mentioned that the microwave power beam may not only be influenced by its environment but will have on its part an effect on the environment. However, reference must be made to the literature also here (see e.g. Chiu, Y.T., et al., 1979; Livingstone, F.R., 1978).

#### References:

AEG-TELEFUNKEN, DORNIER System und Institut für Luft- und Raumfahrt der Technischen Universität Berlin, 1975, "Analyse der technologischen Entwicklungsprobleme für den Einsatz orbitaler Systeme zur Energieerzeugung im bzw. der Energieübertragung aus dem Weltraum", Studie im Auftrag der Gesellschaft für Weltraumforschung, Auftrags-Nr. RV 11 - V 67/74 - PZ - BB 74.

English translation of the foregoing: "Analysis of Technological Development Problems Posed by Use of Orbital Systems for Energy Conversion and Transfer in and from Space", NASA - TT - F - 16923.

AEG-TELEFUNKEN, DORNIER System und Institut für Luft- und Raumfahrt der Technischen Universität Berlin, 1975, "Betrachtungen zur Durchführbarkeit und Technologie von Sonnenenergie-Satelliten und Energieübertragungs-Satelliten", short version of the foregoing study.

Boeing Aerospace Co. Seattle/Wash., 1977, "Solar Power Satellite System Definition Study", NASA - CR - 151666 to 151673.

Brown, W.C., 1970, "The Receiving Antenna and Microwave Power Rectification", J. Microwave Power 5(4).

Brown, W.C., 1970, "High Power Microwave Generators of the Crossed-Field Type", J. Microwave Power 5(4).

Brown, W.C., 1971, "Transportation of Energy by Microwave Beam", Proc. of the 1971 IECEC, Boston.

Brown, W.C., 1974, "The Technology and Application of Free-Space Power Transmission by Microwave Beam", Proc. IEEE 62, 11.

Chiu, Y.T., and Barbara K. Ching, 1979, "Environmental Factors of Power Satellites, Final Report", Aerospace Corp., El Segundo, Contract F 04701 - 78 - C - 0079, NASA - CR - 157951.

Livingstone, F.R., 1978, "Views Change on Power Satellite Work", Aviation Week & Space Tech-  
nology, 17.

Livingstone, F.R., 1976, "Evaluation of a Microwave High-Power Reception-Conversion Array for Power Transmission", JPL CalTech Pasadena, NASA - CR - 14625.

Livingstone, F.R., 1976, "Microwave Transmission System for Space Power", Proc. Internl. Conference of Space Shuttle and Spacelab, Bonn (FRG).

Livingstone, F.R., 1976, "Satellite Power Systems (SPS) Microwave Subsystem Impacts and Mitigation", JPL CalTech Pasadena, NASA - CR - 157951.

Livingstone, F.R., 1976, "Microwave Power Transmitting Phased Array Antenna Research", JPL CalTech Pasadena, NASA - CR - 157843.



- Ehrlicke, K.A., 1974, "The Power Relay Satellite" Part I and II, Rockwell Intern. Corp., El Segundo, Calif.
- Falcone, jr, V.J., 1970, "Atmospheric Attenuation of Microwave Power", J. Microwave Power 5(4).
- Glaser, P.E., 1970, "Power Without Pollution", J. Microwave Power 5(4).
- Glaser, P.E., O.E. Maynard, J. Mockovciak, jr, and E.L. Ralph, 1974, "Feasibility Study of a Satellite Solar Power Station", NASA - CR - 2357.
- Goubau, G., 1970, "Microwave Power Transmission From an Orbiting Solar Power Station", J. Microwave Power 5(4).
- Hanley, G.M., 1978, "Satellite Power Systems (SPS) Concept Definition Study", Rockwell Internat. Corp., Downey, Calif., NASA - CR - 150700
- Holzer, W., 1965, "Atmospheric Attenuation in Satellite Communications", Microwave Journ. March.
- Livingston, F.R., 1978, "Satellite Power System (SPS) Environmental Impacts, Preliminary Assessment", JPL Cal Tech Pasadena, NASA - CR - 157952.
- Chic, C.M., 1979, "A Ground Based Phase Control System for the Solar Power Satellite", Lin Com Corp., Pasadena, NASA - CR - 160458
- Medhurst, R.G., 1965, "Rainfall Attenuation of Centimeter Waves", IEEE Trans. on Antennas and Propagation AP-13.
- Ozeroff, M.J., 1978, "Satellite Power System (SPS) Military Applications", Pacific Palisades, Calif., NASA - CR - 158109.
- Patha, J.T., and G.R. Woodcock, 1974, "Feasibility of Large-Scale Orbital Solar/Thermal Power Generation", J. Spacecraft 11.
- Raytheon Co., Wayland, Mass., 1978, "Solar Power Satellite (SPS) Pilot Beam and Communication Link Subsystem Investigation Study", Phase 1, Final Report, NASA - CR - 161161.
- Robinson, W.J., 1970, "Wireless Power Transmission in a Space Environment", J. Microwave Power 5(4).
- Ruina, J.P., and C.M. Angulo, 1963, "Antenna Resolution as Limited by Atmospheric Turbulence", IEEE Trans. on Antennas and Propagation AP-11.
- Stuhlinger, E., "Power without Pollution - A Dream That Must Become True", J. Microwave Power 5(4).
- Taylor, R.W., 1976, "POWERSAT A Viable Solar Power Option", Supplement to Statement Before The U.S. Senate Subcommittee on Aerospace Technology and National Needs.
- Williams, J.R., and J.D. Clement, 1973, "Satellite Nuclear Power Station: An Engineering Analysis", Georgia Institute of Technology, Atlanta, Georg., NASA Grant NGR-11-002-145.

Potential Impact of the  
Satellite Power System on Communication and Electronic Systems and the Ionosphere

W. B. GRANT, C. M. Rush, and E. L. Morrison  
U.S. Department of Commerce - NTIA/ITS  
325 Broadway, Boulder, Colorado 80303

ABSTRACT

A Satellite Power System (SPS) concept has been under intensive study in the United States by the Department of Energy (DOE) and the National Aeronautics and Space Administration (NASA) for the past four years. The system presently under study uses a large solar panel (approximately 0.5 km by 5 km by 10 km) to convert the sun's energy to dc power. The dc power is then converted to microwave power at 2.45 GHz by over 100,000 50 kW klystrons. The energy is beamed to earth to a large receiving antenna (rectenna) with an active intercept area of 78.2 km<sup>2</sup>. At the rectenna, the 2.45 GHz energy is converted to dc power by approximately a billion dipoles with diode rectification.

At the Institute for Telecommunication Sciences (ITS), a program to assess the impact of the operation of the SPS upon the ionosphere and telecommunication systems has been actively underway for two years. Analysis of possible functional and operational degradation of electromagnetic systems (communication systems, radars, navigation aids, satellites) and environment-sensitive instruments and systems (computers, sensors, electronic medical instruments and security devices) due to direct SPS power coupling has been studied in detail. The studies also include the development of mitigating techniques when unacceptable degradation is discovered in a given equipment or system.

In this paper, some results of these investigations are described. Assessments of possible impacts upon telecommunication systems and implications for electromagnetic compatibility are discussed. Experimental studies undertaken to determine the degree the ionosphere will be modified by the passage of the microwave power beam and what impact this modification has upon telecommunication systems are also discussed. Theoretical efforts to simulate SPS operational impacts are described.

1. SYSTEM DEFINITION

The United States Department of Energy (DOE), in its quest to provide a source of baseline electrical power for the future, has under study a solar power system as one of the possible systems of the future. This system consists of a large satellite (10 km by 5 km by 0.5 km thick) which uses photo-voltaic cells to produce direct current (dc) from the sun's energy. The dc then drives over 100,000 high power klystrons or other candidate power devices in a phased array antenna 1 km in diameter operating in 2.45 GHz ISM Band. The phased array is made up of modules of power amplifiers arranged such that the aperture power distribution is Gaussian, with approximately a 10 db taper as shown in Figure 1. The microwave beam at a frequency of 2.45 GHz is transmitted to earth where it is received at an elliptical antenna approximately 13 km by 10 km for a site in the southern United States of America. The antenna is made up of bays of dipoles where rectification of the microwave energy takes place. The dc is summed at summing busses, and the total is conditioned to interface with utility grids with an output of 5000 megawatts.

Because of the large amount of rf power involved and the environmental impacts associated with the rf power transmission and the satellite and receiver site physical characteristics, DOE has initiated a very comprehensive assessment program paralleling the concept design program of The National Aeronautics and Space Administration (NASA). The list of the major concerns and the organizations involved in the research area are shown in Figure 2. For this complex program, a continuing data exchange and review process between assessment and design agencies is obviously essential.

The electromagnetic compatibility (EMC) task area under the environmental assessment programs has three basic task areas being studied by the Institute for Telecommunication Sciences:

1. habitable structure penetration and resonance possibilities,
2. potential ionospheric modification by the power beam and associated telecommunication impact,
3. and microwave power coupling effects to a large variety of equipments and systems.

## 2. METHODOLOGY

The radiated power and planned operating frequency of the SPS indicate the importance of the EMC evaluation relative to radio frequency systems and other susceptible electronic systems that operate within the continental U.S. and adjacent international areas. This EMC investigation includes all emissions from the SPS (primary, harmonic, and spurious; and associated spatial patterns), with the determination of interference power densities at the earth's surface, airspace and orbit areas. This includes ionospheric and atmospheric media effects on the primary and sidelobe beam characteristics. Interference power densities are used to determine the character of performance degradation for rf and electronic systems, scored relative to the ranges of signal to interference ratios possible over the operational geographical areas. A pictorial representation of the SPS and candidate interference problems in Figure 3 indicates the scope of this investigation.

In evaluating the impact of equipment/system performance degradation, resultant operational compromises are derived. Operational considerations address, for example, equipment/system criteria relationships to the safety and effectiveness of supported activities (e.g. public transportation, traffic control, military surveillance/weapons delivery, communications network efficiency), in terms sufficient to support national impact extrapolation and cost-benefit analyses to derive degraded system mitigation recommendations.

The basic analysis elements including the SPS environment, equipment/system degradation, and operational implications are depicted in Figure 4. This includes propagation media, affected system performance, and representative operational impact areas.

Mitigation techniques emphasize degraded equipment energy penetration and coupling mechanisms; antennas, circuitry, and cabling, etc. Recommendations for equipment modifications will concern these areas, including cost-benefit tradeoff results.

A series of technical reports are being developed: functional system degradation and the operational support implications for the areas near proposed rectenna sites, hemispherical SPS power densities for one through multiple satellites, mitigation technique analyses and recommendations for the various interfered system categories; and guidelines for EMC analyses of future system deployments in the rectenna areas to assure an acceptable performance.

## 3. STATE OF KNOWLEDGE

This EMC evaluation program uses various propagation models to determine SPS illumination power at specific locations and general areas within the continental United States (CONUS), and equipment/system functional models to derive signal-to-interference degradation characteristics for the SPS primary and harmonic emissions. The propagation modes include line-of-sight attenuation, hydrometer and particulate attenuation and scatter, atmosphere anomaly refraction, and terrain and structural reflections. Primarily because of the high power level of the SPS, limited media model refinements in particulate scatter and anomaly refractive effects are required.

System degradation models for communications, radars, and other radio frequency components are adequate for military, industrial, and commercial applications. These models include in-channel and out-of-band interference effects.

Existing coupling and effects descriptors for optical and EM sensors, and various computer and processing/control circuitry (distributed and integrated circuit configurations) provide an adequate base for the initial analyses. Additional measurements will be implemented to allow sufficient definition of modular effects to support realistic mitigation technique specification. These measurements and sensitivity testing using existing functional and circuit models are also necessary to support the cost-benefit trade-off exercises for the mitigation techniques.

The SPS system data required for these EMC analyses are provided by the SPS Concept Definition Program. Data required include satellite spectral and spatial emission characteristics, rectenna candidate locations and functional parameters, and control processes.

## 4. PRELIMINARY ASSESSMENT

### 4.1. Habitable Structures Penetration

The question was raised whether local free-space field-strength maxima (hot spots) inside habitable structures can exceed the uniform power density of incident SPS, coherent, plane-wave radiation. The answer lies in the assessment of two electromagnetic effects:

1. Coupling and penetration of field energy into an enclosure.
2. Storage of field energy in the interior space.

To gain some handle on the rather loosely defined term "habitable structure," we categorize it by means of the enclosure material:

Case	Microwave Properties	Real Structure Equivalent
1	lossy dielectric	brick, frame, stone house
2	composite of lossy dielectric & metal	trailer, house with metal sidings, plant building
3	metal with lossy dielectric layer plus aperture	vehicle interior, aircraft cabin

The crux of the hot spot problem lies in the conversion of traveling, incident, plane wave radiation with the same power density at any given time and location into a resonant, standingwave field storing equal amounts of electric and magnetic energy and displaying locally varying field amplitudes. The incident radiation provides the energy to cover the losses encountered by the resonant field. A local-field energy maximum at the internal space coordinates  $x, y, z$  is described in terms of the electric field components,

$$E_i^2 = E_x^2 + E_y^2 + E_z^2$$

and compared with the incident uniform field  $E_o^2$ . The hot spot problem is defined by means of a power transmission coefficient

$$T = E_i^2 / E_o^2 > 1.$$

If a quality factor  $Q$  (ratio between time-averaged energy stored in the resonance field and the energy loss per period) and a coupling factor  $\eta$  (ratio between the energy available to excite a resonance and the incident energy), are introduced the hot spot problem can be reformulated as

$$T = \eta Q > 1. \quad (1)$$

One speaks of a resonance when  $Q > 1$ ; the coupling will be generally so that  $\eta \leq 1$ . The condition of Eq. (1) will exist for a volume element as small as  $(0.1 \lambda_o)^3$  assuming the maximum spatial periodicity between field maxima and minima to be  $\lambda_o/4$ . Even before discussing the electromagnetic effects that might lead to  $T > 1$ , one has to take note of the complexity of the problem by reckoning the fact that an average habitable space has millions of such probable volume elements to look at (e.g., the room size 4m x 5m x 2.5m has about  $3 \times 10^7$  elements).

In summary, habitable space presents a poorly defined problem electromagnetically. It has the potential of being a complicated resonant system with many coupled oscillations for the coherent SPS radiation but, for all practical purposes, the product of quality and coupling factors (Eq. 1) is not expected to exceed unity. Field hot spots become even more unlikely if a few preventive measures are observed (see below).

#### 4.2. Measures to Mitigate a Potential Hot Spot Problem

Two principal means exist to achieve complete certainty that there is no hot spot problem; namely to avoid penetration into the interior and/or to secure a uniform internal field distribution.

##### a) Measures to accomplish the first objective are:

- Use shielding by natural obstructions (e.g., tree grove).
- Increase reflectivity of the outer shell by metal sidings especially towards the south.
- Shade apertures with metal awnings or wire mesh (mesh size  $< 1.5$  cm).
- Cover apertures with resistive sheet material or embed absorbing cord around the edges (highest field strength).
- Keep unnecessary openings (slots, cracks, etc.) away from the exposed side or keep them below 2 cm. in size.

##### b) Measures for control of the internal free field distribution:

Field uniformity is the desired objective for anechoic chambers and has been studied extensively in this context. The requirements for the free field VSWR of habitable space are less stringent (we suggest a tolerance of about  $\pm 5$  db) than for a test chamber ( $< \pm 0.5$  db).

Proposed measures:

- Apply absorbing material with a thickness  $> 3$  cm to all surfaces.
- Perform in suspected areas (open resonator!) a three-dimensional field scan with a resolution  $< 1$  cm and ascertain by rearrangement of reflecting objects of application of absorbers that the free field VSWR is below  $\pm 5$  db.
- Use, as a last resort, a moving reflector such as a fan (mode stirrer) or a mechanically oscillating metal sheet to mix up the field.

A complete report on this subject has been written and is now in editorial review.

## 5. ELECTROMAGNETIC COMPATIBILITY

Before the EMC evaluation was begun, it was necessary to determine the radiation pattern of the spacenna. This would help us to determine the field intensity distribution on the earth and the EM environment systems would have to operate in should the SPS become a reality. Figure 5 shows the gain versus angle from boresight of the spacenna.<sup>2</sup> Figure 6 shows a smoothed version of what the power density distribution would be for a single satellite with rectenna in mid-CONUS. Power density distributions were also plotted for multiple satellite systems.

Electromagnetic energy coupling modes were studied to determine how coupling takes place as well as what level of penetration would cause functional impacts. This included the study of antenna apertures, electronic circuit, circuit module, subsystem interconnections (shielded and unshielded cables, printed circuit wires, strip lines, etc.), and inter-modulation responses including non-linear elements such as lightning protection devices and other power line coupling.

The effects analysis also included the study and development of mitigation techniques which would allow acceptable operation of systems which show operational degradation due to SPS EM environment.

To assess the impact on systems near four representative candidate rectenna sites, an area 145 km by 145 km with a proposed rectenna site at the center was chosen as our data sample area. All government and non-government EM systems operating within this geographic boundary between 75 MHz and 5 GHz were tabulated.

For purposes of this initial environmental statement, the equipment/system categories identified in the file retrieval are listed:

1. Military Development and Operational Test and Evaluation.
  - a. Instrumentation radars - conical scan and monopulse modes.
  - b. Traffic monitor/control radars.
  - c. Radar transponders.
  - d. Radar signal and functional replicators.
  - e. Wideband monitor receivers with recognition/decision software scan instantaneous frequency modes.
  - f. Television cameras for target position track.
  - g. EM system operational monitors - multiple wideband receivers with processing software.
  - h. Range command/control communications nets.
  - i. Range telemetry communications networks.
2. Industrial Communications.
  - a. Utility network command/control and telemetry.
  - b. Pipeline network command/control and telemetry.
  - c. Water resource telemetry.
  - d. Multiplexed carrier networks - two major service systems.
3. Transportation Support Systems.
  - a. Railroad mobile equipments -yards and enroute complex.
  - b. Air traffic control network.
  - c. Emergency services - mobile, base station, and relay equipment - medical and general emergency applications.
  - d. Railroad "car condition" monitors.
4. Public Service Communications.
  - a. State backbone microwave communication networks.
  - b. Law enforcement systems - state, county, city - mobile, relay, and base station equipments.
  - c. Forest service units.
  - d. Fire and government emergency systems - county and city operations.
  - e. Common carrier networks - telephone, data, television services - remote area voice links.
5. Specialized Services.
  - a. Space tracking and monitoring facilities.
  - b. Railroad hump radars.

Following is a summary of potential SPS illumination effects on a few chosen systems showing degradation without and with mitigation techniques. Figure 7 shows the effect of the microwave power transmission system (MPTS) on selected microwave communication links. The message throughput efficiency degrades as a system is exposed to greater SPS field intensity, shown here as decreasing efficiency with closer proximity to the rectenna site (increased field intensity). The vertical spread in data (e.g. the cross-hatched area) is due to the variety of manufacturers' equipment used as a data base. Some equipment was much more susceptible to SPS interference than others.

The shaded area shown as "mitigated" was data taken after filtering was added in the amplifiers as well as using better shielded interconnecting cables, power line filtering, and supply voltage circuit decoupling. Most systems studied could be made to perform in an acceptable manner with fairly simple mitigation techniques.

Figure 8 shows the degradation of microprocessor accuracy measured by the testing of information flow from the input port through various registers, computational exercises, using data and program control storage, and through the output buffer. Again, the spread of data is due to differences in susceptibility of a variety of manufacturers' equipment. Here it can be seen that the accuracy of some microprocessor equipment dropped by almost 50% at exposure levels of 4.5V/m. The shaded area marked "mitigated" shows the error reduction due to shielding of plastic housing areas with wire screen with grid size 1 cm x 1 cm or less, and single point ground, the use of dual shielded coax and other well shielded cables for message and subsystem interconnecting cables, and bias supply filters with transient protection circuit modification.

Figure 9 represents effects of the MPTS on optical systems such as high-resolution television scanners and infra-red sensors used in security applications. Here the mitigation techniques used were the addition of wire mesh with 1 cm x 1 cm grid over the optical apertures, wire mesh shielding in other unshielded areas where plastic covering or other apertures (cooling holes, etc.) existed, and circuit modifications such as the use of power and bias supply filters.

Radio astronomers have been particularly concerned about the interference potential of a satellite power system. ITS chose a few sites to study, one of which is reported on here. There is a Very Large Array (VLA) in southern New Mexico used for radio astronomy purposes. With a receiver bandwidth of 50 MHz and the widest filter bandwidth setting of 24 MHz, the calculated threshold power density estimates beyond which unacceptable performance would occur are:

At the SPS fundamental frequency	2.45 GHz	-	$8.2 \times 10^{-6}$ mw/cm <sup>2</sup>
At the second harmonic	4.9 GHz	-	$6.5 \times 10^{-16}$ mw/cm <sup>2</sup>

The power density at the VLA site due to SPS from the closest proposed rectenna site in northeast Arizona would be:

At the SPS fundamental frequency	2.45 GHz	-	$1.1 \times 10^{-4}$ mw/cm <sup>2</sup>
At the SPS second harmonic	4.9 GHz	-	$1.2 \times 10^{-11}$ mw/cm <sup>2</sup>

By comparing these calculated figures with those that would cause unacceptable performance it can be seen that SPS poses a potential problem for VLA if the site in northeast Arizona were actually picked as a site for a rectenna.

There are mitigation techniques presently under study at ITS. The first is the use of rejection filters for the SPS fundamental frequency and harmonics exceeding receiver thresholds. Preliminary designs are based on interdigital and elliptic function configurations. These filters would be connected to the receiver input port. Current designs indicate a null depth of 50 to 55 db with a ripple factor of less than 1 db. Phase stability across the rejection band is approximately 30°. These characteristics are being refined by iterative parameter tests. Parameter stability and methods to reduce noise temperature are yet to be investigated. A second method (the most attractive method at the moment) is to use signal cancellation techniques involving sampling of harmonic and fundamental components. This method used signal sampling at a convenient point in the receiver coaxial cable or waveguide input and generates a cancelling signal through a phase-locked oscillator configuration. The initial design provides a dynamic range of about 30 db. A parametric analysis is required to determine optimum loop arrangement to minimize instantaneous error spectra (including interference noise sidebands), particularly with media induced fluctuation spectra ranges. Means of limiting input noise temperature and low level phase locked oscillator noise are being investigated.

## 6. IONOSPHERIC HEATING ASSOCIATED WITH OPERATION OF SPS

In the previous sections we discussed the impact on telecommunication systems of an SPS operating with a frequency of 2.45 gigahertz and transferring between 5 and 10 gigawatts of power from geostationary orbit to the surface of the earth. In this section we will briefly discuss some potential effects of the operation of the SPS upon the ionosphere. The energy density associated with the passage of the power beam through the ionosphere is on the order of 23 milliwatts /cm<sup>2</sup> at the beam center. This energy density is the same order as the energy density required to give rise to substantial heating of the lower ionosphere and could lead to the creation of irregularities and striations in the ionospheric plasma at F-region heights (250 to 400 kilometers).

The heating of the ionosphere that is associated with the passage of the SPS microwave power beam is believed to result from ohmic type interactions between the microwave beam and the ionospheric constituents, primarily the ionospheric electrons. This heating could result in a substantial increase in the electron temperature in the D- and lower E-region of the ionosphere (70 to 100 kilometers) and could have an effect on telecommunication systems whose electromagnetic energy passes through the modified ionosphere. Figure 10 provides an artist's concept of how telecommunication systems could be impacted by the operation of a satellite power system. The Figure shows a SPS beaming energy to the surface of the earth, giving rise to an enhanced electron temperature in the D-region, and the formation of irregularities in the F-region. Telecommunication systems, whether they be situated on the surface of the earth or in space, can be affected by the modified ionosphere. Thus it is necessary to determine the extent to which the ionosphere may be modified by the operation of the satellite power system. This determination is being conducted as part of a national program within the United States involving the government, industry, and university personnel.

The basic philosophy behind the program of research and development is the utilization of existing ground-based heater facilities to simulate the effects on the ionosphere of the operation of the SPS, to undertake measurements of telecommunication systems in conjunction with the operation of the ground-based heater facilities, to make diagnostic measurements of the ionospheric plasma as it is being heated by intense radio waves, and to develop the theoretical capability to explain the observations and to extrapolate to the SPS operational scenario.

#### 6.1. Ground-based Simulation of SPS

It is currently believed that any heating of the ionosphere that will result from the passage of the SPS microwave power beam will be due to ohmic interactions between the power beam and the ionospheric constituents. This being the case, the amount of energy that will keep the ionospheric plasma at the SPS operational frequency can be related to the amount of energy that goes into heating the ionosphere at another frequency using the relationship  $P_{SPS}$  over  $F_{SPS}$  is equal to  $P_{HF}$  over  $F_{HF}^2$  where  $P_{SPS}$  is the energy density associated with the SPS power beam,  $F_{SPS}$  is the operational frequency of the satellite power system (2.45 gigahertz),  $P_{HF}$  is the energy density due to the ground-based heating facility, and  $F_{HF}$  is the operational frequency of the ground-based heating facility. The above relationship indicates that the amount of energy associated with the operation of the SPS that goes into heating the ionospheric plasma can be realistically simulated using much lower frequencies and energy densities provided that the heating is done with radio waves that simulate the SPS operational scenario, that is with radio waves that pass through the ionosphere.

The ground-based heating facility located at Platteville, Colorado, and operated by the Institute for Telecommunication Sciences, and the new heater facility located at Arecibo, Puerto Rico, funded by the United States National Science Foundation, both have adequate power to simulate the SPS heating effects on the lower portion of the ionosphere, the D- and E-region. These facilities can transmit radio waves vertically into the ionosphere between the frequency range 5 to 10 MHz. These frequencies are generally much higher than the characteristic frequencies associated with the lower ionosphere. Thus, they pass through the lower ionosphere in a manner comparable to the SPS power beam. Table A shows the SPS comparable power density and size of the modified ionospheric region associated with a 5 and 10 MHz operation of the Platteville Heater Facility and the Arecibo Heater Facility. It is readily apparent from the table that heating with HF waves of 5 MHz provides SPS comparable power density--23.0 milliwatts/cm<sup>2</sup> to the lower ionosphere. Heating with radio waves at higher frequencies, 10 MHz, for example, shows that the energy density is not sufficient to simulate the SPS operation. However, plans are being developed for more powerful ground-based facilities in order to provide SPS comparable energy density at higher frequencies and at higher ionospheric heights.

#### 6.2. Telecommunications Studies of SPS Impact

In August, September, and October 1979, a number of telecommunications studies were conducted in conjunction with the operation of the Platteville Ionospheric Heating Facility. The telecommunication studies emphasize the performance of electromagnetic systems whose energy is either reflected from the lower ionosphere or whose overall system sensitivity is strongly dependent upon the structure of the lower ionosphere. Telecommunication systems operating in the VLF, LF, and MF portions of the electromagnetic spectrum were investigated. Signals from an OMEGA station located in Hawaii operating at 11.8 kHz (VLF); from two LORAN-C stations, one located at Fallon, Nevada, the other at Dana, Indiana, and operating on a frequency of 100 kHz (LF); and numerous AM broadcast stations operating between 550 and 1600 kHz (MF) were monitored at locations in eastern and northern Colorado. Table B gives the details of the stations that were monitored along with the locations where they were monitored. Figure 11 provides an illustration of the geometry of the signal sources, the monitor locations, and the area of the ionosphere above Platteville that was modified by the high-powered transmitter. Figure 12 provides an indication of the type of data that was observed on the OMEGA path from Hawaii to Brush, Colorado. This particular set of data was observed on August 16, 1979. The figure shows both phase in microseconds and amplitude in db of the signal transmitted from Hawaii to Brush, Colorado. The hatching on the scale above the time indicators refers to times at which the ionospheric heater at Platteville was operating. These are heater "ON" periods. All other time periods for which there is no hatching, the heater was not operating. It is apparent from this figure that there is very little indication of a change in the overall system performance when the heater was turned "ON" compared to when it was not. Figure 13 provides a similar illustration for the data observed on the LORAN-C path from Fallon, Nevada to Brush, Colorado. These data were observed on August 16 and 17, 1979. As was the case with the previous figure, there is little or no indication at all that the phase of the LORAN signal differed during times when the heater was "ON" compared to when the heater was not "ON." Figure 14 is an example of three MF signals that were observed at Brush, Colorado, on August 24, 1979. Shown in the figure are the relative amplitudes of the skywave signals from station KSL located in Salt Lake City, Utah, and station KNX located in Los Angeles, California. As was the case in Figures 12 and 13, there is no apparent difference between the system performance during times when the heater was "ON" compared to when the heater was not "ON."

Tables C, D, and E provide a summary of the observations taken during August, September, and October 1979. Table C shows for each day the average value of the amplitude and phase of the OMEGA signals during time periods when the heater was "ON" compared to when the heater was "OFF". Table D shows the average values of the LORAN phase signal monitored at Brush from Fallon, Nevada, during time periods when the heater was "ON" and "OFF". In Table E, we show, for specific broadcast stations on specific days, the average values of the relative amplitude at time periods when the heater was "ON" and when the heater was "OFF". It is readily apparent from these tables that there is no significant difference between the system performance of the OMEGA system, the LORAN system, and the AM broadcast systems at times when we were heating the ionosphere compared to when we were not. Since we were heating with radio waves that for the most part provided energy power densities to the ionosphere that are comparable to the SPS power density, it would appear that the impact of the SPS operation on the performance of VLF, LF, and MF telecommunication systems would be minimal.

The set up of the experiments that were undertaken in August, September, and October 1979 utilized transmitters of opportunity in order to simulate telecommunication system performance. It is quite possible that some of the signals did not pass exactly over the Platteville transmitter or, more to the point, did not pass through the ionospheric region that was modified by the Platteville transmitter. It is also possible that, because of the scale sizes involved in these systems, the relatively small heated volume of the ionosphere that is above Platteville is inconsequential to affect substantial system change. However, we hasten to point out that at the frequencies used to simulate the SPS operation--5 to 6 MHz--the diameter of the heated volume is on the order of 40 to 50 kilometers. This is about 4 times the size of the 10 kilometer diameter associated with the passage of the SPS power beam through the ionosphere. Thus, from the viewpoint of spatial effects, the simulations that were conducted are a worse-case estimate.

### 6.3. Experimental Studies of SPS Effects

Efforts to determine the degree to which the ionosphere is heated and electron density changed by the passage of the SPS power beam revolve around the Arecibo National Ionospheric Observatory. The incoherent back scatter radar at Arecibo provides a unique diagnostic tool in order to sense changes in electron density and electron temperature, as SPS comparable energy density is incident upon the ionosphere. A detailed program of observation is scheduled to begin in April of 1980. These observations will emphasize the determination of the threshold at which substantial changes in electron density and electron temperature may occur.

### 6.4. Theoretical Studies of SPS Effects

The theoretical studies of the effects of the operation of the solar power satellite on the ionosphere revolve principally around two regions. One region is the effects of SPS operation on the D-region, the other is the effects of SPS operation on the F-region. The D-region studies are emphasizing the degree to which the lower ionosphere will be heated by the passage of the SPS power beam, and to what extent the electron density in the lower ionosphere will be changed by this additional heat. It would appear from the results of the telecommunications experiment that the degree to which the ionosphere is modified is so small that it is of little consequence to the performance of VLF, LF, and MF telecommunication systems.

In the F-region, studies are being directed toward assessing the possibility that plasma instabilities driven by ohmic heating will arise as the result of the passage of the SPS power beam. Emphasis is placed on thermal cell focusing instabilities and the degree to which the onset of these instabilities can be predicted.

## 7. CONCLUSIONS

A detailed technological program is being undertaken in order to assess the potential impact of the operation of the satellite power system upon the ionosphere and ionospheric dependent telecommunication systems. The program revolves around ground-based heating facilities in order to simulate the ionospheric heating expected from SPS operation. Studies undertaken thus far seem to indicate that the operation of the SPS will not adversely impact upon the performance of telecommunication systems that operate in the VLF, LF, and MF portion of the spectrum. Whether such conclusions will be reached with regard to systems operating at HF and above remains to be demonstrated. In addition, studies about to be undertaken in order to determine the absolute magnitude of the changes in electron density in the lower ionosphere as a result of SPS comparable power density will provide needed answers concerning the thresholds for substantial ionospheric changes. Theoretical studies are necessary in order to explain the results of the simulation studies and to extrapolate these results to the actual SPS operational scenario.

There is no doubt that SPS will present some EMC problems with many types of systems particularly within 50 to 100 km of a rectenna site. However, the ITS study is not only tasked to make an effects analysis, but is also tasked to study mitigation techniques. The output of the ITS program will produce effects summaries, mitigation recommendations, and guidelines for designers, manufacturers, and users of EM and electronic systems which may have to operate in a SPS environment in the next century.



Some reports that are in peer review and being prepared are:

"FIELD MAXIMA INSIDE HABITABLE STRUCTURES EXPOSED TO 2.45 GHz  
PLANE WAVE RADIATION"

"THE ELECTROMAGNETIC COMPATIBILITY ANALYSIS FOR A SOLAR POWER  
SYSTEM RECEIVING SITE IN THE MOJAVE DESERT"

"ANALYSIS OF INTERFERENCE BETWEEN A SPS AND CONVENTIONAL  
SATELLITE SYSTEMS"

"SPS EFFECTS ON OTHER SATELLITES IN BOTH GEOSYNCHRONOUS ORBIT  
AND LOW EARTH ORBIT"

"ELECTROMAGNETIC COMPATIBILITY OF A SOLAR POWER SYSTEM -  
VOLUME I"

Future work at ITS will include the following:

Propagation - "Heat Island" effects

Propagation - Atmosphere anomaly characteristics

Mitigation technique verification - electronic systems

Energy coupling and control

Structure intermodulation product evaluation and control

#### REFERENCES

OTT, R. H., E. L. Morrison, and W. B. Grant, 1979, "Antenna Patterns for  
the Solar Power Satellite", NTIA Technical Memorandum TM-79-5,  
Jan., pp. 1-12.

SPS Equivalent Power Density and Size of Heated Region for  
Existing Platteville and Arecibo Facilities

Facility	5 MHz			10 MHz		
	100 km	200 km	300 km	100 km	200 km	300 km
<u>Platteville</u>						
SPS-Equivalent Power Density (mW/cm <sup>2</sup> )	23.	5.8	2.6	4.3	1.1	0.48
Diameter of Heated Region (km)	40.	79.	118.	21.	42.	62.
<u>Arecibo</u>						
SPS-Equivalent Power Density (mW/cm <sup>2</sup> )	24.	6.0	2.7	6.1	1.5	0.7
Size of Heated Region (km)	18x9	35x17	53x27	9x4	18x9	27x13

TABLE B

Data on Facilities and Sites Used in the DOE Experiment

Station	Function	Frequency	Power (Watts)	Coordinates		Bearing from Field Site (°)	Distance to Field Site (km)
				Lat.(N)	Long.(W)		
Platteville	Heater	5-10 MHz	1.6 Megawatts	40.18	104.6	Brush Boulder 258.0 71.2	Brush Boulder 78.2 62.8
Brush	Field Site #1	-----	-----	40.33	103.7	-----	-----
Boulder Bennett	Field Site #2 Field Site #3	----- -----	----- -----	39.8523 39.8	105.263 104.4	----- -----	----- -----
OMEGA (Hawaii)	VLF Source	11.8 kHz	-----	21.4	157.83	Brush Boulder 264.33 263.1	Brush Boulder 5481.16 5345.27
LORAN-C Fallon, NV	LF Source	100.0 kHz	-----	39.5	118.8	Brush	Brush 270.79 1289.25
LORAN-C Fallon, IN	LF Source	100.0 kHz	-----	39.8523	87.4869	Boulder	Boulder 84.87 1516.16
KIIX Fort Collins	AM Broadcast	600 kHz	1,000	40.5	105.1	Brush	Brush 279.52 119.99
KHOW Denver	AM Broadcast	630 kHz	5,000	39.7	105.1	Brush	Brush 238.09 130.98
KERE Denver	AM Broadcast	710 kHz	5,000	39.7	105.1	Brush	Brush 238.09 130.98
KOA Denver	AM Broadcast	850 kHz	50,000	39.7	105.1	Brush	Brush 238.09 130.98
KLMO Longmont	AM Broadcast	1060 kHz	10,000	40.15	105.15	Brush	Brush 261.23 124.66
KNX (CA) Los Angeles	AM Broadcast	1070 kHz	50,000	34.0	118.5	Brush	Brush 246.42 1485.26
KREX Grand Junction	AM Broadcast	1100 kHz	50,000	39.1	108.5	Brush	Brush 253.12 432.58
KSL (UT) Salt Lake City	AM Broadcast	1160 kHz	50,000	41.7	112.0	Brush	Brush 285.41 712.37
KADE Boulder	AM Broadcast	1190 kHz	1,000	40	105.3	Brush	Brush 255.41 140.79
KFKA Greeley	AM Broadcast	1310 kHz	5,000	40.3	104.7	Brush	Brush 268.07 84.83
KSIR Estes Park	AM Broadcast	1470 kHz	5,000	40.25	105.55	Brush	Brush 267.35 157.12
YBOL Boulder	AM Broadcast	1490 kHz	1,000	40	105.3	Brush	Brush 255.41 140.79

TABLE C

## Average Values of OMEGA Amplitude and Phase Recorded During Times of Platteville Facility "ON" and "OFF"

Date	Amplitude Facility "ON" (dB)	Amplitude Facility "OFF" (dB)	Phase Facility "ON" ( $\mu$ s)	Phase Facility "OFF" ( $\mu$ s)
August 16, 1979	14.9 $\pm$ 1.30	15.1 $\pm$ 0.90	3.82 $\pm$ 1.54	2.82 $\pm$ 1.45
August 17, 1979	12.4 $\pm$ 2.72	13.1 $\pm$ 3.07	4.05 $\pm$ 3.33	4.17 $\pm$ 3.50
August 19, 1979	14.9 $\pm$ 0.59	14.9 $\pm$ 0.76	2.35 $\pm$ 2.07	3.10 $\pm$ 1.89
August 20, 1979	13.8 $\pm$ 1.34	14.1 $\pm$ 1.50	7.05 $\pm$ 2.38	8.00 $\pm$ 1.70
August 22, 1979	9.7 $\pm$ 1.83	10.0 $\pm$ 1.51	6.28 $\pm$ 2.14	6.02 $\pm$ 2.28
August 23, 1979	9.39 $\pm$ 1.69	9.08 $\pm$ 1.83	4.59 $\pm$ 3.12	3.63 $\pm$ 2.70
September 26, 1979	16.7 $\pm$ 1.20	16.9 $\pm$ 1.20	6.93 $\pm$ 1.55	7.73 $\pm$ 1.32
October 3, 1979	1.54 $\pm$ 5.10	1.83 $\pm$ 5.50	2.73 $\pm$ 2.88	2.56 $\pm$ 2.54

TABLE D

## Average Values of LORAN-C Phase and Amplitude Data Recorded During Times of Platteville Facility "ON" and "OFF"

Date	Phase Facility "ON" ( $\mu$ s)	Phase Facility "OFF" ( $\mu$ s)	Amplitude Facility "ON" (dB)	Amplitude Facility "OFF" (dB)
August 16, 1979	0.91 $\pm$ 0.02	0.90 $\pm$ 0.04		
August 17, 1979	0.46 $\pm$ 0.30	0.46 $\pm$ 0.26		
August 19, 1979	0.65 $\pm$ 0.17	0.71 $\pm$ 0.12		
August 20, 1979	0.50 $\pm$ 0.23	0.49 $\pm$ 0.24		
August 23, 1979	0.26 $\pm$ 0.06	0.49 $\pm$ 0.28		
Sept. 26, 1979	0.53 $\pm$ 0.32	0.32 $\pm$ 0.24	-0.21 $\pm$ 1.06	-0.58 $\pm$ 0.85
Oct. 3, 1979	0.37 $\pm$ 0.21	0.57 $\pm$ 0.27	0.62 $\pm$ 1.48	-0.17 $\pm$ 1.78

TABLE E

## Average Values of AM Broadcast Station Relative Amplitude Recorded During Times of Platteville Facility "ON" and "OFF"

Date	Amplitude Facility "ON" (dB)	Station	Amplitude Facility "OFF" (dB)	Station
August 16, 1979	0.49 $\pm$ 0.05	KOA	0.38 $\pm$ 0.11	KOA
	0.45 $\pm$ 0.12	KLMO	0.34 $\pm$ 0.11	KLMO
August 17, 1979	0.42 $\pm$ 0.09	KADE	0.45 $\pm$ 0.08	KADE
	0.34 $\pm$ 0.13	KLMO	0.33 $\pm$ 0.14	KLMO
August 20, 1979	0.33 $\pm$ 0.24	KSIR	0.37 $\pm$ 0.24	KSIR
	0.40 $\pm$ 0.07	KBOL	0.39 $\pm$ 0.08	KBOL
August 22, 1979	0.44 $\pm$ 0.18	KSIR	0.40 $\pm$ 0.18	KSIR
August 23, 1979	0.63 $\pm$ 0.34	KSIR	0.63 $\pm$ 0.36	KSIR
	0.17 $\pm$ 0.12	KNX	0.13 $\pm$ 0.06	KNX
	0.35 $\pm$ 0.07	KSL	0.41 $\pm$ 0.17	KSL

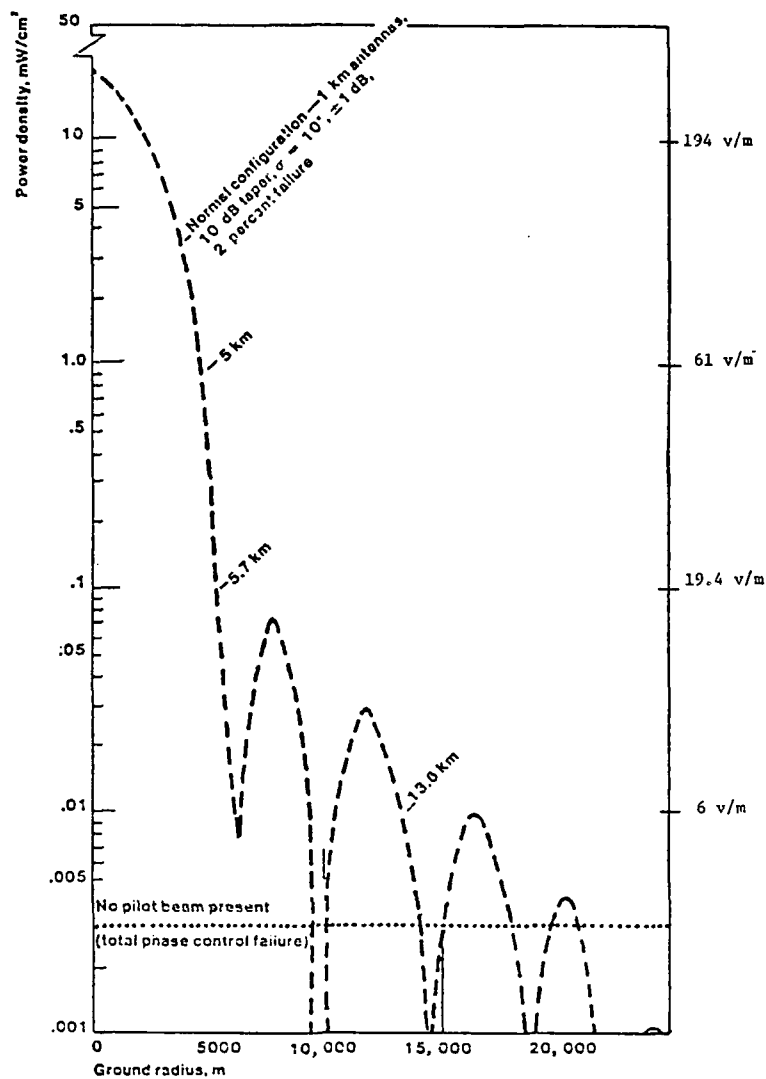


Fig.1 SPS antenna pattern on the ground

Program Responsibility

- Department Of Energy

Project Management

- Department Of Energy
- National Aeronautics & Space Administration

Systems Definition

- National Aeronautics & Space Administration
  - Johnson Space Center
  - Marshall Space Flight Center

Environmental Assessment

- Environmental Protection Agency
- Lawrence Berkeley Laboratory
- Ames Research Center - NASA
- Argonne National Laboratory
- Los Alamos Scientific Laboratory
- Institute For Telecommunication Sciences
- Pacific Northwest Laboratories

Societal Assessment

- Planning Research Corp.

Comparative Assessment

- Argonne National Laboratory

Fig.2 SPS key organization

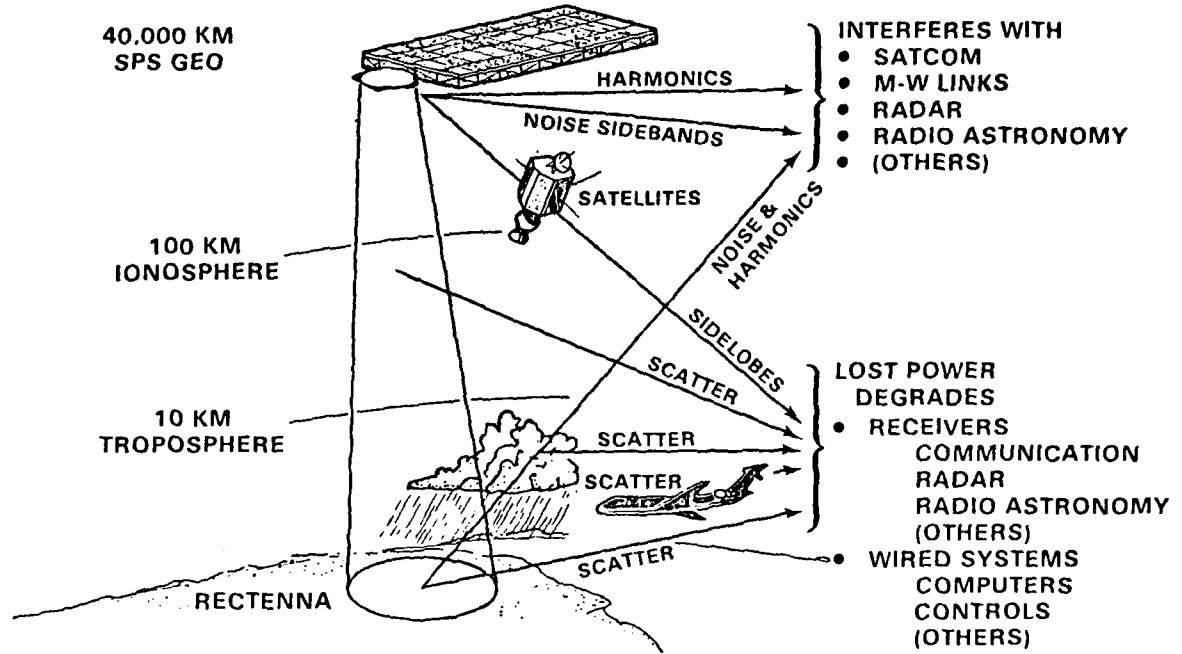


Fig.3 SPS radio frequency and electromagnetic interference

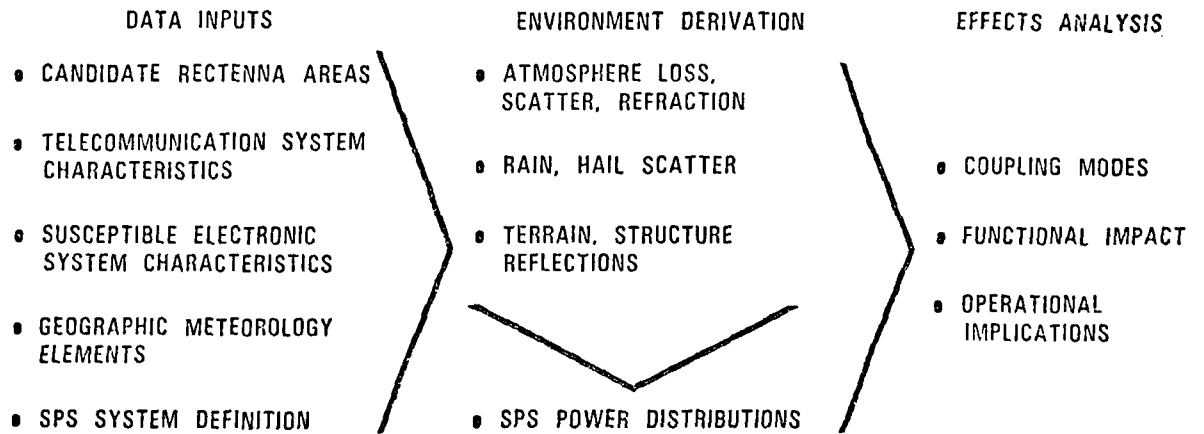


Fig.4 SPS EMC analysis - functional effects evaluation

AD-A090 850

ADVISORY GROUP FOR AEROSPACE RESEARCH AND DEVELOPMENT--ETC F/6 20/14  
PROPAGATION EFFECTS IN SPACE/EARTH PATHS. (U)  
AUG 80 H J ALBRECHT

UNCLASSIFIED

AGARD-CP-284

NL

6 of 6  
AD-A090 850

END
DATE
FORMED
11-80
DTIC

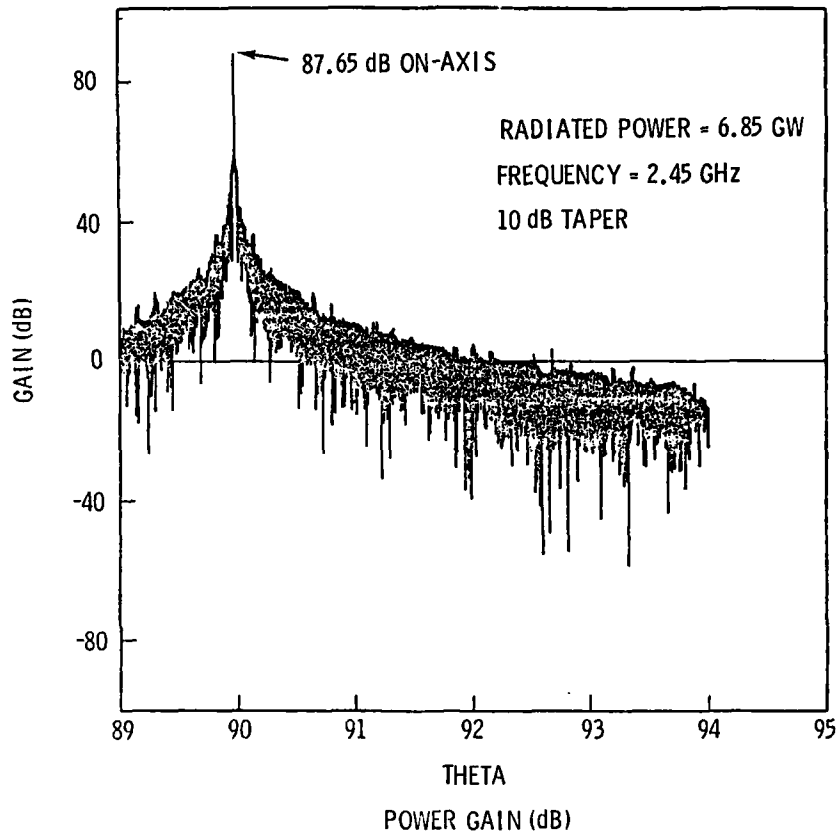
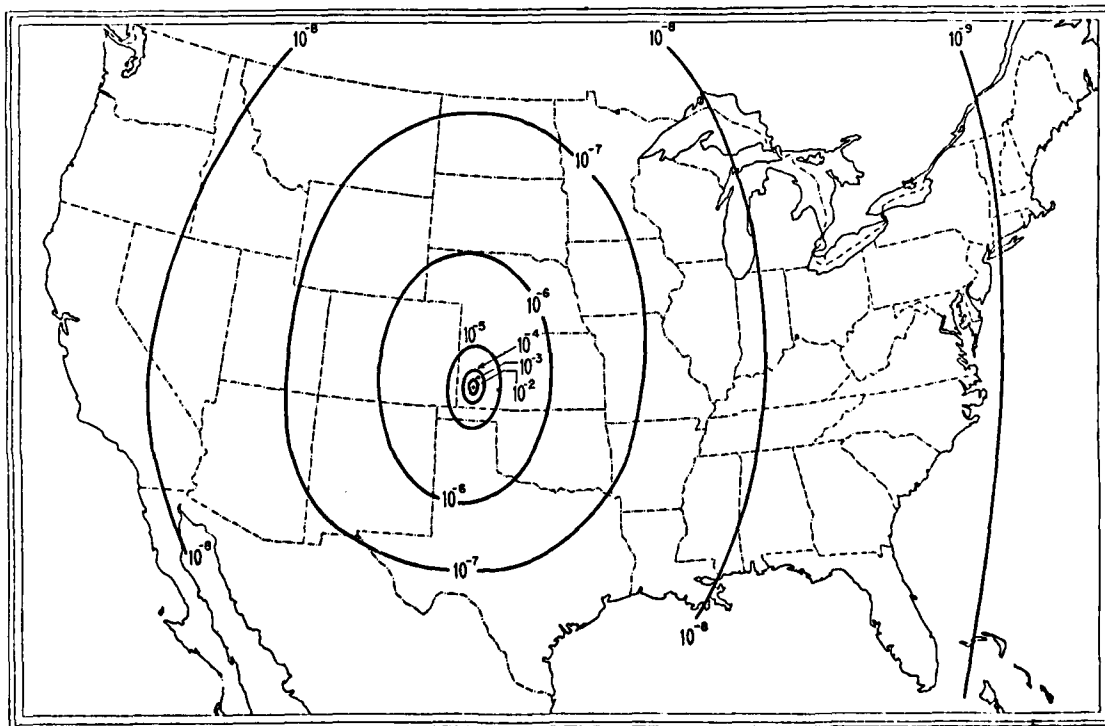


Fig.5 Gain versus angle from boresight

Fig.6 SPS single satellite power density distribution, mw/cm<sup>2</sup>

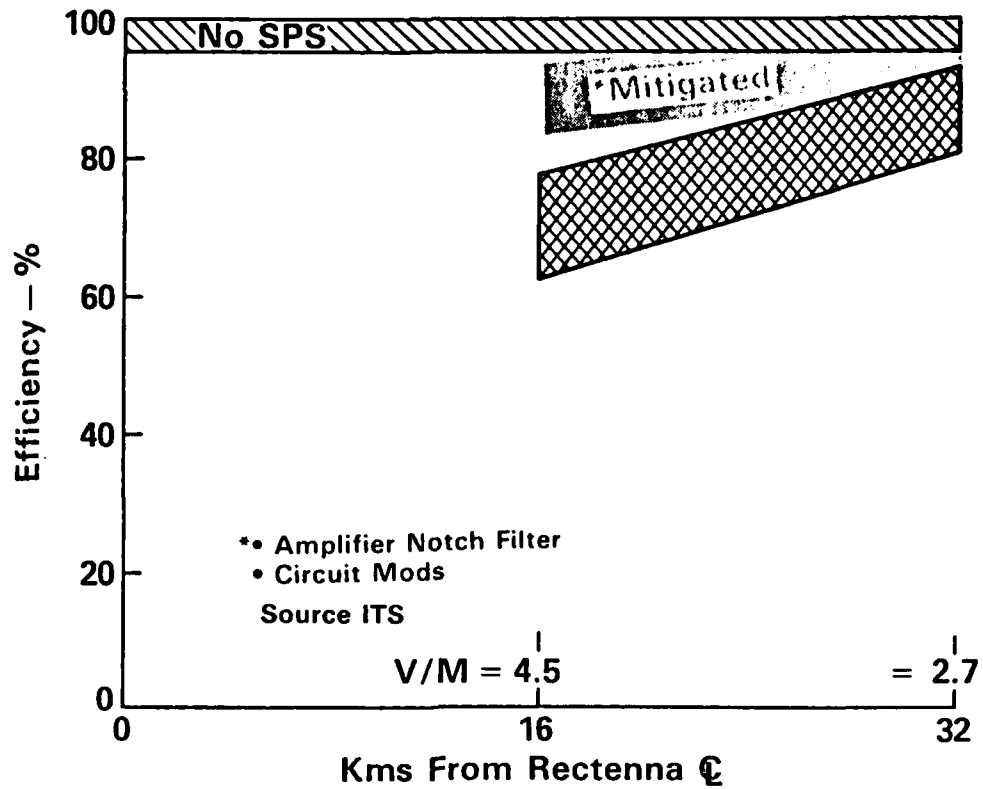


Fig.7 SPS results – electromagnetic compatibility effect of MPTS beam on M-W communications links

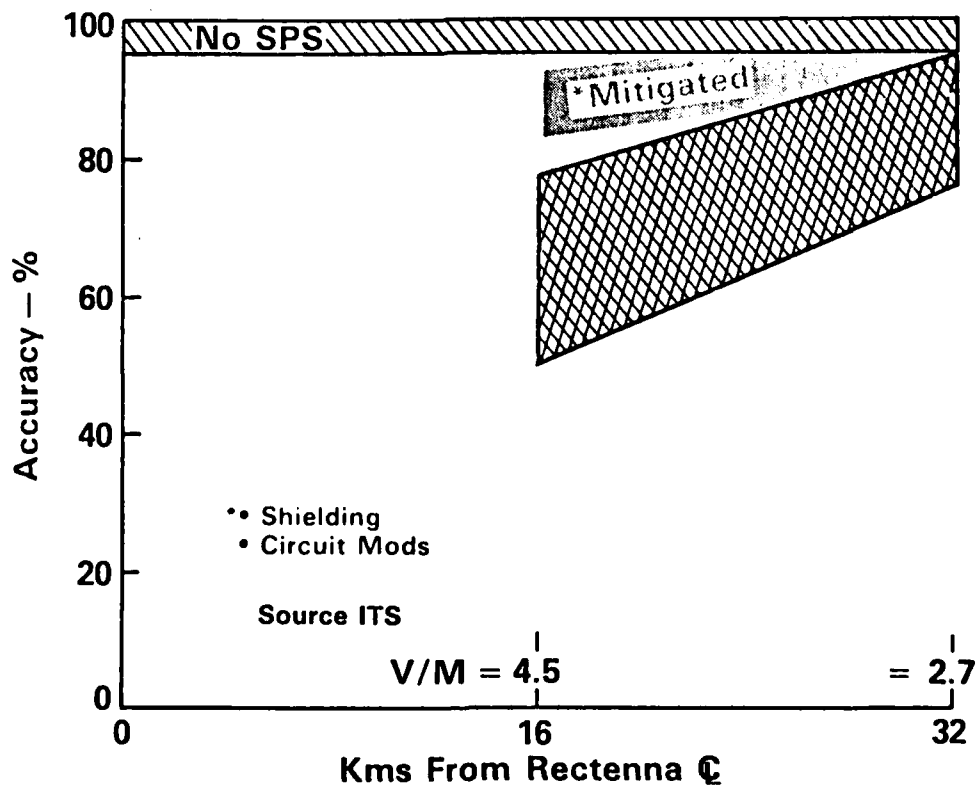


Fig.8 SPS results – electromagnetic compatibility effect of MPTS beam on microprocessor accuracy



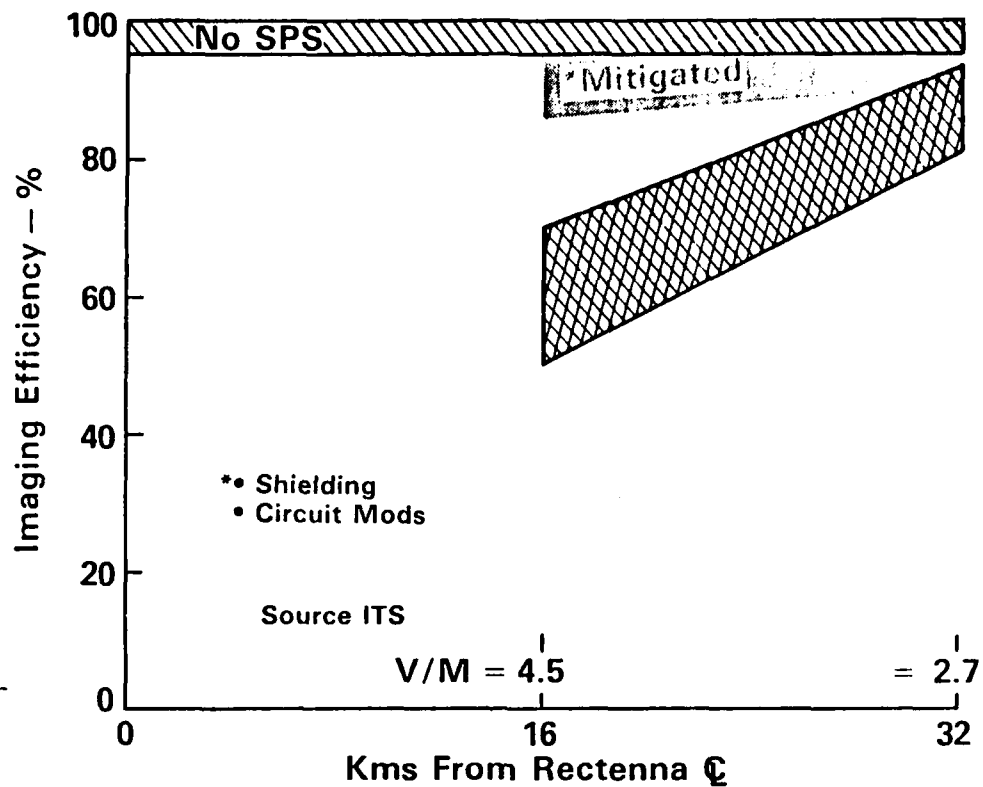


Fig.9 SPS results – electromagnetic compatibility effect of MPTS beam on security systems (Hi-resolution TV and IR sensors)

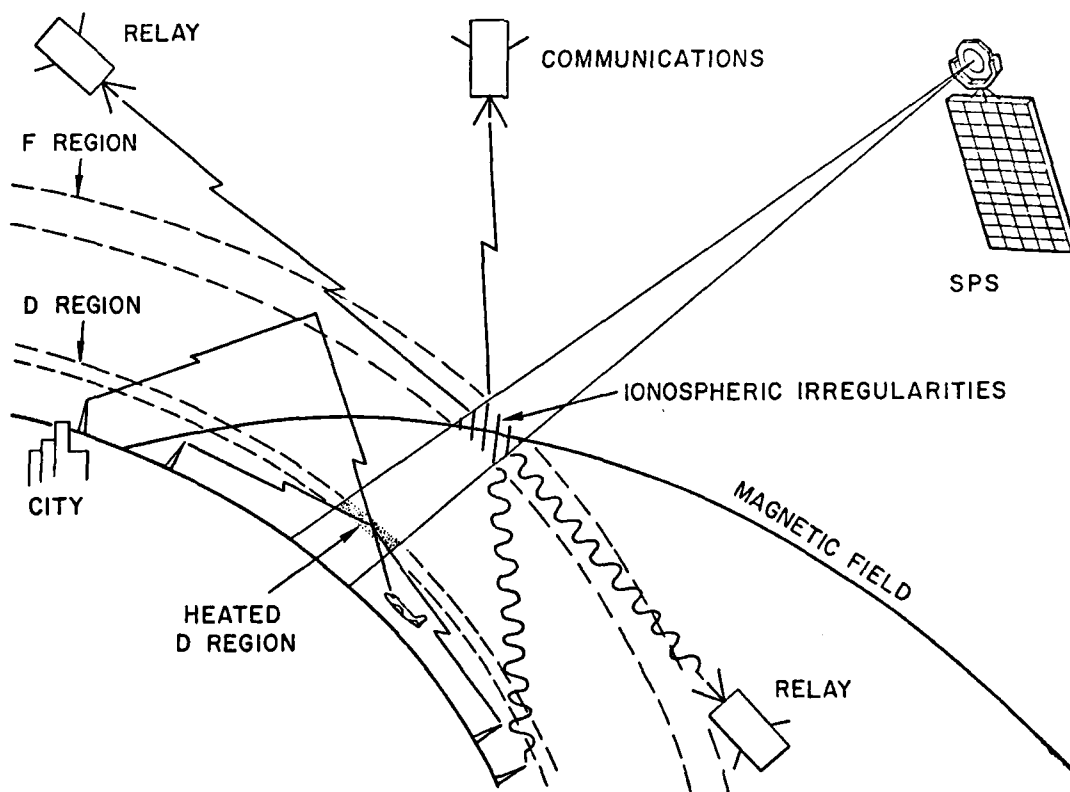


Fig.10 Potential telecommunication system impact due to SPS ionospheric heating

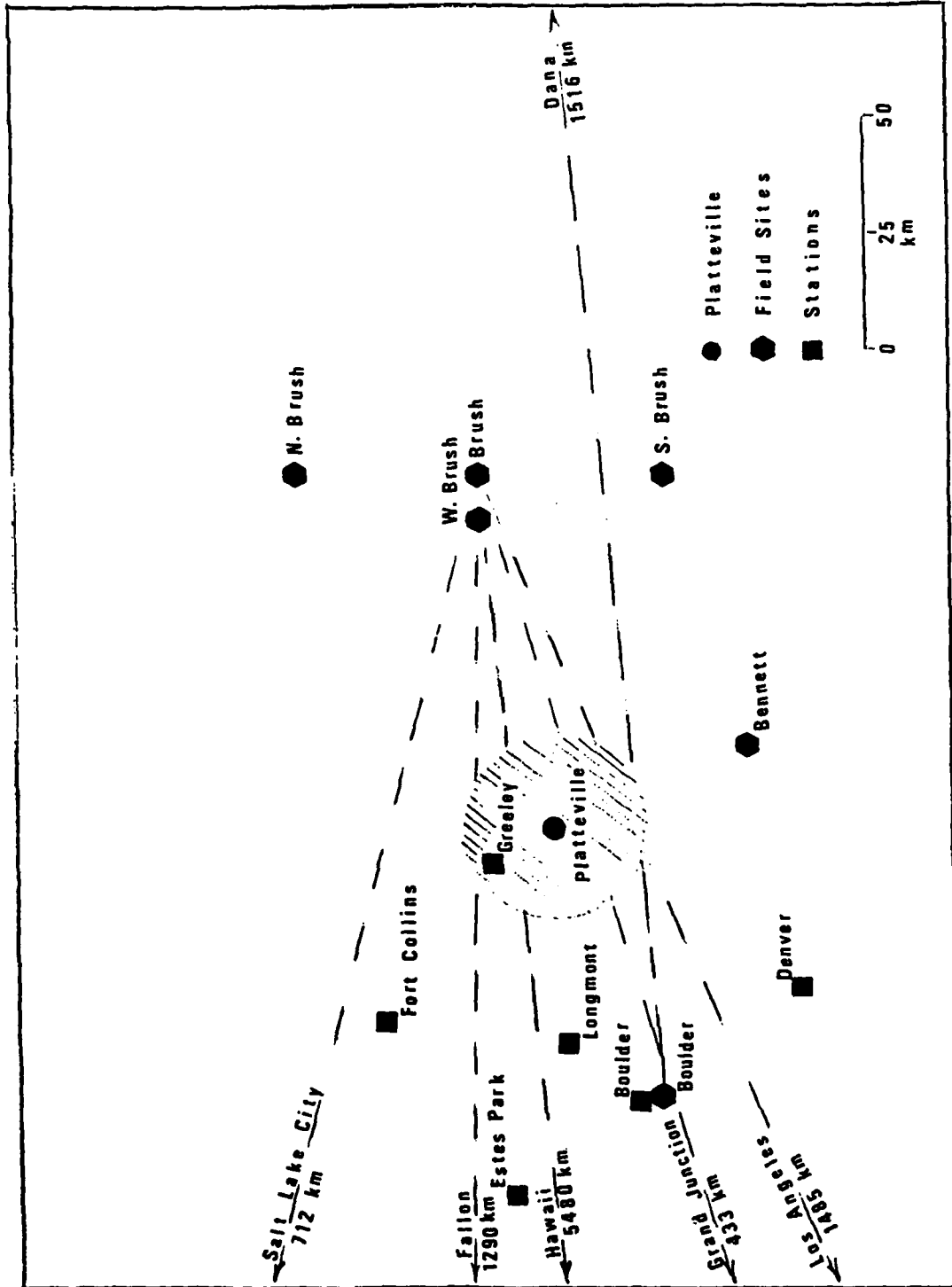


Fig. 11 Map of signal sources and recording sites in relationship to the ionosphere modified by the Platteville facility

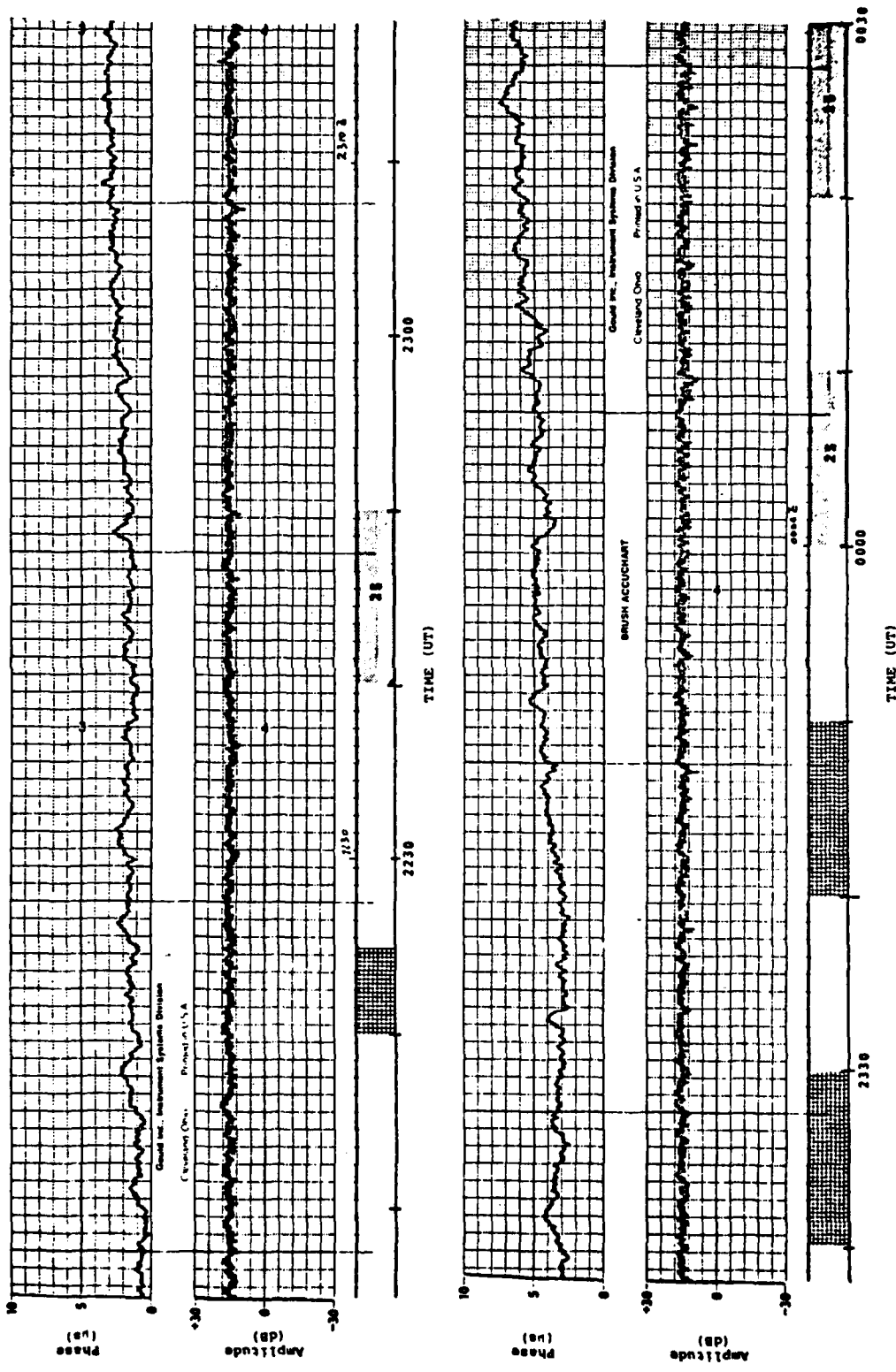


Fig.12 OMEGA phase and amplitude recorded at Brush, CO from Hawaii at 11.8 KHz on August 16, 1979

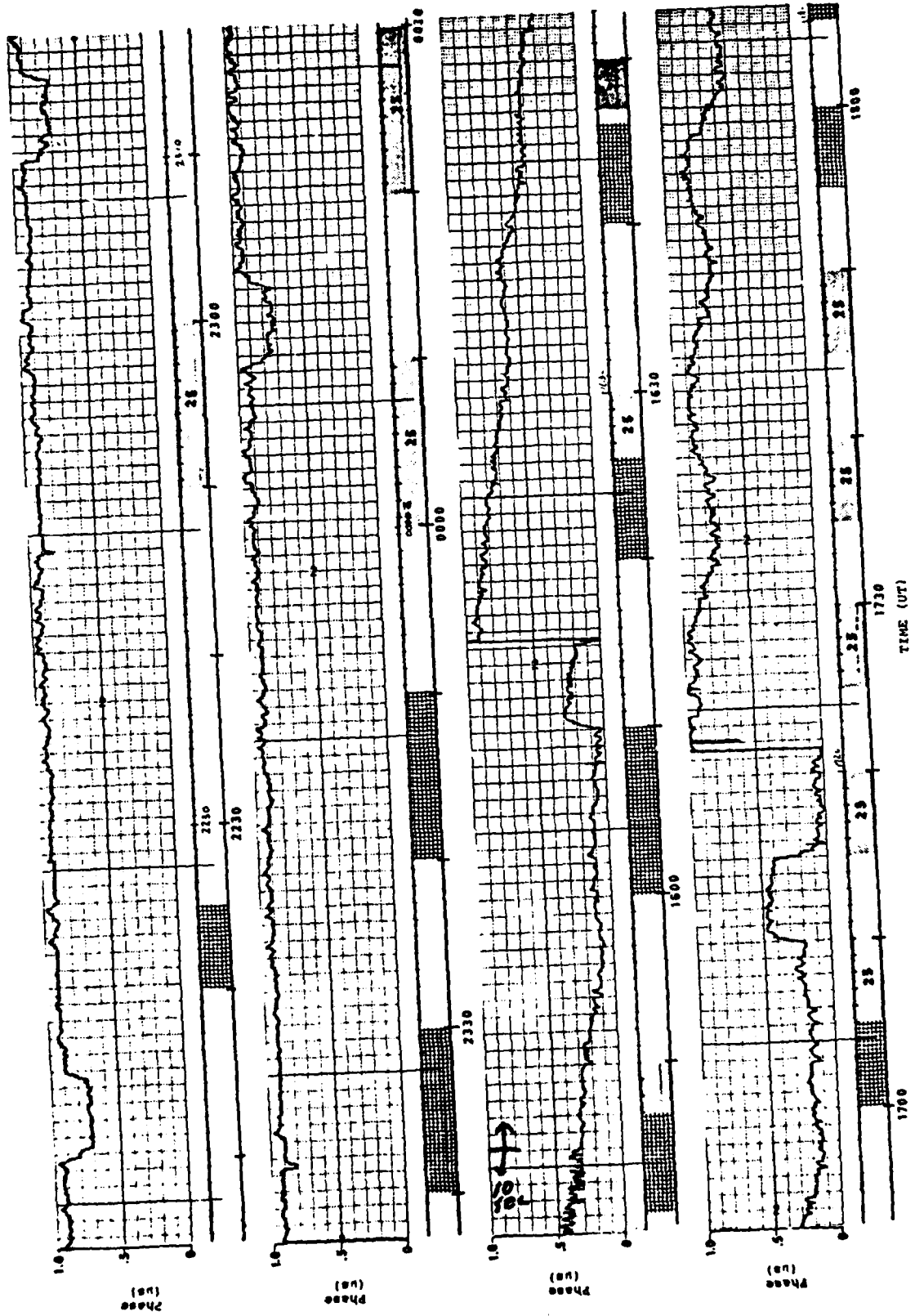


Fig. 13 LORAN-C phase recorded at Brush, CO from Fallon, NV at 100 KHz on August 16 and 17, 1979

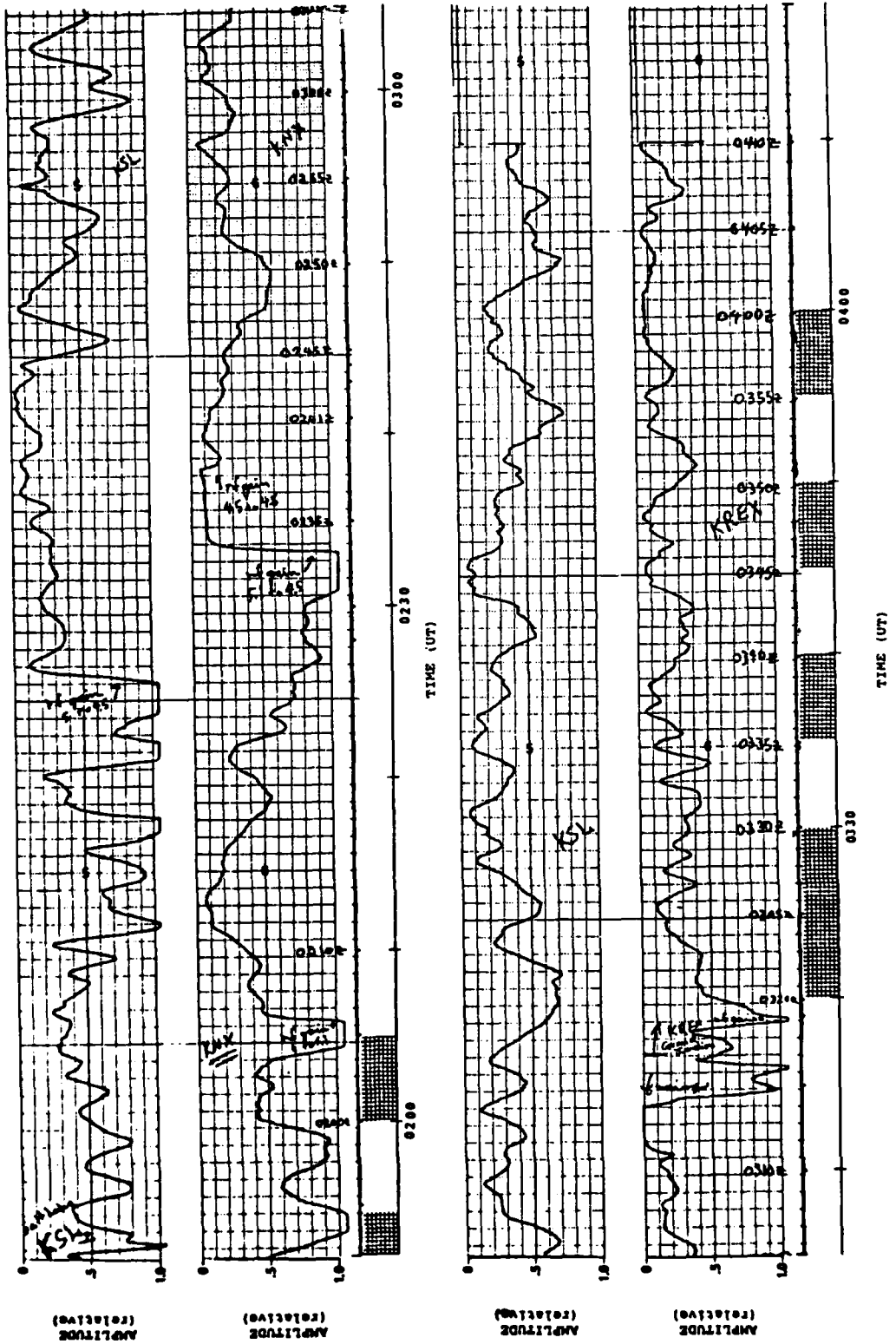


Fig.14 Amplitude signals recorded from KSL, KNX and KREX at Brush, CO on August 24, 1979

## DISCUSSION ON PAPERS

For a comprehensive record of all discussions, contributors and authors had been requested to write, on forms provided, their questions, comments, or replies, respectively. In case of any deletion desired, the form had to be marked accordingly. To complete the overall record, and in lieu of forms not forwarded by 21st July 1980, the Editor made use of appropriate tape recordings taken during discussion periods. (Editor)

### SESSION I

#### Paper No. 1

##### D.J.Fang

I cannot agree with you more on your remark that collecting statistics alone is not adequate, one has to study physics and mechanism as well for a characterization of microwave degradation in a precipitation medium. In that regard, may I ask you the effect of drop-size distribution (DSD). As you are certainly aware, meteorologists have documented extensively the fact that DSD is as much a variable as other rain parameters (such as canting angle spread, rain-rate fluctuations), for individual rain events as well as integrated events. Since your paper did not go into the details of DSD, does that mean: (i) DSD is not important or (ii) any DSD effect has been taken care of implicitly and empirically by calibration?

##### P.A.Watson

My paper emphasized the importance of DSD effects in relation to attenuation. With regard to cross-polarisation, the relationship between cross-polarisation and attenuation is not particularly sensitive to DSD. For example, if one compares the cross-polarisation-attenuation relationships predicted using the Laws-Parsons and Joss thunderstorm distributions, a very small difference is observed. The figure shown overleaf shows the median data points from Figure 4 of my paper, compared with theoretical predictions for zero canting angle using these two drop-size distributions. (See Figure on page D-2.)

##### M.P.M.Hall

With regard to the question as to the variability with position along the Earth-satellite path of the statistical distribution of drop-sizes, Figure 3 of P.A.Watson's paper (and Figure 5 of Paper 8) showed considerable changes of drop-size characteristics with position. It was because of the variability of drop-size characteristics from one compact rain cell to another that the dual-polarisation radar technique had been developed at the Rutherford and Appleton Laboratories.

##### J.Goldhirsh

We at APL/JHU have been making disdrometer measurements for years. In particular we measure drop-size distributions over an entire storm period and convert these to best-fit, attenuation coefficients  $R$  versus reflectivity factors  $Z$ , regression relationships. For each rain storm we examine the data base of drop-size distributions and arrive at a respective  $R-Z$  relation. We find the drop-size distributions over the course of the rain storm change because the rain-rates change. However, these distributions fall, in general, into the same "family". For example, when considering the disdrometer results corresponding to 10 rain days (17 hours), the scatter of the  $R$  values about the best fit  $R-Z$  lines for the various rain days deviates on the average about 25% rms.

##### A.Paraboni

We made calculations about the comparative effects on XPD of the distribution of the canting angles of drops and of the rain drop-size distributions. We found out that the uncertainty on XPD due to the first effect is of the order of 20-25% on the average while the second is of the order of 5%.

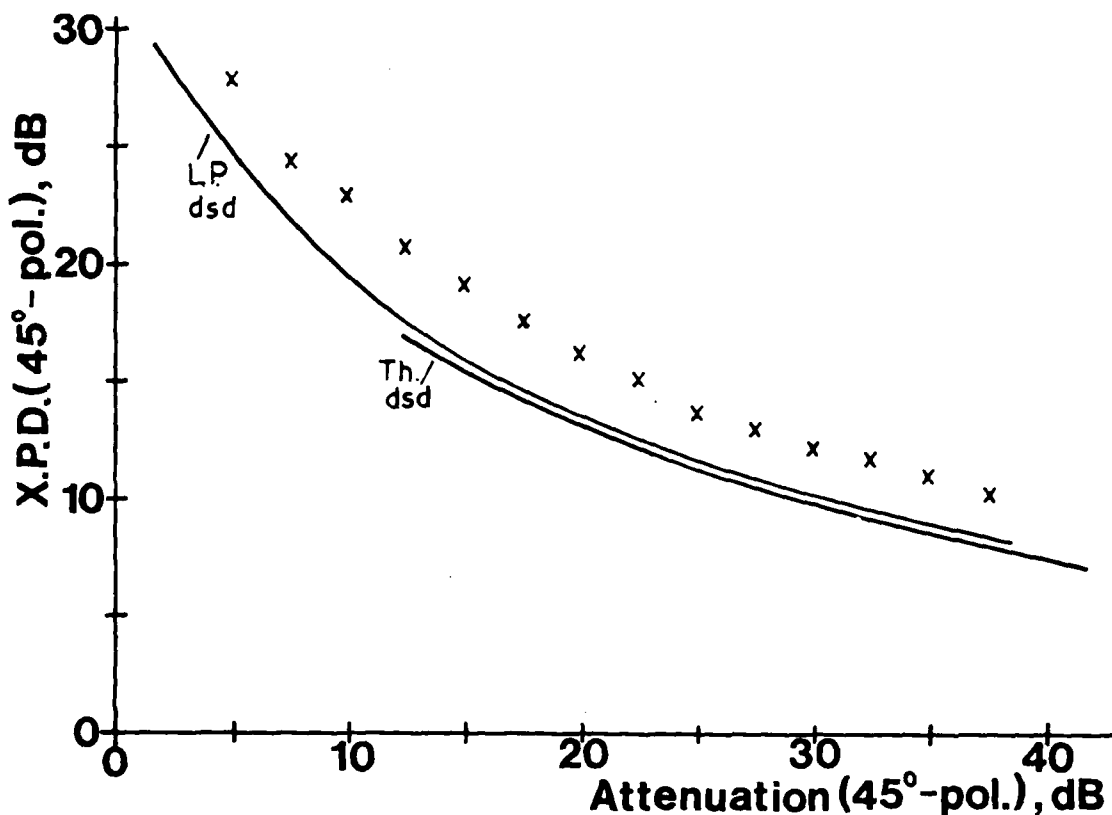
##### J.Thirlwell

Is it appropriate to refer to a tendency for an effective atmospheric absorber temperature of about 260 K for the radiometer equation at this stage? At the Post Office Research Centre we have calibrated 20 and 30 GHz radiometers against the ATS-6 satellite beacons and obtained effective absorber temperatures of 275K in both cases. A similar calibration of 12 and 14.8 GHz radiometers using the OTS satellite transmissions is currently being carried out and preliminary results indicate an effective absorber temperature of about 280K at 14.8 GHz but only about 260K at 12 GHz. Although this latter value is in some agreement with several other results obtained in Europe

during the OTS experiment our immediate reaction is to thoroughly check our 12 GHz radiometer system in view of the 20, 30, and 14.8 GHz results we have obtained. It seems unlikely that the effective absorber temperature at 12 GHz should be significantly different to that at 15, 20, and 30 GHz.

**P.A. Watson**

At 11 GHz, for the range of attenuations measured by a radiometer (up to  $\sim 12$  dB), one is concerned with significantly heavier rainfall than that for the same range of attenuation at 20 or 30 GHz. The opportunity for errors associated with the spatial inhomogeneity of rainfall is thus much greater at 11 GHz than at 20 or 30 GHz. For the latter two frequency bands the statistics of attenuation in the range 0–12 dB may well be dominated by occurrences of widespread rain.



Paper No.3

**D.J. Fang**

Your brief remark on the advantages and limitations of different numerical techniques are well taken. I may give a supplement here based on our experience with the uni-moment method which was used at COMSAT laboratories for evaluation of the forward scattering amplitudes of single rain-drops. The method is very time consuming for large rain-drops at high frequencies. (At 4 mm diameter, 20 GHz, it took more than 10 minutes of cpu on IBM 360/?). Incidentally, our program was developed by Prof. K.K.Mej, the inventor of the uni-moment method. We managed to have all the forward scattering amplitudes calculated for 4–33 GHz frequency, 0.5–7 mm diameter,  $0^\circ$  to  $90^\circ$  incident angle, and at either  $20^\circ$  or  $10^\circ$  temperature. The results are published in COMSAT Technical Review. From our results, we observed two features: (1) The results depend on which expression of complex dielectric constant equation is being employed, either Debye's equation or Ray's equation. This point was also noted by Morrison and Cross. Do you have any feelings on this? (2) The results are sensitive to temperature, a point you have mentioned when comparing  $20^\circ$  and  $0^\circ$  data. In this regard, may I ask your opinion on the most appropriate temperature of a rain-drop to be assigned for microwave studies?  $20^\circ$  is certainly too high in my opinion,  $0^\circ$  is perhaps low, how about  $5^\circ$  or  $10^\circ$ ?

**E.G. Evans**

I am interested that you have positive information on the problems of using the uni-moment method for rain-drop scattering. We have now extended the Fredholm Integral method to 230 GHz but this has only been possible by employing some sophisticated numerical techniques. We feel that the F.I.M. technique is now perhaps in the best position to tackle millimetre wave scattering from precipitation particles.

As regards the refractive index used for the scatterer we have used the values from Ray's paper. I would not expect

there to have been much difference between the refractive index given by Debye's equation or Ray's. However we have not checked this. We have demonstrated that the temperature of the water does change the scattering from rain-drops significantly. We have published some results in Electronics Letters and in the URSI symposium in Canada 1980. The temperature to be chosen will, I think, depend on the type of link, terrestrial or satellite, also on the elevation angle and the season of the year. I guess that there will be variations of temperature on any given path and that one may have to stratify the link to get better results. If a mean-path average temperature is chosen my guess is that somewhere between 5–10° would not be too far out.

**D.P.Haworth**

I noticed you mentioned about your scattering coefficient that you had to determine the precise frequency, for which the coefficients were evaluated, does this mean that you are predicting significant dispersion effects in your results for these scatterers?

**E.G.Evans**

No, I think the point was that you really get a different theoretical prediction for attenuation if you choose a frequency of, say, 11.0 GHz rather than 11.455 GHz. The scattering amplitudes are significantly different and it tends to make a difference when you are actually dealing with ratios, as many people are in trying to extrapolate attenuation at one frequency to another frequency. I do not think I was referring to anything about dispersion particularly – what I was referring to is that you have got to get your frequency right in your theoretical evaluation, if you are tying it up with predictions from an experimental evaluation.

**Paper No.5**

**L.Boithias**

En ce qui concerne l'affaiblissement par la pluie, un loi Affaiblissement/Frequence extremement simple a eté obtenue sur les trajets terrestres – entre 10 et 30 GHz on a approximativement,

$$\frac{A_1}{A_2} = \frac{F_1 - 6}{F_2 - 6}$$

Cette loi peut s'expliquer si on trace le graphe de l'affaiblissement spécifique (dB/km) en fonction de la fréquence pour les intensités de pluies données. Toutes les courbes obtenues sont approximativement des droites qui passent par un point fixe de coordonnées: 6 GHz, 0 dB.

**E.Altshuler**

In Figure 7 you stated that the very low attenuation ratio data that occur for low attenuations are probably due to experimental error. We have made slant path attenuation measurements at 15 and 35 GHz and also obtained much lower attenuation ratios than would have been predicted from ground level drop-size distributions of Marshall-Palmer or Laws-Parsons. I should like to suggest that these low attenuation ratios do exist and that they are produced by very widely dispersed large drops. It may be that drop-size distributions aloft are quite different from those that are measured on the ground.

**P.T.Thompson**

The data in Figure 7 was obtained by simultaneous measurement of 20 and 30 GHz beacon attenuations on the same antenna by the U.K. Post Office.

The exact physical explanation of the wide variance in the ratio at low attenuations cannot be substantiated by these measurements due to inherent uncertainties in the system calibration and short term stability.

Indeed the total variance of the ratio can be accounted for by approximately  $\pm 0.2$  dB system variation.

Consequently although the effect indicated by E.Altshuler may have occurred it is unreasonable to try and verify this using the measured results.

In addition, ice attenuation, water vapour content, and antenna surface wetting effects may also be influential on such low attenuation data.

**P.Watson**

It has been shown that, at 20 to 30 GHz, the ratio you would expect from added water vapour is quite low. If you look at the water-vapour-resonance curve – when you move from 20 to 30 GHz in frequency – the ratio works out to be less than two, so that there is a grouping of points around the 1 dB figure at ratios of 1.5 that would in fact be consistent with a saturated atmosphere during rain, so that, although there is undoubtedly a large error superimposed on that, there may also be some indication of an extra effect from added water vapour. Now here, I think, there is an important point because the error that you see is large partly because it is a beacon measurement. If one had a radiometer and would observe water vapour, which is nearly a pure absorber, then one would expect to observe the correct ratio with very little error. You could average the clear sky value of a long period, the clear sky temperature and then, during a wet but not very heavily rainy atmosphere, look at the ratios on the radiometer and



hope that the scattering contributions may not be so significant during very light rain, fog, and so on. But where the atmosphere is nearly saturated – and you certainly do have more than a standard-atmosphere-water-vapour-content – with the radiometer you should then see the ratio that corresponds to the water vapour line while, with the beacon measurement, you have a very large error due to the absolute calibration of the two receivers.

**A.Paraboni**

Do you not think that the major cause of the variation of this ratio is the effective rain-path length and the effective rain intensity. In other words, you always talk about effects of temperature, effects of rain-drop sizes, but do you not think that the major cause is the fact that you do not know what the length of this rain-path is and what the medium rain intensity in it is. We attempted to interpret the measured pair of the attenuations at two different frequencies, even in terms of effective rain intensity and in terms of effective rain-path length. You can make a very large error due to the temperature in the subdivided cumulative effect in rain-path length and rain intensity but, when you extrapolate to higher frequencies, the product must be almost the same. You can make a large mistake and intend, for example, 50 mm/hr instead of 20 mm/hr, but when you translate the attenuation of one frequency to another one, I think that this effect can be very low, and what effectively remains important is the effect of the temperature of the water, the rain-drop distribution, and so on. I would like to ask if you attempted to interpret this error, due to temperature, e.g., in terms of rain intensity which would be needed in order to obtain this given ratio.

**P.T.Thompson**

No, I do not think we have. The data on this graph (Figure 7) is really put there to indicate the measured ratio and the lines are to indicate just some simple factors which may well influence the scaling factor. And you can see that the curve with a 0.1 dB error in the measurements at 20 GHz, and not including any ice attenuation ratio, makes a fit to the measured results, and that the bottom line represents just -0.1 dB error and with some water vapour content addition. So the whole measurement can be encompassed by just these few influences, without worrying about what the rainfall rate was, what the drop-size distribution was, what the temperature was. I think the purpose of this graph is just to show that measurement errors and a few influences can cover just about all the possibilities of the measured results.

**P.Watson**

I wanted to add to that since I was responsible for drawing that curve. In fact, I chose an 8 km rain cell because that gave the best fit to the data. Now, if one turns the problem the other way around and uses Laws-Parsons conditions, what happens is that you must have then inferred that you have 14 km long rain cells in order to interpret those results. So that I think it is a very dangerous thing to do to infer an equivalent radio path length from a diagram of that sort because there are so many variables, so many factors involved. It is much more sensible to think about the sensitivity of the situation of various parameters than to fix one and interpret another. It is a multivariate problem with about eight variables.

**A.Paraboni**

You found such a result, but, limiting attenuation below two or three dB, with large attenuation we found realistic results on the average. In a single measurement, you are right you can find an absurd equivalent parameter, but interpreting this in statistical terms by comparing ratios, not instantaneous ratios between two frequencies, but ratios obtained by cumulative distributions we obtained results which agree with rain cell dimensions of well-known models.

**Paper No.7**

**A.Paraboni**

- (1) How did you take into account the bright band in your indirect measurements of attenuation?
- (2) What kind of rain intensity did you take as normalization basis in your attenuation statistics?

**J.Goldhirsh**

Answer to (1): By examining signatures of RHI's and Z-h profiles we were able to establish the rain type; namely whether the rains were stratiform or convective. For the case of stratiform rains, the RHI's showed well defined bright bands (i.e., melting layers). For such cases, we integrated up to the base of the bright band which was further identified in detail by the Z-h profile. On the other hand, convective rains are characterized by RHI signatures showing intense long cellular columns of rain penetrating often well above the 0°C isotherm. For such cases, we integrated along the entire path.

Answer to (2): The attenuation statistics presented in the first part of the paper were initially conditioned on a 2 dB "attenuation event". That is, if during the sampling of path attenuation, there existed in a vertical plane at least one parallel path having an attenuation which exceeded 2 dB, all the paths in the plane were sampled; otherwise none were. After the statistics were accumulated, the equivalent rain rate for a 2 dB attenuation event at 30 GHz was deduced using the "two frequency method" as described in the text (equations (6) and (7)). In this way the 2 dB attenuation event was found to correspond to an "equivalent rain rate" of approximately 1 mm/hr.

**D.J.Fang**

The basic parameter used for modelling is the so-called equivalent path length, a pseudo quantity which does not have much meaning in meteorology but a necessary one for engineering predictions. It enables one to estimate microwave degradation based on point-rain rate alone. With your results of fade distributions of 5 frequencies and at various elevation angles, you are in a very good position to assess the equivalent path length provided that you have point-rain data available, which I assume you do. Have you looked into this? What are your conclusions? Specifically, does the equivalent path depend on frequency, elevation angle and percentile?

**J.Goldhirsh**

The attenuation statistics were derived during the summer of 1973 at Wallops Island, Virginia. Unfortunately no point-rainfall measurements were made from which statistics could be compiled. Hence we are not able to relate our attenuations to path length based on point-rainfall statistics. I might add that we are at present analysing a 3 year data base of path attenuation using radar modelling. During this period we have made simultaneous disdrometer as well as rain rate measurements. We hope to develop a data base of path attenuations for these new measurements in much the same way as described in the text except we plan now to condition our attenuation results to point-rainfall rate. Analysis of such statistics should provide the answers for the questions you raise.

**Paper No.8****A.Paraboni**

Did you attempt to measure also depolarisation with your radar?

**M.P.Hall**

No. The radar is designed to obtain drop-size distributions in rain from which rainfall rate and specific attenuation due to rain may be computed. This paper has presented first results of such computation. It may in future be possible to comment on hydrometer types and consequent depolarisation, but not to measure depolarisation directly.

**E.P.Attema**

- (1) Could you comment on the radar calibration procedure used for your system?
- (2) In comparing radar derived attenuation and attenuation on the OTS beacon, did you have to adjust the radar calibration factor to match both data sets?

**M.P.Hall**

- (1) The absolute reflectivity calibration was determined using metal sphere targets well below tethered and free flight balloons. The error is found to be less than 1 dB. The differential reflectivity calibration was determined by looking vertically at hydrometers and by looking at the sun. In both cases no difference should occur for the two polarisations. The error is found to be less than 0.1 dB (see our seventh reference). The consequences are discussed in this paper.
- (2) We did not adjust this calibration to match the data sets, but regard the good match obtained as a confirmation of both the technique and the calibration.

**SESSION II****Paper No.9****H.J.Albrecht**

A relationship between the diversity advantage factor and a prevailing wind direction with respect to the sites is certainly interesting and would be helpful in system applications. However, two questions should be answered:

- (1) which of the various possible wind directions did you use? (certainly not the one measured 30 to 50 m above the ground? )
- (2) how did you measure the direction and how significant were the results?

**P.G.Davies**

The information relating to the directions from which storms approached and crossed the triangular diversity network was not derived directly from meteorological sources. It was deduced from an analysis of the times at which fades occurred in the network as described in section 4.4 of the paper by Davies (1976). For frequencies near 30 GHz, the direction of the prevailing wind will be an important parameter in establishing an optimum two-site diversity system. However, since not all large storms approach from the same direction, a three-site triangular system should provide better reliability.

**F.Dintelmann**

I wonder whether you could comment on the residual attenuation for the larger time percentages?

**P.G.Davies**

The Appleton Laboratory Sun-tracker data at 19, 37 and 71 GHz were analysed for levels of attenuation of 0.5 dB and greater in excess of the clear day values. The Post Office data at 12 GHz were analysed in a similar, but slightly different manner. The more recent OTS and SIRIO satellite measurements were analysed only for fades greater than 3 dB above the clear air values.

**P.T.Thompson**

Considerable advantages may be achieved particularly at higher frequencies by employing up-link power control. Data is required on the rate of change of attenuation in order to reasonably dimension the control algorithm and its speed of response.

Have you analysed your extensive set of data in a manner by which rate of change of fading is evaluated?

**P.G.Davies**

We have not, as yet, analysed our data to extract the particular type of information which you mention. However, it is possible to do this, particularly for the SIRIO and OTS data.

**Paper No.10**

**C.H.Liu**

- (1) Have you ever seen the 1 minute oscillation on occasions other than 2° elevation? At different oscillation frequency?
- (2) Have you considered the possibility of atmospheric waves in causing these oscillations?

**J.Thirwell**

- (1) No. The oscillations were only observed during two ATS-6 transmission periods when the satellite was at 2°, or less. No other oscillation frequencies were noticed.
- (2) No, we have not looked into this possibility.

**A.Paraboni**

Did you attempt to interpret the discrepancy between experimental points and theoretical models of XPD in terms of spreading of the raindrop axes orientation?

**J.Thirwell**

The depolarisation model used assumed a uniform canting angle for all the raindrops and a wind direction perpendicular to the vertical plane of the satellite slant path. This represents a worst case, as pointed out in the paper, and the theoretical curves do indeed appear to correspond to the lower measured values of XPD. A Gaussian distribution of canting angles will be fed into the model and this will certainly bring closer agreement between the mean of the measured and the theoretical data (which is already reasonably good). However, it should be noted that the canting angle distribution will vary with rainfall rate (fade depth), as seen from the paper of D.C.Cox et al., presented at this conference. The model, as presented in the present paper, should not be underestimated since it is more useful for a system designer to know the lower values of XPD to be expected, rather than to be given optimistic estimates.

**P.T.Thompson**

With reference to scaling in frequency from 20 to 30 GHz our sensitivity studies have shown that this may not be difficult, similarly with scaling from 11 to 14 GHz.

However caution must be exercised when scaling OTS or SIRIO 11 GHz data to 20 and 30 GHz as the peak of the sensitivity of attenuation due to temperature and drop-size distribution occurs at around 11 GHz.

**Paper No.11**

**E.Altshuler**

For your low elevation angle measurements you mentioned that attenuations down to about 2° elevation angle followed a secant law. I should like to mention that in a paper entitled "Atmospheric Attenuation at 15 and 35 GHz for Very Low Elevation Angles" which was published in the September - October 1978 issue of *RADIO SCIENCE*, we derived an expression for the path length through the troposphere for a curved earth. It would be interesting to compare your results with this expression.

**T.Pratt**

I am grateful to E.Altshuler for drawing my attention to the curved-atmosphere model of a low-elevation radio path. The results in the paper were based on a plane-atmosphere model to which the small data sample fitted quite well down to  $2^\circ$ .

**D.J.Fang**

I am very interested in your Figures 7 and 8 in which you present, respectively, the variation of S/N and BER due to precipitation for single and dual polarized links. This is vital information required by the system design engineers for designing communication links. For that purpose, proper understanding on the assumptions you used to derive S/N and BER is essential. Two questions in that regard: (1) How do you model the interference from orthogonal channels? Do you consider the orthogonal signal simply as noise? If so, it is important to note that random noise is commonly peak-limited (particularly for FM), while the orthogonal signal is not. Consequently, your results may require some modification in heavy rainfall conditions. (2) In your evaluation of link performance due to rain, have you taken the increase of sky noise temperature into consideration? If so, how much is contributed by sky noise temperature increase?

**T.Pratt**

The analysis on which Figures 7 and 8 of the paper is based is not rigorous, and is intended only to show the feasibility of frequency re-use at 20 and 30 GHz in Europe. The orthogonal channel was assumed to be noise-like, and no account was taken of increase in sky noise temperature for small percentages of time. However, in most 20/30 GHz systems the latter effect would be small, since the system noise temperature of the earth station would generally be higher than for a 4/6 GHz earth station. For example, an earth station with a system noise temperature of 500 K might see a sky noise of 80 K for 20% of the time, rising to 260 K for 0.1% of time. Assuming an antenna efficiency of 70%, the increase in sky noise temperature would degrade the C/N ratio by 1 dB for 0.1% of time. This would barely affect the shape of the curves in Figures 7 and 8.

**J.Thirwell**

You described one of the depolarisation events which you observed as being due to refractive bending of the incident beam on the receive antenna. At the time of this event the co-polar received signal showed less than 1 dB attenuation. Can you explain why you attributed this event to refractive beam bending rather than the presence of high altitude ice particles in the atmosphere?

**T.Pratt**

The clear-air cross-polarization event described in this paper was not attributed to high altitude ice particles for two reasons. Firstly, the sky was optically clear at the time of the event; even low density ice clouds such as cirrus can be easily seen by eye, and give very little cross-polarization. For cross-polarization to occur at the levels seen in this event, a very dense ice-cloud would be necessary. Secondly, the increase in cross-polar signal correlates well with the decrease in co-polar signal which would be expected for a signal arriving off-axis in the elevation plane, as shown by the scattergram in Figure 2.

**J.Belrose**

An important conclusion of this paper is that circular polarization is worse than linear polarization if good cross-polarization discrimination is desired. This I do not understand, since the ionosphere rotates the polarization vector, and I suppose ice crystals in the troposphere must also, and therefore the plane of the polarization at the receiving antenna must be rotated along with these changes. Surely circular polarization would circumvent this problem. On the loss of frequency re-use, it is certainly technically possible (but somewhat more difficult perhaps) to transmit and receive left- and right handed circularly polarized waves.

**T.Pratt**

The question of using circular rather than linear polarization for frequency re-use on satellite links has been studied by many workers, both theoretically and experimentally, with the general conclusion that linear polarization is better than circular polarization. This conclusion results from the fact that in rain, and also in ice on most occasions, the major symmetry axis of the hydrometeors with respect to the radio path has an orientation around the local horizontal. (See for example, ref. 1). The signals with vertical or horizontal polarization will suffer the least depolarization and linearly polarized signals oriented at  $45^\circ$  to the horizontal will be affected most severely.

Circular polarization can be considered as two orthogonal, linearly polarized waves in phase quadrature. Differential attenuation of the linearly polarized waves, or differential phase shift between them will result in a departure from circular polarization. If we subtract a true circularly polarized wave (with the same sense as the originally transmitted wave) from the resultant elliptically polarized wave, we will have a residue which contains a component of a circularly polarized wave with the opposite sense. Since this is the operation performed by an ideal, dual circularly polarized antenna, the elliptically polarized wave which is received under conditions of atmospheric depolarization will be interpreted by the antenna as the sum of a co-polar and a cross-polar wave.

Rain-drops tend to become asymmetric with their axes very close to vertical/horizontal. Ice crystals tend to be pulled away from horizontal alignment by intense electric fields in thunderstorms. Thus rain cross-polarization is markedly less for linear polarization oriented vertically or horizontally than for circular polarization, whereas this is not always true for ice cross-polarization.

Ref. 1: H.W.Arnold, D.C.Cox, R.H.Hoffmann and R.P.Leck, 'Characteristics of rain and ice depolarization for a 19 and 28 GHz propagation path from a Comstar satellite', Proc. ICC. Boston, Mass, USA. June 1979.

#### Paper No.12

##### A.Paraboni

I just want to comment on the phase measurements on the cross-polarized signal we intend to do in the future. We decided to give a tilt angle to the linear polarization in order to increase the level of about -20, -25 dB under the coplaner signal in order to have the best identification of this channel. We are all aware that this measurement is not significant for the real applications in the future but we wanted to have the channel characteristics and so we looked for the best conditions to measure the channel. The decision we took was to tilt the angle and to introduce some stronger depolarization just to have a better measurement.

##### D.C.Cox

When we started off we had designed to have a polarization vertical and horizontal at our facility and, life being what it is, we ended up with 21°; the satellites were not put where they were designed to be put. If you are going to do the complete set of measurements that we did, what you will find is that when you look at vertical/horizontal, all the information which you want is in the differential quantities between the two orthogonal polarizations. All the information lies in the differential phase, in the differential attenuation because the depolarization is so low that it does not matter, if you are measuring at the minimum of depolarization. When you move with the polarization approximately 45°, or circular polarization, a lot of the information is in the depolarization, amplitude and phase.

The accurate phase measurements and the accurate amplitude measurements have to be made between the differential quantities, between the differential attenuation and the differential phase at the two orthogonal components. The accuracy of the phase measurement to the cross-polarized signal is not quite so precise, i.e. the requirements there are not so precise. We did some studies on that and some computer calculations that were written up in the Bell System Technical Journal, about five or six years ago. I wanted to explain that these measurements do have to be made quite accurately, more accurately than you would have to make them for providing systems information, if you are going to do the calculations from them. Otherwise the calculations will not yield very good results.

#### Paper No.13

##### L.Boithias

Le rapport des atténuations mesurées aux deux fréquences (figure 3) est égale à 2.2 - La valeur prévue par la formule empirique:

$$\frac{A_2}{A_1} = \frac{F_2 - 6}{F_1 - 6}$$

est égale à 2.1, c'est à dire extrêmement proche de la valeur mesurée.

##### A.Paraboni

We have tried to study a bit in detail this matter about the ratio between the two frequencies and we found that this is a very critical point and the result can depend on the way you compare the two attenuations. The most correct way should be the one of obtaining the instantaneous ratio and then statistically classify this ratio as a physical variable per se. If you do this you obtain somehow different ratios, with respect to the ones I gave in my report, if one does not pretend to give a very detailed explanation of a physical phenomenon. This is simply what we obtained by comparing the probability distributions without any attempt to interpret it in physical terms or in model terms.

I suppose that the rule you obtained is real accurate and can sure be used for extrapolating at all statistical results to higher frequencies. I agree with P.Thompson, however, that this kind of relationship should be taken with caution when extrapolating to higher frequencies in the range of 20 and 30 GHz, in which case I suppose that this simple rule of obtaining relationships is no more adequate.

#### Paper No.14

##### M.P.Hall

Could you please explain the processes you have used in producing figures 8 and 9.

- (1) It seems that you have used the radar data and attenuation data to derive a and b in  $A = a Z^b$ , and then used these to compare A and Z in Figures 5 and 8. Why is it that you get such good agreement at 1348 GMT, but much less good agreement elsewhere? Was the satellite data used to modify the radar calibration?
- (2) Figure 9 compares cross-polar discrimination measured directly and that computed from radar. How was the latter derived?

**J.P.Mon**

- (1) Figure 8 results from a best-fit of the observed attenuation to the *whole* set of radar samples collected between 13.29 and 14.03. The best-fit computer program we used consisted of matching observed attenuation samples  $A_{oi}$  with radar attenuation samples  $A_{ri}$  calculated as follows:

$$A_{ri} = \sum_{j=1}^{6h} a Z_{ij}^6$$

where  $i$  refers to time ( $i = 1 \rightarrow 20$ ) and  $j$  refers to range along the path (1 to 6h). The program makes  $\sum_{i=1}^{20} |A_{oi} - A_{ri}|^2$  minimum. It just incidentally happens for that particular event that perfect agreement is observed when maximum attenuation is reached.

- (2) Figure 9 was produced in the same manner as above except using observed XPD values instead of  $A_{oi}$  and shows no correlation between observed XPD and best-fit XPD.

**SESSION III****Paper No.20****A.Vander Vorst**

- (1) Is the radiometer working in the same polarization at the various frequencies?  
 (2) How did the model take into account the direction of the wind speed at the sea surface?

**R.K.Moore**

- (1) It always measures both V and H, but we used the one least sensitive to wind speed ( $T_H$ ).  
 (2) Wind direction does not affect radiometer (we believe). The orthogonal scatterometer measurements are made to determine wind direction.

**J.Goldhirsh**

What is the error introduced with the SMMR to determine the 18 GHz attenuation in view of variability of water vapor profiles? Are these errors negligible?

**R.K.Moore**

I believe it is of order  $\pm 0.1$  dB, which has negligible effect on windspeed determination. We calculated this a good many years ago, so my recollection of *size* may be wrong. I know the conclusion is correct.

**SESSION IV****Paper No.22****T.R.Larsen**

You mentioned that paths from geostationary altitude to Northern Scandinavia pass through the mid-latitude trough. How stable is this trough during disturbances? Can it happen that such paths at times pass inside the trough and at other times outside? This would probably increase the variation in TEC values at stations like Tromsø and Kiruna.

**K.Davies**

I think the answer is YES. There is evidence that the trough(s) move equatorward when magnetic indices increase. G.Hartmann may have further comments.

**G.K.Hartmann**

During disturbed ionospheric conditions the trough moves southwards and thus propagation paths from Scandinavia to a geostationary satellite may pass through this region and thus be affected. The stronger the ionospheric disturbances the more scintillations are observed and the less accurate TEC determinations get. However this is more problematic for low orbiting satellites than for the observation of geostationary satellites. There might be occasions where no TEC can be calculated because of too strong scintillations.

**J.A.Klobuchar**

Replying to G.Hartmann's comments on capability of making TEC measurements at high latitude during aurorally disturbed conditions, we have been routinely making measurements of Faraday rotation from VHF radio waves transmitted from geostationary satellites at a ground station at Goose Bay, Labrador, for almost nine years. During

times when auroral precipitation is observed along the ray path, as evidenced by strong amplitude scintillation, we observe Faraday polarization fluctuations, as well as increases in the total Faraday rotation, but we rarely have difficulty in following the total Faraday rotation angle changes. Hence TEC measurements are not lost during these periods.

**L.Kersley**

You commented that the protonospheric/plasmaspheric contents measured from USA during Phase III of the ATS 6 programme with the satellite at 140°W showed a daytime maximum even in northern hemisphere winter. What was the minimum L-shell encountered by the ray path for these observations and did this flux tube terminate in the ionosphere in the conjugate hemisphere at a latitude outside the Antarctic Circle? If this were the case the ionosphere would not be sunlit 24 hours per day in local midsummer and so would be expected to show normal behaviour. Can this explain the Np results?

**K.Davies**

The minimum L-values are:—

$$\text{ATS 6 - Boulder} \approx 1.86$$

$$\text{ATS 6 - Lorman} \approx 1.70$$

The corresponding conjugate geographic latitudes are near 50°S which lie outside the Antarctic Circle.

The answer to your question as to whether this can explain the diurnal variation of Np is, I think, no. This subject is discussed in a paper:—

Davies, K., and M.P.Paul, 1980, ATS 6 Measurements of Plasmaspheric Electron Content during Phase III at Boulder, Colorado and Lorman, Mississippi, to be published in the Proceedings of the COS PAR/URSI Symposium: Scientific and Engineering Uses of Satellite Radio Beacons, Warsaw, Poland, May 1980.

**H.Soicher**

What is the solar-cycle variability of Np?

**K.Davies**

In Phase III 1976–1977, the slant plasmaspheric content for ATS 6 to Boulder is around  $4 \times 10^{16} \text{ m}^{-2}$  and essentially independent of time of day. This is roughly twice the values in 1974–1975, i.e. there is an increase of Np with sunspot number.

**D.P.Haworth**

Have you any physical explanation of the small scale irregularities that you report?

**K.Davies**

None that are entirely satisfactory. There is a discussion of several possibilities in the Davies and Whitehead (1977) reference.

**J.Aarons**

- (1) Middle latitude isolated irregularities are "freaks" or "sports" or anomalies and the important irregularities from this system point of view are at high and equatorial latitudes.
- (2) From a point source (a satellite beacon) we have not found low S4s at low frequencies (with higher S4s at higher frequencies) when we have observed at 137 MHz and higher.

**K.Davies**

- (1) My emphasis was on understanding the physical basis for certain strong diffraction patterns. Exceptions often provide clues to this understanding.
- (2) As pointed out by C.L.Rino, the reason that you may not see the decrease of S4 with radio frequency is because the spectrum follows a power law rather than a Gaussian law. See also C.L.Rino, this volume, paper 28, Figures 11 and 12, that support this frequency dependence of S4. See C.L.Rino's comments.

**C.L.Rino**

The peaking of S4 with changing frequency has an exact statistical analogue (see Figures 11 and 12 in paper No.28). With regard to J.Aarons' comment, one would expect to see strong focussing only if the distributions were characterized by a Gaussian spectrum or a steeply sloped power-law spectrum. This is not the case in a randomly disturbed ionosphere. Thus one does not observe strong focussing.

**Paper No.23**

**H.Soicher**

Since the ultimate quantity to be predicted is TEC does the modelling of slab thickness offer any advantages over modelling TEC directly?

**L.Kersley**

The day-to-day variability of slab thickness is generally less than that of TEC and, in addition, to obtain TEC from slab thickness necessitates the use of foF2 so that information on the actual state of the ionosphere at the time of interest can be incorporated in the estimation.

**T.R.Larsen**

Please correct me if I am wrong but I guess you did not try to account for chemical changes in the F-region. I guess those are still present in the data?

**L.Kersley**

Yes, we are just using the raw data and developing empirical models from there. There is no physics in this.

**Paper No.26****D.J.Fang**

Presumably, your exercise in determining the degradation of a pulse is inspired by radar applications. The dispersion (and time delay) of a pulse will cause intersymbol interference in a digital communications system. Although the modern digital systems are much more sophisticated than that of transmitting square and/or Gaussian pulses, it still will be interesting for the digital transmission engineers to see what is the maximum pulse rate you can propagate through the ionosphere without causing intersymbol interference. Have you done this?

**G.H.Millmann**

We have not evaluated ionospheric dispersion effects in this manner. We were more interested in the dispersion effects as applied to radar pulse transmissions. It should not be too difficult to perform an analysis to determine the maximum pulse rate that can be propagated through the ionosphere!

**Paper No.27****J.A.Klobuchar**

I have two concerns.

- (1) Why do you redefine slab thickness as  $\tau = \frac{N_T(\text{slant})}{N_{\text{max}}}$ , rather than the standard  $\frac{N_F(\text{vertical})}{N_{\text{max}}}$  especially since  $N_T$  contains a (presumably) non-F region component of up to 25% (see page 27-6 in preprint).
- (2) Could this account for the "considerable day-to-day variability" in your defined slab thickness and perhaps your mean slab thickness "dominated by a semi-annual variation", rather than a clear annual term dominance with relatively small monthly standard deviations as seen in figures 1, 7a and 7b of the paper number 23 by Kersley, using data taken also from the UK?

**J.K.Hargreaves**

I think I did say that the *slant* slab thickness was being derived. As soon as one converts it to the vertical slab thickness an approximation is being made. Similarly, since the separation of  $N_T$  into  $N_F$  and  $N_p$  is also model-dependent, we preferred to stick to the quantities actually measured, as  $N_T$ ,  $F$  and  $\tau$ , for the main presentation. Although we do treat  $N_p$ , this does not have such a precise meaning. Our intention here was to present the measurements actually made, rather than to derive secondary quantities - users can easily do that for themselves. For example, the Faraday slant thickness is given by  $\tau_F = \tau \cdot F/\bar{F}$ , where  $\bar{F}$  is the longitudinal gyrofrequency appropriate to the ionosphere. Regarding your second point, I do not think the day-to-day variability of the slab thickness is excessive, but this point, and the question of how well  $N_T$  (or  $N_F$ ) and the maximum electron content are correlated, are things we could look at again in the data. I do not know why our results for 1975-76 differ from those of L.Kersley for 1967 to 1974, unless different solar activity has something to do with it. It does appear from his Figure 2 that the annual variation of the daily means decreases as the sunspot number decreases. The variation shown on our Figure 3 is actually relatively small over the year. The amplitude of the diurnal component (Figure 5) has a larger relative variation over the year, and this is not dissimilar to L.Kersley (his Figure 5).

**H.Soicher**

The relative merits of empirical and/or physical models have been previously discussed in AGARD meetings. The consensus was that at present the only improvements to be realized are through the incorporation of understood physical processes into the models. Your paper indicates that such an effort is being implemented.



## SESSION V

## Paper No.28

## J.Aarons

The intensity decorrelation prediction technique described can only be used for low altitude satellites since synchronous or high altitude satellite scintillations show the effect of winds at ionospheric heights. These must be known to predict decorrelation for the latter paths.

## C.L.Rino

It is true that all results that pertain to time structure depend on irregularity drift and decay rates as well as satellite drift rates. These parameters must be known or founded to extrapolate system effects.

## C.H.Liu

Regarding the fact that theoretical results derived from phase-screen theory agree with the experimental results very well, can you then imply or conclude that the ionosphere behaves as a phase-screen?

## C.L.Rino

The phase-screen should be thought of as an *equivalent or lumped-parameter* representation of the actual ionosphere. The work of Bramley and Fante shows that little error is made when this approach is taken. One need not have an actual plane of zero amplitude scintillations to use such a model.

## Paper No.29

## J.Aarons

"Too much data" is never "too much" as shown by the scintillation observations of the current peak of the solar cycle which is quite different from the data from the peak of the cycle around 1968-1969.

## G.K.Hartmann

Too much just means too much of one type, in order to get it clearer. We have to have a good balance between temporal and spatial resolution, i.e. there is no further benefit if we increase temporal resolution at one location without simultaneous increase of spatial resolution, but this mostly implies to bring together data from various different agencies, mostly with different formats, which makes processing time consuming and difficult.

## D.J.Fang

If I understand correctly, the talk by C.L.Rino, the previous speaker, contains three messages. One, due to complicated nature of the problem, there is no simple and consistent law to characterize the first order statistics of ionospheric scintillations. Two, for communications applications, however, to consider scintillation simply as amplitude fluctuation of Nakagami distribution is probably adequate. Three, using power-law phase-screen methods, we can effectively model the parameters for communication applications. If so, the communications community will very much like to see ionospheric physicists devote their effort to come up with a useful (although perhaps not theoretically precise) model for engineering applications, such as those available in HF communications. If such a model cannot be made available soon, then the communications community may elect to ignore ionospheric scintillation when it moves ahead to 14/11 GHz and 20/30 GHz systems. In that case, it will make the communications community even less sympathetic than now to the "wish list" and/or "wish schedule" on ionospheric research as presented in your paper.

## C.L.Rino

We always have the problem in the applied fields that the system designer has to wait indefinitely for the solution to the problem so that he can proceed with his system design, and he obviously cannot do that. But I think we have a situation now that is very encouraging in that regard and I have seen this happening in a number of areas. I think we now know how to parameterize the problem, and the system designer himself can also parameterize the vulnerabilities of his system in terms of a complimentary set of parameters when those two come together (there will be, of course, uncertainties which J.Aarons constantly reminds me of), because I can do a good job in closing a loop on a data set where I have all the parameters I need available. That is by no means the solution to the problem of predicting whether it is going to be tomorrow or whether it is going to be somewhere else. But it can put very reasonable bounds on that. Communication systems after all, communication systems particularly are the best example in that, if you "knock them around" a little bit about their design parameters, if they are well-designed, they do not fail catastrophically. If the fading margin is 3 or 4 dB, it is a very bad system. If it is 10 dB or more, the fading structure, and so on, is not so critical and you can put reasonable bounds on the expectation of those systems that they will encounter, for certain fractions of the time, certain types of disturbances which can then be related to system effects. So, it is moving in the right direction if we bring the physics into it eventually, and I am not so pessimistic in that area, because considerable progress is being made there. It is not showing perhaps so much in these papers unfortunately, because the community of people who are doing that work is at another meeting right now but a lot is happening in that field.

I like to make one brief comment on G.Hartmann's paper too. I think he has for some time been discussing this problem of how we handle our data bases. I want to point out that the two major agencies that are funding scientific research in the United States, the National Aeronautic and Space Administration and the National Science Foundation, are both strongly urging – in fact more than strongly: they are insisting on it – that the people who are supported by those agencies start to think in terms of common data bases, so that we break the cycle of the data flowing through the single experimenter who took the data, rather that those data go into an orderly way into a central data pool, so that the entire community of users can have direct access to it. The technology that allows computers to talk to one another in rapid communications is the vehicle for doing that and it is becoming an integral part of the projections of almost all the planning of the major experiments that is going on right now. The defence community or particularly the defence research project agencies are operating very much in that way right now.

#### Paper No.30

##### C.L.Rino

It is very nice to see the universal parameters that K.C.Yeh derived from quite a different method that I used, are showing essentially the same results, i.e. the U-parameter that I described in my talk, I think (we need to check carefully to see whether it is the same parameter, it is certainly proportional to the weak scatterer S4 index), is the same parameter that C.H.Liu derived by working through the parabolic wave equation directly. So it is a good progress.

##### L.Bothias

Dans les exposés déjà présentés sur les scintillations dues aux irrégularités ionosphériques, on ne semble pas se préoccuper des effets sur les télécommunications et des moyens de se protéger de ces effets (par exemple réception en diversité). Il faudrait éviter le renouvellement de ce qui s'est passé il y a une quinzaine d'années pour le "troposcatter" où des études très semblables à celles ci ont sombré dans l'oubli à cause du manque d'applications.

##### C.H.Liu

I think the study here, e.g. the statistic moments, like the S4, the features of the intensity fluctuations, like the correlation interval and also the probability distribution of the amplitude of the compact signal, all these are very closely related to the tactical points that you mentioned, like the error-bit rate, error-bit computation and all these things can be applied to a specific system if you know the statistical characterization of the channel. And, at least in my case, I am essentially indicating a way to try to characterize this channel.

##### C.L.Rino

You are no doubt quite familiar with the research that is going on in the troposphere where the classical methods that have been applied to neutral turbulence have been used rather well. It is very interesting in that work, which was originally developed by Kolmogorov who set up the methodology that eliminates these trend-like variations from the data, that the parameterization that falls out of that approach naturally is the one that I think we are coming to adopt now for radio-wave scintillation and for much the same reason. So these two theoretical approaches which seem on the face to be very different, are coming together very nicely and again if you look carefully, that same parameterization leads to the universal characterization of the scattering phenomena.

The ionospheric turbulence has many more configurations than neutral turbulence can take, because electric fields interact with the medium and velocity flow structures play a very more dynamic role. So, I think that the analysis in this case is more intimately tied to the physics, i.e. there is not a single universal characterization of the power-law index, the 8/3-law does not seem to apply. There is no reason why it should.

I hope we can answer confidently that maybe we can look again at the analysis, even in the case of neutral turbulence.

##### C.H.Liu

Even in the neutral atmosphere or optical case, the multiple scattering theory has only been developed recently which we are also using.

#### Paper No.31

##### D.J.Fang

How comfortably can we take your statement that an increase of magnetic activity increases scintillation activity? I recall some early data indicating that the correlations between the two are not very convincing, also some data show actually slightly negative correlation. I recall that one of the SRI reports mentioned that. I am not sure I am right.

##### J.Aarons

First of all, I do not think I said that. I said that, after midnight, in most seasons, the increase in magnetic activity produced increased scintillation activity. In some seasons, there is no correlation between scintillation activity and magnetic activity. And in other seasons, increased magnetic activity produced decreased scintillation activity. But

those charts that are in the book will give that, and the Guam data give similar data. During May, June and July, one to seventy degrees west you have increased magnetic activity producing increased scintillation activity, and during November, December, January in the Guam region the same thing happens. But for example I cannot forecast what is going to happen over India, where there is not enough data to show what is going to happen in that region.

**T.R.Larsen**

In the light of your 1979 measurements, do you expect scintillations also at L-band frequencies at high latitudes?

**J.Aarons**

We have recorded hours of scintillation activity of 40 dB peak-to-peak at 250 MHz. There will therefore be fluctuations of several dB at L-band at polar latitudes during years of very high solar flux.

**C.L.Rino**

Could you clarify one point. In terms of the sheet-like structure, we have never seen any evidence of sheet-like irregularities in day-time. Scintillation data only occur in the evening, at midnight, and early morning sectors.

**J.Aarons**

My comment on that is that you are really not in a good geometrical position to observe that and the sheet-like irregularities which were seen by the SRI group, and we saw them too earlier, are true in the midnight time sector, for example, it may well be so that at higher latitudes or different times of the day the actual geometry changes from 10 to 10 : 1, or whatever it is. So that there may be sheet-like structures that are changing as far as the dimensions are concerned, as a function of time and as a function of latitude. We have very limited data.

## SESSION VI

### Paper No.35

**P.T.Thompson**

I just like to see if I can understand more clearly the statement you made on the use of polarization. You mentioned problems of Faraday rotation but in the EHF bands I understand this will not be a problem and that linear polarization could be adopted here. And the depolarization will be less significant if you use linear polarization rather than circular; so are there overriding reasons for employing circular polarization in the EHF bands?

**J.M.Goodman**

The question is: Are there any reasons why one should not use linear polarization in the EHF bands. I think the answer probably is no. You can use circular polarization at EHF or basically vertical and horizontal, it would not make any difference. You do not have any polarization rotation to speak of anyway, I guess. There is a problem of rainfall attenuation and I do not feel competent to answer that question thoroughly. My main point was that the problem of Faraday rotation is not an important one; it is an ionospheric problem. I think you find from other work that was discussed earlier that linear polarization may well have significant advantages.

**J.Aarons**

Looking back over the history of work done in ionospheric studies for various systems, we have to say that we do not know enough about what is needed. For example, I have been looking through the HF-field. If we want to do some work in HF adaptive systems, there is a lot more research that has to be done to determine, e.g., Doppler spreading, multipath problems, than has already been done. And referring to the field of UHF, it is a lot simpler to use UHF frequencies for the military, for example, than to go to some of the very high frequencies with very complex equipment. And so one would want to do some more work to utilize the band there, to make up for the deficiencies of the ionosphere. A.L.Johnson, e.g., talked about interleaving, etc., for correcting for scintillation. And to go on with this, one of the reasons for the choice of L-band was that we would not have any ionospheric problems, and yet when the needs of the NAVSTAR GPS system were examined carefully you found you had to take into account the ionosphere. So with greater use of all of the bands, with greater accuracy demanded, and with some new systems planned, it looks as if one would have to keep a core of people who would understand the ionospheric limitations and keep producing creative research in the field. I do not think we can stop here because the needs are going to be different and the demands are going to be different.

**J.M.Goodman**

Thank you. I appreciate your comments and I agree with it. Higher data rates, for example, require much better information about the statistics and characteristics of the inhomogeneities which exist there. They are going to mean that ionospheric research is needed because certainly, at least I would guess, it would be quite impossible to characterize the ionosphere that fully at this point. I think you would attest that even more needs to be known about the basic geomorphology itself, for example the mere fact that there has recently been discovered in the last several years not only the well-known latitudinal variation, in the geomagnetic sense, of scintillations but also a longitudinal variation which I think was some sort of a surprise, perhaps of lower order, but we can look for those

kinds of things. They would suggest that, if there is that longitudinal dependence and if it is repetitious, there may be holes there, or regions where one can propagate or not propagate for long periods of time and one can take advantage of those kinds of notions. That opens whole new vistas for lower frequencies which have other charms. So I think there is, definitely I agree, a good need to continue ionospheric research and I think much can be gained from it.

**J.S.Belrose**

J.Aarons has discussed new data on ionospheric scintillations in equatorial regions; A.L.Johnson has commented on these data and he has given details on other equatorial phenomena. In the present paper J.M.Goodman has shown a diagram (after Klobuchar) that shows peaks in ionospheric delay at 1.6 GHz located at  $\pm 10 - 20^\circ$  each side of the equator. The night-time F-layer shows similar peaks in the height of constant electron density isopleths (in fact Klobuchar's data may have been calculated from these data).

The night-time equatorial ionosphere, when solar control is absent, is strongly influenced by dynamics and vertical drift. The height of surfaces of constant electron density (isopleths) measured by top-side sounders (Alouette and ISIS) reveal the latitudinal/time variations of the equatorial ionospheric structure. Since ionospheric irregularities are measured by  $\Delta N/N$ , if  $N$  changes rapidly so does  $\Delta N$ . It seems to me that greater insight can be got into the phenomena of equatorial scintillations by studying top-side sounder electron density-latitude data. I do not know if this has been made, since I have not worked in the field, but the various speakers did not mention such comparisons. Certainly the differences in time of the onset, but not perhaps the occurrence, of scintillations illustrated by J.Aarons must be directly associated with the movement of such ionospheric structure into the satellite-earth path.

**J.Aarons**

I would like to answer Belrose. We are doing this right now and it is very important in the equatorial studies to utilize the electron density variations as a function of latitude in the equatorial region, particularly the anomaly region, both the anomaly in electron density maxima and the time of the maxima and we are doing a serious study of this right now.

**Paper No.36**

**E.Altshuler**

How is the tropospheric range error correction going to be handled?

**J.A.Klobuchar**

A model developed by the US Jet Propulsion Laboratory, Pasadena, Ca. is to be used. On some specific locations provisions have been made for near-real-time updates by local measurements of P, T and water vapor content.

**Paper No.41**

(Order of papers as presented)

**H.Soicher**

How well are the potential SPS transmission effects (at 2.45 GHz) on the ionosphere simulated by HF heating experiments?

**W.Grant**

The SPS-simulated effects in the D and E region rely upon an extrapolation based on Ohm's law. This law is well-known to hold over all frequency ranges. The HF experiment must be conducted with appropriate power densities and frequencies to enable the  $1/f^2$  Ohmic Law scaling to yield SPS-comparable power densities. The Platteville operation at 5.2 MHz yields a scaled SPS power density of 23 mw/cm<sup>2</sup> that is in agreement with the current SPS design criterion.

**W.F.Utlaut**

I think that W.Grant gave the correct answer for the D-region, i.e. as far as we know, it will be an Ohmic loss and therefore an inverse frequency-squared dependence is applicable. However, when one goes up into the higher portion of the ionosphere, up into the F-region, it is less clear that it will be only an Ohmic loss, there will be plasma instabilities which will develop and it turns out that some of the more recent theory would indicate that there may be a frequency-cubed dependence. It may be easier to essentially affect the F-region than first believed but the theory is very complicated there.

**A.C.Marvin**

You mentioned intermodulation products from the rusty bolt effect on the rectenna structure. Surely I.M. products from the rectenna elements will be much greater.

**W.Grant**

We are going to look at that.

**C.L.Rino**

The environmental impact of actually putting the SPS in space was not discussed in your talk. How is this important concern being factored in the overall planning?

**W.Grant**

The environmental impacts of SPS are being studied under the direction of Anthony Valentino of the Argonne National Laboratory. Referring to page 41-11 of the AGARD Conference preprint, the organizations studying the various aspects of the environmental impact are listed under *Environmental Assessment*; I believe ANL, LASL and EPA are the particular organizations looking at launching impacts of very large space vehicles.

**J.A.Klobuchar**

Please comment on the likely interference from the SPS beam to VHF and UHF television receivers, which are of generally minimum cost design.

**W.Grant**

Because of the large separation in frequency we have not seen problems with coupling into VHF/UHF receivers which would be large enough to degrade picture or voice quality. More tests are to be accomplished in this area in the near future.

**Paper No.38**

**H.J.Albrecht**

I wish to refer to the table you have shown, indicating the rain scatter. You used the two climates, climate 2 and 4 as specified in CCIR documents. Do you not agree that actually there is not too much difference between the two or, just to turn it the other way around, the rather artificial subdivision of climates, with climate 2 representative of the US and climate 4 representative of the UK, is rather courageous? In the CCIR texts, this categorization was not meant to be used as definite boundary line. I do not know whether you agree but I think the effects should be regarded to be almost the same as far as the order of magnitude is concerned.

**K.A.Hughes**

Yes, I would agree with that.

**J.Belrose**

You commented on the scattering of power out-of-the-beam for the case of normal ionospheric irregularities, of a magnitude which causes  $\pm 5$  dB fading at 2.45 GHz. However, when the beam is switched on, the generation of extended striations, which you have later referred to, will also have a fine structure of irregularities superimposed. The end result could be an enormous increase in the power levels scattered out-of-the-beam. The process is a very non-linear one, and so above a certain power level these effects could be very large indeed. Have you given consideration to calculating such effects?

**K.A.Hughes**

It is true that the formation of further irregularities in the F-region by mechanism such as thermal self-focussing will make matters far worse as regards scattering power outside of the main beam. Unfortunately, I have not undertaken calculations to quantify this increase in scattered power.

**Paper No.40**

**K.A.Hughes**

Do you know of any likely sites in Europe to locate the rectenna; has the possibility of siting the rectenna over the sea been ruled out yet?

**D.Koehn**

The answer to both questions is "no". But placing rectennae over the open sea (e.g. the North Sea, the Baltic, the Bay of Biscay) would probably be a bit risky, bearing in mind the problems of oil-well platforms there. Moreover, the rectennae should be sited in the vicinity of industrial centers (although of course in relatively uninhabited areas what may be somewhat contradictory).

But after all, satellite power stations will certainly only be installed if dictated by sheer necessity, and then rectenna sites have to be made available – this is then a question of setting priorities. To illustrate the actual area requirements of rectennae: if the total production of electric energy of the Federal Republic of Germany in 1971 (275 billion kWh) should have been provided by SPS, six of them would have been necessary. The involved six rectennae would require an area of 1,700 km<sup>2</sup> (including the surrounding safety zone) which equals approximately 0.7% of the total area of the FRG (or, incidentally, less than one third of the public road network area). Moreover, the rectenna area could probably be used on a secondary basis under some safety precautions for other purposes (cf. Ehrlicke, K.A., 1974).

**E.Lampert**

Considering the overall amount of energy necessary to set up such a SPS it would be interesting to know how long it would take to get this energy back and what would be the total lifetime of the system.

**D.Koehn**

A detailed analysis of the energy balance (or energy profitability) of a SPS is somewhat difficult to carry out since many input data are not readily available; however, one can assume that the lion's share of the invested energy goes into the production of the solar cells. Current production techniques require about 7 MWh electrical energy for 1 m square of solar cells (Wolf, M., Proc. 9th IEEE Photovoltaic Specialist Conference, 1972); this corresponds to approximately 41.5 MWh per KW generated in space. If one assumes that the total energy required to set up a SPS system is twice as high as the energy needed to produce the solar cells and if the power transmission efficiency equals 60%, the invested energy could be recouped in approximately 18 years. Since the lifetime of a power satellite is generally assumed to be 30 years, an (although not overwhelming) energy profitability is almost certain. But the present solar cell production methods are not energy-optimized; it is estimated that improvements can reduce the required energy by a factor of 10 to 20 (Wolf, M., Proc. Internat. Conf. on Photovoltaic Power Generation, 1974). If this turns out to be true and if the other production processes can be economized in the same way, a SPS could recoup the invested energy in about 2 (perhaps 3) years.

**Final Comments H.J.Albrecht**

We in our Panel attempt to cover in more or less regular intervals certain areas of importance and we felt that a sufficient number of years had gone by without a scientific meeting on space/earth paths, with the various possible system applications. And this was the main reason for deciding finally on the type of meeting we have had here.

We have covered the general tropospheric effects, then we have given an opportunity to all those who have experimented — and there is an increasing number of institutions doing this — with the reception of satellite beacon transmissions. As they have tried it on EHF, they have found out that rain does behave the same way in the United States and also in Europe, as long as you specify the appropriate drop-size distribution and the rain cell as such; it will most likely behave very similarly also in other parts of the world.

We have paid attention to remote sensing. It was a mini-session but, on the other hand, I think, even there, we have been able to highlight some of the important aspects and also to discuss the present state of the art.

Then the general ionospheric dispersion effects have been dealt with. In a subsequent session this was supplemented by new data on ionospheric irregularities and their characteristic behaviour.

Thereafter, the final session concerned propagation limitations in systems. When introducing this session, I did mention that on the one hand, our AGARD community, is responsible for scientific work, but, on the other hand, we should never forget the application to systems; suitable aspects were covered.

## APPENDIX

## LIST OF ATTENDEES

AARONS, J. Dr Panel Chairman	Senior Scientist, Air Force Geophysics Lab. L.G. Hanscom Field, Bedford, MA 01731, USA
ALBRECHT, H.J. Dr Panel Member	FGAN, Königstrasse 2, 5307 Wachtberg-Werthhoven, Germany
ANGLADE, Mr	Fort de Montrouge, 94114, Arcueil, France
ALTSCHULER, E. Dr	RADC/EPP, Hanscom AFB, MA 01731, USA
ATTEMA, E.P. Ir.	Delft University of Technology, EE Dept. Mekelweg 4, 2628 CD, Delft, Netherlands
AURIA d', G. Prof.	Istituto di Elettronica, Facolta di Ingegneria, Universita di Roma, Via Eudossiana 18, 00184, Roma, Italy
BAKKEN P. Dr	S.T.C. P.O.Box 174, 2501 CD The Hague, Netherlands
BARBATI, S. Mr	Contraves Italiana S.p.A. Via Affile 102, 00131, Roma, Italy
BARCLAY, L.W. Mr	Home Office, Directorate of Radio Technology, Waterloo Bridge House, London SE1 8UA, UK
BECKER, K.D. Prof.	Theoretische Elektrotechnik Universität des Saarlandes, D 6600 Saarbrücken, Germany
BELROSE, J. Dr Panel Deputy Chairman	C.R.C. P.O.Box 11490, STNH Ottawa K2H 8S2, Canada
BERGER, F. Mr	DRET/DGA, 26, Bld Victor, 75015 Paris, France
BLYTHE, J.H. Dr Panel Member	Marconi Research Lab. Great Baddow, Essex CM2 8HN, UK
BOITHIAS, L. Mr Panel Member	CNET, PAB, 38, rue du Général Leclerc, 92131, Issy-les-Moulineaux, France
BOSSY, L. Prof.	Institut Royal Météorologique, 3, Avenue Circulaire, B 1180, Brussels, Belgium
BRAMLEY, E.N. Mr	Rutherford & Appleton Lab, Ditton Park, Slough, SL3 9JX, UK
BROWNING, D.J. Dr	RF Technology Centre, ERA Technology, Cleeve Road, Leatherhead, Surrey, KT 227 SA, UK
BRUSSAARD, G. Mr	ESTEC, P.O.Box 299, 2200 AG, Noordwijk, Netherlands
BURGESS, B. Dr Panel Member	Radio and Navigation Department, Royal Aircraft Establishment, Farnborough, Hants, UK
CHERRY, S.M. Mr	Rutherford & Appleton Laboratories, Ditton Park, Slough, SL3 9JX, UK
CHRISTOPHE, F. Mr	ONERA, 92320 Châtillon, France
CLAYDON, B. Dr	RF Technology Centre, ERA Technology, Cleeve Road, Leatherhead, Surrey, UK
COOKE, G.A. Mr	Civil Aviation Authority, Room K 320, CAA House, 45-59 Kingsway, London WC2 B 6TE, UK
COURTHOLD, M.J.D.	SRC, Rutherford & Appleton Labs. Ditton Park, Slough, SL3 9JX, UK
COX, D.C. Dr	HOH R 127, Bell Laboratories, Holmdel, N.J. 07733, UK
COYNE, V.J. Mr Panel Member	Chief, Strategic Surveillance Branch, Surveillance Division, Rome Air Development Center/OCS, Griffiss AFB, N.Y. 13441, USA
CUTOLO, M. Prof. Panel Member	Via G. Santacroce 60, 80129, Naples, Italy
DAVIES, K. Dr	NOAA/SEL, Boulder, CO 80303, USA
DAVIES, P.G. Dr	SRC, Rutherford & Appleton Laboratories, Ditton Park, Slough, SL3 9JX, UK

DINTELMANN, F. Dr	Forschungsinstitut der Deutschen Bundespost, D 6100 Darmstadt am Kavalleriesand 3, Germany
DORMAN, C.J.B. Mr	P 160 Building, Royal Aircraft Establishment, Farnborough, Hants, UK
DOLD, B. Dr	Ionosphäreninstitut, 7831 Rheinhausen, Germany
EVANS, B. Mr	University of Essex, Wivenhoe Park. Colchester, COA 3SQ, UK
FANG, D.J. Dr	COMSAT Labs. P.O.Box 115, Clarksburg, MD 20734, USA
GALE, D.J. Mr	Dept. of Electronic & Electrical Engineering, University of Surrey, Guildford, Surrey, GU2 5XH, UK
GELSTHORPE, R.V. Dr	RFTC, ERA Technology Ltd., Cleeve Road, Leatherhead, Surrey, UK
GJESSING, D.T. Prof.	NTNF/PFM, P.O.Box 25, N-2007 Kjeller, Norway
GODDARD, J.W.F. Mr	Rutherford & Appleton Laboratories, Ditton Park, Slough, Berkshire, UK
GOLDHIRSCH, J. Dr	Applied Physics Lab., John Hopkins University, Laurel, MD 20810, USA
GOLE, Mr	CNET/RPE, 38, 40, rue du Général Leclerc, 92131, Issy-les-Moulineaux, France
GOODMAN, J.M. Dr	Code 7560, 4555 Overlook Avenue, Washington D.C. 20375, USA
GRANT, W.B. Mr	Institute for Telecommunication Sciences, NTIA, Department of Commerce, Boulder, CO 80303, USA
GREEN, D.W. Mr	GEC-Marconi Electronics Lab., Great Baddow Research Lab., Great Baddow, Chelmsford, CM2 8HN, UK
HALL, M.P.M. Mr	Rutherford & Appleton Laboratories, Ditton Park, Slough, Berkshire, UK
HALL, W.J. Mr	British Aerospace Dynamics Group, Site B, Gunnels Wood Road, Stevenage, Herts, SG1 2AS, UK
HALLEY, P. Mr	12, rue du Dr Kurzaune, 78350, Jouy en Josas, France
HARGRAVE, P.J. Dr	Standard Telecommunication Lab. Ltd., London Road, Harlow, Essex CM17 9NA, UK
HARGREAVES, J.K. Dr	Dept. of Environmental Sciences, University of Lancaster, Lancaster LA1 4YQ, UK
HARTMANN, G.K. Dr	Max-Planck Institut für Aeronomie, Postfach 20, D 3411 Katlenburg Lindau 3, Germany
HAWORTH, D.P. Dr	RSRE, T3 Div. Steamer Point, Christchurch, Dorset, UK
HOPPONEN, J. Dr	Lockheed Missiles and Space Company Inc., P.O.Box 504, Sunnyvale, CA 94086, USA
HUGHES, K.A. Dr	Home Office, Waterloo Bridge House, Waterloo Road, London SE1 8UA, UK
IASELLI, P. Col. Panel Member	Ministera della Difesa TELECOMDIFE, Via Università 4, 00100 Roma, Italy
JOHNSON, A.L. Mr	Avionics Lab., AF Wright Aeronautical Lab., Wright Patterson AFB, Ohio 45433, USA
KERSLEY, L. Dr	Dept. of Physics, University College of Wales, Penglais, Aberystwyth, UK
KLOBUCHAR, J.A. Mr	Air Force Geophysics Lab., PHP Hanscom AFB, Bedford, MA 01731, USA
KOCH, R. Prof.	Fondazione Ugo Bordononi, Viale Trastevere 108, Roma, Italy
KOEHN, D. Dr	AEG Telefunken, Friedrich Ebert Allee 26, 5300 Bonn, 1, Germany
KRAUSE, J. Col.	AEG Telefunken, Friedrich Ebert Allee 26, 5300 Bonn, 1, Germany
LAMPERT, E. Dr Panel Member	Siemens AG, Wv FU MS EF2, P.O.Box 70 00 74, D 800 München 70, Germany
LANGE HESSE G. Dr Panel Member	Max-Planck Institut für Aeronomie, Postfach 20, D 3411 Katlenburg-Lindau 3, Germany
LARSEN, R. Mr	Marconi Research Lab., Great Baddow, Chelmsford, Essex, UK
LARSEN, T.R. Dr Panel Member	N.D.R.E., P.O.Box No.25, N-2007 Kjeller, Norway
LAW, D. Mr	Government Communications Hqs., Room B/0303, Oakley, Priors Road, Cheltenham, Glos., UK
LIU, C.H. Dr	Department of Electrical Engineering, University of Illinois at Urbana Champaign, Urbana, Illinois, 61801, USA



LORENZONI, A. Dr	Aeronautica Militare, Centro Consultivo Studie Ricerche, Via dei Pontefici, 3, 00100 Roma, Italy
LOW, K. Mr	AEG Telefunken, Abt. N.1 E 331, Elisabethen Strasse 3, 7900 Ulm/Donau, Germany
MAANDERS, E.J. Dr Ir.	Eindhoven University of Technology, Department of Electrical Engineering, Eindhoven, Holland
MADAMS, C.J. Dr	Admiralty Surface Weapons Establishment, Portsmouth, Cosham, Portsmouth, PO6 4AA, UK
MARVIN, A. Dr	Dept. of Electronics, York University, York, YO1 5DD, UK
McKENZIE, E.C. Mr	Rutherford & Appleton Lab., Slough, Berkshire, UK
MENDES, A.S. Prof. Panel Member	Instituto Nacional de Meteorologia e Geofisics, Rua C, Aeroporto de Lisboa, 1700 Lisboa, Portugal
METZIG, G. Mr	Institut für Geophysik u. Meteorologie der Universität zu Köln, Albertus Magnus Platz/Kerpener Str.13, 5000 Köln 41, Germany
MILLMAN, G.H. Dr	General Electric Cy, Bld 4, Rm 57, Court Street Plant, Syracuse N.Y.13221, USA
MON, J.P. Dr	CNET/RPE, 38, 40 rue du Général Leclerc, 92131, Issy-les-Moulineaux, France
MOORE, R.K. Prof.	Remote Sensing Lab., University of Kansas, Lawrence, KS 66045, USA
NEESEN, J.T.A. Mr	Dr Neher Labs., St Paulusstraat 4, Leidschendam, Holland
NEWELL, D. Lt. Col.	European Office (EOARD), 223 Old Marylebone Road, London NW1 5TH, UK
ONG, Jin Teong Dr	Cable and Wireless Ltd., Mercury House, Theobalds Road, London WC1X 8RX, UK
PARABONI, A. Mr	IROE, Via Panciationi 64, 50127 Firenze, Italy
PILLET, G.M. Melle.	CNET, DICET, 38, 40, rue du Général Leclerc, 92131, Issy-les-Moulineaux, France
POSSENTI, Ing.	Telepazio vorso d'Italia, 42-43, 0001, Roma, Italy
PRATT, T. Dr	University of Birmingham, P.O.Box 363, Birmingham, B15 2 TT, UK
RINO, C.L. Dr	SRI International, 333 Ravenswood Ave., Menlo Park, CA 94025, USA
RÜCKER, F. Mr	Forschungsinstitut der Deutschen Bundespost, D 6100 Darmstadt am Kavalleriesand 3, Germany
SCHMERLING, E.R. Dr Panel Member	ST-5/NASA Headquarters, Washington D.C. 20546, USA
SCHROTT, A. Dr	DFVLR Institut für Hochfrequenztechnik, 8031 Oberpfaffenhofen, Germany
SCHMITH, B.G. Dr	Smiths Associates, 45/57 High Street, Cobham, Surrey, UK
SOICHER, H. Dr Panel Member	US Army Communications Reseach and Development Command, CENCOMS-DRDCO-COM-RH-5, Fort Monmouth, N.J. 07703, USA
SPRENKELS, C. Col. Panel Member	Commandant 22 LOGW. Quartier Roi Albert I, rue de la Fusée 70, B.1130 Brussels, Belgium
STANNARD, E.J. Mr	Admiralty Surface Weapons Establishment, Portsmouth, Cosham, Portsmouth, PO6 4AA, UK
STEIN. H.T. Mr	DFVLR, Institut für Hochfrequenztechnik, 8031 Oberpfaffenhofen, Germany
SUTTELS, R. Mr	Bell Telephone Manufacturing Cy, Francis Wellespless B 2000 Antwerp, Belgium
TAAGHOLT, J. Mr Panel Member	Ionosphere Laboratory, Technical University of Denmark, Bldg 349, 2800 Lyngby, Denmark
THIRLWELL, J. Mr	Post Office Telecommunications, Martlesham Heath, Ipswich IP5 7RE, UK
THOMPSON, P.T. Mr	S.T.C. The Hague, Netherlands
TISCHER, W.S. Mr	Bundesakademie für Wehrverwaltung und Wehrtechnik, Seckenheimer Landstrasse 8-10, 6800 Mannheim-Neuhostheim, Germany
UTLAUT, W.F. Dr Panel Member	Deputy Director, NTIA/ITS, Boulder, CO 80302, USA
VAN CAPELLEN, J. Mr	St Paulusstr. 4 Leidschendam, Holland

VANDER VORST, A. Mr  
Panel Member  
VIDDELEER, R. Prof.  
Panel Member

Professeur à l'Université de Louvain, Laboratoire des Télécommunications et  
d'Hyperfréquences, Batiment Maxwell, B-1348, Louvain-la-Neuve, Belgium  
Eutelsat c/o ESA/ESTEC, Postbus 299, 2200 A6 Noordwyk, Holland

WATSON, P.A. Dr  
WEBBER, R.V. Dr  
WHITE, M.B. Dr  
Panel Member  
WHICHER, P.G. Mr

University of Bradford, Dept. of Electrical Eng., Bradford BD7/CP, UK  
C.R.C., P.O.Box 11490, Station H, Ottawa K2H 8S2, Canada  
Office of Naval Research, Eastern Central Regional Office, 666 Summer St.,  
Bld. 114, Sect.D, Boston, Mass.02210, USA  
MOD (Room 2311) Whitehall, London SW1, UK

**REPORT DOCUMENTATION PAGE**

<b>1. Recipient's Reference</b>	<b>2. Originator's Reference</b>	<b>3. Further Reference</b>	<b>4. Security Classification of Document</b>								
	AGARD-CP-284	ISBN 92-835-0269-8	UNCLASSIFIED								
<b>5. Originator</b>	Advisory Group for Aerospace Research and Development North Atlantic Treaty Organization 7 rue Ancelle, 92200 Neuilly sur Seine, France										
<b>6. Title</b>	PROPAGATION EFFECTS IN SPACE/EARTH PATHS										
<b>7. Presented at</b>	the Electromagnetic Wave Propagation Panel Symposium held in London, UK on 12-16 May 1980.										
<b>8. Author(s)/Editor(s)</b>	Various	<b>9. Date</b>	August 1980								
<b>10. Author's/Editor's Address</b>	Various	<b>11. Pages</b>	536								
<b>12. Distribution Statement</b>	This document is distributed in accordance with AGARD policies and regulations, which are outlined on the Outside Back Covers of all AGARD publications.										
<b>13. Key words/Descriptors</b>	<table> <tr> <td>Electromagnetic wave transmission</td> <td>Depolarization</td> </tr> <tr> <td>Spacecraft communication</td> <td>Tropospheric propagation</td> </tr> <tr> <td>Atmospheric attenuation</td> <td>Ionospheric propagation</td> </tr> <tr> <td>Atmospheric refraction</td> <td></td> </tr> </table>			Electromagnetic wave transmission	Depolarization	Spacecraft communication	Tropospheric propagation	Atmospheric attenuation	Ionospheric propagation	Atmospheric refraction	
Electromagnetic wave transmission	Depolarization										
Spacecraft communication	Tropospheric propagation										
Atmospheric attenuation	Ionospheric propagation										
Atmospheric refraction											
<b>14. Abstract</b>	<p>These Proceedings include the papers and discussions presented at the AGARD Electromagnetic Wave Propagation Panel Symposium on "Propagation Effects in Space/Earth Paths" held in London in May 1980. The Symposium addressed both military and civil applications and problems in satellite communication. Theoretical and experimental aspects of slant path propagation through both ionized and non-ionized media are addressed. Atmospheric effects included attenuation, refraction, and depolarization and resulting scintillation, multipath, absorption and scatter.</p> <p>The 38 papers were divided as follows; 8 on tropospheric effects, 10 on experimental data of SHF/EHF Paths, 3 on remote sensing, 6 on general ionospheric dispersion, 6 on ionospheric irregularities, and 5 on propagation limitations in systems.</p>										

<p>AGARD Conference Proceedings No.284 Advisory Group for Aerospace Research and Development, NATO <b>PROPAGATION EFFECTS IN SPACE/EARTH PATHS</b> Published August 1980 536 pages</p> <p>These Proceedings include the papers and discussions presented at the AGARD Electromagnetic Wave Propagation Panel Symposium on "Propagation Effects in Space/Earth Paths" held in London in May 1980. The Symposium addressed both military and civil applications and problems in satellite communication. Theoretical and experimental aspects of slant path propagation through both ionized and non-ionized media are addressed. Atmospheric effects included</p> <p>P.T.O.</p>	<p>AGARD-CP-284</p> <p>Electromagnetic wave transmission Spacecraft communication Atmospheric attenuation Atmospheric refraction Depolarization Tropospheric propagation Ionospheric propagation</p>	<p>AGARD Conference Proceedings No.284 Advisory Group for Aerospace Research and Development, NATO <b>PROPAGATION EFFECTS IN SPACE/EARTH PATHS</b> Published August 1980 536 pages</p> <p>These Proceedings include the papers and discussions presented at the AGARD Electromagnetic Wave Propagation Panel Symposium on "Propagation Effects in Space/Earth Paths" held in London in May 1980. The Symposium addressed both military and civil applications and problems in satellite communication. Theoretical and experimental aspects of slant path propagation through both ionized and non-ionized media are addressed. Atmospheric effects included</p> <p>P.T.O.</p>	<p>AGARD-CP-284</p> <p>Electromagnetic wave transmission Spacecraft communication Atmospheric attenuation Atmospheric refraction Depolarization Tropospheric propagation Ionospheric propagation</p>
<p>AGARD Conference Proceedings No.284 Advisory Group for Aerospace Research and Development, NATO <b>PROPAGATION EFFECTS IN SPACE/EARTH PATHS</b> Published August 1980 536 pages</p> <p>These Proceedings include the papers and discussions presented at the AGARD Electromagnetic Wave Propagation Panel Symposium on "Propagation Effects in Space/Earth Paths" held in London in May 1980. The Symposium addressed both military and civil applications and problems in satellite communication. Theoretical and experimental aspects of slant path propagation through both ionized and non-ionized media are addressed. Atmospheric effects included</p> <p>P.T.O.</p>	<p>AGARD-CP-284</p> <p>Electromagnetic wave transmission Spacecraft communication Atmospheric attenuation Atmospheric refraction Depolarization Tropospheric propagation Ionospheric propagation</p>	<p>AGARD Conference Proceedings No.284 Advisory Group for Aerospace Research and Development, NATO <b>PROPAGATION EFFECTS IN SPACE/EARTH PATHS</b> Published August 1980 536 pages</p> <p>These Proceedings include the papers and discussions presented at the AGARD Electromagnetic Wave Propagation Panel Symposium on "Propagation Effects in Space/Earth Paths" held in London in May 1980. The Symposium addressed both military and civil applications and problems in satellite communication. Theoretical and experimental aspects of slant path propagation through both ionized and non-ionized media are addressed. Atmospheric effects included</p> <p>P.T.O.</p>	<p>AGARD-CP-284</p> <p>Electromagnetic wave transmission Spacecraft communication Atmospheric attenuation Atmospheric refraction Depolarization Tropospheric propagation Ionospheric propagation</p>

<p>attenuation, refraction, and depolarization and resulting scintillation, multipath, absorption and scatter.</p> <p>The 38 papers were divided as follows: 8 on tropospheric effects, 10 on experimental data of SHF/EHF Paths, 3 on remote sensing, 6 on general ionospheric dispersion, 6 on ionospheric irregularities, and 5 on propagation limitations in systems.</p> <p>Copies of papers and discussions presented at the Electromagnetic Wave Propagation Panel Symposium held in London, UK on 12-16 May 1980.</p> <p>ISBN 92-835-0269-8</p>	<p>attenuation, refraction, and depolarization and resulting scintillation, multipath, absorption and scatter.</p> <p>The 38 papers were divided as follows: 8 on tropospheric effects, 10 on experimental data of SHF/EHF Paths, 3 on remote sensing, 6 on general ionospheric dispersion, 6 on ionospheric irregularities, and 5 on propagation limitations in systems.</p> <p>Copies of papers and discussions presented at the Electromagnetic Wave Propagation Panel Symposium held in London, UK on 12-16 May 1980.</p> <p>ISBN 92-835-0269-8</p>
<p>attenuation, refraction, and depolarization and resulting scintillation, multipath, absorption and scatter.</p> <p>The 38 papers were divided as follows: 8 on tropospheric effects, 10 on experimental data of SHF/EHF Paths, 3 on remote sensing, 6 on general ionospheric dispersion, 6 on ionospheric irregularities, and 5 on propagation limitations in systems.</p> <p>Copies of papers and discussions presented at the Electromagnetic Wave Propagation Panel Symposium held in London, UK on 12-16 May 1980.</p> <p>ISBN 92-835-0269-8</p>	<p>attenuation, refraction, and depolarization and resulting scintillation, multipath, absorption and scatter.</p> <p>The 38 papers were divided as follows: 8 on tropospheric effects, 10 on experimental data of SHF/EHF Paths, 3 on remote sensing, 6 on general ionospheric dispersion, 6 on ionospheric irregularities, and 5 on propagation limitations in systems.</p> <p>Copies of papers and discussions presented at the Electromagnetic Wave Propagation Panel Symposium held in London, UK on 12-16 May 1980.</p> <p>ISBN 92-835-0269-8</p>

B338  
4

**AGARD**

NATO  OTAN

7 RUE ANCELLE · 92200 NEUILLY-SUR-SEINE  
FRANCE

Telephone 745.08.10 · Telex 610176

**DISTRIBUTION OF UNCLASSIFIED  
AGARD PUBLICATIONS**

AGARD does NOT hold stocks of AGARD publications at the above address for general distribution. Initial distribution of AGARD publications is made to AGARD Member Nations through the following National Distribution Centres. Further copies are sometimes available from these Centres, but if not may be purchased in Microfiche or Photocopy form from the Purchase Agencies listed below.

NATIONAL DISTRIBUTION CENTRES

**BELGIUM**

Coordonnateur AGARD - VSL  
Etat-Major de la Force Aérienne  
Quartier Reine Elisabeth  
Rue d'Evere, 1140 Bruxelles

**CANADA**

Defence Science Information Services  
Department of National Defence  
Ottawa, Ontario K1A 0K2

**DENMARK**

Danish Defence Research Board  
Østerbrogades Kaserne  
Copenhagen Ø

**FRANCE**

O.N.E.R.A. (Direction)  
29 Avenue de la Division Leclerc  
92320 Châtillon sous Bagneux

**GERMANY**

Fachinformationszentrum Energie,  
Physik, Mathematik GmbH  
Kernforschungszentrum  
D-7514 Eggenstein-Leopoldshafen 2

**GREECE**

Hellenic Air Force General Staff  
Research and Development Directorate  
Holargos, Athens

**ICELAND**

Director of Aviation  
c/o Flugrad  
Reykjavik

**ITALY**

Aeronautica Militare  
Ufficio del Delegato Nazionale all'AGARD  
3, Piazzale Adenauer  
Roma/EUR

**LUXEMBOURG**

See Belgium

**NETHERLANDS**

Netherlands Delegation to AGARD  
National Aerospace Laboratory, NLR  
P.O. Box 126  
2600 A.C. Delft

**NORWAY**

Norwegian Defence Research Establishment  
Main Library  
P.O. Box 25  
N-2007 Kjeller

**PORTUGAL**

Direcção do Serviço de Material  
da Força Aerea  
Rua da Escola Politécnica 42  
Lisboa  
Attn: AGARD National Delegate

**TURKEY**

Department of Research and Development (ARGE)  
Ministry of National Defence, Ankara

**UNITED KINGDOM**

Defence Research Information Centre  
Station Square House  
St. Mary Cray  
Orpington, Kent BR5 3RE

**UNITED STATES**

National Aeronautics and Space Administration (NASA)  
Langley Field, Virginia 23365  
Attn: Report Distribution and Storage Unit

THE UNITED STATES NATIONAL DISTRIBUTION CENTRE (NASA) DOES NOT HOLD STOCKS OF AGARD PUBLICATIONS, AND APPLICATIONS FOR COPIES SHOULD BE MADE DIRECT TO THE NATIONAL TECHNICAL INFORMATION SERVICE (NTIS) AT THE ADDRESS BELOW.

PURCHASE AGENCIES

*Microfiche or Photocopy*

National Technical  
Information Service (NTIS)  
5285 Port Royal Road  
Springfield  
Virginia 22161, USA

*Microfiche*

Space Documentation Service  
European Space Agency  
10, rue Mario Nikis  
75015 Paris, France

*Microfiche*

Technology Reports  
Centre (DTI)  
Station Square House  
St. Mary Cray  
Orpington, Kent BR5 3RF  
England

Requests for microfiche or photocopies of AGARD documents should include the AGARD serial number, title, author or editor, and publication date. Requests to NTIS should include the NASA accession report number. Full bibliographical references and abstracts of AGARD publications are given in the following journals:

Scientific and Technical Aerospace Reports (STAR)  
published by NASA Scientific and Technical  
Information Facility  
Post Office Box 8757  
Baltimore/Washington International Airport  
Maryland 21240; USA

Government Reports Announcements (GRA)  
published by the National Technical  
Information Services, Springfield  
Virginia 22161, USA



Printed by Technical Editing and Reproduction Ltd  
Harford House, 7-9 Charlotte St, London W1P 1HD

REF ID: A6602108